HIBERNIA THREE-PHASE RELATIVE PERMEABILITY MEASUREMENTS AT RESERVOIR CONDITIONS

By Daniel R. Maloney and Brad E. Milligan, ExxonMobil Upstream Research Company

ABSTRACT

The purpose of this study was to provide three-phase relative permeability versus saturation data to support investigation of double-displacement process (DDP) and water-alternating-gas (WAG) schemes for the Hibernia Field in East Canada. Goals were to measure three-phase steady-state relative permeabilities, gain description of hysteresis during WAG, and to reduce uncertainty of three-phase trapped gas saturation magnitude. Innovative aspects include the design of saturation trajectories to mimic saturation changes during DDP and WAG, and measurement of three-phase steady-state relative permeabilities at saturation conditions along those trajectories using live fluids and reservoir conditions.

Hibernia core plugs of this study were the same used in a previous study.[1] The plugs were previously characterized as oil-wet. The reservoir-condition DDP test of that study began with live brine and live oil injection at a ratio of 9:1 until a steady-state condition was established, then continued by flooding with pre-equilibrated gas until residual oil saturation was achieved. Results described a saturation path or trajectory during DDP. In this work, two-phase steady-state gas-oil and oil-brine relative permeability tests were performed to confirm agreement with previous measurements. Gas-brine relative permeability tests were also performed. For three-phase testing, the fluid injection sequence was designed to approximate the same saturation path or trajectory as that of the previous DDP test. At specific saturations along that trajectory, three-phase relative permeabilities were measured under steady-state conditions. After finishing the double displacement trajectory, steady-state testing continued with gas and brine injection representing several cycles of water-alternating-gas. Measurements from additional saturation trajectories provided good coverage of the three-phase saturation envelope.

Under conditions of three-phase flow, for this oil-wet rock, the gas phase exhibited the greatest amount of saturation-history-dependent hysteresis. The two-phase gas-brine curves, in addition to gas-oil curves, were found to be useful for understanding when and why either brine or oil had the greatest influence on three-phase gas relative permeabilities. The process of following a specific saturation trajectory for three-phase testing provided an efficient means for completing the three-phase tests in a relatively short time period (3.5 months). This protocol of performing relatively quick displacements (gas flood after waterflood or waterflood after gas flood) is recommended to identify saturation paths to follow during subsequent three-phase steady-state flow tests.

INTRODUCTION

Measurements of this project relate to the Hibernia Field, which is located 300 km southeast of St. John's Newfoundland and Labrador, Canada in the Jeanne D'Arc Basin. It is 250 km offshore with 80 m water depth. A concept being considered is gas flooding some of the Hibernia Formation waterflood blocks when secondary recovery is complete. Screening calculations and field experience with gas injection in the northern fault blocks indicate that WAG injection in blocks currently undergoing waterflood has potential to yield additional oil recovery.[2] Objectives of SCAL studies are to provide the most representative three-phase relative permeability curves for pilot and full-field studies, to investigate WAG three-phase hysteresis effects, and to assist in the estimation of recovery efficiency.[2]

In 2006, Wang *et al.*[1] reported results from gas injection following a waterflood on core plugs from the Hibernia B-16-17 well in the V-Block. During the experiment, gas injection began after the foot-long composite core was flooded at a 9:1 water-oil injection ratio. The authors describe that some evaporation of water and oil may have occurred during the test. They made corrections to account for the loss. The blue "target" trend on Figure 5 shows the saturation path or trajectory that resulted during the double-displacement test, after saturations were corrected for fluid loss because of evaporation. This trend shows that, during the early stage of the gas flood, mostly brine was produced until brine saturation (fraction of pore volume) decreased to about 0.35. Thereafter, injected gas displaced mostly oil until oil saturation was reduced to about 0.10.

Data from the 2006 investigation[1] left some uncertainty in relative permeability curves, because three-phase relative permeabilities were calculated using a modification of the JBN[3] unsteady-state method, and because of questions related to "evaporation" losses. To reduce uncertainty, additional testing was warranted. The additional tests are the subject of this paper.

TEST METHODS AND DESCRIPTIONS

Fluids and Conditions

Brine was of the same Hibernia recipe used in the previous investigation. The brine composition, as well as various other rock and fluid properties (USBM wettability index, capillary pressure curves, two-phase relative permeability curves, interfacial tensions, and pore size distribution) can be found in ref. 1. Live Hibernia oil and equilibrium gas were used for reservoir-condition steady-state gas-oil, oil-brine, and brine-oil-gas tests. Synthetic solution gas was prepared and recombined with stock tank oil to match the reservoir fluid composition. Bubble point at 213 °F was 3241 psig. Table 1 provides descriptions of fluids, test conditions, and viscosities of fluids used in tests of this project. Viscosities listed in the table are those measured during flow tests after fluids were equilibrated.

For wettability restoration, within confining pressure cells, plugs were centrifuged at 3200 rpm (120 psi capillary pressure) in gas-displacing-brine mode to initial brine saturation, flooded with degassed or "dead" Hibernia oil to displace gas, and aged 6 weeks at 213°F.

Table 1 Test fluids and conditions.							
Test Type	Fluids	T, °F	Pore pressure, psig	Net confining pressure, psi	μ_w, cP	μ_o, cP	μ_g, cP
g-w	nitrogen, brine	120	1000	4000	0.915	**	0.020
g-o	live gas, live oil	213	3241	4000	**	0.793	0.031
o-w	live oil, live brine	213	3241	4000	0.411	0.793	**
w-o-g	live brine, live oil, live gas	213	3241	4000	0.411	0.793	0.031

Core Plugs
Core plugs were the same plugs used for an earlier double-displacement experiment.[1] Plugs were stacked to build a composite with the same arrangement as in the earlier investigation, and loaded into a coreholder. With 4000 psi net confining pressure, permeability of the composite to gas (nitrogen) was 2045 mD, whereas the harmonic average from individual plug properties was 2052 mD. Permeability of the composite to brine was 2200 mD, compared to the harmonic average of 2051 mD from individual plug properties. When arranged in a composite, k_w was slightly greater than k_g. This was also observed in the prior investigation (see Table 2, ref. 1). The reason for this difference has not been resolved. At the beginning of the gas-oil test, oil permeability was 1514.8 mD at residual water saturation (Swirr = 0.042). This permeability value (1514.8 mD) was used as the basis for normalizing all permeabilities to express results as relative permeabilities.

Flow Apparatus
The flow apparatus is depicted in Figure 1. All components are mounted within a temperature-controlled environment. The apparatus is a "closed-loop" recirculating system. Compared to a "single-pass" system, fluid volume requirements are less, fluids are better equilibrated, and experimental anomalies such as mass transfer and evaporation losses are reduced or eliminated.

At upstream and downstream locations with respect to the composite sample, pressures P_1 and P_2 are measured by high accuracy quartz transducers. Quizix pumps are used for fluid injection. The pumps refill by drawing fluids from the three-phase acoustic separator. A servo pump maintains downstream pressure constant by pushing gas into or withdrawing gas from the separator. Saturation changes within the composite are determined continuously during a test by volumetric balance. Increases and decreases in brine, oil, and gas volumes within the composite are reflected by corresponding changes in fluid volumes within the separator, pumps, and tubing. By knowing the volumetric contents of the separator, pumps, and tubing at all times, saturations within the composite are determined. After finishing a test, volumes of fluids extracted from the composite confirmed results from volumetric balance. Additional descriptions are available elsewhere.[4, 5]
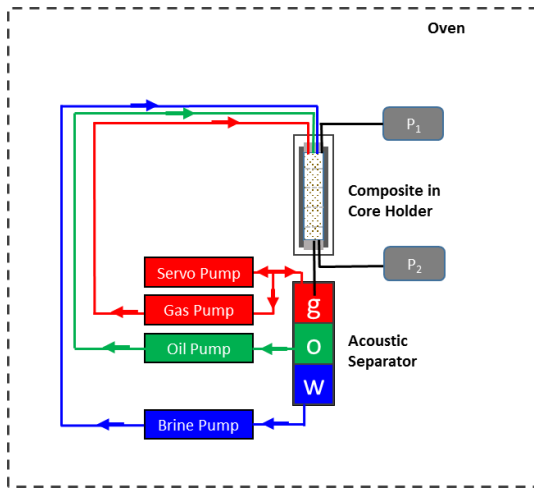
Figure 1 Simple schematic of the steady-state relative permeability apparatus.

Permeability and Relative Permeability Equations

Steady-state permeabilities were calculated using the Darcy equation. For gas,

$$k_g = 2\,P_1\,Q_{g1}\,\mu_g\,L \,/\, [A(P_1^2 - P_2^2)] \tag{1}$$

where k_g is permeability to gas, Q_{g1} is the upstream gas injection rate or delivery rate of the gas pump when injecting gas into the composite, μ_g is viscosity of the gas (which is approximated as a constant over the pressure range from P_1 to P_2 for these experiments), L is length of the composite, A is cross sectional area of the composite, P_1 is upstream pressure, and P_2 is downstream pressure. ("Pressure drop" equals P_1 minus P_2.)

For the liquid phases, at steady-state, flow rates and viscosities are assumed constant throughout the sample over the pressure range from P_1 to P_2. Thus, brine permeability is calculated from

$$k_w = Q_{w1}\,\mu_w\,L \,/\, [A(P_1 - P_2)], \tag{2}$$

and oil permeability is calculated from

$$k_o = Q_{o1}\,\mu_o\,L \,/\, [A(P_1 - P_2)]. \tag{3}$$

To express results as relative permeabilities, effective permeabilities are normalized by dividing by a common basis. For this work, the basis was k_o at S_{wirr}.

Data Labels and Saturation History Description

In sections that follow, saturations are expressed as fractions of pore volume, with brine, oil, and gas saturations abbreviated as S_w, S_o, and S_g. Relative permeabilities are represented by k_r followed by a letter representing the fluid of interest; for example, k_{rw} means brine relative permeability.

The convention used in this document is to label data sets with direction of saturation change of brine, oil, and gas sequentially, using letter "D" for decreasing, "I" for

increasing, "R" when the phase is at or near residual saturation and is not being injected, and "Ø" when the phase is absent. A number associated with each "D" or "I" indicates the number of cycles of decreasing or increasing saturation that the fluid phase has experienced. The same convention is used for labeling two- and three-phase data to facilitate comparison. For example, with residual brine saturation present, a first displacement of oil by gas is (R, D1, I1). The first cycle of water displacing oil beginning at Swirr without gas present in the pore system is (I1, D1, Ø), and if followed by gas injection to displace oil and brine, continues as (D2, D1, I1).

Two-Phase Steady-State Tests
<u>Gas-Brine</u> – A gas-brine steady-state test was performed, beginning with a measure of k_w at $S_w=1$ followed by gas-displacing-water (D1, Ø, I1) and water-displacing-gas (I1, Ø, D1). After the test, the composite was cleaned. The test was run again as a consistency check.

<u>Gas-Oil with S_{wirr} Present</u> – Steady-state relative permeability testing included measurements in cycles of oil saturation decreasing (R, D1, I1) and then increasing (R, I1, D1). The last step of the sequence was an oil flood and compress-back to put gas back into solution.

<u>Oil-Brine</u> – Beginning with S_{wirr}, oil-brine relative permeabilities were measured in steps of increasing brine saturation (I1, D1, Ø) to the launch point for three-phase flow.

Three Phase Steady-State Tests
Once steady-state is achieved at a particular saturation condition, the process of measuring two- and three-phase relative permeabilities is similar in that permeabilities are calculated from rates and pressure drops, permeabilities are divided by the basis to yield relative permeabilities, and average saturation is quantified using the acoustic separator. In a two-phase test, controlling the direction of saturation change is straightforward: implement a sequence of increasing or sequence of decreasing fractional flows. Controlling direction of saturation change with three flowing phases is more challenging; the direction of saturation change depends on rates of three fluid phases and the saturation history. The sequence of flow rate adjustments during a three-phase test is important for following a defined saturation path.

The first three-phase trajectory was designed to approximate saturation history during the previous double-displacement test.[1] It was important not to stray off path, because the first trajectory would be most representative and least affected by prior three-phase saturation history. Target saturations were selected in sequence along the trajectory. The challenge was to develop a schedule of brine, oil, and gas injection rates to pilot along the desired saturation trajectory without unintended saturation reversals or excessive pressure drops. The approach taken was to first graph results from the two-phase tests as phase relative permeability versus phase saturation to identify trends. The k_{ro} versus S_o plot showed that oil relative permeability was essentially a function of oil saturation, so a fit to all of the two-phase k_{ro} versus S_o data was used to estimate k_{ro} for a given target oil saturation

condition. From the plot of k_{rw} versus S_w using two phase data, the relative lack of hysteresis from the gas-water test attracted the use of the gas-water trend to predict k_{rw} from S_w. In retrospect, a better predictor would have been to use the trend from the (D2, I2, Ø) oil-brine cycle. There was enough variability in k_{rg} versus S_g that the arbitrary choice was to use a trend from the combined gas-water (I1, Ø, D1) and gas-oil (Ø, I1, D1) data to predict k_{rg} from S_g. These trends were then used to predict relative permeabilities for each target saturation along the trajectory. Relative permeabilities were multiplied by the basis of normalization to yield permeabilities. Finally, for a given pressure drop, flow rates (brine, oil, and gas) were calculated from permeabilities. This approach was not perfect, but was found to be adequate.

During the first saturation trajectory, after approaching residual oil saturation with three-phase flow, oil injection was stopped and cycles of increasing and decreasing brine and gas saturations were imposed. Thereafter, three phase flow was reinitiated to trace a path back toward a residual brine saturation condition. The last step of the sequence was to flood with oil at elevated pore pressure in an attempt to put gas back into solution to prepare for additional saturation trajectories.

For labeling purposes, after finishing a trajectory and compressing to put gas back into solution, it was assumed that the next trajectory would start over on the (I1, D1, Ø) cycle.

Two additional three-phase saturation trajectories were performed, beginning with higher S_w condition. The final saturation trajectory was a constant-rate waterflood to S_{or}, from which relative permeabilities were calculated by the Jones-Roszelle graphical method.[6]

RESULTS
From the entire data set, highest injection rates for brine, oil, and gas were 8.7 cm^3/min, 8 cm^3/min, and 83 cm^3/min respectively. The highest recorded pressure drop was 31 psi.

Two Phase
Two-phase data trends were fitted with Corey functions. These Corey functions are shown on graphs of two-phase and three-phase relative permeability results. For two-phase measurements, saturations are estimated to be accurate to within 0.03 saturation units. For three-phase flow, saturations are estimated to be accurate to within 0.04 saturation units.

Gas-Brine - Results from two tests (a, b) on the same composite are shown in Figure 2. Residual brine saturation at the end of (D1, Ø, I1) in test (a) was 0.23 compared to the value of 0.15 from test (b). These results were achieved by gas flooding, which does not provide enough drainage capillary pressure to achieve irreducible brine saturation. In this case, even though residual brine saturation from test (a) was greater than that from test (b), results from both tests are comparable. Without oil in the pore system, there is little if any cycle-dependent hysteresis in brine phase relative permeability versus brine saturation, whereas I1 and D1 curves are quite different for the gas phase.

Gas-Oil - Results from gas-oil steady-state relative permeability versus saturation measurements are shown in Figure 3. The oil and gas relative permeability curves show little if any hysteresis.

 Oil-Brine - Two-phase brine-displacing-oil steady-state relative permeabilities (I1, D1, Ø) were measured only to the saturation state at which three-phase flow was initiated (Trajectory 1). After the fourth steady-state (I1, D1, Ø) measurement with $S_w = 0.25$, a valve error briefly caused S_w to increase to about 0.55 before the issue was identified and corrected. After correction, the next two (I1, D1, Ø) brine relative permeabilities with brine saturations of 0.41 and 0.46 respectively follow the (D2, I2, Ø) Corey trend (Fig. 4 and 6).

Figure 4 compares this limited data with results from Ref. 1, Figure 11. Reference 1 data is denoted "2005" in the figure legend.

Another two-phase oil-brine data set was obtained in this investigation as a fourth saturation trajectory after all other measurements were completed. Prior to the fourth trajectory, the composite had undergone multiple cycles of increasing and decreasing brine, oil, and gas saturations, finishing with an oil-flood to residual brine saturation and compress-back that put gas back into solution. Trajectory 4 consisted of a constant-rate waterflood from which relative permeabilities were calculated by the Jones-Roszelle method.[6] As shown in Figure 4, the unsteady-state results, labeled as (Ix, Dx, Ø) with cycle number denoted "x" to indicate many cycles of increasing and decreasing saturation, are in reasonable agreement with (D2, I2, Ø) trends from steady-state measurements. Although it was a brine-saturation-increasing test, the brine relative permeability data follows the D2 trend. Apparently, when the system contains oil, after the first cycle of increasing brine saturation, brine relative permeabilities from subsequent decreasing and increasing brine saturation cycles follow the D2 trend. The figure shows little if any cycle-dependent hysteresis in oil-phase relative permeability versus saturation.
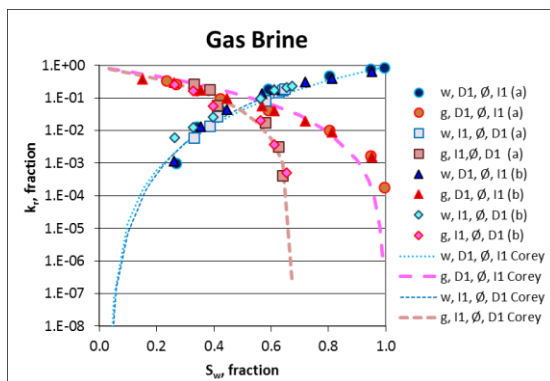

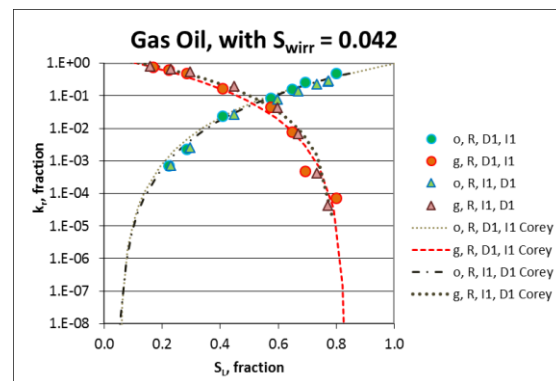**Figure 2 Gas-brine k$_r$ (2 tests) and Corey fits.**   **Figure 3 Gas-oil k$_r$ (with S$_{wi}$) and Corey fits.**
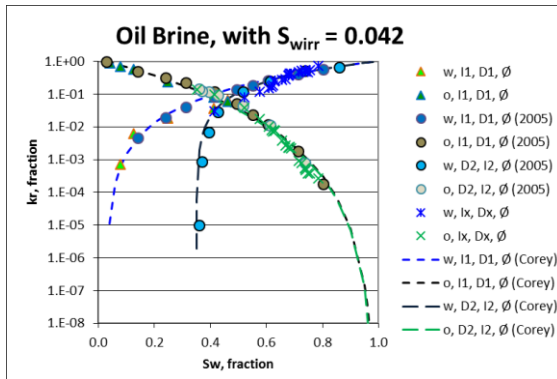
Figure 4 Oil-brine k_r and Corey fits.

Three Phase

Trajectory 1 – Figure 5 shows saturations at which relative permeabilities were measured during Trajectory 1. The trajectory was close to that of the Target path. On this type of plot, saturation (fraction of pore volume) equals one for the phase of interest at the apex and zero at the opposite side of the triangle. Lines between the apex and opposite side are in 0.1 saturation fraction increments.

The last sequence of Trajectory 1 was to oil flood and compress-back (to put gas back into solution by flooding with high pressure drop and increased backpressure) in an attempt to return to a S_{wi} condition. The data indicates that after this step, residual gas saturation was 0.08.

Trajectory 1 brine, oil, and gas relative permeability versus saturation results are shown in Figures 6 through 8. Subsets of the trajectory are denoted by different symbols and legend labels. After the initial saturation reversal when three-phase flow was initiated, for the most part, brine relative permeability versus brine saturation follows the (D2, I2, Ø) trend. Since S_w was near residual for most of the three-phase flow measurements, oil relative permeabilities are mostly on the two-phase gas-oil trend. For (D2, D1, I1), gas relative permeabilities follow the (R, D1, I1) trend, but for (I2, D1, D1) and subsequent cycles, gas relative permeabilities follow the (I1, Ø, D1) trend.
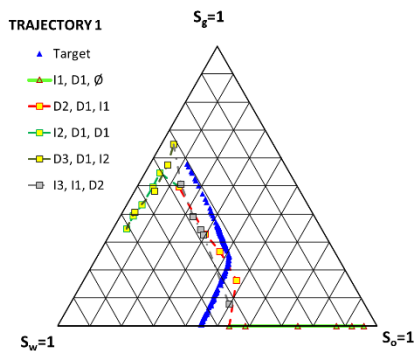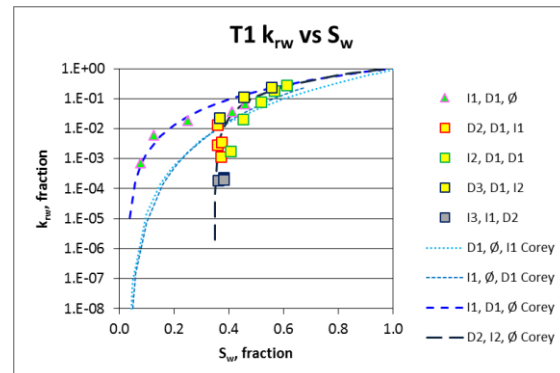

Figure 5 Saturation Trajectory 1.
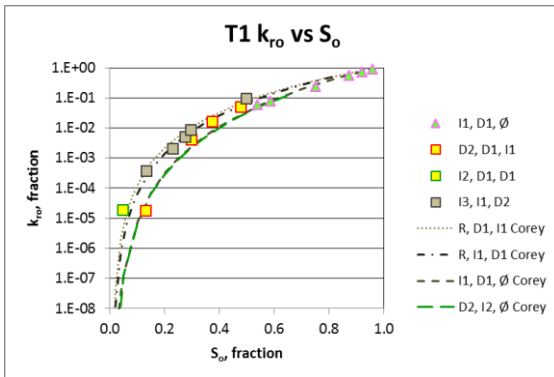

Figure 6 k_{rw} versus S_w, Trajectory 1.

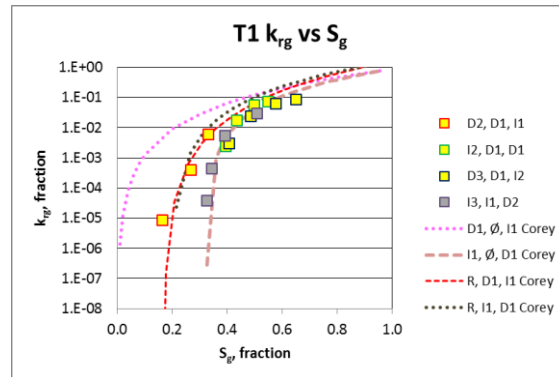**Figure 7 k_{ro} versus S_o, Trajectory 1.**

Figure 8 k_{rg} versus S_g, Trajectory 1.

Trajectory 2 – At the start of Trajectory 2, brine saturation was 0.35. Gas saturation, as determined from the three-phase separator, was 0.08. Several steady-state oil-brine measurements were recorded with increasing brine fractional flow to increase brine saturation to 0.44. The first part of the trajectory was designed to measure three-phase relative permeabilities with brine saturation maintained close to the 0.44 starting condition while oil saturation decreased and gas saturation increased. After completing this segment of the Trajectory, near S_{or}, brine and gas injection rates were varied in steps for cycles of increasing and then decreasing brine saturation. The final segment of the test was to flood with oil and compress-back to S_{wi}.

Figure 9 shows saturations at which relative permeabilities were measured during Trajectory 2. Trajectory 2 brine, oil, and gas relative permeability versus saturation results are shown in Figures 10 through 12. Brine relative permeabilities mostly follow the (D2, I2, Ø) trend. Oil results mostly follow the (D2, I2, Ø) trend. Gas results are predominantly on the (R, D1, I1) trend.
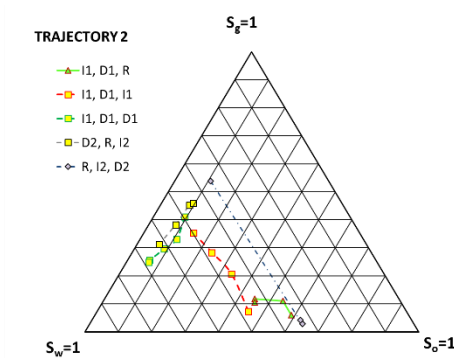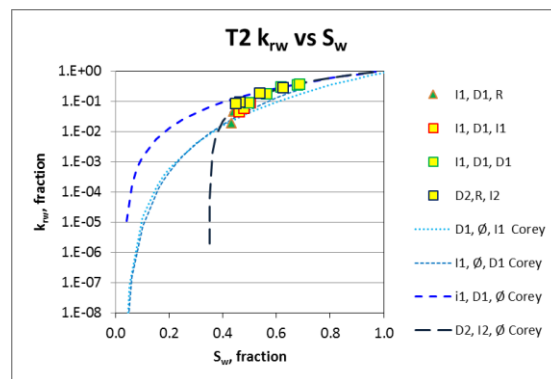

Figure 9 Saturation Trajectory 2.
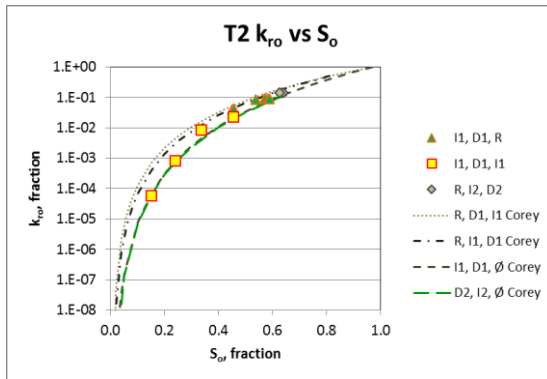

Figure 10 k_{rw} versus S_w, Trajectory 2.

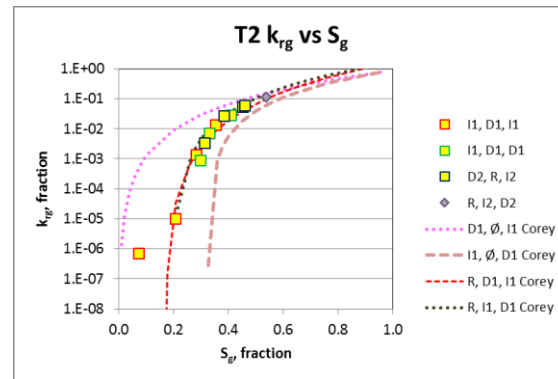**Figure 11 k_{ro} versus S_o, Trajectory 2.**

Figure 12 k_{rg} versus S_g, Trajectory 2.

Trajectory 3 - The compress-back step following the preceding saturation trajectory did not put all gas back into solution. At the start of Trajectory 3, brine saturation was 0.35. Gas saturation, as determined from the three-phase separator, was 0.07. Several steady-state oil-brine measurements were recorded with increasing brine fractional flow to increase brine saturation to 0.58. The first part of the trajectory was designed to measure three-phase relative permeabilities with increasing brine and gas saturations and decreasing oil saturation. After completing this segment of the Trajectory, near S_{or}, brine and gas injection rates were varied in steps for cycles of increasing and then decreasing brine saturation. The final segment of the test was to flood with oil and compress-back to S_{wi}. During this step, separator volumes indicate that all gas was put back into solution. The next test, Trajectory 4, was a waterflood without gas injection.

Figure 13 shows saturations at which relative permeabilities were measured during Trajectory 3. Trajectory 3 brine, oil, and gas relative permeability versus saturation results are shown in Figures 14 through 16. Brine results are mostly on the (D2, I2, Ø) trend, although saturations are in the range where (I1, D1, Ø) and (D2, I2, Ø) trends overlap. Oil results are mostly on the (D2, I2, Ø) trend. Gas results are between (D1, Ø, I1) and (R, D1, I1) trends, perhaps because for most of the test, gas saturation was increasing and oil saturation was low to moderate.
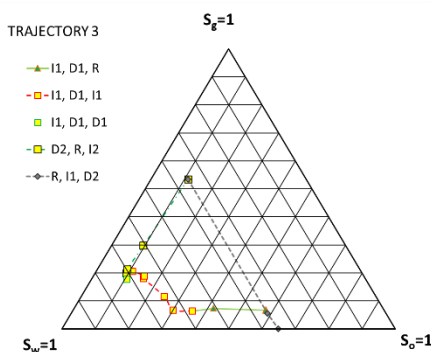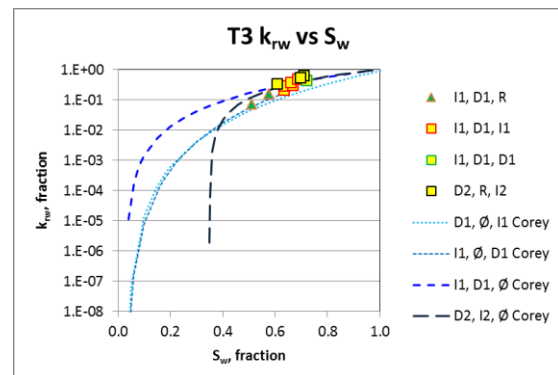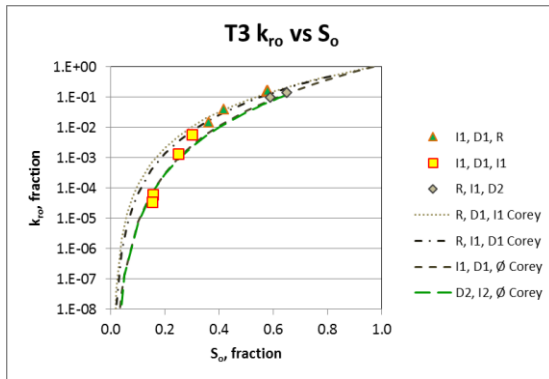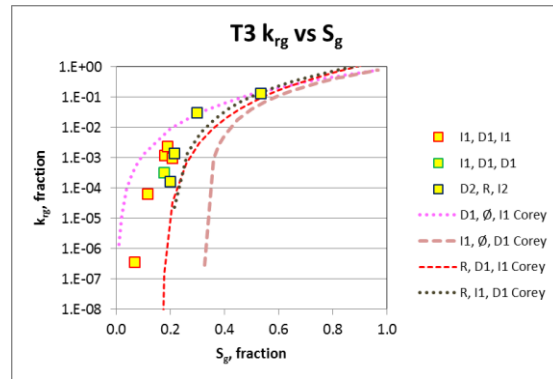

Figure 13 Saturation Trajectory 3.

Figure 14 k_{rw} versus S_w, Trajectory 3.

Figure 15 k_{ro} versus S_o, Trajectory 3.

Figure 16 k_{rg} versus S_g, Trajectory 3.

Figures 8, 12, and 16 show that gas relative permeability in this three-phase flow system is influenced by saturation history and all three flowing phases. To estimate three-phase relative permeabilities from two-phase relative permeability functions, gas-brine as well as oil-brine and gas-oil functions are useful.

Trapped Gas - Trapped gas saturation from two- and three-phase measurements of this investigation and from the previous work are shown in Figure 17. The plot shows trapped versus initial gas saturation from measures before and after the first WAG cycle. Trapped gas saturation is lower when less gas is initially put into the pore system.
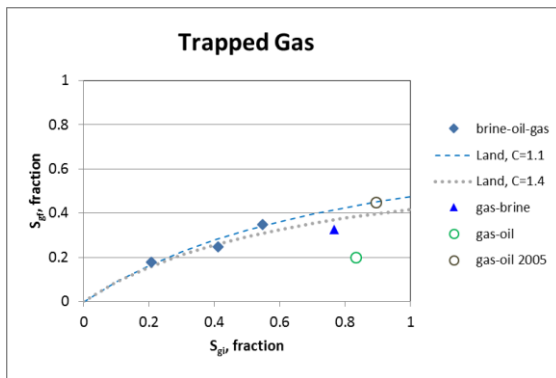
Figure 17 Trapped gas versus initial gas saturation.

CONCLUSIONS

- Sufficient resolution was achieved to reveal saturation-history-dependent hysteresis trends.
- Trapped brine saturation was approximately 0.35 (fraction of pore volume). After increasing S_w above 0.35 during the first cycle of increasing brine saturation, brine saturation did not reduce below 0.35 during subsequent saturation cycles.
- Oil relative permeabilities with three phase flow for the most part were similar to those for two-phase oil-brine flow.
- The gas phase exhibited the greatest amount of hysteresis.

- Two-phase gas-brine curves, in addition to gas-oil curves, are useful for understanding gas relative permeability versus gas saturation in this three-phase system.
- Trapped gas saturation for the most part followed a Land trend, with trapped gas saturation increasing with increasing initial gas saturation.
- Part of the challenge in designing three-phase flow experiments is to follow saturation paths similar to the field process under investigation. For this experimentation, saturation trajectory guidance was available from a previous displacement test. For future three-phase testing, it will be useful to follow a similar protocol of performing relatively quick displacements (gas flood after waterflood or waterflood after gas flood) to identify saturation paths to follow during subsequent three-phase steady-state flow tests.

ACKNOWLEDGEMENTS

REFERENCES

1. Wang, F., M. Honarpour, N. Djabbarah, and F. Haynes: Characterization of Multiphase Flow Properties for Tertiary Immiscible Displacement Processes in an Oil-Wet Reservoir. Paper SCA2006-33 presented at the International Symposium of the Society of Core Analysts, Trondheim, Norway (12-16 September, 2006).
2. Lawrence, J., H. Sahoo, G. Teletzke, J. Banfield, J. Long, N. Maccallum, R. Noseworthy, and L. James: Optimization of Gas Utilization to Improve Recovery at Hibernia. SPE 165240 presented at the SPE Enhanced Recovery Conference, Kuala Lumpur, Malaysia (2-4 July 2013). (OnePetro document ID 10.2118/165240-MS).
3. Johnson, E., D. Bossler, and V. Naumann: Calculation of Relative Permeability from Displacement Experiments. Petroleum Transactions AIME, V. 216 (1959). pp. 370-372. (OnePetro document ID SPE 0123-G.)
4. Wang, F., E. Braun, J. Kuzan, N. Djabbarah, M. Honarpour, C. Chiasson, and B. Milligan: Application of Unique Methodology and Laboratory Capability for Evaluation of Hydrocarbon Recovery Processes. Paper IPTC 12418 presented at the International Petroleum Technology Conference, Kuala Lumpur, Malaysia (3-5 December 2008). (OnePetro document ID 12418-MS.)
5. Braun, E., and R. Blackwell: A Steady-State Technique for Measuring Oil-Water Relative Permeability Curves at Reservoir Conditions. Paper SPE 10155 presented at the SPE Annual Technical Conference and Exhibition, San Antonio, TX (5-7 October 1981). (OnePetro document ID 10155-MS.)
6. Jones, S. and W. Roszelle: Graphical Techniques for Determining Relative Permeability From Displacement Experiments. Journal of Petroleum Technology (May, 1978), pp. 807-817. (OnePetro document 6045-PA SPE.)

ULTRA FAST CAPILARY PRESSURE AND RESISTIVITY INDEX MEASUREMENTS (UFPCRI) COMBINING CENTRIFUGATION, NMR IMAGING, AND RESISTITY PROFILING

Pierre Faurissoux, Alison Colombain, Ghislain Pujol, Oscar Fraute, Benjamin Nicot
TOTAL

ABSTRACT

The knowledge of water saturation is essential to determine hydrocarbon in place in an early discovery and also to monitor the sweep efficiency during the production phase. Water saturation can be measured using different logging techniques such as: resistivity, NMR (Nuclear Magnetic Resonance), dielectric, and pulsed neutrons. However resistivity measurement is the only means capable of giving information in the virgin zone around the well. These electrical measurements are used to estimate the water saturation using Archie's law.

Archie's law requires the knowledge of certain parameters such as the cementation factor (m) and the saturation exponent (n). These parameters can be measured in the laboratory and the time required to obtain these values differs considerably. While the cementation factor can be measured in hours, the saturation exponent measurement may take up to six months and therefore the cost associated to the experiment is higher.

The common technique to derive the saturation exponent is based on the use of a porous plate to ensure the uniformity of the saturation profile along the rock sample, but the price to pay is a very long and expensive experiment, driven by the low permeability of the porous plate.

This paper presents a new and radically faster alternative approach to measure both capillary pressure and saturation exponent. The general idea is to remove the porous plate and to generate a saturation profile in the sample using centrifugation. The generated saturation profile is then characterized by NMR and a multiple electrode resistivity profiling method developed "in house". This method can be applied together with the GIT (Green Imaging Technologies) patented capillary pressure method and therefore provide capillary pressure and resistivity index values in parallel.

This method has been tested and validated on outcrop samples from Bentheimer (sandstone) and Estaillades (carbonate). Also, it has been successfully applied to reservoir samples from a gas field under drainage and imbibitions processes.

INTRODUCTION

Accurate evaluation of hydrocarbon in place requires the knowledge of rock volume, porosity and fluid saturations. Resistivity measurements, performed during logging

operations, are converted into saturations using Archie's equation [1]. Thus, the knowledge of the Archie parameters "m" and "n" is essential. The cementation exponent "m" is easily and quickly determined in the laboratory from electrical measurements performed on 100% water saturated samples. In contrast, classical measurements of the Archie saturation exponent "n" are long and prone to experimental artifacts. The classical method relies on the establishment of a homogeneous water saturation profile along the sample using a porous plate, but this process can be extremely long. It may take from weeks (continuous injection method- no capillary equilibrium) to months (classical porous-plate method). Often, the results of laboratory measurements of the factor "n" arrive too late to be used in the electrical logs interpretation.

Attempts have been made in the past to shorten this experiment. Fleury proposed the FRIM method [2], which is much faster, but does not allow for simultaneous measurement of capillary pressure. Bona *et al*. [3] proposed a method based on centrifuge and saturation profiling. Assuming the validity of Archie's law, they calculate a saturation exponent "n".

Another drawback of the classical methods (porous plate or continuous injection) is that they are very sensitive to the heterogeneity of water saturation (Sw) in the sample. The only way to circumvent this issue is to use in-situ saturation monitoring techniques: Bona *et al*. [4] proposed to use MRI; Durand [5] proposed X-ray CT together with a first attempt to introduce resistivity profiling.

The method proposed in this paper combines centrifugation, NMR profiling and local resistivity measurements to derive the capillary pressure and the saturation exponent. It consists in generating a saturation profile along the sample by centrifugation at a given speed. Then, NMR is used to measure the saturation profile and resistivity is measured using an "in house" multi electrode device. This process is performed at different speeds in order to cover different ranges of capillary pressures and saturations. Results are available in weeks and the method is applicable to heterogeneous samples.

OUTLINE OF THE METHOD

This method starts with samples saturated 100% by brine, measuring NMR and resistivity profiles. Next, samples were centrifuged. This creates a saturation profile along the plug induced by the capillary pressure gradient applied in the centrifuge. NMR and resistivity profiles are measured again, and then converted respectively to saturation and resistivity index profiles using the data acquired at 100% water.

The resolution of the resistivity profile is limited by the electrode spacing, creating N virtual slices (for N+1 electrodes). Matching the saturation to the resistivity in each slice, N points are obtained in the Rt=f(Sw) plot at each centrifuge step.

An example is given on Figure 1 on which 7 electrodes were used (6 slices), Following this method, we obtain for each of the 6 slices a triplet [Pc, Sw, RI]; and therefore are able to plot the RI=f(Sw) curve together with the Pc=f(Sw) curve (as already proposed by Green *et al*.[6][7].

Minimal redistribution of fluids was observed during the timescale of NMR and resistivity measurements, and affected neither NMR nor resistivity profiles.

EQUIPMENT AND PROCEDURE
Resistivity Measurements

Electrical resistivity measurements were performed using a tailor made device with a Keysight E4980A Precision LCR meter at 1V and 1 KHz. In this device two parallel plates are used as current electrodes, and ΔV measurements are made using several 2mm thick ring electrodes spaced by 3mm electrical insulation.The classical 4 contacts resistivity method presented by Garrouch and Sharma [8] is used.

Saturation Measurements

Saturation measurements were performed using NMR profiling on a 2MHz Geospec from Oxford Instruments, equipped with Green Imaging software. The classical SE-SPI saturation profiling proposed by GIT has been used. NMR profiling allows the measurement of the volume of water in the sample as a function of the position along the sample. For a given sample, an NMR profile is acquired at Sw=100% and after each centrifuge step. Therefore, the saturation profile at any given centrifuge step can be obtained by dividing the NMR profile by the NMR profile at Sw=100%.

PROCEDURE

Sample characterization: 1) Clean with sequences of toluene and iso-propanol; dry by nitrogen flushing then heating at 80°C. 2) Measure permeability and Helium porosity. 3) Saturate with synthetic brine (Sw=100%) to determine pore volume.

Fully saturated properties: 4) Determine brine resistivity Rw. 5) Measure NMR and resistivity profile @ Sw=100%.

$$P_c(r)=1/2\ \Delta\omega^2(r_2{}^2-r^2)$$

plug, then the calculated NMR Sw for each slice, and finally the measured Rt.

Determination of first drainage PCRI curves: 6) Spin the core in the centrifuge in drainage mode until stabilization of the production during few hours. 7) Obtain the NMR and resistivity profile. 8) Loop to step 6 for next centrifuge speed.

Determination of imbibition PCRI curves: 9) Perform a capillary rise experiment putting the core in a foot bath (3mm) monitored with a balance. 10) Measure the NMR and resistivity profile. 11) Spin the core in the centrifuge in imbibition mode. 12) Measure the NMR and resistivity profile. 13) Loop to step 11 for next centrifuge speed.
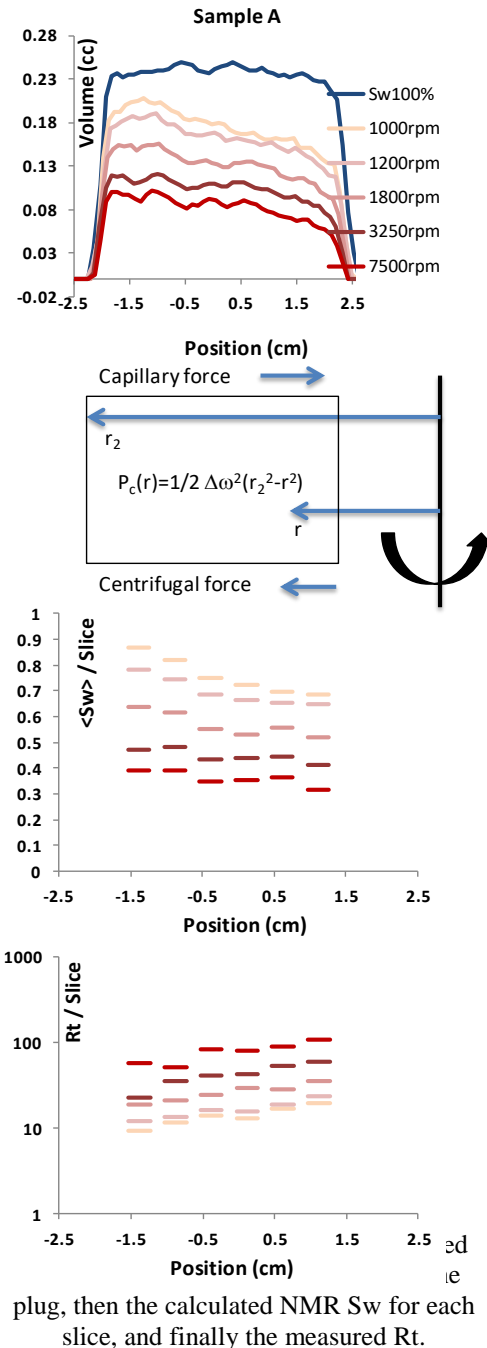
VALIDATION OF THE TECHNIQUE ON OUTCROP ROCKS
In order to validate the UFPCRI technique, electrical measurements were performed on the same samples, with the continuous injection (CI) method [9]. The classical porous plate was not considered due to the long time required to get the results.

Two outcrop samples (diameter 38mm and length 45mm) were selected: Bentheimer sandstone (28p.u., 2.2D) and Estaillades carbonate (31p.u. & 288mD). All measurements were performed at ambient conditions using mineral oil (non wetting fluid) to displace brine (wetting fluid), using confining stress of 15 bars only for CI.

Once the experiment was completed, the samples were cleaned, dried and saturated to 100% with the same brine used in the continuous injection technique. Then, the UFPCRI method was applied. The experiment was conducted twice in drainage mode, using gas and mineral oil. The purpose was to verify that the same Archie exponent "n" was found for both cases and to show that there was no experimental bias due to the fluid used.

With this technique, one centrifuge step would be enough to determine Archie's saturation exponent "n" (*i.e.* the slope of the RI=f(Sw) log-log curve). This is due to the multiple resistivity measurements on the different slices of the sample. However, it is better to cover a larger range of water saturation to determine "n". For this reason we performed 3 centrifuge steps to investigate a wider Sw range and to derive the capillary pressure curve.

Figure 2 shows the resistivity index vs water saturation plot, for each plug, using data derived from measurements with the CI method and the proposed UFPCRI with oil/brine and gas/brine couples. We observe that:
- The two UFPCRI results (oil/water and gas/water) overlay for both Bentheimer and Estaillades. This confirms the independence of the method versus the fluid used.
- UFPCRI gives consistent results when compared to the CI method for both samples.
- For Bentheimer a deviation from linearity on the CI data is observed. This is a commonly known issue of the CI method [9]. In any case, the determination of "n" being done by a linear regression forcing the zero intercept, the high Sw part of the curve has almost no effect on the "n" value obtained.

Despite the overlay of the experimental data, derived from both methods, the resulting saturation exponent are not identical. Thus, the impact on the calculation of saturation was also verified. This is important for small values of Sw, corresponding to the oil zone in a reservoir.

In order to validate the technique, we need to verify not only the overlay of the experimental data in the RI vs Sw log-log plot, but also the impact of the different values of n found on the saturation calculations, particularly for the small values of Sw, corresponding to the oil zone in a reservoir. For this, Sw calculated using the different values of n are compared, at a mean Sw of 10s.u.:

- For the Bentheimer sample, the maximum difference between the UFPCRI and CI is Δn=0.05. This translates to ΔSw=0.7s.u. at Sw=10s.u.. For higher Sw, the maximum error remains below 1.1s.u..
- For the Estaillades sample, the maximum difference between the UFPCRI and CI is Δn=0.06. This translates to ΔSw=0.6s.u. at Sw=10s.u.. For higher Sw, the maximum error remains below 1.0s.u..
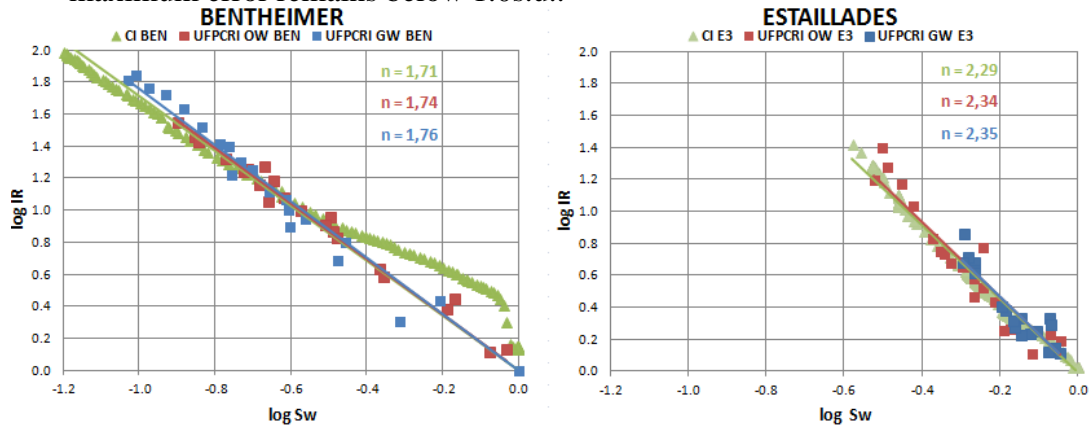

Figure 2: Comparison of Resistivity Index curves obtained by CI method (Oil/Water) in green and our UFPCRI method for both Oil/Water (red) and Gas/Water (blue): Bentheimer (left) and Estaillades (right).

The observed repeatability of the UFPCRI method regardless of the fluid used (gas or oil) and its good agreement with the CI method, clearly validate the UFPCRI technique.

The proposed method allows the joint determination of the Archie parameter "n" and the capillary pressure curve (as presented and already validated by Green [6]) in less than a week for drainage, compared to:

- Several weeks for RI only using the CI method,
- Several months for RI and Pc with the porous plate method.

APPLICATION TO REAL CASES

The UFPCRI method has been applied to a set of three reservoir samples. These rocks are heterogeneous carbonates. As shown in Figure 3, these limestones do not have the same amount and size of vugs. Observing their pictures they can be sorted as sample B the most heterogeneous with the presence of many surface vugs (up to 1mm) while sample A and C seem to be more homogenous with less pronounced vugs. Their basic petrophysical properties are summarized in Table 1.

Drainage (Gas displacing brine saturated sample)
All measurements were performed at ambient conditions. The samples were centrifuged in drainage mode at various speeds (1000, 1200, 1500, 1800, 2500, 3250, 7500rpm). Each time the samples were spun until stabilization of the production. NMR and resistivity profiles were then measured.

Figure 4 presents the drainage results: NMR profiles at various rotating speed are presented in the left column; while the resulting RI curves are presented in the middle column and the resulting Pc curves in the right column.

Because the three samples have different permeability, 7 centrifuge steps were required to cover the whole range of saturations.

Figure 3: Pictures of the samples used. From left to right: sample A, B and C.

Property	A	B	C
Porosity / p.u.	20.5	23	27.2
Permeability / mD	80	12	4
Diameter / mm	38.12	38.11	37.72
Length / mm	40.7	38.53	28.18

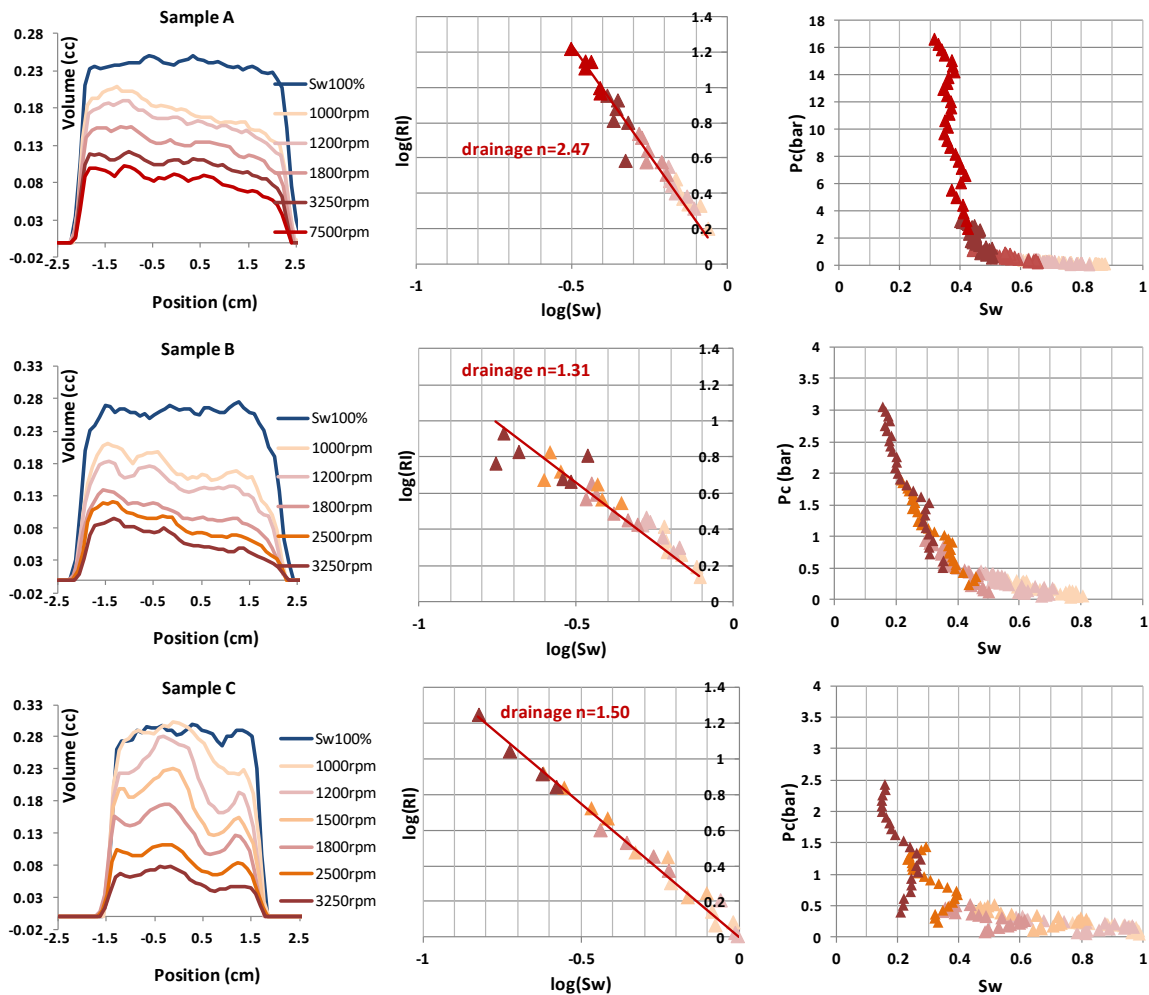Table 1: Basic petrophysical properties of the three reservoir samples

Figure 4: UFPCRI results for drainage of samples A, B and C. NMR profiles (left), resulting RI curves (middle) and Pc curves (right)

The number of NMR profiles is not the same for all the samples. These types of measurements were only performed if significant brine production was observed between the centrifuge steps. Moreover, the NMR acquisition time for samples containing limited amount of water was too long (up to days for a SNR close to 100).

In this case, if there was not enough production for a given sample at a given centrifugal speed, neither saturation profiles nor resistivity profiles were acquired. This explains, for example, why there is no data presented for samples B and C at 7500rpm. These latter did not produce enough brine from 3250rpm to 7500rpm and the NMR acquisition time for samples containing limited amount of water were too long. So samples B and C have also been spun to 7500rpm but no data is presented.

From the NMR profiles, sample A seems homogeneous, while sample B shows heterogeneities and sample C is the most heterogeneous. The impact of the heterogeneity on the results will be discussed below in a separate section.

The RI curves show a straight line for the three samples, verifying the validity of Archie's law for these samples. Sample B data dispersion will be covered in the heterogeneity section. The following Archie's saturation exponents can be derived:

- For sample A: $n_{drainage} = 2.47$
- For sample B: $n_{drainage} = 1.31$
- For sample C: $n_{drainage} = 1.50$

Capillary pressure curves were computed using the Green-Imaging GIT-Cap-Pressure software. The shape of the Pc curve for sample C can be attributed to the heterogeneity and will be discussed in detail later in this paper.

With the centrifuge steps used, many points overlap. Thus this result could have been achieved with a reduced number of centrifuge steps. As proposed by Green *et al*. [6], as few as three centrifuge steps can be used for this purpose.

Imbibition (Brine displacing gas from the sample at residual water saturation)
Once the drainage was completed, the next step was to perform the spontaneous imbibitions by capillary rise to create a saturation profile. Then, NMR and resistivity profiles were measured.

Imbibition under centrifugation was performed at 800, 1000 and 2500 rpm. The criteria to change the centrifuge speed were the same as used during the drainage experiments.

Figure 5 presents the results for imbibition. NMR profiles at various rotating speed are presented in the left column, while the resulting RI curves are presented in the middle column and the resulting Pc curves in the right column.

As expected, the heterogeneities highlighted on the NMR profile during drainage were also observed during imbibition. Sample C is clearly the most heterogeneous of the group. The heterogeneity will be discussed in a dedicated section. As shown in Figure 5, a peak at the top of plugs B and C can be observed. This peak increases with the centrifugal speed despite the fact that at this position Pc is close to 0. This could be attributed to remaining water droplets in surface vugs of the samples which may be blocked during the manipulation between the centrifuge and NMR measurements. The values from the extremities were not considered in the calculation of either the Pc or RI.
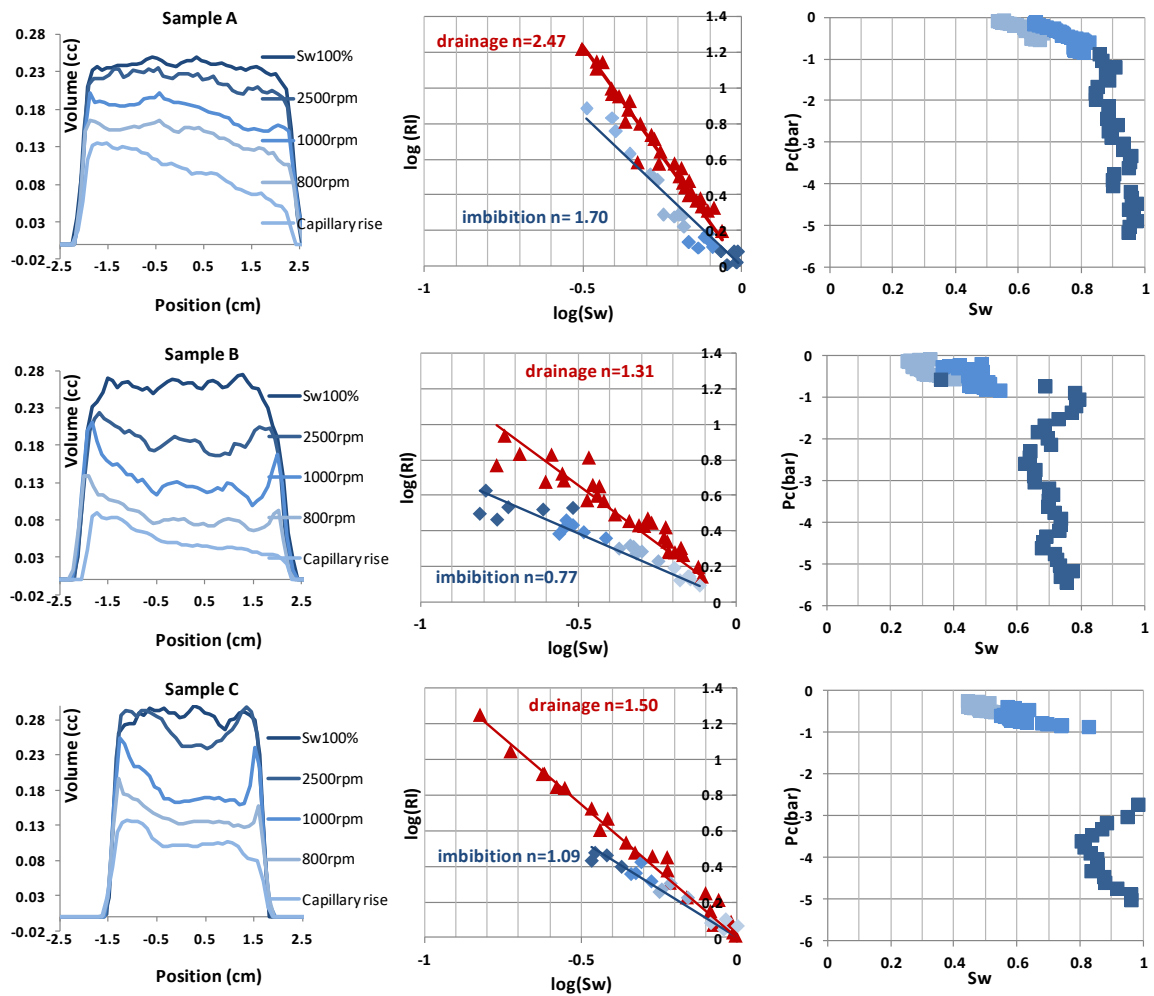
Figure 5: UFPCRI results for imbibition of samples A, B and C. NMR profiles (left), RI curves (middle) and Pc curves (right)

RI curves show a straight line for the three samples, verifying the validity of Archie's law for these samples. A greater dispersion of the points in the RI plot can be observed for sample B; this will be discussed in details in the section dedicated to heterogeneity. The following Archie's saturation exponents can be derived:

- For sample A: $n_{imbibition} = 1.70$, while $n_{drainage} = 2.47$
- For sample B: $n_{imbibition} = 0.77$, while $n_{drainage} = 1.31$
- For sample C: $n_{imbibition} = 1.09$, while $n_{drainage} = 1.50$

Pc curves were computed using the GIT-Cap-Pressure software. The surprising shape of the Pc curve for sample C can be explained by heterogeneity. Its small length highlights the limit of UFPCRI to describe a whole range of Sw especially with local heterogeneity.

DISCUSSION

For drainage, the following observations can be made:

Sample A: the most homogenous based on the NMR profiles at 100% Sw, $n_{drainage} = 2.47$. The RI vs. Sw plot shows good linearity. Despite having the largest permeability (80mD),

Swi (37 s.u) is higher than the rest of the samples with lower permeabilities.

Sample B and C: NMR profiles highlight their heterogeneities and identify sample C as the most heterogeneous. Their saturation exponents, respectively $n_{drainage} = 1.31$ and $n_{drainage} = 1.50$, seem relatively low when compared to sample A. Furthermore, their Pc curves reach similar Sw.

For the imbibition curves:

Samples A and C: $n_{imbibition} = 1.70$ and $n_{imbibition} = 1.09$, a significant ratio of approximately 1.4 is observed against drainage, and a poorer linearity than others plugs for sample A. Furthermore, NMR profiles and Pc show that its irreducible gas saturation seems close to zero with $<Sw> = 93\%$.

Sample B: $n_{imbibition} = 0.77$, a large ratio of 1.7 is observed between drainage and imbibition. The trend follows a pretty good linearity with a really good match between slices close to zero.

These results emphasize the importance of measuring the saturation exponent for both drainage and imbibition.

All the samples show the same behavior upon the transition to the imbibition cycle: the points, in the RI vs. Sw plots, corresponding to the imbibitions are always located below the ones measured in drainage. This type of hysteresis has already been observed ([10], [11]). Such behavior was successfully modeled by Toumelin *et al*. [12] and Man [13]. Comparison of experimental data with the model available in the literature requires NMR profile at Swi, which was only measurable for Sample A. During measurements, the saturation profile was not acquired at maximum centrifuge speed for Sample B and C as mentioned above. Hence, we will focus the discussion of hysteresis between drainage and imbibition of Sample A. As shown in Figure 6 the RI data for sample A follow the trends modeled by Toumelin[12] for a water wet system. In fact, the drop of n could be described as a water film thickening. Following this theory, the imbibition in Figure 6 could be decomposed into three parts:

- P1: the water film thickness increases rapidly at the pore throat,
- P2: rising of surface layers,
- P3: water film thickening reaches a critical gas saturation where the air phase is disconnected.
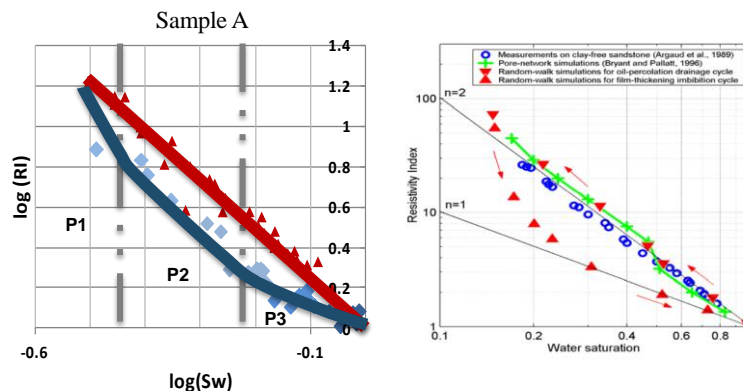

Figure 6: RI data acquired on sample A (left) and the model proposed by Toumelin [12] (right).

Heterogeneity:
The UFPCRI method provides directly the local saturation and resistivity. Therefore this method is independent of the Sw heterogeneity.
Heterogeneity of the studied samples can be inferred from the NMR profiles at Sw=100%, and after each centrifuge step. For sample C, the most heterogeneous, NMR profiles shows bumps and valleys; certain regions of the plug de-saturate faster than others despite the Pc gradient imposed by centrifugation.

Figure 7 shows NMR profiles and the resulting Pc curve for sample C where two trends can be observed and each response can be attributed to a particular section of the sample. Considering only the bottom part of the plug (orange rectangle in NMR profiles), all the points in the Pc curve corresponding to this section fall on the orange line. Similarly the Pc curve corresponding to the middle of the plug (red rectangle in NMR profiles) is represented in red. Thus, the shape of the Pc curve for sample C is not due to uncertainties of the technique but rather reveals the heterogeneity of the sample. Additionally, data from both trends could be used to derive Pc curves for both "rock types". The heterogeneity observed in the Pc curve of sample C does not translate into the RI curve as the RI vs. Sw plot showed linearity between the different values. This means that the two "rock types" present in the bottom and the middle of sample C have different Pc curves, but have the same electrical characteristics.
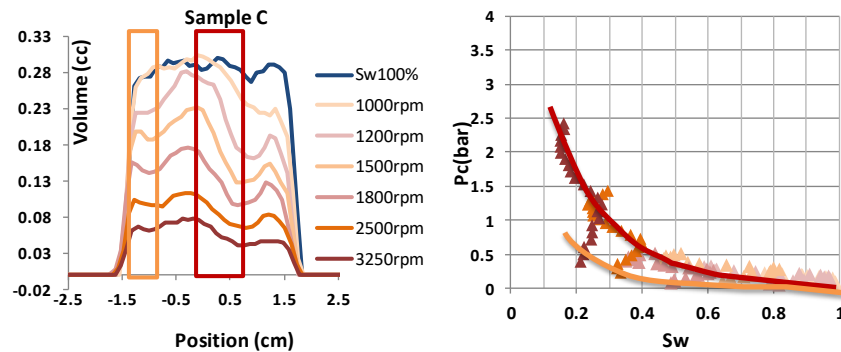
Figure 7: NMR profiles from sample C (left) and the resulting Pc curve. Pc curves obtained from the bottom of the sample (orange rectangle) and the middle (red rectangle) are drawn in corresponding colors.

An interesting result was obtained on sample B for drainage and imbibition: RI curves in Figure 8 were presenting dispersed points (i.e. the points were not aligning clearly on a straight line). However, two trends can be observed when plotted as a function of the position of the measurement. While the Slices 1, 2, 3 & 5 behave linearly in the RI plots; Slices 4 and 6 have a different behavior with flattening of the RI curves at low Sw.

Neither Pc curve nor NMR profiles showed similar deviation for this sample. The non-Archie behavior observed on slices 4 and 6 could be attributed to a dual porosity system in this vuggy carbonate. Such behavior has previously been reported by Fleury et al.[14]. Indeed, Fleury proposed a model to fit the results and obtain a non-Archie law [15]. This example demonstrates the capacity of the UFPCRI technique to capture heterogeneities.

Figure 8: RI curves obtained on sample B in drainage (left) and imbibition (right). Slice are sorted from the bottom (slice 1) to the top (slice 6) of the sample.
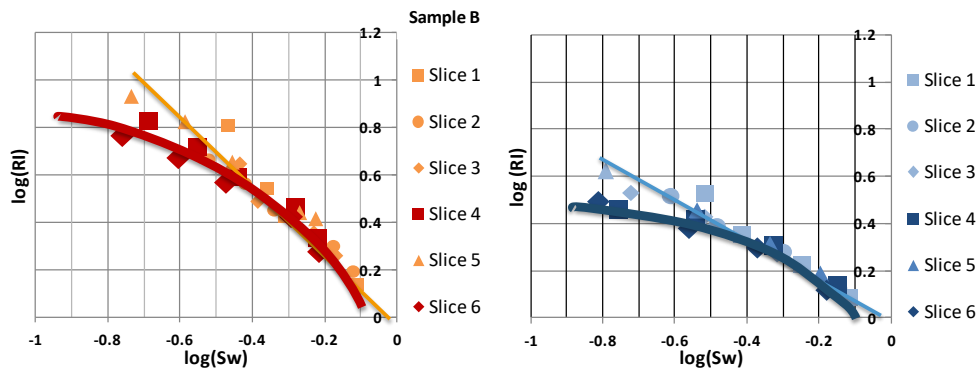
CONCLUSION

We present for the first time an experimental method (UFPCRI) allowing the simultaneous acquisition of capillary pressure data and resistivity index in a matter of weeks (drainage and imbibitions). This technique combines the method proposed by Green [6] to derive capillary pressure with a novel approach to provide resistivity index. The electrical measurements were clearly validated by comparing the results with the continuous injection method on outcrop samples, and a set of results are presented on heterogeneous carbonates. We present numerous centrifuge steps in order to have an extensive dataset, but three well chosen centrifuge steps could be sufficient to acquire enough data, therefore shortening even more the acquisition time.

UFPCRI has the advantage of avoiding the porous plate and its drawbacks (loss of capillary contact, long equilibrium time, risk of leaks).

Additionally, *classical methods* (porous plate, continuous injection) are completely blind against the heterogeneity of the sample since they report only the *average* values of: capillary pressure, saturation and resistivity. On the other hand, we propose an innovative technique *UFPCRI* which allows the measurement of the *local* properties (porosity, saturation, capillary pressure and resistivity). While core samples are often heterogeneous even at the plug scale, UFPCRI captures local properties and provides reliable petrophysical answers. Would the heterogeneity be a perturbation or a zone of no interest (*e.g.* shale layer), UFPCRI could capture it and discard it from the interpretation.

In summary, the proposed method:
- Is very fast, and therefore can provide Pc and "n" data in the range of operational timeframe, allowing the n results to effectively be used in log interpretation.
- Is able to capture heterogeneity, therefore leaving the choice to the interpreter to use or discard this information in the global n and Pc.

ACKNOWLEDGEMENTS

REFERENCES

[1] G. Archie, "Electrical Resistivity Log as an Aid in Determining Some Reservoir Characteristics," *Petroleum Transactions AIME,* 1942.

[2] M. Fleury, "FRIM, a Fast Resistivity Index Measurement Method," in *SCA*, 1998.

[3] N. Bona, E. Rossi and B. Bam, "Ultrafast Determination of Archie and Indonesia m&n Exponents for Electric log Interpretation: a Tight Gas Example," *IPTC,* 2014.

[4] N. Bona, B. Bam, M. Pirrone and E. Rossi, "Use of a New Impedance Cell and 3D MRI to Obtain Fast and Accurate Resistivity Index Measurements from a Single Centrifuge Step," *Petrophysics,* 2012.

[5] C. Durand, "Combined Use of X-Ray CT Scan and Local Resistivity Measurments: A New approach to Fluid Distribution Description in Cores," *SPE,* 2003.

[6] D. Green, J. Dick, J. Gardner, B. Balcom and B. Zhou, "Comparison Study of Capillary Pressure Curves Obtained Using Traditional Centrifuge and Magnetic Resonance Imaging Techniques," in *SCA*, 2007.

[7] D. Green, J. McAloon, P. Cano-Barrita, J. Burger and B. Balcom, "Oil/Water Imbibition and Drainage Capillary Pressure Determined by MRI on a Wide Sampling of Rocks," in *SCA*, 2008.

[8] A. Garrouch and M. Sharma, "Techniques for the Measurment of Electrical Properties of Cores in the Frequency Range 10Hz to 10MHz," in *SCA*, 1992.

[9] H. Zeelenberg and B. Schipper, "Developments in I-Sw Measurements," in *Advances in Core Avaluation II, Reservoir Appraisal*, Gordon and Breach Science Publishers, 1991, p. 257.

[10] M. Han, M. Fleury and P. Levitz, "Effect of the Pore Structure on Resistivity Index Curves," in *SCA*, 2007.

[11] R. Knight, "Hysteresis in electrical Resistivity of Partially Saturated Sandstones," *Geophysics,* vol. 56, no. 12, 1991.

[12] E. Toumelin, C. Torres-Verdin, S. Devarajan and B. Sun, "An Integrated Pore-Scale Approach for the Simulation of Grain Morphology, Wettability, and Saturation-History Effects on Electrical Resistivity and NMR Measurements of Saturated Rocks," in *SCA*, 2006.

[13] H. Man and X. Jing, "Network Modelling of Mixed-Wettability on Electrical Resistivity, Capillary Pressure and Wettability Indices," *Journal of Petroleum Science and Engineering,* vol. 33, 2002.

[14] M. Fleury, M. Efnik and M. Kalam, "Evaluation of Water Saturation from Resistivity in a Carbonate Field. From Laboratory to Logs," in *SCA*, 2004.

[15] M. Fleury, "Advances in Resistivity Measurments using the FRIM MEthod at Reservoir Conditions. Application to Carbonates," in *SCA*, 2003.

HOW CAN NMR ASSESS THE WETTABILITY OF A CHALK RESERVOIR

Wim Looyestijn, Xiangmin Zhang and Albert Hebing

PanTerra Geoconsultants B.V., Netherlands

This paper was prepared for presentation at the International Symposium of the Society of Core Analysts held in Vienna, Austria, 27 August – 1 September 2017

ABSTRACT

Knowing the wettability of a reservoir at an early date is important for every oil reservoir, but can be vital in low-permeability reservoirs such as in off-shore chalk fields. Therefore, an extensive wettability program was designed for this field, including USBM and Amott-Harvey tests on a set of core samples. These tests followed the standard protocol of ageing in dead crude, followed by imbibition and drainage cycles with mineral oil. As a novel addition, we took individual NMR core measurements at each of the nine laboratory steps. We found a good correlation between USBM and Amott-Harvey, and also with the NMR wettability index. Whereas the USBM and Amott-Harvey techniques provide just one number, NMR can be interpreted at each analytical laboratory step. We found that the wettability index remains roughly constant during the process. This implies that the protocol of imbibing and draining mineral oil in aged samples does not affect the wettability condition.

Subsequently, the analysis was applied to the NMR logs in the same well. The wettability in the oil zone was found to be similar as what was found in the core data. As expected, the wettability gradually changes to fully waterwet over the transition zone down to the OWC. SCAL measurements at transition zone conditions are cumbersome, but this information allows modeling changes in flow properties in the transition zone.

INTRODUCTION

Nuclear Magnetic Resonance (NMR) derives its popularity as a logging technique from the sensitivity of the measured relaxation times of hydrogen nuclear spins of the wetting fluids to an interaction with the pore surface. Whereas this is normally only observed for water, it has long been known [1] that a similar effect exists for oil in non-waterwet rock. Over the years, many publications appeared showing empirical correlations, e.g. [2] or

through more complicated analyses, e.g. [3]. Recently we developed a method to derive a quantitative NMR wettability index (NWI) from just a single NMR measurement [4]. The index is computed through detailed modeling of the NMR response as a function of saturation and wetting over the pore size distribution. The validity of this method was verified on a large set of core samples against standard laboratory wettability index data (USBM). This method has been adapted to be used with NMR log data [5] allowing the wettability to be determined over the entire reservoir interval as a continuous curve, rather than on a few samples, from any standard NMR log.

The NMR Wettability Index

The surface of pores provides an additional relaxation mechanism, which adds to the bulk relaxation of the nuclear hydrogen spin of the saturating fluid. The effect is that the ith fluid in a pore relaxes a single exponential decay $exp(-t/T_{2,i})$, with :

$$\frac{1}{T_{2,i}} = \frac{1}{T_{2,bulk,i}} + \rho_i \frac{A}{V} \frac{f_i}{S_i} \tag{1}$$

with $T_{2,i}$ observed relaxation time
$T_{2,bulk,i}$ relaxation time of bulk fluid
ρ_i surface relaxivity
A / V surface-to-volume ratio of the pore
f_i wetted fraction of the surface
S_i saturation of the pore by fluid i

The wetting index can thus be defined as the relative fraction of the total surface wetted by water minus that by oil: $NWI = f_{water} - f_{oil}$. In words:

$$NWI = \frac{Surface\ wetted\ by\ water - Surface\ wetted\ by\ oil}{Total\ Surface} \tag{2}$$

To conform to existing indices, NWI, scales from +1 for fully water-wet, through 0 for neutral, to -1 for fully oil-wet. In reality, rocks have a certain range of pore sizes (A/V values), and thus a range of T2 amplitudes. Furthermore, f_i and S_i may vary with poresize. NWI is thus computed by integration of eq. (1) over T_2. Full details of the method may be found in an earlier publication [4].

It is emphasized that the definition of NWI has some resemblance with the traditional Amott and USBM indices. However, since it is based on entirely different grounds, there is no fundamental numerical equality implied other than at the endpoints of fully water-wet and fully oil-wet. Similar to any index, it provides an indication of flow properties, but being a single number, it cannot replace a full set of SCAL data.

The challenge in the computation of NWI is in determining $f_i\ (T2)$ and $S_i\ (T2)$. In many practical cases, the oil and water distributions have significant overlap, causing the position of the oil peak to be shifted, or even to be indistinguishable. This problem has

been solved by inversion of a detailed forward model of the NMR response, taking into account as a function of pore size: (1) the microscopic distribution of oil and water, (2) the wetting fraction, (3) the T2 distributions of the rock at Sw=1 and of the bulk fluids.

NMR wettability on core samples during SCAL program

The objective of the present study was to apply the method at every preparation step of the traditional wettability workflow for the combined Amott-Harvey / USBM method.

NMR measurements were made using a Maran spectrometer, operating at 2 MHz in a homogenous field. Measurements were made on 6 samples from an oil bearing chalk reservoir, at the following steps of preparation:

1   Cleaned, Sw =1
2   Swi-crude before ageing
3   Swi-crude after ageing
4   Displace by isopar-L
5   Swirr desaturation
6   Spontaneous imbibition water
7   Forced imbibition water
8   Spontaneous imbibition oil
9   Forced imbibition oil

The samples were first vacuum-saturated with synthetic formation brine, then de-saturated to initial saturation (Swi) in crude oil–brine system by single-speed centrifuge. After aging at reservoir temperature and pressure, the samples were flushed with mineral oil (Isopar-L) in a core holder, first with decalin oil and then with isopar-L oil. The samples were further de-saturated to irreducible water saturation (Swirr) by single-speed centrifuge. The spontaneous imbibitions (step 6 step 8) were carried out in Amott cells and forced imbibitions (step 7 and step 9) were performed in multi-speed centrifuge.
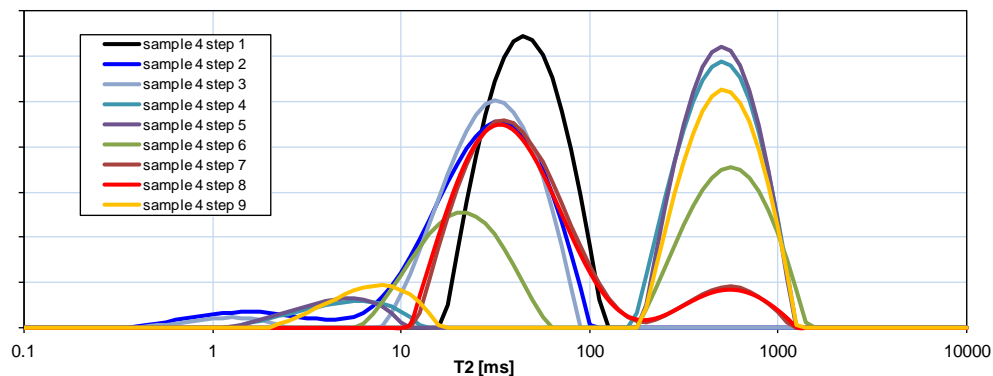

Figure 1   Observed NMR T2-distribution of sample 4 after steps 1 to 9.

The observed NMR T2-distribution after each step is shown in Figure 1 for sample 4; all other samples showed a very similar response. The interpretation of the response in terms

of fluid distribution and wettability is given in the next sections, starting with the more straightforward cases where the oil is a light refined oil (isopar-L)(steps 4 to 9), leaving the more complicated case of crude oil to the end.

Wettability interpretation after step 4 and 5

The interpretation of the T2-distribution after step 4 is relatively straightforward. An example is shown in Figure 2 for sample 4; all other samples look very similar.
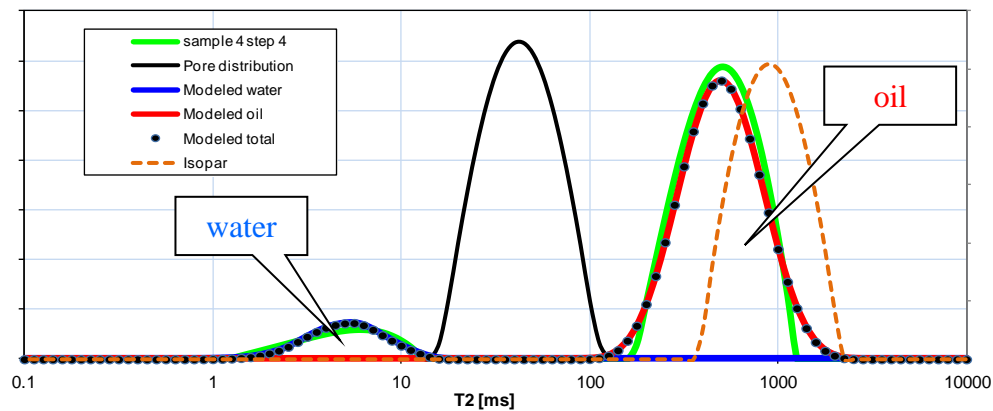

Figure 2   Observed and modeled T2-distribution of sample 4 after step 4

The "Pore distribution" (black curve) is the T2-distribution measured on the water-filled sample (step 1). Upon imbibition with crude, and subsequently isopar-L, the water saturation has reached a low value. Consequently, the amplitude is reduced, but also its T2 has shifted to a lower value. This shift can be understood from eq.(1): the volume of water has now been reduced to V*Sw. Roughly speaking, this means that T2 has reduced to T2*Sw. The actual modeling is more refined, as it takes into account that the larger pores are stronger imbibed than the smaller pores.

The stronger peak, at longer T2, is due to isopar-L. As can be seen, it has been shifted to lower T2 compared to the bulk relaxation. This is the result of wetting. The degree of shift depends on the value of ρ in eq.1; it appears that no explicit value of ρ is required, but only the ratio of the surface relaxivity of isopar-L compared to that of water [4]. Previous experience has shown a relative value of 0.2 for oils in chalk. The quantitative wettability interpretation furthermore includes pore-size dependent saturation and wetting, and integration over all pore sizes (i.e. over the T2-distribution).

As can be seen, the modeling reproduces the observed T2-distribution very well. This is seen on all samples. The water saturation can now be calculated precisely since there is a clear separation between water and oil. The integrated area under the water peak gives Sw.

The NMR response hardly changes between steps 4 and 5; the wettability index remains virtually the same.

Wettability interpretation after step 6

After step 6 water saturation has increased by spontaneous imbibition. As a consequence, the water peak has grown, and shifted to a larger T2, both by the same mechanism as explained in the previous section. The wettability index remains approximately the same.
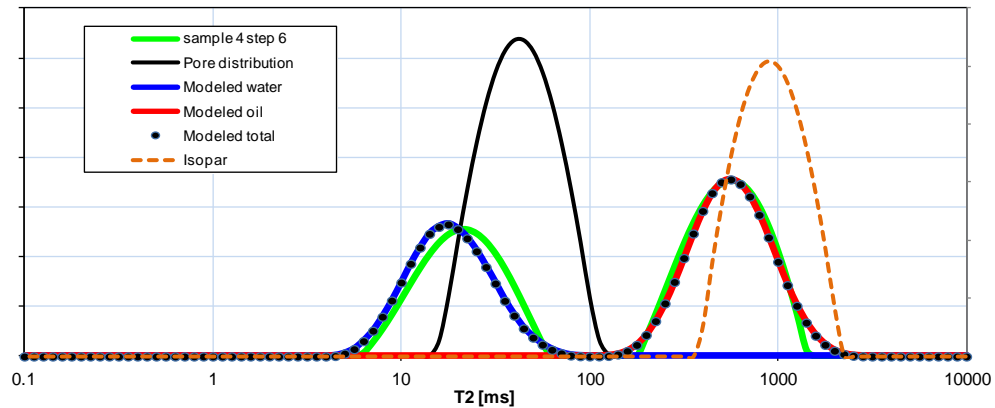
Figure 3   Observed and modeled T2-distribution of sample 4 after step 6

Wettability interpretation after step 7

Forced water imbibition continued to increase the water peak, leaving a small peak of oil. The oil peak is still lightly shifted from the bulk response as a result of partial wetting. Because the oil saturation is low, the wettability index has a larger uncertainty than in the other steps, but is still about the same as before.

Figure 4   Observed and modeled T2-distribution of sample 4 after step 7

Wettability interpretation after step 8 and 9

Spontaneous and forced oil imbibition in steps 8 and 9 has reduced water saturation more or less back to the situation after step 5; the NMR response is also virtually the same as after step 5.
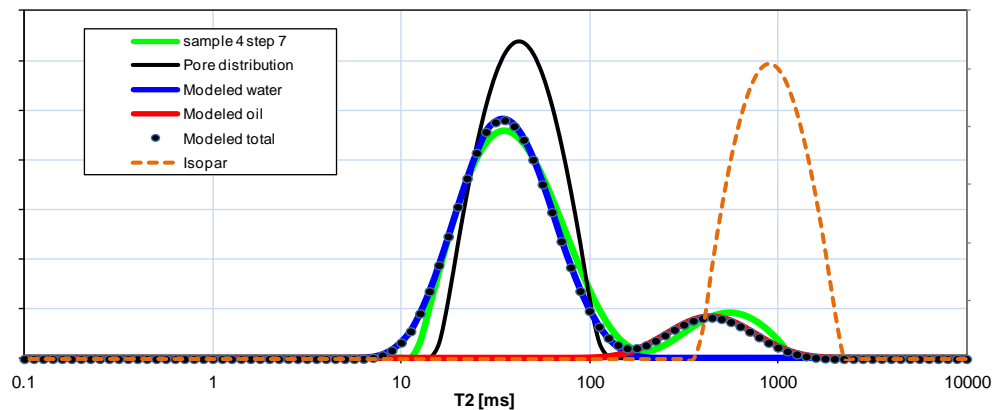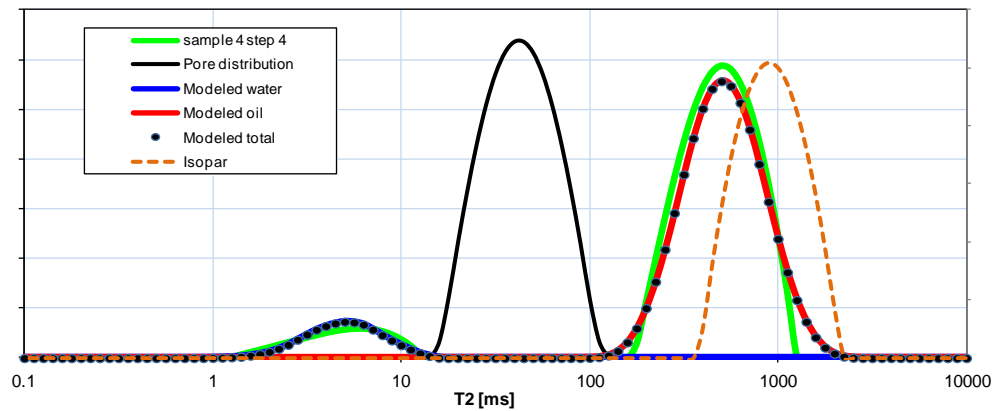

Figure 5   Observed and modeled T2-distribution of sample 4 after step 9

Wettability interpretation after step 2 and 3

When the responses of water and oil overlap, the interpretation gets more complicated. In the present case the situation is even worse: for all samples the Sw=1 response and crude oil fully overlap, which renders the interpretation virtually impossible. Even if the water saturation is taken from the SCAL analysis, the model allows almost any level of wettability. A further complication is that there was no NMR measurement made of the crude after ageing. Studies elsewhere have occasionally seen some alteration of the crude (evaporation of lighter ends) that do not impact on the ageing, but give additional uncertainty in the NMR wettability analysis. Consequently, no interpretation can be given for steps 2 and 3, except, qualitatively, that the sample is not fully water-wet.

Figure 6   Observed and modeled T2-distribution of sample 4 after step 2

Discussion of results on core-derived wettability

The interpretation results are summarized in Table 1, together with the corresponding Amott and USBM indices.

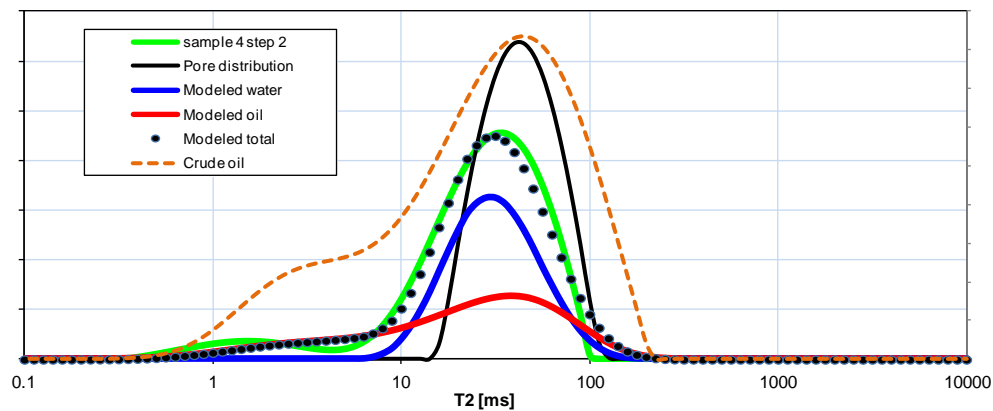| Sample		After preparation step nr.						Amott	USBM
		4	5	6	7	8	9	Index	Index
1	Sw_core	0.10	0.10	0.22	0.70	0.70	0.16		
	Sw_NMR	0.13	0.12	0.26	0.80	0.82	0.29		
	NWI	0.64	0.65	0.73	0.82	0.84	0.76	0.20	0.12
2	Sw_core	0.18	0.12	0.33	0.80	0.80	0.15		
	Sw_NMR	0.19	0.15	0.37	0.84	0.82	0.17		
	NWI	0.71	0.74	0.83	0.79	0.83	0.71	0.30	0.24
3	Sw_core	0.17	0.17	0.47	0.77	0.77	0.20		
	Sw_NMR	0.15	0.16	0.45	0.80	0.77	0.19		
	NWI	0.71	0.69	0.83	0.90	0.92	0.71	0.50	0.42
4	Sw_core	0.12	0.12	0.46	0.86	0.86	0.14		
	Sw_NMR	0.11	0.10	0.43	0.87	0.87	0.16		
	NWI	0.72	0.72	0.86	0.95	0.95	0.76	0.46	0.43
5	Sw_core	0.15	0.10	0.43	0.74	0.74	0.15		
	Sw_NMR	0.14	0.13	0.46	0.71	0.71	0.15		
	NWI	0.82	0.82	0.88	0.90	0.90	0.84	0.53	0.30
6	Sw_core	0.13	0.13	0.44	0.76	0.76	0.19		
	Sw_NMR	0.15	0.14	0.49	0.73	0.73	0.17		
	NWI	0.84	0.85	0.84	0.78	0.78	0.76	0.50	0.24

Table 1   Saturation and Wettability Index by NMR

As explained in the previous sections, the NMR-derived saturations of steps 4 - 9 are very robust because the water and oil peak are well separated. The agreement with the independent Sw_core from SCAL volumetrics is excellent, see Figure 7. The largest exceptions are with sample 1 for which the Sw_core values are somewhat questionable because of significant observed grain losses.
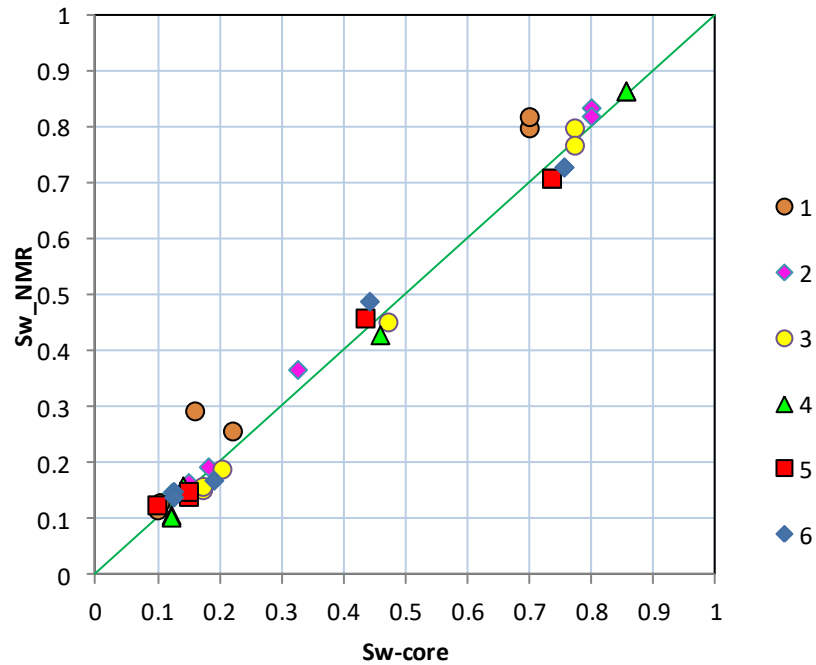
Figure 7   NMR-derived saturation versus SCAL-derived saturation for samples 1 to 6

The NMR Wettability Index correlates well with the Amott (and USBM) index, see Figure 8. As mentioned in the Introduction, there is no one-to-one relationship between these indices, but rather a positive trend between the common endpoints [-1,-1] and [+1,+1]. The observed trend implies that a given NMR Wettability Index corresponds to a lower Amott value, at least for positive index values.

There appears to be a slight trend between the NMR Wettability Index and Sw, see Figure 9. When analyzed against step number, Figure 10, it appears that the samples become more water-wet with every subsequent step; the most water-wet values are seen at steps 7 and 8, which have the lowest oil saturation. Part of this residual oil is present in the form of snapped-off droplets that have no contact with the surface; this is not properly incorporated in the model, and will result in a too high index. The interpretations of steps 7 and 8 thus have the largest uncertainty.

If this trend were true, it would mean that flooding mineral oil has some effect on the wetting condition of the samples. However, the evidence is not strong enough to support this concern. Suijkerbuijk et al [6] reported a study in which Berea samples were aged with various crudes, and subsequently flooded with mineral oil. They did not observe a change in wetting.
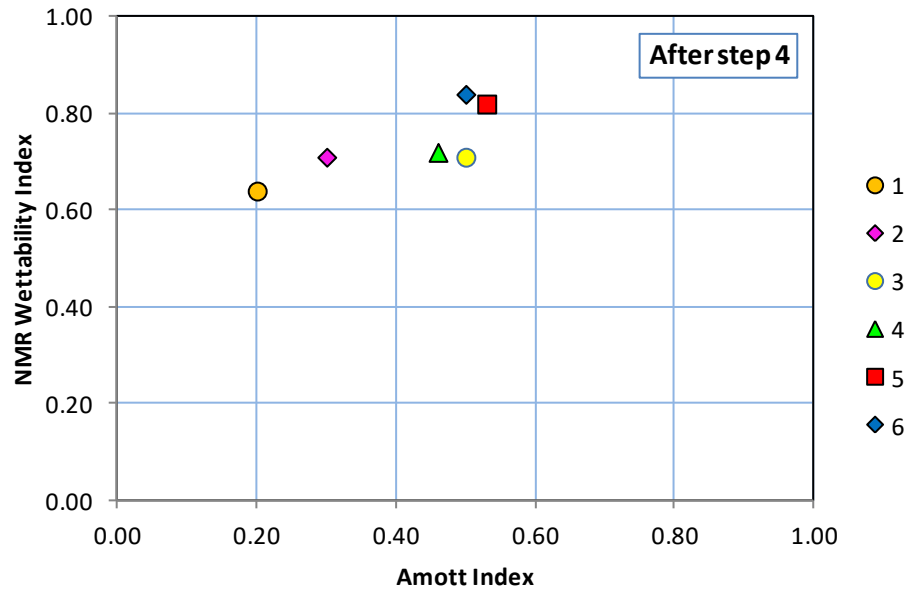
Figure 8   NMR Wettability Index (after step 4) versus Amott Index
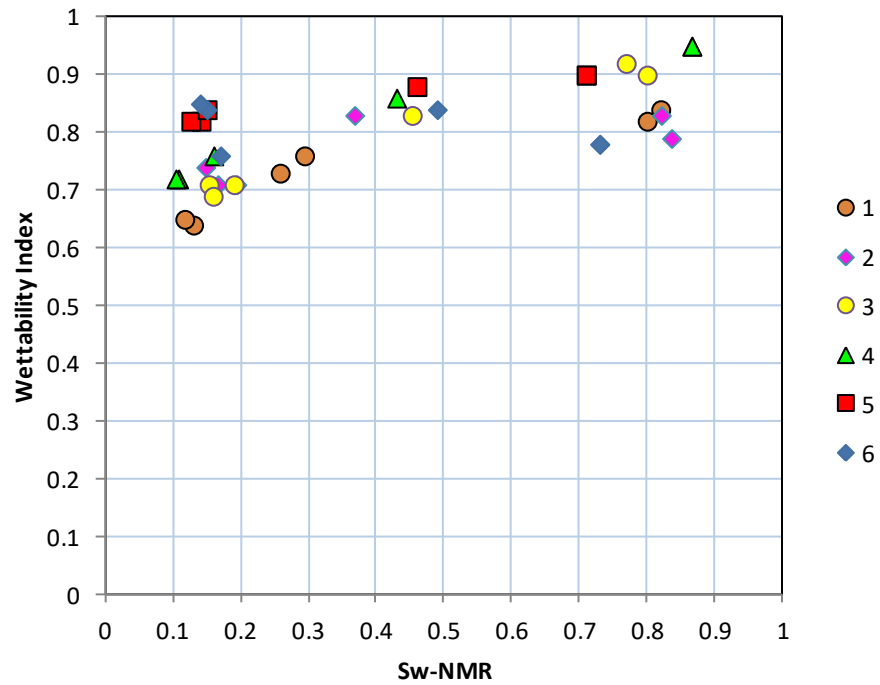

Figure 9   NMR-derived Wettability against water saturation at the various preparation steps 4-9.
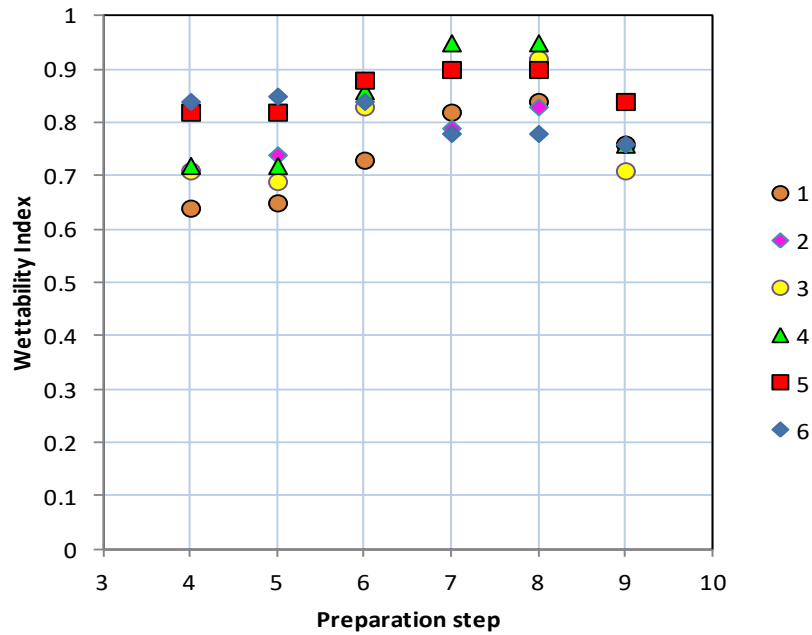
Figure 10   NMR Wettability Index at subsequent preparation steps

Wettability interpretation of the NMR log

The same method was applied to the NMR log run in the same well. The additional challenge is now that the Sw=1 response is unknown. However, from the core data it appears that the shape of this response is rather constant, and the position on the T2-axis shifts with permeability. A first estimate of permeability could be obtained from the k-phi correlation. Furthermore, the water saturation could be estimated from the Rxo log which measures the resistivity at about the same depth of investigation as the NMR log. In the process of matching the actual response with the modeled response both permeability and saturation may be adjusted, in addition to the wetting profile. Details of this approach can be found in previous publications [5,7].

An example of the interpretation in the oil zone is shown in Figure 11. Contrary to the situation in the core analysis, the live crude has a much longer relaxation time, which results in a good sensitivity to wettability. The wetting index in the oil zone was found to be 0.5 ± 0.2; this is slightly less waterwet than found in the core analysis. The most likely reason for this difference is the value of the surface relaxivity; we assumed the same value for mineral oil and crude oil as these have not yet been measured. The interpretation of the continuous NMR log, Figure 12, shows that the wetting index gradually changes to fully water-wet over the transition zone towards the OWC; this is expected because in the transition zone a larger portion of the rock remains fully water bearing, and thus has no chance to develop any oil-wetness [8]. This observation is important because, even if transition zone SCAL is lacking, it allows the use of more waterwet flow properties in the transition zone.
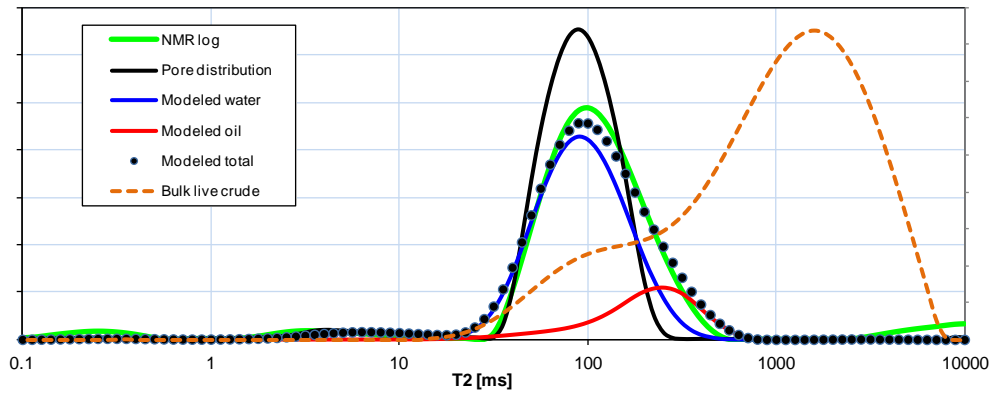
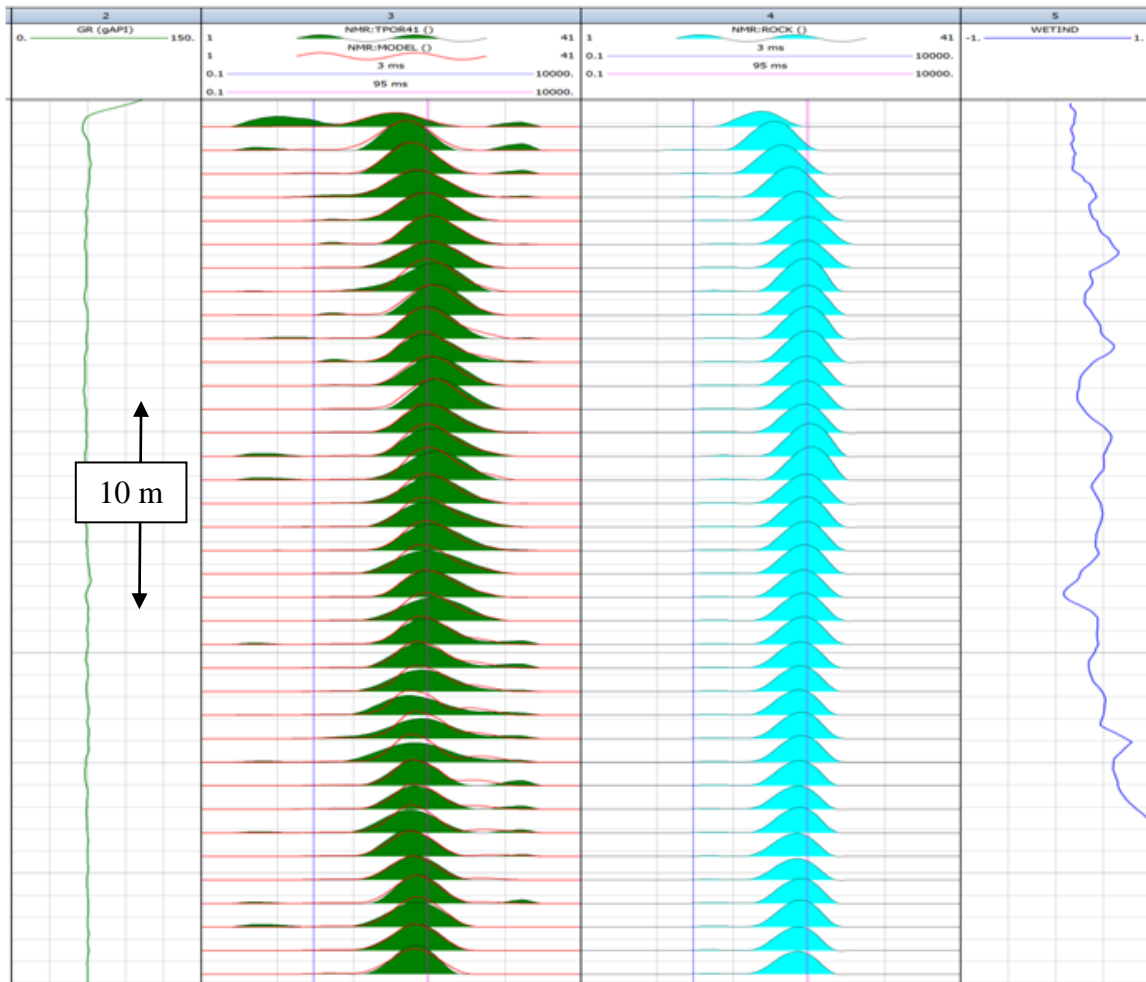Figure 11   Observed and modeled response from the NMR log in the oil zone.

Figure 12   Overlay of the measured NMR log (TPOR) with the modeled result (MODEL), and the modeled water-filled response (ROCK); the derived NMR wettability index (WETIND).

CONCLUSIONS

NMR measurements performed at various stages of Amott and USBM wettability determination show a consistent fairly water-wet wettability (NWI ≈ 0.75 $\pm$ 0.15) for the chalk samples in this study.

Water and oil responses can be precisely modelled for the situations with refined oil.

NMR measurements on samples with crude oil could not be interpreted because the water and oil responses completely overlap.

The NMR Wettability Index correlates well with the Amott and USBM index, but is numerically different because it has a different definition.

NMR-derived saturations are in excellent agreement with independently derived Sw_core values.

Since NMR measurements are non-destructive, they may provide a relatively inexpensive indication of the wettability of samples at any stage of SCAL analyses.

Analysis of the continuous NMR log shows an in-situ wettability of NWI ≈ 0.5 $\pm$ 0.2 in the oil zone, trending to fully water-wet over the transition zone to the OWC.

ACKNOWLEDGEMENTS

REFERENCES

1. Brown, R.J.S., Fatt, I.: "Measurements of Fractional Wettability of Oilfield Rocks by the Nuclear Magnetic Relaxation Method", (1956) Trans. AIME, 207, 262-264.
2. Fleury M, Deflandre F., Quantitative evaluation of porous media wettability using NMR relaxometry. Magn Reson Imaging. 2003 Apr-May;21(3-4):385-7.
3. Howard J.J., 1994, Wettability and Fluid Saturations Determined from NMR T1 Distributions, Magn. Reson. Imaging, vol. 12, no.2, pp 197-200.
4. Looyestijn, W.J. and Hofman, J.P., 2005, Wettability Index Determination by Nuclear Magnetic Resonance, SPE 93624, presented at the MEOS, Bahrain, March 2005. Published in SPEREE April 2006, pp 146 – 153.
5. Looyestijn, W.J., 2007, Wettability Index Determination from NMR Logs, SPWLA 48th Annual Symposium, Austin, TX, paper Q.; published in Petrophysics, April 2008.
6. Suijkerbuijk, B.M.J.M, Hofman J.P., Ligthelm D.J., Romanuka, J., Brussee, N., van der Linde H.A. and Marcelis, A.H.M., 2012, Fundamental investigations into Wettability and low salinity Flooding by Parameter Isolation, SPE 154204.
7. Looyestijn W.J. and Steiner S., 2012, New approach to interpretation of NMR logs in chalks, SPWLA 53rd Annual Symposium, Cartagena, Colombia, paper HH, published in Petrophysics, April 2013.
8. Kovscek, A.R., Wong H., and Radke C.J., A Pore-Level Scenario for the Development of Mixed Wettability in Oil Reservoirs, AIChE J., 39(6), 1072-1085 (1993).

A BLIND STUDY OF FOUR DIGITAL ROCK PHYSICS VENDOR LABS ON POROSITY, ABSOLUTE PERMEABILITY, AND PRIMARY DRAINAGE CAPILLARY PRESSURE DATA ON TIGHT OUTCROPS

Shreerang S. Chhatre[§], Hemant Sahoo [§], Sergio Leonardi [§], Keili Vidal [§], Jennifer Rainey[§], Edward M. Braun[€], and Prateek Patel[§]

§ - ExxonMobil Upstream Research Company, € - Consultant

ABSTRACT

Estimation of reservoir rock properties using multi-scale imaging of the pore structure, followed by mathematical modeling of the segmented images *i.e.* Digital Rock Physics (DRP) is a promising technique. However, DRP workflows are highly variable in terms of imaging tools, resolution of those tools, segmentation algorithms, handling of unresolved porosity, gridding of the resolved pore structure, and mathematical modeling of flow properties. As a result, users familiar with physical measurements of reservoir properties struggle to judge the quality of DRP data, and to incorporate DRP data in commercial workflows in a suitable manner.

In this work, we present a DRP study on tight rocks ($k_{abs} < 10$ mD) conducted at 4 digital vendor labs, anchored to high quality physical measurements conducted in our lab. We selected core plugs from a set of six outcrop rocks. We cleaned the plugs, measured porosity (φ) and absolute permeability (k_{abs}), and then split the plugs in 4 quarters. Four commercial DRP labs conducted blind porosity and permeability predictions on those quarter plugs using (a) only micro-CT based tools, and (b) all the tools accessible to DRP service providers. We also compare primary drainage capillary pressure (P_c) calculated by 4 DRP vendors on quarter plugs with centrifuge based gas-water measurements conducted in-house on companion plugs.

As a result of this blind study, we gained insights into workflows, strengths/weaknesses of DRP predictions carried out by 4 vendors. Various levels of physical measurements (lab-based k_{abs}, and φ data, MICP, or none) are used by different vendors to anchor DRP data. DRP predictions for porosity were from 37% to 96% of the measured values, whereas permeability is within a factor of 0.4 to 4 from the experimental measurements. At low P_c values, predictions by the 4 DRP vendors generally agreed with each other, and with experimental measurements. However, the values diverged significantly at high P_c. Based on this study, we conclude that the dominant source of error in DRP data is highly specific to a given sample, technique, or operator. A lot more uncertainty quantification is necessary to allow DRP data to be used instead of physical measurements for business decisions on tight rocks. We outline learnings for hydrocarbon resource owners and DRP data providers so that commercial workflows could benefit from DRP-based data.

INTRODUCTION

DRP on hydrocarbon reservoir rock aims to provide a pore-scale understanding of the fluid displacement phenomena and predict flow properties of reservoir rocks. Due to recent advances in high resolution imaging and high performance computing, even individual pore-scale flow events can be dynamically observed [1]. Despite significant potential of DRP, the level of confidence to apply DRP data for business decisions is highly variable. The value of DRP data depends on the owner of an asset, expertise of the DRP lab, rock quality/homogeneity, presence of analog data, and timescale of evaluation.

Frederich *et al*. compared DRP with experimentally measured rock properties [2]. They claimed that DRP-based measurements were predictive and approved for business use. Masalmeh *et al*. conducted a joint experimental and DRP-based approach to evaluate the predictive capability of pore-scale modeling for a homogenous carbonate reservoir [3]. They tuned the DRP predictions of primary drainage and primary imbibition capillary pressure to the corresponding experimental data. They used these matched parameters to predict relative permeability and compared with experimental data measured on the same rock samples. They indicated a good match between tuned-DRP and experimental data for water relative permeability, while oil relative permeability showed discrepancies.

Cense and Marcelis compared 3 pore-scale reconstruction and pore-network extraction techniques on high quality sandstones [4]. They observed a 3% mismatch in porosity (φ), and up to a 3x mismatch in permeability (k), indicating a good match in the threshold pressure; but poor match with experimental data regarding the shape and endpoint of the capillary pressure curve. Kalam *et al*. conducted a DRP validation study on 95+ reservoir cores from 4 reservoirs and concluded that DRP is capable of generating fairly accurate SCAL data [5]. Schembre-McCabe *et al*. showed two examples where digital rock data was used along with experimental data to reduce uncertainty to create business value [6]. They found that the image segmentation process is subjective due to the presence of sub-resolution features, and therefore additional independent information can improve the quality of DRP-based predictions. DRP-based predictions have also been used for tight rocks with extremely low permeability or during Enhanced Oil Recovery studies [7] [8] [9] [10]. ExxonMobil Upstream Research evaluated the use of DRP on a Middle Eastern carbonate reservoir for SCAL measurements, and concluded that DRP was unable to provide an acceptable substitute to experimentally measured, high-quality SCAL data [11]. However, since this evaluation the number of DRP service providers, resolution of imaging tools, and the perceived quality of DRP data has improved significantly.

Sorbie and Skauge reviewed the success of pore-scale network modeling for multiphase flow in porous media [12]. They concluded that pore-scale modeling cannot reliably predict two-phase flow functions in pores with mixed wettability in "blind" tests. Therefore in this work, we restricted the scope to water-wet systems. We picked 6 outcrops (3 carbonates, and 3 sandstones), with tight but measurable porosity and permeability. We then compared experimental data for k, φ and primary drainage P_c with values reported by 4 DRP vendors in blind tests for the 6 outcrop plugs.

Objectives of This Study
1) To understand whether porosity (φ), absolute permeability (k), and primary drainage capillary pressure (P_c) can be estimated using DRP for tight rocks
2) To understand the limitations of the technology, which will allow the user to incorporate DRP data in the right context for a given business need
3) To test whether DRP-based predictions are consistent among 4 selected vendors offering commercial DRP services, and whether these values are consistent with physical measurements carried out in our lab
4) To develop a working knowledge about DRP workflows, data quality, and potential pitfalls in interpretations of DRP data
5) To present a "DRP user perspective" and to motivate research on topics that enable the use of DRP data in the right context along with other sources of data

What is Not Addressed in This Study (Out of Scope)
We made best efforts to minimize extraneous variables that might influence the outcome of this study. However, we would like to recognize the following aspects before the reader proceeds to interpret the findings from our study: (1) Proprietary steps in image acquisition and analysis could not be influenced. (2) Only the primary drainage process was evaluated using DRP, as the rock is water-wet during this process. All other displacement processes are expected to be wettability sensitive, and those are beyond the scope of this study. (3) Routine properties (k and φ) were measured in our lab on plugs. Then the plugs were cut in 4 quarters along their axes. The DRP study on quarter plugs was conducted in parallel at 4 vendor sites, so there was no possibility to conduct a "post DRP" measurement in our lab. Primary drainage P_c was measured in our lab on companion plugs, which were chosen based on the good match in their k-φ values (e.g. within 10%) to the DRP plugs, and taken from the same piece of outcrop rock sample.

EXPERIMENTAL PROCEDURE AND DRP WORKFLOWS
Three carbonates – Austin Chalk (AC), Indiana Limestone (I), Carthage Marble (CM), and 3 sandstones – Scioto (S), Torrey Buff (T), and Crab Orchard (CO) were picked (0.01md < k < 1 mD). Plugs were cleaned using a flow-through method with a methanol-water mixture to remove salt from the lubricating fluid used during plugging. Fresh batches of fluids were used intermittently, and the effluent was tested for the presence of salt. Sample cleaning took 1 week for the 4 better quality plugs (AC, I, S, and T), and 3+ weeks for the 2 tightest plugs (CO and CM). Once no salt was detected for 24+ hours, the plugs were dried in a humidity oven to retain clay-bound water. Pore volume, porosity, grain volume, and Klinkenberg corrected gas permeability were measured under a net confining stress of 800 psi (typical condition for routine core analysis). K-φ measurements for the 2 tightest rocks involved special care to avoid artifacts due to leaks, temperature variations in the lab, and large dead volumes. The experimental results are summarized in Table 1 (shaded grey). Plugs were then cut in 4 quarters without using any lubricating fluid and quarters were sent for DRP studies. Companion plugs used for P_c measurements were cleaned following the

same protocol, saturated with brine and centrifuge based primary drainage air-brine P_c measurements were conducted.

In phase I, we restricted the DRP labs to only use µCT based imaging tools that have resolution of ~1 µm. All labs took a scoping scan of the whole plug at a resolution of 20-30 µm to qualitatively evaluate the plug and to select a location for a sub-plug. Vendor C conducted physical poro-perm measurements on the 6 quarter plugs they received. Three vendors (B, C, and D) drilled sub-plugs and imaged the sub-plugs at a higher resolution of ~1 µm. Two vendors (C and D) also conducted Mercury Injection Capillary Pressure (MICP) measurements on part of the quarter plug supplied to them. All vendors used proprietary workflows to segment the collected µCT image to simulate phase distribution and flow. In phase II, the DRP labs used the highest resolution tool available to refine their digitally calculated k-φ values on the same samples. Using either nano-CT or FIB-SEM based tools with resolutions of 20 – 50 nm, DRP labs calculated primary drainage P_c. The P_c results were normalized to a consistent interfacial tension (IFT = 28 mN/m) and contact angle ($\theta = 0°$ for primary drainage) for typical oil-water fluid properties.

RESULTS AND DISCUSSION

Phase I: Porosity (φ) and Absolute Permeability (k) Based on Micro-CT

DRP-based poro-perm results reported by 4 vendors are summarized in Table 1 along with experimental measurements on core plug. For the 2 tightest samples, three vendors were unable to calculate permeability due to lack of sufficient resolution based on the µCT tool to resolve pore throats in the 2 tightest rocks. MICP based pore-throat size distributions for all samples are plotted in Figure 1, and the portions of the pore throat sizes "visible" to the µCT are shaded grey. For the 2 tightest samples (CO and CM), none of the pore throats could be resolved, and therefore no connected pathway could be extracted from µCT images. Reported permeability values from vendor A were based on extrapolation of poro-perm trends from better quality rocks, so permeability of CO and CM reported by vendor A was deemed unreliable and excluded in subsequent analysis.

If the resolved image has a sufficient number of connected pathways, then permeability will be controlled by those dominant pathways. However, a significant number of voxels have a CT contrast in-between the bright grains and dark pores. These voxels containing sub-resolution porosity contribute to the total porosity but may or may not significantly affect the permeability. The CT number of each voxel could be used to calculate the total amount of pore space within that voxel, but the CT number does not indicate how the sub-resolution porosity is distributed and connected within the voxel. Each DRP vendor used their own proprietary poro-perm transforms to handle sub-resolution porosity.

Phase II: k-φ Based on Highest Resolution Tool Available for DRP

Three DRP labs (B, C, and D) used either nano-CT or SEM-based techniques to recalculate k and φ. The hatched area in Figure 1 highlights the new connected pathways visible using nano-CT/SEM but not to µCT based rock evaluation. Vendor A did not have access to any

higher resolution techniques, therefore it did not provided any new data in Phase II. K-φ values in Table 1 indicate that whenever a DRP-based permeability was calculated in phase I, the value did not change appreciably in phase II. This is despite the higher number of pore throats being visualized in phase II. Nano-CT or SEM enabled analysis of the tightest rocks (CO and CM) by resolving pore throats that were previously not resolved using μCT. Therefore, it is essential to use a DRP technique with the appropriate resolution for a given rock fabric and for a desired level of accuracy.

K-φ calculated in phase II using the DRP approach on quarter plugs by 4 vendors are compared against experimentally measured values on the intact plug in Figure 2. Porosity calculated from imaging was found to be less than the measured porosity, *i.e.* all points in Figure 2(a) lie below the 45 degree line. Slopes of the best fit lines through the 6 data points for each vendor indicate the fraction of total porosity captured using DRP. Vendors B and C reported the maximum (86% and 96% respectively) fraction of measured porosity. However, it is important to remind the reader that vendor C carried out physical measurements for k and φ on their quarter samples. Therefore, vendor C had an opportunity to compare DRP predictions with physical measurements on the same sample, while the other 3 vendors did not. Vendor A reported 72%, whereas D could visualize only 37% of the total porosity. The slopes calculated above are based on at best 6 pairs of data (3 carbonates and 3 sandstones). The regression minimizes the sum of squares of the error between DRP data and a model, so the slope is biased by higher porosity rocks. Therefore, these slopes should not be used in a quantitative manner.

A similar regression exercise is summarized for absolute permeability in Figure 2(b). DRP-based permeability data on 4 quarters of the same plug had a variation of up to one order of magnitude. Based on a regression model, vendors A and C over predicted permeability by a factor of 4.4 and 1.6, respectively. On the contrary, B, and D under predicted lab measurements of permeability by a factor of 0.49 and 0.40, respectively. The caveat about physical measurements carried out by vendor C applies here as well. Vendor A systematically over predicted DRP permeability compared to experimentally measured data. DRP workflow employed by vendor A was the simplest of the 4 vendors evaluated in this study. Vendor A takes a single CT scan of the whole plug, and runs a DRP simulation to get "digital" k and φ values. The vendor has conducted physical and DRP measurements on numerous sandstones and carbonates. From this catalog, vendor A derived an empirical correlation between digital and physical values. The "digital" values obtained from imaging were plotted on this catalog, and "corrected digital" values were reported. From the cross-plot, it is clear that vendor A under predicts porosity, while systematically over predicting permeability.

Vendor B did not perform any physical measurement or benchmarking. They slightly under predicted porosity, while under predicting permeability by a factor of 2. Vendor D's workflow involves MICP measurements, which were used to select optimal imaging parameters. Vendor D did not use MICP as a fitting parameter. Vendor D systematically under predicts both k and φ. Vendor C also took a scoping scan followed by a detailed scan

on a mini-plug, as well as conducted a physical MICP experiment on part of the sample. They measured k and φ experimentally on the quarter plugs, but claimed that the physical data was not used in any benchmarking of digital P&P data. DRP data reported by vendor C slightly under predicts porosity, while over predicting permeability by 60%.

Based on the numbers from Table 1 and Figure 2, the variation among the 4 DRP vendors seems unacceptable. Possible reasons for the mismatch include (1) imaging of non-representative elements, (2) issues with segmentation, (3) inaccurate physical measurements, or (4) inherent variability within a core plug. Three vendors conducted a scoping scan to pick the best region to investigate in detail, but still the issue of non-representative sampling cannot be discounted. Segmentation algorithms are proprietary for all vendors, so we could not understand their differences, or whether any algorithm could lead to systematic errors. Segmentation is not completely automated, so some degree of subjectivity might be involved. The DRP vendors could not quantify the level of uncertainty in segmentation. In contrast, physical measurements were conducted on an experimental setup where the pressure transducers and pump flow rates have been calibrated against traceable standards. We took utmost care to minimize and quantify leaks and dead volume, and all measurements were repeated 3 times. Uncertainty in measurements was found to be smaller than the size of the symbol plotted in Figure 2 for the 4 higher quality outcrops. For the 2 lower quality samples, uncertainty in porosity was about 2% (as shown in Table 1).

Phase II: Primary Drainage Capillary Pressure (P_c) Measurements Using DRP
Vendors B, C, and D used a combination of µCT and higher resolution techniques, whereas vendor A used only µCT images to derive P_c (Figure 3, assuming oil-water IFT γ_{ow}= 28 mN/m.) MICP data are also rescaled for water-oil IFT and plotted. For conventional systems, primary drainage P_c is crucial to determine the original in-place volume, to calibrate well log data, and to quantify the transition zone. In Figure 3, oil-water P_c is plotted up to 160 psi, which will correspond to more than 1000 feet oil column above free water level assuming typical light oil and brine properties.

DRP data from the 4 quarters are consistent with MICP measurements on 2 out of the 4 quarter plugs for the Austin Chalk outcrop in Figure 3(a). DRP data from B (■) indicate higher irreducible water saturation (S_{wir}) than C (▲). DRP-based P_c data from A (◆), and D (●) are measured only up to 5 psi and 25 psi respectively, so we could not define the asymptotic S_{wir} from these 2 datasets. Vendor A used only µCT based images with a nominal resolution of 1 µm, so it was expected that vendor A would only be able to define part of the capillary pressure curve. For a simplistic pore model with a spherical geometry, capillary pressure (P_c) can be converted to pore-throat radius (r) using the Young-Laplace equation $P_c = 2\gamma_{ow} \cos\theta / r$. When images are acquired at a resolution of 1 µm, we expect digital P_c up to about 15 psi. When the image resolution is ~40 nm, the highest reported P_c is expected to be ~400 psi.

MICP can measure P_c to a significantly higher value than DRP-based predictions, however, several limitations with MICP are documented in literature [13] [14]. Mercury is not a reservoir fluid, and it interacts with the rock differently than oil, water, or gas. Due to extremely high pressures imposed at the end of a MICP test (~60,000 psi), mercury can damage clays and intricate pore structure, leading to non-representative S_{wir} values. MICP data can also be erroneous due to conformance correction or lack of sufficient equilibration time at each pressure step [15]. DRP data by C (▲) in Figure 3(a) track closely with MICP (▬) measured on part of the same quarter of the Austin Chalk outcrop plug, even at high pressures. As a result, C reported S_w < 2% at the highest DRP-based P_c = 130 psi. Displacement of water to such low saturation seems surprising given the low permeability of the rock. S_{wir} extrapolated from DRP data from B and D are in the 10-20% range, which appears reasonable. For Austin Chalk, the DRP-based P_c measured by B, C, and D using different workflows match well at low P_c values. A (♦) under predicted P_c, possibly due to strong anchoring to an erroneous MICP-based model.

Primary drainage P_c was calculated on 3 other outcrops and plotted in Figure 3. DRP predictions for "I" indicate higher variation within the 4 DRP vendors. When S_w > 0.6, DRP data from vendors A, B and C agree, whereas for S_w < 0.6, C (▲) reported significantly higher capillary pressure than B (■) and D (●). For S_w < 0.6, P_c is controlled by submicron pore throats, *i.e.* micrite in carbonates. According to the MICP pore throat distribution in Figure 1, "I" has a much wider pore throat size distribution than "AC" and has significant number of pores in the sub-micron scale. Therefore, treatment of micrite using multi-scale imaging techniques in DRP becomes much more crucial for *I* compared to AC. Although, vendors B, C and D had sufficient resolution to visualize most of the micritic porosity in these rocks, they used different techniques to transition from P_c controlled by larger pore throats to P_c controlled by micrite. Differences in these proprietary workflows associated with this transition could be a reason for this mismatch.

Another important finding is the inconsistency between the MICP-based P_c curve measured by C (▬) and D (▬) on their respective quarter plugs. For all 4 higher permeability samples, C reported a more optimistic (lower P_c at a given S_w) P_c curve than vendor D. Sample heterogeneity is unlikely as the data are based on 2 quarters of the same plugs. D (▬) selected fewer pressure steps than C (▬), so we postulate that the differences in the experimental protocol might be the reason for this mismatch. Given the low quality of these samples, it is likely that relative permeability effects interfered with MICP [15]. This interference might have contributed to the mismatch between MICP reported by C and D. If the data were affected by any relative permeability artifact, the real P_c curve could be even more optimistic than MICP-based curve from C (▬).

Comparison of DRP-Based Pc with Centrifuge Measurements

A set of companion plugs from the 4 better quality outcrops (AC, I, S, and T) were used for centrifuge based primary drainage gas-brine P_c measurements. Based on the MICP and poro-perm measurements on the two tighter samples (CO and CM), it was estimated that the conventional centrifuge would not provide sufficient driving force to displace fluids

out of these rocks. Therefore, P_c was not measured using a centrifuge for these 2 plugs. Average saturations obtained from the centrifuge tests were converted to face saturations using the Hassler-Bruner technique. A power-law relationship between normalized water saturation (S_{wn}) and capillary pressure *i.e.* $P_c = P_{cth} + A(S_{wn}^B - 1)$ was assumed, where $S_{wn} = (S_w - S_{wir})/(1 - S_{wir})$. Irreducible water saturation (S_{wir}), threshold capillary pressure (P_{cth}), and two other fitting parameters in the model (A, and B) were varied to obtain a set of solutions for which calculated average saturations at each centrifuge speed are within 2% of the experimental values. From these solutions, centrifuge based optimistic bound (COB), and pessimistic bound (CPB) were chosen and plotted in Figure 4. P_c calculated by 4 DRP vendors, along with 2 MICP measurements were re-scaled to gas-brine fluid properties (IFT = 72 mN/m) and plotted alongside experimentally calculated bounds.

A comparison of DRP and physical measurements in Figure 4 indicates that both datasets agree at low P_c, but diverge as S_w declines and P_c increases. In general, the agreement is better for the 2 sandstones compared to 2 carbonate samples. A comparison of MICP and centrifuge P_c data indicates that MICP erroneously asymptotes towards $S_{wir} = 0$, which might lead to overestimation of the in-place hydrocarbon volumes. We have high confidence in centrifuge based measurements for capillary pressure, due to validation with the porous plate technique and decades of experience comparing those data with saturations found in hydrocarbon reservoirs. DRP based P_c measurements by A ($\blacklozenge$) and C ($\blacktriangle$) are anchored to MICP data. Therefore these DRP data are expected to have the shortcomings of the underlying MICP data. DRP data from B and D are not anchored to MICP, however those data differ from experimental measurements as shown in Figure 4. In general, DRP-based P_c data appear more optimistic *i.e.* indicate a higher amount of hydrocarbon in-place compared to centrifuge measurements. Due to large differences between centrifuge vs. DRP-based P_c data, we recommend that DRP-based Pc data should not be used for in-place estimation in absence of calibration to experimental data.

Centrifuge based optimistic (COB) and pessimistic bounds (CPB) indicate the level of uncertainty based on experimental data. Uncertainty in DRP-based P_c is non-trivial to calculate, and not reported by any DRP vendor in this study. In the absence of uncertainty quantification of DRP-based data, it becomes hard to compare it against P_c data measured using centrifuge. Therefore, we recommend that the DRP vendors should comment about level of uncertainty in the P_c calculations so that the data can be used in the right context.

CONCLUSION
DRP-based k, φ and primary drainage Pc data: DRP based data reported by 4 vendors did not quantitatively match the physical measurements for *k*, *φ* and primary drainage P_c carried out at our lab, despite commercial DRP services being available for almost 10 years. So, we suggest caution when using DRP results in a quantitative manner without validation with experimental data on at least a subset of plugs. DRP-based permeability was off by a factor of up to 4x, whereas porosity was off by up to 60% for tight rocks. The *k-φ* trends reported by each vendor are internally consistent, and clustered around physical data. However, the DRP predictions for *k-φ* are not consistent among the 4 selected vendors, e.

g. up to 1 order of magnitude scatter in permeability. DRP-based P_c data agreed with centrifuge data at low values of P_c, but deviated at higher values.

DRP workflows and user's perspective: We gained working knowledge about the DRP service offered by each vendor in terms of the number of scans with various resolutions and degrees of experimental calibration. Plug selection, imaging, segmentation, and modeling can all introduce errors. Dominant sources of error could be highly specific to a given sample, technique, or operator. Most physical measurements are carried out on a plug-scale, whereas most DRP measurements are carried out on multiple length scales like plugs (1 inch), sub-plugs (mm), and SEM images (10 – 100 µm). Representative sampling and upscaling techniques are available and employed to overcome this problem. However, a user should be careful when dealing with DRP data for heterogeneous rocks. Currently, DRP service providers typically provide one value of a rock property, without providing any quantification of uncertainty. DRP measurements are carried out on a voxel scale, which allows the technique to quantify heterogeneity of the plug/mini-plug. Such analysis should be utilized to quantify error and uncertainty. Uncertainty quantification in DRP-based data is necessary to enable appropriate comparisons with physical measurements and improve the utility of DRP data for subsurface assessments.

ACKNOWLEDGEMENTS

REFERENCES
[1]   S. Berg, H. Ott, S. A. Klapp, S. A., R. Neiteler, A. Makurat, L. Leu, F. Enzmann, K. M. Schwarz J., S. Irvine and M. Stampanoni, "Real-time 3D imaging of Haines jumps in porous media flow," PNAS, vol. 110, no. 10, pp. 3755-3759, 2013.

[2]   J. T. Fredrich, D. L. Lakshtanov, N. M. Lane, E. B. Liu, C. S. Natarajan, D. M. No and J. J. Toms, "Digital Rocks: Developing An Emerging Technology Through To A Proven Capability Deployed In The Business," in SPE Annual Technical Conference and Exhibition, Amsterdam, Netherlands, 2014.

[3]   S. Masalmeh, X. Jing, S. Roth, C. Wang, H. Dong and M. Blunt, "Towards Predicting Multi-Phase Flow in Porous Media Using DRP: Workflow to Test Predictive Capability of Pore-Scale Modeling," in Abu Dhabi International Petroleum Exhibition and Conference, Abu Dhabi, UAE, 2015.

[4]   A. Cense and F. Marcelis, "A Comparative Study of Three Pore-scale Reconstruction and Pore-Network Extraction Techniques," in Annual Symposium of the Society of Core Analysts, Abu Dhabi, UAE, 2008.

[5]   Z. Kalam, M. Gibrata, M. Al Hammadi, A. Mock and O. Lopez, "Validation of DRP Based Water-oil Capillary Pressure and Saturation Exponents in Super Giant Carbonate Reservoirs," in SPE Middle East Oil and Gas Show and Conference, Manama, Bahrain, 2013.

[6]   J. Schembre-McCabe, R. Salazar-Tio and J. Kamath, "Two Examples of Adding Value through Digital Rock Technology," in The Annual Symposium of the Society of Core Analysts, Aberdeen, Scotland, UK, 2012.

[7]   M. A. Gibrata, V. D. R. and S. Geiger, "Pore Scale Modeling and Its Advantage for EOR of Near Miscible 3-Phase Flow WAG Flooding in Carbonate Reservoir," in International Petroleum Technology Conference, Kuala Lumpur, Malaysia, 2014.

[8]   H. Li, M. Dawson and D. C. Standnes, "Multi-Scale Rock Characterization and Modeling for Surfactant EOR in the Bakken," in SPE/CSUR Unconventional Resources Conference, Calgary, Alberta, Canada, 2015.

[9]   N. Fishman, J. Guthrie and M. Honarpour, "The Stratigraphic Distribution of Hydrocarbon Storage and its Effect on Producible Hydrocarbons in Eagle Ford," in Unconventional Resources Technology Conference, Denver, Colorado, USA, URTeC 1579007, 2013.

[10]   A. Almarzooq, T. Al-Ghamdi, S. Koronfol, M. Dernaika and J. Walls, "Shale Gas Characterization and Property Determination by Digital Rock Physics," in SPE Saudi Arabia Section Annual Technical Symposium and Exhibition, SPE 172840, 2014, 2014.

[11]   K. Guice, L. Lun, B. Gao, R. Gupta, G. Gupta, J. G. Kralik, R. Glotzbach, E. Kinney, G. Leitzel, J. Rainey, R. Kudva and M. O. Al Jawhari, "An Evaluation of Digital Rock Physics Technology for the Prediction of Relative Permeability and Capillary Pressure for a Middle Eastern Carbonate Reservoir," in IPTC, Doha, Qatar, 2014.

[12]   K. S. Sorbie and A. Skauge, "Can network modeling predict two-phase flow functions?," in Annual Symposium of the Society of Core Analysts, Austin, TX, 2011.

[13]   H. N. Greder, V. Gallato, D. Laran, V. Munoz and O. d'Abrigeon, "Forty Comparisons of Mercury Injection Data with Oil/water Capillary Pressure Measurements by the Porous Plate Technique," in Annual Symposium of the Society of Core Analysts, paper 9710, Calgary, Canada, 1997.

[14]   J. Shafer and J. Neasham, "Mercury Porosimetry Protocol for Rapid Determination of Petrophysical and Reservoir Quality Properties," in Annual Symposium of the Society of Core Analysts, Abu Dhabi, UAE, 2000.

[15]   J. G. Maas, N. Springer and A. Hebing, "Relative Permeability Effects Overlooked in MICP Measurements - Transition Zones Likely to be Smaller," in Annual Symposium of the Society of Core Analysts, Snowmass, Colorado, USA, 2016.

Table 1. Porosity (φ, %) and absolute permeability (k, mD) measurements (shaded grey) with DRP-based predictions by 4 vendors based on micro-CT workflow (resolution ~ 1 µm, phase I), and based on a combined micro-CT and SEM or nano-CT based workflow (resolution ~ 40 nm, phase II) are summarized.

| Phase I (µCT only)	Lab φ (%)	DRP A	B	C	D	Lab k (mD)	DRP A	B	C	D
Austin Chalk (AC)	29	17.80	22.37	29	9.35	7.81	35.2	■	8.8	3.104
Indiana Limestone (I)	17	12.70	19.49	16.50	6.44	5.92	24.9	26	15.2	2.409
Carthage Marble (CM)	2 – 4	4	2.35	■	0.70	0.002	0.036	■	■	■
Scioto Sandstone (S)	18	15.40	15.15	17.50	8.58	1.38	8.1	0.6	1.2	0.539
Torrey Buff (T)	16	15.50	14.22	7.50	6.33	1.2	3.9	1.7	1.13	0.337
Crab Orchard (CO)	4 – 6	1.10	6.10	■	4.17	0.005	0.001	■	■	■
Phase II (all tools)		A	B	C	D		A	B	C	D
Austin Chalk (AC)	29	17.80	22.37	29	6.87-10.40	7.81	35.2	5.4	8.8	1.43
Indiana Limestone (I)	17	12.70	19.49	16.50	6.44	5.92	24.9	31.6	14.2	2.41
Carthage Marble (CM)	2 – 4	4	2.35	1.3	0.70	0.002	0.036	0.008	0.001	■
Scioto Sandstone (S)	18	15.40	15.15	18	8.58	1.38	8.1	1.5	1.2	0.54
Torrey Buff (T)	16	15.50	14.22	13.6	6.33	1.2	3.9	0.8	1.3	0.34
Crab Orchard (CO)	4 – 6	1.10	6.10	4.3	4.17	0.005	0.001	0.002	0.008	■
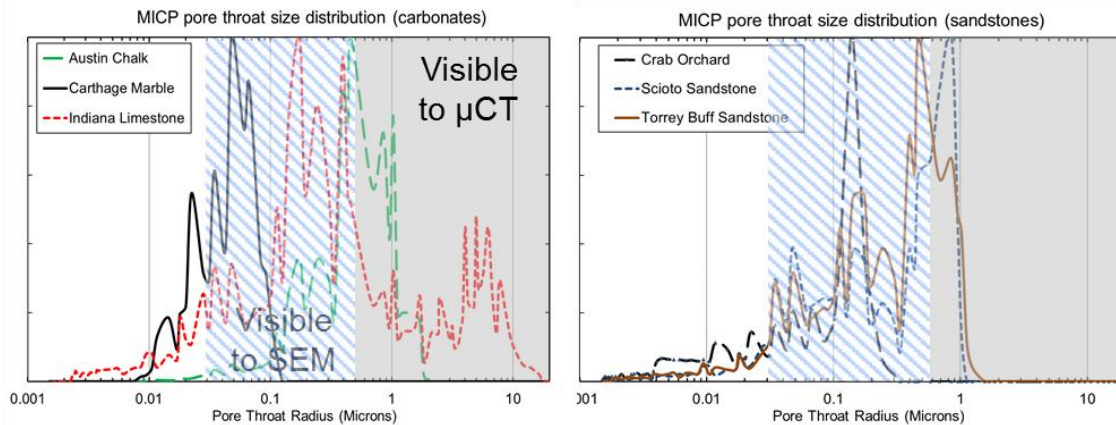
Figure 1. Pore throat size distribution interpreted from MICP measurements on all 3 carbonates (left), and 3 clastics (right) outcrop conducted on portions of the quarter plugs supplied to vendor C. Shaded area represents the pore throats visible to µCT, whereas the hatched area indicates the pore throats visible in a SEM with 40-50 nm resolution that are not visible during µCT based evaluation.
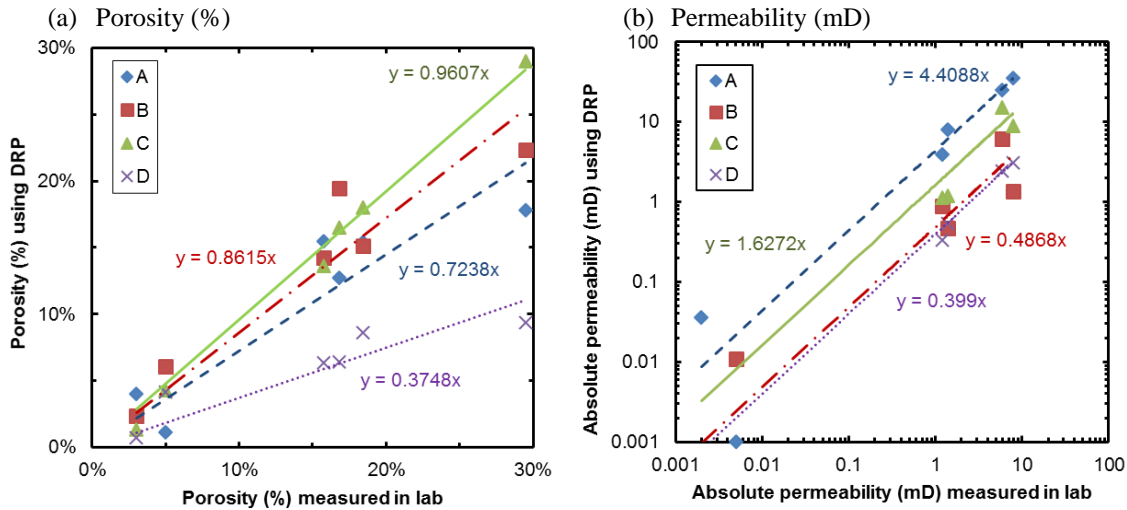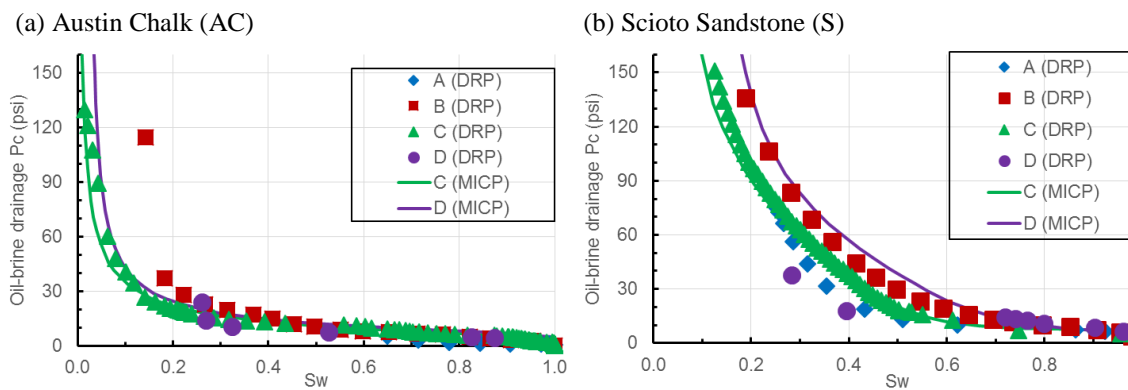

Figure 2. Cross-plots of (a) porosity (%), and (b) permeability (mD, log scale) measurements in lab vs. calculated using DRP based on highest resolution tool by 4 DRP vendor labs are shown.
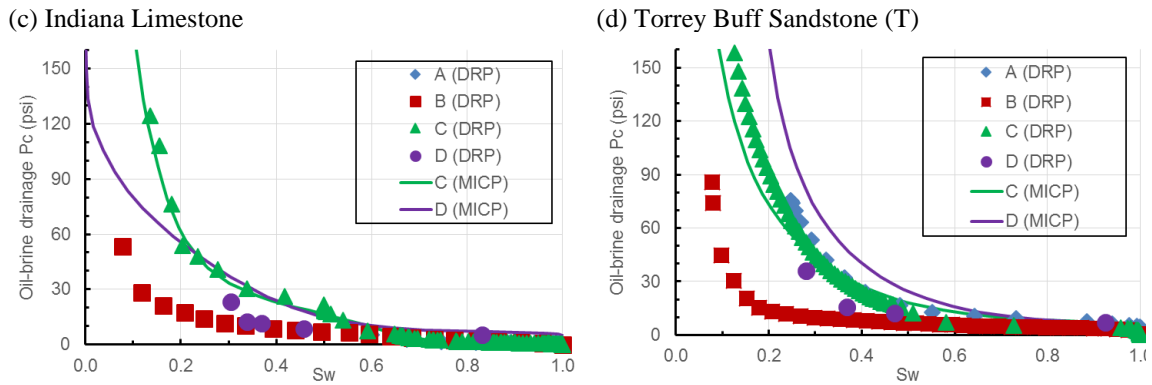
Figure 3. A comparison of DRP-based primary drainage P_c for Austin Chalk (AC), Indiana Limestone (I), Scioto (S), and Torrey Buff (T) calculated by 4 vendors is plotted along with IFT-scaled MICP curve.
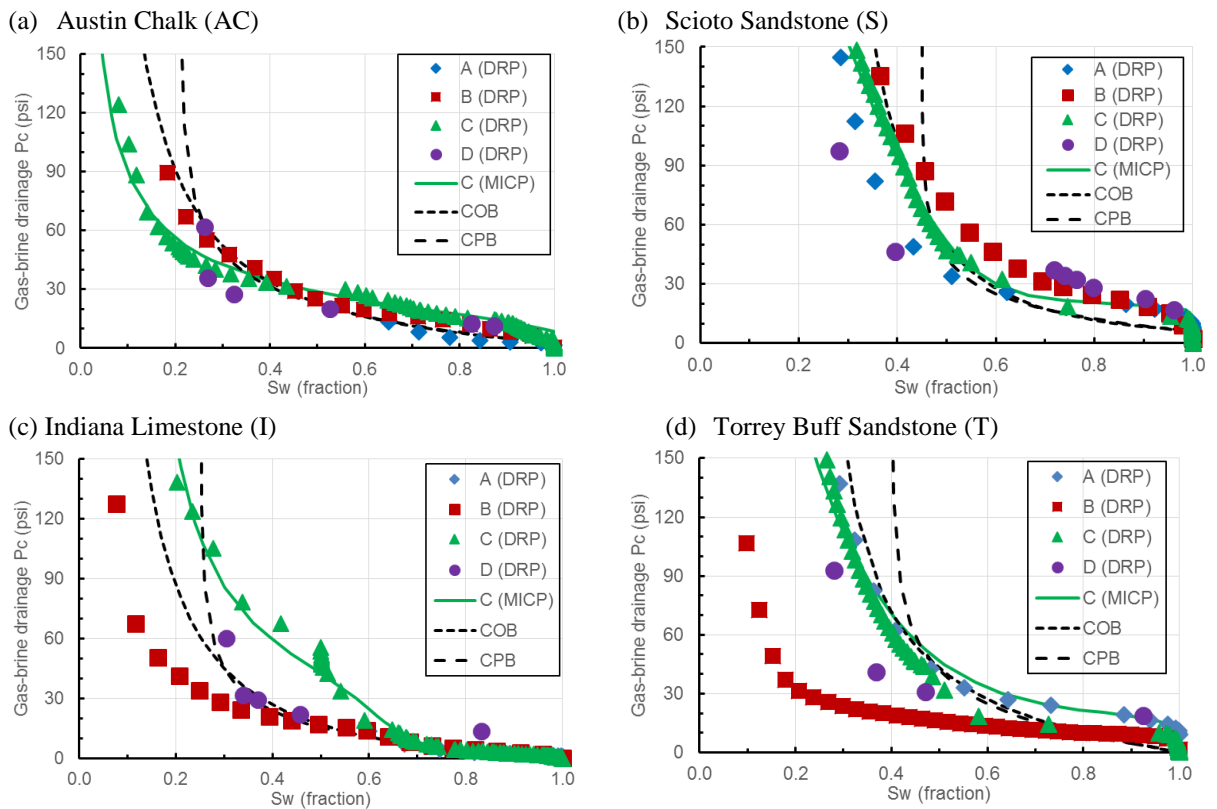

Figure 4. A comparison of DRP-based primary drainage P_c by 4 vendors on four quarters of the same plugs, along with MICP measurements conducted by vendor C on parts of the quarter plugs. Centrifuge based optimistic bound (COB) and pessimistic bound (CPB) are plotted for comparison for the four outcrops.

PORE-SCALE DISPLACEMENT DURING FAST IMAGING OF SPONTANEOUS IMBIBITION

W.-B. Bartels[1,5], M. Rücker[2,5], M. Boone[3], T. Bultreys[2,4], H. Mahani[5], S. Berg[5], S.M. Hassanizadeh[1] and V. Cnudde[4]

[1] Earth Sciences department, Utrecht University, 3584 CD Utrecht, NL
[2] Department of Earth Science and Engineering, Imperial College London, SW7 2AZ UK
[3] XRE, Technologiepark-Zwijnaarde, 9052 Ghent, BE
[4] UGCT- PProGRess, Ghent University, Krijgslaan 281 S8, 9000 Ghent, BE
[5] Shell Global Solutions International B.V., Kesslerpark 1, 2288 GS Rijswijk, NL

ABSTRACT

Amott spontaneous imbibition tests are well-established methods to investigate wettability and wettability alteration in oil saturated rock samples. Usually the cumulative volume of produced oil versus time is used as qualitative indicator of the wettability or wettability alteration of the sample. In this study, we used fast X-ray CT imaging aimed at linking the observed oil production to underlying pore-scale processes. In this study, we developed novel core holders suited for HECTOR (Higher Energy CT Optimized for Research) micro-CT scanner and EMCT (Environmental Micro-CT) scanner from the Centre for X-ray Tomography of the Ghent University (UGCT). We demonstrate these capabilities for a crude oil-brine-carbonate rock (Ketton) system to visualize the pore-scale fluid distribution during Amott tests. We performed experiments on mini-plugs (diameter: 4 mm, length: 20 mm) to capture dynamic processes during spontaneous imbibition by fast imaging (up to 15s per full rotation) with a voxel size of 13 µm and SCAL plugs (diameter: 2.54 cm, length: 5 cm). We monitored oil configuration changes over a period of several months, to verify consistency of oil production behaviour across length scales. After initialization with oil and water, the samples were surrounded by formation water for imbibition. From 3D reconstructed and segmented images, we observed movement of the oil phase in the pore space of the rock in real time in water-wet (mini-plug and SCAL plug) and mixed-wet (SCAL plug) systems. Both the mini-plug and SCAL plug seemed to show preferred production sites. Furthermore, the pore-scale images of the mini-plug showed production due to snap-off in boundary adjacent pores. The pore-scale information aids in assessing the standard sample preparation and handling protocols in Amott tests. Moreover, the pore-scale information was used to interpret the cumulative production versus time curve of the SCAL plugs.

INTRODUCTION

Spontaneous imbibition is the capillary-driven invasion of wetting-phase into the pore-

space of a porous medium, thereby displacing a non- or less-wetting phase initially in place. This process is seen in daily life when ink sinks into paper or water infiltrates soils. The process is also relevant in petroleum engineering. For instance, spontaneous imbibition occurs in an unsteady state displacement where in absence of capillarity we have a shock-front, but in presence of capillarity the shock-front becomes a smooth curve. Also, spontaneous imbibition plays a role in recovering oil from matrix blocks surrounded by fractures.

The imbibition capillary pressure-saturation curve consists of a forced and a spontaneous part. The forced part is measured in centrifuge or porous plate set-up. The spontaneous part is measured in tests such as the Amott test [1, 2], see Figure 1a, which ultimately provides a value for the saturation at a capillary pressure of zero. These laboratory tests are numerous [3-6]. The main variable that is measured in these tests is cumulative oil production versus time, see Figure 1b. With the part of the capillary pressure curve obtained from this data, these tests aim to indicate the (change of the) wettability state by assigning an index to the crude oil, brine, rock (COBR) system, see Figure 1c. Since wettability influences flow behavior, an accurate representation of the wettability of a rock type is imperative in predicting flow dynamics.

To make sure the variation in capillary pressure curves is because of wettability, different scaling groups were proposed to eliminate the effect of initial water saturation, mobility and viscosity, and interfacial tension variations, e.g. [7-9], on the cumulative production versus time curves. It has been shown that in many cases of uniform wettability, the scaling groups are effective [8]. However, [10] has shown that natural systems are most likely mixed-wet systems because of the connate water that is in the pore-space which prevents direct contact between oil and rock. Besides, there are general problems with wettability indices. For instance, indices computed from the Amott and USBM methods are often misleading when it comes to predicting sample wettability and associated flow behavior [11]. One reason for this is that the index represents a non-unique measure of wettability since different combinations may lead to the same index.

In summary, at least for mixed-wet systems, the wettability index that followed from curves of total production versus time, may not reflect the wettability following from the sum of the local pore-space wettability states. Since wettability finds its origin below the core scale, this is not necessarily surprising. Therefore, interpretation of the production curves and consequently wettability may be improved by adding the pore-scale information, as suggested by [12]. In addition, pore-scale information can be used to verify the experimental protocols for Amott tests. Issues like trapped gas or a significant capillary end-effect that may impact the result can be detected. In this study, we use SCAL plugs to examine those two effects.

Finally, there is the fundamental question about where and how the oil is produced from the sample. To address this question, we use a water-wet mini plug, because there is often no onset before spontaneous imbibition starts in water-wet systems. This eliminates some uncertainty in monitoring the dynamics of spontaneous imbibition. The visualized volume contains both (part of) the sample and the surrounding fluid, making this a suitable dataset for pore-scale simulation of the imbibition process as suggested by [12].
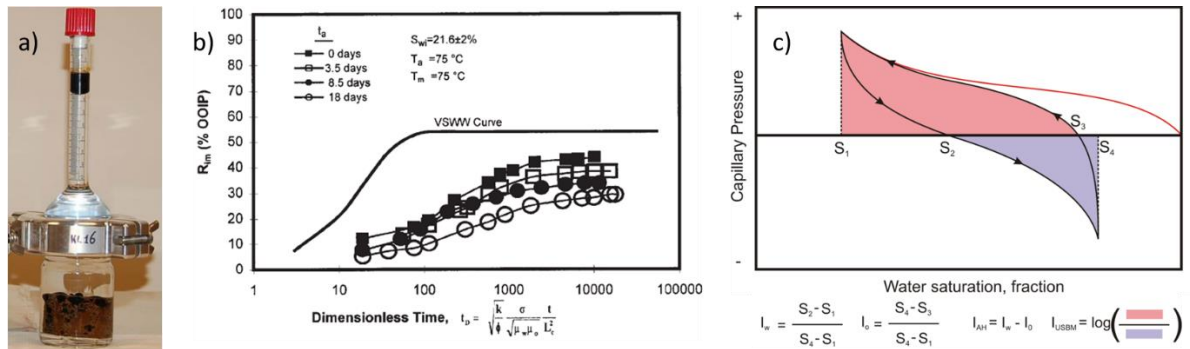
Figure 1: a) Amott spontaneous imbibition test with all faces open. b) Example of spontaneous imbibition oil production versus time and as function of ageing, after [3]. c) Definitions of wettability indices, taken from [13].

We used three novel set-ups in combination with HECTOR and EMCT micro-CT scanners [14, 15]. The imaging systems were developed by the Centre for X-ray Tomography of the Ghent University (UGCT, www.ugct.ugent.be) in collaboration with XRE (www.xre.be). They were used to visualize the pore-scale fluid distribution during Amott tests. We present pore-scale behavior as well as the observed cumulative oil production versus time curves.

MATERIALS AND METHODS

Crude oil, brine, rock systems

For the experiments, we used Ketton carbonate (Oolite) rock [16], porosity $\varphi_{MICP} = 23\%$ and $K_{brine} = 5.7$ Darcy, formation water (FW) (density $\rho = 1.152$ g/cm^3, viscosity $\mu = 1.550$ mPa·s, at T = 20°C, composition see Table 1), decane ($\rho = 0.730$ g/cm^3, $\mu = 0.920$ mPa·s, at T = 20°C) and crude oil ($\rho = 0.8833$ g/cm^3, $\mu = 11.486$ mPa·s, at T = 20°C, composition see Table 2). Both decane and crude A were doped with 20 wt% Iodo-decane to obtain higher X-ray attenuation.

Table 1: Composition of FW

Ion	Na$^+$	K$^+$	Mg^{2+}	Ca^{2+}	Sr^{2+}	Cl$^-$	SO$_4^{2-}$	HCO$_3^-$	TDS	Ionic Strength [mol/L]	pH
FW [mg/L]	49.9	0	3.25	14.5	0	112	234	162	180	3.659	6.9

Table 2: Crude oil specification

IFT FW – doped crude oil	TAN (mg KOH/g)	TBN (mg KOH/g)	Asphaltene (g/100ml)
20 mN/m @ 20°C	0.5	1.0	0.244

A list of systems used in this study, together with their initialization methods can be found in Table 3. The mini-plugs were difficult to machine to the desired diameter; they would easily break. Therefore, the mini-plugs that survived contained a higher volume percentage of cement compared to the SCAL plugs. Cement contains micro-porosity that

cannot be resolved in the used micro-CT scanners and can make up to 40% of the total porosity in Ketton (see Figure 3) which is consistent with the initial water saturations for the SCAL plugs. In that case, the role of the water saturated micro-porosity is limited to slightly increasing the water connectivity. In addition, since the pores in the observable pore-space are well connected, there should not be events in the micro-pores.

Table 3: List of samples used in this paper. We used two types of plugs: small SCAL plugs (5 cm length and 2.54 cm diameter) and mini-plugs (20 mm length and 4 mm diameter). The initial water saturation (S_{wi}) excludes the water in the micro-pores for the mini-plug. The oil phases were doped with 20 wt% Iodo-decane.

Rock	Oil phase	S_{wi}	Desaturation	Ageing	Wetting
KET1_06	Decane	0.37	Centrifuge	40°C/24 hrs	Water-wet
KET1_08	Crude oil	0.34	Centrifuge	40°C/24 hrs	Mixed-wet
KET1_09	Crude oil	0.38	Centrifuge	40°C/24 hrs	Mixed-wet
Mini-plug	Crude oil	0.06	Flooding	40°C/24 hrs	Water-wet

Experimental workflow
Sample saturation
Both the SCAL plugs and the mini-plugs were saturated by placing the samples in a sleeve and applying vacuum (~10^{-2} mbar). Subsequently, de-aerated FW was added. As final step, the samples were placed in a pressure chamber at 30 bars for two hours to dissolve any gas bubbles that may still exist in the sample.

Sample desaturation: centrifuge and micro-coreholder
The SCAL plugs were brought to initial water saturation in a centrifuge (URC-628, Coretest Systems Inc., used at 3500 RPM for SCAL plugs) in 24 hours. To prevent gradual heating during centrifuging, the temperature was fixed at 40°C. By automatic recording of the production and material balance calculation, initial water saturations shown in Table 3 were achieved. Because centrifuging was done at elevated temperature, aging of the rock took place for the samples saturated with crude oil. Therefore, we ended up with one water-wet SCAL plug and two mixed-wet SCAL plugs, see Table 3.

For the mini-plug, we used a specially designed micro-coreholder to (de-)saturate the samples by flooding, see Figure 2a. The core holder consisted of Hastelloy steel and X-ray transparent polyether ether ketone (PEEK). This way, the saturation state of the sample could be monitored during or after (de-)saturation. The bottom of the cell consisted of a pressure vessel that regulated the sleeve pressure, which was set by water (up to 30 bars). Because of the pressure vessel there was no need to keep any pressure line attached to the set-up, allowing 360 degrees rotation in a micro-CT scanner. The micro-coreholder could be used for both static (e.g. aging tests) and dynamic (e.g. flow tests) experiments at elevated temperatures up to 80°C. Properties of the mini-plug can be found in Table 3.

Experimental protocols
We used standard experimental protocols for SCAL spontaneous imbibition tests. An exception was the aging for SCAL plugs as addressed above. One part of the SCAL plug Amott protocol is to roll the sample on a tissue saturated with oil to remove oil attached to the outside of the sample. However, this may create suction on the surface pores if the

tissue is not wet enough or it may not remove all oil from the outside of the sample when the tissue is too wet. Both scenarios may influence the cumulative oil production versus time curve. Still, it was decided to adhere to the standard protocols. For mini-plugs, similar protocols were used. However, because of the small volume of resolvable pore space and because the production was not measured, it was decided to refrain from rolling this sample. In addition, because spontaneous imbibition may be a sub-second process, it is relevant to note that the delay between filling the cells with brines and starting of the scans was around one minute for the mini-plugs and around five minutes for the SCAL plugs.
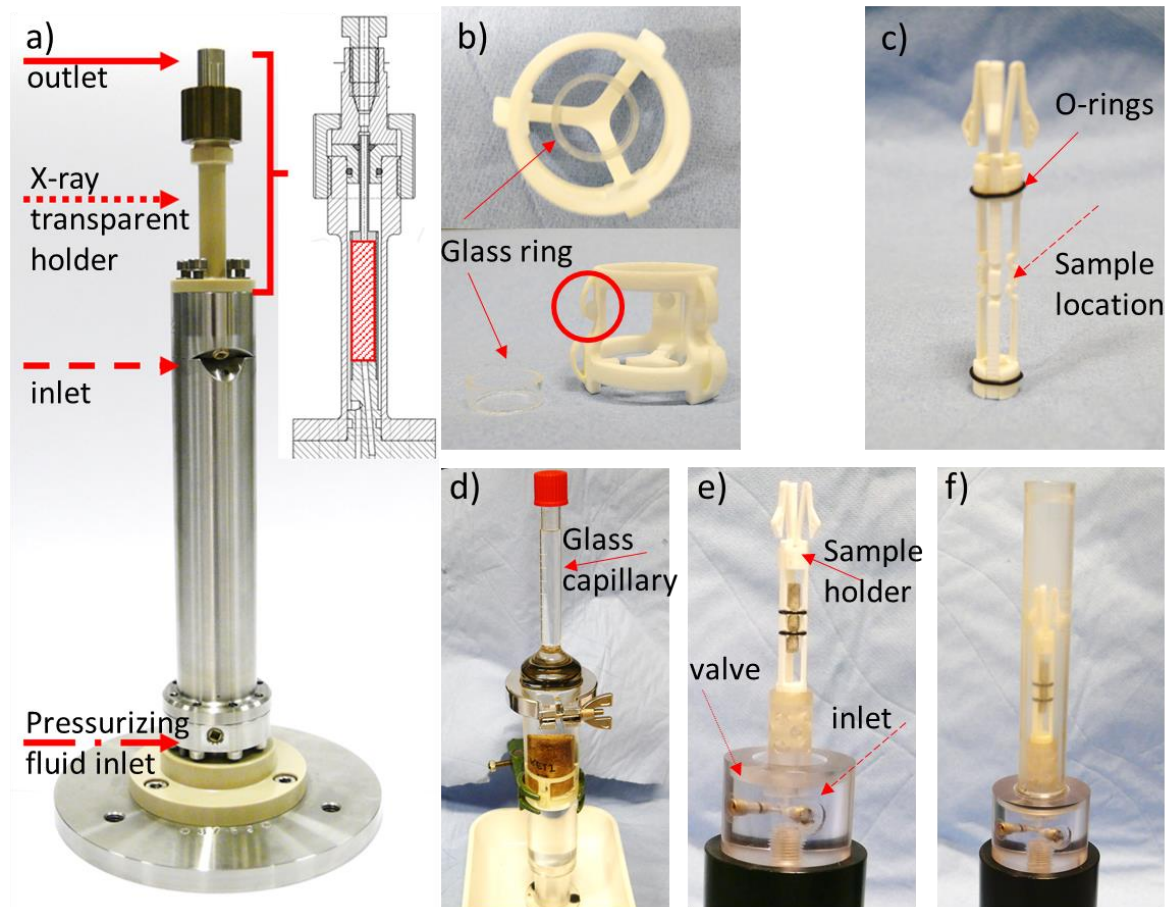

Figure 2: a) Micro-coreholder for de-saturation of mini-plugs and flow experiments. The bottom cylinder is a pressure vessel, with water as pressurizing agent. The PEEK top holds the sample and allows for X-ray scanning. This section is shown again in the inset in which a typical mini-plug (4 mm × 20 mm) is indicated by the red square. Flow lines for de-saturation can be attached at the top and bottom of the PEEK section. Sample holders for the spontaneous imbibition cells (b, c) and the Spontaneous imbibition cells for SCAL (d) and mini-plug (e, f).

Spontaneous imbibition set-ups
Two different set-ups were used for spontaneous imbibition: one for the SCAL plug Amott tests (a slightly modified standard Amott cell) and one for the mini-plug Amott test, see Figure 2d-f**Error! Reference source not found.**. Both cells can be used for different types of spontaneous imbibition tests and are made of crude-oil-resistant and X-

ray-transparent materials. For all faces open spontaneous imbibition tests, the rock sample needs to be well consolidated. For other types of imbibition experiments (one end open or two ends open) a sleeve can be used, which also poses less stringent requirements on the consolidation state of the sample. The cells can handle samples of various sizes.

The sample holders – depicted in Figure 2b, c – that are placed in the cell are constructed to minimize contact with the sample whilst simultaneously fixing the sample position in the cell. It is vital that the samples do not move during the scans to prevent blurring of the images. In the case of the SCAL plugs, the points where the sample holder touches the sample were made of water-wet glass to prevent oil from spreading along the holders.

Micro-CT scanners: HECTOR and EMCT

HECTOR [14], was used for time lapse imaging of the SCAL plugs. The X-ray tube was operated at 160 kV with a power of 14 W. The plug was imaged using 4 consecutive scans along the vertical axis of the sample, which were merged together, resulting in a total reconstructed volume of $2000 \times 2000 \times 4700$ voxels, with a voxel size of 14.25 µm. Individual consecutive scans were used to reduce the scan time (100 minutes per scan) and limit motion blurring during the acquisition.

EMCT, also known as the Environmental MicroCT scanner [15], was used for fast dynamic imaging of the mini-plugs. Unlike conventional micro-CT systems, the sample remains immobile in the EMCT, while the X-ray tube and detector rotate around the samples in a horizontal plane. This fixed sample configuration makes the system ideal for continuously monitoring dynamic in-situ processes. The mini-plugs were imaged at different spatial and temporal resolutions related to the assumed rate of the process that was monitored. The onset of the imbibition was imaged with a high temporal resolution of 15 seconds for a full rotation and a spatial resolution of 13 µm. Later stages of the process were imaged at a spatial resolution of 6.7 µm and a temporal resolution down to 70 seconds for a full rotation.

Image analysis

All scans were reconstructed using the dedicated reconstruction tools in the Acquila software package from XRE. Further post-processing and visualization of the data were done using Avizo 9.2.0 (FEI) and GeoDict, (Math2Market). The images were first filtered with a non-local means filter and subsequently segmented by comparing the data of the dry scan with the wet scans captured during the spontaneous imbibition experiment, following the procedure described in [17].

RESULTS AND DISCUSSION

Verification of the production curve in SCAL-sized samples and Amott protocols

In the initial state of both the SCAL and the mini-plugs, no air was observed throughout the sample, indicating that the standard procedures to initialize plugs were correct and working. For all samples, no capillary-end effect was detected even though the centrifuge was used for the SCAL plugs. This is based on estimations made using the mercury intrusion porosimetry curve and the centrifuge inlet pressure, see Figure 3. However, we observed a considerable amount of cement in the matrix in the micro-CT images, giving rise to a large fraction of micro-porosity which may influence the results. The cement is difficult to indicate in wet samples, because the attenuation is close to that of the oil

phase. Rolling the samples on a tissue pre-wetted with oil, did not seem to have any effect on the interior of the sample.
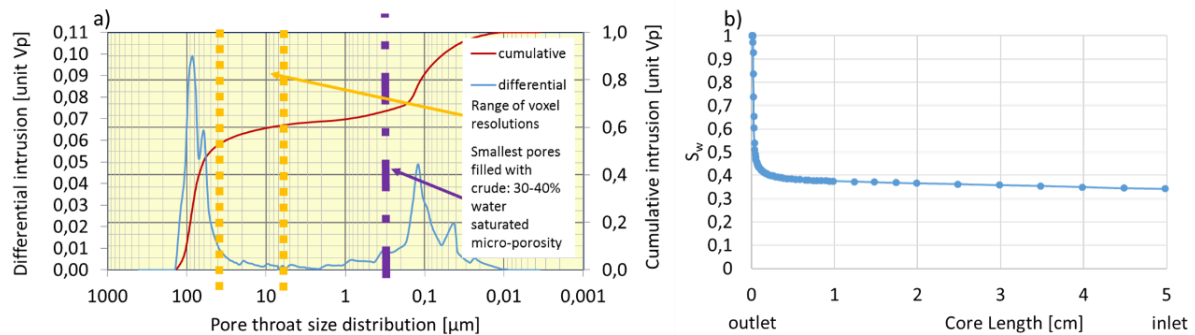

Figure 3: a) Mercury intrusion curve of one of the SCAL Ketton samples. The dotted lines indicate the voxel resolutions of the different scans that were made. The dash-dot line indicates the smallest pores filled with crude by the centrifuge. All scans capture the larger pores and are well above the sizes of the micro-porosity. In b) the estimation of the capillary end effect along the length of the SCAL plug.

For the mini-plugs, the sample holder (Figure 2c and Figure 7) was oil-wet which means it may have led to draining of oil from near-surface pores. Therefore, only spontaneous imbibition that was isolated from other parts of the pore-space, i.e. disconnected oil that is moving out, could be examined.
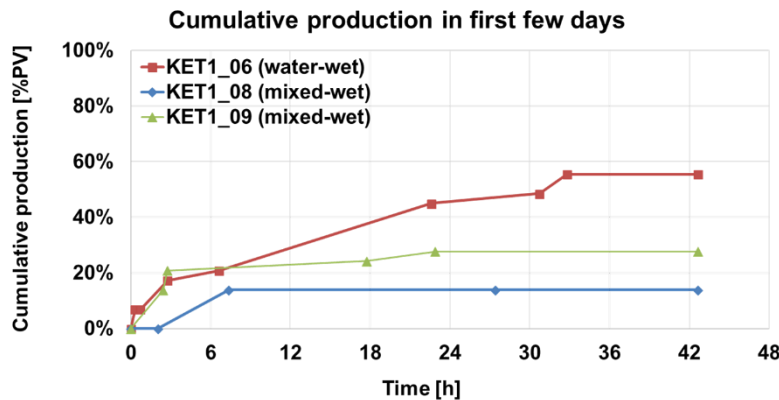

Figure 4: All production in % of visible pore volume, for both water-wet and mixed-wet samples, occurs right after immersion in brine. KET1_08 was kept for a total of 122 days in which no additional production occurred. The wettability state of the samples is based on the curves in this figure and on the pore scale images of protruding droplets (and their contact angle with rock surface) in Figure 5, Figure 8 and Figure 9.

Next, it was investigated whether the produced oil, as measured in the production curve, see Figure 4, reflected the pore-space of the sample as mentioned in [12]. The water-wet SCAL plug shows more production than the two mixed-wet SCAL plugs, see Figure 4. For the water-wet SCAL plug production coincides with pore-scale displacement as can be seen from the imbibition front in Figure 5b, c. For the mixed-wet case, production does not coincide with pore-scale changes in fluid configuration, as can be seen in Figure 5e, f and Figure 6. This means that the oil volume in the glass capillary reflects neither the rate at which the oil is produced nor the volume of produced oil, but probably relates to oil attached to the outside of the sample. To get a production of 1 ml, the film of oil covering the sides of the cylindrical plug would have to be ~0.25 mm thick. For the

water-wet plug we used doped decane. Therefore, the oil film on the sample is expected to be negligible. The production of the water-wet mini-plug was not measured but the significant amount of cement in the pore-space may explain the lack of response to brine exposure.
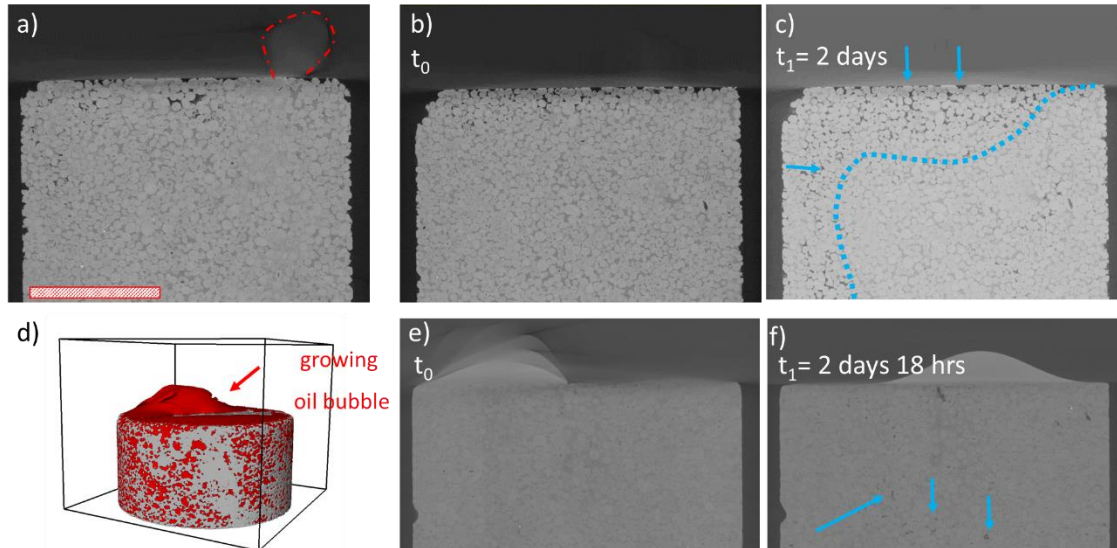

Figure 5:a, b, c) the water-wet SCAL sample (KET1_06). The red bar in a) indicates 1 cm. d,e,f) a mixed-wet SCAL sample (KET1_09). In a) and d-f) an oil droplet is seen growing at the top of the SCAL samples. b) initial saturation of water-wet SCAL sample at t_0=~105 minutes c) saturations after 2 days for the water-wet SCAL sample. A clear imbibition front has formed, indicated by the blue line and arrows. The center of the sample shows very little change. e) initial saturation of mixed-wet SCAL sample at t_0=~105 minutes. f) Almost no change in the mixed-wet sample after ~2 days. The little change there is, is indicated by blue arrows.
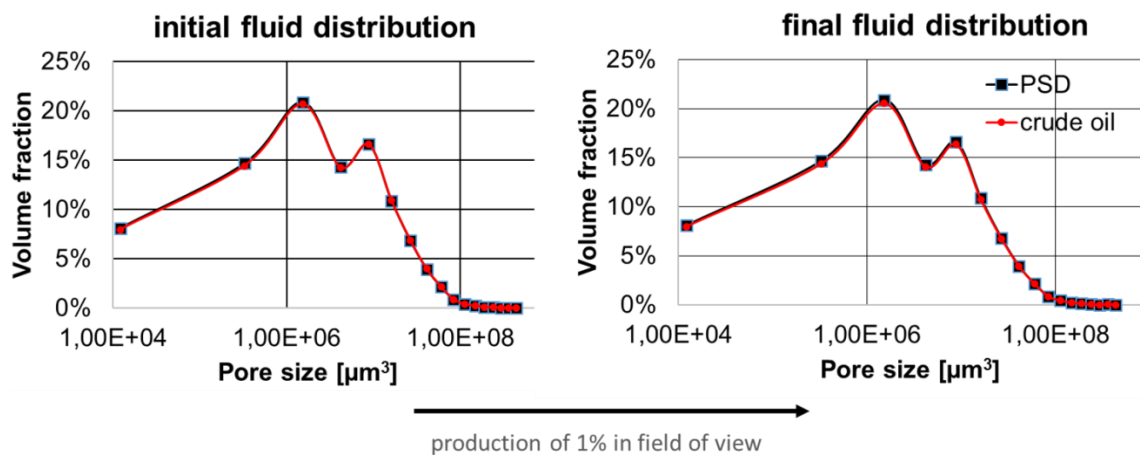

Figure 6: Change in oil distribution (red dotted line) compared to the Pore Size Distribution (PSD, black line with squares) for the mixed-wet SCAL plug (KET1_09) in Figure 5e, f. The change is minimal whereas the production in the glass capillary at the top reaches almost 1 ml.

Observations from micro-CT images

The SCAL plugs, both water-wet and mixed-wet, showed large oil blobs protruding from the top, see Figure 5a, d–f, at a single location. Visual observation also indicated that the drop detached and grew back again several times for the water-wet case, which was in

line with the preferred production sites mentioned in [12]. The mixed-wet sample – in contrast to the water-wet sample – did not show an imbibition front. In addition, there was no significant change in the occupancy of the pores, whereas production was observed, see Figure 4 and Figure 6.

A similar observation was made for the mini-plug in Figure 7. However, because of the limited field of view (FOV) this cannot be confirmed. In the mini-plug, preferential production sites were also observed. The observed process has some similarity to that hypothesized by [12] when discussing the generation of capillary back pressure at a wetted open surface during imbibition. They stated that [18, 19] found that when air is the non-wetting phase it tends to *"...emerge as a stream of very fine bubbles, often at a single location, which indicates that snap-off is occurring a short distance in from the open face."* The stream of fine and larger bubbles was observed by eye, but it was not possible to image this, because it fell out of the FOV for the mini-plug or out of the temporal resolution for the SCAL plug. However, the bubble that emerged in our FOV of the mini-plug shows snap-off at a short distance from the open face, see Figure 8.
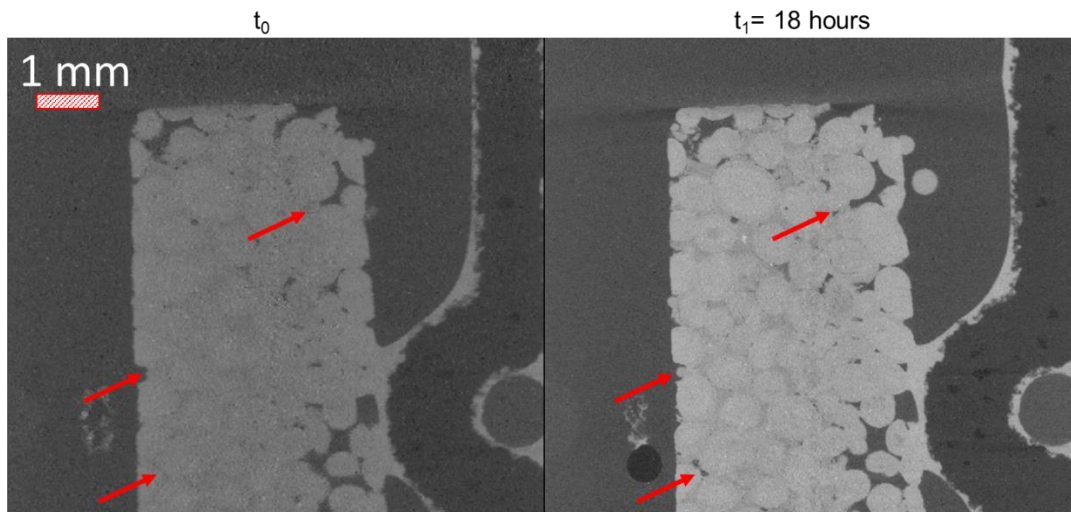

Figure 7: Spontaneous imbibition dynamics in the water-wet mini-plug are indicated by the red arrows. The sample holder is also clearly visible. The bright phase coating the holder is doped crude oil.

The effect of buoyancy on spontaneous imbibition

We observe that the outside of the mixed-wet SCAL sample is covered with crude oil, see Figure 9a. However, there seems to be less crude towards the bottom of the sample. Combined with the imbibition front observed in Figure 5c and the rising oil drop observed in the mini-plug, see Figure 8, this could mean that gravity effects dominate the imbibition process in our samples. However, the buoyancy/capillary force computation in Figure 9b indicates otherwise: it shows that for oil clusters of a length equal to that of the sample, gravity forces are an order of 10,000 less than capillary forces. Buoyancy would dominate inside the pore space for contact angles around 90 degrees. However, the effect of contact angle in the force balance is uncertain, since advancing and receding contact angles may show significant hysteresis, see e.g. [20]. When oil starts protruding from the sample, the restrictions of the pore-space fall away and gravity dominates over capillary

forces. Buoyancy may play a role in 'sucking out' oil and creating space for water to imbibe as indicated in Figure 8. Depending on the crude oil and liquid-liquid interface properties (such as interface elasticity, interfacial tension, composition), and pore geometry, the protruding oil drop may grow before snap-off disconnects the drop from the interior of the sample, see Figure 8b, c. Interestingly, after snap-off, the droplet retains a non-equilibrium shape for minutes (Figure 8c), before moving toward a more stable configuration on the rock surface (Figure 8d).
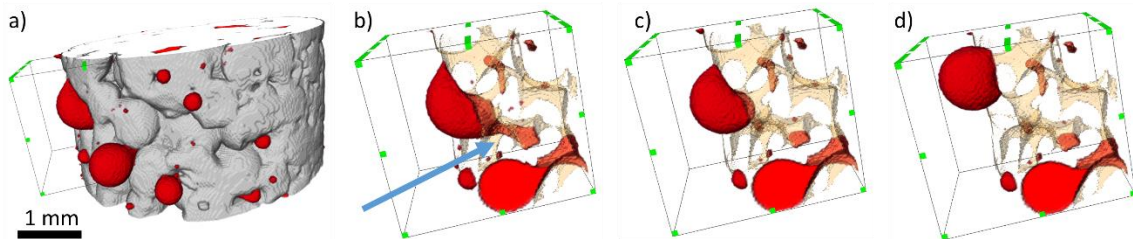

Figure 8: Oil droplet movement out of pore space and snap-off event in mini-plug. a) shows the grains (white) and oil (red) configuration in the plug. b-d shows time steps of 11 minutes, 4 hours after starting the experiment. The snap-off event is clearly visible between steps b) and c) [indicated by the blue arrow]. From c) to d) the drop moves towards a more spherical/equilibrium shape.
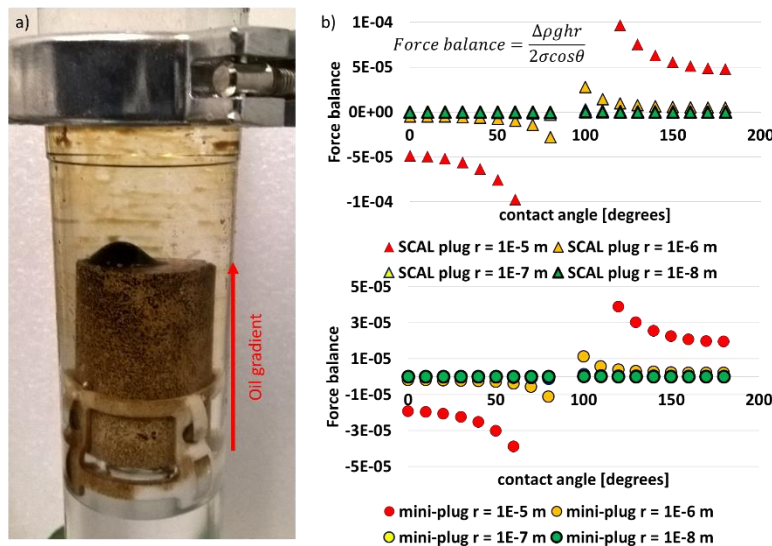

Figure 9: a) SCAL plug (KET1_09) showing gradient of oil coverage on the outside of the sample which cannot be due to centrifuge desaturation. Notice also the bubble on top. Together with the dynamics of production in the mini-plug, see Figure 8 this hints that buoyancy is important in spontaneous imbibition of this rock b) Computation shows that gravity drainage is very unlikely inside both samples for h=sample/cluster length, Δρ= density difference of fluid phases, σ=interfacial tension, θ = contact angle, and r=pore diameter.

CONCLUSION

We used three novel coreholders and fast benchtop micro-CT scanners to study spontaneous imbibition both on long (months) and short time scales (seconds to minutes). From 3D reconstructed and segmented images, we observed movement of the oil phase in the pore space of the rock in water-wet (mini-plug and SCAL plug) and mixed-wet (SCAL plug) systems using benchtop X-ray micro-tomography.

We found the *sample preparation* protocols to be adequate i.e. no air bubbles were trapped in the pore space and homogeneous oil saturations were achieved. However, we showed that there is a discrepancy between production as measured in the capillary of the Amott cell and the pore-scale observations in some SCAL plugs. The fluid distribution in the interior of the plugs remained unchanged whereas production was still accumulating in the capillary. The produced oil may have come from the oil layer attached to the outside of the sample: a rough estimate indicates an oil film of ~0.25 mm would be sufficient produce 1 ml of oil. In that sense, rolling the sample per protocol may still influence the production curves even though the rolling did not seem to affect the pore space distribution of oil. For water-wet plugs, the measured production matches the observed pore-scale events better. Since we used decane in this case, the oil film on the sample is expected to be negligible because of the water-wetness of the system. For both cases, oil drops would protrude from the sample without being recovered.

Furthermore, we observed an 'oil gradient' on the outside of the sample (mixed- wet SCAL plug), a big oil droplet on the top of both water-wet and mixed-wet SCAL plugs and a pore-scale snap-off event in the water-wet mini-plug. In addition, we observed preferred production sites for all water-wet samples. They all hint that buoyancy is important for the displacement of oil. However, force balance computations show that buoyancy is not important inside the samples, but may be very important outside of the sample as demonstrated by the mini-plug pore-scale imbibition.

The next part of this study focusses on investigating spontaneous imbibition when changing brine salinity. This finds its application in Amott tests that are conducted to investigate the response of a COBR system to Low Salinity Flooding.

ACKNOWLEDGEMENTS

REFERENCES

1. Amott, E., "Observations relating to the wettability of porous rock", *Petroleum Transactions*, AIME (1959).
2. Donaldson, E.C., R.D. Thomas and P.B. Lorenz, "Wettability Determination and Its Effect on Recovery Efficiency", *SPE Journal* (1969), March, 13-20.
3. Tang, C.Q., and N.R. Morrow, "Salinity, Temperature, Oil Composition and Oil Recovery by Waterflooding", This paper was presented at the SPE Annual Technical Conference and Exhibition held in Denver, Colorado, 6-9 October 1997.
4. Zhou, X., N.R. Morrow and S. Ma, "Interrelationship of Wettability, Initial Water Saturation, Aging Time and Oil Recovery by Spontaneous Imbibition and Waterflooding", *SPE Journal* (2000), 5 (2), 199-207.
5. Graue, A., E. Aspenes, T. Bognø, R.W. Moe and J. Ramsdal, "Alteration of wettability and wettability heterogeneity", *Journal of Petroleum Science and Engineering* (1999), **33**, 3-17.

6. Fischer, H., and N.R. Morrow, "Spontaneous Imbibition with Matched Liquid Viscosities", This paper was presented at the SPE Annual Technical Conference and Exhibition held in Dallas, Texas, U.S.A., 9-12 October 2005, *SPE 96812*.
7. Mattax, C.C. and J.R. Kyte, "Imbibition oil recovery from fractured water-drive reservoir", *SPE Journal* (1962), June, 177-184.
8. Ma, S., N.R. Morrow, and X. Zhang, "Generalized scaling of spontaneous imbibition data for strongly water-wet systems", *Journal of Petroleum Science and Engineering* (1997), **18**, 165-178.
9. Schmid, K.S., and S. Geiger, "Universal scaling of spontaneous imbibition for arbitrary petrophysical properties: Water-wet and mixed-wet states and Handy's conjecture", *Journal of Petroleum Science and Engineering* (2013), **101**, 44–61.
10. Salathiel, R.A., "Oil Recovery by Surface Film Drainage In Mixed-Wettability Rocks", *Journal of Petroleum Technology* (1973), 1216-1224.
11. Dixit, A.B., J.S. Buckley, S.R. McDougall and K.S. Sorbie, "Core wettability: should I_{AH} Equal I_{USBM}", *SCA9809* (1999).
12. Mason, G., and N.R. Morrow, "Developments in Spontaneous Imbibition and possibilities for future work", *Journal of Petroleum Science and Engineering* (2013), **110**, 268-293.
13. Abdallah, W., J.S. Buckley, A. Carnegie, J.E.B. Herold, E. Fordham, A. Graue, T. Habshy, N. Seleznev, C. Signer, H.Hussain, B. Montaron, and M. Ziauddin, "Fundamentals of wettability", *Oilfield Review* (2007), **19** (2), 44 – 61.
14. Dierick, M., D. van Loo, B. Masschaele, J. Van den Bulcke, J. Van Acker, V. Cnudde and L. Van Hoorebeke, "Recent micro-CT scanner developments at UGCT", *Nuclear Instruments and Methods in Physics Research B* (2014), **324**, 35-40.
15. Bultreys, T., W. de Boever, and V. Cnudde, "Imaging and image-based fluid transport modeling at the pore scale in geological materials: A practical introduction to the current state-of-the-art", *Earth-Science Reviews* (2016), **155**, 93-128.
16. Muir-Wood, H.M., 1952, "Some Jurassic Brachiopoda from the Lincolnshire limestone and upper estuarine series of Rutland and Lincolnshire", *Proceedings of the Geologists' Association* (1952)*, **63** (2), 113–42.
17. Berg, S., R.T. Armstrong, H. Ott, A. Georgiadis, S.A. Klapp, A. Schwing., R. Neiteler, N. Brussee, A. Makurat, L. Leu, F. Enzmann, J.-O. Schwarz, M. Wolf, F. Khan, M. Kersten, S. Irvine and M. Stampanoni, "Multiphase flow in porous rock imaged under dynamic flow conditions with fast X-ray computed microtomography". *Petrophysics* (2014), **55** (04), 304-312.
18. Unsal, E., G. Mason, N.R. Morrow, D.W. Ruth, "Bubble snap-off and capillary-back pressure during counter-current spontaneous imbibition into model pores", *Langmuir* (2009), **25** (6), 3387–3395.
19. Li, Y., G. Mason, N.R. Morrow, D.W. Ruth, "Capillary Pressure at the Imbibition Front During Water-Oil Counter-Current Spontaneous Imbibition", Transport in Porous Media, **77**, 475-487.
20. Raeesi, B., N.R. Morrow and G. Mason, "Effect of surface roughness on wettability and displacement curvature in tubes of uniform cross-section", *Colloids and Surfaces A: Physicochemical and Engineering Aspects* (2013), **436**, 392 – 401.

Primary Drainage Relative Permeability in Hydrocarbon Reservoirs Interpreted Using Digital Rock Physics

Sven Roth [#], Hu Dong [#], Martin J. Blunt [#,◊], Zubair Kalam*, Ahmed Al Ratrout*◊,
Djelloul Hammadi*
[#] iRock Technologies, Beijing, P.R. China.
◊ Department of Earth Science and Engineering, Imperial College London, London, UK.
* Abu Dhabi Company for Onshore Oil Operations (ADCO), Abu Dhabi, UAE.

ABSTRACT

We apply multi-scale interrogation of complex carbonate reservoir rocks from whole core – plug – micro – nano scale, and then work backwards to upscale and integrate the properties to an acceptable 3D representation. This is achieved through imaging at different resolutions: for each image an equivalent network model is constructed. The smaller-scale networks are upscaled to generate effective properties for input into a plug-scale network representation of the rock.

We study 54 samples from three reservoir zones of a Lower Cretaceous reservoir. Using the Dunham rock classification scheme we see a range of rock types from grainstone to mudstone-dominated. For primary drainage, the higher quality grain-dominated samples show better connectivity and a higher oil relative permeability than the poorer quality rocks. However, for waterflooding the situation is reversed: the better quality rocks tend to be more oil-wet, with a large water relative permeability which leads to early breakthrough and a poor local displacement efficiency. In contrast, the mudstones are mixed-wet and more poorly connected, which impedes the movement of water, leading to a more favourable local recovery.

This study demonstrates how employing the state-of-the-art in multi-scale imaging and modeling, the behavior of complex carbonates can be quantified and interpreted, allowing an assessment of recovery based on pore structure and facies type.

INTRODUCTION

The computation of multiphase properties using Digital Rock Physics and pore-scale modeling, DRP, is extremely valuable as the tests are quick compared with physical laboratory test protocols, and typical costs are about one-half of conventional Special Core Analysis (SCAL) tests using live fluids at full reservoir conditions. Such data are the typical building blocks of dependable field development models of multiphase flow in hydrocarbon reservoirs. Acquisition of accurate representative data minimizes uncertainty in model validations, and opens the possibilities for future sensitivity studies with respect to changes in wettability as well as micro-porosity present in typical Middle Eastern carbonate reservoirs [1, 2].

The goal of this DRP campaign was to complement the SCAL work program for a Lower Cretaceous Reservoir with three reservoir zones (Zone 1, 2, and 3) to provide essential input to the reservoir simulation model.

For every sample, we acquired images at different scales (multi-scale imaging approach), including a full-plug X-ray scan, micro-CT images (tens of micron resolution), micro-CT subsample images (micron resolution) and nano-CT subsample scans (tens of nanometre resolution). An example of such a multi-scale imaging work flow can be found in [3]. Additional QEMSCAN analysis for mineral identification was complemented by high-resolution, large-area electron microscopy mosaics (BSE) to obtain seamless pore-size information.

From the multi-scale rock models, constructed from these images, single and multiphase flow properties were predicted. We predicted electrical properties (resistivity index and the related m and n exponents), elastic properties (elastic constants and acoustic wave speeds), porosity, permeability, capillary pressure and relative permeability, for drainage and waterflooding with detailed scanning curves to investigate relative permeability and capillary pressure hysteresis. Additionally, a series of wettability sensitivity studies have been performed to simulate the effect of low-salinity floods.

For every property, we used an upscaling technique that incorporates the impacts of micro-porosity (characterized at nanometre resolution) with macro-porosity (micron-sized features), together with vugs (mm-sized pores) and fractures. Because wettability is a key control on waterflood capillary pressure and relative permeability it adds a level of complexity when studying the impact of pore structure on relative permeability. The core samples during primary drainage, however, are assumed to be water-wet and so variability in relative permeability is controlled entirely by the pore structure.

In this manuscript, we focus on the effects of rock types and porosity systems on the shape of the water-oil primary drainage relative permeability curves to develop an understanding of how individual rock types and their pore structure shape the primary drainage relative permeability – or vice versa, can primary drainage relative permeability help to refine the current geological- or petrophysical- based rock typing procedure. This could then explain the impact of wettability changes on individual rock types during waterflooding. The combination of pore connectivity at different scales and wettability allows us to identify representative multiphase flow behavior, which is different in primary drainage and waterflooding.

MATERIAL AND METHODS
Formations And Rocks Studied
Twenty-four samples from Reservoir Zone 1, sixteen samples from Reservoir Zone 2, and fourteen samples from Reservoir Zone 3 – a total of 54 samples – were analysed using digital rock physics.

The reservoir zones represent porous units of a Lower Cretaceous formation. Zone 1 has an average thickness of 45ft and Zone 2 has an average thickness of 24ft. Both reservoir zones are composed of limestone, mainly deposited in an open platform, middle ramp to restricted platform subtidal to intertidal environments. Zones 1 and 2 carbonates have been subjected to multiple diagenetic events that have occurred at different post-depositional

times. The present reservoir quality is controlled by four major diagenetic events, including meteoric leaching, cementation, early (meteoric) and late (deep burial) calcite cementation and compaction and stylolitization. Zones 1 and 2 show a high degree of reservoir heterogeneity, which is mainly due to depositional facies and diagenetic overprint. Although most of the lithofacies units show a wide range of porosity and permeability within each lithofacies, they also show large overlapping. Reservoir zone 3 is on average 28 foot thick, and is predominated by bioclastic wackestones to mudstones at the top and base, with intercalated bioclastic pelloidal wackestones to grainstones in the central section. Sequence related reservoir-facies distribution based on geological and petrophysical data properties was used to define flow units and to establish a Reservoir Rock Typing Scheme (RRT). This rock typing scheme is based on the lithofacies identified from core, thin section analysis, and petrophysical results. The reservoir quality of the rock types from Zones 1 and 2 decrease with increasing number, while the permeability of rock types in Zone 2 are generally lower than their counterparts in Zone 1. Within the rock types, moderate to good reservoir quality rock types are mainly developed in the crestal areas (indicated with A) showing preserved primary porosity. Rock types labeled with "B" and "C" are low to moderate reservoir quality rocks with increased cementation and compaction, which occur at the flanks of the reservoirs. The rock typing for Zone 3 is based on lithofacies unit and porosity-permeability range, with smaller numbers being better rock types.

Digital Rocks Work Flow
A generalized work flow for multi-scale imaging and pore-scale modeling is illustrated in Figure 1. Here, the work flow starts with a plug screening using X-ray micro-CT, followed by controlled subsampling and further micro-CT and nano-CT imaging. The acquired images are used to build the multi-scale digital rock models including numerical pore network models, which are then used to calculate and simulate the single phase and multiphase properties. All properties are finally upscaled to the core plug.

Subsampling And Multi-scale Imaging
The multi-scale imaging work flow starts with a full-plug X-ray scan with voxel sizes ranging from 20-40µm. This overview scan provides information about the heterogeneity in the individual core plugs and is used to design a subsampling strategy for the multi-scale imaging. Additionally, this plug CT builds the rock model for later upscaling of all properties. While vugs can be resolved on the plug-overview scan, volumes of macroporosity and microporous matrix can be observed only qualitatively in micro-CT images on the plug level (as areas of different gray shades) - the resolution is not sufficient to resolve the macro- and micropores. For this subsampling and imaging work flow, however, it is mandatory to determine the nature, amount, size, and distribution of all pore types, present in the plug – from vuggy porosity down to microporosity.
The plug X-ray CT was thus complimented with high-resolution, large area backscatter electron microscope images (BSE), acquired with a scanning electron microscope. These BSE mosaics cover large areas (ideally the entire sample surface) down to a resolution that captures even the smallest pores present (nanometer resolution) and provide a continuous

pore-size information of the sample. Although this is a 2D analysis and, as such, derived pore sizes will be slightly offset towards smaller sizes due to stereological effects, all present pore classes can be determined accurately from centimeter to sub-micrometer. This enables us to identify, characterize, and quantify the volumes of sub-resolution pores, which were detected in the plug X-ray CT as volumes of different grey shades.
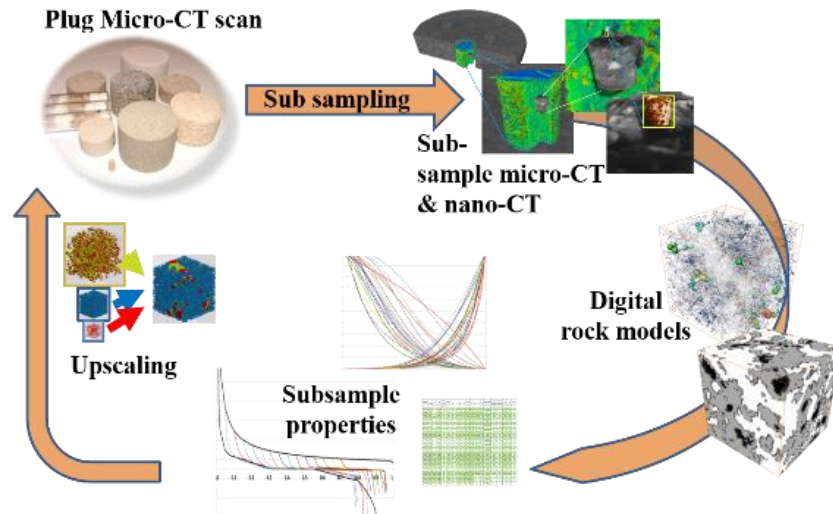

Figure 1. Generalized digital rock work flow, modified from [3].

Additionally, mineralogy was determined on the plug scale using QEMSCAN analysis. QEMSCAN technology provides 2D mineralogy mapping from the same surfaces as used for the BSE images, providing mineral distribution and quantification.

The rock-framework information from the X-ray core-plug screening complimented with the quantitative mineralogy and the detailed BSE-derived pore size information are then utilized to understand the flow characteristics of the core plugs. The most important parameters for successful subsampling are present porosity types, their distribution and interconnection, as well as, the pore sizes in the individual pore classes. This information decides on the location of subsample extraction, the volume of subsamples to be extracted (to be representative for this pore class) and the deployment of imaging instruments, a critical step in the multi-scale 3D rock model construction and subsequent data acquisition. All subsamples were imaged at appropriately high resolution to resolve the pore space. Depending on the facies and pore types, the subsample for micro-CT is typically a cylinder of 2 mm to 16 mm in diameter corresponding to voxel sizes of 1-8 μm. Very fine grained facies, such as micrite and cemented regions, require a much higher resolution than micro-CT equipment can achieve. These facies were imaged using a nano-CT device providing 3D images with a voxel size of 65 nm. Due to the heterogeneity of carbonate rocks, any combination of instrumental 3D image acquisition might be applied – 2 x micro-CT, 1 x micro-CT plus 1 x nano-CT, 2 x nano-CT, etc.

All X-ray micro-CT imaging was performed with a Micro XCT 200, the nano - CT imaging with an Ultra XRM L200, both manufactured by Xradia. The BSE images were acquired

on a Helios NanoLab 650, the mineralogy was investigated with a QEMSCAN 650 F (both from FEI company).

Digital Rock Models And Numerical Pore Networks
Prior to any simulations the 3D X-ray images must be processed and segmented. The processing includes image enhancement (noise reduction) and cropping the 3D volume into a three-dimensional rock model. Noise reduction is performed using an edge preserving smoothing algorithm, which removes noise from the individual rock phases (such as pores, grains) but leaves the phase boundaries untouched. The segmentation into rock phases: pore, microporosity volume, and solid is done using the gray-shade histogram and including the local gradient information. This procedure, noise reduction and filtering, is performed on all multi-scale images. The topology of the pore space is determined using a revised maximal ball algorithm pioneered by [4].

Property Calculations
On these multi-scale rock models, we predicted single and multiphase flow properties, such as electrical properties (resistivity index and the related m and n exponents), porosity, permeability, capillary pressure and relative permeability, for primary drainage. The absolute permeability and formation factor are calculated directly on the grid-based images by solving the Stokes equation and Laplace equations, respectively. The porosity stems directly from segmentation of the individual scale images. The multiphase fluid flow properties are simulated based on the pore scale modeling technology introduced by [5] and adopted and modified by iRock Technologies: capillary-dominated displacement is assumed and so the complexities of ganglion dynamics and viscous effects are ignored.

Upscaling Of Properties
Upscaling of the results is performed using a proprietary three-stage approach. The basis of the method is to construct a multi-scale network model of the rock, see [6] for more details: rather than being an explicit representation of large "pores" connected by "throats" as in traditional pore-network modelling approaches, we instead consider interconnected elements. These elements may indeed be real pores and throats, or could represent an averaged behavior of a region of micro-porosity: this average behavior accurately captures the combined response of the smaller-scale network. In this way, we can construct a network at any scale, representing features spanning many orders of magnitude in scale. Furthermore, we can still retain the semi-analytical computation of conductance and local capillary pressure in each element.
The three stages outlined below and illustrated in Figure 2 deal with the three generic types of porosity encountered in complex carbonate rocks: micro-porosity (Stage 1); combined micro- and macro- porosity (Stage 2); and then combined micro-, macro- and vuggy porosity (Stage 3).
The rock models in Stage 1 capture the smallest pore types present in the rock, which in carbonates is the microporosity. The single-phase properties, absolute permeability and formation factor, etc. is calculated directly on the grid-based representations of the rock. Capillary-dominated two-phase flow through this smallest pore-network system is

simulated to predict two-phase properties such as capillary pressures, relative permeability and resistivity index. The key outputs from this model are capillary pressures and the conductances of oil, water and gas computed as a function of local saturation (which in turn is related to local capillary pressure).
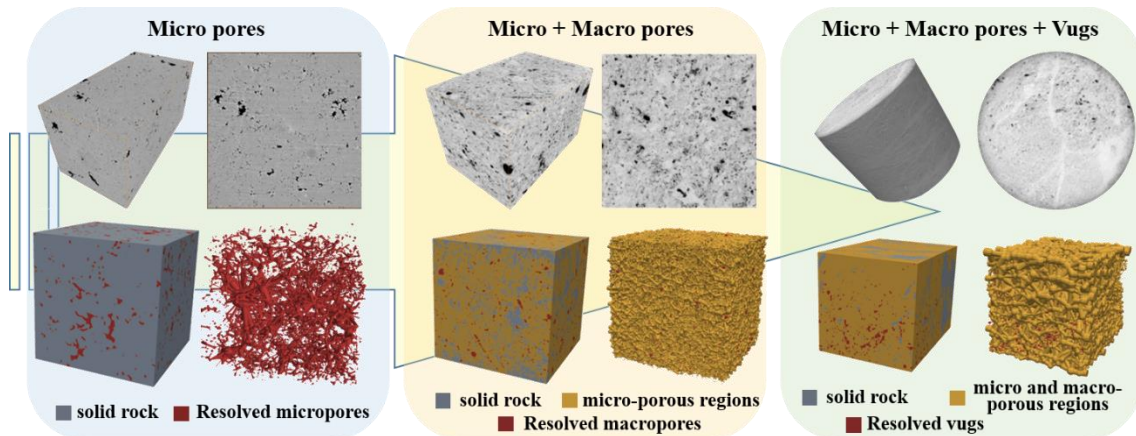

Figure 2. Upscaling work flow illustrating the three-step approach discussed in the text.

The Stage 2 images capture a larger volume of the rock and can resolve macro-pores directly but they cannot directly see the micro-porous voids. However, the presence of micro-porosity can be deduced from intermediate grey-scales in the image. Thus, the image voxels are partitioned into three types: solid voxels, pore voxels and voxels containing micro-scale pores (micro-porosity).

A novel method is used to extract a network of the resolved macro-pore space combined with micro-porosity volumes. We refer to the resolved pore and throats as well as the micro-porosity volumes constituting the combined network simply as "elements". The pore elements detected at this scale are called macro-pores to differentiate them from the micropores generated in Stage 1. The micro-porosity elements from Stage 1 are combined with the macro-porous network; the micro-porosity creates additional connections across the rock resulting in a network of generalized elements whose conductance can be computed as a function of local capillary pressure.

An extended two-phase flow modeling code is used to model the flow through the combined network. The flow through the micro-porosity elements is described using the multiphase Darcy law with the flow properties obtained from the Stage 1. The network model works by gradually increasing the oil pressure in oil-injection cycles and decreasing it in water-injection cycle, which is similar to the displacement sequence in experimental measurements. The water-saturation, the flow and electrical conductivity of the micro-porosity elements are calculated from the capillary pressure curve, the relative permeability and resistivity indices obtained in Stage 1, respectively. The flow equation for the combined network of the macro pores and micro-porosity elements are put together using the mass conservation equation and solved to obtain the single and two-phase flow properties for the Stage 2 micro-CT image.

The same technique is used to upscale the properties of the combined micro- and macro-porosity (Stage 2) to the plug size. By solving the flow equations for the combined network of vugs, micro- and macro- porous elements we obtain the capillary pressure curve, absolute and relative permeabilities, formation factor and resistivity index for the whole sample.

RESULTS AND DISCUSSION

Figure 3 summarises the porosity-permeability of all studied rocks and formations, colour coded after the Dunham classification [7] and labeled according to the rock type scheme described above. The accordance of laboratory derived and upscaled digital porosities and permeabilities for all rocks is illustrated in Figure 4. This comparison is an important step in validating the accuracy of the digital rock models and the data derived from these models [8].
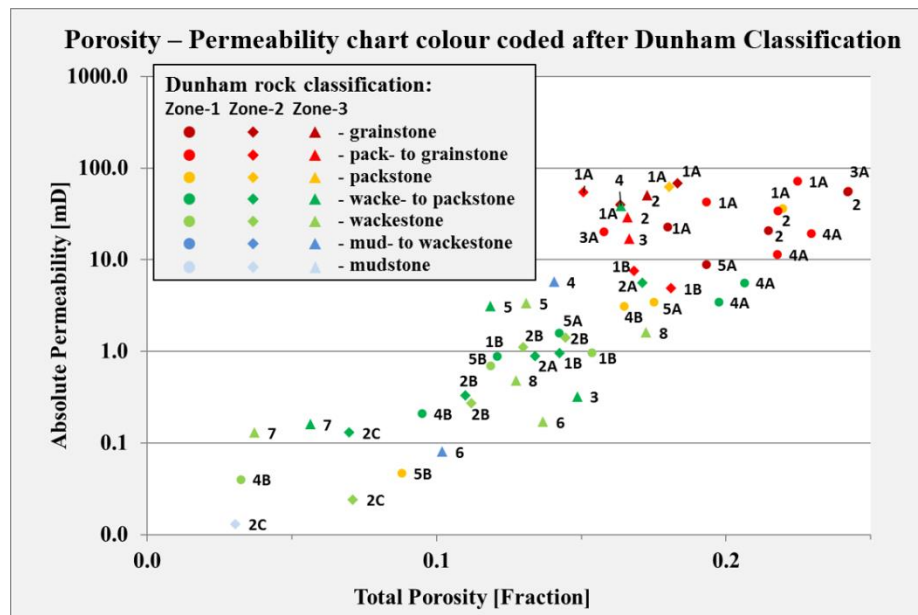

Figure 3. Porosity versus permeability cross plot colour-coded after Dunham Classification and labeled with rock types. Rock type definitions are explained in the text.

The relative permeability curves for all the rocks investigated are shown in Figure 5. As expected the curves show a considerable variability caused by the wide range of rock types and their porosity systems. In order to unravel the behavior of individual rocks the data set was reduced to the cross-over points of the relative permeability curves assuming that this points reflect both, the behavior of the water- and oil relative permeability curves.

Figure 6 shows the extracted cross-over points marked after reservoir zones (different symbols) and color-coded. Two methods were used to discriminate between the rocks: (1) a characterization according to tri-modal versus bi-modal pore systems (left graph) and (2) according to the classical Dunham classification (right graph). The classification into tri- versus bi- modal pore system (1) was further subdivided depending on which pore class is

dominating the overall porosity system – macroporosity or microporosity or vugs. Then each of the encoded assemblages were enclosed into lower and upper bounding curves to find the fields where the categorized crossover-points plot.
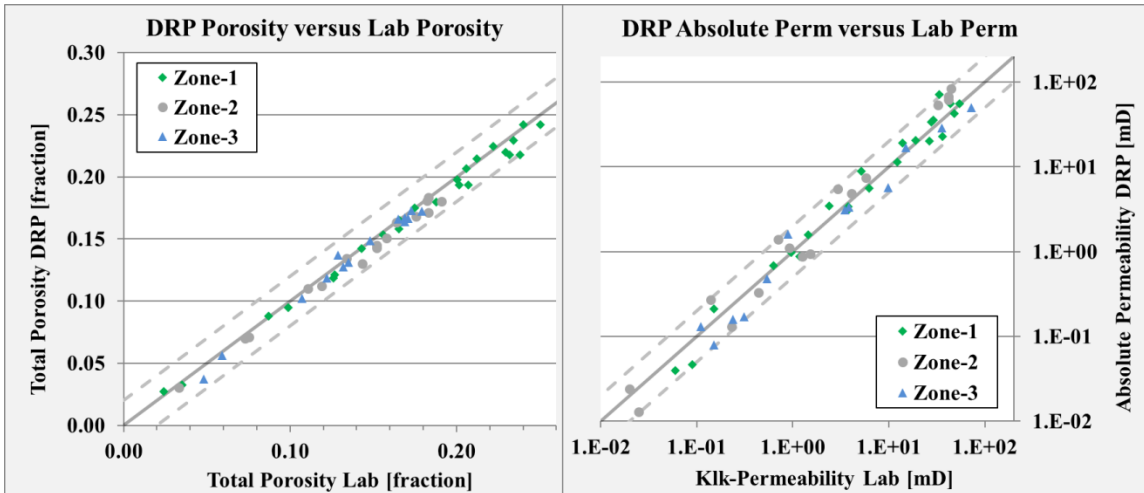

Figure 4. Comparison of laboratory derived total porosities (left) and permeabilities (right) versus digital rock data. The gray solid lines are the 1:1 relations, the broken lines indicate the envelopes for ± 2 units deviation in porosity (left graph) and a factor of two for permeability (right graph).
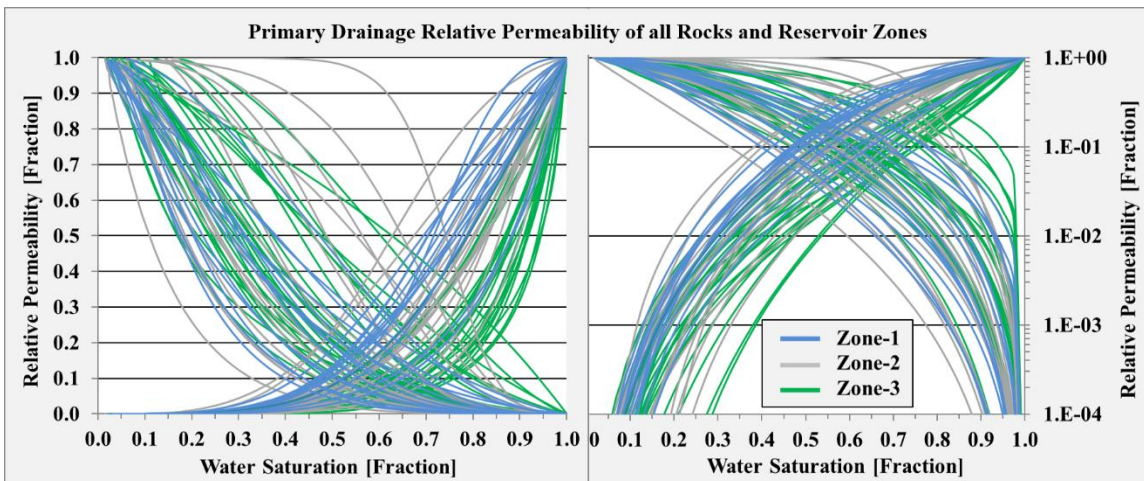

Figure 5. Primary drainage relative permeability of Reservoir Zones 1, 2, and 3.

While classification into tri- and bi- modal pore systems (1) is relatively straightforward, the Dunham classification (2) is more like a continuous transition. Here the boundary was drawn between the grain-dominated and mud-dominated rocks. The latter comprise mudstones, wackestones and wacke- to packstones (blue bounding curves and field), while grainstone, pack- to grainstone and packstone belong to the grain-dominated rocks (red bounding lines and red field). Both categorizations result in very similar fields of cross-over points. Although it was expected that the much more detailed classification in pore systems (1) would result in more distinct cross-over accumulation fields, Figure 6 exhibits

that further subdivision into macroporosity- or microporosity- dominated bi- and tri- modal pore system does not yield advantages over the 'coarser' Dunham classification. The likely explanation for this is that we are only considering volumes of pore classes, neglecting the important effect of how these volumes are distributed and interconnected. We therefore follow the easier Dunham classification for the rest of this manuscript.
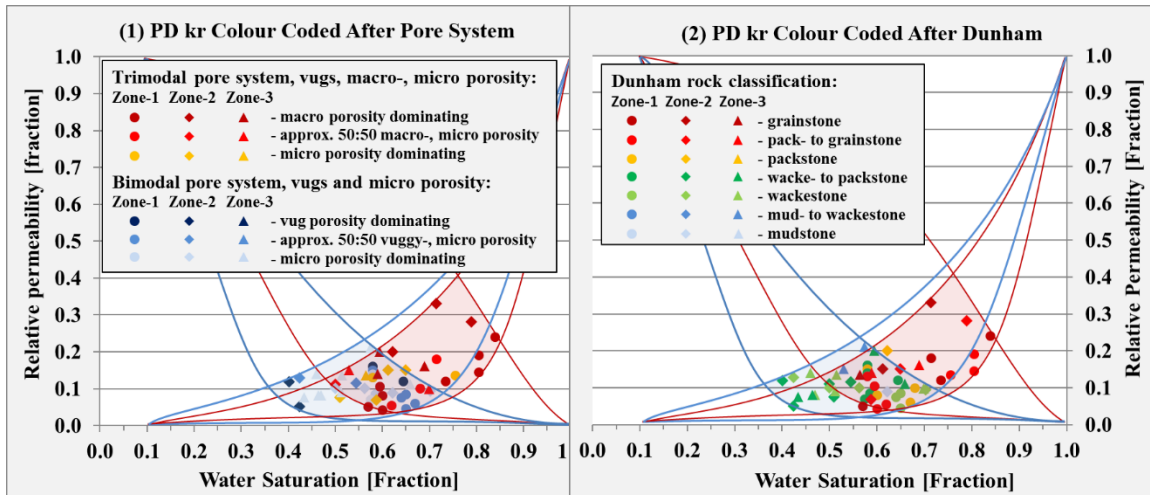

Figure 6. Primary drainage relative permeability cross-over points of all three reservoir zones colour coded after pore system (left) and Dunham classification (right).

In the next step we populated the Dunham-colour coded primary drainage cross-over points with absolute permeability, formation factor data, as well as rock types and wettability indication (Figure 7). The permeability and the formation factor show a clear inverse overall trend from higher saturation/higher relative permeability towards lower saturation/lower relative permeability cross-over points. The mud-dominated rock types (blue to green colours and blue field) plot in a narrower range of water saturations between 0.4 - 0.7, and relative permeability between 0.05-0.2. The grain dominated rocks (orange to red colours and red field) show a larger variability between 0.57-0.84 water saturation and 0.04-0.33 relative permeability. This is insofar intuitive as the mud-dominated rocks have only one governing pore system – the microporosity, while the grain dominated facies usually have two generations of conducting pore systems: macroporosity and microporosity. The behavior of their relative permeability curves and thus the location of the cross-over points are governed by the contribution of each of the pore systems to the overall rock, which is dependent on their relative volume, their hydraulic properties and their interconnection.

Figure 7 (lower left), also illustrates the link between the rock types and the location of cross-over points. The individual rock types plot well within the blue, mud-dominated and the red, grain dominated fields, which were based on the bounding curves of pore classes and Dunham classification.

The implication for wettability is shown on the lower right of Figure 7. At a distinct level in the reservoir (at any given capillary pressure) the grain dominated facies tend to be more mixed to oil wet, while the mud-dominated rocks show a more mixed to water wet behavior.

The wettability indication plotted in Figure 7 is based on the understanding of the reservoirs and rock types. Insofar the shape of the primary drainage curves or their cross-over points analysed through pore-network modeling could be used to indicate wettability for subsequent modeling of waterflooding.
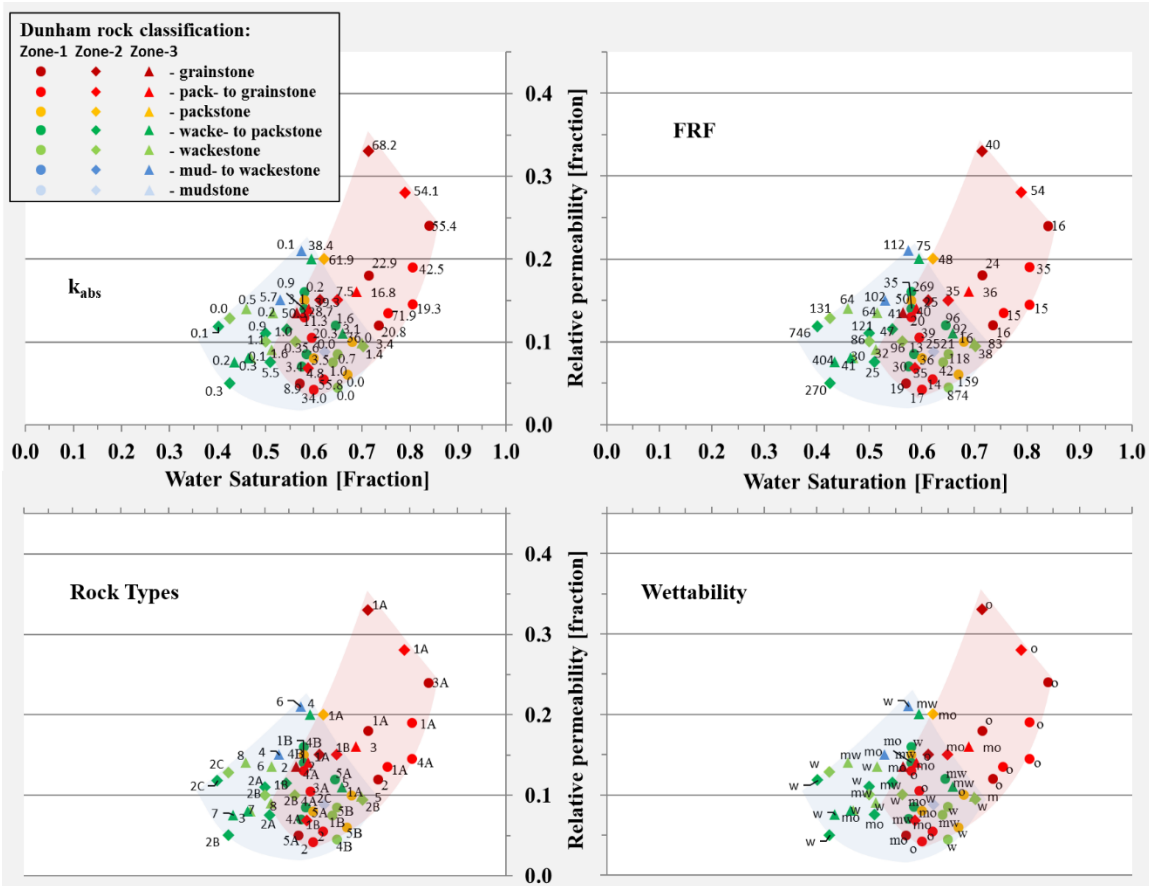

Figure 7. Primary drainage relative permeability cross-over points colour coded after Dunham classification and labeled with absolute permeability (upper left), formation factor (upper right), rock types (lower left) and wettability (lower right; o: oil wet, mo: mixed to oil wet, mw: mixed to water wet, w: water wet). The reservoir quality of the rock types generally decreases with increasing number. For Zones 1 and 2, "A" indicates moderate to good, while "B" and "C" are low to moderate reservoir conditions.

Figure 8 illustrates the results of waterflood modeling with the given wettability indications. The different behavior of the waterflood relative permeability curves between mixed to water-wet (blue) and mixed to oil-wet (red) rocks.

The results help to indicate the likely waterflood performance of the samples. The more grain-dominated facies are likely to have a lower initial water saturation in the reservoir and tend to be oil-wet during waterflooding. Now the good connectivity of the larger pore spaces allows the rapid movement of water, leading to high water relative permeabilities and a low cross-over saturation, which is associated with poor local displacement efficiency, see Figure 8 and page 329 in [9]. Instead, the mud-dominated samples are mixed to water-wet and have a less well-connected path of larger pores. This leads to a lower

water relative permeability, a higher cross-over saturation and more favourable recovery. Note that this is the opposite trend than seen for primary drainage and indicates the significance of both pore structure and wettability in the behavior.
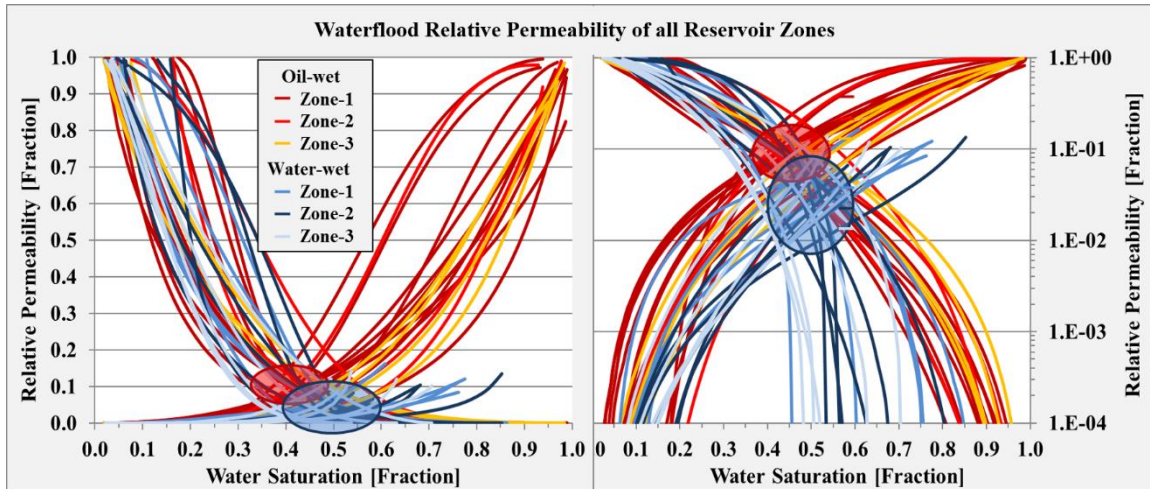

Figure 8. Waterflood relative permeability of Reservoir Zones 1, 2, and 3. Red and blue circles indicate the fields of cross-over points for the oil-wet samples and the water-wet samples, respectively.

It has been demonstrated in this study that individual rock types and their petrophysical properties have a distinct impact on the corresponding relative permeability curves, which then could be used for more dynamic rock classification/rock typing.

In this study, we have discriminated only between mud-dominated and grain-dominated facies based on the presence of different pore classes (digital; Figure 6, left) and based on the geological Dunham classification (Figure 6, right). This was then backed-up with absolute permeability measured in the laboratory, formation factor (digital) and the rock typing (petrophysical) and wettability indication. The data set presented here is promising - however, especially the grain-dominated facies show a too large variability (too wide a cross-over field) to be used for improved rock typing. A possible solution would be to study more in detail the contribution of individual pore classes within bi-, and tri- modal pore systems – not only volumetrically as done in this study but based on volume, distribution and connectivity of individual pore classes, incorporating their hydraulic properties.

CONCLUSIONS

We have demonstrated how the rapid and comprehensive prediction of multiphase flow properties using Digital Rock Physics, employing a multi-scale imaging and modeling work flow, can be used to interpret and quantify trends in behavior and assign rock types. In this study we show that the more grain-dominated facies give – for primary drainage relative permeability – a cross-over at high water saturation, indicating high-conductivity pathways of the larger pore spaces. These rocks tend to be more oil-wet for subsequent waterflooding which reverses the behavior: the cross-over is now pushed to low water saturation, indicating poor recovery, as the larger pores are filled rapidly by water as the

non-wetting phase. The more mud-dominated samples show the opposite behavior, tend to be more mixed to water wet, and provide more favourable waterflood recoveries.
This work offers a promising application of modeling technology and could be applied to a wider range of rocks using a more detailed classification of the pore structure and its connectivity.

ACKNOWLEDGEMENTS

REFERENCES

1. Kalam, M.Z., "Digital Rock Physics for Fast and Accurate Special Core Analysis in Carbonates", In: *New Technologies in the Oil and Gas Industry*, J.S. Gomes (eds), (2012), DOI:10.5772/52949.
2. Al-Ratrout, A.A., M.Z. Kalam, J.S. Gomes, M.S. Jouini, S. Roth, (2014). "Narrowing the Loop for Microporosity Quantification in Carbonate Reservoirs Using Digital Rock Physics and Other Conventional Techniques – Part II", *International Petroleum Technology Conference, Doha, Qatar*, (2014), IPTC 17702.
3. Roth, S., Y. Hong, H. Bale, T. Zhao, S. Bhattiprolu, M. Andrew, C. Weichao, J. Gelb and B. Hornberger, "Fully Controlled Sampling Workflow for Multi-Scale X-Ray Imaging of Complex Reservoir Rock Samples to be Used for Digital Rock Physics", *Search and Discovery*, (2016), Article #41840.
4. Dong, H. and M.J. Blunt. "Pore-network extraction from micro-computerized-tomography images", *Physical Review E*, (2009), **80**, 3, 036307.
5. Valvatne, P.H. and M.J. Blunt, "Predictive pore-scale modeling of two-phase flow in mixed wet media," *Water Resources Research*, (2004), **40**, 7, W07406.
6. Roth, S. "Porous Media Analysis System and Method." *International Patent Filing No.:PCT/CN2015/089409, filed September 2015*.
7. Dunham, R.J., "Classification of carbonate rocks according to depositional texture", In *Classification of carbonate rocks*, W.E. Ham (eds), American Association of Petroleum Geologists, **Memoir 1**, (1962), pp. 108–121.
8. Kalam, M. Z., T. Al Dayyani, A. Clark, S. Roth, C. Nardi, O. Lopez, P.-E. Øren, "Case study in validating capillary pressure, relative permeability and resistivity index of carbonates from X-Ray micro-tomography images", *SCA International Symposium, Halifax, Canada*, (2010), paper SCA2010-02.
9. Blunt, M.J., *Multiphase Flow in Permeable Media – A pore-scale perspective*, Cambridge University Press, Cambridge, (2017), DOI: 10.1017/9781316145098.

THE EFFECT OF SPREADING COEFFICIENT ON RECOVERY OF WATERFLOOD RESIDUAL OIL USING GAS INJECTION IN FRACTURED CARBONATE ROCKS: A MICRO-SCALE EXPERIMENTAL INVESTIGATION USING X-RAY MICROTOMOGRAPHY

M. Sabti, A.H. Alizadeh, E. Lowry, and M. Piri
Department of Petroleum Engineering, University of Wyoming,
1000 E. University Ave., Laramie, WY 82071-2000, USA

This paper was prepared for presentation at the International Symposium of the Society of Core Analysts held in Vienna, Austria, 27 August – 1 September 2017

ABSTRACT

Fractured carbonate reservoirs host a significant fraction of oil reserves around the world. Enhancing the recovery of oil from these reservoirs requires a considerably improved understanding of the displacement mechanisms governing the fluid transport from the matrix to the fracture network. During the last few decades, a considerable amount of effort has been dedicated to developing laboratory and field technologies to overcome the challenges associated with the complex flow behavior in these reservoirs during recovery processes. In this paper, we present the results of a pore-scale experimental study of tertiary gas injection in a fractured carbonate rock sample. A state-of-the-art, three-phase miniature core-flooding apparatus integrated with a high-resolution micro-CT scanner was employed to conduct two sets of three-phase brine/oil/gas experiments under spreading and nonspreading conditions. The initial two-phase, oil-water saturation conditions prior to gas injection were similar for both spreading and nonspreading fluid systems. The core sample, 10 mm in diameter and 48 mm long, was partially fractured to the middle, along the length of the specimen, in order to probe multiphase flow behavior in various topological locations of the sample including the matrix and the fracture in order to better understand matrix-fracture interactions. We developed an image processing workflow to map the pore fluid occupancies and fluid connectivity in both the fracture and the matrix. This allowed us to examine the impact of the spreading phenomena on oil extraction from the matrix to the fracture. During gas injection, since gas-liquid capillary pressures were negligible in the fracture conduit, gas displaced brine first. By increasing the gas flow rate in the spreading system, gas accessed trapped oil globules in the neighboring matrix, resulting in formation of spreading oil layers and re-connection of trapped oil globules. It was found that the ability of oil to maintain its hydraulic connectivity between the matrix and fracture by forming stable spreading layers, sandwiched between brine in the corners of pore elements and gas in their centers, improved the oil recovery efficiency significantly. Oil layer drainage, however, was not observed in the experiment performed with the nonspreading fluid system, resulting in higher remaining oil saturation.

INTRODUCTION

The infrequent discovery of new, producible oil fields has led the petroleum community to research new approaches to enhance the extraction of the remaining oil after primary or secondary recovery, particularly for complicated reservoir rock morphologies, such as fractured reservoirs. This type of reservoirs is one of the most important geological formations targeted for oil recovery by petroleum industry since they host a vast fraction of oil reserves worldwide. Further oil production from these reservoirs often requires the injection of a new fluid phase, in addition to oil and brine already present in the reservoir, to enhance the oil displacement efficiency from the matrix to the fractures. The coexistence of three fluid phases, such as brine, oil, and gas, within a fractured system introduces technical challenges in addition to the disparate hydraulic conductivity of the matrix blocks compared to the fracture network. The displacement mechanisms taking place under three-phase flow conditions, such as layer drainage, however, may play a significant role in connecting the matrix to the fracture by forming spreading oil layers and hence increasing the oil recovery. Layer drainage, in a porous medium saturated with brine, oil, and gas, refers to a process under which oil is displaced by gas in the presence of brine through stable and connected layers. Although a number of studies in the literature [1-4] have been dedicated to understanding the spreading phenomena and their impacts on remaining oil saturation, most of these investigations probed nonfractured porous media and did not consider the presence of fractures. Blunt et al. [2] discussed the importance of the spreading layers theoretically and experimentally. They performed gravity drainage experiments using sand columns and capillary tubes and concluded that the stability of oil layers in the spreading system provided hydraulic continuity for the oil phase and resulted in higher oil recovery. For the nonspreading system, however, less oil recovery was observed. Vizika and Lombard [3] investigated the effect of spreading characteristics on residual oil saturation. They carried out secondary gravity assisted inert gas injection experiments on a consolidated porous medium using fluid systems with positive and negative spreading coefficients. Under water-wet conditions, the oil relative permeability was almost identical at high oil saturations for both the spreading and nonspreading systems but showed differences at low oil saturations where layer flow played a more significant role. Zhou and Blunt [5], Sahni et al. [6], Alizadeh and Piri [7], and Øren and Pinczewski [8] also observed the impact of the flow through spreading layers experimentally. A recent study by Zolfaghari and Piri [9] investigated the formation and collapse of the spreading oil layers and oil cusps using thermodynamically consistent threshold capillary pressures and a three-phase pore-scale network model. The authors extensively investigated the effect of layer and cusp stability on three-phase relative permeabilities and validated their predictions against core-scale results reported by Alizadeh and Piri [7] and others in the literature.

Despite the knowledge gained through the above-mentioned studies on non-fractured systems, laboratory and field studies can be further expanded to improve our understanding about the fundamentals of multi-phase flow in fractured porous media. Over the last few years, researchers and scientists have been motivated to use the so-called "digital rock physics" workflow, which includes the interpretation of rock properties and in-situ fluid occupancies using advanced imaging technologies, such as X-ray microtomography [10].

This approach provides a mean for direct observation of pore space topology and fluid occupancy on a wide range of scales from millimeters to nanometers. This methodology allows researchers to verify previously-hypothesized multi-phase flow displacement theories.

In this study, a state-of-the-art experimental system including a high-resolution micro-CT scanner integrated with a three-phase core-flooding apparatus was utilized to perform two- and three-phase flow experiments on a miniature fractured carbonate core sample. The study was designed to demonstrate the role of spreading phenomena in displacing oil from the matrix to the fracture at the pore scale. The pore fluid occupancies were compared under spreading and nonspreading conditions during gas injection experiments.

MATERIALS AND METHODS
Rock sample and fluids
Fond Du Lac limestone quarried from an outcrop area in Wisconsin, USA, was selected for this study. It is a water-wet rock consisting mainly of calcium carbonate. A core plug, 38 mm in diameter and 120 mm long, was cut from a block of the selected rock using water and then oven dried at 110° C for 24 hours. Subsequently, a fracture was introduced into half of the core plug, i.e., from one of the end faces to nearly the middle of the medium as shown in Figure 1 (a, b). The fracture was induced by applying a non-uniform stress parallel to the stress axis of the core plug using the modified Brazilian test [11, 12]. The core plug was then X-ray imaged using a medical CT scanner to visualize the fracture and its orientation throughout the pore space. A miniature core samples, 10 mm in diameter and 48 mm in length, was cut from the fractured core plug using air as a coolant. The miniature sample was drilled in a way that the fracture was positioned in the middle of its cross section as illustrated in Figure 1 (b, c). The end faces of the miniature core sample were trimmed so that the fracture extended only over half of sample's length. The dimensions and the petrophysical properties of the miniature core sample are given in Table 1.
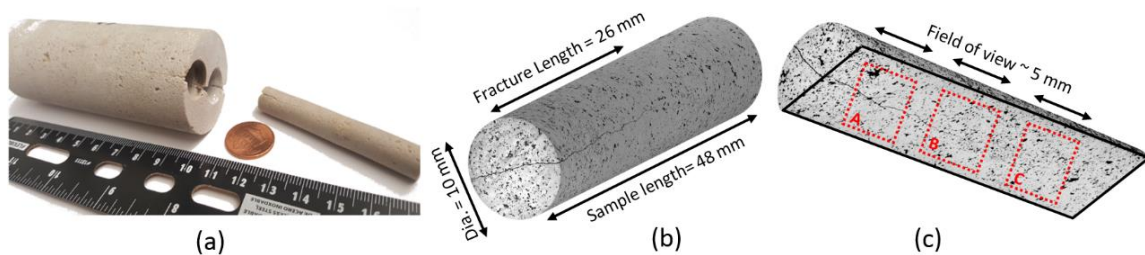

Figure 1. (a) The miniature sample drilled from the core plug, (b) a three-dimensional representation of the miniature sample, and (c) scan locations (i.e., A, B, and C) and their fields of view.

The core-flooding tests were carried out using two fluid systems with different spreading coefficients. The only difference between the two fluid systems was the oil phases used. The aqueous phase (i.e., the wetting phase) was prepared using distilled water, 2 wt% $CaCl_2$, 15 wt% NaI as an X-ray doping agent, and 0.01 wt% NaN_3 as an anti-bacterial

growth agent. A sacrificial limestone core was immersed in the aqueous solution for 24 hours in order to equilibrate the brine with the rock minerals and prevent rock dissolution during injection sequences. The oil phases (i.e., the intermediate-wetting phase) were Soltrol 170 for the spreading system and White Mineral Oil for the nonspreading system. Both oils were well purified prior to use by passing them through a gravity column filled with aluminum oxide (alumina) and silica gel to remove polar components and surface active impurities that could alter the wettability of the medium. In both fluid systems, 5 vol% 1-iodooctane ($C_8H_{17}I$) was added to the oils as an X-ray dopant. Sodium iodide and 1-iodooctane were used to establish sufficient contrasts among the fluid phases. The gaseous phase (i.e., the most nonwetting phase) was nitrogen with 99.9% purity. Table 2 lists the properties of the fluids used.

Table 1: Dimensions and petrophysical properties of the miniature core sample used in the experiments.

Rock	Length (mm)	Diameter (mm)	Porosity of the matrix (%)[*]	Gas permeability of the matrix (mD)[*]	Pore volume (ml)
Fond Du Lac limestone	47.98	9.98	10.9	13.8	0.4

[*]Porosity and permeability were measured on the core plug before creating the fracture using an automated helium porosimeter-permeameter.

Table 2: Properties of the fluids used in this study.

Fluid	Viscosity (mPa.s)	Density (kg/m[3)]
Brine (2 wt% $CaCl_2$ + 15 wt% NaI + 0.01 wt% NaN_3)	1.145	1138.12
Spreading oil (Soltrol 170)	2.526	802.13
Nonspreading oil (white mineral oil)	26.367	805.02
Gas (Nitrogen)	0.0187	62.84

Experimental apparatus

The experimental apparatus used in this work consisted of a three-phase core-flooding setup coupled with a high-resolution micro CT scanner (Xradia 510 Versa). As shown in Figure 2, the core-flooding setup included a miniature core holder, Rosemount® differential pressure transducers with different ranges, a three-phase separator, two accumulators, and six dual-cylinder Quizix® pumps. Three of the pumps were utilized to inject brine, oil, and gas into the core, one pump to maintain overburden pressure, one pump to receive the fluids produced from the core and regulate the pore pressure, and the last pump to compensate for fluctuations in the separator pressure caused by fluid withdrawal/accumulation. The wetted parts were made of Haselloy C-276 to prevent corrosion. Inside the micro-CT enclosure, the core holder was connected to high pressure PEEK (polyetheretherketon) tubing. This tubing is light-weight and flexible so it minimizes the amount of torque exerted on the core-holder during the rotation, which could severely impact the quality of images. An in-house custom-designed core holder was fabricated from carbon fiber because it is fully X-ray transparent and lightweight as well as having a high strength-to-weight ratio. It helps to significantly reduce scanning time and noise. The design of the core-flooding setup allowed for the equilibration of the three fluids (water/oil/gas) in a closed-loop bypassing the core prior to starting the experiment to avoid any mass transfer between the

phases. This system also allowed to dynamically scan the medium while injecting the fluids into the core sample. This feature enabled us to compare the pore fluid occupancies at exactly the same locations in the core sample during the course of the experiments without altering the pore configurations and fracture aperture. More details of the three-phase core-flooding setup can be found elsewhere [13].
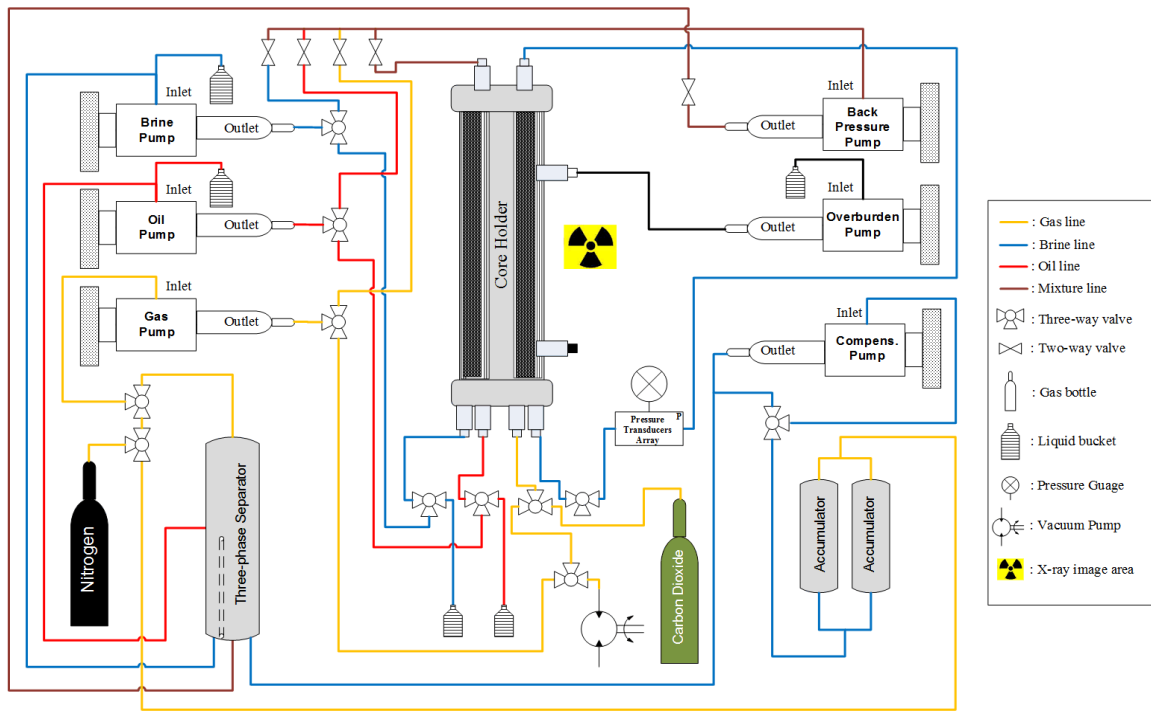

Figure 2. Experimental setup employed to perform the core-flooding experiments. The core holder was placed inside the micro-CT scanner's enclosure [14].

Experimental procedure

The core holder was placed vertically inside the micro-CT scanner, and then an overburden pressure of 100 psig was applied on the core sample. The fractured end face of the sample was placed at the bottom where the phases were injected from. After acquiring a reference scan with a resolution of 2.5 μm, the sample was flooded with gaseous CO_2, vacuumed, and subsequently fully saturated with degassed brine. The pore and overburden pressures were then concurrently increased to 500 and 600 psig, respectively, and several pore volumes of brine were injected into the sample. The net confining pressure of 100 psi was maintained in the course of all displacements to avoid any undesirable changes in the aperture of the fracture. After saturating the medium with brine, the core sample was scanned again to acquire a new reference image. Subsequently, it was subjected to an oilflood to establish initial water saturation (approximately 24%) followed by a waterflood to reach residual oil saturation. Upon establishment of the initial two-phase oil-brine saturation condition, gas was injected into the sample at increasing flow rates. During all steps of the oilflood, waterflood, and gas injection processes, the core sample was regularly

scanned with a low resolution of 5 μm to monitor fluid saturations. A high-resolution scan with a resolution of 2.5 μm was taken at the end of each step when saturations no longer changed. Table 3 lists the microtomography parameters used in each type of scan. It was intended to study the pore-scale displacement physics in three different locations of the sample labeled as *A, B,* and *C* in Figure 1 (c). These sites were selected to study fluid displacements and pore fluid occupancies at topologically different areas of the medium while using different fluid systems. All the displacements in the experiments were conducted at 20° C and under the capillary-dominated regime. The unsteady-state approach was used to perform the experiments, in which only one phase was injected in each displacement sequence. Furthermore, the core sample was cleaned thoroughly with isopropyl alcohol between the spreading and nonspreading experiments in an attempt to use the same specimen under both conditions. Details of the cleaning process can be found elsewhere [15].

Table 3: Microtomography parameters used to scan the core sample during the core-flooding experiments.

Recipe	Projections counts	Exposure time (s)	Camera binning	Resolution (μm)	Image size (pixel)	Objective
High-resolution scan	3201	6.5	1	2.5	2032 x 2032	4.0 X
Low-resolution scan	1601	2.0	2	5	1014 x 1014	4.0 X

RESULTS AND DISCUSSION

In this section, we present the results of the two sets of experiments performed using the spreading and nonspreading fluid systems. In both sets, similar waterflood residual oil saturation conditions were established prior to gas injection. Gas was then injected into the core sample in each case and possible reduction in residual oil saturation was monitored. The subtle governing displacement mechanisms responsible for the reduction of oil saturations in both systems are highlighted.

Two-phase flow condition

The initial two-phase oil-brine condition prior to gas injection in each experiment was established by injecting oil into a fully brine saturated sample to reach an average initial brine saturation (S_{wi}) of approximately 24%. This was followed by a waterflood to establish residual oil saturation (S_{orw}). The waterflood residual oil saturations obtained in the spreading and nonspreading experiments were 52 and 47%, respectively. We attempted to reach similar initial two-phase oil-brine saturation conditions in both spreading and nonspreading experiments to examine the impact of the spreadability of the oil on recovery of waterflood residual oil during gas injection. Since the oil viscosities in this study were different by an order of magnitude (see Table 2), a modified capillary number equation, $N_{ca} = \frac{\mu_w v_w}{\gamma_{ow} \varphi} (\frac{\mu_w}{\mu_o})^{0.4}$ [16], that accounts for the viscosity of the defending fluid (i.e., oil), was used to determine the waterflooding flow rate preceding the gas injection tests. In this equation, μ is viscosity, φ is porosity, γ is interfacial tension between the pairs of fluids, and v is Darcy velocity. The subscripts w and o denote brine and oil, respectively.

By analyzing the images, it was observed that oil, the nonwetting phase with respect to brine, initially filled the fracture as it constituted the path of the least resistance. As primary oil drainage progressed and the capillary pressure increased, oil started to invade the large brine-filled pore elements in the neighboring matrix. Brine, as the wetting-phase, covered the surface and the roughness of the pore and fracture walls and formed wetting layers in the corners of the pores. Figures 3(a) to (c) show the pore fluid occupancy of brine and oil starting from a dry void space to an initial brine saturation condition in an intra-fracture spacing. The brine was connected through the wetting layers that covered the solid surface throughout the medium. During the waterflood, which was conducted under the capillary dominated flow regime ($N_{ca} \sim 10^{-6}$), brine initially invaded small pore elements of the matrix as well as the narrow parts of the fracture aperture. By increasing the brine flow rate, local oil-water capillary pressure decreased allowing water to invade into larger elements and wider openings of the fracture as well. As expected, the imbibition threshold capillary pressures regulated the displacement sequence. As brine flow rate was increased to higher values, the brine layers swelled in many of the pore elements that in turn led trapped oil in the matrix and the narrow openings of the fracture by the snap-off displacement mechanism. This can be seen in Figure 3(d) where trapping of an oil globule in a selected fracture opening is illustrated.

Three-phase flow condition
Upon establishment of the waterflood residual oil, gas (the most nonwetting phase) was injected into the core sample. When gas is introduced to a water-wet porous medium having oil and brine, various possible displacement scenarios may result in the drainage of oil and brine: (1) gas displaces oil (gas-to-oil), (2) gas displaces brine (gas-to-brine), (3) gas displaces oil and oil displaces brine (gas-to-oil-to-brine), and (4) gas displaces brine and brine displaces oil (gas-to-brine-to-oil) [17]. The occurrence of these scenarios depends on many factors including the pore occupancy established before gas injection.

The analysis of the micro-CT images revealed that the injected gas initially propagated the fracture conduit due to the minimal gas-water threshold capillary pressure required. At very low gas flow rates, gas did not virtually invade the pore elements of the matrix adjoining the fracture and no oil displacement was observed in the surrounding matrix. By increasing the gas flow rate, the gas-brine capillary pressure overcame its displacement threshold values and gas invaded the matrix. At this juncture, the gas displaced brine first since brine was mobile and then reached the trapped oil blobs. After reaching these blobs, gas started to displace oil. The displaced oil could in turn displace brine, resulting in a double displacement event. This gas-to-oil-to-brine event was observed to be more favorable and frequent than gas-to-brine-to-oil. This finding has also been reported in previous studies [4,8,18]. The scenario during which gas displaces oil but oil does not displace brine was not observed in this study because the oil was initially trapped. This displacement event, however, was observed in our previous studies under secondary gas injection into a fractured porous medium where the wetting phase, brine, was immobile [15,19]. One should note that the spreadability of oil will also impact the oil displacement, which is explained in the next section.
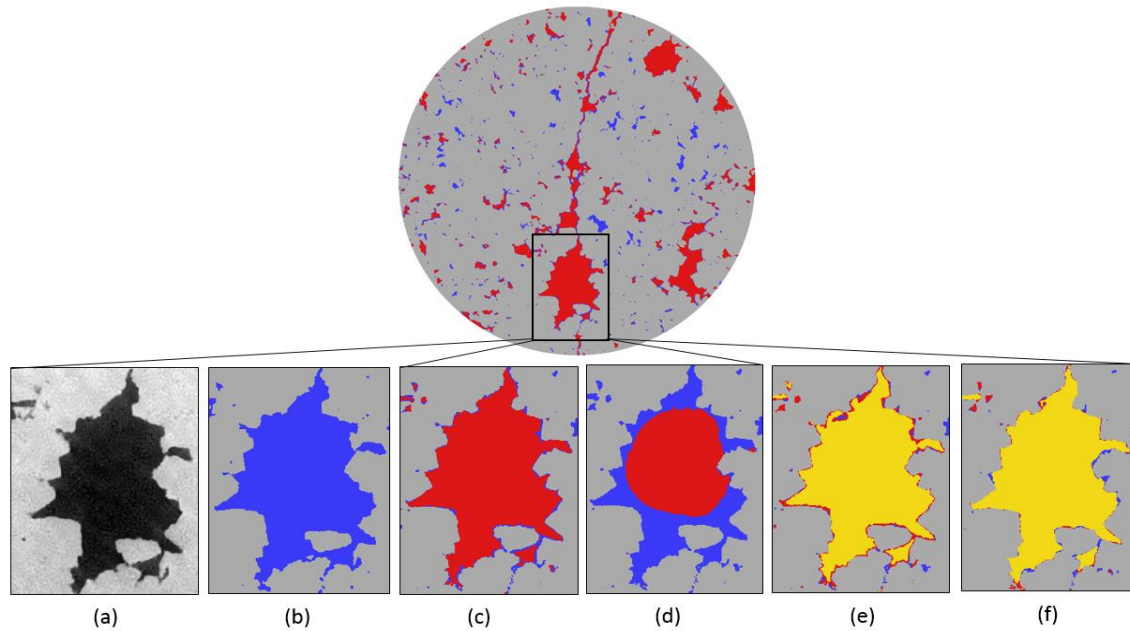
Figure 3. Segmented images showing the fluid occupancy map of an intra-fracture spacing at Location A during gas injection; (a) gray-scale image of the void space, (b) after fully saturation with brine, (c) after primary oil drainage, (d) after the waterflood, (e) after gas injection (in the spreading system), and (f) after gas injection (in the nonspreading system). Black, blue, red, yellow, and gray represent the void space, brine, oil, gas, and grains, respectively. The images were taken with a resolution of 2.5 μm and a field of view of 5 mm.

Spreading and nonspreading systems

The ability of oil to spread on water in the presence of gas is characterized by the oil spreading coefficient. It is defined as $S = \gamma_{gw} - (\gamma_{go} + \gamma_{ow})$, where $\gamma_{gw}, \gamma_{go},$ and γ_{ow} are the interfacial tension of gas-water, gas-oil, and oil-water pairs, respectively. When water, oil, and gas coexist in a system at equilibrium, the spreading coefficient can be either zero or negative. A zero or slightly negative value implies that oil will spread as a thin layer between water and gas with a non-negligible hydraulic conductivity. In contrast, a negative value means that oil will form a disconnected lens on the surface of water in the presence of gas and, hence, will not sustain its phase connectivity across the medium. The thickness and the stability of these layers depend on the spreading coefficient, pore geometry, and gas flow rate [7,8,9,20].

In the spreading experiment, as gas flow rate was increased (resulting in increasing the gas-water capillary pressure), gas reached the trapped oil globules. At this point, oil started forming continuous and stable spreading oil layers between brine and gas, which allowed oil to get reconnected. Subsequently, gas started to drain oil through these layers from the matrix to the fracture and towards production site. Figure 4 illustrates the tendency of oil to spread on the surface of water in the presence of gas. In this figure, a gas cluster invaded

a pore element that held trapped oil in the center and brine in the corners. As shown, oil spread and evolved into oil layer between the gas cluster and the brine. The analysis of the CT images of the spreading experiment further confirms that the spreading characteristics aided in maintaining oil-phase connectivity from the matrix to the fracture and hence enhanced the oil production (Figure 5). As seen in this figure, the oil formed a continuous layer that spread between the brine and gas and allowed for hydraulic connectivity of the oil in both the fracture and the matrix. However, in the nonspreading experiment, as the gas flow rate was increased, the oil globules did not possess the tendency to form spreading layers, thereby limiting the amount of oil that could be drained from the matrix to the fracture.

The ternary diagrams depicted in Figure 6 show the saturation paths for both the spreading and nonspreading oil experiments in both the neighboring matrix of the fractured portion of the core as well as the matrix-only site. In both locations, it can be seen that the gas initially displaced a large amount of brine at a relatively low flow rate of gas and then displaced more oil in the spreading system. However in the nonspreading system, the oil and the brine were displaced simultaneously with lower efficiency due to the characteristics of this system and the larger pressure required to displace the highly viscous disconnected trapped oil phase. This is evident by comparing the reduction of oil saturation in both spreading and nonspreading systems in Figure 6. As a result of the differences in the displacement mechanisms between the spreading and nonspreading systems, the saturation of oil at the end of gas injection reached as low as 14% for the spreading system compared to 27% in the nonspreading system.
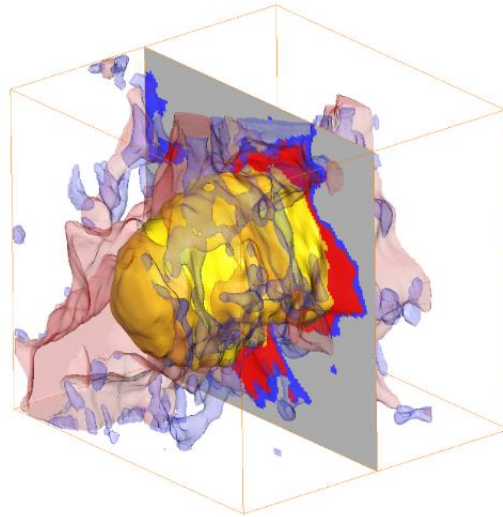

Figure 4. Segmented image showing the fluid occupancy map obtained during gas injection with a resolution of 2.5 μm. Faded blue/blue, faded red/red, yellow, and gray colors represent brine, oil, gas, and grains, respectively.
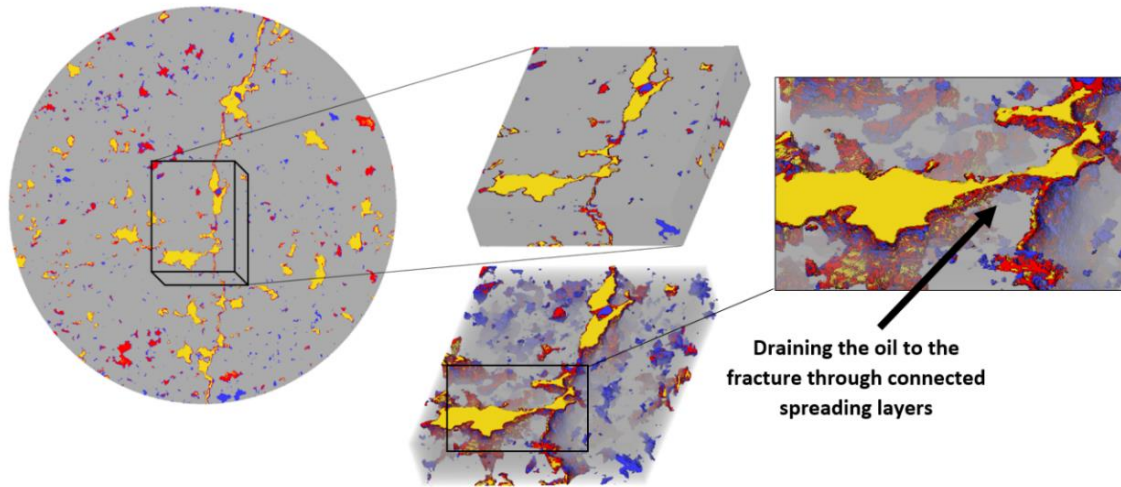
Figure 5. Segmented images showing the fluid occupancy during gas injection. Oil was drained from a pore element to the fracture through spreading layers. Faded blue/blue, faded red/red, yellow, and gray colors represent brine, oil, gas, and grains, respectively. The images were taken with a resolution of 2.5 μm.
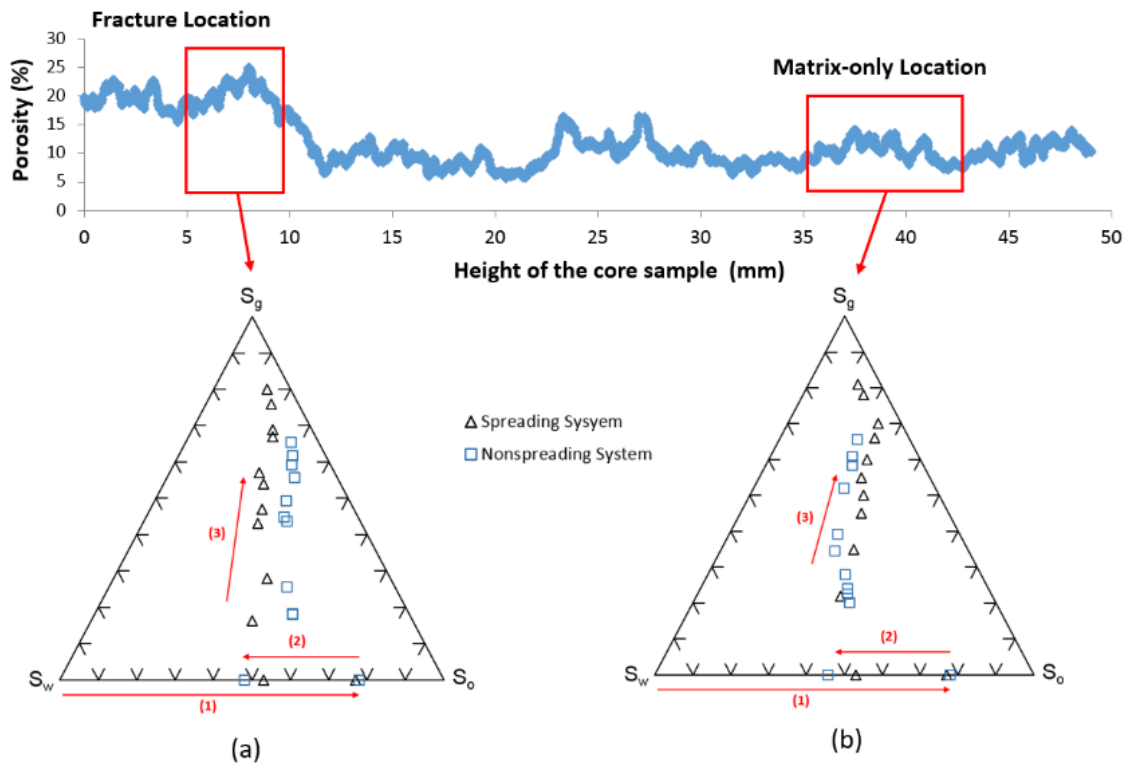

Figure 6. Saturation trajectories taken during the flow tests under spreading and nonspreading systems. The points represent fluid saturations measured (a) at Location A (matrix surrounding the fracture) and (b) at Location C (only matrix). (1), (2) and (3) represent oil drainage, waterflood and gas injection displacement sequences, respectively.

CONCLUSION

The formation of spreading layers strongly enhanced the hydraulic conductivity of the reconnected trapped oil from the matrix to the fracture, which resulted in much higher ultimate oil recovery as compared to the nonspreading system. This was confirmed by capturing a detailed map of the pore space and fluid distributions in the intact matrix and the matrix adjacent to the fracture under two- and three-phase flow conditions using X-ray micro-computed tomography. These pore-scale maps demonstrated the importance of the spreading phenomena to fluid displacements under three-phase flow conditions in a fractured porous system. The saturation profile over the course of gas injection (Figure 6) showed that brine was predominately produced first since it was the most well-connected phase. The nonspreading system showed lower initial displacement of oil and brine due to the higher gas pressure required to displace the highly viscous, trapped nonspreading oil. After increasing the gas flow rate, the gas obtained sufficient capillary pressure to invade areas containing trapped oil at which point oil layers began to form and re-connect the oil phase in the spreading system. In the nonspreading system, however, these layers were not clearly observed. This study demonstrates that recovery from fractured reservoirs can be vastly improved by directly leveraging the spreading characteristics of the fluids in fractured reservoirs under tertiary gas injection.

ACKNOWLEDGEMENTS

REFERENCES

1. Vizika, O., "Effect of the spreading coefficient on the efficiency of oil recovery with gravity drainage," proceedings of the Symposium on Enhanced Oil Recovery (1993) Denver, Colorado USA.
2. Blunt, M., D. Zhou, and D. Fenwick, "Three-phase flow and gravity drainage in porous media," *Transport in Porous Media*, (1995) **20,** 77-103.
3. Vizika, O., and J. Lombard, "Wettability and spreading: Two key parameters in oil recovery with three-phase gravity drainage," *SPE Reservoir Engineering*, (1996) **11**, 1, 54-60.
4. Keller, A., M. Blunt, and P. Roberts, "Micromodel observation of the role of oil layers in three-phase flow," *Transport in Porous Media* (1997) **26**, 277-297.
5. Zhou, D., and M., Blunt, "Effect of spreading coefficient on the distribution of light non-aqueous phase liquid in the subsurface," *Journal of Contaminant Hydrol*ogy, (1997), **25,** 1-2.
6. Sahni, A., J. Burger, and M. Blunt, "Measurement of three phase relative permeability during gravity drainage using CT scanning," paper SPE 39655, proceeding of SPE/DOE Improved oil recovery Symposium (1998), Tulsa, Oklahoma, USA.

7. Alizadeh, A.H., and M. Piri, "The effect of saturation history on three-phase relative permeability: An experimental study," *Water Resources Research*, (2014) **50**, 1636-1664.

8. Øren, P., and W. Pinczewski, "The effect of wettability and spreading coefficients on the recovery of waterflood residual oil by miscible gasflooding," *SPE formation evaluation*, (1994) **9**, 2,149-156.

9. Zolfaghari, A., and M. Piri, "Pore-scale network modelling of three-phase flow based on thermodynamically consistent threshold capillary pressure: I: Cusp formation and collapse," *Transport in porous media*, (2017) **116**, 1093-1137.

10. Andrä, H., N. Combaret, J. Dvorkin, E. Glatt, J. Han, M. Kabel, Y. Keehm, F. Krzikalla, M. Lee, and C. Madonna, "Digital rock physics benchmarks–Part I: Imaging and segmentation", *Computer & Geosciences*, (2013) **50**, 25–32.

11. Guo, H., N.I. Aziz, and L.C. Schmidt, "Rock fracture-toughness determination by the Brazilian test, "Engineering Geology, (1993) **33** (3), pp.177-188.

12. Alajmi, A., and A. Grader, "Analysis of Fracture-Matrix Fluid Flow Interactions Using X-ray CT," SPE 65628, Proceedings of the SPE Eastern Regional Meeting, Morgantown, West Virginia, 2000.

13. Alizadeh, A.H., M.A. Ioannidis, and M. Piri, "CO_2-saturated brine flooding: An effective process for mobilization and recovery of waterflood residual oil," paper SCA2011-07, proceeding of the Symposium of the Society of Core Analysts, (2011), Austin, Texas, USA.

14. Piri, M., Recirculating. Constant back pressure core-flooding apparatus and method., *Patent W02012/082797* (University of Wyoming, 2012).

15. Sabti, M., A.H. Alizadeh, and M. Piri, "Three-phase flow in fractured porous media: experimental investigation of matrix-fracture interactions," paper SPE 181891, presented at the SPE Annual Technical Conference, (2016), Dubai, UAE.

16. Abrams, A., "The influence of fluid viscosity, interfacial tension, and flow velocity on residual oil saturation left by waterflood," *Society of Petroleum Engineers*, (1974) **15**, (05).

17. Kantzas, A., I. Chatzis and F. Dullien, "Enhanced oil recovery by inert gas injection," paper SPE 17379, presented at SPE Enhanced Oil Recovery Symposium (1988).

18. Khishvand, M., A.H. Alizadeh, and M. Piri, "In-situ characterization of wettability and pore-scale displacement during two- and three-phase flow in natural porous media," *Advances in Water resources*, (2016) **97**, 279-298.

19. Sabti, M., A.H. Alizadeh, and M. Piri, "Matrix-fracture interactions during gas injection: A pore-scale experimental study," paper SCA2016-029, proceeding of the Symposium of the Society of Core Analysts, (2016), Snowmass, Colorado, USA.

20. Piri, M., and M. Blunt, "Three-phase threshold capillary pressures in noncircular capillary tubes with different wettabilities including contact angle hysteresis," *Physical Review E*, (2004) **70**, 061603.

NEW EXPERIMENTAL EVIDENCE ON THE DOMINANT MECHANISM OF OIL RECOVERY BY LOW SALINITY WATER INJECTION IN CARBONATE ROCKS

Mohamed AlHammadi, Pedram Mahzari, and Mehran Sohrabi
Centre for Enhanced Oil Recovery and CO2 Solutions, Institute of Petroleum
Engineering, Heriot-Watt University, Edinburgh, UK

ABSTRACT

In the past two decades, several investigations have shown an improvement in oil recovery by low salinity water injection (LSWI) in core flood experiments and some pilot tests have been performed. Despite numerous publications on this matter, the underlying mechanisms leading to improved oil recovery have not yet been confirmed. It has been recently reported that certain crude oil-brine interactions take place during LSWI that lead to formation of water in oil micro-dispersions. The role of this mechanism, which is linked to the natural surface active components of the oil, has already been demonstrated in improving oil recovery in clastic rocks. In this work, we will test whether micro-dispersion formation could also be applicable to carbonate reservoirs.

This experimental investigation was performed on crude oil and rock samples obtained from a carbonate oil reservoir in the Middle East. Firstly, using an in-house methodology, a crude oil sample with high propensity to form micro-dispersion was identified. This crude oil (Crude-A) was then used in a series of oil/brine interaction tests involving formation brine and various diluted versions of it, to quantify the micro-dispersion formation capacity of the oil. Another sample from the same crude oil was then prepared by removing the compounds responsible for micro-dispersion formation (Crude-At). The two crude oil samples, one capable and the other incapable of forming micro-dispersion, were then characterised and prepared for core-scale experiments.

We observed that the crude oil with high micro-dispersion resulted in additional oil recovery during tertiary LSWI compared to the crude oil with low micro-dispersion. Therefore, the presence or absence of the oil compounds behind micro-dispersion formation can make the system respond positively or negatively to LSWI. The effluents of the coreflood experiments were also analysed. Interestingly, identical behaviour in terms of both pH and ionic concentrations was obtained with the two different oil recovery profiles, indicating that the micro-dispersion formation propensity of the crude oil is the main factor determining the efficacy of LSWI in carbonate rocks. The results provide useful new insights into the role of crude-oil/brine interactions during LSWI in carbonate reservoirs and their impacts on the response of a reservoir to LSWI.

INTRODUCTION

Enhanced oil recovery methods (EOR) are widely used in oil reservoir management. Recently, the process of injecting high salinity brine (HS) in secondary mode and low salinity brine (LS) in tertiary mode, has shown promising results in terms of recovering crude oil in carbonate reservoir rock [1]. The underlying mechanisms behind LSWI EOR at the pore level for certain conditions of crude oil and rock properties have been investigated for a period spanning around 30 years [2]. Among the mechanisms behind LSWI EOR, wettability alteration have been found to be more widely accepted as the underlying cause, from many experimental analyses and design data.

The fundamental principle of wettability alteration is the change in rock properties from oil-wet and/or mixed wet toward water-wet conditions, due to molecular interactions among the oil, brine, and rock minerals [2]. Further, the possible mechanisms behind wettability alterations can be broadly classified as rock-fluid interaction mechanisms and fluid-fluid interaction mechanisms. In a rock-fluid interaction mechanism, the involvement of multicomponent ionic exchange (anionic exchange and/or substitution reaction [3,4], mineral dissolution [5], and surface charge change [6]) in the rock matrix during LSWI EOR has been considered as the main cause of wettability alterations and hence, improved oil recovery during tertiary flooding. A close look at the proposed mechanism(s) in carbonate rocks would indicate many contradictory views.

In fluid-fluid interaction mechanisms, the formation of water micro-dispersions [7], due to the fluid-fluid interaction effect of oil-water contact flows, has been linked to improved oil recovery during LSWI EOR. It has been reported recently, Emadi and Sohrabi [12] that, certain crude oil-brine interactions take place during LSWI that lead to the formation of water-in-oil micro-dispersions. The role of this mechanism, which is linked to the natural surface active components of the oil, Mahzari and Sohrabi [13], has been demonstrated by improving oil recovery in clastic rocks. The aim of this work is to investigate whether the micro-dispersion mechanism can also control EOR by LSWI in carbonate reservoir rocks. To investigate this mechanism, a systematic analysis was carried out.

In this paper, we demonstrate the importance of the formation of micro-dispersion to additional oil recovery during LSWI EOR in carbonate reservoir rock. This is done by a targeted experimental design to study both fluid-fluid and rock-fluid interactions, to answer the question of whether a link can be observed between the role of micro-dispersion formation during oil-brine interaction and process of oil recovery during tertiary LS EOR in carbonate reservoir rock.

The paper is organised as follows: section 2, provides a brief introduction to the mechanism of micro dispersion due to oil-brine interaction, causing wettability alterations. Sections 3 explains the experimental design and the procedure used to investigate the cause of LSWI EOR. The results of these experiments are discussed in section 4 and, finally, we conclude this paper with a summary and future outlook in section 5.

BACKGROUND OF MICRO-DISPERSION AS A CAUSE OF WETTABILITY ALTERATION

Micro-dispersions are essentially packets (micelles) of water surrounded by certain indigenous surface active compounds of the crude oil [9]. In [10], the authors proposed two mechanisms that link the formation of these micelles to oil recovery by LSWI EOR.

- Wettability alteration due to migration of natural surface active components of the oil from the interface into the bulk of the oil
- Transport of micro-dispersion in the oil, in a manner similar to the osmotic effect, and their coalescence at the interfaces between crude oil and high salinity water, expelling oil from dead-end pores

Further the authors of [10], illustrated how the salinity variation would cause the pre-adsorbed natural surface active materials to migrate from the rock surface toward to the bulk of the oil phase, bringing about mobilization of trapped oil.

Error! Reference source not found.1 shows the formation of micro-dispersions during LSWI, at different scales. Figure 1A is a snapshot of a micro model experiment of LSWI at the macro scale. Figure 1B shows the interface between the oil and the low salinity brine during the low salinity brine flooding (images obtained from micromodel), showing that when low salinity brine contacts certain crude oils the colour of the oil becomes dark. Further, in Figure 1B, we can observe the formation of dark particles in the oil phase near the interface. Based on a series of micromodels and experiments, it was found that there is a correlation between the appearance and disappearance of these dark particles (which are referred to as micro-dispersion) and salinity of the brine [9]. Figure 1C, which is an ESEM (Environmental Scanning Electron Microscope) image of a sample taken from where the dark particles formed, shows white spots (determined as droplets of water using EDS). Further, each droplet of water (i.e. a nucleus of water) is composed of some ions taken from the LS brine and surrounded by particular components from the crude oil [8]. Analysis of these white spots showed that these micro-dispersions consist of both organic and inorganic compounds, arranged so that they have a centre, which is a water nucleus, and around it a layer of organic polar components coming from the oil (i.e. the oil encapsulates the water molecule) [10]. Figure 1D shows the micro-dispersion structure: a water molecule surrounded by polar molecular components of crude oil [8]. Figure 1E shows the arrangement of indigenous surface-active materials of oil in HS and LS systems. In high salinity systems, surface-active agents tend to adhere to the rock surface, creating an oil-wet condition. In the LS system, water, in the form of oil micro-dispersion, and indigenous oil surfactants leave the rock surface, accumulating around the water micro-dispersion [10].

Injection of LS brine results in the activation/release of the crude oil's natural surface active agents from the oil-water interface and brings about development of water micro-dispersion. This alters the oil surface charges, which itself changes the balance between repulsive and binding forces between the oil and the rock surface [11].

EXPERIMENTAL DESIGN

This section describes the experimental procedure followed in the lab to validate micro-dispersion as the mechanism for wettability alteration resulting in additional oil recovery during tertiary LSWI. This experimental study has two parts, namely, a fluid-fluid interaction test and a rock-fluid interaction test. These two parts are detailed in the two sections below.

(A) – Experimental Setup:
This section explains part 1 of the experimental set up and analysis **Error! Reference source not found.**. In this part, crude oils with the capability of forming micro-dispersions with low salinity brine were identified by conducting series of crude oil-brine interaction tests. A set of five crude oil samples was selected for the fluid-fluid characterization test (i.e. the crude oil-brine interaction test). These crude oil samples were filtered through centrifuging at $70\,^{0}$ Celsius to remove any solid or suspended particles from it. We then selected four formation brine samples of different salinities, ranging from 200,000 ppm to 1,000 ppm. We placed each brine sample in an in-house set-up and each crude oil sample was added on top of the brine, thus providing 20 combinations of brine-oil contacts. After 24 hours, the brine was drained slowly from the bottom, with a very low flow rate. Following the complete drainage of brine from the oil-brine samples, we took a sample of each crude oil which was interfacing with the brine prior to drainage. These samples of crude oil were finally used to measure the amount of micro-dispersion formed during the oil-brine interface interactions. Karl-Fischer Titration was employed to quantify the amount of micro-dispersion. After the complete analysis of the oils in part 1, Crude oil A was identified as the one with the highest propensity to form high micro-dispersions, compared to other samples of crude oil, when contacted with low salinity brine. A detailed explanation of this experimental methodology can be found in the paper [8]
Further to this, to conduct a fluid-rock interaction test, we prepared an additional crude oil, At, from Crude oil A, in such a way that crude oil At had a low capability to form micro-dispersion when contacted with low salinity brine compared to crude oil A. The preparation of crude oil At was carried out by selecting only the upper two thirds of Crude oil A, where no micro-dispersion was formed during the contact of Crude oil A with the low salinity brine sample.

(B) Recovery validation by core flooding:
This section explains part 2 of the experimental procedure and analysis. In part 2, the crude oil with high micro-dispersion was shown to recover additional oil during tertiary LSWI. In this validation process, two crude oils, Crude oil A and Crude oil At were selected to undergo LSWI for EOR.

First, two long cores with similar properties were selected for tertiary LSWI (12 inches long by 1.5 inch in diameter from a Middle East carbonate reservoir). The selected cores were then cleaned by flush cleaning at high temperature with toluene and methanol. The basic properties of each core were then measured, Table 1, which demonstrates acceptable similarities between the cores in terms of porosity, brine permeability, and initial water saturation. Next, the initial water saturation was established using mineral oil, followed by

aging the two cores by injecting the Crude oils A and At through the respective cores at the reservoir temperature for 21 days. During the aging period, the differential pressure (dP) across each core was measured and the crude oils were injected continuously at a rate of 1.5 PV per week until the dP across the cores became stable. An average initial oil saturation of 0.91 was established in the two core samples. Each core was then subjected to forced displacement by water using a flow rate of 4 cc/hr at a temperature of $80\,^{0}$C and pressure 1000 psi. The sequence of fluid injection consisted of secondary high salinity water injection, followed by tertiary low salinity water injection for an extended time period. Throughout the experiment, the oil recovery and dP profiles were recorded. In addition, the pH value and ionic composition of the core effluent were measured. The HSWI was continued until no further oil production was observed. After no oil production was seen in the core effluent, three bumped floods were then performed at rates of 50, 70, and 80 cc/hr to check for any capillary end effect. LSWI was injected in tertiary mode with the same injection rate. In tertiary modes, the improved oil recovery by low salinity was found to be directly related to the presence of micro-dispersion.

RESULTS AND DISCUSSION

Figure 1 summarises the variation in micro-dispersion formed during the contact of Crude oil A and Crude oil At with the brines of different salinity, ranging from 1,000ppm to 208,600 ppm. From Figure 3, we can clearly identify that crude oil A has a great deal of potential to form micro-dispersion at low salinity conditions compared to Crude oil At. Furthermore, the amount of micro-dispersion formed by Crude oil A increases as the salinity of the brine decreases. However, in contrast, Crude oil At did not show any formation of micro-dispersion at all salinity levels of the formation brine. The reason for selecting very dilute salinity (1,000ppm) is to demonstrate the role of the crude oil's ability to form micro-dispersion in helping to enhance the oil recovery during tertiary LSWI. Since Figure 3 shows that crude oil A has more capability to form micro-dispersion, one may expect high oil recovery during tertiary LSWI compared with this oil compared to crude oil At, which has a poor capability to form micro-dispersion.

Figure 2 (a) shows the plot of oil recovery and the plot of dP versus injected pore volume during secondary high salinity flooding in the two cores, displacing Crude oil A in the first core and displacing Crude oil At in the second core. From the figure, we can observe that the trend of the oil recovery profile does not show significant variation, irrespective of the large difference between crude oil A and crude oil At in their propensity for micro-dispersion. However, the slight difference in the oil recovery could be due to the initial wettability of each core and the pore geometry (i.e. structure). Prior to tertiary recovery, we ensured that all the other artefacts, associated with low injection resulting end effects, which might contribute to oil recovery in the tertiary LSWI, for example, capillary end effects, which may contribute to low salinity EOR [12], are reduced substantially. This reduction of the artefacts is carried out by employing a series of bump floods. The results of the bump flood in the two cores after secondary recovery, shown in Figure 2 (b), indicate that there is no capillary end effect

Figure 3 shows the outcome of the tertiary LSWI in this carbonate system. 6.3% additional oil recovery was achieved in the coreflood experiments where Crude oil A was used. On the other hand, when crude At was used, tertiary low salinity water could not improve the oil recovery. The results confirm the positive response of this carbonate system to LSWI when a crude oil with high propensity to form micro-dispersion was used. Thus as far as these carefully designed experiments could reveal, micro-dispersion formation would be the main cause for additional oil recovery.

The core effluent was analysed to obtain the profiles of ionic concentration and pH value, as presented in Figure 4 and Figure 5. To obtain a better understanding of the geochemical process in terms of rock-brine interactions, we first measured the pH of the water, because this provided an indication regarding the rock-brine interactions. The pH value during tertiary LSWI showed a higher value, due to calcite dissolution which had occurred inside the core. In terms of ionic concentration of the effluent, the ionic concentration for LSWI is a diluted version of that in HSWI (1,000 ppm): thus, the ratios of the ions in both floods are the same. Because of this, we have plotted the ratio of the ions, instead of plotting the concentration of the ions in the conventional way (i.e. C/Co). The ratios of both calcium and magnesium to sodium have increased compared to the ratio in the injected concentration. This shows that there is a possibility of mineral dissolution from the rock causing this increase. Moreover, the ratio of sulphate to chloride exhibits an increase after one pore volume of LSW was injected, which reached the maximum value at two pore volumes, and then gradually decreased and fell to its lowest value. This increase in sulphate would be related to the release of ions from the rock surface and was probably due to dissolution of anhydrite.

Thus, we observed a similar increase in pH value, together with mineral dissolution, and also anhydrite dissolution, when using Crude oil A and Crude oil At in the respective core flood tests during LSWI. However, the resultant increases in oil recovery for the core flood test using only Crude oil A, which has high micro-dispersion, imply that the fluid-rock interaction mechanism has not played a significant role in additional oil recovery during tertiary LSWI. The results of this study reveal that pH increase, mineral dissolution (include calcite and anhydrite) are not needed for LSWI to work in carbonate rock. Nasralla [13], also conclude that mineral dissolution is not the dominant mechanisms in increasing oil recovery in LSWI. However, this conclusion was based in brine unable to dissolve calcite, whereas some brines which dissolved calcite produce no additional oil recovery. Furthermore, the finding of this study that anhydrite dissolution is not necessary for improved oil recovery conflict with Austad's [14] conclusion that increase oil recovery is linked to anhydrite dissolution, Moreover, the result shown in Figure 3 indicates that Crude A, with high propensity to form micro-dispersion, results in high oil recovery and leads us to conclude that the micro-dispersion mechanism would be the primary mechanism for wettability alteration, thereby increasing the oil recovery during tertiary LSWI.

CONCLUSION

In this paper, the underlying mechanisms leading to improved oil recovery during tertiary LSWI were analysed. The results provide new experimental evidence on the underlying mechanism causing the improved oil recovery during LSWI, which is micro-dispersion formation. Two crude oil samples having high and low propensity to form micro-dispersion were selected and the core flood experiments have verified the link between the formation of micro-dispersion and the improvement in oil recovery. Furthermore, the experiments also confirmed that geochemical interactions such as mineral dissolution, sulphate interactions, and pH variations are not the primary mechanism for such additional recovery. From the experimental outcome, it is conceivable that identifying the crude oil propensity to form micro-dispersions can be a feasible method to evaluate the effectiveness of LSWI.

ACKNOWLEDGEMENTS

REFERENCES

.
1.   Yousef, A., Al-Saleh, S., Abdulaziz, A., & Mohammed, A. (2010). *Laboratory investigation of novel oil recovery method for carbonate reservoirs*. Paper SPE 137634 presented at Canadian Unconventional Resources and International Petroleum Conference, Calgary, Alberta, Canada, 19–21 October.
2.   Morrow, N., & Buckley, J. (2011). *Improved oil recovery by low-salinity waterflooding*. Journal of Petroleum Technology, *63*(05), 106-112.
3.   Lager, A., Webb, K., Black, C., Singleton, M., & Sorbie, K. (2006). *Low salinity oil recovery-an experimental investigation*.
4.   Austad, T., et al. (2009). *Is wettability alteration of carbonates by seawater caused by rock dissolution*. International Symposium of the Society of Core Analysts held in Noordwijk, The Netherlands, SCA2009-43
5.   Hiorth, A., et al. (2010). "*The impact of pore water chemistry on carbonate surface charge and oil wettability*." Transport in Porous Media 85(1): 1-21.
6.   Mahani, H., et al. (2015). *Driving mechanism of low salinity flooding in carbonate rocks*. EUROPEC 2015, Society of Petroleum Engineers
7.   Sohrabi, M., et al. (2015). *Novel insights into mechanisms of oil recovery by low salinity water injection*. SPE Middle East Oil & Gas Show and Conference, Society of Petroleum Engineers
8.   Mahzari, P. and M. Sohrabi (2014). *Crude oil/brine interactions and spontaneous formation of micro-dispersions in low salinity water injection*. SPE Improved Oil Recovery Symposium, Society of Petroleum Engineers.
9.   Emadi, A., & Sohrabi, M. (2013). *Visual investigation of oil recovery by lowsalinity water injection: formation of water micro-dispersions and wettabilityalteration*.

10.   Sohrabi, M., Mahzari, P., Farzaneh, S. A., Mills, J. R., Tsolis, P., & Ireland, S. (2016). Novel insights into mechanisms of oil recovery by use of low-salinity-water injection. *SPE Journal*.

11.   Kanicky, J. R., Lopez-Montilla, J.-C., Pandey, S., & Shah, D. (2001). *Surface chemistry in the petroleum industry*. Handbook of applied surface and colloid chemistry*, 1*, 251-267.

12.   Masalmeh, S. K., Sorop, T., Suijkerbuijk, B. M. J. M., Vermolen, E. C. M., Douma, S., van del Linde, H. A., & Pieterse, S. G. J. (2014). *Low salinity flooding: experimental evaluation and numerical interpretation*.

13.   Nasralla, R. A., Sergienko, E., Masalmeh, S. K., van der Linde, H. A., Brussee, N. J., Mahani, H., . . . Alqarshubi, I. (2014). *Demonstrating the potential of low-salinity waterflood to improve oil recovery in carbonate reservoirs by qualitative coreflood*. Paper presented at the Abu Dhabi International Petroleum Exhibition and Conference

14.   Austad, T., et al. (2011). "*Conditions for a low-salinity enhanced oil recovery (eor) effect in carbonate oil reservoirs*." Energy & Fuels 26(1): 569-575.

Table 1 properties of the cores and brines used in this study

Brine used				
Salt	Formation water, g/l	Diluted formation water, g/l		
$CaCl_2*2H_2O$	101.28	5.96 times dilution	41.72 times dilution	208.6 times dilution
$MgCl_2*6H_2O$	13.96			

NaCl	150.2			
Na$_2$SO$_4$	0.55			
	208,600 ppm	35,000 ppm	5,000 ppm	1,000 ppm
Cores properties				

	Core flood test -1	Core flood test-2
Length, cm	30	30
Diameter, cm	3.75	3.75
Porosity, frac.	0.268	0.272
K brine,mD	2.6	2.43
Swi, frac.	0.09	0.1
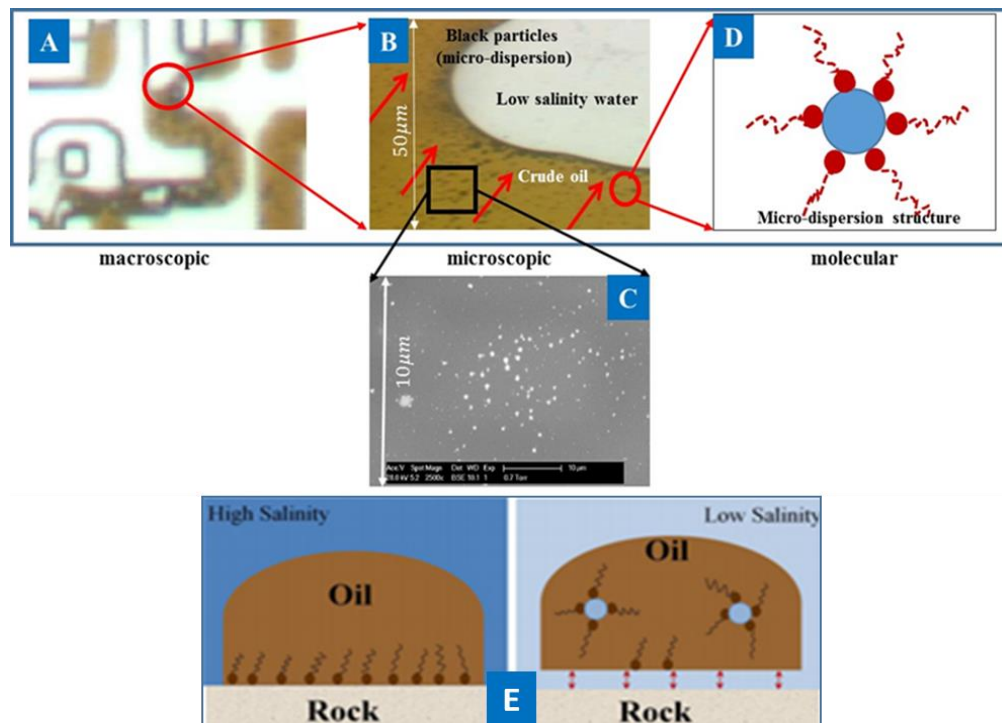
Figure 1 Spontaneous formation of micro-dispersion during the displacement of crude oil by low salinity water. A: formation of micro-dispersion in the oil phase during LSWI in the micromodel. B: a highly magnified section of the micromodel showing the instantaneous formation of micro-dispersion when LS brine contacts the crude oil. C: crude oil contact with LS brine under ESEM image, note the light spots (i.e. dark particles as seen in micromodel). D: illustration of micro-dispersion structure, representing the dark (B)/light (D) particles; these include organic and inorganic components: the polar compounds of the crude oil encapsulate the water molecules. E showing the arrangements of indigenous surface active materials of oil in HSWI and LSWI.
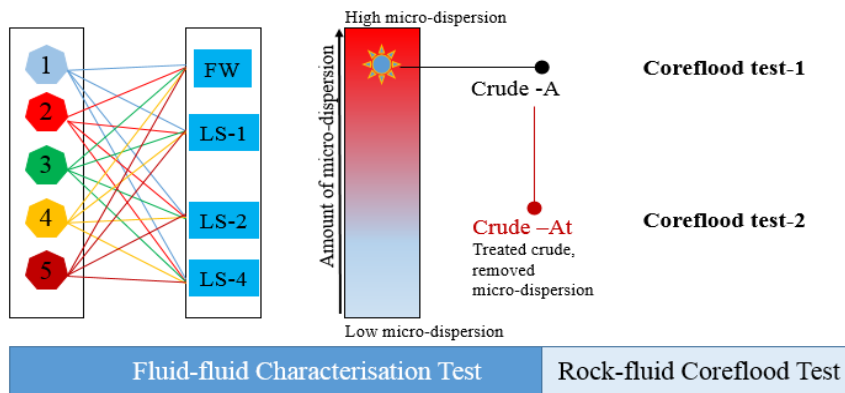
Figure 2: Experimental design: screening propensity of crude oils for micro-dispersion at different salinities and design of the fluid displacement efficiency test, accordingly. Crude A is prone to form high micro-dispersion; Crude At is the same as Crude A; the only difference is that we have removed micro-dispersion from the original crude oil. Crude A and Crude At are sharing the same reservoir oil but crude At is treated by removing micro-dispersion (i.e. polar components); columns 1 and 2 respectively represent oil and water samples. The left side (columns 1 and 2) shows a mixed matrix where heptagons 1 to 5 represent different crudes brought together with 4 different water compositions.
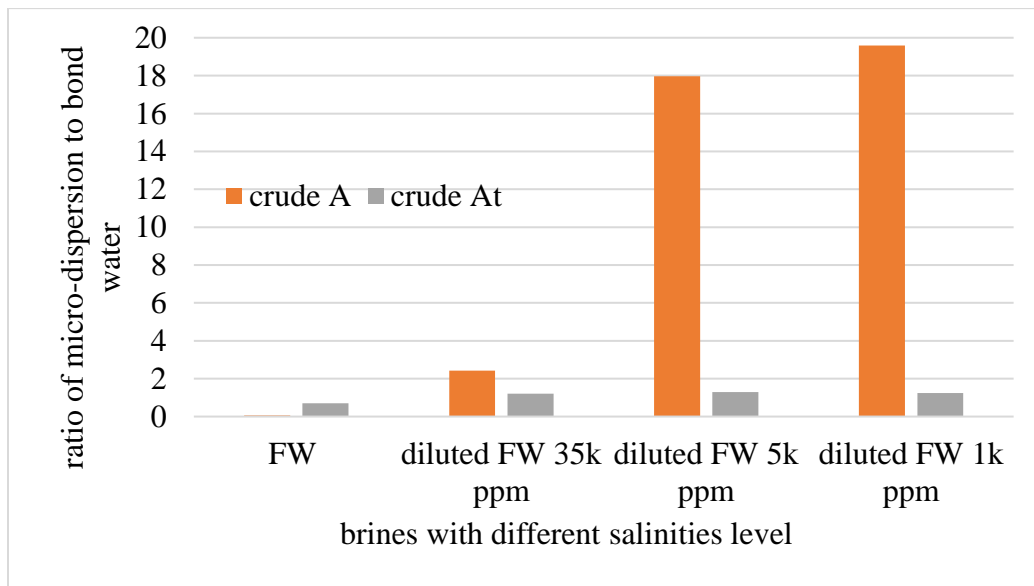

Figure 1: The two selected crude oils were contacted with brines of different salinities to quantify the amount of micro-dispersion in each crude oil. Y-axis shows the ratio of amount of micro-dispersion to the bond water (original crude oil pre-contacted). A LSW with 1,000 ppm was selected for the tertiary coreflood tests.

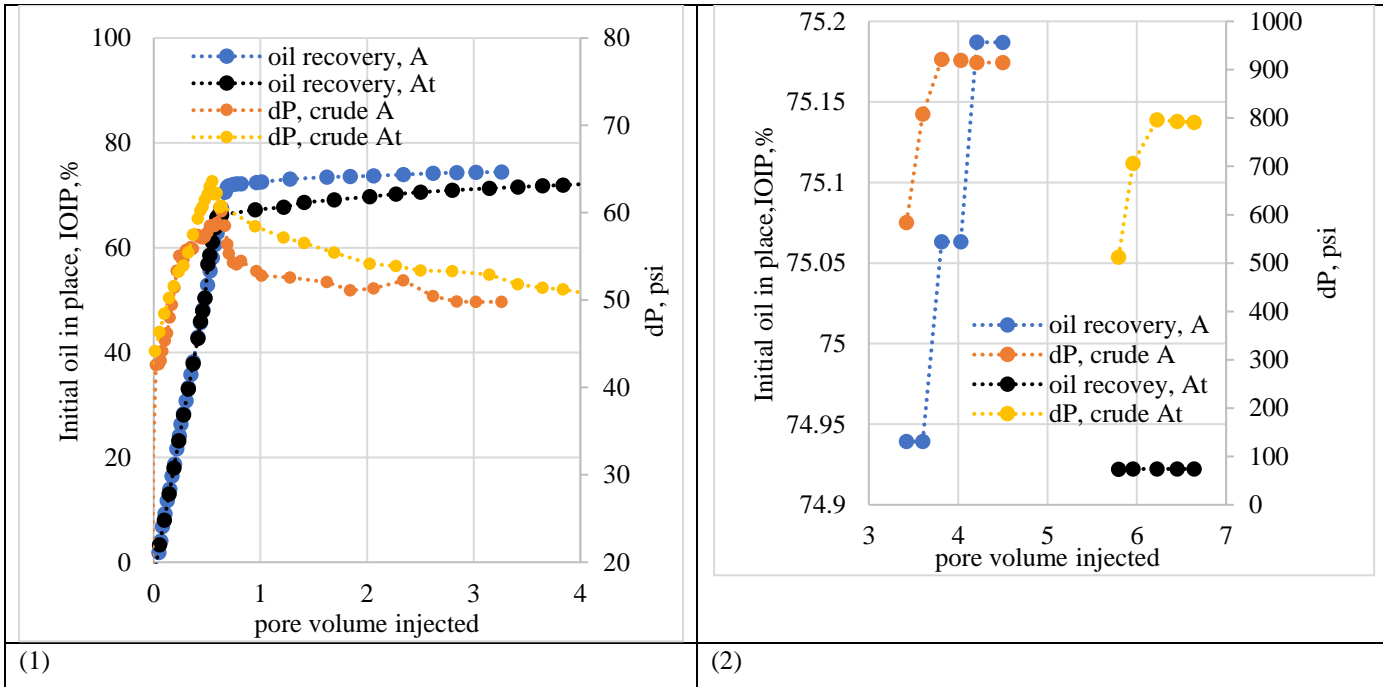(1)   (2)

Figure 2 plot 1 shows secondary high salinity water injection result for both crude A and At respectively and plot 2 result of secondary high salinity bump flood at the end of 4cc/hr (equivalent to reservoir flow advance rate 1ft/day)
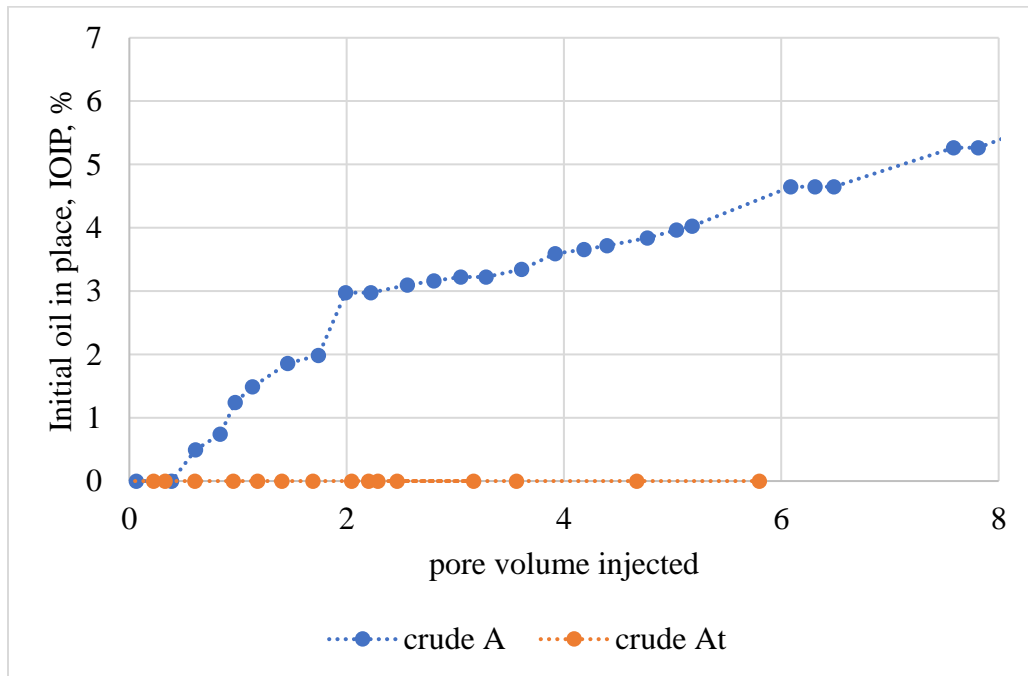

Figure 3 Tertiary low salinity water injection: effect of the presence and/or absence of micro-dispersion on the improved oil recovery during LSWI
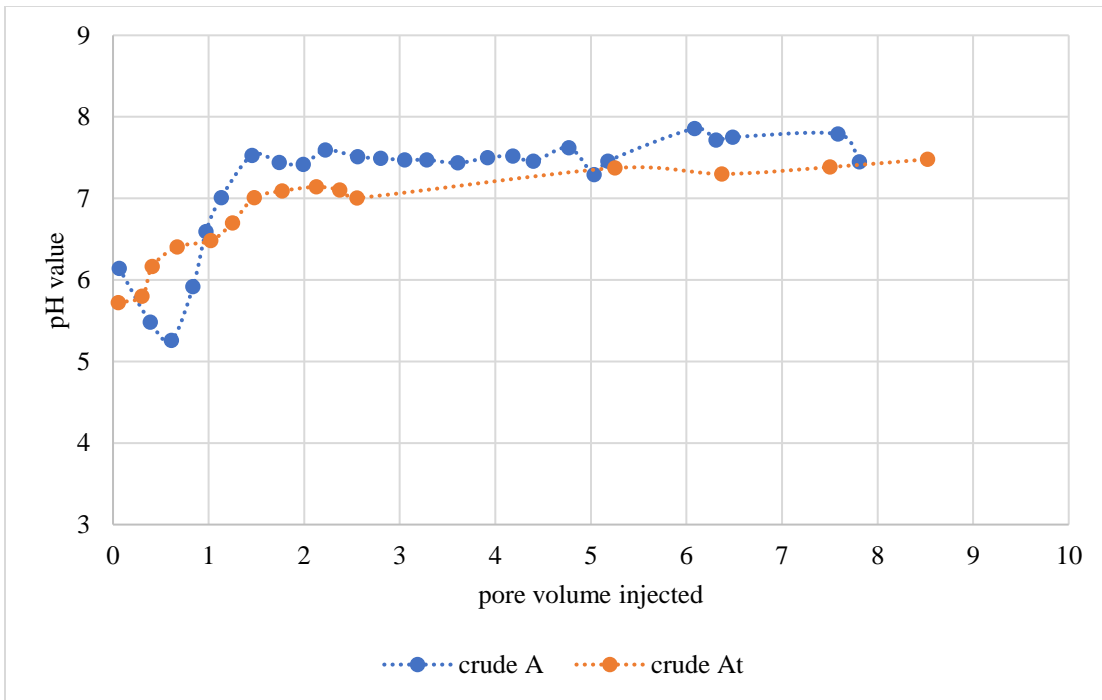
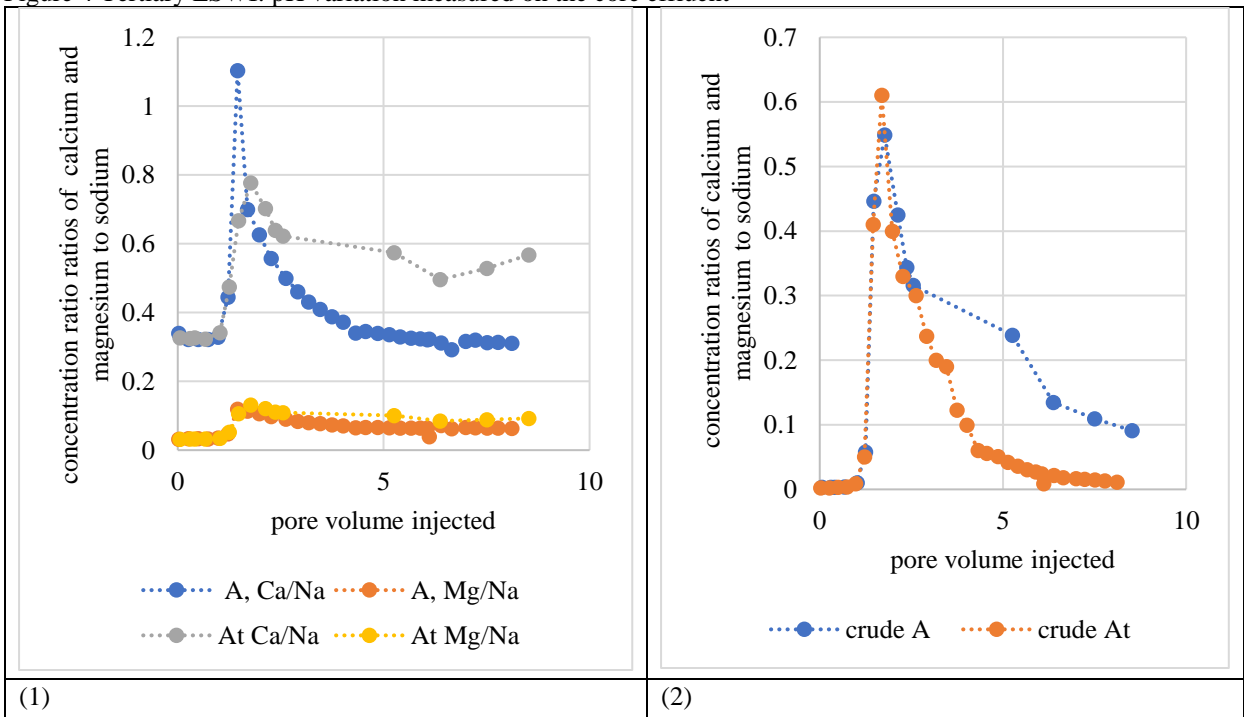Figure 4 Tertiary LSWI: pH variation measured on the core effluent

(1)

(2)

Figure 5: Graph 1 shows tertiary LSW Ca^{2-} /Na^{1+} and Mg^{2+} /Na^{1+} versus pore volume LS injected. Graph 2 tertiary LSWI SO_4^{2-} /Cl^{1-}

RESIDUAL OIL SATURATION UNDER MIXED-WET CONDITIONS: A DIRECT COMPARISON BETWEEN INDIANA LIMESTONE AND ITS MICROFLUIDIC ANALOGUE

Yukie Tanino, Magali Christensen, Xanat Zacarias Hernandez
School of Engineering, University of Aberdeen, UK

ABSTRACT

We present laboratory measurements of residual oil saturation established by secondary waterflood in packed beds of crushed calcite assembled in a microfluidic channel under mixed-wet conditions. The measurements are compared with analogous measurements in Indiana limestone cores using the same test fluids and comparable injection rates. The wettability is characterized by the advancing contact angle of the flood water on a mineralogically representative substrate submerged in the oil phase, which ranged from θ_a = 90° to 160°.

While residual oil saturation is larger in the microfluidic analogue than the limestone cores over the full range of θ_a considered presently, its dependence on θ_a is qualitatively similar for both media and is well described by a concave-up quadratic function. Maximum recovery occurs at moderately oil-wet conditions of θ_a = 130° in Indiana limestone and 120° in its microfluidic analogue. These findings demonstrate that salient features of oil/brine flow through $O(10)$cm-long cores are conserved in two-dimensional microfluidic models under conditions considered presently.

INTRODUCTION

Salient features of waterflood oil recovery under mixed-wet conditions where the oil-contacted grain surfaces are strongly oil-wet are well established. However, there is no consensus on the optimal wettability for waterflood oil recovery. While some laboratory studies and pore network simulators report the dependence of oil recovery on contact angle, their findings are contradictory, with maximum recovery reported at neutral wettability in some studies [1, 2] and under strongly oil-wet conditions in others [3].

In this paper, we focus on residual oil saturation, S_{or}, established by secondary waterflood from high initial oil saturation under capillary-dominated conditions, and its dependence on contact angle under mixed-wet conditions. We compare measurements in Indiana

limestone and a quasi-monolayer of marble grains assembled in a microfluidic channel. Numerical simulation is used to quantify the impact of capillary end effects. An empirical model is proposed to describe the dependence of S_{or} on the advancing contact angle on a mineralogically representative substrate, θ_a, which is valid over the range $90° \leq \theta_a < 160°$.

METHODS

Porous Medium

The cross-sections of the limestone and its microfluidic analogue captured by X-ray micro tomography (Xradia Versa) are shown in Figure 1. The Indiana limestone cores had a mean porosity and permeability of $\phi = 0.15$ and $k = (6.5 \pm 2.7) \times 10^{-15}$ m^2, respectively, and were $L = 3.5$ in.-long and 1.5 in. in diameter [4]. Mercury injection porosimetry and NMR data are available in Refs. [4, 5].

The microfluidic analogue was a quasi-monolayer bed of crushed marble from Carrara, Italy, with a mean equivalent diameter of 53 ± 24 μm [6], packed in a $W = 1200$ μm-wide, $H = 55$ μm-deep channel etched in soda lime (Dolomite Centre Ltd.). The grains were prepared and wet-packed following the protocol described in Ref. [6] with minor modifications. The mean porosity of the marble packed bed was estimated from X-ray micro tomography scans of a microfluidic analogue to be $\phi = 0.27$. The length of the packed beds ranged from $L = 1280$ to 2440μm.
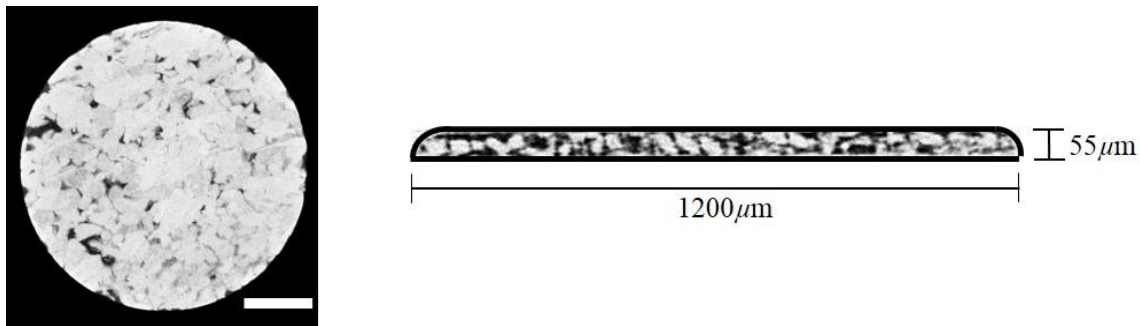

Figure 1. A two-dimensional cross-section of three-dimensional X-ray scans of Indiana limestone (left, [5]) and its microfluidic analogue (right). The diameter of the limestone sample is 5 mm; the white horizontal bar depicts 1200 μm, the width of the microfluidic analogue. Voxel size is 2.7551 μm for the limestone and 2.9586 μm for the microfluidic analogue.

Fluids

The aqueous phase was a solution of 5wt.% sodium chloride and 1wt.% potassium chloride saturated in limestone, as used previously [4, 5, 7, 8]. Four oils were considered: 6.6×10^{-2} M solutions of cyclohexanecarboxylic acid, cyclohexanepropionic acid, cyclohexanebutyric acid, and cyclohexanepentanoic acid in n-decane. In-situ adsorption of these acids render Indiana limestone and its microfluidic analogue mixed wet to different degrees [4, 10]. In the lab-on-a-chip measurements, the oils were dyed with Oil Red O

(ORO) to facilitate visualization; details are presented in Ref. [9]. At ambient conditions, the dynamic viscosity of the brine is $\mu_w = 1.087$ mPa s. The dynamic viscosity of the dyed and undyed oils range from $\mu_o = 1.027$ to 1.116 mPa s [10] and $\mu_o = 0.880$ to 0.910 mPa s [4], respectively.
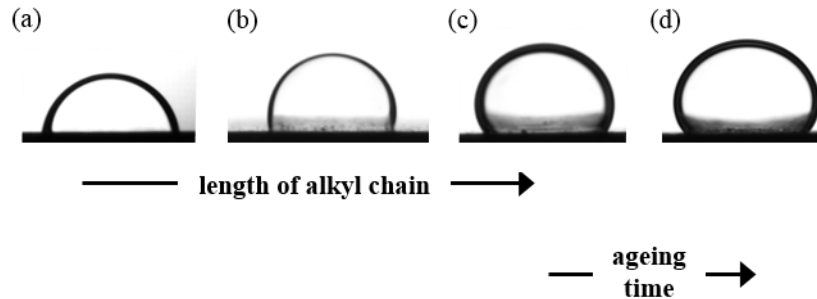

Figure 2. A drop of brine on a polished marble substrate that had been pre-equilibrated in brine then submerged in 6.6×10^{-2} M cyclohexanecarboxylic acid (a), cyclohexanebutyric acid (b), and cyclohexanepentanoic acid (c, d) for $t_a = 1$h (a-c) or 75h (d). The drop volumes are approximately the same in all images.

Contact Angle

Each oil/brine pair is characterised by the advancing contact angle, θ_a, on a mineralogically representative substrate that had been submerged in the test oil for ageing time t_a relevant to the displacement experiments (e.g., Fig. 2). Because cores were saturated in oil for much longer than the duration required for contact angles to asymptote (~ 50h [4]), their wettability is represented by equilibrium (long-time) values of θ_a. For dyed oils, t_a was matched to the duration that the microfluidic analogues were saturated in the test oil prior to waterflooding.

Table 1. Interfacial tension and advancing contact angle of each oil/brine pair. The reported uncertainty is standard error of the mean. All measurements were collected at ambient temperature.

oil	θ_a [°]		σ [mN/m]	
	with dye (t_a) [10]	without dye [4]	with dye [10]	without dye [4]
6.6×10^{-2} M cyclohexanecarboxylic acid	$89 \pm 3°$ (1h)	$108 \pm 0°$	29.7	33.10 ± 0.003
6.6×10^{-2} M cyclohexanepropionic acid	N/A	$127 \pm 2°$	22.5	28.50 ± 0.006
6.6×10^{-2} M cyclohexanebutyric acid	$113 \pm 2°$ (1h)	$134 \pm 2°$	23.0 ± 0.1	23.67 ± 0.006
6.6×10^{-2} M cyclohexanepentanoic acid	$140 \pm 2°$ (1h)	$150 \pm 0.6°$	19.3 ± 0.1	16.50 ± 0.010
	$155 \pm 5°$ (75h)			

The values of θ_a for the test oils and t_a corresponding to the experiments reported in this paper are summarized in Table 1. In the discussion that follows, all θ_a are rounded to the nearest 5°. Also reported are the interfacial tensions, σ, for each oil/brine pair.

Displacement Experiments

Two techniques were used to measure the remaining oil saturation as a function of time during waterfloods, $S_o(t)$: lab-on-a-chip methods [9] and conventional corefloods [4]. In both methods, each experiment comprised three stages: complete saturation of the porous medium with the brine, primary drainage, and waterflood at constant Darcy velocity, U_w. To remove ambiguity in the wettability of the system, cores and microfluidic analogues were not reused once they were exposed to oils containing organic acid.

Corefloods

Details of the coreflood apparatus and procedure can be found in Ref. [4]. The key steps were as follows:

1. Each core was alternately evacuated and flushed with gaseous CO_2 to remove air, then flushed with degassed brine to fully saturate it.
2. The test oil was injected into the core at constant pressure to establish initial oil saturation, S_{oi}, using the porous plate method.
3. Up to 100 pore volumes (pv) of degassed brine was injected at constant $U_w = 30$ μm/s in one experiment and 1.5 or 3.0 μm/s (= 0.43 and 0.85 ft/d) in all others.

The corresponding microscopic capillary number,

$$\text{Ca} = \frac{\mu_w U_w}{\sigma} , \tag{1}$$

varied between Ca = 5×10^{-8} and 1×10^{-6}. The corresponding macroscopic capillary number [11],

$$\langle \text{Ca} \rangle = \frac{\mu_w U_w L/k}{P_b} , \tag{2}$$

where $P_b = 2\sigma \cos \theta_a / r_{p,b}$ and $(S_w, r_{p,b})$ corresponds to the inflection point in the mercury injection (drainage) capillary pressure curves, varied between 0.43 and 6.3 (Table 2). Data to date suggest that S_{or} is not a strong function of U_w within this range [4, 8, 12].

S_{oi} and S_{or} were determined by mass balance on the core. In this paper, we consider maximum S_{oi} (≈ 0.9) only.

Lab-on-a-Chip Experiments

The lab-on-a-chip method combines, with modifications, the coreflood protocol of Tanino & Blunt [7] and the lab-on-a-chip protocol developed by Bowden et al. [6]:

1. The packed bed was first saturated with the brine to establish connate water saturation.
2. Oil was injected until a uniform oil saturation of $S_{oi} \cong 1$ was established. Fresh oil was circulated through the packed bed for $t_a = 1$h or 75h to allow the acid in the oil phase to render grain surfaces oil-wet to different degrees.

3. Brine was injected at $U_w = 26\mu$m/s ($= 7.3$ft/d) using a high precision syringe pump; the corresponding capillary number ranges from Ca $= 9 \times 10^{-7}$ to 1×10^{-6} and $\langle$Ca$\rangle$ $= 2 \times 10^{-3}$ to 7×10^{-2} (Table 2).

Because we do not have a method for measuring $P_c(S_w)$ in the microfluidic rock analogues at this time, the breakthrough capillary pressure was estimated as

$$P_b = J(S_{w,b})\sigma \cos\theta_a \sqrt{\frac{\phi}{k}} ,$$ (3)

where $J(S_{w,b})$ is the Leverett-J scaling

$$J(S_{w,b}) = \frac{P_c(S_{w,b})}{\sigma \cos\theta_a}\sqrt{\frac{k}{\phi}}$$ (4)

corresponding to the inflection point in primary imbibition oil/water capillary pressure curve in a packed column of mixed-wet spheres [13].
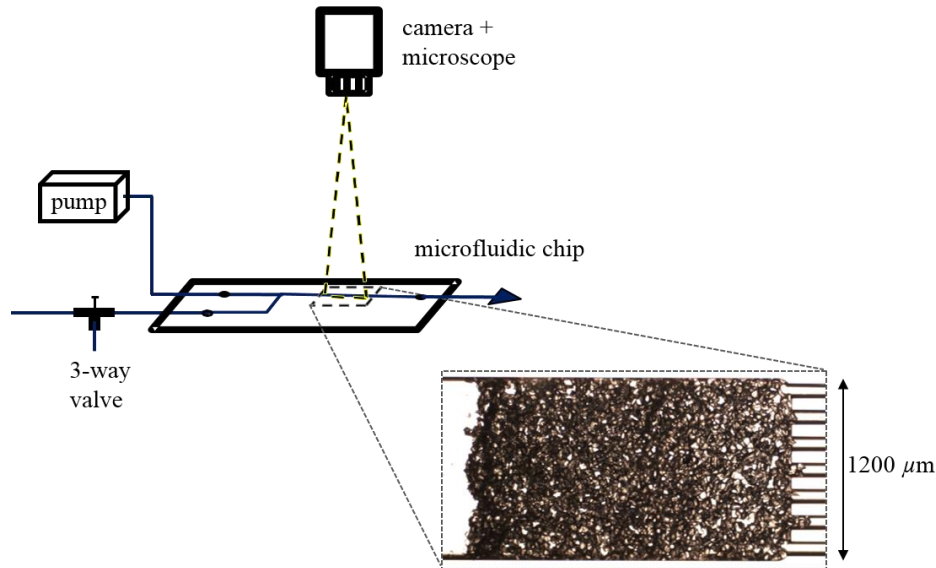

Figure 3. Setup for the lab-on-a-chip experiments. The chip is back lit from below. Adapted from Tanino et al. [8].

Flow Visualization

The evolution of the depth-integrated oil distribution inside the packed bed was captured using a high-speed camera coupled to an optical microscope at a resolution of 2.4 to 4.0 μm/pix; the chip was lit from below (Fig. 3).

The distribution of oil within the packed bed and its evolution were determined as follows:
1. The red channel field of the acquired still images, $i_R(x, y, t)$, was subtracted from the green channel field, $i_G(x, y, t)$.
2. A 3×3 median filter was applied to the resulting $i_G - i_R$ field.

3. A segmentation threshold, $i_c(y)$, was determined for each half-width of the packed bed.

The remaining oil saturation at a given instance as a fraction of the initial oil saturation was determined as:

$$\frac{S_o(t)}{S_{oi}} = \frac{n_o(t)}{n_o(t<0)},$$

(5)

where n_o is the number of pixels in the packed bed for which i_G-$i_R < i_c(y)$; $t = 0$ corresponds to the time when water first enters the packed bed. All post-processing was performed using MATLAB (Mathworks, Ltd.). Additional details are provided in Ref. [9].

Capillary end effects are a concern in microfluidic experiments and, indeed, oil saturation tends to be larger near the downstream end of the packed bed than the upstream end. However, this phenomenon is observed at $\theta_a < 90°$ also, which suggests that it is largely due to imperfections in the channel cross-section at the downstream end of the packed bed rather than the capillary discontinuity. For simplicity, the last 300 μm (= 5.5H) of the packed bed was excluded from consideration to prevent end effects from unrealistically increasing the estimated $S_o(t)$ (e.g., Fig. 4, white rectangle). As will be shown below, the reduction in $S_o(t)$ that arises from expanding the excluded region to 550 μm (= 10H) falls within experimental uncertainty (Fig. 6, dashed-dotted).

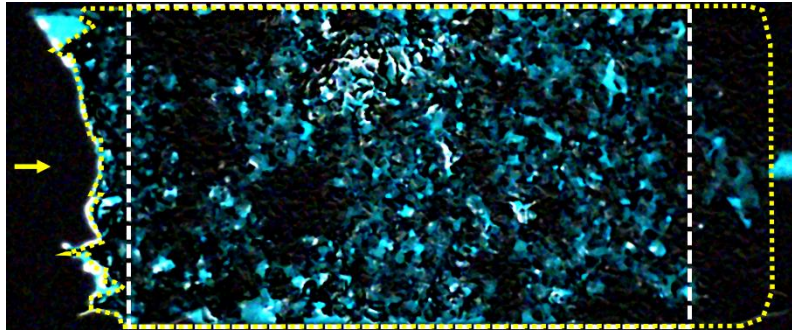**Figure 4.** A microfluidic analogue at residual oil saturation for $\theta_a = 155°$; $S_{or}/S_{oi} = 0.50$. An image at initial oil saturation has been subtracted from the image and a 3×3 median filter applied; the bright pixels represent invading water. The yellow polygon demarcates the boundaries of the packed bed. The white dashed box demarcates the region over which $S_o(t)$ is evaluated. Mean flow is left to right.

Numerical simulation

Numerical simulations of the corefloods were performed using CYDAR^{TM} (CYDAREX). First, waterflood (secondary imbibition) capillary pressure, $P_c^B(S_w)$, and relative permeability, $k_r^B(S_w)$, curves of a Berea sandstone pore network from Ref. [5] were predicted for each oil/brine combination using a two-phase pore network simulator developed by Valvatne & Blunt [14]; details of the pore network are available in Ref. [5]. To account for differences in S_{or}, water saturation was rescaled as

$$S_w^* = \frac{S_w - (1 - S_{oi})}{(1 - S_{or}) - (1 - S_{oi})}. \tag{6}$$

Similarly, P_c^B was scaled using the Leverett-J function, i.e.,

$$P_c(S_w^*) = P_c^B(S_w^*)\sqrt{\frac{k^B/\phi^B}{k/\phi}}, \tag{7}$$

where superscript B denotes properties of the Berea sandstone pore network. $P_c(S_w^*)$ and $k_r^B(S_w^*)$ were used as input parameters for the simulations.

RESULTS

Figure 5 presents the residual oil saturation distribution along the length of the Indiana limestone core as predicted by the simulator for each θ_a. At all θ_a considered, the oil saturation at the upstream end of the core ($x = 0$) agrees with the "true" S_{or}, i.e., the oil saturation corresponding to $k_{ro} = 0$, to within -0.09% to 0.07%. As x increases, oil saturation remains uniform within the first $x < 5$ mm ($\theta_a = 110°$) to 5 cm (150°), then increases gradually with increasing x until $x/L \approx 0.95$. Finally, in the last 4 mm of the core, oil saturation increases sharply to $\approx S_{oi}$ to accommodate the $P_c = 0$ boundary condition at $x = L$. Because capillary end effects are constrained to a small region, the core-averaged residual oil saturation is only 2 to 4% larger than the residual oil saturation at the upstream end of the core, $S_{or}(x = 0)$.
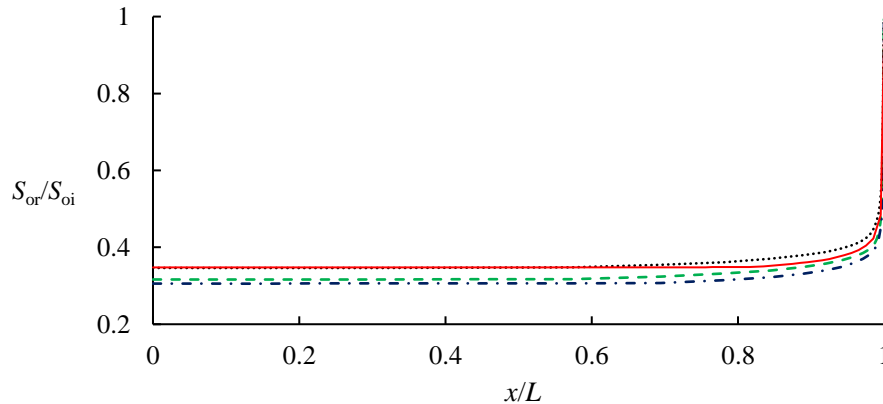

Figure 5. Residual oil saturation in Indiana limestone cores at $\theta_a = 110°$ (black dotted), 125° (green dashed), 135° (blue dashed-dotted), and 150° (red solid line). Mean flow is left to right. $L = 8.9$cm; $\phi = 0.15$; $k = 6.597$mD; $S_{oi} = 0.9$.

Figure 6 presents the evolution of the remaining oil saturation from Indiana limestone (blue) and its microfluidic analogue (red, magenta) under weakly oil-wetting and strongly oil-wetting conditions. Time $\tilde{t}$ is defined from the onset of waterflood in units of cumulative pv of brine injected. During any waterflood, S_o decreases as waterflood progresses until it asymptotes to its residual state. The constant, long-time value is taken

to be S_{or} for Indiana limestone. For simplicity, S_{or} in the microfluidic analogues is taken to be S_o time-averaged over $\tilde{t} = 30 \pm 0.5$ after water breakthrough.
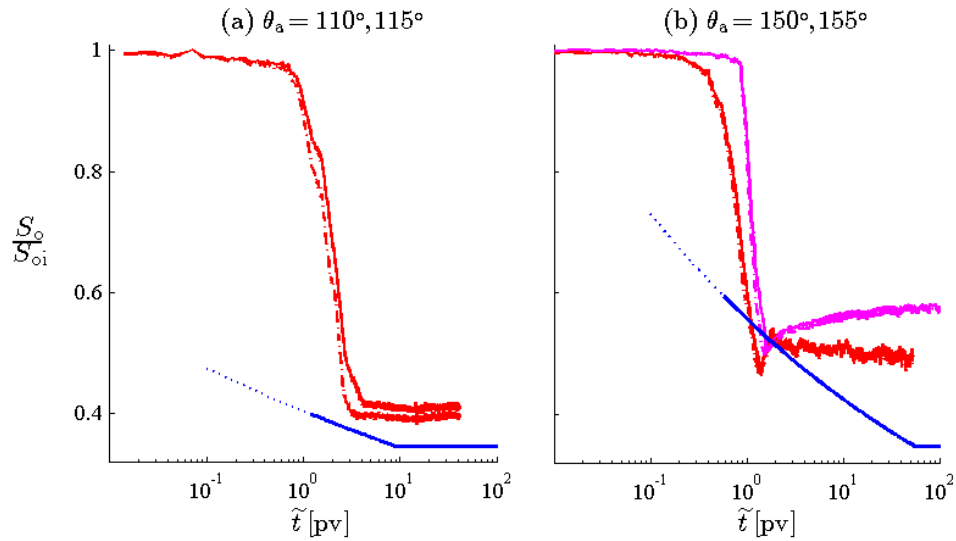

Figure 6. Evolution of the remaining oil saturation during waterflood at $\theta_a = 110°/115°$ (a) and $150°/155°$ (b) in cores (blue) and microfluidic analogues (red, magenta). Recovery from cores are represented by the best-fit power functions to data [4]. For microfluidic analogues, solid and dashed-dotted lines depict saturation excluding the last 300 and 550μm of the packed beds, respectively.

Table 2. Summary of experimental conditions.

porous medium	θ_a	$\langle Ca \rangle$		ϕ	S_{or} / S_{oi}
		min.	max.		
Indiana limestone [4, 7]	$108 \pm 0°$	0.63	0.69	$0.149 - 0.155$	0.35 ± 0.008
	$127 \pm 2°$	0.54	6.3	$0.143 - 0.154$	0.32 ± 0.02
	$134 \pm 2°$	0.43	1.3	$0.139 - 0.156$	0.31 ± 0.02
	$150 \pm 0.6°$	1.4	1.5	$0.133 - 0.139$	0.35 ± 0.01
microfluidic analogue	$89 \pm 3°$	7×10^{-2}		-	0.52
	$113 \pm 2°$	3×10^{-3}		-	0.41 ± 0.03
	$140 \pm 2°$	2×10^{-3}		-	0.45 ± 0.02
	$155 \pm 5°$	2×10^{-3}		-	0.58 ± 0.03
		3×10^{-3}		-	0.50

Figure 7 presents S_{or} as a fraction of the OOIP as a function of θ_a. In both Indiana limestone and the microfluidic analogue, residual saturation displays a non-monotonic dependence on contact angle. In the former, S_{or}/S_{oi} decreases with increasing contact angle from S_{or}/S_{oi} = 0.35 at $\theta_a = 110°$ to $S_{or}/S_{oi} = 0.31 \pm 0.02$ at $135°$, then increases back to $S_{or}/S_{oi} = 0.35 \pm$

0.01 at $\theta_a = 150°$ (squares). Similarly, S_{or}/S_{oi} decreases from $S_{or}/S_{oi} = 0.52$ at $\theta_a = 90°$ to $S_{or}/S_{oi} = 0.41 \pm 0.03$ at $\theta_a = 115°$, then increases to $S_{or}/S_{oi} = 0.54 \pm 0.04$ at $\theta_a = 155°$ in the microfluidic analogue (circles). The data are well described by the best-fit quadratic function in the least-squares sense (dotted lines):

$$\frac{S_{or}}{S_{oi}} = 8.3 \times 10^{-5} \theta_a^2 - 0.021\theta_a + 1.7 \tag{8}$$

and

$$\frac{S_{or}}{S_{oi}} = 1.1 \times 10^{-4} \theta_a^2 - 0.026\theta_a + 2.0 \tag{9}$$

for Indiana limestone and its microfluidic analogue, respectively. For the same θ_a, S_{or}/S_{oi} in the microfluidic analogues exceeds that in Indiana limestone cores by 17% to 47% over the full range of θ_a considered presently, with the fractional difference increasing monotonically with θ_a.
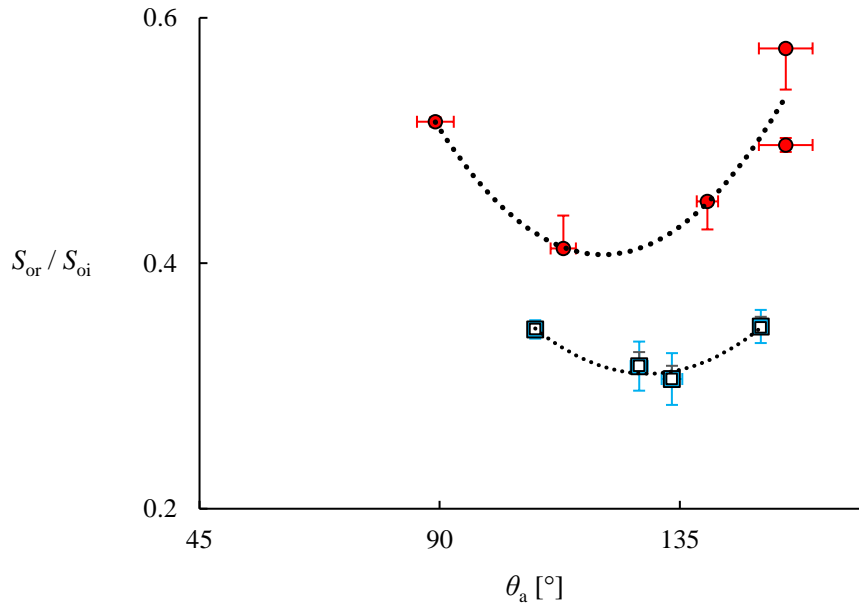

Figure 7. Residual oil saturation in Indiana limestone cores (blue squares; [4]) and microfluidic analogues (red circles). Each marker represents a single experiment for the microfluidic analogues and the average over two or three independent corefloods for Indiana limestone. Horizontal bars depict standard errors of the mean. Vertical bars depict the standard errors of the mean for Indiana limestone and the uncertainty in the segmentation threshold for microfluidic analogues. Dotted lines depict polynomial functions of degree two fitted to data in the least squares sense [Eqs. (8, 9)]. Superposed are residual oil saturation at the upstream end of the core determined from numerical simulation (open squares); vertical bars depict the core-averaged S_{or} in the simulations.

As discussed above, capillary end effects tend to elevate the porous medium-averaged S_{or} at $\theta_a > 90°$. To demonstrate that the observed non-monotonic trend is not an experimental artefact arising from two competing mechanisms – a reduction in true S_{or} and an increase in capillary end effects – we consider the θ_a dependence of the simulated S_{or}. $S_{or}(x = 0)$

displays a concave-up dependence on θ_a similar to the core-averaged S_{or}, with the same optimal contact angle of $\theta_a = 130°$ (Fig. 7, open squares). The positive correlation between $S_{or}(x = 0)$ and θ_a at high θ_a in the simulations suggests that previous observations of such correlations in corefloods are not an experimental artefact. Furthermore, the occurrence of the same correlation in the present microfluidic experiments suggests that the non-monotonic dependence is a salient feature of multiphase flow in mixed-wet media at low $\langle Ca \rangle$.

CONCLUSIONS

Residual oil saturation in two-dimensional packed beds of calcite grains and three-dimensional limestone cores under mixed-wet conditions were compared. The main findings are:

- S_{or} decreases, then increases as θ_a increases from 90° to 160° in both systems.
- The non-monotonic dependence is well described by a concave-up quadratic function.
- Optimal wettability (minimum S_{or}) occurs at moderately oil-wetting conditions.
- S_{or} was larger in the microfluidic analogue than in Indiana limestone cores over the full range of θ_a considered presently.
- Numerical simulations of the corefloods demonstrate that the positive correlation between S_{or} and θ_a at large θ_a is not a result of two competing mechanisms – a reduction in S_{or} and an increase in oil retention due to capillary end effects – but a true behaviour of S_{or}.

Ongoing laboratory work is focused on an analogous comparison of relative permeability of Indiana limestone [15] and its microfluidic analogue.

REFERENCES

1. Kennedy, H. T., E. O. Burja & R. S. Boykin (1955) An investigation of the effects of wettability on oil recovery by water flooding. *J. Phys. Chem*. 59(9), 867-869. doi: 10.1021/j150531a015.
2. Morrow, N. R., P. J. Cram & F. G. McCaffery (1973) Displacement studies in dolomite with wettability control by octanoic acid. *Soc. Petrol. Eng. J*. 13(4), 221-232. doi: 10.2118/3993-PA.
3. Owens, W. W. & D. L. Archer (1971) The effect of rock wettability on oil-water relative permeability relationships. *Soc. Petrol. Eng. J*. 23(7), 873-878. doi: 10.2118/3034-PA.
4. Christensen, M. & Y. Tanino (2017) Waterflood oil recovery from mixed-wet limestone: dependence on contact angle. *Energy Fuels*, 31(2), 1529-1535. doi: 10.1021/acs.energyfuels.6b03249.
5. Tanino, Y. & M. J. Blunt (2012) Capillary trapping in sandstones and carbonates: dependence on pore structure. *Water Resour. Res*. 48(8), W08525. doi: 10.1029/2011WR011712.
6. Bowden, S. A., Y. Tanino, B. Akamairo & M. Christensen (2016) Recreating mineralogical petrographic heterogeneity within microfluidic chips: assembly, examples, and applications. *Lab Chip* 24(16), 4677-4681. doi: 10.1039/C6LC01209D.
7. Tanino, Y. & M. J. Blunt (2013) Laboratory investigation of capillary trapping under mixed-wet conditions. *Water Resour. Res.* 49(7), 4311-4319. doi: 10.1002/wrcr.20344.
8. Tanino, Y., B. Akamairo, M. Christensen & S. A. Bowden (2015) Impact of displacement rate on waterflood oil recovery under mixed-wet conditions. In *Proc.,* International Symposium of the Society of Core Analysts. St. John's Newfoundland and Labrador, Canada, 16-21 August.
9. Tanino, Y., M. Christensen & X. Zacarias Hernandez (2017) Dynamic, pore-scale imaging of water invasion in microfluidic packed beds, *Appl. Sci*., in prep.
10. Christensen, M., X. Zacarias Hernandez & Y. Tanino (2017) Impact of Oil Red O on physical and interfacial properties of *n*-decane+acid solutions, in prep.
11. Hilfer, R. & P.-E. Oren (1996) Dimensional analysis of pore scale and field scale immiscible displacement, *Transp. Porous Med.* 22(1), 53-72.
12. Christensen, M. & Y. Tanino (2017) Capillary desaturation curves under mixed-wet conditions: a microfluidic study, in prep.
13. Murison, J. L. (2013) Wetting heterogeneities in porous media: Insights from experiments on the displacement of immiscible fluids, PhD thesis, Georg-August-Universität, Göttingen, Germany.
14. Valvatne, P. H. & M. J. Blunt (2004) Predictive pore-scale modeling of two-phase flow in mixed wet media. *Water Resour. Res.* 40(7), W07406. doi: 10.1029/2003WR002627.
15. Christensen, M. & Y. Tanino (2017) Enhanced permeability due to apparent oil/brine slippage in limestone and its dependence on wettability, *Geophys. Res. Lett*. doi: 10.1002/2017GL073603.

PREDICTION, CONTROL AND VALIDATION OF ROCK DISSOLUTION DURING SMART WATER INJECTION AND ITS IMPACT ON WATERFLOOD PERFORMANCE IN HEAVY OIL CARBONATE RESERVOIRS

Heron Gachuz-Muro, Mehran Sohrabi
Pemex E&P, Heriot Watt University

ABSTRACT

Smart water injection studies are rewriting the rules and the understanding of water injection as a method for improving oil production. The voluminous research being undertaken in this area has enabled us to better understand the significant impact that the water composition and salinity can make in the outcome of waterflood. A universal consensus has not yet been reached on the main mechanism of oil recovery by smart water injection but it appears that in most previous works the role of injected water/crude oil interactions has been overlooked.

A first approach would be to systematically analyse the fundamental knowledge of such fluid-fluid and rock-fluids interactions. Once this knowledge is defined, we might be able to predict its direct impact in terms of oil production. Then, the presence of such mechanisms could be controlled and validated through more complex multi-variable experiments.

This paper provides new evidence by means of fluid-fluid interactions and coreflood experiments that natural generation of acidic water in the reservoir is responsible for improvement of oil recovery by smart water injection in carbonate rocks through rock dissolution. Laboratory experiments were performed at 92 ºC using a dolomite rock. Four coreflood experiments were conducted by injecting either seawater or low salinity seawater and showed significant additional oil recovery when smart waters were injected in both secondary and tertiary modes. Changes in permeability of the core, derived from rock dissolution, were observed and the magnitude of the changes was bigger when the crude oil was basic in comparison with an acidic one. The rock permeability increased by up to 100% if the injection water was low salinity whereas, if seawater was injected, rock damage was observed. The results indicate that the migration of water-soluble compounds of the crude oil becomes more important for basic oils and causes a drop in the pH of injected water. The results show that it is possible to predict the extent of the rock dissolution based on fluid-fluid contact tests. The findings also show that the amount of oil recovered by smart water depends on the type of crude oil. Less oil production was detected when acidic crude oils were used in the same rock under the same conditions.

INTRODUCTION

Since it has been analytically established that the interactions of crude oil/smart water (especially low salinity waters) can naturally generate acidic water during water injection in carbonate rocks (Gachuz et al, 2016), the goal of this work will be the validation of these observations. The lack of equilibrium in the fluid/rock system may be the underlying cause of changes in wettability and rock dissolution due to such chemical interactions between invading fluids and the initial native fluids, principally with the crude oils. For this reason, one cannot confirm these facts without considering the flow of fluids throughout the cores at reservoir conditions. Moreover, the possibility that these conditions would involve the pressure and its influence cannot be excluded either. Considering that dissolution has been identified as part of the effects that occur during smart water injection, especially in low salinity waters, coreflood experiments should enable us to observe the difference in the enhanced oil recovery if different brines and crude oils are used. This will make it possible to distinguish where and when this vital mechanism occurs.

As indicated by us in 2016, there is probably a pattern that proves that dissolution plays an important role during the additional oil production. Therefore, this technical paper will mainly focus on more elaborate experiments such as coreflood experiments where it will be demonstrated how the simple models previously presented (Gachuz et al., 2016) can be used to predict if dissolution of the rock is taking place in the fluid/rock interaction and then to evaluate its impact on final oil production. Subsequently, coreflood experiments were then carried out under both secondary and tertiary injection modes, in order to experimentally investigate the performance of smart water injection for heavy oils. The effects of the composition of the crude oil on the dissolution of rock were also studied and compared in terms of additional oil recovery. Water composition changes, pH measurements, permeability variation and oil recovery before and after the experiments were all performed during the experiments. That will allow us to examine the fundamentals of fluid flow and analyse whether changes occur, where they occur and how they are influenced by the injected waters. The article ends with the discussion of what implications these results will have for the oil production of carbonate heavy oil reservoirs. The results of this work will supplement previous findings.

EXPERIMENTAL

Two crude oil samples were selected for this research from a group of carbonate formations with similar reservoir conditions. Table 1 shows the basic properties of the selected crude oils. The core was taken from a dolomite core. The dimensions for this used core were as follows: diameter = 5.09 cm, length = 15.20 cm, pore volume = 58.15 cc, brine permeability = 142.21 mD and porosity = 18.80 %. The presence of sulphate was not detected using an Environmental Scanning Electron Microscope (ESEM), however, ionic analysis of the effluents during water saturation confirmed the presence of

sulphate into the core. Brines were made in the laboratory from original compositions. Four brine solutions were prepared for this research (Table 2). Seawater composition from Gulf of Mexico was considered for this study because oil reservoirs are located offshore. Formation brine only contains small amounts of magnesium and sulphate, details may be consulted in Gachuz et al., 2016.

Table 1.- Crude Oil Properties.

Crude Oil	Density* (ºAPI)	Viscosity* (cp)	Asphaltene Content (% wt)	Water Content (ppm)*	Resins Content (% wt)	TAN (mgKOH/g)*	TBN (mgKOH/g)*
A	14.12	53,484.31	13.20	208.40	31.70	1.00	3.50
E	19.27	1,251.80	0.82	2,920.52	16.85	2.40	2.10

*Measured at 20 ºC

Table 2.- Brine Compositions.

Brine/Ion	Na^+	Ca^{2+}	Mg^{2-}	K^+	Cl^-	SO_4^{2-}	HCO_3^-	TDS (mg/l)
FW (mg/l)	9,614	320	218	-	15,117	550	1,135	25,670
SW (mg/l)	11,429	429	1,361	351	20,040	3,500	47	37,198
LSSW10 (mg/l)	1,142	42	136	35	2,004	350	4	3,719
LSSW50 (mg/l)	228	8	27	7	400	70	1	743

*Measured at 20 ºC

The working temperature was at 92 ºC and an overburden pressure of 1,500 psi (reservoir conditions) was kept the same during the whole study. The orientation of the coreflood experiments was horizontal with a back pressure of 500 psi. The formation water was injected into the core at constant rate, which didn't exceed 1 ft³/day. Once the specific water saturation was established using crude oils, the core was aged and flooded with fresh crude oil at different times for 20 days to restore the original wetting conditions. Injection of working brines through the core was performed at 2 cm³/hr. In all the experiments, once the oil production finished, a change in the water injection rate was applied to make sure that there was no more produced oil. The oil volume (expressed as a percentage of the original oil in place) was recorded as a function of pore volume injected. The same core was used for all the reported coreflood tests followed the same experimental procedures.

RESULTS AND DISCUSIONS

For the first coreflood experiments (first and second coreflood experiment) the crude oil "A" was selected and dolomite core was firstly flooded with a diluted version of seawater called LSSW10 (refer to Table 2 for composition brine) as a secondary process. Pressure, pH and effluent composition were constantly monitored, Figure 1. After 22 pore volumes were injected, a 24-hour soak period was applied. No extra oil was recovered after this closure. Because of the high permeability of the core, a high rate was applied at the end of each stage (20 cm³/hr). The LSSW10 injection resulted in the final recovery of 69.30 % OOIP. With respect to pH, after rising slightly and staying almost stable during the injection of 9.5 pore volumes, it fell at 10 pore volumes injected and fluctuated between 7.2 to 7.3 units.

For the effluents of the LSSW10 injection period (Figure 2a and 2b), it may be clearly seen that the calcium and bicarbonate concentrations rose and those of sulphate and magnesium also exhibited small variations in comparison with the original composition of the injected water. The effluent samples were treated with methyl orange and then titrated with hydrochloric acid once it was not possible to detect bicarbonate concentrations using ion chromatography analysis.
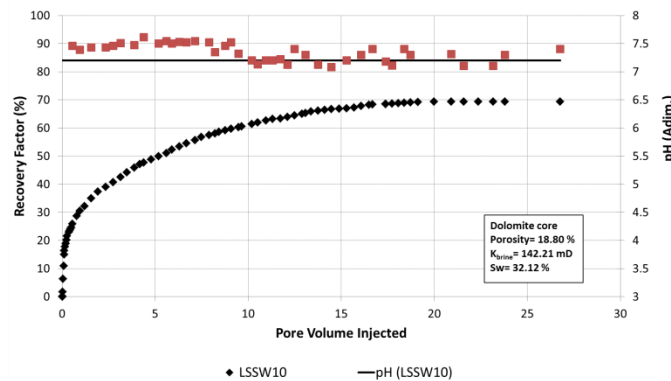

Figure 1.- Cumulative oil recovery with low salinity seawater at 92 ºC.

The concentrations of the rest of the elements remained constant (sodium, potassium and chloride). This production may be linked to the reaction of the injected water, firstly with the crude oil and subsequently with the rock, leading to a possible dissolution effect. Later, this assumption was supported by the measurement of the new permeability, which turned out to be higher, 180.28 md. Permeability changes were studied using Darcy´s Law. A tertiary programme was not applied for this test.

Once the experiment with low salinity seawater was finished, the core was cleaned and reused later. The same process was repeated, except the type of injected brine was changed. This time (second coreflood experiment), the core was brought into contact with seawater. High oil volume was produced at early time. Before 4 pore volumes had been injected, the recovery factor was around 31 %, as shown in Figure 3. From 5 to 10 pore volumes, the recovered oil was around of 2 % more. Later, pH measurements were obtained from the effluents. The pH tended to drop from 7.8 to 7.0, approximately. Alotaibi et al. (2010) obtained similar results using dolomite cores at 90 ºC. In their tests, the recovery factor was around 35.5 % after 2.5 pore volumes. The reactivity of the core towards the divalent ions appeared to be negligible, except for magnesium, Figure 4. This divalent ion and also sulphur showed small variations on their concentrations, staying active at high temperature. The bicarbonate ion was completely inert.
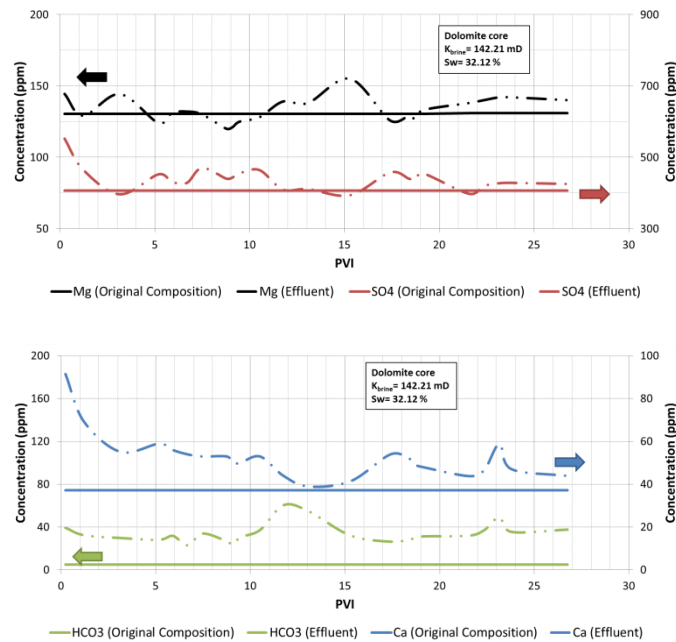
Figure 2.- Changes in ion concentrations of magnesium, sulphate (above), bicarbonate and calcium (below) when low salinity water is flooded through the core at 92 °C.
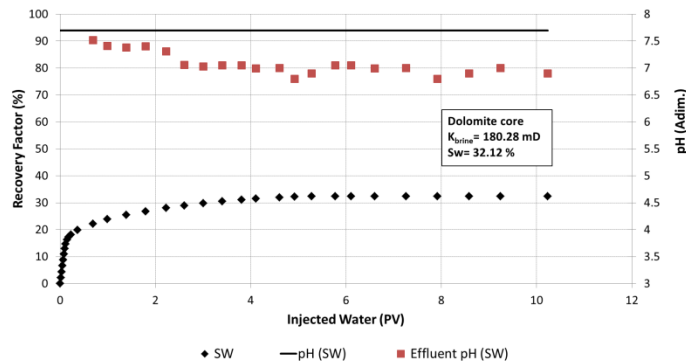

Figure 3.- Oil recovery versus pore volumes of injected seawater at 92 °C.

Calcium, magnesium and sulphate have been reported as potential determining ions for improving oil recovery in carbonate rocks. For these experiments, the effect of such ions on the wettability change is not in good agreement with the results described by Austad's group (2009 to 2012).

However, there is a contrast between the ion evaluation and the permeability measurements after the experiment. The water permeability decreased dramatically to a stable value of 64.08 md, which was around 65 % below its initial permeability (180.28 md). The decrease in permeability denotes that the permeability was dominated by the damage resulting from the seawater injection. The lack of ion production and the loss of permeability may be linked to this damage caused by seawater injection. Overall, this core was found to suffer permeability loss when seawater is used as a smart fluid.
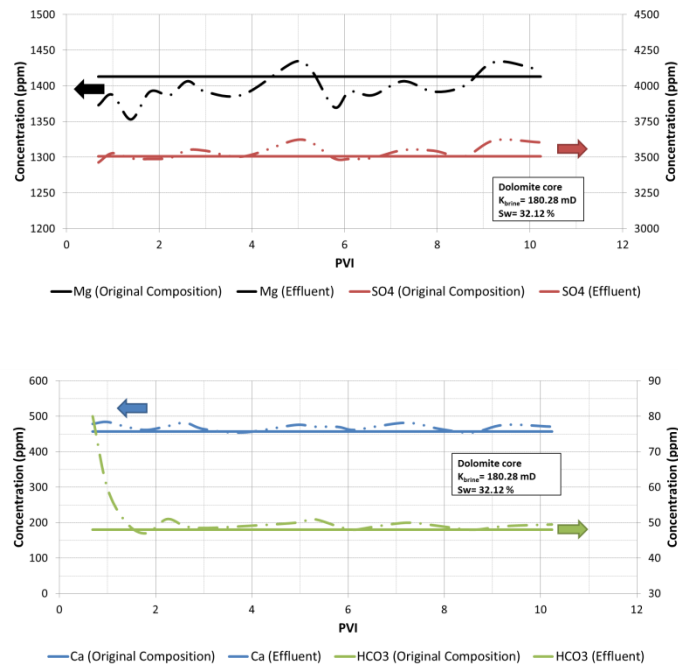
Figure 4.- Changes in ion concentration of magnesium, sulphate (above), calcium and bicarbonate (below) when seawater is flooded as a secondary process.

From the differential pressure curves in Figure 5, it is evident that during each experiment, the pressure first increased then decreased slowly, and later the trend was stabilised. In addition, from this Figure, some small variations of pressure were noticed when both high rates and shut-in periods were applied. Thereafter, other major changes in pressure were not detected or the differential pressure response did not give an indication of any instability and hence unusual behaviour.

For the dolomite core, the seawater was supersaturated (SI>0) at high temperatures. That is, the seawater is fully saturated with diverse ions in solution, so, this state does not allow that material from the rock become dissolved and/or transported. Thus, this condition of saturation set up the potential for particular events such as precipitation, pore blocking (plugging) or loss of permeability.

In the case with inject seawater, it is clear that saturation condition of this fluid will favour the permeability reduction (up to 65 % for the dolomite core), as shown in Table 3. If the saturation index is negative (SI<0) as for the low salinity waters (Gachuz et al., 2016) then no precipitation will take place. Consequently, the low salinity waters may adequately dissolve and transport the released material from the rock, which originated from the action of the acidic water derived from the crude oil/low salinity brine interaction. Crude oil with low TAN was especially prone to create acidic water because of the highest amount of water-soluble compounds that are diffused in the aqueous phase, allowing the hydrogen to be released, creating a more acidic environment (Gachuz et al., 2016).
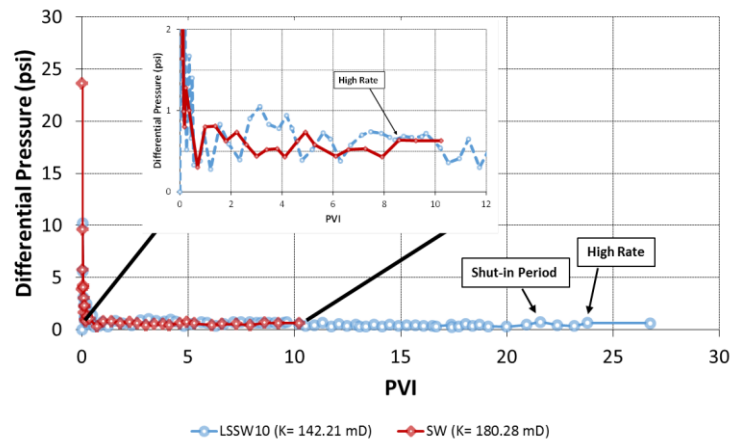
Figure 5.- Differential pressure across core versus pore volumes for the dolomite core with two brines.

Over the long term this process will lead to improving the internal conductivity in the porous media, generating a better permeability, as seen in Table 3 for low salinity water injection (from 142.21 to 180.28 md, respectively). Dissolution of the rock is usually studied in the context of room conditions and hence research for elevated temperatures or pressures is limited in the published literature (Morey, 1962; Plummer et al., 1978; Zhang et al., 2007). For instance, calcite and dolomite minerals have been investigated in terms of the importance of transport control vs pH changes. When the temperature goes up diffusion will control the system. At low temperatures, dissolution is a chemical control mechanism (Sjoberg, 1976 and 1978; Sjoberg et al., 1983-1985; Brantley et al., 2008).

Table 3.- Change of core permeability after coreflood experiments.

Experiment	Initial K_{brine} (mD)	Process	Injected Fluid	RF (%)	Final K_{brine} (mD)
1	142.21	Secondary	LSSW10	69.30	180.28
2	180.28	Secondary	Seawater	32.43	64.08

In order to verify that the oil recovery factor may also be associated with the dissolution effect, other parallel coreflood experiments were conducted using the same core (third coreflood experiment). In this case, the core was saturated with crude oil "E", which is more acidic. The results are plotted in Figure 6. For the first experiment with this crude oil, low salinity seawater was intentionally injected. The aim was to firstly remove the damage which existed. Only 42 % of OOIP was recovered during low salinity water injection as a secondary program. When the brine was changed to another low salinity water, LSSW50, an increase in oil production was noticed. After 10 PV of injection, the recovered oil exceeded 45 %. The effect of the low salinity water was less than that observed in the coreflood experiments for the basic crude oil (crude oil "A"). This demonstrates that low salinity fluids play an important role in the wettability change processes.
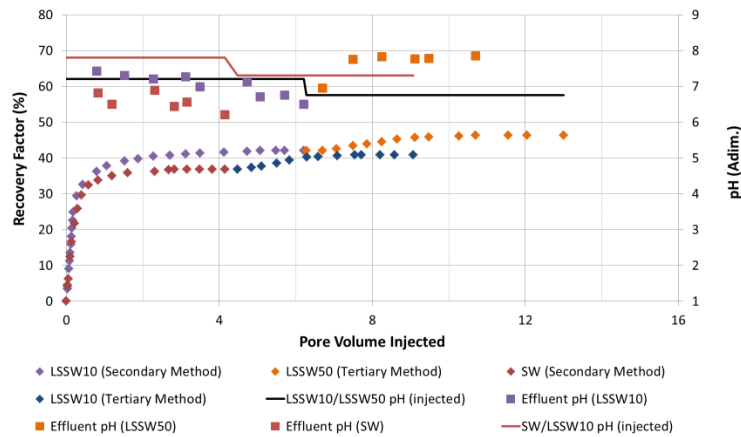
Figure 6.- Oil recovery versus pore volumes of injected seawater at 92 ᵒC.

In the second case (fourth coreflood experiment), seawater injection was first flooded as a secondary process then low salinity water was injected. The oil recovery for a secondary process using seawater reached a plateau of 36.87 % of OOIP after 4 PVI. The injection fluid was then changed to LSSW10, which resulted in a small increase in oil production with a maximum plateau of 40.62 % after 8 PVI. Previous experiments with the same core and a basic crude oil resulted in higher oil production for low salinity water but slightly lower production for seawater.

Figure 7 illustrates the variations of ion concentrations in terms of pore volumes injected for the low salinity waters system. The concentration of magnesium and sulphate ions did not change for the first period of injection with LSSW10. This is comparable to what was previously observed for the basic crude oil, as shown in Figure 4. The effluents maintained a continuous production of calcium and bicarbonates. When the concentration of the injected fluid was dropped, the production of these ions remained high. As the change in concentration became great enough, the effluents continued producing bicarbonates but the sulphate exhibited a sudden change. This change is perceptible from 7 to 10.70 PVI. The effect of this additional production during the whole experiment can be explained by considering the probable removal of the core damage. Notice also that this low salinity water (LSSW50) has the ability to be less saturated, as it was explained by us in 2016, revealing that the salts in the brine may increase. These results were later confirmed with the permeability measurement, where the final value was 158.57 md, as shown in Table 4. As the low salinity water was injected, the damage was practically removed. The lower the concentration of the brine, the more active the brine will become. Due to contamination with the previous water samples, no analyses were obtained from 10.7 to 13 pore volumes injected. The oil recovery factors, changes in core permeability and ion concentration variations imply that the mechanism of rock dissolution is practically negligible for the experiments using an acidic crude oil (crude oil "E"). Moreover, the wettability change, where it occurred, was relatively lower.

Table 4.- Changes in core permeability after the coreflood experiments for two crude oils.

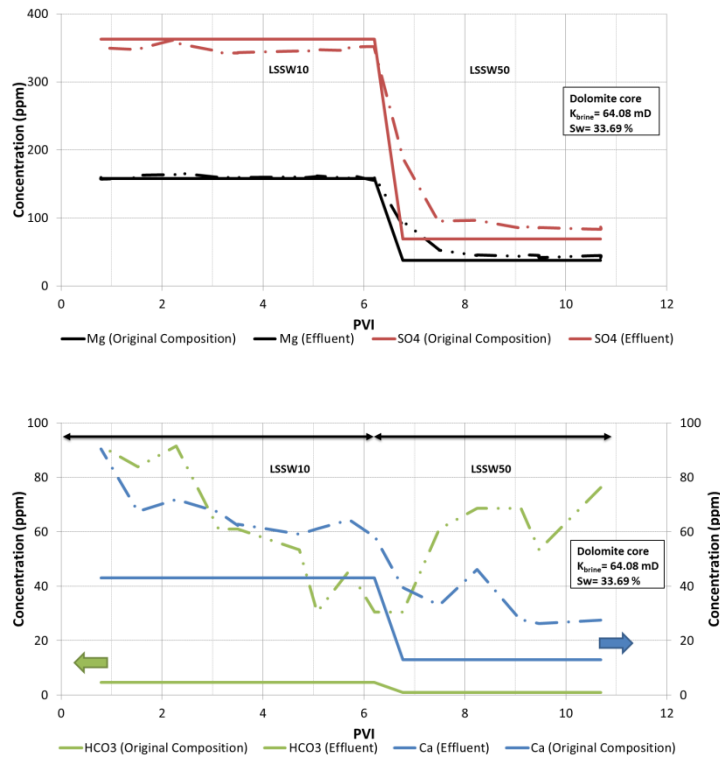| Experiment	Initial k_{brine} (md)	Process	Injected Fluid	RF (%)	Final k_{brine} (md)
Crude Oil "A"					
1	142.21	Secondary	LSSW10	69.30	180.28
2	180.28	Secondary	Seawater	32.43	64.08
Crude Oil "E"					
3	64.08	Secondary/Tertiary	LSSW10/LSSW50	42.05/4.29	158.57
4	158.57	Secondary/Tertiary	Seawater/LSS10	36.87/3.75	141.83

Figure 7.- Changes in ion concentrations of Mg^{2+}, SO_4^{2-} (above), HCO_3^- and Ca^{2+} when low salinity waters were injected through the core using an acidic crude oil (Crude oil "E").

In Figure 8, only very small pressure variations can be noticed during the injection processes. Injection at a high rate caused a rise in pressure to a maximum value of 3 psi. Modification of the rate was not accompanied by an increase in oil recovery. The pressure continued to drop smoothly and stabilised after a while. Additional oil recovery was never gained with high injection rates. In spite of the fact that the permeability changed, no direct experimental evidence is accessible to support the possibility that either dissolution or blockage can be detected by analysing differential pressure across a core, so far. No significant changes can be observed in the pressure behaviour, apart from injection rate adjustments at the end of each sequence.
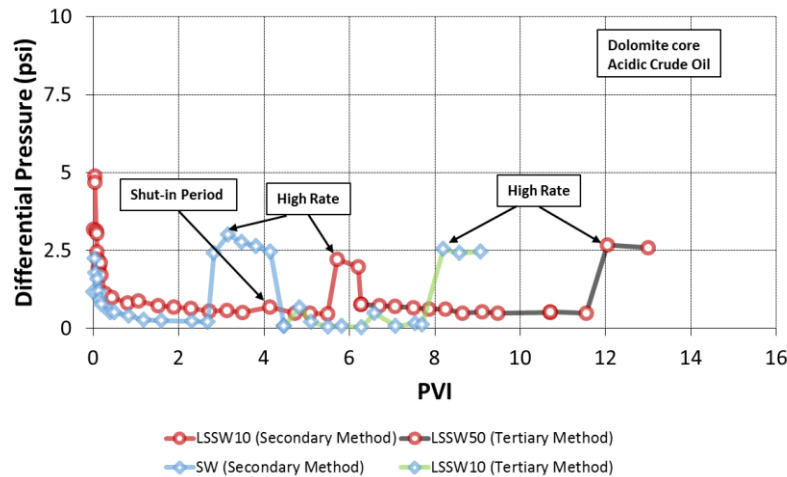
Figure 8.- Differential pressure across core versus pore volumes for the core with four brines.

Morse and Arvidson (2002) compiled dolomite dissolution data as a function of pH from published values. The experiments of Zhang et al. (2007) indicate that the mechanisms of dissolution of dolomite at low temperatures differ from those at high temperatures. Their results indicate that there are linear correlations between concentrations of calcium and magnesium in the aqueous phases. The release rates of calcium and magnesium are proportional (1:1), especially at temperatures below 100 $^{\circ}$C. However, the dissolution product is not proportional (1≠1) at higher temperatures.

Thus, a vast number of studies have provided evidence that the rate of dissolution is highly dependent on diverse variables. Under reservoir conditions where such variables are important, smart waters may then apparently mobilise the released material from the core and produce/transport it to the outside. The observation that smart waters may mobilise this material also suggests that movement and transport are likely to occur during coreflood experiments, in either secondary or tertiary oil recovery methods at high pressure and high temperature, even at reservoir scale, where reservoir conditions could favour better situations for dissolution and transport.

CONCLUSIONS

The effect of the smart waters on rock dissolution has been studied in more detail at dynamic conditions in a dolomitic core. Some conclusions can be drawn as follows:

- The tests of these studies proved that is possible to predict the occurrence of the dissolution phenomenon during smart water injection using simple fluid-fluid contact tests where acidic water generation is easily detected.

- Effluent analysis and permeability evaluations validated the influence caused by low salinity water as acidic water in contact with the rock. The presence of rock

dissolution was principally detected by coreflood experiments through changes in ion concentrations of calcium and bicarbonates and permeability values.

- Crude oil is an important agent playing a vital role in improvement of oil recovery and the rock dissolution effect will be more important at reservoir scale. The findings described here differ from Mahani et al. (2015), where they affirmed that the rock dissolution was only relevant on a laboratory scale and not at reservoir scale. The crude oil, itself, is governing the effects of the smart water injected into the reservoirs.

- Damage to the core occurred when seawater was used for improvement of the oil production. Permeability measurements corroborated these findings.

- Positive effects derivate from the use of seawater were not observed here. In spite the fact that the permeability changes occurred, no direct experimental evidence is accessible to support the possibility that either dissolution or blockage can be detected by analysing differential pressure across the used core, so far.

Therefore, these dissolution studies have help to better understand and verify many of the variables which are taking part during the dissolution in coreflood experiments such as pressure, temperature, rate controlling mechanisms, type of aqueous phase, pH and ionic strength.

ACKNOWLEDGEMENTS

REFERENCES

Alotaibi, M. B.; Nasralla, R. A.; Nasr-El-Din, H. A. 2010. Wettability Challenges in Carbonates. SPE-129972, The 2010 SPE Improved Oil Recovery Symposium, Oklahoma, U.S.A.

Austad, T.; Shariatpanahi, S. F.; Strand, S. 2012. Conditions for a Low-Salinity Enhanced Oil Recovery (EOR). Effect in Carbonate Oil Reservoirs. Energy & Fuel, 26, 569-575.

Brantley, S. L.; Kubicki, J. D.; White, A. F. 2008. Kinetics of Water-Rock Interaction. Springer.

Fathi, J.; Austad, T.; Strand, S. 2011. Water-Based Enhanced Oil Recovery (EOR) by Smart Water": Optimal Ionic Composition for EOR in Carbonates. Energy & Fuels, 5173-5179.

Gachuz-Muro, H.; Sohrabi, M.; Benavente, D. 2016. Natural Generation of Acidic Water as a Cause of Dissolution of the Rock During Smart Water Injection in Heavy Oil

Carbonate Reservoirs. The SPE Latin America and Caribbean Heavy and Extra Heavy Oil Conference, Lima, Peru.

Mahani, H.; Levy, A. K.; Berg, S.; Bartels, W. B.; Nasrall, R.; Rossen, W. R. 2015. Insights Into the Mechanism of Wettability Alteration by Low Salinity Flooding (LSF) in Carbonates. Energy & Fuels, 29, 1352-1367.

Mahani, H.; Levy, A. K.; Berg, S.; Bartels, W. B.; Nasrall, R.; Rossen, W. R. 2015. Driving Mechanism of Low Salinity Flooding in Carbonate Rocks. SPE-174300, the EUROPEC 2005, Madrid, Spain.

Morey, G. W. 1962. The Action of Water on Calcite, Magnesite and Dolomite. The American Mineralogist, Vol. 47, 1456-1460.

Morse, J. W.; Arvidson, R. S. 2002. The Dissolution Kinetics of Major Sedimentary Carbonate Minerals. Earth-Science Reviews, Vol. 58, 51-84.

Puntervold, T.; Strand, S.; Austad, T. 2009. Coinjection of Seawater and Produced Water to Improve Oil Recovery from Fractured North Sea Chalk Oil Reservoirs. Energy & Fuel, 23, 2527-2536.

Plummer L. N.; Wigley T. M. L.; Parkhurst D. L. 1978. The Kinetics of Calcite Dissolution in CO2-Water Systems at 5 to 60∘C and 0.0 to 1.0 atm CO2. American Journal of Science Vol. 278, 179-216.

RezaeiDoust, A.; Puntervold, T.; Strand, S.; Austad, T. 2009. Smart Water as Wettability Modifier in Carbonate and Sandstone: A Discussion of Similarities/Differences in the Chemical Mechanisms. Energy & Fuels, 23, 4479-4485.

Shariatpanahi, S. F.; Strand, S.; Austad, T. 2010. Evaluation of Water-Based Enhanced Oil Recovery (EOR) by Wettability Alteration in a Low-Permeable Fractured Limestone Oil Reservoir. Energy & Fuels, 24, 5997-6008.

Shariatpanahi, S. F.; Strand, S.; Austad, T. 2011. Initial Wetting Properties of Carbonate Oil Reservoirs: Effect of the Temperature and Presence of Sulphate in Formation Water. Energy & Fuels, 25, 3021-3028.

Sjoberg, E. L.; Rickard, D. T. 1985. The Effect of Added Dissolved Calcium on Calcite Dissolution Kinetics in Aqueous Solutions at 25o C. Chemical Geology, Vol. 49, 405-413.

Sjoberg, E. L.; Rickard, D. T. 1984. Calcite Dissolution Kinetics: Surface Specification and the Origin of the Variable pH Dependence. Chemical Geology, Vol. 42, 119-136.

Sjoberg, E. L.; Rickard, D. T. 1983. The Influence of Experimental Design on the Rate of Calcite Dissolution, Geochimica et Cosmochimica Acta, Vol. 47, 2281-2286.

Sjoberg, E. L.; Rickard, D. T. 1984. Temperature Dependence of Calcite Dissolution Kinetics between 1 and 62o C at pH 2.7 to 8.4 in Aqueous Solutions, Geochimica et Cosmochimica Acta, Vol. 48, 485-493.

Sjoberg, E. L. 1978. Kinetics and Mechanism of Calcite Dissolution in Aqueous Solutions at Low Temperatures. Stockholm Contrib. Geol., Vol. 32, No.1.

Sjoberg, E. L. 1976. A Fundamental Equation for Calcite Dissolution Kinetics. Geochimica et Cosmochimica Acta, Vol. 40, 441-447.

Zhang, R.; Hu, S.; Zhang, X.; Yu, Wenbin. 2007. Dissolution Kinetics of Dolomite in Water at Elevated Temperatures. Aquatic Geochemistry, Vol. 13, 309-338.

STRESS SENSITIVITY OF MERCURY INJECTION MEASUREMENTS

P. Guise[1], C. Grattoni[1], S, Allshorn[1], Q.J. Fisher[1], A. Schiffer[2]
1 – School of Earth and Environment, University of Leeds, Leeds, LS2 9JT, UK
2 – InfLogik H-7630 Pecs, Hungary

ABSTRACT

Many petrophysical properties (e.g. permeability, electrical resistivity etc.) of tight rocks are very stress sensitive. However, most mercury injection measurements are made using an instrument that does not apply a confining pressure to the samples. Here we further explore the implications of the use and analysis of data from mercury injection porosimetry or mercury capillary pressure measurements (MICP). Two particular aspects will be discussed. First, the effective stress acting on samples analysed using standard MICP instruments (i.e. Micromeritics Autopore system) is described. Second, results are presented from a new mercury injection porosimeter that is capable of injecting mercury at up to 60,000 psi into 1.5 or 1 in core plugs while keeping a constant net stress up to 15,000 psi. This new instrument allows monitoring of the electrical conductivity across the core during the test so that an accurate threshold pressure can be determined.

Although no external confining pressure is applied (unconfined) when using the standard MICP instrument, this doesn't mean that the measurements can be considered as unstressed. Instead, the sample is under isostatic compression by the mercury until it enters the pore space of the sample. As an approximation, the stress that the mercury places on the sample is equal to its threshold pressure. Thus, the permeability calculated from standard MICP data is equivalent to that measured at its threshold pressure. Not all the samples have the same stress dependency thus comparing measured permeabilities at a single stress with values calculated from standard MICP data, corresponding at different threshold pressures, can lead to erroneous correlations. Therefore, the estimation of permeabilities from standard MICP data can be flawed and uncertain unless the stress effect is included.

Results obtained from the new mercury injection system, porosimeter under net stress, are radically different from those obtained from standard MICP instruments such as the Autopore IV. In particular, the measurements at reservoir conditions produce threshold pressures that are three times higher and pore throat sizes that are 1/3rd of those measured by the standard MICP instrument. The results clearly indicate that calculating capillary height functions, sealing capacity, etc. from the standard instrument can lead to large errors that can have significant impact on subsurface characterization.

INTRODUCTION

Mercury injection analysis has been extensively used to estimate the capillary pressure of rocks for the petroleum industry. Initially, measurements were made in an instrument in which core plugs were placed in a core holder with a confining pressure of up to 10,000 psi and mercury was injected manually into the sample at pressures of up to 2,000 psi. It is possible to make electrical measurements during this test so that the pressure at which mercury spans across the length of the sample, often referred to as the *threshold pressure*[1], can be identified. More recently, the trend within industry is to use automated porosimeters that can inject mercury at up to 60,000 psi; this will be referred to as unconfined mercury injection capillary pressure (MICP). MICP is usually conducted on small samples (~1-10 cm^3). Two key criticisms of MICP are that the samples are not placed under a confining stress and that electrical measurements cannot be made to identify a threshold pressure. Conducting mercury injection experiments without a confining pressure is a particular worry for tight samples whose petrophysical properties are known to be highly stress sensitive. Attempts have been made to pre-stress samples prior to the mercury injection test but only a few results have been published and confining pressures are generally limited to a fixed hydrostatic stress of around 5,000 psi although some measurements at stresses of 16,000 psi have been reported (Mitchell et al., 2003). It has also recently been argued that MICP tests should not be regarded as unstressed measurements because mercury will place an isostatic pressure on the samples, inducing a pore volume compression, until it enters their pore space (Mitchell et al., 2003; Brown, 2015). Indeed, Brown (2015) presented a methodology to take into account the effect that the isostatic pressure has on MICP results when being used to calculate permeability.

The following paper aims to increase understanding of the impact of stress on mercury injection measurements by presenting and analysing results from mercury injection experiments conducted using both an industry-standard instrument and a newly developed mercury injection porosimeter that allows standard core plugs to be confined at very high net stress (up to 15,000 psi) and mercury intruded at pressures of up to 60,000 psi. The new instrument, here referred to as Porosimeter Under Confining Stress (PUCS), which also allows electrical measurements to be made so that the threshold pressure can be identified. The paper begins by describing the samples and methods used including the methodology and analysis process of the new PUCS instrument. The paper compares results from both instruments and discusses use of these results to estimate permeability. Finally, the implications of the results are discussed in relationship to the common uses of mercury injection data such as sealing capacity and saturation height functions.

---

[1] For a homogeneous rock with a unimodal and narrow pore size distribution the terms entry pressure, threshold pressure and breakthrough pressure are interchangeable. In this paper they will be used with this concept in mind, however, for many natural samples they are different.

METHODS
Samples And General Methodology
A range of tight samples were analysed during this study including:-

- Approximately 250 tight gas sandstone samples were analysed; small samples of each were tested using the standard MICP instrument and 18 core plugs tested with PUCS. The samples were mainly from Jurassic, Triassic, Permian and Carboniferous from onshore and offshore Europe but some samples from Australia, Oman and Ukraine were also tested.

- Seven fault rock samples were tested with both methods; four are from faults outcropping in the UK and Miri, Malaysia, three were from core taken from a Triassic reservoir in the Central Graben of the North Sea, UK.

- Three caprocks from petroleum reservoirs of undisclosed locations were tested with both methods.

All samples were supplied as 1.5 in core plugs with off-cuts. Cubes of around 1.5 x 1.5 x 1.5 cm were cut from the offcuts for unstressed Hg-injection analysis. The 1.5 in core plugs were trimmed so that their ends were parallel. The samples were then thoroughly cleaned in a Soxhlet extractor using a 50:50 mixture methanol-toluene or dichloromethane. The samples were then dried in an oven at 65°C until constant weight was obtained. A thorough core analysis program was conducted on each core plug including: (i) X-ray CT using a medical CT scanner; (ii) helium porosimetry only at ambient stress; and (iii) gas permeability vs stress using a pulse decay permeameter during a loading cycle at net stresses of 500 to 7000 psi. The Klinkenberg corrected value was determined by measuring apparent permeability, k_{ap}, at four gas pressures, P_p, and extrapolating plots of k_{ap} vs. $1/P_p$ to $1/P_p = 0$. The microstructure of all samples were examined using optical and scanning electron microscopy to identify the presence of fractures as well as the key microstructural controls on flow properties (e.g. clay distribution etc.).

Unconfined mercury porosimetry analysis was conducted on all samples using the methodology described below. Mercury injected under stress was conducted on 28 samples (tight gas sandstones, fault rocks and caprocks) using the methodology described later in this section. The unconfined and under net stress porosimetry are both performed in a temperature controlled laboratory at 21 ^{o}C. The preparation of each sample for mercury injection under stress takes approximately two days due to the larger sample size.

Unconfined Mercury Injection
The unconfined mercury injection (MICP) was performed using a Micromeritics Autopore IV 9520 system. This model has four low pressure ports and two high pressure chambers. Clean and dry samples are loaded into a penetrometer and evacuated. The penetrometer is automatically backfilled with mercury. The pressure is then increased to 25 psi (0.17 MPa) in the low pressure port and up to 60000 psi (413MPa) in the high pressure chamber

following pre-selected pressures. The change from one selected pressure to the next can be at fixed times or when injection rate becomes less than a user defined value (0.001 µl/g/s was used in this work). The Autopore software does an automatic blank cell correction and data reduction. For more details see the Micromeritics documentation. If necessary a manual volume conformance and bulk rock compressibility corrections (Shafer and Neasham, 2000; Comisky et al., 2011) can be applied during data interpretation.

Mercury Injection Under Stress
A new equipment has been designed to perform mercury Porosimetry Under Confining Stress (PUCS) on competent porous and permeable rocks. A net stress equivalent to reservoir conditions (generally 3000 to 7,000 psia), which is the difference between confining stress and pore pressure, is applied and kept constant on the rock sample during mercury injection. The range of net stress applicable is between 1000 and 15000 psi (6.9 -103 MPa) and the maximum mercury pressure is 60,000 psia (413MPa). The resolution per unit volume of sample of the new equipment is comparable to the Autopore. All aspects of control as well as data collection and display are automatic and processed by computer software. The bespoke software for this system was developed in Labview by InfLogik. The post processing and data reduction of the data collected during the experiment is dealt with separately in Excel.

Overview Of The Analysis Process
A clean and dry sample is prepared, loaded into a sample assembly before beginning the analysis. The first phase is the evacuation of the rock sample and filling the sample assembly with mercury. The second phase consists of placing the sample assembly in the pressure vessel and a confining pressure equal to the reservoir net stress is applied for approximately 12 hours (overnight). A sample information file that describes the sample and gives the analysis conditions and other parameters is loaded into the software. Separate files are also loaded to define the pore pressure table, which lists the pressure points at which data are collected during the loading and unloading cycle. The system is initialised and the software automatically controls both mercury and confining pressure whilst recording both volumes. Mercury is injection from one side of the sample and once each mercury pressure point is reached the flow rate is monitored until it becomes less than a pre-set value (typically $0.001 mm^3/cm^2/s$) the pressure and volumes are recorded. The top and bottom of the sample assembly are electrically isolated and before mercury injection the core sample is a non-conductor so there is a very large resistivity across the sample. As soon as the mercury spans the length of the sample the conductivity is significantly increased, which is used to accurately determine the breakthrough pressure.
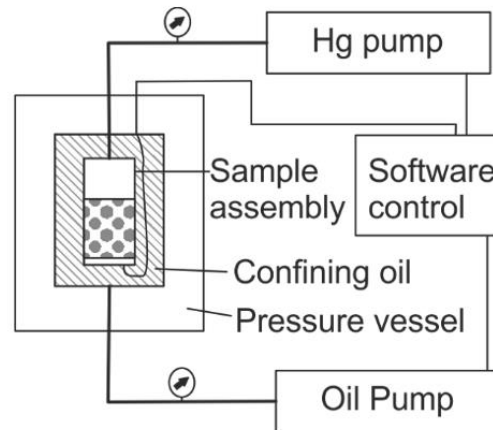
Figure 1. Picture and schematic diagram of the new porosimeter under confining stress.

The data collected during the test is manually processed to obtain capillary pressure as a function of saturation and pore throat size distribution. The porosity under stress is calculated using volume of mercury injected at maximum pressure (pore volume), the sample weight and grain density (grain volume). The pore volume at net stress is calculated by determining the volume injected corrected for system and mercury compressibility effects. The pore diameter at each pressure is calculated using Washburn (1921) equation.

RESULTS
Comparison Of Methodologies

To validate the methodology of the new instrument a standard ceramic sample from Soilmoisture Equipment Corp. (15 Bar) was tested in both the Autopore and PUCS. The properties of ceramic disks are likely to be far less stress dependent than core material as they haven't experienced the dramatic changes in stress that core samples experience during extraction. A disk of 38 mm diameter and 5 mm thickness (~5.5 cm^3) was used, to minimize the stress effect, in the new system and a sample of 2 x 1.5 x 0.5 (~1.5 cm^3) was used for MICP. A very good agreement between results of both systems was obtained and shown in Figure 2. A breakthrough pressure of 4000 psig at a saturation of 24.5 % was determined using the resistivity measurement in the new instrument.
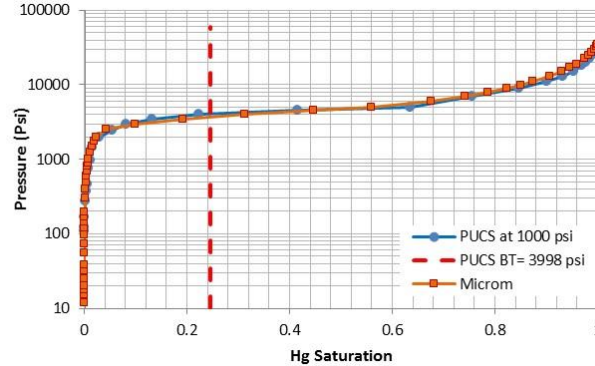
Figure 2. Plot of pressure vs. Saturation for comparing MICP and PUCS.

Permeability Estimates From Unconfined MICP Data Of Tight Gas Sandstones

Purcell (1949) was the first to estimate permeability from MICP data by assuming that flow could be calculated applying Poiseuille theory to a bundle of capillaries whose diameter was estimated using the Washburn (1921) equation. The equation of Purcell (1949) contained a term referred to as the lithology factor to account for tortuosity but was obtained by calibration against samples with known permeability. Katz and Thompson (1986, 1987) used percolation theory to derive a method for calculating permeability from MICP data without the need for calibration. Comisky et al. (2007) presented a comparative study of the accuracy of various methods to calculate permeability of tight gas sandstones from MICP data and found that the Purcell (1949) and Katz and Thompson (1986, 1987) performed the best.

A conformance correction was applied to all MICP data by removing any data, low pressures, at points below where no mercury intrusion should occur. Permeability was calculated from the mercury injection data using a wide range of published methods but only the results from the method of Swanson (1981) are presented here;

$$K_{gas} = A \left(\frac{S_{Hg}}{P_c} \right) apex^B \qquad (1)$$

where K_{gas} is the gas permeability (mD), S_{Hg} is the mercury saturation (%) and P_c is the capillary pressure (psi) corresponding to the apex of a hyperbolic log-log MICP injection plot. The constants A and B are fitting parameters, which Swanson suggested were 339 and 1.691 respectively. As suggested by Pittman (1992), the apex was obtained by plotting Hg saturation against (Hg saturation/capillary pressure). In the current study, the Excel solver was used to optimize the constants A and B in order to provide the best fit with the Klinkenberg corrected permeability measured at a net confining pressure of 5000 psi. The optimal value of A and B that produced a correlation close to 1:1, between the estimated and measured gas permeability (Figure 3a), are 26 and 1.63 respectively. It should,

however, be noted that the method appears to systematically underestimate the permeability of many of the low permeability samples (i.e. <0.0001 mD).

It is often argued that MICP analysis is an unstressed measurement because no confining pressure is applied to the sample during the analysis. However, this is not strictly true as the mercury actually applies an isostatic pressure before it enters the pore space, which becomes important for samples with a high entry pressure. Brown (2015) argued that many of the mercury injection based permeability predictors are broadly based on the assessment of the pore throat diameter of the key pore systems that control flow. So as a first approximation, the permeability values obtained can be regarded as being equivalent to a stress at which the mercury spans across the pore system. The threshold pressure usually increases as the pore size of the network decreases, so a permeability estimated from MICP data of tight rocks should be compared to permeability measured at high confining stress. On the other hand, for high permeability samples it should be compared to permeability measured at lower confining stress. The isostatic pressure effect can easily explain why the permeability estimated using MICP and the method of Swanson is generally lower than measured values for the low permeability samples.

To test the concept presented by Brown (2015) the permeability, of tight gas sandstones, at a stress equivalent to the mercury threshold pressure was obtained from the stress vs gas permeability data. The Excel solver function was then used to estimate the optimal values of A and B to produce the best correlation between the Klinkenberg corrected gas permeability at stress and the value estimated using the Swanson method. The values of 500 and 1.8 for the constants A and B were found to produce the best 1:1 correlation between measured and estimated values (Figure 3b). The correlation coefficient is similar to that produced when plotted against gas permeability measured at 5000 psi net confining pressure but there is no underestimation of permeability for the tight rocks.
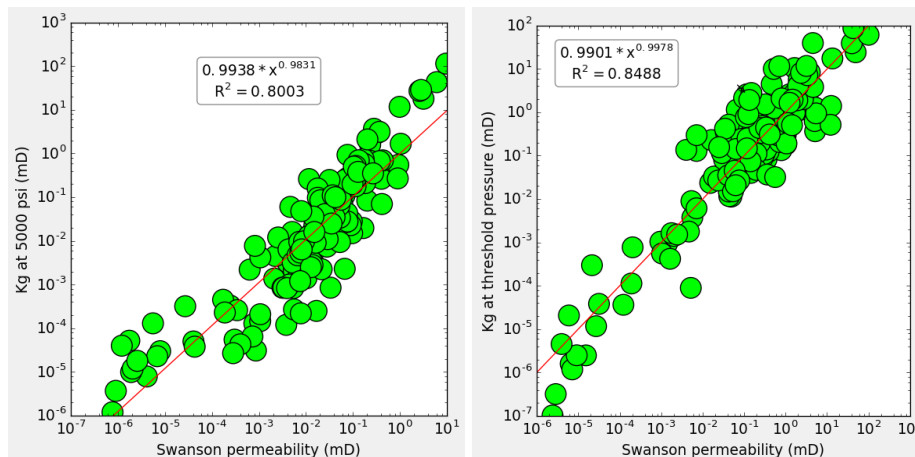

Figure 3. Plot of a) permeability estimated using MICP and the Swanson method (Eqn.1) against Klinkenberg gas permeability measured at 5000 psi confining

pressure and b) permeability estimated using the Swanson method against the gas permeability measured at the mercury-air threshold pressure of each sample.

Stressed Mercury Injection Results Of Tight Gas Sandstones

The PUCS results at reservoir net stress are radically different from those obtained using the unconfined MICP (e.g., Figure 4). For example, the threshold pressures are an average of 3 times larger for the unconfined MICP compared to the stressed PUCS (Figure 5a) and the peak pore diameters are on average a third of the values for the unconfined MICP (Figure 5b). An unequivocal test has not yet been identified to be absolutely certain that these differences are totally due to stress-related variations in pore structure as oppose to differences in experimental details (e.g. sample size, pressure steps etc.). However, the results are entirely consistent with the stress-dependence of permeability of the samples (e.g. pore size is reduced by a factor of 3 and permeability is reduced by an order of magnitude). In addition, as discussed above, the results obtained from the ceramic disk are very similar for the PUCS and MICP instruments.
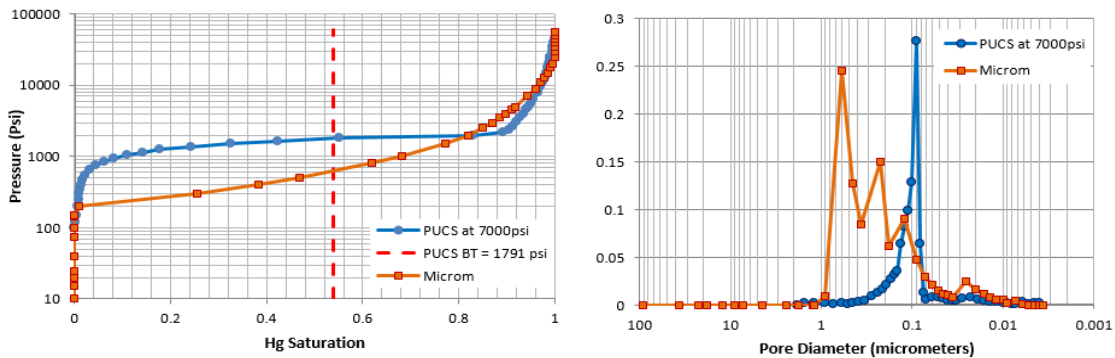

Figure 4. Typical, mercury injection results from the unconfined MICP (orange) and the new stressed Hg porosimeter (blue). The red dashed line marks the threshold pressure as measured using the electrical conductivity measurement.
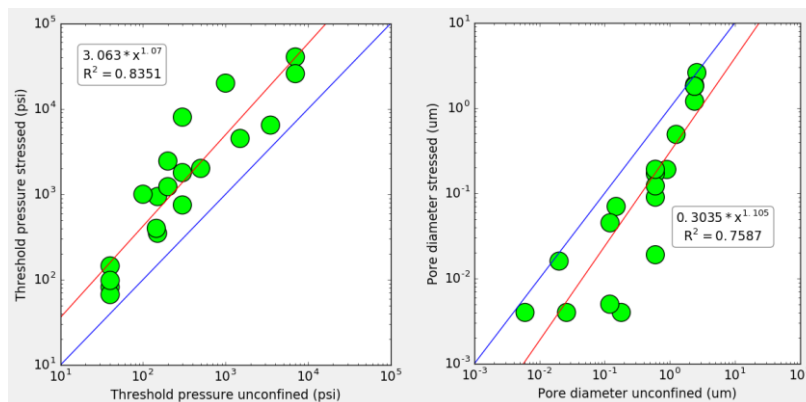
Figure 5 Plot of a) threshold pressure of tight gas sandstones measured PUCS vs MICP, and b) peak pore diameter; the blue lines represent the 1:1 relationship whereas the redlines are the power-law regressions.
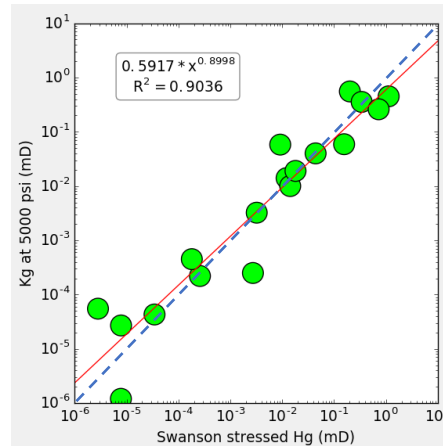

Figure 6 Plot of permeability calculated using PUCS data and Swanson's method vs the Klinkenberg corrected gas permeability measured at 5000 psi net confining pressure. The blue line represent the 1:1 relationship whereas the redline is the power-law regressions

The Excel solver function was then used to estimate the optimal values of A and B to produce the best correlation between the Klinkenberg gas permeability at and the value estimated using the Swanson method. The values of 560 and 2.05 for the constants A and B were found to produce the best 1:1 correlation between measured and estimated values (Figure 6). The correlation coefficient is slightly better to that produced when plotted against gas permeability measured at net stress of 5000 psi but there is no systematic underestimation of permeability for samples with k_g of <0.001 mD.

Threshold Pressures of Tight Gas Sandstones, Fault Rocks and Top Seals

The breakthrough pressure represents the capillary pressure at which a non-wetting phase will start to flow and is useful for identifying the sealing capacity of seals and faults as well as the height above the free water level that the critical gas saturation is reached. Figure 7 shows a plot of threshold pressure measured by PUCS at reservoir conditions against that estimated from unstressed MICP data. It shows that on average the threshold pressure measured by PUCS is over four times that estimated from MICP data. However, the threshold pressure at reservoir conditions can be up to an order of magnitude higher that the estimated by MICP.
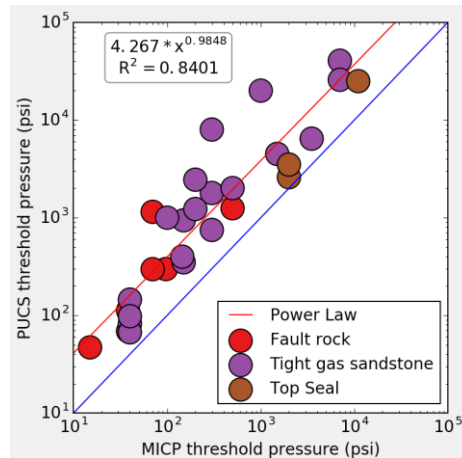
Figure 7. Plot of threshold pressure measured using PUCS against that estimated from MICP data. The blue line represents the 1:1 relationship whereas the red line is the power-law regression.

DISCUSSION

Mercury injection porosimetry is one of the most widely used experimental methods to estimate the capillary pressure characteristics of reservoirs and seals; it is also often used to estimate permeability. Like many other petrophysical properties, MICP results are stress sensitive. The stress sensitivity of many properties (e.g. electrical resistivity, permeability, capillary pressure, etc.) tends to be proportional to pore size. This relationship is not so straight forward for MICP results. In particular, despite often being perceived as an unstressed measurement, the traditional high pressure unconfined measurement, will place an isostatic pressure on the sample inducing a pore volume compression before entering the pore space. The mercury will place a stress of at least the entry pressure onto the sample. This means that mercury injection data conducted on low permeability samples, with a high threshold pressure, will have effectively been measured at a higher stress than those of high permeability samples.

An example of the determination of isostatic pore volume compression and entry pressure for MICP has been presented for an Eagle Ford Shale by Comisky et al. (2011). They used a bulk compressibility model to separate the conformance correction, pressure range 10 to 30 psi, isostatic pore volume compression (up to 4000 psi) and intrusion volume (4000 to 60000 psi). Thus, the entry pressure for their shale is 4000 psi but the estimated breakthrough pressure is 18000 psi. However, based on the depth of their logs the reservoir is approximately at a net stress of 5000 psi and as a consequence none of the properties estimated from MICP (mainly porosity, permeability and capillary pressure) are representative of the reservoir due to an excessive isostatic compression.

There is currently not agreed method to stress correct capillary pressures obtained from MICP experiments. However, the assumption that the permeability estimated from MICP

data using methods such as Swanson (1981) is equivalent to the permeability measured at the mercury injection threshold pressure appears to improve interpretations for the samples used in this paper.

Threshold pressures obtained under constant net stress are on average four times higher than those estimated from traditional MICP measurements. These results are highly significant in that standard MICP data may have been underestimating the sealing capacity of faults and top seals by at least a factor of four. The results also indicate that using traditional MICP data to estimate saturation height functions in tight gas reservoirs could result in a significant overestimation of mobile gas.

CONCLUSIONS

The results from mercury injection analysis are very sensitive to the net stress applied to the sample. Traditional high pressure mercury injection analysis is often thought of as being an unstressed measurement but this is not the case as the mercury provides an isostatic compression to the sample before it enters its pore space. Therefore, if it is assumed that the permeability estimated from the traditional MICP corresponds to the permeability measured at a net stress, equivalent to the sample threshold pressure, a better correlation over a wider range is obtained.

A new mercury porosimeter that performs the analysis under constant net stress has been built and tested. The results indicate that for tight gas sandstones the threshold pressure under reservoir conditions are three times higher than those estimated using the traditional high pressure mercury porosimeter which operates under unconfined conditions. While the average for all the rocks tested is over four times higher. These results are significant when calculating both sealing capacities and saturation height functions. We have not yet attempted to use the results to assess whether it is possible to stress correct unconfined MICP data.

ACKNOWLEDGEMENTS

REFERENCES

1. Brown, A.A. "Interpreting permeability from mercury injection capillary pressure data". (2015) AAPG Annual Convention and Exhibition, Denver, Colorado, May 31 – June 3. Search and Discovery Article #41660.
2. Comisky, J.T., Newsham, K.E., Rushing, J.A., and Blasingame, T.A. "A comparative study of capillary-pressure-based empirical models for estimating absolute permeability in tight gas sands". (2007) SPE 110050.
3. Comisky, J.T., Santiago, M., McCollom, B., Buddhala, A. and Newsham, K.E. "Sample size effects on the application of mercury injection capillary pressure

for determining the storage capacity of tight gas and oil shales". (2011) CSUG/ SPE 149432.

4. Katz, A. J. and Thompson A. H. "Quantitative prediction of permeability in porous rock". (1986), *Physical Review Letters B*, **34**, 11, 8179-8181.

5. Katz, A. J. and Thompson A. H. "Prediction of rock electrical conductivity from mercury injection measurements". (1987) *Journal of Geophysical Research B*, **92**, B1, 599-607.

6. Mitchell, P., Sincock, K., and Williams, J. "On the effect of reservoir confining stress on mercury intrusion-derived pore frequency distribution". (2003) Proc. International Symposium of Society of Core Analysts, Paper SCA2003-23.

7. Pittman, E. D. "Relationship of porosity and permeability to various parameters derived from mercury injection-capillary pressure curves for sandstone". (1992) *AAPG Bulletin*, **76**, 191-198.

8. Purcell, W. R. "Capillary pressures-their measurement using mercury and the calculation of permeability therefrom" (1949) *American Institute of Mechanical Engineers, Petroleum Transactions*, February, 39-48. (SPE-949039-G)

9. Shafer, J., and Neasham, J. "Mercury porosimetery protocol for rapid determination of petrophysical and reservoir quality properties". (2000) Proc. International Symposium of Society of Core Analysts, Paper SCA2000-21.

10. Swanson, B. F. "A simple correlation between permeability and mercury capillary pressures". (1981) *Journal of Petroleum Technology*, Dec., 2488-2504.

11. Washburn, E. W. "Note on a method of determining the distribution of pore sizes in a porous material". (1921) *Proc. Nat. Acad. Sci. of the USA*, **7**, 115-116.

CAL-X: AN X-RAY RADIOGRAPHY TOOL FOR HIGH THROUGHPUT COREFLOOD EXPERIMENTATION. APPLICATIONS IN THE EOR CONTEXT.

Souhail Youssef, Matthieu Mascle, Yannick Peysson, Olga Vizika

IFP Energies nouvelles, 1&4 avenue de Bois-Préau, Rueil-Malmaison, France

This paper was prepared for presentation at the International Symposium of the Society of Core Analysts held in Vienna, Austria 28 August - 1 September 2017

ABSTRACT
To speed up coreflood experiments, we have developed a state of the art experimental setup (CAL-X) designed for high throughput coreflood experimentation. The setup is composed of an X-ray radiography facility, a fully instrumented multi-fluid injection platform and a dedicated X-ray transparent core holder. The equipment was designed to handle small samples of 10 mm in diameter and 20 mm in length, and can be operated at up to 150 bar and 150 °C. The X-ray facility consists of a high-power X-ray tube and a high speed-low noise detector allowing real-time radiography acquisition and offering sufficient density resolution to use dopant-free fluids. The injection platform is fully automated and allows the control and monitoring of different parameters (pressure, temperature, flow rate…). 1-D and 2-D saturation profiles are followed in real-time, allowing a precise determination of the recovery curve, reducing thus drastically time-consuming effluent measurements. Using this setup, a typical coreflood experiment can be run in less than a day. To validate the setup, we have run a series of experiments on water-wet sandstone samples to determine capillary desaturation curve, steady-state relative permeabilities and recovery factor for a formulation designed for high temperature conditions (110°C). The results show good repeatability as well as good agreement when compared to standard coreflood experiments. In the recovery factor experiment, during surfactant injection, the formation and displacement of an oil bank was observed, yielding a recovery factor of 92% OOIP.

INTRODUCTION
Demonstrating the viability of a chemical EOR project requires a meticulous and intensive laboratory study that involves complex, time-consuming workflows and optimization processes. These workflows include successive or iterative steps starting from reservoir fluid and rock characterizations followed by surfactant formulation screening and optimization, coreflood validation and simulation, and sensitivity studies [1]. In this context, High Throughput Experimentations (HTE) are necessary to decrease time and cost of laboratory studies [2]. On the chemical

side, formulation design is already performed via an efficient High Throughput Screening (HTS) methodology using a robotic platform. On the petrophysical side, fast coreflood experiments are also needed to measure EOR related petrophysical properties on different rock-facies and evaluate the efficiency of the selected formulations at reservoir conditions.

To develop HTE, three main concepts are used: automation, parallelization and sample size reduction [3]. In the field of core analysis, automation has been developed since the 80's to accelerate workflow [4,5]. A work recently reported [6] describes a fully automated coreflood laboratory based on standard core plugs sizes. With regards to size reduction, miniaturization of coreflood experiments have been also developed recently [7–9]. In these works, the objective was to image pore scale mechanisms and local fluid saturation and not experimental time reduction. Yet, it has allowed to overcome some technical challenges related to core holder miniaturization and physical properties measurement. In the present work, we combined automation and miniaturization to accelerate SCAL measurements. To that purpose we developed a dedicated setup (CAL-X) that allows to measure different properties needed in an EOR workflow like capillary desaturation curve (CDC), relative permeability and recovery factor while reducing by an order of magnitude the time needed to run these experiments.

MATERIAL AND METHODS
Experimental setup
The setup is composed of an X-ray radiography facility, a fully instrumented multi-fluid injection platform and a dedicated X-ray transparent core holder. The X-ray facility consists of a high-power X-ray tube (up to 150 kV and 500 µA) and a high speed-low noise detector allowing real-time radiography acquisition (up to 30 fps) and offering sufficient density resolution to use dopant-free fluids. The different components are embedded in a large X-ray protection cabinet (see Figure 1.a). The core holder was adapted to small samples (mini-plug) of 10 mm in diameter and 20 mm in length, and can be operated at up to 150 bar and 150 °C. The core holder body was made of beryllium to guarantee maximum X-ray transparency and temperature resistance. Each side of the core holder is equipped with three ports (inlet, outlet and pressure tap) as well as a temperature transducer. Figure 1.c shows a possible connection configuration. The injection platform (see Figure 1.b) is equipped with eight pumps and is fully automated allowing the control and monitoring of different parameters (absolute and differential pressure, temperature, flow rate…).

X-ray Radiograph Processing
The radiographs were captured using an energy of 60 kV and current of 300 µA. The use of low voltage allows for a higher contrast between components. The spatial resolution was set to 30 µm. Radiographs were captured each second. Due

to the difference in the X-ray attenuation coefficient of the injected fluid, the X-ray radiograph shows a variation in the gray-scale intensity throughout the sample. This variation can be used to estimate the fluid saturation in specific parts of the rock. The X-ray radiographs at each second are displayed and stored on the monitoring workstation as digital images of 16-bit precision. An image consists of 1800 rows and 1450 columns of pixels. Figure 2 shows a radiograph which emphasizes the sample shape and the basic components of the core holder.
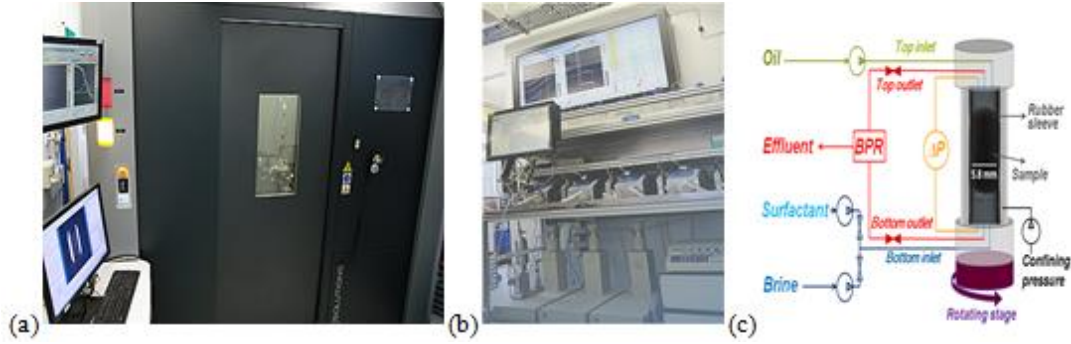

Figure 1 CAL-X setup composed of an X-ray radiography facility (a), a fully instrumented multi-fluid injection platform (b) and a dedicated X-ray transparent core holder (c).

To infer the oil saturation from the radiographs, we use Beer-Lambert's law for multi-material:

$$I = I_o \, e^{\sum_i (-\mu_i X_i)} \qquad\qquad \text{Eq.1}$$

where I and I_0 are respectively transmitted and emitted X-ray intensities, μ_i is the X-ray absorbance of the phase i, and X_i is the length of phase i.

Considering two reference states (100% water saturation and 100% oil saturation), we define I_{water} and I_{oil} as transmitted X-ray intensities:

$$I_{water} = I_o \, e^{-\mu_w X + \alpha} \qquad\qquad \text{Eq.2}$$

$$I_{oil} = I_o \, e^{-\mu_o X + \alpha} \qquad\qquad \text{Eq.3}$$

where μ_w and μ_o are the water and the oil attenuation coefficients, X is the length of the X-ray path in the fluid volume and α is a constant corresponding to the attenuation due to the solid part of the rock and the different components of the cell crossed by the X-ray. If the sample is saturated with oil and water, the transmitted X-ray intensity I_t is governed by the following equation:

$$I_t = I_o \, e^{-(\mu_o X_o + \mu_w X_w) + \alpha} \qquad\qquad \text{Eq.4}$$
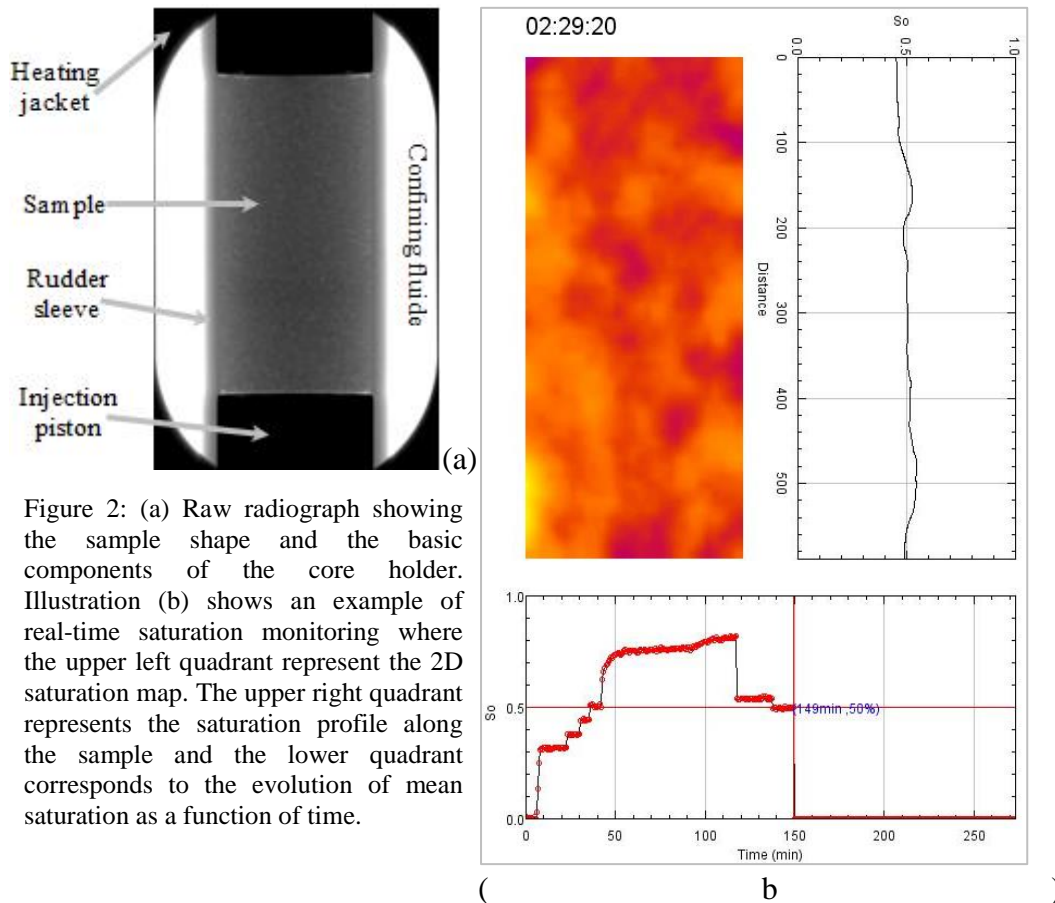
where X_o and X_w are respectively the oil and the water portions in the path of the X-ray. Furthermore, by definition, we obtain the following equation:

$$X_o + X_w = X \qquad \text{Eq.5}$$

The oil saturation S_o can be obtained as follows:

$$\frac{\ln\left(\frac{I_{water}}{I_0}\right) - \ln\left(\frac{I_t}{I_0}\right)}{\ln\left(\frac{I_{water}}{I_0}\right) - \ln\left(\frac{I_{oil}}{I_0}\right)} = \frac{-\mu_w X + \mu_o X_o + \mu_w X_w}{-\mu_w X + \mu_o X} = \frac{X_o}{X} = S_o \qquad \text{Eq.6}$$

The transmitted X-ray intensity is measured by each pixel of the X-ray detector and represented by a proportional gray value. Therefore, Eq.6 can be applied directly to the gray level images to estimate local and average saturations. The results of the image processing are presented as illustrated in Figure 2.b. The upper left quadrants represent the 2D saturation map. The upper right quadrant represents the saturation profile along the sample and the lower quadrant corresponds to the evolution of mean saturation as a function of time. The radiographs are processed instantaneously allowing a real-time monitoring of experiments.

Figure 2: (a) Raw radiograph showing the sample shape and the basic components of the core holder. Illustration (b) shows an example of real-time saturation monitoring where the upper left quadrant represent the 2D saturation map. The upper right quadrant represents the saturation profile along the sample and the lower quadrant corresponds to the evolution of mean saturation as a function of time.

Rock samples

Samples used in this work are water wet outcrop sandstones from different quarries with porosity ranging from 12% to 23% and permeability ranging from 200 mD to 2030 mD (see Table 1). Samples are cored with a diamond core drill with 1 cm internal diameter and cut to a length of 2 cm. Then, they are dried in an oven for at least 48 hours at a temperature of 60 °C.

Table 1 Petrophysical properties of the plugs used in this work

Plug name	Benth_28	Benth_12	Clash_22	GDF_15
Origin	Bentheimer		Clashach	Fontainebleau
Porosity (%)	23%	22%	14%	12%
Permeability (mD)	2030	1350	950	200

APPLICATIONS AND RESULTS

Steady state relative permeability

Relative permeabilities are fundamental properties required to describe an immiscible two-phase flow using Darcy's equations. Relative permeabilities are functions of the saturation and the capillary number at which the immiscible displacement occurs. When neglecting gravity effect, Darcy's equation can be written as:

$$q_i = \frac{K_a k_{ri}(S_i, N_c) S}{\mu_i} * \frac{\Delta P_i}{L} \qquad \text{Eq.7}$$

where q_i is the volumetric flow rate of the phase i (m³/s), K_a is the absolute permeability (m²), k_{ri} is the relative permeability of the phase i, μ_i is the fluid viscosity (Pa.s), S_i the saturation of the phase i, ΔP_i the differential pressure measure in the phase i, between the outlet and the inlet of the plug (Pa), L the length of the plug (m) and S the cross section (m²).

In the case of two phase flow, Steady State Method (SSM) can be used to derive relative permeability. The SSM method involves the injection of both fluids at the inlet of the plug while measuring the differential pressure and the saturation within the core. Eq.7 can then be solved analytically if capillary pressure is neglected. This condition can be assessed when fluids are injected at high flow rate. Yet, negligible capillary effect and laminar flow (i.e Reynolds number less than 10) have to be confirmed. Laminar condition is verified since a linear relation between flow rate and pressure drop is respected in mono-phasic injection. To neglected capillary pressure (Pc=0) we verify that the saturation at steady state condition is

uniform along the sample (see example on Figure 2 (b)). In this case relative permeability can be derived from Eq.7 for each fluid as:

$$\begin{cases} k_{rw}(S_w, N_c) = \dfrac{\mu_w L}{K_a S} * \dfrac{q_w}{\Delta P_w} \\ k_{rnw}(S_w, N_c) = \dfrac{\mu_{nw} L}{K_a S} * \dfrac{q_{nw}}{\Delta P_w} \end{cases} \qquad \text{Eq.8}$$

where indices w and nw refer respectively to wetting and non-wetting fluids. If capillary end effects is observed, simulations must be used to derive the relative permeabilities by data history matching.

The Steady State method is usually considered as one of the most reliable methods to perform relative permeability measurements, but one of its limitations is the time required to conduct such an experiment, ranging from several days to several weeks for classical core-plug sizes. With CAL-X, the size of plugs has been decreased to reduce experimental time by an order of magnitude (i.e. few hours to few days). An example of SSM imbibition relative permeability measurement protocol is presented in Figure 3. The experiment is conducted on a water-wet Bentheimer sandstone at ambient temperature, using 25 bars of confinement pressure and 15 bars of pore pressure. For this experiment we used a 33 g/l NaCl brine and dodecane synthetic oil with respectively a viscosity of 1.07 cP and 1.52 cP. In this example, the sample is first saturated with brine for absolute permeability measurement. Then, the oil is injected at a rate of 1cc/min until steady saturation reached. Next, oil and brine are co-injected at a total flow rate of 1cc/min corresponding to a capillary number of 5 10^{-6}. The saturation S_w was computed from the X-ray imaging, the differential pressure (ΔP_w) was measured and the fluid flow rates were imposed. The relative permeabilities were measured for different saturations, S_w, by varying the fractional flow (f_i) of each phase while maintaining the total flow rate constant and then resolving Eq.8.
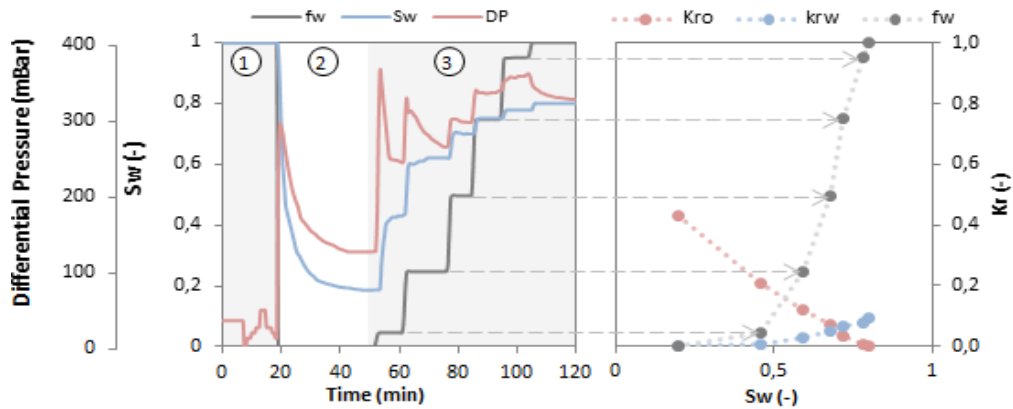

Figure 3 : Example of differential pressure ($\boldsymbol{\Delta P}$), water saturation ($\boldsymbol{S_w}$) and water fractional flow ($\boldsymbol{f_w}$) acquisition for kr measurement using SSM. The 3 steps mentioned on the 1st plot refer to the

experimental protocol. During step 3, $k_{or}(S_w), k_{rw}(S_w)$ are measured for each f_w value, when the system reaches the steady state. The acquisition was conducted on a water-wet Bentheimer sandstone, with $q_{tot}^{inj} = 1\ cc/min$ during step 3.

Left graph of Figure 3 illustrates the parameters measured during the experiment. It shows that the total time needed to run the full injection sequence is few hours. For each fractional flow, steady state is reached in about tens of minutes.

Relative permeabilities illustrated on the right graph of Figure 3 have a typical shape of Relative permeabilities measured on water-wet homogeneous sandstone. To validate the representativeness of the measurements, results are compared to macro-scale experiment. Figure 4 shows a superimposition of relative permeabilities for Benth_12 measured in this work and for a 40 mm in diameter Bentheimer plug documented in [12]. Results show a very good agreement. They demonstrate that for this homogeneous case a mini-plug can be considered to be above the representative elementary volume (REV) for multiphase flow behaviour.
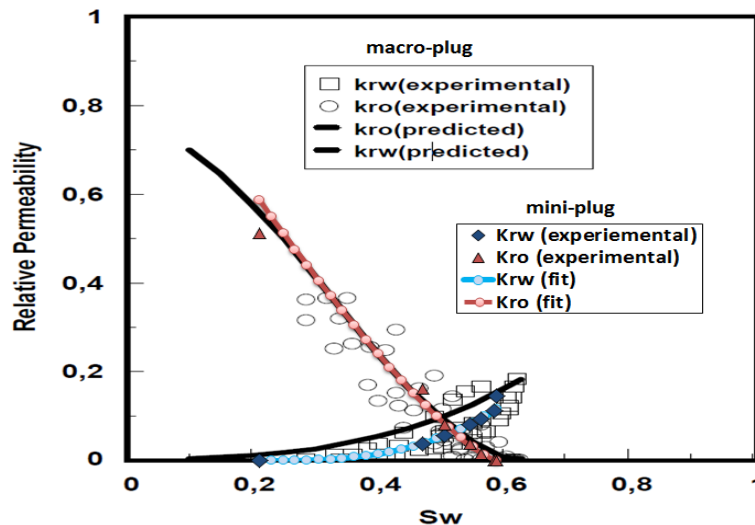

Figure 4: Relative permeability measurements conducted on the mini-plug Benth_12 compared to the ones conducted on a standard macro-plug extracted from the work of Oren et al [12].

Capillary Desaturation Curves (CDC)

The Capillary Desaturation Curve expresses the saturation of the trapped oil in a porous medium (usually expressed as the reduction of the remaining oil in place $S_{or}(N_c)/S_{orw}$) with the increase of the capillary number Nc [10]. Capillary number value is adjusted varying the injection flow rate or fluid/fluid interfacial tension. For example, by adding surfactants in the brine the interfacial tension is decreased leading to an increase of the capillary number.

In a typical CDC measurement workflow, the plug is initially fully saturated with brine. The absolute permeability can be measured at this step. Then the plug is set

to residual water saturation (Swr) by injecting oil (dodecane) from the top of the plug to reduce the impact of gravity on the fluid displacements. Brine is first brought in contact with the plug by leaching the bottom face to perform a spontaneous imbibition and then injected at 0.05 cc/min, to set the plug to residual oil saturation (Sorw). Finally, surfactant solution is injected at increasing flow rates, from 0.005 cc/min to 1 cc/min. The reduction of the interfacial tension and the increase of the injection flow rate contribute to progressively produce the trapped oil. At each step, the corresponding capillary number and the average saturation are calculated. An illustration of saturation monitored during a CDC measurement is given in Figure 5. The CDC is measured using the saturation computed from radiographs. The saturation profile So(z) can be used to correct the measured average saturation from capillary end effects. The time needed to measure a CDC is in the range of hundreds of minutes (see Figure 5). The protocol described above to perform CDC measurements has been applied on various homogenous water-wet rock types previously presented in Table 1.
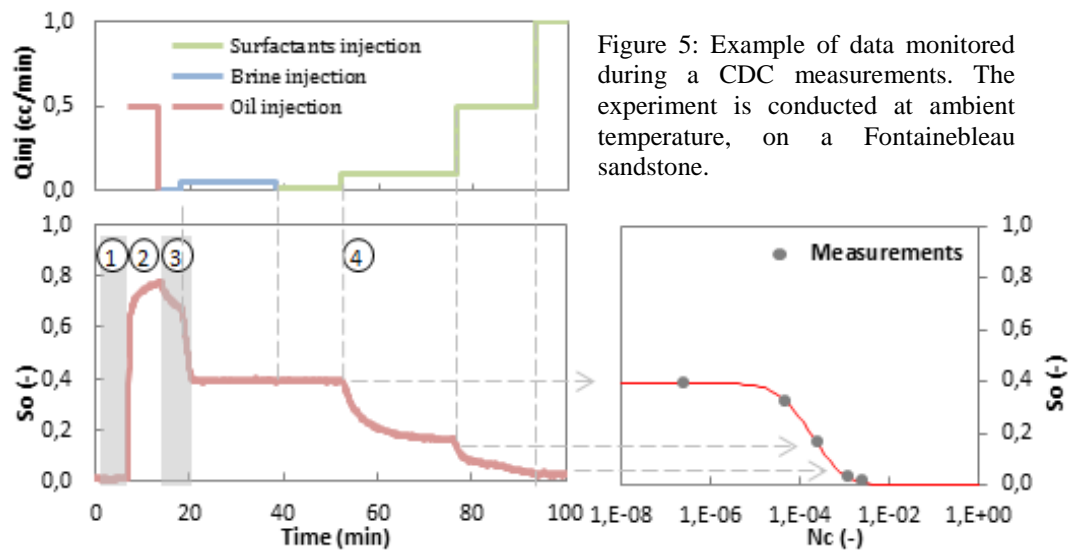

Figure 5: Example of data monitored during a CDC measurements. The experiment is conducted at ambient temperature, on a Fontainebleau sandstone.

The interfacial tensions between the surfactant solutions and oil for each test are listed in Table 2. The experimental CDC presented below are fitted using an analytical solution expressed as follows [11]:

$$\frac{S_{or}(N_c)}{S_{orw}} = \frac{1}{2}\,\text{erfc}\left[a.\ln\left(\frac{N_c}{N_{c0}}\right)\right]$$

Eq.9

where $\text{erfc}(x)$ is the complementary error function, a and N_{c0} are two fitting parameters. The four measured CDC for the different mini-plugs are given in Figure 6 with the analytical fit (solid redline). Results show that all CDC have comparable tendencies with the residual oil starting to be produced for capillary

numbers higher than 10^{-5}, and half of the residual oil produced close to $N_c = 1.3 \ 10^{-4}$.

Reproducible measurements have also been conducted to assess the robustness of the protocol on sample (Benth_12). The results, given in Figure 7 show very good reproducibility of the experimental CDC. To validate the representativeness of the measurements, results are compared to macro-scale experiment. The aim is to demonstrate that neither the reduced size of the mini-plugs used with CAL-X nor the measurement protocol impact the quality of the measurements. A CDC was measured on a 33 mm diameter Bentheimer sample (BH1), more detail on the experiment can be found in [13]. The results show a very good agreement between the CDC measured on mini- and macro-plug (see Figure 7).

Table 2 : The interfacial tension (IFT) is measured between the wetting phase (surfactants formulation) and the non-wetting phase (dodecane). Residual Oil Saturation reached with the brine water flush (Sorw) for the different CDC measurements. The two parameters (Nc0 and a) correspond to the fitting parameters of the analytical CDC expression.

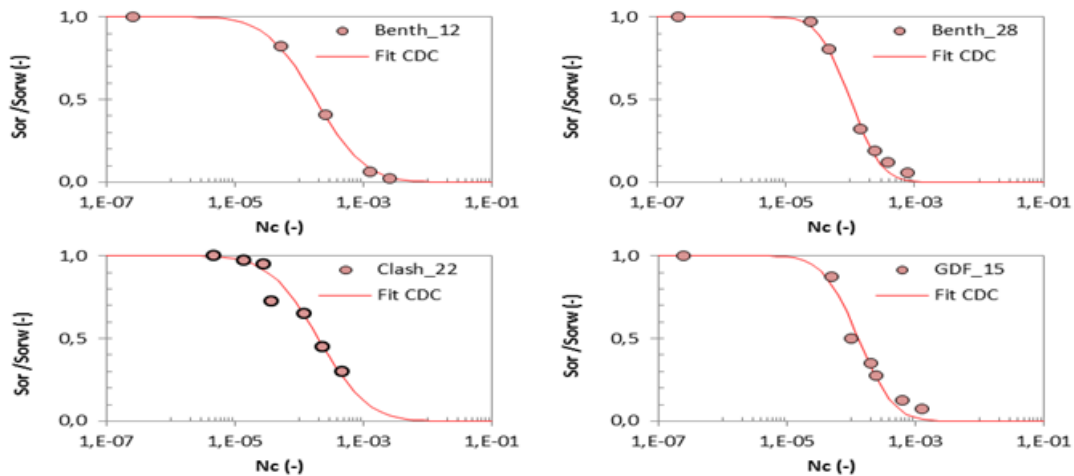|	Benth_28	Benth_12	Clash_22	GDF_15
IFT (mN/m)	0.45	0.10	0.10	0.50
Sorw	0.36	0.4	0.4	0.4
Nc0	$1. \, 10^{-4}$	$1.8 \, 10^{-4}$	$2. \, 10^{-4}$	$1.3 \, 10^{-4}$
a	0.8	0.5	0.5	0.7

Figure 6 : Experimental CDC measured on four rock-types. The residual oil saturation Sorw reached before injecting the surfactants are given in Table 2. The four experimental curves are fitted using Eq 9, the fitting parameters are given in Table 2.
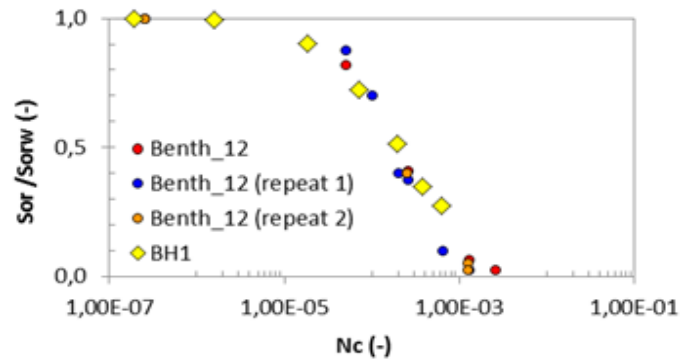
Figure 7 : CDC reproducibility measurements conducted on the mini-plug Benth_12 (circle) compared to a CDC measured on a macro-plug (BH1).

Production curves and Recovery factor (RF)

Production curves help assess the oil recovery kinetics and recovery factor when using enhanced oil recovery techniques, by reproducing the injection sequences of fluids planned in the EOR process. Recovery factor, which evaluates the recoverable part of the original oil in place (OOIP), constitutes a convenient way to compare the efficiency of different injection sequences and chemical products.

In this section, we present the use of the new equipment (CAL-X) to study infinite surfactant slug injection tests at high temperatures. The objective was to check the efficiency of a formulation designed to minimise the interfacial tension between the oil phase (dodecane) and the water phase (a 33 g/l NaCl brine) at 110°C. Experiments were conducted on Benth_28 sample. The injection sequence consisted first of injecting oil in the fully brine saturated sample, from the top, to reach Swi. Then brine is injected from the bottom of the sample until Sorw is reached. At this stage, surfactant formulation is injected from the bottom at a rate of 0.005 cc/min, which corresponds to a linear velocity of 1.6 ft/day.

Figure 8 shows snapshots of 2D saturation maps and saturation profiles taken at different time intervals. The two first profiles, at 32 min and 50 min, show respectively the saturation profile at Swi and Sorw. It can be seen that the capillary end effect observed at Swi is reduced after the brine imbibition resulting in a more uniform saturation profile. Once surfactant reaches the sample, we can see the development of an oil banc traduced by a local increase of the oil saturation. The mean saturation during surfactant injection is reported on Figure 9 as a function of the injected pore volume. We can note that the oil production begins at almost 1.5 PV and that the final oil saturation after 3.3 PV is of 5%, which leads to a recovery factor of OOIP of 92% for an additional oil production of 35%. The small increase in the oil saturation that can be observed at the beginning of surfactant injection (about 5%) is attributed to residual oil trapped at the surface of the sample after waterflood and reintroduced in the sample when surfactant is injected.
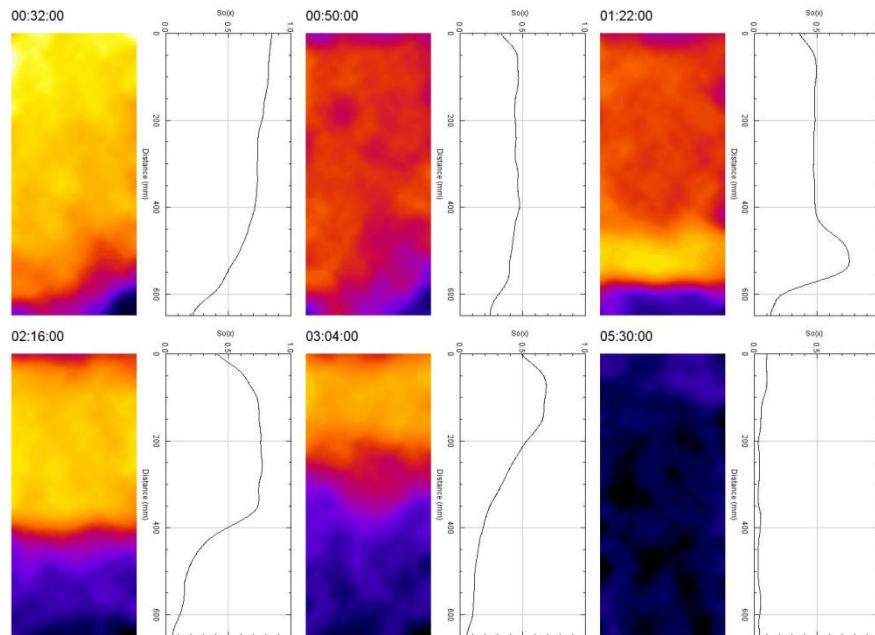
Figure 8 Snapshots of 2D saturation maps and saturation profiles taken at different time intervals for the 110°C experiment (left to right then down left to right). The two first profiles at 32 min and 50 min show respectively saturation profile at Swi and Sorw. Profiles from 1h:22 min to 5h:33 min correspond to surfactant injection at a linear velocity of 1.6 ft/day.
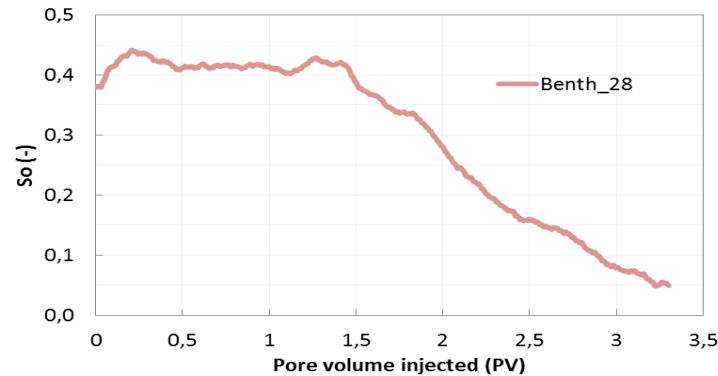

Figure 9 Production curve during the surfactant formulation injection obtained at 110°C. Experiments were conducted on the mini-plug Benth_28.

CONCLUSIONS

In this work, we have presented a new setup and methodologies designed to speed up coreflood experiments by an order of magnitude. The setup (CAL-X) was designed to run experiments on small sample size of 10mm diameter and 20mm length. To validate the setup, we have run a series of experiments on water-wet sandstone samples to determine capillary desaturation curves, steady-state relative permeabilities and recovery factors. Results were satisfactorily compared to standard size core experiments. Integrating this setup in a chemical EOR validation

workflow will not only shorten experimental durations and give quick insights, but also enable exploring a greater parameter space for minimizing uncertainties in the model calibration. Complementary studies are ongoing to extend the workflow to heterogeneous rock type and altered wettability cases.

REFERENCES

[1] Bazin B; Morvan M; Douarche F. and Tabary R. "An Integrated Workflow for Chemical EOR Pilot Design". SPE IOR Symposium, Tulsa, Oklahoma, USA (2010).

[2] Newsam J. M. "High Throughput Experimentation (HTE) Directed to the Discovery, Characterization and Evaluation of Materials". Oil Gas Sci. Technol (2015); 70:437.

[3] Selekman J. A; Qiu J; Tran K; Stevens J; Rosso V; Simmons E. and Xiao Y. et al. "High-Throughput Automation in Chemical Process Development". Annual Review of Chemical and Biomolecular Engineering (2017); 8.

[4] Keelan D. K. "Automated core measurement system for enhanced core data at overburden conditions" Rocky Mountain Regional Meeting of the Society of Petroleum Engineers, Billings, Montana. (1986) SPE-15185.

[5] Maloney D. "X-ray imaging technique simplifies and improves reservoir-condition unsteady-state relative permeability measurements". Petrophysics (2003); 44.

[6] Griffiths D, Gagea B, Couves J, Spearing M, Webb K. "The Advantages of the Application of Automated Work Flows to Coreflood Testing: Introducing the Next Generation of BP's Advanced EOR Testing Capability" International Petroleum Exhibition and Conference, Abu Dhabi, UAE (2015).

[7] Berg S; Ott H; Klapp S. A; Schwing A; Neiteler R; Brussee N. and Makurat A. et al. "Real-time 3D imaging of Haines jumps in porous media flow". Proceedings of the National Academy of Sciences of the United States of America (2013); 110:3755–9.

[8] Youssef S; Deschamps H; Dautriat J; Rosenberg E; Oughanem R; Maire E. and Mokso R; "4D imaging of fluid flow dynamics in natural porous media by ultra-fast X-ray microtomography", Int. Sym. of the Society of Core Analysts Napa Valley, California; (2013).

[9] Youssef S; Bauer D; Bekri S; Rosenberg E. and Vizika O; "Towards a better understanding of Multiphase flow in porous media: 3D In-Situ fluid distribution imaging at the pore scale", Int. Sym. of the Society of Core Analysts, Noordwijk aan Zee, The Netherlands; (2009).

[10] Oughanem R; Youssef S; Bauer D; Peysson Y; Maire E. and Vizika O. "A Multi-Scale Investigation of Pore Structure Impact on the Mobilization of Trapped Oil by Surfactant Injection". Transport in Porous Media (2015); 109:673–92.

[11] Douarche F; Da Veiga S; Feraille M; Enchéry G; Touzani S. and Barsalou R. "Sensitivity analysis and optimization of surfactant-polymer flooding under uncertainties". Oil Gas Sci. Technol. – Rev. IFP Energies nouvelles (2014); 63.

[12] Oren P.-E; Bakke S. and Arntzen O. J. "Extending predictive capabilities to network models". SPE journal (1998); 3:324–36.

[13] Oughanem R; Youssef S; Peysson Y; Bazin B; Maire E. and Vizika O. "Pore-scale to core-scale study of capillary desaturation curves using multi-scale 3D imaging". Int. Sym. of the Society of Core Analysts (2013).

Quick and Simple Porosity Measurement at the Well Site

M.J. Dick[1], D. Green[1], T. Kenney[1], D. Veselinovic[1], J. Tallarita[2], and M.A. Smith[2]
[1]Green Imaging Technologies, Fredericton, NB, Canada
[2]ALS Oil & Gas, Houston, TX, USA

Abstract

Porosity is the single most important petrophysical property. Typical measurements of porosity are done via down hole logging tools and core analysis. These methods either do not generate immediate porosity data while drilling, are complex, expensive, or prone to error. Furthermore, modern drilling produces cuttings that are not suitable for most conventional porosity measurements as they are crushed into very small "grain like" pieces. Nuclear Magnetic Resonance (NMR) measurements overcome the shortcomings of traditional porosity measurements allowing porosity to be determined efficiently and accurately on drill cuttings. In addition, the NMR measurement of the cuttings provides not only the porosity but the pore size distribution as well (assuming the cuttings are not crushed beyond the pore size).

In this work, we propose a simple measurement of porosity using benchtop NMR on modern drill cuttings. The NMR technique has been tested on both shale and sandstone samples to date. For the shale samples, T_2 distributions were used to determine the porosity of core plugs, crushed core plugs and drill cuttings. The results showed excellent agreement between porosities derived for each sample. For the sandstone samples, T_2 distributions were used to determine the porosity of core plugs and drill cuttings which were saturated with water in the lab. The results showed good agreement between the porosity derived for each sample. Some error was observed due to extra water present on the surface of the cuttings. We have completed extensive work in optimizing our experimental technique to minimize this error. This refinement of our experimental technique will be described in this paper. Currently we are furthering our testing by using samples from different fields predominately from unconventional reservoirs.

Introduction

Knowing the porosity of the rocks in an oil field is vital to the profitable development of the field. The porosity is reflective of the amount of oil present in a field. The earlier porosity is known the earlier decisions can be made about how to best retrieve the oil from the field. Typical measurements of porosity are done via down hole logging tools and core analysis. These methods either do not give immediate feedback of the porosity while drilling, are complex, expensive, or prone to error. Nuclear Magnetic Resonance (NMR) is widely used in the oil and gas sector to investigate both the types of fluids present and the porosity of the oil bearing rocks [1]. NMR measurements are well suited to overcome the shortcomings of traditional porosity measurements allowing porosity to be determined efficiently and accurately on drill cuttings.

NMR measurement of the cuttings provides not only the porosity but also the pore size distribution (provided the cuttings are not crushed beyond the pore size). Ignoring diffusion, the relationship between the NMR property T_2 and the pore size is governed by the following equation.

$$\frac{1}{T_2} = \frac{1}{T_{2-Bulk}} + \rho\, \frac{S}{V} \tag{1}$$

Where S/V is the surface to volume ratio of the pore, ρ is the relaxivity parameter and T_2-bulk is the T_2 relaxation time of the fluid. The surface, S, to volume, V, ratio is the pore size and if the other terms are ignored, is directly related to the T_2 through the relaxivity parameter, ρ. Therefore, a plot of volume (retrieved from NMR signal) vs T_2 is the pore size distribution. The pore size distribution offers complimentary information to porosity i.e. what size pores the oil is in and hence how hard it will be to retrieve. The ability of NMR measurements to determine the pore size distribution of drill cuttings makes it superior to traditional measurements done on cuttings which don't provide the pore size distribution. In this paper, we summarize work that has been completed on developing an effective technique to measure the porosity and pore size distributions on drill cuttings.

Experiment

In the initial tests, T_2 NMR acquisition scans for the dry or as received sandstone and shale plugs, crushed plugs and cuttings were recorded using an Oxford Instruments GeoSpec 2-53 rock core analyzer [2]. Data acquisition and data analysis of the T_2 data was achieved via Green Imaging Technology software [3]. Comparison between the T_2 data for the plugs, crushed plugs and cuttings validated the ability of NMR to accurately measure the pore size distributions of drill cuttings.

Next the ability of NMR to accurately determine the porosity of cuttings was tested by, again, comparing data derived from plugs, crushed plugs and cuttings. The porosity of the cuttings and crushed plug were determined using the following procedure.

1. Run an NMR T_2 scan on a vial filled to a pre-determined level with the saturating fluid to measure the total volume, V_{total}.

2. All the samples were vacuum saturated with brine (2% KCl in water) for approximately an hour.

3. The samples were then removed from the brine and their pore volumes and T_2 distributions were retrieved.

For the core plugs this is the end of the procedure. The pore volume retrieved along with the bulk volume is used to determine the porosity of the plug. For the cuttings and crushed core plugs, pore volumes retrieved from the NMR data corresponded to the volume of the cuttings ($V_{cuttings}$). This data was used in the remainder of the procedure to determine the porosity of the cuttings and crushed plugs. In order to capture any possible residual bulk water signal, the following NMR parameters were employed; Tau was set at 100μs, recycle delay was 28,125ms and T_2 max was 3,750ms.

4. Place the saturated cuttings or crushed core plug into the vial from Step #1 and remove any fluid above the pre-determined level. Run a T_2 scan to measure the volume of the vial's contents, $V_{cuttings+fluid}$.

5. Calculate the porosity of the cuttings using the equation:

$$Porosity = \frac{Pore\ volume\ of\ cuttings}{Bulk\ volume\ of\ cuttings} = \frac{V_{cuttings}}{V_{total} - V_{cuttings+fluid} + V_{cuttings}} \qquad (2)$$

This procedure is straightforward and easy to implement. However, it was found to overestimate the porosity of the cuttings and crushed plugs due water stuck to the surface of the cuttings. This water has NMR signal and as a result $V_{cuttings}$ is often inflated in the NMR data leading to a higher than expected porosity value. The majority of the work summarized in this paper has centered on deriving an optimal technique for removing this surface water without compromising the water in the pores of the cuttings. These efforts will be described in the following section.

Results
Pore Size Distribution Of As Received Samples:

Figure 1 shows a comparison of the pore size distribution for a core plug (green trace), a crushed core plug (blue trace) and cuttings (red trace). All samples came from the same shale formation and were tested in their as received or dry state. Each sample had the same pore size distribution with a peak near a relaxation time of 0.2 ms. This relaxation time is typical of shale samples. The excellent agreement between the pore size distribution of each sample indicated that pore size distribution and hence the porosity of samples is invariant from core plug to cuttings. Several shale samples were tested in this manner and all showed good agreement of their pore size distributions for core plugs, crushed core plugs and cuttings.

The pore size distribution for core plugs, crushed core plugs and cuttings of several sandstone samples were also compared. They also showed good agreement of the retrieved pore size distributions. The only difference between shale and sandstone was that if the sandstone cuttings were crushed to a size smaller than the typical pore size then the pore size information derived from the cuttings would be compromised. This is not the case for shales which have very small pores making it unlikely that the cuttings would ever be crushed smaller than the typical pore size.

Pore Volume Retrieval Of Saturated Sandstone Samples:

Figure 2 compares the pore size distribution for a plug (blue trace) and a crushed plug (red trace) taken from the same sandstone formation. The porosity of the crushed plug was determined using the procedure outlined in the last section. The area under each curve is the cumulative porosity for each sample. If all else is equal, the cumulative porosity for each sample should be very similar as the samples were derived from the same formation. From the figure, it is clear that the porosity derived from the crushed core plug is higher

than that derived from the core plug. This is due to extra NMR signal from water stuck to the surface of the crushed samples.

This becomes more obvious when the pore size distributions in Figure 3 are examined. In this case, the water on the exterior of the crushed plug has a longer T_2 relaxation time than the water in the pores. This results in a shoulder present on the peak of the porosity distribution for the crushed core plug (red trace) and yields a higher cumulative porosity as compared to the core plug (blue trace). Table 1 summarizes the difference between porosities derived from NMR data for core plugs vs. crushed core plugs for several sandstone samples tested. In each case the porosity derived from the crushed plug overestimates the porosity by between 2.4 and 6.8 porosity units.

Pore Volume Retrieval Of Drill Cuttings:

The overarching goal of this work has been to determine a quick, efficient and effective method of determining the porosity characteristics of cuttings such that this process can be performed on-site, while drilling. A set of cuttings was provided to us by ALS from one of their drill sites for refinement of our procedure. This was meant to be a blind study and ALS provided us no information on the type rock the cuttings originated from. The conventional method of removing excess liquid by means of a dampened paper towel (API 5.2.4.6.2 [4]) was not viable in this case due to the delicate and fragile nature of the cuttings in question. So instead, the procedure outlined in the Experimental section was modified as follows; steps one and two were followed as described, step three was skipped and finally step four was also followed as described. Once $V_{cuttings+fluid}$ was determined, the brine solution was displaced from around the ALS cuttings by means of introducing a more dense, NMR invisible, fluid, namely fluorinert (FC-40). After the FC-40 was introduced the water, now floating on top of the emulsion, was siphoned off by pipette; at this stage $V_{cuttings}$ could be established by performing a T_2 NMR scan.

However, as with the original procedure, the $V_{cuttings}$ T_2 NMR scan provided an erroneously high volume value for the cuttings; giving porosity values of 55% and higher, which exceeds the generally accepted sandstone porosity range of 10-40% [5], to say nothing of shale. It was hypothesized at this point, that the spurious signal seen in the $V_{cuttings}$ scans was due to contamination of the cuttings caused by the drilling mud ALS used for boring; thus, ALS was consulted and new cuttings, cleaned per their standard Soxhlet based procedure, were provided. However, after repeating the above described procedure to derive V_{total}, $V_{cuttings+fluid}$ and $V_{cuttings}$, the average porosity of the three retested samples was still 54%. Due to there being no significant impact on the calculated porosity figures after cleaning the cuttings it was then hypothesized that the FC-40 was not displacing all of the brine. As a result, the new experimental procedure was still subject to surface water contamination and hence artificially inflating the $V_{cuttings}$ value, leading to an overestimation of the cuttings' true porosity.

Development Of A Technique To Remove Surface Water From Crushed Samples:

As a result of the failure of our experimental procedures to accurately predict the porosity of both crushed core plugs and drill cuttings, it was decided that a more controlled development of a technique to remove surface water was needed. A sandstone plug with known parameters, NMR peak, pore volume and porosity, was selected. A slice of this plug, approximately 0.5cm in length, was removed from the main body. Both the plug and the slice of the plug were then immersed in methanol and cleaned using the Dean-Stark cleaning procedure. After the methanol cleaning, the plug and slice were transferred to toluene for removal of possible oil content, again, via the Dean-Stark cleaning procedure. After cleaning was completed, the slice was pulverized into pieces 1 to 3 mm in diameter. The porosity of the plug was then determined using the pore volume measured by NMR and the bulk volume. This porosity would act as the standard all further tests on the pulverized pieces would be compared against.

The initial test on the crushed plug was to employ the procedure outlined in the last section on the crushed pieces. The left most bar in Figure 4 shows the percent difference between the porosity retrieved from the crushed plug with the porosity of the plug itself. The 97% difference between the two porosities was a clear indication that the technique of FC-40 displacement of surface water did not work effectively.

To further understand how to best eliminate surface water from the crushed plug pieces, six experimental assay groups were tested. They are as follows; screening or size differentiation, D_2O washing, variable centrifugal speed, surfactant infused fluorinert, $CuSO_4$ doped H_2O and sonication. These methods were devised to eliminate the persistent surface or bulk water signal in the $V_{cuttings}$ derived from NMR analysis. For each assay, the original procedure outlined above was followed to generate, clean and saturate the crushed plug pieces. A comparison of the porosity derived from each procedure with the known porosity of the standard core plug is shown in Figure 4.

The screening assay underwent the same procedure as the original cuttings, however, immediately after pulverization of the plug slice, the cuttings were poured over a wire screen with openings of 1.45 mm. This yielded a percent difference in the calculated porosity of 90%.

The D_2O washing assay followed the original procedure to generate, clean and saturate the crushed plug pieces. The difference in the D_2O washing assay arose after the $V_{brine+cuttings}$ scan was completed. The brine surrounding the cuttings was removed, as much as possible, by pipette. Afterwards, instead of immediately introducing FC-40 to displace the brine, 5ml of D_2O was first mixed in with the remaining brine. It was thought that the D_2O would mix with any remaining surface water on the crushed core pieces so that any water that remained bound to the cuttings by surface tension would be NMR invisible. After the D_2O was mixed with the brine, FC-40 was introduced to displace and remove the D_2O to prevent it from infiltrating the pore spaces of the cuttings. A variation on this method, D_2O rinsing, simply used the 1.45mm screen to hold the cuttings while 5ml of D_2O was poured over them instead of introducing the D_2O directly into the vial. According to Figure 4, the percent difference for these two methods were 38% for the D_2O washing and 20% for the D_2O rinsing.

The surfactant assay followed the original procedure but the FC-40 was mixed with a surfactant, SDS, before being introduced to the vial. It was thought that this might aid in the mixing of the existing brine and FC-40 such that it would encourage the removal of the cuttings' surface water. This yielded a percent difference in the calculated porosity of 96%.

The $CuSO_4$ doped H_2O assay was identical in procedure to the original method but, before the introduction of FC-40, the brine present in the vial was removed via pipette and doped H_2O was then mixed in with the remaining brine in the vial. It was hoped that the doped H_2O would mix enough with the surface bound water on the cuttings such that it would separate the surface water signal from that of the water in the pores of the crushed pieces, at which point it could be easily and definitively subtracted. The concentration of $CuSO_4$ used was approximately 260g/L. This yielded a percent difference in the calculated porosity of 76%.

The next tested method was sonication. A Branson 3800 sonicator was filled with water and used to vigorously vibrate a partially immersed vial with the crushed core pieces and FC-40 in it. It was thought that such high frequency vibrations would remove any brine still clinging to the outside of the cuttings; the sonication lasted a total of 30 minutes. This yielded a percent difference in the calculated porosity of 64%.

The final methods tested involved the use of a centrifuge. The variable centrifuge speed method followed the original method. However, after the introduction of FC-40 to the vial, the immersed samples were spun at a range of centrifuge speeds. This centrifugal assay began at 100 RPM and increased in speed up to 7500 RPM with T_2 NMR scans ($V_{cuttings}$) being taken after each speed, each speed step lasted for 15 minutes. Figure 5 shows the detected volume at each centrifuge speed. From the figure, a clear drop in the detected volume is seen between 500 and 600 rpm and between 1000 and 1100 rpm. The T_2 NMR scans taken at these speeds show significant reduction to the long T_2 components. We interpret this reduction to be water leaving the surface of the crushed pieces. If the $V_{cuttings}$ is taken as the detected volume at 1100 rpm then the percent difference is 9.4% between the calculated porosity and known porosity. We interpret any further decrease in detected volume beyond 1100 rpm to be due to water leaving the pore volume due to the ever-increasing centrifugal force. This is further confirmed by the T_2 NMR scans at these speeds which show any further reduction in detected volume coming from the shorter T_2 components corresponding to water in the pores.

Another experimental assay involving centrifugation was time varied centrifugation. Based on the results from the variable centrifuge speed method, 1100 rpm was selected as the centrifuge speed which captured most of the crushed pieces surface water loss. The pieces were then spun at 1100 rpm for varying amounts of time. The detected volume was then measured via T_2 NMR scans after each spin time. After 36 minutes of centrifugation the detected volume yielded a porosity within 4 % of the expected porosity.

To determine the repeatability of the centrifugation technique, four samples of crushed pieces were processed using centrifugation at 1100 rpm for 35 mins. The retrieved volumes after centrifugation all yielded porosities within 3% of the expected porosity.

Testing of the centrifugation technique using ALS cuttings

Once a reliable method for determining the porosity of crushed pieces was determined, our investigation turned back to the drill cuttings provided by ALS Oil & Gas. These cuttings were processed using the centrifugation technique described in the last section with centrifugation taking place for 35 min at 1100 rpm. Unfortunately, the porosities retrieved after centrifugation were still higher than expected for a reservoir rock. However, the T_2 spectra recorded after centrifugation showed no sign of surface water indicating that the extra porosity observed is of another origin. As mentioned above, we have investigated the possibility that the cuttings have been contaminated by drilling mud yielding higher than expected porosities. Cleaning and drying the cuttings has not yet yielded a reasonable porosity. Another possibility is that the cuttings have been crushed beyond the assumed pore size of the rocks (the actual pore size for these samples is not known) rendering NMR analysis ineffective. Investigations continue into retrieving an accurate porosity of the ALS cuttings.

Conclusion

A method has been presented for using NMR to determine the porosity of crushed rock samples. An intensive investigation has gone into first showing that crushing or cutting rock samples does not compromise their pore networks. As a result, NMR remains a feasible way of determining the porosity of crushed rock samples. Next an extensive investigation into determining the best method to accurately determine the porosity of crushed samples has been carried out. It was discovered that during water saturation of the crushed samples, their surfaces become contaminated with water. Removing this water without removing water in the sample's pore network has proven to be difficult. A procedure involving centrifuging the samples was developed and seems to be effective in eliminating the unwanted surface water without eliminating the water in the pores. When the centrifugation procedure was carried out on drill cuttings provided by ALS Oil & Gas, the porosities derived were too high. Work continues on determining why our experimental technique was not effective on the ALS cuttings.

References

1. Coates,G.R., Xiao, L., and Prammer, M.G., *NMR Logging. Principles & Applications*, Halliburton Energy Services, Houston, 1999.
2. Geo-Spec 2-53 User Manual, Version 1.8, Oxford Instruments.
3. GIT Systems and LithoMetrix User Manual, Revision 1.9, Green Imaging Technologies.
4. American Petroleum Institute, *Recommended Practices for Core Analysis*, API Publications, Washington, D.C., (1998), p. 5-7.
5. Pittman, E. D., *Porosity diagenesis and productive capability of sandstone reservoirs*, (1979).

Tables and Figures:

Sandstone	A	B	C	D
Core Plug	16.7	14.1	16.0	15.2
Crushed Core Plug	23.2	16.3	18.4	22.0

Table 1: NMR porosities for core plugs vs. crushed core plugs
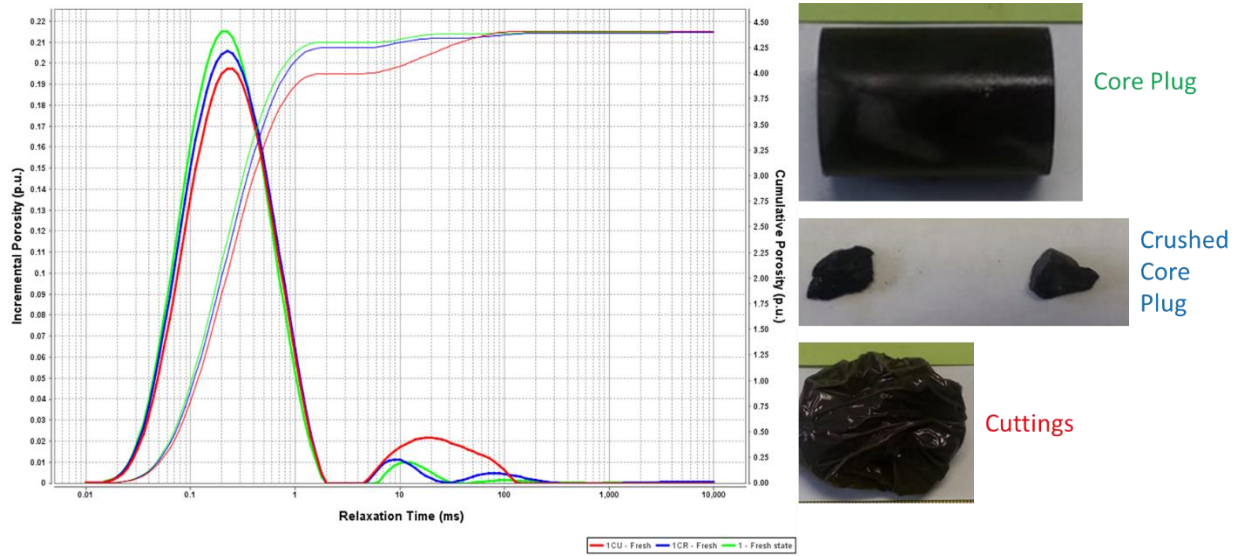

Figure 1: Comparison of the pore size distribution for a shale core plug (green trace), a crushed core plug (blue trace) and cuttings (red trace).
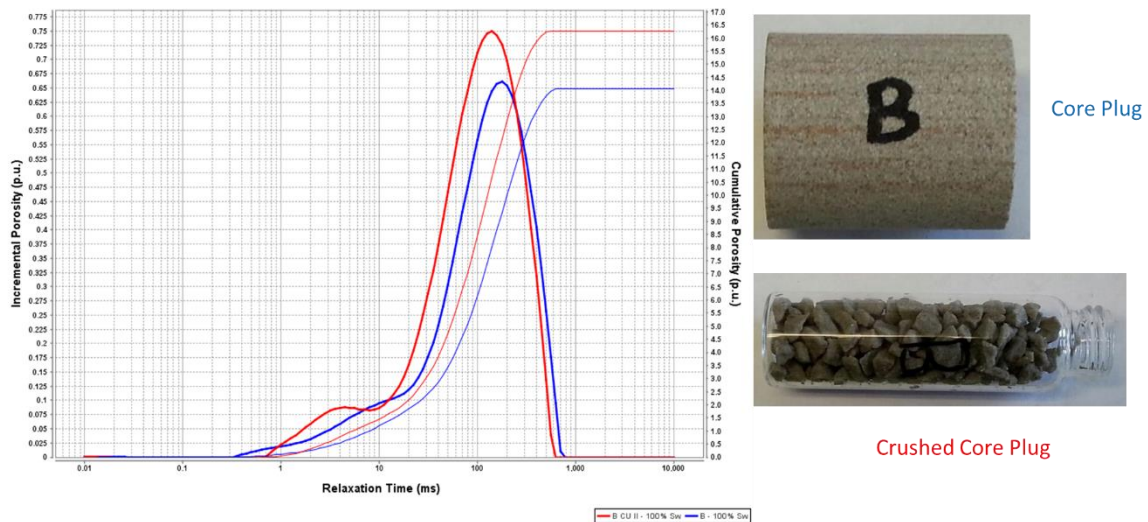

Figure 2: Comparison of the pore size distribution for a sandstone core plug (blue trace) and a crushed core plug (red trace).
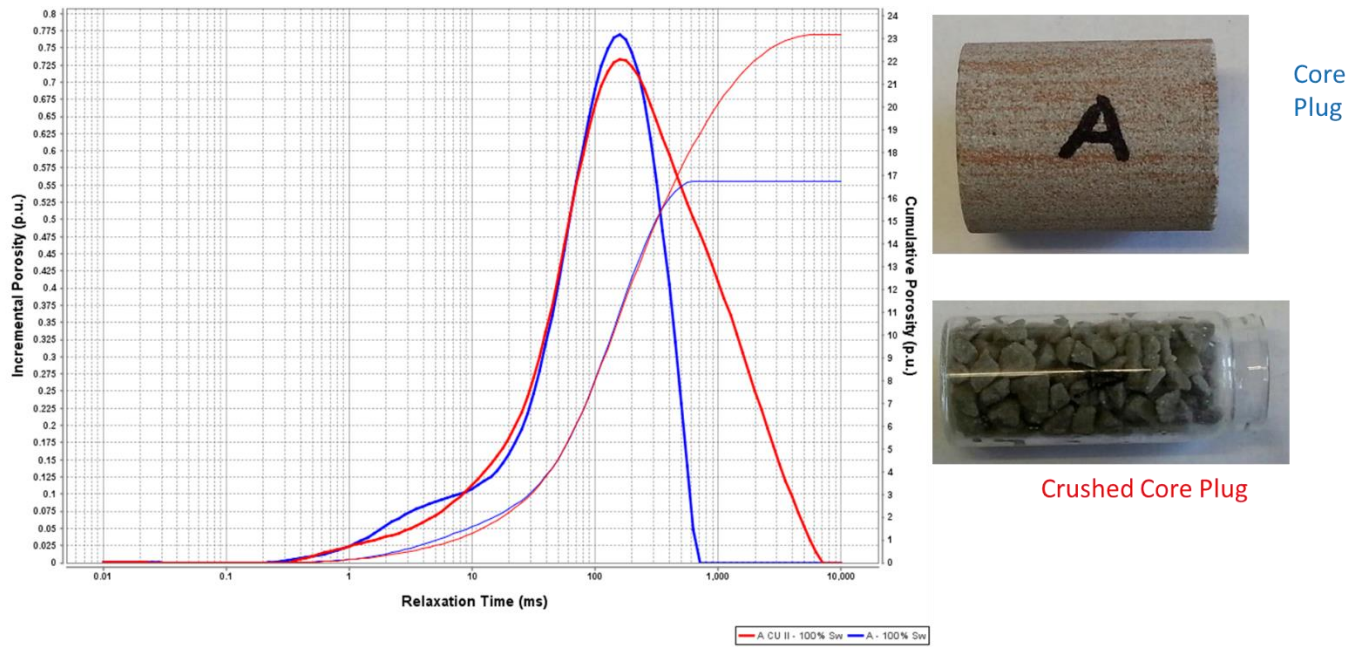
Figure 3: Comparison of the pore size distribution for a sandstone core plug (blue trace) and a crushed core plug (red trace).
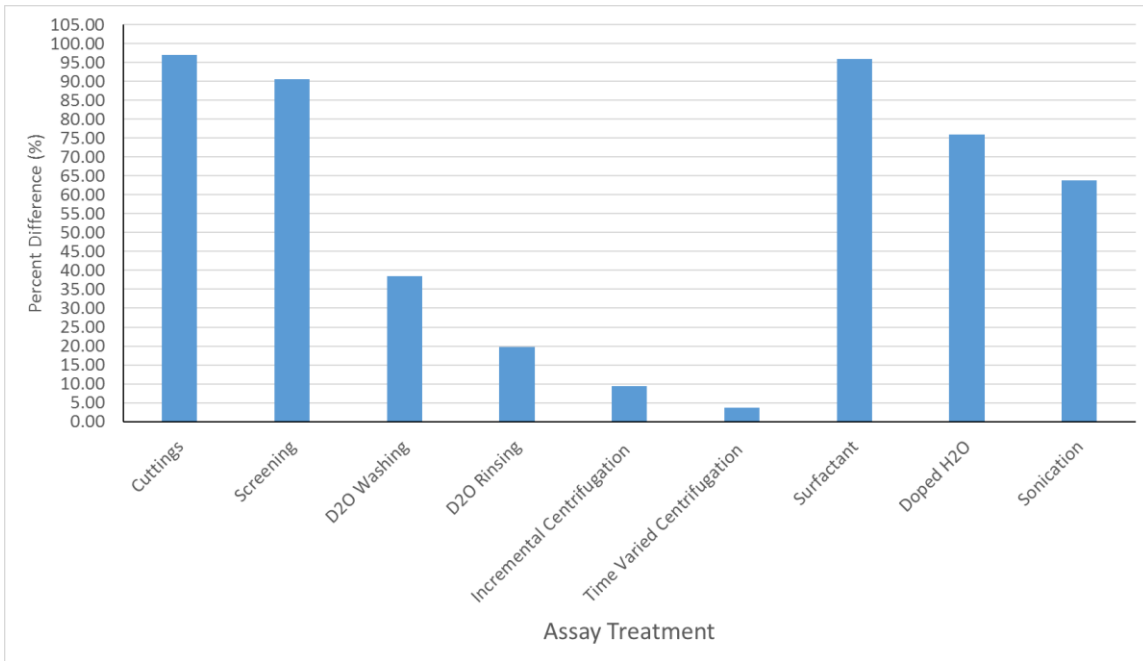

Figure 4: Bar graph comparison of the porosity determined for each procedure derived to eliminate the persistent surface water with the known porosity of the standard core plug
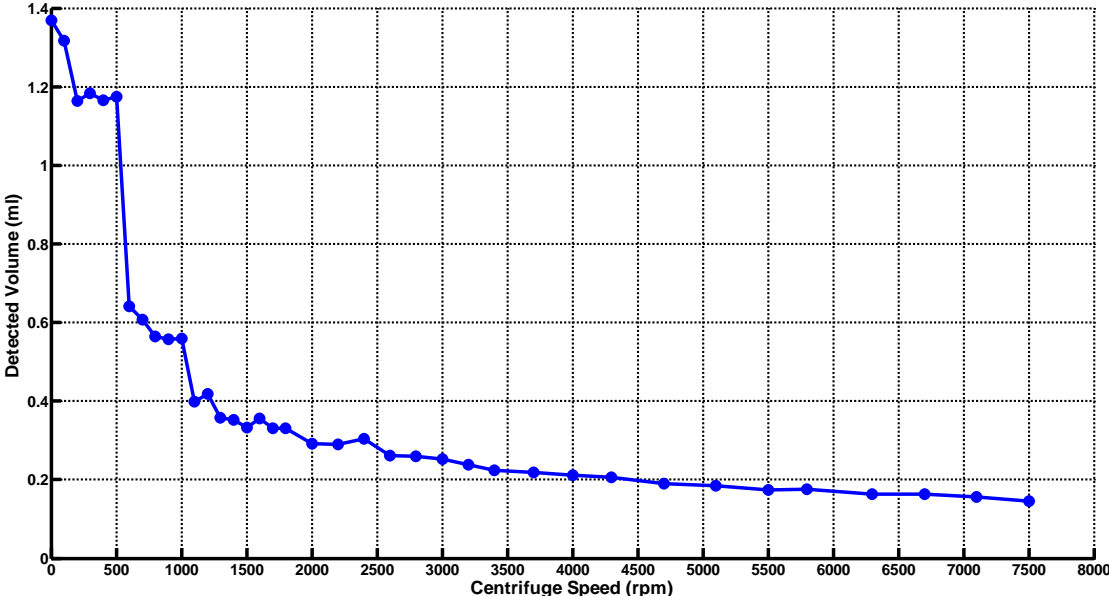
Figure 5: Detected volume in crushed sandstone pieces as a function of centrifuge speed

USING DIGITAL ROCK TECHNOLOGY TO QUALITY CONTROL AND REDUCE UNCERTAINTY IN RELATIVE PERMEABILITY MEASUREMENTS

Josephina Schembre-McCabe and Jairam Kamath
Chevron Energy Technology Company

This paper was prepared for presentation at the International Symposium of the Society of Core Analysts held in Vienna, Austria, 27 August – 1 September 2017

ABSTRACT

Digital Rock Technology (DRT) has experienced tremendous progress in the last decade, with an increasing number of companies providing imaging hardware, modeling software and digital core analysis services. While prediction remains the most discussed application of DRT, this paper discusses its use to quality control water displacing oil relative permeability (k_r) experimental measurements. The k_r data was collected from three wells over a span of seven years, and it showed a very large spread. To identify potential outliers, we performed micro-CT imaging on six samples that were selected based on similarity in rock properties but differences in measured relative permeability behavior. The three-phase segmentation process was guided by measured values of porosity and clay. Consistency checks verified that we could reproduce permeability, drainage capillary pressure, and gas oil relative permeability. Water displacing oil relative permeability was then calculated using pore network models for water-wet and oil-wet conditions, and used to establish a maximum range for each sample. This range was instrumental in identifying suspicious behavior, and reducing uncertainty in recovery predictions.

INTRODUCTION

DRT based prediction of primary drainage and imbibition water-oil relative permeability can be in good agreement with experimental data if the pore structure, connectivity, and wettability of the porous media is captured accurately [1,2,3,1,2,3,4]. However, accurate characterization of wettability inputs such as contact angles and distribution of oil-wet surfaces is a challenge [8,9]. In this work, we use wettability measurements only as a guide, and focus on comparing experimental results with pore network simulations of strongly water-wet and oil-wet relative permeability behavior. We expect these simulations to be reasonably accurate [10,11].

RELATIVE PERMEABILITY AND WETTABILITY DATA

Water displacing oil Unsteady State (USS) relative permeability data was collected on three wells over a seven-year period. The data was fitted using a power law model, and Figure 1 displays the normalized relative permeability curves. The same testing protocols (reservoir temperature, preserved, unsteady state) were used over the years, but the data showed a very large variation with remaining oil saturation (SO) from fractional flow

calculation ranging from 30 to 65% OIP after 1 pore volume injected (PVI). Fractional flow is calculated assuming water-oil viscosity ratio of 0.13. The objective of this work was to understand the reasons for this large variability and to identify potential outliers.
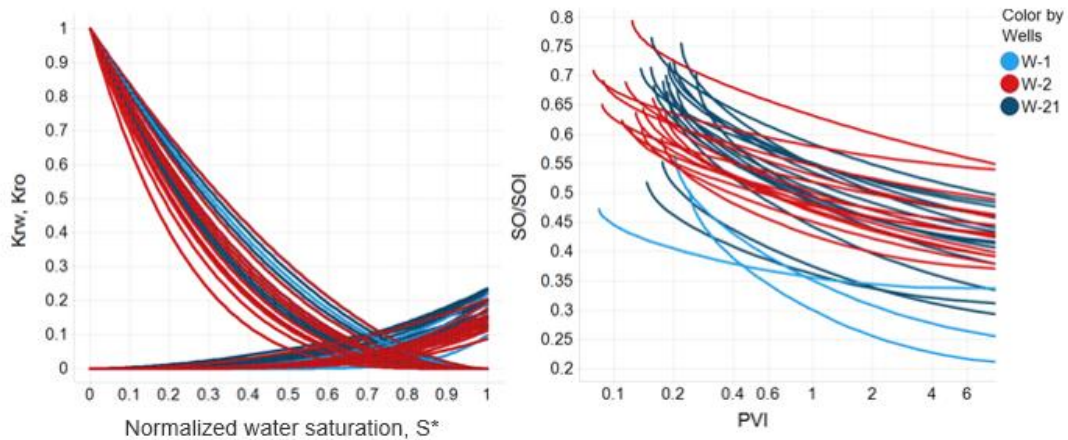

Figure 1: Imbibition Water-Oil Relative Permeability (Left) and So / Soi from fractional flow calculations (Right).

Figure 2 displays Amott and USBM index for samples in wells W-1 and W-2, in which measurements (reservoir temperature, preserved) were performed in a combined sequence on the neighboring plugs. Marked symbols indicates samples that are close to those we analyzed in this study. This plot is also useful to understand the distribution of oil-wet surfaces – the line [12] for Fractional Wet (randomly distributed water-wet and oil-wet) is shown for reference.
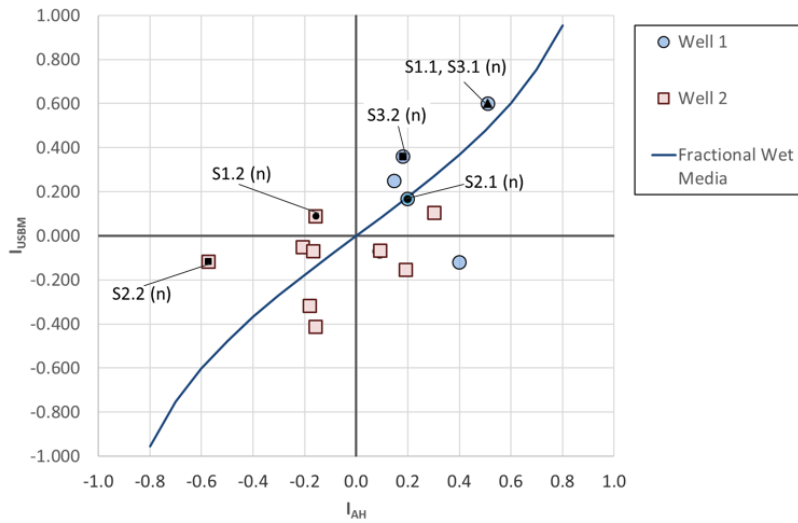
Figure 2: Amott and USBM indices for samples from well 1 and 2. Marked symbols indicate samples that were close to those analyzed in this study – well 1 (samples 1.1,2.1,3.1and 3.2); well 2 (samples 1.2 and 2.2).

WORKFLOW

The workflow consists of five stages:

- Selection of Samples
- Micro-CT and Segmentation
- Pore Network Simulation - Consistency Checks
- Comparison of Calculations for Water Wet and Oil Wet Scenarios with Measured Data
- Uncertainty Reduction

Selection of Samples

Table 1 shows the 3 sample groups used in this study. Each group contains two samples that have similar porosity and permeability (**Figure 3**) and pore throat size distributions (**Figure 4**).

Table 1: Properties of samples used in the analysis

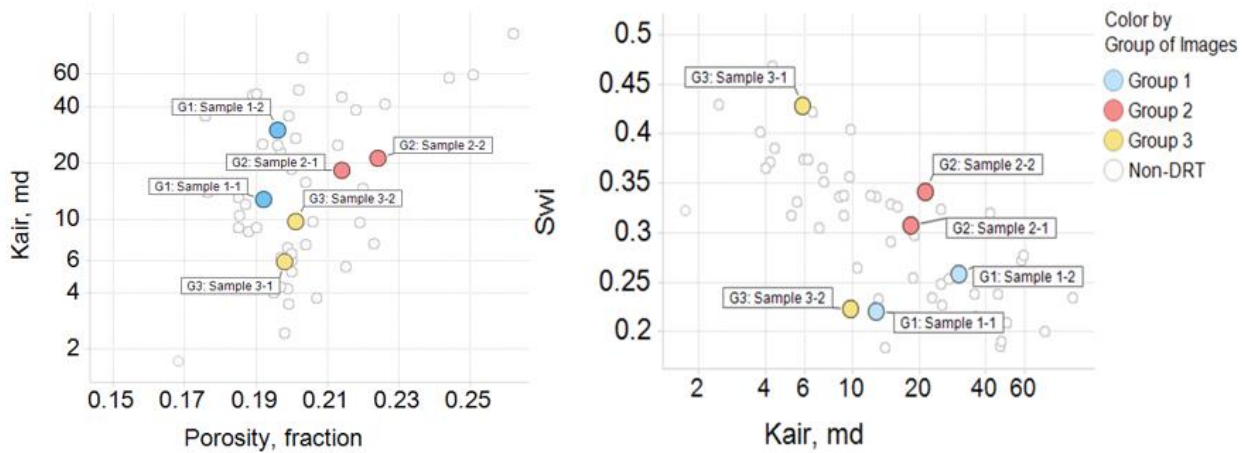| Group	Sample	Well	Formation	Porosity	Permeability	Clay Cont (total)
1	1-1	W-1	F2	20	19	16
	1-2	W-2	F2	20	25	14
2	2-1	W-1	F1	21	18	17
	2-2	W-2	F1	22	16	22
3	3-1	W-1	F1	20	6	23
	3-2	W-1	F1	20	10	23

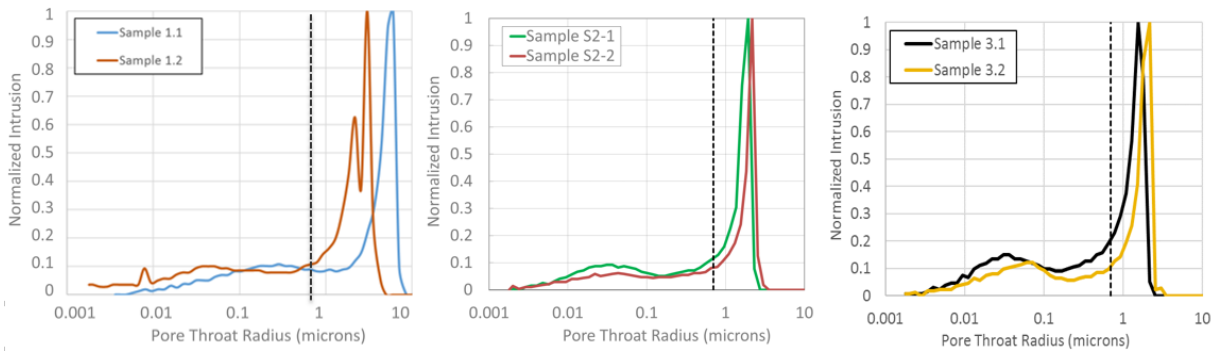**Figure 3: Groups of Samples selected for the study**

Figure 4: Pore Throat Size Distribution for selected samples, dashed lines indicate voxel size for reference

The relative permeability data and corresponding remaining oil saturation, ROS are in figures 5-7. Similar samples can exhibit significantly differing behavior.
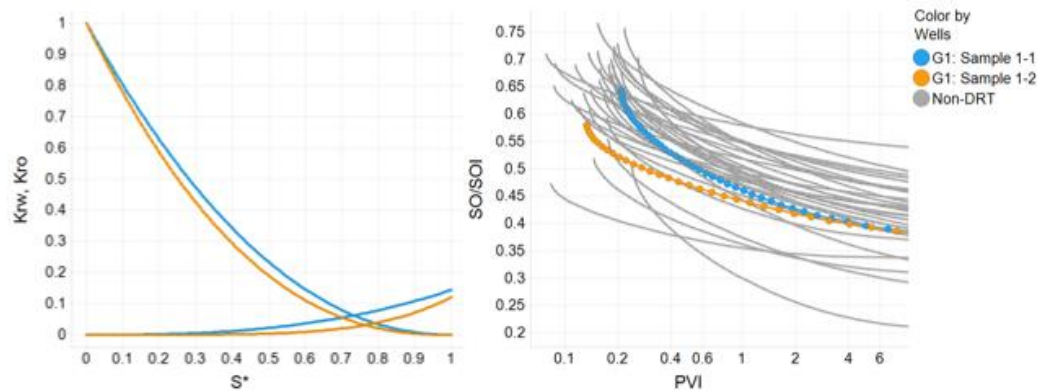

Figure 5: Group 1 - Relative Permeability (Left) and ROS from fractional flow calculations (Right)
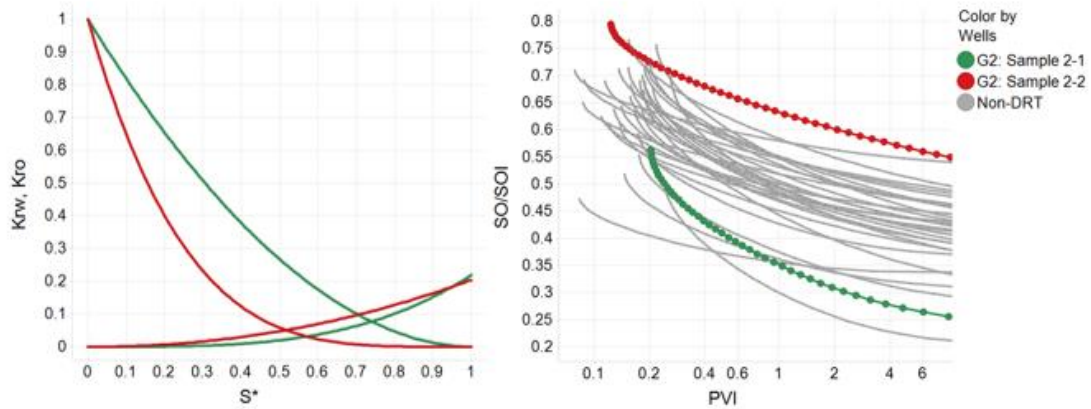
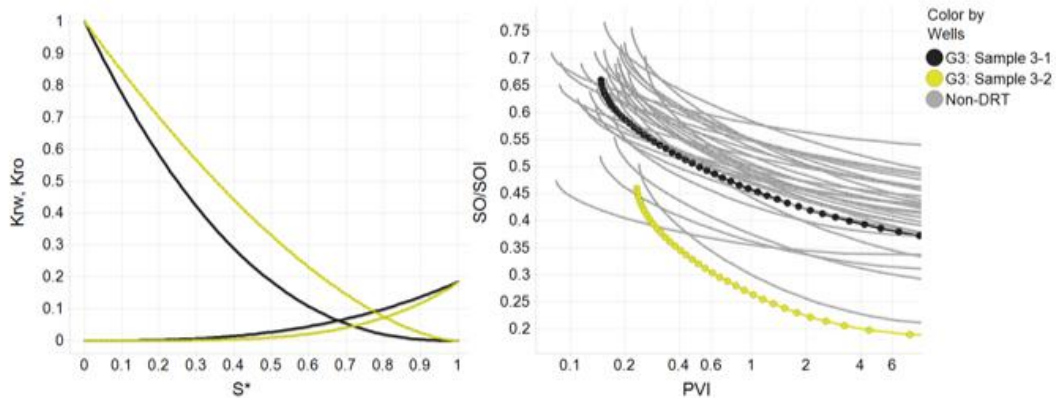**Figure 6: Group 2 - Relative Permeability (Left) and ROS from fractional flow calculations (Right)**

Figure 7: Group 3 - Relative Permeability (Left) and ROS from fractional flow calculations (Right)

Micro-CT and Segmentation

Micro-CT 3D images at 0.7 μm voxel size were obtained on samples of 3mm diameter using X-Radia VersaXRM-500, Figure 8 shows a slide of 3D Micro-CT before segmentation. Due to the amount of clay and their distribution, the segmentation process was guided by values of porosity (resolvable and total) and clay estimated from other laboratory measurements (PKS, MICP, QXRD, 2D QEMSCAN® (2μm/pixel) to narrow the uncertainty in the segmentation process [13, 14]. We used an in-house enhanced histogram thresholding method to perform segmentation. This partitioning yields at least 3 regions -- pore phase, a sub-resolution-porosity, and a solid phase.
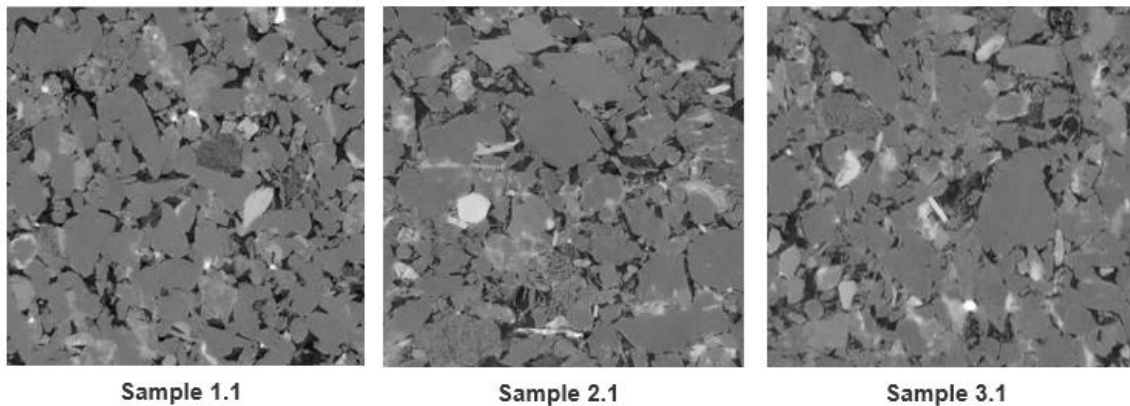
Sample 1.1   Sample 2.1   Sample 3.1

Figure 8: Two-dimensional section of Micro-CT (μm voxel size) scans for sample 1.1, 2.1 and 3.1. Voxel resolution is 0.7 μm.

Pore Network Simulation - Consistency Checks

Once the segmentation was completed, we performed consistency checks for absolute permeability, drainage capillary pressure, and gas-oil relative permeability using REV sub-volumes (800^3 pixels) to test the pore network representativeness of the samples. We used commercial software (e-core) [10] to extract the pore network and perform numerical simulations.

We show one example of the consistency checks performed in each of these samples using results from sample 1.1. **Figure 9 -left** reveals that computed permeability agrees well with measurements on sample 1.1. **Figure 9-right** compares the drainage capillary pressure (MICP) of sample 1.1 and pore network simulation.
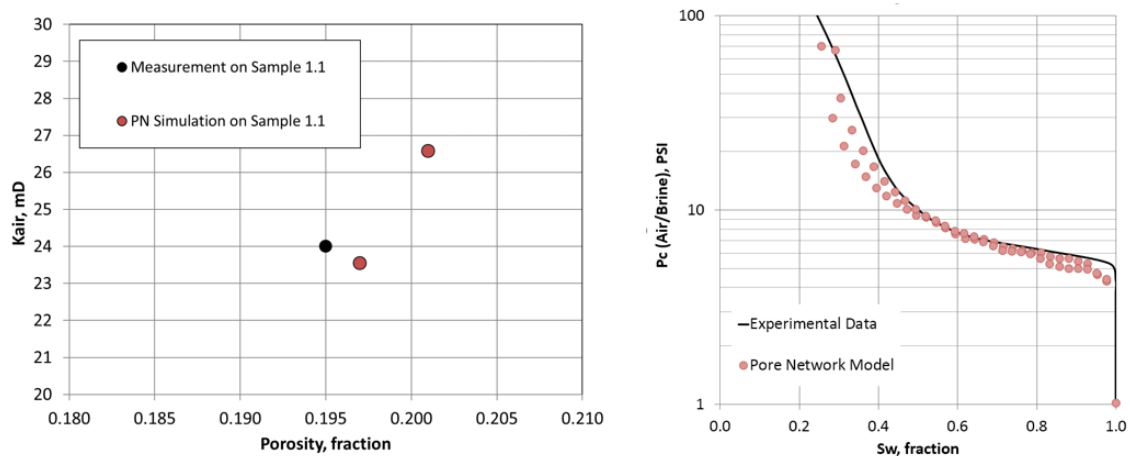

Figure 9: Consistency check for sample 1.1: Permeability vs porosity (left); primary drainage capillary pressure (right)

Figure 10 demonstrates the good agreement between calculated and measured gas-oil centrifuge relative permeability and pore network model.
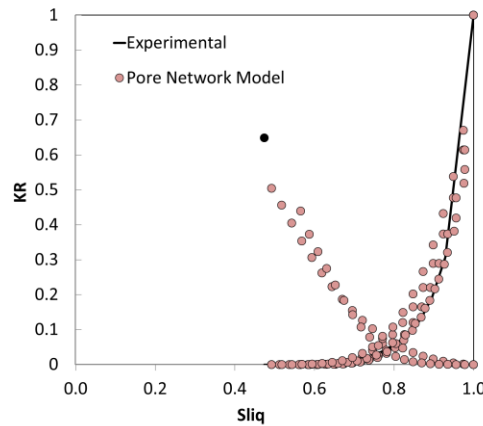
Figure 10: Consistency check for sample 1.1. Comparison of Experimental and Simulated Gas-Oil Kr

COMPARISON OF CALCULATIONS FOR WATER WET AND OIL WET SCENARIOS WITH MEASURED DATA

The sensitivity studies on imbibition were performed for scenarios representing water-wet (contact angle 30-70^0) and oil-wet (contact angle 120-150^0) conditions [10]. The comparisons of experimental and results from the pore network simulation consisted of relative permeability and fractional flow plots. Information from wettability tests (**Figure 2**) on neighboring samples in wells 1 and 2 was used to check for consistent behavior.

Group 1: Relative permeability for the two samples in this group are shown in **Figure 11** Displacement efficiency plots calculated with each relative permeability set are shown in in **Figure 12**. A comparison of experimental results with the pore network model simulations suggests that sample S1.1 is in the water-wet to mixed-wettability range, and this is consistent with the wettability tests. However, sample S1.2 is outside even the water-wet range, and this is contrary to the wettability data. Samples belonging to well 2 with the same behavior were removed from the sample pool.
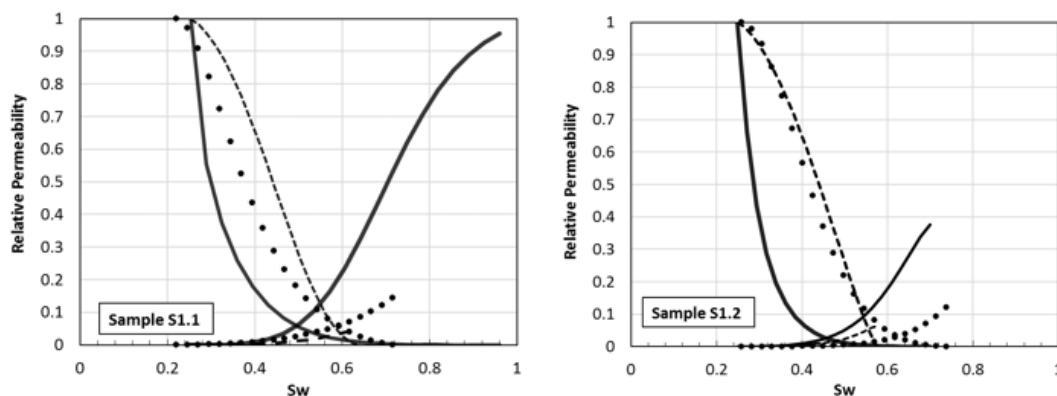

Figure 11: Group 1 - Comparison of experimental (solid circles) and calculated imbibition water/oil kr for water-wet (dashed line) and oil-wet (solid lines) scenarios for S1.1 and S1.2
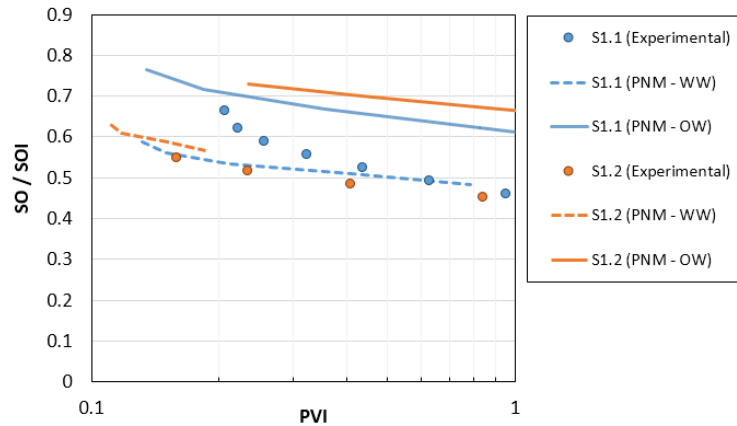
Figure 12: Group 1 - Comparison of So /Soi vs PVI using k$_r$ from Figure 10

Group 2: Relative permeability for the two samples in this group are in **Figure 13**; displacement efficiency plots calculated with each relative permeability set are in in **Figure 14.** The comparison of experimental results with the pore network model simulations are consistent with the wettability data in that sample S2.1 is more water wetting than sample S2.2. However, it is worth noting that sample S2.1 is in extreme water wetting range and sample S2.2 in the highly oil wet range. Samples with similar pore structure exceeding the oil-wet and water-wet thresholds in **Figure 14** were flagged for further analysis.
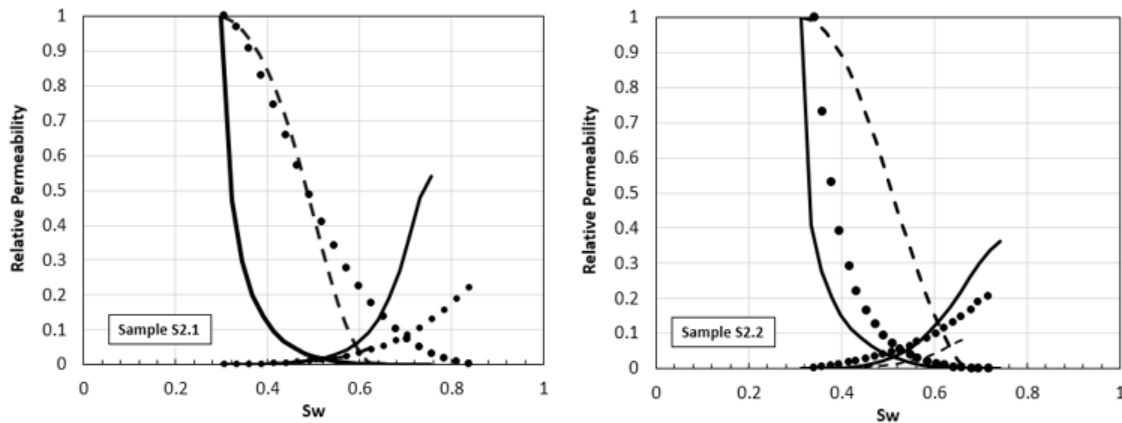

Figure 13: Group 2: Comparison of experimental (solid circles) and calculated kr for water-wet (dashed line) and oil-wet (solid lines) for S2.1 and S2.2

Figure 14: Group 2 - Comparison of So/Soi vs PVI using k$_r$ from figure 12

Group 3: The samples in this group are the most challenging due to the low permeability and comparatively large amount of clay. This causes more uncertainty in the segmentation. Relative permeability for the two samples in this group are shown in **Figure 15;** displacement efficiency plots calculated with each relative permeability set are shown in in **Figure 16.** Comparison of experimental results with the pore network model simulations suggests that results of sample S3.1 are consistent with the wettability data. However, sample S3.2 appears very water-wet and this this sample was flagged for further analysis as it is inconsistent with the wettability data.
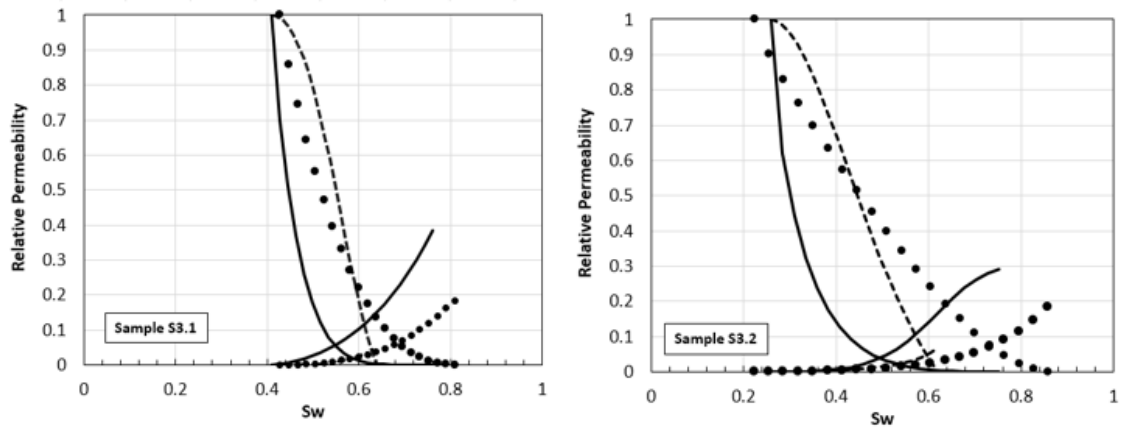
Figure 15: Group 3: Comparison of experimental (solid circles) and calculated kr for water-wet (dashed line) and oil-wet (solid lines) for S3.1 and S3.2
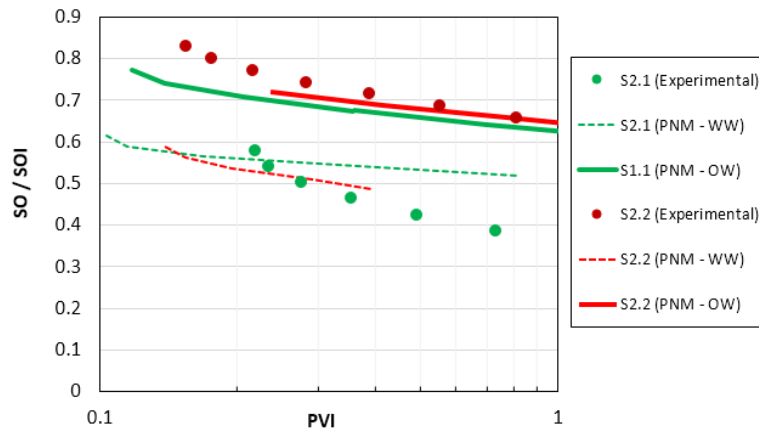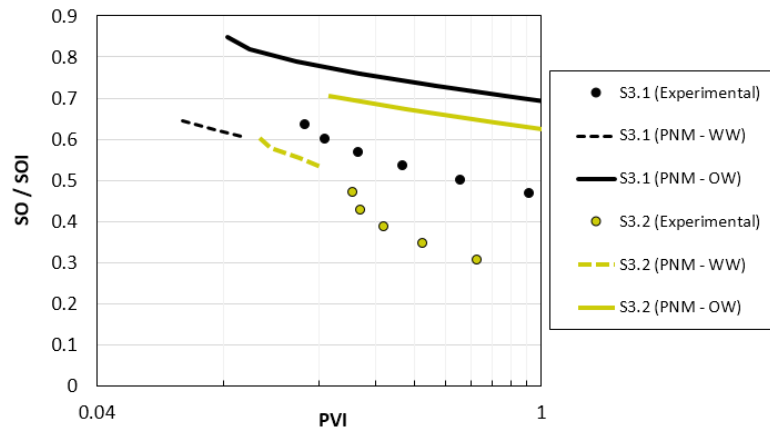
Figure 16: Group 3 - Comparison of ROS vs PVI using k_r from figure 14

UNCERTAINTY REDUCTION

Results from this analysis provided a guideline to confirm suspicious behavior, especially in well 1. **Figure 17 - left** shows water displacing oil relative permeability data after removal of samples. The effect of removal of samples in the reduction of the uncertainty in waterflood uncertainty is highlighted in **Figure 17-right,** where the range of oil saturation after 1 PVI decreases from 30% - 60% OIP (**Figure 1-right**) to 42% – 58% OIP.
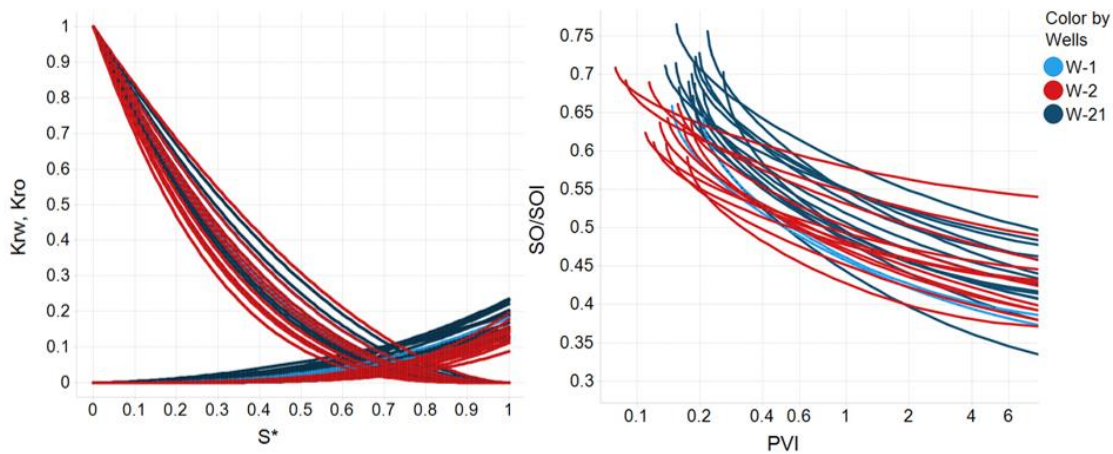
Figure 17: Relative Permeability (Left) and So / Soi from fractional flow calculations (Right) after identification of outliers and removal of samples

CONCLUSIONS

- Digital rock technology was used to reduce the uncertainty in waterflood ROS after 1 PVI from the prior range of 30% - 60% OIP to 42% – 58% OIP. The extreme wetting scenarios used in pore network calculations, along with guidance from wettability data, was instrumental in identifying outliers.

- Pore network models successfully reproduced permeability, drainage capillary pressure, and gas oil relative permeability measurements; and these were important in gaining confidence in water oil relative permeability calculations.

ACKNOWLEDGEMENTS

REFERENCES
1. Bakke, S. and P.E. Øren, "3D Pore-Scale Modeling of Sandstone and Flow Simulations in the pore Networks, SPE Journal (1997), **2**, 136-149
2. Blunt, M. J., M. D. Jackson, M. Piri, and P. H. Valvatne, "Detailed physics, predictive capabilities and macroscopic consequences for pore-network models of multiphase flow, Adv. Water Resour (2002), **25**, 1069-89.
3. Øren, P. E., S. Bakke, and O. J. Arntzen, "Extending Predictive Capabilities to Network Models," *SPE Journal*, (1998), **3**, 324-336.
4. Golab A, A. Arena, I. Barranco, R. Salazar-Tio, J. Hamilton, N Idowu, P. Rajan, S. Sommacal, B. Young, A. Carnerup, and J. M. Schembre-McCabe, "Mineralogical and Petrophysical Characterization of a Fine-Grained Sandstone With Significant Clay Coating Using 3-D Micro-CT and SEM Imaging From a 5mm Plug,". International Conference & Exhibition 2015 Sep 16.
5. Masalmeh, S. K., Jing, X., Roth, S., Wang, C., Dong, H., and Blunt, M. "Towards Predicting Multi-Phase Flow in Porous Media Using Digital Rock Physics: Workflow to Test the Predictive Capability of Pore-Scale Modeling", SPE 177572 presented at the International Petroleum Exhibition and Conference, Abu Dhabi (2015).
6. Al-Kharusi AS and M. J. Blunt, "Multiphase flow predictions from carbonate pore space images using extracted network models," Water Resources Res (2008), 44, W06S01.
7. Idowu, N. A., C. Nardi, H. Long, T. Varslot, and P.E. Øren, "Effects of segmentation and skeletonization algorithms on pore networks and predicted multiphase-transport properties of reservoir-rock samples,". SPE Reservoir Evaluation & Engineering (2014) Nov 1;17(04):473-83.
8. Idowu, N.A., H. Long, P. E. Øren, A. M. Carnerup, A. Fogden, I. Bondino, and L. Sundal, "Wettability analysis using micro-CT, FESEM and QEMSCAN, and its applications to digital rock physics," Proceeding of the International Symposium of the Society of Core Analysts, St. John's Newfoundland and Labrador, Canada (2015) SCA2015-010.
9. Bondino, I, G. Hamon, W. Kallel, and D. Kachuma,"Relative Permeabilities from Simulation in 3D Rock Models and Equivalent Pore Networks: Critical Review and Way Forward," Petrophysics, Vol. 54, No. 6 (2013), 538-546
10. Øren, P. E. and S. Bakke, "Reconstruction of Berea sandstone and pore-scale modeling of wettability effects," *J. Petroleum Science and Engineering* (2003), **39**, 177-199.

11. Valvatne, P.H. and M. J. Blunt, "Predictive pore scale modeling of two-phase flow in mixed water wet media," Water Resource Research, (2004) 40(7), W07406.
12. Dixit, A.B., Buckley, J.S., McDougall, and S.R., Sorbie, K.S., "Core Wettability: Should I_{AH} equal I_{USBM}?, *Proceeding of the International Symposium of Core Analysts* (1998), SCA1998-09.
13. Schembre-McCabe, J., Salazar-Tio, R., Ball, G., and J. Kamath, "A framework to validate Digital Rock Technology," *Proceedings of the 2011 International Symposium of the Society of Core Analysts*, Austin (2011), SCA 2011-028.
14. Schembre-McCabe, J., R. Salazar-Tio and J. Kamath, "Two examples of adding value through Digital Rock Technology," Proceedings of the 2012 Annual Symposium of the Society of Core Analysts, Aberdeen, Scotland, UK (2012), SCA 2012-081.

INVESTIGATION OF SALT-BEARING SEDIMENTS THROUGH DIGITAL ROCK TECHNOLOGY TOGETHER WITH EXPERIMENTAL CORE ANALYSIS

Marisa B. Rydzy, Ben Anger, Stefan Hertel, Jesse Dietderich, Jorge Patino,
Matthias Appel

Shell International Exploration and Production, Houston, TX

ABSTRACT

In this study, we combined digital rock analysis with a variety of experimental core analysis measurements to investigate the effect of salt saturation and distribution on the permeability and porosity of halite-cemented core samples. Medical and micro X-ray CT scans of core sections and 2.54 cm-diameter plugs indicated that the halite generally occurred in form of distinct layers. High-resolution micro X-ray computed tomography (MXCT) images acquired of 0.6 cm-diameter plugs revealed that, on the pore scale, halite appeared to be pore-filling. Pores were either completely filled with halite or did not contain any halite at all. It was also observed that halite preferentially occurred in the larger pores. The porosity and permeability results, both measured and calculated, demonstrated the obstructive effect of halite on storage and flow as well as the decline of both properties with increasing salt saturation. Comparison of calculated and measured values showed that the measured porosity could be up to 6 porosity units (p.u.) higher than the calculated one while the measured permeability of core plugs after salt removal was lower than the calculated one by an order of magnitude. One possible reason for this discrepancy may be the stratified nature of the samples. While the fully salt-saturated plugs appeared homogeneous in MXCT images, post-flood MRI images revealed that the plug was composed of layers with different MRI intensities, i.e. different amounts of water-filled porosity. Consequently, the petrophysical parameters calculated for the mini plugs may only be representative for a section of the core plug. The results of the MRI-assisted core floods emphasized the importance of considering different scales when interpreting and applying the results of digital rocks analysis.

INTRODUCTION

Understanding of how and to what degree an immobile pore fill, such as salt, obstructs the flow of mobile reservoir fluids (water and hydrocarbons), represents an important step in proper reservoir characterization. Basic petrophysical properties, such as porosity

and permeability, are strongly affected by the presence of salt. Mechanical, chemical and, as such, the electrical properties of the formation may be impacted (e.g. Hartman, 1968; Hamilton and Bachman, 1982; Barnabé et al. 1992; Olivarius et al. 2015). **Figure 1** shows X-ray computed images of salt-bearing sandstone on core, plug and pore scale. The images demonstrate the scale dependency of the salt occurrences. They suggest that hydrocarbon storage and flow in these types of sediment will be not only a function of the salt saturation but also a function of the salt distribution. Consequently, interpretation and quantification of key reservoir parameters based on well-logs and other means of geophysical exploration will require validation through digital image analysis at various scales of the salt-bearing sediment in addition traditional core analysis data.
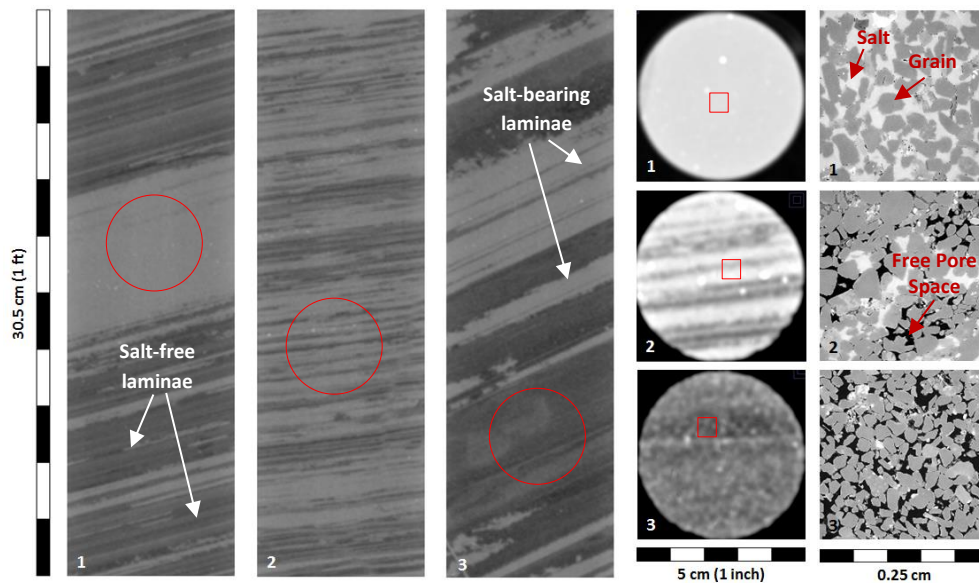
Figure 1: Examples of medical CT scans of 1-ft long core sections and the corresponding 2.54-diameter core plugs that were used in our investigation (Core section CT scans were acquired by CORE LABORATORIES® in Houston, TX). In the MXCT images, black indicates free pore space, grey and light grey/white areas represent sand grains and halite, respectively.

In this paper, we present the findings of our investigation of the porosity and permeability in halite-cemented sandstone. The objective of this study was to characterize the relationship between these key petrophysical parameters with the amount and distribution of the halite. For this purpose, we combined traditional core measurements and core flood (salt dissolution) experiments with imaging techniques, such as macro- and micro-scale X-ray computed tomography (XCT and MXCT, respectively) and magnetic resonance imaging (MRI), as well as qualitative and quantitative image analysis techniques. XCT, MXCT, and MRI have been employed in a variety of geoscience applications (e.g. Sarker and Siddiqui, 2009; Cnudde and Boone, 2013; Thiemeyer et al., 2015), either in the context of quantitative and qualitative analysis of rock structures (e.g. Arns et al. 2005; Wildenschild and Sheppard, 2013) or for monitoring of saturation changes (e.g. Hoffman et al. 1996; Mees et al. 2003; Kneyfsey et al. 2007; Ersland et al., 2009). Quantitative analysis of images through "Digital Rocks Technology" (i.e. calculation and simulation

of rock properties based on pore scale images) has emerged in the early 90's. Even though the technology itself can still be considered to be in its infancy, results of recent geoscientific studies that employed digital rocks technology have already demonstrated its potential and value for the petrophysics community (e.g. Arns et al. 2003; Mock et al. 2007).

SAMPLES AND EXPERIMENTAL PROCEDURES

We performed digital image analysis of micro-X-ray CT scans of sixteen 0.6-cm diameter core plugs ("mini plugs"). Porosity measurements and core flood experiments were conducted on regular 2.54-cm diameter core plugs ("macro-plug").

Eight of the macro-plugs had previously been drilled, trimmed, and cleaned with a mild solvent (cyclohexane) at CORE LABORATORIES© in Houston. These plugs were used for the digital rock work. The clean macro-plugs were transferred to our laboratory, where we performed helium porosimetry (**Table 1**) and acquired plug-scale MXCT images of them (**Figure 2**). Afterwards, we drilled a total of sixteen mini plugs out of the macro-plugs. The number of mini plugs per macro-plug are listed in **Table 1**. Their drilling locations are marked in the MXCT images (**Figure 2**). Note, both macro and mini-plugs were drilled without the use of any liquids but with nitrogen gas to preserve the halite.

Table 1: Overview of full-size plugs from which mini plugs were produced

Sample	Description	He-ϕ, %	# Mini Plugs
SLT_001	Fully salt-saturated	6.2	1
SLT_002	Fully salt-saturated	10.2	1
SLT_003	Partially salt-saturated (layers)	12.8	6
SLT_004	Partially salt-saturated (high saturation)	5.3	2
SLT_005	No pore-filling salt	27.0	3
SLT_006	Partially salt-saturated (low saturation)	27.4	2
SLT_007	No pore-filling salt	28.3	3
SLT_008	Fully salt-saturated	-	1

Four sets of additional macro-plugs were drilled, trimmed, and cleaned at our laboratory facility. These plugs were later used in the core flood experiments. The cleaning process involved circulation of toluene for 3-7 days (until the effluent appeared clear) followed by a 12-hour nitrogen purge to dry the samples. During cleaning and drying, the samples were subjected to an effective stress of 3.5 MPa. From monitoring the flow of toluene, we obtained first permeability estimates (**Table 2**). The plug porosity before and after salt-dissolution was estimated by NMR and helium porosimetry, respectively (**Table 2**).

Digital Rock Analysis

MXCT images of the mini plugs were acquired with a ZEISS Xradia 520 Versa scanner. The standard acquisition parameters[1] for each scan yielded 2048x2048x2048 volume of images with a resolution of about 2 µm. The image volumes were reconstructed with

---

[1] MXCT acquisition parameters: 4X objective, energy of 80 keV/7W and exposure time of 7s yielding an energy count of 7,000, tomography angle = ±180° with 6001 projections. Different source filters (LE#2-4) were applied depending of the transmission value.

default settings, exported and processed as raw files. Image processing included reduction of the image stack to a 1024x1024x1024 volume and application of non-local-means filter (Buades et al, 2005). The volume fractions of free and salt-filled pore space were determined from image segmentation (**Figure 3**) performed in IMAGEJ (https://imagej.nih.gov/ij/) using manual thresholding based on visual judgement. Pore and grain size distribution were then calculated based on the segmented image volumes using the "porosimetry" method (Wiegmann and Blatt, 2017) within the PORODICT® module of the materials properties simulator GEODICT® (www.math2market.com). Finally, the permeability was calculated for each segmented image volume using an in-house single-phase Lattice-Boltzman flow simulator.
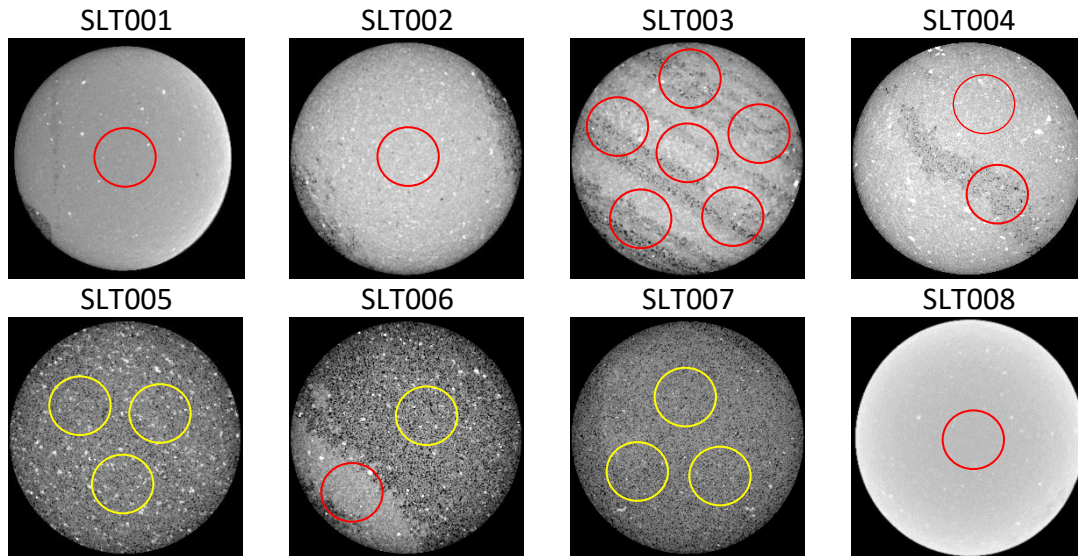
Figure 2: MXCT images of full-size plugs with varying amounts of salt and locations of mini plugs

Table 2: Overview of macro-plugs used in MRI-Flow experiments

Sample	Before salt dissolution					After salt dissolution	
	D, cm	L, cm	NMR-ϕ, %	k_{tol}, md	He-ϕ, %	NMR-ϕ, %	K_{brine}, mD
SLT009-A	2.54	2.51	3.4	4	3.04	23.5	756
SLT010-A	2.55	3.69	3.3	20	4.13	-	669
SLT011-A	2.55	3.72	1.7	25	-	21.1	811

Core Flood Experiments

The core flood experiments were performed in conjunction with magnetic resonance imaging (MRI). The sample was confined inside a sample holder composed of polycarbonate resin (LEXAN™). The sample holder was composed of two halves held together brass screws. Tightening the screws exerted a small confining pressure (less than 10 psi) on the sample. The sample holder was placed inside a vertical bore 2.1T (90.5 MHz for 1H) magnet (ImaCore 3017, MR Solutions and Green Imaging Technologies). The plugs were injected with diluted formation brine (50k ppm equivalent salinity) to initiate salt dissolution. The brine was injected at a constant flow rate (2-5 cc/min) using a Vindum VP-12K pump. Images were acquired at different stages of the core flood

using a Fast Spin Echo (FSE) pulse sequence with three lobe sinc-shaped 90° and 180° pulses of 336 µs duration, echo times TE = 2 ms, 16 signal averages, and eight echoes per RF excitation, leading to acquisition times of 4.3 minutes. The resulting transaxial and/or sagittal 128x128 pixel images provided a field of view of 50 mm and 70 mm, and image resolution of 0.39 mm and 0.55 mm/pixel respectively.
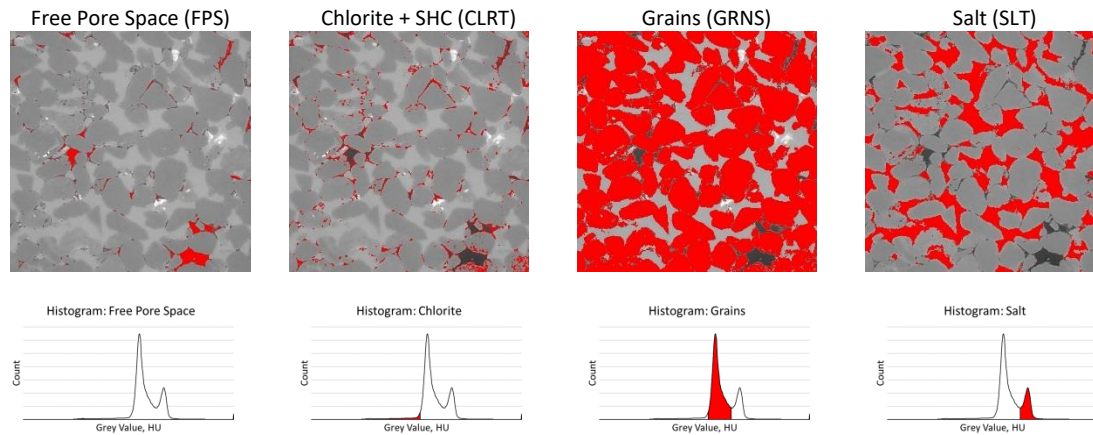
Figure 3: Example of segmentation of MXCT image of mini plugs (SLT006_M1)

RESULTS AND DISCUSSION

Visual inspection of the MXCT images acquired of the mini plugs revealed the principal sediment components that had previously been identified through thin section analysis (M. Jaminski, personal conversation, 2017), namely quartz grains, chlorite overgrowth covered in solid hydrocarbons, and salt (**Figure 4**).
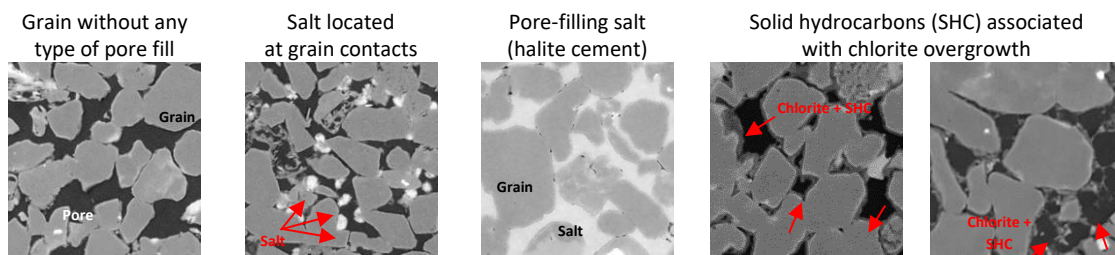
Figure 4: Rock components identified in MXCT images of mini plugs (images shown 1x1 mm^2)

The hydrocarbon-covered chlorite cement was occurred on the grain surfaces as smooth layers that could be several micro-meters thick or in form of thin streaks protruding from the grain surface into the pore space. Salt appeared to occur either as pore-filling halite cement or in form of small polycrystalline agglomerates attached to grain surfaces or located at the grain contacts. At this moment, it remains unclear whether the latter presents a result of cleaning/drying-induced precipitation. In the following, it be treated as part of the rock matrix. The images also revealed that pores were either fully filled with halite or did not contain any salt at all (note, in the following, "partial saturation" will refer to the fraction of salt-filled pore volume compared to the total amount of pore

volume in one mini plug). The salt-filled pores often formed well-defined layers that distinctly stood out in both XCT/ MXCT images of plugs and core sections (**Figures 1** and **2**).

Digital Rock Analysis Results
Based on the calculated salt saturation (S_{salt}), we divided the samples into four groups: 1) fully salt-saturated samples with $S_{salt}>97\%$, 2) partially saturated samples with high salt volume ($97\%>S_{salt}>85\%$), 3) partially saturated samples with medium to low salt volume ($85\%>S_{salt}$), and 4) samples without any pore-filling halite. We determined different types of porosity. The "***resolved porosity***" (PHI) only included the free pore space visible in the MXCT images. For samples that did not contain any pore-filling halite, the resolved porosity ranged between 15 and 18%. Up to 3 porosity units (p.u.) of the resolved porosity in these samples could be occupied by the disconnected polycrystalline salt agglomerates mentioned above. In fully salt-saturated samples, the free pore space rarely exceeded 1%. For partially salt-saturated samples, the resolved porosity fell in between. The ***"paleo-porosity"*** was calculated by adding up free and salt-bearing pore space. For fully and partially salt-saturated samples, we obtained paleo-porosity ranges of 25-33% and 13-33%, respectively. Most samples contained a volume fraction of around 10% of hydrocarbon-covered chlorite cement. Assuming the chlorite contained a ***micro-porosity*** of 50% (Berger et al. 2009), the additional pore space would increase the overall porosity by around 5 p.u. Measured (**Tables 1** and **2**) and calculated porosity followed similar trends and fell into the same range. The results for individual samples, however, could deviate by up to 6 p.u.

The resolved porosity in the partially halite-saturated samples was generally only partially ***percolating***. Especially in samples with higher S_{salt}, the network of connected pores only extended in the directions parallel to bedding. As a result, the ***permeability*** calculated based on the segmented MXCT images was strongly direction-dependent in the partially halite-saturated samples. Due to the lack of pore-network conductivity, no permeability could be calculated for the fully saturated mini plugs. Instead, a "paleo-permeability" was determined, i.e. the permeability for the host sediment without salt. The paleo permeability reached values in the 1000s of md. In comparison, the permeability calculated for samples without any halite only reached values up to a couple 100 md. **Figure 5** shows the paleo-permeability as a function of salt saturation for the fully salt-saturated samples alongside the calculated actual permeability of the partially saturated and halite-free samples (in the direction of bedding). The plot also includes measured permeabilities for halite-cemented and halite-free macro-plugs.
As expected, the permeability decreases with increasing salt saturation. The permeability decrease loosely follows an exponential trend. However, the results for the partially saturated samples exhibit significant scatter which can be attributed to a) the small number of samples and to b) the dependence of the permeability on the halite distribution (or in this case the orientation of the salt layer to the flow direction). The experimental data showed a less steep increase in permeability from 4-20 mD for fully saturated samples to 600-800 mD for the same samples without the salt.

The elevated paleo-permeabilities obtained for the fully halite-filled samples compared to actual permeabilities determined for the halite-free samples can be attributed to a difference in average *pore size*. Pore sizes (D10, D50, D90) calculated for each mini-plug are shown in **Figure 6**. For the halite-free sediment, pore sizes ranged around 30-60 µm, while the paleo-pore sizes for the fully halite-filled sediment ranged between 40-80 µm. A tendency of halite to occupy larger pore spaces was previously reported in literature. Putnis and Mauthe (2001) observed that halite cement in the Solling Sandstone of the Bunter Formation preferentially occurred in the larger pores. Ott et al. (2014) reported similar observation from laboratory experiments where halite was precipitated through evaporation and CO_2 injection inside a multi-porosity system. Putnis and Mauthe (2001) suggested pore size affected the supersaturation limit for NaCl brine which caused the selective cementation. Similarly, Benavente et al. (2004) cited pore space-induced thermodynamic effects on the brine activity as a factor influencing salt precipitation in porous media. Alternative explanations include prevention of sediment compaction during burial by the halite cement (e.g. Schenk and Schmoker, 1993; Nguyen et al. 2013) and pore-space expansion due to crystallization pressure exerted by the precipitate (e.g. Noiriel et al. 2010).
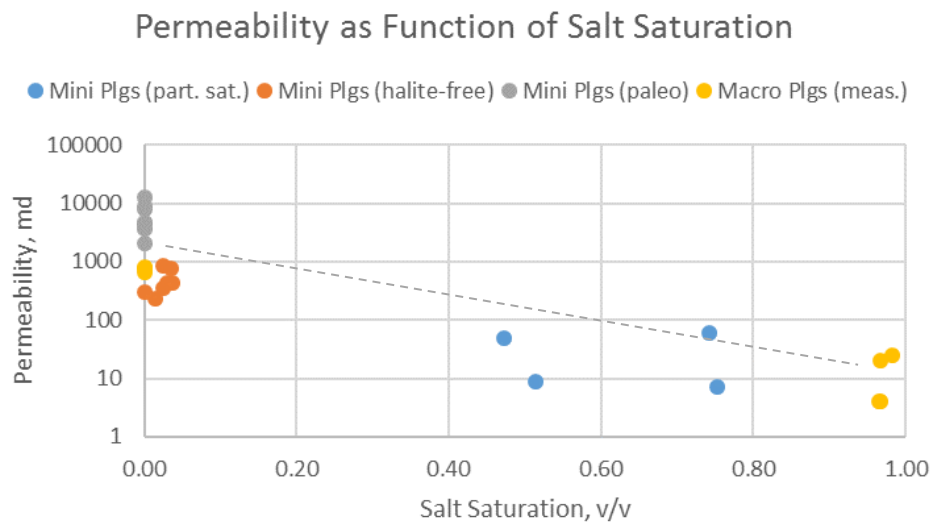
Figure 5: Permeability as function of salt saturation (mini plug permeabilities obtained from simulations)

In this study, the difference in average pore size between fully halite-filled and halite-free sediments can be traced back to a difference in overall *grain size*. This Grain sizes calculated based on the MXCT images of the mini plugs are shown in **Figure 7**. The average grain size for fully halite-filled samples ranged between 10 and 60 µm, while the average grain size for halite-free samples ranged between 5 and 40 µm. Note that the range of grain sizes calculated (10-80 µm) classified the sediment at hand as silty-fine sandstone. Based on the geological analysis of the full core, the sediment was previously classified as fine-medium grained (C. Hern, personal conversation, 2017). The observed

correlation between pore and grain size supports the hypothesis that selective halite precipitation may be influenced by the pore space rather the other way around. Nevertheless, it does not necessarily invalidate alternative explanations, as all the different mechanisms may even act in parallel.
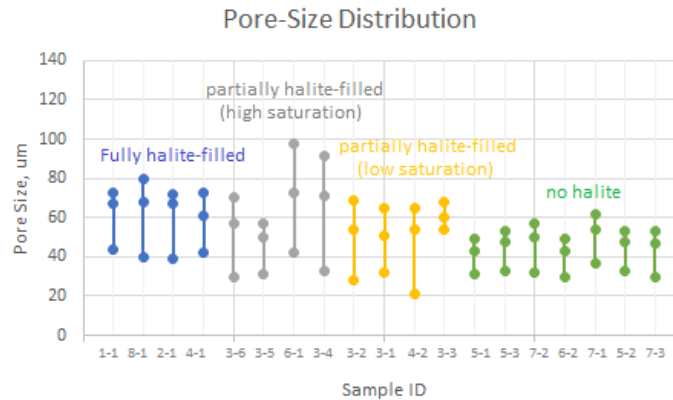
Figure 7: Pore size distribution calculated with PORODICT™ for rock samples with different salt saturations (blue=fully salt-saturated samples, grey=partially salt-saturated (high S_{salt}), yellow= partially salt-saturated (low S_{salt}), green= samples without pore-filling salt, three dots depict D10, D50, and D90)
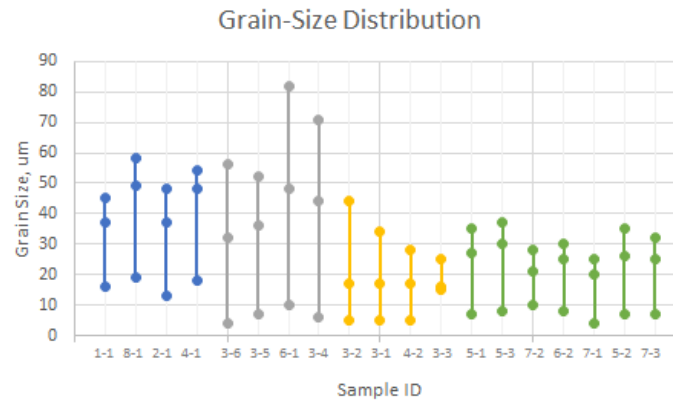
Figure 7: Grain size distribution calculated with PORODICT™ for rock samples with different salt saturations (blue=fully salt-saturated samples, grey=partially salt-saturated (high S_{salt}), yellow= partially salt-saturated (low S_{salt}), green= samples without pore-filling salt, three dots depict D10, D50, and D90)

Salt Dissolution during Core Flooding with Low-Salinity Brine

Figure 7 shows MRI images acquired during the low-salinity water floods of 3 fully halite-cemented macro-cores. MRI measured the nuclear spin density of water within the sample and the water-saturated areas became visible in the MRI scan. The higher water content, the lighter the image appeared. Solid components, such as rock minerals and salt remained undetectable in the MRI. As salt dissolved, more pore space became available for fluid flow and the effective flow cross section increased as can be seen in **Figure 8**. The MRI images that were acquired after salt dissolution had completed show distinct

layers of varying intensity. The different grey values represented different water contents which in turn corresponded to different porosities and potentially different pore sizes. Due to the heterogeneity of the macro-plugs, the porosities and permeabilities of the extracted mini plugs may not have been representative of the whole plug but merely of one layer or two. Consequently, even in fully salt-saturated samples that appear homogeneous in XCT or MXCT images, multiple mini plugs should be extracted for digital rock analysis. Interestingly though, the salt dissolution front did not appear to be impacted by the stratified makeup of the sample as it was observed to cut across layers (**Figure 7**).
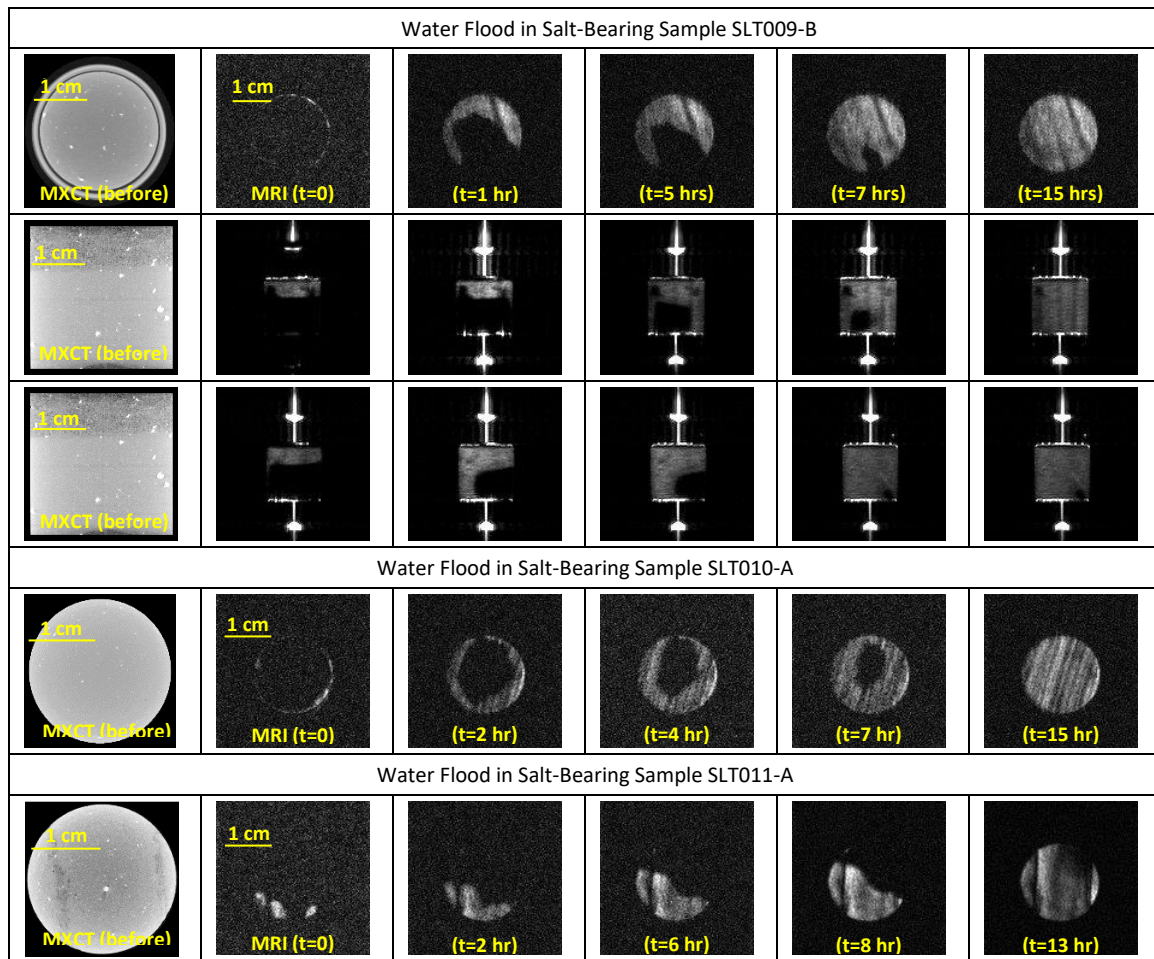
Figure 8: MXCT and MRI images acquired of Samples SLT010-A, SLT011-A, and SLT009-B before, during, and after the water flood experiment. All three planes (coronal, sagittal, and transaxial) were only recorded for the last sample. The duration of the salt dissolution process rarely exceeded 24 hours.

CONCLUSIONS

The combination of core analysis measurements, MRI, and digital rock analysis was shown to be a valuable approach in the investigation of halite-cemented sandstones. The qualitative and quantitative results of the analysis of pore scale images provided useful

insights into the interplay between halite cementation. It was shown that the halite cement occurred primarily in the larger pore spaces which generally arose from larger grain sizes, and that permeability and porosity declined drastically with higher halite content. Furthermore, the MXCT images showed a bimodal halite distribution occurring as layers in the XCT images with either fully cemented pore space or free pore space. While a full quantitative evaluation of the MRI images is still outstanding, it could be shown that the salt masked the stratified makeup of the plugs and that unconformities in the distribution of the halite cement determined that starting point and propagation of the salt dissolution front. As a next step in the investigation of halite-cemented sediments, we will attempt to utilize the combination of core flood, permeability measurements and imaging to better quantify the relationship between salt saturation, its distribution across the core plug, and permeability.

ACKNOWLEDGEMENTS

REFERENCES

Ajayendra,'AJ'Kumar, Z. G.,L. Morales, T. Griffin, and J. Dacy. (2016), Micro-CT Imaging—A Powerful Tool for Screening and Rapid Quantification of Rock Properties, EG Technical Program Expanded Abstracts, 1477-1480

Arns, C.H., A. Sakellariou, T.J. Senden, A.P. Sheppard, R.M. Sok, M.A. Knackstedt, W. V. Pinczewski, and G.F. Bunn (2003) Virtual core laboratory: Properties of reservoir rock derived from X-ray CT images,

Benavente, D., M.A. Garcia del Cura, J. Garcia-Guinea, S. Sanchez-Moral, and S. Ordonez (2004), Role of pore structure in salt crystallization in unsaturated porous stone, Journal of Crystal Growth 260, 532-544

Berger A., S. Gier and P. Krois (2009) Porosity-preserving chlorite cements in shallow-marine volcaniclastic sandstones: Evidence from Cretaceous sandstones of the Sawan gas field, Pakistan. AAPG Bulletin 93(5), 595–615

Bernabé, Y., Fryer, D. T., & Hayes, J. A. (1992). The effect of cement on the strength of granular rocks. Geophysical Research Letters, 19(14), 1511-1514.

Buades, A., B. Coll, and J.M. Morel (2005), A non-local algorithm for image denoising, in Computer Vision and Pattern Recognition, 2005, IEEE Computer Society Conference Vol. 2, 60-65

Cnudde, V., and M.N. Boone, High-Resolution X-ray computed tomography in geosciences: A review of the current technology and applications, Earth Science Reviews 123, 1-17

Ersland, G., J. Husebø, A. Graue, and B. Kvamme (2009). Transport and storage of CO2 in natural gas hydrate reservoirs, Energy Procedia 1(1), 3477-3484

Fredrich, J. T., Lakshtanov, D. L., Lane, N. M., Liu, E. B., Natarajan, C. S., Ni, D. M., & Toms, J. J. (2014, October). Digital rocks: developing an emerging technology through to a proven capability deployed in the business. In SPE Annual Technical Conference and Exhibition. Society of Petroleum Engineers.

Gevantman, L.H., Lorenz, J., Haas, J.L. Jr., Clynne, M.A., & Potter, R.W. II. (1981). Physical properties data for rock salt. United States.

Hamilton, E. L., & Bachman, R. T. (1982). Sound velocity and related properties of marine sediments. The Journal of the Acoustical Society of America, 72(6), 1891-1904.
Hoffman, F., D. Ronen, and Z. Pearl (1996). Evaluation of flow characteristics of a sand column using magnetic resonance imaging, Journal of Contaminant Hydrology, 22(1-2), 95-107.

Kneafsey, T. J., L. Tomutsa, G.J. Moridis, Y. Seol, B.M. Freifeld, C.E. Taylor, and A. Gupta (2007), Methane hydrate formation and dissociation in a partially saturated core-scale sand sample, Journal of Petroleum Science and Engineering 56(1), 108-126.

Laier, T., & Nielsen, B. L. (1989). Cementing halite in Triassic Bunter Sandstone (Tønder, southwest Denmark) as a result of hyperfiltration of brines. Chemical Geology, 76(3-4), 353-363.

Mees, F., R. Swennen, M. Van Geet, and P. Jacobs (2003), Applications of X-ray computed tomography in the geosciences, Geological Society Special Publications 215, 243-249.

Nguyen, B.T., S.J. Jones, N.R. Goulty, A.J. Middleton, N. Grant, A. Ferguson, and L. Bowen (2013), The role of fluid pressure and diagenetic cements for porosity preservation in Triassic fluvial reservoirs of the Central Graben, North Sea, AAPG bulletin 97(8), 1273-1302.

Noiriel, C., F. Renard, M.L. Doan, and J.P. Gratier (2010), Intense fracturing and fracture sealing induced by mineral growth in porous rocks, Chemical Geology, 269(3), 197-209.

Olivarius, M., Weibel, R., Hjuler, M. L., Kristensen, L., Mathiesen, A., Nielsen, L. H., & Kjøller, C. (2015). Diagenetic effects on porosity–permeability relationships in red beds of the Lower Triassic Bunter Sandstone Formation in the North German Basin. Sedimentary Geology, 321, 139-153.

Ott, H., M. Andrew, J. Snippe, and M.J. Blunt (2014), Microscale solute transport and precipitation in complex rock during drying, Geophysical Research Letters 41, 8369-8376
Putnis, A. and G. Mauthe (2001), The effect of pore size on cementation in porous rocks, Geofluids 1, 37-41.

Sarker, M.R.H., and S. Siddiqui (2009), Advances in Micro-CT Based Evaluation of Reservoir Rocks, SPE 126039, presented at the 2009 Saudi Arabia Section Technical Symposium and Exhibition, AlKhobar, Saudi Arabia, May 9-11.

Schenk, C.J. and J.W. Schmoker (1993), Role of Halite in the Evolution of Sandstone Porosity, Upper Jurassic Norphlet Formation, Mississippi Salt Basin, Gulf Coast Association of Geological Societies Transactions 43, 357-362.

Thiemeyer, N., J. Habersetzer, Mark Peinl, Gernold Zulauf, and J. Hammer (2015), The application of high resolution X-ray computed tomography on naturally deformed rock salt: Multi-scale investigation of the structural inventory, Journal of Structural Geology 77, 92-106.

Wiegmann, A. and E. Glatt (2017), Porodict, GeoDict 2017 User Guide, math2market

PREDICTION OF PERMEABILITY FROM EULER CHARACTERISTIC OF 3D IMAGES

Z. Liu[1], A. Herring[2], V. Robins[2], R. T. Armstrong[1]

[1]School of Petroleum Engineering, University of New South Wales, Kensington, New South Wales, Australia

[2]Department of Applied Mathematics, Research School of Physics and Engineering, Australian National University, Canberra, Australian Capital Territory, Australia

ABSTRACT

The determination of absolute permeability in porous media is of great importance in hydrocarbon extraction, subsurface groundwater investigation and carbon dioxide sequestration. Permeability can be determined from empirical formulations, such as Katz-Thompson, which correlates permeability with percolation threshold. Alternatively, recent research using 2D micro-fluidic experiments and numerical simulations have demonstrated that permeability can be derived from the Euler characteristic (a topological invariant) and the number of grains, which is independent of percolation threshold. However, whether or not these new findings are applicable for three-dimensional porous media has not been verified. How to determine the number of grains also remains a question. Herein, we examine new formulations for characterizing permeability in porous media. We generate three types of stochastic models, simulate single-phase flow using Lattice Boltzmann method and calculate absolute permeability. We find that permeability in 3D pore space does not scale with the same correlation as previously published work on 2D porous media. One possible explanation to this difference is that the number of grains does not capture the resistant force in three-dimensional space. We propose a modified equation by incorporating the void ratio, which is pore volume divided by solid volume. We find that the permeability scales with the Euler characteristic, number of grains and void ratio in 3D porous media and that the scaling is unique for distinctly different stochastic models. These findings provide a new means to characterize the absolute permeability of 3D porous media from pore-scale images of distinctly different grain and pore geometries without the need of numerical simulation.

INTRODUCTION

Absolute permeability represents the ability of a porous medium to conduct fluid flow. It was first defined by Henry H. G. Darcy [1]. It is usually measured through core flooding experiment and calculated from Eq. 1, which is known as Darcy's Law.

$$K = \frac{Q\mu L}{A\Delta P} \tag{1}$$

Here K is absolute permeability, Q is flow current, μ is fluid viscosity, L is length of the core, A is cross-sectional area and ΔP, is pressure gradient. While permeability is a

simple concept there exist a wide range of different empirical relationships that link pore structure (geometry and/or topology) to permeability. These correlations are often used in the petrophysical analysis of petroleum reservoirs and/or clustering of rock properties into distinct categories.

The Carman-Kozeny equation is a well-known empirical equation where permeability is dependent on rock porosity [2], which can be seen in Eq. 2.

$$K = \frac{\phi r^2}{8\tau} \qquad (2)$$

Here ϕ is rock porosity, r is effective radius and τ is tortuosity. In Figure 1, we provide the permeability versus porosity relationship for many different rock types [3]. It can be seen that there is no universal relationship between permeability and porosity, *e.g.* at 12% porosity resulting permeability value can range from 1 mD to 1D depending on the rock type. Indeed the underlying pore structure of these rocks are not the same, resulting in different effective radii and tortuosity coefficients for the same porosity. While porosity does have a strong influence in permeability, the underlying geometry and topology of the pore space are major factors that must be considered.
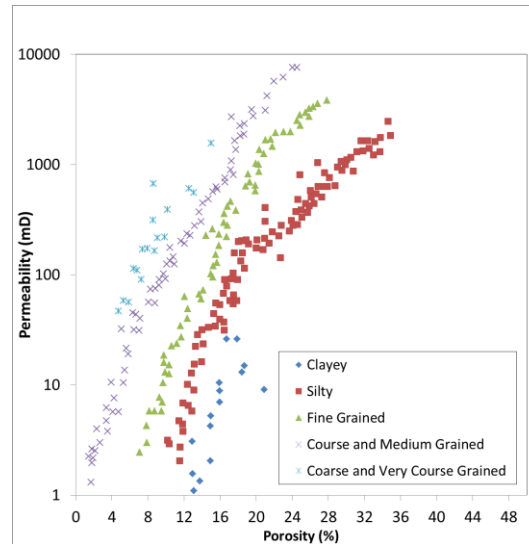
Figure 1: Modified permeability – porosity relation chart from previous work [3].

Another widely used empirical correlation is the Katz-Thompson model [4] as shown in Eq. 3.

$$K = c l_c^2 \left(\frac{\sigma}{\sigma_0}\right) \qquad (3)$$

Here c is the constant on the order of $\frac{1}{226}$, l_c is characteristic length of the pore space, σ is conductivity of rock saturated with a brine solution of conductivity σ_0. Because electrical conductivity is influenced by the topology of the pore space this relationship implicitly captures pore topology while the geometry of the pore space is captured through the

characteristic length term (l_c). The σ/σ_0 term can be linked to porosity according to Archie's law as shown in Eq. 4.

$$\frac{\sigma}{\sigma_0} = \left(\frac{\phi - \phi_c}{1 - \phi_c}\right)^\mu \tag{4}$$

Here ϕ_c is porosity at the percolation threshold and μ is the critical exponent. The Katz-Thompson model has been further developed by replacing the σ/σ_0 term with direct measurements of pore morphology [5]. The new formulated equation is shown is Eq. 5 and we will be referred to it as Scholz's model from hereon.

$$K = cl_c{}^2 \left(\frac{1-\chi_0}{N}\right)^\alpha \tag{5}$$

Here χ_0 is Euler characteristic of the conducting phase and N is number of grains in the granular porous media. Through topological arguments (for a 2D system), it can be shown that as $\phi \rightarrow 1$, $\frac{1-\chi_0}{N} \rightarrow 1$ and as $\phi \rightarrow 0$, $\frac{1-\chi_0}{N} \rightarrow 0$. Therefore $\frac{1-\chi_0}{N}$ is analogous to (σ/σ_0) from Katz-Thompson because as $\phi \rightarrow 1$, $(\sigma/\sigma_0) \rightarrow 1$ and as $\phi \rightarrow 0$, $(\sigma/\sigma_0) \rightarrow 0$. In order to apply Scholz's model to 3D systems, the Euler characteristic of the pore space can be measured from segmented X-ray microtomography (micro-CT) images. However, calculating the number of grains (N) in the context of real reservoir rock is not straightforward. In Scholz *et al.* [5], the number of grains (N) was an input parameter from their stochastically generated models and each grain had constant volume, which is not realistic for geologic materials. For the practical application of Scholz's model, N must be directly measured from micro-CT images and it must accommodate different grain sizes.

Regardless of the practical problems associated with Scholz's model, the results are intriguing because they demonstrate a universal permeability relationship for stochastically generated 2D porous media. The tested porous media displayed different scaling relationships for $cl_c{}^2$ versus ϕ; however, once $cl_c{}^2$ versus $\frac{1-\chi_0}{N}$ was considered the data collapsed onto a single relationship. The main drawback of this study was that only 2D systems were considered and the proposed relationship has yet to be applied to real rock data. The results however warrant further studies and suggest that Scholz's model could provide a universal relationship between permeability and pore topology.

A key parameter in Scholz's model is the 2D Euler characteristic, which is a topological invariant that describes the connectivity of a binary object. The Euler characteristic has been previously used to characterize pore morphology of soils and reservoir rocks [6], two-phase flow and relative permeability [7-10], and non-wetting phase trapping for application to CO_2 sequestration [11]. The Euler characteristic can be determined from segmented pore scale images of reservoir rocks. The most intuitive way to think about the Euler characteristic is in terms of its Betti numbers (β_i).

$$\chi = \beta_0 - \beta_1 + \beta_2 \tag{5}$$

For a 3D object, β_0 is the number of components, β_1 is the number of inequivalent loops and β_2 is the number of cavities (enclosed voids). Take a donut as an example, shown in Figure 2, where the number of components is 1 (β_0=1) and number of inequivalent loops is 1 (β_1=1) since we are considering a solid donut. In describing the topology of the pore space of a porous rock, it can be assumed that the solid matrix is connected, so that $\beta_2 = 0$. In this case, the Euler number reduces to the difference between the number of discrete components and inequivalent loops. If all pore space is connected via one pathway or another, and there are no isolated pore spaces, then $\beta_0 = 1$. As the number of loops decreases the Euler number becomes less negative and will eventually become positive, at which point the system will no longer percolate [12].

Figure 2: A solid donut with a β_0 of 1, β_1 of 1 and β_2 of 0.

Recent developments in digital rock technologies have given us access to detailed information on pore space morphology using micro-CT imaging [13, 14]. One method to calculate permeability from micro-CT images is pore network modelling [15]. In addition to the pore network modelling approach, direct numerical simulations on porous media images have been developed, including finite difference methods [16] and Lattice-Boltzmann methods (LBM) [17], and these achieve reasonable predictions of permeability compared with experiments. The Lattice-Boltzmann method has been shown to be a valid approach in predicting absolute permeability for sandstone with limited resolution [18]. However, we would like to develop a simple approach for estimating reservoir rock permeability by measuring pore morphology.

Herein, we verify Scholz's model by simulating single-phase flow through quasi-two-dimensional (q2D) geometries and 3D systems. For the 2D models, we explore different ways to determine *N* and then extend our studies to 3D systems with different grain sizes. Recent developments in digital rock technology have given us access to detailed information on pore space morphology using micro-CT imaging [13, 14] and Scholz's model provides a novel approach to utilize this information. We attempt to apply Scholz's model to more realistic pore morphologies and thus attempt to provide a simple/convenient methodology to predict the absolute permeability of digital images. This approach could also provide a robust way to characterize rock types that have distinguishably different pore morphologies by providing a universal relationship between permeability and pore morphology.

MODEL GENERATION

We generate quasi-two-dimensional and 3D models for testing and extending Scholz's model. The quasi-two-dimensional (q2D) models generated are similar to Scholz's work including round models (RM) and ellipse models (EM) in a 4000x4000x10 domain size. The round models have a radius of 30 voxels. The ellipse models have a constant aspect ratio $a/b = 8$, where a is the long semi-axis and b is the short semi-axis of the ellipse. Additionally, we add square models (SM) as a new validation model to our work. The three types of q2D models are shown in Figure 3. For all of these models the number of grains (N) is an input parameter and each grain is added to a random location. For the ellipse model, each ellipse also has a random orientation. We control the number of elements (round, ellipse, square) to generate models with a range of different porosities.
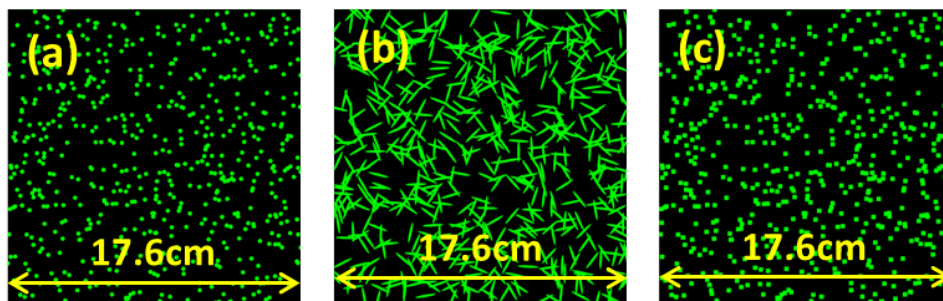
Figure 3: Generated 2D models with 600 Grains, (a) Round Model (b) Ellipse Model and (c) Square Model.

We also test three distinct 3D models as shown in Figure 4: (a) Sphere Model (480x480x480 domain): generated by randomly placing spheres with random radii following a Gaussian distribution (average radius is 20 voxels, standard deviation is 4 voxels) within the domain. The number of grains (N) added controls the porosity; (b) Stick Model (480x480x480 domain): generated by randomly placing sticks with random orientation within the domain. The length-width-height ratio is 2:2:15. The number of grains (N) added controls the porosity; (c) Robuglass Model (1000x1000x572 domain): a synthetic porous media is imaged with micro-CT [19, 20] and then derivative models are generated by running either erosion or dilation filters on the segmented image to reduce/increase the porosity. The number of grains (N) must be measured.
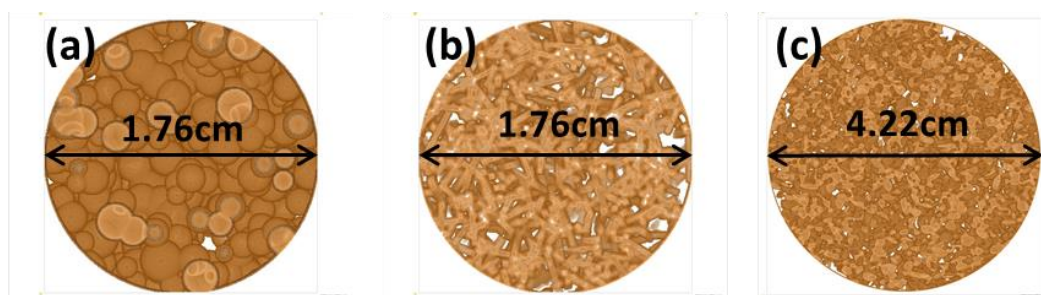
Figure 4 Generated 3D Models with 600 Grains, (a) random sphere model with 600 grains (b) random stick model with 9000 grains and (c) Robuglass model with erosion of 4 voxels.

CRITICAL PORE DIAMETER

For the q2D structures considered here, the critical pore diameter can be limited by the system height h. When the q2D critical pore diameter is larger than the height h, the limiting hydrodynamic length is determined by, h, i.e., $l_c = min(D_c, h)$.

The q2D and 3D critical diameter D_c is calculated from the Euclidean Distance Map (EDM). By thresholding the EDM with different radii r, a percolation test is performed to check if the system can percolate or not, the critical diameter D_c is two times the radius between percolation and non-percolation at the onset of percolation.

GRAIN NUMBER DETERMINATION

Input Grain Number

The input grain number N_i is available in q2D models, 3D Sphere Model and 3D Stick Model as an input. For 3D Robuglass Models, N_i is not available and the grain number must be determined using other methods. We must determine how to measure N if there is to be any practical application of Scholz's model applied to digital rock images. Herein we test two different approaches for measuring N.

Weighted Grain Number

The weighted grain number N_w is the grain number determined by Eq. 6.

$$N_w = \frac{V_{gtot}}{V_{element}} \tag{6}$$

Here V_{gtot} is the total volume of grains and $V_{element}$ is the volume of a single grain, or the mean grain volume as determined from pore-scale images. N_w is directly available in q2D models, 3D Sphere Model and Stick Model and can be measured from all other models by estimating mean grain size after running a grain separation algorithm (watershed) on the segmented images.

Persistence Grain Number

The persistence grain number N_p is calculated from the persistent homology signatures of the data as measured using the software package Diamorse [21]. In the persistent homology analysis, a signed Euclidian distance transform (SEDT) is calculated from the segmented image data; this identifies local minima at the center of pore bodies within the pore space of the system and local maxima at the center of solid grains. A level-set growth process is carried out on this Euclidean distance transform: topological features β_0, β_1 and β_2 are measured for the data set at each level-set distance value; as the level-set value increases from local minima (pore bodies) to local maxima (grain interiors) topological features are tracked, and their "persistence" (the difference in distance values for which individual β features appear and vanish) is measured. For our analysis, a feature whose persistence is less than one unit in the voxel size is considered to be insignificant and merged with an adjacent feature. From this persistent homology

perspective, cavities (β_2 features) will appear in the SEDT as the level-set threshold value increases beyond the grain-pore space interface and local maxima (grains) become separated; the total number of β_2 features that have a persistence greater than one unit of distance provides an estimate for the number of topologically-relevant grains in the sample.

EULER CHARACTERISTIC

Before the Euler characteristic is calculated, a spanning cluster is extracted with a 6-connectivity check, so that dead pores, i.e. pores inside the grains, contribute neither to the total porosity nor the Euler characteristic. Euler characteristic and the Betti numbers are determined using pore-scale image processing software Mango [22].

LATTICE-BOLTZMANN SIMULATION OF SINGLE PHASE FLOW

The Lattice-Boltzmann model used here is the D3Q19 (3D lattice with 19 possible momenta components) in the Morphy software package [18, 23]. The single relaxation time (SRT) Bhatnager–Gross–Krook (BGK) model is used as the collision model. The boundary condition of the inlet and outlet is periodic boundary condition and fluid-solid boundary condition is bounce-back boundary condition. All of the simulations are performed on the Raijin supercomputer from National Computational Infrastructure (NCI). The average velocity is calculated from the velocity field and then used to determine permeability using Eq. 1.

2D VERIFICATION OF SCHOLZ'S MODEL

Figure 5a shows the numerically determined permeability (normalized by ${cl_c}^2$) versus the $(\phi - \phi_c)/(1 - \phi_c)$ according to Eq. 3 and Eq. 4. We can see that each q2D model follows a different trend when only porosity is considered. We also tested Scholz's model and found a relationship between $K/({cl_c}^2)$ and $(1 - \chi)/N_i$ that is similar to what is reported by Scholz *et al.* [5]. In Figure 5b, we can see that each q2D model collapses to a single relationship when the topology of the pore space is considered.
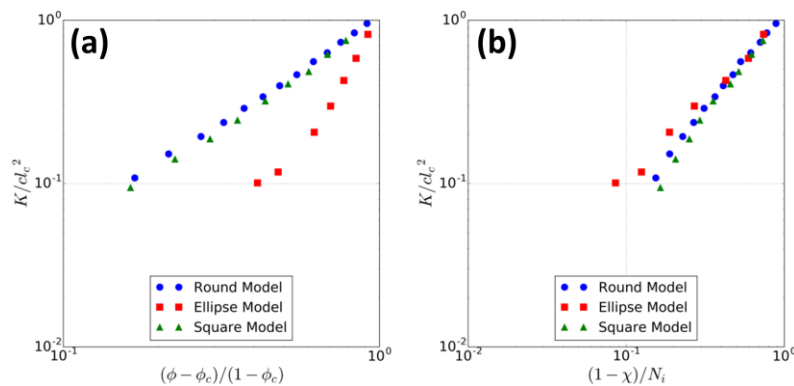

Figure 5: (a) $K/{cl_c}^2$ versus $(\phi - \phi_c)/(1 - \phi_c)$ for q2D models (b) $K/{cl_c}^2$ versus $(1 - \chi)/N_i$ for q2D models using Scholz's model

However, for the data presented in Figure 5b, N is an input parameter. For the practical application of this work, we need to measure N from the pore scale images. For this we test the weighted grain number (N_w) and persistent grain number approaches (N_p). In Figure 6 we show how the persistence model is able to partition the grains for the q2D models. It can be seen that for the spherical and square shaped grains the persistent homology approach appears to capture each grain element whereas for the ellipse grains when multiple ellipses overlap then additional grains are measured. Furthermore in Figure 7, we compare the input grain number (N_i) to the measured grain numbers for all three of the q2D models. We find that for the Ellipse Model, the best match in comparison to N_i is with N_w whereas N_p overestimates the number of grains. It appears that the persistent homology of the SEDT does not accurately identify overlapping grains with irregular oblong shapes. For the round and square models, both N_w and N_p produce lower grain number estimates than N_i at high grain density; the reason behind this is that in model generation the generated grains can overlap with each other but the grain number still adds to N_i. In all three cases, at low grain density the N_w and N_p are able to measure a grain number near N_i. However, as added grains start to overlap, the measured values depart from N_i.

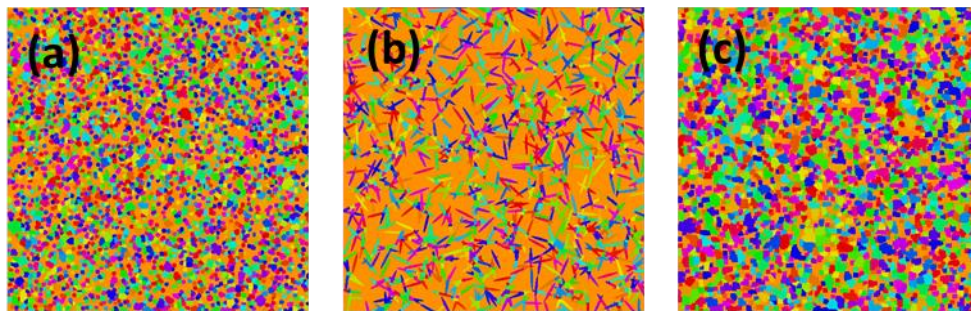**Figure 6:** Grain partition diagrams for (a) Round Model (b) Ellipse Model and (c) Square Model from persistence homology. Orange represents pore space and other colors are used to label individual grains.
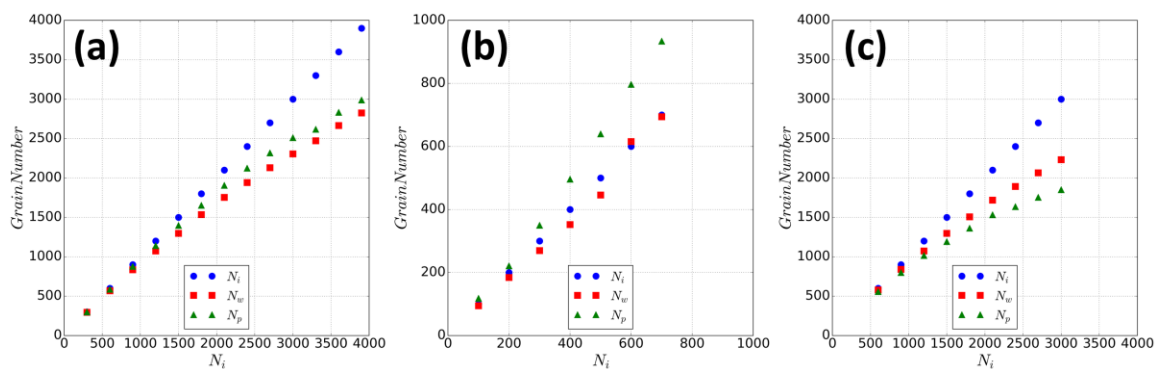
Figure 7: Grain number (input grain number, N_i; weighted grain number, Nw, and persistence grain number Np) versus input grain number for (a) Round Model (b) Ellipse Model and (c) Square Model.

The implication of these results is seen in Figure 8 where the universal relationship presented in Figure 5b (using N_i) no longer holds. At low grain density, we are able to measure a grain number that is consistent with N_i and thus the data collapses to a single relationship. However, as grain density increases, the datasets follow different relationships because the difference between the measured and input grain numbers starts to deviate. While this might not be an issue in real rock samples, because grains do not overlap as in our stochastically generated models, this could be an issue in rock types with irregular or oblong shaped grains.
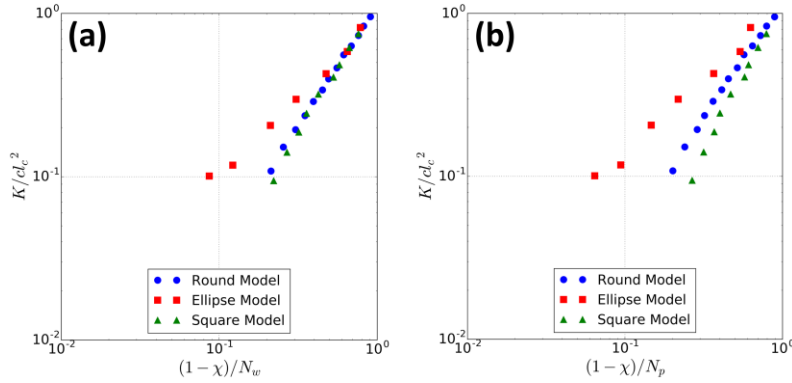
Figure 8: (a) K/cl_c^2 versus $(1-\chi)/N_w$ for q2D models (b) K/cl_c^2 versus $(1-\chi)/N_p$ for q2D models.

3D EXTENSION OF SCHOLZ'S MODEL

First we plot $K/(cl_c^2)$ versus $(\phi - \phi_c)/(1 - \phi_c)$ in Figure 9a. It can be seen that each dataset follows a slightly different scaling relationship. We also plot $K/(cl_c^2)$ versus β_1/N_p in Figure 9b according to Scholz's model. We use β_1 instead of $(1 - \chi)$ because in 3D the Euler characteristic is dominated by β_1, which best represents the connectivity, and we use N_p as the number of grains. Scholz's model does not seem to predict a single trend relationship between $K/(cl_c^2)$ and β_1/N_p. The reason for this can be explained in Figure 10. Intuitively, and as described in the introduction, as $\phi \to 1, \frac{K}{(cl_c^2)} \to 1$, and as $\phi \to 0, \frac{K}{(cl_c^2)} \to 0$-; thus, the same limits will apply to any topological metrics describing permeability. We observe that these limits apply for $(1 - \chi)/N_p$ in 2D, however, this does not occur for $\frac{\beta_1}{N_p}$ in 3D.
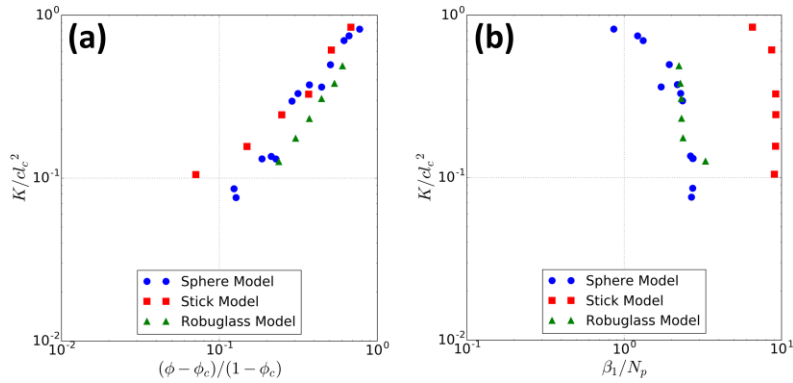
Figure 9: (a) $K/cl_c{}^2$ versus $(\phi - \phi_c)/(1 - \phi_c)$ for 3D models (b) $K/cl_c{}^2$ versus β_1/N_p.
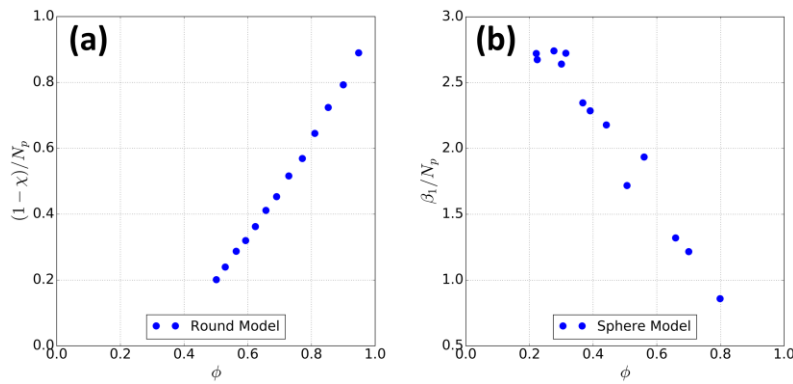
Figure 10: Euler characteristic versus porosity, (a) 2D Round Model (b) 3D Sphere Model.

Noting that the variable N_p perhaps does not fully describe the resistance to flow in 3D, we incorporate the void ratio e, which is equal to $\phi/(1 - \phi)$. When we plot $\beta_1/N_p \times e$ versus porosity, we can generate a trend similar to that observed for the 2D systems, compare Figures 10a and 11a. We plot $K/(cl_c{}^2)$ versus β1/Np*e in Figure 11b and find that all 3 datasets provide very similar scaling relationships, i.e. the slope of each line is similar. The curves could be collapsed to a single relationship by adjusting the constant parameter c; however, at this time we cannot justify the physical significance of this.
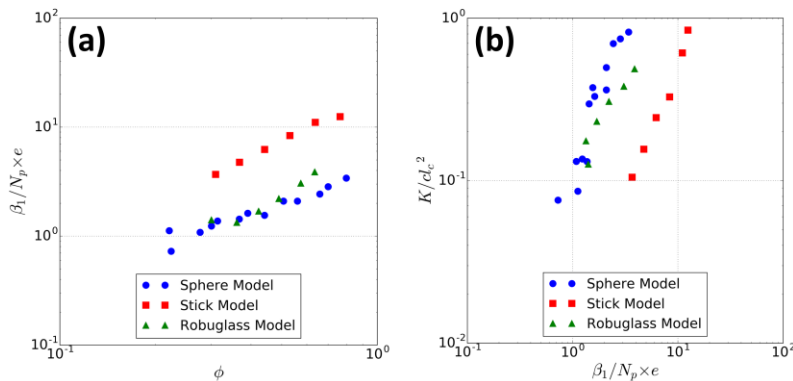
Figure 11: (a) $\beta_1/N_p \times e$ versus ϕ for 3D models (b) $K/cl_c{}^2$ versus $\beta_1/N_p \times e$ for 3D models

CONCLUSION

We verify Scholz's model by simulating single-phase flow in generated q2D models. With regards to the grain number, we implement distinct methods to measure grain count and show that these methods compare well to the input parameter from stochastically generated media when the number of overlapping grains is low. We then extend Scholz's model by simulating single-phase flow in 3D porous media, and we find that by adding a new parameter, the void ratio, the modified Scholz's equation is able to provide a similar scaling exponent for all of the tested models.

ACKNOWLEDGEMENTS

REFERENCES

1.   H. Darcy, *Les fontaines publiques de la ville de Dijon: exposition et application*, Victor Dalmont, (1856).
2.   P.C. Carman, *Flow of gases through porous media*, Academic press, (1956).
3.   D. Tiab and E. Donaldson, "Petrophysics, Theory and practice of measuring reservoir rock and fluid transport properties, Gulf Publ," *Co., Houston, Texas*, (1996), 205-220.
4.   A. Katz and A. Thompson, "Quantitative prediction of permeability in porous rock," *Physical review B*, (1986) **34**, 11, 8179.
5.   C. Scholz, F. Wirner, J. Götz, U. Rüde, G.E. Schröder-Turk, K. Mecke and C. Bechinger, "Permeability of porous materials determined from the Euler characteristic," *Physical review letters*, (2012) **109**, 26, 264504.
6.   H.-J. Vogel, U. Weller and S. Schlüter, "Quantification of soil structure based on Minkowski functions," *Computers & Geosciences*, (2010) **36**, 10, 1236-1245.
7.   Z. Liu, A. Herring, C. Arns, S. Berg and R.T. Armstrong, "Pore-Scale Characterization of Two-Phase Flow Using Integral Geometry," *Transport in Porous Media*, (2017) **118**, 1, 99-117.
8.   R.T. Armstrong, J. McClure, M. Berill, M. Rücker, S. Schlüter and S. Berg, "Flow regimes during immiscible displacement," *Petrophysics*, (2017) **58**, 01, 10-18.
9.   R.T. Armstrong, J.E. McClure, M.A. Berrill, M. Rücker, S. Schlüter and S. Berg, "Beyond Darcy's law: The role of phase topology and ganglion dynamics for two-fluid flow," *Physical Review E*, (2016) **94**, 4, 043113.
10.   S. Schlüter, S. Berg, M. Rücker, R. Armstrong, H.J. Vogel, R. Hilfer and D. Wildenschild, "Pore-scale displacement mechanisms as a source of hysteresis for two-phase flow in porous media," *Water Resources Research*, (2016).

11.   A.L. Herring, E.J. Harper, L. Andersson, A. Sheppard, B.K. Bay and D. Wildenschild, "Effect of fluid topology on residual nonwetting phase trapping: Implications for geologic CO2 sequestration," *Advances in Water Resources*, (2013) **62, Part A**, 47-58.

12.   H.-J. Vogel, *Topological Characterization of Porous Media*, in *Morphology of Condensed Matter*, K. Mecke and D. Stoyan, Editors. 2002, Springer Berlin Heidelberg. p. 75-92.

13.   D. Wildenschild and A.P. Sheppard, "X-ray imaging and analysis techniques for quantifying pore-scale structure and processes in subsurface porous medium systems," *Advances in Water Resources*, (2012) **51**, January 2013, 217–246.

14.   S. Berg, H. Ott, S.A. Klapp, A. Schwing, R. Neiteler, N. Brussee, A. Makurat, L. Leu, F. Enzmann, J.O. Schwarz, M. Kersten, S. Irvine and M. Stampanoni, "Real-time 3D imaging of Haines jumps in porous media flow," *Proceedings of the National Academy of Sciences of the United States of America*, (2013) **110**, 10, 3755-3759.

15.   H. Dong and M.J. Blunt, "Pore-network extraction from micro-computerized-tomography images," *Physical review E*, (2009) **80**, 3, 036307.

16.   P. Mostaghimi, M.J. Blunt and B. Bijeljic, "Computations of absolute permeability on micro-CT images," *Mathematical Geosciences*, (2013) **45**, 1, 103-125.

17.   S. Chen and G.D. Doolen, "Lattice Boltzmann method for fluid flows," *Annual review of fluid mechanics*, (1998) **30**, 1, 329-364.

18.   C.H. Arns, M.A. Knackstedt and N.S. Martys, "Cross-property correlations and permeability estimation in sandstone," *Physical Review E*, (2005) **72**, 4, 046304.

19.   S. Berg, M. Rücker, H. Ott, A. Georgiadis, H. van der Linde, F. Enzmann, M. Kersten, R. Armstrong, S. de With and J. Becker, "Connected pathway relative permeability from pore-scale imaging of imbibition," *Advances in Water Resources*, (2016) **90**, 24-35.

20.   M. Rücker, S. Berg, R. Armstrong, A. Georgiadis, H. Ott, A. Schwing, R. Neiteler, N. Brussee, A. Makurat and L. Leu, "From connected pathway flow to ganglion dynamics," *Geophysical Research Letters*, (2015).

21.   O. Delgado-Friedrichs, V. Robins and A. Sheppard, "Skeletonization and partitioning of digital images using discrete morse theory," *IEEE transactions on pattern analysis and machine intelligence*, (2015) **37**, 3, 654-666.

22.   A. Sakellariou, C.H. Arns, A.P. Sheppard, R.M. Sok, H. Averdunk, A. Limaye, A.C. Jones, T.J. Senden and M.A. Knackstedt, "Developing a virtual materials laboratory," *Materials Today*, (2007) **10**, 12, 44-51.

23.   C. Arns, F. Bauget, A. Sakellariou, T. Senden, A. Sheppard, R. Sok, A. Ghous, W. Pinczewski, M. Knackstedt and J. Kelly, "Digital core laboratory: Petrophysical analysis from 3D imaging of reservoir core fragments," *Petrophysics*, (2005) **46**, 04.

MICROSTRUCTURAL INVESTIGATION OF STRESS-DEPENDENT PERMEABILITY IN TIGHT OIL ROCKS

Hubert King, Michael Sansone, Pavel Kortunov, Ye Xu, Nicole Callen[1]
Shreerang Chhatre, Hemant Sahoo, Antonio Buono[2]

[1] ExxonMobil Research & Engineering Company
[2] ExxonMobil Upstream Research Company

1. ABSTRACT

Recent studies on several core-plug scale samples from tight oil reservoirs have demonstrated that such rocks can exhibit a significant, irreversible permeability decline with increase in net confining stress. Because this effect closely follows the expected stress change during drawdown in the field, the origins of this phenomena as well as a method to predict the magnitude relative to different rock types is valuable information for reservoir management. To better understand this effect, we have undertaken a series of in situ studies that demonstrate how an external stress field translates to microscopic strain at the pore scale and couples to the fluid transport. These studies rely on the coordinated use of low-field Nuclear Magnetic Resonance (NMR) and X-ray Micro-tomography (XMT). Making use of labeled fluids to enhance contrast, we are able to directly resolve how local strains affect fluid transport throughout the core plug. In a similar manner, proton NMR resolves how stress couples to deformation of the various pore systems, affecting the fluid content and their dynamics. Together, these techniques indicate that internal, high-permeability pathways play an important role in the stress dependence. Matrix permeability is much less affected. These higher-permeability zones are not ubiquitous in tight-oil rocks. Characterizing these zones and relating them to mineralogy and rock fabric is an attractive pathway to greater predictability for stress-dependent permeability for reservoir rock types.

2. INTRODUCTION

Over the last few years, technological advances including horizontal drilling and hydraulic fracturing have enabled production of vast amounts of oil and natural gas from shale and tight rocks. Most of the hydrocarbon production from tight rocks is carried out via primary depletion, where rock and fluid expansion provide the necessary driving force. Due to the low permeability of the rock matrix, large changes in pore pressure are expected for regions close to propped hydraulic fractures during hydrocarbon production. While the pore pressure is expected to change significantly, the overburden pressure is expected to be largely invariant during production timescale. As a result, the net confining stress (NCS = overburden pressure – pore pressure) experienced by near-fracture region of the rock matrix is expected to change significantly.

Changes in NCS can alter the permeability for unfractured rocks, matrix for tight/shales, and natural fractures. It can also affect hydraulic fractures, both propped and un-propped. Impairment of flow properties were found to be a function of the magnitude of pressure drawdown and the pressure history (hysteresis) [1-4]. Deterioration of the flow capability of the near-frac region alters the expected drainage area around fractures. Therefore, pressure dependent rock properties could provide key inputs for reservoir development business decisions in terms of well spacing, frac stage spacing, draw-down rates etc.

3. SAMPLES
This work is focused on samples from the productive *Wolfcamp* formation in the Midland Basin in West Texas. However, comparisons with data from the literature[1] suggest similar behavior for other regions.

4. EXPERIMENTS
a.   Microscopy and Composition
The two samples differ in their mineralogy and texture. Sample A is a poorly sorted, calcareous conglomerate with intraclasts and shell fragment, with extensive development of early carbonate (calcite, dolomite) cements, and later microcrystalline quartz cement. Sample B exhibits a succession of intraclast-bearing, bioturbated medium and fine mudstones. Grains are silt-sized quartz and albite. The matrix is clay rich, with fine microcrystalline quartz cement.

b.   Steady State Permeability
Core plugs from the *Wolfcamp* formation from Midland Basin, West Texas were first scanned using a micro-computed tomography (µCT) with a resolution of about 15 µm, eliminating those with any fractures. Plugs were mounted in hydrostatic core holders, thoroughly evacuated, and pressure saturated with toluene. Pressure dependent permeability was measured by increasing the sleeve pressure for fixed pore pressure. The sleeve pressure was changed by applying a mineral oil. The reader is referred to our previous work[1] for detailed description of the experimental setup, and various steps undertaken to ensure complete saturation, dissolution of trapped gas, and avoidance of asphaltene precipitation. Stress creep behavior was observed in these samples, and the measurements were conducted for multiple weeks to ensure steady-state was reached.

c.   Nuclear Magnetic Resonance (NMR)
Following the steady state permeability evaluation, the same two core plugs were provided for NMR analysis. They were stress-free for approximately 1 month.

Plugs were mounted in a hydrostatic core holder and placed in the bore of a 2MHz NMR instrument (Maran-2 manufactured by Resonance Instruments). This NMR transparent core holder is equipped with a confining pressure capability (using pressurized NMR-invisible fluorinated fluid FC40) and a flow-through fluid handling system with precision Quizix pumps that control both pore pressure and flow-rate through the core plug. At low

confining pressure of 1,500 psig, toluene was pumped through the core plug, reaching saturation as confirmed by NMR.

The next step was to measure permeability with continuous flow under fixed pore pressure gradient (ΔP). Owing to the low permeability, we found that a high ΔP~1000 psi was necessary. Following this, we equalized pore pressure, ΔP=0, to ensure equal pre-saturation along the core plug for NMR measurements, and simultaneously increased confining and pore pressure to 4,500 psi and 3,500 psi, respectively, to achieve reference toluene saturation at initial NCS of 1,000 psi. Afterwards NCS was step-wise increased through reduction of pore pressure at fixed confining pressure to mimic downhole conditions during oil production. At each stress state, a waiting time of approximately 24 hours was utilized before beginning NMR measurements.

The NMR analysis consisted of T_2 relaxation decay collected using a typical CPMG pulse sequence with inter-echo time of 400 microseconds and repetition delay of 5 seconds. This well-known method provides total amount of fluid in the sample and allows us to separate signal from fluid in different pore or viscosity phases. The NMR signal was rigorously calibrated against several reference samples with a known amount of bulk toluene diluted in NMR-invisible deuterated toluene to fill a similar to core plug magnet volume. Careful calibration is key to measuring fluids for these low-porosity rocks.
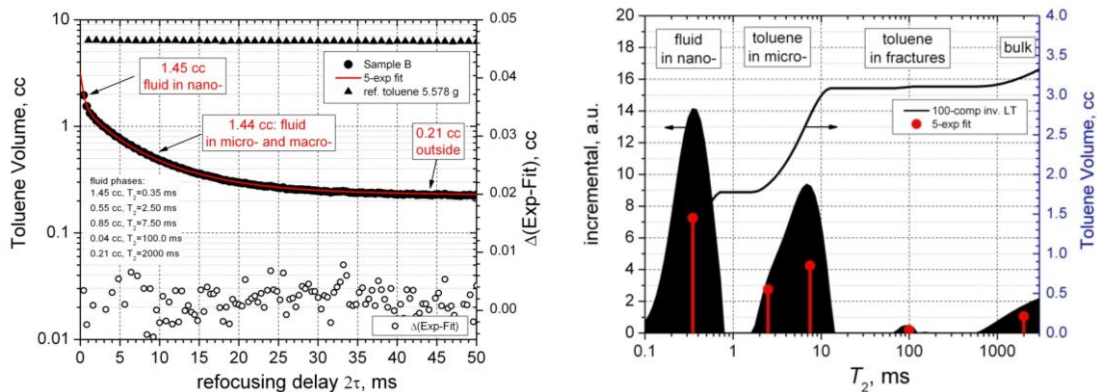
Figure 1. Fluid saturation analysis using NMR measurements: raw NMR signal calibrated against known amount of toluene fitted with sum of five exponential decays (left), inverse Laplace transformation of calibrated NMR signal (right)

Analysis of NMR data was performed by direct fitting raw T_2 relaxation decay curves with a fixed number of exponential decays, usually five, with pre-exponential factors proportional to amount of fluid in a corresponding phase (Fig. 1 left). Determined T_2 values are interpreted as the following fluid phases: fluid in nanopores or heavy hydrocarbons $T_2 < 1$ ms, toluene in micropores 1 ms $< T_2 < 20$ ms, toluene in macropores and/or fracture 50 ms $< T_2 < 100$ ms, bulk toluene outside of core plug $T_2 \sim 2400$ ms. Although inverse Laplace transformation (LT) provides an appealing visual interpretation of T_2 spectrum (Fig. 1, right). The inverse transformation can be significantly altered by

small changes in a few points. We use inverse LT to guide selection of relaxation times, relying on the amplitudes of the exponential fits to quantify amounts.

d. XMT

Plugs were mounted in a hydrostatic core holder and placed in a specialized liquid/gas feed assembly for use on an XTEK X-ray Tomography device. The X-ray device uses a polychromatic source which irradiates the sample with fan-beam geometry. The source and detector area are fixed and are diametrically opposed on a line going through the cylindrical sample center. Rotation of the sample about its long axis provides the data necessary for 3-D tomographic reconstruction. An important modification to this core holder is a rotary tubing tensioner that allows full rotation of the sample while controlling the confining pressure and pore pressure. With the option of applying ΔP across the sample, this device can measure permeability while simultaneously imaging the in situ fluid movement.

The samples were prepared for analysis by ensuring the pore space was empty. This was typically accomplished through evacuation, although some as-received plugs were also found to be nearly fluid free. Fluid filling was evaluated through NMR analysis.

At the beginning of experiments, a base image of the sample, with empty pores, was made to evaluate the internal structure. Typical 3-D data collection for these would consist of 2500 angle views. Following application of a beam-hardening correction, a standard reconstruction algorithm was applied. Standards inserted in small pits in the sample guide calibration of the linear attenuation coefficients. This results in a 3-D volume image at a native resolution of 30-35 µm per voxel.

Evaluation of the transport in the sample was made through use of an imaging gas. For this, we utilized xenon at elevated pressures. In the pressure range above about 75 psi, xenon exhibits an X-ray attenuation comparable to the mineral matrix.

Imaging time-dependent structures, especially those consisting of both fast and slow regimes, required that we utilize a specialized data collection. For-rapid data collection, we use 2-D data taken at a fixed, "Key Angle". Here, we rotationally select an end-on view of parallel bedding planes. For longer-times and slow regimes we utilize a locally-created "Sorted Golden Angle" data collection. Small sub-sets of the data (~10 hours) can be utilized for 3-D tomographic reconstruction following long-term structural changes that occur over several days. All data are corrected to place them on an absolute scale, allowing quantitative analysis of linear attenuation.

The stress protocol followed for these samples is as follows: Change the confining stress, wait a fixed time (~ 1 week), measure permeability and image flow, repeat. The fast permeability, perm-streak, is determined through measurement of the pressure decay for an instantaneous xenon gas pressure increase. Imaging of the associated gas movement is made through "Key Angle" data. At later times, we utilize imaging to follow the much slower diffusion of xenon from the high-perm streaks into the matrix.

5. RESULTS AND DISCUSSION

a. Permeability Results and Discussion:

The *Wolfcamp* formation in the Midland Basin of West Texas represents one of the largest hydrocarbon accumulations discovered to date in the United States. According to USGS, the *Wolfcamp* interval contains about 20 billion barrels of oil, 16 trillion cubic feet of associated natural gas, and 1.6 billion barrels of natural gas liquids.[5] The *Wolfcamp* interval is hundreds of feet thick, and has significant variability in terms of in situ pore pressure, mineralogy, clay content, porosity, and total organic carbon (TOC). Quantification of mechanical and flow properties for such heterogeneous interval could provide key inputs in optimal development and depletion of hydrocarbon resources. An example of rock heterogeneity observed in the *Wolfcamp*, is the steady-state liquid permeability for Samples A and B, core plugs from the same well.

Pressure dependent permeability experiments were conducted at two NCS conditions – (1) NCS = 1,500 psi corresponding to in situ NCS and (2) NCS = 5,500 psi corresponding to a drawdown of 4000 psi. The extrapolated steady-state values at higher NCS were normalized using corresponding permeability values at lower NCS. The ratio is plotted in Fig. 2.
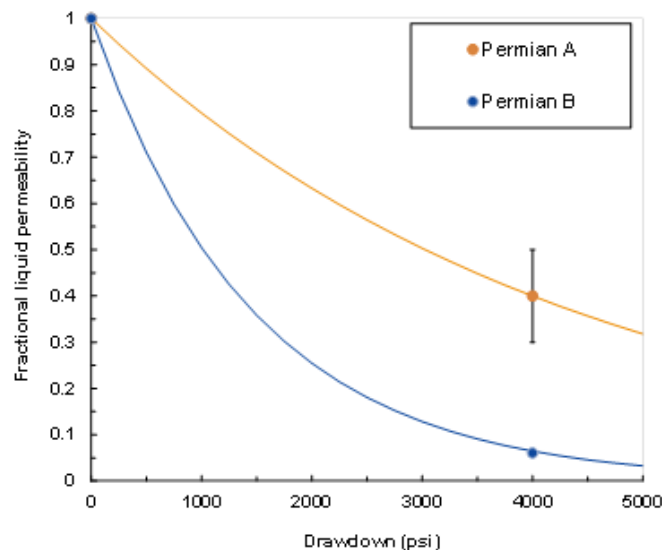
Figure 2. Pressure dependent permeability for two core plugs from *Wolfcamp* are plotted against drawdown assuming the in situ NCS is 1500 psi for this interval. Results here are comparable with those previously published[1], showing a low (Sample A) and high (sample B) stress response. Following that previous work, we describe these responses through use of an exponential function, details of the fit parameters given in the text.

An exponential model provides a good fit to pressure dependent permeability.[1,2] Even though we conducted permeability measurements at only two NCS for these samples, that

experience gave us confidence to use an exponential model. The fractional liquid permeability at an elevated NCS is modeled using the following relationship, and the impairment of permeability is characterized in terms of the permeability exponent "γ."

$$\frac{k}{k_i} = e^{-\gamma(NCS-NCS_i)} \tag{1}$$

where k_i and NCS_i, are respectively the initial permeability and net confining stress.

Sample A (plotted in orange) has lower steady-state permeability ~50 nD at NCS = 1,500 psi, and the permeability declines to ~20 nD at NCS = 5,500 psi. On the contrary, sample B (plotted in blue) has higher permeability of ~990 nD at NCS = 1,500 psi, but the permeability severely declines to ~60 nD at NCS = 5,500 psi. Clearly, sample B displays significantly more pressure dependent permeability than sample A, as shown in Fig. 2. The resulting permeability exponent for sample B is $6.8\pm0.01 \times 10^{-4}$ /psi, which is significantly higher than the permeability exponent for sample A of $2.3\pm0.2 \times 10^{-4}$ /psi.

Data reported in our previous publication [1] on *Vaca Muerta* are similar. It is clear that the level of stress dependence is similar for the 2 plugs of Permian *Wolfcamp* to that of the samples from *Vaca Muerta*. However, *Wolfcamp* and *Vaca Muerta* are very different shale plays in terms of location, age, mineralogy, environment of deposition etc. Therefore, such similarity in pressure dependency is surprising.

Motivated by this finding, we utilize various techniques to probe pore-scale changes as a result of increased NCS, in order to explain the reasons behind pressure dependent permeability behavior observed on core plugs.

b. XMT Analysis of Micro-Structure
The images in Fig. 3 were reconstructed from 3-D XMT data collected on the core plugs at ambient pressure. Two cross-sections are shown: one through the mid-plane with the axis of cylindrical sample vertical and a second taken at the mid-point of the sample. The structures are strikingly different. Sample A, exhibits uniform porosity throughout with less severe stress-dependent permeability, and occasional pyrite inclusions, seen as highly-attenuating white blebs in Fig 3. Sample B, in contrast exhibits a strong variation in porosity, focused in planes running parallel to bedding, likely the result of local changes in sorting and particle size. Occasional dark streaks, low-attenuation features, are seen in the vertical cross-section. These features may be filled with low attenuation organic or could be open fissures, but they do not span the sample length. Because X-ray attenuation is calibrated, sub-voxel porosity is indicated by attenuation coefficients less than the mineral matrix. This, combined with in-situ xenon uptake and any subsequent increases in measured voxel attenuation coefficients enables identification of higher porosity regions in the rocks without spatially resolving sub-voxel pore structure.
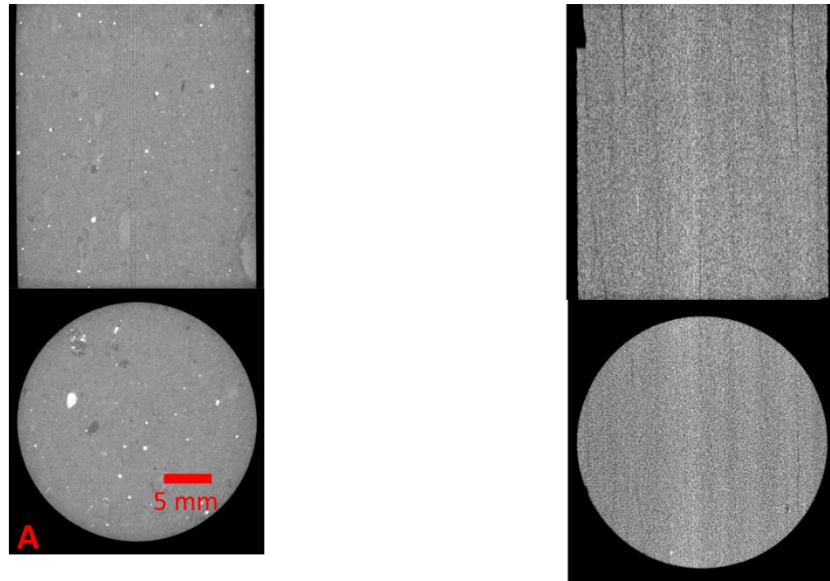
Figure 3. Cross-sections through 3-D reconstruction volumes of Samples A and B. Vertical section along core plug axis, horizontal section at mid plug. The samples are approximately 1 x 1 inch and the resolution of the native images is 30-35 µm per voxel. Sample B exhibits variable-porosity laminae parallel to vertically-oriented bedding planes. These features correlate with high-perm streaks.

c.   NMR Analysis of Stress Dependent Pore Structure

Following our protocol, we investigated how the NMR signal responded to changes in NCS. Similar to previous work[6], we find that the overall tendency is for the amount of fluid in the sample to decrease as NCS increases. However, not every pore size is equally affected. As is recognized, tight-oil T_2 spectra can typically be described by a few key relaxation times going from the shortest ~0.1 ms to longest ~2000 ms. Here, we find the relaxation times can be most efficiently described by five exponential decays. The shortest time we attribute to fluid (toluene or water) in nano pores or heavy hydrocarbons [7, 8], the next three are toluene in micro (best fitted by two components suggesting two types of micropores) and macro pores (which may indicate fractures). The longest-T_2 is for bulk toluene in distribution plugs and delivery lines. Signals from the three intermediate components are stress dependent. The changes can be tracked by comparing the calibrated signal level, as expressed by the amplitude of the exponential fit. The relaxation times themselves show little change, T_2 values for fluid in nano- and macro-pores as well as in the bulk do not change while T_2 values of fluid in micropores shows a slight tendency to decrease at higher NCS, suggesting a reduction of micropore size. Our precision in these measurements is enhanced because the core holder is immobile throughout all of the data collection. In addition, a large number of scans were collected, >30,000, resulting in a high signal/noise, >2000. With an approximate fluid volume of 3 cc, this corresponds to a small uncertainty, ~0.0015 cc.

Figure 4. Reduction of total and pore specific fluid filled porosity at increased NCS as measured by NMR on toluene saturated sample A (left) and B (right) expressed in absolute porosity (left axis) and relative porosity (axis) units.
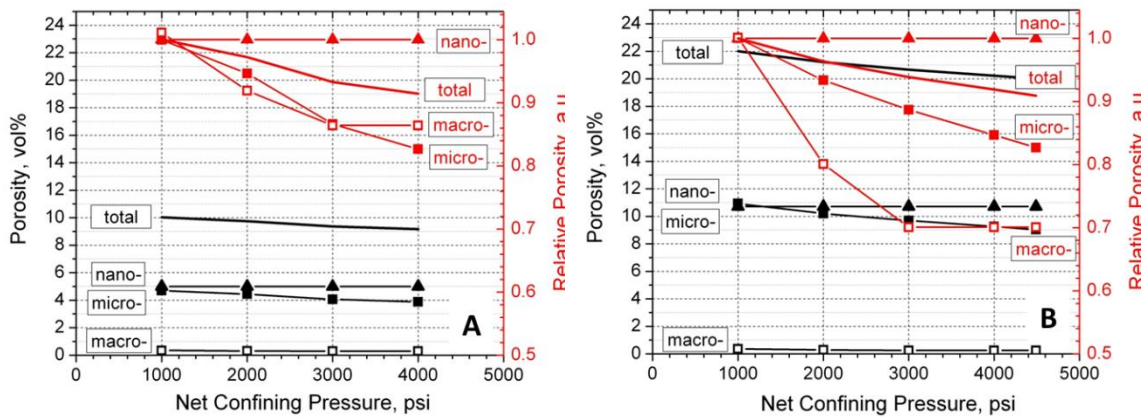
Initial permeabilities measured here are comparable to the initial values, respectively, of 50 nD and 990 nD. We observe reduction of fluid amount in both samples at higher NCS (and confirmed by collection of displaced fluid by Quizix pump), a reduction of pore volume and porosity. Although, the lower porosity sample A is somewhat less compressible, the percent change in total porosity is comparable for both (8% vs. 9%, Fig. 4) with majority of total porosity reduction caused by compression of micropores as they account for approximately half of total porosity. Focusing on behavior of the specific pore systems of higher porosity sample B, we see that the largest percent change is for the macro pores (Fig 4, right), which could include any open fractures as well as the high-perm streaks. While macropore porosity is small (0.34 vol% and 0.36 vol% for samples A and B), the macropore volume decrease by 14% and 30% for samples A and B may be a driver for the strong permeability response. Note how this change occurs over a narrow NCS range of 1,000-3,000 psi and then saturates, perhaps indicating partial closure for high-perm zones. Nevertheless, continuous compression of the micro pores is also observed in both samples and results in approximately 18% reduction of absolute micropore volume, which may also contribute to overall fluid transport through the rock. The component with $T_2 < 1$ ms is the only fluid phase insensitive to NCS. This fluid might be located in either less compressible cemented (nano-) pores of matrix or characterized as a low mobility material (heavy hydrocarbons, bound water, etc.). Given this phase contains approximately half of detected fluid in the rock and might contain valuable hydrocarbons, we continue to study the nature and dynamic behavior of this phase.

d. XMT Analysis of Transport and Structure
Following our protocol, we mounted a companion sample, B2, exhibiting similar structure and porosity to Sample B. NMR evaluation showed the sample pore space was essentially empty. This sample was subjected to 1500 psi confining stress and a full 3-D structure was determined. Layers of high and low porosity were identified, with no visible fractures.
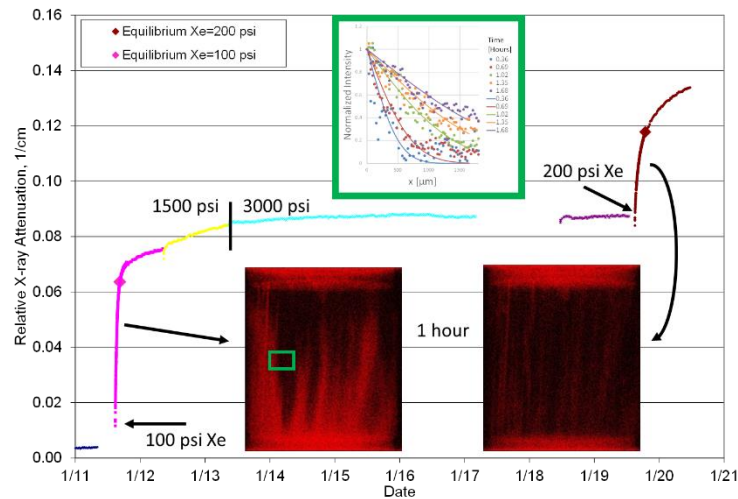
Figure 5 Time transcript of volume-averaged sample attenuation due to xenon flow into the core plug. Data were taken in projection through the cylindrical sample, excluding the porous frits above and below the sample. The individual data points were obtained from image analysis of over 1700 individual frames. Inserts show two of those frames taken one hour after increasing the xenon pressure. Early-time transport is dominated by xenon in high perm zones, and analysis of ΔP yields permeability. Areas adjacent to the high-perm zones fill more slowly. Analysis of xenon concentration, as shown in inset, yields matrix permeability.

The confining stress was maintained at 1500 psi for one week, at which time 100 psi xenon gas was introduced. "Key Angle" scans were initiated prior to gas infusion and by subtracting those initial reference images we obtain a real-time image of the xenon transport. As is clear in Fig. 5, initial transport is concentrated along zones which parallel bedding. The 3-D structure suggests that these high-perm streaks are planar features. After a short time, marked by the solid diamond equilibrium point in the figure, pressure across the sample equilibrates. Further xenon transport is now associated with matrix filling and this proceeds much more slowly. We followed a similar protocol for 3000 psi confining stress. During the 1 week waiting period, the sample attenuation (a measure of xenon content), seems to decline very slightly. 3-D data were reconstructed into 3-D volumes and analyzed for strain, but it was below our detection limit of 2×10^{-3}. At the end of this period, the xenon gas pressure was again increased (to 200 psi), difference images for "Key Angles" (obtained by subtracting reference images at 100 psi) show similar high-perm streaks as at lower stress. This is significant, since we would have expected open fractures to have closed by 3000 psi confining stress.[2] Pressure equilibration occurs rapidly (minutes) followed by slower (hours) matrix filling.

Using conventional pressure jump analysis, we obtain the early-stage sample permeability. Utilizing transport equations for a compressible gas flowing from a fixed upper pressure into a bottom reference volume (several times larger than the pore volume), we obtain the sample permeability. Evaluating the Klinkenberg correction for xenon is problematic, as there are no reported values for the constant, b. Here we used the

N_2 values modified slightly to account for the difference in mean free path between the two molecules. The values applied are b= 100 and 200 psi for 1500 and 3000 psi confining stress. At NCS= 1400 and 2800, permeabilities are 15000±1000 and 3500±500 nD. These values are higher than for sample B, but with transport controlled by the high-perm streaks, it is most likely they are present at a slightly higher density of such features in sample B2. The decline in permeability with NCS is similar for both toluene and xenon transport.

To measure matrix transport we employ the linear relationship between X-ray attenuation and xenon concentration. Careful attention to data collection and processing ensures that the attenuation data are all referenced to a common baseline. We can then use the spatially-resolved change in attenuation with time to measure local xenon concentration. Concentration profiles are analyzed using an assumption of diffusion from a planar source of constant concentration. An example is shown in Fig. 5, with a typical value for diffusion of D=1 x 10^{-6} cm^2/s. To calculate the matrix permeability we utilize the familiar pressure diffusion equation $= D\mu/B$, where the bulk modulus B for a gas is simply the pressure and the viscosity, μ= 2.3 x10^{-5} Pa s, from NIST[9]. At NCS= 1400 and 2800 psi, the resulting permeability values are k= 0.81±0.6 and 0.78±0.6 nD. Consistent with expectations, these are considerably smaller than the perm-streak values, and they show no significant variation with stress. We also analyzed the volume-averaged sample attenuation, obtaining similar values.

6. SUMMARY
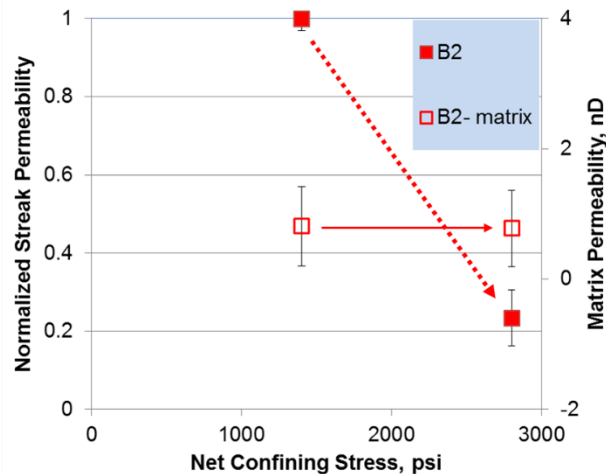
Figure 6. Summary of transport measured via XMT analysis. Solid symbols, showing significant stress dependence, are permeability values associated with perm-streaks The open symbols are for matrix permeability and show no stress response within experimental uncertainty.

The results here show that with changing NCS the NMR-measured micro and macro porosities change, whereas nano porosity is unchanging. We acknowledge that artifacts can be introduced based on workflow (steady-state perm -> NMR -> microCT), and

irreversible hysteresis. There may have been material changes in the microstructure during coring/ surfacing/ handling operations. However, if only the matrix permeability is intrinsic to the rock, our results suggest no stress dependent permeability would occur. We compare those observations to the XMT results showing that perm-streak permeability is affected by changing NCS but not that of the matrix. Transport is highly sensitive to pore-throat changes. With no changes for matrix transport nor for NMR nano porosity, these quantities appear arise from the same structures. This same logic implies that both the NMR micro and macro pores are part of the high perm streak. XMT data support this conclusion. Fig. 5 shows that comparison of the linear attenuation change before equilibrium (perm streak) with that afterwards (matrix) suggests that about 75% of the volume is in the perm-streaks with the remainder in the matrix. NMR analysis is in rough agreement, with about 50% of the volume in micro plus macro pores. With the permeability so strongly affected in Sample B, and an associated sharp change in NMR macro porosity, it is likely those pores which control permeability.

Others have suggested that stress dependent permeability arises from compression of high-perm regions, for example Rydzy et al.[2]. Their analysis found a similar power law behavior for permeability vs. NCS, as first reported by Chhatre et al. [1]. However Rydzy et al. attributed this to fracture closure, with fractures being a probable artifact of exhumation of the core plug.. In conventional rocks, fracture closure effects on permeability are well known. There, permeability of the matrix is investigated by first applying sufficient stress to close fractures.[10] As expected for a stiff rock matrix with an open aperture, fracture closure occurs at low stress, and this leads to a substantial change in permeability[11, 12]. Afterwards the intrinsic matrix permeability is observed. The circumstances for tight oil samples seem distinctly different. The stresses required to alter the permeability are considerably higher. Also, there is a distinct ductile strain component, evident in the long times to reach equilibrium for steady-state permeability. Finally, the high-stress permeability remains larger than the matrix permeability. This suggests a more complex strain phenomena.

7. CONCLUSIONS
- Pressure dependent perm can be characterized accurately
- NMR studies indicate
    - Three distinct grouping of the peaks in the T_2 spectra which are speculated to represent nano, micro and macro pores
    - The three kinds of porosity have different response to increases NCS
- XMT studies indicate the differences between the two Permian samples in terms of the presence of high perm streaks
    - Effective transport properties along and perpendicular to the streaks can be calculated using diffusion of Xenon
    - Response of transport properties with increasing stress is different for the streaks vs inherent matrix

8. ACKNOWLEDGEMENTS

9. REFERENCES

1. Chhatre, S.S., et al., *Steady-State Stress-Dependent Permeability Measurements of Tight Oil-Bearing Rocks.* Petrophysics, 2015. **56**(02): p. 116-124.
2. Rydzy, M.B., et al. *Stressed Permeability in Shales: Effects of matrix compressibility ad fractures – A step towards measuring matrix permeability in fractured shale samples*. in *International Symposium of the Society of Core Analysts*. 2016. Snowmass, CO.
3. Martin, J.A.Q. and D. Devegowda. *Modeling-Based Recommendations for Drawdown Management in Liquids-Rich Shale Wells*. 2015. Unconventional Resources Technology Conference (URTEC).
4. Devegowda, D. *Modelling Based Recommendation for Choke Management in Shale Wells*. in *Unconventional Resources Technology Conference*. 2015. Society of Petroleum Engineers.
5. USGS. *https://www.usgs.gov/news/usgs-estimates-20-billion-barrels-oil-texas-wolfcamp-shale-formation*. 2016.
6. Dick, M., et al. *Understanding Fractures and Pore Compressibility of Shales using NMR*. in *Internatonal Symposium of the Society of Core Analysts*. 2016. Snowmass, CO.
7. Kausik, R., et al., *NMR relaxometry in shale and implications for logging.* Petrophysics, 2016. **57**(04): p. 339-350.
8. Washburn, K.E. and J.E. Birdwell, *Updated methodology for nuclear magnetic resonance characterization of shales.* Journal of Magnetic Resonance, 2013. **233**: p. 17-28.
9. Lemmon, E., M. McLinden, and D. Friend, *Thermophysical Properties of Fluid Systems*, in *NIST Chemistry WebBook, NIST Standard Reference Database Number 69*, P. Linstrom and W. Mallard, Editors. 2015, National Institute of Standards and Technology: Gaithersburg MD.
10. Zhu, W. and T.f. Wong, *The transition from brittle faulting to cataclastic flow: Permeability evolution.* Journal of Geophysical Research: Solid Earth, 1997. **102**(B2): p. 3027-3041.
11. Brace, W.F., J. Walsh, and W. Frangos, *Permeability of granite under high pressure.* Journal of Geophysical research, 1968. **73**(6): p. 2225-2236.
12. Pyrak-Nolte, L. and J. Morris, *Single fractures under normal stress: The relation between fracture specific stiffness and fluid flow.* International Journal of Rock Mechanics and Mining Sciences, 2000. **37**(1): p. 245-262.

UNLOCKING THE POTENTIAL WITHOUT FRACKING – CO$_2$ INJECTION IN TIGHT SHALE OIL

Arthur U. Rognmo, Sunniva B. Fredriksen and Martin A. Fernø
Dept. of Physics and Technology, University of Bergen, Norway

ABSTRACT

We present laboratory results on the feasibility of CO$_2$ injection to produce oil from tight shale oil without fracturing the formation. The hybrid process studied increased recoverable oil by an order of magnitude compared with fracking, and at the same time reduced the carbon footprint by associated CO$_2$ storage. Despite permeability values in the nano-Darcy range, we argue that CO$_2$-based EOR may successfully be implemented in shale oil formations. Core flooding injection tests showed a viscous dominated oil displacement for the initial oil recovery, changing into progressively more diffusional dominated over time. An average oil recovery of 34% of OOIP was obtained from CO$_2$ flooding experiments in reservoir core plugs. The experimental results demonstrate the potential to 1) increase oil recovery from shale oil compared with current production techniques, 2) reduce the need to rely solely on fracking to extract oil from tight shales, and 3) reduce the carbon footprint when combining oil recovery with CO$_2$-storage in un-fractured shale core plugs.

INTRODUCTION

Worldwide energy demand is ever increasing and relies heavily on fossil fuels to provide energy security for the world in the years to come [1]. The last decade's geopolitical focus on decreasing the adverse environmental impacts caused by climate change illustrate the quandary faced by the world leaders; increase economic growth and human prosperity [2, 3] or decrease the concentration of greenhouse gasses in the atmosphere. Efforts to reduce CO$_2$ emissions must include the energy sector, as it is responsible for 60% of the global anthropogenic CO$_2$ emissions [4]. Sustainable supply of affordable and reliable energy urges a relentless focus on energy efficiency to ensure a prosperous future. Economic incentives from utilizing CO$_2$ after capture shifts the focus from pure Carbon Capture and Storage (CCS) to the Carbon Capture Utilization and Storage (CCUS) technology. A successful implementation of CCUS technologies reduces the carbon footprint from the energy sector and have the potential to achieve close to zero emissions [5]. Recent studies indicate the potential for safe long-term storage of CO$_2$ in cap rock shales or in tight gas shales [6]. In addition to the potential for pore space storage, shales (unlike e.g. sandstone) have a large storage potential due to their high sorption capacities.

Shift to Unconventional

As production rates from mature conventional oil fields decline, the petroleum industry is increasing its exploration of unconventional resources, such as shale oil [7-9]. Estimates of technically recoverable reserves in shale oil formations constitutes 10% of global oil resources. Recent significant US production volumes illustrate the large potential in these sources [10]. With recovery rates between 3-7% of oil originally in place (OOIP), and 58 billion barrels of technically recoverable reserves in the US alone, the potential for enhanced oil recovery (EOR) is enormous [10].

Oil recovery from secondary and tertiary production in conventional reservoirs is dominated by waterflooding [7]. However, the implementation of water injection for EOR in unconventional tight reservoirs is less efficient due to the ultra-low permeability associated with matrix composed of micro- and nano-pores [11]. Despite challenges related to the inherently ultra-low matrix permeability in shale oil formations, extracted volumes are viable due to a combination of water injection, horizontal drilling and hydraulic fracturing [12, 13]. However, rapidly declining production rates are frequently observed, resulting in short well operation times; the well economic shut-down time are considerable shorter compared to conventional reservoirs [14]. Water is extensively used in fracking operations as it is readily available at low cost [15]. It is, however, not without controversy and challenges; water is reported to reduce hydrocarbon flow back to the surface [14]. This is associated with additional costs as the flow back water needs to be treated for chemicals and other contaminants. In addition, due to the immense increase in water demand in combination with periods of drought in some parts of the US, water availability issues have emerged. Also, water flooding as a secondary recovery mechanism it is not expected to be feasible for ultra-tight formations, mainly due to low injectivity.

The utilization of CO_2 for EOR is widely proven in conventional reservoirs and has been commercially applied for more than 40 years in the US. Favorable CO_2 properties at reservoir conditions promotes oil recovery, primarily by oil phase swelling, viscosity alteration, interfacial tension reduction and higher degree of crude oil miscibility, compared to other gasses. These conditions are also considered to be present in tight shale oil formations [16], but a comprehensive understanding of its underlying mechanisms is needed. EOR is a relatively new concept in tight oil reservoirs. To date, the reported experimental studies of EOR in tight shale oil focuses on utilizing fractures for contacting, displacing and transporting oil [17-19]. The presumption is that due to the inherently ultra-low permeabilities associated with these formations, conventional core analysis with pressure driven viscous oil displacement and transport is not possible. Hence, recovery relies on the concentration driven oil displacement from molecular diffusion in the fractures to the oil saturated matrix.

This paper presents results from a comprehensive experimental study on CO_2-EOR in reservoir shale oil core plugs, where a high differential pressure was applied. The accelerated effect of, and increased oil recovery from, viscous oil displacement was studied without fracking the formation. Results demonstrate the feasibility of utilizing

CO_2 flooding as a recovery mechanism in shale oil formations. Effects on oil recovery and rate of recovery from varying system length, pressure, time and oil composition were investigated.

MATERIALS AND METHODS

Core Material

Five cylindrical reservoir core plugs with 1" and 1.5" diameters and length of 1.5-2.5" were used, see Table 1. All core plugs were from a producing shale oil formation in the US, with different states of preservation: cores 1, 2 and 3 were considered restored-state cores (subjected to CO_2-injection tests and re-saturated with crude oil); core 4 and 5 were considered native-state upon arrival. All cores were received at ambient temperature and pressure and rock structure of each core was imaged with a medical X-ray computed tomography (CT) scanner located at Haukeland University Hospital. Variations in permeability (0.12 to 2.36 μD) and porosity (4.5 to 9.3%) were expected due to different extraction depths. The oil phase saturating the pore space for the different experiments was either n-Decane (mineral oil: MO) or a light North Sea crude oil (CO, American Petroleum Institute gravity 38) as listed in **Table 2**.

Table 1 – Characteristics of reservoir shale oil core plugs

Core ID	Length [cm] ± 2E-3 [cm]	Diameter [cm] ± 2E-3 [cm]	Porosity [%]	Permeability [μD]
Core 1	3.798	3.796	4.8	0.12
Core 2	3.923	3.796	4.5	0.74
Core 3	2.450	3.820	7.0	1.70
Core 4	5.150	2.520	9.3	1.85
Core 5	5.115	2.540	7.0	2.36

Oil Saturation Procedure

Re-saturating the core plugs with oil after each CO_2 flooding was necessary to perform repeated tests for increased statistical significance. Reproducible initial oil saturations were achieved prior to each experiment by submerging the core plugs completely in the selected oil phase (mineral oil or crude oil) in a high-pressure stainless steel accumulator. The saturation process lasted for four days, with a saturating pressure of 10 MPa for mineral oil and 20 MPa for crude oil. Based on weight differences before and after saturation, along with density of the oil, the OOIP was calculated.

Table 2: Fluid properties

Fluid	Composition	Density [g/cm^3]	Viscosity [cP]	Conditions		Fluid State
				Temperature [°C]	Pressure [bar]	
n-Decane	C$_{10}$H$_{22}$	0.727	0.848	25.0	1.0	Liquid
		0.734	0.952	25.0	100.0	Liquid
		0.709	0.610	60.0	100.0	Liquid
Crude oil	53 wt. % saturated HCs 35 wt. % aromatics 12 wt. % resins 0.90 wt. % asphaltenes	0.849	14.500	20.0	1.0	Liquid
		0.829	-	60.0	1.0	Liquid
Carbon dioxide	> 99.999 % CO$_2$	0.876	0.086	25.0	150.0	liquid
		0.927	0.098	25.0	220.0	liquid
		0.604	0.046	60.0	150.0	supercritical
		0.752	0.064	60.0	220.0	supercritical

Experimental Setup and Procedure for CO$_2$ Injection

The core plugs were installed in a horizontal biaxial Hassler type core holder (*CoreLab Hassler Type Core Holder*) with a Buna-N rubber sleeve, inside a heating cabinet. A net radial confining pressure of 6.0 MPa (870 psia) was applied during the pressurization period and increased to 9.0 MPa (1305 psia) above inlet pressure during the CO$_2$ flooding tests. A total of 14 injection tests on crude oil saturated core plugs were performed at 60°C (±0.5°C), with a constant differential pressure drop of 7.0 MPa (1015 psia) and an inlet line pressure of 22.0 MPa (3190 psia). Hence, the volumetric injection rate varied depending on the fluid flow capacity of the particular core plug and oil was displaced from inlet towards outlet. Four injection tests were performed using n-Decane saturated core plugs with a lower inlet pore pressures (17.0 MPa – 2465 psia) and at 25°C, other properties being equal. The experimental setup is shown in Figure 1. The effluent fluids were cooled by a water based heat exchanger located downstream the back pressure regulator (*Equilibar HC276-5*), measured at ambient conditions (20°C and 1 bar). A camera and an image software with a time-lapse function was used to calculate oil recovery as a function of pore volumes (PV) CO$_2$ injected. Permeabilities were calculated from parameters obtained at steady state conditions, i.e. all recoverable oil was produced. It is therefore reasonable to assume CO$_2$ to be the only flowing phase in the core plugs, and by correcting for viscosity and density differences across the core, the end point effective permeability for CO$_2$ was obtained. The cores were not wrapped in an impermeable barrier (like Aluminum- or Nickel-foil), a common procedure to prevent CO$_2$ from permeating the core sleeve. Access to a new methodology to explicit track CO$_2$ with positron emission tomography [20], revealed that the injected CO$_2$ bypassed the

core, even with a net confinement pressure of 9MPa, when a foil was used. We speculate that small folds and creases in the foil caused minute flow paths for the CO_2 – preferred over the pore space of the tight shale oil samples. All reported injection tests are therefore performed without foil in this work.
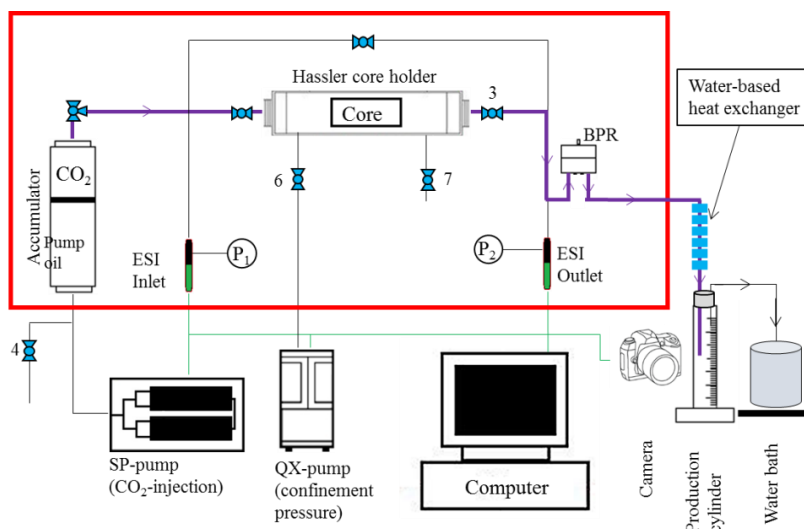

Figure 1: Schematic illustration of the experimental setup used for EOR by supercritical CO_2-injection in tight shale oil reservoir core plugs. Purple lines illustrate injection and production flow paths; arrows indicate flow direction. Green lines illustrate digital information cables from pressure transducers, pumps and camera; connected to a computer for processing and analysis. Black lines illustrate remaining tubing. The heating cabinet is represented by the thick red rectangle.

RESULTS AND DISCUSSION

The main message communicated in this paper is that CO_2-EOR effectively displaced oil during differential pressure driven fluid flow in ultra-tight liquid shales (see Figure 2). Fractures were not introduced before or during the flooding tests, and oil was displaced from the injector (inlet) to the producer (outlet), driven by the pressure gradient over the core. Oil recoveries for all experiments are plotted as recovery factor (R_f) in % of OOIP as a function of PV CO_2 injected, where the starting point was set as the time where the first drop of oil was recorded. Based on repeated CO_2 end-point effective permeability measurements fluid flow potential in the core plugs did not change after each successive CO_2 injection process. Superficial velocities (obtained from permeability measurements at endpoint effective CO_2 permeability) ranged from 0.2 – 2.1 ft/day for the five cores.

CO_2-EOR in Tight Shale Oil

Recovery profiles for four CO_2 floods in crude oil saturated core plugs are shown in Figure 2. The slopes of the recovery profiles indicate the recovery rates, where the highest rate is observed in the early stages of the CO_2 flooding with a progressively decreasing rate of recovery over time. This behavior indicates that the oil displacement became more dominated by molecular diffusion (the spontaneous mixing of miscible fluids due to random motion of molecules down its concentration gradient) over time.

The recovery profiles suggest poor sweep efficiency and early CO_2 breakthrough from CO_2 channeling. The CO_2 was not first-contact miscible with the crude oil, hence, a longer transition zone for development of multi-contact miscibility is needed [21].

Table 3: Key parameters during liquid and supercritical CO_2 injections. Oil saturating the pore space is either n-Decane mineral oil (MO) or a light North Sea crude oil (CO).

| Core ID	Injection ID	Oil phase	Temperature [°C]	Final recovery factor [%]	OOIP [mL]	Final average recovery factor [%]
Core 1	A	CO	60	98.3	1.63	
Core 1	B	CO	60	25.1	1.59	52.7
Core 1	C	CO	60	34.7	1.87	
Core 2	A	CO	60	22.7	1.54	
Core 2	B	CO	60	29.1	1.54	28.1
Core 2	C	CO	60	32.4	1.54	
Core 3	A	CO	60	26.8	1.68	26.1
Core 3	B	CO	60	25.4	1.97	
Core 4	A	CO	60	31.6	1.42	
Core 4	B	CO	60	7.1	1.41	19.8
Core 4	C	CO	60	20.7	1.21	
Core 5	A	CO	60	28.3	1.41	28.3
Large	A	CO	60	55.3	5.07	55.3
Core 1	A	MO	60	60.0	1.58	
Core 3	A	MO	25	73.2	1.84	
Core 3	B	MO	25	81.0	1.79	68.0
Core 3	C	MO	60	57.7	1.73	
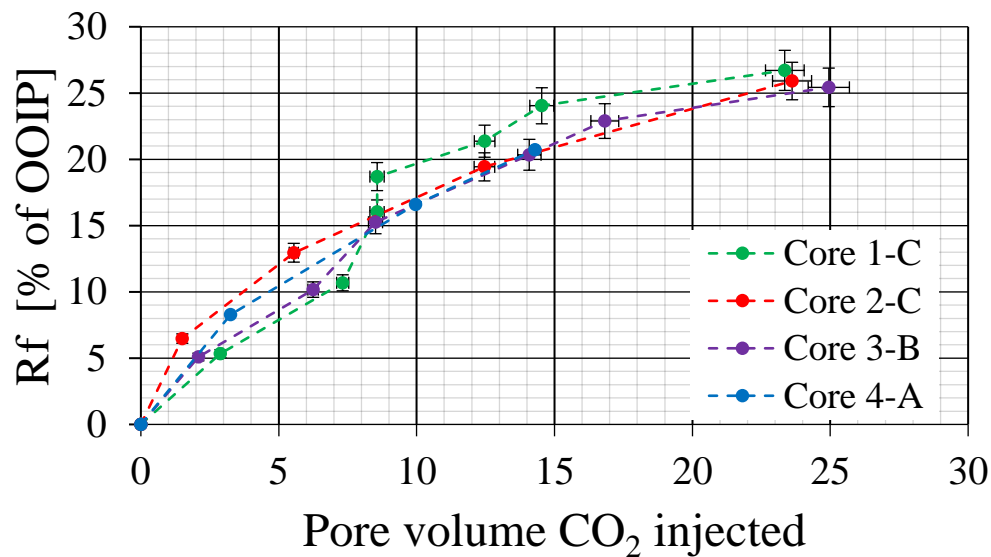
Figure 2: Recovery factor (% of OOIP) vs. time (pore volumes CO_2 injected) for four CO_2-EOR flooding tests in tight shale oil reservoir core plugs, saturated with crude oil. Filled circles indicate measured values. The main observation is that conventional CO_2-EOR can extract fluids from, and flow through, un-fractured tight shales, despite nano-Darcy permeability range.

Effect of Oil Composition

To investigate the effects of first-contact miscible displacements the saturation fluid was changed to mineral oil. This enabled quantitative evaluation of the displacement process and recovery rate. A one-component mineral oil was used (n-Decane) for the oil phase and four first-contact miscible CO_2 flooding tests were performed, at 60ºC and 25ºC. The oil recovery profiles showed an improvement in both final recovery and rate of recovery compared to multi-contact miscible displacements (cf. Figure 3).
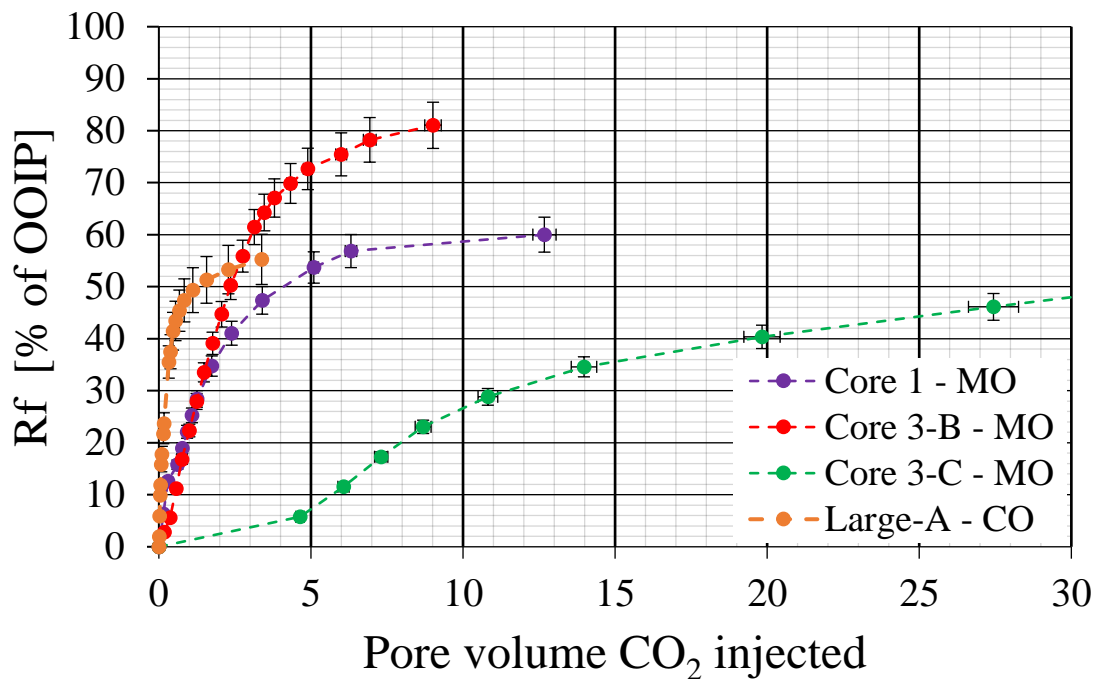

Figure 3: Recovery factor (% of OOIP) vs. time (pore volumes CO_2 injected) for four first-contact miscible CO_2-EOR flooding tests in tight shale oil reservoir core plugs. Core 1-A-MO and 3-C-MO are performed at 60°C and Core 3-A-MO and 3-B-MO are performed at 25°C. The points are measured values and a linear production as function of CO_2 injected from one point to the next is assumed. The graph display fast recovery in the beginning and gradually slower rate of recovery. Note the x-axis has been cropped at 30 PVs injected, final recovery Core 3-C-MO is 57.7 % of OOIP (± 3.2 % of OOIP) at 41.5 PVs (± 1.2 PVs) injected.

Effect of System Size

A larger system (see Table 3 for key properties) was obtained by placing three cores in succession to study the impact of system size on displacement efficiency. Increased length was expected to promote the development of miscibility between injected CO_2 and crude oil by increasing the transition zone length [21]. Two flooding test were performed at 60°C and 7.0 MPa (1015 psia) differential pressure. One flooding test was performed for 3.6 days, yielding a CO_2 injection of 0.18 PVs. Visual inspection of the three cores

showed development of viscous fingers and CO_2 flow influenced by gravitational segregation (cf. Figure 4) at the inlet-end core, whereas no indications of oil displacement was observed for the middle core and the outlet-end core. Due to the high mobility ratio and density difference, CO_2 perturbations occur and override parts of the crude oil phase, causing front instabilities. The second test ran for 8 days, injecting a total of 3.7 PVs CO_2. For the first 5 days, 0.02-0.06 PV CO_2 was injected with low injection rate, assumingly related to the time needed for miscibility to be developed. The viscous driving force was reduced, compared with CO_2 injections in single cores, by a factor of three due to lower pressure drop per unit length. The increased length resulted in a slower front propagation, and, therefore, increased CO_2 exposure to crude oil, favorable for miscibility to develop.
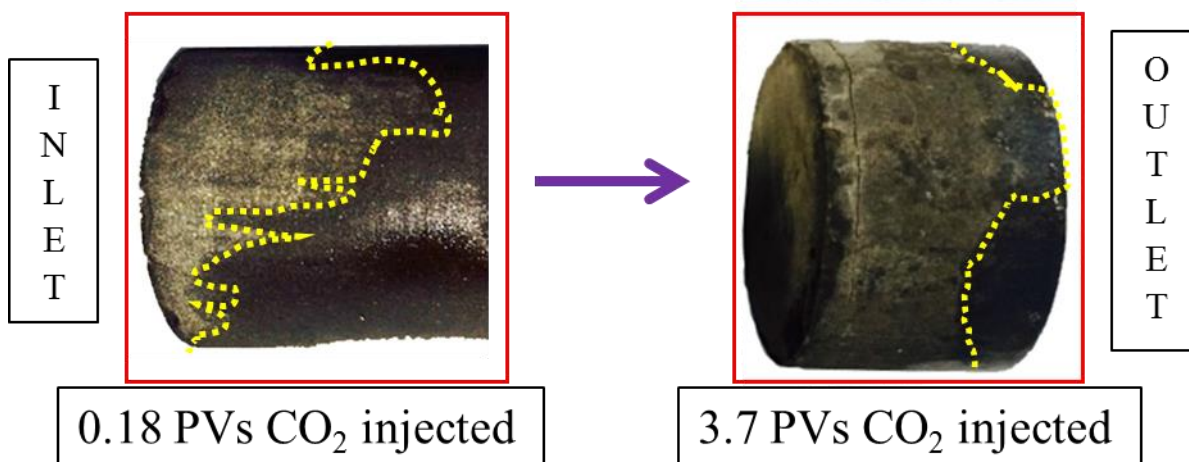

0.18 PVs CO_2 injected   3.7 PVs CO_2 injected

Figure 4: Left picture (after 0.18 PVs CO_2 injected) in large system shows the swept areas (grey) where CO_2 has displaced crude oil. The jagged front (highlighted with dotted yellow line) suggests viscous fingering of the CO2 through the crude oil saturated inlet core. The arrow indicates the direction of flow (the pressure gradient). Right picture (after 3.7 PV CO_2 injected) shows visual observations of swept area (grey) in the outlet core (inlet and middle core completely swept), and display a more homogeneous front development.

Dispersions (and especially diffusion) are likely to dampen the adverse effects of viscous fingers and may explain the shape of the recovery curves obtained; higher rate of recovery early in the injection phase and progressively lower rate of recovery with time. (see Figure 5). Viscous displacement was assumed to dominate in the early stages of injection, whereas oil was recovered by diffusional driven displacement at later stages. Visual observations of the color of produced oil corroborated this, because the heavier components, with relatively lower diffusional coefficients, were produced at the late stage, in agreement with [22]. On larger scales diffusion is perceived as a slower process compared to capillary and viscous driven displacement processes, however it is spontaneous, causing it to be continuous and ubiquitous [6].

The dynamic production profile (see Figure 5) indicates that CO_2 breakthrough occurred after approximately 0.5 PV CO_2 injected (Rf @ CO_2 breakthrough: 41.5% of OOIP). Additional recovery is assumed to mainly occur from the developed multi-contact miscibility caused by molecular diffusion, and a final oil recovery factor yielded 55.0% (± 9.2%) of OOIP after a total of 3.7 (± 0.2) PV CO_2 injected, suggesting high degree of miscibility.
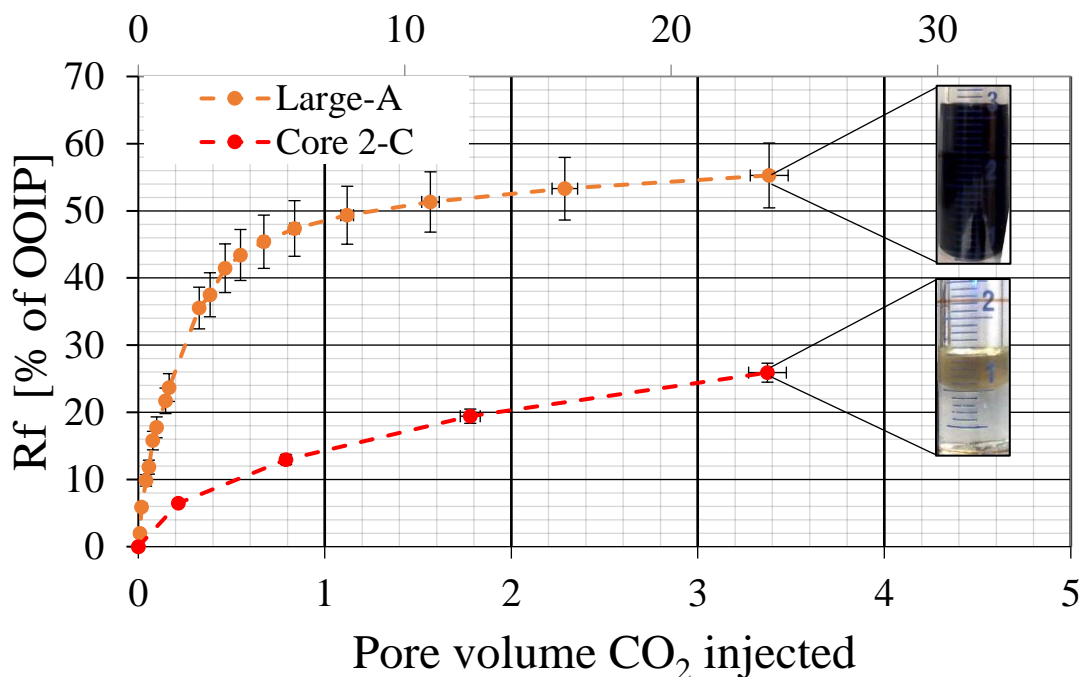

Figure 5: Oil recovery (%OOIP) vs. time (pore volume CO_2 injected) for increased system size (large) and single core plug (core 2). The points are measured values and a linear production as function of CO_2 injected from one point to the next is assumed. The large system size graph display fast recovery in the beginning and gradually slower rate of recovery with a recovery factor yielded 55.0% (± 9.2%) of OOIP after a total of 3.7 (± 0.2) PV CO_2 injected. The single core plug system (Core 2-C) display a slower rate of recovery and the final recovery is lower (23.6 % of OOIP). The produced oil (inset) shows a distinct difference in oil composition further corroborating the importance of system size.

Impact of Time on Oil Recovery

The relationship between PVs of CO_2 injected, injection time and final recovery was calculated for the two main parameters investigated in this work: oil phase (degree of miscibility) and system length. The arithmetic average of oil recovery for three groups (mineral oil, crude oil and large) was used to increase statistical significance in each group (see Figure 6. Area represents the final oil recovery, and indicates a tradeoff between injection rate (volume needed) and flooding time (time needed). Comparison between first-contact miscible displacement (orange circle: Rf= 68% of OOIP) and multi-contact miscible displacement (blue circle: 33.7% of OOIP) show that both the injection

time of CO_2 exposure (hours) and volume of CO_2 injected is considerable lower for systems with higher degree of miscibility. Due to the favorable displacement, the final oil recovery was higher by a factor of two, emphasizing the beneficial impact of diffusion as previous mentioned. Increased system size had a strong effect on the final oil recovery as a function of pore volumes injected. The final recovery was comparable with first-contact miscible displacement at lower pore volumes injected, the tradeoff being the increased time for a high degree of miscibility to develop.
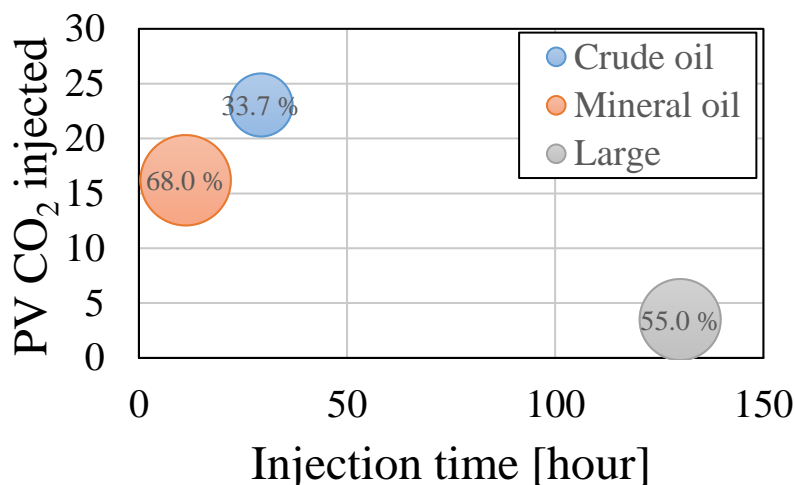

Figure 6: Arithmetic average values of pore volumes CO_2 injected, time of exposure and final oil recovery for seventeen CO_2-EOR flooding tests, performed at reservoir conditions. Time is longer and volumes of CO_2 needed is higher to recover crude oil from single cores, compared to mineral oil recovery. By increasing the time of contact between CO_2 and crude oil, the recovery factor increases and the volumes needed for EOR decreases.

Because some of the miscibility process is assumed to include exchange of particles perpendicular to the direction of flow (by diffusion) and this is time dependent, it seems reasonable that the oil recovery increases due to larger volumetric sweep efficiency as the contacted time increases. However, the surface area of contact is equally important and the stronger effect observed by the cores permeability seems to have larger impact on the rate of developed miscibility and the degree of miscibility.

CONCLUSIONS

In this paper we show that conventional CO_2-EOR can be implemented on ultra tight shale oil core plugs, reaching oil recovery fractions as high as 98.3% of OOIP; without introducing fractures to the system.

An average oil recovery factor of 33.7% of OOIP was achieved for thirteen crude oil saturated core plugs under multi-contact miscible conditions. An average oil recovery factor of 68.0% of OOIP for four mineral oil saturated core plugs under first-contact miscible conditions.

Rate of oil recovery and final oil recoveries are shown to have a positive correlation with system size and CO_2 exposure time.

ACKNOWLEDGEMENTS

REFERENCES
1. Tour, J.M., C. Kittrell, and V.L. Colvin, Green carbon as a bridge to renewable energy. *Nature Materials*, 2010. **9**(11): p. 871-874.
2. Chu, S. and A. Majumdar, Opportunities and challenges for a sustainable energy future. *Nature*, 2012. **488**(7411): p. 294-303.
3. Aldy, J.E., et al., Designing Climate Mitigation Policy. *J.l of Economic Literature*, 2010. **48**(4): p. 903-34.
4. IEA, CO_2 Emissions from Fuel Combustion. 2015: p. 548.
5. Riahi, K., et al., Technological learning for carbon capture and sequestration technologies. *Energy Economics*, 2004. **26**(4): p. 539-564.
6. Busch, A., et al., Carbon dioxide storage potential of shales. *International Journal of Greenhouse Gas Control*, 2008. **2**(3): p. 297-308.
7. Alvarez, J.M. and R.P. Sawatzky, Waterflooding: Same Old, Same Old? 2013, *Society of Petroleum Engineers*.
8. Etherington, J.R. and J.E. Ritter, The 2007 SPE/WPC/AAPG/SPEE Petroleum Resources Management System (PRMS). 2008.
9. Alvarado, V. and E. Manrique, Enhanced Oil Recovery: An Update Review. *Energies*, 2010. **3**(9): p. 1529.
10. EIA, Technically Recoverable Shale Oil and Shale Gas Resources: An Assessment of 137 Shale Formations in 41Countries Outside the United States. 2013: p. 730.
11. Kuila, U., I. Berend, and M. Prasad, Specific surface area and pore-size distribution in clays and shales (vol 61, pg 341, 2013). *Geophysical Prospecting*, 2014. **62**(1): p.196
12. Wang, W., et al., A mathematical model considering complex fractures and fractal flow for pressure transient analysis of fractured horizontal wells in unconventional reservoirs. *Journal of Natural Gas Science and Engineering*, 2015. **23**: p. 139-147.
13. Sheng, J.J., Enhanced oil recovery in shale reservoirs by gas injection. *Journal of Natural Gas Science and Engineering*, 2015. **22**: p. 252-259.
14. Pei, P., et al., Shale gas reservoir treatment by a CO2-based technology. *Journal of Natural Gas Science and Engineering*, 2015. **26**: p. 1595-1606.
15. Middleton, R.S., et al., Shale gas and non-aqueous fracturing fluids: Opportunities and challenges for supercritical CO2. *Applied Energy*, 2015. **147**: p. 500-509.
16. Jarrell, P.M. and R.T. Jones, Practical aspects of CO2 flooding. Henry L. Doherty series. Vol. vol. 22. 2002, Richardson, Tex: Henry L. Doherty Memorial Fund of AIME, *Society of Petroleum Engineers*.
17. Tovar, F.D., et al., Experimental Investigation of Enhanced Recovery in Unconventional Liquid Reservoirs using CO2: A Look Ahead to the Future of Unconventional EOR. 2014, *Society of Petroleum Engineers*.
18. Gamadi, T.D., et al., An Experimental Study of Cyclic CO2 Injection to Improve Shale Oil Recovery. 2014, *Society of Petroleum Engineers*.

19.   Vega, B., et al., Experimental Investigation of Oil Recovery From Siliceous Shale by Miscible CO2 Injection. 2010, *Society of Petroleum Engineers*.
20.   Fernø, M. A., Hauge, L. P., Uno Rognmo, A., Gauteplass, J. & Graue, A. 2015. Flow visualization of CO2 in tight shale formations at reservoir conditions. *Geophysical Research Letters,* 42**,** 7414-7419.
21.   Lake, L.W., et al., Fundamentals of Enhanced Oil Recovery. 2014, 222 Palisades Creek Dr, Richardson, TX 75080, USA: *SPE*.
22.   Darvish, G.R., et al., Reservoir Conditions Laboratory Experiments of CO2 Injection into Fractured Cores. 2006, *Society of Petroleum Engineers*.

JOINT X-RAY AND NEUTRON TOMOGRAPHY OF SHALE CORES FOR CHARACTERIZING STRUCTURAL MORPHOLOGY

Wei-Shan Chiang [1, 2, 3], Jacob M. LaManna [4], Alexander Katsevich [5, 6], Daniel S. Hussey [4], David L. Jacobson [4], Michael Frenkel [5], Daniel T. Georgi [1], Qiushi Sun [1], Yun Liu [2, 3, 7], and Jin-Hong Chen [1]

[1] Reservoir Engineering Technology, Aramco Research Center – Houston, TX 77084
[2] Center for Neutron Research, NIST, Gaithersburg, MD 20899
[3] Department of Chemical & Biomolecular Engineering, U. Delaware, DE 19716
[4] Physical Measurement Laboratory, NIST, Gaithersburg, MD 20899
[5] iTomography Corporation, Houston, TX 77021
[6] University of Central Florida, Orlando, FL 32816
[7] Department of Physics and Astronomy, University of Delaware, Newark, DE 19716

ABSTRACT

To better model the storage and flow of gas and light hydrocarbons in shales, it is necessary to quantify the structural distributions of organic and inorganic components and fractures in shales over a large range of length scales. The combination of neutron and X-ray tomography provides these distributions on the core scale, in contrast to most current µm-scale SEM studies.

We present a new conjoint X-ray and neutron computed tomography (CT) for 3D shale-core characterization. Neutrons are attenuated significantly by hydrogen compared with most other elements. Therefore, the hydrogen-rich areas, i.e. organic matter can be easily distinguished from fractures and inorganic, hydrogen-poor matter. On the other hand, X-rays are attenuated more when the atomic number Z of the element is larger and can be used to identify high-Z elements such as minerals. Therefore, combining X-ray and neutron tomography can provide much more comprehensive information of shale. The combination of neutron and X-ray tomography allows one to identify different minerals, fractures, and organic matter for improved and more realistic representation of the rock 3D structure.

INTRODUCTION

Natural gas production worldwide from shale reservoirs has played an important role for the global energy supplies [1]. Despite its success, many fundamental issues in the gas storage and gas transport are not clearly addressed. It has been reported that most natural gases in shale rocks are stored in kerogens that contain

pores with the characteristic length scale between 1 to 100 nm. Traditional 2D Scanning Electron Microscopy (SEM) and 3D Focused Ion Beam-SEM (FIB-SEM) have successfully revealed the structures of shale rocks at very small length scales comparable to the pores. However, it is also critically important to identify the kerogen distribution at the core scale so that a more statistically representative characterisation of the sample can be constructed to understand the gas flow.

Both neutron and X-ray tomography techniques are widely used to probe a wide range of materials. They are very useful to investigate shale rocks at the core scale. The X-ray tomography technique is more sensitive to the heavy elements with large atomic number Z because X-rays interact with the electron cloud of the elements. Thus, X-ray imaging can easily probe minerals in rocks. Unlike X-rays, there is little correlation of neutron cross sections with atomic number. In particular, neutrons are very sensitive to hydrogen rich materials. Water and organic matter in shale rocks, such as kerogen, bitumen, and heavier immobile hydrocarbons can strongly attenuate neutrons. Thus, neutron imaging is very useful to probe the distribution of hydrogen rich materials. Since the sensitivity for X-rays and neutrons to different elements are very distinct, studying the same rock with both X-ray and neutron imaging techniques can provide more useful information that may not be clearly understood by using only one of them [2]. Dual, sequential neutron and X-ray tomography (i.e. different facilities) has been successfully applied to many other materials such as fuel cells [3], [4], batteries [5], and cultural heritage objects [6], [7].

In this study, we illustrate the use of dual X-ray and neutron tomography to study shales at the core scale. The distributions of minerals, organic matter, and fractures are successfully identified in a Middle Eastern shale.

ATTENUATION OF X-RAY AND NEUTRON

X-ray tomography and neutron tomography are both non-invasive methods and have similar principles. The beam intensity after passing through a sample can be expressed as

$$I_t(l) = I_0 \, e^{-\int_l \, \mu(x)dx} \tag{1}$$

l denotes the transmission path and x is a 3-dimensional position vector. The attenuation coefficient, μ, is related to the attenuation cross sections through

$$\mu = \sum_i \sigma_{t,i} \, N_i \tag{2}$$

$\sigma_{t,i}$ is the total attenuation cross section for X-ray or neutron and N_i is the number density of type i atom.

Table 1. The attenuation coefficient for X-ray and neutron for typical constituents in shales.

Component		μ for X-ray 99.2 keV[a] (cm^{-1})	μ for neutron 1.8 Å[b] (cm^{-1})
Kerogen[c]	$(C_{100}H_{161}N_{1.85}S_{0.7}O_{9.2})$	0.22	6.97
Quartz	(SiO_2)	0.45	0.29
Pyrite	(FeS_2)	1.41	0.44
Siderite	$(FeCO_3)$	1.03	0.67
Calcite	$(CaCO_3)$	0.53	0.35
Dolomite	$(CaMg(CO_3)_2)$	0.51	0.41
Anhydrite	$(CaSO_4)$	0.58	0.29
Celestine	$(SrSO_4)$	1.95	0.34
Kaolinite	$(Al_2Si_2O_5(OH)_4)$	0.45	2.32
Chlorite	$(Mg_5Al_2Si_3O_{10}(OH)_8)$	0.42	2.07
Daphnite	$(Fe_5Al_2Si_3O_{10}(OH)_8)$	0.82	2.30
H_2O		0.17	5.65
C_6H_{14}		0.11	5.39

[a] 99.2 keV is the mean incident energy of X-ray to the sample and attenuation coefficient for X-ray is obtained from the X-Ray Form Factor, Attenuation, and Scattering Tables [9]. [b] The neutrons used in this study are thermal neutrons with a distribution of wavelength centered around 1.8 Å. The attenuation coefficient for neutron is obtained from Neutron Activation and Scattering Calculator [8]. [c] Kerogen formula obtained from literature [23] and the density used is 1.3 g/cm^3.

Table 1 lists the attenuation coefficient, μ, for several common elements found in shales for X-ray and neutron at relevant conditions. Attenuation coefficients for neutrons and X-rays are calculated by using Neutron Activation and Scattering Calculator provided by National Institute of Standards and Technology (NIST) Center for Neutron Research (NCNR) [8] and X-Ray Form Factor, Attenuation, and Scattering Tables provided by NIST Physical Measurement Laboratory [9], respectively. Clearly, hydrogen containing materials have larger attenuation coefficients for neutrons.

In X-ray imaging, μ of organic matter is small compared with the minerals but close to the empty space, i.e. the fractures. It is hard to distinguish between kerogen and fracture using only X-ray data. In contrast, kerogen and any components with a large amount of hydrogens have large μ for neutrons compared to hydrogen-poor minerals: in neutron imaging, μ is 6.97 cm^{-1} for kerogen while μ is only 2.07 cm^{-1} to 2.32 cm^{-1} for clay minerals and below 0.7 cm^{-1} for most of the other shale forming minerals. Thus, kerogen can be easily distinguished from minerals and open fractures using neutron data. In X-ray imaging μ for kerogen is about

half of μ for quartz and some major clays. Overall, the neutron attenuation coefficient provides higher contrast for organic matter than does the X-ray attenuation coefficient.

CORE PLUG SAMPLE

An organic-rich and carbonate-rich source rock sample from Middle East shale was used for this study. The sample was 25 mm in diameter and approximately 19 mm in length. The surfaces on the two ends of the sample are in their original state without being trimmed. Thus, they have rough surface and are not flat.

NEUTRON TOMOGRAPHY

Neutron tomography was conducted at the NCNR at the BT2 neutron imaging facility. This instrument offers a high thermal neutron flux for radiography. Full details of the instrument and applied neutron data reconstruction technique can be found in the following manuscript [10]. Detector resolution was set to 30 µm to keep the sample in the field-of-view at all projection angles. The scan took approximately 18 hours to complete. Volumes were reconstructed from the projection images using the commercial CT software package Octopus[1] using the parallel beam filtered back projection algorithm and visualized with the open-source Drishti Volume Exploration Tool [11].

HELICAL X-RAY TOMOGRAPHY

The raw X-ray projection data was collected at the Aramco Research Center in Houston using a North Star Imaging X5000 Industrial CT Scanner (NSI). The helical cone-beam CT scan was performed using a voltage of 160 keV and a current of 120 µA. The Source-Isocenter Distance (SID) and the Source-Detector Distance (SDD) were 92.2 mm and 999 mm, respectively; 720 projections per revolution were taken over 7 revolutions with a helical pitch of 10 mm per revolution. For the purposes of noise reduction, 8 frames were averaged per radiograph. The magnification factor of 10.8 allows one to achieve a voxel dimension about 20 µm. After the scan, the raw projection CT data was transferred to a stand-alone single GPU laptop to perform raw CT data preprocessing and helical image reconstruction using the iTomography KFBP software package1. Prior to applying 3D image reconstruction, we applied routines to detect and correct bad pixels and accurately determine the central ray position [13], [15].

---

[1]Certain trade names and company products are mentioned in the text or identified in an illustration in order to adequately specify the experimental procedure and equipment used. In no case does such identification imply recommendation or endorsement by the National Institute of Standards and Technology or Aramco Services Company, nor does it imply that the products are necessarily the best available for the purpose.

X-ray CT Reconstruction The volume was reconstructed from the projection images using the theoretically exact Katsevich Filtered Backprojection (KFBP) helical reconstruction algorithm [12], [13]. The algorithm was originally developed for medical CT using a helical scan trajectory and has been shown that the KFBP algorithm can be employed advantageously in core imaging in typical micro-CT setups [13], [14]. KFBP provides theoretically exact reconstruction at any cone angle without cone-beam artifacts, which allows for significant improvement in scan throughput compared to step-and-shoot scanning.

RESULTS

Contrast in acquired X-ray CT images depends on the energy of the X-ray. The mean X-ray energy from X-ray tube is 74.2 keV, 99.2 keV, and 123.0 keV for voltage setting of 110 kV, 160 kV, and 230 kV, respectively, calculated by using SpekCalc [16]. The X-ray energy spectrum is further modified by the sample under study. Fig. 1 shows the calculated X-ray energy spectra after traversing a 1 cm aluminum sample for three different voltages [17].
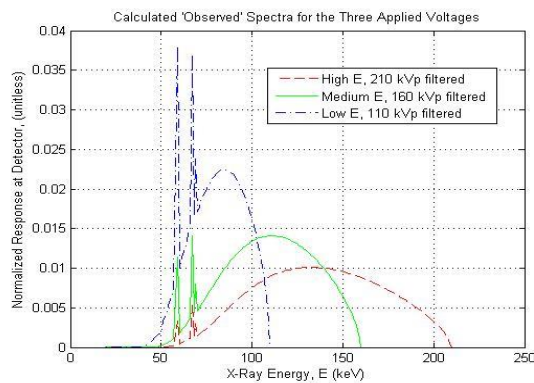

Fig 1. Normalized detector X-ray spectra for 110 keV, 160 keV, and 210 keV energy tube settings after passing through a 1 cm thick aluminum sample phantom calculated by SpekCalc.

Fig. 2 shows representative vertical slice from the X-ray (a) and neutron (b) tomography on the Middle East shale. In both images, the brighter areas indicate regions with larger attenuation, while the darker areas correspond to regions with less attenuation. For X-rays, the cross section of an element is proportional to its atomic number Z and the brighter areas indicate the regions containing more high-Z elements such as heavy minerals. For neutrons, the hydrogen-rich areas are brighter because hydrogen has a larger cross-section and attenuates neutron intensity more significantly. In Fig. 2, the regions outlined by the yellow ovals are bright in the X-ray image but dark in the neutron image and, therefore, are occupied by minerals including high-Z or high-density elements. In contrast, the regions outlined by the blue rectangles are dark on the X-ray image but bright in neutron image and are likely organic matter. The organic matter in this sample

forms continuous layered structures at the top, in the middle, and at the bottom of the sample. This is especially easy to see from the bright bands in the neutron image.
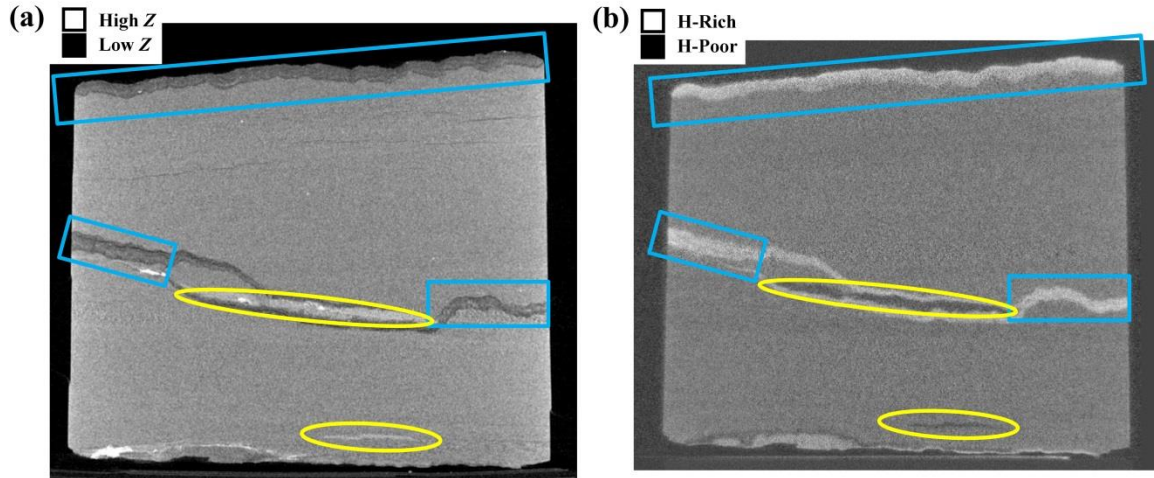

Fig. 2 Representative vertical slice from X-ray (a) and neutron (b) tomography. Blue rectangles label regions of organic matter with lower attenuation in X-ray image but larger attenuation in neutron image. Yellow ovals label regions of high-Z minerals with higher attunation in X-ray but smaller atenuation in neutron image. Note that organic matter forms continuous layers in the sample.

Fig. 3 shows representative horizontal slice from X-ray (a) and neutron (b) tomography. As in Fig. 2, the blue rectangles mark regions including organic matter. It is worthwhile to point out that the black, linear feature in the X-ray image marked by the red rectangle can be easily mistaken for an open fracture if only the X-ray tomography is available. However, it is actually filled with organic matter, as revealed by neutron image; the same feature exhibits a larger attenuation coefficient than the matrix and is hydrogen rich. Also, as in Fig. 2, in Fig. 3 the yellow ovals mark regions with higher X-ray attenuation coefficients but smaller neutron attenuation coefficients. Considering the attenuation coefficient listed in Table 1, it is likely the yellow ovals highlight regions including pyrite while the green ovals mark region with anhydrite.

Fig. 4 shows horizontal slices from X-ray (a) and neutron (b) tomography which include a large area of continuous organic matter and a relatively homogenous matrix. These slices clearly demonstrate the opposite contrast between X-ray and neutron images and indicate that the neutron and X-ray images provide complementary information to each other on formation rocks.

Fig. 5 shows the 3D reconstructed images of the sample for X-ray (a) and neutron (b and c) modes, respectively. Fig. 5c displays only the high-attenuation regions and this gives the 3D distribution of organic matter in shale. Fig. 5c shows that

the organic matter forms clear layered structures in this sample with three layers: at the top, in the center, and at the bottom of the sample. In addition some organic matter is distributed throughout the sample.
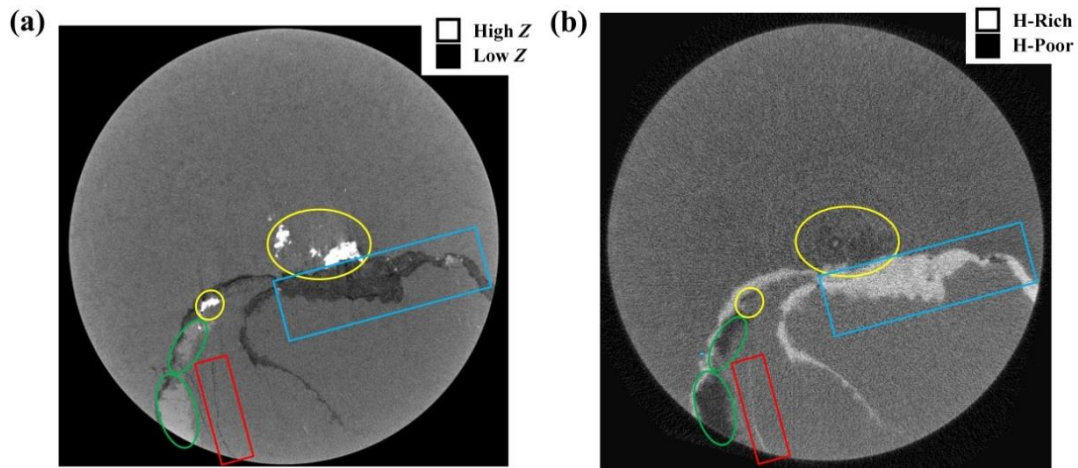
Fig. 3 Representative horizontal slices from X-ray (a) and neutron (b) tomography. Rectangles mark regions of higher organic matter content with lower X-ray attenuation but larger neutron attenuation. The red rectangles mark an organic matter filled fracture. Yellow ovals label regions of high-Z minerals likely pyrite and green ovals contain likely anhydrite.

Fig. 4 Horizontal slice from X-ray (a) and neutron (b) tomography showing opposite contrast between these two imaging technologies.

Fig. 5 3D volume renders of the shale sample for X-ray (a) and neutron (b) tomography and distribution of organic matter (c). Distribut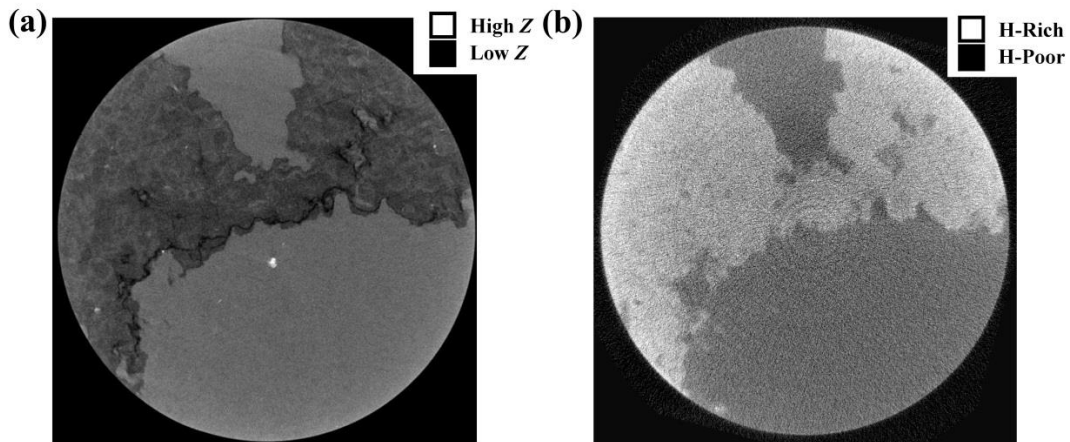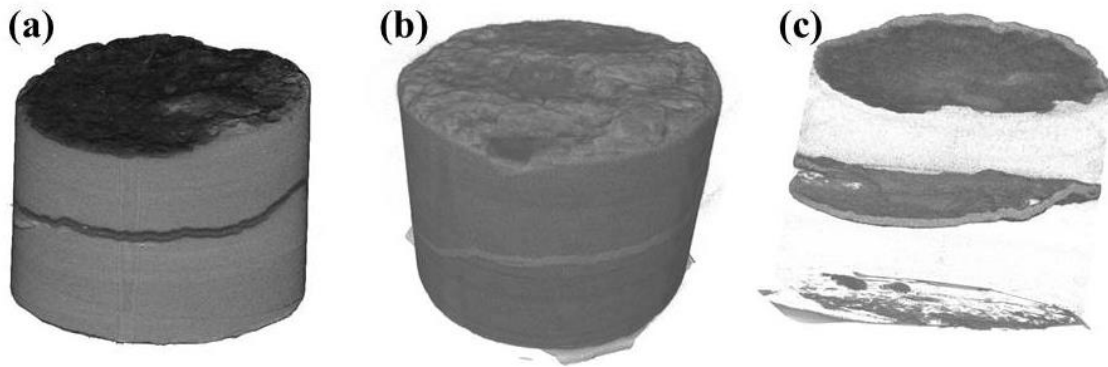ion of hydrogen-rich components, i.e. organic matter, is identified from the high-attenuated (bright) regions in 3D neutron tomography reconstructions.

DISCUSSION

The distribution of different components within the shale rock is crucial for storage and transport of hydrocarbons in the shales. The Middle East shale in the current study is used as an example to demonstrate that dual X-ray and neutron tomography is a powerful tool to identify the distribution of minerals, kerogens, and fractures inside the shale rocks. Since the hydrogen-rich organic kerogens and fractures are both very transparent to X-rays, it is challenging for X-ray CT alone to unambiguously determine the kerogen distributions at the core scale. In contrast, neutrons are very sensitive to hydrogen and are useful to characterize the organic-rich shales. More comprehensive information of material composition and distributions in shale rocks can be obtained by combining X-ray and neutron image.

It is worth mentioning that the structures imaged in this study are on the core scale, rather than in pore scale. Current simulation and modeling of hydrocarbons are mostly based on the rock structure determined at the pore scale constructed from SEM images [18]–[21]. There is about a 10^9 order of magnitude upscaling in length scale from pore scale to core scale. It is important to study the influence of the distribution of different components within the rocks by simulating and modeling the hydrocarbon flow at core scale and larger.

Since the wettability can be very different for the minerals and organic matter, the structure and arrangement in space of these components can directly affect the storage and transport of the hydrocarbons within the shale rocks. The laminar nature of organic-rich mud stones observed in the Middle East shale can dramatically change the current view of hydrocarbon flow and the mechanical properties in the shale rocks.

The organic-rich layers in Fig. 5 span the entire 25 mm diameter plug sample and seem to extend further to the full diameter core, although denser sampling is required to confirm this. The layered structure of the organic matter observed in this study has two important implications: first, the organic-rich bands have very different mechanical properties from the matrix and thus become the weak interfaces for the sample to break. The two ends of this sample were broken at the layer interfaces during plugging which is consistent with the assertion that the interface between organic-rich layer and inorganic-rich layer is a mechanical weak point. The organic layers in this sample are largely parallel to the formation bedding and, thus, perpendicular to the direction of hydraulic fracturing in a horizontal well. Their influence on hydraulic fracturing, however, remains unclear. From a nano-indentation study [22], organic matter was suggested to increase the tensile strength and raise the required pressure for hydraulic fracture initiation. However, the effects of these extensive organic-rich layers on hydraulic fracture require comprehensive study. Second, the organic matter layers can influence the flow of light hydrocarbons. If these layers are predominantly porous kerogen, they could form fast flow-paths for hydrocarbons. In contrast, if these layers are bitumen without pores, they would form barriers that would inhibit hydrocarbon flow. Further investigation is ongoing to delineate the properties of these organic matter layers. It can be argued that only the pore-networks among kerogens are important for light hydrocarbon flow in organic-rich shales. The neutron tomography may be the most sensitive approach to acquire the 3D distribution of kerogen in shale samples.

CONCLUSIONS

Neutron imaging is more sensitive to hydrogen and X-ray imaging is more sensitive to high-Z minerals. The two methods are complementary and can reveal a more comprehensive structure of shales. The theoretical attenuation coefficients of typical components in shales for neutron and for X-ray tomography are presented in this study. The combination of neutron and X-ray tomography allows one to identify different minerals, fractures, and organic matter with voxel size of about 30 µm and field of view about 2 cm. The example shown in this study demonstrates the advantage of the combined use of these two imaging technologies: improved and more realistic representation of the rock 3D structure. The core scale 3D distribution of organic matter and fractures in these rocks could be used to simulate and model the hydrocarbon flow in the future. The layered structure of organic matter found in the studied shale sample is surprising and may significantly change the current explanations of hydrocarbon flow and rock mechanics in the studied reservoir.

ACKNOWLEDGEMENTS

REFERENCES

[1]   Aloulou, F. and V. Zaretskaya, "Shale gas production drives world natural gas production growth - Today in Energy - U.S. Energy Information Administration (EIA)," 2016. [Online]. Available: https://www.eia.gov/todayinenergy/detail.php?id=27512. [Accessed: 11-Apr-2017].

[2]   Chiang, W.-S., J. M. LaManna, D. S. Hussey, D. L. Jacobson, Y. Liu, D. T. Georgi, and J.-H. Chen, "Simultaneous Neutron and X-ray Imaging of 3D Kerogen and Fracture Structure in Shales," *SPWLA 58th Annual Logging Symposium*, (2017).

[3]   Manke, I., C. Hartnig, M. Grünerbel, W. Lehnert, N. Kardjilov, A. Haibel, A. Hilger, J. Banhart, and H. Riesemeier, "Investigation of water evolution and transport in fuel cells with high resolution synchrotron X-ray radiography," *Appl. Phys. Lett.*, **90**, (2007), 174105.

[4]   Banhart, J., A. Borbély, K. Dzieciol, F. Garcia-Moreno, I. Manke, N. Kardjilov, A. R. Kaysser-Pyzalla, M. Strobl, and W. Treimer, "X-ray and neutron imaging – Complementary techniques for materials science and engineering," *Int. J. Mater. Res.*, **101**, (2010),1069–1079.

[5]   Manke, I., J. Banhart, A. Haibel, A. Rack, S. Zabler, N. Kardjilov, A. Hilger, A. Melzer, and H. Riesemeier, "*In situ* investigation of the discharge of alkaline Zn–MnO2 batteries with synchrotron X-ray and neutron tomographies," *Appl. Phys. Lett.*, **90**, (2007), 214102.

[6]   Mannes, D., C. Benoît, D. Heinzelmann, and E. Lehmann, "Beyond the Visible: Combined Neutron and X-ray Imaging of an Altar Stone from the Former Augustinian Church in Fribourg, Switzerland," *Archaeometry*, **56**, (2014), 717–727.

[7]   Mannes, D., F. Schmid, J. Frey, K. Schmidt-Ott, and E. Lehmann, "Combined Neutron and X-ray Imaging for Non-invasive Investigations of Cultural Heritage Objects," *Phys. Procedia*, **69**, (2015),653–660.

[8]   "Neutron Activation Calculator." [Online]. Available: https://www.ncnr.nist.gov/resources/activation/. [Accessed: 27-Apr-2017].

[9]   "NIST X-Ray Form Factor, Atten. Scatt. Tables Form Page." [Online]. Available: http://physics.nist.gov/PhysRefData/FFast/html/form.html. [Accessed: 27-Apr-2017].

[10]   LaManna, J. M., D.S. Hussey, E. Baltic, and D. L. Jacobson, "Neutron and X-ray Tomography (NeXT) system for simultaneous, dual modality tomography,"

Review of Scientific Instruments, (2017).

[11] Limaye, A., "Drishti: a volume exploration and presentation tool," *Developments in X-Ray Tomography VIII*, (2012), 85060X.

[12] Katsevich, A., "Analysis of an exact inversion algorithm for spiral cone-beam CT," *Phys. Med. Biol.*, **47**, (2002), 302.

[13] Katsevich, A., M. Frenkel, M. Feser, Z. Huang, M. Andrew, T. Case, A. Gu, and W. Thompson, "New Fast and Accurate 3D Micro Computed Tomography Technology for Digital Core Analysis," *SPE Annual Technical Conference and Exhibition*, (2015).

[14] Sheppard, A., S. Latham, J. Middleton, A. Kingston, G. Myers, T. Varslot, A. Fogden, T. Sawkins, R. Cruikshank, M. Saadatfar, N. Francois, C. Arns, and T. Senden, "Techniques in helical scanning, dynamic imaging and image segmentation for improved quantitative analysis with X-ray micro-CT," *Nucl. Instruments Methods Phys. Res. Sect. B Beam Interact. with Mater. Atoms*, **324**, (2014), 49–56.

[15] Katsevich, A. and M. Frenkel, "TESTING OF THE CIRCLE AND LINE ALGORITHM IN THE SETTING OF MICRO-CT," *the International Symposium of the Society of Core Analysts*, (2016), SCA2016-080.

[16] Poludniowski, G. G. and P. M. Evans, "Calculation of X-ray spectra emerging from an X-ray tube. Part I. Electron penetration characteristics in X-ray targets," *Med. Phys.*, **34**, (2007), 2164–2174.

[17] Davis, L., "Development of a State-of-the-Art Petrophysical X-Ray CT for Unconventional Reservoirs," Personal Communication (2016).

[18] Saraji, S. and M. Piri, "The representative sample size in shale oil rocks and nano-scale characterization of transport properties," *Int. J. Coal Geol.*, **146**, (2015), 42–54.

[19] Chen, L., L. Zhang, Q. Kang, H. S. Viswanathan, J. Yao, and W. Tao, "Nanoscale simulation of shale transport properties using the lattice Boltzmann method: permeability and diffusivity," *Sci. Rep.*, **5**, (2015), 8089.

[20] Shabro, V., S. Kelly, C. Torres-Verdín, and K. Sepehrnoori, "Pore-Scale Modeling of Electrical Resistivity and Permeability in FIB-SEM Images of Hydrocarbon-Bearing Shale," *SPWLA 54th Annual Logging Symposium*, (2013).

[21] Jiang, W., M. Lin, Z. Yi, H. Li, and S. Wu, "Parameter Determination Using 3D FIB-SEM Images for Development of Effective Model of Shale Gas Flow in Nanoscale Pore Clusters," *Transp. Porous Media*, **117**, (2017), 5–25.

[22] Abousleiman, Y. N., K. L. Hull, Y. Han, G. Al-Muntasheri, P. Hosemann, S. Parker, and C. B. Howard, "The granular and polymer composite nature of kerogen-rich shale," *Acta Geotech.*, **11**, (2016), 573–594.

[23] Siskin, M., C. G. Scouten, K. D. Rose, T. Aczel, S. G. Colgrove, and R. E. Pabst, "Detailed Structural Characterization of the Organic Material in Rundle Ramsay Crossing and Green River Oil Shales," *Composition, Geochemistry and Conversion of Oil Shales*, Dordrecht: Springer Netherlands, (1995), 143–158.

OPTIMIZING NMR DATA ACQUISITION AND DATA PROCESSING PARAMETERS FOR TIGHT-GAS MONTNEY FORMATION OF WESTERN CANADA

Babak Salimifard[1], Mike Dick[2], Derrick Green[2], Douglas W. Ruth[1]
1- University of Manitoba, 2- Green Imaging Technologies

ABSTRACT

With the emergence of unconventional resources as viable sources of producible hydrocarbons, characterization techniques have been modified to accommodate the challenges faced by the complicated pore network and rock structure of such rocks. Nuclear Magnetic Resonance (NMR) is widely used for rock and fluid characterization in both laboratory and at downhole conditions. Proper design of test parameters and analysis of the acquired signal is crucial for proper characterization of the medium. In this study a 1.5" diameter plug of Montney Formation of Northern BC, Canada was used to optimize parameters such as echo spacing, number of echoes, acquisition delays, and number of scans (signal to noise ratios) to ensure data quality while minimizing run time, background signals were sought after to avoid being misinterpreted as micropores, and post-scan data processing was performed to avoid oversmoothing the decay curve.

This study shows that due to the fast relaxing nature of the Montney rock, shorter echo spacing (TE) is more desirable. Ringing effects and background noises are negligible at τ (TE/2) of 50 μs. At longer τs (200 μs) up to 77 percent of micro pore volume is lost while T_{2lm} increases by 130 percent. However, a long acquisition time (up to 1000 msec) should be applied to capture the fluid in the micro and macro fractures if fracture characterization is desired. NMR volume stabilizes at an acquisition time of 250 msec. Shorter acquisition times result in up to 11% loss in NMR volume at a τ of 50 μsec. Longer τs are less sensitive to shorter acquisition times. A recycle delay (RD) study indicates that micro and meso pores are not affected by short recycle delay times; however, a longer recycle delay results in a 44% increase in the macro pore volume. A smoothing parameter of 0.2 was achieved as the optimal smoothing parameter for the Montney rock and proved to generate stable pore size distributions and free-to-bound volume ratios even at low signal to noise (SNR) ratios. A separate study discusses the measurement error in NMR volume as a function of scan duration and finds that at short τs there's up to a 0.5ml reduction in NMR volume per hour of scan time due to heating and 0.1ml reduction per hour due to drying.

INTRODUCTION

Nuclear Magnetic Resonance (NMR) has been used extensively over the past two decades to characterize petroleum reservoir rocks and fluids both in the laboratory and at downhole. NMR characterizes pore network and fluids by monitoring the relaxation rate of the hydrogen nuclei present in the saturating fluids of the porous formation [1,2]. High data quality and proper data processing are key to successful rock and fluid characterization in unconventional resources while small pores, high surface to volume ratios, presence of

heavy hydrocarbons, and presence of organic pores and ferromagnetic minerals make data acquisition and processing much more challenging than that of conventional rocks [3,4].

THE MONTNEY FORMATION

The Montney formation is described as a fluvial sedimentary basin deposited in an open shelf marine environment on the western margin of the North American shield during the Triassic period under arid, mid-latitudinal conditions [5,6]. In the subsurface the Montney Formation extends over 700 kilometers from northern British Columbia to central Alberta and has a thickness of 100 to 300 meters, with thickness and depth increasing from east to west [7]. The Montney Formation is generally characterized as a siltstone-dominated lithology containing abundant dolomitized carbonates and immature feldspars combined with variable amounts of fine-grained shale and clay minerals [6,7]. The Total Organic Carbon (TOC) content of the Montney ranges from 0.1% to 3.6%, with an average of 0.8%. In this study a 1.5" plug sample of the Montney from the gas rich region of Montney in Northern British Columbia, Canada, was scanned and processed to optimize NMR acquisition and processing parameters. XRD and TOC measurements as well as porosity and permeability tests were done on end-pieces of the sample. The results are shown in Figure 1 and Table 1.
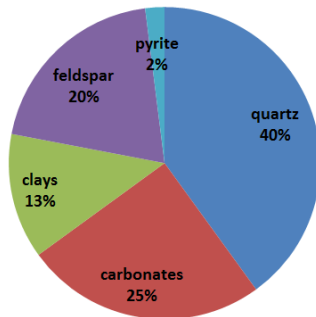

Figure 1 – Summary of XRD results for A13UM1 end-pieces. Carbonates include 9% calcite,12.5% dolomite and 3% ankerite while present clays are only illite and mica.

Table 1 – Summary of porosity, permeability and TOC measurements done on As-Received A13UM1 end-pieces

Well Location	b-070-C/094-A-13
Depth (m)	1855.80
Total Porosity (pu)	5.7
GRI Permeability (nD)	208
Grain Density (gr/ml)	2.71
Bulk Density (gr/ml)	2.56
TOC (%)	1.1

THE CPMG PULSE SEQUENCE AND THE HARDWARE

NMR signals are acquired using a series of pulse sequences consisting of radio frequency (rf) pulses and delay times. Choosing the optimal acquisition parameters requires an understanding of the pulse sequence. The Carr-Purcell-Meiboom-Gill (CPMG) pulse sequence is the most popular pulse sequence used for T_2 measurements. CPMG is initiated with a 90° pulse to align the magnetization vector in the *xy*-plane. After the pulse is turned off, the net magnetization vector disperses as some nuclei with higher Larmor frequency move faster and those with lower Larmor frequency lag behind. To re-phase all the spins a number of 180° pulses (echoes) are applied at specific time periods called "echo spacings" (TE). These pulses flip the spins to the other side of the *xy*-plane. As a result, nuclei with higher Larmor frequency would fall behind the ones with lower Larmor frequency and would eventually catch up to the slower ones and a rise in the magnetization vector is observed as the nuclei realign. Peak magnetization at each echo is captured as the echo

train and is the raw data for T_2 distributions [8,9]. A schematic of the CPMG pulse sequence is shown in Figure 2.

A low-field Oxford Instruments bench-top rock analyzer with a B_o = 0.3 T permanent magnet was used in this study. The rf probe's dimensions are 60 mm long and 40 mm in diameter. Magnet temperature was stable at 35°C and typical 90° and 180° pulse durations are 10 and 20 μs respectively which in combination with recovery time and group delays allows for a minimum CPMG echo time of 50 μs. In this study, all scans were taken at a TE of 100 μs, SNR of 100, RD time of 1000 ms and 10000 number of echoes (acquisition time of 1000 ms) using a 125 KHz digital filter, unless otherwise indicated.
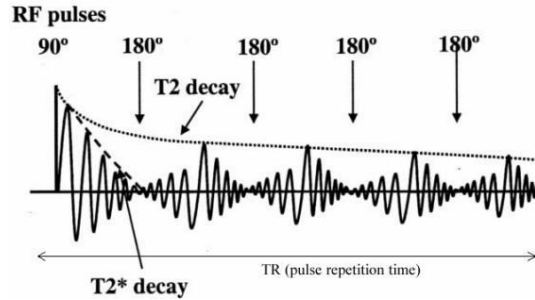

Figure 2 – A sample schematic of the CPMG pulse sequence.

PROCESSING THE NMR SIGNAL

Raw CPMG data is measured as voltage decay versus time in an NMR tool. This decay, in a perfectly homogenous magnetic field, is the result of relaxation of the spins away from the *xy*-plane into their equilibrium state. This curve is then fitted with an exponential decay function to produce the commonly-used T_2 distribution curve. In a porous medium, fluids in different pores relax at different rates; therefore a single exponential function cannot typically be used to fit the decay curve [10]. Assuming that there are *n* echoes, each with a magnitude g_i measured at t_i, the following equation in the form of a summation is used to fit the decay curve and minimize the error [11]:

$$g_i = \frac{M(t_i)}{M_o} = \sum_{j=1}^{m} a_j f_j e^{\frac{-t_i}{T_j}} + \epsilon_i \qquad i=1,2,\dots,n \qquad \text{(Eq. 1)}$$

Here there are *m* known relaxation times, T_j, that are preselected to be equally spaced on the logarithmic scale. $M(t_i)$ is the magnetization of the system at each t_i and M_o is the magnetization at *t=0*. The polarization factor, a_j, is defined as a function of Repeat-Delay (RD) time (the time between successive CPMG sequences) and is typically set to be one if long enough RD times are used. If shorter RD times are used, a_j can be given by

$$a_j = 1 - e^{-RD/T_{1j}} \qquad \text{(Eq. 2)}$$

f_j is the frequency (incremental porosity) of the pores with a T_2 relaxation of T_j, and ϵ_i is the error. Eq. 1 is typically solved using non-negative least square regression on predefined T_2 bins. Such solvers find the particular distribution that minimizes the deviation between the fit and the data with its random noise. As a result, they tend to generate sharp delta-function-like spikes at different T_j values which does not represent the continuous distribution of pore sizes in a porous medium. Also, because the inversion is highly affected

by the noise, the resulting distribution is not repeatable due to the random nature of the noise. To produce a repeatable f_j function, a penalty or regularization function is added to the solution. Although various types of penalty functions have been developed, a general form of regularization is shown here:

$$\varphi(f) = \frac{1}{2}\sum_{i=1}^{n}\left(\sum_{j=1}^{m} f_j e^{\frac{-t_i}{T_j}} - g_i\right)^2 + \alpha R(f_j) \qquad \text{(Eq. 3)}$$

where $R(f_j)$ is the penalty function and α is the smoothing parameter. The smoothing parameter should be adjusted in a way to avoid over-weighting the regularization function while producing stable peaks. Using a large α will increase the weight of the regularization function and produce an over-smooth T_2 distribution. Different Techniques exist to optimize α to be commensurate with the measurement error. In this study BRD, T1-Heel, Full Span and GIT regularization techniques [12] are compared with a fixed smoothing parameter technique (Fixed α). The fixed smoothing parameter was obtained by scanning the sample at different saturations levels. The sample was initially scanned dry. Then it was placed in 2% KCl for 24 hours to imbibe brine. The sample was weighed at both stages and imbibed brine volume was calculated based on a brine density of 1.02 gr/ml (Table 2). The partially saturated sample was scanned and then both the dry and partially saturated NMR decay curves were converted to T_2 relaxation distributions using smoothing parameters ranging from 0 to 1. At each smoothing parameter, the difference between partially saturated (V_i) and dry (V_d) NMR volumes (ΔV_{NMR})(Gray Trace Figure 3-a) was monitored and compared with the volume of the imbibed brine. An optimal smoothing parameter was selected where ΔV_{NMR} matched the volume of imbibed brine. Table 2 and Figure 3 summarize the smoothing optimization process.

Table 2 – Dry and Partially Saturated masses of the sample and calculated brine volume that was imbibed into the sample based on a brine density of 1.02 g/ml

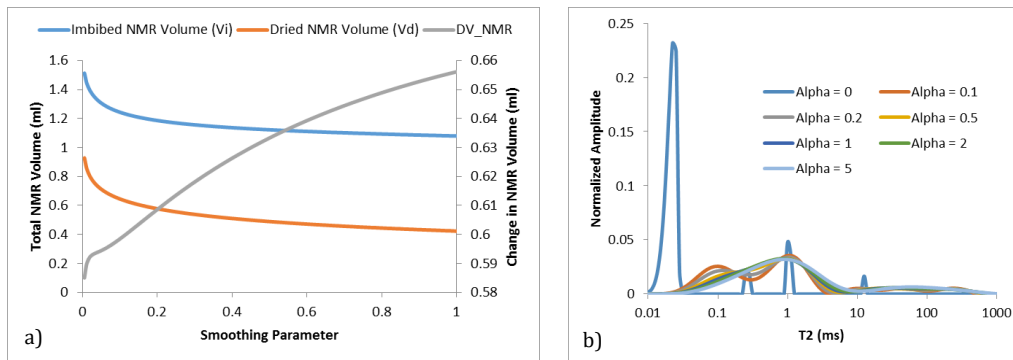| Sample	Dry Mass (gr)	Mass After Imbibition (gr)	Brine Volume Imbibed (ml)
A13UM1	97.243	97.862	0.607

Figure 3 – a)NMR volume at dry and partially saturated (imbibed) using a series of smoothing parameters. The gray line represents the difference between the imbibed and dry volumes at each smoothing parameter. ΔV_{NMR} matches the imbibed brine volume when the smoothing parameter is roughly 0.2. b) Normalized T_2 distribution curve produced using different smoothing parameters. Very small smoothing parameters tend to produce unstable sharp peaks while large smoothing parameters tend to oversmooth the T_2 distribution.

Figure 4 compares T_2 relaxation times derived using each regularization technique. Figure 4 suggests that the T1-Heel and Full Span techniques tend to undersmooth the decay curve

and generate spiky T_2 distributions while the GIT technique oversmooths the decay curve. The BRD technique creates comparable T_2 distributions with distributions created using the fixed smoothing parameter. The BRD and Fixed α techniques both generate stable distributions and produce similar total NMR volumes while T1-Heel and Full Span over-estimate the total NMR volume. GIT's technique generates comparable NMR volume with that of BRD and Fixed α despite oversmoothing the decay curve. Because the T1-Heel and Full Span smoothing techniques could not generate acceptable T_2 distributions, they were excluded from further analysis.
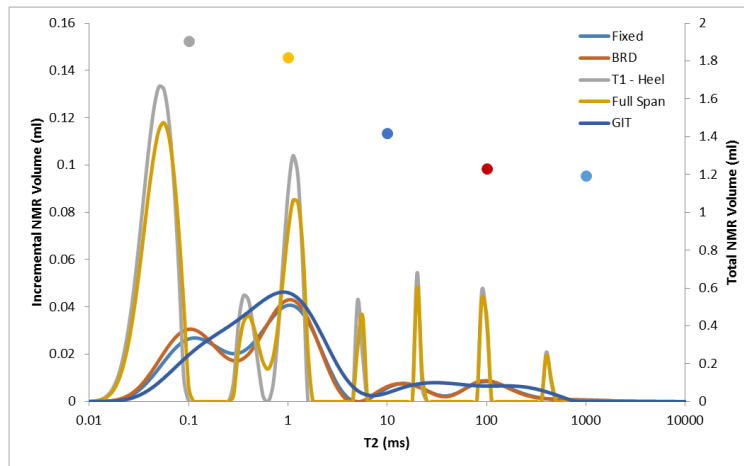

Figure 4 – A comparison of different T_2 distributions using five different regularization techniques. Solid dots represent the total NMR volume calculated using each technique.

SIGNAL TO NOISE RATIO

Although the highest quality data is always desirable, NMR tests are routinely performed at low signal to noise ratios (SNR) to save time. SNR is the ratio of the initial magnitude of the echo train data to the noise amplitude and can be increased by increasing the number of successive scans. SNR would increase by a factor of $\sqrt{2}$ per doubling the number of experiments. The optimal regularization technique should be able to not only produce reliable distributions at high SNR, but also be stable and produce reliable distributions at low SNR. In this study the sample used earlier was scanned at different SNRs. Fixed α, GIT's and BRD regularization techniques were then used to produce T_2 distributions. The tail of the T_2 distribution curve (T_2 larger than 4.5 ms) was taken as the signal coming from micro fractures and was not considered as the in-situ pore network of the rock.

Results (Figure 5Figure 5 – panel (c)) show that Fixed α is able to produce bi-modal distributions even at low SNR while NMR volume stabilizes at SNR of 57. GIT's technique (Figure 5 – panel (a)) produces unimodal distributions even at high SNR (excluding micro-fractures) while showing high stability both in T_2 distribution and NMR volume at very low SNR. The BRD technique (Figure 5 – panel (b)) produces unimodal distributions at low SNR but bi-modal distributions at SNR of 200 and more while NMR volume never stabilizes.
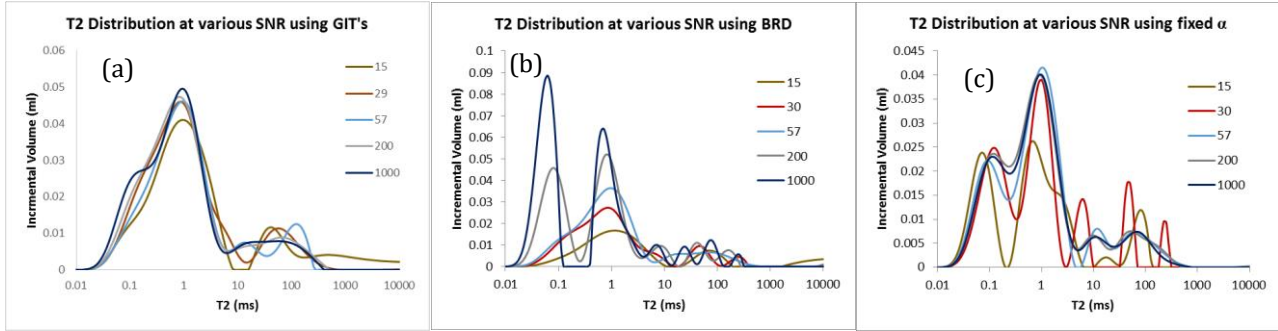
Figure 5 – T_2 distributions generated using GIT's (a), BRD (b), and Fixed α (c) techniques at different SNRs. Tests are run at TE=100 μs, 10,000 echoes and RD time of 1000 ms.

Depending on the application for the NMR data, accuracy and reliability can be interpreted differently. For example, NMR data is routinely used for permeability predictions. Two prominent models frequently used for permeability prediction from NMR data are the Timur-Coates and SDR models [13]. Timur-Coates correlates permeability to free-to-bound fluid volume ratio while SDR correlates permeability to log-mean relaxation time. T_2 distributions generated at different SNRs using the three smoothing techniques were used to calculate free-to-bound fluid volume ratios as well as log-mean relaxation times. The results are shown in Figure 6. Results indicate that the Fixed α regularization technique produces stable T_{2lm} as well as stable free-to-bound volume even at very low SNR. BRD however, while producing reliable T_2 distributions at high SNR, fails to produce consistent T_{2lm} and free-to-bound volumes. GIT's technique fails to produce a bi-modal distribution; however, it outperforms BRD's permeability prediction power at both low and high SNR. In conclusion a fixed smoothing parameter of 0.2 is used for all future inversions in this study.
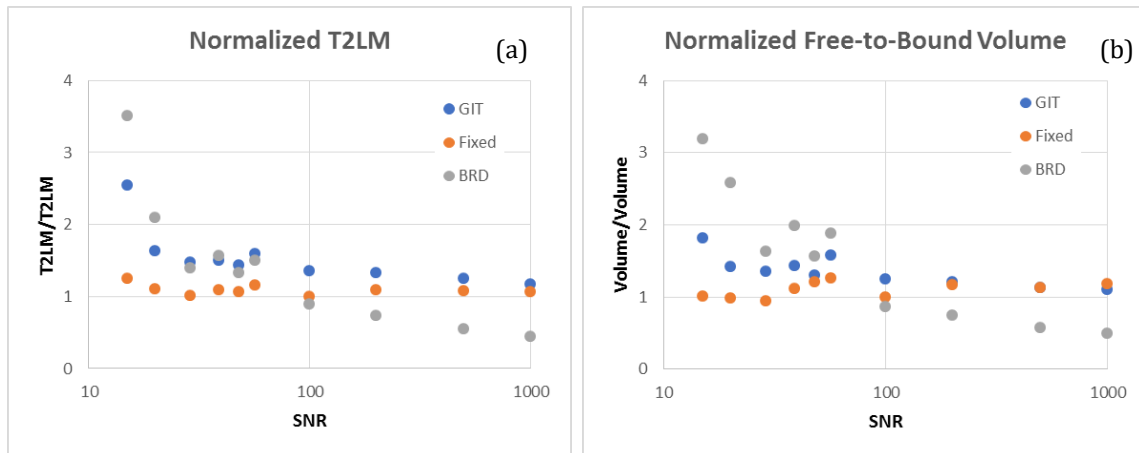

Figure 6 – A comparison of T_{2lm} and Free-to-Bound volumes calculated from T_2 distributions generated using GIT's, BRD and Fixed α techniques at different SNRs. The results are normalized for T_{2lm} and Free-to-Bound volume calculated from T_2 distributions generated using Fixed α technique at SNR of 100.

DATA ACQUISITION OPTIMIZATION
BACKGROUND SIGNALS

In the laboratory samples are typically put in sample holders or wrapped in Teflon wraps and placed in the spectrometer. As a result there exists the possibility of detecting signal from probe ring down, the holder, wrap or ambient moisture which can be interpreted as signal detected from the rock. In high porosity rocks, the background signal is negligible compared to the main signal coming from the rock; however, in low signal samples such as unconventional rocks,

Figure 7 – Background signal captured from the sample holder at different τs using the 1MHz digital filter

background signals can be very misleading as they can be interpreted as microporosity and result in overestimating the storage capacity of the medium. It is common practice to use digital filters to narrow the frequency range of the signal received from the sample and improve data quality [14]; however, each filtering process imposes an acquisition time delay known as "group delay" [1]. In this study digital filters were used to filter out the background signal. To do so, the holder was placed in the spectrometer and scanned at different echo spacing using different available filters while total NMR signal received by the coil was monitored. To avoid adding noise to the data, the SNR of the background signal was set to match the SNR of the scans that were ran on the sample for other measurements in this study. Initially a 1 MHz filter was used to allow for shorter τs. The 1 MHz filter was able to filter out most of the background signals at τ of 70 μsec and higher (Figure 7). At lowest τ, the signal captured from the holder using the 1MHz filter amounted to double the signal captured from the sample at partially saturated state. The 125 KHz filter however, was able to filter out the entire background signal although the smallest τ available on the 125 KHz filter was 50 μsec. Therefore the 125 KHz filter was used as the optimum filter for future runs.
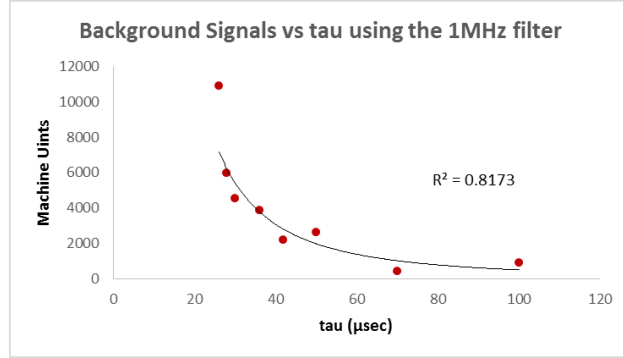
ECHO SPACING (TE)

The sooner data acquisition starts, i.e. shorter TE, in a CPMG process the more spin echoes are detected [in a given experimental time]. Specifically in fast relaxing unconventional rocks these early time signals play an important role in characterizing heavy hydrocarbons as well as the micro-pore space while rocks with larger pore network and light hydrocarbons are less sensitive to echo spacing. Using the 125 KHz filter, a minimum τ of 50 μsec could be achieved. The effect of echo spacing on the T_2 distribution curve was studied by running the same test at different echo spacings, ranging from 50 μsec to 200 μsec in increments of 10 μsec. Figure 8 summarizes the results, showing that micro-porosity (representing fast relaxing atoms) significantly decreases as τ is increased and at τ of 200 μsec 77% of micro-porosity volume is lost and T_{2lm} increases by 130 percent while meso and macro-porosity volumes are unchanged.
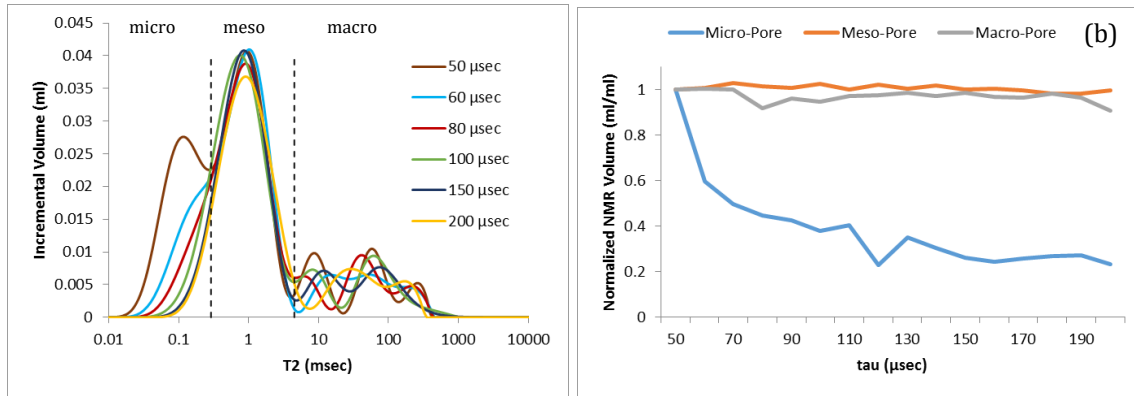
(a)

Figure 8 – A comparison between NMR volumes at different echo spacings, processed using the fixed α method. Results highlight the fact that at higher echo spacings signal from fast relaxing components of the medium (can be organic porosity or heavy hydrocarbons) is not captured

NUMBER OF ECHOES

At any given TE, the number of echoes dictates the length of each NMR scan. In unconventional rocks, due to small pore structure and mineralogy, hydrogen nuclei relax faster. Typically scans with a small number of echoes are run to save time, especially during NMR logging operations, dismissing the fact that enough echoes are required to capture all the hydrogen nuclei with different relaxation rates. Acquiring data with an insufficient number of echoes results in discounting the slow relaxing hydrogen nuclei, typically occupying the micro fractures, and underestimating porosity. It is recommended to increase the number of echoes until the echo train data decreases to the noise level.

In this study, the sample is scanned with different numbers of echoes, ranging from 500 to 10,000 echoes. All scans are run at τ=50μsec and Repeat-Delay time of 3000 ms. The results (Figure 9) show that at a lower numbers of echoes, 45% of the macro-porosity and 10% of the micro-porosity is not captured. As number of echoes increase, both volumes increase while meso-porosity is unchanged. However, because macro-porosity is a small fraction of the total porosity in this specific sample, total NMR volume is only affected by 10% throughout this analysis.
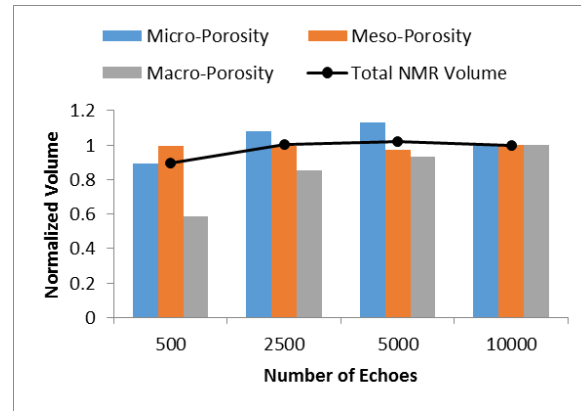
Figure 9 – Study of susceptibility of NMR volumes to number of echoes. In the presence of larger pores and micro-fractures more echoes (longer scans) are required to capture the signal. Volumes in the graph are normalized for volumes at 10,000 echoes.

REPEAT-DELAY TIME

Typically, multiple successive CPMG sequences are run to minimize the noise and maximize the signal-to-noise ratio (SNR). Wait times are applied between each successive CPMG sequence to let the spins relax to their equilibrium state. This wait time is referred to as the Repeat-Delay time (RD). In a complex system, where different fluids exist in a complex pore structure of various sizes, RD is typically chosen as 3 to 5 times the largest T_1 relaxation. Choosing too small of a RD time can result in reduction of the total NMR

signal as some atoms will not have returned to their thermal equilibrium when the next CPMG sequence starts.

In this study, a series of RD times, ranging from 100 ms to 3000 ms, were examined on the Montney sample. All these runs were performed at τ=50µsec. The results (Figure 10-a) show that up to 30% of the macro-pore NMR volume and up to 20% of the micro-pore NMR volume is lost at lower RD times. Meso-pores, occupied by fast relaxing brine molecules, do not show sensitivity to RD time variations. Micro-pore sensitivity to RD time is either an indication of presence of low viscosity hydrocarbons (such as gases) in the micro-pore space or an indication of the presence of fast relaxing heavy hydrocarbons (such as bitumen) in the pore structure. A T_1-T_2 scan performed on the As-Received sample (Figure 10-b) highlights the presence of high viscosity hydrocarbons in the fast relaxing domain. High viscosity hydrocarbons show higher T_1-T_2 relaxation ratios compared to low viscosity hydrocarbons. As a result, in the presence of heavy hydrocarbons, the T_1-T_2 map will deviate from the 1-1 line. It should be kept in mind that the T_1-T_2 map was obtained from the As-Received sample with residual water saturation.
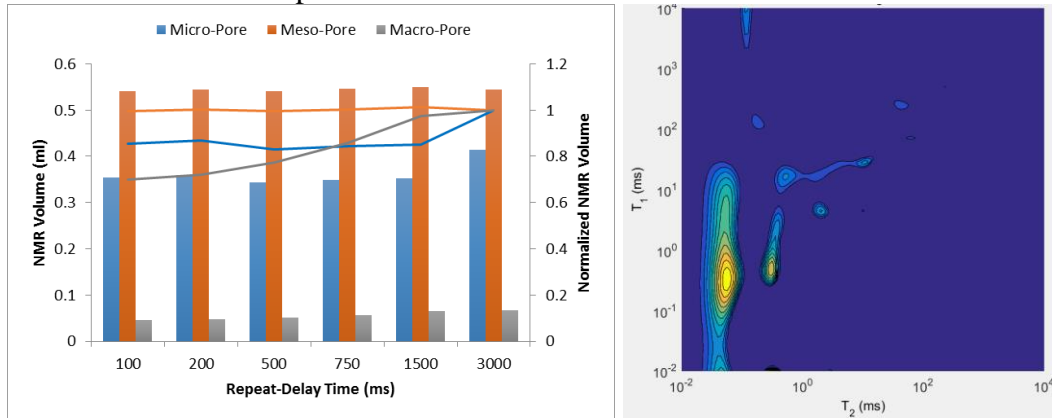

Figure 10 - (a) shows the effect of RD time on NMR volumes while (b) highlights the presence of heavy hydrocarbons in the sample.

REPEATABILITY OF T_2 MEASUREMENTS

On a separate set of samples, an investigation was undertaken into repeatability and error associated with the measurement of T_2 distributions. This data was also used to explore the effect of heating of samples by the rf excitation pulses. All the T_2 relaxation data acquired was fit using the GIT regularization technique.

In the first series of experiments, a calibration sample with a fixed volume of water was used. Its NMR volume was determined repeatedly via 500 T_2 measurements (see Table 3 for experimental parameters) done in succession allowing the error in the measurement to be calculated. The series of T_2 measurements was repeated with $\tau = 100$ µs and 500 µs. By comparing the $\tau = 100$ µs and 500 µs data, the effect of scan sequences with short τ and long echo trains versus long τ and short echo trains could be examined. The results of the T_2 measurements can be seen in Figure 11, the top panel showing the $\tau = 500$ µs data and the bottom panel showing the 100 µs data. Both sets of measurements show a sharp decrease in the NMR volume over the first two to three scans. This is most likely due to heating of the sample during the first few scans. The NMR signal will decrease approximately 0.3% per degree Celsius for temperatures near room temperature. The decrease in signal is not due to a real loss of volume as the sample is sealed. The 100 µs data shows a continual decrease in the NMR volume due to continued heating over the

entire experiment. The same effect is not as pronounced in the 500 µs measurements indicating that heating of the sample is more pronounced for scan sequences with short τ and long echo trains.

The measurement error is hard to determine for either set of measurements due to heating of the sample. The best estimate of the error comes from the last fifty measurements in each data set where temperature is most stable and hence having the least effect (i.e. $\tau =$ 100 µs, measurement error $= \pm 0.033\%$ and $\tau = 500$ µs, measurement error $= \pm 0.068\%$). The lack of shorter τ data makes the determination of the NMR volume from the 500 µs data more prone to error leading to a larger measurement error.

In the second series of experiments, a brine saturated sandstone sample was employed. As with the fixed volume sample, its NMR volume was determined repeatedly via 500 T_2 measurements done in succession. The rock chosen had a T_2 distribution similar to the fixed volume sample so that the same scan parameters could be employed (see Table 3 for experimental parameters).

Again, a series of T_2 measurements was repeated with $\tau = 100$ µs and 500 µs. The results of the T_2 measurements can be seen in Figure 12, the top panel showing the $\tau = 500$ µs data and the bottom panel showing the 100 µs data. Neither data set showed heating effects as pronounced as with the fixed volume sample. This indicates that heating of the sample by the rf pulses is not as much of an issue in rock samples as in fixed volume samples.

For rock samples, care must be taken to ensure that any decrease observed is due to heating of the sample and not due to drying as the sandstone was not sealed. From mass measurements before and after the NMR experiments, it was determined that the rock loses about 0.1 ml/hour of brine due to drying. Removing this drying rate from the NMR data, it is determined that for the $\tau = 500$ µs data the entire change in volume over the experimental time is due to drying, while some of the volume change in the $\tau = 100$ µs data is due to heating.

Table 3 – Experimental Parameters for Fixed Volume and sandstone samples

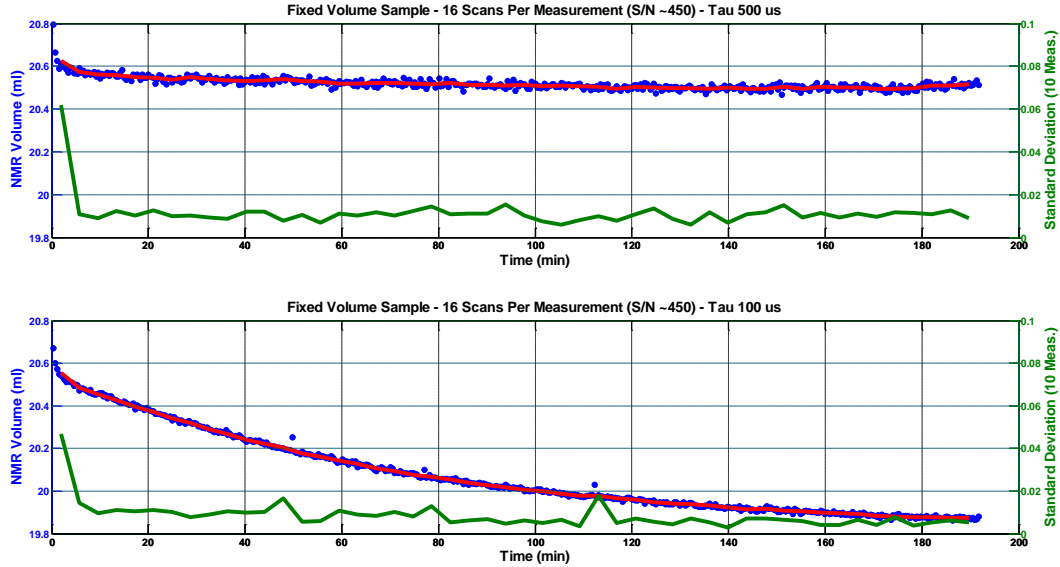| Sample	Fixed Volume Sample	Fixed Volume Sample	Sandstone Sample	Sandstone Sample
Expected Volume	20.75 ml	20.75 ml	12.4 ml	12.4 ml
Number of Scans	16	16	16	16
Number of Echoes	2500	500	2500	500
Recycle Delay	750 ms	750 ms	750 ms	750 ms
Filter	125 KHz	125 KHz	125 KHz	125 KHz
T2 Max	100 ms	100 ms	100 ms	100 ms
τ	100 µs	500 µs	100 µs	500 µs
Approx. SNR	450	450	250	220

Figure 11 – T2 volume measurements for a fixed volume sample versus time at two different echo spacings. The graph shows that at smaller τ heating effects are more severe and lead to major variations in NMR volume

The measurement error is hard to determine for either set of measurements due to the temperature/drying effects observed in the rocks. The best estimate comes from the last fifty measurements in each data set where temperature is most stable and hence having the least effect (i.e. τ = 100 μs, measurement error = ±0.304% and τ = 500 μs, measurement error = ±0.596%). The lack of shorter τ data makes the determination of the NMR volume from the 500 μs data more prone to error leading to a larger measurement error.
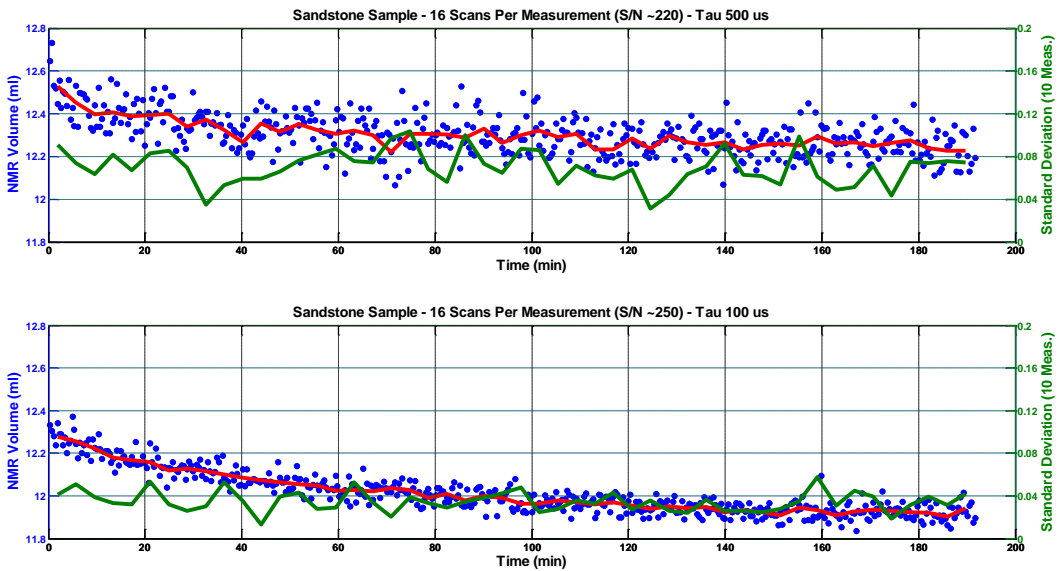

Figure 12 - T2 volume measurements for a sandstone sample versus time at two different echo spacings. The graph shows that at smaller τ drying effects are more severe and lead to major variations in NMR volume

CONCLUSIONS

This study was performed on a tight rock sample to analyze the challenges imposed on NMR data acquisition and analysis due to the presence of fast relaxing hydrogen atoms in the pore space of such rocks. Factors such as smoothing parameter, echo spacing, repeat-delay times, background signals, number of echoes, and repeatability of the measurements were examined. In this study we were able to show that

- Due to the fast relaxation of the hydrogen nuclei in unconventional rocks, NMR data inversion is more challenging in these rocks compared to conventional rocks. A Fixed α inversion technique was compared with other available techniques and proved to be capable of producing reliable and consistent T_2 distributions even at low SNR. It should be noted that the Fixed α was achieved in a lab setting by scanning the sample at two saturation levels. In the field or where scanning samples at various saturation levels is not possible, it is still recommended to run an initial scan with high SNR and calculate α using a trusted inversion technique and use the same α at lower SNR to save time to achieve reliable results.

- A 125KHz digital filter proved to be able to eliminate the entire background signal. Although it was possible to run shorter echo spacings, as small as 26 µs, with the 1MHz filter, the filter could remove the majority of the background signal only at τ=70 µs and larger.

- Short echo spacing, with a large number of echoes should be used to capture all the signal form the micro-pore space to the micro-fractures. Long Repeat-Delay times should be used to let all atoms relax to their thermal equilibrium before the commencement of the next re-phasing. Using short RD times would result in the loss of signal specially from heavy hydrocarbons as well as the macro-pore space.

- Heating and drying effects should be accounted for when consecutive NMR measurements are performed on samples. Particularly at short echo spacings heating/drying effects are more significant and can lead to discrepancies.

REFERENCES

[1] Saidian, M., and M. Prasad. "Nuclear Magnetic Resonance (NMR) Measurements for Mudrock (Shale) Characterizations: Challenges in Data Acquisition and Signal Processing" *Journal of Magnetic Resonance*, Submitted (2015)

[2] Kenyon, W. E., 1992, "Nuclear magnetic resonance as a petrophysical measurement", *Nuclear Geophysics*, v. 6, no. 2, p. 153-171.

[3] Saidian, M., "A comparison of measurement techniques for porosity and pore size distribution in mudrocks: a case study of Haynesville, Niobrara, Monterey and Eastern European Silurian Formations." *AAPG Memoir* 110 (2015): 60

[4] Passey, Q. R., K. M. Bohacs, W. L. Esch, R. Klimentidis and S. Sinha, 2010, "From oil-prone source rock to gas-producing shale reservoir–geologic and petrophysical characterization of unconventional shale-gas reservoirs" *International Oil and Gas Conference and Exhibition,* SPE Paper 131350

[5] Chalmers G. and R. Bustin, "Geological Evaluation of Halfway–Doig–Montney Hybrid Gas Shale–Tight Gas Reservoir, Northeastern British Columbia," *Marine and Petroleum Geology*, vol. 38, no. 1, pp. 53-72, 2012

[6] Wüst R. A., B. R. Nassichuk and R. M. Bustin, "Porosity Characterization of Various Organic-rich Shales from the Western Canadian Sedimentary Basin, Alberta and

British Columbia, Canada," *M102-Electron Microscopy of Shale Hydrocarbon Reservoirs, American Association of Petroleum Geologists*, 2013, pp. 81-100

[7] Ghanizadeh A., S. Aquinto, C. R. Clarkson, O. Haeri-Ardakani and H. Sanei, "Petrophysical and Geomechanical Characteristics of Canadian Tight Oil and Liquid-Rich Gas Reservoirs," *SPE/CSUR Unconventional Resources Conference*, Calgary, Alberta, Sep 30 - Oct 2, 2014.

[8] Meiboom, S., and D. Gill, 1958, "Modified Spin‐Echo Method for Measuring Nuclear Relaxation Times," *Review of Scientific Instrument*, Vol. 29, No. 8, P. 668-691

[9] Carr, H., and E. Purcell, 1954, "Nuclear magnetic resonance: Petrophysical and logging applications," *Physical Review*, v. 94, No. 3, P. 630-638

[10] Coates, G. R., X. Lizhei, and M. G. Prammer, *NMR Logging Principles and Applications,* Haliburton Energy Services Publication, 1999

[11] Dunn K. J., D. J. Bergman and G. A. LaTorraca, *Nuclear Magnetic Resonance: Petrophysical and Logging Applications*, Elsevier, 2002

[12] Song, Y-Q., et al. "T1–T2 correlation spectra obtained using a fast two-dimensional Laplace inversion." *Journal of Magnetic Resonance* 154.2 (2002): 261-268.

[13] Salimifard B., D. W. Ruth, D. Green and D. Veselinovic, "Developing a Model to Estimate Permeability from Other Petrophysical Data," *International Symposium of the Society of Core Analysts,* Avignon, France, 2014

[14] Moskau, D., 2001, "Application of Real Time Digital Filters in NMR Spectroscopy, Concepts," *Magnetic Resonance*, v. 15, no. 2, p. 164-176

COMPARISON OF DISPERSION DESCRIBED BY TRACER TESTS AND NMR PROPAGATORS USING THE SMIM MODEL.

M. Fleury[1], S. Stona[1], D. Bauer[1], M.C. Neel[2]

[1]IFP Energies nouvelles, Rueil-Malmaison, France
[2]Université d'Avignon et des Pays de Vaucluse

This paper was prepared for presentation at the International Symposium of the Society of Core Analysts held in Vienna, Austria, 27 August – 1 September 2017

ABSTRACT

Dispersion in porous media has been studied for a long time from breakthrough curves using a tracer. The NMR propagator technique is an alternate way for deriving dispersion from local velocimetry. In this work we compare the results obtained with both techniques on model porous media. Tracer tests were performed on homogeneous and heterogeneous grain packs using potassium iodium as a passive tracer detected at the outlet by a UV detector. On the same columns, NMR propagators were measured at different flow-rates for the same conditions

The data were analyzed using a general model called SMIM partially developed previously. With 4 parameters in addition to the dispersion coefficient, the model is able to reproduce two important features in dispersion: delayed breakthrough in dual porosity systems for example, and early breakthrough in the presence of preferential paths. For the analysis of NMR data, the SMIM model is described using analytical expressions reproducing directly the NMR signals, whereas for the tracer data, a numerical simulation is needed to calculate the breakthrough curve. NMR data were inverted to obtain the different dispersion parameters and then the breakthrough curves calculated and compared to measurements. Both techniques give comparable results; detailed discrepancies and limitations/advantages of the NMR approach are discussed.

INTRODUCTION

Dispersion in porous media has been studied for a long time from breakthrough curves (BTC) using a tracer [1]. Typically, one monitors at the outlet of a porous medium the spreading of a spike of tracer (a miscible fluid) injected at the inlet. In the simplest case (normal dispersion), the concentration vs. time curve is Gaussian and analyzed using an advection-dispersion equation (ADE) to obtain a dispersion coefficient D. It is well known that such approach is limited to homogeneous porous media and difficulties to analyse non-symmetric curves has long been recognized [2]. When more advanced models are used to reproduce for example trapping mechanisms in non-flowing porosity

fraction, or fast flow in preferential pathways, a single BTC is not sufficient and more information is required such as the spatial evolution of the BTC measured using local concentration along the core length [3]. The Pulsed Field Gradient (PFG) NMR technique is an alternate and much more direct method since the distribution of molecule displacements (propagator) is measured, and this is a unique information at the origin of dispersion mechanisms. Indeed the variance (or second moment) of the measured distribution is directly linked to the dispersion coefficient D without any assumption. This property has been used by many authors and results from both tracer and NMR methods gives comparable results (see Seymour et al. [4] for a compilation of results), although NMR tend to give lower D values. This simple approach does not apply in porous media with a complex structure such as double porosity carbonates [3], or in two phase flows performed in homogeneous systems [5]. When dispersion is anomalous, D will vary as a function of time as observed in NMR experiments [5], and for tracer experiments, a single value of D cannot be found when the length of the porous media is varied (i.e. D depend on space [3]). Hence models can truly be tested when appropriate experimental information is available and the final goal is to characterize a porous media with a unique set of parameters valid at all times and all locations.

In this work, we propose to test a new model (SMIM an acronym for Stochastic Mobile Immobile Model [6]) in a system containing important non flowing zones. In essence, the concepts in this model are not new and stochastic models such as CTRW (Continuous Time Random Walk [1]) are also able to reproduce similar physical mechanisms with the help of numerical simulations. However, the availability of analytical expressions for deriving the NMR signal allows inverting the model parameters in a very efficient way. The analytical expressions describe directly the NMR signal, and not its Fourier transform (propagator) avoiding some important difficulties. It uses also all the information contained in the signals, and not only the second moment that takes only into account the smallest wave numbers. Another objective of this work is to simulate the BTC and compare the results to measurements performed in the same porous media. For this purpose, a numerical simulator was developed to solve an equation applicable for a tracer (SMIMt).

THEORY

Dispersion from NMR data

The proposed model SMIM [6] is very general and attempts to reproduce two important mechanisms: (i) the possibility for a molecule to be temporarily trapped in non–flowing zones and (ii) the possibility for a molecule to travel large distances due to for example a highly contrasted velocity field. Hence, we reproduce deviations from the Gaussian case either by modifying the short or long displacement tails on both sides of the distribution. Empirical choices for representing these mechanisms were made: for the first mechanism, the well-known Mobile –Immobile concept is used [1,2], and for the second mechanism, the idea of Levy motions [7] is exploited with the important advantage that it includes the

Gaussian case. The complex PFG-NMR signal is given by the following analytical expressions [6]:

$$E(q,\Delta t) = <e^{-iq\Delta x}> = (F_- + GM)e^{r_-\Delta t} - (F_+ + GM)e^{r_+\Delta t} \tag{1}$$

where:

$$F_\pm = \frac{\eta}{K+1}\frac{A_\pm}{r_\pm} \quad G = \frac{K\eta}{K+1}\frac{1}{\sqrt{\Delta}} \qquad M = e^{-\omega(K+1)t_1} \qquad \eta = iqv_m + D|q|^\alpha\left[1 + \tan\frac{\pi\alpha}{2}sign(q)\right]$$

$$2r_\pm = -(\eta + \omega(K+1)) \pm \sqrt{\Delta} \quad A_\pm = \frac{\omega(K+1)-\eta}{2\sqrt{\Delta}} \pm \frac{1}{2} \quad \Delta = \eta^2 + 2\eta\omega(K-1) + \omega^2(K+1)^2$$

where q is the NMR wave number (described later). The model has 5 parameters D, α, K, ω, v and an auxiliary parameter M with the following significance:

D: generalized dispersion coefficient [m^α/s],

α: stability exponent of the Levy distribution,

K: ratio of average immobile to mobile times,

ω: parameter describing the distribution of immobile times, exponentially distributed with a rate ω,

v_m: average velocity while moving (thus larger than the measured average velocity $<v>$),

v=$<v>$(1+K),

M: a parameter describing memory effects.

These parameters are better understood when considering the corresponding dispersion equation below describing tracer tests.

Dispersion from tracer tests

The partial differential equation describing tracer experiments and corresponding to the SMIM model is the following:

$$\frac{\partial C}{\partial t} + K\omega e^{-\omega t} * \frac{\partial C}{\partial t} = -v\frac{\partial C}{\partial x} - D\frac{1}{\cos(\pi\alpha/2)}\frac{\partial^\alpha C}{\partial x^\alpha} \tag{2}$$

The parameter α is present in the fractional derivative of order α (definition given in [6]), and the trapping mechanism is identified by a supplementary term in the time derivative (the symbol * indicates a convolution). When α=2 and K=0, equation 2 corresponds to the standard ADE. This equation has been solved numerically by using a finite difference scheme of order 2. To properly represent diffusion, an operator splitting technique has been used. The calculation are made by introducing an initial Dirac impulse and integrating the curve to represent a stepwise continuous injection of tracer. Boundary conditions are more crucial. At the inlet of the column, the computation domain has been slightly augmented by a very small (0.02cm) transition zone in which the diffusivity smoothly decreases from D down to zero. For the present diffusivity and velocity values, this condition has no influence on the results. At the outlet and to avoid numerical perturbations, the computation domain has also been taken larger than in the experiments: homogeneous Dirichlet boundary condition has been imposed 4 cm after the physical outlet where break-through curves are recorded.

MATERIAL and METHODS

Porous media

A homogeneous pack was first prepared using well sorted glass beads with sizes in a narrow range [50 – 70 µm]. For this system, a porosity of 36.0% and a permeability of 2390 mD were obtained (length of the pack 27.73cm, inner diameter 2.40 cm). A second heterogeneous system was built by crushing a heavily micritized wackestone from the Eastern Paris basin (labeled GUD in Vincent et al. [8]). Before crushing, the bloc had a porosity of 22.7% and a permeability of 0.45 mD. The grains were sorted in the range [30-125 µm]. The porosity of the grain pack is 50.1%, composed of an inter-granular and intra-granular porosity respectively of 38.5% and 11.6%. The permeability of this heterogeneous system is 2380 mD (length 20.46 cm, inner diameter 2.40 cm).
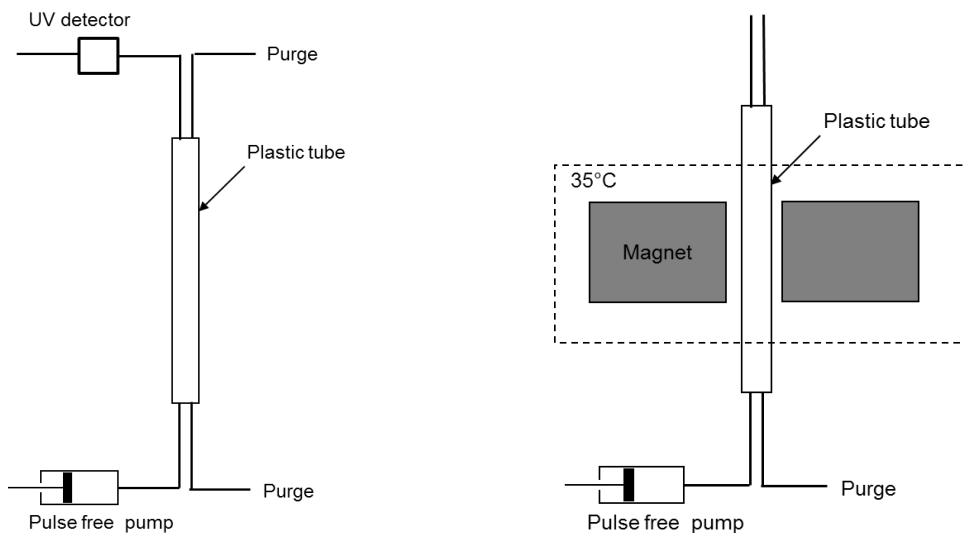

Figure 1: Experimental set-up for measuring breakthrough curves (left) and propagators in the NMR device (right). The column has an outer diameter of 30mm and a length up to 27 cm.

Propagator measurements

To perform propagator measurements (i.e. a measure of the spin bearing molecule displacement distribution in a given volume), the grain pack tube was placed in a 20MHz Oxford Instrument imaging system (Figure 1). The sequence used to measure displacement distributions is a bipolar pulsed field gradient stimulated echo sequence with z-storage in which a slice selection has been inserted to select a given volume in the column (Figure 2, more details are given in Guillon et al. [5]). To build the NMR signal $E(q,t)$ and the displacement distribution for a given observation time t, echo amplitudes are collected for different values of the wave number q defined as :

$$q = \frac{\gamma g_{\max} \delta}{2} \qquad P(\xi,t) = \int_{-\infty}^{+\infty} E(q,t) e^{i2\pi\, q\xi}\, dq \qquad\qquad (3)$$

where $g_{\max}$ is the maximum amplitude of the gradient pulse, and γ the proton giromagnetic ratio ($\gamma/2\pi$=42.58 MHz/T). The factor of 2 in the q calculation originates from the gradient shape. The gradient amplitude $g_{\max}$ was varied in 42 steps adequately spaced up to the noise level depending on the time t and injection velocity.
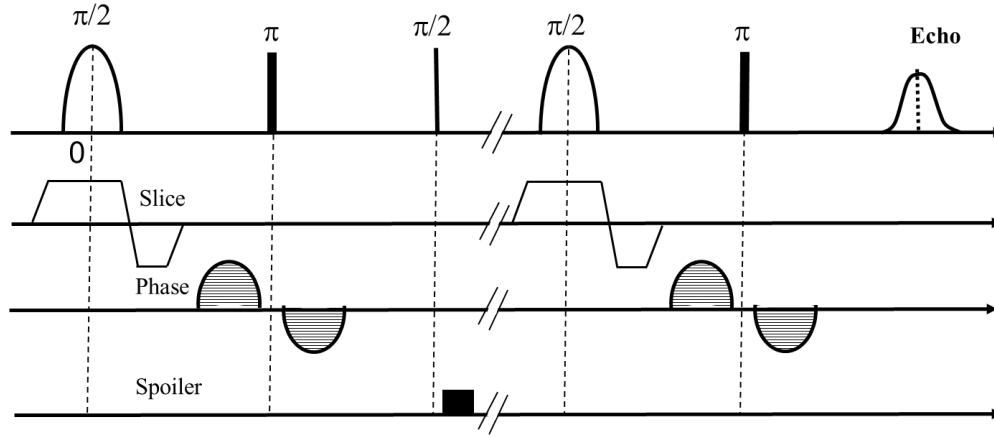

Figure 2: NMR sequence for measuring propagators, 20 MHz Oxford Instrument imaging system. The sequence comprises essentially a slice selection (2 cm thickness) and a bipolar phase encoding performed along the flow direction.

Dispersion can be evaluated from NMR propagator measurements providing (i) the mean displacement is much larger than the grain size ($\langle\xi\rangle > 5d_g$ [5,9]) (ii) the molecular diffusion is large enough to allow particles to probe several streamlines (criterion $L_d = \sqrt{2D_m t} > 0.3d_g$ where D_m is molecular diffusion [9]). Thus, the first criteria requires that <v>t be large enough; in practice, depending on the mean velocity, observation time above 200 or 500 ms are required. With such values, the second criteria is also met. Furthermore, in the context of the SMIM model, it is the time dependence of the propagator that allows determining the numerous parameters of the model, and not only one measurement at a single time. Hence, usually 4 measurements were performed at times varying from 500 up to 1400 ms. We verified that 4 measurements are enough to obtain the desired information by performing one experiment with 16 times varying from 500 up to 2000 ms. We also verified for each experiment that the mean velocity measured by NMR is coherent within experimental uncertainties with the mean velocity deduced from the imposed flow rate and porosity. This implies also that the gradient amplitudes are properly calibrated yielding accurate dispersion coefficients.

For the homogeneous system with a single longitudinal or transverse relaxation time, NMR measurements were performed with the column fully saturated with water and observation time t varying from 500 ms up to 1000 ms. For the bimodal system saturated

with water, the transverse relaxation time is non-unique and has two peaks (T_2=300 and 35 ms) corresponding respectively to the inter and intra-granular porosity. Hence, when large observation times are used (200 ms and more), the displacements inside the grains cannot be detected because the magnetization originating from this porosity fraction has relaxed to zero . Hence, we saturated this porous medium with cyclohexane, a non-polar molecule with very weak surface interaction; as a result, a single relaxation time is observed at about 700 ms, allowing propagator experiments to detect without bias the displacements in the entire pore volume. This is a key issue in many non-strictly homogeneous natural porous media in which there is a relaxation time distribution generating a T_1 or T_2 weighted propagator [10].

Tracer measurements
Using the same porous media, breakthrough curves were measured using a water solution containing 20 ppm of potassium iodure (KI). The concentration of this tracer is then detected by a UV detector at a wavelength of 226 nm (Figure 1). We checked that the response of the detector as a function of the KI concentration is accurate and linear. The detector is placed as close as possible to the outlet of the cell (a few cm). To minimize the dispersion effects close to the inlet and outlet, the inlet and outlet end-pieces, equipped with two tubings, are first saturated with the KI solution, while the grain pack is fully saturated with (pure) water. Then the KI solution is continuously injected and the data acquisition started. As a result, the recorded signal shows several phases (Figure 3): (i) the KI solution contained in the tubing connecting the outlet to the UV detector is first detected; the absorbance decreases from a maximum down to zero (ii) the water inside the porous media is detected; absorbance is zero until (iii) the injected KI solution is detected; the signal increases from zero up to a maximum. After normalization of the curve by the largest absorbance (i.e. the curve varies from 0 to 1, 1 being the 100% tracer concentration relative to the injected solution), a time origin is defined as the time at which the tracer concentration is equal to 0.5 during phase 1. Hence, the time shift between the outlet and the detector is taken into account. In a similar way, injecting pure water after the sequence described above also provides a breakthrough curve. Hence, several experiments could be repeated.
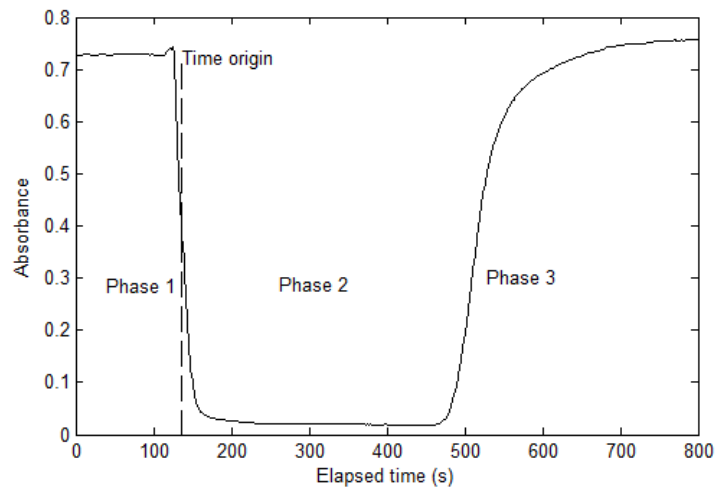
Figure 3: Typical aspect of a recorded signal when measuring breakthrough curves.

RESULTS

The general approach is to determine the dispersion properties from NMR measurements and the SMIM model. Then the same parameters are utilized in the tracer model SMIMt to predict a breakthrough curve. This curve is then compared to the tracer measurement. We present the results and comparisons for the two grain packs below. Four injection flow rates were used varying from 600 up to 1200 ml/h. Peclet numbers Pe vary between 20 and 40 ($Pe = vl/D_m$ where D_m is the molecular diffusion coefficient of water at 30°C, 2.6 10^{-5} cm^2/s, l is taken as the mean bead diameter).
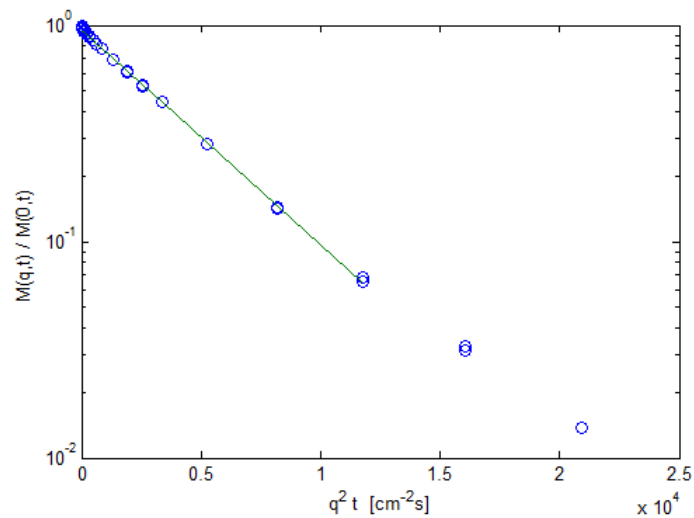

Figure 4: Example of the determination of the dispersion coefficient for the glass bead pack. Flow rate 800ml/h (<v>=0.136 cm/s), observation time t=599.4 ms. The slope D is 2.28 10^{-4} cm^2/s. The last two points not taken in the fitting are influenced by noise.

Homogeneous bead pack

For this system, we observed that the propagators are Gaussian. Indeed, when the magnetization is plotted vs. q^2t, a single exponential decay can be fitted (Figure 4) down to the noise level. Hence, the dispersion coefficient can be determined in a simple way according to :

$$\ln\left[\frac{M(q,t)}{M(0,t)}\right] = -Dq^2t \tag{4}$$

The Gaussian case is one particular case of the SMIM model ($\alpha=2$, all other coefficients K, ω, M equal to zero). For each flow rate, we determined a dispersion coefficient D (Table 1) as an average of the coefficient measured as a function of time (6 values from 500 up to 1000 ms). Indeed, D does not depend on time within experimental uncertainties (Table 1). As expected, D increases with the pore velocity or Peclet number. The dispersivity D/v expected to be constant increases however slightly with the pore velocity from 16 up to 19 µm.

The measured and simulated breakthrough curves are shown in Figure 5. The measured curves are much larger than the simulated ones. We indicate also as a guide the analytical solution of the ADE taking a dispersivity equal to the mean bead size (D/l=60 µm or D=8.2 10^{-4} cm^2/s). In this case, we cannot conclude about the coherency between NMR and tracer tests; with such a small dispersivity, small perturbations in the tracer tests are critical. Indeed, although the experimental set-up has been designed with the shortest distance between the outlet and detector, the measured breakthrough curves are not symmetric due to dispersion occurring between the outlet and the detector. This aspect will be analyzed further in the section the Discussion section.
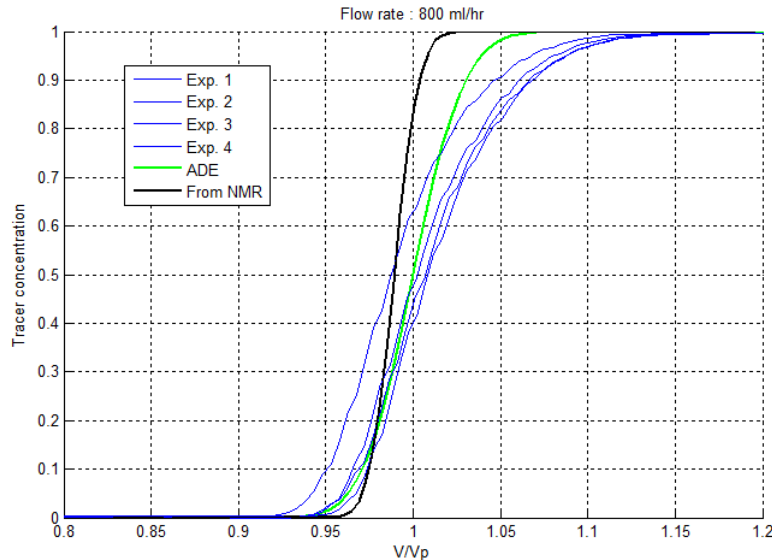

Figure 5: Measured breakthrough curves compared to simulations for the homogeneous bead pack.The blue curves are 4 repeated experiments, the green curve correspond to a standard ADE taking D=8.2 10^{-4} cm^2/s, the black curve corresponds to a simulation in which the NMR dispersion coefficient has been taken.

Bimodal grain pack

To obtain the parameters of the SMIM model, several E(q,t) signals were fitted simultaneously [6]. In most cases, 4 or 5 signals with observation time varying from 200-500 up to 1400 ms were used (Figure 6), yielding large average displacements, much larger than the mean grain size (Table 2). By fitting these signals for different α values spanning from 1.7 up to 2 [6], we found that the value yielding the lowest objective function was always close to 2 (from 1.90 up 1.98). Hence, it was decided to impose α=2 when inverting the SMIM parameters. Therefore, the SMIM model becomes a classical MIM model in which molecules can be trapped in non-flowing zones, and such model is presumably well suited for the present situation. The most interesting parameter is K, the ratio of immobile to mobile particles. For this system, we expect a ratio of the order of the ratio of intra to inter-granular porosity (11.6/38.5=0.30); we find indeed a value in the range [0.21-0.36], increasing with the mean velocity (Table 2). The dispersion coefficient increases with the mean velocity or Pe number, but the dispersivity is nearly stable (51±4 μm).
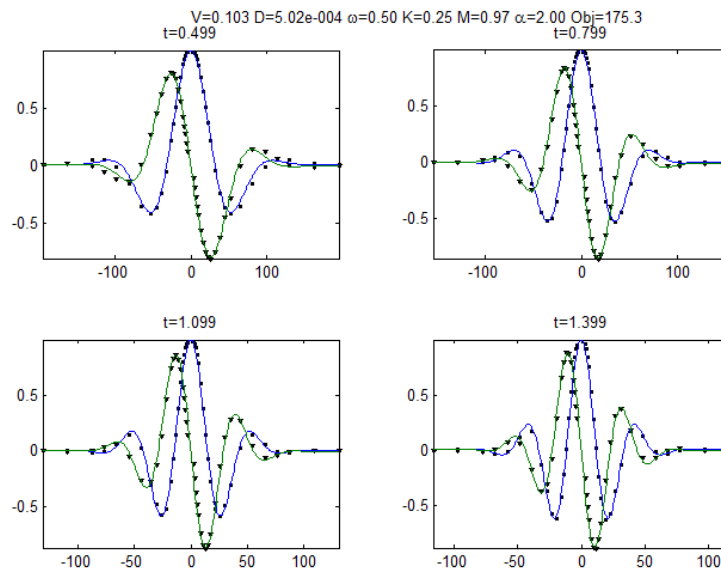

Figure 6: Real and imaginary E(q,t) NMR signals (square and triangle) fitted with the SMIM model (green and blue lines) for the heterogeneous bimodal grain pack. The observation times t are indicated in units of seconds. Flow rate: 800 ml/h. The resulting parameters are: D=5.02 10^{-4} cm^2/s, v_m=0.103 cm/s, K=0.25, ω=0.50, M=0.97.

The comparison between the simulated and measured breakthrough curves is also very instructive (Figure 7 for a flow rate of 800 ml/h). Although the agreement is not perfect, we see clearly that the model in which we used the parameters determined from NMR measurement is able to reproduce the early breakthrough at V/Vp~0.8 and a slight asymmetric shape. The asymmetry is more pronounced for the measured curves. The results obtained for other flow rates are all similar to this one. To obtain a physically sound result, the simulated curves were not scaled by the pore volume but by the volume in which particles are moving (V_p/(1+K)).
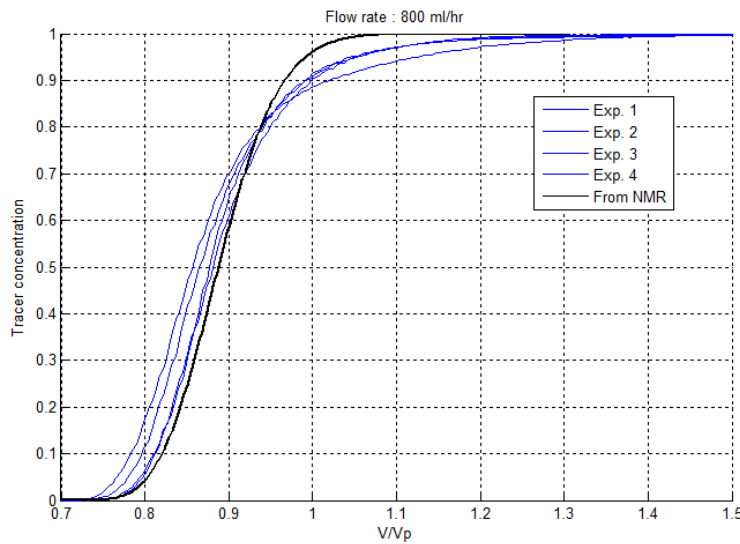
Figure 7: Comparison of simulated and measured breakthrough curves for the heterogeneous bimodal grain pack.

DISCUSSION

The direct use of the NMR signals in the inversion process is very important numerically; however, they have no direct physical meaning. Here, we compare the propagators obtained from the NMR signal in the bead pack and the grain pack for the same pore velocity (about 0.1 cm/s) and two observation times (Figure 8). For the bimodal grain pack, there exist a tail at zero or negative velocities, whereas this is not the case for the homogeneous bead pack. This tail subsist even at large observation times (1400 ms). This is actually the information provided by the signals and used to find the existence of a certain porosity fraction in which little or no flow is occurring (parameter K~0.3 in agreement with micro-porosity fraction in this system). Surprisingly, the propagator for the bimodal grain pack does not show a distinctive peak around zero velocities; this means that the exchange between the intra and inter-granular porosity due to molecular diffusion has a time scale shorter than the observation time. For this system, the micro-porosity is well connected to the macro-porosity.

The agreement between the BTC calculated from NMR data and the measurements is convincing for the bimodal grain pack, but not for the homogeneous bead pack. One source of discrepancy is that the NMR is a local measurement performed over about only 10% of the column, whereas the tracer experiment is valid for the entire column in which small packing defects can accumulate. But the most important aspect is that the tracer experiment has a limited resolution in terms of dispersion coefficient compared to NMR. Indeed, the dispersion of the tubing connecting the outlet face of the sample to the detector, even reduced to a minimum, has a large impact; a 1/8" or 1/16" tubing of a few centimeter with an inner diameter 10 or 100 times larger than the grain size can have a similar dispersion as the entire column only about 5 times longer. The applied protocol can give some information about these effects. Indeed, for each experiment, the

dispersion of the outlet line is measured in order to set the time origin (Figure 3); therefore the width of the BTC cannot be smaller than the width of this early signal. Indeed, for the homogeneous bead pack, we observed that the slope estimated at a concentration C=0.5 characterizing the outlet line and later the porous media are nearly identical. Thus, the tracer experimental device as designed in these experiments is capable of determining dispersivity only larger than about 60 μm, whereas NMR has no limitation and can characterize motions down to molecular diffusion.

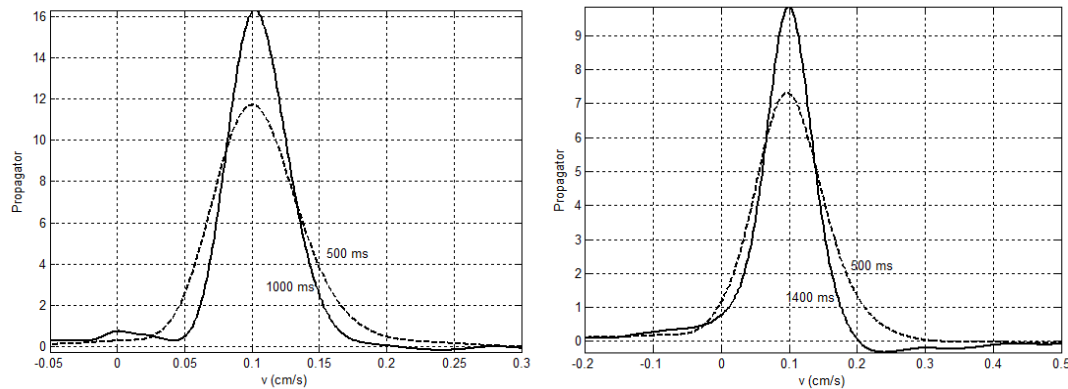Figure 8: Propagators calculated for the homogeneous bead pack (left, Q=600ml/h) and the bimodal grain pack (right, Q=800 ml/h).

CONCLUSION

For two model systems, we performed NMR propagator and tracer measurements in order to compare the NMR prediction on the shape and position of the breakthrough curve (BTC). The NMR analysis is performed using a model (SMIM) able to reproduce the most important features in dispersion: (i) trapping mechanisms in non- flowing zones and (ii) preferential pathways. The BTC are simulated using a numerical model taking as input the parameters determined in the NMR experiments. In this study, we tested the case of non- flowing zones by packing a bimodal system made of porous grains obtained by crushing a carbonate system of known porosity and permeability.

The results show that the early breakthrough observed on the BTC in the bimodal system is well reproduced by the NMR prediction. Furthermore, the NMR model used to interpret propagators also predicts a non-flowing porosity fraction in agreement with the intra-granular porosity. For the homogeneous case, the NMR dispersivity is smaller than the one deduced from BTC due to the important and unavoidable effect of outlet line dispersion.

Table 1: Results of NMR measurements for the homogeneous beak pack. Mean bead size: 60 µm. . $\langle l_D \rangle$ is the range of mean displacement for a given flow rate ($\langle v \rangle$t), $\langle v \rangle$ is the average velocity.

Flow rate (ml/h)	$\langle v \rangle$ (cm/s)	$\langle l_D \rangle$ (µm)	D *10^4 (cm^2/s)	Dispersivity (µm)	Pe
600	0.102	510-1020	1.62±0.03	15.9	23.5
800	0.136	680-1360	2.36±0.02	17.4	31.4
1000	0.170	850-1700	3.08±0.02	18.1	39.2
1200	0.204	408-2243	3.90±0.04	19.1	47.1

Table 2: Results of NMR measurements for the heterogeneous bimodal grain pack. Mean grain size: 75 µm. $\langle l_D \rangle$ is the range of mean displacement for a given flow rate ($\langle v \rangle$t), $\langle v \rangle$ is the average velocity.

Flow rate (ml/h)	$\langle v \rangle$ (cm/s)	$\langle l_D \rangle$ (µm)	D *10^4 (cm^2/s)	D/v (µm)	v_m (cm/s)	K	ω (1/s)	M	Pe
600	0.074	366-1024	3.53	47.5	0.077	0.21	0.50	1.00	21.4
800	0.098	488-1366	5.02	51.4	0.103	0.25	0.50	0.97	28.2
1000	0.119	244-1708	6.03	50.5	0.129	0.30	0.78	0.98	34.5
1200	0.143	293-2094	7.86	55.0	0.154	0.36	0.70	0.98	41.3

References

[1] M. Sahimi, Flow and Transport in Porous Media and Fractured Rock, Wiley-VCH, 2011.
[2] K. H. Coats and B. D. Smith, Dead-end pore volume and dispersion in porous media, Soc. Pet. Eng. J. 73 (1964).
[3] M. Fourar, G. Radilla, Non-Fickian Description of Tracer Transport Through Heterogeneous Porous Media, Transport in Porous Media 80 (2009) 561–579.
[4] J.D. Seymour, P.T. Callaghan, Generalized approach to NMR analysis of flow and dispersion in porous media, AIChE Journal 43 (1997) 2096–2111.
[5] V. Guillon, M. Fleury, D. Bauer, Neel, M. C., Superdispersion in homogeneous unsaturated porous media using NMR propagators, Physical Review E 87 (2013) 043007.
[6] M.-C. Néel, D. Bauer, M. Fleury, Model to interpret pulsed-field-gradient NMR data including memory and superdispersion effects, Physical Review E 89 (2014) 062121.
[7] R. Metzler, J. Klafter, The random walks guide to anomalous diffusion: A fractional dynamics approach, Physics Reports 339 (2000) 1–77.
[8] B. Vincent, M. Fleury, Y. Santerre, B. Brigaud, NMR relaxation of neritic carbonates: An integrated petrophysical and petrographical approach, Journal of Applied Geophysics 74 (2011) 38–58.
[9] U.M. Scheven, P.N. Sen, Spatial and temporal coarse graining for dispersion in randomly packed spheres, Physical review letters 89 (2002) 254501.
[10] J. Mitchell, Graf von der Schulenburg, D. A., D.J. Holland, E.J. Fordham, M.L. Johns, L.F. Gladden, Determining NMR flow propagator moments in porous rocks without the influence of relaxation, Journal of Magnetic Resonance 193 (2008) 218–225.

Combining core floods and numerical simulation to measure flow properties in heterogeneous rocks

Samuel Krevor, Simeon Agada, Sam Jackson, Catriona Reynolds, Ben Niu
Department of Earth Science & Engineering, Imperial College London, London, United Kingdom

This paper was prepared for presentation at the International Symposium of the Society of Core Analysts held in Vienna, Austria, 27 August – 1 September 2017

ABSTRACT
This paper develops the combined use of numerical simulation with core analysis to account for the impact of multi scale rock heterogeneity on equivalent relative permeability. In this workflow laboratory measurements that are a variation of conventional SCAL tests are used to derive properties for the parameterisation of an accurate digital rock model for simulation. An equivalent relative permeability at the range of capillary numbers relevant to flow in the reservoir is derived from numerical simulations of core floods that include capillary pressure heterogeneity. We present results in which digital rock models have been developed alongside core flood observations for three applications: (1) A Bentheimer sandstone with a simple axial heterogeneity to demonstrate the validity and limitations of the approach, (2) a reservoir rock from the Bunter sandstone in the UK North Sea targeted for CO_2 storage, and (3) a Berea sandstone with small layered heterogeneities for which a CO_2-EOR coreflooding program is planned. There are layered heterogeneities present in each rock ranging from multi-cm scale for the Bentheimer to mm-scale for the Berea sandstone. Simulation results on the Bentheimer and Bunter sandstone models show that equivalent relative permeability at low flow rates will be lower than viscous limit relative permeability by a factor of 5.

INTRODUCTION
Understanding the flow of multiple fluid phases in the subsurface has been of significant interest to scientists and engineers working in petroleum and groundwater hydrology for over a century. A key component in the analysis of these flows involves sampling rocks from the subsurface and characterising their flow properties. For single phase flow, this involves the analysis of porosity and absolute permeability. When multiple fluid phases are involved, capillary pressure and relative permeability characteristics are also characterised. The multiphase flow properties depend on the fractional pore occupancy of the fluid phases, i.e. the saturation, and hysteresis in the property-saturation relationships are sometimes also evaluated, along with the irreducible, or residual, saturations of each of the fluid phases.

Rock samples obtained from subsurface wells provide some of the most detailed information about the petrophysics of the reservoir. At the same time, there are a number

of practical issues which limit the nature of subsurface samples that can be analysed: (1) Rock samples obtained from wells (rock cores) are small. Conventional rock samples are 10-13cm in diameter. (2) The size scale of samples is also limited by size scales that can be practically evaluated in the laboratory setting. The length of the rock cores can vary, but it is rare to evaluate rock cores of a meter in length in the laboratory, although it is possible to acquire such cores from the field.

The theoretical justification for the use of flow properties derived from rock core analysis is based in Effective Medium Theory. See *Renard and de Marsily (1997*) [1] and more recently *Ringrose and Bentley (2015)* [2] for reviews. There is a prescription inherent in this that measurements of properties be made in a representative elementary volume of material. In the presence of heterogeneity, however, effective multiphase flow properties cannot be obtained [1]. This basis thus requires that laboratory observations of multiphase flow properties be obtained from homogenous and isotropic rock samples. Even in the context of this theoretical construct, the size of the representative elementary volume for multiphase flow properties is unclear [3]. It may be larger than samples that are readily obtained or practically used in the laboratory.

A number of studies have shown how saturation heterogeneity, and thus relative permeability heterogeneity, will arise in rocks with small variations in capillary pressure characteristics [4-7]. This is particularly true for flow conditions relevant to those of the reservoir system. In reservoir systems, typically low flow rates will allow for capillary redistribution to control fluid saturations over the centimeter length scales at which laboratory measurements are made. Thus, even rock cores which have been identified as homogenous by single phase tracer tests are unlikely to be so at conditions relevant to the reservoir system [7]. By extension a relative permeability curve obtained at high flow rates in the laboratory such that a homogenous saturation distribution can be obtained will have little relevance or predictive value for describing flow in the reservoir system.

The remaining alternative is to derive *equivalent* properties on the naturally heterogeneous samples. This term is typically reserved for flow properties obtained from observations where flow through the sample experiences and is affected by heterogeneity in the same manner as it would in the reservoir [1]. The derivation of relevant equivalent properties, however, also places severe demands on the observation - flow rates, fluids and fluid properties, and the orientation of rock heterogeneity with respect to flow must all be as they are experienced in the reservoir. This set of constraints has been seen to be insurmountable, and no attempts have been made to develop a protocol for measuring properties on heterogeneous rocks. Despite the clear violation of theoretical assumptions, the general protocol remains to perform multiphase flow property measurements at high fluid flow rates in the most homogenous rock cores that can be obtained.

In this work we show that advances in both observational and modeling techniques can be combined to overcome the problems associated with measuring equivalent properties on heterogeneous rocks. Recent work has demonstrated that fluid saturation heterogeneity

observed in rock cores using X-ray imaging can be used as a sensitive measure to characterise capillary pressure heterogeneity [5-8]. This is the principal heterogeneity of interest for characterising multiphase flow. We build on those approaches and combine this with recent developed modeling techniques, primarily those of *Krause et al. (2013)* [6], to build a numerical representation of the rock core. The salient heterogeneous features included in the models are principally heterogeneity in the capillary pressure characteristic curves.

It is the digital model that is used to derive the relevant equivalent relative permeability curve. This digitally derived relative permeability is the one to be used as the basis for upscaling and field scale reservoir simulation. An accurate digital model can generate this information at flow rates and simulating fluids that were not necessarily the ones used in the observation. There is also some ability to reorient the rock core with respect to the fluid flow direction. In this paradigm, the goal of the observations also shifts. Conventionally the focus of observations is on obtaining the most accurate relative permeability curve directly from the observations, often with a simulated based history match of the data. In the approach presented here, the goal becomes to parameterise the numerical model with the highest degree of accuracy.

MATERIALS AND METHODS

We developed the approach using observations made on three sandstone rock cores, a Bentheimer sandstone with a simple heterogeneity parallel to the axis of flow and described in *Reynolds and Krevor (2015)* [7], a rock core from the Bunter sandstone of the Southern North Sea of the UK [8], and a Berea sandstone rock core with parallel bedding. The rock cores were cut to 3.81 cm (1.5 inches) in diameter. The length, permeability, porosity, and capillary pressure characteristics for the rocks are provided in Table 1. The average porosity along the length of each rock core is shown in Figure 1.

The Bentheimer sandstone is a shallow marine sandstone which forms the unit for oil reservoirs in the Netherlands and Germany. It is frequently used in petrophysical studies due to its availability in quarries, high permeability, and homogeneity. The sample used was 95% fine to medium grained quartz with minor feldspar, and clay with a well sorted grain size distribution.

The Bunter sandstone sample was a medium-grained sandstone composed mainly of sub-angular to sub-rounded quartz grains with a minor component of detrital K-feldspar, clay, and carbonate clasts with a well sorted grain size distribution. The core sample was obtained from the British Geological Survey Core Store. It was derived from the Cleethorpes-1 well at 1312 m depth. This was a geothermal borehole located just onshore near the town of Cleethorpes in North East Lincolnshire, UK. Further details about the rock and experimental observations can be found in *Reynolds, (2016)* [8].

The Berea sandstone was an outcrop rock from the United States and is widely used in studies as a benchmark for petrophysical work [12]. The sample was heated above 700C for over 4 hours to stabilise kaolinite clay.

Observations were chosen to parameterise the numerical model accurately with the minimum number of observations. The following formed the principle observations: average absolute permeability, porosity, relative permeability in the viscous flow limit (high flow velocities), and heterogeneous saturation maps of the rock core at a wide range of average saturations. Relative permeability data was obtained by performing steady state relative permeability experiments using an approach described in detail in *Reynolds and Krevor (2015)* [7,8]. Saturation maps were obtained during various fractional flow steps of the steady state relative permeability tests.

In the Bentheimer sandstone, observations were made during primary drainage with nitrogen and water at 50°C and 15.5 MPa pore pressure. The total fluid flow rate of the viscous limit relative permeability observation was $Q_T = Q_{N2} + Q_{water} = 40$ ml min^{-1}. Equivalent relative permeability was simulated at $Q_T = 7$ ml min^{-1}. In the Bunter sandstone, observations were made during primary drainage with a CO_2-brine (1M NaCl) system at 53°C and 13.1 MPa pore pressure. The viscous limit relative permeability was obtained at $Q_T = 20$ ml min^{-1}. Equivalent relative permeability was simulated at $Q_T = 0.2$ ml min^{-1}. Observations in the Berea sandstone were obtained during primary imbibition using N_2 and water at 22°C and 10 MPa. The experimental flow rate was $Q_T = 20$ ml min^{-1}. Simulations have not been completed for the Berea sandstone. In all cases, the capillary pressures that can be obtained in laboratory core floods with low viscosity fluids are limited, and the use of nitrogen also limits the possibility of making observations at high non-wetting phase saturation [12].

Saturation maps were used to characterise the capillary heterogeneity [5,9]. The saturation, including the 3D saturation maps were obtained using an X-ray CT scanner during the flow experiments. For the 3D saturation maps, scans were repeated three times at each step. Averaging imagery over multiple scans allows for a boost in precision in the X-ray imagery which is affected by significant, but random, noise.

A capillary pressure curve derived from mercury porosimetry was assumed to represent the upscaled character of the rock core (Figure 2). During a flow experiment, initially it was assumed that the capillary pressure was constant at a given location along the axis of flow, i.e., that each "slice" of the core had a constant capillary pressure. The average saturation in the slice of the rock core was assumed to map to the capillary pressure obtained from the mercury porosimetry experiment. Thus, the range of saturation in a given slice was indicative of the heterogeneity in the capillary pressure characteristic curve functions for that slice. This is similar to the initial guess used by *Krause et al. (2013)* [6]. In this work, we use simple vertical scaling to vary the capillary pressure characteristic curves,

$$P_c(x, y, z, S) = \kappa(x, y, z)P_{c,a}(S) \qquad (1)$$

where $P_{c,a}$ is the average characteristic curve, a function of saturation, and P_c is the curve for a given location and saturation. These are related to the average through the location-specific scaling parameter, κ. The scaling parameter is initially obtained from the experimental data following the approach of *Pini and Benson (2013)* [9]. This extended the whole-core technique developed by *Lenormand and Eisenzimmer (1993)* [10] to millimetre scale capillary pressure characteristics.

In fitting curves for a given location, the slice averaged saturation (average at a given axial location) was mapped to the capillary pressure using the curves derived from mercury porosimetry. One point on the capillary pressure-saturation relationship was obtained for each fractional flow of the experiment. This was used to construct a capillary pressure dataset for a given location. The core representative capillary pressure curve (from mercury porosimetry) was then scaled by varying the entry pressure (Equation 1) in a regression algorithm until a best fit was obtained for the location.

The assumption of constant capillary pressure at a given location along the axis of flow, however, appears to be valid only at the inlet face of the rock core [6]. Here it is a boundary condition imposed by the experimental apparatus [10,11]. In *Krause et al. (2013)* [6] this assumption was relaxed through an iterative process - capillary pressure characteristic curves in a simulation grid block were updated until local saturations matched the experiment. The parameter was subsequently varied during the matching process to obtain a best fit of saturation. In the matching of saturation data beyond the initial guess, we stretched the distribution of scaling factors, κ, by increasing the variance in the distribution, while preserving the order of scaling factors throughout the domain of the rock model.

We represent the rock core using a model grid with grid cells the same dimension as the voxels obtained from the experimental observations, resulting in a grid of $16 \times 16 \times 40$. In this way, a direct location-specific comparison could be made between the observations and simulations. The ECLIPSE 100 simulator was used. The inlet and outlet boundaries were represented with a slice of grid cells with high permeability and no capillary pressure. The absolute and relative permeability for each grid cell was set to that observed in the experiments with flow rates in the viscous limit. The capillary pressure characteristic curve for each cell was set using vertical scaling. The base capillary pressure curve used a table of values from the mercury porosimetry data, converted to approximate a nitrogen-water system using the standard technique of scaling based on the respective interfacial tensions.

RESULTS

The relative permeability data and best fit curves are shown in Figure 3. The saturation range observed in the experiments was from 20 - 70% non-wettingphase (either nitrogen or CO_2) saturation. In the cases of the Bentheimer and Bunter sandstones, the relative

permeability to nitrogen remained $k_r < 0.12$ across this range. This is typical of coreflood experiments using low viscosity fluids where the maximum capillary pressure achievable is limited by the viscous pressure variation between the upstream and downstream ends of the rock core, i.e., saturation and relative permeability approaching the capillary endpoints are not approached [12]. Relative permeability of the Berea sandstone is far to the right of the saturation axis relative to the Bentheimer and Bunter sandstone data. This is due to either or both the differences in heterogeneity between the Berea and other sandstones, and the difference in displacement process. Relative permeability for the Bentheimer and Bunter sandstones were obtained during primary drainage. Relative permeability for the Berea sandstone was measured during primary imbibition, corresponding to the water-flood stage of an oil recovery process.

The heterogeneity in the capillary pressure characteristic curves are visualised with three-dimensional maps of the scaling parameter, κ, in Figure 4. A principle layering parallel to the long axis of the Bentheimer sandstone is apparent and most prominent at the downstream end of the rock core. Only a single layer can be seen indicating that the size scale associated with layering is larger than the diameter of the rock core. In the Bunter sandstone, there were repeated layers oblique to the long axis, some of which pinched out against the confining sleeve holding the rock core. The spacing between the layers was of similar dimension as the diameter of the rock core itself, i.e., 1-3 cm. Layering parallel to the axis of the rock core is evident in the Berea sandstone. The distance between these layers is far less than that of the Bentheimer and Bunter sandstones, around 5mm. The contrast in capillary characteristics was greater in the Bunter than in the Bentheimer sandstone, but greatest in the Berea sandstone.

A 2D saturation map of a central cross section of the Bentheimer sandstone is shown at steady state for a fractional flow $f_{N2} = 0.4$ in the top panel of Figure 5. The prominent single layer is manifest most clearly in the saturation distribution at the downstream end of the rock core. There also appears to be a gravitational effect at the inlet of the core, with a high nitrogen saturation in the uppermost part of the rock core which is subsequently distributed by capillarity about halfway through the rock core.

The central and lower panel of Figure 5 show the saturation map of the same cross section in the 3D simulation based on the heterogeneity model shown in Figure 4. The central panel shows the distribution with the first guess in capillary heterogeneity and the lower panel shows the simulation results when the variance of the κ distribution is scaled by a factor of 1.2. In both cases the layer is prominent and as with the experimental observation, more clearly defined towards the downstream end of the rock core. The simulation, however, does not appear to capture the gravitational effect at the inlet of the rock core, and is likely due to the boundary condition imposed in the simulation (constant injection, evenly distributed throughout the inlet boundary grid blocks). The simulation with the scaled variance in the κ distribution has a better fit to the observations than the initial unscaled input.

Figure 6 shows the 2D saturation maps of the observed and simulated coreflood for the Bunter sandstone for a fractional flow $f_{CO2} = 0.63$. The observations at the central and downstream ends of the rock core are well matched in the simulations. However, a region of prominent high CO_2 saturation at the upstream end of the observed core flood is not matched in the simulations. Additionally, there is a stronger capillary end effect apparent in the downstream end of the observed coreflood than in the simulations.

The impact of heterogeneity is evident in comparing the calculated equivalent relative permeabilities with the viscous limit relative permeabilities used as input into the numerical simulations (Figure 7). In both cases, the equivalent relative permeability is lower by approximately a factor of 5 than the viscous limit permeability, indicating a less efficient flux of fluid through the rock core due to the impact of capillary heterogeneity.

CONCLUSION

A workflow has been demonstrated for the use of heterogeneous rock cores in reservoir characterisation of multiphase flow properties. The workflow involves the use of corefloods with 3D saturation imaging as the basis for parameterising detailed numerical models of the rock cores. These models can then be used to derive equivalent relative permeability functions at the flow rates or other reservoir conditions of interest for reservoir modelling. In this work three rock cores with different length scales of layered heterogeneities were used in steady state core flood experiments of relative permeability. The saturation maps from the experiments were used to generated 3D models of capillary heterogeneity in the rock cores. Equivalent relative permeabilities derived from two the rock cores showed that equivalent relative permeabilities are significantly lower when obtained at flow rates significantly lower than the viscous limit.

ACKNOWLEDGEMENTS

REFERENCES

1. Renard, P. and de Marsily, G. (1997), Calculating equivalent permeability: a review, *Advances in Water Resources*, 20, 5-6, 253-278
2. Ringrose, P., Bentley, M., (2015) Reservoir Model Design: A Practitioner's Guide. Springer, New York
3. Armstrong, R.A., Georgiadis, A., Ott, H., Klemin, D., Berg, S. (2014), Critical capillary number: Desaturation studied with fast X-ray computed microtomography, *Geophysical Research Letters*, 41, 55-60.
4. Ringrose, P.S., Sorbie, K.S., Corbett, P.W.M., Jensen, J.L. (1993), Immiscible flow behaviour in laminated and cross-bedded sandstones, *Journal of Petroleum Science and Engineering*, 9, 103-124.

5. Egermann, P., Lenormand, R. (2005), A New Methodology to Evaluate the Impact of Localized Heterogeneity on Petrophysical Parameters (kr; Pc) Applied to Carbonate Rocks, *Petrophysics*, 46, 5, 335-345.
6. Krause, M., Krevor, S., Benson, S.M. (2013), A Procedure for the Accurate Determination of Sub-Core Scale Permeability Distributions with Error Quantification, *Transport in Porous Media*, 98(3), 565-588.
7. Reynolds, C.A., and Krevor, S. C. (2015), Characterizing flow behaviour for gas injection: Relative permeability of CO_2-brine and N_2-water in heterogeneous rocks, *Water Resources Research*, 51, 12, 9464-9489.
8. Reynolds, C.A. (2016) Two-phase flow behaviour and relative permeability between CO_2 and brine in sandstones at the pore and core scales. PhD Thesis. Department of Earth Science & Engineering, Imperial College London
9. Pini, R., Benson, S.M. (2013), Simultaneous determination of capillary pressure and relative permeability curves from core-flooding experiments with various fluid pairs, *Water Resources Research*, 49, 3516-3530
10. Lenormand, R., Eisenzimmer, A. (1993) A novel method for the determination of water/oil capillary pressures of mixed wettability samples, *SCA Conference Paper Number 9322*
11. Ramakrishnan, T.S., Cappiello, A. (1991), A new technique to measure static and dynamic properties of a partially saturated porous medium, *Chemical Engineering Science*, 46, 4, 1157-1163.
12. Krevor, S., Pini, R., Zuo, L., Benson, S.M. (2012) Relative permeability and trapping of CO_2 and water in sandstone rocks at reservoir conditions, *Water Resources Research*, 48, 2

Rock	ϕ [−]	K [D]	L [m]	P_e [kPa]	λ [−]
Bentheimer	.22	1.81	.198	1.6	0.92
Bunter	.26	2.2	.151	0.95	.91
Berea	.18	.17	.204	2.5	0.67

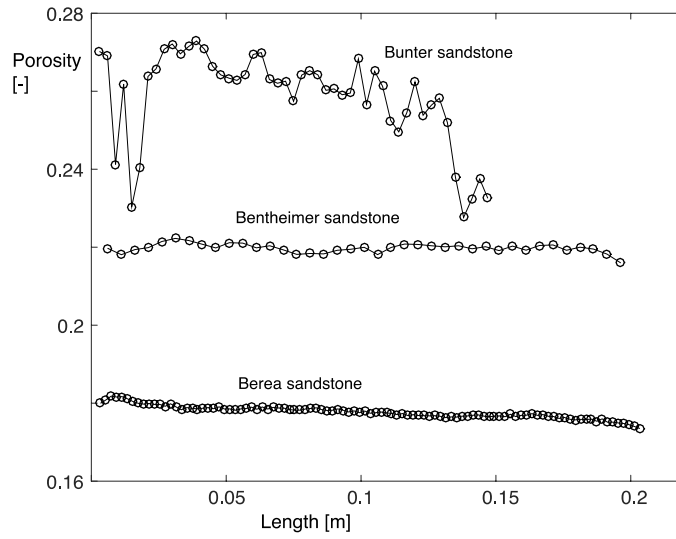Table 1. Properties of the rock samples

Figure 1. Average porosity along the length of the rocks for the samples investigated in this work
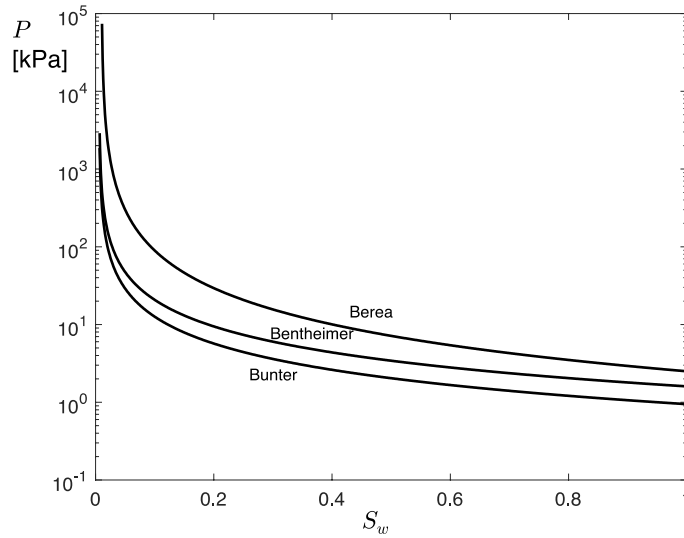

Figure 2. Best fit Brooks-Corey curves to the capillary pressure data measured using mercury porosimetry (Table 1). Saturation is normalised to the intrusion volume.
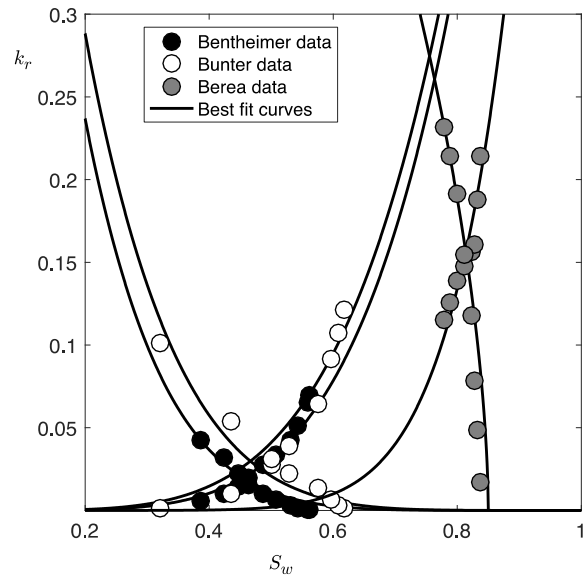
Figure 3. Relative permeability data and best fit curves for the three rocks investigated in this work. The data for the Bentheimer and Bunter sandstones are primary drainage observations. The data for the Berea sandstone is during primary imbibition
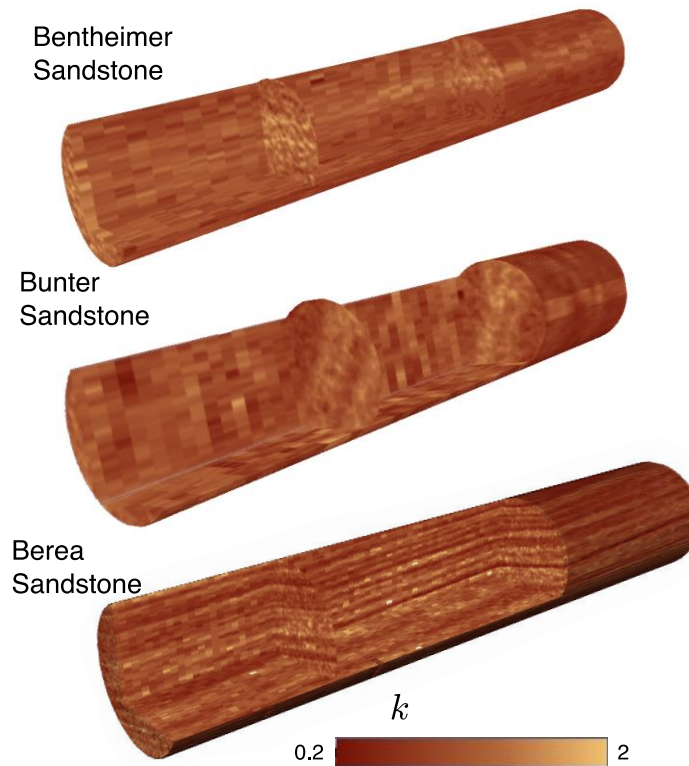

Figure 4. Rendering of the three dimensional maps of the capillary pressure scaling value, κ, for the rocks used in this study.
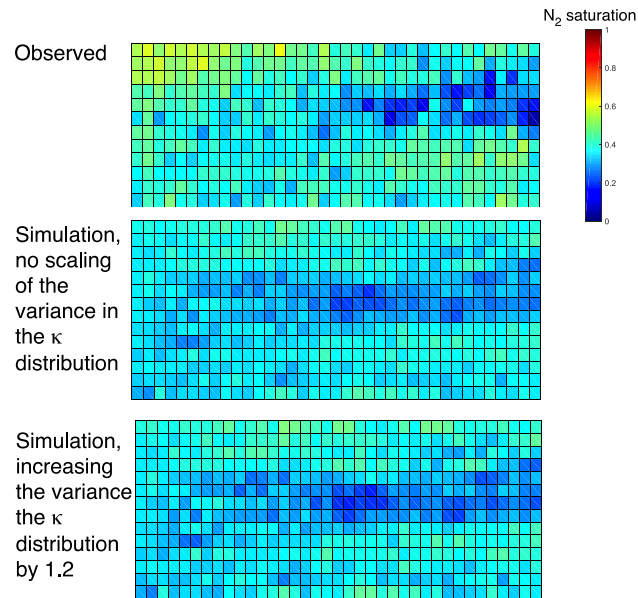
Figure 5. Experimental observations of saturation and simulated saturations in a central slice of the Bentheimer Sandstone at steady state for $f_{N2} = 0.4$. Flow was from left to right. The vertical and horizontal lengths are shown at different scales. See Table 1 for the rock core dimensions.
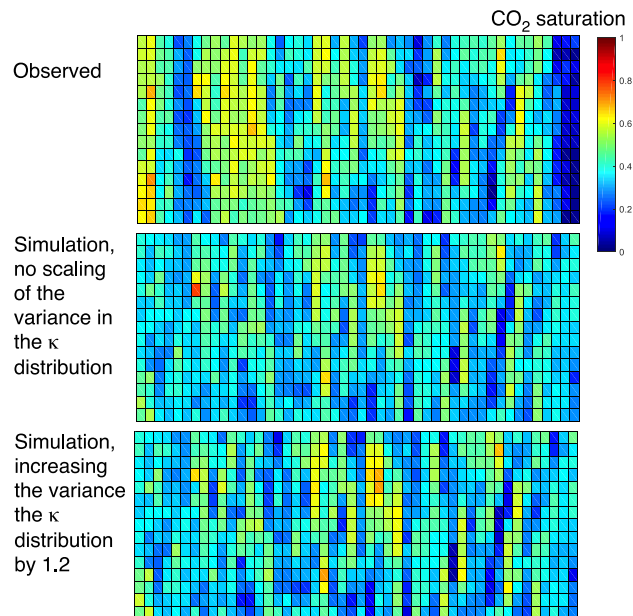

Figure 6. Experimental observations of saturation and simulated saturations in a central slice of the Bunter Sandstone at steady state for $f_{CO2} = 0.63$. Flow was from left to right. The vertical and horizontal lengths are shown at different scales. See Table 1 for the rock core dimensions.
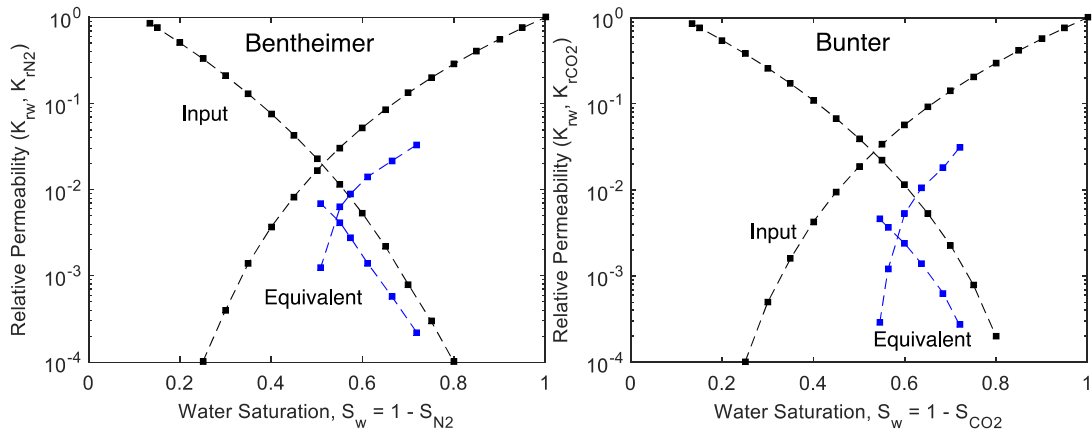
Figure 7. Input relative permeability measured in the viscous limit (in black) and simulated "synthetic" equivalent relative permeability obtained at low fluid flow velocities (blue)

RELATIVE PERMEABILITY EXPERIMENTS MONITORED BY NMR

P.O. Mangane, G. Dubes, B. Nicot

Total

ABSTRACT

Executing successful waterflood recovery projects in field requires prior laboratory core flooding studies, in order to better understand fluid displacement and to predict the recovery efficiency. When dealing with reservoir rocks that display complex fluid distribution (due to pore size heterogeneity, capillary end effect, wettability heterogeneity …), the use of technique with a strong imaging capacity is crucial to evaluate the flow characteristics. Traditionally, fluid saturation changes during core floods are monitored using X-Rays. However, the use of dopants is usally required in order to improve the density contrast between fluids. These dopants could alter the wettability of the rock or could chemically inhibit some EOR operations, such as low salt salinity injection for example.

In this work, we conduct core flooding tests using NMR as monitoring tool on a D_2O brine/oil/rock system. Previous works evidenced that NMR is promising for monitoring core flood experiments, due to its sensitivity to volume, fluid saturation, pore size and wettability. Saturation variation and wettability change can be captured by a T_2 experiment. As D_2O has no NMR signal, its use avoids adding dopants. Running other specific NMR pulse sequences, the fluid distribution within the rock can be computed either in bulk (e.g. saturation profile) or per pore size class (e.g. spatial T_2). This spatially resolved T_2 can be useful in systems that display complex fluid distribution, due to its pore size heterogeneity. To apply this monitoring technique, imbibition experiments were conducted on a low-field spectrometer into oil saturated outcrop plugs, bumping successively the flow rate to reduce the capillary end effects. In association with NMR data, relative permeability simulation was computed to determine the residual saturations and to better evaluate the fluid displacement efficiency during the water injection. Compared to traditional methods like X-ray techniques, the use of NMR to monitor water-flooding experiments can provide further understanding of flow mechanisms, especially in complex carbonate systems such as carbonate.

INTRODUCTION

Relative Permeability data are commonly determined in laboratory from dynamic displacement tests such as coreflood experiments based on unsteady or steady

techniques[1][2] [3]. The coreflood experiments provide principally two time-dependent flow data - the pressure differential across the sample and the volume of displaced fluid recovered, and define the end-point effective permeability (i.e. effective permeability at Swi and at Sor). Then, an automated tool (e.g. CYDAR^{TM}) can be used to numerically calculate the corresponding relative permeability curve [3], adjusting specific Kr and Pc models until they reroproduce the volume of oil recovered and the pressure drop (i.e. the past behavior): history matching.

Corefloods tests can be monitored using gamma/X-Rays techniques which enable measuring local saturations and more importantly visualizing saturation profiles as a function of core length during the flood[4]. This powerful monitoring technique is commonly used in the core analysis domain. However, it has a significant drawback due to the need of doping one phase (e.g. usually Sodium Iodide or Cesium Chloride for the water and/or iododecane for the oil phase). Actually, add dopants allow increasing the difference in attenuation between fluids saturating the core sample, then improving the accuracy of the saturation meausrements. When studying the effect of low salinity brines for example, the addition of dopant is not recommended as it is suspected to potentially alter the wettability of the rock during the coreflooding test; therefore dopant could considerably change the fluid displacement (i.e. relative permeability – Kr) efficiency during the waterflooding experiment.

Recent published works showed that NMR technology is an alternative to monitor fluid displacement in the laboratory and in the well too[5][6][7][8][9]. They evidenced that NMR is quite promising, due to its sensitivity to volume, fluid saturation, pore size, wettability, and particularly due to its strong imaging capacity[9]. Another advantage of NMR for monitoring corefloods is the possibility of using a common physic of measurements at multiple scales (i.e. lab scale and well scale). J Mitchell *et al.* [5] and A Al-Yaaraubi *et al.*, [8] have determined oil and brine saturation change during the flood and estimated the final remaining oil distribution, by conducting in-situ measurements of oil and brine saturations during laboratory corefloods on a low-field bench-top NMR magnet with a defined fluid injection sequence, using diffusion and relaxation measurements. Furthermore, they displayed non-uniform oil saturation during the EOR process from spatially resolved T_2 analysis. In this study, the obtained saturations values are shown to be in quantitative agreement with gravimetric measurements of recovered oil, displaying the accuracy and reliability of the NMR data. Arora *et al.* [7] performed a downhole rock flooding experiment from a micropilot single-well in situ EOR evaluation. They estimated the saturation change across the flood zone from the partitioning of the porosity map scaled in relaxation versus diffusion. Washburn and Madelin [9] have shown the strong capacity of imaging multiphase fluid saturation via sodium NMR. All these studies demonstrate the high potential of the NMR technique for monitoring multiphase flow, in terms of saturation change quantification and visualization of the fluid phase distribution during multiphase flow.

In this study, two unsteady-state imbibition experiments were performed on a low-field DRX spectrometer (MARAN DRX2-HF from Oxford ltd) in an attempt to constrain the computaion of relative permeabilities with the NMR derived saturation profiles within

core at key stages of the waterflood. This paper begins with a brief description of the involved cored plugs and fluids. Next, in the experimental section, we describe the way to set the irreducible water saturation, Swirr and wettability state of the core samples. The experimental setup and protocol used for performing the waterflood tests are also described. We finally discuss the potential of NMR to monitor a coreflood experiment for *Kr* calculation, by analyzing the acquired flow and NMR data.

SAMPLES

Fluids

- **Crude oil and Synthetic oil**

At 25°C, the used crude oil has a density ρ of 0.864 g/cm3 and a viscosity μ of 20.92 cP. The synthetic one was a mineral oil, Marcol 52, manufactured by ExxonMobil. At 25°C, Marcol 52 has a density ρ of 0.830 g/cm3 and a viscosity μ of 12.2 cP.

- **Synthetic brine**

The synthetic brine used for establishing the initial water saturation Swirr and for the waterflood experiments consisted in heavy water (i.e. D_2O) with dissolved salts (see Table 1) at 70 g/l salinity. In addition to major elements (i.e. Na and Cl), this brine was also composed of divalent cations (i.e. Ca^{2+}).

NaCl	CaCl$_2$	Density, ρ, at 25 °C	Viscosity, μ, at 25 °C
mol/l	mol/l	g/cc	cP
0.40	0.33	1.148	0.8

Table 1.   Chemical composition of the synthetic brine used in the waterflood tests.

The interest of using such brine is twofold:

1. According to Shabib-Asl et al., [10], using divalent ions on top of NaCl, has been referred to assist in adsorption of oil onto the surfaces of rock (i.e. favoring the core to become oil wet during the aging step).

2. The use of D_2O is an experimental trick. Actually, heavy water (i.e. D_2O brine) has no NMR signal and was consequently used to prevent adding dopants, in order to discriminate oil from water in the NMR experiment. Only the oil phase will be visible to NMR, using D_2O.

Core plugs

For the waterflood tests, quarried outcrop plugs were used, instead of actual reservoir rocks: Bentheimer sandstone and Sireuil carbonate. Figure 1 presents the 1D T_2 distributions (top) and the oil volume profile (bottom) acquired on both plugs 100% saturated in "normal" brine (i.e. the same synthetic brine described above, with H_2O instead of D_2O). The T_2 distributions display a single pore size class (i.e. unimodal T_2 distribution) for Bentheimer Sandstone and a bimodal porosity (i.e. Bimodal T_2

distribution) for Sireuil carbonate, respectively. The NMR profiles at 100% Sw appear relatively flat for the two samples, indicating that the cores are homogeneous in terms of porosity. Both core plugs were cylindrically sampled to dimensions of 38 mm in diameter and 50 mm in length. The characteristics of both samples are reported in Table 2.
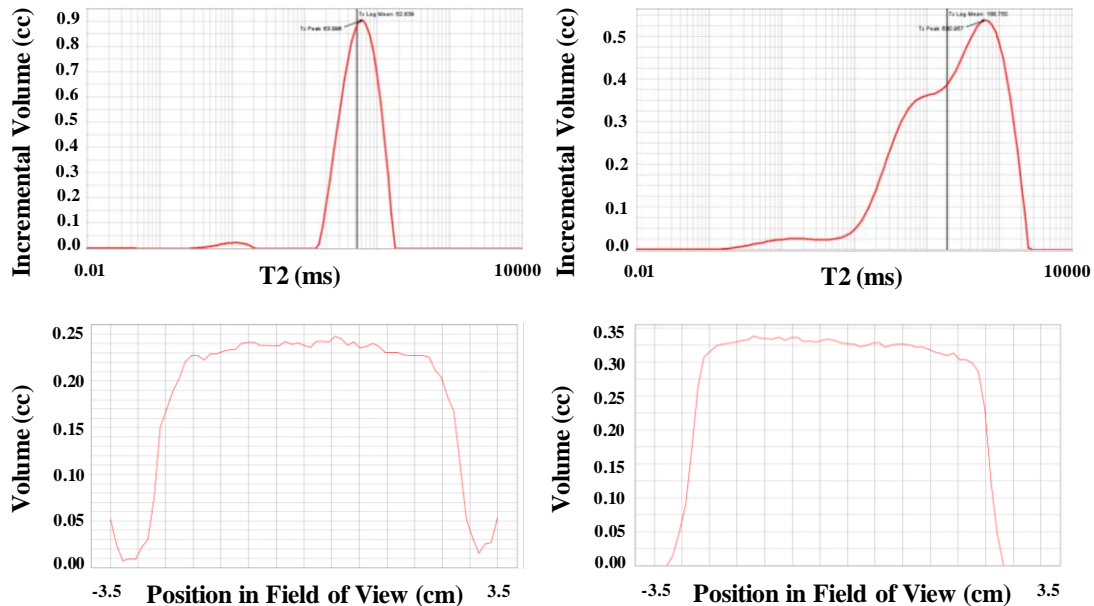

Figure 1 1D T2 distribution (top) and NMR profile along core (bottom), on 100% water saturated plug for Bentheimer (left) and Sireuil (right).

Sample	ϕ (p.u)	K (mD)	PV (cc)	$Swirr$ (frac)
BEN	26.2	2000	14.80	0.09
SIR	29.0	978.8	16.36	0.10

Table 2.   Characteristics of core sample used in the waterflood tests

EXPERIMENTAL

Core preparation

Prior to the saturation state, plugs were cleaned during four days at a temperature of 60 °C, using chloroform then isopropanol. After that, plugs were dried at 80 °C during 48 hours, then placed under vacuum and saturated with synthetic brine under pressure.

- **Setting Swirr**

The brine-saturated plugs were flooded by viscous displacement with crude oil under confining pressure, Pconf = 65 bars, to provide an initial oil saturation.

To ensure obtaining a homogeneous initial oil saturation along the core, the viscous displacements were successively conducted in both directions along the core length. A graduated tube at the outlet, collecting the effluents, allowed monitoring the variation of the average water saturation from material balance.

- **<u>Ageing step</u>**

The core plugs at irreducible water, Swirr, were aged statically under crude oil during 3 weeks at 80 °C, in an attempt to change the rock surface wettability from initially water-wet to oil-wet. This test was performed at 80°c, under 65 bars of confining pressure and 20 bars of pore pressure. This 20 bars pore pressure were maintained into the core plug, in order to prevent, at the ageing temperature, gas bubble formation from the crude oil and fluids evaporation. To prevent the establishment of wettability gradients along the core, the crude oil was renewed once per week by viscous displacement, successively following the two different directions along the core length (i.e. one pore volume PV per direction, successively). This was performed at flowrate slightly lower than the one for the Swirr setting, to prevent an additional water production.

At the end of the aging step, the crude oil was replaced by flooding it with toluene, followed by synthetic oil (Marcol 52). This mineral oil injection viscous was also performed at flowrate below the one for the Swirr setting.

NMR Hardware and measurements

The NMR system (MARAN DRX2-HF from Oxford ltd) consists in a 2MHz low-field DRX spectrometer, equipped with magnetic field gradients on the vertical axis. Two sets of NMR data were acquired during these experimental studies, at different saturation states and especially at different strategic times according to the acquisition duration of the different NMR pulse sequences:

- 1D saturation profile (needed for the history matching of the Kr curve and 1D T_2 relaxation times distribution were acquired during all the core flooding tests, due to their short acquisition time (i.e. between 20 minutes to 2 hours, depending on the oil saturation – the lower the oil saturation, the longer the acquisition time) and for their high interest in monitoring the saturation variation.

- Spatially resolved T_2 relaxation time map was run at the end of each flow rate step. The strategy of these acquisitions is to quantify the saturation profile of each pore size class after each flow rate step. This acquisition can take between 3 hours to 10 hours and the flow rate step can take up to 5 hours.

Waterflood experimental set up

The core flooding tests were conducted using an NMR compatible core holder, manufactured by Deadalus Innovations. This core holder consists of an overburden core cell equipped with dual port end plugs; one port for injecting fluids and a second for measuring the pressure drop across the core plug, which is required for Kr estimation. Collected at the outlet into a graduated tube, the produced volumes were continuously weighted and monitored using a high resolution camera. This setup was put into place to capture the volume of displaced oil recovered, which is an important input data for Kr computation. Note that the production from gravimetric data (i.e. volume from weigh data – see section oil production computation) was considered as the reference and its quality was punctually controlled with volumes measured from the image of the outlet

tube. To calculate the produced oil volume, from weigh data, we had to consider separately distinct block times according to the nature (i.e. density) of the effluent fluids: 1) Time before breakthrough, where only Marcol was produced; 2) Time after breakthrough, where effluents consist of both Marcol and brine.

Core flood protocol

The core plug, saturated with Marcol at Swirr, was vertically mounted under confining pressure (i.e. 65 bars) into the core holder. Flooding fluids were injected, at room temperature, from below using a dual piston pump to maintain constant flow rate. Prior carrying out the waterflood, the end-point effective oil permeability at irreducible water saturation (Ko @Swirr) was determined, by injecting the synthetic oil at several flow rates and measuring their corresponding ΔP. Then, the water injection was conducted at low rate (i.e. capillary number Nc ~10^{-7}, Table 3). This first low flow rate was maintained until the cumulative oil production stabilized. Commonly in coreflood experiments, capillary end effects arise at the outlet of the core sample from the discontinuity of capillarity in the wetting phase (i.e. build up of the wetting phase at the outlet of the sample). This important issue can artificially reduce the relative permeability to water, particularly in the oil-wet case for a rock/water/oil system [3]. Traditionally, high flow rates are used to reduce capillary effects. Thus, the flow rate was successively bumped several times, until reaching the residual oil saturation, Sor. At each bump, the new flow rate is maintained constant until the stabilization of the resulting cumulative oil production. At the end of the last flow rate step, the end-point effective permeability at residual oil saturation (Kw @Sor- The final point of a water flood) was determined, by injecting the synthetic brine at several flow rate steps (lower or equal to the final Q) and measuring the corresponding ΔP.

RESULTS AND DISCUSSIONS

As previously mentioned, the setting of the initial saturations and both water-flood tests were performed using heavy water. Thus, all the resulting 1D and 2D NMR distributions presented here, from the Swirr state to the Sor state, display uniquely the oil signal (from Figure 2 to Figure 4), since D_2O has no NMR signal.

For the bimodal core (Sireuil), it is worth noticing that the oil localization in the pore space was determined at initial oil saturation $So_{init,}$ (i.e. state prior to the water flood) from the 1D T_2 distributions and the spatial T_2 maps (Figure 2 and Figure 3): with an $So_{init} = 90\%$, the oil volume was located in both the big pores (i.e. 90%-95% of the So_{init}) and the small pores (i.e. 5%-10% of the So_{init}).

The waterflood tests were conducted, from So_{init}, injecting a volume of synthetic brine equal to 11 PV and 8.2 PV in the core plug for Bentheimer and Sireuil, respectively (the PV of water injected at each flood stage are presented in Table 3).

Bentheimer Sandstone				Sireuil Carbonate			
Flow rate, Q	Nc	Injected PV	ROS	Flow rate, Q	Nc	Injected PV	ROS
c/h		cc	frac	cc/h		PVI	frac
2	3,69E-08	2,3	0,19	0,5	8,38E-09	0,7	0,75
6	1,11E-07	1,7	0,18	2,2	3,69E-08	3,1	0,56
12	2,22E-07	2,5	0,17	4,5	7,55E-08	2,4	0,46
24	4,43E-07	4,5	0,16	6	1,01E-07	2,1	0,36

Table 3.   Capillary number Nc, Number of pore volume PV injected and remaining oil saturation ROS, at each flood stage

Notice that NMR measurements, particularly the oil volume profile along core length needed for *Kr* history matching, could not be acquired during the test performed on the Bentheimer sandstone. This was due to a technical issue. Thus, proper NMR could be only obtained before and after the imbibition experiment, when the flooding was stopped. Afterward, this issue was fixed by improving our experimental setup. This has allowed acquiring in-situ NMR profiles at each stage of the flood, during the test on the Sireuil carbonate.

NMR results

In Figure 2 we present the T_2 distributions and 1D NMR profiles obtained at irreducible water saturation (Swirr) and at the end of each flow rate step for both Bentheimer and Sireuil samples. On both samples, the 1D T_2 distributions highlighted a decrease in oil saturation from the So_{init} to remaining oil saturation (Table 3), during the waterflood. The ROS (e.g. Average remaining oil saturation, including the end effect) was evaluated to be 15.5% and 36% for the Bentheimer sandstone and the Sireuil carbonate, respectively. Moreover, the position of the T_2 peak remained unchanged during all the brine injections, denoting that there was no wettability alteration during both the waterflood tests. For the bimodal carbonate (Sireuil), the T_2 distributions show that the oil was recovered from the big pores (90 ms < T_2) as well as from the small pores (T_2 < 90 ms). Figure 2 also reports the NMR saturations profiles consisting in the stack of individual oil volume profiles by slice along the core, compared to linear X-ray scanning technique where saturation profiles are often taken in a section along the axis of the cylinder. This allows capturing all the pore heterogeneity along the core, typically when dealing with complex rocks such as the bimodal Sireuil carbonate. In addition to the oil saturation decrease (Table 3), the NMR profile has also evidenced an end effect at the outlet of both samples (Figure 2). This discontinuity is present over the last 0.6 cm for the Bentheimer and 1.5 cm for Sireuil sample. This difference can be attributed either to the difference in the applied *Nc* (Table 3) or to wettability. An interpretation in term of wettability can be made between both tests only with equal *Nc*.
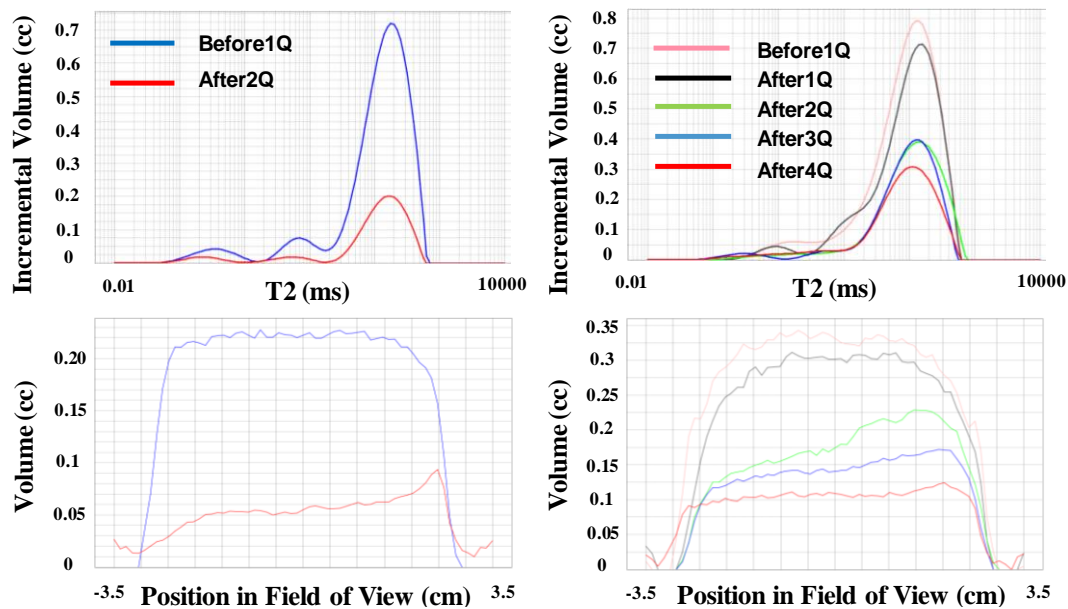
Figure 2 T_2 distribution (top) and oil volume profiles (bottom) at each flood stage (Q corresponding to flow rate step), for Bentheimer (left) and Sireuil (right).

Figure 3 presents the spatially resolved T_2 relaxation time maps obtained at irreducible water saturation (Swirr) and after each flow step for both samples. These measurements provide a partitioning of the porosity map scaled in relaxation (x-axis) versus saturation profile (z-axis). Moreover, individual T_2 distributions by slice along the core can be generated from these maps, allowing the localization of the remaining oil in space (z-axis) and pore size (T_2 axis). On both samples, the spatial T_2 maps and the individual T_2 stack show:

- A decrease of the oil volume during the waterflood (Table 3).
- The resulting capillary end effect at the outlets (Figure 3).
- Oil volume change into the small and big pores, for the Sireuil carbonate.

Figure 4 illustrates the total oil volume profile along the Sireuil sample, the saturation profiles for the small pores ($T_2 < 90ms$) and the big pores ($T_2 > 90ms$) at each stage of the waterflood, evaluated from the spatially resolved T_2 maps. This partitioning of the porosity allows evaluating the oil saturation change in each pore class. It confirms the decrease of the oil volume in both small and large pores. Moreover, both pore size classes display an end effect at the outlet of the sample. Surprisingly, non-uniform oil saturation is evidenced in both pore size classes prior to the water injection (black profiles in Figure 4). This non-uniformity seems to disappear during the flooding. Probably, this could have occurred during the setting of the initial saturation by drainage or during the ageing phase (wettability gradient into the small pores). This phenomenon will be investigated in more details in the future. However, the observation of this saturation gradient into the different pore size groups is specific to NMR and could not have been observed using the X-ray technique.
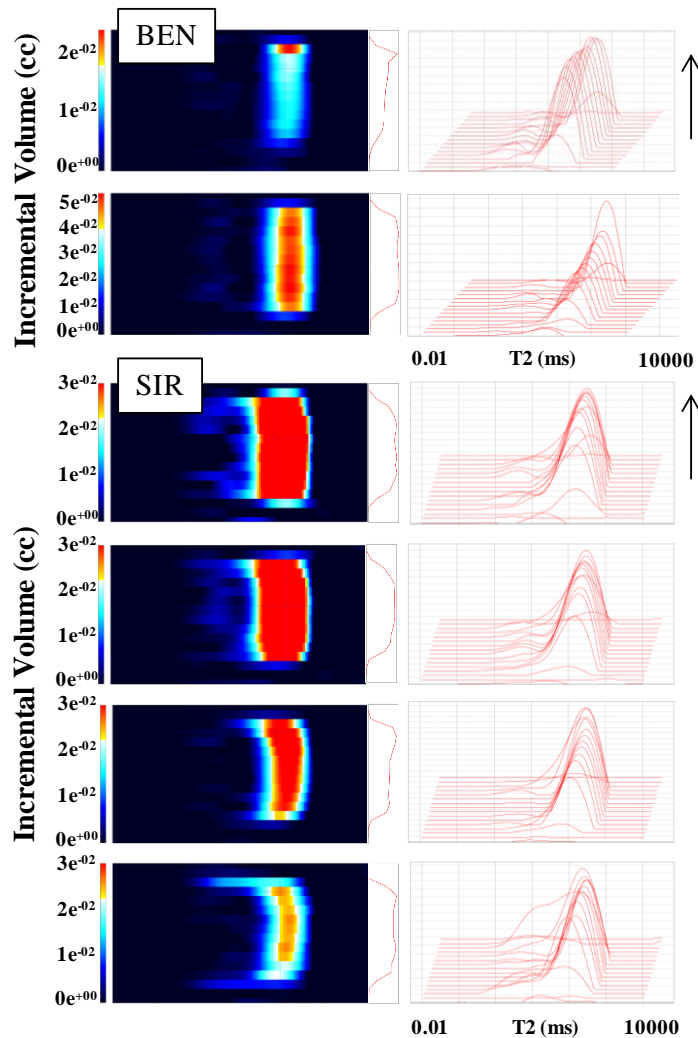
Oil Recovery

Figure 3 Spatial T_2 at each stage of the waterflood test. Arrows indicate direction of flow, for Bentheimer sandstone (top) and Sireuil carbonate (bottom).

The oil production curves of both samples are reported in Figure 5. Comparing both curves, the Bentheimer sandstone appears more "water-wet" than the Sireuil carbonate. Actually, the behaviour of the carbonate core is characterized by earlier breakthrough where more than 80% of the oil recovery has occurred from the flow rate bumps. On the other hand, the sandstone core exhibits a later breakthrough where most of the recovery happens before breackthrought (i.e. more than 90% of the oil recovery has appeared during the first flow rate step).

The presence of end effects at the outlet of both samples evidences (Figure 2) that the crude oil ageing has rendered the cores less water wet than they were initially.

Kr computation

The relative permeability behavior of the waterflood tests was computed by history matching, from CYDAR^{TM} using experimental data (i.e. Volume of oil recovered and pressure drop) and some analytical functions for relative permeability (i.e. LET function) and capillary pressure curve (i.e. Logbeta function). Actually, no experimental Pc data is available for both tests. The history matching of *Kr* and *Pc* curves is performed by optimizing the parameters for *Kr* and *Pc*. The optimization adjusts these models until they reproduce the experimental data.

About the saturation profile data, the purpose is not to get a perfect match with the experimental data, but to drive the *Kr* computation with a capillary pressure as realistic as possible. Note that the NMR and the gravimetric saturation measurements agree within 5

saturation units (s.u) at maximum (Figure 6). In both imbibition tests, the simulated oil recoveries reproduce the input experimental data (Figure 5).
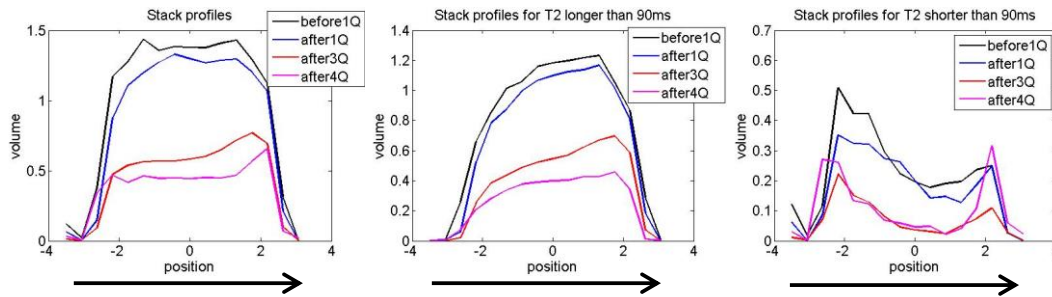

Figure 4 **Sireuil carbonate**: Oil volume profile deduced from the Spatial T_2 maps, at each stage of the waterflood. From left to right, total NMR profile, NMR profile of the big and small pores. Arrows indicate direction of flow.
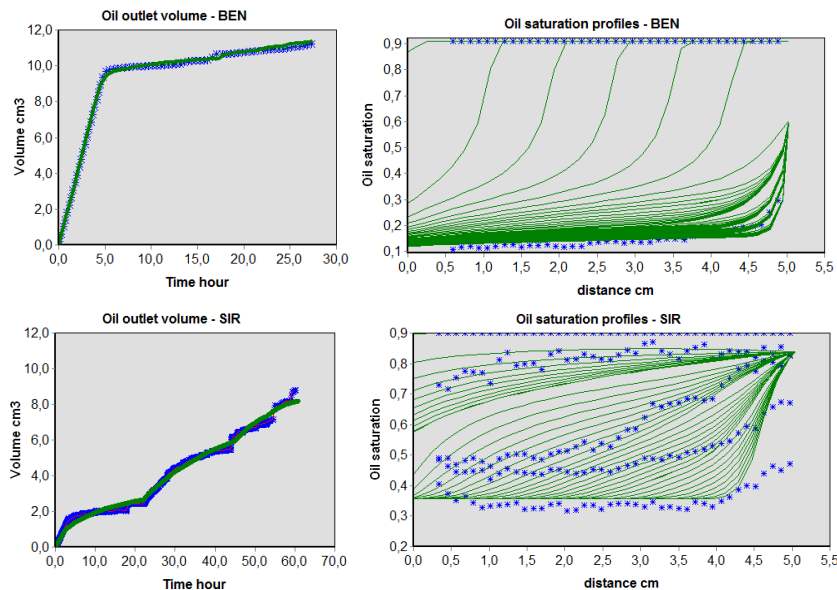

Figure 5 Volume of oil recovered and NMR saturation profile for Bentheimer sandstone (top) and Sireuil carbonate (bottom) – Experimental data in blue and simulated data in green.

Pc would have been better constrained by experimental data. Unfortunately, this data was not available.

As observed on the experimental data, the simulated end effect at the outlet face appeared more pronounced for the Sireuil carbonate (simulated Ros = 36% to 80%) than for the Bentheimer sandstone (simulated Ros = 15% to 50%). This can be attributed either to the oil-wet nature or to the bimodality of the Sireuil carbonate. In this paper we present only the *Kr* computation on the homogeneous Bentheimer sandstone. The difficulty of computing *Kr* curves in the case of heterogeneous such as Sireuil carbonate is out of the scope of this paper.

Reported in Figure 6, the two simulated *Kr* curves (i.e. *Kro* and *Krw,* determined using Corey model) on the Bentheimer sandstone display a shape relatively soft where the water relative permeability *Krw* appears relatively low at high water saturations: *Kr* cross-point is >50% Sw, *Krw*(Sor) around 0.15 and the alpha coefficients are 2.1 and 3.6 for the *Kro* and *Krw*, respectively. The fractional flow curve (described by Buckley and Levrett [11] and extended by Welge [12], Figure 6), deduced from the *Kr* curve, exhibits

a late critical water saturation (saturation above which the water becomes mobile). This behavior indicates the water-wet nature of the sandstone and confirms the late breakthrough and the low oil recovery from the flow rate bumps.
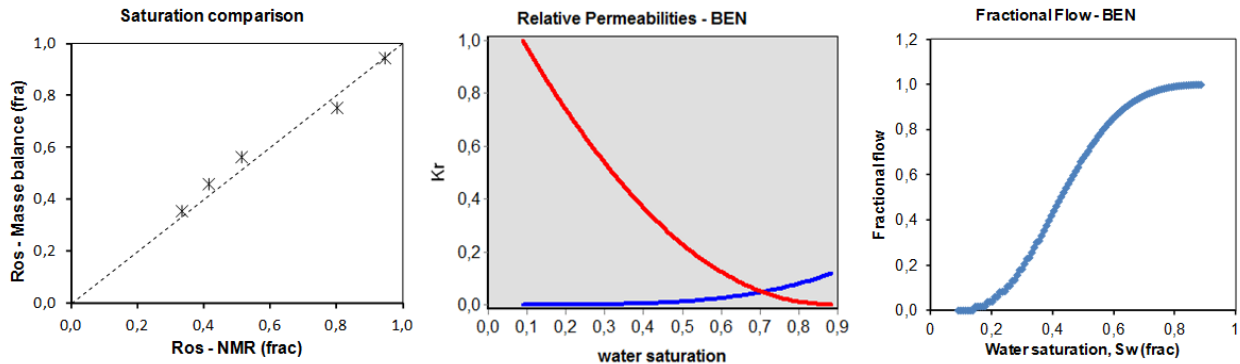

Figure 6 **Sireuil (left):** comparison of remaining oil saturation determined by NMR and by mass balance from the flood effluent. **Bentheimer (right):** the computed *Kr* curve and the water fractional flow.

CONCLUSION

Two unsteady-state waterflood experiments were performed on a low-field DRX spectrometer (MARAN DRX2-HF from Oxford ltd) in an attempt to constrain the computation of relative permeabilities with the NMR derived saturation profiles within core at key stages of the waterflood. NMR, as a monitoring technique, has provided an evaluation of the remaining oil saturation at each flood stage (from T_2 distributions and saturation profiles). The gravimetric (considered as reference) and NMR saturation measurements agree within 5 saturation units (s.u) at maximum. Monitoring the T_2 distribution of the oil in the rock during the flooding experiment allowed evidencing that no wettability alteration occurred. This would be useful in the case of a low salinity water-flood, where an alteration of wettability during the flooding can be suspected.

Furthermore, the spatially resolved T_2 maps have allowed partitioning the porosity and determining oil saturation per pore size classes, on the bimodal Sireuil carbonate. Another interest of theses 2D maps was to evidence the oil localization in space, in addition to the pore size class. For example, even if the oil saturation profile looked uniform on Sireuil carbonate at Swi, the spatially resolved T_2 experiment oil evidenced saturation gradients. This is specific to the pore size sensitivity of NMR and could not have been observed using X-ray technique. With the ability to monitor a waterflood regarding to the different pore size classes, the use of NMR (compared to traditional methods like X-ray techniques) could provide further understanding of flow mechanisms, especially in complex system such as carbonate. As the time-dependent flow data were continuously measured, the reliable in situ NMR saturation profiles before and after the waterflood were used to further constrain the computation of relative permeability on the Bentheimer sandstone. The acquisition of in situ NMR measurements at each flow stage on Sireuil carbonate opens the range of possibilities for improving the difficult *Kr*

computation on heterogeneous rocks by providing valuable information on the localization of the remaining oil (along the flow direction and by pore size).

ACKNOWLEDGEMENTS

REFERENCES

[1] J. Heaviside and C. Black, "Fundamentals of Relative Permeability: Experimental and theoretical Considerations," in *SPE*, 1883.

[2] C. McPhee and K. Arthur, "Relative Permeability Measurement: An Inter-Laboratory Comparison," in *SPE*, 1994.

[3] C. McPhee, J. Reed and I. Zubizarreta, Core Analysis: a Best Practice Guide, Amsterdam: Elsevier, 2015.

[4] A. Hove, J. Ringen and P. Read, "Visualization of Laboratory Corefloods with the aid of Computerized Tomography of X-rays," in *SPE*, 1987.

[5] J. Mitchell, J. Edwards, E. Fordham, J. Staniland, R. Chassagne and P. Cherukupalli, "Quantitative Remaining Oil Inerpretation Using Magnetic Resonance: From the Laboratory to the Pilot," in *SPE*, 2012.

[6] R. Ramamoorthy, M. Kristensen, J. Edwards, C. Ayan and K. Cig, "Introducing the Micropilot: Moving Rock Flooding Experiments Downhole," in *SPWLA*, 2012.

[7] S. Arora, D. Horstmann and P. Cherukupalli, "Single Well In-Situ Measurment of Residual Oil Saturation after an EOR Chemical Flood," in *SPE*, 2010.

[8] A. Al-Yaarubi, J. Edwards, J. Guntupalli, L. Al-Qasmi, J. Kechichian, G. Al-Hinai and M. Appel, "Field Experience of NMR Logging Through Fiber-Reinforced Plastic Casing in an Observation Well.," in *SPWLA*, 2015.

[9] K. Washburn and G. Madelin, "Imaging of multiphase fluid saturation within a porous material via 7 sodium NMR," *Journal of Magnetic Resonance,* 2010.

[10] A. Shabib-Asl, M. Ayoub and K. Elrais, "Laboratory Investigation into Wettability Alteration by Different Low Salinity Water Compositions in Sandstone Rock," in *SPE*, 2015.

[11] S. E. Buckley and M. C. Leverett, "Mechanism of Fluid Displacement in Sands," *SPE,* no. doi:10.2118/942107-G, 1942.

[12] H. J. Welge, "A Simplified Method for Computing Oil Recovery by Gas or Water Drive," *SPE,* no. doi:10.2118/124-G, 1952.

Magnetic Resonance Imaging with a Variable Field Superconducting Magnet that can be rotated for Vertical or Horizontal Operation

Sarah Vashaee[1], Ming Li[1], Bryce MacMillan[1], Razieh Enjilela[1], Derrick P. Green[2], F. Marica[1], Bruce J. Balcom[1]

[1] UNB MRI Research Centre, Department of Physics, University of New Brunswick, E3B 5A3, Canada

[2] Green Imaging Technologies, Inc., 520 Brookside Drive, Suite B Fredericton, NB, E3A 8V2, Canada

ABSTRACT

Magnetic Resonance (MR) is widely employed in the petroleum industry for down-hole logging and for laboratory core analysis. Sensitivity of the magnetic resonance experiment to fluid type and fluid environment makes it uniquely well suited to these applications. The same advantages should accrue to Magnetic Resonance Imaging (MRI) measurements of core flooding experiments. The ability of MRI to directly measure fluid saturation and fluid environment in three dimensions, as a function of time, has to this point, not been fully realized for core flood applications.

Bulk ^{1}H relaxation time measurements are near universally undertaken at low magnetic field to reduce magnetic susceptibility mismatch effects. These fields, typically 0.05 Tesla (2 MHz for ^{1}H), are too low for MRI studies. Higher magnetic fields (3 Tesla and above) are commonly employed for biomedical MRI studies with superconducting magnets. Susceptibility mismatch effects at these field strengths can be severe for many core plug samples and these higher field are generally inappropriate for rock core studies. What is the best field for petroleum core plug MRI studies? It will be sample dependent as one seeks to balance greater sensitivity at high field with susceptibility effects which decrease the transverse signal lifetimes (T_2 and T_2^*) as field increases.

New generation superconducting magnets, actively cooled rather than passively cooled, are permanently connected to the magnet power supply and thus have the possibility of variable field operation. We have recently installed a variable field superconducting magnet MRI instrument which permits operation in the field range 0.01 Tesla to 3 Tesla. This magnet permits one to maximize the sample magnetization for high sensitivity core flooding MRI measurements, while controlling the effect of susceptibility mismatch on the signal lifetime. Because of the elimination of liquid cryogens the new magnet is a fraction of the size and weight of conventional superconducting magnets. The magnet can easily be rotated, from horizontal to vertical, by one person.

Variable field operation permits MRI measurement of other nuclei of interest and importance in core flooding studies. The gyromagnetic ratio of sodium ^{23}Na and fluorine ^{19}F are each less than that of hydrogen ^{1}H but one may increase the static field strength to compensate for the decrease in gyromagnetic ratio such that the RF probe employed to excite and detect the MRI signal has an unchanged frequency. This provides the experimentalist an entirely new way to undertake multi-nuclear MRI studies of core plug systems.

INTRODUCTION

Magnetic Resonance (MR) and Magnetic Resonance Imaging (MRI) are commonly employed for rock core and petroleum studies. MRI resolves structure in rock core plugs under study, as does X-ray CT. The MRI measurement is however a direct measurement of the ^{1}H containing fluids in the core plug, unlike X-ray measurements where absorption is principally due to the matrix [1]. In addition, the MRI measurement has the potential to investigate different nuclei, for example sodium, but more importantly is sensitive to the local dynamics and environment of the fluid. A very wide variety of MR measurements may be spatially resolved with MRI, including measurements of fluid self-diffusion and velocity. MR/MRI measurements may be interpreted to yield a wealth of petrophysical information including fluid viscosity, fluid type, fluid saturation, rock wettability, permeability, capillary pressure and the pore size distribution [2-11]

The fact that MR/MRI can measure so many different petrophysical parameters, with so many different protocols, is a practical weakness when compared to the simpler X-ray CT measurement. Which MR/MRI measurement should be executed, and how, is a common question. This highlights the importance of expert advice and experience in petrophysical MR/MRI studies.

There is considerable interest in monitoring oil displacement processes with Magnetic Resonance Imaging (MRI) methodologies to understand and improve enhanced oil recovery. The ability of MRI to directly measure fluid saturation and fluid environment in three dimensions as a function of time has not been fully realized for core flood applications because of long measurement times at low magnetic fields which can hamper monitoring the displacement [12, 13]. 1D and 2D MRI measurements are instead often undertaken to monitor the oil displacement since they are faster. Although these images may characterize well the overall oil distribution in a homogeneous core sample, the image may be misleading in a heterogeneous core plug, or for a process which is heterogeneous. Fast Spin Echo (FSE) imaging methods have been applied to investigate the 3D fluid content in core-plugs [2, 13].

^{1}H relaxation time measurements are generally performed at low field to reduce magnetic susceptibility mismatch effects. These fields, typically 0.05 Tesla (2 MHz for ^{1}H) with permanent magnets, are too low for MRI studies. The shift to low-field is accompanied by an essential reduction in signal-to-noise ratio. Biomedical MRI is usually conducted at

higher magnetic field strengths with superconducting magnets. MR spectroscopy studies of molecular structure are usually undertaken with high field superconducting magnets.

Higher magnetic fields for MRI provides better SNR and therefore allows high sensitivity and higher resolution imaging, in principle. However, the magnetic susceptibility mismatch decreases the T_2^* in rock cores which hinders both resolution and contrast with conventional high speed MRI methods. The B_0 field distortion in the pore space due to susceptibility mismatch creates so called 'internal' magnetic field gradients. The strength of the internal magnetic field gradients scales with B_0 and the susceptibility mismatch ($\Delta\chi$). It is important to know the best static magnetic field for petroleum core plug MRI studies to balance greater sensitivity at high field with susceptibility effects which decrease the transverse signal lifetimes (T_2 and T_2^*) as field increases. A decrease in the T_2^* lifetime manifests as a less of signal intensity in pure phase encode SPRITE MRI images [14], as shown below. A decrease in T_2^* and T_2 due to susceptibility contrast results in a loss of signal intensity, loss of resolution and may lead to geometric distortion in frequency encode measurements, such as the fast spin echo method employed below.

New generation cryogen free superconducting magnets, actively cooled rather than passively cooled, are permanently connected to the magnet power supply and consequently have the option of variable field operation. We have recently installed a variable field superconducting magnet MRI Instrument which permits operation in the field range 0.01 Tesla to 3 Tesla. This magnet permits one to maximize the sample magnetization for high sensitivity core flooding MRI measurements, while controlling the effect of susceptibility mismatch on the signal lifetime. The cryogen free variable field magnet is a field changing magnet, it is not a field cycling magnet. Fast field cycling is increasingly employed for T_1 dispersion measurements in petroleum systems [15, 16].

A cryogen free magnet with active cooling permits one to enjoy the benefits of a superconducting magnet, which includes field homogeneity and temporal field stability without employing liquid helium. Liquid helium is required as a cryogen for conventional superconducting magnets. Helium cost and stability of supply are of increasing concern in many parts of the word. Permanent magnet based MR/MRI instruments are well-known to suffer from poor innate field homogeneity and temporal field instability due to ambient temperature change.

Due to the elimination of liquid cryogens for cooling, the new magnet is a fraction of the size and weight of conventional, liquid-based, superconducting magnets. The new magnet is small enough and light enough to permit rotation. The ability to rotate the magnet is advantageous for experiments in which the sample orientation matters, for example when gravity and buoyancy are important [17]. Examples include gas injection in petroleum systems, including two phase gas-liquid flow.

We show in this paper results from the variable field magnet in which nuclei (^{1}H and ^{19}F) were employed for core flood imaging. The ^{19}F resonance is ideally suited for MR imaging

since it has a high gyromagnetic ratio, spin 1/2, and 100% natural isotopic abundance [18]. One pulse [1]H Free Induction Decay (FID) results are shown during magnet rotation. We also show MR measurement of [23]Na in a brine saturated rock core plug. The same RF probe was employed for ^{1}H and [23]Na experiments but the magnetic field was changed to maintain the same resonance frequency.

EXPERIMENTAL

MR/MRI measurements were performed on a variable field magnet, maximum field 3T (MR Solutions, Guildford, Surrey, UK) with a 17 cm bore. The RF probe was a birdcage (Barthel HF-Technik, Aachen, Germany). The magnet is 325 kg, 66 cm in diameter and 80 cm in length. It was initially configured for operation at 0.79 T, 1.5 T and 3T. The 3D gradient coil was driven by gradient amplifiers (Performance Controls, Inc., PA, US), providing maximum gradient strengths of 66.4 G/cm, 64.9 G/cm and 87.8 G/cm in the x, y and z directions. The magnet is permanently connected to a magnet power supply (Cryomagnetics, Inc., TN, US).

3D Conical-SPRITE MRI measurements were undertaken on three different rock core plugs (Bentheimer and Berea (Kocurek Industries, Caldwell, TX), and Wallace (Wallace Quarries Ltd., NS, Canada)), length 5 cm and diameter 3.8 cm, at both 1.5 T and 3 T. All three core plugs were fully saturated with 2% brine. SPRITE imaging parameters were: signal averages = 2, field of view = $100 \times 100 \times 100$ mm^3, 64^3 k-space points were acquired each with a phase encoding time of 100 μs. The T$_1$ recovery delays were 2s, 800 ms and 400 ms for Bentheimer, Berea and Wallace core plugs, respectively. The 90° pulse duration was 63 μs at 1.5 T and 38 μs at 3 T. The RF flip angle was 10° for SPRITE measurements.

For flooding measurements Fluorolube oil MO-10 (Gabriel Performance Products, OH, United States) was utilized as the oil phase. The viscosity of the fluorinated oil was 50 mPa s at 25 °C. H$_2$O brine, 1 wt% NaCl, was employed for core plug saturation. A Bentheimer core plug (Kocurek Industries, TX, USA) was employed with length 5.1 cm, diameter 3.8 cm, pore volume 13 cm^3 and a porosity of 23%. The pore volume was calculated gravimetrically. An ISCO pump (Teledyne ISCO, Lincoln, NE, US) was employed for fluid injection. A homemade low pressure core holder was employed for flooding experiments.

The Bentheimer core plug was dried at 100 °C to a constant weight and then saturated with 1 wt% NaCl H$_2$O brine. The pore volume of the core plug was calculated gravimetrically. FID, 3D conical SPRITE [19] and 3D Fast Spin Echo (FSE) MRI measurements were undertaken at 1.5 T for [1]H.

To establish the initial oil saturation, fluorinated oil was injected into the core plug with a syringe until no water production was observed at the outlet end. The initial oil volume inside the sample was 10.2 ml which provides an initial oil saturation of 0.79. FID and 3D FSE measurements were performed at both 1.5 T for ^{1}H and 1.6 T for [19]F. 3D SPRITE MRI was undertaken at 1.5 T for [1]H. Change of nucleus was achieved by changing the

static magnetic field strength with the resonance frequency constant at 63.5 MHz (no change in RF probe).

H_2O brine, 1 wt% NaCl, was employed to displace the fluorinated oil. FID and 3D FSE measurements were undertaken at 1.6 T for ^{19}F to monitor the oil displacement. The sample and the magnet were horizontal. The flooding measurement ceased when the FID signal intensity was constant. After displacement of the oil with H_2O brine, approximately 4.3 ml oil remained inside the sample. Water flooding was undertaken at ambient temperature. The water flooding flow rate was 0.045 ml/min.

2D slice-selective FSE measurements were undertaken to monitor the progression of flooding. The FSE measurement required 16 signal averages with a total imaging time of 12 minutes. The acquisition is sufficiently fast to permit observation of the flooding front displacement. 34 slices (Figure 4) were acquired in the *x* direction to give a 3D data set. The slice thickness was 1.2 mm. 16 k-space frequency encode lines (spin echoes) were acquired per excitation. The echo time was 8 ms. The center of k-space was acquired with the first echo. The field of view was 7 cm in the frequency and phase encode directions. The repetition time between each excitation was 2s. The 2D images were 128×128 pixels.

Preclinical scan software (MR Solutions, Guildford, Surrey, UK) was employed to execute the FSE MRI images. A home built MATLAB program (MathWorks, Natick, MA, USA, written in MATLAB) was employed to visualize 3D FSE images. GIT system software (Green Imaging Technologies, Inc., NB, Canada) was employed to execute FID, CPMG and double-half-k SPRITE [19] measurements.

RESULTS AND DISCUSSION
Variation of B_0 to control sensitivity and susceptibility mismatch effects
The variable field superconducting magnet MRI Instrument permits operation in the field range 0.01 Tesla to 3 Tesla. This permits one to maximize the sample magnetization for high sensitivity core flooding MRI measurements, while controlling the effect of magnetic susceptibility mismatch on T_2^* and T_2. Chen and Balcom have shown [14] that the internal magnetic field distortion is proportional to the external magnetic field strength (B_0) and the susceptibility difference ($\Delta\chi$). The single exponential T_2^* behavior observed arises from an effective Lorentzian distribution of the internal field, induced by the large susceptibility contrast and an intrinsic disordered pore structure. The linewith ($1/(\pi T_2^*)$) measured at different magnetic field strengths (B_0) for a Chatsworth Formation sandstone, water saturated Berea and a carbonate are shown in Figure 1. The slope differs for each sample due to a different susceptibility mismatch ($\Delta\chi$). The new data point corresponds to a new brine saturated Berea plug measured with the new magnet set to 3T.

Figure 2 shows, 2D planes extracted from the 3D SPRITE images for Bentheimer, Berea and Wallace core plugs at both 1.5 T and 3 T. The image intensity for Berea and Wallace core plug images is decreased at higher field. Short T_2^* lifetimes of water in the Berea and Wallace core plugs at 3 T diminish the sensitivity of the SPRITE measurement [14].

However, for the Bentheimer core plug with substantially longer T_2^* the image intensity increases when the B_0 field increases from 1.5 T to 3 T. The image intensity is a balance between sample magnetization which increases with B_0 field strength, sample porosity which varies between the three samples, and T_2^* which varies with the sample and decreases with field strength.
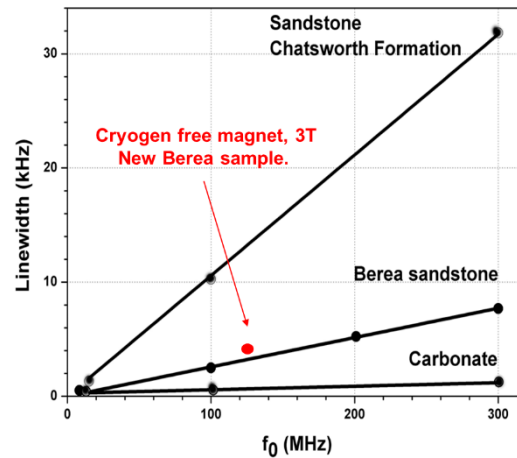

Figure 1. The linewidth ($1/(\pi T_2^*)$) measured at different magnetic field strengths (B_0) for a Chatsworth Formation sandstone, water saturated Berea sandstone and a Carbonate. The measurements at frequencies other than 125 MHz were performed on other MRI instruments in the UNB MRI center. There is a linear relationship between the linewidth and the product of the $\Delta\chi$ and Larmor frequency (f_0). The best fit line for a Berea sandstone is given by $\Delta v = 0.26\ \Delta\chi\ f_0$.
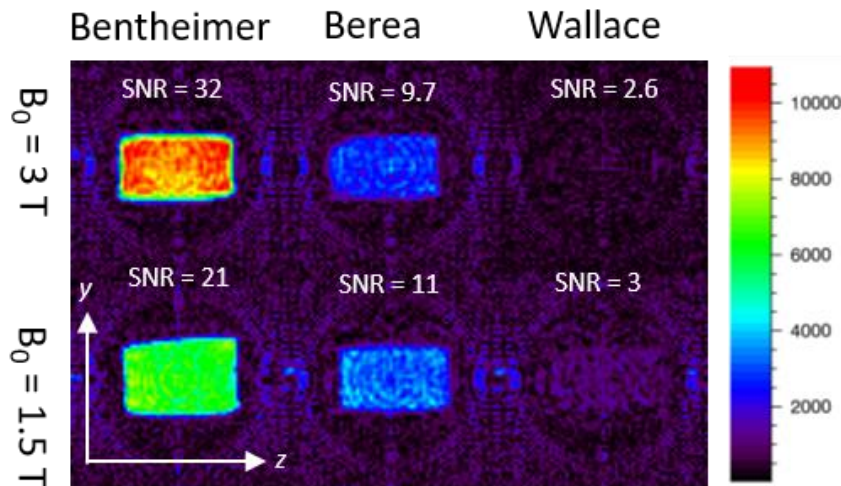

Figure 2. 2D slice images of Bentheimer, Berea and Wallace core plugs from 3D SPRITE images at 3 T and 1.5 T. For each sample a slice from the centre of the 3D core plug image is displayed. There is a probe background signal apparent in all images. Measurement time was 8.5 minutes, 7 minutes and 6 minutes for Bentheimer, Berea and Wallace core plugs, respectively. In each case, 2 signal averages were acquired; the difference in measurement time is due to the T_1 recovery delay. The signal-to-noise ratio (SNR) varies due porosity differences between the core plugs, but also due to sample magnetization change with field, and with the field dependent T_2^* lifetime variation of water in the pore space.

Magnet rotation

The cryogen free magnet is small enough and light enough to permit rotation. Measurement at different orientations is very advantageous for petroleum flooding measurements in which gravity and buoyancy may be important. The one pulse ^{1}H FIDs from a doped water phantom were measured during magnet rotation at 3 T. The FID results with different magnet orientations are shown in Figure 3. When the magnet rotates from horizontal to vertical, as shown in Figures 2a-2c, the FID goes off resonance but the field homogeneity in the sample space (T_2^*) is unchanged. When the magnet is horizontal, the earth's field (0.5 gauss) is at right angles to B_0 (30,000 gauss) and thus there is no effect on the resonance frequency. When the earth's field and the static field B_0 are co-linear, in the vertical orientation, the addition of the two fields changes the Larmor frequency. The predicted change is an increase in frequency of 2 kHz. An increase of 1.95 kHz was observed.
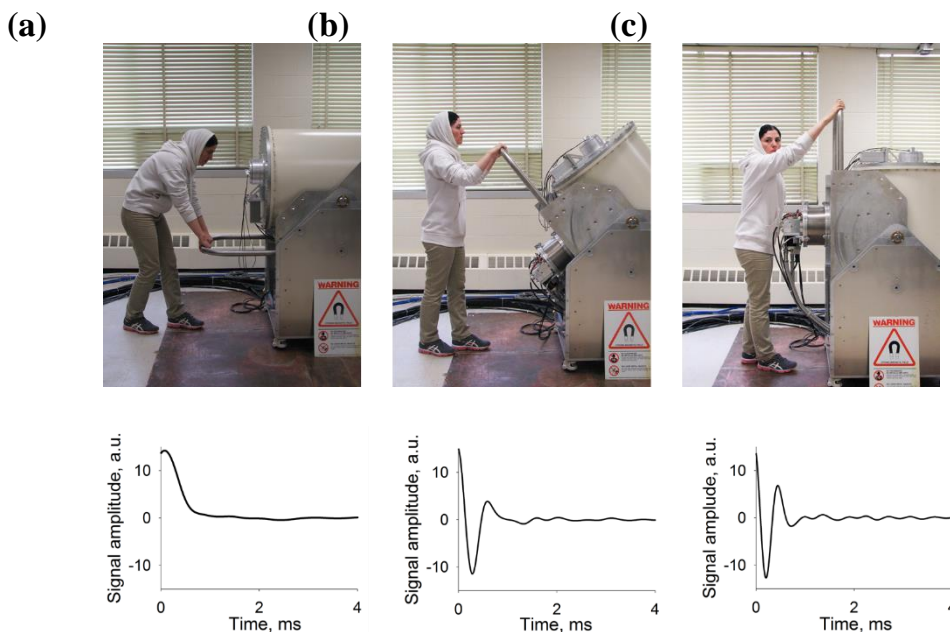
(a)   **(b)**   **(c)**

Figure 3. FIDs from a doped water sample acquired during magnet rotation. The Gifford-McMahon (GM) cryocooler permits vertical or horizontal operation (indeed any orientation) unlike a pulse tube cryocooler. The magnet may be easily rotated by one person.

Multi-field, multi-frequency operation

Switch from ^{1}H at 1.5 T to ^{19}F at 1.6 T with fixed 63.5 MHz frequency RF probe

Figure 4 shows the oil saturation distribution in 2D FSE slices for a Bentheimer core plug during water flooding. The average initial oil saturation was 0.79 in the core plug.

Water flooding displaced oil to an average residual oil saturation of 0.33. A non-piston like displacement was apparent. High intensity oil signal was observed at the interface of the

PEEK distributor and the core plug. The oil signal intensity is proportional to oil saturation. An inhomogeneous initial oil saturation was observed.

Higher water saturation is observed at one end of the core plug (Figure 4). This may be due to a capillary end effect for the short sample [20]. The ^{1}H images of the fully brine saturated Bentheimer, before flooding and after flooding are shown in Figure 4. Change of nucleus to ^{1}H was achieved by changing the static magnetic field strength. The resonance frequency was constant at 63.5 MHz. The same RF probe was used for both ^{1}H and ^{19}F imaging measurements.

If the sample T_2 is longer than tens of ms, and T^*_2 is not less than 1 ms, frequency encode spin echo MRI measurements, such as the 2D slice-selective FSE, are suggested for rapid fluid saturation imaging in core flooding studies. The measurement time of 12 minutes ensured high quality images in our studies. The measurement time may be reduced to 5 minutes with a decrease in SNR. If the T_2 is less than tens of ms, or the T^*_2 is less than 1 ms, then a Centric Scan SPRITE method is recommended for fluid saturation imaging, although the imaging time will increase.

Switch from ^{1}H at 0.79 T to ^{23}Na at 3 T with fixed 33.7 MHz RF frequency Variable field operation also permits MR measurement of ^{23}Na with the same RF probe employed for ^{1}H measurements. ^{1}H and ^{23}Na FID signals, 1D double-half-k profiles and T_2 distributions for a fully 2% brine saturated Bentheimer sample are shown in Figure 5.

The T_2^* was approximately 1.6 ms for both ^{23}Na and ^{1}H (Figures 4a and 4b). As expected, for the same measurement time (2.5 minutes), the ^{1}H and ^{23}Na measurements signal to noise ratios differ by a factor of 100. The ^{1}H signal has higher SNR.

The T_2 distribution for ^{1}H in the Bentheimer core plug has two peaks, $T_{2peak} = 400$ ms and 28 ms. The ^{23}Na T_2 distribution was unimodal, $T_{2peak} = 44$ ms. CPMG experiment parameters for ^{1}H T_2 measurement were: echo time = 2.6 ms, number of echoes = 1541, number of averages = 32 and recycle delay = 6 s. The CPMG parameters for ^{23}Na T_2 measurement were: echo time = 2.6 ms, number of echoes = 193, number of averages 128 and recycle delay = 2 s. The measurement time for CPMG measurement was approximately 5.5 minutes. For the same measurement time for ^{1}H and ^{23}Na measurements the SNR for the ^{1}H signal is 160 time larger than that for ^{23}Na signal. The 90° pulse length and magnetic field gradient strengths employed for ^{23}Na measurements were approximately four times greater than that for ^{1}H measurement ($\gamma_{23Na}/\gamma_{1H} = 3.8$).
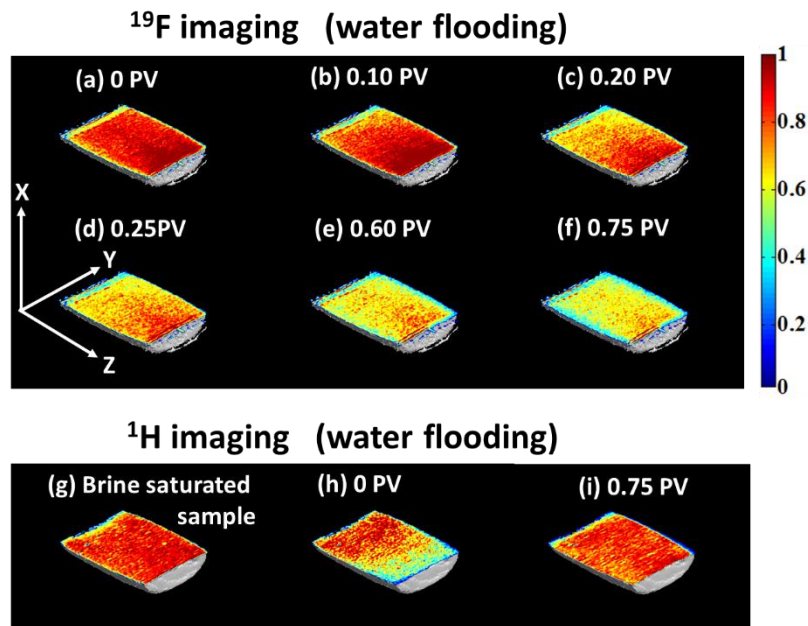
Figure 4. (a-f) The oil saturation distribution ^{19}F, 2D FSE image slices, superimposed on a cut 3D image background for a Bentheimer core plug during water flooding. The observed signal is solely from oil. The flooding is from $-z$ to z. The average initial oil saturation in (a) was 0.79. Water flooding displaced the oil (b-f) to a residual oil saturation of 0.33 in (f). The oil saturation is directly proportional to the signal intensity. The water saturation distribution from ^{1}H 2D FSE image slices, is shown in (g-i) superimposed on a cut 3D image background for the same Bentheimer core plug before and after the same flooding experiment. Image (g) shows the sample fully saturated with brine; the signal is solely from water, (h) shows the sample saturated with brine and oil (before flooding) while (i) shows the sample after flooding has ceased. Images (b) and (h) correspond to the commencement of flooding. The water and oil saturation distribution is inhomogeneous in these two images. The measurements were done at 1.5 T for ^{1}H, 1.6 T for ^{19}F. Change of nucleus was achieved by changing B_0. The resonance frequency was constant at 63.5 MHz.

^{23}Na MR/MRI can be employed as a complementary approach to conventional ^{1}H MR/MRI for shale fluid typing, taking advantage of the fact that sodium ions are only present in the aqueous phase. ^{23}Na can also be used for investigating brine salinity effects in porous media including conventional rocks, clays, and shale, and may be employed to differentiate hydrocarbon and aqueous phases [3, 21-25].

CONCLUSION

A cryogen free superconducting magnet system is introduced for petroleum MR/MRI studies. The small size and light weight of the magnet (by comparison to conventional superconducting magnets) permits one to rotate the magnet. The cryogen free superconducting magnet permits B_0 field change because the magnet power supply is permanently connected. The ability to change the static magnetic field makes it possible to control susceptibility effects in rock core plugs and to resonate different nuclei (^{19}F, ^{23}Na) by employing a constant frequency RF probe.

The new magnet was employed for core flooding MRI measurements at 1.5 T for ^{1}H and at 1.6 T for [19]F. It also permits one to perform [23]Na measurements for a brine saturated Bentheimer sandstone at 3 T with a resonance frequency of 33.7 MHz. Variable field operation is very advantageous for samples with susceptibility driven inhomogeneous broadening since one can readily control the experimental line width $1/(\pi T_2^*)$ [14].
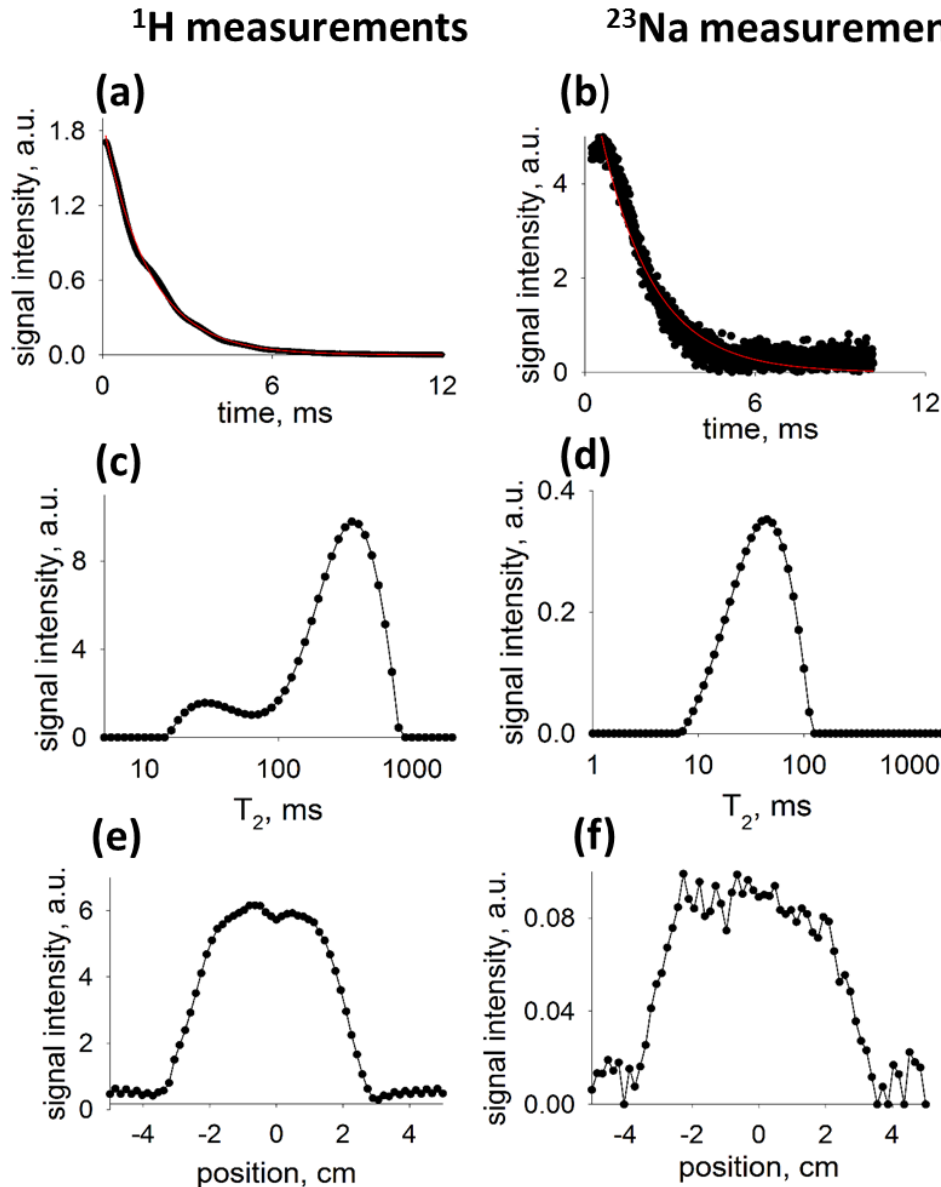

Figure 5. FID signal of brine saturated Bentheimer core plug (2% NaCl) for (a) ^{1}H and (b) [23]Na, the red lines are the fitted plots. (c) [1]H T_2 distribution, (d) [23]Na T_2 distribution. The [1]H T_2 distribution has two components reflecting the pore size distribution. The [23]Na T_2 distribution is unimodal. 1D double half-k SPRITE profile for (e) [1]H (proton density profile) and (f) [23]Na in Bentheimer core plug (salinity profile). FOV is 10 cm with phase encoding time of 400 us.

ACKNOWLEDGEMENTS

REFERENCES

1. C.T. P Chang and A.T. Watson, NMR Imaging of Flow Velocity in Porous Media, AIChE Journal, 45 (1999) 437-444.
2. J. Mitchell, T.C. Chandrasekera, D.J. Holland, F.L. Gladden, E.J. Fordham. Magnetic Resonance Imaging in Laboratory Petrophysical Core Analysis, Phys. Rep. 526 (2013) 165-225.
3. J. Mitchell. Magnetic Resonance Core Analysis at 0.3 T. SCA2014-010, International Symposium of the Society of Core Analysts, Avignon, France, Sept. 8-11, 2014
4. Y. Zhao, Y. Song, Y. Liu, H. Liang, B. Dou. Visualization and Measurement of CO_2 Flooding in Porous Media using MRI, Ind. Eng. Chem. Res. 50 (2011) 4707-4715.
5. D. Green, D. Veselinovic, B.J. Balcom, F. Marica. Applications of a New Technique to Acquire Spatially Resolved NMR Petrophysical Data. SCA2012-32, International Symposium of the Society of Core Analysts, Aberdeen, Scotland, UK, Aug. 27-30, 2012.
6. R. Freedman. Advances in NMR Logging, J. Pet. Technol. 58 (2006) 60-66.
7. A. Brautaset, G. Ersland, A. Graue, J. Stevens, J. Howard. Using MRI to Study in-situ Oil Recovery during CO_2 Injection in Carbonates. SCA2008-41, International Symposium of the Society of Core Analysts, Abu Dhabi, UAE, Oct. 29-Nov. 2, 2008.
8. D. Green, J. Dick, M. McAloon, P.F. de J. Cano-Barrita, J. Burger, B. Balcom. Oil/Water Imbibition and Drainage Capillary Pressure Determined by MRI on a Wide Sampling of Rocks. SCA2008-01, International Symposium of the Society of Core Analysts, Abu Dhabi, UAE, Oct. 29-Nov. 2, 2008.
9. G.R. Coates, L. Xiao, M.G. Prammer. NMR Logging Principles and Applications; Halliburton Energy Services: Houston, USA, 1999.
10. M. Li, D. Xiao, M. Shakerian, A. Afrough, F. Goora, F. Marica, L. Romero-Zerón, B. Balcom, Magnetic Resonance Imaging of Core Flooding in a Metal Core Holder. SCA2016-064, International Symposium of the Society of Core Analysts, Colorado, USA, Aug. 21-Aug. 26, 2016.
11. C.E. Muir, O.V. Petrov, K.V. Romanenko, B.J. Balcom, Measuring Miscible Fluid Displacement in Porous Media with Magnetic Resonance Imaging Water Resour. Res. 50 (2014), 1859–1868.
12. M. Li, D. Xiao, L. Romero-Zerón, F. Marica, B. MacMillan, B.J. Balcom, Mapping Three-Dimensional Oil Distribution with π-EPI MRI Measurements at Low Magnetic Field, J. Magn. Reson. 269 (2016) 13-23.
13. M. Li, D. Xiao, L. Romero-Zerón, B.J. Balcom. Monitoring Oil Displacement Processes with k-t Accelerated Spin Echo SPI, Magn. Reson. Chem. 54 (2016) 197-204.

14. Q Chen, A.E. Marble, B.G. Colpitts, B.J. Balcom, The Internal Magnetic Field Distribution, and Single Exponential Magnetic Resonance Free Induction Decay, in Rocks, J. Magn. Reson. 175 (2005) 300-308.

15. E. Anoardo', G. Galli, G. Ferrante, Fast-Field-Cycling NMR: Applications and Instrumentation, Appl. Magn. Reson. 20 (2001) 365-404.

16. J.P. Korb, G. Freiman, B. Nicot, P. Ligneul, Dynamical Surface Affinity of Diphasic Liquids as a Probe of Wettability of Multimodal porous media, Phys. Rev. B. 061601 (2009) 1-12.

17. K. Alba, S. M. Taghavi, I. A. Frigaard, Miscible Heavy-light Displacement Flows in an Inclined Two-dimensional Channel: A Numerical Approach, Phys. Fluids. 26 (2014) 1-22.

18. G.N. Holland, P.A. Bottomley, W.S. Hinshaw, [19]F Magnetic Resonance Imaging, J. Mag. Reson. 136 (1977).

19. M. Halse, D.J. Goodyear, B. MacMillan, P. Szomolanyi, D. Matheson, B.J. Balcom, Centric Scan SPRITE Magnetic Resonance Imaging, J. Magn. Reson. 165 (2003) 219-229.

20. K. Romanenko, B.J. Balcom, An Assessment of Non-wetting Phase Relative Permeability in Water-wet Sandstones Based on Quantitative MRI of Capillary End Effects, J. Petrol. Sci. Eng. 110 (2013) 225-231.

21. D. Yang, R. Kausik, ^{23}Na and ^{1}H NMR Relaxometry of Shale at High Magnetic Field, Energy Fuels, 30 (2016) 4509-4519.

22. K. E. Washburn, G. Madelin. Imaging of Multiphase Fluid Saturation within a Porous Material via Sodium NMR. J. Magn. Reson. 202 (2010) 122−126.

23. P. Tutunjian, H. Vinegar, J. Ferris, Nuclear Magnetic Resonance Imaging of Sodium-23 in Cores. Log Analyst. 34 (1993), 34 (03) 11-18.

24. H.T. Hu, L.Z. Xiao, X.L. Wu, Corrections for Downhole NMR Logging. Pet. Sci. 9 (2012), 46−52.

25. J. Mitchell, E.J. Fordham, Contributed Review: Nuclear Magnetic Resonance Core Analysis at 0.3 T, Rev. Sci. Instrum. 85 (2014) 1-17.

COMPARISON OF RESIDUAL SATURATIONS OF AN UNCONVENTIONAL RESERVOIR ROCK MEASURED BY DIFFERENT CAPILLARY PRESSURE LABORATORY METHODS

N. Schleifer[1], Alexandra Amann-Hildenbrand[2], Jim Bell[3], Philipp Aurin[1] and Roman Scheliga[2]

(1) Wintershall Holding GmbH, Central Laboratory, Germany; (2) RWTH Aachen, Institute of Geology and Geochemistry of Petroleum and Coal, Germany;(3) Advanced Rock Properties Group, Core Laboratories (U.K.) Ltd

ABSTRACT

An extensive Special Core Analysis study was carried out on an unconventional gas reservoir from the Carboniferous sandstone. As the ambient porosity of the rocks is below 12 % and Klinkenberg corrected permeability is ranging in between 0.001 and 1 mD the laboratory study took almost two years. Saturation measurements were near the detection limit of all applied techniques while running the experiments following best practice procedures.

After finalizing the study the question arose whether such time consuming and cost expensive programs running at the limit of accuracy are appropriate for a proper reservoir characterization or whether a different "more easy" approach is required to deliver data, which would rather give trends and reduce measurement uncertainty by found statistics.

Accordingly a research program was started to compare the existing results with a different approach. Advanced core analysis capillary pressure methods as ultracentrifuge, porous plate and mercury injection (MICP) at overburden stress were compared to cost effective methods like ambient MICP, vapor desorption and adsorption as well as counter current imbibition (CCI) delivering a large amount of data, however at ambient conditions.

The paper shows the results of the different approaches under the consideration of accuracy and the governing physical principles/processes. However, their comparison is not straightforward as each method covers different pressure ranges and partially involve usage of non-reservoir fluids, which requires the transfer to representative wettability conditions. The results of this study show the advantages and disadvantages of characterizing such low porosity reservoir rocks and tries to define a complementary laboratory program delivering valuable results within acceptable time for a proper reservoir characterization.

INTRODUCTION

In 2012 about 130 m of core were taken from a Carboniferous tight gas reservoir in the Northern German Lower Saxony Basin. The six cored intervals cover a depth range from 3832.5m down to 4380.0m and comprise sediments from the Westphalian C to D or even Stephanian. The underlying Westphalian A-C coals are the origin of the accumulated gas. The sedimentological sequences of the reservoir mainly consist of thick sequences of fining upward fluvial sandstones which are separated by conglomerate and silty claystone units as well as anthracite coals. The gas-bearing fluvial sandstones have their origin in braided as well as meandering systems and were deposited in a broad alluvial plain in the northern forland basin of the Variscan mountain belt.

CORE ANALYSIS PROGRAM

A core logging and core analysis program was designed to characterize reservoir quality and rock mechanical behaviour. After running Routine Core Analysis on 230 fresh plugs a selection of 40 plugs was sent to CoreLab Aberdeen for Special Core Analysis. This program was finished in 2014. In 2015 a Master Thesis at RWTH Aachen (Scheliga, 2016) followed to apply complementary capillary pressure methods and to compare the results to the results generated by the SCAL program.

RESERVOIR ROCK CHARACTERIZATION

Core Analysis data shows that the reservoir quality varies in a narrow range. Ambient data give porosities below 12 % and Klinkenberg permeability between 0.001 and 1 mD. Based on this data a sedimentology and petrography study identified four main reservoir rock types (Table 1) where the main parts of RRT 3 and 4 are characterized by porosities below 5% and are commonly assigned to non-reservoir rock (Table 1).

Pore-throat-sizes (PSD) of all rock is below 1 µm (Fig. 1) with only a few samples showing macroporosity. X-ray diffraction analysis was carried out on all 40 SCAL plugs. Quartz and quartz cement content are between 54 and 90 wt.-%. Further abundant minerals are dolomite (1-18 wt.-%) and siderite (1-11 wt.-%). Clay minerals found are illite, mica, kaolinite and chlorite. The clay content varies between 11 and 29 wt.-%.

Thin section petrography by PanTerra Geoconsultants B.V. showed two diagenetic phases having an impact on the current porosity network. In a first stage the primary intergranular pore space was reduced by mechanical compaction and quartz cement precipitation during shallow burial. Secondary porosity was thereafter created by dissolution of feldspar under deep burial conditions. Illite and kaolinite formed due to feldspar dissolution, which filled the new pore space and reduced secondary porosity. Ductile grains were identified.

SAMPLE PREPARATION

Plugs of 1.5inch diameter are used for Routine and Special Core Analysis to maximize available pore volumes. Further 40 "twin"-plugs with 1 inch diameter were drilled for MICP at ambient and overburden conditions close to the SCAL plugs.

Plug cleaning for Special Core Analysis was done dependent on sample permeability. Lowest permeability samples were first saturated and immersed in 2 wt.-% KCl-brine while monitoring electrical conductivity. This should give an indication of the dissolution of precipitated salts in the pore space. The immersion cleaning of the samples indicated predominantly water wet behavior. Dependent on permeability increase samples were then either flow-through cleaned and or immersion cleaned in a Toluene-Methanol solvent mixture. No residual oil appeared while plug cleaning. Samples used in the Master Thesis were immersion cleaned in a mixture of iso-propyl alcohol and de-ionized water until no further dissolution of salt could be observed by measuring the electrical conductivity of the brine. Overall cleaning time took weeks to month.

LABORATORY METHODS APPLIED

The following methods (McPhee et al., 2015; Newsham et al. 2003 & 2004) were applied to measure capillary pressure and to define residual saturations for the static and dynamic reservoir model. Pore volumes vary between 0.25 mL and 5 mL. Given a measurement accuracy of 0.05 mL or 0.01g, partial saturations have an uncertainty of up to 20 %. Each method covers different pressure ranges and partially uses non-reservoir fluids (Table 2).

Porous Plate 1re Drainage Gas-Brine Pc at Reservoir Pressure

Porous plate measurements deliver a uniform fluid distribution while being able to run experiments at reservoir conditions and with reservoir fluids. As such no corrections need to be applied to consider overburden stress effects and wettability. Porous plate experiments are considered time consuming as sufficient time is required to achieve saturation stability. Porous Plate experiments are non-destructive.

Centrifuge 1re Drainage (Gas-Brine) and 1re Imbibition (Brine-Decane)

Ultracentrifuge runs are quick and achieve high capillary pressures. However viscous forces must be considered associated to the high spin speeds. As the capillary pressure varies along the plug axis centrifuge runs result in non-uniform fluid saturations which require a correction of the production data. This is regarded a source of error of the method. Running a gas-brine imbibition cycle requires to replace the gas phase by Decane to be able to monitor production and to ensure a proper displacement front.

MICP at overburden pressure (NOB 5000 psig)

The setup of mercury Pc measurements at overburden are comparable to porous plate Pc measurements. Mercury injection pressure is stepwise increased until mercury saturation becomes constant. As overburden pressure must be adjusted to the injection (pore) pressure to keep the net overburden pressure constant equilibration time to establish constant pressure conditions is a critical point. As the tests are run with two non-wetting fluids Pc curves must be corrected for interfacial tension and contact angles at reservoir conditions. Although reservoir wettability does not influence the experimental curve mercury displacing gas is considered an imbibition Pc curve.

MICP ambient
  Commercial ambient mercury injection instruments were originally designed to measure pore throat size distributions of porous media. The benefit of these systems is that high Pc's can be applied delivering a high amount of data-points. The benefit of these systems is that either small plugs or cuttings can be tested. Cuttings might require correction for surface roughness and porosity deviations to He-porosity. As with overburden experiments true wettability of the rock does not influence the experimental outcome. Ambient MICP systems allow the measurement of large samples series as analysis is quick and cheap.

Counter Current Imbibition (CCI)
  CCI is cheap, easy to apply and allows quick analysis of large sample series. In this study Toluene was used as wetting fluid and gas the non-wetting phase. CCI does not apply a measurable capillary pressure. Toluene is spontaneously imbibed till end-point saturation is achieved. Initial saturation is set by evaporation (drainage). Confining pressure was not applied and whole sample surface was accessible to the wetting fluid.

Vapour desorption and adsorption
  Vapour sorption curves are limited to high Pc's and is dominated by the affinity of the pore surface to adsorb/desorb water vapour (physisorption). In comparison to proper Pc measurements saturation changes are not directly related to pore throat sizes. In this study desorption (drainage) and adsorption (imbibition) curves were measured in a climate chamber using a large sample group simultaneously. Saturation changes were monitored by weighting.

Capillary Pressure conversion
The conversion of the capillary pressure curves measured with different confining stresses and different fluid is based on the Leverett J-Function (1941),

$$Pc_1 = (\sigma_1 * \cos \vartheta_1)/(\sigma_2 * \cos \vartheta_2) * Pc_2 * \sqrt{(\Phi_1/\Phi_2 * K_2/K_1)}, \text{ where} \qquad (1)$$

Pc_1 indicates the references system, e.g. reservoir, and Pc_2 gives the capillary pressure to be converted, e.g. laboratory. Table 2 gives an overview of interfacial tension and contact angles of the rock-fluid systems. IFT at ambient conditions were measured by pendant drop method. Values for overburden measurements were taken from literature, e.g. Mc Caffrey (1972). A contact angle of 30°C was assumed for the air-brine system.

EXPERIMENTS
Dry weight was recorded and the samples saturated either using a pressure of 2000 psig (CoreLab) or atmospheric pressure after initial vacuum period. Synthetic reservoir brine with a TDS = 211 g/L was used for porous plate and centrifuge testing.

Porous Plate 1re Drainage (at 8700 psig overburden stress)
Porous plate measurements with a net confining stress of 8700 psi were part of the SCAL program. Method was performed on six samples using porous discs with a threshold pressure of 1500 psig. A maximum capillary pressure of 500 psig was applied.

Ultracentrifuge (ambient conditions)
Capillary pressure drainage and imbibition was measured by Ultracentrifuge within the SCAL program. No confining stress was applied. The drainage cycle was run using brine as the displaced fluid and air as the displacing fluid. The imbibition curve was run replacing air with decane as the displaced fluid. This is to avoid spontaneous brine imbibition during test loading. A maximum capillary pressure of 550 psig was applied. Capillary pressure curves were generated using Forbes equation (Forbes, 1994).

MICP at 5000 psig overburden stress
Five samples previously used for NMR testing were sent to Core Laboratories Houston for MICP curves at a net confining stress of 5000 psig. Maximum confining pressure of the setup allows 10 000 psi with a maximum mercury-air Pc of up to 5000 psia. Confining stress was continuously adjusted to keep net confining stress constant.

MICP at ambient conditions
Mercury injection capillary pressures (MICP) at ambient conditions were done with a Micromeritics® Autopore IV 9520™ porosimeter. Injection pressures up to 55 000 psi can be applied. In total 10 cylindrical samples of 1 inch diameter and 1 inch height were analyzed. Plug samples were hot solvent cleaned prior to testing.

Counter Current Imbibition (CCI) using Toluene at ambient conditions.
The experiments were run on 17 cleaned and dried samples (diameter 1.5 inch), saturated with toluene in a desiccator under vacuum conditions. Subsequently Toluene is evaporated at room temperature aiming for an initial target saturation of the plugs between 30 and 50 %. This range was defined by well-log interpretation. After setting initial saturation samples are wrapped with aluminum-foil and stored in a refrigerator at T=4°C for 24 h to keep the saturation constant and to achieve a homogeneous fluid distribution. Partially saturated sample were finally immersed in toluene and weight increase measured with an electronic balance. Imbibition was considered complete when no change of weight was observed within 0.5 h. Duration of one experiment was 15 to 20 hours. To avoid temperature variations all CCI experiments were run in a climate controlled laboratory room. CCI is a time- but no pressure controlled method; end-points saturations being determined are initial gas saturation S_{gi} and trapped gas saturation S_{gt} interpreted as residual gas saturation $S_{gr.}$

Vapour Desorption and Adsorption
Application of vapour sorption was adapted from soil science where relative humidity is set by using supersaturated brines. Core analysis adapted the method to achieve low initial water saturations (Newsham et al., 2003). Pressure achieved (10 000 psi) can

commonly only measured with MICP. The application assumes that the vapour pressure in the pores is in equilibrium with the fluid pressure and thus can be regarded equivalent to a capillary pressure. A climate chamber is used where temperature and relative humidity can be set with an accuracy of 0.1 °C and 0.5% rH. Samples were saturated with 2 wt.-% KCl. The brine was selected to avoid clay swelling. Temperature was set to T=35°C to allow a wider humidity range. Starting at 85% rH humidity was decreased down to 65% rH using incremental steps of 5 to 10% rH. The weight of the samples was recorded twice a week. In case no weight changes appeared between two consecutive records humidity was changed. Adsorption started immediately after desorption by increasing relative humidity up to 90% rH. Duration of the entire cycle was 5 month.

CHANGES OF PORE SIZE DISTRIBUTION WITH CONFINING STRESS

In Figure 1 the pore size distributions measured by MICP with and without confining stress are compared. Nearby plugs of reservoir rock type 1 and reservoir rock type 2 with similar basic petrophysical properties are shown. Ambient pore throat sizes are below 1 µm with a distinct peak at 0.4 µm for RRT 1 and a dual porosity distribution for RRT 2 with peaks at 0.4 and 0.015 µm.

Applying confining pressure leads to a single peak at 0.12 µm without any distinct secondary peak. At NOB pore size distribution of sample 41A varies between 0.02 and 0.4 µm. Sample 160A shows pore throat sizes starting from 0.5 µm. As injection pressure is limited to 5000 psi no information on pore throat sizes below 0.02 µm can be given.

RESULTS AT AMBIENT CONDITIONS

Centrifuge, MICP, CCI and vapor de- and adsorption were applied under ambient conditions. Only two: ultracentrifuge and vapor sorption, cover drainage and imbibition cycle. MICP data are converted to air-brine system assuming a water wet system with a contact angel of 0°. IFT of the synthetic reservoir brine is 78 mN/m. Figure 2 shows a comparison of the capillary drainage curves using the samples 123 (UC), 135 (MICP) and 137 (VD). MICP threshold pressure is higher than with ultracentrifuge. At a P_c of 100 psig (PTR 0.2 µm) and $S_w=0.6$ curves are crossing leading to a lower S_{wi} at 550 psig with MICP compared to centrifuge P_c. This is a general observation when comparing these two methods. A sample set representing rock type 3 ($\Phi = 4\%$, $K_L = 0.01$ mD) shows the same cross-over at 100 psig and a $S_w=0.92$. To bring both curves to an overlap different sets of converting parameters would be necessary for MICP. One before and one after the cross-over. VD curves are shifted to higher capillary pressures compared to MICP leading to higher S_W at identical Pc. Comparing samples of same permeability the initial water saturation increases with the method applied (Fig. 4): $S_{wi}(VD) \leq S_{wi}(MICP\ A-B) \leq S_{wi}(CCI) \leq S_{wi}(UC)$.

RESULTS AT OVERBURDEN STRESS

Comparing Porous Plate P_c and MICP at overburden pressure gives differences in S_{wi} of up to 0.4 (Fig. 6 and 7). Converting the MICP curve to 8700 psi by reducing porosity and

permeability S_{wi} can only be slightly increased. The example in Figure 3 shows an increase of 0.05. As a contact angle of 0° is already selected the only increase in MICP A-B NOB can be achieved by increasing the IFT of 52 mN/m or to assume different compressibility behavior of the plug. The overburden Pc curves show a parallel decrease of S_{wi} with K_L. The S_{wi} decrease is steeper (Fig. 4.) compared to ambient methods.

INITIAL VESUS RESIDUAL GAS SATURATION

Correlating S_{gi} with S_{gr} (Fig. 5) the methods ultracentrifuge, CCI and vapor de- and adsorption can be compared. Ultracentrifuge delivers lowest S_{gi} (0.2< S_{gi}< 0.7) and lowest S_{gr} (S_{gr} < 0.4). CCI covers an intermediate range as S_{gi} was experimentally set to 0.5 to 0.8. These starting saturations result in a S_{gr} between 0.2 to 0.55. VD gives an S_{gi} above 0.8 with adsorption leading to a S_{gr} between 0.5 up to 0.8. Linear trend lines for S_{gi} vs S_{gr} of the three methods differ (Fig. 5). Vapor shows the steepest increase of S_{gr} with S_{gi} followed by CCI and ultracentrifuge measurements. CCI shows the largest scatter of residual saturations. Distinct trends for rock types are not recognizable (Fig. 6).

DISCUSSION

Tight sandstone samples were investigated with porosities below 12%. At such low porosity levels, any experimental errors in the detection of the partial saturations has large impact on the results. This is especially true for measurements at overburden stress.

Ambient MICP versus ambient air-brine Pc

In Figure 4 it is shown that MICP curves partly overlap with air-brine capillary pressure curves. A more complex conversion of MICP curves dependent on pore size would be required. To do so, interfacial tension and contact angles at reservoir conditions must be known. A constant contact angle of 30° was assumed in this study.

Overburden MICP versus Porous Plate at Reservoir Pressure

Comparing overburden MICP curves with porous plate air-brine Pc curves at overburden stress differ significantly (Fig. 3). There are no reasonable air-brine wettability parameters that bring both curves to an overlap. One reason for the large offset of both curves might be a varying NOB while MICP. Maximum P_c is set to 5000 psi with a maximum applicable NOB of 10 000 psi. Proper adjustment of overburden stress is therefore needed to guarantee a constant NOB and assumes that pore size distribution stays constant throughout the experiment. Saturation equilibration may another reason and have large impact on ambient Pc curves which increases with decreasing permeability, e.g. Maas at al. (2016).

S_{wi} versus Klinkenberg permeability

Although MICP and A-B Pc show a large offset in S_{wi} both method show almost parallel trends of S_{wi} versus K_L. The trend achieved of the overburden methods shows a steeper increase of S_{wi} with K_L than achieved by applying ambient methods (Fig. 4). An extension of the trend observed with ambient methods can not be extended to reservoir conditions. Vapor desorption results in lowest S_{wi} as highest pressures up to 10 000 psi

are applied. Ambient MICP converted to air-brine system and CCI show an overlap in residual saturations. CCI values were adjusted to a S_{wi} between 0.2 to 0.5 as this is the saturation range found by log interpretation. Application of centrifuge leads to highest initial water saturations also overlapping with CCI data.

S_{gi} versus S_{gr}

Plotting S_{gr} verus $S_{gi}=1-S_{wi}$ (Holtz, 2003) further discriminates the methods. Equal to S_{wi} applying VD leads to highest S_{gr} (0.5 to 0.8), CCI delivers intermediate values $(0.2<S_{gr}<0.55)$ and ultracentrifuge testing leads to lowest S_{gr} (< 0.4). These correlations lead to different trends between S_{gi} and S_{gr} which depends on the applied methods (Fig. 5 and 6). Centrifuge testing uses brine as wetting fluid representing one of the reservoir fluids. Water wet behaviour of the rock leads to highest S_{wi} and thus lowest S_{gi}. VD has its benefit in achieving very low S_{wi} but adsorption is limited to a narrow saturation range. Using a different complementary method for achieving S_{gr} would improve the benefit of VD.   Saturations measured with CCI are scattered allowing the extension of the trend derived from UC to higher saturations or the trend derived from vapor towards lower saturations. Obtaining a trend within the saturation range of interest, CCI would have to be applied starting with a wider range of initial saturations.

CONCLUSION

- Although at the detection limit, ambient and overburden Pc methods can be applied on low porosity ($\Phi< 12\%$) tight sandstone reservoir rock.
- Logarithmic trend of S_{wi}-K_L found with ambient Pc methods can not be extended to reservoir conditions.
- MICP curves need to be compared to A-B Pc data to achieve a reasonable conversion to the reservoir fluid systems.
- MICP NOB data can not be brought in agreement with A-B Pc measured at overburden stress.
- CCI method must be applied using a wide range of S_{gi} to derive a valid S_{gi}-S_{gr} relation in the saturation range of interest.
- S_{gi}-S_{gr} relations of the reservoir rock types are dependent on the applied methods.
- Vapor desorption as imbibition capillary pressure method is not recommended.

NOMENCLATURE

A-B, ABRI: Air-brine capillary pressure (combined with resistivity index RI)
CCI: Counter Current Imbibition
Φ: porosity
IFT: interfacial tension σ
K, K_a K_L: Permeability, Air permeability, Klinkenberg Permeability
MICP: Mercury Injection Capillary Pressure
NOB: net overburden pressure, net confining stress
Pc: Capillary Pressure
PSD: Pore throat size distribution
P_{sig}, p_{sia}: Pressure in psi relative to atmospheric pressure (g) and vacuum (a)

RRT: reservoir rock type
RCA, SCAL: Routine and Special Core Analysis
S_{gi}: initial gas saturation ($S_{gi} = 1 - S_{wi}$)
S_{gr}, S_{gt}: residual gas saturation, trapped gas saturation
S_w, S_{wi}: Water saturation, initial water saturation
TDS: Total dissolved solids
ϑ: contact angle
UC: ultracentrifuge
VD: Vapor desorption

ACKNOWLEDGEMENTS

REFERENCES

1. *Forbes P.L. (1994):* Simple and Accurate Methods for Converting Centrifuge Data into Drainage and Imbibition Capillary Pressure Curves, The Log Analyst, 35/4, pp. 31-53.
2. *Holtz, M. (2002):* Residual Gas saturation to aquifer influx: A calculation method for 3-D computer reservoir model construction. SPE paper 75502. Society of Petroleum Engineers (SPE).
3. *Leverett, M. C. (1941):* Capillary Behavior in Porous Solids. Trans AMIE, 142, pp. 152–169
4. *Maas, J.; Springer, N. and Hebing, A. (2016):* Relative Permeability Effects Overlooked in MICP Measurements; Transition Zones Likely to be Smaller. Petrophysics, Vol.58, No. 1, pp. 19-27.
5. *McCaffrey (1972):* Measurement of interfacial tensions and contact angles at high temperature and pressure. Journal of Canadian Petroleum Technology, JCPT 72-03-03, July-Sept., pp. 26-32.
6. *McPhee, C, Reed, J. and Zubizarreta, I. (2015):* Core Analysis: A Best Practice Guide, Volume 64. Developments in Petroleum Science. Elsevier B. V., 1st ed.
7. *Newsham, K.; Rushing, J. and Lasswell, P. (2003):* Use of vapor desorption data to characterize high capillary pressures in a basin-centered gas accumulation with ultra-low connate water saturations. SPE paper 84596. Society of Petroleum Engineers (SPE).
8. *Newsham, K.; Rushing, J.; Lasswell, P. and Blasingame, T. (2004):* A comparative study of laboratory techniques for measuring capillary pressures in tight sands. SPE paper 89866.
9. *Scheliga, R. (2016):* Comparison of Capillary Pressure measurement methods applied to rock samples from a tight gas sandstone. Master Th. RWTH Aachen.
10. *Suzanne, K.; Hamon, G and Billiotte, J. (2003):* Experimental relationships between residual gas saturation and initial gas saturation in heterogeneous sandstone reservoirs. SPE paper 84038. Society of Petroleum Engineers (SPE).

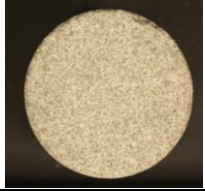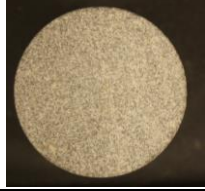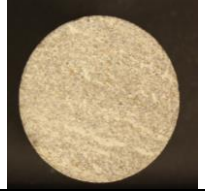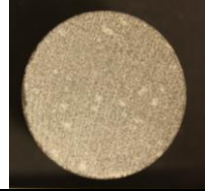Table 1: Images and properties of representative rock type samples.

	RRT 1	RRT 2	RRT 3	RRT 4
Φ (fract.):	7 – 10	5–7	0–7	0–5
K_L (mD):	0.2-0.8	0.08-0.2	0.02-0.08	0.002-0.02
Grain density (g/mL):	2.65-2.67	2.67-2.71	2.70-2.78	2.70-2.78
Grain sizes:	Grain size tends to be medium to very coarse sand.	Medium sand grains	Grain size fine or medium sand.	Grain size fine or medium sand,
Deposit:	Braided channel deposits	Meandering to braided channel sediments.	Meandering channel to distal braided	Sheetflood sediments, very high content of ductile grains

Table 2: Overview of applied methods, capillary pressure ranges, fluid systems and fluid
properties (* measure with pendant drop method).

| Pc Method	Drainage (Swi)	Wetting Fluid	Non-wetting Fluid	IFT	Contact Angle
A- B Pc	x	Brine	Air	78	30
Centrifuge	x	Brine	Air	78	30
MICP @ NOB	x	Air	Brine	480	140
MICP amb.	x	Air	Brine	480	140
CCI					
Vapor	x	Brine	Air	72	30
Pc Method	Imbibition (Sgr)	Wetting Fluid	Non-wetting Fluid	IFT	Contact Angle
A-B Pc					
Centrifuge	x	Brine	Decane	50.6*	0
MICP @ NOB					
MICP amb.					
CCI	x	Toluene	Air	28.4*	0
Vapor	x	Brine	Air	72	30
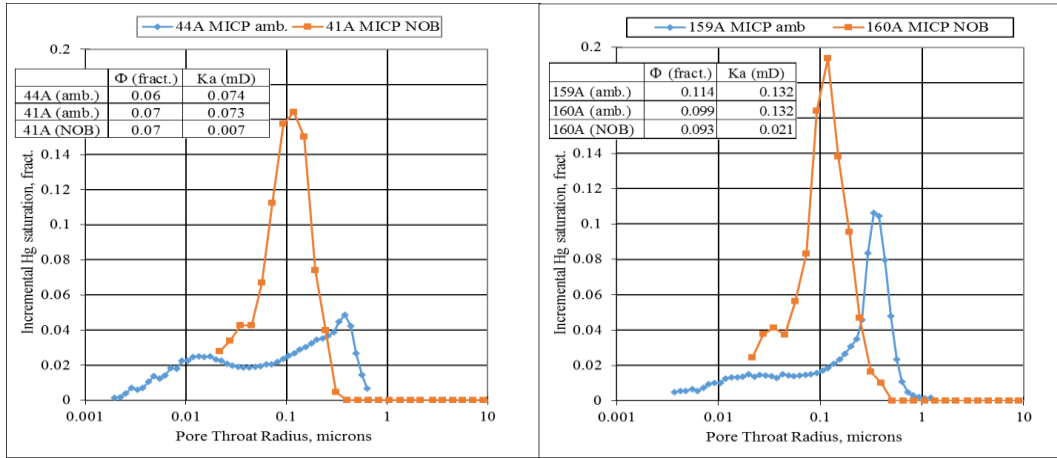
Figure 1: PSD at ambient and confining stress. Left: RRT 2. Right: RRT 1.
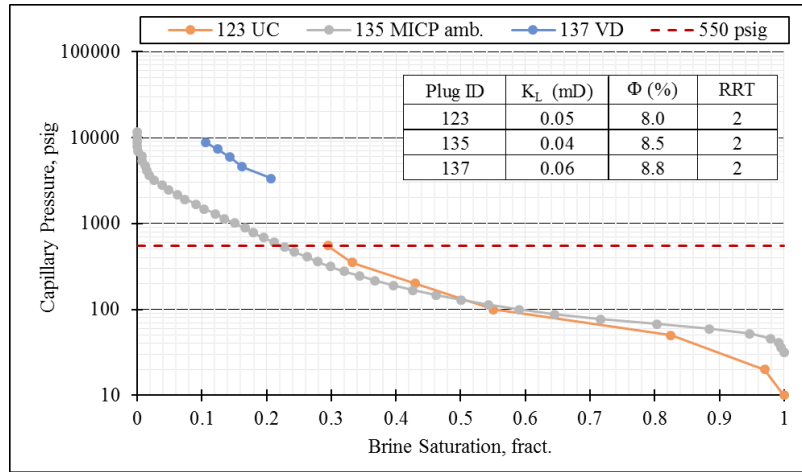

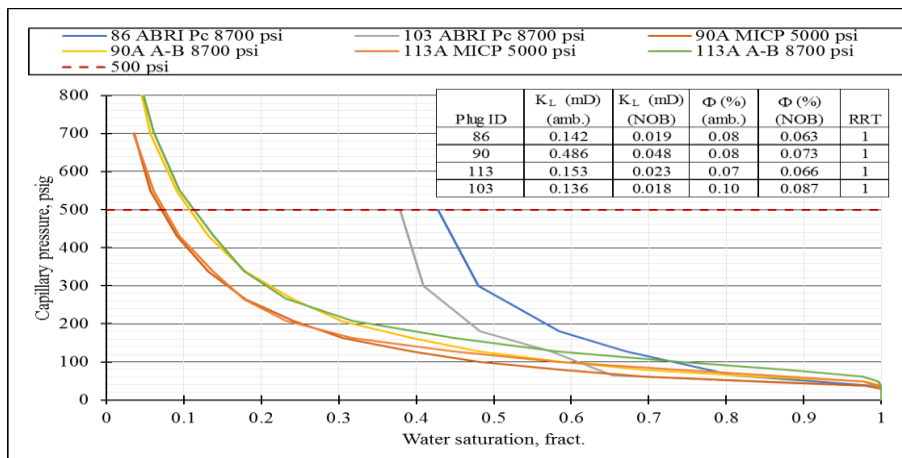*Figure 2: Pc from ultracentrifuge (UC), MICP ambient and vapor desorption (VD).*

Figure 3: Pc curves from MICP NOB and porous plate (ABRI). Table in the graph gives petrophysical properties at measurement conditions and rock type of the samples.
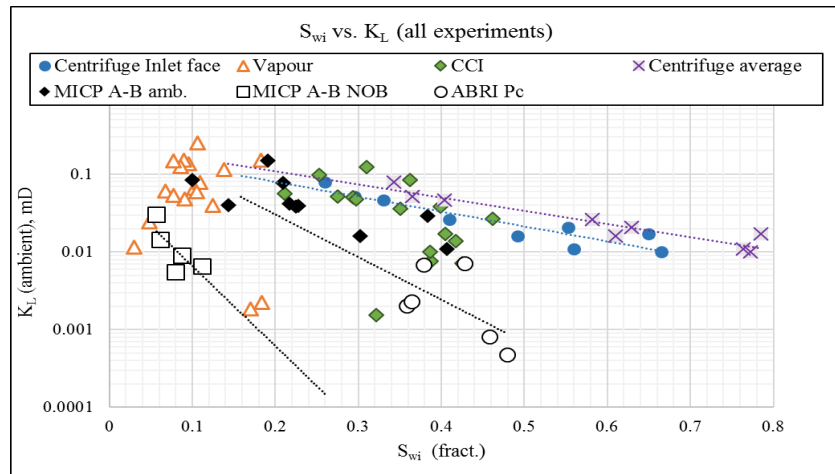
Figure 4: S_{wi} versus K_L (all experiments). MICP converted to A-B Pc and S_{wi} @ 500psig. Logarithmic trends are indicated.
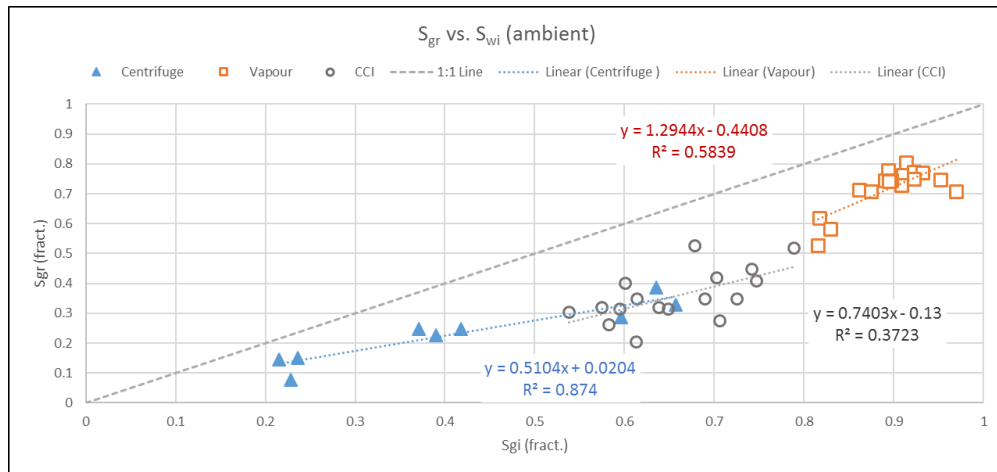

Figure 5: Initial gas saturations versus residual gas saturation sorted by experimental method.
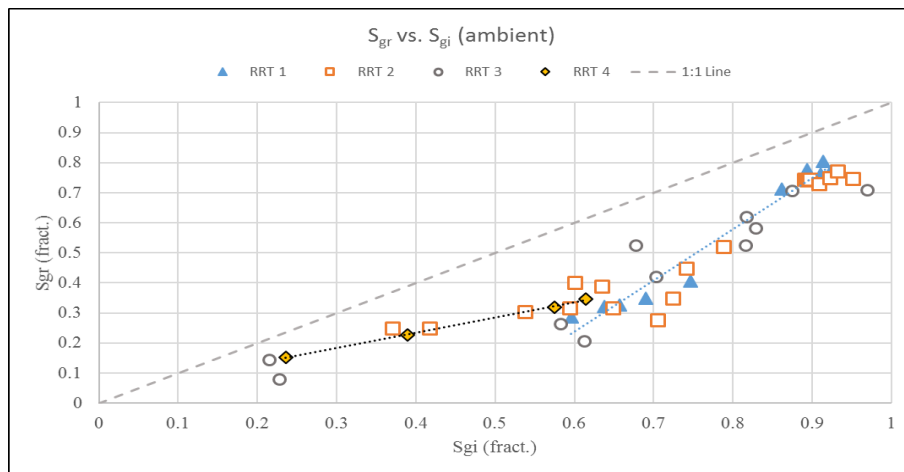

Figure 6: S_{gi} versus S_{gr} sorted by reservoir rock type (RRT).

A THERMOPOROELASTIC (T-P-E) MODEL DEVELOPED FOR CORE TRIPPING FAILURE ANALYSIS

Rahman Ashena[*], Gerhard Thonhauser[*], Holger Ott[*],
Vamegh Rasouli[**], Siroos Azizmohammadi[*], Michael Prohaska[*]
* Department Petroleum Engineering, Montanuniversität Leoben, 8700 Leoben, Austria
** Department of Petroleum Engineering, University of North Dakota, USA

ABSTRACT

During tripping of cores to the surface, the core properties, in particular the mechanical properties, are adversely altered due to the drop of the confining pressure, pore pressure drop (i.e. hydraulic effect), and the temperature drop (i.e. the thermal effect) at the boundary of the core sample. This is while, depending on the core properties, the inner pore pressure and temperature may not change as quickly as at the outer boundary. This differential change of properties between the inner and outer part of the core sample may consequently cause the tensile failure of the core resulting in micro-fractures in the rock matrix. In this study, a safe core retrieval procedure is presented considering the hydraulic diffusivity using a thermoporoelastic (T-P-E) approach.

We developed a T-P-E model that incorporates the change of the confining pressure and temperature and the associated hydraulic and thermal effects in the core. The model calculates the pore pressure distribution and the tensile induced stresses within the core sample. Then, the induced stresses are summed-up to compare with the limits in the Griffith's tensile failure criterion to determine if the sample can be retrieved in a preserved manner. The T-P-E method will be applied to study the core retrieval of a very tight sample for different initial bottomhole depths.

The simulations show comparable results with another method developed in Fluent. The results indicated that the contribution of thermally induced stresses is much less significant than the hydraulically induced stresses for sample failure. We further show that the hydraulic diffusivity coefficient and the in-situ stress state conditions are the controlling parameters for safe tripping operations.

INTRODUCTION

A major challenge in coring during the oil and gas drilling operations is the potential for mechanical core damage which can occur during tripping [1–3]. This occurs due to tensile failures developed as a result of an extremely fast tripping rate. This phenomenon is more manifest in retrieving tight core samples. The resulting micro-fractures created in the sample due to this process alter the physical and mechanical rock properties such as porosity, permeability, Uniaxial Compressive Strength (UCS), Young's Modulus (E) and

might lead to misinterpretation of subsequent core analysis. Therefore, the lab results may not represent the real rock properties, which will be used to characterize the reservoir.

To date, most of the core retrieval procedures and schedules have been generally based on generic methods and rules of thumb [4]. Most of these tripping-out schedules just indicate that the tripping should be conducted more slowly in an interval near the surface (e.g. 100-400 m). The recent research studies do not consider the changes in the mechanical and thermal properties of the core due to the tripping [5–7]. In the present study, we aim for a T-P-E model simulating the induced stresses and possible tensile failure during core tripping process.

TRIPPING INDUCED STRESSES AND FAILURE CRITERION

During tripping of the core to the surface, the pore pressure at the outer boundary of the core drops as it is in contact with the hydrostatic pressure exerted by the drilling fluid. This is while the change in pore pressure and temperature of the core does not equally distribute moving towards the center of the core.

During tripping, the induced stresses in the core body as a function of external stresses are the radial and tangential (hoop) stresses as depicted in Figure 1. The induced radial stresses (σ_{rr}) are created in radial direction of the sample. The induced hoop stresses ($\sigma_{\theta\theta}$) are the compressional stresses around the circumference of the sample.
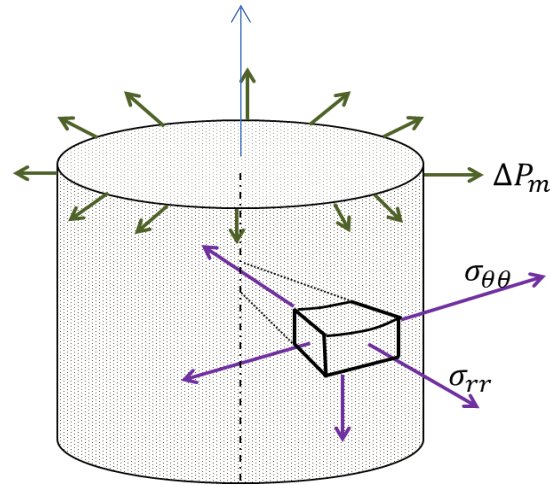

Figure 1: Two dimensional Induced Stresses in the Core during tripping out

If the tripping-induced stresses in the core exceed its tensile strength, the core may undergo tensile failure [5, 6, 8]. It has been noted that this tensile failure attributes the induced tensile stresses to the pore pressure and fluid flow/diffusion out of the core [1, 5, 6, 8] and the Griffith's failure criterion has been applied [9, 10]:

$$\Delta\sigma_3' - T_s \geq 0 \qquad\qquad \text{if} \quad (\Delta\sigma_1' + 3\Delta\sigma_3') > 0, \qquad\qquad (1)$$

where for the case of core tripping, $\Delta\sigma'_1$ and $\Delta\sigma'_3$ are the induced effective maximum and minimum principal stresses, respectively. For the cylindrical sample, $\Delta\sigma'_3$ can be either the differential effective radial $\Delta\sigma'_{rr}$ or the hoop stress difference $\Delta\sigma'_{\theta\theta}$ as depicted in Figure 2.
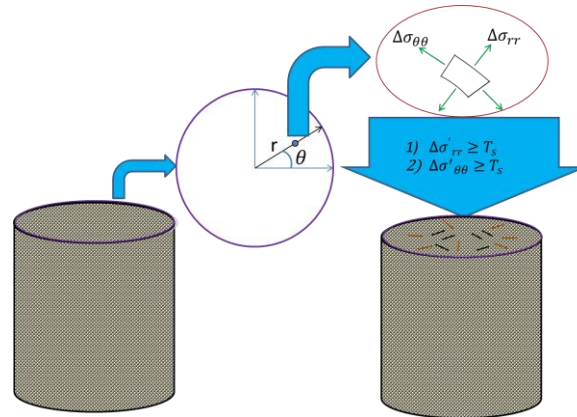

Figure 2: Griffith's Tensile Failure Criterion to Predict Failure during Core Tripping

THERMOPOROELASTICITY (T-P-E)

T-P-E is the study of rock mechanical behavior and how the rocks undergo deformation and failure in response to the effects of imposing a change or difference to confining stress, pore pressure, and also temperature [11–13]. In other words, it describes the interaction and coupling between the confining stress difference, the pore fluid pressure difference and the temperature difference.

Basically, in T-P-E the initial state constitutes the basis of the problem. Therefore, the T-P-E parameters are considered as their difference from their initial values. These parameters include the confining stress/pressure difference ΔP_c, the pore pressure difference ΔP_p, and the temperature difference ΔT. Therefore, the initial T-P-E parameters are considered zero. It is also assumed that these imposed changes occur immediately at the time of nearly zero (t=0$^+$). Then, the new conditions last for a certain period of time Δt (Figure 3). At the end of each time period, the effects of the changes in the conditions on the interested parameters can be analytically determined. The interesting parameters for each problem can be the induced pore pressures or the induced stresses. It is noted that the core tripping cannot be represented by the original T-P-E as the sample is not retrieved from the bottomhole immediately, but it is being tripped gradually during a time interval.

To use this method, first the T-P-E constitutive equations are considered. Then, the diffusivity equations, their initial and boundary conditions are taken into account. Next, the corresponding analytical solutions are found. Finally, using the constitutive equations, the equations for the induced radial and hoop stresses can be analytically derived.
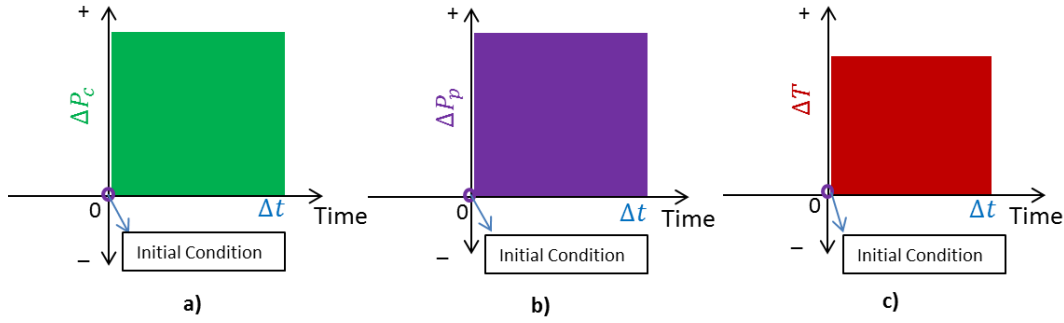
Figure 3: Initial and Boundary Conditions Using Original Thermoporoelasticity

CONSTITUTIVE EQUATIONS

The main constitutive equations used in T-P-E are [1, 11, 12, 14, 15]:

$$\Delta\sigma_{rr} = 2G\epsilon_{rr} + 2G\frac{\upsilon}{1-2\upsilon}(\epsilon_{rr} + \epsilon_{\theta\theta}) - a\Delta P_p \tag{2}$$

$$\Delta\sigma_{\theta\theta} = 2G\epsilon_{\theta\theta} + 2G\frac{\upsilon}{1-2\upsilon}(\epsilon_{rr} + \epsilon_{\theta\theta}) - a\Delta P_p \tag{3}$$

$$\Delta\sigma_T = K_{T(}\epsilon_T - \frac{\alpha_m}{3}\Delta T) \tag{4}$$

Where G is the shear modulus; υ is the Poisson's ratio; ϵ_{rr} is the radial strain; $\epsilon_{\theta\theta}$ is the tangential strain; ΔP_p is the differential induced pore pressure; $\Delta\sigma_T$ is the differential induced thermal stress; K_T is the isothermal bulk modulus; ϵ_T is the thermal strain; α_m is the bulk thermal expansion coefficient.

DIFFUSIVITY EQUATIONS

There are two hydraulic and thermal diffusivity equations. The coupled T-P-E diffusivity equation is expressed as [14–16]:

$$\frac{\partial\Delta P_p}{\partial t} = \eta\left(\frac{\partial^2\Delta P_p}{\partial r^2} + \frac{1}{r}\frac{\partial\Delta P_p}{\partial r}\right) + \eta'\frac{\partial\Delta T}{\partial t}, \tag{4}$$

where t is the time; η is the hydraulic diffusivity coefficient; η' is the corresponding coupling coefficient by the differential temperature on the pore pressure. The first and second terms on the right, respectively, pertain to the pressure diffusion and temperature gradient.

The thermoelastic equation is:

$$\frac{\partial\Delta T}{\partial t} = \eta_T\left(\frac{\partial^2\Delta T}{\partial r^2} + \frac{1}{r}\frac{\partial\Delta T}{\partial r}\right) + \eta'_T\left[\frac{\partial T}{\partial r}\frac{\partial\Delta P_p}{\partial r} + T\left(\frac{\partial^2\Delta P_p}{\partial r^2} + \frac{1}{r}\frac{\partial\Delta P_p}{\partial r}\right)\right], \tag{5}$$

where η_T is the thermal diffusivity coefficient; η'_T is the coupling coefficient by the pore pressure difference on the temperature. The first, second, and third terms on the right hand side of the above equation, respectively, indicate the heat conduction, the heat convection, and the pore pressure diffusion due to the temperature effect.

INITIAL CONDITIONS

In T-P-E, the initial state constitutes the basis of the problem. Therefore, prior to tripping, the initial conditions within the sample are:

✓ The confining pressure difference at t=0:
$$\Delta P_c(r, 0) = 0 \tag{6}$$
✓ The pore pressure difference at t=0:
$$\Delta P_p(r, 0) = 0 \tag{7}$$
✓ The temperature difference at t=0:
$$\Delta T(r, 0) = 0 \tag{8}$$

BOUNDARY CONDITIONS:

Using the original T-P-E, there are three conditions at the boundary of the core sample as follows:

✓ The confining pressure difference at the boundary (for t>0):
$$\Delta P_c(R, t) = \Delta P_{c,0} \tag{9}$$
✓ The pore pressure difference at the boundary (for t>0):
$$\Delta P_p(R, t) = -\Delta P_0 \tag{10}$$
✓ The temperature difference at the outer boundary $(r = R)$, and the center (for t>0):
$$\Delta T(R, t) = -\Delta T_0, \tag{11}$$
$$\checkmark \quad \frac{\partial}{\partial r} \Delta T(0, t) = 0 \tag{12}$$

In the above equations, $-\Delta P_{c,0}$ indicates the induced confining pressure drop from bottomhole to the surface; $-\Delta P_0$ is the pore pressure drop from bottomhole to the surface; and $-\Delta T_0$ represents the temperature drop from bottomhole to the surface.

REPRESENTATIVE T-P-E FOR CORE TRIPPING

As it was discussed earlier, the original T-P-E formulation can only simulate the core retrieval corresponding to the immediate time of its transportation to the surface. To model the complete core retrieval process from the bottom of the hole to the surface, the T-P-E formulation needs to be modified to include the time evolvement during the core tripping process. Therefore, it is assumed that the core is being raised from the bottomhole in a number of discrete steps *n* and after implementation of each single step, the conditions of the sample are maintained for a specified duration until the next step is taken. This process continues until the core reaches the surface. The total number of steps, *N*, should be chosen large enough for exactness of the model. Depending on the chosen value *N*, each step carries specified three effects of reduction in confining mud pressure, pore pressure and the temperature at the boundary of the core, as shown in Figure 4. The impact of these three effects over the entire tripping period will be considered in the T-P-E modeling. The time intervals between the two successive steps is defined based on the selected tripping speed, bottomhole depth and *N*.

Therefore, when the core starts to be raised from bottomhole (during the first raising step from the bottomhole, $n=1$), the confining pressure, pore pressure, and temperature at the core boundary experience a specified difference or drop (this step is shown in Figure 4). The sample will continue experiencing these drops at its boundary until it reaches the surface. Therefore, the duration that the effects of the first step will last (that must be considered in T-P-E modeling) is equal to the whole tripping time. As the core is being raised for the second step ($n=2$), the same changes are induced to the sample and it will continue experiencing them until it reaches the surface. Obviously, the duration that the effects of the second step will last (that should be considered in the T-P-E modeling) is less than that of the first step. This process, shown in Figure 5, continues so forth until the core reaches the surface. It is noted that at each depth, the changes in the fluid properties such as viscosity and isothermal compressibility of gas have been considered.
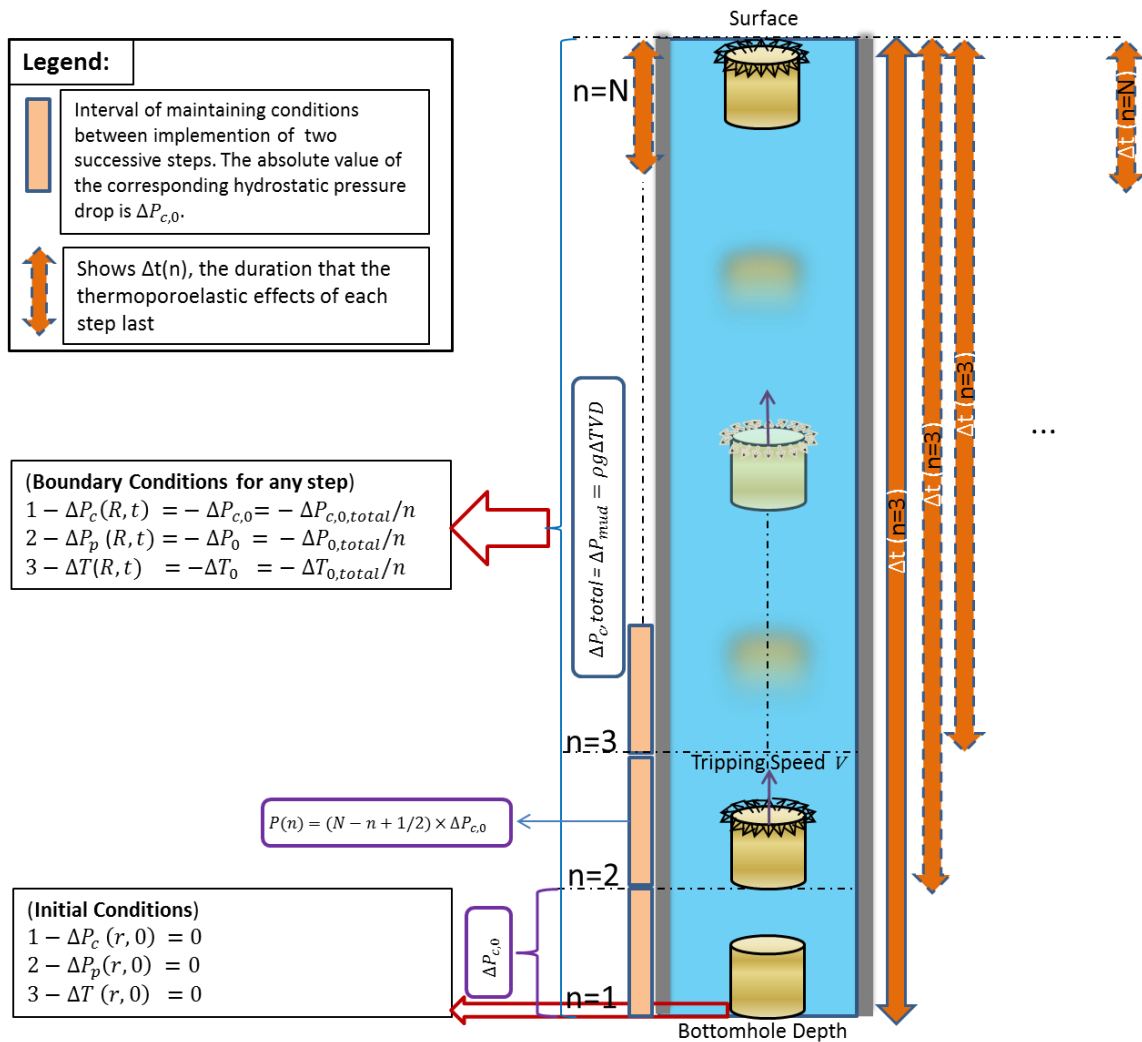

Legend:

Interval of maintaining conditions between implemention of two successive steps. The absolute value of the corresponding hydrostatic pressure drop is $\Delta P_{c,0}$.

Shows $\Delta t(n)$, the duration that the thermoporoelastic effects of each step last

(Boundary Conditions for any step)
$1 - \Delta P_c(R,t) = -\Delta P_{c,0} = -\Delta P_{c,0,total}/n$
$2 - \Delta P_p(R,t) = -\Delta P_0 = -\Delta P_{0,total}/n$
$3 - \Delta T(R,t) = -\Delta T_0 = -\Delta T_{0,total}/n$

$P(n) = (N - n + 1/2) \times \Delta P_{c,0}$

(Initial Conditions)
$1 - \Delta P_c(r,0) = 0$
$2 - \Delta P_p(r,0) = 0$
$3 - \Delta T(r,0) = 0$

$\Delta P_{c,total} = \Delta P_{mud} = \rho g \Delta TVD$

$\Delta P_{c,0}$

Surface

$n=N$

$n=3$

Tripping Speed v

$n=2$

$n=1$

Bottomhole Depth

$\Delta t(n=3)$ $\Delta t(n=3)$ $\Delta t(n=3)$

$\Delta t(n=N)$

Figure 4: Step-wise progression of the core during its Trip from the bottomhole to the surface.
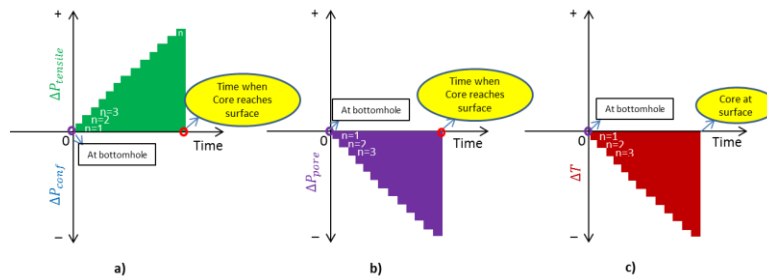
Figure 5: Initial and boundary conditions considering step-wise core decompression from bottomhole to the surface, simulating the real gradual core tripping using thermoporoelasticity

DEVELOPED MODEL

The diffusivity equations were used to develop the boundary and initial conditions corresponding to the pore pressure and temperature distribution within the sample. This requires intensive math exercises including Laplace transformation of the Partial Differential Equations, derivations, integrations, rearrangements, and taking inverse Laplace transformation. This allows calculation of the induced radial and hoop stresses as well as pore pressures based on the T-P-E model for each time step. Using the superposition principle, the total induced stresses and pore pressure corresponding to the sample when brought to the surface is found as the summation of the values for all steps. Then, the effective induced tensile stresses are calculated by including the effect of pore pressure. The final step is to apply the failure criterion to determine if the sample can reach the surface under preserved condition and if so, what the optimum safe tripping speed is to avoid any type of failure. The proposed model was fully developed in Matlab-2015.

RESULTS AND DISCUSSION

Before the implementation of the developed model, it is important to compare its results with some published work to determine if the new model provides more realistic results. For this purpose, the published data in the literature which was conducted using *Ansys-Fluent* software was utilized. The results are presented in this section, followed by analysis of a typical core tripping case.

Benchmarking

In this section, the results of the developed T-P-E model are compared with the Ansys-Fluent simulations performed [5]. They assumed a core sample of 4-inch (10.16 cm) with 2% porosity, and permeability of 2×10^{-4}mD, and gas viscosity 0.02 cp, is retrieved from the depth of 1502.46 m to the surface. The drilling mud weight in the wellbore was 12.5 ppg (1259 Kg/m^3) equivalent to 18.65 MPa as the initial bottomhole pressure. The initial sample pore pressure is assumed to be equal to the initial mud hydrostatic pressure. The surface and bottomhole temperatures are 10˚C and 34˚C respectively. Based on the tripping schedule mentioned in their paper, the core is raised from 1502.46 m to 914.5 m at 0.31 m/s; from 914.5 to 198 m at 0.065 m/s; and from 198 m to the surface at 0.05 m/s tripping

speed. Using this data, the hydraulic diffusivity coefficient η of $4\times10^6\ \frac{m^2}{s}$ was obtained. This value will be used in the T-P-E model.

Similar to other studies, *Zubizarreta et al.* (2013) ignored the impact of the mechanical and thermal effects on the induced pore pressured and stresses. However, in the T-P-E model presented in this work, the contribution of the mechanical and thermal properties of the sample in its response during the tripping are considered. In order to perform the analysis based on the T-P-E model, further input data is required, which was assumed based on the best correspondence to the rock description in the published work. The data used for this purpose include Poisson's ratio $v = 0.18$, Undrained Poisson's ratio $v_u = 0.28$, Biot's coefficient $a = 0.7$, Young's modulus E=10 GPa), thermal expansion coefficient $10^{-5}\ \frac{1}{°C}$, and thermal diffusivity coefficient of $8\times10^{-7}\ \frac{m^2}{s}$.

The analysis was conducted based on the T-P-E model and the results were compared against those published by a literature work [5]. Figure 6 shows a good agreement between the results of the two models. However, the T-P-E model presents a larger induced pore pressure which is due to the fact that the Fluent model has not included the mechanical and thermal properties of the sample in its analysis. The black curve in Figure 6 (left) represents the induced radial stress in the center of the core, which the difference between the value of the pore pressure inside the core (blue) and the mud pressure in its boundary (red). The critical core internal pressure (shown in green color) is found as the summation of the outside mud pressure and the equivalent tensile strength.
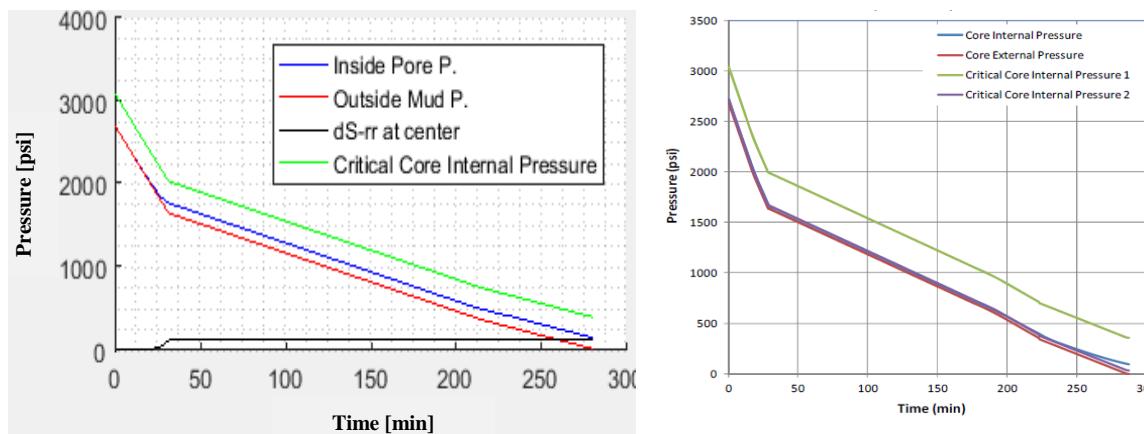

Figure 6: Comparison of the Results of the T-P-E model developed here (a) and model of *Zubizarreta et al.* (2013). (b)

A Typical Core Tripping Case
A set of input data representing the properties of a typical gas-bearing tight core sample is shown in Table 2. For single phase fluids, gas is the worst case because of its compressible nature. The data of Table 2 is taken from *Chen and Ewy (2005)* and *Hettema et al. (2002),*

in addition to the data from the industry core analysis results. The T-P-E model was run and the potential failure of the core sample was investigated.

Running the T-P-E model, the induced stresses were evaluated for two scenarios: 1) considering both the hydraulic and thermal effects, and 2) ignoring the thermal effect. Comparing the results of the two cases allows evaluating the extent of the impact of the thermal effect on the induced stresses. Next, to investigate the possible failure within the sample when it reaches the surface, the Griffith' failure criterion was applied for three cases of the induced radial and hoop stresses and the induced radial stress in the center of the sample, evaluated by subtracting the mud pressure from the pore pressure in the center of the core.

Table 1: Input data corresponding to a typical tight gas-bearing Core sample used for T-P-E core tripping analysis

Parameter	Value	Evaluation Method
Depth at bottomhole [m]	Mostly 500	
Diameter of core [in]	2 (≈5 cm)	
Porosity, ϕ [%]	40	Estimated/Measurable
Permeability of core, K [mD]	10^{-3}	Estimated/Measurable
Viscosity of gas, μ_g [cp]	0.02-0.04 (surface)	Measured
Viscosity of water, μ_g [cp]	1	
Molecular Weight of gas, M_g	16 (Methane)	Depending on the gas
Specific Gravity of gas (Surface)	0.65	Depending on the gas
Compressibility of rock, C_r [1/pa]	5×10^{-10}	Estimated/Measurable
Compressibility of gas (surface), C_g [1/Pa]	9.869×10^{-6}	Estimated/Measurable
Compressibility of water, C_w [1/pa]	5×10^{-10}	Estimated/Measurable
Interstitial Water Saturation, $S_{w,i}$	20%	Estimated/Measurable
Total Compressibility, $C_{t,g}$ [1/Pa] (gas-bearing core)	7.89×10^{-6}	$C_t = C_r + S_w C_w + S_g C_g$ [Ahmed & McKinney, 2005]
Hydraulic-Diffusivity, η [m^2/s] (Gas-bearing at surface)	10^{-8}	$\eta = 9.869 \times 10^{-13} \dfrac{K}{\varphi \mu_g C_{t,g}}$ [Ahmed & McKinney, 2005]
Thermal Expansion Coefficient, α_m [1/˚C]	10^{-5}	Estimated/Measurable [Timoshenko, 1934)]
Thermal Diffusivity, η_T [m^2/s]	8×10^{-7}	Estimated
Geothermal Gradient [˚C/m]	0.044	Estimated/Measurable
Uniaxial Compressive Strength, UCS [Mpa]	20	Measurable/Estimated
Young's Modulus [GPa]	4.2	Calculated/Estimated
Tensile-Strength, T.S. [Mpa]	1.7–2	$T.S. = UCS/m$, m=7–15 [Jaeger et al., 2007]
Biot's coefficient, a	0.7	0.6-0.7 (for shales)
Poisson's Ratio, ν	0.3	Estimated/Measurable
Undrained Poisson's Ratio, ν	0.4	Estimated/Measurable

Mud Weight, ρ_m [kg/m3]	1078	$MW[ppg] \times 119.826 = MW\left[\frac{kg}{m3}\right]$
Mud Cake Pressure Drop		Zero
Coupling Coefficient, η' and η'_T	0.17–0.3	Estimated
Initial Bottomhole Pressure [Mpa]	5.4	
Initial Pore Pressure		Equal to initial hydrostatic pressure

Figure 7 a and b show the induced radial and hoop stresses within the sample. The constant values of the tensile strength of the sample, 2MPa is shown in red color. Figure 7-c displays the induced radial stresses in the center of the core as well as the core's tensile strength, versus time. Comparing the effective induced stresses with the tensile strength of the sample determines whether failure and microfracturing can occur or not.
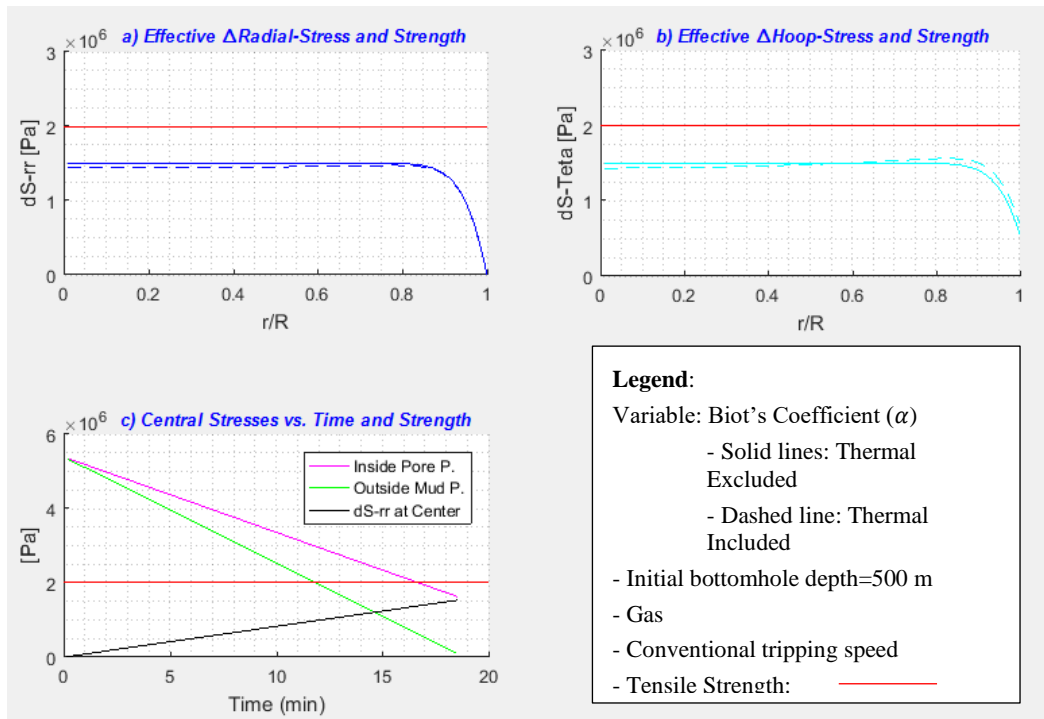
Figure 7: Thermal Effect Excluded and Included during Tripping

The results of Figure 7 show that the tight core sample located at 500 m, can be tripped in a preserved manner to the surface. In addition, the thermal effect corresponds to only ≈6% of the total induced stresses.

The initial bottomhole depth of the core sample is also an important parameter affecting the sample's T-P-E behavior during tripping. To simulate this effect using the T-P-E model, the data of Table 2 was used. The industry suggestion for conventional coring in very tight formations is to use a tripping speed of 0.45 *m/s*.

Figure 8 shows that failure occurs for all the in-situ bottomhole depths, except for bottomhole depth of 500 *m*, as only at this depth the induced radial and hoop stresses are less than the sample tensile strength. This indicates that the suggested 0.45 *m/s* tripping speed is not a proper value to use. The results of Figure 8 show the greater the depth, the greater the initial bottomhole confining pressure of the mud and the initial pore pressure of the sample will be. Therefore, the total differential confining and pore pressure that the sample will experience during tripping longer distances, would be larger. In short, tripping from deeper bottomhole corresponds to larger induced stresses being applied to the sample while its tensile strength remains constant. This means that the possibility of the failure increases with greater bottomhole depths.
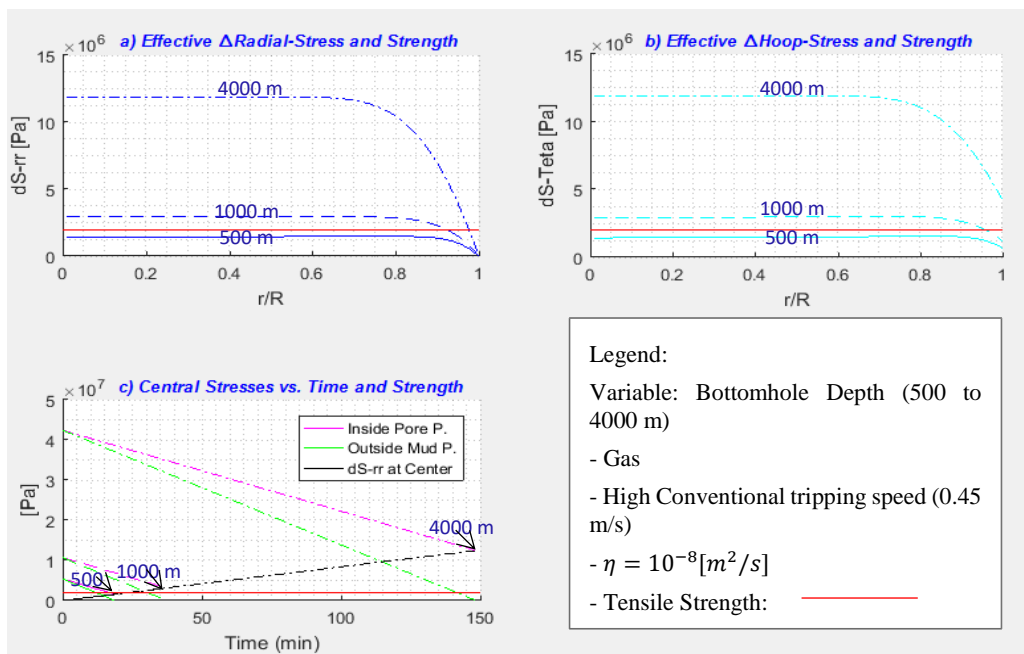
Figure 8: The effect of tripping from deeper bottomhole on the induced T-P-E stresses and sample failure

SUMMARY AND CONCLUSIONS

A thermoporoelastic (T-P-E) model was developed to investigate the magnitudes of stresses applied to a core sample and its potential failure when it is tripped from bottomhole to the surface. The model considers the effect of differential confining mud pressure, pore pressure and the temperature drop at the core boundary during tripping. The improvement yielded from this model were shown by comparing its results against the published data in the literature. The model provides enhanced performance as it also considers the mechanical and thermal effects. Also, analyzing the data corresponding to a typical tight core sample indicated that the contribution of thermally induced stresses is much less significant than the hydraulically induced stresses. We also have shown that very tight core

samples with hydraulic diffusivity coefficient of $10^{-8} m^2/s$ cannot be retrieved in a preserved manner to the surface unless its initial bottomhole depth is shallower than 500 m.

REFERENCES

1. Bouteca, M.J., Bary, D., Piau, J.M., Kessler, N., Boisson, M., & Fourmaintraux, D. (1994) "Contribution of Poroelasticity to Reservoir Engineering: Lab Experiments, Application to Core Decompression and Implication in HP-HT Reservoirs Depletion", Presented at the Eurock SPE/ISRM Rock Mechanics Conference.
2. Rosen, R., Mickelson, B., Fry, J., Hill, G., Knabe, B., & Sharf-Aldin, M. (2007) "Recent Experience with Unconsolidated Core Analysis", SCA 2007, 41.
3. McPhee, C., Reed, J., & Zubizarreta, I. (2015) "Core Analysis: A Best Practice Guide", Published by Elsevier, p.52-57. ISBN: 9780444635334.
4. American Petroleum Institute (1998) "Recommended Practices for Core Analysis", RP 40.
5. Zubizarreta, I., Byrne, M., Sorrentino, Y., & Rojas, E. (2013) "Pore Pressure Evolution, Core Damage and Tripping Out Schedules: A Computational Fluid Dynamics Approach", SPE-163527-MS, SPE/IADC Drilling Conference, 5-7 March, Amsterdam, The Netherlands.
6. Byrne, M., Zubizarreta, I., & Sorrentino, Y. (2015) "The Impact of Formation Damage on Core Quality, SPE 174189-MS", Presented in SPE European Formation Damage Conference and Exhibition, 3-5 June, Budapest, Hungary.
7. Hoeink, T., Van Der Zee, W., & Arndt, S. (2015) "Optimal Core Retrieval Time for Minimizing Core Decompression Damage", Presented at SPE Pacific Unconventional Resources Conference and Exhibition, 9-11 Nov., Australia.
8. Hettema, M.H.H., Hanssen, T.H., & Jones, B.L. (2002) "Minimizing Coring-Induced Damage in Consolidated Rock", SPE 78156 MS, Presented at SPE/ISRM Rock Mechanics Conference, Irving, Texas, Oct. 20-23.
9. Griffith, A.A. (1921) "The Phenomena of Rupture and Flow in Solids", The Philosophical Transactions of the Royal Society London (Series A), 221 (1921), pp. 163–198.
10. Fjaer, E., Holt, R.M., & Horsrud, P. (1992) "Petroleum Related Rock Mechanics", 2nd edition, p.59.
11. Wang, H. (2000) "Theory of Linear Poroelasticity with Applications to Geomechanics and Hydrogeology", Princeton University Press.
12. Detournay, E., & Cheng, A. (1993) "Fundamentals of Poroelasticity, Comprehensive Rock Engineering", Pergamon Press.
13. Zoback, M. (2010) "Reservoir Geomechanics", Cambridge University Press.
14. Chen, G., & Ewy, R.T. (2005) "Thermoporoelastic Effect on Wellbore Stability", SPE Journal, J. Eng. Material Technology 123(4), 409-416.
15. Timoshenko, S. (1934) "Theory of Elasticity", Published by McGraw-Hill Book Company.
16. Li, X., Cui, L., and Roegiers, J.C. (1998) "Thermoporoelastic Modeling of Wellbore Stability in Non-hydrostatic Stress Field", Journal of Rock Mechanics Science.

MECHANISMS OF WATER IMBIBITION
IN CARBONATE-RICH UNCONVENTIONAL
RESERVOIRS

Robert L. Krumm and James J. Howard
Premier Oilfield Laboratory

ABSTRACT

The interaction between water and fine-grained source rock has been a widely-discussed subject since the beginning of the shale revolution. It's well understood in carbonate-rich "shales" that some of the water used during hydraulic stimulation leaks-off or imbibes into the formation never to be recovered during flow-back or production. There is no consensus on the mechanisms for water uptake into shale, especially given the large volumes and rate at which the water is lost into the formation. A mechanism associated with capillary forces that result from the very small pore sizes is countered by arguments that the driving force is set up by osmotic pressures generated by differences in water's chemical. A set of Imbibition experiments that examined the effect of water activity were performed on several clay-rich carbonate (marls) core plugs. Drainage and imbibition experiments were done at room temperature in standard Amott cells as several water compositions were allowed to displace oil in a set of equivalent core plugs. Lithium chloride (LiCl) was chosen to make these different salinity brines because it allowed for the identification of any formation water that might be displaced during imbibition along with other geochemical changes. Cation analysis of the pre- and post-imbibition brines was acquired by ICP. Analysis of the post-imbibition brines found evidence of carbonate and silicate dissolution in the samples with the extent of dissolution decreasing with increased LiCl concentrations. Volumetric results for oil and brine from the imbibition tests found that the impact of initial water activity was statistically insignificant suggesting osmosis played a very limited role in water uptake in these samples. These results suggested that in a carbonate-rich unconventional reservoir rock that large differences in water activity were insufficient to create suitable osmotic pressure gradients that would drive water imbibition. In this case the presence of strong capillary forces associated with small pores provide a reasonable mechanism for water uptake.

INTRODUCTION

The injection of large volumes of water into unconventional reservoirs is a critical step in producing hydrocarbons from low-porosity, very low-permeability rock. The injected water generates a network of fractures in the near-wellbore region that aids in production and helps to overcome the nano-darcy permeability of the matrix. In some of these tight-rock reservoirs much of the injected water does not return to the well upon pressure draw

down, suggesting that it trapped in the low-permeability matrix [1,2]. Imbibition of this water into the matrix is the most common explanation for the loss of flow back water, though the mechanisms associated with this process remain unclear. The list of possible mechanisms includes the standard capillary action, osmotic flow and water sorption by clay minerals (3-5). Many of the laboratory studies focus on water and oil imbibition in gas shale where the liquid displaces gas at very low residual liquid saturations. In these studies, the implication is that the imbibed water lost during hydraulic fracturing can become a means for enhanced oil recovery [6]. Recovery efficiency in these studies can exceed 40% Original Oil in Place (OOIP).

The challenges in designing an experiment that focuses on water imbibition as an oil-displacement mechanism center around the petrophysical properties of these rocks. The low porosity and low permeability result in measurements that require more time and have less sensitivity because of errors in volume measurements. Uncertainty with initial water composition and the inability to remove residual liquids add to the difficulty. This study attempts to resolve some of these issues by relying on NMR methods to monitor fluid volume changes and a tailored water chemistry that allows for a clearer understanding of potential mixing of formation and injected waters.

SAMPLES AND METHODS

A set of core plugs from a carbonate mineral-rich unconventional reservoir were selected for the imbibition tests. The samples were selected from a common lithology defined by a mineralogy dominated by calcite with 10-20 wt percent clay minerals. The samples also included organic material that was 5 to 10% of the total volume.

The samples were standard 2.54 cm diameter core plugs, 3 to 4 cm in length. The liquid saturations of the "as-received" plugs were approximately half of the total volume, the remaining liquids were lost during the coring and transportation operations. A liquid filled saturation was determined by NMR techniques. The gas-filled pore volume was measured with a Helium porosimeter, and this value was combined with the NMR-based liquid-filled volume to create a sum-of-fluids total pore volume. The gas-filled pore volume was then filled with light mineral oil (n-Decane) under 2500 psi for several days. The saturated sample was then re-measured in the NMR spectrometer for a total liquid-filled pore volume that was compared with the sum-of-fluids pore volume. Porosity of these samples ranged from 0.10 to 0.13 with an average pore size of 0.3 microns. Permeability to oil for these samples was in the 50 to 500 nD range, with most samples at the high end.

The imbibition tests were set up in standard glass imbibition cells with the graduated tube oriented either up or down depending on whether imbibing water or oil. Four different salinities based on total dissolved solids were prepared using LiCl as the salt. The idea behind the use of a lithium salt was to monitor the water chemistry after the test and any measured cations would result from either exchange with the residual formation water found in the samples or from dissolution of the matrix. The salinities ranged from 100 to 100,000 ppm of LiCl. Oil production was monitored throughout the test over a period of

10 days, with more observations collected in the first few hours. After the test the samples were re-measured with NMR and mass balance to determine changes in saturation. Aliquots of water from each test cell were collected for chemical analysis (ICP) and pH measurements.

The samples were dried after the water imbibition tests with a NMR measurement to determine any residual fluid. The samples were then re-saturated with one of the different LiCl brines, followed by another NMR T_2 measurement. The water-saturated samples were then reloaded into the imbibition cells that were filled with decane. The cells were inverted, the collection column was located on the bottom, to collect any produced water. A final NMR measurement was acquired to compare with observed water production and weight changes.

RESULTS

The initial water saturations of these samples were established by flushing decane through the plugs in a steady-state flow apparatus for a period of several weeks, sufficient time to move several pore volumes of liquid through the samples. The liquid-filled pore volumes of these samples ranged from 3.0 to 5.0 cm^3. NMR relaxation time measurements at this state defined the initial water saturations between 0.08 and 0.30 for most with a value of 0.39 in an outlier low porosity sample.

The water imbibition tests required 10 days for measurable oil production to stabilize. Many of the samples had an initial production of 0.1 to 0.2 cm^3 of oil before the first sample point at 90 minutes after start (Figure 1). After the initial surge of oil collected in the tube, the rates of oil production were similar for the different imbibing water concentrations. The erratic staircase nature of the imbibition curves resulted from the episodic observations and the resolution of the collection tube, approximately 0.05 cm^3. The produced oil represented 6-12% of original oil in place (OOIP) in these samples, though the uncertainty associated with estimates was high.

NMR T_2 measured post-water imbibition showed distinctive changes in the intensity of the fast and slow relaxation components (Figure 2). The fast component increased in intensity and shifted towards slower times in agreement with the idea of a water-wet pore system accepting water. The slow component generally decreased in intensity following the loss of oil. The difference in the slow component intensity between post- and pre-imbibition measurements corresponded to the amount of oil collected in the imbibition cell (Figure 3).

NMR interpretation was based on assumption that these samples were predominately water-wet such that water filled the smaller pores and oil fills the larger pores. This was manifested in bi-modal relaxation time distributions where the fast component corresponded to the water phase and the slower component to the oil (Figure 2). Numerous displacement tests on samples from this carbonate-rich lithology suggested that this was a

valid interpretation, but exceptions abound. There was a pore volume component in the organic matter as visualized with SEM images. These pores fall in the less than 100 nm diameter range, though gas adsorption measurements indicate that volumetrically these organic matter pores are 10-20% of the total pore volume. Most of the pore volume is associated with the mineral matrix, with pores in the 50 to 1000 nm range.

While the samples were not cleaned in a conventional sense, they were dried after the water imbibition test and then re-saturated with the different salinity brines. The dried samples (150°C for several days) have a small amount of detectable liquids, approximately 10% of the original 3.0 to 5.0 cm^3. The brine-saturated samples also have a bimodal distribution of relaxation times, with most of the incremental volume associated with the slower relaxation times (Figure 4). The intensity of the fast component was less than that from the pre-imbibition stage, which suggested that the model of having only water associated with the fast component was overly simplified. The pore system of these samples likely included two sizes or types of pores.

The oil imbibition tests were allowed to run for 12 days. The amount of collected water ranged from 0.05 to 1.2 cm^3, roughly 1 to 50% of the original water in place (OWIP). There was no obvious connection with the concentration of the water, and since the pore systems of the samples were selected because of their similarity there was no obvious explanation. The NMR T_2 distribution were less illuminating in tracking the changes between pre- and post-oil imbibition samples that with the water imbibition. The changes in sample weight, however, did provide a useful correlation with the amounts of water production (Figure 5). The positive correlation, however, was not sufficient in this case since the volume of produced water is twice what would be expected from the changes in mass, even after correcting for the density of the decane. The non-quantitative nature of the oil imbibition was troubling with no obvious explanation or understanding of the phenomenon. It was suggested by a reviewer that the harsh drying conditions may have damaged the pore system, especially the smaller pores, so that subsequent brine saturation did not restore all of the original pore volume in the allotted time. Whatever the cause for the poor mass balance in this test, this does highlight the need to reconsider many of the sample preparation protocols for fine-grain, organic-rich reservoir rocks.

Analysis of the different salinity brines defined the purity of the LiCl. Since there was 0.2 mg of Na, 0.002 mg of Ca and 0 mg of K per gram of Li in the salt only the 100K ppm brine had measureable amounts of these other cations. The concentration of these cations defined the baseline for the analyses of the brines used in the imbibition tests (Table 1).

The Li content in the post-imbibition brines was the same as the initial brine composition, indicating that Li was neither extracted or added to the rock. The extracted brine compositions were dominated by the presence of excess Ca, Na and Si. The maximum Si concentration in the extracted brines was 7 mg/l, near the solubility of Si at room temperature. Very little Al was detected in the post-imbibition brines, < 0.3 mg/l with no obvious trend associated with the different salinities. The Si:Al ratio suggests that the

soluble Si was associated with the dissolution of quartz phases rather than feldspars or clay minerals, though at these low concentrations it is possible that some of the Al was precipitated in a new alumino-silicate phase [7].

The pH of the initial brines varied from 7.0 to 5.3 with the lower salinity mixtures having the higher pH values. After the imbibition tests the pH of the extracted water was 1 to 2.5 pH units higher (Table 2)

There were two sources of cations in the post-imbibition brines, those produced by the dissolution of minerals and those extracted or exchanged with the initial formation brine that remained in the core plugs. The relationship between Ca and pH indicated a dissolution mechanism with the increased pH in the extracted brine relative to the initial brine composition (Figure 6). The high Na concentrations in the post-imbibition brines represents exchange with the residual formation water found in these samples. There was no correspondence between Na concentration in the post-imbibition water and initial composition. Since there is little evidence of dissolution of Na-bearing phases, (e.g. feldspar) it was likely that the Na came from the residual fluids or precipitated salts. Higher Na concentrations were detected in the lower salinity imbibition brines that suggest chemical potential as a driving force for the movement of Na into the post imbibition brine.

The absence of a correlation between brine chemistry and produced oil volume from water imbibition discounted the osmotic pressure model for imbibition. The lack of correlation between produced oil volume and clay mineral content in these samples discounted the water adsorption model on clay mineral surfaces. The low clay mineral content in these samples may be misleading since the sub-micron particle sizes are all capable of adsorbing some water. The chemical results of the post-imbibition brine indicated some carbonate mineral dissolution, that may have enhanced pore throat sizes and improved capillary-driven processes.

REFERENCES

1. Cheng, Y., "Impact of Water Dynamics in Fractures on the Performance of Hydraulically Fractured Wells in Gas-Shale Reservoirs", *Journal of Canadian Petroleum Technology*, (2012)*51*,2, 143–151.
2. Roychaudhuri, B., Tsotsis, T. T., & Jessen, K., "An experimental investigation of spontaneous imbibition in gas shales", (2013).
3. Ren, W., Li, G., Tian, S., Sheng, M., & Geng, L., "Analytical modelling of hysteretic constitutive relations governing spontaneous imbibition of fracturing fluid in shale", *Journal of Natural Gas Science and Engineering*, (2016)*34*, 925–933.
4. Wang, F., & Pan, Z., "Numerical simulation of chemical potential dominated fracturing fluid flowback in hydraulically fractured shale gas reservoirs", *Petroleum Exploration and Development*, (2016)*43*,6, 1060–1066.
5. Xu, M., & Dehghanpour, H., "Advances in Understanding Wettability of Gas Shales", *Energy & Fuels*, (2014)*28*,7, 4362–4375
6. Wang, D., Butler, R., Liu, H., and Ahmed, S., "Flow-rate behavoir and imbibition in shale", *SPE Reservoir Evaluation & Engineering*, (2011), 14, 505-512.

7. Bethke, C., *Geochemical and Biogeochemical Reaction Modeling*, (2008), 2nd ed., Cambridge University Press.

Table 1. Composition of initial brines

Brine Salinity (mg/L)	Li (mg/L)	Na (mg/L)	Ca (mg/L)	pH
100	15.6	<0.5	<0.01	7.05
2000	357	<0.5	<0.01	6.72
20,000	3649	<0.5	0.19	5.95
100,000	19330	37.5	1.04	5.29

Table 2. Composition of post-imbibition waters

Samples/ Salinity	pH post Imbibition	delta pH	Ca (mg/L)	Na (mg/L)
100	8.6	1.6	4.1	118.6
2000	7.9	1.2	22.5	99.4
20000	7.0	1.1	73.4	82.7
100000	7.8	2.5	37.8	38.7

FIGURES
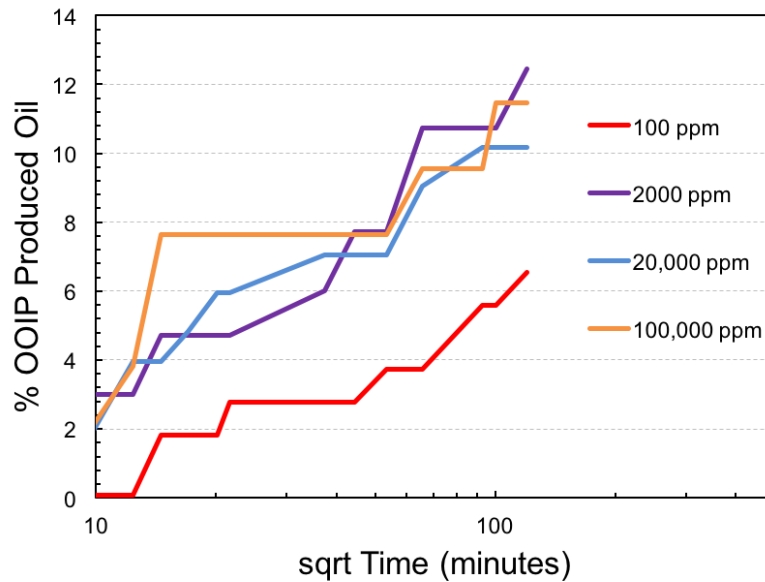
Figure 1. Averaged oil production rate for water imbibition test for the different water concentrations. Produced oil volume was converted to %OOIP using NMR-based estimates of initial water saturation and total pore volume.
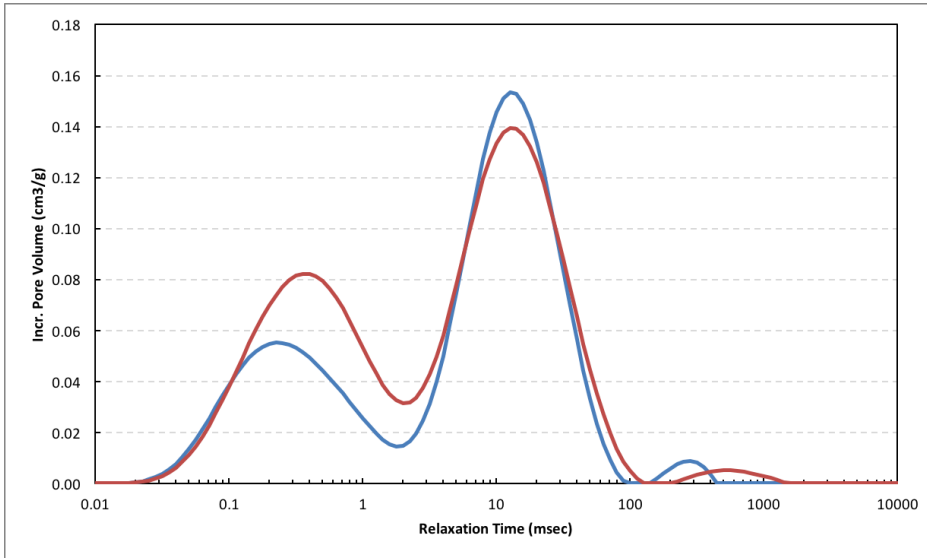
Figure 2. NMR T2 distributions of Pre (blue) and Post (red) water imbibition. The addition of water to the sample is shown by an increase in intensity of the fast component and concomitant decrease in the slower component.
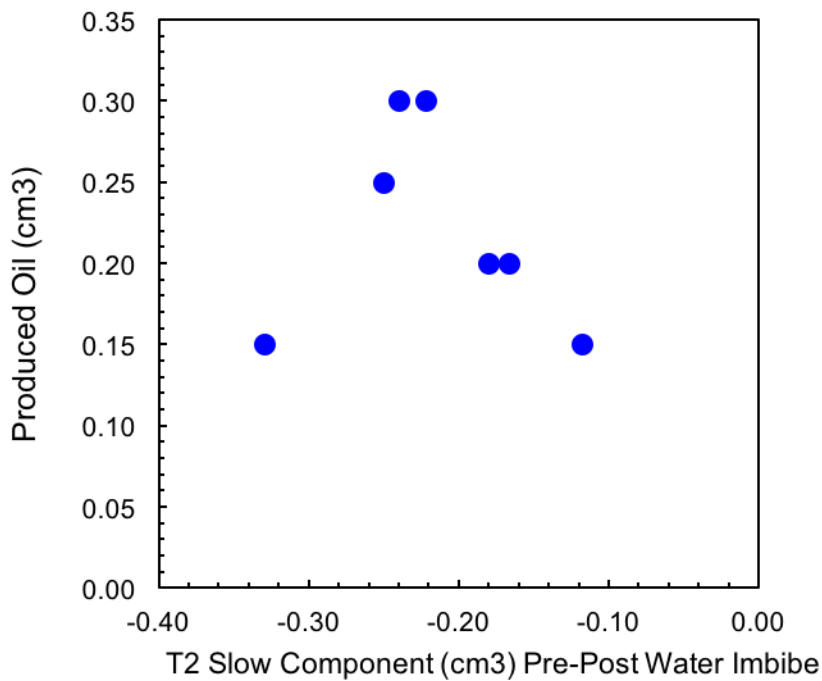
Figure 3. Produced oil volume from water imbibition test compared to the loss of intensity of the T2 distribution slow component after imbibition. There was one outlier from a -1:1 relationship that had a greater change in the NMR intensity than measured in the imbibition cell.
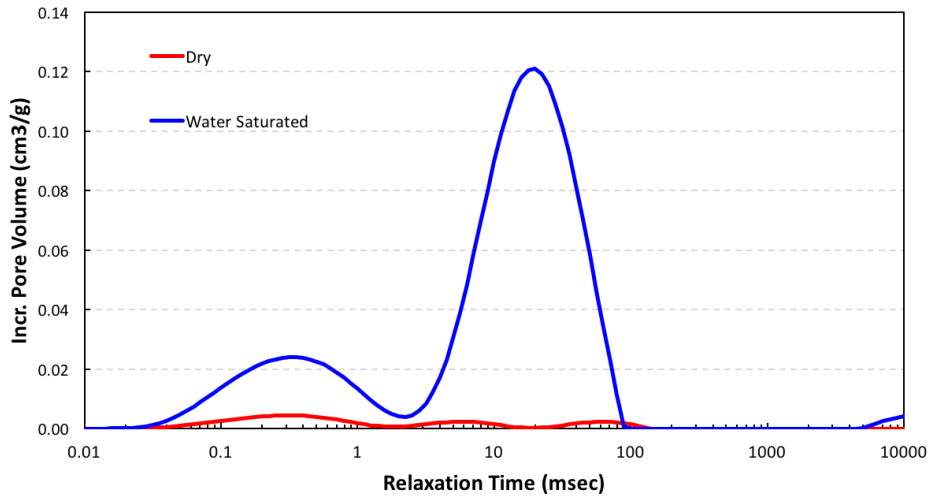
Figure 4. NMR T2 distribution of the dried sample (red) and after saturation with a brine. The dried sample retains a small fraction of liquid. 0.1 to 0.2 cm3). The bimodal distribution of the saturation sample indicates two distinct pore regimes.
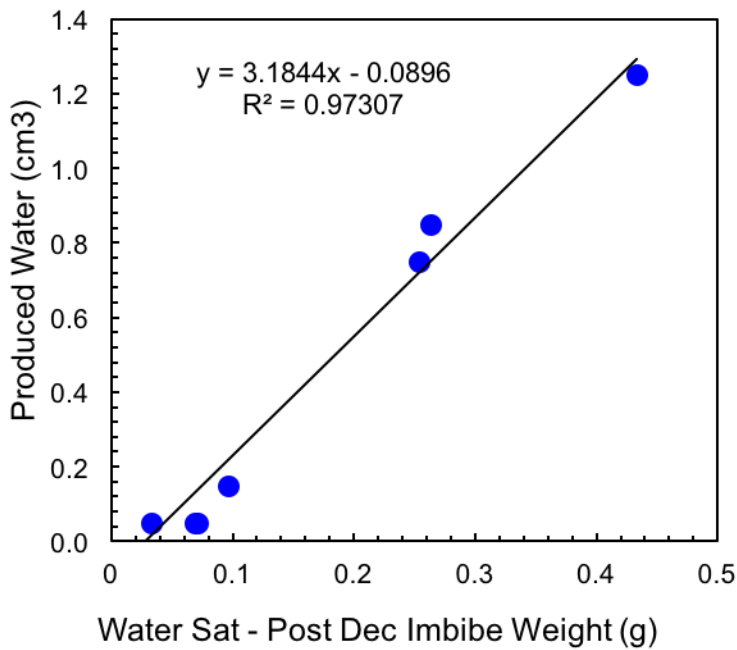
Figure 5. Correlation between the volume of produced water from oil imbibition test and the change in sample weight. While the correlation is positive, the mass balance is off significantly.
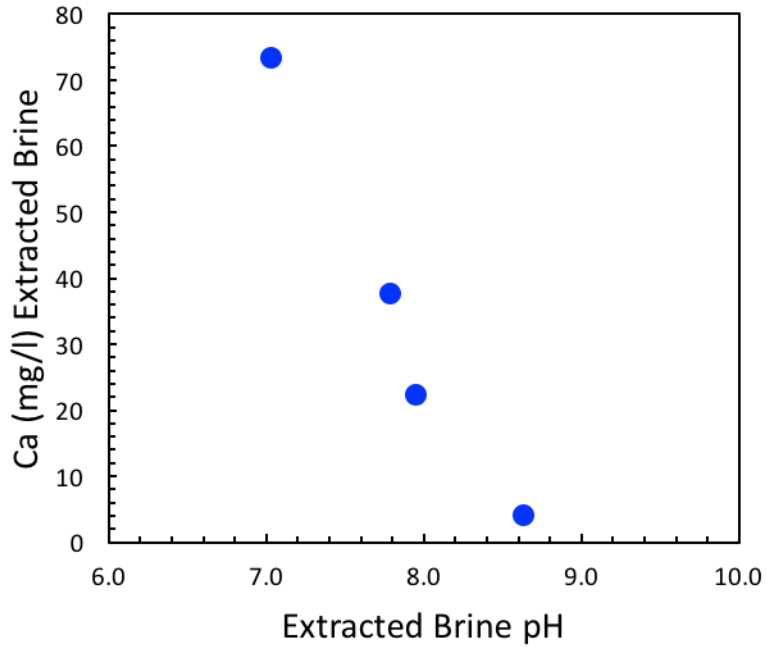
Figure 6. Changes in water chemistry after the water imbibition test. More Ca detected in solution generated by the dissolution of carbonate in the matrix test matches the lower pH.

INTEPRETATION OF NMR RESPONSE TO HYDROCARBONS: APPLICATION ON MISCIBLE EOR EXPERIMENTS

S. T. Dang, C. H. Sondergeld and C. S. Rai
Mewbourne School of Petroleum and Geological Engineering
University of Oklahoma

ABSTRACT

Estimation of total reserves in shale gas and shale oil reservoirs is challenging but critical. Different types of logging tools and core evaluation procedures are utilized in an attempt to address this challenge. NMR plays a vital role in understanding fluid content, rock-fluid interaction, and determination of pore body size distributions. Hydrocarbon (HC) hosting pore systems in shale include both organic and inorganic pores. Recoverable HCs include bitumen and light hydrocarbons. Their relative fractions are strongly dependent on thermal maturity. Regardless of detailed chemical characterization, 'bitumen' is simply defined based on mobility in this study. The apparent mobility of HCs depends on fluid composition, solubility and reservoir temperature. Historically, while verifying interpreted parameters from NMR logs (nominally 2MHz) through core measurements are done at room temperature ($25\text{-}35^{\circ}C$). This study highlights the importance of running NMR tests at reservoir temperature. Experiments were performed for both bulk fluids and fluids within rock samples.

The results show that at a particular temperature, NMR only responds to the fraction of HCs present in the liquid phase. For routine NMR measurement, at $31^{\circ}C$, only the relaxation signals of compounds more volatile than C17 are acquired. Thus, the C17+ fraction would be invisible to NMR at room temperature, but perhaps not at reservoir temperature. This is critical to interpret NMR log response within the early oil and condensate windows, in which C17+ can be a major fraction. Engineers can underestimate movable HCs using routine core data as a basis for interpretation.

Based on NMR experiments for several oil samples, we observed T1-T2 distribution depends on the overall composition of total HCs and effective mobility. The results also show that in case of both light and heavy HCs, which coexist in a single phase, T1-T2 distributions for these fractions are indistinguishable. NMR parameters were used to monitor the amount, composition and effective mobility of remaining HCs after each injection and discharging cycle, during miscible EOR huff and puff experiments on Eagle Ford samples.

INTRODUCTION

NMR has been proven as a useful tool to evaluate formation characteristics in both the field and the laboratory. Historically, the tool is utilized to estimate porosity, pore body size distribution, from which permeability is inferred (Coates et al. 1991[1]; Kenyon et al. 1988[2]). NMR signals, or magnetization vector are induced during the relaxation of a nuclear spin. In petroleum applications, scanning frequency is tuned to resonate with the Lamour's frequency of hydrogen at a specific magnetic field strength (Kleinberg and Jackson, 2001[3]). Hydrogen is found in water, hydrocarbons (oil and gas), bitumen, and macromolecular kerogen. NMR response to each of these components is different (Bryan et al., 2002[4] and Brown, 1961[5]) and should be evaluated. Moreover, the interaction between pore system and included fluids elevate the complication of interpreting the NMR response. **Fig.1** presents different pore systems, and included fluids which can possibly coexist in a rock formation.
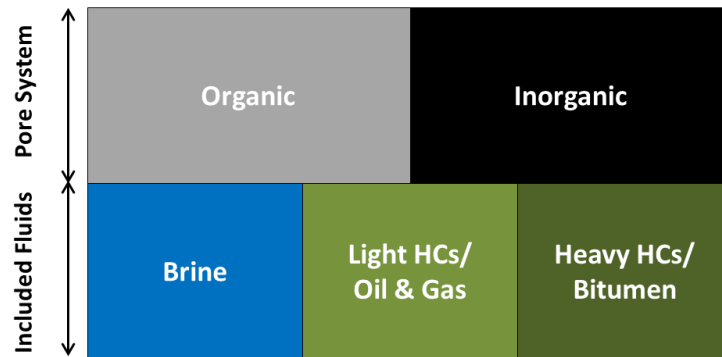
Fig. 1 General schema for different fluids and pore systems in shale. Shale is complicated by the coexistence of inorganic pores, which can be oil or water wet, and organic pores, which are generally assumed to be oil wet.

Unlike conventional rock, with a simple single inorganic pore system, with organic rich tight rocks, the interaction between fluids and void spaces are highlighted, from the pore size effect to the pore wettability effect (Yassin et al., 2016[6] and Deglint et al., 2016[7]). **Fig.2** show a fine scale SEM image of an Eagle Ford shale sample, in which pore spaces can be found among and within carbonate matrix, clay minerals, and organic matter.
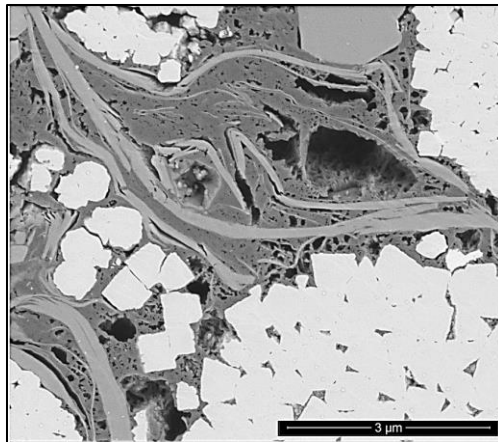
Fig. 2 Backscattered electron (SEM) image of an Eagle Ford shale sample. The image shows different pore systems, within inorganic matrix, within organic matter, or between them. The very bright features are pyrite. The darker masses are organic.

Understanding the NMR response of brine within rock sample is well established. Many previous studies, which use simple hydrocarbon components or mixtures, such as methane, dodecane (Odusina et al., 2011[8]), and isopar L (C11-C13) (Nicot et al., 2016[9]), were successful in demonstrate the presence of a dual-wettability system in organic rich shale. However, the interpretation of NMR data cannot be complete without the understanding the response from reservoir hydrocarbons (HC), which are a multi-component system. This study emphasizes the compositional and temperature effects upon the induced NMR signal from bulk HCs and HCs within the pores.

EXPERIMENTAL INSTRUMENT & SAMPLES

HCs samples used in this study include a set of pure n-alkanes, with a carbon chain length ranging from C6 to C20. The detailed density, melting point, and vaporization temperature of these alkanes are found in Nistchem (Nistchem webbook). According to **Table.1**, C17 is the highest n-alkane occurring in the liquid phase at 31°C. A set of synthetic samples was created from the distillation of a produced crude under inert condition. Crude, or Oil 1 was heated to elevated temperatures to generate Oils 2, 3, 4, 5, and 6 with successively increasing heavy fractions of HCs. Nitrogen was continuously flowed through the heated sample container during the distillation to prevent oxidation. **Table.2** shows the detailed distillation temperatures, and sample stages at room temperature.

An Agilent™ GC-FID-MS system was used to perform compositional analyses on the set of synthetic oils. The analyses provides the detailed concentration of alkanes within each oil sample. With the benchmark as 32.5 minutes or the retention time of C17, the fraction of C17- decreases from Oil 1 to Oil 6 (see **Fig. 3**). In other words, the mean molecular weight increased respectively, which results in the reduction of mobility.

Table. 1 Melting point, vaporization temperature and density of pure n-alkanes used in this study. Notice C17 is the highest alkane occurring in liquid phase at 31ºC

Alkane	C6	C7	C9	C10	C12	C16	C17	C20
Density, g/cc	0.66	0.68	0.72	0.73	0.75	0.77	0.78	0.79
Melting Point, ◦C	-95	-91	-54	-30	-10	18	21	37
Boiling Point, ◦C	69	98	151	174	216	287	302	343
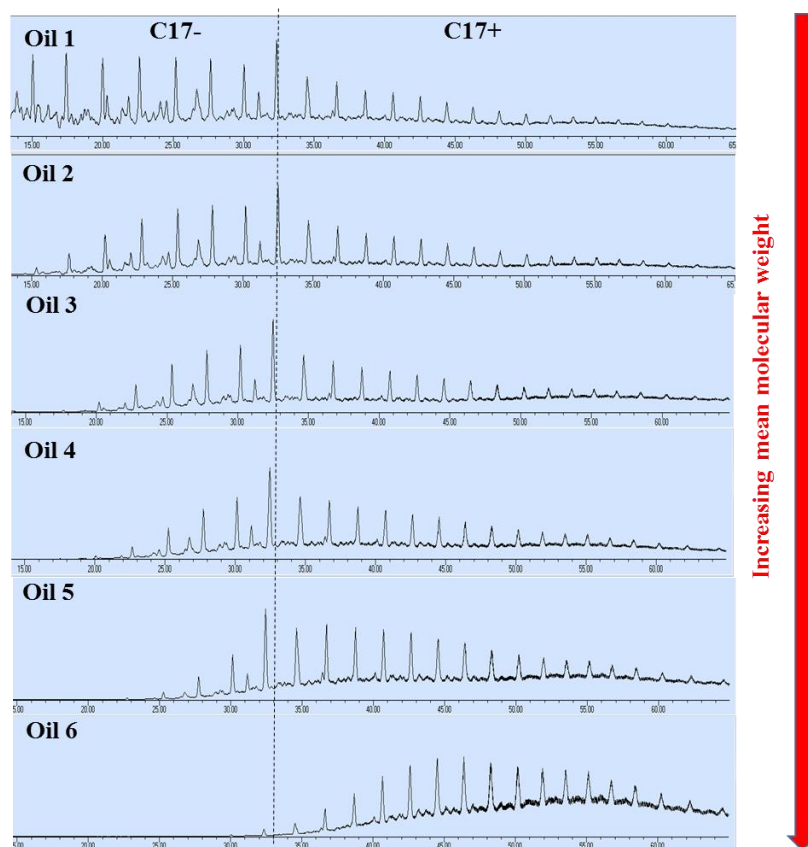
Fig. 3 Compositional analysis, GC-FID spectra for Oil 1, 2, 3, 4, 5, 6 with retention times range from 15 to 65 minutes. With the increasing of heavy HCs fraction (C17+) corresponding to the systematic decreasing of oil mobility. C17 alkane appears at 32.5 minute (dash line).

Table. 2 The set of synthetic oils generated from a produced crude through heating to different temperatures. At room temperature, Oil 1 and 2 occur in the liquid phase; Oil 3 appears as wax (semi-solid); and Oil 4, 5, 6 appears as solid.

Oil ID	Crude/1	2	3	4	5	6
Distillation T, ◦C		100	150	200	250	300
Phase	liquid	liquid	wax	solid	solid	solid

Source Rock Analysis (SRA) or Rock-Eval® is an anhydrous pyrolysis technique, utilized to estimate parameters relating to source rock maturity and productivity level. It is also applied to measure producible HCs, from the FID response to HC components evaporated at temperature less than 300ºC, i.e., the S1 peak in a pyrogram. According to **Table.1**, the producible HC measured from SRA correlated to C17- fraction. Figure.4 shows the FID pyrograms for Oil 1, 2, and 5. Respectively, S1, or C17- fraction reduces relative to C17+ fraction.
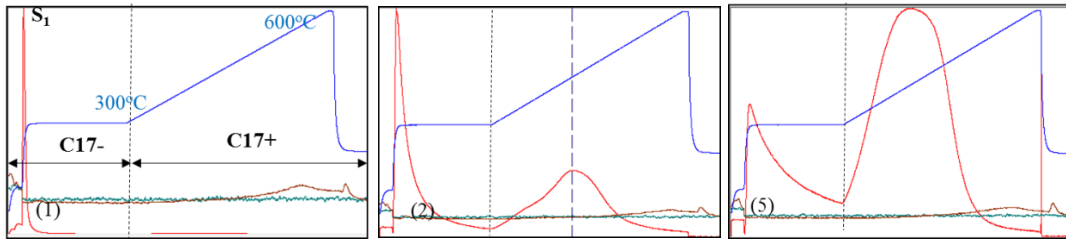
Fig. 4 (Left to right) FID pyrograms of Oil 1, 2 and 5 (red lines.) S1 or C17- fraction includes HC components, which vaporize at temperatures (blue lines) less than 300ºC. S1 or C17- reduces systematically from Oil 1 to Oil 6.

NMR spectra were acquired using two benchtop GeoSpec Oxford™ instruments with operating frequencies of 2 MHz and 12 MHz. The temperature for each instrument was set 31ºC. We performed T2 relaxation and T1-T2 map measurements with an echo spacing of 114 µs. This optimum echo spacing was chosen to capture fast relaxation components from shale samples, while prevent the interference of the fluorine signal from internal machine parts made of Teflon. **Fig.5** demonstrates the difference in acquired NMR signal as a function of echo spacing. The selection of echo spacing is extremely important while running NMR on oil prone shales, which include fast relaxation components, such as low mobility fluids or fluids in small pores (ref.)
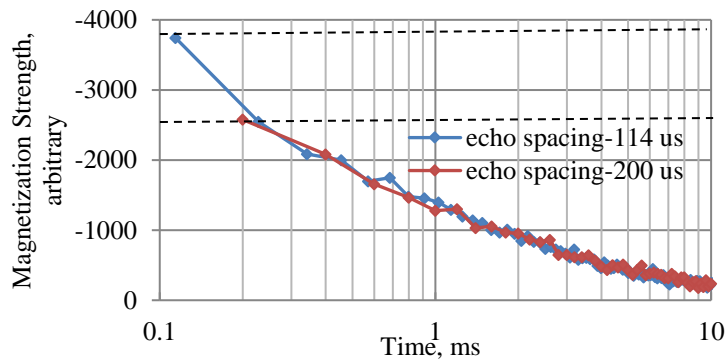

Fig. 5 NMR data recorded on a highly viscous fluid. With smaller echo spacing, acquired signal is lower, due to the capture of signals from fast relaxation component. The total signal increase 30% in this fluid sample with echo spacing of 114µs.

RESULTS

Simple T2 relaxation spectra were acquired for six bulk pure n-alkanes (**Fig. 6**). The data attained by using 12 MHz NMR system, with echo spacing of 114 µs and temperature of 31ºC. The calculated log mean T2 values has a negative correlation with the length of carbon chain. This is due to the viscosity of the fluid that restricts the rotational diffusion, which makes the nuclear spin relax faster (Bloembergen, 1961[10]). However, there is no NMR signal acquired for C17 higher alkanes, which appear as solid phase at these testing conditions.

To confirm the temperature effect on NMR response of HCs, an experiment was performed on C17 alkane. First, bulk C17 was solid frozen at 4ºC; then it was brought into testing condition of 31ºC and NMR was continuously measured as the sample warmed.   As the results of partial melting of the bulk fluid, the total amplitude increases while the $T2_{log\ mean}$ shifts to the right (**Fig.7**.) This response indicates that temperature governs which component in a HC mixture yields a measureable NMR signal. For example, when NMR measurement was obtained on an alkane mixture at 31ºC, only alkanes lower C17 response to the magnetization. On the other hand, temperature affects the liquid-solid interaction happening on the surface of the grain, which contribute to the overall relaxation rate of fluids inside pore spaces (Godefroy et al., 2001[11]). However, the focus of this study is to identify HCs components responding to NMR at a particular temperature.
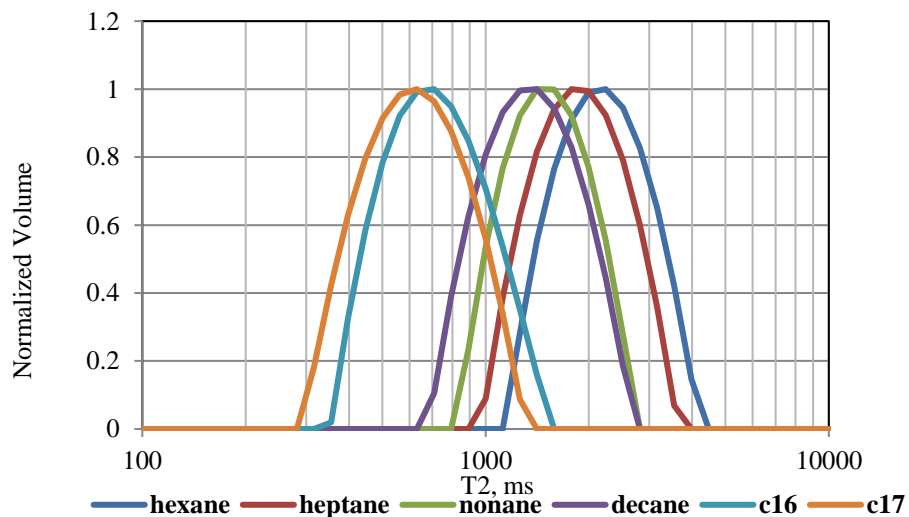

Fig. 6 T2 distribution for different pure n-alkanes. The curves shift to the left for higher n-alkanes. $T2_{log\ mean}$ and its inverse relation with carbon length. There is no NMR response for higher C17 n-alkanes at temperature of 31ºC.
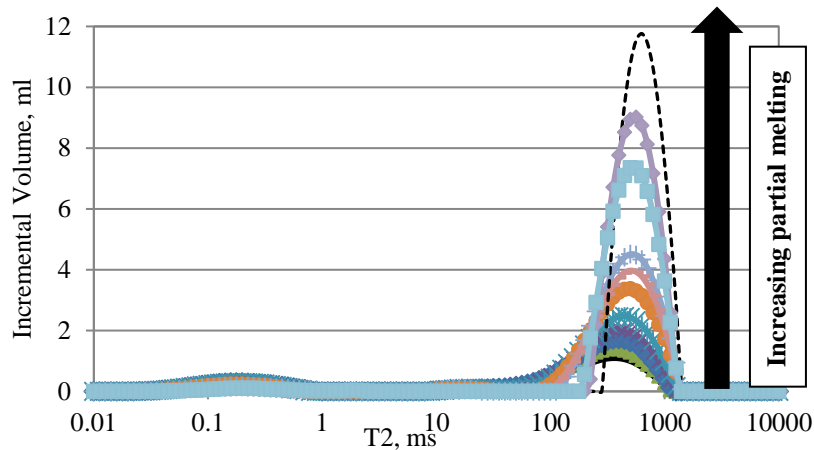
Fig. 7 Continuous NMR response for bulk C17 alkane undergoing warming and increasing partial melting. Cumulative response increases until complete melting at 31°C (black dash line.)

NMR T1 and T2 measurements were also obtained for the set of synthetic oils, using both 2 MHz and 12 MHz instruments at 31°C. As the above results suggested, NMR response for this set of oils– Oil 1 to Oil 6– correlates well with SRA-S1 amplitude, which is sensitive to C17- or light HC fraction. The S1 signal from SRA is reported in mg/g of total HCs. Using compositional analysis for each oil samples, Hydrogen Index and mean density were estimated. These parameters are subsequently applied to convert NMR volumetric amplitudes to mg/g of total HCs. **Fig.8** shows good agreement between S1 and NMR response for the set of synthetic oils as well as HCs in some Eagle Ford shale samples.
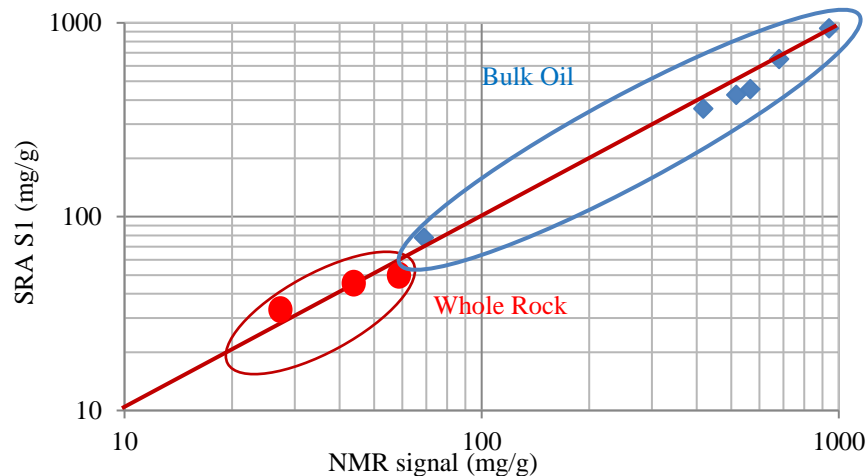

Fig. 8 The agreement between S1, characterize for the mass of light HCs/ C17-, and NMR amplitude under the experimental temperature of 31°C.

The results suggest that at reservoir conditions, different fractions of the total HCs can be detected by NMR tools due to the tool configurations and echo times; additionally, due to

the combination fluid composition and temperature. At a specific NMR configuration, total HCs from a rock sample can be underestimated, especially with a source rock in the oil window.

Although at a specific temperature, NMR amplitude only responds to a certain HC fraction, NMR parameters, such as T1 and T2 distribution are functions of overall fluid composition. **Fig.9** shows T1-T2 maps at 12 MHz for samples Oil 1, 3, 4, and 6. With increasing viscosity or higher mean molecular weight, the signals move further from 1:1 line. **Fig.10** shows the positive relationship between T1/T2 and fluid viscosity. The separation between T1 and T2 is more pronounced in the higher frequency NMR measurement. Previous studies (Nicot et al., 2007[12]; Lo, 2000[13]) suggest using this ratio as an index for fluid mobility. With 12 MHz instrument, the clear separation between T1 and T2 can only be observed in Oil 3, 4, 5, and 6, which appear from the wax to solid form. Korb (2015)[14] presents experimental data reported in the literature (Latorraca et al., 1998[15] and Zhang, 2002[16]), which confirms the observation, that low frequency NMR is limited in differentiating the mobility of fluids. For 2 MHz measurements, the true split between T1 and T2 curves can only be observed with viscosities larger than 1000cP. However, higher operating frequency can help to estimate fluid mobility.
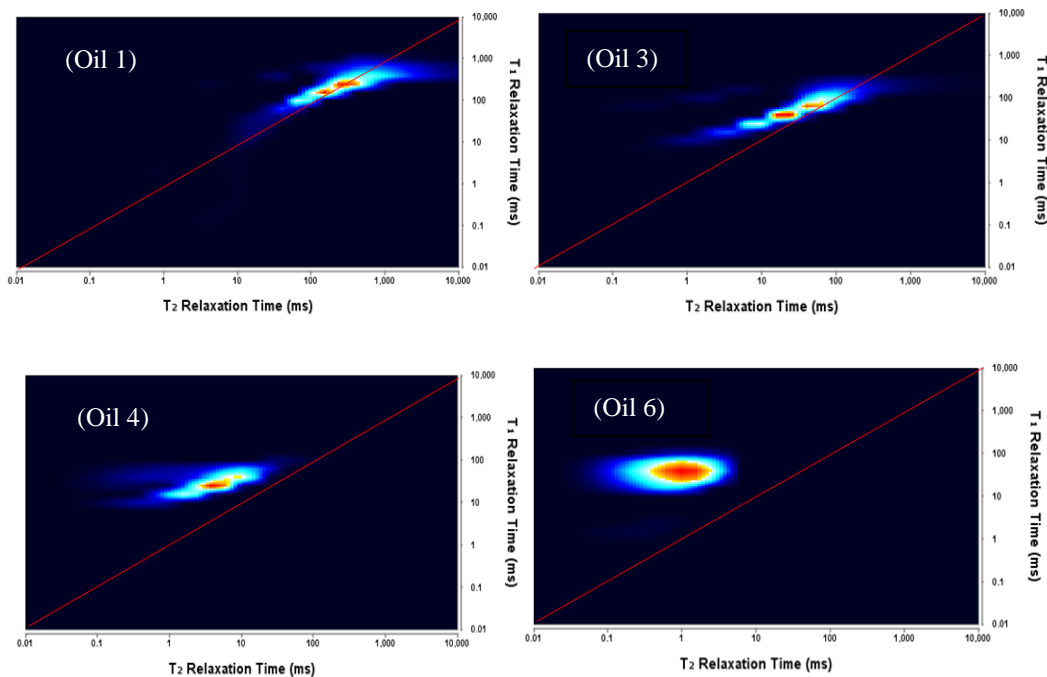

Fig. 9 T1-T2 maps at 12 MHz for Oil 1, 3, 4 and 6. In all images, the red line represents 1:1 correlation between T1 and T2. The more viscous fluids show more separation between T1 and T2. Although the amplitude corresponds to C17- fraction, the distribution depends on the overall composition of a fluid.
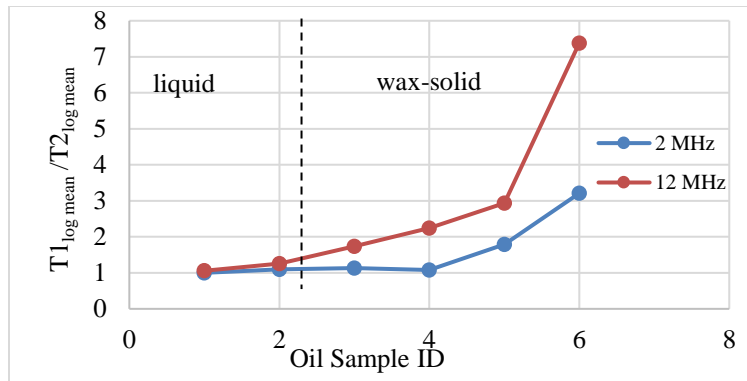
Fig. 10 T1/T2 ratio for the set of synthetic oils. The separation between T1 and T2 is more visible for the more viscous oil, and the split is more pronounced for the higher NMR operating frequency.

CASE STUDY APPLICATION

With the low price of produced crude oil and gas, economic success in newly drilled wells requires reducing cost and risk. Enhanced oil recovery is considered economically attractive for increase crude output at a marginal cost. Miscible gas injection, such as huff and puff, is the most feasible EOR method for unconventional tight reservoirs. Some preliminary field tests suggested the process could help to improve the recovery by up to 30%. The success of the project partially depends on the detection and monitoring reservoir fluid quality and quantity after each injection cycle. With an attempt to capture the change in remaining HCs through huff-and-puff, carried out a laboratory experiment to measure the NMR response from an Eagle Ford shale sample after each cycle of CO_2 injection; injection pressure was 3500 psi at a temperature of 170°F. The injection and production scheme is summarized in **Figure 11.**
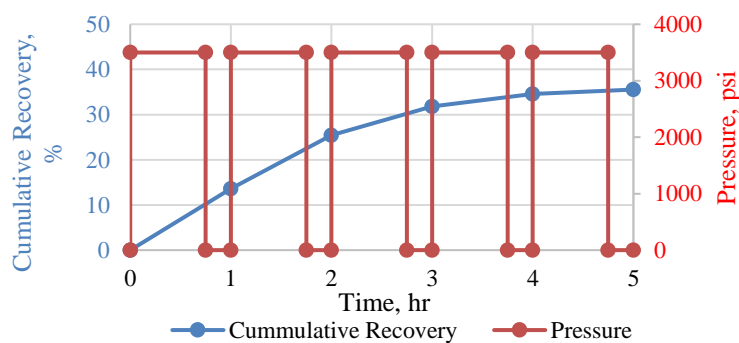

Fig. 11 Huff and puff scheme for miscible gas injection experiment for an Eagle Ford sample. Injection pressure is 3500 psi at 170°F. Blue line represents the cumulative recovery with maximum recovery of 35%.

After each cycle, a fraction of light HCs is recovered along with the solvent gas. The T2 response helps to quantify the amount of HC that has been released after each cycle

(**Fig.12**), while the remaining fraction within the rock sample becomes heavier. T1-T2 maps provide evidence for our conclusion. In **Fig.13**, after each cycle, we observe the increasing of water signal (close to 1:1) relative to HC signal. HC signal also shifts to smaller T2, and T2 separates further from T1.
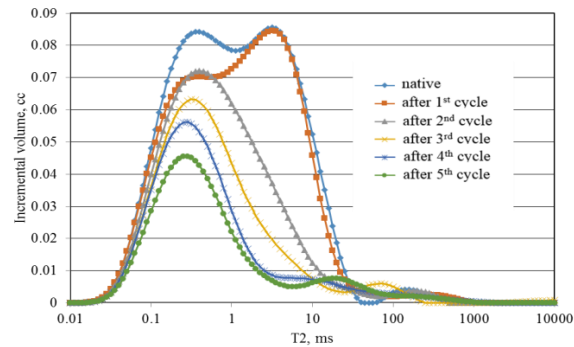

Fig. 12 T2 distribution for the remaining fluids in the rock sample after each huff-and-puff cycle. We observe the reduction in T2 amplitude due to the recovery of light HCs from the bulk rock. Note T2$_{log\ mean}$ shifts to the left.
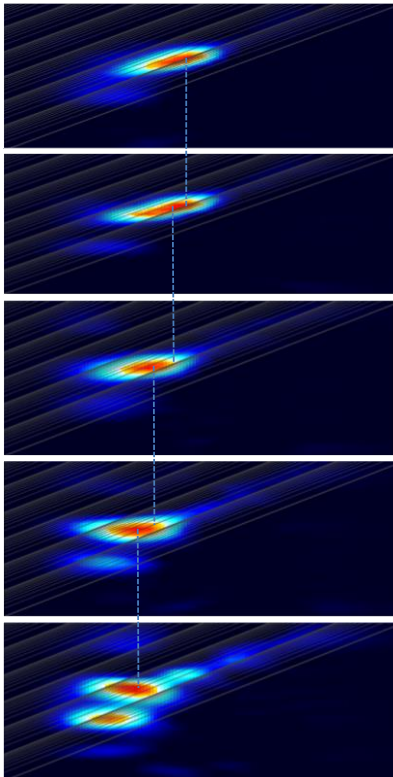

Fig. 13 T1-T2 distributions for the fluids remaining inside the rock sample after each huff-and-puff cycle. Y-axis represents T1, while x-axis represents T2; both are in scale of 0.01-10000ms. We observe the reduction in overall amplitude due to the recovery of light HCs from sample, which results in the highlight of water signal (close to 1:1). HCs signal moves further to the left. Note the color scale in each spectrum had been auto scaled.

With conventional core flooding experiment, the amount of collected fluid after each cycle is used to compute the recovery. However, with EOR experiments on tight rocks, this quantitation becomes unreliable due to the limitation of pore volume. Therefore, we propose the workflow, in which collected fluids are analyzed to understand extracted composition, while the recovery is calculated using the NMR parameters measured from the remaining HCs fraction in rock samples. With the removal of water signal (close to 1:1 line) from T1-T2 spectra, the recovery for 5 cycles of huff and puff done on an Eagle Ford sample, are plotted in **Fig.14.** Note the experiment was conducted on crushed samples with sample size from 6-8mm. Future experiments with core flooding with live monitoring using high pressure and high temperature NMR sample cell are planned.
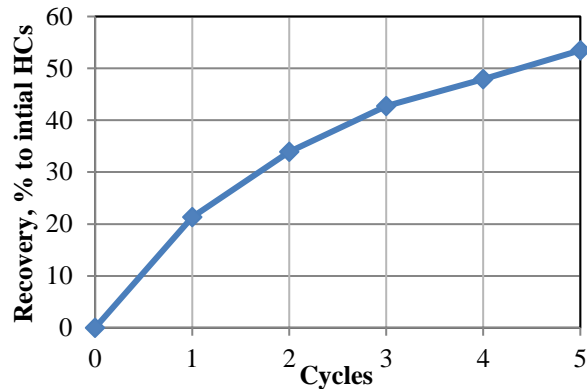

Fig. 14 HCs recovery after each cycle of huff and puff with CO_2. The total recovery is 52%. Note the experiment was performed on crushed samples with sample size from 6-8mm.

CONCLUSIONS

With the coexistence of HC gases, oil, bitumen, and macromolecular kerogen within a shale rock, the interpretation of NMR response has become more complicated. This study highlights the dependence of NMR response on operating configuration, HC composition and reservoir temperature. This is critical when laboratory measures are used to verify NMR log inferred parameters.

NMR only responds to the fraction of HCs present in the liquid phase. For routine NMR measurements, with temperature ranging from 25-35°C, only the relaxation signals of compounds more volatile than C17 are acquired; whereas, at the reservoir condition, relaxation signals of heavier HCs fraction can also be detected.

Although at a specific temperature, NMR amplitude only responds to a certain HC fraction, NMR parameters are functions of overall fluid composition, and NMR operating frequency. The separation between T1 and T2 is more recognizable when the apparent mobility of HC mixture decreases. Moreover, this effect is more pronounced at higher NMR frequency. From this study and literature, for NMR tool with frequency lower than 2 MHz, T1/T2 can only be used as a viscosity index when viscosity is greater than 1000 cP.

REFERENCES

1. Coates, G. R., R. C. A.Peveraro, A. Hardwick. A. and D. Roberts, 1991, The magnetic resonance imaging log characterized by comparison with petrophysical properties and laboratory core data: Paper   12723, Society of Petroleum Engneers 66th Annual Technical Conference and Exhibition, (1991)

2. Kenyon, W. E., P. I. Day, C. Straley and J. F. Willemsen, A three-part study of NMRlongitudinal relaxation properties of water-saturated sandstones: *SPE Formation Evaluation*, (1988), v. 3, n. 3, 622-636.

3. Kleinberg, R. L., and J. A. Jackson, J. A, An introduction to the history of NMR well logging, (2001)

4. Bryan, J., F. Manalo, Y. Wen, and A. Kantzas, Advances in heavy oil and water property measurements using low field nuclear magnetic resonance. Society of Petroleum Engineers, (2002)

5. Brown, R. J. S., Proton relaxation in oils. *Nature*, (1961) 189, p. 387-388

6. Yassin, M. R., H. Dehghanpour, J. Wood and Q. Lan, A Theory for Relative Permeability of Unconventional Rocks With Dual-Wettability Pore Network, (2016)

7. Deglint, H. J., C. DeBuhr, C. R. Clarkson, F. F. Krause, S. Aquino, A. Vahedian and A. Ghanizadeh, Understanding Wettability Heterogeneity at the Micro and Nano Scale in Unconventional Light Oil Reservoirs. Unconventional Resources Technology Conference, (2016)

8. Odusina, E., C. H. Sondergeld, and C. S. Rai, An NMR study on shale wettability. Canadian Unconventional Resources Conference, (2011) SPE 14737

9. Nicot, B., N. Vorapalawut, B. Rousseau, L. F. Madariaga, G. Hamon and J. P. Korb, Estimating Saturations in Organic Shales Using 2D NMR. Society of Petrophysicists and Well-Log Analysts, (2016)

10. Bloembergen, N., 1961, Nuclear magnetic Relaxation.

11. Godefroy, S., M. Fleury, F. Deflandre and J. P. Korb, Temperature effect on NMR surface relaxation. SPE ATCE, (2001), SPE 71700

12. Nicot, B., M. Fleurry and J. Leblond, Improvement of viscosity prediction using NMR relaxation, 48th SPWLA symposium, (2007)

13. Lo, S. W, Correlation of NMR relaxation time with viscosity/ temperature, diffusion coefficient and gas/oil ratio of methane-hydrocarbon mixture. Doctoral Thesis, (2000) Rice University

14. Korb, J. P., N. Vorapalawut, B. Nicot, and R. G. Bryant, Relation and correlation between NMR relaxation times, diffusion coefficients, and viscosity of heavy crude oils. *Journal of physical chemistry*, (2015)

15. LaTorraca, G. A., K. J. Dunn, P. R. Webber and R. M. Carlson, Low-field NMR determinations of the properties of heavy oils and water-in-oil emulsions. *Magnetic resonance imaging,* (1998), 16, p. 659-662

16. Zhang, Y., NMR relaxation and diffusion characterization of hydrocarbon gases and liquids. Doctoral Thesis, Rice University, (2002)

APPLICATION OF AN OPTIMISATION METHOD FOR THE RESTORATION OF CORE SAMPLES FOR SCAL EXPERIMENTS – Part II

Edison Sripal, L.A. James
Memorial University of Newfoundland

ABSTRACT

The restoration of wettability in reservoir rock core samples to its original state is highly critical in preliminary core preparation for SCAL experiments. Conventional core restoration methods to either strongly or weakly oil-wet are largely influenced by increasing or decreasing the aging time at reservoir temperature. There is a lack of consistent or reliable methods to restore core to its original state which is normally obtained from preserved core samples. This paper is a continuation of the work that was presented in SCA2016-002 where we examined the optimum level of three important parameters, brine salinity, restoration temperature, and restoration time (age in number of days) for restoring wettability. In this paper, we extend the Box Behnken model of surface response methodology to analyze wettability determined via three methods: contact angle, Amott-USBM, and via a new method using SEM-MLA over extended ranges of brine salinity (10,000, 100,000 and 200,000 ppm total dissolved salts), temperature (60, 90 and 120°C), and age of conditioning (2, 4 and 8 weeks). The samples for this study included 15 Berea sandstone and Silurian dolomite samples aged in crude oil and brine of varying salinity. The samples for this work underwent extended aging time to overcome the shortcoming in the previous work which again was carried out using coreholders under confining pressure. The wettability was experimentally validated using contact angle measurements, Amott-USBM tests, and a novel SEM-MLA imaging (at low vacuum conditions). A seminal effort in applying SEM-MLA image analysis for wettability determination was also explored. Linear regression models were developed and the adequacy of predicting the output variables (wettability) to nearly all conditions were verified. The study showed a comprehensive influence of brine salinity, aging time, and temperature towards wettability restoration. Further 2-D and 3-D surface plots were generated to show the interaction between the three independent variables in establishing a wettability value.

INTRODUCTION

Specialised Core Analysis (SCAL) data, specifically capillary pressure (P_c) and relative permeability (K_r) are important for reservoir characterization, production optimization and simulation. In this study, we developed an optimization methodology to restore wettability in core samples for SCAL experiments as laboratory experiments are routinely performed

on core samples from restored state [4]. In practice, aging strategies vary between organizations and there is no one commonly accepted restoration process. In this paper, we try to determine the optimal value of the three parameters that are generally agreed upon as contributing to the aging process [2, 15]: brine salinity, aging time, and aging temperature for a given rock mineralogy and oil composition. While it is understood that mineralogic composition of the reservoir rock and oil composition (polar components, asphaltenes) play a significant role in wettability alteration and aging, the interest of this study is to establish optimal aging time for a given reservoir rock and oil. Our interest is to determine the optimal aging conditions using Hibernia light crude oil (35°API) with an asphaltene content of < 1% for aging the core samples. The crude oil composition is presented in Table 6. A Berea core sample with 80% quartz content and less than 2% clay content was used for this study. Although wettability is largely influenced by rock minerology and crude oil composition, the restoration process is impacted by the aging time, temperature and brine salinity.

Aging time and temperature are generally accepted to be the two most important factors contributing to the aging process. Anderson (1986) indicated that 1,000 hours (40 days) of aging at reservoir temperature is sufficient for wettability equilibrium. Additionally, during the aging process, it is important to saturate the core with brine prior to oil to ensure the wettability effects due to brine chemistry are not ignored. Numerous studies [5, 13] have demonstrated the effect of increased brine salinity on oil wet characteristics exhibited in Berea sandstone.

Wettability is generally quantified by contact angle measurements or by USBM method or both. For a reservoir rock to be deemed oil-wet, the contact angle in an oil-brine-rock system should be $> 105°$ (Anderson 1986) or wettability index to be -1. USBM wettability index is calculated from the drainage and imbibition capillary pressure curves and Robin (2001) demonstrated a qualitative differentiation between oil-wet to water-wet capillary pressure curves. Lately, USBM wettability methods are increasingly applied on understanding the wettability nature of shale formations in unconventional oil productions [3, 6, 8]. In addition to the above two methods, digital imaging methods like SEM analysis are increasingly applied for wettability characterization. CRYO SEM and ESEM methods [7, 9, 10, 11] were initially used to analyse wettability in rocks and packed glass beads that were saturated with reservoir fluids. But these analyses were not accurate as it often compromised the sample integrity due to extreme changes in the physical state because of cooling and polishing. In a seminal method, we have applied SEM-MLA method by testing the sample without any changes in its physical state.

This paper is a continuation of the work that was presented in SCA 2016 [12]. We have extended the range of three input parameters that influence wettability to address the gaps that were identified in the past work [12]. Additionally, we have extended the model to include three response factors instead of one for determining wettability, they include contact angle measurement, USBM wettability index and organic content from SEM-MLA analysis.

EXPERIMENTAL METHODOLOGY

For this study we have chosen statistical design of experiments (DOE) as it provides an understanding of the parametric effects controlling a process with the benefit of a decrease in the number of experiments required. Box Behnken response surface methodology was applied to optimise the input parameters i.e., aging time, temperature and brine salinity for the desired output parameter that is wettability. Box Behnken requires only 15 trials for a three factor experiment and providing maximum efficiency for a surface model. In the previous work, the model was tested using one response factor i.e. wettability using contact angle. In this study, we have extended the model to include three response factors: contact angle measurement, USBM wettability index method and organic content (%) from SEM-MLA analysis.   Table 2 summarises the experimental plan and the real values for input parameters. Trials at optimal levels were duplicated twice to ensure repeatability. Design Expert ® software was used for the DOE, response surface model analysis, and input parameters optimisation.

A wider range of brine salinities from 10,000 to 200,000 ppm were used for this work which was markedly different from 60,000 to 120,000 ppm that was used in the previous study [12]. The composition of brine includes some divalent calcium and magnesium ions and the complete composition is presented in Table 1. The aging period was increased from 6 weeks to 8 weeks with the maximum aging temperature changed from 90 to 120°C. Hibernia (offshore Newfoundland) dead crude oil with 5.9 cP viscosity and 878 kg/m^3 density was used for saturation. The oil was filtered and degassed by vacuuming it for 48 hours to prevent any gas production during the drainage. During the aging process the core samples were circulated with few pore volumes of oil on a weekly basis. Berea Sandstone used for this work came from Cleveland Quarries with porosity in the range of 18 - 20% and gas permeability ~ 150 mD.

The core samples for testing were initially cut to 6.3 cm length with two 5 mm sections cut from the top and bottom of the core. The idea was to use the core sample for capillary pressure measurement (USBM wettability measurement) and the thin section being used for contact angle measurement and SEM-MLA analysis. The samples were then sonicated twice for 20 minutes each for a total of 40 minutes and dried in an oven for 24 hours before being saturated with the representative brine as outlined in the experimental plan.

In the first stage of experiment, the core samples were brought to connate water condition and oil saturation. The brine saturated samples (core + thin section) were loaded in to a core holder at overburden pressure of 3000 psi and centrifuged in drainage mode. A Rotosilenta 630RS refrigerated centrifuge from Vinci Technologies was used for this purpose. The drainage test with oil displacing brine was carried out in 7 centrifugation steps starting from 500 rpm to a maximum of 3,500 rpm with 3 hours of equilibration time per rpm step.

After centrifuging, the core holders were disassembled to inspect the oil saturation in the core samples. The samples were again loaded in the core holder and the overburden

pressure was adjusted prior to placing them in the oven for aging. Once the aging was completed, the top (thin) section of the core sample was loaded in a Vinci IFT 700 instrument to measure the contact angle by sessile drop method using brine as the drop fluid. The measured contact angles for the aged Berea Sandstone are listed in Table 2. Figure 1 shows representative contact angles for the brine sessile drop in the presence of air for some of the rock samples.

In the second stage, the bottom (thin) section of the aged core sample was utilised for SEM-MLA analysis. FEI Quanta 650 FEG scanning electron microscope, equipped with Bruker high throughput energy dispersive x-ray (EDX) system and backscattered electron detectors was used for this purpose. Imaging on the flat sample surfaces was carried out at very low vacuum conditions (0.6 Torr) to prevent evaporation of fluids [7]. Additionally, the samples were not subject to any metallic or carbon coating on the surface, except for liquid graphite coating on the sample holder. Instrument conditions and parameters include a high voltage of 25 kV, spot size of 5.75, working distance of 13.5 mm, 10 nA beam current, 16 µs BSE dwell time, 10 pixel minimum size (400 pixel frame resolution for 1mm HFW), and 12 ms spectrum dwell for EDX. Each of these MLA acquisitions was completed using version 3.1.4.683 MLA™ software and took between 3-4 hours per sample. Minerals and fluids in the core sample were calculated through a custom classification script that accounted for porosity and minerals. The results for individual samples were acquired as digital map of the minerals and a data table listing their mineral composition. Figure 3 is an example of mineral map and BSEM image of a sample aged for 4 weeks at 90°C. Wettability assessment was based on the organic (oil) content of the sample in direct comparison to brine and mineral composition prior to saturation. Values are in Table 2.

After the primary drainage test was completed, the imbibition step was started to force brine into the aged core sample to displace oil. The core samples were loaded in the core holder (in imbibition mode) with overburden pressure of 3000 psi. The receiving tubes were filled with the representative brine for each sample and the samples were centrifuged from 500 to 3500 rpm in seven 3-hour steps. At the end of the imbibition test, the secondary drainage step was carried out by forcing oil through the brine saturated samples. The secondary drainage process was also carried out in seven steps. The secondary drainage data and the imbibition data were analysed and the area under each curve was calculated. Figure 2 is the capillary pressure curves generated for samples saturated with oil at different brine concentration (secondary drainage) and displacement of oil under different brine concentrations (imbibition). The USBM wettability index was calculated based on the area under the curve for both secondary drainage (A_1) and imbibition (A_2) using the formula $W = \log (A_1/A_2)$. Typically, the wettability index ranges from > 0 for water wet to <0 for oil wet and 0 for neutrally wet. In comparison with the contact angle measurement, the USBM method provides a macroscopic average of the core plugs used in this study [8]. The wettability index calculated for the 15 samples are listed in Table 2.

RESULTS AND DISCUSSION

Box Behnken response surface methodology, with three factors and three responses, was chosen to investigate and optimise the core restoration (wettability) process. The experimental results are shown in Table 2 and Design Expert ® Software was used for statistical analysis. The optimal aging conditions were predicted using a first order polynomial model which was fitted to correlated relationships between brine salinity, aging temperature and time (input variables) and contact angle, wettability index and organic content i.e., oil content (responses). The experimental data was analysed by multiple regression analysis through least squares method. Analysis of Variance (ANOVA) was applied to compute regression coefficients of the linear and higher order (quadratic and polynomial) models with interaction effects. Statistical validation of the model was done using F-test where a "fitted" model is deemed significant if the probability level is low, i.e. p-value $\leq$ 0.05. The regression model was used to develop the response surface plots in order to visualise the relationship between the three input variables and responses. Finally, the developed models were used to suggest optimal conditions for aging. The experimental sequence was randomized in order to minimise bias and variability in measurements.

The results of the analysis of variance (ANOVA) tests were carried out individually for the three response factors i.e. contact angle, USBM wettability index and organic content from SEM-MLA and are presented in Tables 3, 4 and 5, respectively. For the contact angle measurement and organic content using SEM-MLA, the ANOVA test indicated only the quadratic model to be significant over other models. This is evidenced by the overall model p-values of 0.0464 and 0.0095, respectively. The resultant quadratic equations for the model developed using contact angle is presented in Equation 1. Aging time was the only significant parameter affecting wettability. Brine salinity and temperature were found to influence wettability only when they were considered with aging time, but independently they were found to be inadequate in influencing contact angle measurement. In comparison with the linear model developed in our previous study [12], the model equation is different but it is still in close agreement with aging time and its contribution to the aging process.

$$Contact\ Angle = +65.12 - 3.62{\times}10^{-4}\,[Salinity\ (ppm)] + 0.59[Temp\ (\text{℃})] +$$
$$13.38[Age\ (Weeks)] + 0.031[Temp\ x\ Age] - 1.843[Age^2] \qquad \textbf{(1)}$$

In the case of the USBM wettability index, a linear model was found to be best suited for predicting the experimental outcome which is confirmed from very low p-value of < 0.0001. Among the three parameters, aging time was found to have the highest F value thereby significantly influencing the restoration process. The linear model equation using USBM wettability index (USBM WI) is shown in Equation 2.

$$USBM\ WI = \ 0.782 - 1.9{\times}10^{-6}[Salinity\ (ppm)] + 3.02[Temp\ (\text{℃})] - 0.179[Age] \qquad \textbf{(2)}$$

In order to evaluate the significance of each input parameter on the outcome wettability measurement, F-tests were conducted on the three models. In the model based on contact angle measurement, aging time had higher F-values compared to temperature and salinity. Whereas in the model considering wettability by SEM-MLA, temperature and salinity had

higher F-values respectively. For the model developed based on wettability index, aging time was the significant factor contributing to the restoration process. Additionally, p-values for input parameters in all three cases were calculated to be less than the model F-value which is an indication that the statistical models are statistically significant. A diagnostic test was carried out to compare the experimental data with the model predicted results. Figure 4 shows a plot of experimental versus predicted values for both contact angle and USBM wettability index. Both analyses showed strong agreement between the experiment and model data as observed through most data points lying close to or on the diagonal line. A similar trend with predicted and actual values was observed in the organic content using SEM-MLA, but the results are withheld as we are progressing with further analysis.

From the developed statistical model we were able to produce 3-D response surface plots and 2-D contour plots for the three input parameters (aging time, temperature and salinity) against contact angle. Figure 5 represents the contour plot and 3-D RSM. The 2-D and 3-D plots provide an understanding of the interaction between two input parameters (e.g. age and salinity), while keeping the third parameter constant (temperature). The time of aging was found to be the most significant factor in impacting the aging process as observed through contact angle measurement. As the aging period was extended from 2 weeks to 8 weeks, the contact angle increased indicating a shift from intermediate oil-wet to strongly oil-wet characteristics. A similar trend was reported by Morrow (2000) and Anderson (1986) where strong oil wet characteristics was observed when aging time was extended to more than 40 days. Increasing temperature resulted in more oil-wet behavior whereas increasing brine salinity resulted in decreasing contact angle hence more water-wet behavior. This is in close agreement with published work [14, 15] on wettability alteration in sandstone when the brine concentration was increased from 0.3 % to 20%.

Optimisation: The regression models developed using three different wettability characterizations were utilised for optimising the input parameters such as temperature, aging time and brine salinity. As previously mentioned, the wettability criterion for an oil-rock-brine system with a contact angle $>105^o$ is considered oil-wet. Applying the optimisation criteria of maximizing the contact angle, numerical solutions were generated to establish the optimum value for Brine Salinity, Temperature and Time to be 104,257 ppm, 95°C & 5.5 weeks, respectively, for restoring wettability. The results are graphically represented via 3D response surface in Figure 6, where the peak points region is observed in both 2-D and 3D plots. In the case of wettability index, the optimal conditions for restoration were found to be aging time of 6.2 weeks, brine salinity of 115,000 ppm and temperature of 99°C. The optimal values were determined by setting a criteria of wettability index in the range of 0 to -0.6.

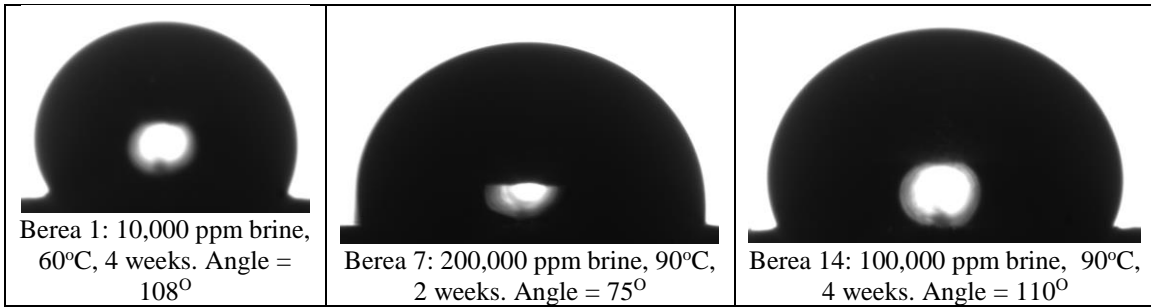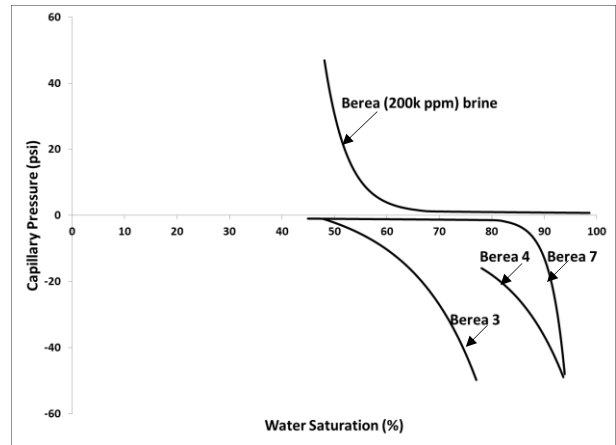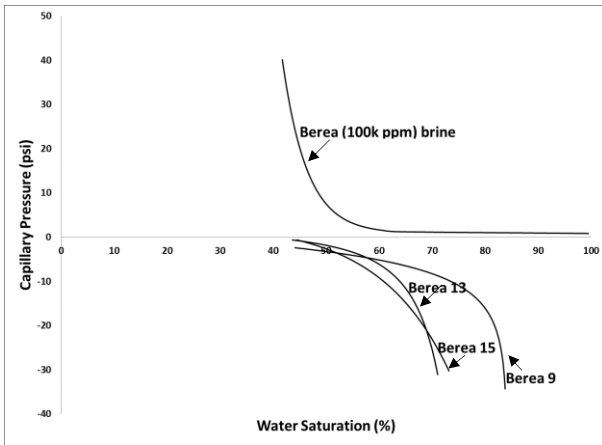| Berea 1: 10,000 ppm brine, 60ºC, 4 weeks. Angle = 108° | Berea 7: 200,000 ppm brine, 90ºC, 2 weeks. Angle = 75° | Berea 14: 100,000 ppm brine, 90ºC, 4 weeks. Angle = 110° |

Figure 1. Contact angle measurements for Berea.

Figure 2. Capillary pressure curves for Berea samples (Imbibition and Drainage) Figure 3. (a) BSEM images of Berea sample 15 (b) Mineral map of Berea sample 15
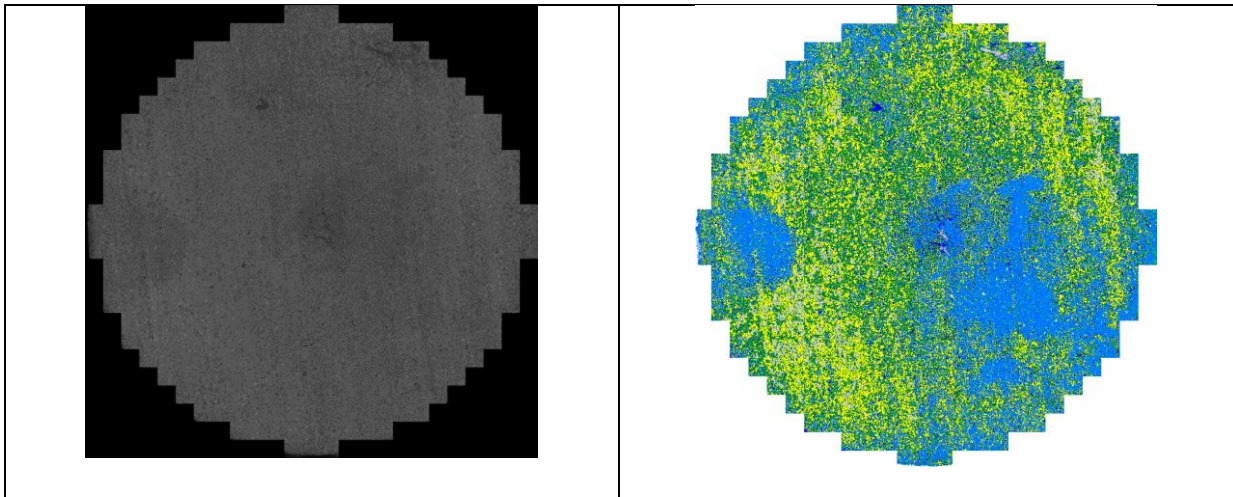

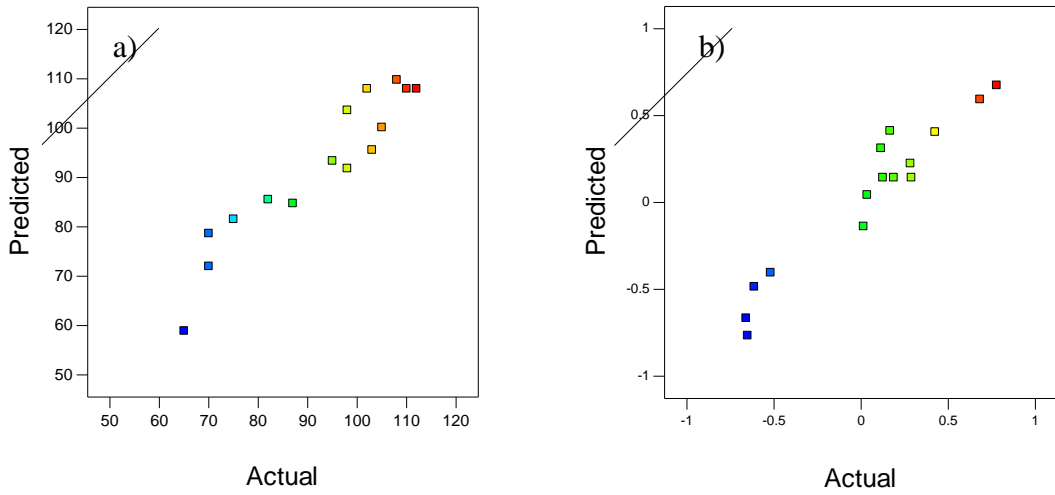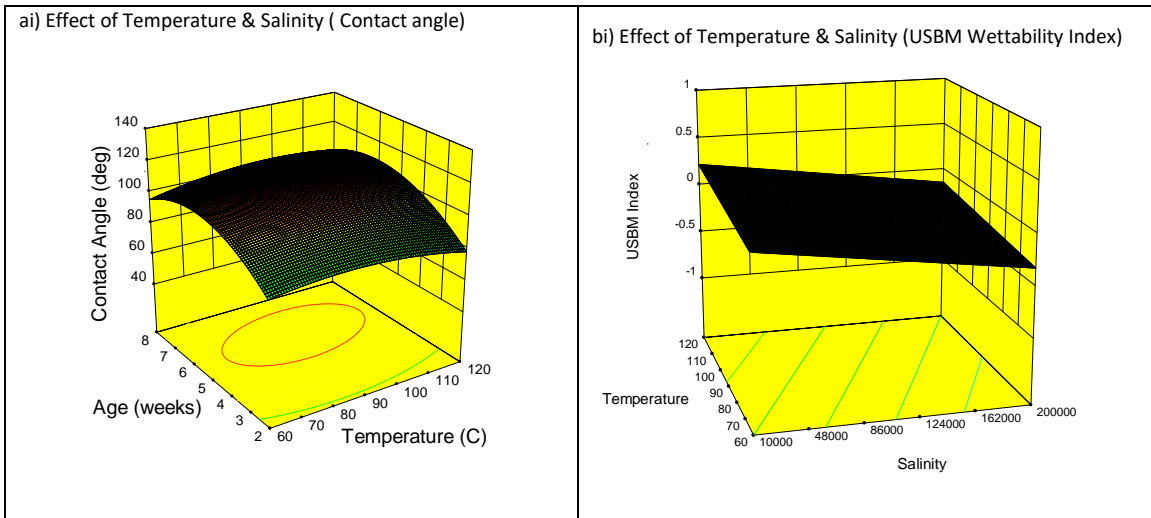**Figure 3. (a) BSEM images of Berea sample 15 (b) Mineral map of Berea sample 15**

Figure 4. Predicted vs Actual for Berea Sandstone (a) Contact Angle (b) USBM Wettability Index
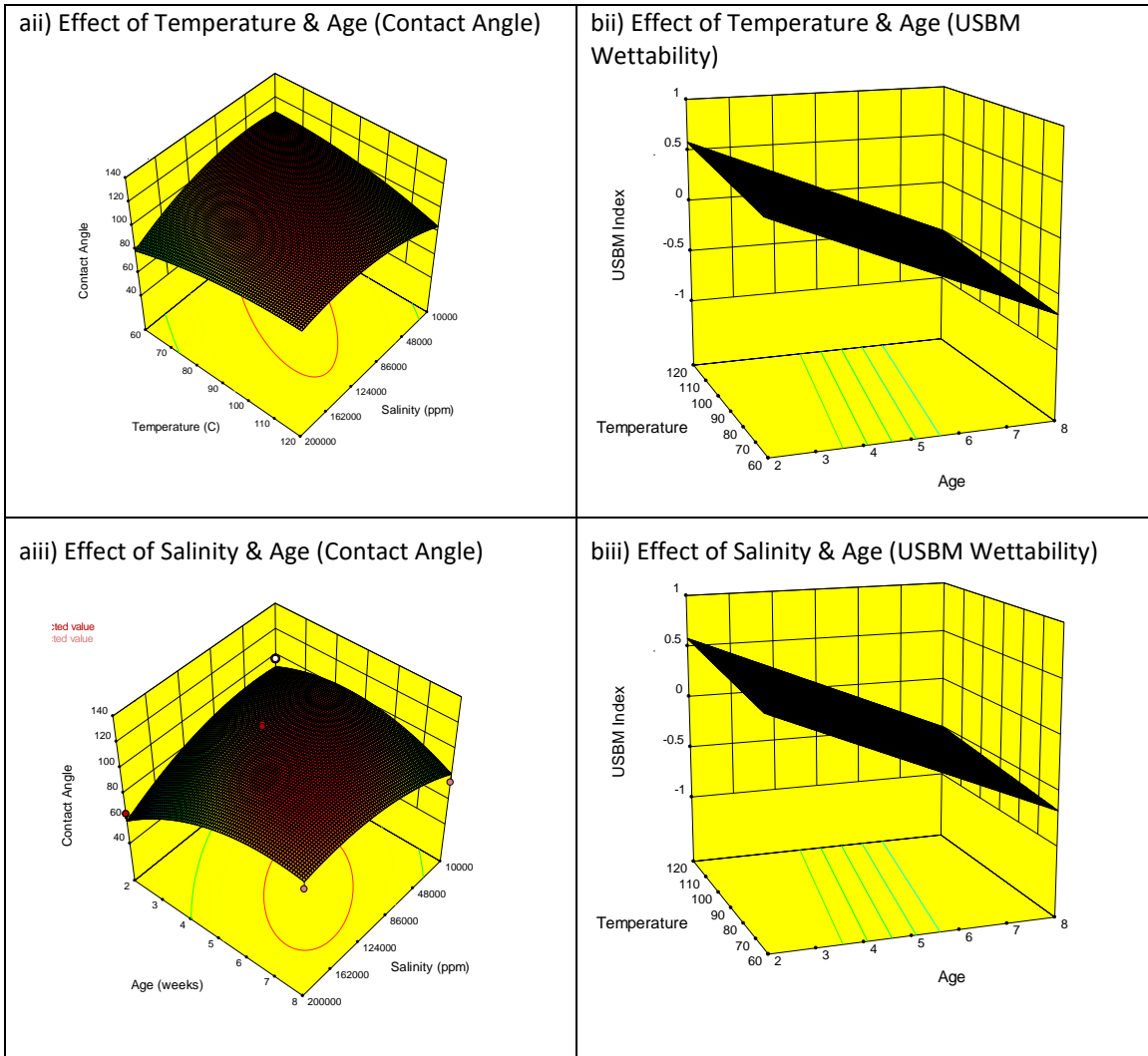**Figure 6. Optimal Aging Conditions (contact angle, 5.5 weeks, 95ºC, 104,257 ppm)**

Figure 5. Contact Angle 3D Surface Models & 2D Contour Plots of Temperature, Salinity & Age
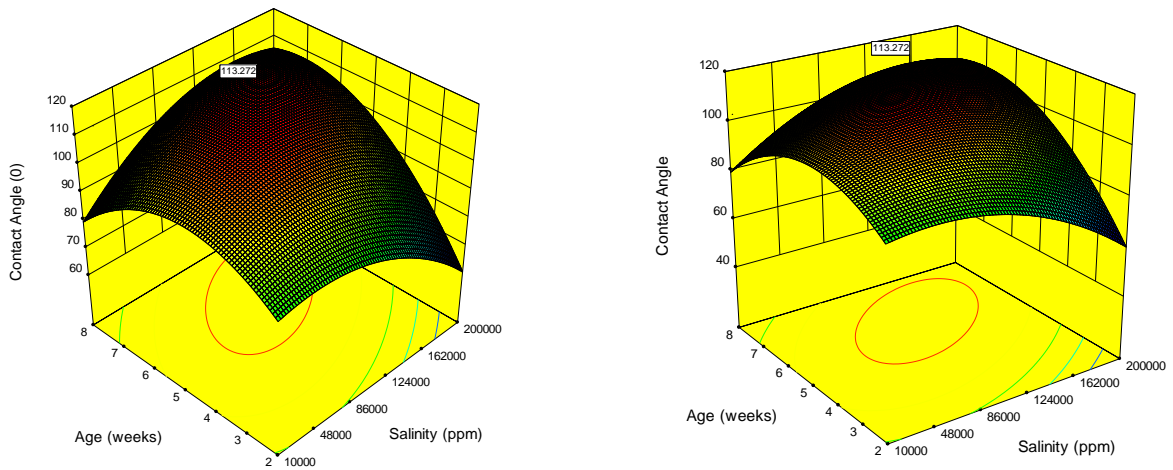

Figure 6. Optimum Ageing Conditions (contact angle, 5.5 weeks, 95ºC, 104,257 ppm)

CONCLUSIONS

Response Surface Modelling (RSM) using three factor Box Behnken Design was successfully applied to study and optimise brine salinity, temperature of aging and aging time for wettability restoration in core samples.

1. A suite of 15 Berea sandstones were prepared and aged following Box Behnken design of experiments. Wettability was validated based on three response factors i.e., contact angle, USBM wettability index and organic content using SEM-MLA analysis.
2. The Berea samples used for this study were initially water-wet and under saturation with crude oil with little or no asphaltene content we were able to develop an optimization strategy for restoring core samples to desired wettability conditions found in the reservoir.
3. The experimental results were analyzed statistically using a regression model and analysis of variance (ANOVA). The ANOVA results for the three response factors showed high coefficient of determination values, ensuring a fit of the developed mathematical model with the experimental data.
4. Applying the optimization methodology, the optimum value of input parameters for restoring oil-wet conditions using contact angle measurement was calculated as brine salinity at 104,257 ppm, temperature at 95°C and time of aging at 5.5 weeks.
5. Optimization results for restoring wettability using USBM method provided an optimum brine salinity of 115,000 ppm, temperature of aging at 99°C and aging time for 6.2 weeks.
6. Optimal solution for restoration using SEM-MLA method is under process and the final results will be presented in a future paper.
7. Response surface models and 2-D contour plots were successfully developed for analyzing the interaction between the three input parameters on contact angle measurement. The results for Berea were in strong agreement with proven results.

ACKNOWLEDGEMENTS

REFERENCES

1. Alotaibi, M.B., Azmy, R., & Nasr-El-Din, H.A. (2010, January 1). Wettability Challenges in Carbonate Reservoirs. Society of Petroleum Engineers. doi:10.2118/129972-MS
2. Anderson, W.G. (1986, October 1). Wettability Literature Survey- Part 1: Rock/Oil/Brine Interactions and the Effects of Core Handling on Wettability. Society of Petroleum Engineers. doi:10.2118/13932-PA

3. Begum, M., Reza Yassin, M., Dehghanpour, H., & Dunn, L. (2017, February 15). Rock-Fluid Interactions in the Duvernay Formation: Measurement of Wettability and Imbibition Oil Recovery. Society of Petroleum Engineers. doi:10.2118/185065-MS

4. Hirasaki, G. J., Rohan, J. A., Dubey, S.T., & Niko, H. (1990). Wettability Evaluation During Restored-State Core Analysis. Society of Petroleum Engineers. doi:10.2118/20506-MS

5. Jadhunandan, P.P., & Morrow, N.R. Effect of Wettability on Waterflood Recovery for Crude-Oil/Brine/Rock Systems. Society of Petroleum Engineers. (1995) 22597

6. Karimi, S., Kazemi, H., & Simpson, G. A. (2017, March 27). Capillary Pressure, Fluid Distribution, and Oil Recovery in Preserved Middle Bakken Cores. Society of Petroleum Engineers. doi:10.2118/185095-MS

7. Kumar, M., Fogden, A., Senden, T., & Knackstedt, M. A. (2012, March 1). Investigation of Pore-Scale Mixed Wettability. Society of Petroleum Engineers. doi:10.2118/129974-PA

8. Luo, P., & Li, S. (2017, February 15). Simultaneous Capillary Pressure and Wettability Determination for Tight Bakken Cores Using an Ultra-High-Speed Centrifuge. Society of Petroleum Engineers. doi:10.2118/185067-MS

9. Robin, M., Combes, R., Degreve, F., & Cuiec, L. (1997, January 1): "Wettability of Porous Media from Environmental Scanning Electron Microscopy: From Model to Reservoir Rocks," Society of Petroleum Engineers. doi:10.2118/37235-MS

10. Robin, M., Combes, R., & Cuiec, L. (1998, November 1). Two SEM Techniques to Investigate Reservoir-Rock Wettability. Society of Petroleum Engineers. doi:10.2118/1198-0077-JPT

11. Schmatz, J., Klaver, J., Jiang, M., & Urai, J. L. (2017, February 1). Nanoscale Morphology of Brine/Oil/Mineral Contacts in Connected Pores of Carbonate Reservoirs: Insights on Wettability from Cryo-BIB-SEM. Society of Petroleum Engineers. doi:10.2118/180049-PA

12. Sripal, E.A., James, L.A., "Application of an optimization method for restoration of Core samples for SCAL experiments" Proceedings of the Annual Symposium of the Society of Core Analysts, Snowmass, USA, 2016

13. Tang. G.Q, and N.R. Morrow, "Influence of Brine composition and Fines Migration on Crude Oil/Brine/Rock Interactions and oil recovery. Journal of Petroleum Science and Engineering. (1999) 24 (2-4):99-111.

14. Vijapurapu, C.S., & Rao, D.N. (2003). Effect of Brine Dilution and Surfactant Concentration on Spreading and Wettability. Society of Petroleum Engineers. doi:10.2118/80273-MS

15. Zhou, X., Morrow, N.R., & Ma, S. (2000). Interrelationship of Wettability, Initial Water Saturation, Aging Time, and Oil Recovery by Spontaneous Imbibition and Waterflooding. Society of Petroleum Engineers. doi:10.2118/62507-PA

Table 1. Brine Properties

Brine Salinity (ppm)	Density (kg/m³)	Viscosity (cP)	IFT with oil (Nm/m)
10,000	1010	1.05	70.8
100,000	1070	1.21	22.4
200,000	1140	1.50	5.32

*Brine Composition: NaCl 84.38%; CaCl$_2$*2H$_2$O 12.32%; MgCl$_2$*6H$_2$O 2.57%; KCl 0.4%; Na$_2$SO$_4$ 0.32%*

Table 2. Experimental Measurement for Berea Sandstone

Berea Sample	Porosity (%)	Salinity (ppm)	Temp (°C)	Time (weeks)	Contact Angle (°)	SEM-MLA Oil %	Wettability Index (USBM)
B1	18.45	10,000	60	4	108	0.1	0.282
B2	18.19	10,000	120	4	70	0.2	0.424
B3	19.71	200,000	60	4	87	1.2	-0.013
B4	20.69	200,000	120	4	95	1.3	0.034
B5	18.24	10,000	90	2	98	0.59	0.778
B6	18.24	10,000	90	8	65	0.07	0.519
B7	18.12	200,000	90	2	75	1.81	0.113
B8	21.13	200,000	90	6	98	0.53	-0.651
B9	18.40	100,000	60	2	82	1.57	0.165
B10	18.45	100,000	60	8	70	0.39	-0.660
B11	18.52	100,000	120	2	103	2.54	0.681
B12	19.46	100,000	120	8	105	1.58	-0.613
B13	18.00	100,000	90	4	112	1.02	0.2881
B14	18.60	100,000	90	4	110	1.39	0.1870
B15	18.47	100,000	90	4	102	1.72	0.1249

Table 3. ANOVA test results for Berea Sandstone (Contact Angle)

Analysis of variance table [Partial sum of squares - Type III]					
Source	Sum of Squares	df	Mean Square	F Value	p-value (Prob > F)
Model	0.42	9	0.047	4.95	0.0464
A-Salinity	8.5E-003	1	8.5E-003	0.90	0.3863
B-Temperature	6.5E-005	1	6.5E-005	6.8E-003	0.9372
C-Age	0.082	1	0.082	8.65	0.0322
AB (Salinity x Temp)	0.070	1	0.070	7.35	0.0422
AC (Salinity x Age)	0.12	1	0.12	12.16	0.0175
BC (Temp x Age)	4.9E-003	1	4.9E-003	0.52	0.5042
A^2	0.061	1	0.061	6.45	0.0519
B^2	0.013	1	0.013	1.41	0.2890
C^2	0.097	1	0.097	10.20	0.0242

Table 4. ANOVA test results for Berea Sandstone (USBM Wettability Index)

Analysis of variance table [Partial sum of squares - Type III]					
Source	Sum of Squares	df	Mean Square	F Value	p-value (Prob > F)
Model	2.77	3	0.92	48.00	<0.0001
A-Salinity	0.26	1	0.26	13.65	0.0035
B-Temperature	0.066	1	0.066	3.41	0.0919
C-Age	2.45	1	2.45	127.00	<0.0001

Table 5. ANOVA test results for Berea Sandstone (SEM-MLA Wettability Analysis)

Analysis of variance table [Partial sum of squares - Type III]					
Source	Sum of Squares	df	Mean Square	F Value	p-value (Prob > F)
Model	6.28	9	0.70	10.38	0.0095
A-Salinity	0.52	1	0.52	7.68	0.0393
B-Temperature	0.18	1	0.18	2.63	0.1659
C-Age	0.14	1	0.14	2.13	0.2039
AB (Salinity x Temp)	1.10	1	1.10	16.39	0.0098
AC (Salinity x Age)	0.17	1	0.17	2.48	0.1758
BC (Temp x Age)	0.40	1	0.40	5.91	0.0593
A^2	2.12	1	2.12	31.55	0.0025
B^2	0.83	1	0.83	12.42	0.0168
C^2	0.25	1	0.25	3.72	0.1118

Table 6. Hibernia crude oil composition

Composition of Hibernia Crude Oil			
Component	Mass fraction	Mole fraction	Volume fraction
CO_2	0.0000	0.0000	0.0000
N2	0.0000	0.0000	0.0000
C1	0.0000	0.0000	0.0000
C2	0.0000	0.0000	0.0000
C3	0.0002	0.0009	0.0003
i-C4	0.0003	0.0012	0.0005
i-C5	0.0018	0.0070	0.0026
n-C5	0.0028	0.0086	0.0040
C6	0.0054	0.0165	0.0075
C7+	0.0163	0.0427	0.0206

T_2-STORE-T_2 RELAXATION EXCHANGE NMR TO CHARCTERISE EFFECT OF ASPHALTENES ON WETTABILTY DYNAMICS IN SILICEOUS SYSTEMS

Igor Shikhov, Rupeng Li, Ji-Youn Arns, Christoph H. Arns
University of New South Wales, Sydney, Australia

ABSTRACT

The asphaltene fraction of crude oils is one of the main factors defining wettability conditions and ultimate oil recovery. At reservoir scale asphaltenes may cause reservoir compartmentalization and at pore scale govern wettability phenomena. To reproduce reservoir conditions, aging in oil is a common step in laboratory core analysis. Oils relevant to the origin of the plugs are the apparent choice for aging, while for outcrop rocks various hydrophobic chemicals and anti-wetting agents or arbitrary oils are often used. We evaluate alteration properties of synthetic oils represented by various proportions of commercially available bitumen, aromatics and alkane for studies requiring wettability alteration.

Low-field NMR relaxation measurements have been applied in the past to characterise the wettability of rocks by introducing an NMR wettability index. However, the latter requires multiple reference measurements at end-point saturation states. NMR correlation techniques have a higher prediction capacity, e.g. T_2-store-T_2 (REXSY) experiment is naturally sensitive to spatial variation of physical properties by detecting diffusion exchange between different environments. It has been applied to study the connectivity of the pore space in aqueous systems such as gypsum, cement pastes, soils, etc. We applied REXSY to study effect of asphaltenes deposition on wettability of siliceous systems. The change of wettability over aging time in different synthetic oils was tracked using T_2 relaxation measurements, providing estimates of aging dynamics useful in designing wettability-related experiments. Quantitative information about fraction of altered surface area and deposition pattern was inferred from combination of T_2 experimental and numerically simulated responses and from T_2-store-T_2 experiments. Results show that the wettability alteration process is strongly sensitive to both chemical composition of synthetic oils and asphaltenes origin (light or heavy oil). It can be performed in controlled manner to set variety of heterogeneous wetting conditions. Elements of resulting deposition pattern and wetting state of the core were identified using low-field NMR relaxation and relaxation exchange techniques.

INTRODUCTION

Asphaltenes: Understanding their behavior is among the major problems in upstream and downstream petroleum engineering as they may change wettability and create barriers to flow at various scales. Wetting properties of natural rocks motivate studies of

mechanisms governing wettability change, relationships between wettability and rock petrophysical and reservoir properties, detection techniques, and methods allowing restoration and control of wettability change and associated chemo-physics at reservoir conditions. Asphaltenes' dynamics represents a complex process considering their flocculation behavior, interaction with other fluid components and minerals over a broad range of temperature and pressure. On the molecular level asphaltenes dynamics can be well described using Yen-Mullins model [1]. Here we focus mainly on the effect of pore-scale asphaltene-to-solid interaction and their accumulation in rock void space rather than stability/solubility chemistry.

Wettability: a mutual solid-fluid property defined as the tendency of a fluid to spread over or adhere to a solid surface in the presence of other immiscible fluid(s), wettability is one of the main factors governing oil recovery since it controls initial fluids distribution, capillary pressure and relative permeability. It is a multi-scale phenomenon depending on mutual intermolecular interactions between fluids and solids, chemical potential of components, excess of free energy in the solids in contact with fluids (surface energy) and surface roughness (topology). Wetting properties of rocks in context of petroleum engineering are considered qualitatively, ranging from strongly water-wet to strongly oil-wet. These states are often expressed either through contact angle (which is a microscopic property) or more often through one of wettability indices which relate observable change of saturation and saturation history to rock wetting capacity (macroscopic average property), such as Amott [2] and US Bureau of Mines (USBM) methods. The Amott wettability index relates the ratio of spontaneous to forced displacement of oil and water on a -1 to +1 scale. A comprehensive description of these techniques can be found elsewhere, [3]. Alternative approaches include direct measurement of zeta potential [4], various contact angle measurements using e.g. telescope-goniometry [5], Wilhelmy balance method [6].

NMR Wettability Index and Surface Relaxivity Heterogeneity: NMR is widely used for petrophysical characterization of rocks, including applications to wettability [7]: NMR relaxation is sensitive to the wetting state of the rock through surface relaxivity, which lead to the definition of NMR indices correlating very well to standard USBM [8] and Amott [9]. Further improvements were achieved with the aid of numerically modelled NMR responses using simplified pores geometries, e.g. 2D triangular [10]. These models assume homogeneity of surface relaxivity and wettability. The significance of wettability heterogeneity on relative permeability is long known [11]. Effects of surface relaxivity heterogeneity on log mean relaxation time and associated permeability correlations were investigated numerically using simulated NMR relaxation experiments and 3D micro-CT representations of rock and various spatial relaxivity distributions [12]. A systematic experimental study of surface relaxivity heterogeneity on relaxation rates using sand packs altered with ferrihydrite is given in [13]. There is clear proof that variations of wettability of a given mineral constituent of the rock correspond to variations of surface relaxivity. However, it is less obvious how precipitation of asphaltenes following various scenarios (favoring pore topology or mineralogy or combination of both) would affect such interpretation.

Wettability Reversal/Alteration in SCAL (Ageing): Core analysis for the purpose of evaluation of reservoir quality and petrophysical studies requires restoration of core wettability state. This is typically achieved by making a core strongly water-wet using a variety of cleaning procedures and subsequent alteration of the core wettability to some degree of oil wetness. The latter can be achieved either using special hydrophobic chemicals and anti-wetting agents (e.g. dimethyldichlorosilane $Si(CH_3)_2Cl_2$) or using a so-called ageing process – exposure of the rock to crude oil (native to rock origin or arbitrary) at a certain elevated temperature. Where possible, crude oils native to core samples are used. However, in many cases, e.g. for benchmark studies on outcrop rocks or phenomenological studies the selection of oil is arbitrary, which complicates comparison of results. Wettability and asphaltene deposition studies typically involve at least two steps: setting initial conditions of solid (porous) system and alteration of wettability by exposure of solid to long-chained hydrocarbons - ageing at certain conditions (temperature and pressure). In this work we systematically study the effect of two cleaning solvents (light alkane and basic aromatic) as well as the effect of oil composition on strength and rate of wettability alteration.

Distribution and Rate of Asphaltene Deposition: mechanisms and dynamics of asphaltene deposition are of significant importance in upstream and downstream petroleum engineering. At given conditions, asphaltenes likely precipitate on rock surfaces non-uniformly, depending on mineralogy, pore shape, surface roughness, etc. Understanding the influence of these factors will assist in improving multiphase flow models. One apparent effect of asphaltenes deposition is porosity and permeability reduction. There are many techniques and their combinations which have been applied for direct and indirect detection of the deposition process. One work utilised SEM observation and pressure drop in capillary, concluding that submicron asphaltene aggregates are likely responsible for fouling rather than large matured ~0.5 µm aggregates [14]. Other works often rely on various optical microscopy/ photomicrography techniques. Wang *et al.* (2004) [15] investigated deposition rates of asphaltenes mixed with n-alkanes on metallic surfaces in the temperature range of 20 to 60°C. They concluded that governing factors include base crude oil properties, oil/alkane ratio and alkane carbon number. Two base crude oils were used with very similar composition and properties and deposit thickness was measured indirectly: by pressure drop in capillary and by mass balance (asphaltenes in influent and effluent). The thickness of deposits varied between 2 and 70 µm depending on conditions. 3D optical microscopy was applied to investigate the effect of carbon dioxide on asphaltenes deposition at various pressures by detecting size of asphaltene aggregates and glass surface area covered by deposit [16]. Direct or 3D detection of asphaltene deposition processes has an apparent advantage over the indirect or 2D measurements. 3D optical microscopy was applied to measure deposition rate in a glass microchannel as function of pumped volume at a constant and variable flow rate [17]. Experiments were conducted for 4-14 hours at constant temperature 21°C. There was no apparent flow rate dependency on deposition thickness, while fraction and especially type of n-alkane and oil in the mixture changes thickness sometimes significantly, Figure 1 [a,b]. Zhao *et al.*

(2016) [18] studied the impact of asphaltenes precipitation on sandstone during CO_2 flooding using high resolution micro-CT tomography to directly detect deposits. Other examples include a combination of multiple techniques, where micro-CT is used to determine oil and water distribution within pore space, while asphaltene deposition is evaluated using FESEM and optical profilometry providing 3D surface maps [19]. Examination of wetting characteristics of 55 crude oils and pure samples by measuring advancing contact angle values as function of aging time revealed that deposition of surfactants and asphaltenes gradually renders the surface progressively more oil-wet with respect to time as the system ages [20], Figure 1 [c]. Note, both deposition [17] and contact angle time-series data [20] follow very well the logarithmic trend.

Oil Composition and Wettability: Published experimental results show different wettability effects caused by asphaltenes originating from heavy and light oils [21]. This stresses the importance of molecular-level studies targeting the influence of asphaltenes structure. In this study we used natural and synthetic oils containing asphaltenes from light and heavy oils in the various ratios: 1:0, 0.6:0.4, 0.3:0.7 and 0:1. We discuss our observations regarding this effect. The present work focusses on the following aspects relevant to the influence of asphaltenes on rock petrophysical/reservoir properties:

- rate of asphaltenes deposition in sandstone saturated with various synthetic oils after ageing process (after cleaning/re-saturation with n-alkanes),
- rate of wettability change and potential correlation to deposition rate,
- effect of asphaltene deposition and wettability change on NMR T_2 relaxation and T_2-store-T_2 relaxation exchange NMR measurements, characterization of deposition pattern and evaluation of wettability heterogeneity,
- influence of oil composition on aging efficiency.

We aged bead packs and outcrop sandstone with a variety of crude and synthetic oils to investigate the relationship between asphaltene accumulation and wettability change over time depending on oil composition. Wettability change was tracked by measuring NMR relaxation responses. NMR relaxation responses were modelled using random walk simulations with high-resolution micro-CT images as morphological inputs. To interpret results we modelled asphaltene deposition over time using two scenarios: (1) uniform (random) precipitation and accordingly uniform random change of surface relaxivity (with different mean and variance of the affected surface spots); (2) non-uniform, deposition is preferential in crevices defined using radius thresholds on a covering radius transform. Furthermore, for a given ageing time of 14 days depositions were detected directly (within resolution limit) using differential imaging techniques.

EXPERIMENTS

Fluids: In this study we used five synthetic oils composed of various proportions of C170 grade bitumen, toluene, hexadecane and crude oil (Tables 1-3). Asphaltene fraction in these oils varied from 1.6 to 6.6 wt% and resins from 3.4 to 17.4%. All oils are diamagnetic with susceptibility values in a range of -8.0 to -8.5 µSI. Oil 1.b with highest degree of resins and asphaltenes has lowest mean diffusion coefficient of 385 µm^2/s,

while two oils, 3.d and 4.e, with similarly low resins and asphaltene content (though of different origin) show fastest mean diffusion coefficient of 610 μm^2/s (Table 3).

Samples: The rate of asphaltene deposition and wettability change was studied using two porous systems: (1) six borosilicate bead packs plus reference and (2) 36 Bentheimer sandstone core plugs plus two reference plugs. Bead packs we used to test aging capacity of all available oils over the single aging time of 14 days, while 36 sandstone plugs were organized as three sets of 12 plugs aged with three synthetic oils (1.b, 2.c, 3.d) over the 12 time intervals.

We selected borosilicate beads of large size to create bead packs (mean radius r=0.766±0.055 mm) to diminish possible capillary effects on asphaltene precipitation. Beads underwent aging with crude and five different synthetic oils described above (base oil TD, 0.a, 1.b, 2.c, 3.d, 4.e) at room temperature for 4 days following 10 days of ageing at 60°C. Then beads were cleaned in hexane, dried at 60°C for 24 hours and packed in borosilicate bottles (Figure 2 [a-g]). Lastly, bead packs were saturated with n-decane.
We cored 38 Bentheimer sandstone plugs (32~34 mm long and 12.7 mm diameter): two reference cores, never exposed to oils and another 36 were cleaned in methanol, dried and saturated with three types of synthetic oils (1.b, 2.c, 3.d) using the desiccator/vacuum pump setup, 12 samples per each oil type. The average porosity of these plugs is 24.18±0.22%. These three sets are used to measure oil wettability alteration capacity, ageing rate (and cleaning procedure efficiency).

Rock samples fully saturated with oil were held at room temperature for four days and at the end one sample was spared as reference. Then we start ageing at elevated temperature of 60°C following the time schedule shown in Table 4. Accordingly, each sample was aged once for scheduled aging time and then was cleaned in n-hexane at room temperature for six days. Subsequently, cores were dried and saturated with n-decane (in this work water was not used).

MODELLING
To enhance our understanding about the influence of rock topology and morphology (in addition to chemistry) and to evaluate the potential of NMR relaxometry we employed simulated NMR relaxation experiments utilizing a random walk technique on segmented tomographic images [12]: In the pore space, the random walkers can progress towards any one of the 6 possible directions under internal gradient arising from different susceptibilities. The interactions between fluid and solid phases are simulated by assigning relaxivities to interfaces between phases of non-zero hydrogen index. Then we use a numerical CPMG technique to acquire the signals of an ensemble of spin-packets (isochromats) followed by inversion of the resultant magnetization decay.
During the aging process asphaltenes readily deposit in the following two environments: (a) in the high S/V pore space surfaces, pore crevices and kaolinite patches; (b) onto low S/V grain surfaces, likely with much slower rate if any solvent involved. Alternatively, deposition and change of wetness may occur uniformly on all solid surfaces as a thin layer. These scenarios can be expressed through material balance for asphaltenes phase as following: $V_{a,total} = M_a/(\rho_a \varphi_{a'}) = V_{a,agg} + V_{a,surf} = V_{a,agg} + f_a A_s (\delta_a \varphi_a)$, where $V_{a,total}$ − total

volume of precipitated asphaltene, $V_{a,agg}$ – asphaltene accumulations in crevices, $V_{a,surf}$ – asphaltenes attached on the surface, A_s, f_a and δ_a – surface area of solids, fraction covered with asphaltenes and average layer thickness, ρ_a and φ_a – deposit density and porosity. From experiment M_a and A_s are known, ρ_a can also be measured or evaluated based on literature and minimum value of δ_a can be assumed between 1.5 to 5 nm based on modified Yen-Mullins model [1].

To test these two deposition scenarios against observable NMR relaxation data, we mimic these by relabeling a segmented micro-CT image of Bentheimer sandstone. Initially we have three segmented phases: #1 void/pore space; #2 clay patches; #3 solids (quartz and feldspar). Two additional phases corresponding to asphaltene deposition during the aging process are added as following: #4 accumulations in high S/V regions of initially void space performed by relabelling part of phase #1 by thresholding a covering radius field (CRT, the maximum radius of the sphere which can cover the voxel of a phase) [22]. The deposition process on low S/V surfaces is mimicked by creating an imaginary phase #5 at the expense of solid phase #3 (thresholded Euclidean Distance field, EDT – in our case a voxel layer normal to the solid phase surface). This new phase is combined with a uniform random voxelized field so that total fraction of relabelled surface is changed, e.g. as 0%, 50% and 100% (Figure 3 [b-d]). These morphological operations enable us to reproduce a partial or uniform change of surface properties of a solid. Simulated T_2 responses for different wettability/relaxivity scenarios are given in Figure 4, and conceptual and actual spatial relaxivity assignments are given in Figure 3. Main unknown input properties are decane effective diffusion in clay phase and asphaltene patches, diffusion exchange with macro-pores, porosity of asphaltene deposit.

RESULTS

Bead packs: Visual inspection of aged and cleaned bead packs reveals a slight change of beads color after aging in crude oil (Figure 2 [g]); four synthetic oils change beads color to quite similar extent, to medium brown (Figure 2 [c-f]) and aging with oil 4.e resulted in a strongest change of color, to dark brown (Figure 2 [f]). Relaxation time measurements used to calculate the difference of surface relaxivity to n-decane as a function of oil type used for ageing. Relaxation measurements and evaluated surface relaxivity are summarised in Table 5. Oil 4.e demonstrates the strongest increase of relaxivity of aged beads by 40%, oils 1.b, 2.c show significant increase by ~10%, oil 3.d just by 5% and the mixture with the highest fraction of asphaltenes shows the least increase of relaxivity, by 3%. Aging beads in natural crude oil surprisingly decrease relaxivity by 15%, which may be explained by the chemical nature of the deposit (likely wax rather than asphaltenes).

Sandstones: Change in appearance of cores from set 1 (oil 3.d) after aging, cleaning and drying is shown on Figure 5. Cores from this set look much darker (from approx. 17 days of aging, Figure 5 [c]) comparing to cores aged with oils 1.b. and 2.c (all are light to medium brown in color even after 72 days of aging). This has a certain correspondence to the amount of precipitate (Figure 6), but also to precipitate type. The amount of precipitate and degree of color change anti-correlate with regard to the initial amount of

asphaltenes in the oil (which agrees with reported field experience [23]). Surface relaxivity of cores aged with low-asphalte oil 3.d also increased to a higher extent (from 4.2 µm/s to 9.0 µm/s after 52 days of aging). In comparison, surface relaxivity of plugs aged with high-asphaltene content oil 1.b increased rather little, up to 5.9 µm/s after 52 days (compare to 5.5 µm/s in five days), i.e. remained nearly constant. The main peak of T_2 distributions (Figure 7) moves clearly towards shorter relaxation times and becomes coupled to the short component, the amplitude fraction of which is almost doubled when 3.d oil was used (comparing reference sample and aged for 52 days short-time part of the signal <100 ms increased from 4% to 7%).

The average thickness of deposit and portion of surface it covers can be evaluated if surface area is known. Yan al. (1997) [24] estimated thickness following aging of Berea sandstone of 3.1 nm (for one oil), concluding the presence of a nearly uniform asphaltene monolayer; for another oil the calculated value of 1.7 nm led to the conclusion of a partially covered surface. Similarly, using specific surface area from MICP experiment of 0.5 m^2/g and assuming a minimum layer thickness of 3 nm we can estimate the possibility of uniformly covered grain surfaces: plugs aged with oil 3.d, 2.c and 1.b may reach that state (if no accumulation occurs) in approximately 20, 25 and 50 days respectively based on total precipitate amount, Figure 6 [a]. We can test this estimate by comparing several experimental T_2 distributions, e.g. for samples aged with oil 3.d (BH1.7, BH1.9, BH1.11 aged for 22, 36 and 72 days respectively) with the set of simulated responses where uniform relaxivity was used (Figure 4 [a]). Distributions match is obtained with following relaxivity values (experiment vs simulation): BH1.7: 6.8 vs 5.5 µm/s; BH1.9: 7.8 vs 7.0 µm/s; BH1.11: 10.2 vs 11.0 µm/s; non-aged core: 4.2 vs 4.2 µm/s. Assuming fractional additivity of responses for non-altered and fully altered surfaces, the altered surface fraction is: BH1.7: 15~35%; BH1.9: 40~60%; BH1.11: 90~100%. We can test that finding for the core BH1.9 against simulations performed using 50% of solid surface altered with different relaxivities; experiment expected to match simulated T_2 distribution if 50% of solid surface accept relaxivity 10-11 µm/s. One can see that the experimental distribution overlaps with the simulated curve corresponding to a surface relaxivity of 10 µm/s (Figure 4 [b]). This is rather a solid prediction of the partially altered surface or equally a wetting heterogeneity.

T_2-store-T_2: Similarly to T_2 relaxation, REXSY [25,26] detects the increase of short-time component fraction in total 2D signal amplitude as function of ageing time (peak CC and exchange cross-peaks CB and BC) as well as decrease of the long-time component (peak AA), Figure 9 [b,c]. The evolution of the peak AA over time may be used to track changes of effective surface relaxivity and wettability (calibration to reference sample required, than it recovers relaxivity evaluated from 1D T_2 data within 2-5% difference). More interestingly, based on 2D maps we may suggest certain morphological similarity between responses from kaolinite and asphaltene deposits (Figure 9 [a-c]). Properties of kaolinite in Bentheimer rock are well-known and can be found elsewhere. Comparing the intensity of peaks CC, CB and BC of aged samples to reference and noting the known total amount of deposit, we can evaluate deposit apparent porosity of 0.73 (oil 3.d) and 0.75 (oil 1.b) for samples aged for 22, 36 and 52 days.

DISCUSSION

Our results demonstrate that surface relaxivity of aged sandstone changes with the rate specific to oil chemical composition. Oil with the highest asphaltene content (1.b) demonstrates the least wettability alteration capacity, while oil different from 1.b only in factor 2.5 lower asphaltenes fraction (3.d) much higher alteration strength. In a long aging time (17–72 days) relaxivity changes with time linearly (Figure 6 [b,c]), with the rate ratio 3 : 6 : 1 for oils 3.d, 2.c and 1.b respectively. The highest rate of relaxivity change in sandstone is ten folds slower comparing to published data for the case of flow in capillary, [17], Figure 1 [a,b]. This signifies difference in asphaltenes concentration condition and the impact of a cleaning step. For borosilicate beads aged over 14 days a little difference was found in ageing capacity in three oils of interest (1.b, 2.c and 3.d), with slight preference to the one with highest asphaltene content (10.4, 9.9 and 9.6 µm/s respectively). In our opinion these results evidence that the surface to volume ratio of the aged medium is among the primary factors governing deposition rate and accordingly rate of wettability change. Experimental results of sandstone ageing rate (Figure 6) show that mobility of oil constituents (or bulk-self diffusion coefficient) may be as important as amount of asphaltenes in the oil. Comparing oils 1.b and 2.c with similar asphaltenes content (3.9 % vs 3.4%) we can see that the latter changes wettability/relaxivity 6 times stronger/faster. The higher mobility of oil 2.c together with presence of asphaltenes originated from both light and heavy oils enhanced wettability alteration capacity of the mixture. REXSY technique provides estimate of deposit apparent porosity and together with material balance may be utilized to evaluate deposition pattern.

CONCLUSION

We demonstrated that low-field NMR is suitable to monitor wettability state in time-series experiments. Data show that wettability alteration can be performed in a controlled manner, i.e. by adjusting synthetic oil composition. Experiments demonstrate feasibility of NMR relaxation-exchange technique to identify deposition pattern - fraction deposited as the surface layer and fraction precipitated as aggregate, as well as porosity (packing factor) of the latter. Understanding the dynamics of wettability alteration/restoration in the laboratory improves our ability to reproduce reservoir conditions before performing core tests and aid to ensure representativeness of laboratory data. It also provides pathway for solution of a forward pore-scale wettability problem of unknown spatial distribution and magnitude of surface relaxivity by numerical NMR relaxation experiment.

ACKNOWLEDGEMENTS

REFERENCES

1. Mullins, O.C., 'The modified Yen model', *Energy Fuels*, (2010) **24**, 2179.
2. Amott, E., 'Observations relating to the wettability of porous rock', *Trans. AIME*, (1959) **216**, 156.
3. Dandekar, A.Y., *Petroleum Reservoir Rock & Fluid Properties*, *CRC Press*, (2013).

4. Bassioni, G. *et al.*, 'Wettability studies using zeta potential measurements', *J. Chem.*, (2015) 743179, 1.

5. Bigelow, W.C. *et al.*, 'Oleophobic monolayers. I. Films adsorbed from solution in non-polar liquids', *Coll. Interface Sci.*, (1946) **1**(6), 513-538.

6. Wihelmy, L.A., 'Über die Abhängigkeit der Kapillaritäts-Constanten des Alkohol von Substanz und Gestallt des benetzten festen Körpers', *Ann. Phys.,* (1863) **119**, 177.

7. Fleury, M. *et al.*, 'Quantitative evaluation of porous media wettability using NMR relaxometry', *Magn. Reson. Imag.*, (2003) **21**, 385.

8. Looyestijn, W. *et al.*, 'Wettability-index determination by nuclear magnetic resonance', *SPE Res. Eval. Eng.*, (2006) **9**(2), 146.

9. Chen, J. *et al.*, 'NMR wettability indices: Effect of OBM on wettability and NMR responses', *J. Petr. Sci. Eng.*, (2006) **52**, 161.

10. Al-Mahrooqi, S.H. *et al.*, 'Pore-scale modelling of NMR relaxation for the characterization of wettability', *J. Petr. Sci. Eng.*, (2006) **52**, 172.

11. Blunt, M.J., 'Effects of heterogeneity and wetting on relative permeability using pore level modeling', *SPEJ*, (1997) **2**(1), 70.

12. Arns, C.H. *et al.*, 'NMR petrophysical predictions on digitized core images', *Petrophys.*, (2007) **48**(3), 202.

13. Keating, K. *et al.*, 'The effect of spatial variation in surface relaxivity on nuclear magnetic resonance relaxation rates', *Geophys.*, (2012) **77**(5) , E365.

14. Hoepfner, M.P. *et al.*, 'A fundamental study of asphaltene deposition', *Energy Fuels,* (2013) **27,** 725.

15. Wang, J. *et al.*, 'Asphaltene deposition on metallic surfaces', *J. Dispers. Sci. Technol.*, (2004) **25**, 287.

16. Zanganeh, P. *et al.*, 'Asphaltene deposition during CO2 injection and pressure depletion: a visual study', *Energy Fuels,* (2012) **26**, 1412.

17. Zhuang Y. *et al.*, 'Three dimensional measurements of asphaltene deposition in a transparent micro-channel', *J. Petr. Sci. Eng.*, (2016) **145**, 77.

18. Zhao, Y. *et al.*, 'Visualization of asphaltene deposition effects on porosity and permeability during CO2 flooding in porous media', *J. Vis., (2016)* **19**, 603.

19. Kumar, M. *et al.*, 'Patterned wettability of oil and water in porous media', *Langmuir*, (2010) **26**, 4036.

20. Treiber, L.E. *et al.,* 'A laboratory evaluation of wettability of fifty oil-producing reservoirs', *SPE J*, (1972) **12**(6), 531.

21. Dashti, H. *et al.*, 'The comparison between heavy and light oil asphaltene deposition during pressure depletion and CO2 injection at reservoir condition, a visual laboratory study', *Chemeca Conf.,* (2013) 30298, *Brisbane, Australia.*

22. Arns, C.H. *et al.*, 'Cross-property correlations and permeability estimation in sandstone', *Phys. Rev. E*, (2005) **72**:046304:1.

23. de Boer, R. *et al.*, 'Screening of crude oils for asphalt precipitation: Theory, practice, and the selection of inhibitors', *SPE Prod. & Fac.*, (1995) **10**(1), 55.

24. Yan, J. *et al.*, 'Wettability changes induced by adsorption of asphaltenes', *SPE Prod. & Fac.*, (1997) **12**(4), 259.

25. Lee, J.-H. *et al.*, 'Two-dimensional inverse Laplace transform NMR: Altered relaxation times allow detection of exchange correlation', *J. Am. Ceram. Soc.*, (1993) **115**, 7761.

26. Washburn, K.E. *et al.*, 'Tracking pore to pore exchange using relaxation exchange spectroscopy', *Phys. Rev. Let.*, (2006) **97**, 175502:1.

TABLES AND FIGURES

Table 1. Component of mixtures representing five synthetic oils.

Hydrocarbon	Bitumen, wt.%	Crude oil, wt.%	n-$C_{16}H_{34}$, wt.%	Toluene, wt.%
Synth. Oil "0.a"	41.7	0.0	0.0	58.3
Synth. Oil "1.b"	25.0	0.0	40.0	35.0
Synth. Oil "2.c"	15.0	30.0	15.0	40.0
Synth. Oil "3.d"	10.0	0.0	50.0	40.0
Synth. Oil "4.e"	5.0	30.0	30.0	35.0

Table 2. SARA analysis of base hydrocarbons and mixtures.

Hydrocarbon	Saturates, %	Aromatics, %	Resins, %	Asphaltenes, %	Volatiles + LOC
Crude oil	38.40	5.60	4.20	3.49	48.30
Bitumen C170	12.90	28.80	41.70	15.72	0.90
Synth. Oil "0.a"	5.38	70.31	17.39	6.56	0.38
Synth. Oil "1.b"	43.23	42.20	10.43	3.93	0.23
Synth. Oil "2.c"	28.46	46.00	7.52	3.41	14.63
Synth. Oil "3.d"	51.29	42.88	4.17	1.57	0.09
Synth. Oil "4.e"	42.17	38.12	3.35	1.83	14.54

Table 3. Physical properties, Total Acid Number, Total Base Number and magnetic susceptibility.

Hydrocarbon	Density, /cc	Viscosity, cP	D, $\mu m^2/s$	AN, mg KOH/g	BN, mg KOH/g	χv, μSI
n-hexadecane	0.7713	3.25	402	-	-	-8.08
n-decane	0.7277	0.89	1328	-	-	-7.64
Toluene	0.8625	0.60	2163	-	-	-7.57
Crude oil	0.8134	16.41	198	1.19	0.66	-8.56
Bitumen C170	1.0304	-	-	1.90	3.80	-9.76
Synth. Oil "0.a"	0.9325	6.04	478	0.79	1.58	-8.48
Synth. Oil "1.b"	0.8792	3.61	385	2.37	1.00	-8.32
Synth. Oil "2.c"	0.8529	2.42	510	1.14	0.78	-8.27
Synth. Oil "3.d"	0.8240	1.78	610	1.63	0.32	-8.04
Synth. Oil "4.e"	0.8235	1.85	607	1.40	0.40	-8.22

Table 4. Ageing schedule (at 60°C).

Step/sample No	1	2	3	4	5	6	7	8	9	10	11	12
Time step, dt [days]	0	1.5	2	2.5	3	4	5	6	8	16	24	28
Total aging time, t [days]	0	1.5	3.5	6	9	13	18	24	32	48	72	100

* All samples were initially aged at room temperature of 22°C for four days (our initial condition).

Table 5. Average weight gain and calculated average deposit thickness

Beadpack sample	Ref 1	Ref 2	0.a	1.b	2.c	3.d	4.e	TD
N beads, estimated [pcs]	5114	5260	5059	5135	5092	5107	5076	5006
S/V calculated [μm^{-1}]	0.0068	0.0070	0.0069	0.0072	0.0070	0.0070	0.0071	0.0070
S/V evaluated $3/r$ [μm^{-1}]	0.0255	0.0255	0.0255	0.0255	0.0255	0.0255	0.0255	0.0255
Relaxition time, T_2 [ms]	1028.9	1049.6	1023.1	1007.6	1010.4	1011.8	1026.7	1064.4
ρ_2 (e) effective [$\mu m/s$]	3.41	3.50	3.56	3.94	3.73	3.63	4.17	2.99
ρ_2 evaluated [$\mu m/s$]	9.01	9.23	9.39	10.38	9.85	9.57	11.01	7.89

Calculated S/V used known weight of beads; Evaluated S/V used surface area of inscribed spheres.
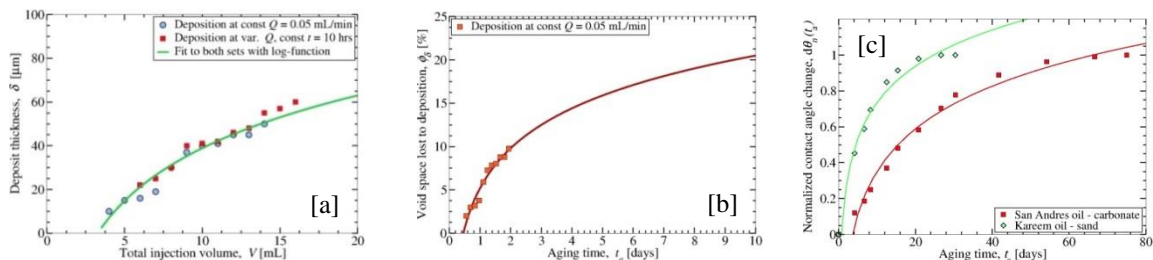
Figure 1. **[a]** Growth of asphaltenes in a capillary tube at constant flow rate over 48 hrs / variable rate at constant time 10 hrs, [17]. **[b]** Constant flow rate data is replotted as normalized void space loss over time. **[c]** Contact angle change during aging in native crude oils for two reservoir rocks excerpted from [20]: re-plotted as normalized contact angle change d$\theta_n(t_a)$. All data [a-c] fitted with log-function: $A + B \ln (t)$.

Figure 2. Reference 20 cc borosilicate beadpack **[a]** and beadpacks aged 14 days in different natural and synthetic oils (dried): **[b]** oil 0.a; **[c]** oil 1.b; **[d]** oil 2.c; **[e]** oil 3.d; **[f]** oil 4.e; **[g]** crude oil.
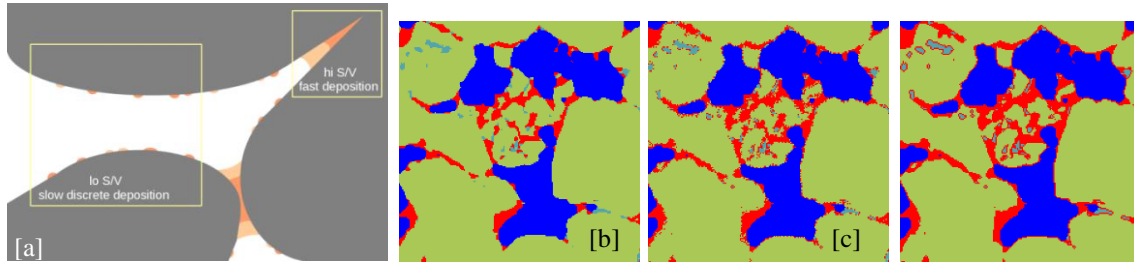

Figure 3. **[a]** Concept of two competing deposition processes, rates of which governed by local surface-to-pore ratio. **[b-d]** The slice through the segmented Bentheimer sandstone µ-CT image altered using morphological transforms to create an additional phase following three deposition scenarios: **[b]** deposition occurs in the pore crevices only (high S/V); **[c]** same as [a], in addition 50% of grain surface is randomly altered (no volume assigned); **[d]** whole surface is uniformly altered.
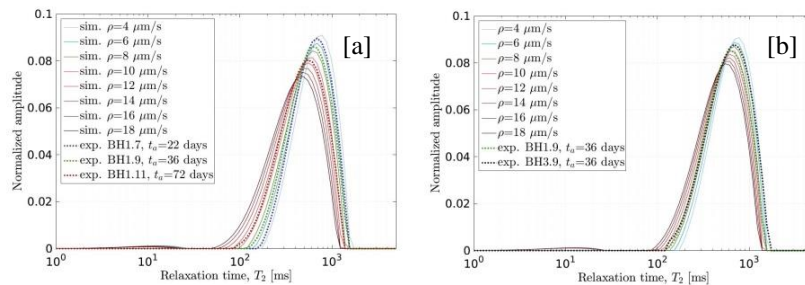
Figure 4. Simulated T_2 distributions of decane-saturated Bentheimer for two deposition scenarios: **[a]** surfaces are altered uniformly. **[b]** deposition in the crevices and 50% of grain surface is altered.
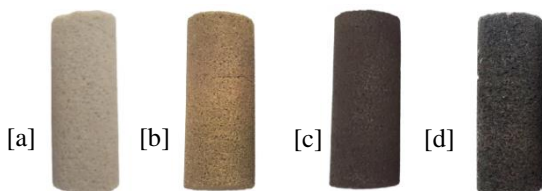
Figure 5. Bentheimer cores **[a]** non-aged reference; aged in synthetic oil 3.d over **[b]** 10 days; **[c]** over 22 days; **[d]** 36 days. Cores were pictured after cleaning in n-hexane and drying.
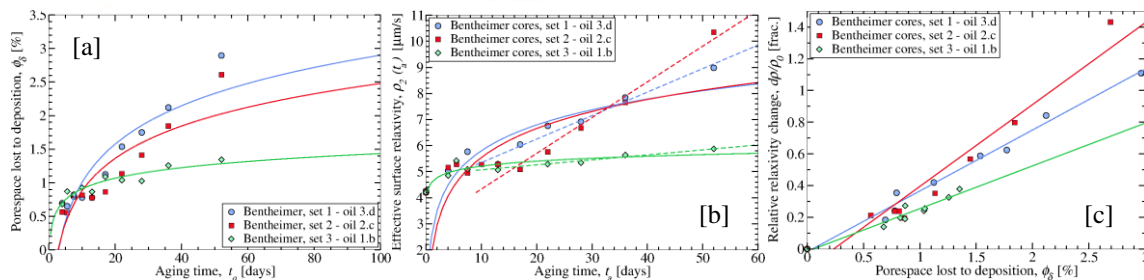
Figure 6. **[a]** Porespace fraction of cores lost to precipitate deposition φ_δ (from weight gain) for synthetic oils 1.a, 2.c and 3.d. **[b]** Change of surface relaxivity over aging time $\rho_2(t_a)$. **[c]** Porespace fraction lost to deposition plotted vs normalized relaxivity change for three sets of cores aged up to 52 days.
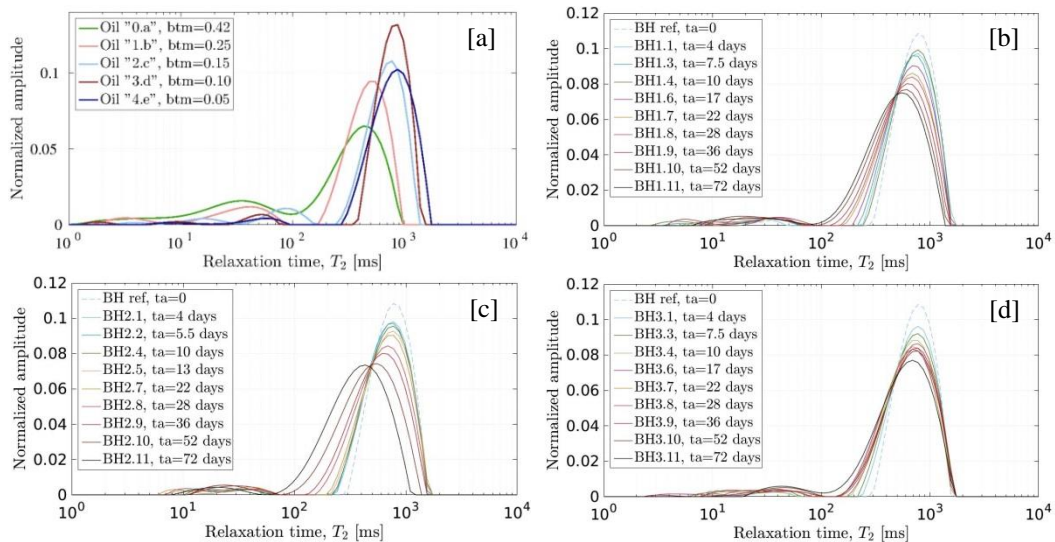
Figure 7. T_2 distributions of **[a]** synthetic oils mixed with different proportions of bitumen (Table 1-3); Bentheimer plugs aged over different time, up to 72 days in three synthetic oils: **[b]** oil 3.d (plugs BH 1.1-1.11); **[c]** oil 2.c (plugs BH 2.1-2.11); **[d]** oil 1.b (plugs BH 3.1-3.11).
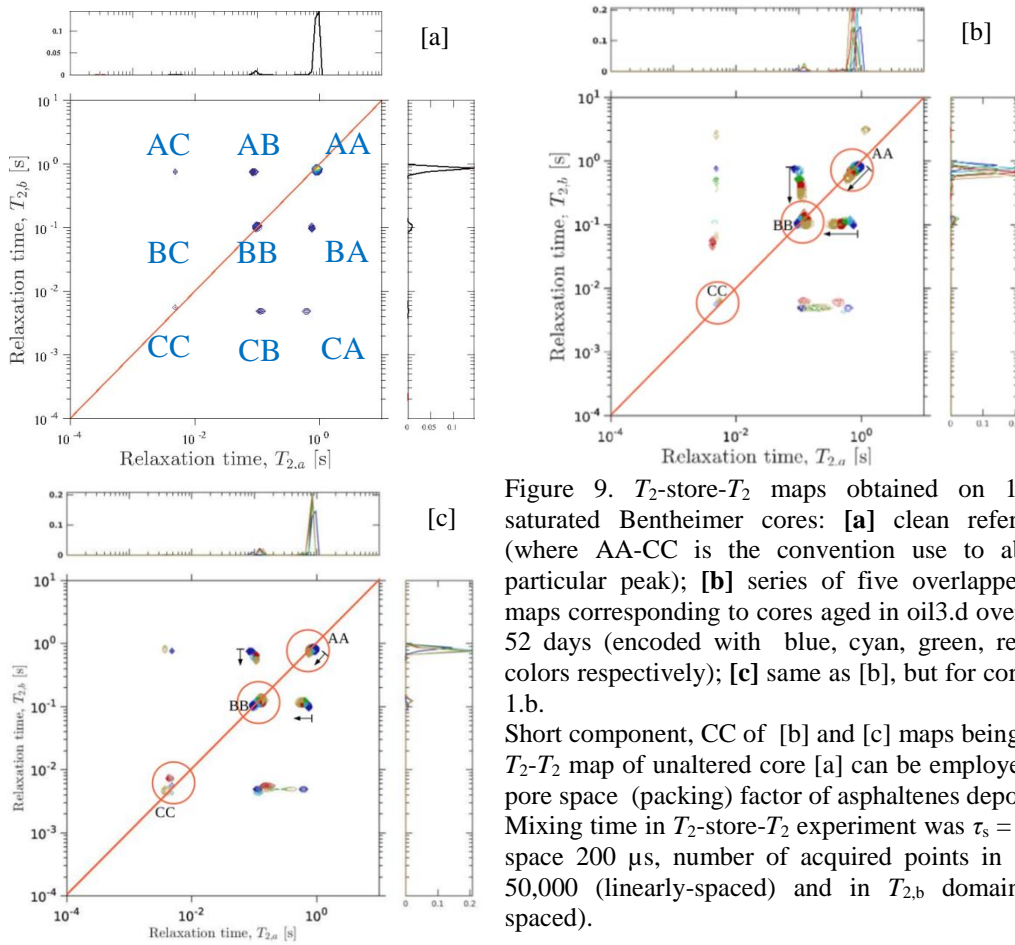
Figure 9. T_2-store-T_2 maps obtained on 100% decane saturated Bentheimer cores: **[a]** clean reference sample (where AA-CC is the convention use to abbreviate the particular peak); **[b]** series of five overlapped T_2-store-T_2 maps corresponding to cores aged in oil3.d over 0, 4, 22, 36, 52 days (encoded with blue, cyan, green, red and brown colors respectively); **[c]** same as [b], but for cores aged in oil 1.b.

Short component, CC of [b] and [c] maps being calibrated to T_2-T_2 map of unaltered core [a] can be employed to evaluate pore space (packing) factor of asphaltenes deposits.

Mixing time in T_2-store-T_2 experiment was $\tau_s = 100$ ms, echo space 200 µs, number of acquired points in $T_{2,a}$ domain - 50,000 (linearly-spaced) and in $T_{2,b}$ domain - 80 (log-spaced).

INTEGRATION OF MULTI-SCALE TECHNIQUES TO EVALUATE RESERVOIR WETTABILITY FOR CARBONATE RESERVOIRS IN MIDDLE EAST

Peila Chen[3], Areej Hussain Al Katheeri[2], Mohammed Zubair Kalam[2], Edmond Shtepani[1]
1. Intertek Westport Technology Center, Houston, Texas, USA
2. Abu Dhabi Company for Onshore Oil Operations, Abu Dhabi, UAE
3. University of Houston, Houston, Texas, USA

ABSTRACT

This work is to evaluate reservoir wettability and its effects on oil recovery from carbonate reservoirs in the Middle East, by integrating multi-scale laboratory techniques. We employed contact angle measurement, Amott-Harvey (AH) index and USBM method to evaluate the rock wettability. NMR wettability indices were also used to quantify rock wettability.

Contact angles of oil droplets on aged calcite plates under reservoir conditions have proved that the live crude oil was able to render the calcite surface towards oil-wet. The AH index and USBM method implied that some reservoir cores as received were water-wet. After core cleaning and wettability restoration, we found that the wettability of reservoir cores has become neutral wet to slightly oil-wet; and the degree of oil wetness varies on the rocks from the different petrophysical groups. We quantified the NMR wettability index using Fleury and Deflandre (2003) model and Chen and Hirasaki (2006) model. Correlations show that both NMR indices generally agree with the AH and USBM index, suggesting that quantitative information of reservoir rock wettability can be gained from NMR measurements. The advantage of NMR wettability indices is to gain an in-depth understanding of the evolution of multi-phase saturation and pore-scale trapping of residual phases. The effects of rock wettability on the residual oil saturation (ROS) after forced water imbibition process were also investigated.

The reservoir wettability determination in multiple-scales, show consistent trends in reservoir characteristics, and show slightly variations in different rock types. The integration of the techniques offers an in-depth understanding of the reservoir properties for potential investigations in further field development using IOR/EOR techniques.

INTRODUCTION

Carbonate reservoirs account for approximately half of the world hydrocarbon reserves. Majority of these are located in Middle East and North America. Many carbonate reservoirs tend to be highly heterogeneous or highly fractured, and oil-wet, in which capillary force opposes imbibition of water into the matrix.

Wettability is a very important concept in oil recovery processes and has a strong influence on distribution, location and flow of multiple phases during hydrocarbon production. Wettability also significantly affects capillary pressure, relative permeability and residual oil saturation [1-4]. A fully understanding of reservoir wettability significantly improves reservoir modeling and the development of an IOR/EOR process [5, 7]. Many methods have been developed for the determination of wettability, as listed in Table 1. Anderson W.G. has reviewed the advantages and limitations of all three industry-standard quantitative methods in use today: contact angle, Amott-Harvey (AH) index and U.S. Bureau of Mines (USBM) method [6].

The AH index, which measures the spontaneous displacement potential of water and oil, varies from +1 from strongly water-wet rocks to -1 for stongly oil-wet rocks. The USBM index is quntified by comparing the amount of work required to displace each of the fluids by the other. It is generally accepted that values below -0.3 are considered preferentially oil-wet, whereas values greater than 0.3 are considered preferentially water-wet. Values between -0.3 nd 0.3 are either mixed-wet (inhomogeneous wettability) or intermediate wet (lacking a strong wetting preference).

As a fast-evolving method for wettability measurement, nuclear magnetic resonance (NMR) is a technique that has been proved to be very sensitive to rock-fluid interface. NMR surface relaxation dictates that the fluid in contact with the mineral surface has a relaxation time shorter than its bulk value. For a system of intermediate wettability, both water and oil molecules will have access to the pore surface and the relaxation time depends on the amount of wetted surface and strength of the interactions. Therefore, NMR can be considered as a quantitative method for wettability index determination.

The reservoirs of interest are two thin and heterogeneous reservoirs, reservoir A and B, within a Lower Cretaceous producing field (Barremian age) in Middle East. They are separated from the overlaying Upper reservoir by a dense layer of 45 ft (average thickness). A very thin layer of around 5 ft separates reservoir A from reservoir B. The average thicknesses of these reservoirs are about 20 ft for reservoir zone A and 30 ft for reservoir zone B. These two reservoirs contain an estimated total of 197 MMSTB OOIP.

This work is to evaluate reservoir wettability and its effects on oil recovery from these carbonate reservoirs by integrating multi-scale laboratory techniques. We employed and compared the results from contact angle test, Amott-Harvey index and USBM method, and NMR wettability index techniques. The effects of wettability on the distribution of multi-phase saturation and local trapping of residual phases were discussed.

THEORY

Wettability and NMR surface relaxation are related to each other. The basic physics is that NMR surface relaxation dictates that the fluid in contact with the mineral surface has a relaxation time shorter than its bulk value. It has been noticed that the reduction in relaxation time of oil from its bulk value can be utilized as a qualitative wettability indication [8, 9], and in specific cases, as a quantitative method [10, 11].

For a system of intermediate wettability, both water and oil molecules will have access to the pore surface and the relaxation time depends on the amount of wetted surface and strength of the interactions. *Fleury and Deflandre* (2003) proposed a NMR wettability index based on fluid distributions. Their NMR wettability model has the form below [10]:

$$I_{NMR} = \frac{S_w(\frac{1}{T_w} - \frac{1}{T_{bw}}) - C_\rho S_o(\frac{1}{T_o} - \frac{1}{T_{bo}})}{S_w(\frac{1}{T_w} - \frac{1}{T_{bw}}) + C_\rho S_o(\frac{1}{T_o} - \frac{1}{T_{bo}})} \quad \dots\dots\dots\dots\dots\dots\dots\dots\dots\dots\dots\dots\dots\dots\dots\dots \text{(1)}$$

$$C_\rho = \frac{\rho_w}{\rho_o} = \frac{1/T_{w,Sw=1} - 1/T_{bw}}{1/T_{o,So=1} - 1/T_{bo}} \dots\dots\dots\dots\dots\dots\dots\dots\dots\dots\dots\dots\dots\dots\dots\dots\dots\dots\dots \text{(2)}$$

Chen and Hirasaki (2006) proposed a concept of effective surface relaxivity, which quantified rock wettability by two NMR wettability indices from either water or oil response [11].

$$I_{NMR} = I_W^{NMR} - I_O^{NMR} = \frac{(\frac{1}{T_w} - \frac{1}{T_{bw}})}{(\frac{1}{T_{w,S_w=1}} - \frac{1}{T_{bw}})} * S_w - \frac{(\frac{1}{T_o} - \frac{1}{T_{bo}})}{(\frac{1}{T_{o,S_o=1}} - \frac{1}{T_{bo}})} * S_o \dots\dots\dots\dots\dots\dots\dots\dots\dots\dots \text{(3)}$$

where, I_W^{NMR} is water index and I_O^{NMR} is oil index. $T_{w,S_w=1}$ and $T_{o,So=1}$ correspond to T_2 relaxation time when $S_w = 100\%$ or $S_o = 100\%$, respectively. T_{bw} and T_{bo} are T_2 relaxation times of bulk brine or bulk oil, respectively. S_w and S_o are the end-point water or oil saturation after forced displacement in centrifuge, respectively. T_w and T_o are T_2 relaxation time @ any Sw and any So, respectively.

METHODS AND MATERIALS

Sample Description and Preparation

The sample selection and preparation was focused on having the widest possible range of wettability from various rock types within a carbonate reservoir in Middle East. The selected core plugs had a porosity range of 13-24% and wide permeability range of 0.2 to 350 md. Since a rigorous core-preservation program was not implemented, the fluid saturation and wettability of these core samples were not preserved. The core samples "as-received" were reconditioned to initial water saturation in centrifuge without aging. Then NMR, AH and USBM tests were conducted on these plugs. Next, the same batch of core samples was cleaned by hot solvents, in the sequence of toluene, azeotrope and methanol, using vigorous flow-through cleaning program. The core plugs were then saturated with brine and oil, and then reached to initial water saturation (S_{wi}). A restored wettability state was established by aging the plugs with live crude oil under high pressure and elevated temperature conditions. The formation brine used in this study contains 22% total dissolved salts (TDS), and the crude oil has an API gravity of ~ 40.0.

Contact Angle Measurements

Contact angle measurement was conducted on the polished calcite plates under both ambient condition and reservoir conditions (Temp = 250degF, Pressure = 3800psig). These calcite plates were aged in crude oil for 4 weeks at an elevated temperature. It should be noted that we the contact angle measurement under high temperature and high pressure (HTHP) conditions was performed using a designed apparatus by Intertek Westport Technology Center in Houston, Texas, which can be set up to temperature of 350 degF and pressure of 5000 psi.

Amott-Harvey and USBM Data Acquisition

Eight 1.5" diameter plugs were selected for capillary pressure and Amott-Harvey & USBM wettability measurements on their as-received state and restored state. The forced imbibition and drainage capillary pressure tests were performed in a BECKMAN L8-M model centrifuge with imaging system using the fluid pairs. The rotational rates were increased incrementally to generate equivalent capillary pressures ranging from 1.0 to approximately 150.0 psi (inlet face). The industrial standard procedures were followed in setting up experimental procedures and calculation of AH and USBM index [12, 13].

NMR Data Acquisition

The proposed NMR wettability index requires the measurement of T_2 relaxation time distribution for at least four different saturation states: 1) 100% Sw; 2) 100% So; 3) after forced imbibition to S_{or}; 4) after forced drainage to S_{wr}. The reasons for selecting the two extreme saturation cases are that the saturation for brine after forced imbibition and for oil after forced displacement is relatively higher, so that better resolution of the NMR measurement is gained for the corresponding water and oil phases. Additionally, we added the T_2 measurements before and after aging to investigate the effects of wettability restoration on T_2 profiles.

NMR T_2 relaxation time measurements were performed simultaneously with capillary pressure measurements by centrifuge on the same 8 plug samples. NMR measurements were made using NUMAR's CoreSpec - 1000[TM] at a Larmor frequency of approximately 1 MHz. Each sample was stored in an air-tight vial and allowed to equilibrate at system temperature prior to loading into the NMR instrument. The tests were performed under a homogenous magnetic field at interecho spacings (T_E) of 0.6 ms.

RESULTS AND DISCUSSIONS

1. Interpretation from Contact Angle Measurements

Calcite was used as a model mineral to perform contact angle measurement since the reservoir of interest is a carbonate reservoir. The objective of measurement is to study if a crude oil could render the calcite oil-wet. The contact angle measurements of at least three oil droplets were performed in each test and the average contact angle was reported.

The test conditions are listed in Table 2. Under ambient test conditions, an average contact angle of oil droplets on calcite plates was determined to be $144.7 \pm 3.2°$, as shown

in Figure 1A. While under reservoir conditions (temperature of 250 deg F and pressure of 3800 psig), the contact angle on the calcite plates reduced significantly to 111.4 ± 2.6^o. In summary, the synthetic live oil was able to render the calcite plates towards oil-wet.

2.   Amott-Harvey Index and USBM Method

The summary of AH index and USBM index is presented in Table 3. In the samples of as-received state, the wettability varies from strongly water-wet (RRT 6 and 8) to slightly oil-wet (RRT 2). After cleaning and being wettability-restored, these samples became towards more oil-wet, expecially in RRT- 4, 6 and 8. As seen in Figure 2, the absolute values of AH index and USBM index agree very well, especially in the range of [-0.5, 1], indicating that both tests are equivalent.

3.   Quantitative Interpretation from NMR T_2 Relaxation Times

As described in theory and method section, the NMR index requires the determination of the dominant relaxation times at at least 4 saturation states. An example of a measurement sequence is shown in Figure 3. The vertical dashed line shows that the surface relaxation time shifted towards shorter time after aging process. It implies that more oil molecules have contacted with mineral surface after aging and some portion of surface became oil-wet.

Since wettability index is a macroscopic term reflecting the average property of core samples, we extracted the avearge property of T_2 relaxation time, including T_2 mode and T_2 log mean values, instead of focusing on the microscopic behaviors. As an example, Table 4 presents the summary of data for NMR wettability study from sample 6A. After feeding the data into Equations 1-3, the NMR wettability index was obtained from both the Fleury and Hirasaki Models, as shown in Table 5.

As shown in Figure 4, the NMR wettability indices derived from two models are in good agreement with a correlation coefficient $R^2 > 0.90$, especially in the range of [-0.5 0.5]. There is difference in NMR index calculated using T_2 mode or T_2 Log mean for the same wettability test, while they correlate well with each other ($R^2=0.86$), as shown in Figure 5. Moreover, NMR wettability index correlates reasonably well with Amott-Harvey index and USBM index in the range of [-0.3, 1], as seen in Figure 6. Therefore, all three wettability indices (AH, USBM, NMR) have shared the same confidence in the measurement when the sample wettability lies between neutral and water-wet state.

4.   Effects of Wettability on Residual Oil Saturation

After centrifuge-based forced imbibition test, the residual oil saturation (ROS) in each plug samples varies. In order to understand the physics behind ROS, it is helpful to calculate the Trapping number (N_T) for each test. Trapping number is a dimensionless number to integrate the effects of both capillary and viscous forces [14, 15]. Viscous force is negligible in a centrifuge-based forced imbibition test. It is then assumed that the Trapping number equals to the microscopic Bond number, *i.e.*

$$N_T \approx N_B = \frac{k \cdot \Delta\rho \cdot \omega^2 R}{\sigma} \quad \ldots\ldots\ldots\ldots\ldots\ldots\ldots\ldots\ldots\ldots\ldots\ldots\ldots\ldots\ldots\ldots\ldots\ldots\ldots\ldots$$

(4)

where k is absolute permeability (m^2), ω is angular velocity (revolution/second), R is the distance from the center of rotation to the center of the plug (m). $\Delta\rho$ is the difference of phase densities (kg/m^3), and σ is the water/oil interfacial tension (N/m).

The values and correlations of ROS (at the inlet) and Bond numbers are presented in Table 6 and Figure 7 for each imbibition test associated with wettability studies. As expected, the values of ROS continue to drop when the Bond number of a centrifuge displacement increases in carbonate rocks, with no presence of definitive critical trapping number [15, 16]. The ROS drops to 0.15 PV when trapping number is around 10^{-5}.

The effect of rock wettability on ultimate oil recovery and residual oil saturation (ROS) has been generally focused on water flood. In this study, we presented the correlation of ROS versus wettability index for carbonate rocks in a forced imbibition process. As shown in Figure 8, the plot of ROS as a function of wettability index indicates a gradually decrease in ROS from strongly water-wet to neutral wet conditions. A clear plateau of lowest ROS exists when the wettability is near intermediate-wet domain.

CONCLUSIONS

1. The wettability study of a carbonate reservoir in the Middle East by integrating multi-scale lab techniques has shown that the reservoir is neutral wet to slightly oil-wet. The degree of oil wetness is varied on the rocks from different petrophysical groups.

2. Contact angles of oil droplets on aged calcite plates under HTHP reservoir conditions have shown that reservoir crude is able to render oil-wetness on the calcite surfaces.

3. Comparing with restored wettability after aging, the "as-received" state was towards more water-wet, possibly due to the contamination of drilling fluid.

4. NMR wettability index was calculated using *Fleury and Deflandre* (2003) model and *Chen and Hirasaki* (2006) model. Correlations show that both NMR indices generally agree with the AH and USBM wettability index, suggesting that quantitative information of reservoir rock wettability can be gained from NMR measurements.

5. In a capillary desaturation curve (CDC), the post-imbibition residual oil saturation (ROS) decreases while trapping number increases in carbonate rocks, without a critical trapping number. There is a lowest plateau of ROS when the sample possesses the neutral wettability.

6. The full integration of reservoir wettability determination in multiple scales showed consistent trends in reservoir characteristics, and show slightly variation in different rock types.

ACKNOWLEDGEMENT

REFERENCES

1. Anderson, W.G., "Wettability Literature Survey - Part I: Rock/Oil/Brine Interactions and the Effects of Core Handling on Wettability," *Journal of Petroleum Technology*, (1986) **38**: 1125-1144

2. Morrow, N.R., "Wettability and Its Effect on Oil Recovery," *Journal of Petroleum Technology*, (1990) **42**, 12: 1476-1484

3. Cuiec, L.E., "Evaluation of Reservoir Wettability and Its Effects on Oil Recovery," In *Interfacial Phenomena in Oil Recovery*, N.R. Morrow, ed., Marcel Dekker, Inc., New York City, 1991, 319-375.

4. Anderson, W.G., "Wettability Literature Survey – Part 4: Effects of Wettability on Capillary Pressure," *Journal of Petroleum Technology*, 1987, 1283-1300.

5. Looyestijn, W. and J. Hofman, "Wettability Index Determination by Nuclear Magnetic Resonance," SPE-93624-PA, *SPE Reservoir Evaluation & Engineering*, (2006)

6. Anderson, W.G., "Wettability Literature Survey – Part 2: Wettability Measurement," *Journal of Petroleum Technology*, 1986, **38**: 1246-1262.

7. Dernaika, M.R., M.Z. Kalam, M.A. Basioni, S.M. Skjæveland, "Hysteresis of Capillary Pressure, Resistivity Index and Relative Permeability in Different Carbonate Rock Types," *Petrophysics*, (2012) **53**, 5, p315-331

8. Borgia, G.C., P. Fantazzini, E., Mesini, "Wettability effects on oil–water configurations in porous media: a nuclear magnetic resonance relaxation study," *J. Appl. Phys.* (1991) **70**, 7623–7625

9. Howard, J.J., "Quantitative estimates of porous media wettability from proton NMR measurement," *Magnetic Resonance Imaging* (1998) **16**, 529–533.

10. Fleury, M. and F. Deflandre, "Quantitative evaluation of porous media wettability using NMR relaxometry," *Magnetic Resonance Imaging* (2003) **21**: 385-387

11. Chen, J., G.J. Hirasaki and M. Flaum, "NMR Wettability Indices: Effects of OBM on wettability and NMR responses," *Journal of Petroleum Science and Engineering* (2006) 52: 161–171

12. Ferno, M.A., Treiner R. and Graue, A., "Experimental Measurement of Capillary Pressure With the Centrifuge Technique-Emphasis on Equilibrium Time and Accuracy In Production", paper *SCA2007-22*, September 2007, Calgary, Canada

13. Forbes Pierre, "Centrifuge Data Analysis Techniques: An SCA Survey on the Calculation of Drainage Capillary Pressure Curves from Centrifuge Measurements," SCA-9714, International Symposium of the Society of Core Analyst.

14. UTCHEM Technical Manual (http://www.cpge.utexas.edu/sites/default/files/research/ UTCHEM_Tech_Doc.pdf).

15. P. Chen, "Enhanced Oil Recovery in Fractured Vuggy Carbonates", 2014, Dissertation (https://repositories.lib.utexas.edu/handle/2152/31396), The University of Texas at Austin.

16. Kamath, J., Meyer, R.F., Nakagawa, F.M., "Understanding Waterflood Residual Oil Saturation of four Carbonate Rock Types," Paper SPE-71505 presented at the Annual Technical Conference and Exhibition, New Orleans, October.
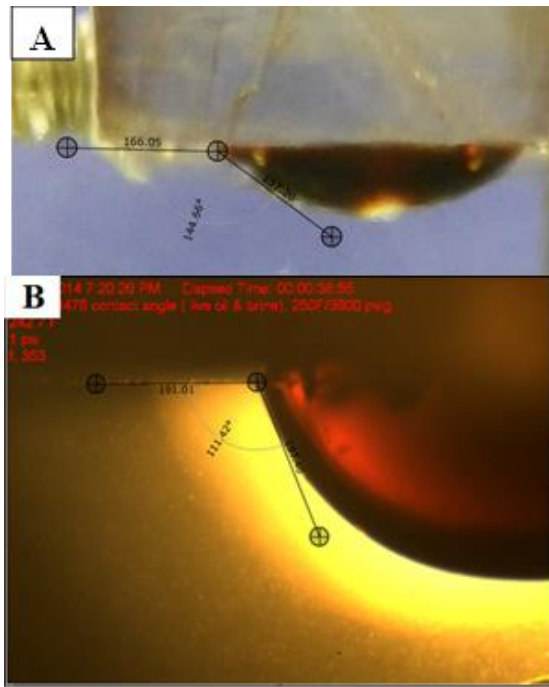
Figure 1. Contact angle measurement on aged calcite plates. (A) Average θ = 144.7° under ambient conditions; (B) average θ = 111.4° under reservoir conditions.
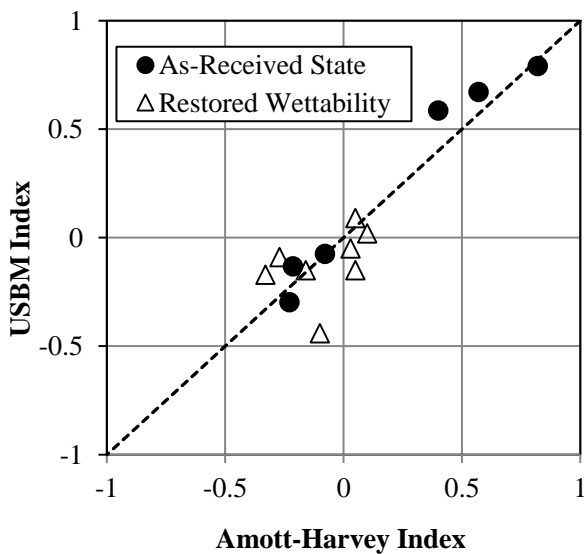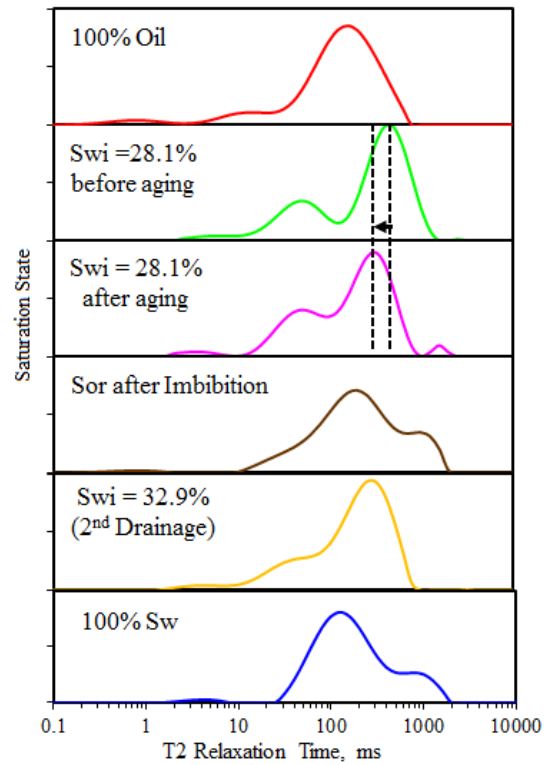

Figure 3: The NMR T_2 relaxation times ate different saturation states. The vertical dashed lines indicate the T_2 mode relaxation time is reduced after aging process.
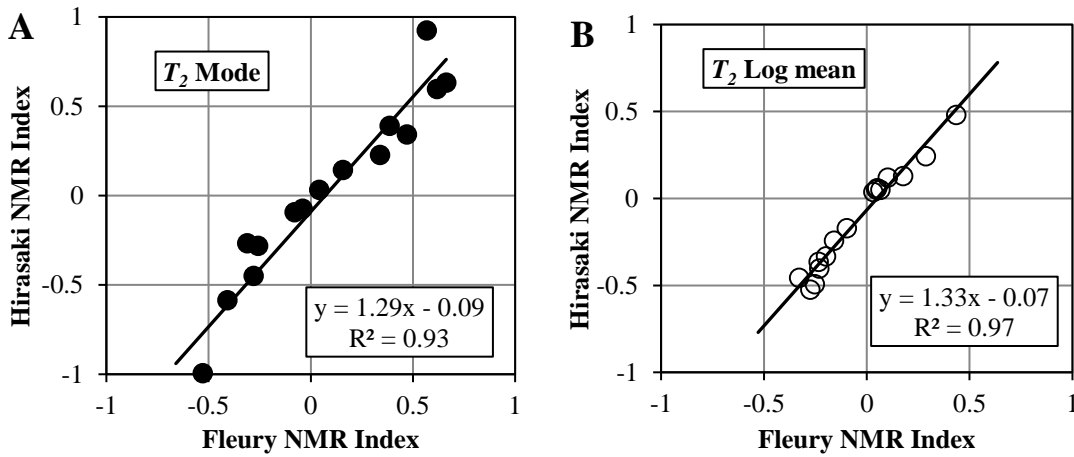

Figure 2. The cross-plot of Amott-harvey index with USBM index.

Figure 4: Comparison of NMR Wettability Indices derived from Fleury and Hirasaki Models. A) T_2 Mode was used for calculation; B) T_2 Log mean was used for calculation.
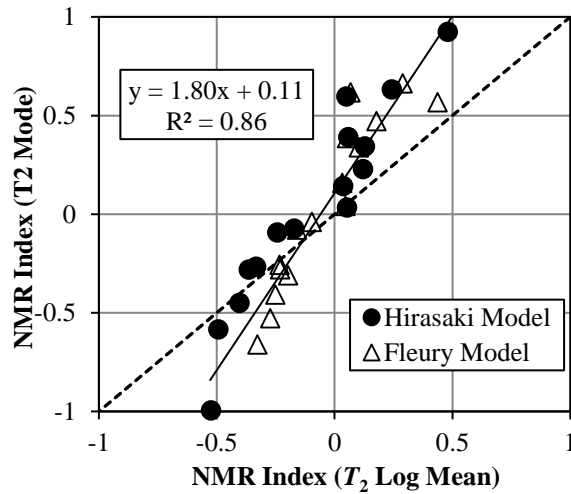
Figure 5. NMR Wettability Index derived from T_2 Log mean and T_2 mode.
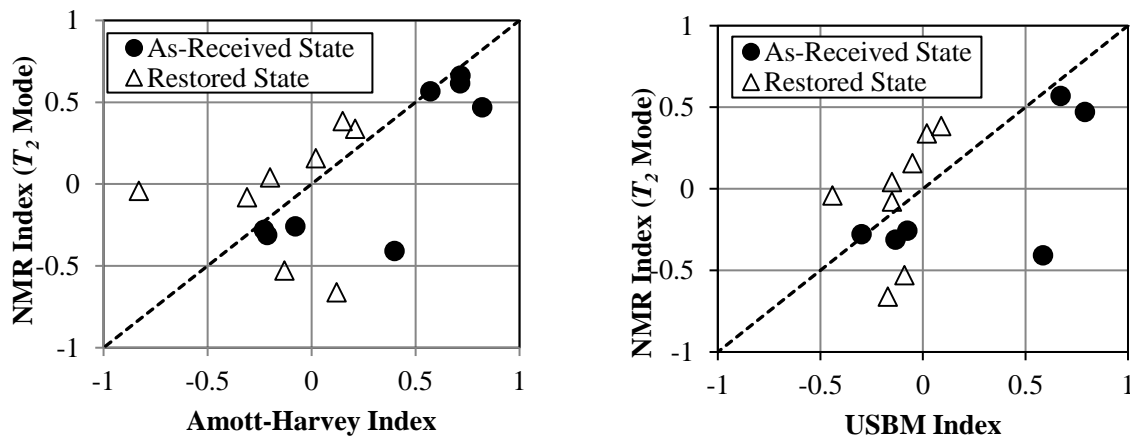
Figure 6. Cross-plots of NMR Wettability Index and AH Index (A) and USBM Index (B).
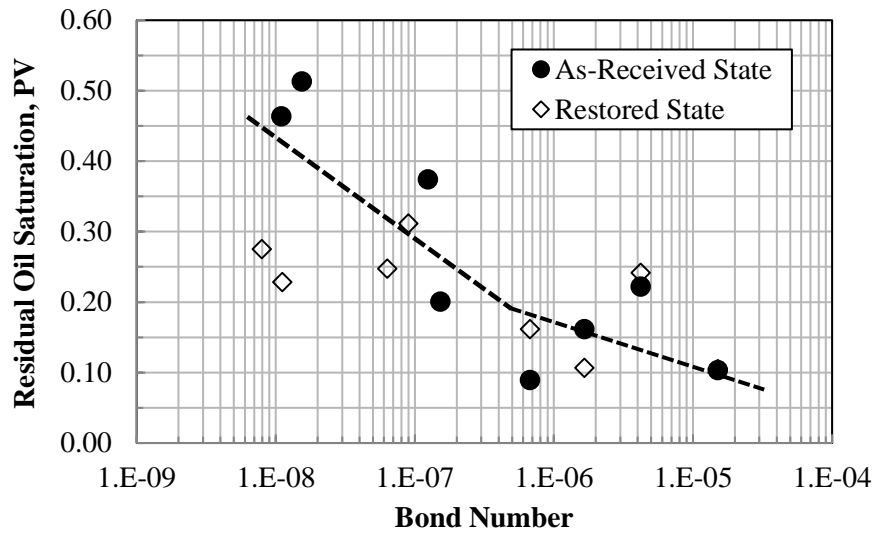
Figure 7: The residual oil saturation (inlet S_{or}) vs. microscopic Bond number in carbonate rocks. The dashed line indicates the continuous reduction of ROS along the increase of Bond number in the non-water wet cores, without the presence of critical Bond number.
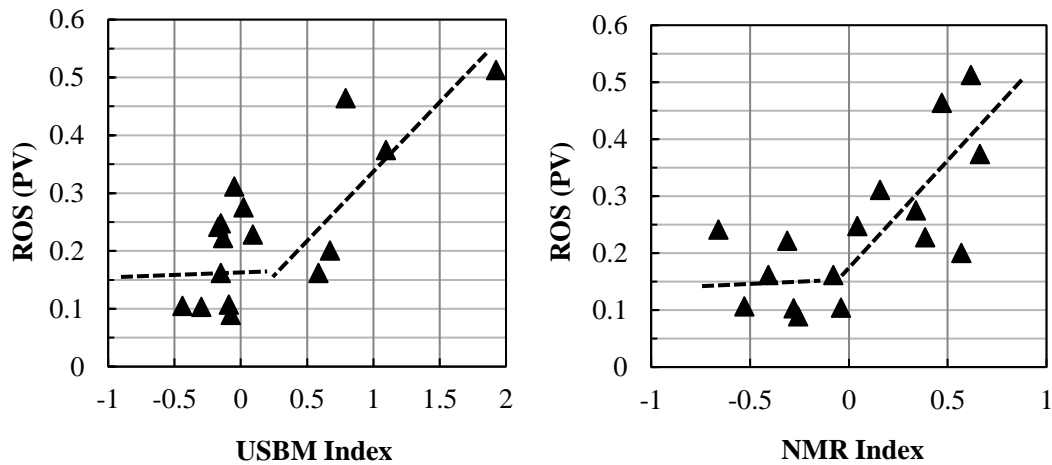
Figure 8: The residual oils saturation vs. wettability indices. The dashed lines imply the presence of stabilized ROS when the wettability index less than 0.

Table 1: The lists of quantitative and qualitative methods to measure wettability

Quantitative Methods	Qualitative Methods
Contact Angle	Imbibition
Amott-Harvey	Floatation
USBM	Relative Permeability
Amott-USBM	Capillary Penetration
NMR Measurement	Glass slide
	Electrical resistance

Table 2. The results of contact angle measurement (1A: ambient; 1B: reservoir conditions)

Figure No.	Temp °F	Pressure Psig	Formation Brine Density g/cm³	Oil Density g/cm³	Contact Angle degree
1A	71	0	1.140	0.816	144.7
1B	250	3800	1.108	0.685	111.4

Table 3: Summary of AH and USBM indices for four rock types

Wettability State	Sample	RRT	Depth (ft)	AH Index	USBM Index	Wettability Description
As-Received State	2A	2	8289.75	-0.23	-0.30	Slightly oil-wet
	2B	2	8384.00	-0.21	-0.13	Slightly oil-wet
	4A	4	8289.90	-0.08	-0.07	Neutral wet
	4B	4	8289.50	0.40	0.59	Water-wet
	6A	6	8297.30	0.57	0.67	Strongly water-wet
	6B	6	8396.98	0.72	1.09	Strongly water-wet
	8A	8	8363.90	0.71	1.92	Strongly water-wet
	8B	8	8374.61	0.82	0.79	Strongly water-wet
Restored Wettability State	2A	2	8289.75	-0.10	-0.44	Slightly oil-wet
	2B	2	8384.00	-0.33	-0.17	Slightly oil-wet
	4A	4	8289.90	-0.16	-0.15	Neutral wet
	4B	4	8289.50	-0.27	-0.09	Neutral wet
	6A	6	8297.30	0.05	-0.15	Neutral wet
	6B	6	8396.98	0.03	-0.05	Neutral wet
	8A	8	8363.90	0.05	0.09	Neutral wet
	8B	8	8374.61	0.10	0.02	Neutral wet

Table 4: Summary of core saturation and NMR T_2 relaxation time for Plug 6A

DESCRIPTION	CORE S_w%	T_2 Mode (ms)	T_2 Log Mean (ms)
As-Received Wettability State			
100% S_w	100.0	125.9	167.9
S_{wi} to Oil	15.9	501.2	159.6
S_{or} to brine	23.7	79.4	167.6
S_{wi} to Oil 2nd drainage	12.6	398.1	200.5
100% S_o	0.0	158.5	98.7
Restored Wettability State			
100% S_w	100.0	125.9	167.9
S_{wi} to Oil before aging	28.1	398.1	203.5
S_{wi} to Oil after aging	28.1	316.2	148.2
S_{or} to brine	31.6	199.5	187.1
S_{wi} to Oil 2nd drainage	32.9	316.2	146.6
100% S_o	0.0	158.5	98.7
Bulk Fluid T_2 Measurement			
Crude Oil ($T_{2b, oil}$)	Bulk fluid	1259	711
Formation brine ($T_{2b,w}$)	Bulk fluid	2512	2512

Table 5. The wettability index derived from Fleury model and Hirasaki Model

Sample	RRT	Depth (ft)	Fleury Model		Hirasaki Model	
			NMR Index (T_2 Mean)	NMR Index (T_2 Mode)	NMR Index (T_2 Mean)	NMR Index (T_2 Mode)
Wettability Index: As-Received State Plugs						
2A	2	8289.75	-0.23	-0.28	-0.23	-0.30
2B	2	8384.00	-0.20	-0.31	-0.21	-0.13
4A	4	8289.90	-0.23	-0.26	-0.37	-0.28
4B	4	8289.50	-0.25	-0.41	-0.49	-0.59
6A	6	8297.30	0.44	0.57	0.48	0.92
6B	6	8396.98	0.29	0.66	0.24	0.63
8A	8	8363.90	0.07	0.62	0.05	0.60
8B	8	8374.61	0.18	0.47	0.13	0.34
Wettability Index: Restored State Plugs						
2A	2	8289.75	-0.10	-0.04	-0.17	-0.07
2B	2	8384.00	-0.33	-0.66	-0.46	-1.12
4A	4	8289.90	-0.16	-0.08	-0.24	-0.09
4B	4	8289.50	-0.27	-0.53	-0.53	-0.99
6A	6	8297.30	0.05	0.04	0.05	0.03
6B	6	8396.98	0.03	0.16	0.04	0.14
8A	8	8363.90	0.05	0.39	0.06	0.39
8B	8	8374.61	0.10	0.34	0.12	0.23

Table 6. Residual oil saturation after forced imbibition vs. wettability indices

Wettability State	Sample	NMR Index (T_2 Mode)*	USBM Index	Abs. Perm Kw, md	Trapping Number	S_{or} after imbibition*
As-Received State	2A	-0.28	-0.30	357.03	1.51E-05	0.10
	2B	-0.31	-0.13	103.79	4.22E-06	0.22
	4A	-0.26	-0.07	16.16	6.75E-07	0.09
	4B	-0.41	0.59	40.28	1.66E-06	0.16
	6A	0.57	0.67	1.62	1.53E-07	0.20
	6B	0.66	1.09	2.24	1.24E-07	0.37
	8A	0.62	1.92	0.28	1.54E-08	0.51
	8B	0.47	0.79	0.20	1.10E-08	0.46
Restored Wettability State	2A	-0.04	-0.44	357.03	1.51E-05	0.10
	2B	-0.66	-0.17	103.787	4.22E-06	0.24
	4A	-0.08	-0.15	16.16	6.75E-07	0.16
	4B	-0.53	-0.09	40.28	1.66E-06	0.11
	6A	0.04	-0.15	1.62	6.35E-08	0.25
	6B	0.16	-0.05	2.24	8.99E-08	0.31
	8A	0.39	0.09	0.28	1.12E-08	0.23
	8B	0.34	0.02	0.20	7.95E-09	0.28

*Note: S_{or} was calculated as the inlet oil saturation using Forbes 2nd solution.

TOWARD A METHOD FOR MEASURING WETTABILITY IN POROUS MEDIA BY NMR WATER VAPOR ISOTHERM TECHNIQUE

Hyung T. Kwak and Ahmad M. Harbi
Saudi Aramco, Dhahran, Saudi Arabia, 31311

Yan Song
Department of Applied Physical Sciences, University of North Carolina, Chapel Hill, NC 27599-3255, USA

Alfred Kleinhammes and Yue Wu
Department of Physics and Astronomy, University of North Carolina, Chapel Hill, NC 27599-3255, USA

ABSTRACT

The wettability of reservoir rocks is one of the most important factors in evaluating hydrocarbon reserves and producibility. Reservoir rocks contain considerable amounts of pore spaces to trap and transport fluids including hydrocarbons and brine. Although those pore spaces are essential and beneficial for hydrocarbon production, the porous nature of reservoir rocks, on the other hand, poses difficulties for measuring the wettability. Macroscopic experiments, such as a contact angle determination, are of limited value because the wettability needs to be determined within the rock pore structure. Here, we propose a new method for measuring the wettability of porous media by Nuclear Magnetic Resonance (NMR) water vapor isotherm technique. It could provide insight into the molecular dynamics at the interface between fluids and surfaces by analyzing different total amount of adsorbed water vapor and shapes of the measured water vapor isotherm as a function of relative vapor pressure. Since the NMR water vapor isotherm is affected not only by water molecule affinity for the pore surface but also by other factors controls wettability of the surface, it could provide the wettability information of pore surface within porous materials. An additional advantage of NMR water vapor isotherm wettability measurement is it is able to measure the wettability of nano-sized pore surface since gas is injected instead of liquids in the case of other conventional wettability measurement methods.

In the current work, the isotherms taken on the soda lime glass beads with different wetting properties prove that our approach is indeed capable of distinguishing between hydrophobic and hydrophilic surface states which are directly related to the wettability. The consistency of the contact angle measurement is also discussed. The new NMR method can be further applied to

study reservoir core rocks, leading to new insights that are needed in optimize hydrocarbon production.

INTRODUCTION

The wettability of the porous structure within rocks is one of the key parameters that determine the fluid flow through those rocks. Consequently, it is one of the essential input variables for geophysical models that predict flow through reservoir rocks. Wettability is often used as a distinguishing characteristic of materials, designating them as hydrophobic (water fearing), or hydrophilic (water loving). However, it is not just a material parameter characteristic of a given rock but depends on other factors as well, such as surface roughness, surface size, existence of primary adsorption sites, and specific ion effect. Therefore, it is not sufficient to determine the wettability of an idealized surface by using a water drop and measuring the contact angle as a decisive indication of the ability of the surface to attain moisture. Moreover, in terms of rock pore structure, macroscopic experiments, i.e. contact angle determination, are of limited value. Other common wettability measurement methods for porous media, such as Amott-Harvey and USBM methods are indirect method which are prone to a considerable margin of errors from the unavoidable multiple experimental procedures. In addition, these methods only measure the global wettability which has is not sufficient for porous media with heterogeneous pore structures such as carbonate.

Two forces determine the wettability of solid surface, adhesion and cohesion force. The adhesion force is the tendency of liquid molecules to create an attraction to a different substances and the cohesion force is that of liquid to create the minimum possible surface area. The affinity of water molecule to the solid surface, which is the hydrophobicity (or hydrophilicity) of solid surface, is caused by the adhesive force between liquid and solid. Thus, the hydrophobicity is directly relate to the wettability of solid surface.

NMR has been proven to be a good technique to determine the hydrophobicity within porous materials. For example, using NMR, Wang et al. shows that the shape of water adsorption isotherm in micropore environments strongly depends on the surface hydrophobicity; hydrophobic surfaces produce a concave shape, while hydrophilic surfaces lead to a convex isotherm, corresponding to Type III and Type I, II, respectively of the IUPAC classification of isotherms [1]. In addition to the isotherms, NMR can also provide insight into the molecular dynamics at the interface by probing the relaxation processes (T_1, T_2) [2, 3]. This additional information sheds light on the interactions between the water molecules and the hydrophilic or hydrophobic surface [4].

In the current work, we focus on surfaces where external stimuli can trigger changes in surface hydrophobicity. The resulting change in surface wetting is observed by monitoring the change in the static contact angle and NMR-detected water vapor isotherm. Clear differences of the NMR water vapor isotherm curves from hydrophilic and hydrophobic porous materials has been observed and analyzed.

Methods
Materials

The soda lime glass beads and microporous silica beads (> 98% SiO_2 and < 2% B_2O_3) are purchased from Mo-Sci Corporation and used as purchased without further purification. The soda

lime glass beads are solid and nonporous; their morphologies are shown in Figure 2. Three different soda lime glass beads are used: 20, 40 and 400 μm in diameter, respectively. The diameter of microporous silica beads is 8 μm. Sulfuric acid solution (4N), glass wafers made of soda lime and Chloro(dodecyl)dimethylsilane (purity > 95%) are purchased from Fisher Scientific.

Surface Wettability Modification

The surface hydrophobicity (or wettability) of glass beads and glass wafers are modified by two different chemical treatments. Hydrophilic surface is obtained through acid wash treatment. Clean glass beads or glass wafers are immersed in 2M sulfuric acid solution for 24 h. The acid-treated samples are subsequently rinsed with distilled water and dried in the lab for two days. Hydrophobic surface is obtained via the silane-coating method [6-8]. Clean glass beads or glass wafers are immersed in the Chloro(dodecyl)dimethylsilane for 24 h. The reaction can be represented as follows.

$$CH_3(CH_2)_{11}Si(CH_3)_2Cl + -Si-OH \rightarrow -Si-O-Si(CH_3)_2(CH_2)_{11}CH_3 + HCl \qquad (1)$$
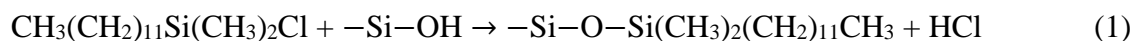
Following the silane coating, the treated sample is rinsed with ethanol to wash off any remaining organic materials.

Contact Angle Measurement

Static contact angles are measured using CAM 200 optical contact angle meter (KSV instruments). A water droplet of 2 μL is formed at the end of the syringe and carefully deposited onto the sample surface. The images of static contact angle are taken within 5s of water deposition by a charge coupled device (CCD) camera. Static contact angle is calculated by vendor-supplied software.

NMR-detected Isotherm

The water isotherms are measured at a home-made in situ NMR system on a 34 MHz magnet at 293 K. The in situ NMR isotherm system enables us to selectively detect the adsorbed water on the surface with high sensitivity. As illustrated in Figure 1a, the basic components are a vacuum chamber connected to a mechanical pump, a pressure gauge, the NMR sample tube, and the source of water vapor. Shown in the left figure of Figure 1b, in each measurement, equal amounts of treated 20-μm and 400-μm beads are first mixed thoroughly and then loaded into the sample tube. The inner diameter of the sample tube is 3.9 mm and the length (height) of packed sample is 5 cm. The sample tube with the loaded sample is then shaken carefully to get random close packing. The ^{1}H free-induction-decay (FID) signal of the dry sample is then acquired by a single-pulse excitation with pulse duration of 8 μs. The waiting interval between each repetition of the pulse sequence is set long enough, longer than $5T_1$, to ensure that the signal is fully recovered after each scan. A broad peak of 500 ppm (full width at half-maximum, FWHM) is observed in the background spectrum and is subtracted from subsequent spectra. Water vapor is then loaded to the sample at varying vapor pressures, and the NMR spectra of the hydrated samples are acquired. The intensity of the ^{1}H NMR signal is calibrated with a test tube of bulk water of known mass.
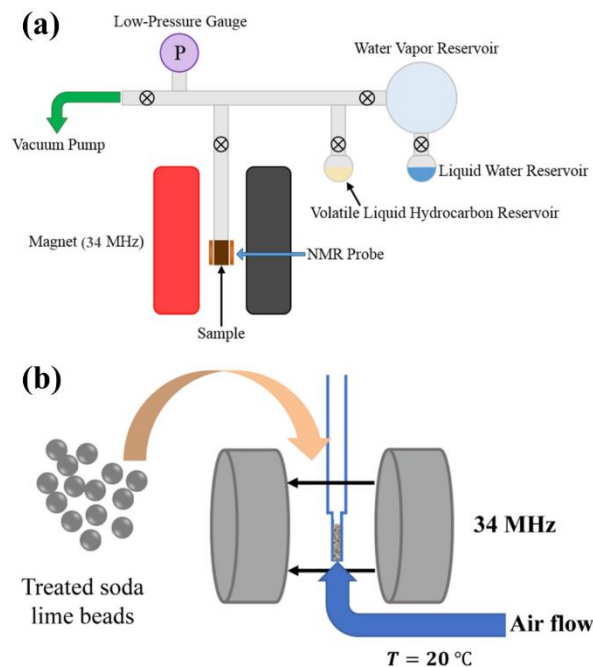
Figure 1. (a) 34 MHz magnet and water vapor delivery system with vapor expansion bulb, distribution chamber, pressure gauge, pump connection, and sample tube. (b) Treated glass beads are first loaded into the sample tube. The sample tube is subsequently attached to the water vapor delivery system and maintained at 20 ℃ by air flow.

Results and Discussion

Two different chemical treatments have been applied to modify the surface wettability. The morphology and particle size of soda lime glass beads before and after surface modifications are determined by scanning electron microscope (SEM). In Figure 2, SEM images show that the three representative samples, assigned as unmodified, hydrophilic and hydrophobic glass beads, have uniform spherical morphology in large domains. All three samples contain uniform spheres with a size of approximately 40μm, which agrees well with the supplier's characterization (particle size ranging from 38 to 45μm).
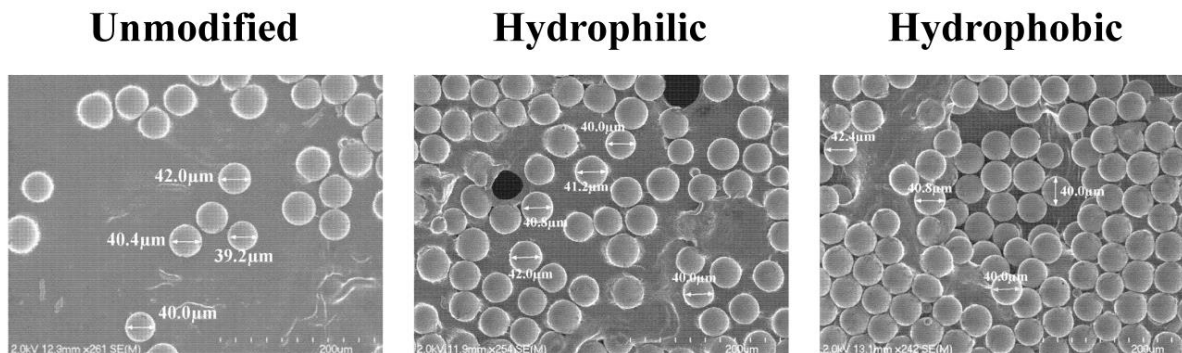
Figure 2. SEM images of soda lime glass beads with unmodified (left), hydrophobic (right) and hydrophilic (middle) surface, respectively.

The resulting change in surface wetting is characterized by monitoring the change in static contact angle and NMR-detected water isotherm. Figure 3 shows the static contact angles of water on

unmodified, hydrophilic and hydrophobic treated glass surfaces, respectively. The macroscopic contact angle of the unmodified glass surface is ~59°, indicating that soda lime glass surface is intrinsically mildly hydrophilic. After Silane coating, the contact angle increases to ~95° , indicating a much better degree of hydrophobicity compared to the unmodified surface. The strong hydrophobicity of the silane-coated surface comes from the outermost long alkyl chains ($-(CH_2)_{11}CH_3$), which is verified by the strong ^1H NMR signal in the dry sample (see Figure 4). Soda lime glass surface after acid wash is clearly tuned to hydrophilic with contact angle ~24°. Hence, through different chemical modification methods, the wetting behavior of the surface can be controlled from hydrophobic to hydrophilic. In the following isotherm measurements, identical chemical modification methods are applied to soda lime glass beads. Since the chemical composition of glass beads and glass surfaces are similar, it is assumed that the chemical treatments also work for glass beads, resulting similar surface wettability.
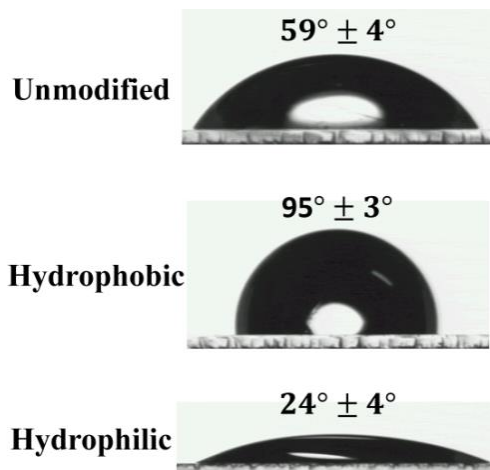
Figure 3. Images of water drops on glass wafers with unmodified, hydrophobic and hydrophilic treatment, respectively.
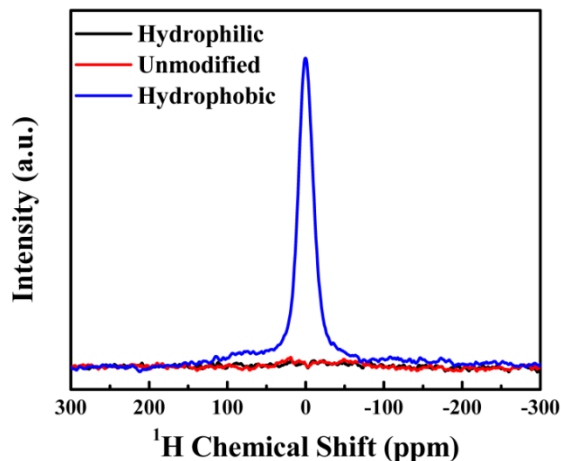
Figure 4. ^1H NMR spectra of dry glass beads after different chemical modifications. A strong ^1H signal is observed in the hydrophobic treated glass beads due to the long chained coating polymer ($-(CH_2)_{11}CH_3$). The ^1H peak of hydrophobic coated glass beads is set at 0 ppm. The bulk water proton peak is hence centered at 4.19 ppm.

NMR-detected water vapor isotherms of hydrophilic (red), hydrophobic (blue) and unmodified (black) soda lime glass beads at 20 °C are shown in Figure 5. For the hydrophobic treated glass beads, the water isotherm is nearly flat to the P/P_0 axis over its entire range and therefore demonstrates that the silane coated glass beads are more hydrophobic than the unmodified beads. This isotherm data is consistent with the contact angle result above. In contrast, compared with the hydrophobic treated glass beads, a significantly larger amount of water adsorption is observed on the hydrophilic-treated glass beads. Specifically, the amount of water adsorbed on the hydrophilic beads at the same relative pressure is larger than both the unmodified and hydrophobic sample, indicating a greater degree of hydrophilicity. As expected, the water vapor isotherm of unmodified glass beads lies between the hydrophilic and hydrophobic curves. The above isotherm results agree very well with the wetting properties obtained from the contact angle measurement. It demonstrates that water vapor isotherms can clearly distinguish between hydrophobic and hydrophilic surfaces embedded in a granular or porous structure, which the contact angle measurement cannot achieve. This is of particular importance in determining the wetting properties of rocks.
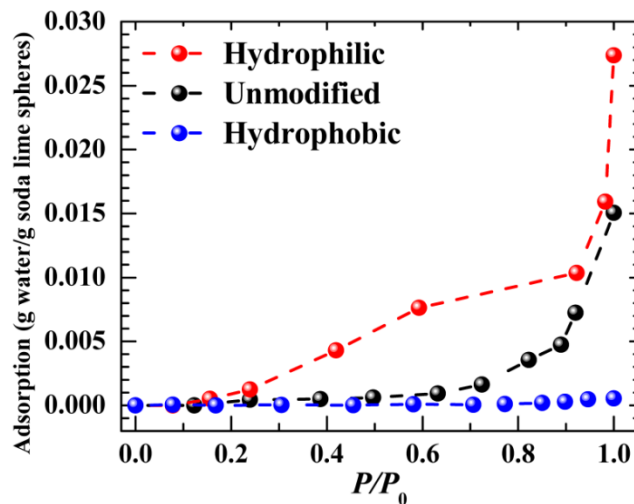
Figure 5. NMR-detected water isotherms of hydrophilic (red), hydrophobic (blue) and unmodified (black) soda lime glass beads at 20 ℃.

Figure 6 and 7 show NMR-detected water vapor isotherms of glass beads with 2 different sizes, 20 and 400 μm in diameter with different surface hydrophobicity. The pore sizes created by these glass beads when packed separately are similar to those of macro- and micropores of Middle East Arab formation carbonates, ~5 and ~100μm, respectively [9]. Figure 6 illustrates the mass ratio of adsorbed water to glass beads with respect to the relative pressure. Not surprisingly, the sample (black curve), consisting of hydrophilic treated 20 μm and hydrophilic treated 400 μm beads, adsorbs the largest amount of water. This is because all the exposed surfaces of this sample have been rendered hydrophilic, leading to strong water adsorption. The amount of adsorbed water on another sample (yellow curve), containing hydrophilic treated 20 μm and hydrophobic treated 400 μm beads, is close to the sample with both hydrophilic beads. In contrast, the sample (blue curve), consisting of hydrophobic treated 20 μm and hydrophobic treated 400 μm beads, adsorbs the least amount of water.
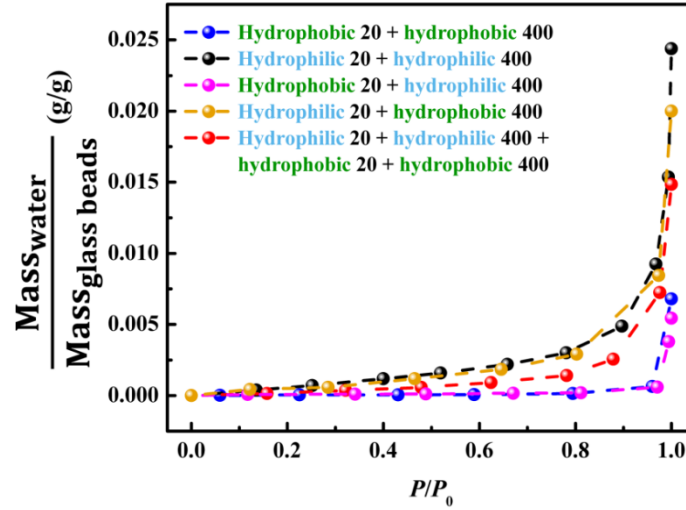
Figure 6. NMR-detected water vapor isotherms of glass beads with 2 different sizes, 20 and 400 μm diameter with different surface hydrophobicity.

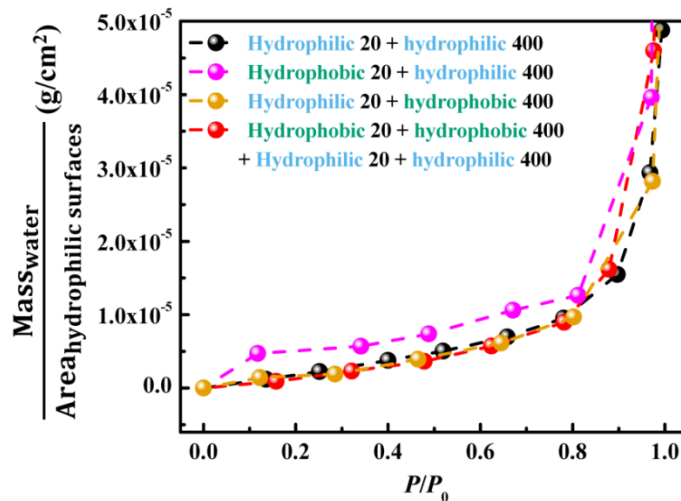In order to understand the adsorption mechanism, a quantitative relationship between the relative pressure and the ratio of water adsorption mass to the total hydrophilic surface area in each sample is analyzed. Figure 7 shows the $Mass_{water}/Area_{hydrophilic\ surface}$ vs. P/P_0. The total hydrophilic surface area is determined as follows, for example, for the hydrophilic 20 μm and hydrophilic 400 μm glass beads mixture sample,

hydrophilic surface area =

$$\frac{mass(20\ \mu m\ beads)}{\frac{4}{3}\pi*(10\ \mu m)^3*1.3g/cm^3}*4\pi*(10\ \mu m)^2 + \frac{mass(400\ \mu m\ beads)}{\frac{4}{3}\pi*(200\ \mu m)^3*1.3g/cm^3}*4\pi*(200\ \mu m)^2 \qquad (1)$$

,where $mass(20\ \mu m\ beads)$ and $mass(400\ \mu m\ beads)$ are the masses of the glass beads with diameter of 20 μm and 400μm, respectively. 1.3 g/cm^3 is the bulk Density of Dry Beads. Eq. (1) can be applied to all the samples. The sample, consisting of hydrophobic treated 20 μm and hydrophobic treated 400 μm beads, is not included in Figure 7 because it contains no hydrophilic surface area. Different from Figure 6, all curves in Figure 7 overlap with each other very well, indicating that the water vapor adsorption mainly depends on the total hydrophilic surface area. Moreover, it can be concluded that the water vapor adsorption in our glass beads sample is dominated by the surface adsorption. This conclusion is crucial for core rock surface modification and further analysis.

Figure 7. The quantitative relationship between the relative pressure and the ratio of water adsorption mass to the total hydrophilic surface area: $Mass_{water}/Area_{hydrophilic\ surface}$ vs. P/P_0.

To further elucidate the new water vapor isotherm technique, microporous silica beads of 8 μm in diameter are tested. In Figure 8, the isotherm obtained with the silica beads as received is shown in blue dots. Untreated beads adsorb water within the micropores, diameter about 5μm, at low relative pressure ($P/P_0 < 0.2$). Above $P/P_0 \sim 0.2$, water vapor starts filling the macropores, diameter about 100μm, between beads due to capillary condensation. A big difference in adsorption is observed for the hydrophobic treated surfaces. The red triangles show the isotherm after the beads are rendered hydrophobic via the silane coating. In the initial nanopores filling stage, $0 < P/P_0 < 0.2$, Silane coating has no influence on the water vapor adsorption. This is because the nanopores are too narrow to accept the long chained Chloro(decyl)dimethylsilane and remain uncoated, which allow the much smaller water molecules to adsorb. However, above $P/P_0 \sim 0.2$, water vapor adsorption occurs in the intergranular space between beads, which has been turned to hydrophobic via Silane coating. Thus, the isotherm changes to flat when $P/P_0 > 0.2$.
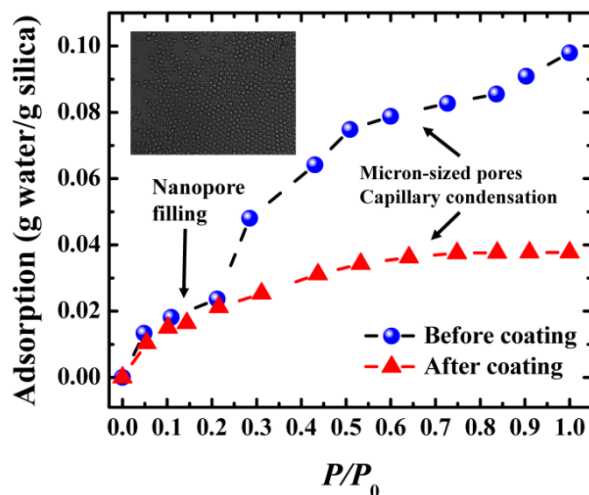
Figure 8. NMR-detected water isotherms of unmodified (blue) and hydrophobic treated (red) microporous silica beads at 20 ℃. Insert: SEM image of beads.

CONCLUSION

Wettability of reservoir rocks plays an important role in hydrocarbon recovery. However, characterizing the wettability of reservoir rock is particularly challenging due to the complex porous network inside the rock. In this paper, we propose a new method for measuring the wettability of porous media by NMR water vapor isotherm technique. The NMR-detected water vapor isotherms are taken on soda lime glass beads with different wetting properties vary from hydrophilic to hydrophobic, which are obtained through different chemical modifications. The contact angle measurements show that the silane coating can make water contact angle increase from 59° (unmodified surface) to 95°, indicating a stronger hydrophobicity; the acid wash can decrease the contact angle to 24°, indicating a stronger hydrophilicity. NMR-detected isotherms show that no water adsorbs on the hydrophobic glass beads. In contrast, a significantly larger amount of water adsorption is observed on the hydrophilic-treated sample. All of the isotherm data are consistent with contact angle measurements. The new NMR method can be further applied to study the wettability of core rocks, leading to new insights that are needed in improved oil production. Currently, we are further developing the current method to quantify the degree of pore surface hydrophobicity from reservoir rocks core sample, in the form of hydrophobicity index which is directly related to wettability index [10].

REFERENCES

1. Wang, H.-J.; Xi, X.-K.; Kleinhammes, A.; Wu, Y. Temperature-Induced Hydrophobic-Hydrophilic Transition Observed by Water Adsorption. *Science* **2008,** *322* (5898), 80-83.
2. Bloembergen, N.; Purcell, E. M.; Pound, R. V. Relaxation Effects in Nuclear Magnetic Resonance Absorption. *Physical Review* **1948**, 73 (7), 679-712.
3. Carr, H. Y.; Purcell, E. M. Effects of Diffusion on Free Precession in Nuclear Magnetic Resonance Experiments. *Physical Review* **1954**, 94 (3), 630-638.
4. Wang, H.-J.; Kleinhammes, A.; McNicholas, T. P.; Liu, J.; Wu, Y. Water Adsorption in Nanoporous Carbon Characterized by in Situ Nmr: Measurements of Pore Size and Pore Size Distribution. *The Journal of Physical Chemistry C* **2014,** *118* (16), 8474-8480.
5. Song, Y.; Chong, Y.; Raghavan, A.; Xing, Y.; Ling, Y.; Kleinhammes, A.; Wu, Y. Nucleation and Growth Process of Water Adsorption in Micropores of Activated Carbon Revealed by Nmr. *The Journal of Physical Chemistry C* **2017**, *121* (15), 8504-8509.
6. Fuji, M.; Iwata, H.; Takei, T.; Watanabe, T.; Chikazawa, M. The Change in Wettability and Structure of Silica Powder Surfaces Modified with Hexamethyldisilazane. *Advanced Powder Technology* **1999,** *10* (2), 187-198.
7. Naono, H.; Fujiwara, R.; Yagi, M. Determination of Physisorbed and Chemisorbed Waters on Silica Gel and Porous Silica Glass by Means of Desorption Isotherms of Water Vapor. *Journal of Colloid and Interface Science* **1980,** *76* (1), 74-82.
8. Takei, T.; Yamazaki, A.; Watanabe, T.; Chikazawa, M. Water Adsorption Properties on Porous Silica Glass Surface Modified by Trimethylsilyl Groups. *Journal of Colloid and Interface Science* **1997,** *188* (2), 409-414.
9. Cantrell, D.L.; Hagerty, R.M. Microporosity in Arab Formation Carbonates, Saudi Arabia. *GeoArabia* **1999**, 4 (2), 129-154.
10. Kwak, H.T.; Al-Harbi, A.M. Nuclear Magnetic Resonance Gas Isotherm Technique to Evaluate Reservoir Rock Wettabilty. US Patent 2016/0313267 A1 **2016.**

Evaluation of Core Heterogeneity Effect on Pulse-decay Experiment

Bao Jia, Jyun-Syung Tsau and Reza Barati
University of Kansas

ABSTRACT

Microcrack and heterogeneity are essential to tight oil and gas production, but there exits great uncertainty and challenge to evaluate them even at the core scale. Pulse-decay experiments are routinely used to measure petrophysical properties of tight cores. In this study, effects of permeability magnitude and location of the microcrack on pulse-decay experiments are numerically evaluated based on our experimental scenarios. The simulation model is three dimensional with dual permeability and concentrates the fracture in the middle of the core. Permeability value of the core in each grid is populated homogeneously and heterogeneously, and different correlation lengths are used to describe the spatial distribution patterns.

Pulse-decay experiments are performed on a tight carbonate core by flowing helium in both forward and reverse directions under different pressures. A preferential flow path is discovered even when the microcrack is not present in a tight core. We suggest that very early pressure response in a pulse-decay experiment should be closely examined to identify the preferential flow path, and failure to identify the preferential flow path leads to significant porosity and permeability underestimation.

INTRODUCTION

Table 1 chronologically lists representative work of exploring petrophysical properties using pulse-decay method since 1968. Among them the work by Kamath et al. (1992), Ning (1992), Cronin (2014) and Alnoaimi (2016) are highlighted for this study as they explored heterogeneity/microcrack related petrophysical properties. Kamath et al. (1992) combined two separate cores with different values of permeability and flowed water through them from forward and reverse directions. They evidenced qualitatively that the pressure responses are direction dependent, implying that heterogeneity plays a role affecting the pulse-decay experiment. They also demonstrated the dual porosity phenomenon in a fractured core. Ning (1992) analytically and numerically explored the dual porosity and dual permeability phenomenon in a fractured core. Cronin (2014) proposed a layered simulator to continuously study effects of heterogeneity and fracture on the pressure response in a pulse-decay experiment. Alnoaimi (2016) performed pulse-decay experiments in fractured shales using helium and carbon dioxide, and made efforts to history match the pressure curves.

Authors	Contributions
Brace et al. (1968)	Firstly applied pulse-decay method to measure permeability of granite
Lin (1977)	Put forward the basic numerical model for pulse-decay process
Hsieh et al. (1981)	Presented complete and restrictive analytical solution for pulse-decay process
Dicker and Smits (1988)	Simplified the complete analytical solution with acceptable accuracy
Kamath et al. (1992)	Characterized heterogeneity and microcrack of synthetic cores using pulse-decay method
Ning (1992)	Explored dual porosity and dual permeability of fractured cores analytically and numerically
Jones (1997)	Proposed valuable recommendations for pulse-decay experimental set-up design, for example, using cores with large diameter and short length
Cui et al. (2009)	Extended the flowing fluid from non-adsorptive gas to adsorptive gas
Civan (2010), Civan et al. (2010)	Incorporated other important variables in the numerical settings of pulse-decay
Cronin (2014)	Numerically explained impacts of anisotropy and microcrack on pulse-decay pressure response
Alnoaimi (2016)	Numerically matched pressure curves of non-adsorptive gas and adsorptive gas during a pulse-decay experiment
Jia et al. (2017a)	Comprehensively investigated flow behaviors of adsorptive and non-adsorptive gas in a wide range of pressure in a tight core using pulse-decay method

Table 1 Representative work regarding pulse-decay method in tight cores

In the light of the previous work, we constructed a three dimensional, dual permeability numerical model to demonstrate clearly how the permeability magnitude and different location of the microcrack in a tight core, and how the permeability heterogeneity and spatial distribution patterns affect pressure responses in a typical pulse-decay experiment. Kamath et al. (1992) investigated heterogeneity effect by flowing water and combing two separate cores, and in this work we use one core and flow gas from both the forward and reverse directions to observe the different flow behaviors. During the course of the experiment a preferential flow path is discovered in a natural heterogeneous core sample even a microcrack not present. We suggest the very early beginning of pressure response reveals the preferential flow path, and it should be emphasized in a general pulse-decay experiment.

Procedure

Fig. 1 shows the pulse-decay experimental set-up. It is mainly composed of four components: first upstream reservoir U_1, second upstream reservoir U_2, core holder and downstream reservoir D. To investigate properties of a tight core under a certain pore pressure, one needs to inject gas into the system by constant pressure with valves V_1 and V_2 opened, and V_3 closed. Subsequently, a pressure pulse is introduced into U_1 with V_2 closed. Finally after V_2 is opened and V_1 closed, the upstream pressure starts to decline and the downstream pressure rise. Analyzing these two pressure curves enables one obtain petrophysical properties of the core sample.
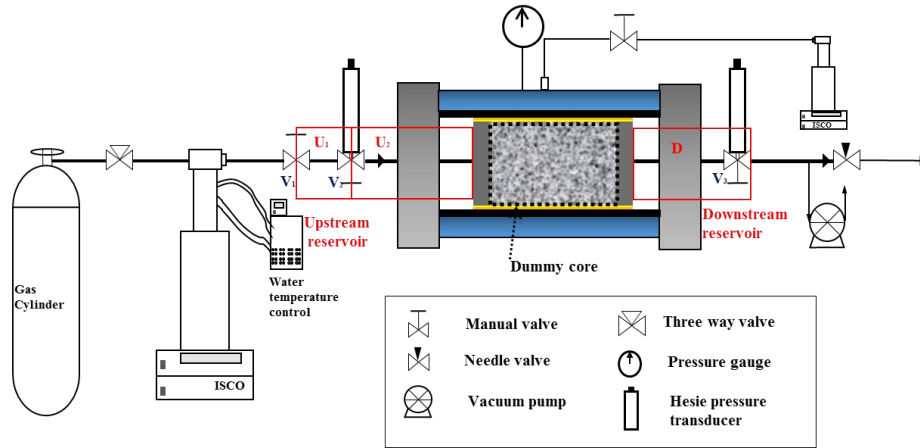
Fig. 1 Pulse-decay experimental set-up

Based on the experimental scenarios, a three dimensional model is constructed to numerically evaluate effects of microcrack and heterogeneity on the pressure response. Table 2 lists the details of the numerical setting of the core. A commercial reservoir simulator is used in this study (IMEX, 2015). The circular section is squared with the same cross-sectional area. The fracture is located in the fifth layer of the core.

length, cm	5.08	grid number	16*8*8
width, cm	3.38	porosity, fraction	0.02
grid size, cm	0.32*0.42*0.42	matrix permeability, mD	0.1

Table 2 Numerical setting for the core
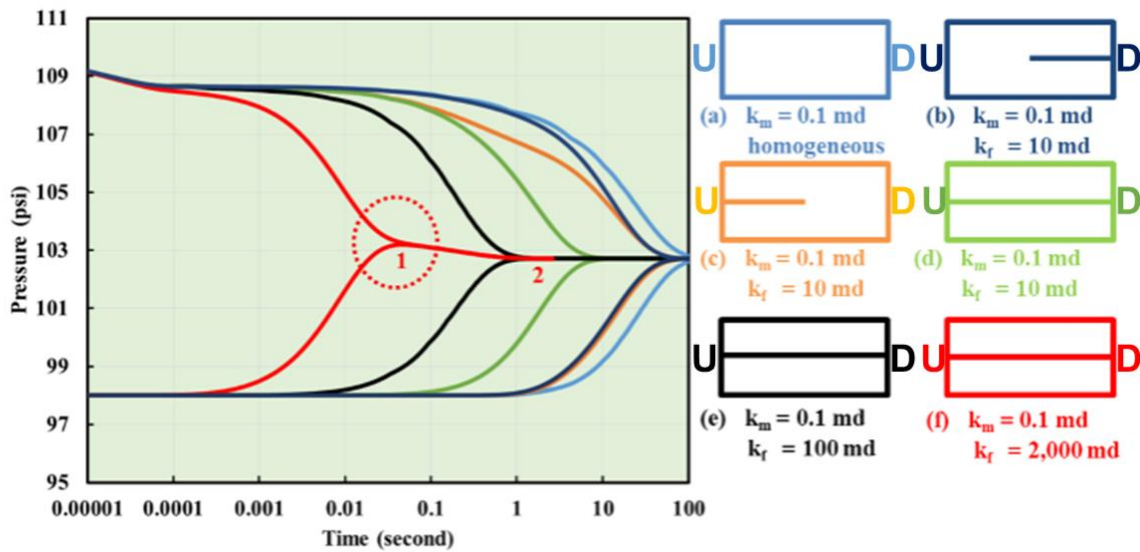
Fig. 2 Comparison of upstream and downstream pressure responses in six different core model configuration (a) homogeneous core with permeability of 0.1 mD (b) heterogeneous core with fracture of 10 mD at the rear half of the core (c) heterogeneous core with fracture of 10 mD at the front half of the core (d) heterogeneous core with fracture of 10 mD throughout the core (e) heterogeneous core with fracture of 100 mD throughout the core (f) heterogeneous core with fracture of 2,000 mD throughout the core. U represents upstream and D represents downstream.

Initially the core is saturated with helium and the downstream reservoir is maintained at 98 psi. A 10% of the initial pressure pulse was applied in the upstream reservoir. One homogeneous and five heterogeneous simulation scenarios are constructed to observe the impact of the microcrack. Fig. 2 plots pressure curves in the upstream and downstream in the six scenarios. An abrupt pressure decrease is observed at the very beginning as gas expands freely from the first upstream reservoir to the second upstream reservoir. Comparing the homogeneous scenario (a) and heterogeneous scenarios shows fracture expedites gas flow process, which is as expected. Comparing (b) and (c) shows that upstream pressure is sensitive to the microcrack location but downstream pressure is not. Upstream pressure curve in (c) declines much faster than that in (b), but downstream pressure curves come closest to coinciding in shape between (b) and (c).When permeability of the fracture increases to 10 mD and 100 mD in scenario (d) and (e), respectively, less time is required for the gas pressure in the upstream and downstream to reach equilibrium with a more permeable microcrack. As the permeability of microcrack increases to 2,000 mD, a "hump" region (red dashed circle) is formed before final pressure equilibrium (Alnoaimi, 2016). This behavior is caused by the "flow back" phenomenon (Fig. 3). Gas in the fracture travels faster and arrives at the downstream earlier than in the matrix, causing a "pseudo" equilibrium pressure at point 1 (Fig.2) when upstream pressure curve and downstream pressure curve converge. Afterwards gas in the downstream starts to flow back towards the upstream direction, and pressure continues to decrease until reaching the final equilibrium pressure at point 2 (Fig. 2).
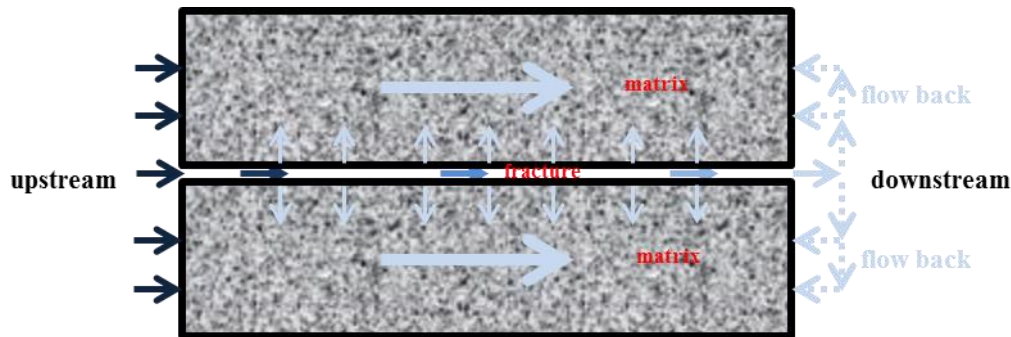
Fig. 3 Flow back phenomenon if a microcrack is present in the core.

Comparing (d), (e) and (f) reveals that, to identify a microcrack in a typical pulse-decay experiment, the difference of permeability between matrix and fracture must be large enough. After performing a series of sensitivity analysis by changing reservoir volume and pressure pulse size, two approaches are suggested to help identify the microcrack if the permeability difference is small: one is to reduce the reservoir volume and the other one is to reduce pressure pulse size. Actually, Kamath et al. (1992) experimentally concluded that using small vessels helps detect core heterogeneity. It is worthwhile to notice that, if a steady-state method is used to measure the permeability, the result should be independent of the microcrack location, as the permeability is calculated based on the total pressure drop across the core.
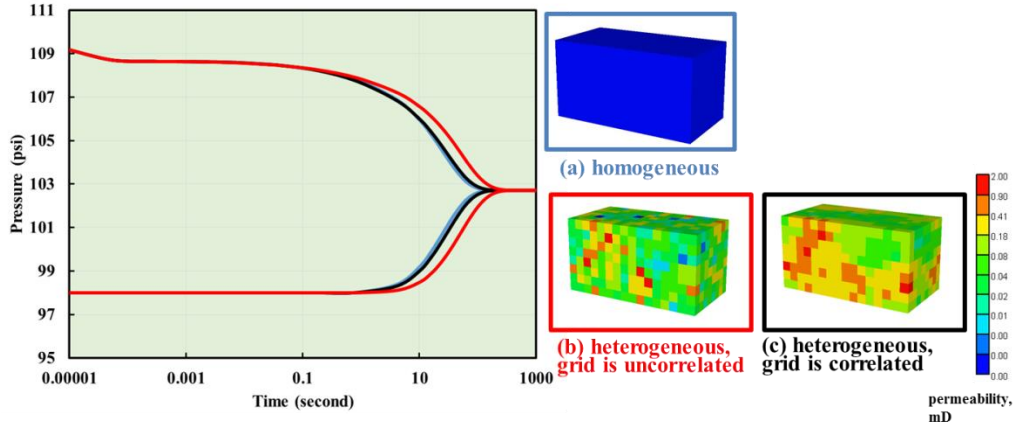
Fig. 4 Comparison of pressure response in upstream and downstream of the core in three simulation scenarios (a) homogeneous core with permeability of 0.1 mD (b) heterogeneous core with correlation length of one grid size (c) heterogeneous core with correlation length of the width of the cross section.

Subsequent simulations investigate effects of heterogeneity and correlation length on pressure responses if a microcrack is not present in the core. Permeability distribution is generated geostatistically by Stanford Geostatistical Modeling Software (SGeMS) (Remy et al. 2009). Mean value is 0.1 mD in all the simulation scenarios shown in Fig. 4, and the heterogeneity degree of heterogeneous scenarios, evaluated by Dykstra-Parsons coefficient, is the same. In this figure, (a) is homogeneous, (b) is heterogeneous, but each grid is not correlated, which means the correlation length is set as the grid size (0.32 cm). (c) and (b) share the same permeability values quantitatively implies that the degree of heterogeneity is the same, but their permeability distributions are different. Correlation length in (c) is the width of the cross section (3.38 cm).

Comparing (a) and (b) shows that, more time is needed to reach pressure equilibrium in the heterogeneous scenario, implying that heterogeneity hampers the gas flow process in the porous media. This difference is caused by the energy dissipation occurring along the flow path when the porous media is heterogeneous. However, as the correlation length is increased in scenario (c), time to reach pressure equilibrium is close to that of the homogeneous scenario, implying that a longer correlation length reduces energy dissipation and favors gas flow if the degree of heterogeneity is the same. Therefore, the core behaves similar to the more permeable scenario.

A series of pulse decay test was conducted on a tight carbonate core, of which the pore size distribution was analyzed with nuclear magnetic resonance (NMR) spectroscopy.

Two relaxation time are involved in NMR: T1 and T2. T1 is longitudinal relaxation time and T2 is spin relaxation time. Both T1 and T2 are important for characterizing PSD, but T2 measurement is much faster, thus it is more practical (Arnold 2007).

$$\frac{1}{T_{2A}} = \frac{1}{T_{2F}} + \frac{1}{T_{2S}} + \frac{1}{T_{2D}}$$

(1)

In equation (1), the subscript A, F, S, D denote apparent, free fluid, surface-induced, and diffusion-induced respectively. Free fluid relaxation time is several seconds, but T1 and

T2 are of several milliseconds, thus the free fluid term could be ignored. In heterogeneous local magnetic fields, the diffusion-induced term contribution is negligible. Therefore, equation (1) could be approximated as

$$\frac{1}{T_{2A}} \approx \frac{1}{T_{2S}}$$

(2)

The surface-induced term equals

$$\frac{1}{T_S} = \rho_2 \frac{S}{V}$$

(3)

Where ρ_2 is surface relaxivity related to mineral surfaces properties (e.g. iron(III) content), the value is estimated to be $5 \sim 30$ μm/s for mudstone and sandstones, and $0.15 \sim 3.6$ μm/s for carbonate, and the value applied to generate the pore size distribution in this study is 1 μm/s. S is surface area and V is volume. If the grain is assumed to be spherical, the ratio of surface area and volume could be correlated with diameter d as follow:

$$d = \frac{6}{S/V}$$

(4)

Thus, the reciprocal of the relaxation time equals:

$$\frac{1}{T_2} = \rho_2 \frac{6}{d}$$

(5)

Figure 5 presents the size distribution of the core which ranges from 0.6 nm to 6 nm peaking at about 1.3 nm. Porosity obtained from the NMR is 0.037.
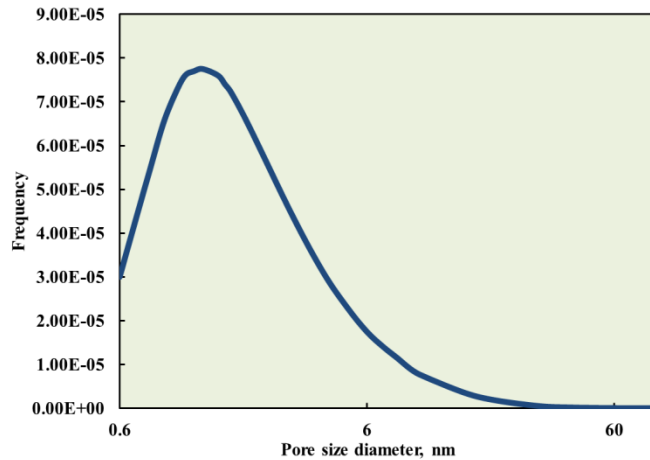
Fig. 5 Pore size distribution by NMR.

Fig. 6 shows entire pressure curves in a pulse decay experiment. Initially, core sample and downstream are saturated with helium under pressure of 98 psi (p_d), and the first upstream reservoir is saturated with helium under pressure of 110.1 psi (p_u). Valve V1 is opened at the 10th second. Helium expands freely to the second upstream reservoir and flows into the core inlet. Heise pressure transducers in this set-up record data points every second. Upstream reservoir pressure drops abruptly at the 11th second. It firstly drops to a lowest point and then increases slightly to 106.6 psi (p'_u) due to the Joule-Thomason effect. At the

same time, pressure response in the downstream is also observed. The downstream pressure is increased to 98.3 psi (p'_d).
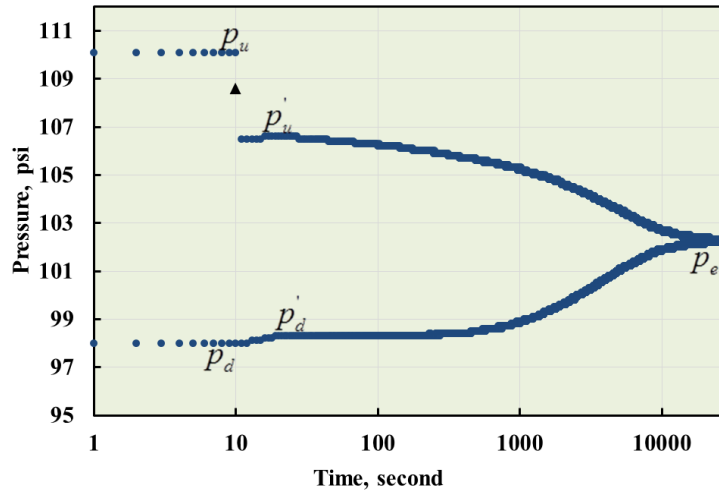
Fig. 6 Pressure data points in estimating total porosity and secondary accessible porosity in a pulse-decay experiment

$$\frac{p_u V_{u1}}{Z_u} + \frac{p_d (V_{u2} + V_p + V_d)}{Z_d} = \frac{p_e (V_{u1} + V_{u2} + V_p + V_d)}{Z_e} \tag{6}$$

$$\frac{p'_u (V_{u1} + V_{u2})}{Z_u} + \frac{p'_d (V'_p + V_d)}{Z_d} = \frac{p_e (V_{u1} + V_{u2} + V'_p + V_d)}{Z_e} \tag{7}$$

	p_u	p_d	p'_u	p'_d	p_e
pressure, psi	110.1	98	106.6	98.3	102.3
compressibility factor, Z	1.0040	1.0036	1.0039	1.0037	1.0038

Table 3 Pressure and compressibility factor of data points in Fig. 6.

Two methods using Bolye's law are employed to calculate porosity. Equation (6) is formed based on the pressure of p_u, p_d and p_e, and equation (7) is formed based on the pressure of p'_u, p'_d and p_e, V_{u1}, V_{u2} and V_d are volumes of the first upstream reservoir, second upstream reservoir and downstream reservoir, and the values are 3.147 cm³, 0.431 cm³ and 3.183 cm³, respectively. Table 3 lists the corresponding compressibility factor under the specific pressure and 86 ˚F. V_p and V'_p are pore volumes estimated by the two equations. Ideally, for a homogeneous core, porosity values estimated from equation (6) and (7) should be the same. However, noticeable difference exists between the two values. As we are dealing with very small volumes of the reservoir, the result might be misleading even if the measured volume of the reservoir deviates slightly from the real value. To validate our results, a dummy core with zero porosity is placed inside the core holder, in order to measure the reduced pressure after opening valve V₁. This pressure is marked with black triangle in Fig. 6, and it is compared with the result estimated using our measured volumes of the first upstream and second upstream reservoir. This step ensures the accuracy of our test result.

Based on the pressure responses during the test, we suggest that the preferential flow path exists in a natural, tight and heterogeneous core even if a microcrack is not present. Gas will choose different flow paths through the core from upstream to downstream. The flow path is preferential if it is less tortuous and with higher permeability. On the other hand, the flow path is described as the secondary flow path when the tortuosity increases and permeability decreases. We examined closely the pressure curves throughout the experiment and found that gas flow in the preferential flow path occurs at the very beginning of the pulse-decay experiment, which finishes within one second based on our observation, and it is much faster than in the secondary flow path. Thus, the concepts of total and secondary accessible porosity, estimated from equation (6) and (7), respectively, are proposed in this work to differentiate the two types of flow path.

Prior to the constant pressure injection, vacuuming is applied to excavate air in the system as the flowing gas is helium in tests. Then constant pressure gas injection from the ISCO pump is performed until the final pressure equilibrium is obtained in the system. Fig. 7 plots upstream and downstream pressures during this process. Unlike the scenario that pore space is already under a certain level of pressure, no pressure response occurs instantaneously at the downstream reservoir as a constant pressure is exerted at the upstream, even though the pressure pulse is more than 100 psi. This observation implies that the preferential flow path forms in the tight porous media only when gas has fully saturated the core.
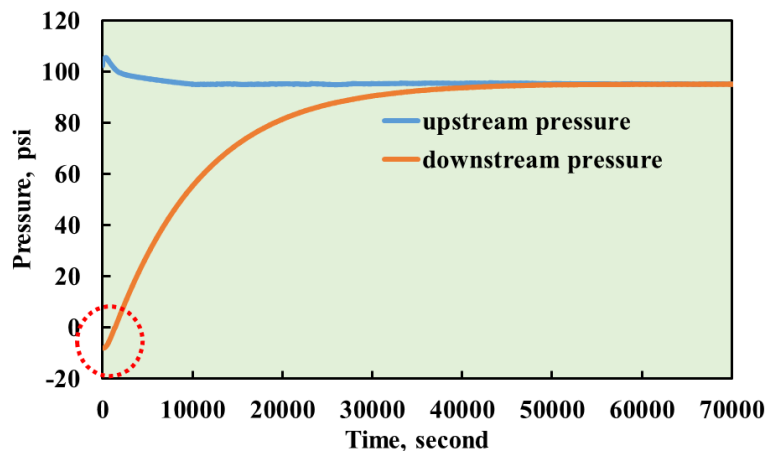
Fig. 7 Constant pressure gas injection to form gas saturation in the pulse-decay set-up.

Subsequent tests are performed by continuously increasing the pore pressure. The effective stress is kept constant at 2,000 psi by controlling the confining pressure. After reaching the pore pressure of approximately 300 psi, pressure in the system is relieved and the core sample is reverted and placed in the core holder to repeat the experiment under the same pressure. Fig. 8 shows two types of porosity calculated from the test at different pressures. Significant difference exists between the total porosity and secondary accessible porosity during the pressure range from 100 psi to 300 psi. Total porosity is approximately 0.035 for both forward and reverse directions. Secondary accessible porosity is approximately 0.012 and 0.025 in the forward and reverse directions, respectively, the difference is because p_u' is lower in the forward direction, which is caused by the heterogeneity

characteristic of the core. Moreover, the fact that p_u' is lower in the forward direction actually reveals that the front half of the core is more permeable than the rear half of the core.
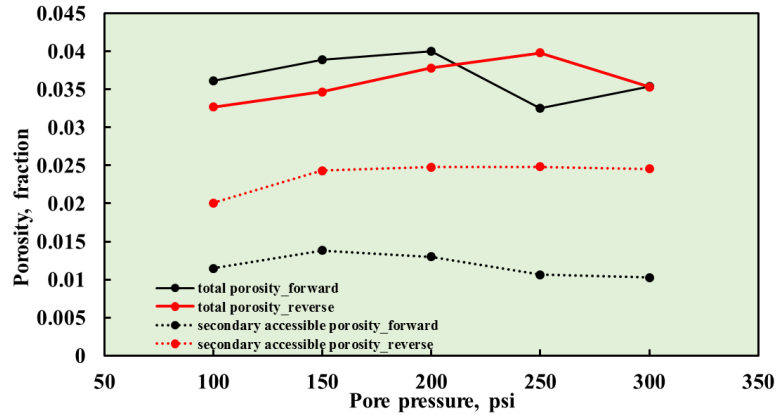

Fig. 8 Total porosity and secondary accessible porosity in the core in the forward and reverse directions.

Fig. 9 shows experimental and simulated pressure curves under the initial pore pressures approximately of 100 psi, 150 psi, 200 psi, 250 psi and 300 psi of flowing gas from the forward and reverse directions. The simulating process requires initial pressures in the upstream and downstream, reservoir volumes, core configuration including diameter, length and porosity. Permeability value is finely tuned in the simulator to history match experimental curves, the matched permeability is apparent permeability of the porous media taking into account of the non-Darcy flow behavior occurred in tight porous media, including slip flow and Kundsen diffusion. Surface diffusion will also occur if the flowing gas is adsorptive. Sensitivity analysis was performed using various grids number, and the result shows that the pressure curves are insensitive to the grids number in the model. Using the matched permeability values, simulated pressure curves are also plotted as in forward/reverse directions in Fig. 9. In this work, no specific optimization algorithm is developed to obtain permeability value, thus the matched permeability is an approximation. Matched permeability value is very close in the forward and reverse directions, and the difference is within 20 nD which is negligible compared with the total value, thus, the permeability as a function of pressure is represented as one value, as shown in Fig. 10. Dummy core pressure tests referred previously for each pore pressure further validates the accuracy of our measured reservoir volumes.
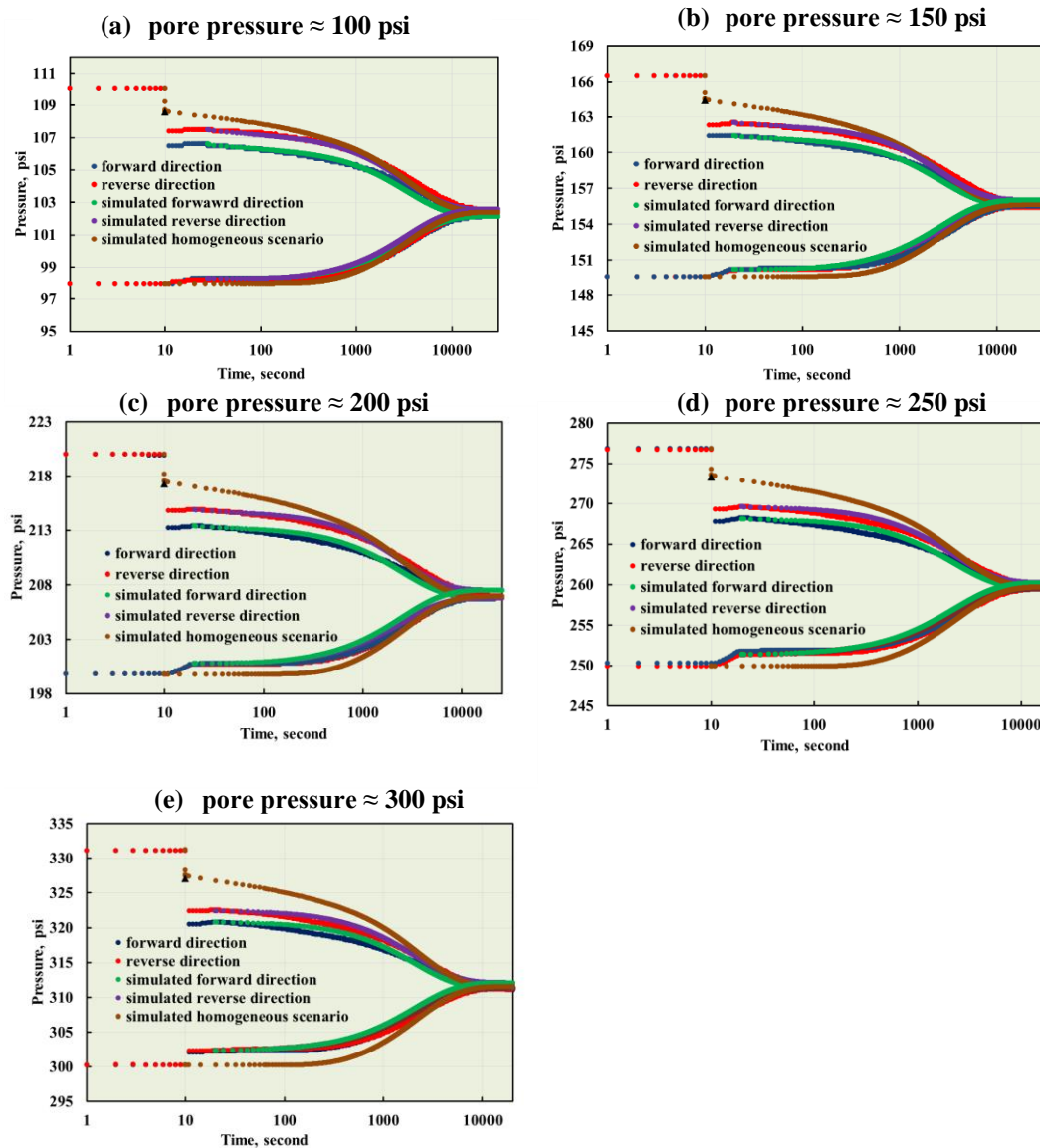
Fig. 9 Experimental and simulated pressure curves in the pulse-decay experiment. Experiment results include pressure curves by flowing helium in the forward and reverse directions, pressure ranges from 100 psi to 300 psi (from (a) to (e)). Pressure curve is adjusted within ± 0.2 psi for better visualization of comparing pressure responses in different directions. The black triangle point is the experimental reduced pressure after gas freely expands from the first upstream reservoir to the second upstream reservoir if a dummy core replaces the natural core sample. Simulated pressure curves are generated by matching the late-time pressure response using the secondary accessible porosity, and the homogeneous scenarios are constructed based on the averaged permeability obtained from the matching results using the total porosity.

Fig. 10 also shows the first order Klinkenberg equation to describe the slip flow behavior, where k_∞ is intrinsic permeability of the porous media and b is slip factor describing the degree of permeability deviation from Darcy's law. Matched permeability varies from 600 nD to 400 nD under the pore pressures ranging from 100 psi to 300 psi. Gas behaves more permeable under low pressure due to the slip flow and Knudsen diffusion behavior (Jia et al. 2017b).

$$k = k_\infty (1 + \frac{b}{p})$$ (7)

Using the matched permeability, an idealized homogeneous scenario is simulated starting from the initial pressure p_u and p_d. Thus the three sets of simulated pressure curves share the same permeability and reach the final equilibrium pressure almost at the same time. However, as the permeability in the preferential flow path must be much larger than that in the secondary flow path, as the pressure decrease in the preferential finishes within one second. We could reasonably infer that purely estimating permeability starting at p_u' and p_d' significantly underestimates both porosity and permeability.

The preferential flow path is more important under a higher pressure. As pore pressure increases, larger deviation of p_u' from the reduced pressure using the dummy core is observed, which is the value should be obtained if the core is homogeneous. More rapid response is observed at the downstream, as the difference between p_d' and p_d becomes more pronounced and the time for p_d to reach p_d' is shorter. For example, in the 300 psi scenario, 300.2 psi increases to 302.3 psi within only one second.
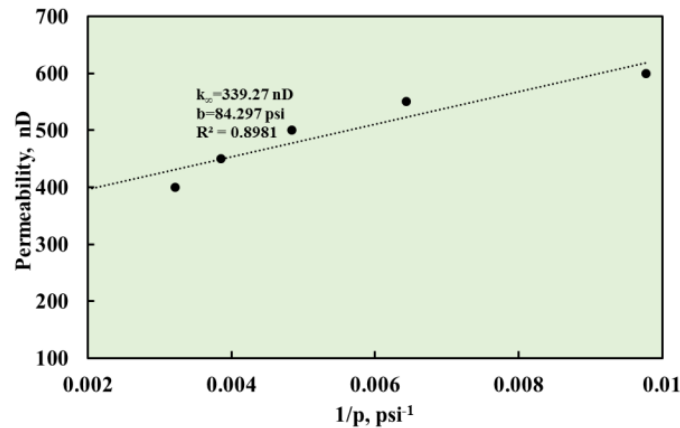
Fig. 10 Permeability as a function of 1/p.

The permeability curve in Fig. 10 behaves a downward curvature, which is unlike the result of steady-state permeability measurements. This phenomenon is also observed by Lenormand et al. (2010) and Rushing et al. (2004), which is more evident in more permeable core samples. This effect is due to the non-Darcy flow effects, mainly slip flow caused by the non-slip boundary condition and inertial flow in the transient flow regime.

The effect of the preferential path on permeability discussed in this study might be confirmed by experimental tracer tests. Gas can be applied if the permeability is too low. In addition, simulation of tracer tests on the heterogeneous scenarios might also be helpful. These can be next research focuses of this subject.

Conclusions

The following conclusions are obtained from this study:

- A microcrack can be detected by the pulse-decay experiment when it causes a "hump" region.

- The preferential flow path exits in a natural, tight and heterogeneous core even when microcrack is not present.
- Gas flows through the preferential flow path at the very early beginning. Failing to take the early pressure response into account leads to significant underestimation of porosity and permeability.
- The formation of a preferential flow path in heterogeneous porous media is more pronounced under an elevated pore pressure.
- In a typical pulse-decay experiment, the upstream reservoir pressure is sensitive to the core heterogeneity but the downstream reservoir pressure is not.
- Performing a pulse-decay experiment in both the forward and reverse directions assists differentiating which part of the core is more permeable.

Acknowledgements

REFERENCES

1. Alnoaimi, K. R. 2016. Influence of Cracks and Microcracks on Flow and Storage Capacities of Gas Shales at Core-level. Ph.D. thesis, Stanford University.
2. Arnold, J. 2007. Mobile NMR for Rock Porosity and Permeability. Ph.D. thesis, RWTH Aachen University.
3. Brace, W. F., Walsh, J. B., and Frangos, W. T. 1968. Permeability of Granite under High Pressure. *Journal of Geophysical Research* **73** (6): 2225-2236. http://doi.org/10.1029/JB073i006p02225.
4. IMEX. IMEX user's guide-version. Canada: Computer Modelling Group, Ltd; 2015.
5. Civan, F. 2010. A Review of Approaches for Describing Gas Transfer through Extremely Tight Porous Media, AIP Conference Proceedings, Montecatini, Italy, 20-25 June. http://doi.org/10.1063/1.3453838.
6. Civan, F., Rai, C. S., and Sondergeld, C. H. 2010. Intrinsic Shale Permeability Determined by Pressure-Pulse Measurements Using a Multiple-Mechanism Apparent-Gas-Permeability Non-Darcy Model, SPE Annual Technical Conference and Exhibition, Florence, Italy, 19-22 September. SPE-135087-MS. http://doi.org/10.2118/135087-MS.
7. Cronin, M. B. 2014. Core-scale Heterogeneity and Dual-Permeability Pore Structure in the Barnett Shale. Master thesis, University of Texas at Austin
8. Cui, X., Bustin, A. M. M., and Bustin, R. M. 2009. Measurements of Gas Permeability and Diffusivity of Tight Reservoir Rocks: Different Approaches and Their Applications. *Geofluids* **9** (3): 208-223. http://doi.org/10.1111/j.1468-8123.2009.00244.x.
9. Dicker, A. I., and Smits, R. M. 1988. A Practical Approach for Determining Permeability From Laboratory Pressure-Pulse Decay Measurements, International Meeting on Petroleum Engineering, Tianjin, China, 1-4 November. SPE-17578-MS. http://doi.org/10.2118/17578-MS.

10. Hsieh, P. A., Tracy, J. V., Neuzil, C. E., Bredehoeft, J.D., and Silliman, S.E. 1981. A transient Laboratory Method for Determining the Hydraulic Properties of 'Tight' Rocks—I. Theory. *International Journal of Rock Mechanics and Mining Sciences & Geomechanics Abstracts* **18** (3): 245-252. http://doi.org/10.1016/0148-9062(81)90979-7.

11. Jia, B., Tsau, J., and Barati, R. 2017. Different Flow Behaviors of Low-pressure and High-pressure CO2 in Shales, Unconventional Resources Technology Conference, Austin, Texas, USA, 24-26 July. URTEC-2690239-MS. http://doi.org/10.15330-URTEC-2017-2690239.

12. Jia, B., Li, D., Tsau, J., and Barati, R. 2017. Gas Permeability Evolution During Production in the Marcellus and Eagle Ford Shales: Coupling Diffusion/Slip-flow, Geomechanics, and Adsorption/Desorption, Unconventional Resources Technology Conference, Austin, Texas, USA, 24-26 July. URTEC-2695702-MS. http://doi.org/10.15330-URTEC-2017-2695702.

13. Jones, S. C. 1997. A Technique for Faster Pulse-Decay Permeability Measurements in Tight Rocks. *SPE Formation Evaluation* **12** (01): 19-26. http://doi.org/10.2118/28450-PA.

14. Kamath, J., Boyer, R. E., and Nakagawa, F. M. 1992. Characterization of Core Scale Heterogeneities Using Laboratory Pressure Transients. *SPE Formation Evaluation*: **7** (03) 219-227. http://doi.org/10.2118/20575-PA.

15. Lenormand, R., Bauget, F., Ringot, G. 2010. Permeability Measurement on Small Rock Samples, International Symposium of the Society of Core Analysts, Halifax, Nova Scotia, Canada, 4-7 October. SCA2010-32.

16. Lin, W. 1977. Compressible Fluid Flow through Rocks of Variable Permeability, Lawrence Livermore Laboratory, Livermore, California.

17. Ning, X. 1992. The Measurement of Matrix and Fracture Properties in Naturally Fractured Low Permeability Cores Using a Pressure Pulse Method. Ph.D. thesis, Texas A&M University.

18. Remy, N., Boucher, A., and Wu, J. 2009. Applied geostatistics with SGeMS: A user's guide. Cambridge, UK: Cambridge University Press.

19. Rushing, J. A., Newsham, K. E., Lasswell, P. M., Cox, J. C., Blasingame T. 2004. Klinkenberg-Corrected Permeability Measurements in Tight Gas Sands: Steady-State Versus Unsteady-State Techniques, SPE Annual Technical Conference and Exhibition, Houston, Texas, USA, 26–29 September. SPE-89867-MS. https://doi.org/10.2118/89867-MS.

A METHOD FOR RAPID DETERMINATION OF OIL AND WATER CONTENT IN GEOLOGICAL FORMATIONS

D. Vartsky[1,*], M. B. Goldberg[2], V. Dangendorf[3], I. Israelashvili[1,5], I. Mor[4], D. Bar[4], K. Tittelmeier[3], M. Weierganz[3], B. Bromberger[3], A. Breskin[1]

[1] Weizmann Institute of Science, Rehovot, 76100, Israel
[2] Herzbergstr. 20, 63584 Gründau, Germany
[3] Physikalisch-Technische Bundesanstalt (PTB), 38116 Braunschweig, Germany
[4] Soreq NRC, Yavne 81800, Israel
[5] Nuclear Research Center of the Negev, P.O.Box 9001, Beer Sheva, Israel

This paper was prepared for presentation at the International Symposium of the Society of Core Analysts held in Vienna, Austria, 27 August – 1 September 2017

ABSTRACT

A novel method utilizing Fast Neutron Resonance Transmission Radiography is proposed for rapid, non-destructive and quantitative determination of the weight fractions of oil and water in cores taken from subterranean or underwater geological formations. Its ability to distinguish water from oil stems from the unambiguously-specific energy-dependence of the neutron cross-sections for the principal elemental constituents. Furthermore, the fluid weight fractions permit determining core porosity and oil and water saturations. In this article we show results of experimental determination of oil and water weight fractions in 10 cm thick samples of Berea Sandstone and Indiana Limestone formations, followed by calculation of their porosity and fluid saturations.

The technique may ultimately permit rapid, accurate and non-destructive evaluation of relevant petro-physical properties in thick intact cores. It is suitable for all types of formations including tight shales, clays and oil sands.

INTRODUCTION

Routine oil-drilling core analysis consists of measuring porosity, permeability, and fluid or gas saturation [1,2]. Most prevalent analysis techniques are based on destructive analysis of small plug samples removed from the core. More recent techniques include X-ray CT [3] and MRI analysis [4,5] that could, in principle, be applied non-destructively to larger core samples.

Nuclear geophysics is a discipline that assists oil, gas and uranium exploration, both in nuclear borehole-logging and analysis of core samples [6]. Middleton et al, [7], investigated thermal neutron radiography to estimate the rock porosity and relative fluid saturation in 5 mm-thick rock slices. The use of thermal neutrons does not permit distinguishing between water and oil, because it relies mainly on the attenuation of hydrogen. De Beer et al [8] also used thermal-neutron radiography to provide internal structure images of rocks, in order to determine the effective porosity of the object. Nshimirimana et al [9] examined the precision of porosity calculations

---

*Corresponding author
e-mail: david.vartsky@weizmann.ac.il

in 14-17 mm thick rock samples using thermal neutron radiography. Lanza et al, [10] investigated thermal neutron computerized tomography to image the distribution of hydrogenous liquids (oil or water) in a 25.4 mm-diameter core. As in the above-mentioned studies it cannot distinguish between oil and water either. In certain cases deuterated water is introduced into the porous media, in order to study immiscible fluid flow by thermal neutron tomography [11]. A recent review [12] of thermal-neutron imaging of hydrogen-rich fluids in geo-materials discusses the non-destructive visualization of such fluids within diverse porous media.

In our previous work [19] we described a proof-of-principle study of the Fast Neutron Resonance Transmission (FNRT) radiography method for core analysis using synthetic samples of sand saturated with oil or water. In this paper we further evaluate the technique using thick, real formation cores.

FAST NEUTRON RESONANCE TRANSMISSION RADIOGRAPHY

A description of FNRT radiography has been given in [13-18] and its specific application for core analysis was detailed by Vartsky et al.[19]. Briefly, FNRT radiography is a method that exploits characteristics (resonances) in the neutron attenuation of the analysed constituents in order to determine the identity and proportions of substances within an object. A typical neutron energy-range is 1-10 MeV.
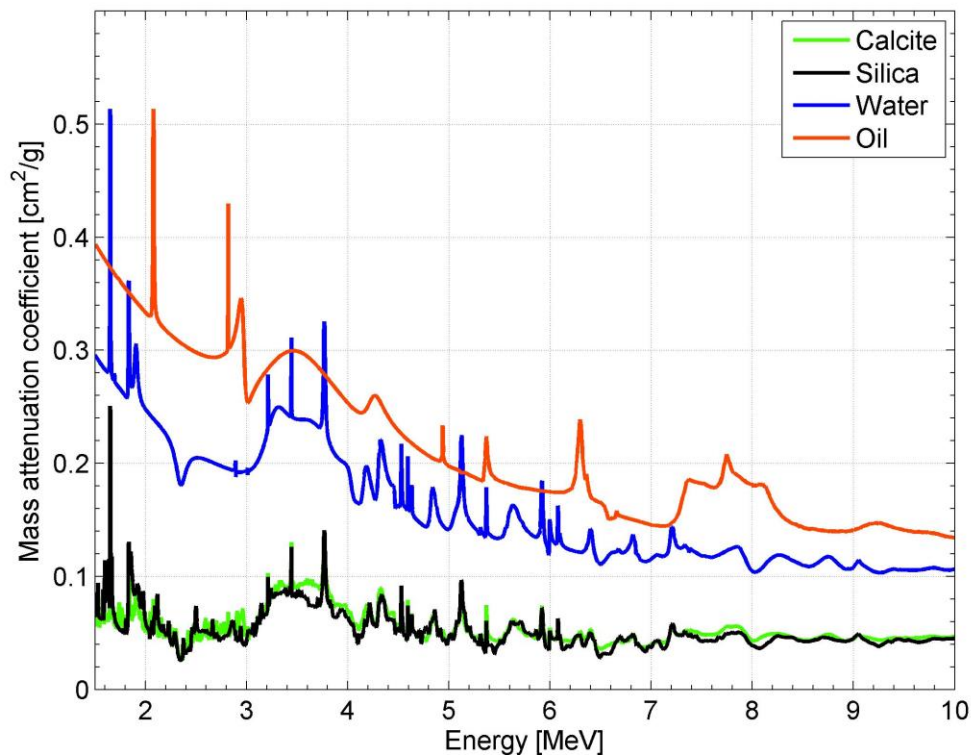
Fig. 1 Mass-attenuation coefficients of silica, calcite, oil and water vs. neutron energy.

Fig. 1 shows the energy dependence of the mass attenuation coefficients of calcite, silica, (the principal constituents of limestone and sandstone rocks respectively), oil and water. The values were calculated for the above substances using compiled

neutron cross-sections [20] of their elemental constituents. It can be observed that the attenuation coefficients of the four substances exhibit different characteristic behaviour with neutron energy. This is due to resonances in the neutron interaction with the most abundant elements in materials, such as carbon in oil, oxygen in water, oxygen and silicon in silica and calcium, oxygen and carbon in calcite. In most elements the resonances occur mainly at lower neutron energies (below 8 MeV) and are due to compound nucleus formation. In such reaction the probability of interaction increases, when the energy of the incident neutron corresponds to an excited nuclear state of the resulting compound nucleus. Following this stage a neutron may be reemitted leading to elastic or inelastic resonance scattering. Hydrogen, present in oil and water does not exhibit any resonances in its attenuation coefficient, which decreases smoothly with neutron energy. Thus, for example, the resonant features in water are all due to resonances in cross-section of oxygen, which ride on a smooth hydrogen cross-section curve.

In FNRT the inspected object is irradiated with a broad spectrum of neutrons in the above-mentioned energy range. Dependent on the nature of the inspected object the transmitted neutron spectrum will exhibit dips and peaks at specific energies-thus carrying information about the object's composition. This is similar to observing characteristic absorption lines observed in other analytical spectroscopic techniques; for example atomic absorption method.

Fig. 2 schematically shows the FNRT irradiation configuration. An intact core within its protective sleeve is subjected to a broad-energy neutron beam in the energy range 1-10 MeV. The transmitted neutron spectrum is detected by a fast-neutron position-sensitive detector to provide mm-resolution imaging capability. In addition to position resolution the detector must be spectroscopic, i.e. it should provide information on the energy of the detected neutrons.
The shape of the core can be arbitrary and the method can provide the relevant information regardless of its geometry.
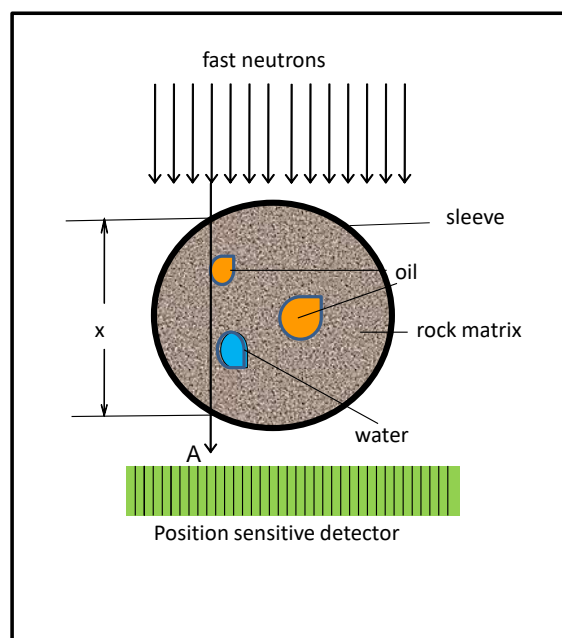
Fig. 2 Schematic description of FNRT irradiation configuration of a core in its protective sleeve. The arrow marked "A" stands for part of the beam of fast neutrons that traverses the thickness x of the sample and impinges on a specific pixel within the array.

If we assume that the inspected object, such as an oil-drilling core, consists mainly of porous rock matrix (eg. sandstone), oil and water; (we can ignore the presence of few mg/g of Cl which may be part of high salinity water, since for MeV energy neutrons its cross section is only few barns), the ratio R_i of the transmitted-to-incident neutron flux at an energy **i** and at the position indicated in the drawing by the arrow (A) is:

$$R_i = \exp[-(\boldsymbol{\mu}_i^s \rho_s x + \boldsymbol{\mu}_i^o \rho_o x + \boldsymbol{\mu}_i^w \rho_w x)] \quad \text{Eq.1}$$

Where $\boldsymbol{\mu}_i^s$, $\boldsymbol{\mu}_i^o$, $\boldsymbol{\mu}_i^w$ and $\rho_s x$, $\rho_o x$, $\rho_w x$ are the mass attenuation coefficients and areal densities of dry formation (sandstone, limestone), oil, and water, respectively (see also Fig. 1). The densities ρ in Eq. 1 are not the intrinsic physical densities of the substances, they represent the mean densities averaged over the trajectory x.

Since the spectrum may consist of **n** discrete neutron-energies, one can write **n** such equations. By taking a natural logarithm of R_i one obtains a set of **n** linear equations where the areal densities are the unknowns of interest. This is an over-determined system, in which there are **n** linear equations with three unknowns (of these **n**, not all have the same sensitivity: in other words, depending on the element in question, the effective number of equations may be considerably smaller than the nominal **n**. Such a problem can be solved by a least-squares solution with bootstrapping or a Bayesian minimization method [21-23].

Once a solution for the 3 areal densities is found for a given detector pixel, we can determine the areal-density-ratio of oil or water to that of the dry rock. This yields the local weight-fractions of oil and water **f_o** and **f_w** in the traversed core, independent of sample thickness or shape. It must be noted that the fluid weight-fractions in the sample are determined independently, thus the oil-to-rock weight-ratio is independent of water content.

One can now display the map of oil or water weight-fractions for each individual pixel. Alternatively, by multiplying each pixel areal density by a pixel area we obtain the mass of each component in a volume defined by pixel area and height x and by integrating over all pixels obtain the total weight of oil, water and dry rock in the entire core, from which the average weight-fractions of oil and water F_o and F_w in the core can be determined regardless of the object shape, thickness or fluid distribution.

Prior to analysis of the core of interest we must calibrate our system using substances of known composition and physical densities. To this end we must determine experimentally the values of the mass attenuation coefficients vs. neutron energy for pure dry-rock of known grain-density, oil and water. This calibration procedure is necessary since there could be significant differences between rock and oil types from one drilling site to another.

Alternatively, or if such standards are unavailable, one may use calibrated elemental standards, such as Si, O, C, H, Ca Al and Mg to measure their mass-attenuation

coefficients. In such a case, solving Eq. 1 will yield elemental areal densities, from which one can deduce the content of oil and water in the core.

From the determined oil and water average weight fractions F_o and F_w it is further possible to calculate the dry weight of the core (**DWC**), the average rock porosity (**Φ**) and average oil and water saturation levels (S_o, S_w) of the analysed core, provided we can measure the total weight-(TW_c) and volume (V_c) of the analysed core and that the grain-density of the rock, as well as the densities oil and water ($ρ_G$, $ρ_o$, $ρ_w$) are known, using the following equations:

$$DW_c = \frac{TW_c}{(1+F_o+F_w)\cdot} \qquad \text{Eq. 2}$$

$$Φ = 1 - \frac{TW_c/V_c}{(1+F_o+F_w)\cdot ρ_G} \qquad \text{Eq. 3}$$

$$S_o = \frac{F_o \cdot (TW_c/ρ_o)}{V_c \cdot (1+F_o+F_w) - (TW_c/ρ_G)} \qquad \text{Eq.4}$$

$$S_W = \frac{F_W \cdot (TW_c/ρ_W)}{V_c \cdot (1+F_o+F_w) - (TW_c/ρ_G)} \qquad \text{Eq. 5}$$

EXPERIMENTAL PROCEDURES

Preparation of Formation Samples

Evaluation of the technique was performed using rock formation samples of known properties. Three Berea Sandstone and three Indiana Limestone cubical samples 10x10x10 cm³ in dimensions were prepared by Kocurek Company [24]. After cutting to the desired dimensions the samples were dried at 82°C in core-drying oven. Their weight was recorded. Two samples of each formation type were then inserted into a vacuum chamber and evacuated for approximately 1 hour. Following this step, the given fluid was pulled into the sample from the bottom at a very slow rate using a vacuum pump. After saturation the samples were weighed, the direction of "top" and "bottom" was marked and they were sealed in a container immersed in the saturation fluid for shipping. The saturation fluids were water and Odorless Mineral Spirit (OMS, density=0.748 g/cc) supplied by the Univar Company.

Fig. 3 Indiana Limestone (left) and Berea Sandstone (right) samples

Fig. 3 shows the dry limestone and sandstone samples and Table 1 summarizes the weights of all samples. The bulk volume of the samples was measured to be 1000±2.3 cc. Based on the weights, volumes and literature values of grain densities of sandstone and limestone (2.66 and 2.71 g/cc respectively) [25] we calculated the sample porosity and oil and water saturation levels, also shown in Table 1.

Table 1 Weights, porosity and fluid saturation values of the analyzed samples

Sample No.	Sample type	Weight (g)	Porosity (%)	Saturation(%)
1	Dry limestone (LS)	2257.7±0.1	16.8±0.23	---
2	LS+oil	2380.9±0.1	*	97.9±0.23
3	LS+water	2403.3±0.1	*	86.6±0.23
4	Dry sandstone (SS)	2112.3±0.1	20.6±0.23	---
5	SS+oil	2270.0±0.1	*	102.4±0.23
6	SS+water	2323.7±0.1	*	102.7±0.23

*Assumed to be the same as for dry sample

The higher than 100% saturation values for sandstone samples could result from inaccurate grain density taken from literature. Porosity calculation and the resulting saturation values are rather sensitive to variations in grain density. A change in grain density by less than 1% can result in porosity change of about 3%.

For determining the mass-attenuation coefficients μ_i^s, μ_i^o, μ_i^w we used the dry samples of limestone and sandstone, pure OMS liquid supplied by Univar and regular tap water.

Neutron Irradiation Procedure
The experiment was performed using the CV28 isochronous cyclotron at the Physikalisch-Technische Bundesanstalt (PTB), Braunschweig, Germany. Neutrons were produced by a 12 MeV deuterium beam impinging on a 3 mm thick Be target. The useful part of the neutron energy spectrum ranges from ca. 1 MeV up to 10 MeV [26].

Neutron spectroscopy was performed by the time-of-flight (TOF) method. In this method the time the neutron travels over a known distance between the target and the detector is measured and is converted to neutron energy. The deuteron beam was pulsed at a pulse repetition rate of 2 MHz and a pulse width of 1.7 ns. Average beam current was approximately 2 μA.

Neutrons were detected using a cylindrical 25.4 mm diameter x25.4 mm long liquid scintillator detector (NE213 type) positioned at 1247 cm from the target.

The analyzed samples were positioned between target and detector at a distance of 245 cm from the latter. The angle subtended by the detector was 0.058°, thus the diameter of the inspected region in the sample was 2 cm. The measurement time per sample ranged from 100-1000s.

RESULTS AND DISCUSSION

Uniformity Tests

As the samples were saturated with the fluids by pulling the liquid from the sample bottom, it was important to determine the uniformity of the fluid distribution along the direction of saturation. For this purpose the samples were scanned with the neutron beam directed perpendicularly to the direction of saturation from the bottom to the top of the sample in steps of 1 cm. The scans indicated that the fluids were uniformly distributed along the saturation direction to within ±2%.

As the samples were uniform in dimensions and composition there was no need to perform a high resolution radiographic scan and transmission measurements at a single point were performed using the liquid scintillator detector mentioned above.

Neutron Transmission Spectra

All transmission measurements were performed using the time-of flight (TOF) spectroscopy. In such measurements it is common to present the spectra vs. TOF rather than converting them to neutron energy. Fig. 4 shows the TOF spectra of the transmitted neutrons through a dry limestone and through water and oil-saturated limestone cores.
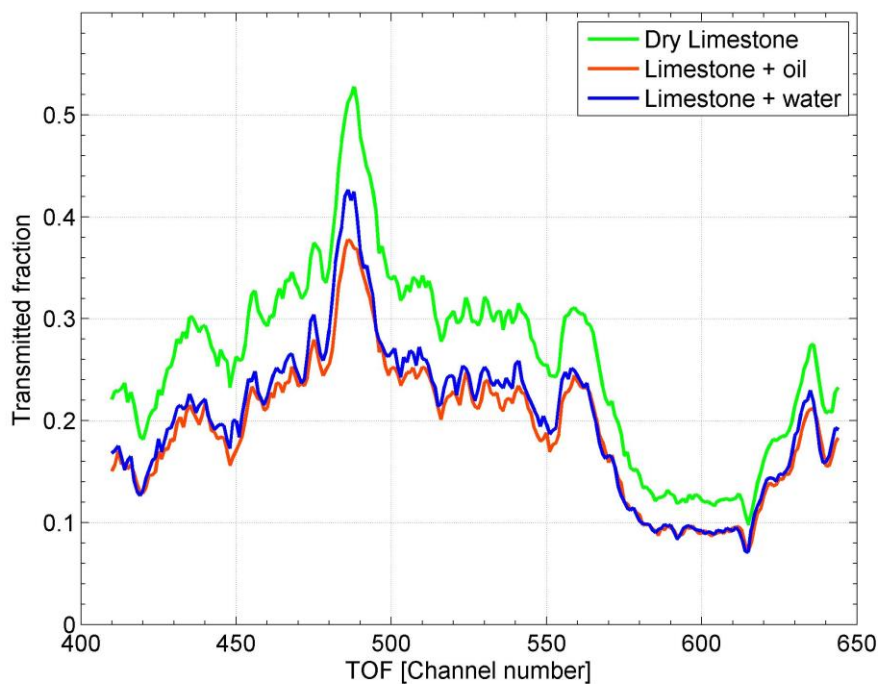
Fig. 4 Transmission spectra vs TOF (expressed in channels) through 10 cm thick samples of dry limestone, limestone+oil and limestone+water. TOF range corresponds to neutron energy range of 1.7-4.2 MeV

As can be observed the spectrum is dominated by the shape of the dry limestone spectrum (the dominant absorber), nevertheless the proportions of various features are different for each configuration.

Fig. 5 shows the experimentally determined mass-attenuation coefficients of limestone, sandstone, oil (OMS) and water vs neutron TOF. The coefficients were determined by measuring neutron transmission through calibrated samples of pure dry limestone, dry sandstone, water and oil. Due to limited energy resolution of our experimental system the resonances are substantially broader and less pronounced than those based on compiled values of Fig. 1. These experimentally determined mass-attenuations are used as μ_i^s, μ_i^o, μ_i^w values in Eq. 1 for reconstructing the areal densities of dry rock, oil and water in the fluid saturated core samples. For reconstruction we used only a limited range of neutron TOF's corresponding to 1.7 to 4.2 MeV energy range. We found that this neutron energy range resulted in the best reconstruction.
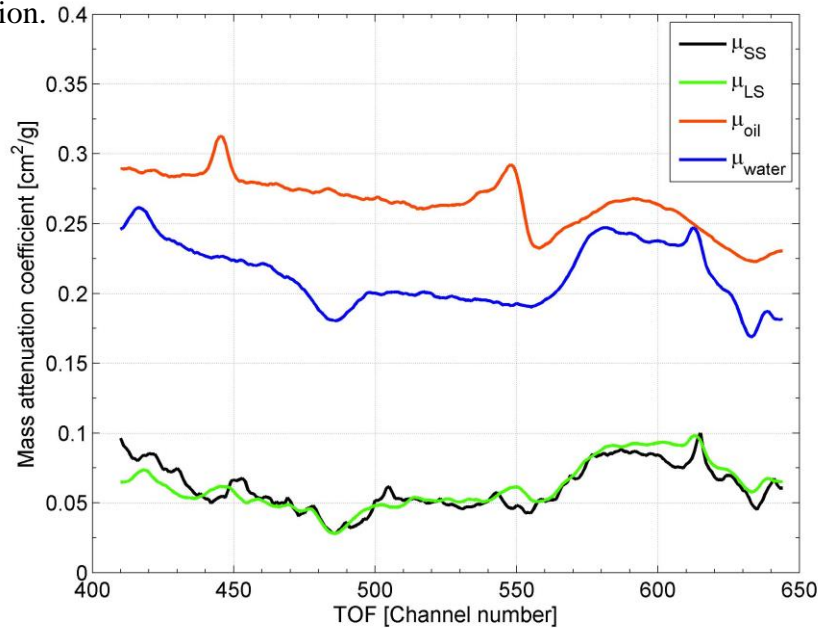
Fig. 5 Experimentally determined mass attenuation coefficients for dry limestone, sandstone, water and oil (OMS).

Reconstruction of Areal Densities

We used two methods for reconstructing the areal densities: 1) least-squares solution with bootstrapping and 2) WinBUGS program (Bayesian Inference Using Gibbs Sampling). [25]. Both types of analysis gave very similar reconstruction results and uncertainties. The reconstruction methods provide a probability distribution of the areal density for each constituent, indicating whether it is likely to be found in the inspected sample and what is the most probable areal density.

Fig. 6 shows the reconstructed experimental areal density distributions of dry sandstone core, oil and water in sandstone+oil (left column) and sandstone+water

(right column). Here we used the least squares method with bootstrapping. The mean and standard deviation of the distributions are also indicated. The distributions for limestone samples are similar in shape.
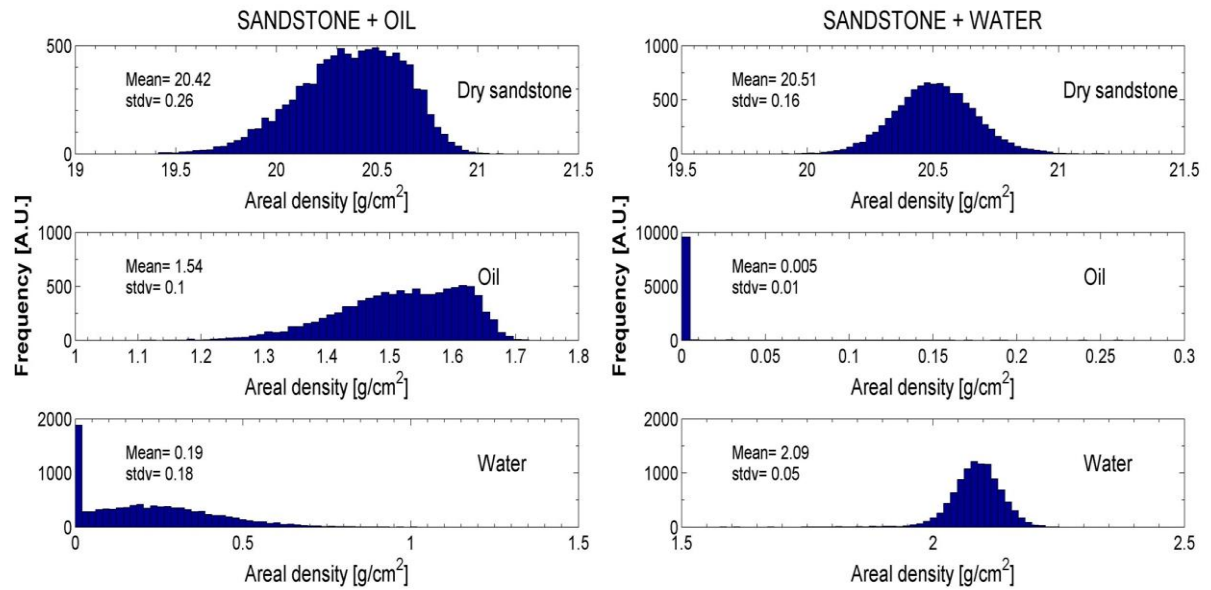
Fig. 6 Distribution of least squares-reconstructed areal density of dry sandstone, oil and water in sandstone saturated with oil (left) and sandstone saturated with water (right).

The ratio of reconstructed areal density of oil (or water) to that of dry core yields the weight fraction of each fluid in the core. Fig. 7 shows the experimentally determined oil *Fo* and water *Fw* weight fractions (in %) in each sample.
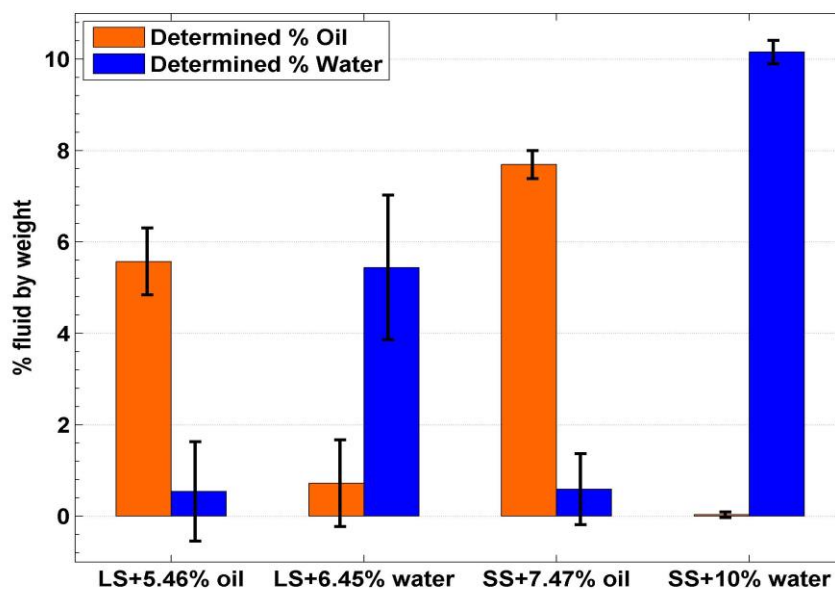
Fig. 7 Experimentally determined weight percentage of oil (orange) and water (blue) in LS+5.46% oil, LS+6.45% water, SS+7.47% oil and SS+10% water

Table 2 summarizes all experimental results: % weight of oil F_o and water F_w, dry core weight-DWc, porosity-Φ, oil and water saturations-S_o,;S_w calculated using equations 2-5. The expected values determined by the prior weight and volume measurements are shown in square brackets.

Table 2 Experimental F_o and F_w and calculated dry weight, porosity and saturations

Case	F_o [%]	F_w [%]	DWc [g]	Φ [%]	S_o[%]	S_w[%]
LS+oil	5.57±0.7[5.46]	0.54±1.1[0]	2243±27[2257]	17.3±0.2[16.8]	96.4±12.7[98]	7±14[0]
LS+water	0.72±0. 9[0]	5.44±1.6[6.45]	2264±39[2257]	16.6±0.2[16.8]	13±17[0]	74.3±22[87]
SS+oil	7.54±0.3[7.47]	0.9±0.8[0]	2093±18[2112]	21.3±0.1 [20.3]	98.9±4.2[102]	9.1±8.6[0]
SS+water	0.030±0.1[0]	10.2±0.3[10]	2108±5[2112]	20.7±0.04 [20.3]	0.36±0.86[0]	103±2.6[103]

[expected value]

The experimentally determined dry weights and porosity of the samples agree quite well with the expected values. The uncertainties in saturation values in limestone core case are relatively large 13-30% and can be mainly attributed to the errors in F_o and F_w. The F and saturation values for fluids not present in the core are consistent with zero within their standard deviation. In addition, the shape of their frequency distributions (Fig. 6) is consistent with a characteristic distribution shape of substances which are not likely to be present in the inspected sample (strongly asymmetric distribution with a large value at zero).

Our previous Monte-Carlo calculations [19] indicated that the fluid content can be determined with sufficiently high accuracy and precision by irradiating a 10 cm thick core with a broad-energy neutron spectrum with no more than 10^6 neutrons. However, the experimentally-calibrated reference values of the mass-attenuation coefficients of the standards (dry rock, oil and water) used in the reconstruction need to be determined with much higher precision than we have done so far, requiring at least ten-fold higher counting-statistics for the FNRTR spectra of these standards. Hence, although we collected about 10^6 neutrons for the fluid saturated rocks in the present work, the uncertainties of the reconstructed experimental values, especially for limestone, appear to be higher than expected. We are confident that this is the sole procedural hurdle that the method still needs to surmount.

CONCLUSIONS

We describe a method based on Fast-Neutron Resonance Transmission (FNRT) radiography for a non-destructive, specific and quantitative determination of oil and water content in core samples. The application of fast neutrons can be useful in screening bulky objects such as thick rock cores, for which alternative probes, such as slow and epithermal neutrons, as well as low-energy X-rays, not only do not distinguish between hydrocarbons and water, but also suffer from limited penetration. The method measures the average fluid/dry-core-weight ratio in the path traversed by the fast neutrons regardless of object shape, thickness or distribution. In principle the entire length of an intact core, within its protective sleeve can be scanned along the core length, providing information about the content distribution. The fluid weight-fractions in the interrogated sample are determined independently, thus the ratio of oil-to-rock weights is independent of the water content.

The measurement time is dependent on the incident neutron flux. Our measurement times/sample were about 1000s. The measurement time can be substantially reduced by using stronger neutron sources, and analysing many cores simultaneously using a large pixelated detector. We estimate that an operational facility will be able to analyse a core within minutes.

The experimentally determined fluid weight fractions F were determined with uncertainties of about 13-30%. We attribute these relatively large errors to insufficient counting statistics for our standards. The weight fraction values for fluids not present in the core are consistent with zero within their standard deviation. In addition, the shape of their frequency distributions (Fig. 6) is consistent with a characteristic distribution shape of substances which are not likely to be present in the inspected sample (strongly asymmetric distribution with a large value at zero).

We have demonstrated that if the total weight and volume of the core is available one can use the measured fluid weight fractions for the determination of the global core porosity and oil/water saturation. The experimentally determined dry weights and porosity of the samples agree quite well with the expected values. The uncertainties in saturation values in limestone core case are relatively large and can be mainly attributed to the errors in F_o and F_w.

The FNRT method permits determining the fluid weight-fractions in any type of cores including tight shales, clays and oil sands. The method is also applicable for fluid-content evaluation in drill cuttings held in containers or bags.

REFERENCES

1.   American Petroleum Institute, 1998, *Recommended practices for core analysis*, API Publications and Distributions 2nd Edition, February 1998. http://w3.energistics.org/RP40/rp40.pdf

2.   Andersen M.A., B. Duncan and R. McLin, 2013. Core truth in formation evaluation, *Oilfield Review*, 25, 2, 16-25.

3.   Boone M., T. Bultrjs, B. Masschaele, D. Van Loo, L. Van Hoorebeke, and V. Cnudde, 2016, In-situ real time micro-CT imaging of pore scale process, the next frontier for laboratory-micro-CT scanning. *Int. Symposium of Society of Core Analysts*, Snowmass Colorado SCA2016-018

4.   Chen Q., F.R. Rack and B.J. Balcom, 2006, Quantitative magnetic resonance imaging methods for core analysis, *New Techniques in Sediment Core Analysis*, 267, 193-207

5.   Mitchell J, T.C. Chandrasekera, D.J. Holland, C.V. Gladden and E.J. Fordham, 2013. Magnetic resonance imaging in laboratory petrophysical core analysis, *Physics Reports* 526, 165-225.

6.   Borsaru M, 2005, Selected topics in nuclear geophysics, *Proceedings of the Romanian Academy series* A, 6, 3/2005.

7.   Middleton M.F., I. Pazsit and M. Solymar, 2001. Petrophysical application of neutron radiography, *Nondestr. Test. Eval*. 16, 321-333.

8.   de Beer F.C., M.F. Middleton and J. Hilson, 2004. Neutron radiography of porous rocks and iron core, *Applied Radiation and Isotopes* 61, 487-495.

9.   Nshimirimana R., M. Radebe and F. de Beer, 2015, Precision of porosity calculation from "Material stopping power" using neutron radiography, *Physics Procedia* 69, 358-365.

10.   Lanza R.C., E.W. McFarland and G.W. Poulos, 1991, Computerized neutron tomography for core analysis, *SCA-9128 in 5th annual technical conference proceedings: Society of Professional Well Log Analysts*, Vol 3, p.12

11.   Murison J., R. Moosavi, M. Schulz, B. Schillinger and M. Schroter, 2015, Neutron tomography as tool to study immiscible fluids in porous media without chemical dopant, *Energy Fuels* 29 (10), 6271-6276

12. Perfect E., C.L. Cheng, M. Kang, H.Z. Bilheux, J.M. Lamanna, M.J. Gragg, D.M. Wright, 2014. Neutron imaging of hydrogen-rich fluids in geomaterials and engineered porous media: A review, *Earth Science Reviews* 129, 120-135

13. J.C. Overley, 1985, Determination of H, C, N, O content of bulk materials from neutron attenuation measurements *Int. J. Appl. Rad. & Isot*. 36, 185-191

14. Miller T. G., P.K. Van Staagen, B.C. Gibson, J.R. Orthel and R.A. Krauss, 1997, Contraband detection using neutron transmission, *SPIE proceedings*, Vol. 2936, 102

15. Dangendorf V., D. Bar, B. Bromberger, G. Feldman, M.B. Goldberg, R. Lauck, I. Mor, K. Tittelmeier, D. Vartsky, M. Weierganz, 2009. Multi-frame energy selective imaging system for fast neutron radiography. *IEEE Transactions on Nuclear Science* 56, 1135-1140

16. Mor I., D. Vartsky, D. Bar, G. Feldman, M.B. Goldberg, D. Katz, E. Sayag, I. Shmueli, Y. Cohen, A. Tal, Z. Vagish, B. Bromberger, V. Dangendorf, D. Mugai, K. Tittelmeier, M. Weierganz, 2009. High Spatial Resolution Fast-Neutron Imaging Detectors for Pulsed Fast-Neutron Transmission Spectroscopy *JINST 4 P05016* , http://arxiv.org/abs/0905.4399

17. Brandis M., D. Vartsky, V. Dangendorf, B. Bromberger, D. Bar, M.B. Goldberg, K. Tittelmeier, E. Friedman, A. Czasch, I. Mardor, I. Mor, M. Weierganz, 2012. Neutron measurements with Time-Resolved Event-Counting Optical Radiation (TRECOR) detector, *JINST 7 C04003* (2012)

18. Israelashvili I., M. Cortesi, D. Vartsky, L. Arazi, D. Bar, E.N. Caspi, A. Breskin, 2015. A Comprehensive Simulation Study of a Liquid Xe Detector for Contraband Detection, *JINST 10* , PO3030

19. Vartsky D., M.B. Goldberg, V. Dangendorf, I. Israelashvili, I. Mor, D. Bar, K. Tittelmeier, M. Weierganz, B. Bromberger and A. Breskin, 2016. Quantitative discrimination between oil and water in drilled bore cores via Fast-Neutron Resonance Transmission radiography, *Applied Radiation and Isoptopes* 116, 87-94

20. Evaluated Nuclear data File, (ENDF), 2015, https://www-nds.iaea.org/exfor/endf.htm

21. Efron B.,1979. Bootstrap Methods: Another Look at the Jackknife. *The Annals of Statistics*. 7 (1), 1-26

22. Lunn D. J., A. Thomas, N. Best, D. Spiegelhalter, 2000. WinBUGS - A Bayesian modelling framework: Concepts, structure, and extensibility, *Statistics and Computing* 10, 325-337

23. Mor I., V. Dangendorf, M. Reginatto, K. Kaufmann, D. Vartsky, M. Brandis, D. Bar, M.B. Goldberg. 2015. Reconstruction of Material Elemental Composition Using Fast Neutron Resonance Radiography, *Physics Procedia* 69, 304-313

24. Kocurek Industries, www.kocurekindustries.com

25. Churcher P.L., P.R. French, J.C. Shaw and L.L. Schramm, 1991, Rock Properties of Berea Sandstone, Baker Dolomite and Indiana limestone, *SPE Int. Symposium on Oilfield Chemistry* Anaheim, CA February 20-22, 1991.

26. Brede H. J., G. Dietze, K. Kudo, U.J. Schrewe, F. Tancu and C. Wen, 1989, Neutron yields from thick Be targets bombarded with deuterons or protons, *Nucl. Instr. and Meth.* 274, 332-344

Maximizing the core value – joint investigations with special emphasis on complex electrical conductivity give new insights into Fontainebleau Sandstone

Matthias Halisch[1], Sabine Kruschwitz[2,3], Andreas Weller[4], Bernadette Mensching[5], Lucinda Gürlich[2,3]

[1] Leibniz Institute for Applied Geophysics (LIAG), Dept. 5 Petrophysics & Borehole Geophysics, Stilleweg 2, D-30655 Hannover, Germany
[2] Bundesanstalt für Materialforschung und –prüfung (BAM), Berlin, Germany
[3] Technische Universität Berlin, Berlin, Germany
[4] Clausthal University of Technology (TUC), Institute of Geophysics, Clausthal, Germany
[5] Leibniz University Hannover, Institute for Geosciences, Hannover, Germany

ABSTRACT

The Fontainebleau Sandstone is supposed to be well known amongst the core analysts' community. It has the reputation of being a reference sandstone, i.e. it is widely used to study and to assess petrophysical relationships and pore scale (mostly flow) related processes, due to its straightforward mineral composition (more than 99% quartz) and its ideal and well connected pore system. The results of these analyses are often used to understand and interpret data from other locations that feature clastic sedimentary reservoirs. Nevertheless, the assumption that the Fontainebleau Sandstone is "easy" to understand is not true, if the entire Fontainebleau Formation, and not only the high porosity zones, are taken into account. Within our joint research project, we are investigating Fontainebleau samples from almost every stratigraphic section of the Formation, covering a wide range of petrophysical data (i.e. porosity ranging from 2 % up to 24 %, and permeability covering five orders of magnitude). Besides classic core analysis, including 2D and 3D imaging, special emphasis has been laid upon the determination of the frequency dependent complex electrical conductivity by using the spectral induced polarization (SIP) method. This method has proven to be very sensitive towards the specific surface area and surface topology, as well as towards the type of pore system. As one result, it has been possible to characterize the different Fontainebleau units in detail, and to assess the highly increasing degree of complexity qualitatively and quantitatively, as this sandstone changes its type of pore system from single porosity towards dual porosity. Amongst the different petrophysical methods, only SIP was able to detect this transition reliably.

INTRODUCTION

Spectral Induced Polarization (SIP) measurements (i.e. "low frequency range" impedance spectroscopy) are used in many different ways to characterize natural rocks and soils. Main

foci of interest are the enhanced characterization of the causes of polarization effects in sedimentary rocks. The interactions between the matrix-fluid-system and within the electrical double layer as well as the correlation with petrophysical parameters, such as specific surface area, permeability, and pore radii distribution as derived from mercury intrusion capillary pressure data are considered. A variety of polarization models, either grain based or pore based, have been developed over the past years to describe the polarization effects of sedimentary rocks [e.g.: 1, 2, 3, 4, 5, 6]. The electric resistivity, as well as electric conductivity are both described as complex quantity values. As explained by [7], complex conductivity ($\sigma*$) of a rock sample is determined by measuring the magnitude of conductivity ($|\sigma|$) as well as the phase shift (φ), relative to a reference resistor. The real (σ') and imaginary (σ'') part of $\sigma*$, which represent the ohmic conduction and polarization charge transport mechanisms, respectively, are directly determined from impedance measurements. The phase shift thereby is defined as:

$$\varphi = \arctan(\sigma''/\sigma') \approx \sigma''/\sigma' \text{ (for } \varphi < 100 \text{ mrad),} \tag{1}$$

which is by convention defined as a positive value in conductivity space. Generally, complex conductivity models are based on two contributing conductivity terms, as denoted amongst others by [8]:

$$\sigma* = \sigma_{el} + \sigma*_{surf}. \tag{2}$$

The first term (σ_{el}) represents the conductivity of the electrolyte filled interconnected pore space, whereas the second term ($\sigma*_{surf}$) reflects conduction and polarization within the Electrical Double Layer (EDL) of the interconnected pore (matrix) surface, respectively. The SIP method itself has developed from classic frequency domain IP, and takes both, electric resistivity as well as phase shift into account. This method has become a potentially good tool for the enhanced characterization of rocks as well as of soils, due to the dependence of the measurements on the internal surface area (S_{por}) of the investigated materials [9]. Additionally, strong efforts have been made to predict permeability by using SIP method [10; 11]. Hence it seems promising to combine SIP measurements with other petrophysical methods such as mercury injection porosimetry (MIP), steady state permeametry, nitrogen adsorption and buoyancy measurements, as well as state of the art imaging techniques, such as environmental scanning electron microscopy (ESEM) and X-ray micro computed tomography (μ-CT).

SAMPLES & METHODOLOGY

The Fontainebleau (FO) sandstone, is often used as a reference sandstone for systematic laboratory studies, due to its high mineralogical "purity" (> 99.6 vol.-% SiO2). In fact, the mineralogical main component is quartz is a young tertiary sediment, for which several, controversial depository models exist [12; 13]. Despite that, the Fontainebleau sandstone features a broad variety of porous systems and hence of petrophysical properties [14]. For this study, we showcase first results of the denser part of the formation. Accordingly, the pore networks consist of pore bodies that are primarily connected via intergranular planes in between the idiomorphic quartz crystals (figure 1).
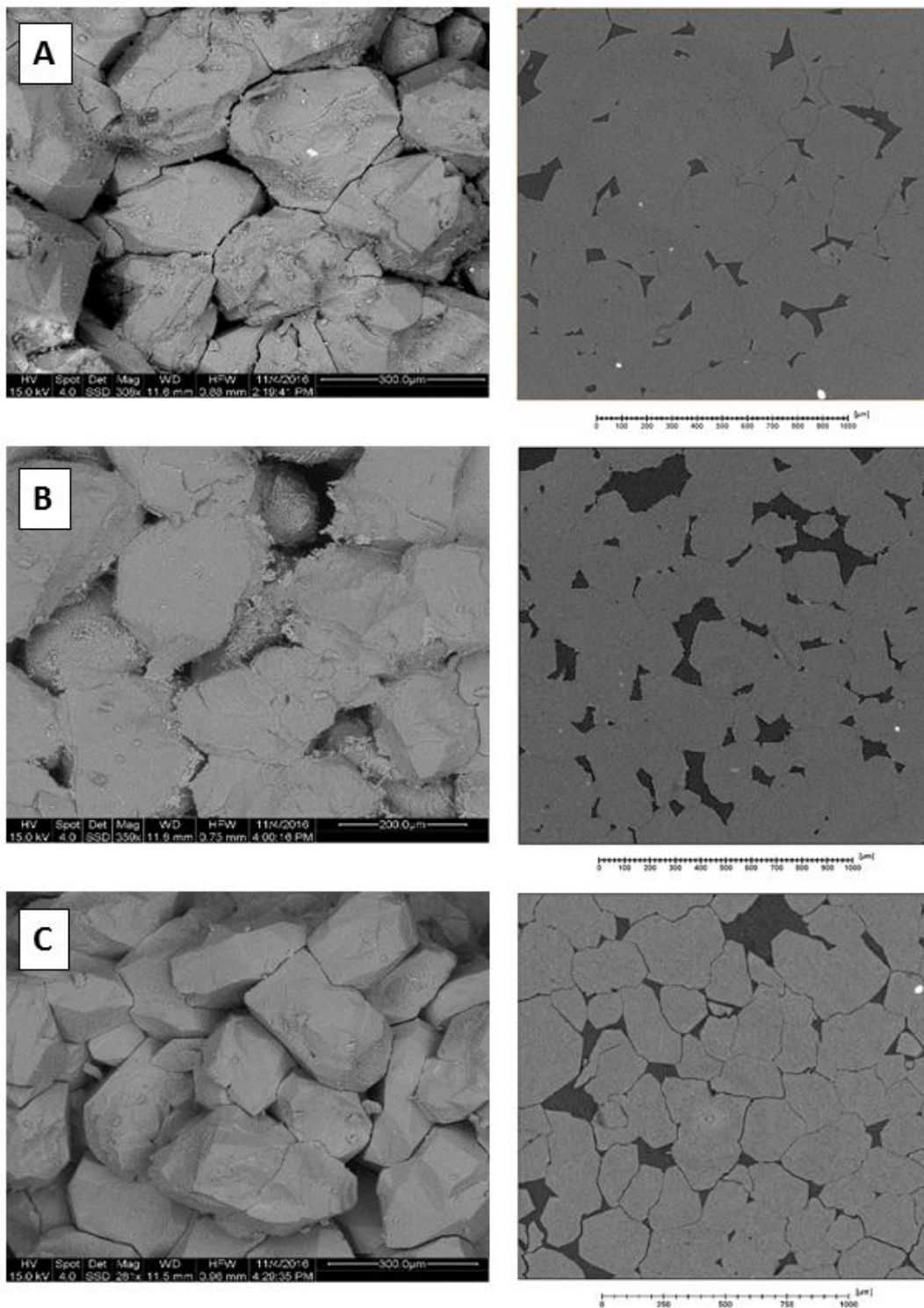
Figure 1: SEM (left hand side) and μ-CT (right hand side) images of representative samples from three different Fontainebleau stratigraphical blocks: A = block 36 (tight strata), B = block 64 (porous strata), C = block 93 (intermediate strata).

The specific surface area was determined by gas adsorption using the Brunauer-Emmet-Teller (BET) method [15]. Measurements were performed with a Quantachrome Autosorb iQ device with approximately 50 g of sample mass. Surface areas have been derived by 7-point BET adsorption measurements for each sample. Additionally, krypton has been used instead of nitrogen, due to the better adsorbent characteristics for the significant lower surface areas of these "clean" rock samples. Measurements were carried out at 77°K in a relative pressure (i.e. measured against ambient atmospheric pressure) range of 0.05 – 0.3. Mercury intrusion porosimetry (MIP) measurements were conducted by using an AutoPore III from Micromeritics within a pressure range from 0.003 MPa to 400 MPa. The calculated differential intrusion versus pore diameter curve has been used to determine the dominant pore throat diameter (D_{dom}). An Environmental Electron Scanning Microscope (ESEM) of the type FEI Sirion D1625 (low vacuum, 0.6 mbar) was used to investigate air-dried sub-samples of the three rock strata. The μ-CT imaging has been performed with a high resolution X-ray CT system (nanotom 180 S, GE Sensing & Inspection Technologies). Effective porosity of these sandstones has been determined by buoyancy method. As saturation fluid, degassed and desalinated tap water was used. The fluid density was presumed as constant (1 g/cm^3). Gas permeability has been determined by a custom built steady-state permeameter under ambient conditions, featuring a special Fancher-type core sleeve for lower overburden pressures (12 bar = 174 psi) and hence less mechanical influence upon the samples. These investigations were conducted following protocols provided by [16]. SIP measurements have been performed with a SIP-ZEL device [17] by using a custom built 4-electrode core holder [18] and within a frequency range from 1 mHz to 20 kHz. Demineralized water has been used for mixing the NaCl-solution with a varying fluid conductivity from 5 mS/m, 10 mS/m, 25 mS/m, 50 mS/m to 100 mS/m at a temperature of 20 °C for sample saturation.

RESULTS

The results from permeability, porosity and surface area measurements are showcased in figure 2. The permeability of the FO sandstone (fig. 2, A) used in this study covers four orders of magnitude (from 0.1 to 300 mD). The results are in good accordance with the data from [14] and follow the known trend. Reference data, provided by Cydarex, over-estimate the permeability for lower porosity samples slightly, due to the decreased accuracy of the used Tinyperm device (personal communication with Roland Lenormand). The different FO strata can be clearly distinguished from each other (block #36 lowest porosity and permeability values, which successively increase from block #93 to block #64) and are coherent with the qualitative results from sample imaging (fig. 1). Figure 2 (B) showcases the correlation between the Klinkenberg corrected gas permeability (k_{kl}) and specific surface area related to the pore volume (S_{por}). Again, the different block strata can be clearly differentiated from each other. Samples from block #36 and block #93 follow a steep trend line, showing a strong dependence of the hydraulic conductivity towards the surface area. Since these samples solely consist of idiomorphic quartz, it can be assumed that the surface area for these strata is dominantly influenced by the accessible pore network and not by the matrix material at all.
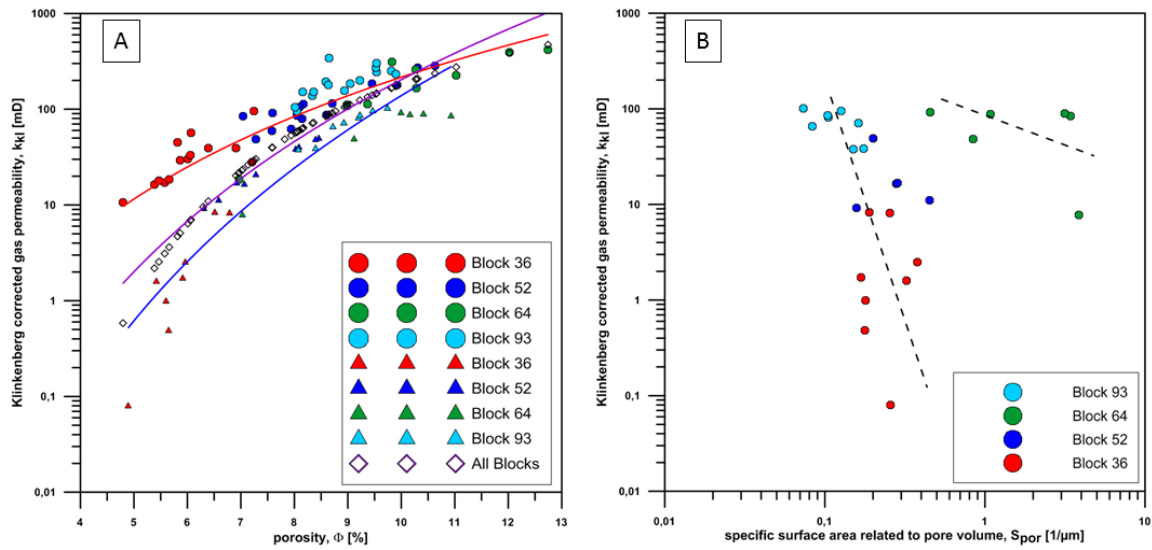
Figure 2: Porosity – permeability (A) and surface area – permeability relationship (B) for the investigated stratigraphical Fontainebleau block units (circles: data from Cydarex, $R^2 = 0.75$; triangles: data from LIAG, $R^2 = 0.88$; diamonds: data from [14] $R^2 = 0.97$).

The samples originating from block #64 follow a significantly different trend than the other strata, showing a less pronounced dependence of the permeability upon the surface area. Here, this effect can be explained by the overgrowth of the idiomorphic crystal surfaces by secondarily precipitated quartz, as shown within figure 1 (B), left hand side. Accordingly, here the influence of the matrix material (or better of the surface topology) dominates over the overall influence of the pore network structure.

Interestingly, SIP measurements on samples of these three different strata show an even higher sensitivity towards the differences in the pore networks and pore surfaces. In figure 3, representative SIP phase shift (left hand side) and resistivity spectra (right hand side) for block #36, #64 and #93 are presented. All investigated samples from block strata #36 and #93 show for low fluid conductivities a pronounced phase shift maximum at low frequencies (approx. at 0.01 Hz for unit #36 and approx. at 0.1 Hz for unit #93). This phase peak vanishes as theoretically expected, for stepwise increasing fluid conductivity according to [7]. Hence, the different relaxation times (i.e. inverse of frequency) can possibly be linked towards the accessible pore pathways, i.e. the lesser connected the pores, i.e. the longer the plane like pores that connect the few pore bodies, the longer the corresponding relaxation time (i.e. the smaller the peak frequency). Contrary to that, the samples from block #64, which feature the distinct secondarily precipitated quartz overgrowth throughout the entire sample set, show a completely different phase shift behavior. For these samples, a double phase peak behavior in the low (peak one around 0.02 Hz) and middle (peak two around 0.35 Hz) frequency range is observed (fig. 3, middle). Furthermore, if the fluid conductivity increases, the middle range phase peak vanishes, whereas the low frequency phase peak can still be assumed, but the peak shifts towards higher relaxation times in the sub-millihertz range.
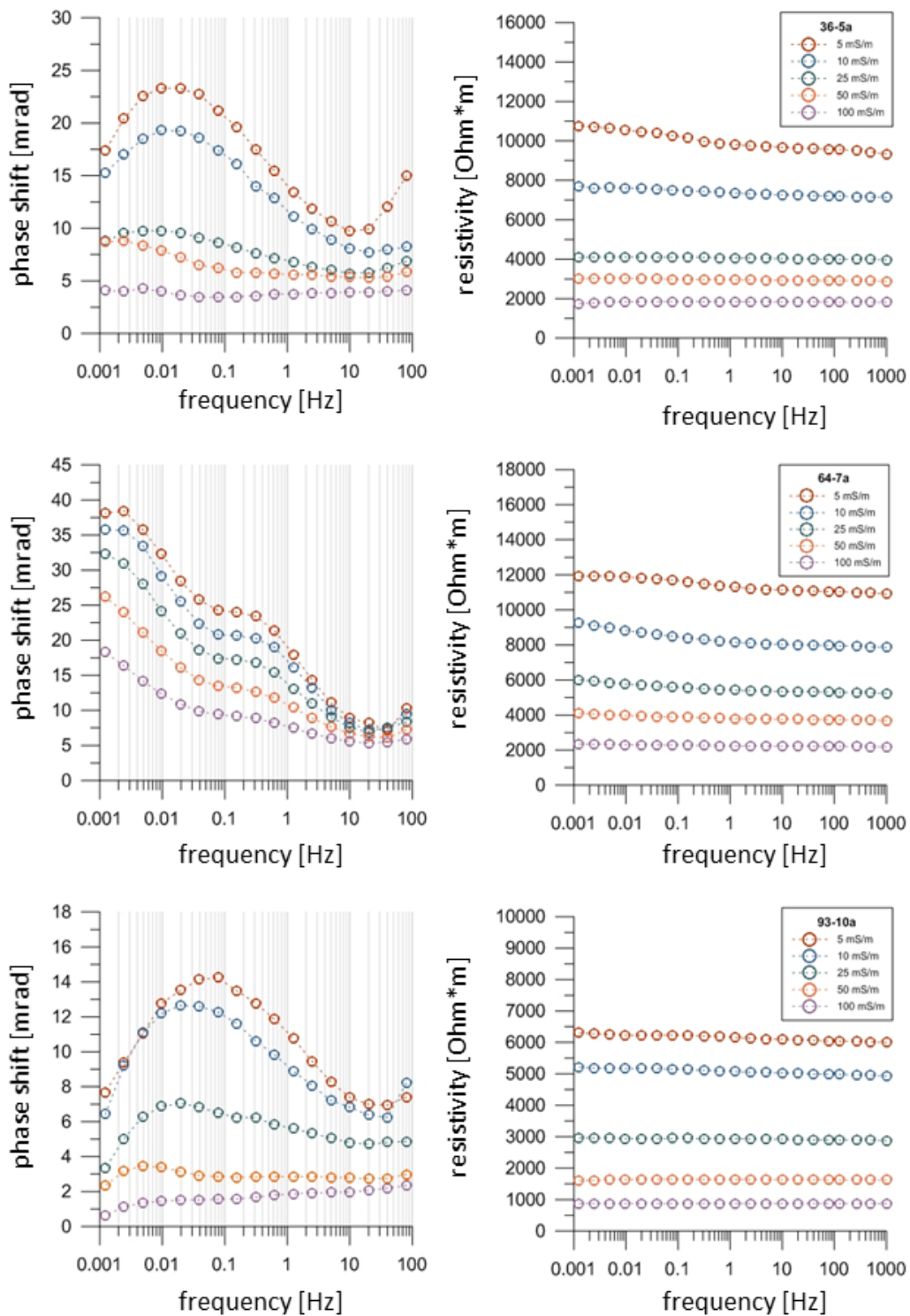
Figure 3: Representative SIP phase spectra (left hand side) and resistivity data (right hand side) for three block units: block #36 (top, sample FO-36-5a), block #64 (middle, sample FO-64-7a), block #93 (bottom, sample FO-93-10a).

Consequently, it seems reasonable to assume that the maximum phase shift peak may be linked with a characteristic (pore or grain) length within the samples (compare [19]). Following this idea, the maximum phase shift has been correlated to the dominant pore throat diameter, which has been measured by MIP. This correlation is presented in figure 4, which also has been observed for other sandstones as reported by [20]. Three possible outliers (marked by dashed circles) for the entire sample set can be identified within the given graph. These measurements either do not indicate a distinct phase shift (i.e. a "true" phase maximum within the measured frequency range), or are influenced by low permeability (< 5 mD), i.e. by a low amount of hydraulically and electrically connected pore space, and hence by an overall low polarization capability. Without these samples, a correlation ($R^2 = 0.76$) between D_{dom} and the related block strata can be detected. By trend, samples from block #93 seem to feature the largest pore throat diameter and samples from block #64 and #36 the lowest. Especially for block #64 this is a surprising result, since these samples are the most porous and permeable of this study.
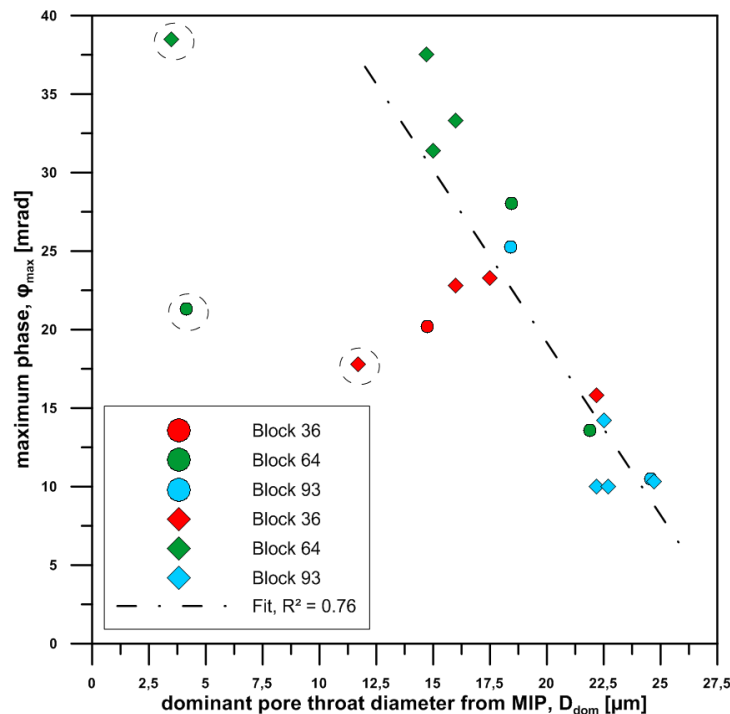
Figure 4: Correlation of the maximum phase shift (measured with SIP) with the dominant pore throat diameter (measured by MIP) for the three investigated Fontainebleau block strata (circles indicate LIAG, diamonds indicate BAM data; $R^2 = 0.76$). Dashed circles mark outliers as mentioned in the text.

SUMMARY & CONCLUSIONS

Within this study we have shown, that spectral induced polarization is a reliable method for the enhanced characterization of the Fontainebleau sandstone in general, and for its related stratigraphical units in particular. Due to its high sensitivity towards pore network and pore surface changes, different stratigraphical units can be clearly differentiated and

probably even classified. We have observed a good correlation between the maximum of the SIP phase shift and the dominant pore throat radius for this rock type, as it has been reported for others sandstones before [20].

OUTLOOK

As part of an ongoing project, research upon the Fontainebleau sandstone is not finished yet. Consequently, all stratigraphical units will be investigated by SIP measurements within the near future. In addition, more multi-salinity conductivity, fluid ion-valence variations, zeta-potential, as well as formation factor measurements will be conducted to gain more insights for the correlation with SIP data. Furthermore, the impact of silica leaching upon the SIP relaxation behavior and upon the pore structure related petrophysical properties will be investigated.

ACKNOWLEDGEMENTS

REFERENCES

1. Schwarz G., "A theory of low-frequency dispersion of colloidal particles in electrolyte solution", *Journal of Physical Chemistry,* (1962) **66**, 2636-2642.
2. Scott J.B.T. and R.D. Barker, "Characterization of sandstone by electrical spectroscopy for stratigraphical and hydrogeological investigations", *Quarterly Journal of Engineering Geology and Hydrogeology*, (2005) **38**, 143-154.
3. Tarasov A. and K. Titov, "Relaxation time distribution from time domain induced polarization measurements", *Geophysical Journal International,* (2007) **170**, 31-43.
4. Kruschwitz S., A. Binley, D. Lesmes and A. Elshenawy, "Textural controls on low frequency electrical spectra of porous media", *Geophysics,* (2010) **75**, 113-123.
5. Revil A., K. Koch and K. Hollinger, "Is the grain size or the characteristic pore size that controls the induced polarization relaxation time of clean sands and sandstones?", *Water Resources Research,* (2012) **48.**
6. Weller A. and L. Slater, "Induced polarization dependence on pore space geometry: empirical observations and mechanistic predictions" *Journal of Applied Geophysics,* (2015) **123**, 310-315.
7. Weller A. and L. Slater, "Salinity dependence of complex conductivity of unconsolidated and consolidated materials: comparisons with electrical double layer models", *Geophysics,* (2012) **77**, 185-198.
8. Vinegar H.J. and M.H. Waxman, "Induced Polarization of shaly sands", *Geophysics*, (1984) **49**, 1267-1287.

9. Weller A., L. Slater, S. Nordsiek and D. Ntarlagiannis, "On the estimation of specific surface per unit pore volume from induced polarization: a robust empirical relation fits multiple data sets", *Geophysics*, (2010) **75**, 105-112.

10. Revil A. and N. Florsch, "Determination of permeability from spectral induced polarization in granular media", *Geophysical Journal International*, (2010) **181**, 1480-1498.

11. Weller A., S. Nordsiek and W. Debschuetz, „Estimating permeability of sandstone samples by nuclear magnetic resonance and spectral induced polarization", *Geophysics*, (2010) **75**, 215-226.

12. Guillocheau F., C. Robin, P. Allemand, S. Bourquin, N. Brault, G. Dromart, R. Friedenberg, J.-P. Garcia, J.-M. Gaulier, F. Gaumet, B. Grosdoy, F. Hanot, P. Le Strat, M. Mettraux, T. Nalpas, C. Prijac, C. Rigollet, O. Serrano and G. Grandjean, "Meso-Cenozoic geodynamic evolution of the Paris Basin: 3D stratigraphic constraints" *Geodinamica Acta*, (2000) **13**, 189–246.

13. Thiry M., M. Bertrand-Ayrault and J.C. Grisoni, "Ground water silicification and leaching in sands: Example of the Fontainebleau Sand (Oligocene) in the Paris Basin", *Geological Society of America. Bulletin,* (1988) **100**, 1283–1290.

14. Bourbie T. and B. Zinszner, "Hydraulic and acoustic properties as a function of porosity in Fontainebleau sandstone", *Journal of Geophysical Research: Solid Earth* (1985) **90 (B13)**, 11524–11532.

15. Brunauer S., P. Emmet and E. Teller, "Adsorption of gases in multimolecular layers", *Journal of the American Chemical Society*, (1932) **60(2)**, 309-319.

16. API, American Petroleum Institute, Exploration and Production Department, "Recommended Practice (RP) 40: Core Analysis", (1988) **2**, API Publishing Services, Washington, DC, USA.

17. Zimmermann E., A. Kemna, J. Berwix, W. Glaas, H. Münch and J. Huisman, „A high-accuracy impedance spectrometer for measuring sediments with low polarizability", *Meas. Sci. Technol.*, (2008) **19(10)**, 105603 ff.

18. Halisch M., T. Grelle, S. Hupfer, J.T. Blanke and C. Lehne, "A new and modular laboratory core holder for high-precision measurements with low frequency impedance spectroscopy on natural rocks", *Annual Symposium of the Society of Core Analysts (SCA) Proceedings*, (2017) Vienna, Austria, SCA2017-021.

19. Kruschwitz S., M. Halisch, C. Prinz, A. Weller, M. Müller-Petke and R. Dlugosch, "Towards a better understanding of electrical relaxation", *Annual Symposium of the Society of Core Analysts (SCA) Proceedings*, (2017) Vienna, Austria, SCA2017-001.

20. Kruschwitz S., C. Prinz and A. Zimathies, "Study into the correlation of dominant pore throat size and SIP relaxation frequency", *Journal of Applied Geophysics,* (2016) **135**, 375-386.

3D-NMR, simultaneous determination of saturations and wettability

Benjamin Nicot, Georges Ibrahim, Gregory Dubes
TOTAL

This paper was prepared for presentation at the International Symposium of the Society of Core Analysts held in Vienna, Austria, 27 August – 1 September 2017

ABSTRACT

The knowledge of saturations and wettability is key in the assessment of the potential of an oil field. Saturations control the hydrocarbon volume in place, while wettability has a strong influence on the recovery. While many techniques are available to derive saturations, both from laboratory and log data, techniques for measuring wettability are limited to the laboratory and are expensive and time consuming.

Traditionally, laboratory measurements of wettability in the laboratory are based on spontaneous and forced drainage and imbibitions (USBM and Amott indexes). Many attempts have been presented in the past to replace these long and expensive measurements by other techniques. Among these techniques, NMR has a strong potential thanks to its natural sensitivity to saturations and wettability. On the one hand, NMR is sensitive to saturations through DT2 maps. On the other hand, T_1T_2 maps are sensitive to wettability. In these maps many authors have already reported that the wetting fluid has a high T_1/T_2 ratio. However one question remains: which fluid is the fluid that exhibits a high T_1/T_2 ratio? The difficulty comes from the fact that there is no fluid identification in the T_1T_2 maps.

In this paper we demonstrate the interest of acquiring 3 dimensional NMR: Longitudinal relaxation time T_1, transverse relaxation time T_2 and Diffusion D. The correlated information between the three NMR parameters allows the simultaneous interpretation of the data in terms of pore size distribution, saturations (thanks to Diffusion), and identification of the wetting fluid (thanks to T_1). This method has been developed on bulk fluids, and successfully tested on real rocks.

INTRODUCTION

Nuclear Magnetic Resonance (NMR) has been used in the oil industry since the early beginning of NMR. Soon after the discovery of NMR by Bloch and Purcell in 1946, the oil industry recognized the interest of this technique and launched laboratory NMR studies of fluids in porous media. Since the first earth's-field NMR logging tool developed by Chevron in 1960, NMR measurements have evolved a lot. NMR can be used to measure different parameters: Quantity of signal, relaxation times T_1 and T_2, diffusion coefficient.

NMR first answer of interest to the oil industry is the quantity of signal. The quantity of signal measured by an NMR device is proportional to the amount of Hydrogen nuclei present in the sample. Therefore, on a rock containing liquids of know Hydrogen density, NMR measures porosity.

Relaxation times are used to get structural information on the rock. Since the discovery of reduced fluid relaxation times in porous media, NMR has been used as a pore size indicator [1], and NMR permeability predictors such as the Schlumberger-Doll Research [2] and the Timur-Coates [3] have been proposed.

Since the 2000's and the pioneering work of Venkataramanan et al.[4], two dimensional NMR has arisen, allowing to correlate two different NMR parameters. The most widely used NMR 2D map has been the Diffusion-T_2 map, allowing the determination of the water and oil saturations thanks to their diffusion contrast. The interest of performing a 2D measurement has been tremendous and dedicated logging tools have been developed to allow the acquisition of the 2D Diffusion-T_2 maps [5].

Meanwhile, the industry recognized the natural sensitivity of NMR to wettability and many papers have been published demonstrating the potential of using T_2 for getting wettability information [6][7][8]. However, the work from Korb et al. [9] demonstrated that a measurement of T_1 is very sensitive to wettability and Valori et al. [10] published a very strong dependence of the T_1/T_2 ratio of oil with wettability. The remaining difficulty being: how to measure the T_1/T_2 ratio of oil.

Here we propose to combine the benefits of the Diffusion-T_2 map to obtain saturations with the potential of the T_1T_2 map to obtain wettability. For this purpose we developed a 3D inversion allowing the simultaneous acquisition and inversion of T_2, T_1 and diffusion. We first give the principle of the method, and then demonstrate the concept on bulk fluids. Last, we provide experimental examples acquired on outcrop and reservoir rocks.

PRINCIPLE OF 3DNMR

The 3D NMR sequence used in this paper consists of three main segments. The first one is a simple inversion-recovery with a waiting time of ΔT_1. This segment is followed by a pulsed gradient stimulated echo of gradient **G** for diffusion encoding. Finally a classical CPMG sequence is used to characterize the T_2 distribution. The overall pulse sequence is presented in Fig.1 where K_{T1} is the longitudinal magnetization kernel, K_D is the diffusion kernel and K_{T2} is the transverse magnetization kernel.

The problem is to find the relaxation times T_1, T_2 and the diffusion coefficient D, knowing the magnetization M. Mathematically, the problem can be written in the following way:

$$M(i, j, k) = \sum_{l,m,n} K_{T_1}(i, l) K_{T_2}(j, m) \, K_D(k, n) F(l, m, n) + \varepsilon(i, j, k) \quad (1)$$

Where $M(i, j, k)$ denotes the magnetization resulting from the ith ΔT_1, the kth G, and measured at the jth nTE. The discretised kernels and the discretised density function F are calculated using the discretisation over T_1, T_2 and D.
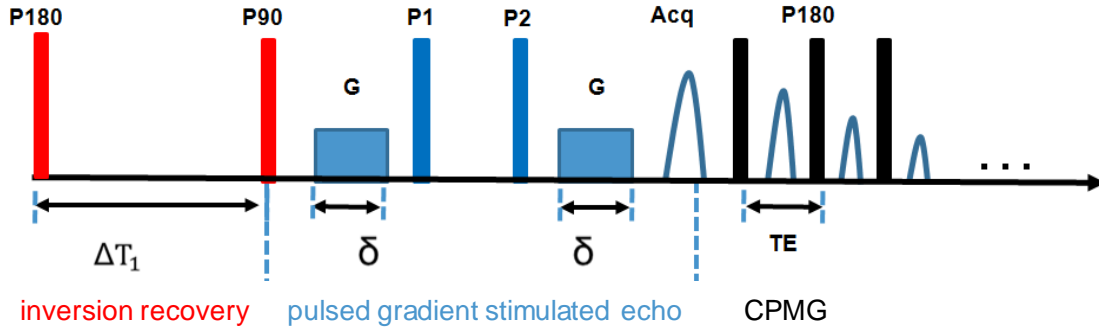

Fig.1: The 3D NMR sequence: ΔT_1 is the inversion time in the inversion recovery segment; in the PGSTE segment δ and G are the duration and amplitude of the gradient pulse; in the CPMG segment TE is the inter echo time. This sequence is run by varying ΔT_1 for encoding T_1 and varying G for encoding diffusion. (time intervals not to scale). Typical parameters are presented in Table 2.

The objective of the inversion is to find the optimal F that best fits the data M. In 2D, the problem can be written as a matrix product and solved using the method proposed in Venkataramanan et al. [4]. In 3D the matrix product no more holds. The mathematical formulation of the problem is given in [11]. We have proposed a way to solve this problem [12] based on a relatively simple strategy detailed in Figure 2:

1. Transform the 3D problem into a 2D problem by combining 2 Kernels. The key idea is to transform a third degree tensor into a second degree tensor by unstacking its elements into the first horizontal plane.
2. Solve the 2D problem using the classical approach proposed in [4],
3. Transform the 2D solution into a 3D solution

This way, the mathematical problem presented in equation (1) (that was impossible to solve) is transformed into a more simple 2D problem defined in equation (2)

$$R(M) = (K_D \otimes K_{T_1}) . R(F) . K'_{T_2} \quad (2)$$

All the details of the inversion strategy are given in [12].
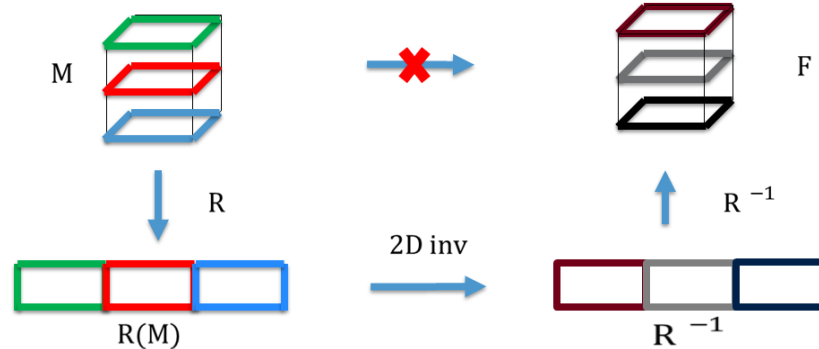
Figure 2: Principle of the 3D NMR inversion: We first transform the problem into a 2D problem by unstacking the 3D tensor into a 2D matrix, solving the problem in 2D, and then re-stacking the results into a 3D matrix to get the solution

EXPERIMENTAL

The NMR acquisitions were performed on a 2MHz Geospec from Oxford Instrument equipped with 1D gradients. Typical pulse length is 13µs for the 90° pulse and 6ms for gradient pulse. Typical inter-echo time is 200µs, and signal is acquired to a minimum SNR of 40, using the sequence described in Fig.1 and the parameters given in

Table 2. Typical acquisition time can range from 10hours on bulk fluids to a few days on rock samples.

RESULTS ON BULK FLUIDS, PROOF OF CONCEPT

The concept of 3D (T_1-T_2-D) NMR was tested on a sample made of bulk fluids: 40% of $MnCl_2$ doped water and 60% of synthetic oil. Since the two fluids have nearly the same hydrogen index, the apparent porosity of the sample is 100%. Its NMR properties are summarized in Table 1.

	$T_1(s)$	$T_2(s)$	$D(m^2 s^{-1})$
Water	0.07	0.05	2.10^{-9}
Oil	0.2	0.2	10^{-10}

Table 1 : NMR properties of the fluid sample

On this sample, the acquisition of a 3D NMR cube was performed using the sequence described in Fig.1 and the parameters given in

Table 2.

	Min	Max	Nb of values
ΔT_1	5ms	3s	25
G	0	20 Gauss/cm	25
nTE	0	1s	5000

Table 2: Acquisition parameters

The result of the 3D inversion gives a cube of intensities; the axis of the cube being T_1, T_2 and D. An example of the cube is given in Figure 3. For practicity, the projections of the cube on the D-T_2 map and on the T_1-T_2 maps are displayed. In these projections, the water and oil signals can be clearly identified from the D-T_2 map: the round signal (signal A on Figure 3) corresponds to water. In the T_1-T_2 map this signal exhibits a high T_1/T_2 ratio; this is due to the use of $MnCl_2$ as a dopant. The elongated signal (signal B in Figure 3) corresponds to the mineral oil.
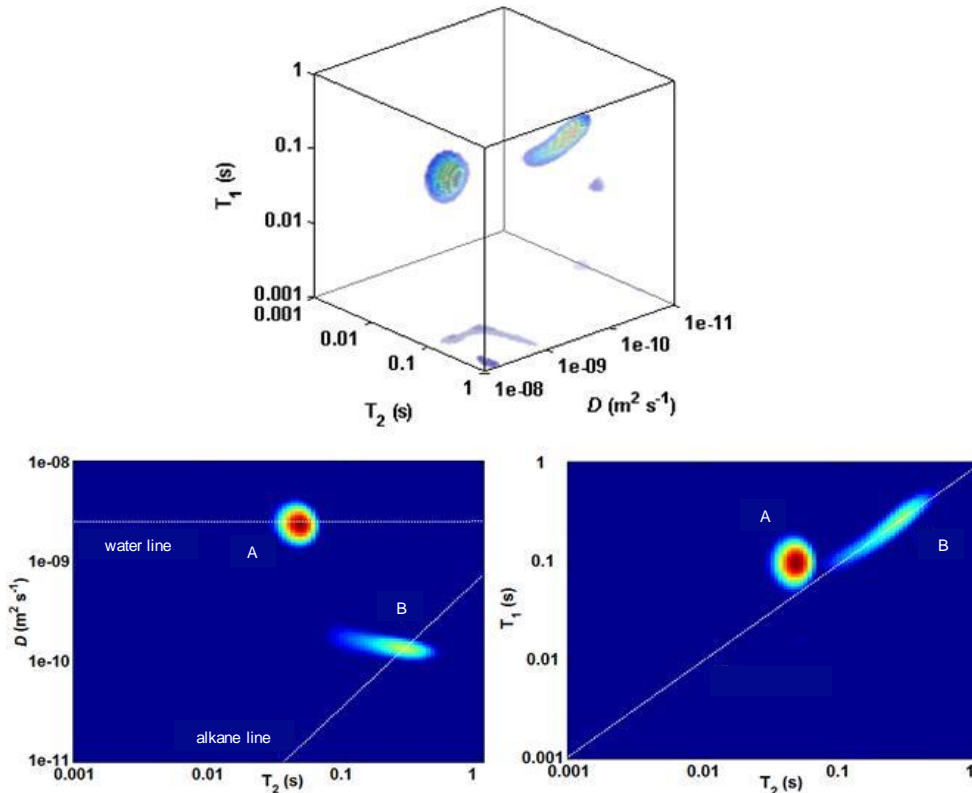
Figure 3: 3D inversion results carried on sample (2). Top panel shows a cube representation of the solution with a resolution of (100,100,100). Bottom left and right panels and represent the projection of the 3D solution on theDT2 and T1T2 planes.

RESULTS ON OUTCROP ROCK

This section discusses the results of the experiments on real rocks. We discuss petrophysical properties of the rock samples, crude oils properties, samples preparation and the results of processing.

Rock and crude oils properties
We present the results from one limestone plugs from the French quarry Estaillades, exhibiting bimodal porosity.
The crude oil used was a viscous crude oil (viscosity~50cP).

Samples preparation

The sample first dried in an oven heated to 80°C, and porosity ϕ=28.5p.u. was determined in the lab measuring total volume and solid volumes, using a pycnometer. The plug was then vacuumed in a cell, and then saturated with brine at 200bars to remove any air. Due to the rock type, the brine was designed to avoid degradation (0.4mol/l NaCl + 0.33mol/l $CaCl_2$).

A suite of NMR acquisitions was performed on these samples at 100% brine saturation, referred later as Sw1.

Samples were set in Hassler cells for setting irreducible water saturation (Swi). The gas confining pressure was set to 75bars, keeping a 25bars pore pressure with crude oil. The plug was slowly swept, monitoring the fluids flowing out. The injected oil volume was equivalent to 4 times the porous volumes, estimated from NMR @ Sw=1. At this stage, the sample was close to (if not at) irreducible water saturation. A second suite of NMR acquisitions was performed after dismounting from the Hassler cell, referred as SwiBA (irreducible water saturation, Before Ageing).

The sample was then replaced in Hassler cell, in the same conditions. After a quick sweep equivalent to 1 Vp, a heating phase was started in order to age the plug and change wettability. Heating jackets were set on Hassler cells and temperature was controlled to 80°C at the plug. This operation lasted 3 weeks, and included a weekly oil sweep with an oil volume equivalent to 1 Vp. A third suite of NMR acquisitions was performed after dismounting from cells, referred as SwiA (irreducible water saturation, Aged).

NMR acquisition

The complete set of NMR acquisitions consisted in: 1D: T_2; 2D: T_1-T_2 map and D-T_2 map; and 3D: T_2-T_1-D cube

As shown in Figure 4, the T_2 distribution obtained on this sample saturated with brine partly overlaps with the bulk crude oil distribution. This already can help predicting that a single T_2 experiment would not be capable of distinguishing oil from water inside this rock.

In fact, as shown in Figure 4, a T_2 experiment is indeed not able to distinguish between oil and water, neither before nor after the ageing process. However, a small shift of the main T_2 peak towards shorter T_2 can be observed during the ageing. In order to interpret this shift into a wettability change, one would have to know if the peak corresponds to a water or an oil signal.
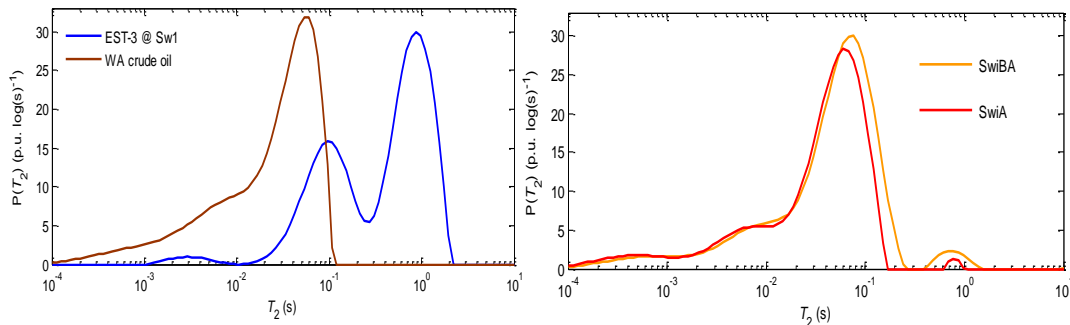
Figure 4 : Left : T_2 distribution of the Estaillade sample saturated with brine (blue) and of the bulk crude oil (brown). Right: T_2 distribution of the Estaillade sample at irreducible water saturation before ageing (orange) and after ageing (red).

In order to distinguish the NMR signals corresponding to oil and water, a diffusion contrast is required. Figure 5 presents the T_2 distribution, D-T_2 maps and T_1-T_2 maps obtained on this sample before and after ageing.

In this case, water and oil NMR signals have similar T_2, but the diffusion contrast is sufficient to separate the water and oil signals. This is the classical way to measure fluid saturations from NMR.

Looking at the T_1-T_2 map in Figure 5, a small increase of the T_1/T_2 ratio can be observed during ageing. As stated by Valori et al. [10], the T_1/T_2 ratio of the oil can be used as a proxy for wettability, however in this case it is not possible to know which fluid (water or oil) is responsible for the increase in T_1/T_2 ratio (i.e. which fluid is the most wetting fluid). The missing information is a connection between the D-T_2 map (allowing identifying the fluids) and the T_1-T_2 map (allowing the estimation of wettability).

The acquisition of 3D (T_1-T_2-D) NMR data can solve this issue. The 3D NMR cube acquired on the Estaillades sample before ageing is presented in Figure 6. The projections of the cube on the DT$_2$ and T_1T_2 maps are also presented. All the interest of the technique resides on the possibility to identify the oil signal on the DT$_2$ projection and to display the corresponding signal on the T_1T_2 projection. In this example, the oil signal has been selected and allows the determination of the T_1/T_2 ratio for the oil. The exact same methodology has been applied on this sample after ageing and the results are presented in Figure 7.

For this example, even if water and oil signal are superimposed in a simple T_1T_2 map, the use of 3D NMR allows the identification of the signals and the calculation of a mean T_1T_2 ratio for the oil. We found $T_1/T_{2oil(before\ ageing)}=1.9$ and $T_1/T_{2oil(after\ ageing)}=2.2$. According to Valori et al. [10] the T_1/T_2 ratio of the oil can be used as a proxy for a wettability index. This method has been used in Figure 10 to estimate the corresponding wettability indexes of $W_{(before\ ageing)}=0.4$ and $W_{(after\ ageing)}=0.2$.
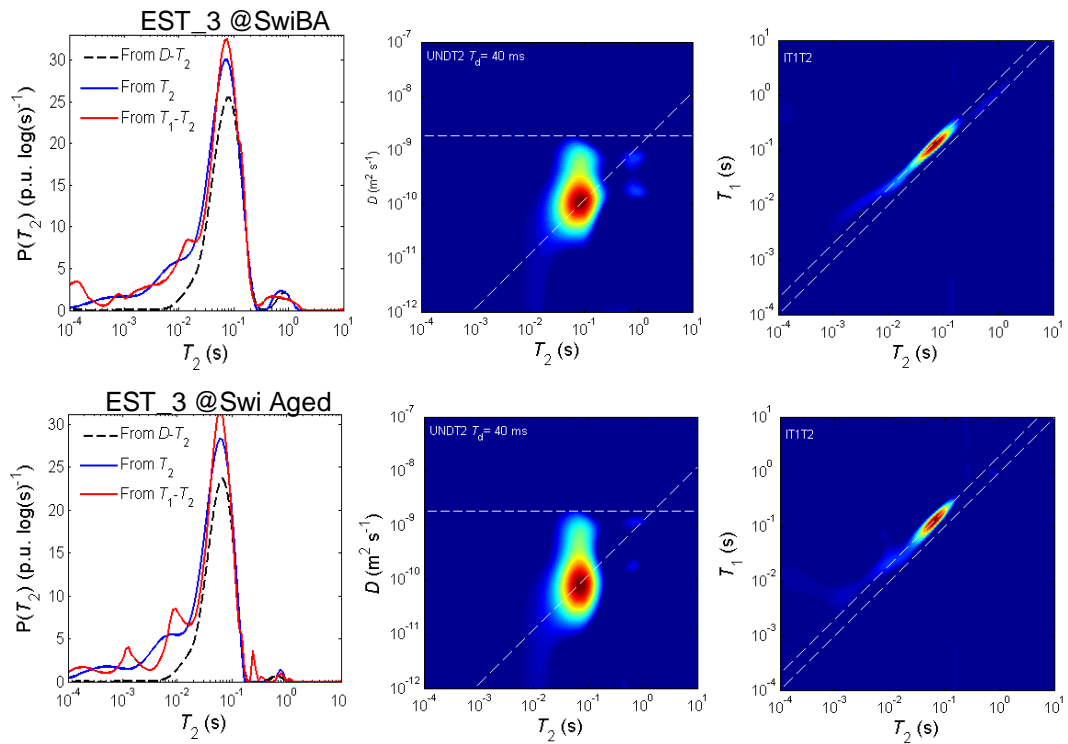
Figure 5: T$_2$, D-T$_2$ map and T$_1$-T$_2$ map obtained on the Estaillades sample before (top) and after (bottom) ageing
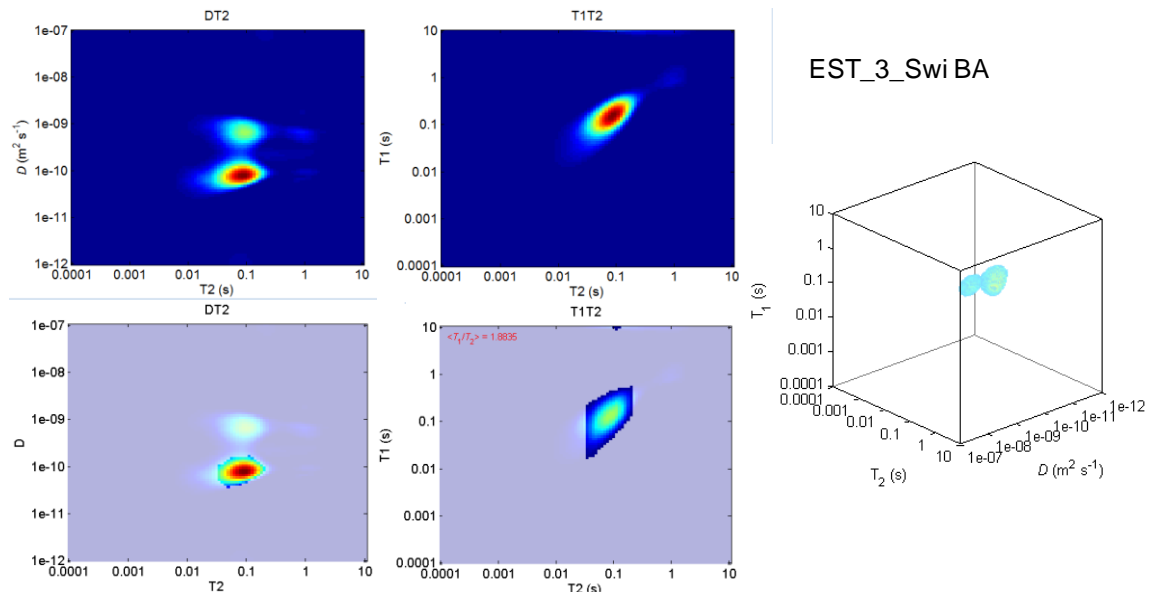
Figure 6: 3D NMR results obtained on the Estaillade carbonate at Swi before ageing. The 3D cube is presented on the right. On the left are presented the DT$_2$ and T$_1$T$_2$ projections. Bottom left are presented the

results of selecting the oil signal in the DT_2 projection and displaying the corresponding signal in the T_1T_2 projection.
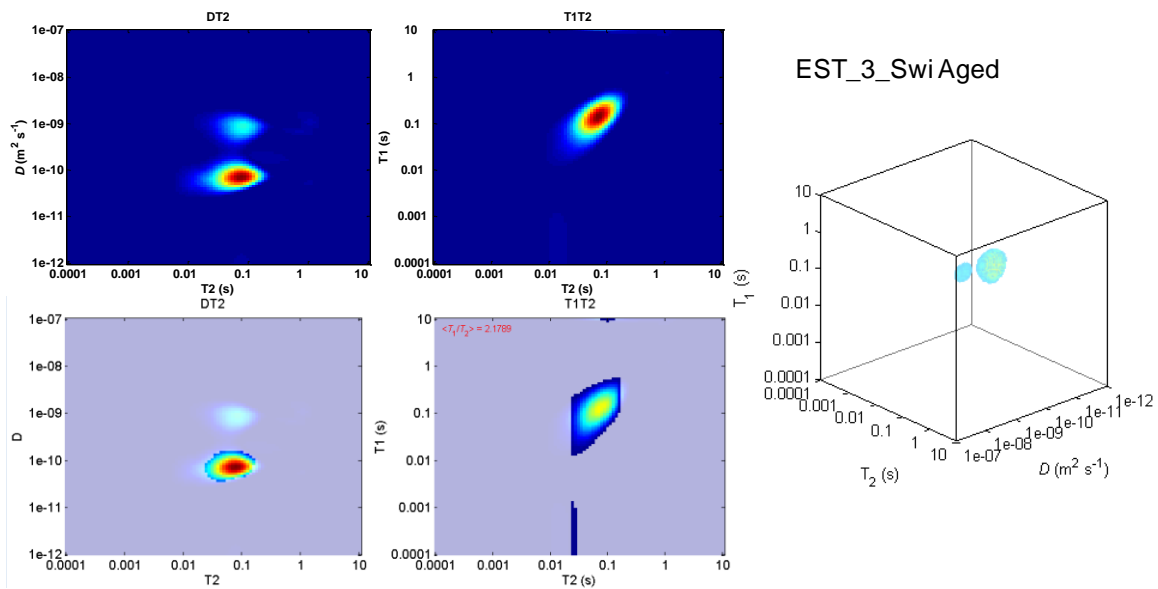

Figure 7 : 3D NMR results obtained on the Estaillade carbonate at Swi after ageing. The 3D cube is presented on the right. On the left are presented the DT_2 and T_1T_2 projections. Bottom left are presented the results of selecting the oil signal in the DT_2 projection and displaying the corresponding signal in the T_1T_2 projection.

RESULTS ON RESERVOIR ROCK

We present here the result of the 3D NMR acquisition on a real reservoir rock. This reservoir rock is a sandstone in the "as received" state, containing a light oil (~1cp). This reservoir is known to be strongly oil wet with Amott index of the order of -0.8.

On the same sample, Amott test and 3DNMR were performed. The Amott test was performed using mineral oil, after ageing at irreducible saturation in dead crude oil.

When performing the 3DNMR acquisition, presented in
Figure 8, the oil and water signals can be separated from the DT_2 projection. This allows the identification of the oil signal on the T_1T_2 projection. In this case, the oil and water signal do not properly separate in the T_1T_2 projection, this is due to a lack of encoding of the T_1 using the parameters presented in
Table 2 (25 points). Once the position of the oil signal is known, a more simple T_1T_2 measurement can be performed, with a much stronger encoding of the T_1. As this stage, a 40 by 40 points encoding of a 3DNMR could have been done, but would have been very time consuming. In this case, the 3DNMR unambiguously assign the signal to oil and water thanks to the diffusion encoding. Once
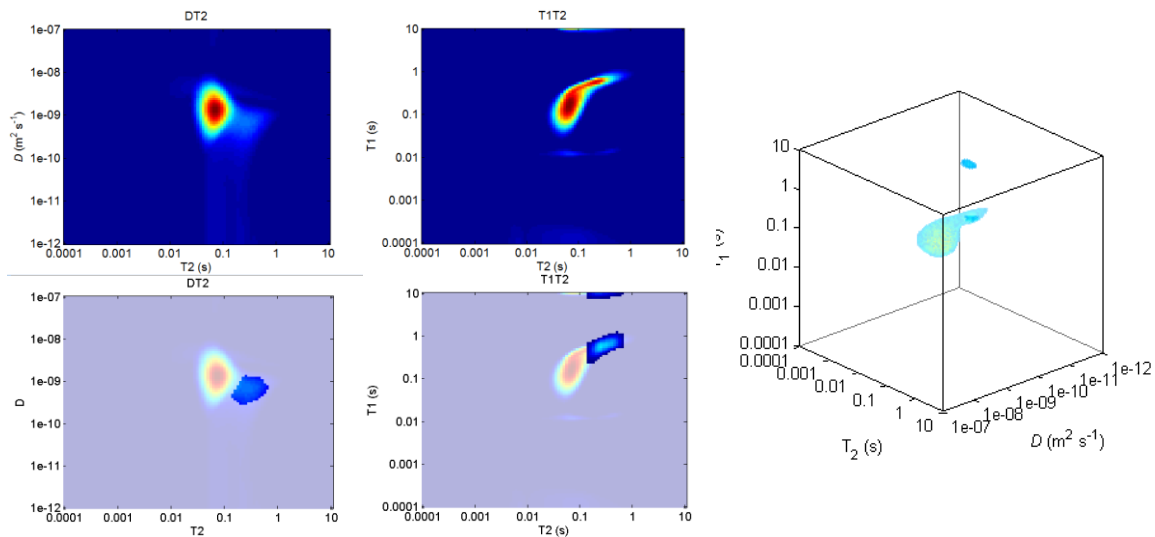
Figure 8: 3D NMR results obtained on the reservoir sandstone. The 3D cube is presented on the left. On the right are presented the DT_2 and T_1T_2 projections. Bottom left are presented the results of selecting the oil signal in the DT_2 projection and displaying the corresponding signal in the T_1T_2 projection.

In Figure 9 we present the 2D D-T_2 and T_1-T_2 maps acquired on this sample with the same parameters as in Table 2 but encoding using 40 points. This allows a much better resolution of the maps, for both DT_2 and T_1T_2. This T_1-T_2 map was then used to calculate the mean T_1/T_2 ratio for the oil. We found T_1/T_{2oil}=3.7, corresponding to a wettability index W=-0.75, following the Valori et al.[10] method presented in Figure 10.
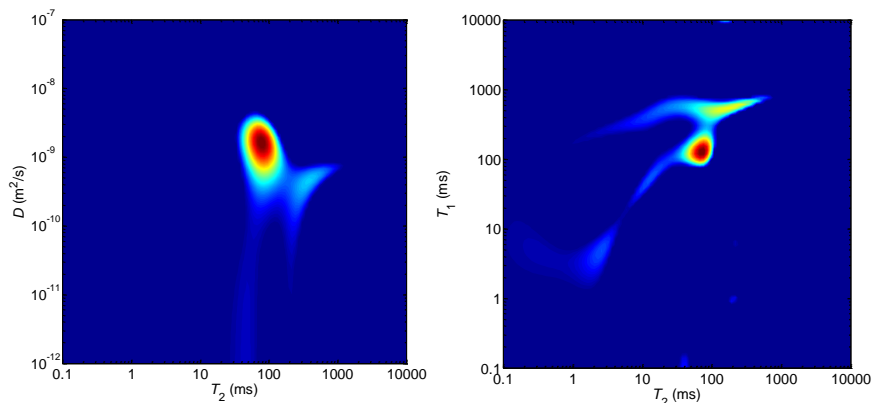
Figure 9: D-T_2 map (left) and T_1-T_2 map (right) obtained on the "as received" reservoir sandstone

In this example, it is arguable that a similar information could have been obtained with 2D maps only. In fact the use of 3DNMR in this case was to unambiguously identify the oil signal in the T_1-T_2 map. However, for samples like the Estaillades samples previously shown, where the oil and water signal have similar T2, 3DNMR is the only way to extract the T_1T_2 ratio of the oil, therefore the wettability.
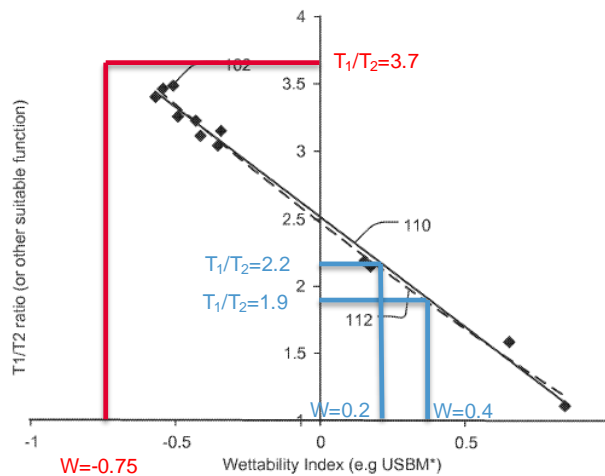
Figure 10: Correlation between the T_1/T_2 ratio of the oil with wettability (from [10]). The results from Estaillades carbonates before and after ageing are presented in blue, the results from the reservoir sandstone are presented in red.

CONCLUSION

We present in this paper the acquisition and processing of 3D NMR data: T_1, T_2 and Diffusion. We demonstrate that the interest of increasing the dimensionality of an NMR measurement is to unlock the fluids identification and to provide several petrophysical answers simultaneously. Examples are given on aged outcrop rocks and reservoir rocks that 3DNMR allows the joint determination of saturation and T_1/T_2 ratio of the oil, which is related to wettability [10].

Compared to the traditional measurement of wettability indexes, the proposed method is fast and does not require any change in saturation.

ACKNOWLEDGEMENTS

REFERENCES

[1] K. Brownstein and C. Tarr, "Importance of Classical Diffusion in NMR Studies of water in biological cells," *Physical Review A,* vol. 19, no. 6, 1979.

[2] W. Kenyon, P. Day, C. Straley and J. Willemsen, "A Three-Part Study of NMR Longitudinal Relaxation Properties of Water-Saturated Sandstones," *SPE-15643.*

[3] G. R. Coates, M. Miller, M. Gillen and C. Henderson, "The MRIL In Conoco 33-1

An Investigation Of A New Magnetic Resonance Imaging Log," in *SPWLA*, 1991.

[4] L. Venkataramanan, "Solving Fredholm Integrals of the First Kind With Tensor Product Structure in 2 and 2.5 Dimensions," *IEEE TRANSACTIONS ON SIGNAL PROCESSING,* vol. 50, no. 5, pp. 1017-1026, MAY 2002.

[5] C. Cao Minh, N. Heaton, R. Ramamoorthy, E. Decoster, J. White, E. Junk, R. Eyvazzadeh, O. Al-Yousef, R. Fiorini, B. Dacion and D. McLendon, "Planning and Interpreting NMR Fluid-Characterization Logs," in *SPE 84478*, 2003.

[6] M. Fleury and F. Deflandre, "Quantitative Evaluation of Porous Media Wettability using NMR Relaxometry," *Magnetic Resonance Imaging,* vol. 21, 2003.

[7] J. Chen, G. Hirasaki and M. Flaum, "NMR Wettability indices: Effect of OBM on Wettability and NMR responses," *Journal of Petroleum Science and Engineering,* vol. 52, 2006.

[8] W. Looyestijn, "Wettability Index Determination from NMR Logs," in *SPWLA*, 2007.

[9] J. Korb, G. Freiman, B. Nicot and P. Ligneul, "Dynamical Surface Affinity of Diphasic liquids as a probe of Wettability of Multimodal Pourous Media," *Physical Reveiw E,* 2009.

[10] A. Valori, B. Nicot, M. Hurlimann and H. Bachman, "Obtaining Wettability from T1 and T2 Measurements". Patent WO2013180752.

[11] C.H.Arns, «Multidimentional NMR inverse Laplace spectroscopy in petrophysics,» *Society of Petrophysicists and Well-Log Analysts,* p. 9, June 2006.

[12] G. Ibrahim and B. Nicot, "Solving Fredholm Integral for 3D NMR Inversion," *Submitted to Journal of Magnetic Resonance,* 2017.

CXBOX: AN INNOVATIVE TOOL FOR FLUID DYNAMIC QUANTIFICATION DURING COREFLOODS

Gilles PUYOU, Michel N'GUYEN and Sabine SAVIN
TOTAL SA, CSTJF, Avenue Larribau, Pau, France

ABSTRACT

Corefloods are very useful to understand the oil recovery mechanisms. These corefloods are usually monitored in petrophysical laboratory by using X-rays to visualize fluids in the rock sample. The 2D visualization and quantification of each fluids (water, oil, gas) are very challenging especially for corefloods carried out under reservoir conditions, owing to the attenuation of the environment (coreholder, confinement,..). As a result in this context, the signal-to-noise ratio is very low. Futhermore, it's usually not desirable to change the nature of fluids by adding contrast agents.

This paper presents a new apparatus, which is a cabinet X-ray system, developed to distinguish fluids in porous media in 2D, and to calculate and visualize the quantity of each fluid. This visualization is performed in a dynamic way, under pressure and temperature (up to 650 bars, 155°C), with quite substantial rock sample sizes (up to 100 mm diameter) and all that without having to change the nature of the fluids (by chemical doping for example). The association of all these features makes this equipment innovative.

Instead of trying to increase the signal with a contrast agent, this equipment includes some systems and methods to minimize the noise. By monitoring a coreflood with this system we obtain a picture of the rock sample in grayscale, similar to a medical radiography. The amount of fluids present in the rock is calculated from this radiograph. A false color image is then created that represents at a particular time t the amount in percentage of fluid present in the rock. An image of the rock sample can be produced every second, so we obtain in this way a succession of images (a film) that allows to see changes in fluid saturation in the rock sample at all stages of the core flooding experiment.

INTRODUCTION

Core flood tests are widely used to produce datasets that serve in reservoir simulations (relative permeabilities) and also help test, understand and improve production techniques. During these tests, a rock sample is placed in a Viton sleeve, sometimes wrapped in aluminum, and then placed in a Hassler-type core holder. The sample is

maintained under pressure using a confinement fluid in order to ensure injection into the rock. Sensors monitor physical parameters during the experiment (pressure, temperature, density, viscosity, pH, etc.). Since the 1990s, benches are equipped as standard with an X-ray generator that produces a photon beam for measuring saturation *in situ*. The beam passes through the medium and the transmitted photons are counted by a NaI photomultiplier. Based on absorption laws (Beer-Lambert), it is then possible to discriminate and calculate the quantity of fluids crossed at the counting point by working out the difference between the number of photons counted at this particular time t with the counting reference (dry rock). During the experiment, the generator/detector assembly is moved along the length of the core sample to ultimately obtain a series of points and generate a 1D saturation "profile" (see references [1] to [6]). Such a process of obtaining the saturation of each fluid is weak (yet possible) for the following reasons:

The fluid attenuation coefficients are low compared to those of the other materials crossed. Water, for example, has a linear attenuation coefficient of around 0.2 cm^{-1} at 80 kV, whereas that of the rock ranges from 0.4 to 1 cm^{-1}, or higher, depending on the rock. In addition, the fluid length the photon beam passes through (i.e. the volume of fluid to be quantified) is relatively short in relation to the total length. In the case of a rock of 5 cm in diameter with 20% porosity for instance, the photons cross a fluid length of 1 cm (5*0.2) on a total attenuating medium of around 15 cm (rock + coreholder and confinement). As a consequence, when it passes through the medium, the photon beam is mostly attenuated by the rock sample and its environment rather than by the fluids.

Moreover, the differential attenuation between the two fluids to be discriminated is minimal: the attenuation coefficient of water at 80 kV is 0.2 cm^{-1}, that of oil is 0.16 cm^{-1}.

To summarize, the signal-to-noise ratio is low both because fluids to be discriminated and quantified are very close to one another in terms of attenuation, and because they are present in a low quantity in a very attenuating environment.

Even though challenging, this measurement can still be performed in 1D, first by limiting the attenuation of the coreholder using carbon material, but also owing to the very high sensitivity of the NaI detector. However this technique has its limitations: total counting time for a profile is relatively long (30 minutes to 1 hour depending on experimental conditions), the 1D profile cannot always be integrated when it comes to heterogeneous flows, the generator/detector assembly usually emits in the open air thus limiting the intensity of the photon beam for radiation protection purposes.

3D X-ray images during core waterfloods have been available for quite a long time [7],[8]. They are very helpful in so far as heterogeneous samples are concerned, to the extent that these samples do actually represent the reservoir (vuggy facies of carbonate reservoir for example). However, this type of *in situ* saturation monitoring represents today a very small fraction of corefloods, because CT scanning technology is 1)

expensive to acquire and maintain 2) has very large footprint 3) suffers from strong limitations when medical technology is used (no vertical scanning).

2D imaging systems have been developed, but mainly for rock slabs [9]. They proved to be very useful for research purposes, but have not been used at reservoir conditions.

In this paper we describe how TOTAL's petrophysical laboratory has developed and designed a new self-protected 2D X-ray bench called the CXBOX, and the associated calculation methods, to apply to reservoir conditions on full size cores.

EXPERIMENTAL SET UP AND METHOD
Description of the way of development
The starting point of this development was the decision to replace the NaI detector with a flat-panel detector in order to obtain a 2D image. However, because this type of detector is far less sensitive than the NaI scintillation detector, the development focused both on how to1) increase the intensity of the signal and 2) reduce the noise.

Several parameters can be thought of to increase the signal. As an example, two of them were discussed but finally given up:
- *Reduction in the experimental pressure and temperature conditions* to obtain a less attenuating environment: this was not acceptable owing to our objectives to continue to propose core flood tests at reservoir conditions.
- *Use of contrast agents (dopants) in one of the phases:* this was rejected due to potential impact on fluid physico-chemical behavior.

After the solutions for enhancing the signal had been reviewed, two were finally selected:
- *Regarding the resolution of the detector:* because our actual need was visualization of fluids and saturations and not of the porous environment, we decided to opt for a sensor with a substantial pixel size (200 µm) contrarily to micro-tomography requirements. This also could help reduce the acquisition time.
- *Regarding the X-ray dose rate:* a self-protected enclosure was designed to house the coreholder in order for the photon beam to be intensified while guaranteeing radiation protection.

A considerable part of the development of the new bench (fig.1) was devoted to reducing and managing noise, and having a signal as stable as possible over the time. A custom-made X-ray generator, able to emit a lasting hyper-stable photon beam, has been purposely developed. The enclosure was also designed such that the operator does not need to stop the generator or to change the configuration inside the enclosure throughout the study (for connecting pumps for example). As a result, the diffuse radiation keeps almost constant over the time and its effect significantly disappears when two images are subtracted. In addition, the technique was also made possible owing to a new type of low-attenuation coreholder made of carbon, without tie bars, able to hold rock samples of up to 100 mm and reach pressures of up to 650 bars and temperatures of 155°C (fig.2).

Setup description
This development resulted in a 2D X-ray bench called the CXBOX (fig.1), that includes:

X-ray source: a few designs with different ranges of power (from 50 to 500W) were developed in order to adapt the generator to a range of applications, especially depending on the size of the reservoir core, which first means to adapt both tension and current (as an example, with a core of 50 mm of diameter, the generator is usually adjusted to 120 kV, 1.8 mA). But most important, these X-ray generators have been designed to be able to emit during a long period without having to be stopped (several weeks) while keeping highly stable. Fluctuations in dose are $< 0.5\%$ over at least 24 hours.

Flat panel detector: amorphous Silicon and Gadox scintillator technology, with an active area of 40 cm * 40 cm, and a pixel size of 200 µm.

The coreholder is placed as close as possible to the detector, and at least 50 cm from the X-ray generator.

Development of saturation calculation methods
The flat-panel detector generates grayscale images which are the 2D projection through the entire rock. From these images, two methods were developed and tested for visualizing fluids and calculating saturation.

Calculation method 1: based on image processing
The calculation is carried out in two steps. The first consists in determining, for each fluid phase present, a reference grayscale image representing the rock that is totally saturated with this fluid. Two methods could be used to establish these references.

The simplest method involves physically saturating the rock at 100% with the fluid, then generating a reference image by averaging over several acquired radiographies (generally 10). This method is used to obtain an image of the rock that is 100% dry or 100% saturated with water. However, 100% saturation of the rock with fluid such as reservoir oil is often very complex and time-consuming especially when the sample has a large pore volume. In that case, a second method is used: the image of the rock 100% saturated with oil is simulated from previous acquisitions. First, the image of the dry rock is subtracted from that of the water-saturated rock. Then based on this 'water-only' image, the image of the reservoir oil, distributed throughout the porous medium, is simulated using the ratio of the oil (μ_o) and water (μ_w) attenuation coefficients. Finally, the image of the dry rock is added to this new image to produce a simulated image of the rock 100% saturated with reservoir oil. The equation 1 below, which is the mathematical transcription of these operations, is applied to each pixel :

$$Image\ @So_{100\%} = \left[\left(Image\ @Sw_{100\%} - Image\ Rock_{empty} \right) \times \left(\frac{\mu o}{\mu w} \right) \right] + Image\ Rock_{empty} \quad (1)$$

As the attenuation coefficients of the fluids are needed to produce these simulated images, a technique was developed to calculate them *in situ*. A standard piece in PEEK with an orifice of a known diameter is placed either side of the rock sample (fig.3). During coreflooding, images of these standards are obtained: empty, 100% water, 100% oil, etc. Based on these, the average grayscale value of the pixels in the centre of the standard piece is extracted for each saturation state. The Beer-Lambert law is then applied to this data to obtain the attenuation coefficient of the fluids in experimental conditions. For instance, to obtain the attenuation coefficient of the reservoir oil μ_o, we select a region of interest (ROI) in the centre of the orifice. Then we calculate:

N_{empty} : average gray value of the ROI when the standard piece is empty

N_{oil} : average gray value of the ROI when the standard is 100% filled with reservoir oil

l : path length of the X photons beam through the standard at the selected area location

As we select a narrow area in the centre of the standard, and due to the CXBOX configuration (the standard piece is facing the centre of the emission cone and it is far enough from the generator to be allowed to consider the X photons beam to be parallel in this location), we usually use the diameter of the orifice for the l value.

Then, according to the Beer-Lambert law, we calculate μ_o according to equation 2 below.

$$\mu_0 = \ln \frac{N_{empty}}{N_{oil}}/l \qquad (2)$$

Once the reference images have been determined, we can then move on to the next step.

During the core flood tests, images of the rock are acquired at regular time steps (e.g. every 10 seconds). For each image, the fluid saturation level in each pixel is calculated based on the gray value by linear regression using the reference images. Equation 3 illustrates the calculation used to establish the water saturation (Sw):

$$Sw = (N_{oil_{ref}} - N_{measured})/(N_{oil_{ref}} - N_{water_{ref}}) \qquad (3)$$

The saturation is then represented by a false color image. By repeating this operation, we obtain a false color film representing the change in saturation in each pixel. This allows us to monitor the changes in a flood front while continuously calculating the quantity of fluid present in the porous medium. IT tools were developed to calculate from these images the fluid saturation in a pre-selected zone and then to extract the data or present them in graphs.

In this application, a linear regression can replace a log linear regression because of the low difference between the attenuation coefficients. This simplification allows us to use a simple imaging software during coreflood and then follow the evolution of saturations in a simple way. After using this calculation method to interpret numerous coreflood tests, we observed that in most cases, we ended up with the same results as those obtained with a material balance. In a small number of cases, however, the results were substantially

different from those of the material balance (five saturation units). This usually happens when a study lasts several months: although the system is relatively stable and the fluctuations are corrected (effect of the temperature variations on the flat-panel, temperature variations of the coreholder, etc), these fluctuations cannot be perfectly compensated for. What is negligible over a short period of time is less so over several months, hence the limitation of this method when measurements are compared with references which may have been established several months before. This led us to develop a second calculation method.

Calculation method 2: using the Beer-Lambert law
Compared to method 1, this method is less affected by the fluctuations of the system because the reference used is the last state of saturation. This second method consists in extracting the information from the dose received (N), in grayscale, in a pre-defined zone (a pixel, a pixel line or the entire rock sample). The saturation of the zone is calculated from these doses by applying the Beer-Lambert law. As with method 1, the standard pieces enable to monitor changes in the fluid attenuation coefficients at all times in the injection or production circuit, and thus adapt the interpretation and calculation to changes in the fluid in the case of composition exchanges for example. The saturation of a fluid is calculated by using Beer Lambert law applied to the difference of saturation of this fluid between two states (two images). Equations 4 to 6 illustrate the calculation of oil saturation (So) during a waterflood after reaching irreducible water saturation (Swi); in this case, the Swi image (N_{swi}) is used as a reference ; the attenuation coefficients of the water injected (μ_{water}) and reservoir oil (μ_{oil}) are calculated from the standard. From Beer-Lambert law, we obtain:

$$So = So_{swi} + \frac{\ln\left(N_{current\_image}/N_{swi}\right)}{\emptyset * l * (\mu_{oil} - \mu_{water})} \qquad (4)$$

With $\emptyset$ = local porosity.

During the first water saturation, Beer-Lambert law gives :
$$N_{water\_initial} = N_{rock\_empty} * e^{(-\mu_{water\_initial}*\emptyset*l)} \qquad (5)$$

From equations (4) and (5), comes equation (6):

$$So = So_{swi} + \frac{\ln\left(N_{current\_image}/N_{swi}\right)}{\ln\left(N_{rock\_empty}/N_{water\_initial}\right) \times \frac{(\mu_{water} - \mu_{oil})}{\mu_{water\_initial}}} \qquad (6)$$

The calculated saturations can then be averaged and presented in a graph. One advantage of these two calculation methods is that the fluid saturation of the rock can be calculated independently of the material balance. One of the limits of this visualization technique is that it is impossible to calculate local porosity. As described with equation (5), we can

calculate the product '∅*l'. However, it is not straightforward to find out for each pixel the exact distance crossed by the X-ray photon beam through the rock sample (= l). One reason is that the relative position of the core in relation to the beam and the detector changes from a study to another one, depending on the size of the core. To make up for this shortcoming, another calculation method has been developed which consists in calculating a porosity map based on the reference images, and at least one piece of information from the material balance to calculate the global porosity. This porosity map can easily be defined when the rock is saturated with water. The image of the dry rock is subtracted from that of the water-saturated rock. We obtain an image in grayscale of the water only. From this image, we extract the average of two areas 1) the entire core and 2) the standard. As we know the porosity of each of these two areas, the image in grayscale is converted to a map of local porosity by using a transfer function.

Comment about the use of Beer-Lambert law in this application:
This law generally applies to a given energy, and the attenuation coefficient of a fluid therefore applies to this same energy too. This law has long been used to calculate saturation in porous media on 1D X-ray benches, as the NaI scintillation detector is capable of classifying the images received by energy type: it is therefore possible to obtain quasi-monochromatic information. But the flat-panel detector does not offer this possibility: the information transmitted (the grayscale in ADU) is actually a dose received, i.e. the energy of the photons of the entire emission spectrum. So we had to check first that Beer Lambert law could be used under such circumstances for interpreting the CXBOX data. Based on a great number of situations tested it could be concluded with confidence that this was indeed the case. One reason for that could be related to the high stability of the X-ray generator which implies that the spectrum arriving at the detector is highly stable over the time. Therefore the coefficients thus measured correspond to an attenuation across the entire spectrum and can be used during the entire study period. It is worthy to note that these coefficients are not transposable from a study to another because in the interim, generator and detector have been stopped and restarted, the overall configuration has changed, and consequently the spectrum received changes.

RESULTS
The new 2D bench and the associated calculation methods have since been tested on many samples, both homogeneous and heterogeneous, in standard and in reservoir conditions (up to 650 bar and 155°C). The time needed to acquire an image is 1 to 10 seconds which means that dynamic imaging can be used. Two examples of the monitoring of fluid saturation during coreflood tests, taken from three different studies on rocks of 50 mm in diameter, are presented below. Study A will be used to compare the calculation methods with the material balance, and to illustrate the results generally achieved with the CXBOX. Studies B presents a case in which it is normally difficult to discriminate and visualize the fluids present.

Study A: comparison between the two CXBOX imaging calculation methods and the material balance during coreflooding on a homogeneous sandstone sample (porosity: 21% +/- 0.2 p.u.)

Achieving irreducible water saturation (Swi) by viscous displacement with oil is illustrated in fig.4, showing images from the film obtained, each tagged with the oil saturation value. Fig.5 shows the simultaneous variations of oil and water saturation over time using method 1 and gives a comparison between the two methods of calculation. Table 1 compares the results obtained for Swi by each method of calculation with the result obtained by material balance.

Table 1: achieving Swi - Comparison of the results of the final balance using the calculation methods (methods 1 & 2) with the material balance

	Using MB	Using method 1	Using method 2
Swi (%)	26.6	26.0	25.8
Uncertainty (s.u.)	+/- 1	+/- 3	+/- 2

The subsequent operation of water injection was similarly monitored. Fig.6 provides some images from the film, with the relevant calculated oil saturation (So) values. Fig.7 focuses on the oil and water saturations over time using method 1, and shows the comparison between the two calculation methods. Table 2 summarizes the results obtained for the final water saturation level reached at the end of the coreflood.

Table 2: water injection - Comparison of the results of the final balance using the calculation methods (methods 1 & 2) with the material balance

	Using MB	Using method 1	Using method 2
So (%)	41.6	40.0	39.2
Uncertainty (s.u.)	+/- 1	+/- 3	+/- 2

As we can see in tables 1 and 2, the imaging techniques developed not only make it possible to view flow in the porous medium in 2D but also to calculate consistent saturation values independently of the material balance at all times during the coreflooding. In addition, 2D imaging takes into account the entire sample, unlike 1D techniques where only part of the sample can be investigated. Indeed, when interpreting the experiments conducted on 1D benches, we must assume that the spot measurements taken by the detector are representative of the entire sample. So, the saturation measured at a point at the centre of the sample is considered as homogeneous across the entire width of the sample at this point. This hypothesis is no more valid when the flood front is heterogeneous [9]. 2D visualization is a first step to take heterogeneity into account.

Study B: imaging monitoring of a miscible tracer test performed on a sand sample using two brines with a very small difference in X-ray attenuation (no dopant added)

The sample is 34% (+/- 0.2 p.u.) porosity. The brine concentrations are respectively: 6 g/l for water n1 and 30 g/l for water n2.

Difference in linear attenuation coefficient between the two brines is only 0.06 cm^{-1}.

The series of images taken during the miscible tracer test (fig.8), show that the two fluids can be visualized without adding a dopant, even in conditions that are not favorable in terms of X-ray contrast. In addition, heterogeneous flow (here, preferential path at the edge of the sample) can clearly be seen on this 2D imaging bench. In the present case, this makes it possible to process the information using a dual permeability model, according to the methodology developed by C.Dauba et al [10]. It is also a help for improving sample selection and detecting a technical problem.

CONCLUSION

This new bench and associated methods gives TOTAL a tool to monitor fluid changes in a porous medium, to dynamically calculate fluid saturation (acquisition time of 1 to 10 seconds per image) in conditions not favorable to imaging (pressures up to 650 bars, temperatures up to 155°C, very low X-ray attenuating contrast, samples of up to 100 mm in diameter), without it being necessary to dope the fluids. This tool is very useful for monitoring changes in fluids and characterizing recovery mechanisms in the case of flooding of heterogeneous samples such as carbonates, or in the event of viscous fingering. It is all the more valuable in that it can be used for samples with a large size. Moreover, the fact of being able to perform the core flood tests at high pressure and temperature conditions is an advantage for understanding mechanisms causing composition exchanges. As the images obtained are averaged over the entire rock, this method is currently limited when it comes to the understanding of heterogeneous material but it paves the way to the development of a new 3D bench.

ACKNOWLEDGMENTS

REFERENCES
1. Boyer R.L., Morgan F. and Muskat M.: "A New Method for Measurement of Oil Saturation in Cores,"*Trans.,* AIME (1947) 170, 15-33

2. Morgan F., McDowell J.M. and Doty E.C.: "Improvements in the X-Ray Saturation Technique of Studying Fluid Flow," *Trans.,* AIME (1950) 189, 183-94

3. Oak M. and Ehrlich R. : "A New X-Ray Absorption Method for Measurement of Three-Phase Relative Permeability " SPERE, February 1988, 199

4. Potter G. and Groves D.: " Displacements, Saturations, and Porosity Profiles From Steady-StatePermeability Measurements ", SPE 19679, 1989

5. Berry J., Little A. and Salt H.: "In-Situ Saturation Measurements Improve Analysis and Interpretation of Laboratory Miscible and Immiscible Displacement Processes" SPERE, November 1991, p 429

6. Maloney D., Wegener D., and Zornes D., "New X-ray Scanning System for Special Core Analyses in Support of Reservoir Characterization" , Paper SCA 9940, 1999

7. Hicks P.J. Jr., Deans H.A. and Narayanan K.R.: "Distribution of Residual Oil in Heterogeneous Carbonate Cores Using X-ray CT," SPEFE (Sep. 1992) 235-240. SPE 20492

8. Hicks P., Narayanan K., Deans H.: "An Experimental Study of Miscible Displacements in Heterogeneous Carbonate Cores Using X-Ray CT" SPEFE, March 1994, p55

9. Mitchell P., Brockley P., and Sincock K.: "Two-dimensional Fluid Saturation Imaging Improves Estimates Of Oil Recovery In Heterogeneous Carbonates", SCA 2004-15, 2004

10. Dauba C., Hamon G., Quintard M. and Cherblanc F.: "Identification of parallel heterogeneities with miscible displacement", SCA 9933, 1999
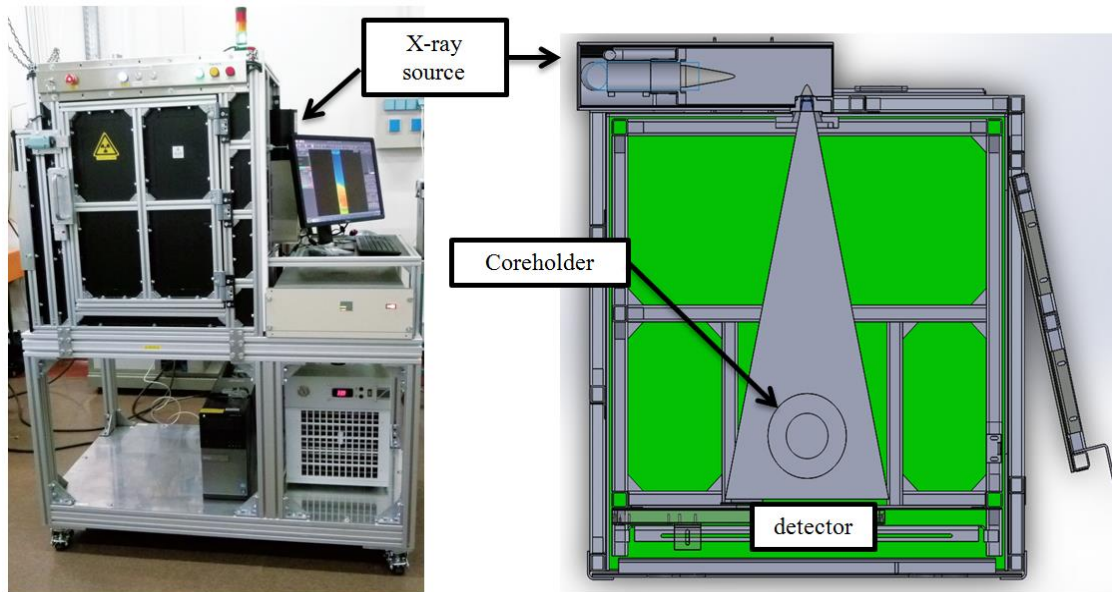
Figure 1: photo and diagram (top view) of the CXBOX1 2D bench after development
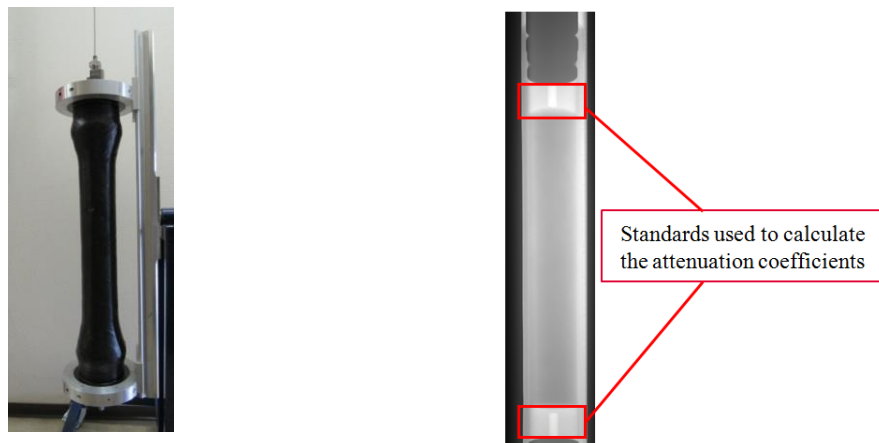
Figure 2 : example of a carbon coreholder used by the petrophysical laboratory - 650 bars, 155°C, for a sample of 50 mm in diameter and with a maximum length of 40 cm

Figure 3 : grayscale image of a sample
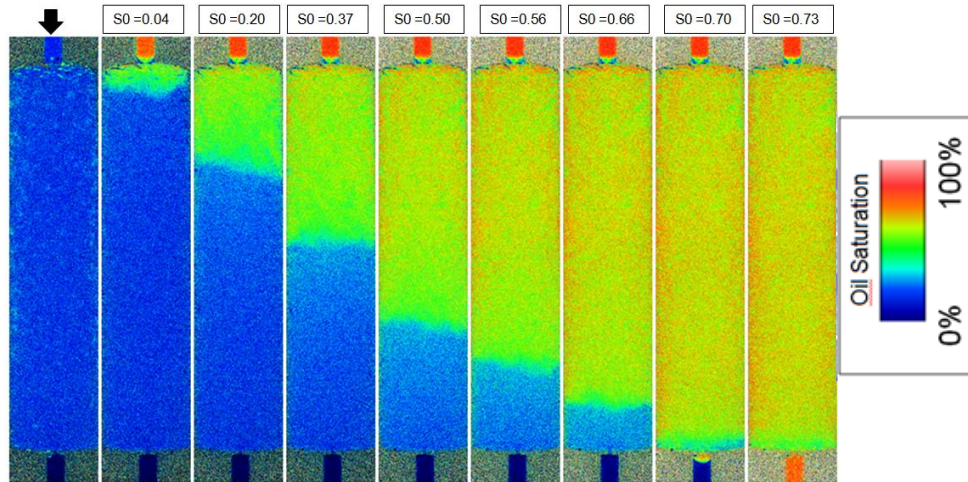
Figure 4: nine images from the film showing saturation states when achieving Swi (oil injection)
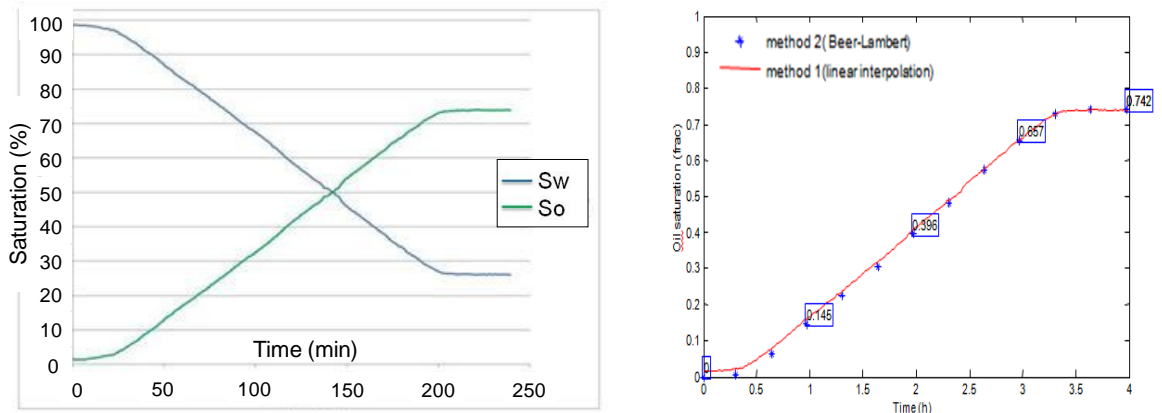
Figure 5 : achieving Swi - Monitoring oil and water saturation over the entire core using method 1 (graph on the left) and the oil saturation of the entire core using method 1 and method 2 (graph on the right)
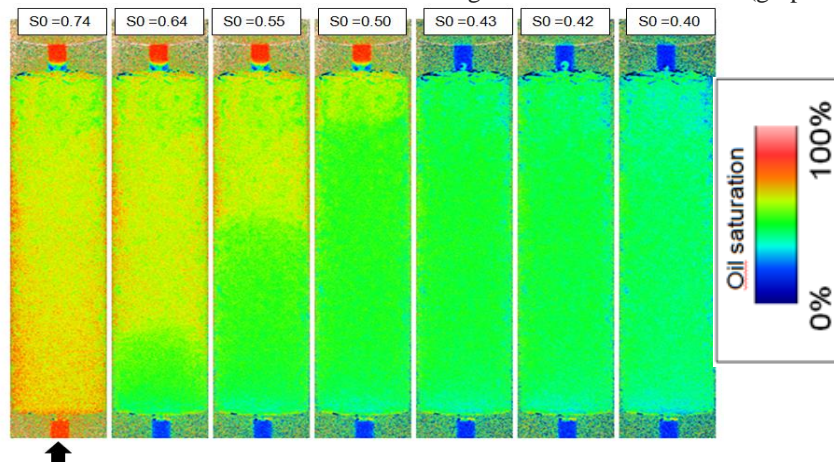
Figure 6 : seven images from the film showing saturation states taken during water injection
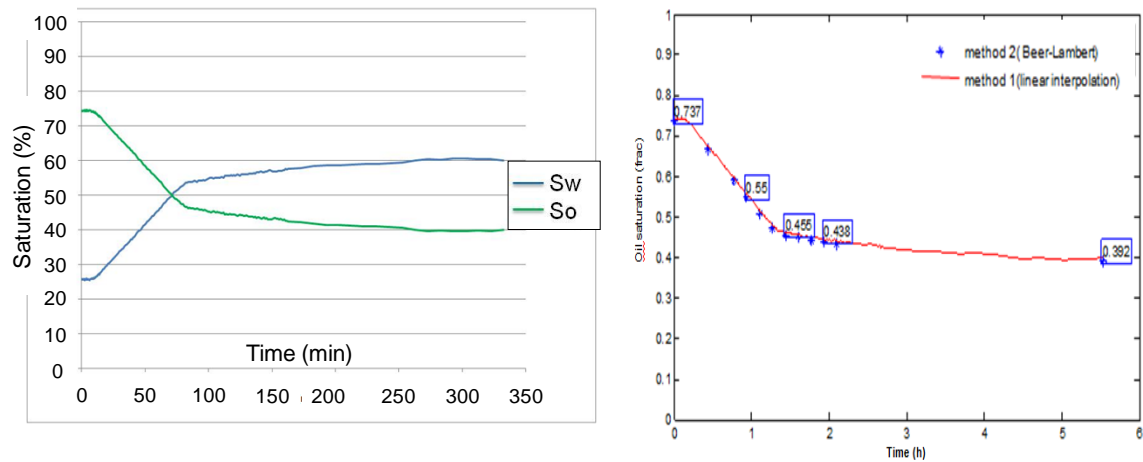
Figure 7: water injection - Monitoring oil and water saturation over the entire core using method 1 (graph on the left) and the oil saturation of the entire core using method 1 and method 2 (graph on the right)
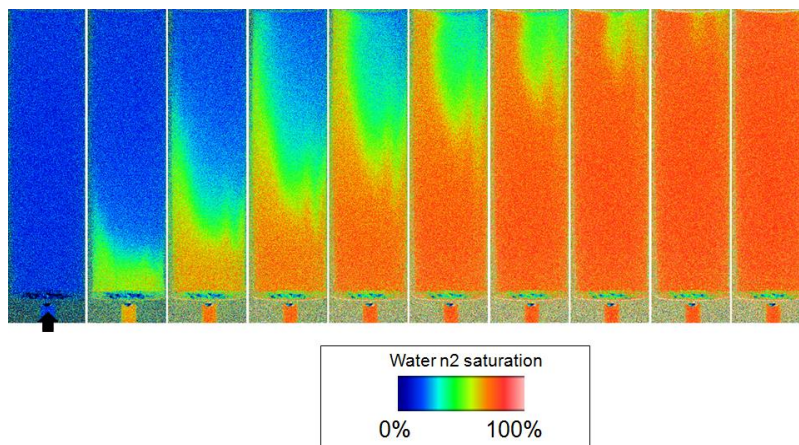
Figure 8: miscible tracer test showing a small difference in salinity between the two brines – Evolution of saturation states during the tracer test

WORKFLOW FOR MEASUREMENT OF STEADY-STATE TO LIQUID PERMEABILITY IN NANO-DARCY RESERVOIR ROCK

Robert L. Krumm and James J. Howard
Premier Oilfield Laboratories, Houston TX

ABSTRACT

A workflow for the measurement of very low permeability unconventional reservoir rocks was developed that accounts for the presence of micro-cracks and fractures in the sample. A rapid low resolution micro-CT scan (~50 microns/voxel) identifies significant cracks and partings in 2.55 – 3.75 cm diameter core plugs that are used in the subsequent petrophysical study. In some instances, these pre-scans eliminate more the 90% of the samples from further testing. In instances of moderately fractured samples, small prisms of non-cracked rock are trimmed and then mounted in a cylindrical mold filled with epoxy. Low-field NMR measurements are used to determine initial liquid content in the core plugs. Initial liquid saturations range from almost 100% to less than 50% in liquid-hydrocarbon shale reservoirs and are strongly dependent upon the nature of the reservoir fluid compositions. In the case of as-received samples with low liquid saturations it is possible to measure a gas-filled pore volume with a standard porosimeter. A summation of fluids approach then is used to determine total porosity. The measurement of merit for permeability is a steady-state to oil flow experiment at elevated temperature and under confining pressure in a standard Hassler cell. The sample's pore volume is filled with a decane by pressure saturation for a period of time prior to loading into the flow cell. Permeability is measured by monitoring differential pressure across the core at two or three constant flow rates. The multi-rate approach allows for a graphical solution to the Darcy equation along with point-by-point values that are averaged over a period. These two approaches differ by less than 5% for good quality data. Flow rates for these sub-microDarcy rocks are in the range of 0.01 to 0.12 cm^3/hr and often these tests require several days to more than a week to complete. NMR measurements are collected on the post SSKo sample to ensure that the test did not change the liquid-filled pore volume or saturations. The technique is very reproducible when the samples remain intact during handling.

INTRODUCTION

There are several challenges in measuring flow properties in very fine-grain reservoir rock. The most notable is the presence of fractures and micro-scale cracks found in standard core plugs in many of these unconventional reservoirs. Early efforts to measure permeability on shale core plugs with the unsteady-state pressure decay method generated uneven results in many cases [1]. The Devonian Shale Gas program created a workflow that handled micro cracks in conventional core plugs by using instead smaller particles crushed to a uniform size. The intent of using smaller "chips" was to avoid micro-cracks that would affect the gas flow in a pressure-decay test. The belief was that crushing samples to a uniform particle sizes (e.g. 20-35 mesh, 500 to 850 microns) that breakage would occur along naturally occurring cracks and partings such that the particles themselves would be free of these cracks. This approach led to a somewhat standardized workflow used by a wide number of industry labs, often referred to as "Crushed Rock Analysis". More recent studies highlighted some of the difficulties in maintaining interlab calibrations and comparisons [2, 3]

A second challenge associated with petrophysical measurements of unconventional reservoir rocks is identifying and quantifying the various liquids found in the sample when it arrives at the laboratory. An ideal measurement of gas-filled pore volume and permeability to gas involves liquid-free pores. Standard core cleaning methods and water extraction techniques are hampered by the very low permeability of the sample, especially in a core plug [1]. Size reduction of the sample to uniform particles improves access to pores that should improve cleaning efficiency, though recent work indicates that saturation estimates from small particles are strongly biased and do not match log-based results [4].

Steady-state permeability to gas measurements in tight unconventional reservoirs are commonly used because of the shorter time requirements, though issues with fluid compressibility and adsorption remain a concern [1]. Steady-state permeability to liquid measurements are easier to interpret, but require longer time periods [5, 6]. The design of these tests is to monitor flow rates generated by constant pressure differences across the core plug. Changes in effective stress and observations of permeability creep with time are common observations.

The proposed workflow returns to the use of standard-sized core plugs and a steady-state to liquid flow test as the best means to measure permeability in these very low permeability rocks. The core plugs are scanned for evidence of micro-cracks that would impact the flow test, which results in many samples discarded from testing. NMR relaxation measurements are used to determine the volume of liquids in the sample at various stages of the testing. A standard steady-state permeability setup was modified slightly in order to adjust for the very low flow rates required to measure nano-Darcy level permeability.

PROCEDURE

Whether the core plug is prepared at wellsite or in the laboratory itself, the first step is to collect a rapid, low-resolution micro-CT image of the plug. The main advantages of micro-CT over other imaging modalities are its speed and resolution along with the ability to scan the sample while still wrapped in any preservation packaging. Images are collected with a Zeiss Versa 510 micro-CT running at 140 kV. Scan times for 58-micron resolution images on standard 2.54 cm diameter core plugs are 60 minutes or less. The use of an auto-sample loader allows for near 24-hour usage of the imager.

These low-resolution images are sufficient to identify micro-cracks and partings that extend along the length of the horizontal core plug. Many of these features are parallel to bedding and result from the stress release of the sample. Smaller cracks and especially those transverse to the long axis of the plug are less likely to affect a flow experiment. An empirical classification scheme based on number and length of these partings was developed to evaluate plug quality and their suitability for testing. While it may be possible to generate an automated classification tool for these images, current experience with these low-resolution images is that edge effects and uneven brightness that the eye overlooks hinder any image processing efforts.

Liquid volumes of the core plugs are measured with a low-field (0.045T) NMR spectrometer (GeoSpec2, Oxford Instruments) equipped with a Q-Sense probe. Standard Free Induction Decay (FID) and Spin-Spin Relaxation (T_2) measurements are acquired on the sample at various stages of the workflow, including in the "as-received" and after the steady-state permeability test. Changes in liquid volume are compared with mass changes in the sample at the various stages. The instrument is calibrated to a known volume standard with reproducibility of 0.19 cm^3 for a 16.7 cm^3 liquid volume, ~1.2% error. The T_2 measurement is acquired with a standard CPMG pulse sequence with an echo spacing of 0.1 msec, a recovery delay of 3 to 5 seconds depending upon the sample and accumulated over 256 scans. This normally leads to a signal-to-noise level between 50 and 100 as determined by the intensity of the first few echoes relative to an averaged baseline determined near the end of the echo train. Pulse widths and resonance frequencies are calibrated for each suite of samples. The raw data is processed with a standard non-negative least squares inversion algorithm with a constant regularization component that is optimized for the hardware (GITSystems Advanced, Green Imaging Technology).

Samples that have more than 50% of their pore volume filled with air/gas in the "as-received" state are placed in a gas porosimeter in order to measure pore volume. A sum-of-fluids approach uses the NMR-based liquid volumes and the gas porosimeter derived volume to determine a total pore volume and porosity. In some cases, after the as-received NMR measurement, samples are dried under mild conditions (vacuum, 80°C) in order to remove as much fluid as possible before the next step.

Regardless of the initial gas content in the as-received core plugs the remaining gas-filled pore volume is replaced by a light liquid hydrocarbon in a pressure-saturation process. The core plugs are placed in Nalgene bottles filled with decane and then placed in a larger pressure vessel. The hydrostatic pressure in the vessel is raised to 2500 psi and 150°F and left there for 1 day. A programmed depressurization process over the ensuing 4 days minimizes breakage of the core plugs due to stress release. Early experience found that rapid depressurization after pressure saturation frequently caused plugs to break. A second set of NMR measurements are collected on these "pressure-saturated" samples and the measured total liquid-filled volume is compared to the sum-of-fluids values generated from the as-received liquid content and its gas-filled content. The pressure-saturation process is repeated when the volume comparison falls outside 10%.

The liquid-saturated core plugs are inserted into a standard steady-state permeability rig for measurement of the hydrocarbon flow (SSKo). The core holder is connected to a precision pump (Quizix 5000 series, Chandler Engineering) on the upstream end and a back-pressure regulator on the downstream. These pumps are capable of stable flow rates down to 0.001 cm^3/hr while monitoring pressure changes of 0.1 psi. Flow rates for nano-Darcy samples are set between 0.01 and 0.2 cm^3/hr with measured inlet pressures between 55 and 135 atm. The back-pressure regulator is set nominally to 34 atm during the test. Hydrostatic pressure applied to the Viton sleeve in the core holder is maintained by a second pump and set to 240 ± 0.07 atm. The core holder is wrapped in a heating mantle that maintains a stable 160°F temperature for the duration of the experiment. Permeability is measured by monitoring the pressure changes at the inlet end of the core plug at constant flow rates and determining an average pressure differential along the length of the plug. Permeability is calculated with the Darcy equation at each data acquisition point, roughly 6 minutes apart, with the constant flow rate value, the measured pressure differential, and the decane viscosity at temperature. The flow rate is changed several times during the test so that sufficient points are available for a graphical solution to Darcy, including an origin point of zero differential pressure at zero flow rate. Each flow rate step requires several days for the pressure differential to stabilize within a tolerance of 3% of the absolute value. A complete permeability test therefore requires 7-14 days to complete. The effluent flow volumes are monitored to ensure mass balance and are sometimes captured for further analysis.

A final set of NMR measurements are collected after the core plug is retrieved from the permeability apparatus to monitor any changes in total liquid volume or saturations.

RESULTS

Samples were selected from a single well in an unconventional reservoir that produces oil. The samples were a fine-grain carbonate-rich rock with varying amounts of clay minerals (marls and argillaceous marls). The core plugs were preserved prior to sending to the special core analysis lab and were accompanied by the results of crushed-rock analysis on companion pieces. Gas-filled porosity of the as-received samples were measured with the crushed-rock analysis method and ranged from 0.02 to 0.12. Gas saturations were estimated to be between 40 and 80%, which suggested that much of the initial liquids were lost during the coring process.

Initial micro-CT scans on the "as-received" core plugs generated images that illustrated a wide range of plug quality (Figure 1). A few of the samples had no discernible cracks at the resolution of these quick-scan images, and were passed along directly to the permeability workflow. Many of these carbonate-rich samples were characterized by significant cracks or partings that extended the entire length or width of the original plug. These samples were candidates for trimming and epoxy potting in preparation for permeability testing.

The as-received samples had liquid-filled volumes that range from 0.5 to 2.5 cm^3. The gas-filled pore volumes of these samples were used to generate a sum-of-fluids total pore volume, which in turn was used to calculate a total porosity. These sum-of-fluids values compared favorably with the total liquid volumes measured by NMR on the pressure-saturated core plugs (Figure 2).

The T_2 relaxation time distributions of the as-received samples were often unimodal and skewed towards faster times in most cases, with a larger relaxation component centered around 1 msec and a second, smaller component around 10 msec or slower. The addition of decane in the pressure-saturation step contributed primarily to the slow component and developed a strong bimodal character (Figure 3). This particular carbonate-rich unconventional reservoir rock was characterized by relaxation behavior similar to many water-wet conventional reservoirs where irreducible water is associated with the faster relaxation components and the slower component represents the light hydrocarbons [7]. As in NMR analysis of conventional reservoirs, the population density of each major relaxation component was transformed into liquid saturation estimates. The addition of decane during the pressure-saturation step did not change the intensity of the fast relaxation component in most of these samples. Only the slow component is affected, which suggested that the added decane was located in larger pores or in water-wet pores, or some combination of both scenarios.

The NMR-based water saturation estimates were in general slightly greater than those generated from the standard Dean-Stark analysis (Figure 4). The data in Figure 4 was

produced from NMR and Dean-Stark extractions on the same pieces of core. The NMR-based estimates were slightly higher due in part to the T_2 distribution's inability to separate signals from water and residual oil or bitumen.

The steady-state permeability tests on selected samples showed well-behaved pressure-drop / flow rate behavior that could be analyzed with the Darcy equation (Figure 5). The monitored pressure differential usually stabilized within 12 hours of changing the flow rate and over a period of several days remained within 0.5 atm of the averaged value. A data analysis tool allowed for user input to select the time period over which the pressure differential was averaged at each flow rate. In some instances, pressure showed a slight decrease in time (i.e. increased permeability), but the opposite condition of permeability creep was not observed [6]. This increase in permeability is due to the dissolution of residual hydrocarbons from the core. The permeability value determined from an average of point-by-point calculated permeability differed by less than 3% from the value estimated from the graphical solution to Darcy in this suite of samples. The linear correlation R^2 of the graphical solution was usually 0.98 or better (Figure 6).

The SSKo results were different from crushed-rock analysis results in two ways (Figure 7). The first was that the total porosity measured in the SSKo workflow covered a narrow range of values compared to the CRA values on extracted samples. The second difference was that at similar range of total porosity the SSKo values were one to two orders of magnitude less than the CRA values. The reproducibility of the SSKo tests was determined by replicate measurements on several samples and found to be within 5% of the original value in the range of 20 to 1000 nD. The broad range of porosity values in the CRA values could result from a combination of incomplete extraction of residual liquids that affected the total gas volume measurement and a sampling bias. The latter could have occurred with SSKo sample selection that emphasized intact lithology.

The constant flow rate approach to measuring steady-state permeability in tight shale samples worked as well as the constant differential pressure approach [6]. Concerns of slower test equilibration with the constant flow rate approach were not a factor in this study, the monitored pressure differential reached steady-state within hours of changing flow rates.

This method for determining permeability in nano-Darcy rock is robust and reproducible. The permeability values provided by this method are relative to whatever residual water saturation is left in the sample and pre/post NMR T_2 measurements confirm that saturations remain constant. Because samples are pre-screened, this is a true measurement of matrix permeability. These types of measurements can define the ranges of permeability of regional lithologies. If higher-frequency permeability data is needed, this method can be used to correct values provided from other methods.

The principal advantages of measuring permeability at steady state to oil compared to other permeability measurements can be summarized as follows:

- There are fewer assumptions in the model (1D-Darcy) compared to the more complicated models used for crushed rock permeability and pulse decay permeability. The results are easier to interpret.
- There is no need to correct for slip or gas compressibility.
- Hot decane solubilizes residual hydrocarbon without use of solvent extraction which would damage the rock matrix.
- Very repeatable and robust measurement.

REFERENCES

[1] Guidry, K., Luffel, D.,and Curtis, J., "Development of laboratory and petrophysical evaluation techniques for evaluating shale reservoirs", *Gas Technology Institute*, GRI final report: GRI-95/0496, (1995)

[2] Spears, R., Dudus, D., Foulds, A., Passey, Q., Sinha, S., and Esch, W., "Shale Gas Core Analysis: Strategies for Normalizing between Laboratories and a Clear Need for Standard Materials", *Society of Petrophysicists and Well Log Analysts*, Transactions of Society of Petrophysicists and Well Log Analysts 52nd Annual Meeting, Colorado Springs CO, Paper A. (2011)

[3] Tinni, A., Fathi, E., Agarwal, R., Sondergeld, C., Akkutlu, Y., and Rai, C., "Shale Permeability Measurements on Plugs and Crushed Samples", *Society of Petroleum Engineers*, SPE Canadian Unconventional Reservoir Conference, SPE-162235. (2012)

[4] Wood, J., "Crushed-Rock Versus Full-Diameter Core Samples for Water-Saturation Determination in a Tight-Gas Siltstone Play", *Society of Petroleum Engineers*, (2015) doi:10.2118/174548-PA

[5] Lasswell, P., "Steady-state permeability analysis in unconventional plays", *geoconvention partnership*, (2013), Presented at GeoConvention, Calgary, Canada, 6 &- 10 May.

[6] Chhatre, S., Braun, E., Sinha, S., Determan, M., Passey, Q., Zirkle, T., Wood, A., Boros, J., Berry, D., Leonardi, S., and Kudva, R., "Steady-State Stress-Dependent Permeability Measurements of Tight Oil-Bearing Rocks", *Petrophysics*, (2015), **51**, no. 2, 116-124

[7] Rylander, E., Singer, P., Tianmin, J., Lewis, R., McLin, R., and Sinclair., S., 2013, "NMR T2 Distributions in the Eagle Ford Shale: Reflections on Pore Size", *Society of Petroleum Engineers*, (2013), Unconventional Resources Conference, SPE-164554.

FIGURES
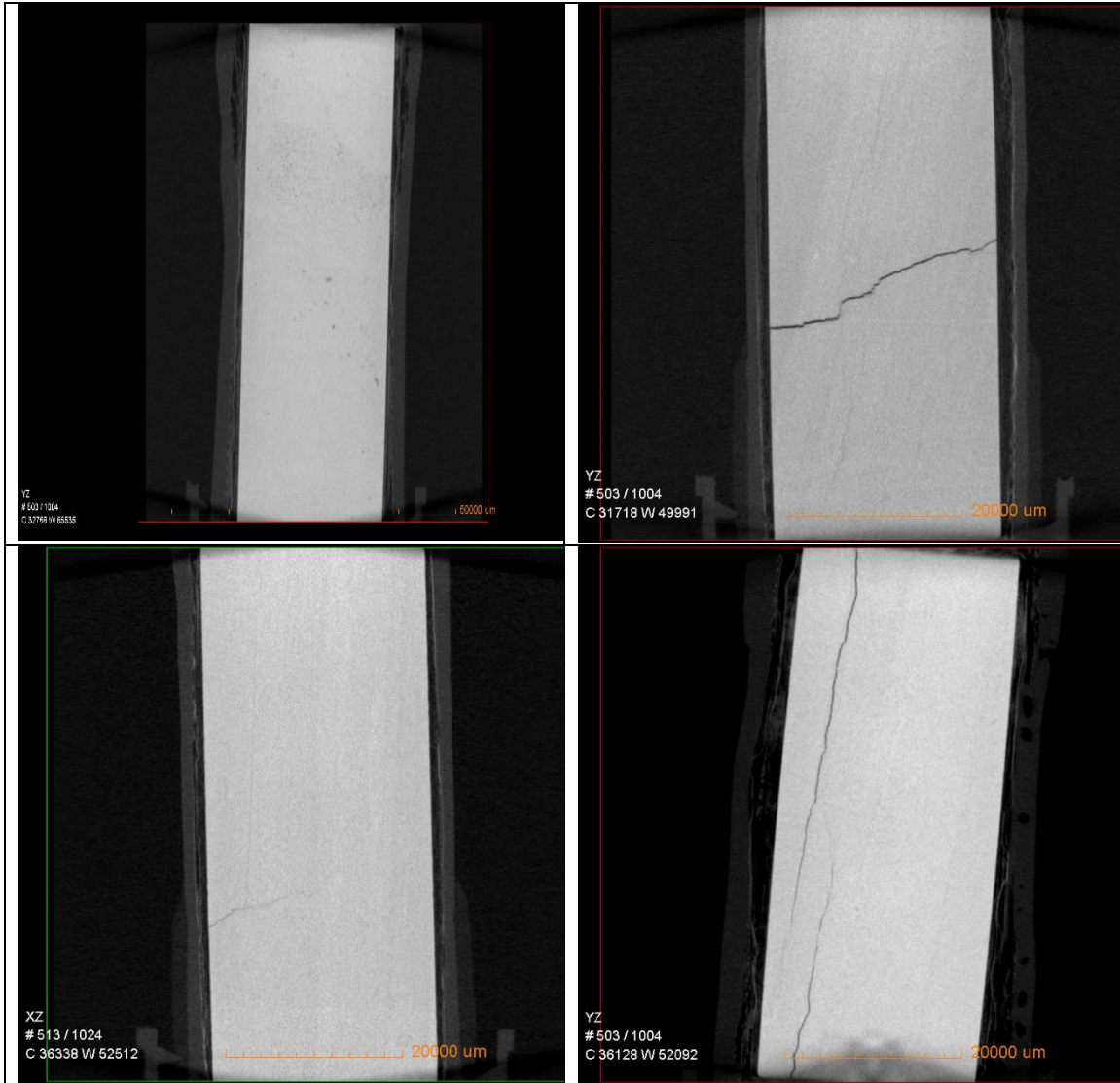
Figure 1. Micro-CT images of selected core plugs that illustrate the range of cracks and partings found in samples selected for permeability testing. Upper left illustrates a high-quality core plug with no visible cracks or partings that is ready for SSKo testing. Lower left shows a sample with a faint transverse crack that could be used in SSKo rig. Upper right image shows a large transverse crack that limits the use of this plug. A trimmed whole diameter shortened plug from either half could be used. Lower right image illustrates multiple longitudinal cracks and partings that make this plug unsuitable for testing. A reduced diameter prism can be trimmed from this piece and epoxy-potted for testing.
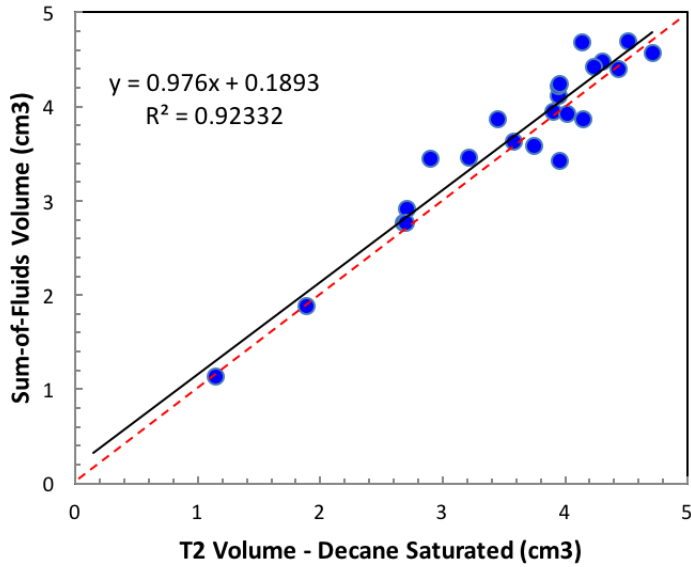
Figure 2. Comparison of total pore volume from NMR on pressure-saturated samples and sum-of-fluids volumes measured on "as-received" samples. The dashed line is unity and the solid line is the actual data trend.
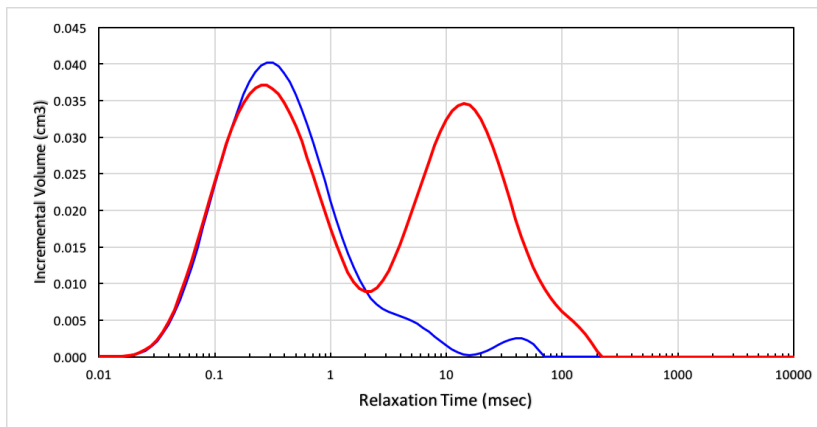
Figure 3. T_2 relaxation time distributions for as received sample (blue) and after pressure-saturation with decane (red). The increase in the slow component with the addition of decane supports the basic interpretation model of water as fast relaxation and mobile oil captured in the slow component.
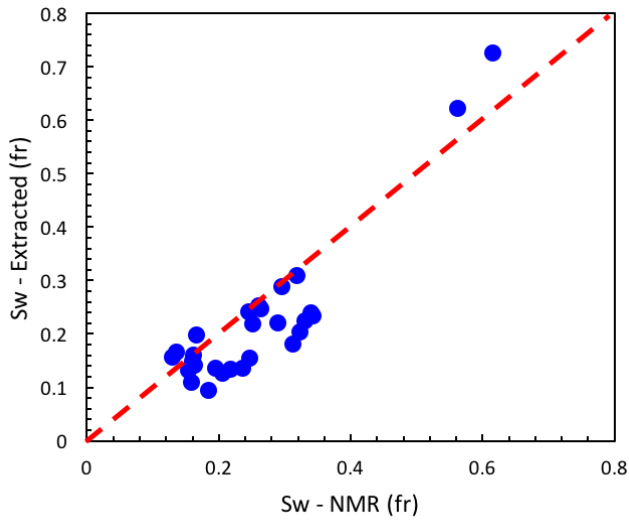
Figure 4. Comparison of crushed-rock-method water saturation versus NMR-based results from pressure-saturated samples. The water saturation values for the crushed rock samples were determined from Dean-Stark extraction of small chips
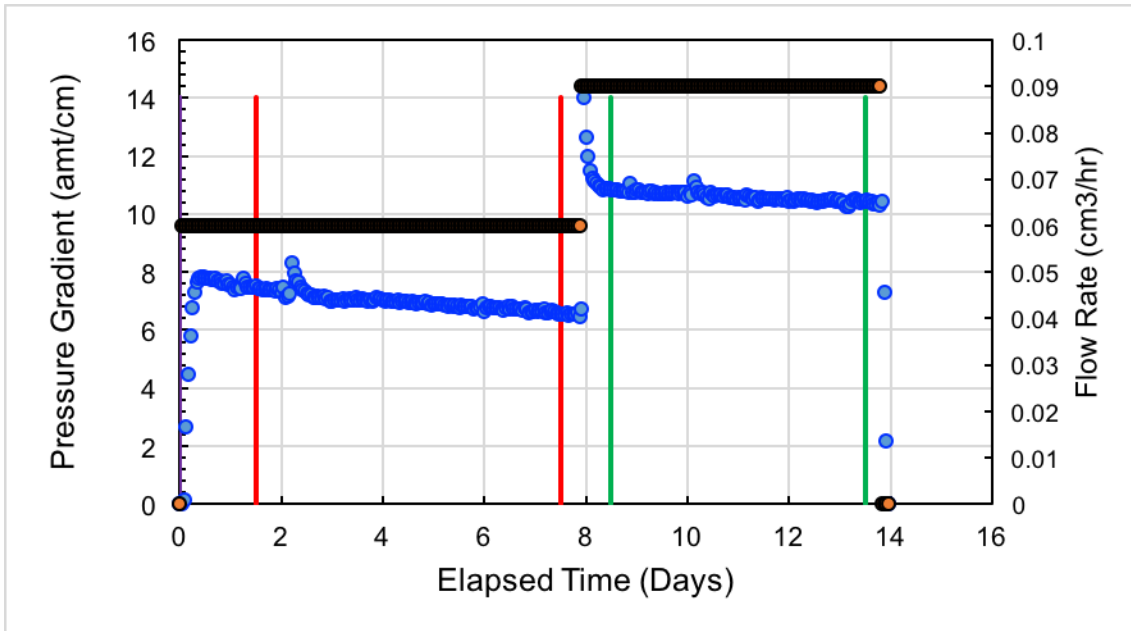
Figure 5. Example of steady-state permeability data where the pressure gradient (blue) was monitored for two flow rates (black) over a period of several days. Gradient values were averaged between the vertical lines for each flow rate for graphical solution. Averaging the gradient values provided better representation of the pressure drop during the steady-state regime.
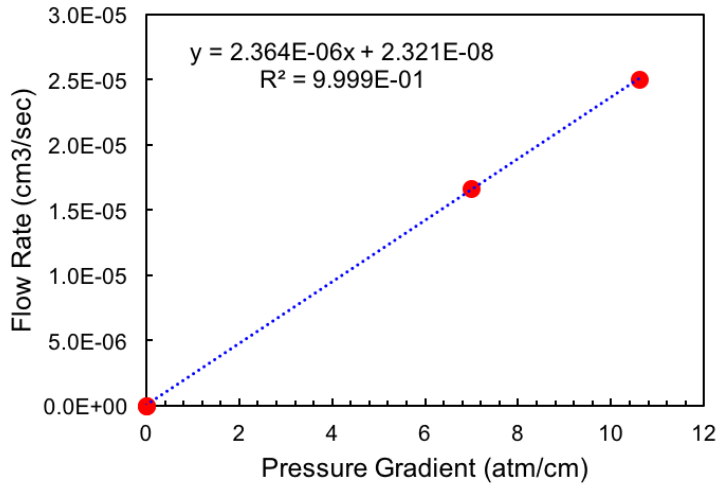
Figure 6. Example of graphical solution of Darcy's equation for permeability using data from Figure 5. Solution includes the use of the zero flow rate, zero pressure gradient origin value.
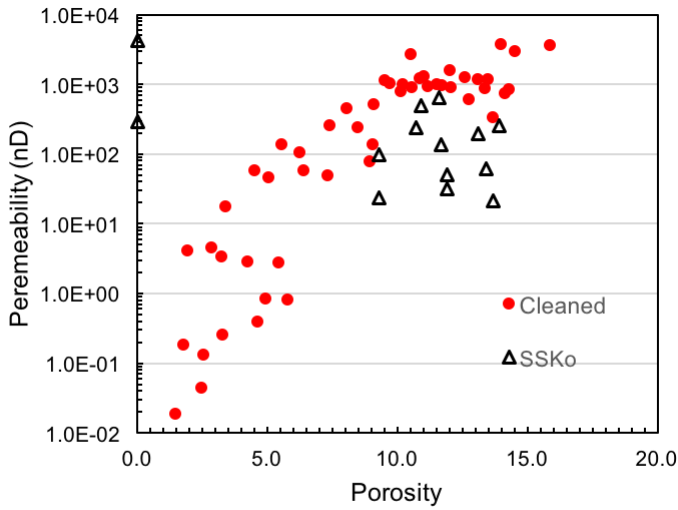
Figure 7. Comparison of steady-state permeability results with previous crushed-rock analysis based values. Porosity used with SSKo-based values is a total porosity value, comparable to the "cleaned" value determined from crushed rock measurements.

USING A DENSITOMETER FOR QUANTITATIVE DETERMINATIONS OF FLUID DENSITY AND FLUID VOLUME IN CORE FLOODING EXPERIMENTS AT RESERVOIR CONDITIONS

Dan Olsen
GEUS, Denmark

This paper was prepared for presentation at the International Symposium of the Society of Core Analysts held in Vienna, Austria, 27 August – 1 September 2017

ABSTRACT

A densitometer is used for quantitative density determinations of fluids being produced from core samples during flooding experiments at reservoir conditions. The densitometer is situated in the flow-line immediately after the core holder, and measures the density of all fluids being produced from the core sample at the actual Pressure/Temperature (P/T) conditions of the flooding experiment. In addition the densitometer provides timing information about dynamic events during the experiment, e.g. water breakthrough or gas breakthrough.

In the case of two-phase experiments, the densitometer may be used for determining the volumes of the two produced phases, if the density of each of the two fluid phases is known. This is the case in many flooding experiments using oil and water. In such cases the densitometer may provide data for the produced volumes of oil and water that agrees reasonably with fluid volumes determined by an acoustic separator. In complex and prolonged flooding experiments the densitometer volume determinations may provide an independent confirmation of the volume determinations of an acoustic separator or possibly other devices.

DENSITOMETER SET-UP

During core-flooding experiments at reservoir conditions it is important to keep track of the fluids being produced from the core sample. For this purpose a densitometer situated in the flow-line immediately downstream to the core sample has proved useful. The densitometer (Paar DMA HPM) has been used at GEUS for obtaining precise density measurements of the fluids being produced from core samples at temperatures up to 115 degree C and fluid pressures up to 420 bara [1]. However, the rating of the device allows use up to 200 degree C and 1400 bara.

The densitometer is situated in the flow-line immediately downstream to the core holder containing a core sample, and measures the density of whatever fluid mixture is produced from the core sample. After passing the densitometer, the fluid flow continues to an

acoustic, two-phase separator (Nisep-200) that measures the produced fluid volumes. A water reservoir, the core sample, the densitometer, and the separator are all situated inside an oven with temperature control better than 1 degree C. Figure 1 gives a sketch of the set-up. Depending on the number of fluid phases in the experiment, the two-phase separator can be replaced by a three-phase separator situated outside the oven. The present paper is only concerned with experiments where the two-phase separator inside the oven is used.

Figure 1. Sketch of the experimental set-up. The dotted line indicates the outline of the oven. Not to scale.
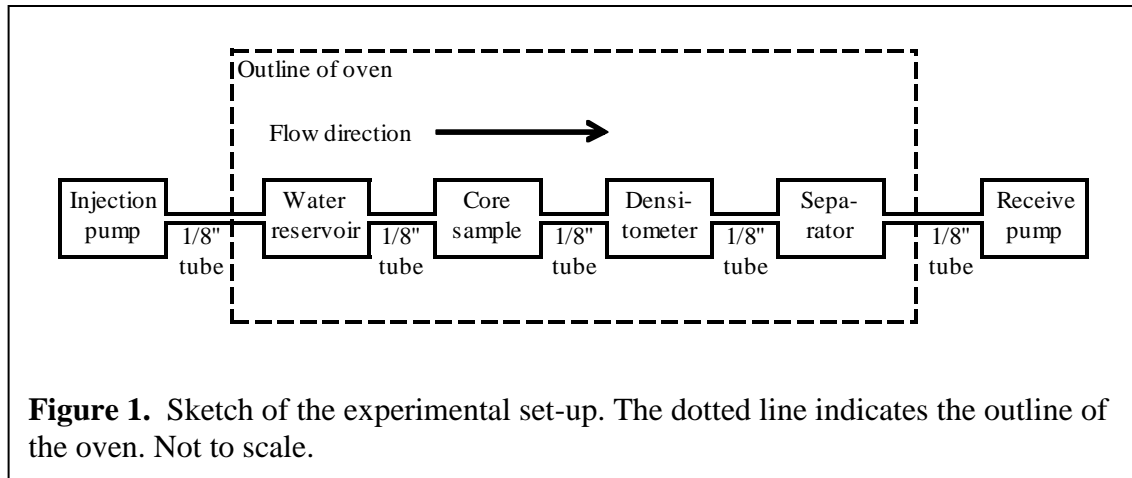
USING THE DENSITOMETER

Data from a core-flooding experiment, Exp-1, on a chalk sample from a North Sea oil reservoir is used to illustrate the use of the densitometer. The core sample was free of fractures, and was initially saturated with live crude oil and simulated formation water, while synthetic sea water was used as injection water for the water-flooding. The experiment was conducted at the P/T conditions of the North Sea reservoir. Figure 2 shows the density log obtained during the water-flooding. Several observations can be made from the log:

(1) Only oil with a constant density of 0.7821±0.0001 g/ml is produced from the core before water breakthrough.

(2) Water breakthrough occurs when the amount of injected water, *Vinj*, reaches 0.481 pore volumes (PV).

(3) After water breakthrough the measured fluid density fluctuates between a density that represents water and a density that represents a mixture of water and oil. This is best seen in the bottom plot of Figure 2 that shows a blow-up of a typical part of the log. It is seen that the majority of the density measurements reports a value around 1.0015 g/ml, which is the density of the injection water. With regular spacing occur narrow downward deflections of the density trace that usually reach down to a fluid density between 0.92

Figure 2. Density log obtained during water-flooding experiment of a chalk core sample at reservoir conditions. The fluids were recombined live oil, simulated formation water, and simulated injection water. The log contains 16785 density measurements. Water breakthrough occurs at Vinj= 0.481 PV. The top plot shows the complete log, the bottom plot, shows a small part of the log in detail.

and 0.965 g/ml. Each of these downward deflections represents an oil drop that passes through the densitometer. The density of the oil was constant during the oil-only production period before water breakthrough, and it is estimated that it remained nearly constant throughout the water-flooding. Whenever the volume of an oil drop entering the measuring cell is smaller than the sensitive volume of the measuring cell volume, the reported density is the average density of the fluids present in the cell. This effect is

termed *the partial volume effect*. Because most of the downwards deflections of the density log only reach between 20% and 35% of the distance from the density of water to the density of oil, it is concluded that the associated oil drops only filled between 20% and 35% of the densitometer cell. The sensitive volume of the cell is approximately 0.35 ml and therefore most of the oil drops were between 0.07 ml and 0.12 ml.

(4) Immediately after water breakthrough the water density is considerably higher than the density of the injection water, i.e. 1.0245 g/ml vs. 1.0015 g/ml. The heavy water represents the connate formation water of the core sample being displaced by the injection water. It is seen that the displacement of the connate water is rather efficient, being completed before Vinj=0.79 PV. Similar behaviour of the connate water being mobilized ahead of the injection water has been observed in other studies, e.g. Brown [2], Nielsen et al. [3], and Korsbech et al. [4].

QUANTIFICATION OF PRODUCED FLUID VOLUMES

In many experiments with flow of water and oil in tubes of more or less transparent materials, e.g. nylon or Teflon, it has been observed that the oil and water moves in sections of fluids separated by curved interfaces, Figure 3. Furthermore, it has been noted that for tubes with inner diameter between 1.0 and 1.6 mm, i.e. commonly used 1/8" tubes, oil and water do not seem to flow past each other, but instead moves as fixed "trains" (Figure 3). The curvature of the oil-water interface indicates that oil is the wetting phase, which agrees with Long et al. [5]. The measuring cell of the densitometer is Hastelloy C-276, and the wetting properties of this alloy against live oil-water are not known. However, because the density log of Exp-1 (Figure 2) and many other experiments show the characteristic movement in "trains", it is reasonable to assume that
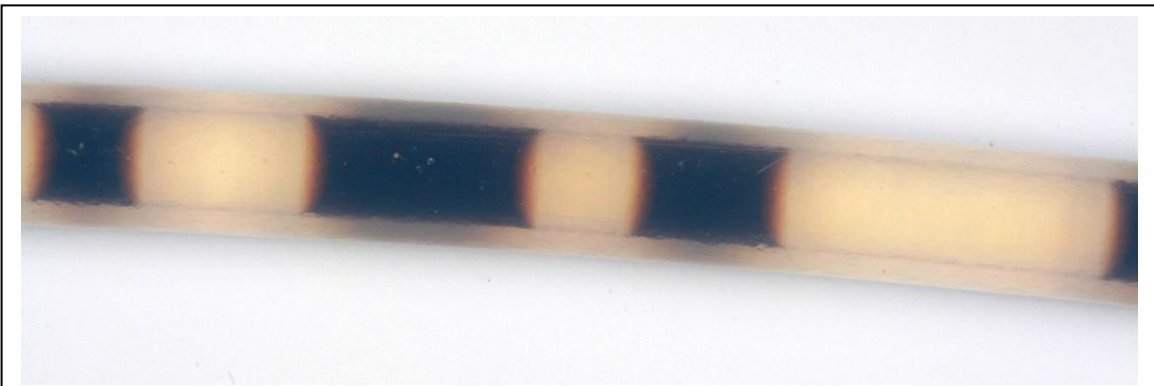
Figure 3. Photo of a Teflon tube filled with alternating sections of water (colourless) and crude oil (very dark brown) during a flow experiment. The curvature of the oil-water interfaces shows that oil is the wetting phase. Note that the inner wall of the tube do not show any oil staining in the water sections, except adjacent to interfaces. The tube has an outer diameter of 3.2 mm (1/8 inch) and an inner diameter of 1.6 mm. Fluid flow was from right to left. While the photo was taken the flow was stopped. Pressure was 1 atm, temperature was 22 degC.

the movement of oil and water is similar in the densitometer, even though it cannot be verified visually. In this treatment it is assumed that water and oil cannot flow past each other in the tube.

A density log may with certain presumptions be used for calculation of a log of produced fluid volumes. The theory of the calculation of oil and water production from densitometer data is given below.

Consider a core flooding experiment conducted at constant pressure and temperature with two immiscible fluids. For ease of reference the fluids are referred to as water and oil, but the presented technique is considered generally applicable for immiscible fluid pairs. The flow rate of the experiment may vary, but is constant in most experiments.

Let *WF* be the fraction of water in a small volume, *dVol*, at a measuring site in the flow line as a function of the total injected volume, *InjVol*, at that site. The cumulative amount of water that has passed the measuring site, *CumProdWater*, is then

$$CumProdWater = \int WF \, dInjVol \tag{1}$$

For measurements in discrete steps from start at zero to end at N Eq. 1 becomes

$$CumProdWater(0, N) = \sum_0^N WF(i) * [InjVol(i) - InjVol(i-1)] \tag{2}$$

The conversion of Eq. 1 to Eq. 2 requires that the density measurements are made so often that every fluid molecule participates in at least one density measurement, i.e. *[InjVol(i)-InjVol(i-1)]* must be less than the measuring volume *dVol*. In the present work *[InjVol(i)-InjVol(i-1)]* is typically between 0.03 and 0.07 ml while *dVol* is 0.35 ml. Therefore each fluid molecule participates in between 5 and 12 density measurement.

Being a system with two phases separated by interfaces, i.e. a water phase and an oil phase, a measured density of the mixture is always intermediate between the density of the water phase and the density of the oil phase. *WF* at step i is then calculated as

$$WF(i) = \frac{MeasDens(i) - LowerEnvelope(i)}{UpperEnvelope(i) - LowerEnvelope(i)} \tag{3}$$

where *MeasDens* is the measured density of the mixture, *LowerEnvelope* is the density of the oil, and *UpperEnvelope* is the density of the water phase.

Combining Eqs. 2 and 3 gives

$$CumProdWater(0, N) = \sum_0^N \frac{MeasDens(i) - LowerEnvelope(i)}{UpperEnvelope(i) - LowerEnvelope(i)} * [InjVol(i) - InjVol(i-1)] \tag{4}$$

Because the experiment is conducted at constant pressure and temperature

$$CumProdOil(0, N) = CumInjFluid(0, N) - CumProdWater(0, N) \tag{5}$$

After defining the functions *LowerEnvelope* and *UpperEnvelope*, Eqs. 4 and 5 can be used to calculate the volumes of produced water and oil in the experiment. The functions *LowerEnvelope* and *UpperEnvelope* must be carefully considered. In many situations the fluid densities are readily available from the densitometer measurements, but in particular the *LowerEnvelope* densities may be difficult to obtain. Whenever possible, the pure fluids should be flowed through the densitometer to obtain the density of the pure fluids.

Because the fluid volumes determined by the densitometer and the separator are made at the same temperature and pressure they are directly comparable, without any P/T corrections.

EXAMPLE OF FLUID VOLUME QUANTIFICATION

A log of produced oil volume calculated from the densitometer data of Figure 2 is given in Figure 4. Also given is a log of produced oil volume calculated from two-phase separator data. The two methods do not share any parameters, and are therefore fully independent volume determinations. The two oil volume traces are seen to match within 1.3% relative. Furthermore, the shapes are nearly identical. The only notable deviation is that the separator log lags a little below the densitometer log immediately after water breakthrough, as oil production according to the separator log seems nearly to stop. This is contrary to the densitometer data, where a significant oil production is documented in the time just after water breakthrough, cf. Figure 5. It is considered most likely that the

Figure 4. Log of produced oil calculated from densitometer data compared with log calculated from two-phase separator data. Each log consists of 16785 data points. PV of the sample is 146 ml.

Figure 5. Enlargement of the densitometer log just after water breakthrough with upper envelope.
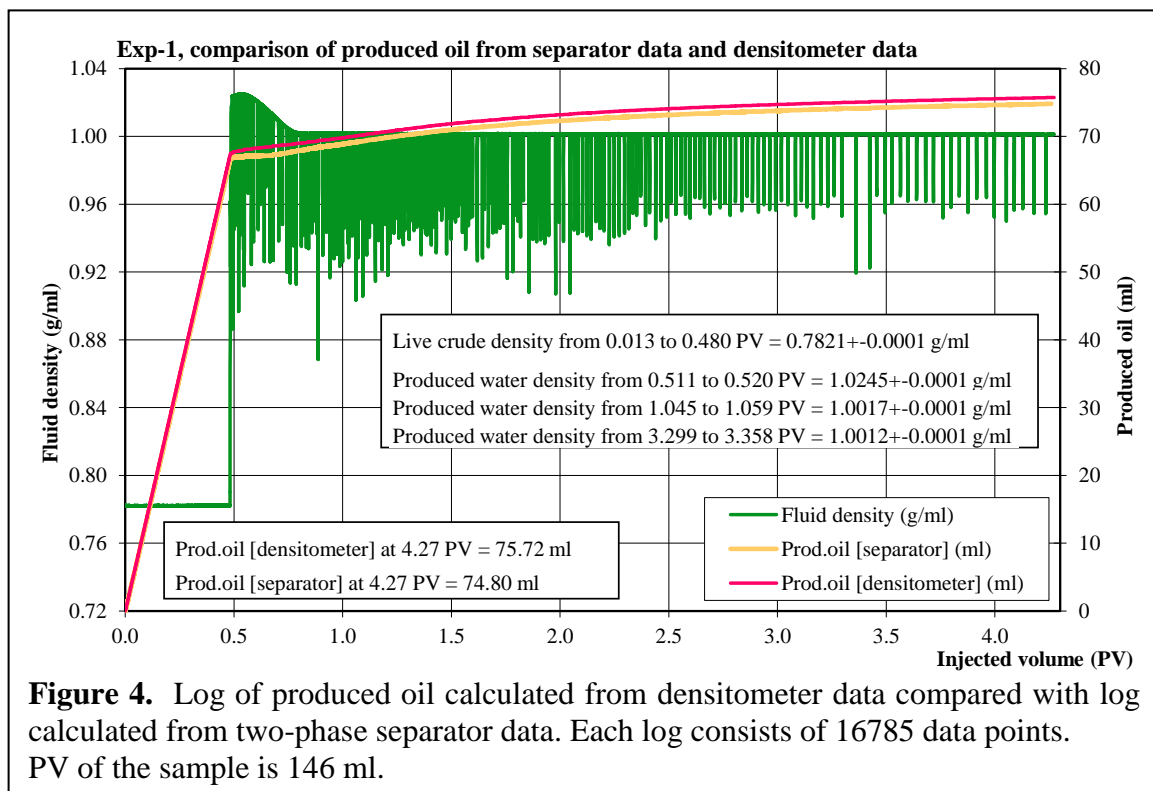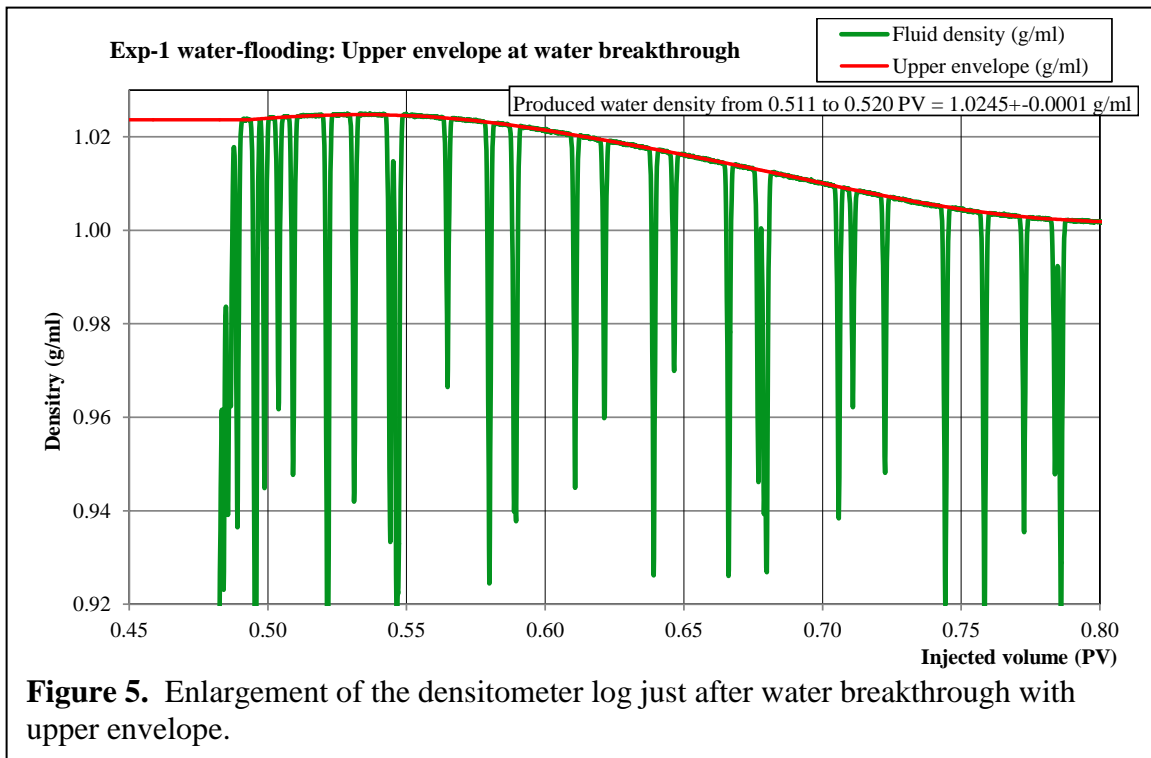
separator data are slightly biased by the influx of heavy formation water just after water breakthrough and that the densitometer data in this instance may actually be more precise.

The use of equations 1 to 5 requires that the lower density envelope and the upper density envelope are defined. The densitometer oil volume log of Figure 4 is based on a constant lower envelope density of 0.7821 g/ml, which is the very stable density of oil recorded before water breakthrough, cf. Figure 4. The upper density envelope is calculated from the densitometer log, and is shown as a red line in Figures 5 and 6. The calculation of the upper density envelope is automated by using an algorithm that identifies sections with nearly constant high density values, and interpolates linearly across the downward deflections of the density log. This is well seen is Figure 5.

The measurement of density in the densitometer and volume in the separator are done downstream to the outlet of the core sample with a separation between the units of several milliliters. In Figures 2, 4, 5 and 6 the densitometer log and the separator log have been shifted by the volume of the connecting flow lines. In this way the densitometer and separator data are shifted to correspond to the outlet of the core sample, i.e. events recorded by the densitometer and separator are shown in the diagrams at the value of the injection volume, *InjVol*, where the corresponding fluids left the outlet of the core sample. In this way the densitometer log and the separator log become directly comparable.

Figure 6. Complete log of densitometer data for Exp-1 with upper envelope shown.
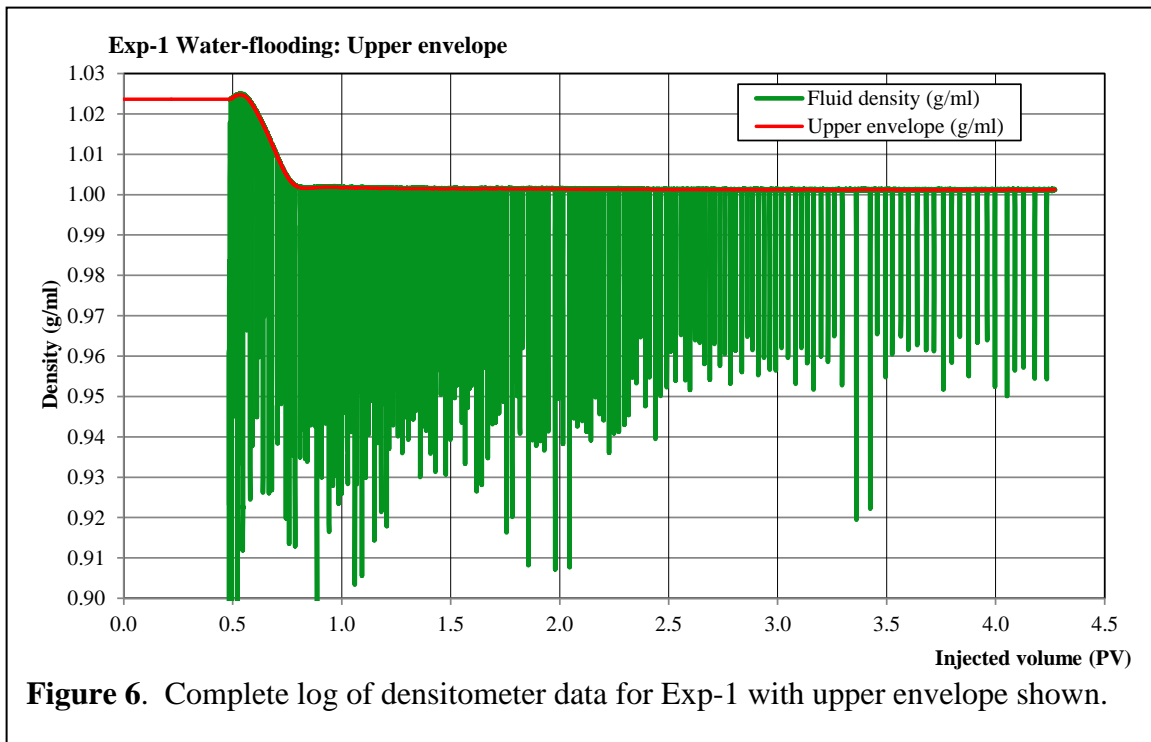
DISCUSSION

The assumption that the fluid phases within the densitometer moves in "trains" without bypassing each other is crucial to the use of the densitometer data for calculation of produced fluid volumes. The main argument that this is the case comes from the fact that the measured fluid density returns exactly to the density of pure water after the passage of an oil drop, cf. Figure 2 bottom plot and Figure 5. If bypassing took place, an amount of oil would sometimes be present in the measuring cell in the intervals between passing oil drops. This is never seen in situations where the oil drops are clearly spaced as in Figure 2. In situations where the measured fluid density returns to the density of water after passage of every drop of oil, both two-phase flow and bypassing of immobile oil within the measuring cell is not possible, and the calculation procedure proposed in this paper is considered valid. In situations where the fractional flow of water and oil are approximately equal, the measured fluid density sometimes stays in an intermediate interval between the density of water and the density of oil (Figure 5). In this situation two-phase flow within the densitometer cannot be ruled out, and the calculation procedure may or may not be valid. In water-flooding experiments this situation has only been seen right after water breakthrough.

The measuring cell of the densitometer consists of a metal tube with an inner diameter of 2 mm (Anton Paar Nordic AB, personal communication). This is slightly larger than the Teflon tube shown in Figure 3, and it is possible that significant bypassing may take place in fluid systems with significantly lower interfacial tension than standard North Sea water-oil systems.

The specifications of the densitometer states that the "amount of sample in the measuring cell" is "approximately 2 ml" [6]. The stated cell volume of 2 ml is clearly larger than the sensitive volume of the measuring cell. At GEUS the sensitive cell volume has been determined to be 0.35 ±0.03 ml by observing the passage of a single water-oil interface through the cell, cf. Figure 7.

Figure 7. Density log of the passage of a water-oil interface through a Paar DMA HPM densitometer. The measured density starts changing at approximately $Vinj$=4.9 ml and ends at approximately $Vinj$=5.25 ml, indicating the volume of the sensitive part of the measuring cell to be approximately 0.35 ml. The density change is not linear as the interface passes through the sensitive volume, indicating that the sensitivity to fluid density varies through the sensitive volume, being largest at the center of the sensitive volume.

It is not known how the densitometer will perform at flow rates above 25 ml/h, and neither how it will perform with oil that are significantly heavier than typical North Sea oil. If a water-oil emulsion is produced, it is estimated that the quantitative volume calculation procedure will probably fail.

In general the densitometer has proved to be very reliable. However, it is susceptible to fines that settle in the measuring cell. Such incidents typically cause the densitometer trace to display a sudden offset towards higher density values. In such case the densitometer data cannot be used for quantitative determination of fluid volumes as the true density values become unknown. In some cases it is possible to flush the fines out of the measuring cell by briefly increasing the flow rate.

The densitometer at GEUS is mounted in a horizontal position. A vertical orientation with the closure of the densitometer U-tube pointing upwards has been considered as a means to avoid settling of fines within the measuring cell. The point should be that gravity then would prevent the fines from settling in the measuring cell. However, this has not been implemented at GEUS, because it seems to introduce a risk of oil collecting at the top of the U-tube.

CONCLUSIONS

An in-line densitometer provides a method for obtaining reliable fluid density data continuously during core-flooding experiments at reservoir conditions. Furthermore, it provides precise timing information of breakthrough events. These applications are possible both for two-phase experiments and three-phase experiments.

In the case of two-phase experiments conducted at constant temperature and pressure conditions, data from an in-line densitometer allows calculation of a log of produced fluid volumes that is comparable in precision to data obtained from an acoustic separator. The application requires the logging time of the density parameter and the injected fluid volume parameter to be so short that every fluid volume molecule participates in at least one density measurement. This method is presently used at GEUS as a secondary method for calculating produced fluid volumes, with separator determination being the primary method.

REFERENCES

1. Olsen, D., "CO2 EOR Production Properties of Chalk", SPE 142993 (2011).
2. Brown, W.O., "The Mobility of Connate Water During a Water Flood", *Trans. AIME*, (1957), **210**, 190-195.
3. Nielsen, C.M., Olsen, D., and Bech, N., "Imbibition Processes in Fractured Chalk Core Plugs with Connate Water Mobilization", SPE 63226 (2000).
4. Korsbech, U., Aage, H.K., Hedegaard, K., Lohmann Andersen, B. and Springer, N., "Measuring and modeling the displacement of connate water in chalk core plugs during water injection", *SPE Reservoir Eval. & Eng.* (2006) **9,3**, 259-265.
5. Long, Z., Shetty, A.M., Solomon, M.J., and Larson, R.G., "Fundamentals of magnet-actuated droplet manipulation on an open hydrophobic surface", *Lab Chip.* **9(11)**, 1567-1575 (2009).
6. Instruction Manual, DMA HPM, Document no. C34IB06A.fm, Anton Paar GmbH, Graz, Austria (2005).

TRANSPORTATION OF NANOCELLULOSE DISPERSIONS THROUGH POROUS MEDIA

Reidun Cecilie Aadland[1], Carter Jordan Dziuba[2], Ellinor Bævre Heggset[3], Kristin Syverud[1,3], Ole Torsæter[1,4], Ian D. Gates[2] and Steven Bryant[2]

1) Norwegian University of Science and Technology (NTNU), Trondheim, Norway
2) Department of Chemical and Petroleum Engineering, University of Calgary, 2500 University Dr. N.W., Calgary, Alberta T2K-1N4
3) RISE PFI, Trondheim, Norway
4) PoreLab, Department of Geoscience and Petroleum, NTNU, 7491 Trondheim, Norway

This paper was prepared for presentation at the International Symposium of the Society of Core Analysts held in Vienna, Austria, 27 August – 1 September 2017

ABSTRACT

Nanocellulose serves as a potential new water additive for enhanced oil recovery (EOR) applications. This is an emerging new type of nanoparticle that is comprised of cellulose fibrils in the nanometer range. Cellulose is a biopolymer and it is the main constituent in the cell wall of plants and trees. Thus, the material is biodegradable, non-toxic and renewable. The particles are different from traditional nanoparticles, such as silica, since they are rod-shaped instead of spherical. This adds a new element of complexity to their flow behavior.

Transportation of nanocellulose through porous media has been investigated where the main objective was to identify retention mechanisms. Experiments consisted of single-phase flow through unconsolidated sandpacks. Two floods were performed for each experiment – a tracerflood and a nanoflood. An ultraviolet (UV)-visible (VIS) spectrometer was used to measure the nanocellulose concentration, and pressure data gave information about permeability alterations. The effects of varying the salinity, sand grain size, particle size and velocity were examined. Two types of cellulose nanocrystals (CNC) were tested: CNC from the U.S. Department of Agriculture (USDA) and CNC from Alberta Innovates Technology Futures (AITF).

From these experiments, it is clear that nanocellulose particles, suspended in aqueous phase, have the ability to flow through porous media. As a general trend, it was observed that larger particles or aggregates resulted in higher retention and permeability impairment. By increasing the salinity, particles started to aggregate more, which resulted in blocking and log-jamming in the sandpack. Thus, salinity was found to be the most important parameter affecting transport. For larger particles, the main retention mechanism was observed to be log-jamming, whereas for small particles adsorption was observed.

Furthermore, higher velocities or larger grain sizes were found to reduce retention and permeability reduction.

INTRODUCTION

Over the last decades, production rates from existing fields have declined since most of the easy and accessible oil has already been produced. The remaining oil is difficult to extract and there is a low proportion of new fields for exploration. As a result, there is a constant need for environmental friendly EOR methods that are more efficient and less expensive than the ones we have today. Chemical flooding with polymers is considered one of the most promising EOR methods and has been researched for over 40 years[1].

The aim of the method is to mix the polymer with water to enhance the viscosity of the injection fluid. By injecting a more viscous fluid, the mobility ratio will become favourable and the macroscopic sweep efficiency will be improved. The viscosity can be enhanced by increasing the size of the polymer (i.e. the molecular weight). However, a larger size increases the risk of plugging of pore throats and formation damage. Polymers are also easily adsorbed onto solid surfaces, which results in loss of chemicals to the formation. Loss of chemicals will in turn increase the injection cost, as it is necessary to inject more polymers to maintain the desired concentration. Thus, the method faces challenges[2]. To increase EOR efficiency of injection fluids, particles should therefore be small enough to allow for long distance transport in the subsurface with minimal retention.

The research reported in this paper focuses on a novel green nanoparticle, nanocellulose, for chemical EOR applications. Nanocellulose is comprised of cellulose fibrils in the nanometer range, hence they are much smaller than polymers. Cellulose is a biopolymer obtained from wood (Fig.1), thus it is a renewable resource with relatively low toxicity. Nanoscale cellulose particles may be classified into three main subcategories: bacterial nanocellulose (BNC), cellulose nanofibers (CNF) and cellulose nanocrystals (CNC)[3]. Only the latter category has been studied in this paper.
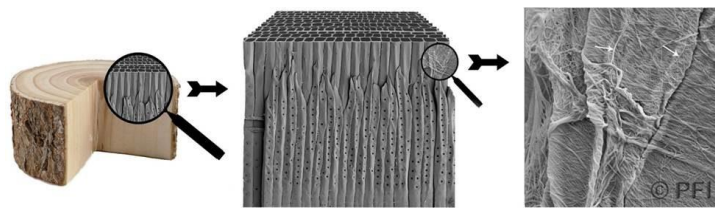
Figure 1. From tree to nanocellulose. Photo by Per Olav Johnsen, RISE PFI

Nanocellulose is an emerging new type of nanoparticle in the petroleum industry. Hence, there does not exist a lot of research on its applications for EOR. Molnes et al. (2016)[4] looked into the premise for use of CNC in EOR. Through their research, it was established that stable dispersions of CNC were obtained when using 1000 ppm NaCl brines as a dispersing medium. In their study cellulose nanocrystal concentrations ranging from 0.5 to 2.0 wt.% were tested. All dispersions remained stable and the stability was verified through zeta-potential measurements. Furthermore, the CNC dispersion was injectable through a

sandstone core. Nevertheless, there were indications that some of the CNC particles became trapped inside the pore matrix, which is a common phenomenon when dealing with polymers[4].

When nanoparticles flow through porous media, there are four potential transport outcomes - adsorption, blocking, bridging (log-jam) or free passage (Fig. 2). The first scenario might occur if the nanoparticle is much smaller than the pore size and there exist some physiochemical interaction between the particle and the pore wall. The particles will then adsorb to the pore wall, which could lead to a wettability change. This adsorption can be reversible or irreversible. Blocking could take place if the particle is much larger than the pore throat. Bridging or log jamming of the pore throat arises when two or more particles with sizes slightly less than a pore throat accumulate together, leading to an obstruction of the pore throat. Free passage happens if the pore throat is large, in which nanoparticles can easily move through[5].
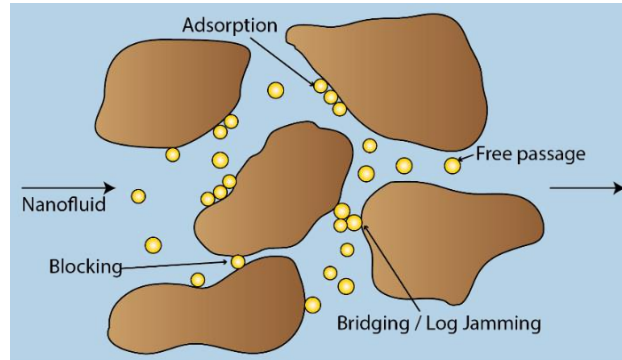
Figure 2. Possible transport outcomes for nanoparticles flowing through porous media.

The aim of this study was to identify the main retention mechanism that affects transport of nanocellulose through porous media. Nanocellulose particles are not spherical, but rod-shaped, which adds complexity to potential flow behavior.

MATERIALS
Porous media
The porous media consisted of a 1-ft-long column (inner diameter = 0.62 inches), which was packed with silica sand grains. The sand grains were purchased from Sigma-Aldrich and Agsco. In the experiments, three different grain sizes were used: large (16-30 mesh), medium (50-70 mesh) and small (140-270 mesh). For the majority of the experiments the medium grain size was used. The average physical properties are listed in Table 1.

Table 1. Average properties of the sandpacks used in retention flooding experiments

Sand Grain Size		Porosity	Permeability	Pore Volume
[mesh]	[μm]	[%]	[D]	[ml]
140-270	53-105	39	3	23.6
50-70	210-297	37	35	22.1
16-30	595-1190	33	284	19.6

Brine

In the majority of the retention experiments 0.1 wt.% brine was used, which was prepared using sodium chloride (NaCl). To test the effect of salinity on nanocellulose transport, experiments were also conducted using 0.3 wt.% and 1.0 wt.% brine.

Nanocellulose

Two types of cellulose nanocrystals (CNC) were used in this study. One was purchased from the University of Maine. This material was manufactured at the Forest Products Laboratory in Madison, USDA (U.S. Dep. of Agriculture). The cellulose nanocrystals were produced using 64 % sulphuric acid to hydrolyze the amorphous regions of the cellulose material, resulting in acid resistant crystals[6]. The stock dispersion is in a gel-form and has a concentration of 12 wt.%. This CNC is denoted CNC (USDA) in this article. The other type of CNC was purchased from Alberta Innovates Technology Futures, and is denoted CNC (AITF). These cellulose nanocrystals were also prepared by using concentrated sulphuric acid. The production process for CNC (AITF) has a spray-drying step so the final nanocelluose product is in powder form instead of gel form.

Both nanocellulose types were diluted to 0.5 wt.% with the respective brine – 0.1 wt.%, 0.3 wt.% or 1.0 wt.% NaCl.

EXPERIMENTAL METHODS

Particle size and zeta potential

The size of nanocellulose aggregates was measured by using dynamic light scattering (DLS). For each solution, 25 sizing measurements were taken and any measurements with an intensity more than one standard deviation from the median intensity were omitted. The remaining measurements were averaged. Zeta potential measurements were taken as the average of six measurements. All dynamic light scattering measurements and zeta potential measurements were performed with a NanoPlus HD zeta/nano particle analyzer.

Flooding setup

Figure 3 shows a schematic of the flooding setup. All experiments were conducted at ambient conditions. A syringe pump was used to inject either nanocellulose fluid or brine through the horizontal sandpack. An in-line ultraviolet (UV)-visible (VIS) spectrometer gave the absorbance readings of the fluid, which was used to calculate a mass balance around the sandpack. The pressure drop across the sandpack was measured throughout the experiment, which gave information about permeability alterations.
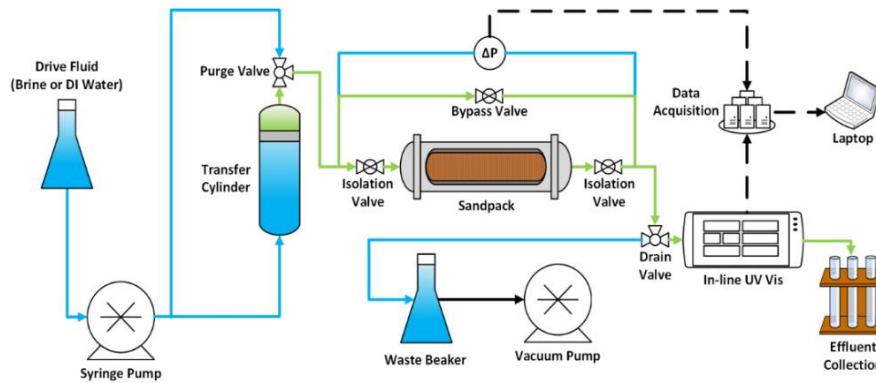
Figure 3. Schematic of the experimental setup used for retention floods

Experimental procedure

One flooding experiment took approximately two days to complete; where day one was injection of a tracer fluid and day two was injection of the nanofluid (NF). There were two main procedures for each experiment: a preparation part and the tracerflood or nanoflood. Four different parameters were varied in these floods: salinity, grain size, particle type and velocity (Table 2).

Table 2. Details over the conducted retention floods. The tables (A-D) list the parameters and values that were tested for each flood. The initial concentration of CNC was 0.5 wt.% for all experiments.

A. Particle type					C. Grain size			
Particle type	Sand grain size [mesh]	Salinity [wt.%]	Darcy velocity [cm/min]		Particle type	Sand grain size [mesh]	Salinity [wt.%]	Darcy velocity [cm/min]
CNC (USDA)	50-70	0.1	0.5		CNC (USDA)	140-270	0.1	0.5
CNC (AITF)	50-70	0.1	0.5		CNC (USDA)	50-70	0.1	0.5
					CNC (USDA)	16-30	0.1	0.5

B. Velocity					D. Salinity			
Particle type	Sand grain size [mesh]	Salinity [wt.%]	Darcy velocity [cm/min]		Particle type	Sand grain size [mesh]	Salinity [wt.%]	Darcy velocity [cm/min]
CNC (AITF)	50-70	0.1	0.05		CNC (USDA)	50-70	0.1	0.5
CNC (AITF)	50-70	0.1	0.5		CNC (USDA)	50-70	0.3	0.5
CNC (AITF)	50-70	0.1	4.1		CNC (USDA)	50-70	1.0	0.5

Preparation of sandpacks

The sand was rinsed over a sieve using deionized water (DIW) and high salinity brine (10 wt. % NaCl). It was then dried in an oven before packing. After packing the tube with sand,

a vacuum pump was used to remove all the water from the lines in the system. The sandpack was afterwards saturated with DIW. The sandpack was prepared for the tracerflood or nanoflood by alternating between injection of DIW at a high rate (29 ml/min) and 10 wt.% brine at a low rate (2 ml/min). This preparation step was done to knock out silica fines that might disturb the UV-Vis absorbance readings during the actual floods. The final step of the preparation part was to purge the sandpack with the salinity that was going to be used in the NF. This purge continued until the UV-Vis signal leveled out.

Sandpack flooding procedure
Sodium Iodide (NaI) was used as the tracer, and the tracerflood was carried out with each sandpack before nanocellulose injection. The tracerflood was injected to characterize the dispersivity in the sandpacks. After each experiment the tracer breakthrough (BT) curve was compared to the nanocellulose BT-curve. Normally, two pore volumes (PV) of tracer was injected, followed by three PV of brine post flush. Afterwards, the sandpack was prepared for the nanocellulose injection by again alternating between DIW and high salinity brine, as described above. The nanocellulose injection followed the same procedure as the tracerflood, with two PV of nanocellulose injection and then three PV of post flush.

Visualizing nanocellulose retention
Nanocellulose shows significant thermal decomposition at high temperatures. Heggset et. al (2017) evaluated the temperature stability of nanocellulose dispersions and found that nanocellulose start to degrade around $110°C$[7]. The thermal decomposition results in production of black ash and some char. After each flood, the sand from the pack was emptied onto a tinfoil sheet by applying low-pressured air to the outlet side of the pack, pushing the sand slowly out. It was then baked in a Thermo Scientific HERATHERM Oven at 300°C to trigger thermal decomposition. Regions of the sandpack containing relatively more nanocellulose would darken more than the rest of the pack due to the presence of ash and char. This allowed for a qualitative visualization of the retention.

RESULTS AND DISCUSSION
Particle size and zeta potential
Table 3 shows the average measured particle size values and the zeta potential for the solutions that were used in the retention flooding experiments. The size of the particles in deionized water (DIW) is also included in the table as a reference for the onset of aggregation. Dynamic light scattering is a technique which is intended for spherical particles, so the measurements in this section is not an exact value of their size, but gives the possibility to compare the samples to one another.

Table 3. Aggregate sizing data (measured by DLS) and zeta potential data for the fluids used in the floods. The zero salinity value corresponds to the nominal particle size.

	0.5 wt.% CNC (USDA)				0.5 wt.% CNC (AITF)	
Salinity [wt.%]	0	0.1	0.3	1	0	0.1
Avg. Aggregate size [nm]	53 ±3	67 ±3	298 ±12	913 ±132	166 ±15	321 ±29
Zeta potential [mv]	-	-30.28 ±1.18	-21.20 ±2.37	-11.01 ±1.32	-	-23.60 ±2.22

Retention flooding results

This section presents a series of selected BT-curves outlining the key findings from the flooding experiments (Fig. 4-6). When reading the BT-curves, note that the black dotted curve is the tracer. The tracer curve was run prior to each experiment, and by comparing all of them against each other the curves overlays with minimal variation to the top-, start- or ending-point. The curve is intended to map the dispersion of the sandpack for an ideal case of no retention. The nanocellulose BT-curves are compared against the tracer curve to identify various transport phenomena occurring during the floods. The graphs also contain the corresponding pressure curves for each experiment. This data gives information about permeability impairment in the sandpack. The results for each tested parameter (particle type, velocity, grain size and salinity) are presented below. The retention and permeability data from the floods is found in Table 4.

1. Impact of particle type

The two tested particle types showed different transport behavior in the porous media when tested with the same salinity (0.1 wt.% NaCl). This difference is theorized to be a result of their size. From the DLS measurements, CNC (AITF) aggregates are presumed to be ~4.8 times larger than CNC (USDA) aggregates in 0.1 wt.% NaCl. The flooding experiments showed that the amount of retained particles was in the same range for both types, 6.2 % for CNC (USDA) and 6.6 % for CNC (AITF). The interesting findings were in the permeability data and study of the nanofluid BT-curve. From Figure 4 it is seen that the nanofluid (NF) CNC (USDA) BT-curve is delayed compared to the tracer curve. It is also seen that the pressure curve increases until it reaches one PV. A pressure increase is expected during the first PV as a slightly more viscous fluid is injected into the sandpack. The pressure is then stable for the second PV. Both these observations suggests that some adsorption is taking place. The CNC (USDA) BT-curve has a smooth tail, which suggests that particles are able to transport out of the porous media with minimal straining occurring.

The CNC (AITF) BT-curve on the other hand, overlays with the tracer curve indicating no adsorption is happening. For this flood, other mechanisms seem to be at play. By comparing the pressure curves for the two particles, CNC (AITF) has approximately one and a half times higher pressure than CNC (USDA) during the two PV of nanocellulose injection. This indicates that particles are blocking of pore throats to a greater degree. This log jamming effect is further supported by the continuous increase in pressure during the second PV, and that the brine from the post flush breaks through earlier than the tracer BT-curve. This suggests that pore throats have been blocked off during the nanocellulose flood,

which gives the post flush a smaller volume to traverse before exiting the pack. At the end of the CNC (AITF) tail there is a small bump, which is believed to be retained particles being released from log jams that have been broken apart during the post flush with brine.

Overall, larger nanocellulose particles and aggregates in the bulk solution result in impaired transport properties through porous media.
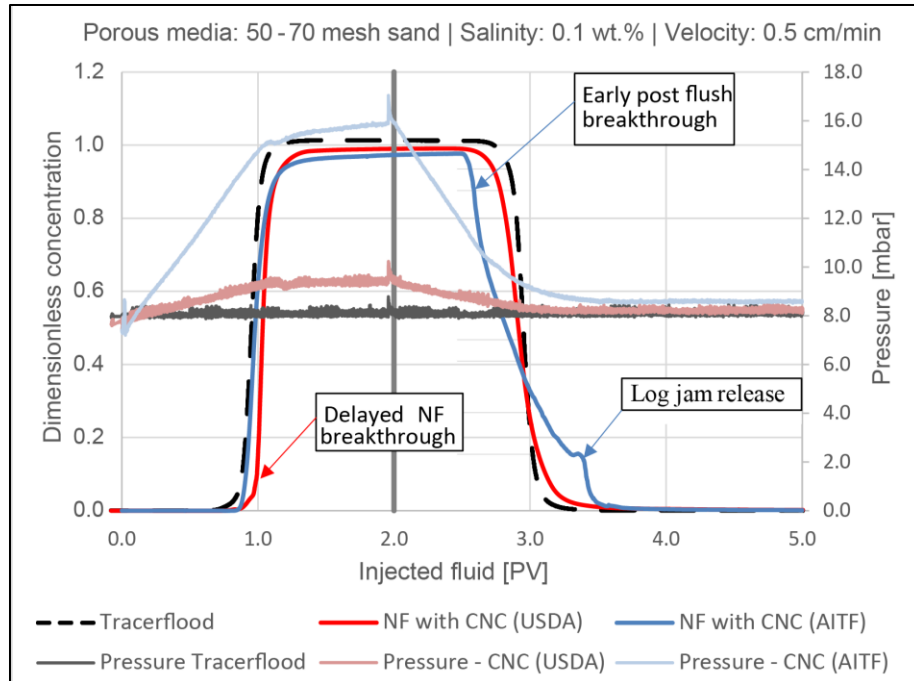
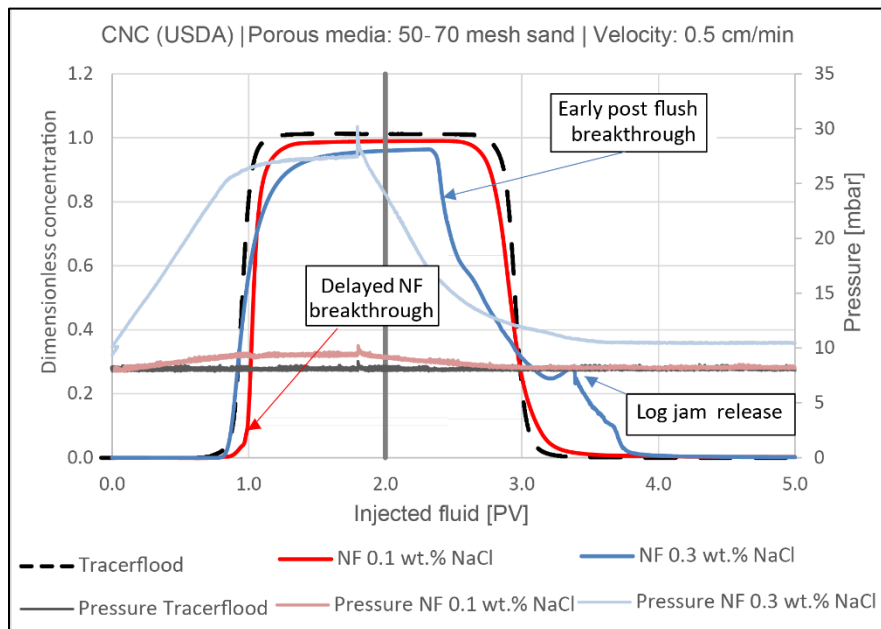**Figure 4.** Breakthrough curve for flood with 0.5 wt.% CNC(USDA) (red line) and 0.5 wt.% CNC (AITF) (blue line). The tracer BT-curve is the black dotted line.

2. Impact of velocity

Three velocities were tested in this experiment: a low (0.05 cm/min), medium (0.5 cm/min) and high (4 cm/min). It is believed that a high velocity will result in a high shear rate, which may break up aggregate log-jams. Since CNC (AITF) caused the highest permeability reduction and appeared to be more susceptible to log jamming, they were the only particles considered for the velocity experiments.

The BT and pressure curves for the flooding experiment using the low velocity is seen in Figure 5. The medium velocity was the CNC (AITF) flood that was previously presented in Figure 4. By comparing the floods it is seen that the flood with the low velocity has a much steeper increase in pressure during the second PV of NF injection. The post flush also has an earlier breakthrough compared to the medium velocity, and both floods have some small bumps in the end of the tail for the BT-curve. It is therefore believed that the low velocity leads to more aggregated log jams based on the interpretation of the pressure data and tail of NF curve. From the computed numbers the retention is 24% for the low velocity and 6.6 % for the medium velocity. The overall permeability reduction with the

low velocity is 90.3%. From Figure 5 it is also seen that the pressure drop is spiky and keeps increasing during the post flush. These spikes likely indicate reordering of the retained nanocellulose aggregates. The BT-curves for the high velocity is not included as it behaved almost like a tracer with no early breakthrough of the post flush brine.
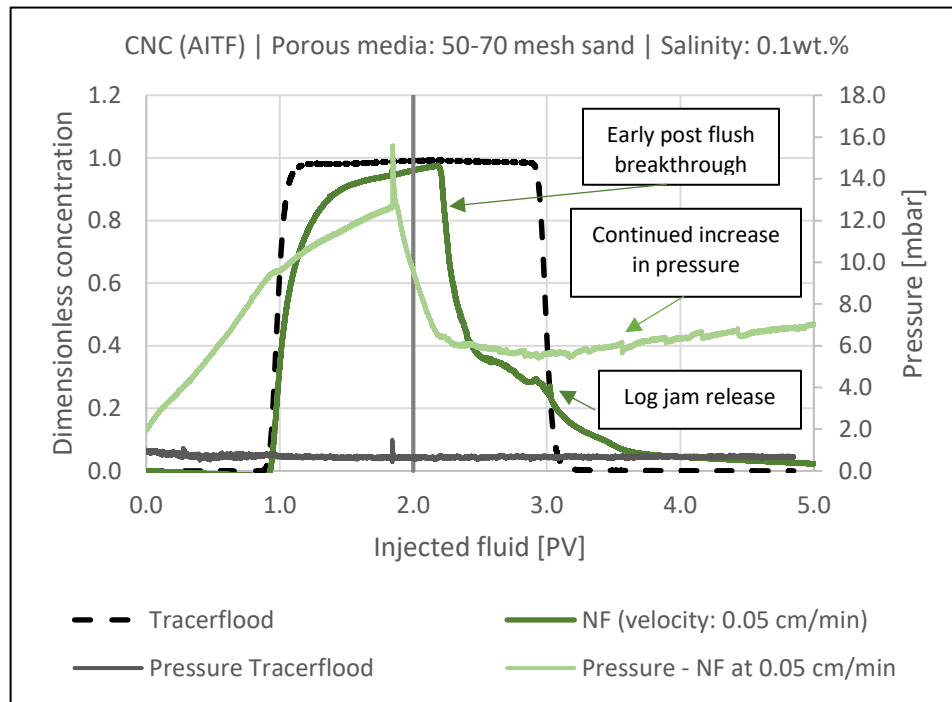
Figure 5. Breakthrough curve for flood with 0.5 wt.% CNC(AITF) (dark green line) using a low velocity (0.05 cm/min). The tracer BT-curve is the black dotted line. The light green and grey line are the corresponding pressure curves.

3. Impact of sand grain size
Only CNC (USDA) was tested with varying the grain size of the sandpack. The major finding from these experiments was that retention and permeability reduction increased as grain size decreased (Table 4). One interesting observation was that the BT-curve for the nanoflood in the medium sand (50-70 mesh) and the small sand (140-270 mesh) were both delayed relative to the tracer curve. The pressure also stabilized during injection of the second PV indicating that no major straining is occurring inside the sandpack. Both these factors suggest that adsorption is occurring, and the effect was slightly more profound for the small sand. The nanoflood BT-curve in the larger sand coincides closely with the tracer curve and there were only 2.3% retention and 3.33% permeability reduction. This implies that this flood was behaving almost like a tracer. No BT-curves are included from these experiments, as they show similar trends as the CNC (USDA) curve in Figure 4.

The grain size will determine how closely packed the sand is, i.e. the diameter in the pores. If the diameter becomes too large, the particles will move relatively unhindered through the porous media with no interaction. In smaller grain sizes, the surface-to-volume ratio is

larger. The results from these three experiments tells us that there seem to be a critical surface area threshold where adsorption starts to come into effect.

4. Impact of salinity

By increasing salinity, the aggregated particle size increases. Thus, this parameter had the most effect on retention and permeability reduction, since larger particles would more easily clog the system. CNC (USDA) was the only particle tested for the effect of salinity, since CNC (AITF) aggregated greatly at salinities above 0.1 wt.%. It was therefore not possible to get a mass balance, as a stable UV reading could not be achieved. Figure 6 show the BT-curve for CNC (USDA) in 0.1 wt.% and 0.3 wt.% NaCl. CNC (USDA) with 0.1 wt.% NaCl has already been explained in Figure 4, where adsorption seemed to be the most dominating mechanism at play. CNC (USDA) in 0.3 wt.% NaCl showed a similar trend in the transport behavior as CNC (AITF) in 0.1 wt.% NaCl (Fig.4). No significant adsorption is occurring as the NF BT-curve is overlaying with the tracer BT-curve in the beginning. The pressure slightly increased during the injection of the second PV of nanofluid and the post flush with brine had an early breakthrough. This suggests that log-jamming or blocking of pore throats inside the pack occurs. By blocking off pores, the pressure in the pack will increase as the permeability is reduced, and the fluid will have a smaller volume to traverse, which results in the early breakthrough. The overall permeability reduction with the higher salinity (0.3 wt.% NaCl) was 24 % (Table 4), and the pressure was almost three times higher compared to the injection with 0.1 wt.% NaCl.

The graph for the highest salinity is not included, as a filter-cake was created at the inlet of the sandpack. This resulted in 100% retained particles and 98 % permeability impairment (Table 4).

Figure 6. Breakthrough curve for flood with 0.5 wt.% CNC(USDA) in 0.1 wt.% NaCl (red line) and 0.3 wt.% NaCl (blue line). The tracer BT-curve is the black dotted line.

Table 4. Retained nanocellulose and permeability data from the flooding experiments.

Parameter changed	Retention [%]	Permeability [Darcy]		Permeability Reduction [%]
		Before	After	
1. Particle type				
CNC (USDA)	6.2	34	32	5.5
CNC (AITF)	6.6	36	31	13.3
2. Velocity				
0.1 ml/min	24.0	36	4	90.3
1.0 ml/min	6.6	36	31	13.3
8 ml/min	8.2	39	36	7.8
3. Grain size				
140-270 mesh	8.4	2.4	1.87	21.8
50-70 mesh	6.2	34	32	5.5
16-30 mesh	2.3	296	286	3.3
4. Salinity				
0.1 wt.% NaCl	6.2	34	32	5.5
0.3 wt.% NaCl	9.9	33	25	23.7
1.0 wt.% NaCl	100	34	0.9	97.5

Visualizing nanocellulose retention

To further elucidate that higher salinity results in higher retention and permeability impairment, visualization of the nanocellulose retention was performed using extensive heating of the post-flood sandpacks (Fig.7). For the flood with CNC (USDA) in 0.1 wt.% NaCl, it appears that the whole sandpack has darkened slightly. This suggests that nanocellulose filled adsorption sites in the pack resulting in a small retention. For the flood with high salt concentration, there is a notable darkening in the front while the outlet seemed to be unaffected. This indicates that the retention favored the front of the pack, which is consistent with a log-jamming phenomena leading to straining and filter cake formation. Both findings are consistent with the results from the BT-curves.
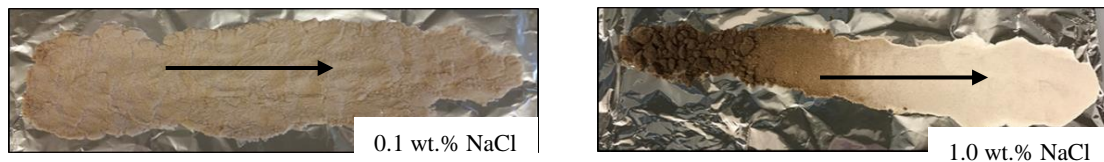
Figure 7. Burning photos of retention floods with CNC (USDA). The picture to the left is with 0.1 wt.% NaCl, while the picture to the right is with 1.0 wt.% NaCl. The arrow indicates the direction of flow.

CONCLUSION

- The two tested nanocellulose types were different in size. Particle size contributed to different transport behavior when flooded with 0.1 wt% NaCl.

- Salinity had the largest effect on retention, since it changed the aggregated particle size in the bulk solution.
- Smaller particles seemed to be dominated by adsorption on sand grains, whereas larger particles were retained in the sandpack by blocking and log-jamming.
- Retention and permeability reduction increases as the velocity decreases, the same trend is seen by decreasing the grain size.

ACKNOWLEDGEMENTS

REFERENCES

1   Kamal, M. S., Sultan, A. S., Al-Mubaiyedh, U. A. & Hussein, I. A. Review on Polymer Flooding: Rheology, Adsorption, Stability, and Field Applications of Various Polymer Systems. *Polymer Reviews* **55**, 491-530, doi:10.1080/15583724.2014.982821 (2015).

2   Sun, X., Zhang, Y., Chen, G. & Gai, Z. Application of Nanoparticles in Enhanced Oil Recovery: A Critical Review of Recent Progress. *Energies* **10**, 345 (2017).

3   Klemm, D. *et al.* Nanocelluloses: a new family of nature‐based materials. *Angewandte Chemie International Edition* **50**, 5438-5466 (2011).

4   Molnes, S. N., Torrijos, I. P., Strand, S., Paso, K. G. & Syverud, K. Sandstone injectivity and salt stability of cellulose nanocrystals (CNC) dispersions— Premises for use of CNC in enhanced oil recovery. *Industrial Crops and Products* (2016).

5   Ju, B. & Fan, T. Experimental study and mathematical model of nanoparticle transport in porous media. *Powder Technology* **192**, 195-202, doi:http://dx.doi.org/10.1016/j.powtec.2008.12.017 (2009).

6   Dong, X. M., Revol, J.-F. & Gray, D. G. Effect of microcrystallite preparation conditions on the formation of colloid crystals of cellulose. *Cellulose* **5**, 19-32 (1998).

7   Heggset, E. B., Chinga-Carrasco, G. & Syverud, K. Temperature stability of nanocellulose dispersions. *Carbohydrate Polymers* **157**, 114-121 (2017).

THE FORMATION OF MICROEMULSION AT FLOW CONDITIONS IN ROCK

M. Ruecker[1,2], W.-B. Bartels[1,3], E. Unsal[1], S. Berg[1], N. Brussee[1], A. Coorn[1], A. Bonnin[4]

[1] Shell Global Solutions International B.V., 2288 GS Rijswijk, NL
[2] Department of Earth Science and Engineering, Imperial College London, SW7 2AZ UK
[3] Earth Sciences department, Utrecht University, 3584 CD Utrecht, NL
[4] Swiss Light Source, Paul Scherrer Institute, CH-5232 Villigen, Switzerland

ABSTRACT

Surfactant flooding is a chemical enhanced oil recovery (cEOR) technique where low concentrations of surfactant are added to the injection water. The surfactant reduces the oil/brine interfacial tension which, in return, increases the capillary number favoring the viscous mobilization of (capillary) trapped oil. In order to reduce the residual oil saturation significantly, ultra-low interfacial tension ($<10^{-2}$ mN.m^{-1}) between crude oil and aqueous phase is required. That is achieved by employing surfactants that solubilizes the oil and form a microemulsion phase. How low interfacial tension can become depends on the phase behaviour of the surfactant/oil/water system which is often studied with equilibrium phase behaviour tests. However, oil recovery is a dynamic process, and microemulsion formation occurs in situ over different time and length scales depending on the flow and porous medium characteristic.

In this study, we investigated in-situ formation of microemulsion and production of oil by solubilization in a core sample. The aqueous solution of an EOR surfactant was injected into the core sample after the waterflood to solubilize the remaining oil. The surfactant was an internal olefin sulfonate (IOS), and had affinity to the oil phase (n-decane); in situ microemulsion formation occurred. The oil phase was doped with iodo-decane as contrast agent, which allowed visualization of the oil-and emulsion phases using X-ray computed micro-tomography technique. The resolution was sufficient to visualize pure and emulsified oil within individual pores. Image analysis of the scans showed that the emulsification during flow took place at shorter time scales than what was observed at static conditions. These results were consistent with findings of micromodel experiments.

INTRODUCTION

It is commonly accepted that residual oil saturation after conventional waterflood can be further reduced by increasing the capillary number [1-4] $N_c = u\eta/\sigma$ (u is the flow rate, η the viscosity of the injected fluid and σ the interfacial tension (IFT) between the oleic and aqueous phase) as illustrated in Figure 1A [4,12]. Various injection strategies have been developed to enhance the oil recovery (EOR) by changing the properties of the injected

fluid in order to increase N_c. To significantly reduce the residual oil saturation an increase in N_c by several orders of magnitude compared to waterflooding may be required. This can be achieved by surfactants that produce an ultra-low IFT ($<10^{-2}$ mNm^{-1}) between crude oil and the displacing aqueous phase [3,5]. These surfactant systems typically form microemulsions where the surfactant solubilizes some of the oil phase [3,5,8]. In general, the emulsification is studied under controlled conditions such as in laboratory, and facilitated by some form of external mechanical energy, i.e. stirring [6]. But in subsurface applications the emulsification occurs in-situ and application of an external energy is not possible. It is commonly expected that for appropriate composition of surfactants and fluids ultimately a microemulsion will form. What is not clear how long this process will take in absence of "stirring" under in-situ flow conditions which are mostly laminar. There is coupling between emulsification and flow; flow dynamics promote the mixing required for the emulsification while resulting (micro)emulsion properties like increase in viscosity and ultralow IFT impact the flow. Microemulsions can consist of structures with feature sizes – a few nm to several 100 nm – which can increase viscosity and can be larger than the pores of the porous medium (Figure 1C) [6]. IFT reduction will increase the N_c and promote displacement, but a higher viscosity may lead to other adverse effects like trapping and bypassing. For example, Figure 1B shows the viscosities of the microemulsion of n-decane and surfactant solution over a range of salinities used in this study. The equilibrium microemulsion viscosity was 4-6 cP, while the surfactant solution viscosity was ~1 cP and the n-decane viscosity was 0.85 cP [7].

Conventional assessment of the effectiveness of surfactants
To assess the oil recovery efficiency of surfactants, typically equilibrium phase behavior tests are performed. In these tests, the surfactant solution and the oil are initially mixed in test tubes by rigorous shaking, and let stagnate while the emulsification takes place which took approximately 1h for the surfactant/oil/water system used in this study [7,8]. The properties of the microemulsion are then assessed by visually inspecting the solubilization, measuring the oil/water IFT and the viscosity of the resulting microemulsion to determine the optimum surfactant solution [8]. These tests are done under static conditions and do not probe the influence the flow and in-situ mixing.

Pore-scale studies on surfactant flooding
Glass micromodels allow direct visualization of the pore space, and provide crucial information to understand the fundamentals of the pore-scale physics which play a role in the emulsification. Studies in micromodels have shown that the microemulsions can form in situ under flowing conditions at shorter time scales than in static conditions [7]. However, the pore structure of a rock is more complex, and, therefore, may have significant influence on the emulsification behaviour. Coreflood experiments can be performed where the aqueous solutions of surfactant are injected in an oil-saturated rock of several centimeters to 1m length [2,3]. These experiments provide an estimate on the average oil recovery values but do not give access to microscopic details at pore scale.
Recent advances at μCT synchrotron beamlines have enabled to study multiphase flow through rock samples at a time resolution of few seconds [9][10]. With this technique also

the effect of surfactant has been studied, however, the surfactant/oil/water system did not form microemulsions with ultralow interfacial tension [11] .
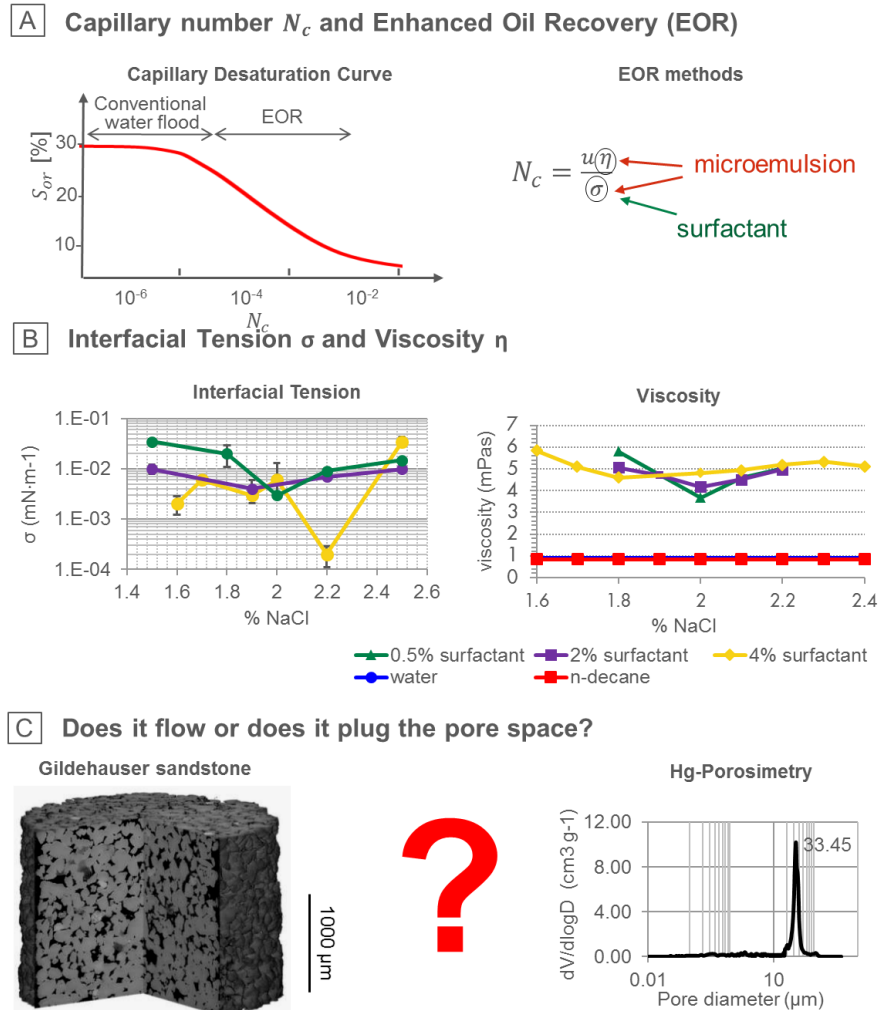
Figure 1: Capillary desaturation curve (A-left: adapted from Lake, 1989 [1]) and capillary number formulation (A-right). IFT and viscosity values of microemulsions in the behavior study (B: adapted from Unsal et al., 2016 [7]). C: flow dynamics in pore space depend on the topology, pore size distribution and feature size of microemulsions.

Here, we present a coreflood experiment using fast X-ray computed micro-tomography. We studied the in-situ emulsification of oil during surfactant flooding. The resolution was enough to visualize pure and emulsified oil which provided a more detailed insight into the time and length scales associated with the in-situ emulsification.

MATERIALS AND METHODS

Sample selection and preparation

Water-wet Gildehauser sandstone was used as the rock sample [10]; its properties are listed in Table 1. The corresponding pore size distribution obtained by Hg-porosimetry is

displayed in Figure 1C. The sample was cleaned and embedded into polycarbonate by heat-shrinking. Prior to the coreflood, the sample was saturated with brine which was then displaced by drainage with oil (n-decane). The oil phase was doped with iodo-decane as a contrast agent (22% iodo-decane / 78% decane).The brine composition is given in Table 2.

Table 1. Core sample details.

Core material	Porosity	Permeability	Core length	Core diameter
Gildehauser sandstone	0.2	1 Darcy	20 mm	4 mm

The surfactant solution consisted of 1% Na_2CO_3, 5% 2-butanol, 1.25% NaCl and 2% surfactant. It was chosen based on its capability to form microemulsions with n-decane at ambient conditions. The surfactant was an internal olefin sulfonate (IOS) with 20-24 carbon atoms (C20-24) and is produced by Shell Chemicals as the ENORDET O series.

Table 2. Brine composition,

Ion	Na^+	K^+	Mg^{2+}	Ca^{2+}	Cl^-	Ionic Strength [mol/L]	pH
FW [mg/L]	4270	7240	20	300	13750	0.396	7

Beamline based fast X-ray computed micro-tomography
The experiments were performed at the TOMCAT beamline of the Swiss Light Source (Paul Scherrer Institute). The fast synchrotron-based X-ray computed micro-tomography facility enabled us to collect a full 3D scan (1500 projections) of a region of interest (ROI: 1400x1400x900 voxels with a pixel size of 3 µm) located 2mm above the inlet in 7s. A white beam with 5%, 250 um Al was used.
The core samples were mounted vertically in a flow setup containing two remotely controlled piston pumps [13], which enabled a continuous rotation for 4D tomography. The injection was done at the bottom of the sample. The injection rate was 30 µl.min^{-1} for both floods, and corresponded to a interstitial velocity of approximately 12 mm.min^{-1} or 1.68 pore volume per minute. The corresponding capillary number was $N_c= 1.1 \times 10^6$. The experimental protocol started with sample saturated with oil after primary drainage. Two consecutive injections were performed; waterflood followed by the surfactant injection. The waterflood was imaged taking a scan at 1 scan at every 7s and surfactant flood was imaged at 1 scan every minute.

Image processing
The images obtained from the beamline were reconstructed using the Paganin method [14,15]. They were then filtered, segmented and processed with Avizo 9.0 (FEI) and Matlab (MathWorks) [10]. Rock, initial water and oil phases were segmented during the conventional waterflood. During the surfactant flood the mixing with remaining oil led to the formation of emulsions with a range of composition and associated of grey levels ranging between (un-doped) water to doped oil levels. The degree of emulsification was assessed from the grey level. In addition to the coreflood images, equilibrated phase

behaviour test tubes were also scanned in a benchtop µCT-scanner Xradia (Zeiss) in order to study the composition of the (fully) equilibrated middle microemulsion phase.

RESULTS

Phase behaviour studies (static)

Based on equilibrium phase behavior analysis of the surfactant solution and n-decane, the optimum salinity was at 1.25% NaCl. Since the oil was doped with iodo-decane, the phase behaviour tests were repeated with the doped n-decane, which did not affect the optimum salinity (Figure 2A).
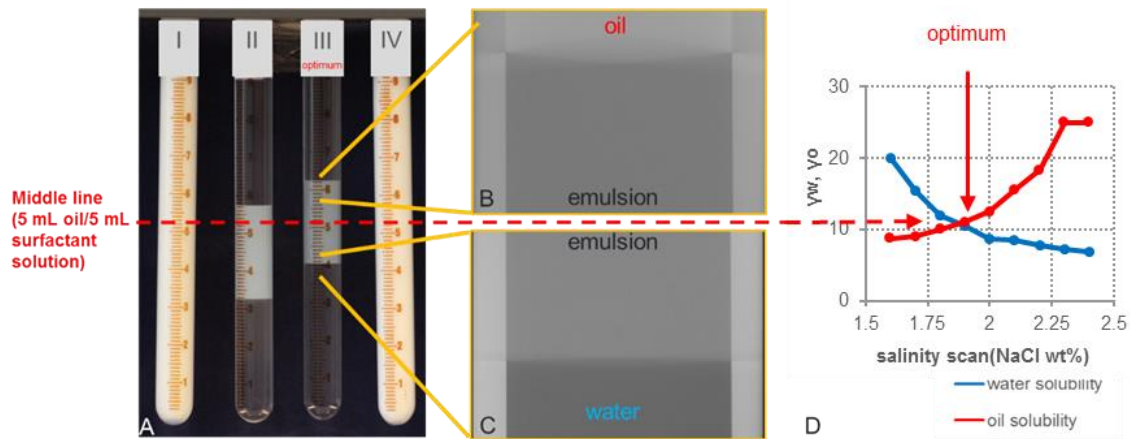
Figure 2: (A) Equilibrium phase behaviour tests of the surfactant/oil/water system used in this study with I: 0.75% NaCl II: 1%NaCl, III: 1.25% NaCl (optimum) and IV:1.5%NaCl. (B+C) exact composition of tube III was further analysed with uCT scanning. Based on the grey values of the image an oil content of 53% and water content of 47%, (D) solubility of the surfactant in oil and aqueous phases for the studied system [7,8].

The 1.25% NaCl test tube was scanned in the µCT-scanner; the oil (top layer), aqueous (bottom layer) and the microemulsion (middle layer) each had a distinctly different grey value (Figure 2B). The aqueous and oil phase content of the microemulsion was estimated using the linear blending rule for X-ray attenuation coefficients expressed here as

$$Gray\ value\ (emulsion) = \gamma_o\ Gray\ value\ (oil) + \gamma_w Gray\ value\ (water), \quad (1)$$

where the oil and water content of the emulsion are γ_o and γ_w, respectively. Based on the grey values of the image of the middle emulsion phase, an oil content of 53% and 47% of the surfactant solution was determined. The test tubes contained a 1:1 ratio of aqueous and oil phases (5mL surfactant solution + 5mL n-decane). At the optimum salinity, the microemulsion was expected to contain 50% aqueous solution and 50% oil phase because the surfactant had similar affinities to the oil and the water. Figure 2D shows the solubility diagram of the surfactant/oil/water system which was obtained by analysing the phase behaviour tubes shown in Figure 2A [7]. It showed that the surfactant had similar solubility in the aqueous and oil phases at the optimum salinity. The values extracted from the µCT-

scanner images indicated that the microemulsion at the optimum salinity, indeed, contained approximately equal volumes of aqueous and oil phases.

In situ formation of microemulsion in rock

Figure 3B shows the oil (grey) and water phase (black) at the end of waterflood and Figure 3C shows the first scan of the surfactant injection 7s after the injection started. At this time, the total injected surfactant solution volume was less than 1PV (~0.8 PV), but it is likely that surfactant breakthrough occurred through preferential pathways and/or quasi-miscible flow and associated fingering [12]. Furthermore, the scan was taken 2mm above the inlet; the surfactant solution has already passed through this segment at 7 s. Figure 3D shows the final scan of the surfactant flooding which was taken approximately 45 mins later. The pore space was flooded by the surfactant for multiple PVs, and it was assumed that any additional displacement due to quasi-miscible was completed. Compared to the first scan with the surfactant, there were subtle differences in the saturation profile; difference in grey levels in the bigger pores were directly visible (compare Figure 3C and 3D).
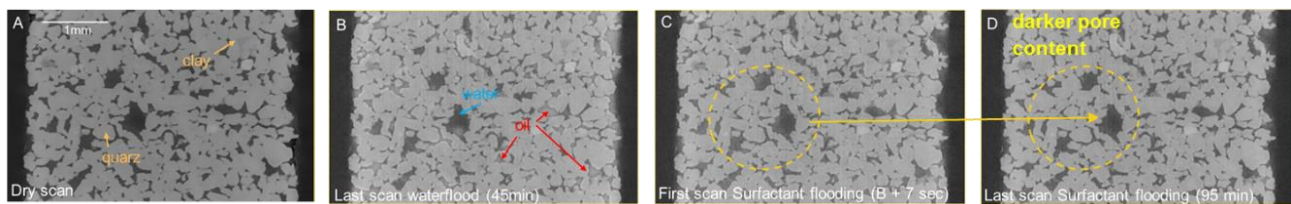
Figure 3: (A) Grey scale image of the sample without any fluid, (B) Last scan of the waterflood: oil-phase appears bright and the water phase dark, (C) 7 s after surfactant flood started, (D) Content of large pores become slightly darker.

The scans taken during the waterflood and surfactant flood were processed for detailed saturation profiles. For improved signal-to-noise ratio, volume averaged grey levels were considered. Corresponding to Equation (1) this averaged grey value of the pore space indicates the composition of the fluid. In Figure 4A the volume averaged grey value over the pore space of each image vs. time is displayed. The total grey value of each slice as a function of vertical position was extracted from the images during the surfactant-flood (Figure 4B). In combination with the oil-saturation obtained from the waterflood, a linear correlation of the oil-saturation and the grey value was determined and used to estimate the oil-content in the pore space during the surfactant flood. Based on this estimation after the surfactant flood around 16% of the oil remained in the core in form of emulsion. Shortly after the surfactant injection started, the oil saturation decreased sharply from 40% to 18%. This sharp reduction suggested that the surfactant was transported quickly, and it covered most of the oil/water interface almost immediately. From these images, it is not possible to infer the emulsification rate, however, it is likely that the IFT reduction was enough to mobilize a relatively significant amount oil in seconds. As the surfactant injection continued, the oil saturation gradually decreased a further 2%, and the residual oil saturation reached 16% (Figure 4B, at 95 mins). During this injection period, the pore space was flooded by the surfactant already for many PVs, and surfactant solubilized over time of the trapped oil (Figure 4C).
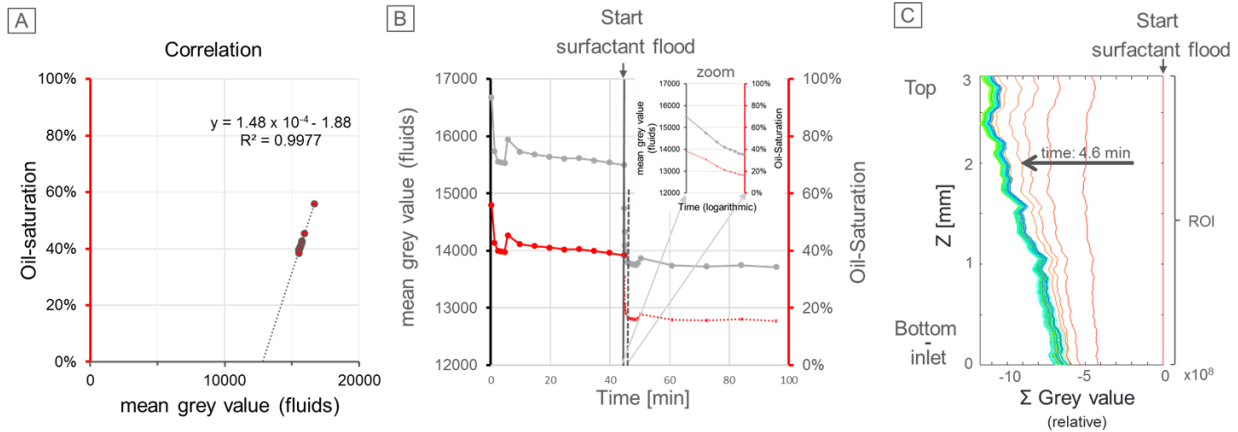
Figure 4: (A) Correlation between the oil saturation computed based on the segmented image and the mean grey value of the fluid phases.(B) Oil saturation vs time (red solid line) for the waterflood imbibition. Total grey value (grey) was used to estimate the oil-content during the surfactant flood (red dashed line). (C) Change of the grey-scale value during the surfactant flood along the z axes is shown relative to the first scan.

Pore-scale processes

The grey value analysis of the images was then used for understanding the pore-scale behavior of the in-situ emulsion formation and quasi-miscible flow. In Figure 5, images from waterflood and surfactant flood are shown. The color-scheme from violet to red highlighted the difference in grey values inside the pore space. Figure 5A was taken at the end of waterflood where the oil is red and the water is blue. Figure 5B shows the scan which was taken 7s after the surfactant flooding started. The initially oil filled (red) pores already changed composition: the color changed from light to dark blue which suggested presence of an aqueous phase, but possibly with different water content, i.e. emulsion with oil solubilized. At the end of the surfactant flooding, the fraction of the dark blue within individual pores increased (Figure 5C). After flooding the sample with the surfactant solution for many PV, the surfactant accessed and solubilized most of the trapped oil. However, it was not possible to mobilize all of the solubilized oil even after that many pore volumes of continuous surfactant injection.

The fact that the surfactant accessed and mobilized a significant potion of the remaining oil during the initial few seconds (Figure 5B) suggested that the emulsification rate was much quicker compared to rates observed at static conditions. Unsal et al. (2016) [7] observed that microemulsion formed faster under dynamic conditions in pore space than expected from static phase behaviour studies. In micromodel experiments, the diffusion controlled processes as in dead end pores (Figure 5C) and turbulence mixture during co-injection of two fluids (Figure 5D) provided the means for stirring and quicker emulsification. Their effects may be even more pronounced in a core as the connectivity in a 3D porous system is significantly higher than in a 2D system such as a microfluidic chip.
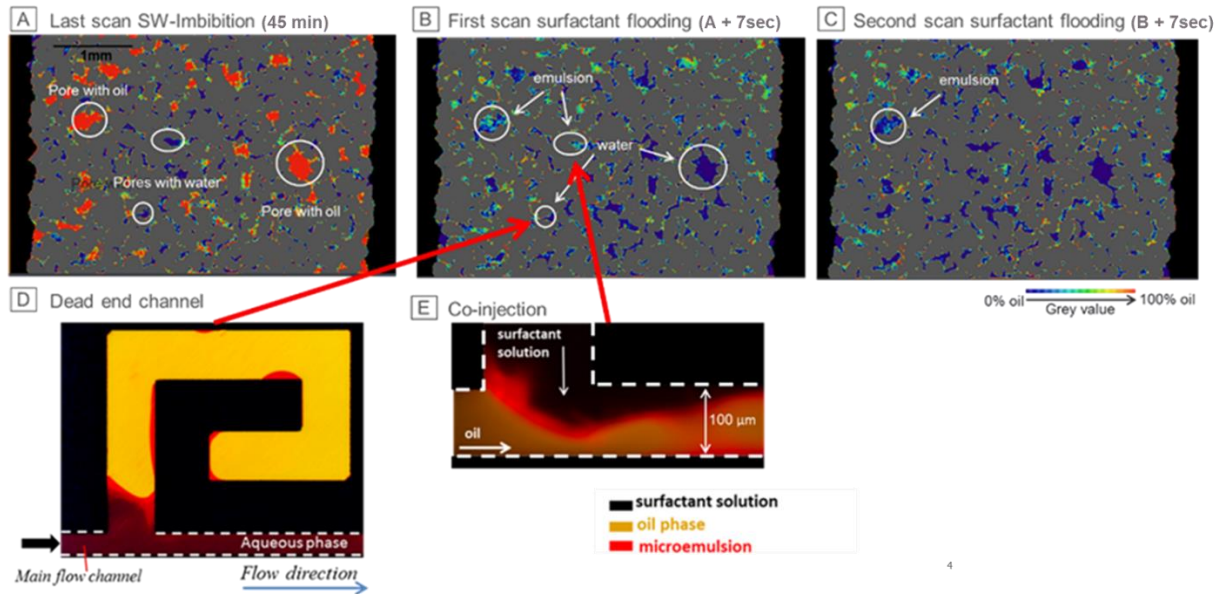
Figure 5: (A) Last scan of the waterflood-imbibition, displaying the oil-(red) and water (blue) distribution, (B) Image of first scan during surfactant flooding showing the rock and the grey values in the pore space in a color-scheme to highlight the variety. (C) Further oil solubilisation during surfactant flooding, (D)Dynamic phase behavior experiments in micromodels [7].

CONCLUSION

In this study, we conducted a flow experiment with surfactant/oil/water system in a rock sample whilst imaging with fast µ-CT. We used a surfactant which formed microemulsions in presence of n-decane, and allowed the visualization of quasi-miscible flow and oil recovery by solubilisation. The resolution within individual pores was sufficient to identify 'pure/clean' and 'emulsified' oil. The image analysis of the images taken from the experiments suggested that the emulsification during flow took place at shorter time scales (seconds) than what would be expected at static conditions. It is probable that the diffusion of surfactant and mixing due to flow in the confined pore space facilitated this relatively faster emulsification rates.

ACKNOWLEDGEMENTS

REFERENCES

1. Lake, L. W. ,1989, *Enhanced Oil Recovery*. Prentice Hall: Upper Saddle River, NJ.
2. Putz, A., Chevalier, J. P., Stock, G., Philippot, J., 1981, A Field test of microemulsion flooding, Chateaurenard Field, France. *JPT, J. Pet.Technol. 1981, 33*, 710−718.
3. Hirasaki, G. J., Miller, C. A., Puerto, M., 2011, Recent advances in surfactant EOR. *Soc. Pet. Eng. Journal* 16, 889−901.
4. Dullien, F. A., & Brenner, H., 1991, *Porous Media: Fluid Transport and Pore Structure* (2 ed.). San Diego Calif.: Academic Press.
5. Salager, J. L., Bourrel, M., Schechter, R. S., Wade, W. H., 1979, Mixing rules for optimum phase behavior formulations of surfactant/oil/water systems. *SPEJ, Soc. Pet. Eng. J.*, 19, 271−277.
6. Sjoblom, J., 1996, *Emulsions and emulsion stability*, Mercel Dekker, New York.
7. Unsal, E., Broens, M., & Armstrong, R. T., 2016, Pore Scale Dynamics of Microemulsion Formation. *Langmuir*, 32(28), 7096-7108.
8. Huh, C., 1979. Interfacial tensions and solubilizing ability of a microemulsion phase that coexists with oil and brine. *Journal of Colloid and Interface Science*, 71(2), pp.408-426.
9. *Proceedings of the National Academy of Sciences*, 110(10), 3755–3759.
10. Rücker, M., Berg, S., Armstrong, R.T., Georgiadis, A., Ott, H., Schwing, A., Neiteler, R., Brussee, N., Makurat, A., Leu, L. and Wolf, M., 2015. From connected pathway flow to ganglion dynamics. *Geophysical Research Letters*, *42*(10), pp.3888-3894.
11. Youssef, S., Rosenberg, E., Deschamps, H., Oughanem, R., Maire, E., Mokso, R., 2014, Oil Ganglia Dynamics in Natural Porous Media During Surfactant Flooding Captured by Ultra-Fast X-Ray Microtomograpy, Paper SCA2014-023 presented at the SCA International Symposium, Avignon, France, 8–11September.
12. Lenormand, R., Toubul, E., Zarcone, C. Numerical models and experiments on immiscible displacements in porous media. *Journal of Fluid Mechanics*, 1988, 189, 165-187.
13. Armstrong, R., Ott, H., Georgiadis, A., Rücker, M., Schwing A., Berg, S., 2014, Subsecond Pore-Scale Displacement Processes and Relaxation Dynamics in Multiphase Flow. *Water Resources Research*, 50(12), 9162–9176.
14. Paganin, D., Mayo, S., Gureyev, T., Miller, P., and Wilkins, S.,2002, Simultaneous Phase and Amplitude Extraction from a Single Defocused Image of a Homogeneous Object. *Journal of Microscopy*, 206(1), 33–40.
15. Marone, F., Stampanoni, M., 2012, Regridding Reconstruction Algorithm for Real-Time Tomographic Imaging. *Journal of Synchrotron Radiation*, 19, 1029–1037.

INVESTIGATION ON THE PETROPHYSICAL CHANGES ON A COQUINA CORE UNDER CARBONATE WATER INJECTION ASSISTED BY COMPUTERIZED TOMOGRAPHY

[1]Eric Yuji Yasuda, [2]Erika Tomie Koroishi, [3]Osvair Vidal Trevisan and [4]Janeth Alina Vidal Vargas

[1]Master's Student – Mechanical Engineering, State University of Campinas, UNICAMP
[2,4]Researcher – Center for Petroleum Studies – CEPETRO
[3]Professor – Department of Energy, State University of Campinas – UNICAMP.

ABSTRACT

Multiple interactions between injected fluid and the reservoir rock occur during oil recovery processes. These interactions are particularly important if CO_2 is used as injection fluid either in enhanced oil recovery (EOR) methods or in CO_2 sequestration projects in deep saline aquifers, especially in carbonate reservors. When CO_2 dissolves in water, carbonic acid (H_2CO_3) is formed. The resulting acid water will react with the carbonate salts, calcium carbonate ($CaCO_3$) and magnesium carbonate ($MgCO_3$) present in the reservoir rock, causing its dissolution. This effect is expected to change the main properties of the reservoir, such as permeability and porosity. This work proposes an experimental investigation on the permeability and porosity changes of a pressurized carbonate rock with the injection of brine saturated with CO_2. Tomography is used to observe the behavior of any wormholes created during the test. The experiment was carried out at 2,000 psi, 18ºC and four different flow rates of 0.025, 0.075, 0.1 and 2 cc/min. Results show that the porosity had a constant increase during the experiment, with a steeper increase on the end of the experiment when the flow rate was higher. Overall permeability showed an increase of about twenty times the initial value. Local permeability showed a similar behavior for each of the sections of the rock, with a reduction at lower flow rates and an increase at higher ones. Some regions had final permeability of up to 4D, an indicator of a wormhole. Tomography highlighted the creation of a wormhole in the beginning of the core.

INTRODUCTION

The acidization and the process of wormhole propagation have been studied by many researchers. Grigg and Svec [1] showed that the injection of CO_2 in carbonate rocks increases the permeability of the sample close to the injection point, due to the formation of a wormhole, and that in the fluid production region the permeability was reduced due to the damage caused by the precipitation of calcium carbonate. These inferences highlight

the importance to control these effects in order to prevent problems, such as clogging the fluid production or bypassing the oil region near the injection point. The findings of this work are related to the rate of the injection fluid, which is higher at the injection point and slower at the production region because of the energy loss while the fluid flows through the reservoir.

The effect of injection rate on the patterns of dissolution was studied through the injection of water into plaster made cores. Also, it was found out an optimal value to form a wormhole as prominent feature. At a high injection rate, the acid has less time to dissolve the rock so that the permeability of the core will not be increased. At low injection rates, the acid has more time to dissolve the rock and therefore to create larger voids near the wellbore, which may cause borehole collapse during production [2,3]. These conditions are not optimal, and cost more acid to create a wormhole. This was corroborated by Hoefner and Fogler [4] with experiments using limestone and dolomite cores. The optimal injection rate decreased as the acid-rock reaction changed from mass transfer control to reaction kinetics control, as described in the results from the experiments of Fredd and Fogler [5]. Other parameters as medium heterogeneity, acid concentration and core size were also studied [6, 7, 8, 9].

Golfier et al. [10] found through experiments that the shape of the wormholes is based on two dimensionless numbers; Péclet (Pe) and Damköhler (Da), the first relates the advection to the diffusion and the second relates the chemical reaction rate to the transport phenomena. These numbers are among other factors, based on the flow rate of injection and the properties of the porous medium. They also created a classification for the different types of wormholes based on its form.

This work proposes an experimental investigation on the permeability and porosity variations of a coquina core subjected to a carbonate water injection. The experimental parameters are: 2,000 psi of both radial and axial pressures, 18ºC, flow rates of 0.025; 0.075; 0.1 and 2 cc/min. A special coreholder with multiple pressure taps along the length of the core is used in order to evaluate the permeability, the porosity is evaluated through computerized tomography and validated by monitoring the calcium concentration of the production fluids.

PROCEDURES

Materials

The carbonate rock used in the study was extracted from a coquina outcrop in the CIMPOR (former Atol) quarry, from Morro do Chaves formation, in the Sergipe-Alagoas basin, Brazil. Three fluids were employed in the experiment: an equilibrated brine at 38 kppm salt concentration as the initial saturation fluid, a sodium iodide (NaI) brine at 38 kppm as the dopant and an equilibrated brine at 38 kppm saturated with CO_2 at 2,000 psi as injection fluid. Table 1 shows the equilibrated brine composition, and it was designed to have no chemical interaction with the core sample.

Table 1. Equilibrated brine composition.

	NaCl	KCl	MgCl₂ . 6 H₂O	CaCl₂ .2 H₂O	SrCl₂ . 6 H₂O	KBr	Na₂SO₄	NaHCO₃
Mass of each component [g/L]	31.288	0.781	0.276	5.403	0.018	0.107	0.176	0.059

Methods

The experimental setup is the same used in the earlier project of 2015 [11], a positive displacement pump, high pressure vessels, a special coreholder with multiple pressure taps, a backpressure system and differential pressure transducers. The coreholder is designed for X-ray tomography, with an aluminum cylinder, with an epoxy and carbon fiber jacket around the sample. The experimental apparatus is schematized in Figure 2.

Legend
1- Positive displacement pump
2- Cylinder containing either carbonate water, NaI brine or seawater brine
3- Coreholder containing the rock
4,5 and 6- Pressure transducers
7- Backpressure system
8- Gas-Liquid separator
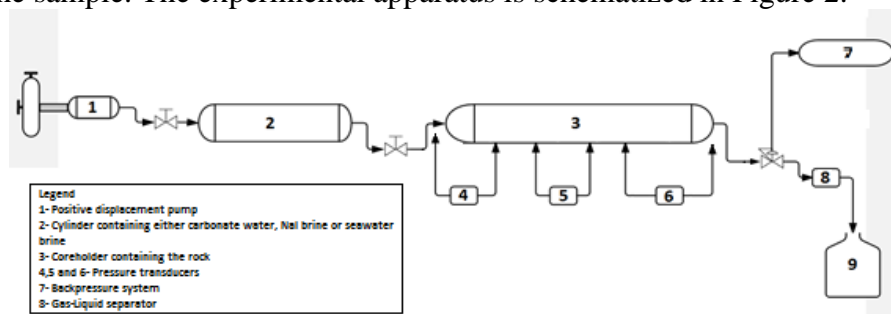
Figure 2. Scheme of the experimental apparatus.

After each carbonate water injection cycle, the sample was flushed with the equilibrated brine in order to isolate the effect of each flow rate. The equilibrated water was injected at 2 cc/min after each flow rate swap until the sample was totally saturated and ready for the next experimental step. Differential pressures were measured at points along the core as shown in the Figure 2 by the transducers (nVision Crystal Engineering Corporation). These ensured the permeability evaluation through the sample length. The pressure was measured in six points and enabled five permeability sections of the rock, presented in Figure 3 by K0, K1, K2, K3 and K4.
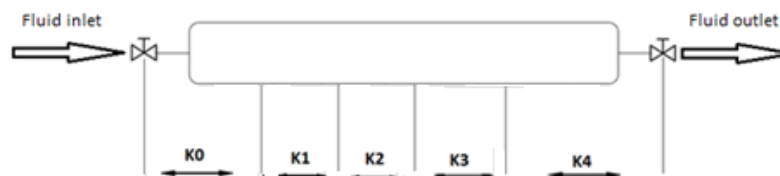
Figure 3. Scheme of the permeabilities evaluated during the test.

Porosity was evaluated by X-ray computerized tomography (Siemens CT scanner model SWFVD30C), using the software Syngo. The images had a 0.5 mm resolution and each scan acquired 69 images along the sample. It was also evaluated, in order to confirm the results, by the analysis of calcium concentration of the production fluid.

RESULTS
Porosity
<u>Tomography Method</u>
A MatLab™ routine, developed by Vargas, was used in order to verify the porosity changes. The mean porosity obtained through the CT values is shown in Figure 4. The absolute variation was from 12.27% to 13.69%. The variation was steady, with a slightly greater increase at the beginning, until the high flow rate of 2 cc/min when the porosity increased substantially.
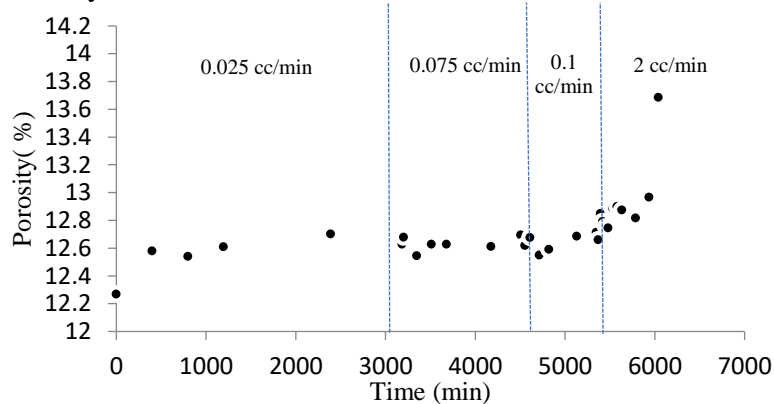
Figure 4. Porosity through time by tomography method.

<u>Calcium Concentration Method</u>
The porosity values obtained from the CT scans were validated by the calcium concentration method. This method evaluates the amount of calcium dissolved on the production fluid by inductively coupled plasma-optical emission spectrometry (ICP-OES), the analysis was carried out by the analytic central from the Chemistry Institute of UNICAMP. Considering the outcrop rock is composed by calcite, the calcium variation can be converted in pore volume variation using Equations 2 and 3 from Mangane [12]:

$$\phi(t) = \phi_0 + \frac{100 . V_{CaCO3}(t)}{V} \qquad (2)$$

$$V_{CaCO_3}(t) = \frac{(\Delta Ca . Q . \Delta t . M_{CaCO_3})}{M_{Ca} . \rho_{CaCO_3}} \qquad (3)$$

$V_{CaCO3}(t)$ is the volume of calcite dissolved, ΔCa is the variation of the calcium concentration on the production fluid, Q is the flow rate, Δt is the time interval, M_{CaCO3} is the molar mass of the calcium carbonate, M_{Ca} is the molar mass of calcium, ρ_{CaCO3} is water density, $\phi(t)$ is porosity along time, ϕ_0 is initial porosity. The results obtained are shown in Figure 5, where the porosity changed from 12.27% to 13.69%.
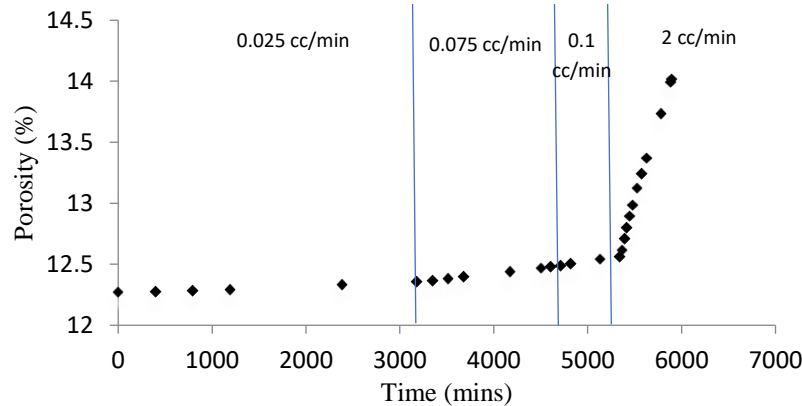
Figure 5. Porosity through time by calcium concentration method.

The methods used to calculate porosity variation presented a similar value. The first method (CT method) showed a variation of 1.75% on porosity, and the second (calcium concentration method) provided 1.42%. The flow rate of 2 cc/min had less experimental time, but injected more acid, hence the steeper increase in the porosity. Also, the higher flow rate probably damaged the porous medium, increasing the pore volume.

Permeability
The permeability had a similar behavior for all the sections, the profile showed a decrease at the beginning of the experiments, when lower injection rates were used. This decrease can be explained by precipitation of minerals. By the end of the experiment the permeability increased, because the dissolution is predominant. The sections near the injection point (K0, K1, K2) showed a much higher increase in permeability, because of the creation of a wormhole. Figure 6 shows the permeability variation for the five sections of the rock, divided by flow rates, where A=0.025 cc/min, B=0.075 cc/min, C=0,1 cc/min, D=2 cc/min.
The observed effect can be related in a field scale, to regions near the injection well for 2 cc/min high flow rate and to regions far from the injection well for the slower flow rates of 0.025 cc/min, 0.075 cc/min and 0.1 cc/min.
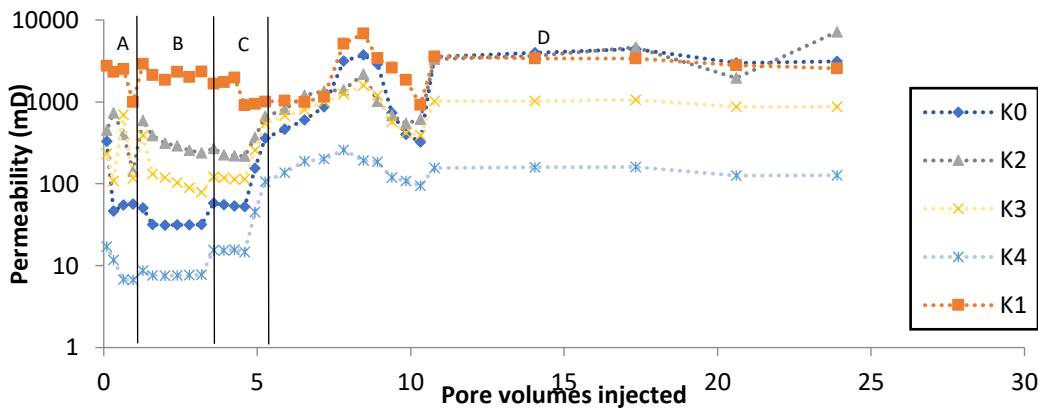
Figure 6. Mean permeability by pore volumes of carbonate water injected.

Damköhler and Péclet numbers
Both Da and Pe numbers were evaluated for this experimental work. Gharbi [13] proposed a method to estimate accurately the Da number using well-established data in the literature. Plummer et al. [14] determined the dissolution rate of calcite in well-controlled batch reactions for different CO_2 saturations and temperatures, but not considering high pressures or brines as in this experiment. Assuming that the reaction rate is related mostly on pH and temperature, it is possible to use Plummer et al.'s data to estimate the reaction rate and by consequence the Da number. This work's conditions were 18°C and the pH was approximately 4.6, using Figure 8 from Plummer et al. [14] the reaction rate is $1*10^{-5}$ moles m^2s^{-1}. The pore-grain area of interface was evaluated through Brunauer–Emmett–Teller(BET) method, with a value of 0.6137. Calcite density is known, and so is its molar mass. Diffusion coefficient for the ion Ca^{2+} is $7.5*10^{-10}$ m²/s [14]. Using the data acquired in the experiments and the approximations of Gharbi [13] it is possible to estimate the Da and Pe numbers with the following equations:

$$L = \frac{\pi.Vb}{S} \tag{4}$$

Where, L is the specific length, Vb is the bulk volume and S is the area of the pore-grain interface.

$$u_{avg} = \frac{Q}{A.\Phi} \tag{5}$$

$$Pe = \frac{u_{avg}.L}{De} \tag{6}$$

u_{avg} is the average interstitial velocity of the flow, Q is the flow rate, A is the area perpendicular to the flow, Φ is the porosity, Pe is the Péclet number, De is the diffusion coefficient for Ca^{2+},

$$k = \frac{r}{\rho.M.L} \tag{7}$$

Where, k is a reaction rate measured in units of inverse time s^{-1}, ρ is the density of calcite, M is the molar mass of calcite.
If the Pe number is higher than one:

$$Da = \frac{k.L}{u_{avg}} \tag{8}$$

If Pe number is lower than one:

$$Da = \frac{k.L^2}{De} \tag{9}$$

Finally, the results are shown in Table 2:

Table 2. Pe and Da numbers for the experiments.

Test Number	Flow Rate [cm³/min]	Pe	Da
1	0.025	2.94E-01	3.44E-02
2	0.075	8.77E-01	3.44E-02
3	0.1	1.16E+00	2.97E-02
4	2	2.29E+01	1.50E-03
5	2	2.23E+01	1.55E-03
6	2	2.06E+01	1.67E-03

According to Golfier et al. [10], with a Pe number ranging from 0.3 to 20.6 and Da from 0.034 to 0.002 should result in either a ramified wormhole or a dominant wormhole. Figure 7 shows the rock after the entire experiment, with what appears to be a dominant wormhole, highlighted in blue dots, near the injection side (left side of Fig. 7).

Figure 8 shows the rock before and after the experiments. The image is a section near the injection point, with the wormhole highlighted in a blue circle. At least three visible channels were created by the end of the experiment, possibly representing a ramified wormhole regime.

Figure 7. Tomography of the sample at the end of the experiment.
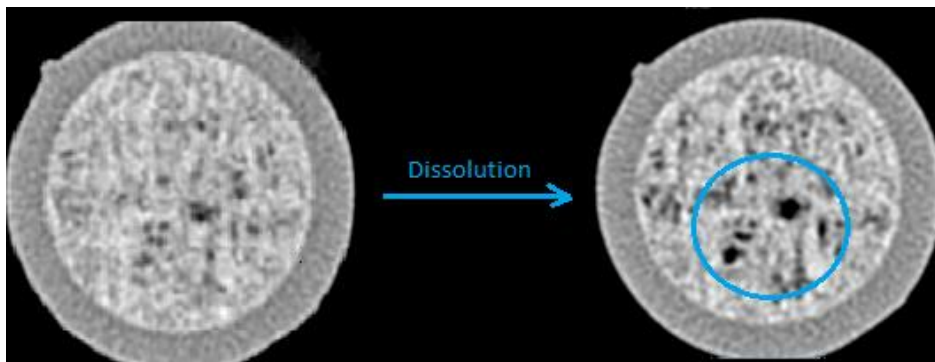
Figure 8. Cross section of the sample near injection face.

CONCLUSIONS

The results provide valuable insight to the mechanism of wormholing with injection of seawater-like brine saturated with CO_2 on carbonates. Differently from result previously shown by Yasuda et al. [11], this one provides data with very low flow rates, which simulates in the field a region far from the injection well. A porosity increase of 1.75% was evaluated by the CT scan method and 1.42% through analysis of calcium concentration of the effluents. The porosity showed a linear increase at the first 6 pore volumes injected (5,300 mins), but then there was bigger change at the injection rate of 2 cc/min. The images provided by CT scan show a wormhole at the beginning of the core, where permeability showed the greatest increase.

ACKNOWLEDGEMENTS

REFERENCES

1. Grigg, R.B., Svec, R.K., Lichtner, P.C., Carey, W., Lesher, C.E., CO2/Brine/Carbonate Rock Interactions: Dissolution and Precipitation, presented at the Fourth Annual Conference on Carbon Capture & Sequestration, (2005) Alexandria, Virginia, May 2-5.

2. Daccord, G., Lenormand, R., Lietard, O., Chemical dissolution of a porous medium by a reactive fluid-1. model for the "wormholing" phenomenon, *Chemical Engineering Science*, (1993) **48**, 1, 169–178.

3. Daccord, G., Lenormand, R., Lietard, O., Chemical dissolution of a porous medium by a reactive fluid-2.Convection vs reaction, behavior diagram, *Chemical Engineering Science*, (1993) **48**, 1, 179–186.

4. Hoefner, M.L., Fogler, H.S., Pore evolution and channel formation during flow and reaction in porous media, *AIChE Journal*, (1998) **34**, 1, 45-54.

5. Fredd, C.N., Fogler, H.S., Optimum conditions for wormhole formation in carbonate porous media: influence of transport and reaction, *SPE Journal*, (1999) **4**, 3, 196–205.

6. Frick, T.P., Mostofizadeh, B., Economides, M.J., Analysis of radial core experiments for hydrochloric acid interaction with limestones, presented at SPE International Symposium on Formation Damage Control, (1994) Lafayette, Louisiana, 7–10 February, SPE27402.

7. Bujise, M.A., Mechanisms of Wormholing in Carbonate Acidizing, presented in the International Symposium on Oilfield Chemistry, (1997) Houston, Texas, February 18-21.

8. Bazin, B., From matrix acidizing to acid fracturing: a laboratory evaluation of acid/rock interactions, *SPE Production and Facilities Journal*, (2001) **16**, 1, 22-29.

9. Ott, H., Pentland, C.H., Oedai, S., CO_2-brine displacement in heterogeneous carbonates, presented at the International Symposium of the Society of Core Analysts (2014), France, Avignon, September 8–11.

10. Golfier, F., Zarcone, C., Bazin, B., On the ability of a Darcy-scale model to capture wormhole formation during the dissolution of a porous medium, *Journal of Fluid Mechanics*, (2002) **457**, 1, 213-254.

11. Yasuda, E. Y., Blini, E. T. K., Trevisan, O. V., Bonet, E. J., Study of Petrophysical Properties Alterations of Carbonate Rocks under Carbonate Water Injection, presented in International Symposium of the Society of Core Analysts (2015), Canada, St. John's Newfoundland and Labrador, August 16-21.

12. Mangane, P. O., Caractérisation des changements dans les propriétés de réservoir carbonaté induits par une modification dans la structure des pores lors d'une injection de CO2: application au stockage géologique du CO2, phD Thesis (2013), Sciences de Techniques du Languedoc-Roussillon, Universite Montpellier II.

13. Gharbi, O., Fluid-Rock Interactions in Carbonates: Applications to CO2 Storage, phD Thesis (2014), Qatar Carbonates and Carbon Storage Research Centre Department of Earth Science and Engineering, Imperial College London.

14. Plummer, L.N., Wigley, M.L., Parkhurst, D.L., The kinetics of calcite dissolution in CO2 – water systems at 5o to 600C and to 0.0 to 1.0 atm CO2, *American Journal of Science*, (1978) **278**, 1, 179-216.

EXPERIMENTAL INVESTIGATION OF THE IMPACT OF SALT PRECIPITATION ON CO₂ INJECTIVITY

Yen Adams Sokama-Neuyam, Jann Rune Ursin
Department of Petroleum Engineering, University of Stavanger, 4036 Stavanger, Norway

This paper was prepared for presentation at the International Symposium of the Society of Core Analysts held in Vienna, Austria, 27 August – 1 September 2017

ABSTRACT

Adequate CO_2 injectivity is required to inject large volumes of CO_2 into the reservoir at acceptable injection flow rates through a minimum number of wells. Salt precipitation induced by brine vaporization in the wellbore vicinity could impair CO_2 injectivity especially in deep saline reservoirs. We conducted core-flood experiments to investigate the development of salt cake at the injection inlet during CO_2 injection into sandstone core samples. We also attempted to quantify the impact of drying and salt precipitation on CO_2 injectivity. We observed severe salt cake deposition at the injection inlet even when the core was still wet with immobile brine. The amount of salt cake deposited at the injection inlet depended on the resident brine salinity and the supercritical CO_2 injection rate. About 29 per cent CO_2 injectivity impairment was induced by drying and salt precipitation. Injectivity impairment was also found to be dependent on CO_2 injection flow rate. The present work provides insight into the underlying mechanisms of salt cake development at the injection inlet during CO_2 injection into deep saline formations.

INTRODUCTION

A successful Carbon Capture, Utilization and Storage (CCUS) candidate must have good containment efficiency, adequate storage capacity and threshold well injectivity, to inject the desired quantity of CO_2 at acceptable rates through a minimum number of wells [1]. Deep saline reservoirs standout in terms of storage capacity and containment efficiency. However, salt precipitation induced by brine vaporization near the wellbore, could threaten CO_2 injectivity in deep saline formations and render them unsuitable for CCUS [2–5]. Miri and Hellevang [6] identified initial rock permeability, CO_2 injection rate, saturating brine salinity, temperature and pressure as important parameters underlying CO_2 injectivity impairment caused by salt precipitation.

The underlying mechanisms of formation brine dry-out and salt precipitation include: (1) immiscible two-phase displacement of brine by injected CO_2, (2) vaporization of brine into the flowing CO_2 stream, (3) capillary-driven back-flow of brine toward the injection inlet, (4) diffusion of dissolved salt in the aqueous phase, and (5) gravity override of injected CO_2 [6]. Low brine evaporation rate in the drying front, may result in homogeneous distribution of precipitated salt throughout the porous medium [3,4,6,7]. For high evaporation rates, there are no sufficient time for the salt concentration gradient to diffuse

away from the drying front, resulting in nonhomogeneous accumulation of salt [4,8]. While numerical experiments by Roels et al.[9] suggested that local salt accumulation occurs far from the wellbore, several research works [3,10–12] suggest that precipitated salt accumulates near the wellbore.

As brine is vaporized, the concentration of salt in the brine increases. Zuluaga et al.[13] explains that salt precipitates out when the brine concentration exceed supersaturation. Several researchers have observed the formation of salt cake at the core inlet in CO_2 core-flood experiments [10,14]. However, the governing mechanism of salt cake development at the injection inlet have not been studied thoroughly but it is believed that capillary backflow of brine towards the injection inlet may result in formation of salt cake if the brine salinity is high enough to reach supersaturation before the brine is swept into the formation. Insight into the development of salt cake during the drying process will improve understanding of its impact on CO_2 injectivity.

In the present work, we have conducted various core-flood experiments using sandstone core plugs where the development of salt cake at the core inlet was monitored. We also present quantitative effect of drying and salt precipitation on CO_2 injectivity.

MATERIALS AND METHODS
Materials
The experiments were conducted on two types of homogeneous cylindrical sandstone core plugs. Berea sandstone core samples were used to study the quantitative effect of drying and salt precipitation because of their suitable range of permeability and porosity. Bentheimer core plugs were used to investigate salt cake development at the injection inlet because of their high permeability. Each cylindrical core samples were 20cm long and 3.81cm in diameter.

The non-wetting fluid used was liquefied CO_2 with purity percentage of about 99.7 %. The liquid CO_2 was injected at 80 bar and 25 °C. During supercritical CO_2 injection, the operational conditions were set to 80 bar and 45 °C. To investigate the effect of brine vaporization and salt precipitation on CO_2 injectivity, we used synthetic Formation Water (FW) with salinity of 105.5 g/l (NaCl 77.4 g/L; $CaCl_2.2H_2O$ 21.75 g/L; $MgCl_2.6H_2O$ 3.56g/L; $SrCl_2.6H_2O$ 2.25 g/L; Na_2SO_4 0.13 g/L; KCl 0.42 g/L)[15]. The Berea sandstone cores were vacuum-saturated with FW prior to CO_2 injection. NaCl brine with equivalent ionic strength as FW (120 g/l) was used to investigate the development of salt cake at the injection inlet. Jeddizahed and Rostami [16] have shown that the total dissolved salt is the main determinant of the precipitated solid salt saturation. Therefore, we expect NaCl brine with the same ionic strength as FW to precipitate solid salt comparable to FW under the same conditions.

Setup and Procedure
The schematics of core flooding apparatus used in the tests are shown in Figure 1. Prior to the test, the core was loaded in a horizontal core-holder. The Quizix pump delivers brine through the connected piston cell into the core inlet. The ISCO CO_2 pump receives liquid CO_2 from the gas container through a pressure regulator. Depending on the injection conditions, either liquid or supercritical CO_2 are injected. The injected fluid passes a piston cell, positioned in the oven, to hold the fluid and secure a pre-set temperature in the oven. A differential pressure gauge and a pressure transducer are connected across the core to monitor the pressure drop and record the absolute pore pressure. A backpressure of 80 bar was set at the outlet during CO_2 injection and effluent fluid was safely collected in a piston cell for analysis and safe disposal.

The core was cleaned and dried at 65 °C for about 24 hours. It was then wrapped in shrinking Teflon and rubber sleeves to prevent CO_2 leakage and mounted horizontally in the core holder. A confinement pressure of about 150 bar was applied in the annular space between the core and the core-holder. The experimental procedure consists of the following steps:
1. Initial liquid CO_2 pressure drop (ΔP_i) across the clean dry core sample were measured and the permeability (K_i) calculated.
2. The core was saturated with either FW or NaCl brine.
3. The saturated core sample was flooded with supercritical CO_2 to vaporize brine.
4. The core was then inspected for salt cake development at the inlet.
5. Final liquid CO_2 pressure drop (ΔP_f) was measured and permeability (K_f) calculated.

In Step 1 and Step 5, liquid CO_2 was injected at 2 ml/min to measure permeability before and after brine vaporization, and salt precipitation. In step 3, about 100 – 300 pore volumes (PV) of supercritical CO_2 was injected at various injection flow rates to vaporize brine and dry the core.

Theory
Fluid injectivity, I is defined as the ratio of volumetric injection flow rate, q to the pressure drop, Δp. Assuming the core has constant absolute permeability k_i and k_f before and after it has been exposed to precipitated minerals respectively and that the viscosity of the fluid used in the measurement (liquid CO_2) is constant, the injectivity before and after salt deposition can be expressed from Darcy's law as:

$$I_i = \frac{q_i}{\Delta p_i} = k_i.C \qquad (1)$$

$$I_f = \frac{q_f}{\Delta p_f} = k_f.C \qquad (2)$$

In Eq. (1) and (2), C is a constant defined as $C = \frac{A}{\mu L}$, for constant A and L. If liquid CO_2 is injected at a constant rate during injectivity measurements ($q_i = q_f$), we can define a Relative Injectivity Change (RIC) index as:

$$RIC = \left(\frac{I_i - I_f}{I_i}\right) = 1 - \left(\frac{I_f}{I_i}\right) \tag{3}$$

Substituting Eq. (1) and (2) into (3) yields:

$$RIC = 1 - \left(\frac{\Delta p_i}{\Delta p_f}\right) = 1 - \left(\frac{K_f}{K_i}\right) \tag{4}$$

Salt precipitation would reduce the flow area and increase Δp. Thus, $\Delta p_f > \Delta p_i$ and $K_i > K_f$ after salt deposition. Consequently, a positive RIC value indicates injectivity impairment. In the present work, RIC is expressed as a percentage.

RESULTS AND DISCUSSION
Salt Cake Development
To investigate the development of salt cake at the injection inlet during CO_2 injection, a clean Bentheimer core was vacuum-saturated with 120 g/l NaCl brine and flooded with about 100 PV of supercritical CO_2 at a rate of 1 ml/min. The core was then taken out and inspected for salt cake. Figure 2 shows pictures of the core taken after the core-flood process.

Figure 2 (A) shows that no salt was observed at the injection outlet. In Figure 2 (B), we observe massive filter salt cake development at the core inlet. Figure 2 (C) shows that the entire core was still wet. When CO_2 is injected into the core, capillary backflow draws the aqueous phase towards the core inlet. Although the same fittings were used at the inlet and the outlet, no salt was precipitated at the injection outlet. This affirms the role played by capillary backflow of brine in salt cake development. The dry supercritical CO_2 removes water from the brine through evaporation. As more water is removed, the salinity of brine increases. When the concentration of salt in the brine exceed supersaturation, salt precipitates out. A filter salt cake could be deposited at the injection inlet if the inlet brine salinity exceed supersaturation before it is swept into the core by the injected gas. For salt cake development at the injection inlet, two conditions must be fulfilled: (1) The brine salinity must be sufficiently high and (2) capillary backflow dominate flow around the injection inlet.

To investigate the impact of brine vaporization rate on salt cake development, we increased the supercritical CO_2 injection flow rate from 1 ml/min to 5 ml/min. We observed that, the amount of deposited salts at the injection inlet decreased when the brine vaporization rate was increased from 1 ml/min to 5 ml/min (Figure 3). At higher supercritical CO_2 injection flow rate, viscous forces overcome capillary forces. The net effect is reduced capillary backflow of brine at the injection inlet. Thus, brine available at the inlet for salt dropout is reduced and lower amount of salt cake is deposited at the inlet.

We then reduced the brine salinity from 120 g/l to 75 g/l, keeping the CO_2 injection flow rate at 5 ml/min. We observed the amount of salt cake precipitated at the injection inlet further decreased significantly when the brine salinity was decreased (Figure 4). At constant injection flow rate, it will take a longer time for the low salinity brine to reach supersaturation. Therefore, a significant portion of the producible brine at the injection inlet could be swept into the core, reducing the chances of salt cake development. Therefore, salt cake could be deposited at the injection inlet during CO_2 injection into saline porous media if the saturating brine salinity is above a certain threshold value and capillary backflow of brine at the injection inlet is high enough.

Effect of Formation Brine Dry-out
It is important to note that in this section, all salt cake at the core inlet was removed before injectivity effects were quantified. Only the effect of complete dry-out and salt precipitation within the core was studied. The clean Berea core with known permeability was initially saturated with FW and flooded with about 300 PV of supercritical CO_2 at a rate of 1 ml/min until the core was completely dried. The permeability of the core after drying was measured and RIC was calculated. The experiment was then repeated for CO_2 injection flow rate of 5 ml/min and 10 ml/min, keeping all other parameters constant, to study the effect of injection flow rate. Figure 5 shows the results of injectivity impairment induced by brine vaporization at varying CO_2 injection flow rates.

CO_2 injectivity was impaired by about 36 % for drying rate of 1 ml/min (Figure 5). Injectivity impairment then decreased from 36% to about 25% when drying rate was increased to 5 ml/min and remained practically unchanged when the drying rate was further increased to 10 ml/min. Several researchers [2,5,17–19] have reported CO_2 injectivity impairment within a range (13% - 83%) that agree favorably with our findings. During CO_2 injection, water is removed from the core through immiscible CO_2-brine displacement and brine vaporization. As brine is vaporized by supercritical CO_2, the concentration of salt in the brine increases within the pore spaces. When the concentration of brine exceed supersaturation, salt precipitates into the pore channels as observed by Zuluaga et al., (2001). The precipitated salts drop out into the pore channels, reducing the CO_2 flow area and consequently the permeability and injectivity [4,16,20,21].

At very low CO_2 injection rate, immiscible CO_2-brine displacement is delayed and the drying rate is lowered, thus increasing the period available for salt precipitation. At high CO_2 injection rates, the resident brine is quickly swept out of the core, leaving out only immobile brine for salt precipitation. With pore volume of about 45 ml, the time taken to sweep out all producible brine will be close for injection rates of 5 ml/min and 10 ml/min and probably that is why injectivity impairment remained practically the same within this interval of CO_2 injection flow rate.

CONCLUSION

Storage capacity and well injectivity are the two most important parameters required to define the storage potential of a geological CCUS candidate. Deep saline reservoirs have the largest storage capacity. However, brine vaporization and salt precipitation in the wellbore region during CO_2 injection, could impair injectivity, thus rendering deep saline formations unsuitable for CO_2 storage. Most of the experimental and theoretical works have investigated salt precipitation in the dry-out region. It is therefore generally assumed that salt precipitation commences when the near well region start to dry-out.

We have conducted laboratory core-flood experiments using sandstone cores to study the mechanisms of salt precipitation from the onset of brine vaporization to the end of the drying process. Some of the highlights of our work include the following:

- Salt could be precipitated in the form of salt cake at the core inlet when the core is still wet with immobile brine. Capillary backflow of brine towards the core inlet could be the main driving force of salt cake development.
- The magnitude of precipitated salt cake depends on the injection flow rate of supercritical CO_2 and the salinity of the resident brine. High brine salinity and low CO_2 injection rate favor salt cake development.
- At complete dry-out, the effect of salt precipitation on CO_2 injectivity is dependent on the drying rate. An average of about 29% injectivity impairment was induced by drying effects.

The present work provides experimental evidence of salt precipitation prior to drying out. Some of the influential parameters underlying the development of salt cake in the inlet region have been identified and studied.

NOMENCLATURE

CCUS   Carbon capture, Utilization and Storage
FW   Formation water
I CO_2 well Injectivity
K_i Initial Permeability
K_f Final Permeability
PV   Pore Volume

Δp_i Initial pressure drop across the core
Δp_f Final pressure drop across the core
q_i Initial injection volumetric flow rate
q_f final injection volumetric flow rate

ACKNOWLEDGEMENTS

REFERENCES
[1]   IEA. Technology roadmap - Carbon capture and Storage. Technol Roadmap 2013:59. doi:10.1007/SpringerReference_7300.

[2]   Bacci G, Durucan S, Korre A. Experimental and Numerical Study of the Effects of Halite Scaling on Injectivity and Seal Performance During CO_2 Injection in Saline Aquifers. Energy Procedia 2013;37:3275–82. doi:10.1016/j.egypro.2013.06.215.

[3]   Peysson Y, André L, Azaroual M. Well injectivity during CO_2 storage operations in deep saline aquifers-Part 1: Experimental investigation of drying effects, salt precipitation and capillary forces. Int J Greenh Gas Control 2014;22:291–300. doi:10.1016/j.ijggc.2013.10.031.

[4]   Miri R, van Noort R, Aagaard P, Hellevang H. New insights on the physics of salt precipitation during injection of CO_2 into saline aquifers. Int J Greenh Gas Control 2015;43:10–21. doi:10.1016/j.ijggc.2015.10.004.

[5]   Muller N, Qi R, Mackie E, Pruess K, Blunt MJ. CO_2 injection impairment due to halite precipitation. Energy Procedia 2009;1:3507–14. doi:10.1016/j.egypro.2009.02.143.

[6]   Miri R, Hellevang H. Salt precipitation during CO_2 storage—A review. Int J Greenh Gas Control 2016;51:136–47. doi:10.1016/j.ijggc.2016.05.015.

[7]   Ott H, Roels SM, Kloe K De. Salt precipitation due to supercritical gas injection : I . Capillary-driven flow in unimodal sandstone. Int J Greenh Gas Control 2015;43:247–55. doi:10.1016/j.ijggc.2015.01.005.

[8]   Peysson Y, Fleury M, Blázquez-Pascual · V. Drying Rate Measurements in Convection-and Diffusion-Driven Conditions on a Shaly Sandstone Using Nuclear Magnetic Resonance. Transp Porous Med 2011;90:1001–16. doi:10.1007/s11242-011-9829-3.

[9]   Roels SM, Ott H, Zitha PLJ. μ-CT analysis and numerical simulation of drying effects of CO_2 injection into brine-saturated porous media. Int J Greenh Gas Control 2014;27:146–54. doi:10.1016/j.ijggc.2014.05.010.

[10]   Bacci G, Korre A, Durucan S. Experimental investigation into salt precipitation during CO_2 injection in saline aquifers. Energy Procedia 2011;4:4450–6. doi:10.1016/j.egypro.2011.02.399.

[11]   Kleinitz W, Koehler M, Dietzsch G, Gmbh PE. The precipitation of salt in gas producing wells. In: SPE, editor. SPE Eur. Form. damage Conf., The Hague: SPE; 2001, p. 1–7. doi:10.2523/68953-MS.

[12]   Pruess K, Muller N. Formation dry-out from CO_2 injection into saline aquifers: 1. effects of solids precipitation and their mitigation. Water Resour Res 2009;45:1–11. doi:10.1029/2008WR007101.

[13]   Zuluaga E, Muñoz NI, Obando G a. SPE 68335 An Experimental Study to Evaluate Water Vaporisation and Formation Damage Caused by Dry Gas Flow Through Porous Media. Media 2001.

[14]   Jeddizahed J, Rostami B. Experimental investigation of injectivity alteration due to salt precipitation during CO_2 sequestration in saline aquifers. Adv Water Resour 2016;96:23–33. doi:10.1016/j.advwatres.2016.06.014.

[15]   Fjelde I, Omekeh AV, Sokama-Neuyam YA. Low Salinity Water Flooding: Effect Of Crude Oil Composition. SPE Improv Oil Recover Symp 2014. doi:10.2118/169090-MS.

[16]   Jeddizahed J, Rostami B. Experimental investigation of injectivity alteration due to salt precipitation during CO_2 sequestration in saline aquifers. Adv Water Resour 2016;96:23–33. doi:10.1016/j.advwatres.2016.06.014.

[17]   Peysson Y. Permeability alteration induced by drying of brines in porous media. Eur Phys J Appl Phys 2012;60:12. doi:http://dx.doi.org/10.1051/epjap/2012120088.

[18]   Tang Y, Yang R, Du Z, Zeng F. Experimental study of formation damage caused by complete water vaporization and salt precipitation in sandstone reservoirs. Transp Porous Media 2015;107:205–18.

[19]   André L, Peysson Y, Azaroual M. Well injectivity during CO_2 storage operations in deep saline aquifers – Part 2 : Numerical simulations of drying , salt deposit mechanisms and role of capillary forces. Int J Greenh Gas Control 2014;22:301–12. doi:10.1016/j.ijggc.2013.10.030.

[20]   Zeidouni M, Pooladi-Darvish M, Keith D. Analytical solution to evaluate salt precipitation during CO_2 injection in saline aquifers. Int J Greenh Gas Control 2009;3:600–11. doi:10.1016/j.ijggc.2009.04.004.

[21]   Kim K-Y, Han WS, Oh J, Kim T, Kim J-C. Characteristics of Salt-Precipitation and the Associated Pressure Build-Up during CO_2 Storage in Saline Aquifers. Transp Porous Media 2012;92:397–418. doi:10.1007/s11242-011-9909-4.

APPENDIX
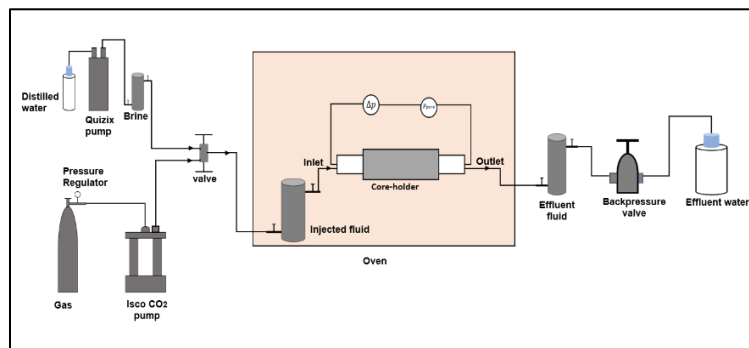
Figure 1. Experimental setup - the CO2 flow rig.
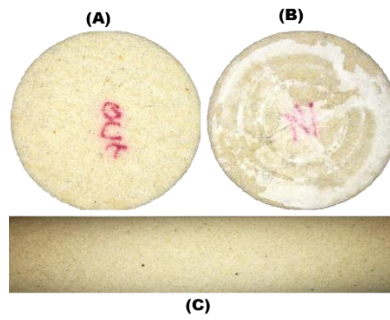
Figure 2. Pictures showing Salt cake development at 1 ml/min CO_2 injection rate into Bentheimer core saturated with 120 g/l NaCl brine. (A) No salt cake observed at the outlet. (B) Massive salt cake developed at the inlet. (C) The entire core is still wet.
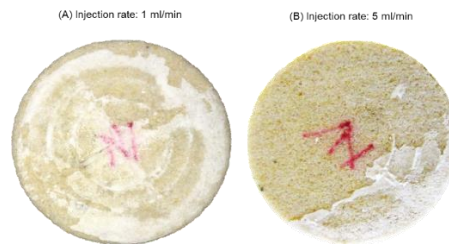
Figure 3. Pictures showing salt cake development as supercritical CO_2 injection rate was increased from 1 ml/min (A) to 5 ml/min (B).
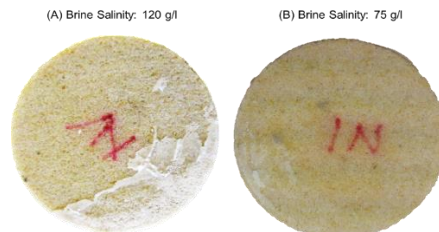
Figure 4. Pictures showing salt cake development as brine salinity was decreased from 120 g/l (A) to 75 g/l (B).
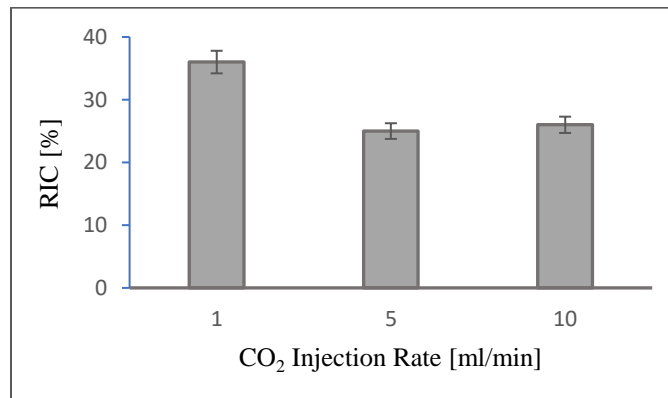
Figure 5. Effect of brine vaporization and salt precipitation on CO_2 injectivity. Injectivity impairment increased with decreasing drying rate.

Carbonate Rock Dissolution under Carbonated Water Injection (CWI)

Rodrigo G. Vaz[1], Rafael Núñez B.[1], Erika T. Koroishi[1], Ricardo D. G. de Freitas Filho[2], Osvair V. Trevisan[1]

1. University of Campinas, Campinas-SP, Brazil, 2. Repsol Sinopec Brazil

This paper was prepared for presentation at the International Symposium of the Society of Core Analysts held in Vienna, Austria, 27 August – 1 September 2017.

ABSTRACT

A set of core-flooding experiments were performed in order to investigate changes in mass, porosity and permeability of dolomite samples due to dissolution and precipitation phenomena occurring during Carbonated Water Injection (CWI). Experiments were carried out under pressure ranging between 7500 and 8500 psi, temperature of 70°C, and flow rate of 2 cm³/min. The core-flooding experimental set-up included two core-holders arranged in series, enabling the recording of differential pressure across each core separately during the tests. X-Ray Computerized Tomography (CT) revealed that the greatest effect of dissolution occurs in the first centimeters from injection point, after which dissolution and precipitation phenomena coexist and porosity tends to remain unchanged. CT data also showed that initial porosity can favor dissolution or precipitation to predominate at pore scale. Differential pressure across dolomite samples were measured using pressure transducers. Results did not show significant changes in samples' permeability in the first core-holder. However, a decrease in permeability was observed in the second core-holder, caused by mineral precipitation.

INTRODUCTION

According to the Earth System Research Laboratory [1], CO_2 concentration in the air has grown 27% from 1965 to 2017, intensifying the greenhouse effect. CO_2 sequestration in geological formations is being considered worldwide as a feasible option to limit the overload of CO_2 emissions. Besides that, CO_2 injection in petroleum reservoirs as an Enhanced Oil Recovery (EOR) method has been showed to increase oil recovery in many studies [2,3,4]. The Brazilian Pre-salt carbonate reservoirs, among the world's most important discoveries over the past decade, has been presenting high content of CO_2 in high pressure conditions (~8500 psi). In this sense, the reinjection of produced CO_2 can be the most attractive option, both environmentally and economically.

Carbonated Water Injection (CWI) has some advantages over other CO_2 injection methods. Due to its density, injected carbonated water moves to lower parts of the reservoir, preventing the formation of bulk-phase CO_2 that will migrate upwards and can lead to CO_2 leakage through seal rock [5]. CWI also leads to a wider CO_2 distribution over the reservoir and can postpone CO_2 breakthrough at production wells [2]. Carbonated water, however, generates carbonic acid (H_2CO_3), which reduces the pH of reservoir fluids. This is particularly important during CWI in carbonate reservoirs, once interactions between carbonated water and host rock will lead to mineral dissolution/precipitation and to

porosity and permeability changes [6,7,8,9,10,11]. Dissolution of carbonate rocks are related with increase in permeability and porosity, while precipitation, with the reduction of these properties [12]. Depending on how the reactive-flow alters rock properties, well injectivity can change severely [13, 14].

Brazilian pre-salt carbonates are highly heterogeneous. Dolomite is a rock type representative of large volumes of the reservoir rock. A small number of experiments are reported in the literature regarding dolomite dissolution under CWI. The experimental procedure used here aimed at mimicking mass transfer as a result of reactive flow at regions near the injection well, and allowing the analysis of porosity and permeability changes in the carbonate rock. In this region, high flow velocity and highly reactive fluid are expected to be present. This paper reports four flow-through experiments in which CO_2-charged brine is pumped at high flow rate through two core-holders at *in situ* conditions of pressure and temperature arranged in series, each one containing a dolomite core plug. X-ray macro tomography imaging is used for the evaluation of porosity at core size level. Pressure drop variations across each of the core plugs were recorded to compute permeability. Chemical analysis of the produced fluids allowed investigation of the dissolution phenomenon. Results focus on the effects of dissolution/precipitation on mass, porosity, and permeability of the rock during CWI and provide a better understanding of conventional petrophysical properties changes during implementation of a CWI project in carbonate reservoirs.

PROCEDURES
Samples
The dolomite samples were gathered from an outcrop belonging to Thornton Formation, from United States. X-ray Diffraction (XRD) technique was used to determine dolomite composition. The XRD technique was done using an X'Pert Philips X-ray Diffractometer, and was performed at the Calibration and Analytical Resources Laboratory, at the University of Campinas. Rock composition was determined to be 100% dolomite – $CaMg(CO_3)_2$. The core plugs had diameter of 3.8 cm, and their properties are presentedon Table 1. Sample mass, effective porosity, and permeability were measured both prior and after reactive flow (except for tests 2 and 3), using a precision scale (Adventurer OHAUS), a gas porosimeter (CoreLab instruments UltraPore 300), and a gas permeabilimeter (CoreLab Instruments Ultra-Perm 500) respectively.
Fluids
Three distinct fluids were used during the experiments: (1) nitrogen, (2) synthetic brine, (3) synthetic brine saturated with CO_2. Nitrogen and synthetic brine are used to saturate samples as part of X-ray tomography procedure. The synthetic brine is chemically balanced with dolomite. Brine saturated with CO_2 is the injection fluid for all tests. To prepare the injection fluid, a stainless steel vessel was filled with deaerated synthetic brine, and then a controlled volume of CO_2 was introduced into the brine. The minimum volume of CO_2 to be mixed with synthetic brine was calculated using a model of CO_2 solubility in sea water [15]. Then, a larger volume of CO_2 was added to brine in order to guarantee 100% of saturation with CO_2 at tests' conditions of temperature and pressure. After that, the carbonated brine was heated to 70°C and pressurized up to test pressure. To ensure brine-

CO_2 mixture, the vessel, which has a free movable sphere inside, was attached to a mechanical device for mixing during 24 hours. During the experiments, carbonated water vessels were kept in vertical position to avoid CO_2 excess volume to be injected along with carbonated water.

Experimental Set-Up

An experimental apparatus was designed to perform CWI in reservoir samples distributed in two core-holders (CH1 and CH2) arranged in series, which enables the recording of differential pressure across each core separately during the test (Figure 1). Each sample was cemented (to fill surface irregularities), wrapped with Teflon tape, aluminum foil, and a heat shrinking film, and then inserted into a rubber to avoid fluid leakage. Confining pressure, in all cases, were set 2000 psi higher than injection pressure. Band heaters connected to temperature controllers were used to keep core-holders and CO_2-saturated brine vessels at constant temperature. A positive-displacement pump was used to inject fluids at continuous flow rate, while a back pressure regulator controlled injection pressure. Fluid sample collection was done at injection system outlet.
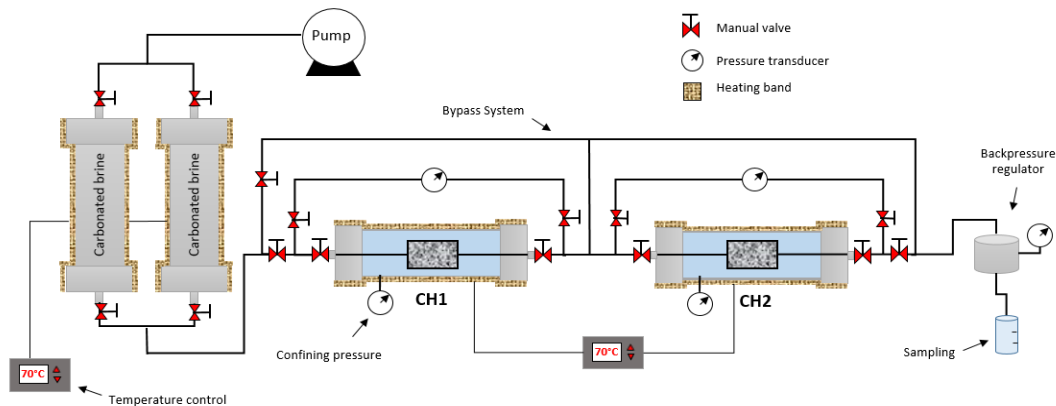
Figure 1. Experimental apparatus.

Experimental procedure

The experiments consisted of the injection of CO_2-saturated brine through core plugs of dolomite at temperature of 70°C. Tests 1, 2, and 3 were performed at the pressure of 8500 psi, while test 4 was carried out at 7500 psi. A constant flow rate of 2 cm^3/min was used in all tests.

Before each core-flooding, both samples were saturated with synthetic brine and pressurized up to test pressure. Synthetic brine flowed first through the bypass and then both core-holders were opened to flow. Once steady-state pressure gradient was stablished across the samples, carbonated brine vessels were opened to flow and bypass system valves were closed. Tests lasted up to 12 hours. The samples were scanned using X-Ray Computerized Tomography (CT) several times during experiment evolution, at a higher frequency in the first two hours. Every CT scanning generated one image for each mm of core length. Absolute porosity was calculated for each image individually, and an average of all image porosity values furnishes the total core porosity [16]. Therefore, porosity

behavior could be analyzed both spatially and along time. For test 2, fluid samples were collected and calcium concentration was obtained using Ion Chromatography (ICS-5000, Thermo Scientific). Differential pressure data registered with both pressure transducers allowed the calculation of core permeability for every second of test through Darcy's law.

RESULTS

Measurements before and after experiments for tests 1 and 4 showed mass reduction in all samples, and mass loss in the CH1 samples was from eight to eleven times greater than in the CH2 ones (Table 1). Effective porosity (measured using the porosimeter) increased 5% in the first samples, while it continued almost unchanged in the second ones. Porosity evolution during reactive flow was obtained for all tests using X-ray Computerized Tomography (CT), and the results are shown on Figure 2, where porosity values are normalized. Overall porosity in CH1 samples tended to remain approximately constant or increase, while the CH2 samples remained constant or decreased. Pressure reduction from 8500 to 7500 psi for test 4 did not change the porosity alteration pattern observed in all tests.

Initial and final porosity distributions along all samples are shown on Figure 3. The greatest increase in porosity (up to 35%) took place within 2 cm from the injection face of CH1 samples, where the phenomenon of dissolution was predominant. CH2 samples porosity tended to remain largely uniform along the cores length. Porosity increase was greater in regions with higher initial porosity, while porosity decrease was greater in regions with lower initial porosity, showing that this phenomenon can be highly influenced by heterogeneities previously present in the dolomite sample. Probably, the sample used in test 3 (CH1) showed a particular characteristic related to mineralogical composition and its degree of consolidation. In fact, each plug sample (CH1) showed a particular behavior in the corresponding tests. That is indicative that dissolution depends on rock heterogeneity as well as on minor changes of the rock mineral composition.

Table 1. Core plugs characteristics before (initial) and after (final) experiments.

Sample	Core Length (cm)	Core Mass (g)		Core Porosity (%)		Core permeability (mD)	
		Initial	Final	Initial	Final	Initial	Final
Test 1 CH1	5.9	161.73	160.4	14.4	15.0	116	58
Test 1 CH2	5.8	160.43	160.27	13.71	13.79	109	85
Test 2 CH1	6.2	166.59	-	16.49	-	403	-
Test 2 CH2	6.4	171.41	-	15.97	-	303	-
Test 3 CH1	5.0	132.63	-	16.84	-	391	-
Test 3 CH2	6.2	167.19	-	15.78	-	315	-
Test 4 CH1	6.4	175.86	174.85	13.43	14.1	119	68
Test 4 CH2	6.1	169.38	169.29	13.79	13.76	122	37

Figure 4 shows calcium concentration in produced fluid against PVs injected during test 2, where the baseline refers to concentration in unaltered brine. Throughout the core-flooding experiment, data remained above the baseline value. Calcium production did not present significant changes after rapidly reaching around 0.04 mol/kg. This is an indicative that dissolution stabilized rather quickly.
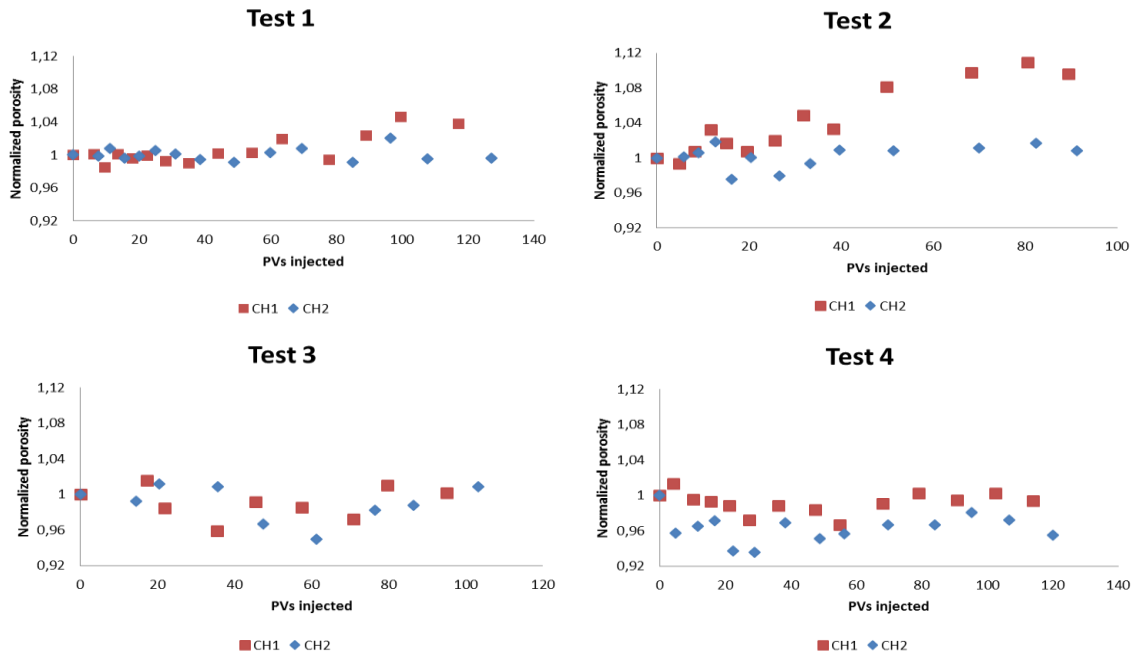
Figure 2. Porosity evolution (normalized) during experiments. Data were obtained with CT.

Measurements in the permeabilimeter showed a permeability reduction that varied from 43% to 50% in the CH1 samples and from 22 to 70% in the CH2 samples (Table 1) for tests 1 and 4. Figure 5 shows permeability data (normalized) obtained from pressure transducers during test 3. Permeability for CH1 sample presented a small decrease in the first PVs injected, and remained unchanged during the rest of the test. A decrease in CH2 sample permeability was observed, mainly during the first 60 pore volumes injected, due to precipitation. It is important to point out that the permeability data obtained from the permeabilimeter (Table 1) are not expected to be the same as the permeability data obtained from pressure transducers during carbonated brine injection (as the ones shown on Figure 4). This is due to differences in effective pressure and in injection fluids between both methods. Furthermore, during apparatus disassembly, the pressure reduction through which the sample goes can have caused mineral precipitation, which can be responsible for permeability decrease indicated by permeabilimeter measurements (Table 1).

Figure 3. Absolute porosity distribution along samples. Data were obtained using CT.

Test 1 (CH2)

Test 2 (CH1)

Test 2 (CH2)

Test 3 (CH1)

Test 3 (CH2)

Test 4 (CH1)

Test 4 (CH2)

—— Initial ----- Final
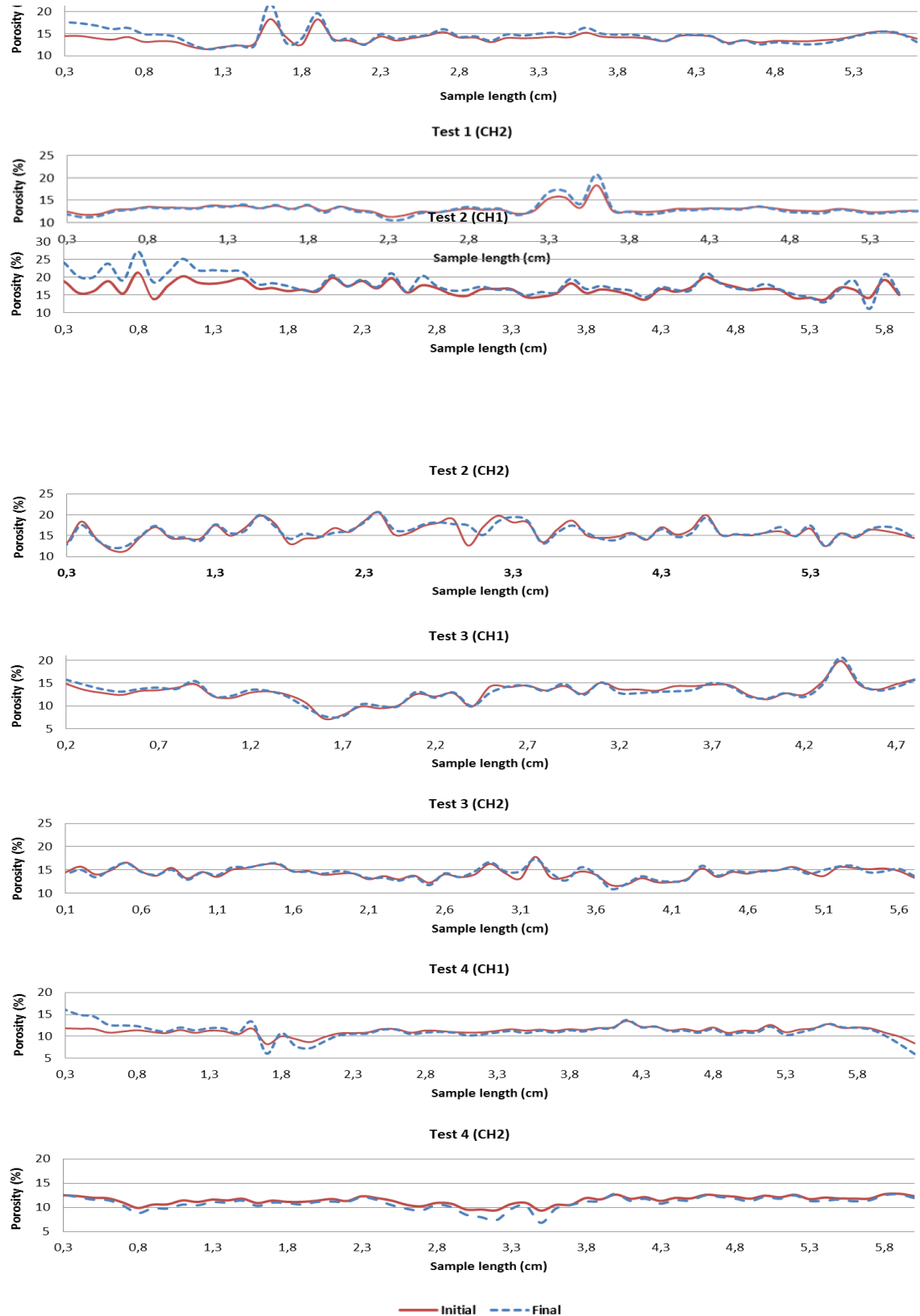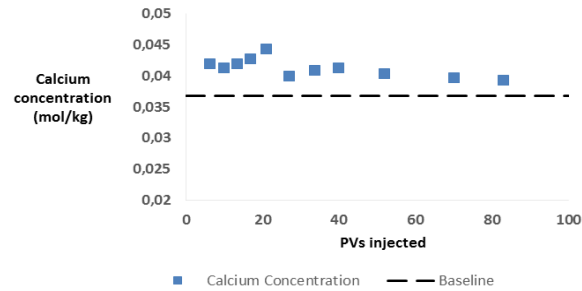
Figure 4. Calcium concentration in produced water during test 2.
The baseline refers to original composition of injected brine.
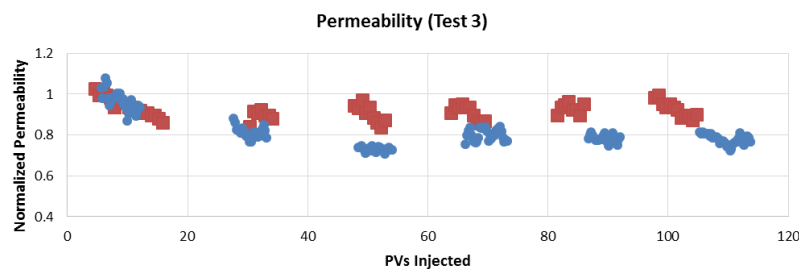
Figure 5 - Permeability (normalized) evolution during test 3.

DISCUSSIONS

Luhmann *et al*. [11] calculated dolomite porosity evolution under CO_2-charged brine based on mass balance, showing porosity increase in all experiments. Here, the experimental porosity data based on CT shows that overall porosity of dolomite does not always increase during carbonic acid injection due to coexistence of dissolution and precipitation phenomena along the samples. Properties related to porous media, such as surface area and initial porosity, will impact on dissolution and precipitation phenomena. Existing heterogeneities will influence fluid-rock reaction. It can be seen in the results that locations with higher initial porosity will be more likely to be dissolved in comparison with their surroundings, once flow velocity will be lower and fluid will have a longer contact time with pore walls. The opposite trend is seen in regions with lower initial porosity. This is especially important for dolomite due to its low dissolution rate. Higher porosity alterations due to dissolution occurring within the first centimeters of the dolomite sample showed that a small volume of rock was sufficient to bring carbonated brine to chemical equilibrium. In this sense, during CWI into dolomite rock, it is not expected that dissolution effects will be important at regions far away from the injection well. However, after injection fluid breakthrough, pressure decreases could lead the saturated fluid to precipitate, thus reducing permeability around production wells.

CONCLUSIONS

1. Significant increase in dolomite porosity due to carbonic acid dissolution occurs within few centimeters from fluid injection point, after which dissolution and precipitation coexist and porosity tends to remain unchanged.

2. Overall porosity of dolomites can experience increase or decrease near injection well during CWI, while permeability is expected to decrease in the cited region.

3. Porous media structure of dolomite can favor dissolution or precipitation to occur. Regions with relatively higher initial porosity will favor dissolution to preponderate, while precipitation can be induced in sections with lower porosity in relation to their surroundings.

NOMENCLATURE

CH1   Core-holder 1
CH2   Core-holder 2
CO_2 Carbon dioxide
CT   X-Ray Computerized Tomography
CWI   Carbonated Water Injection
H_2CO_3 Carbonic acid
PVs   Pore Volumes
XRD   X-Ray Diffraction

ACKNOWLEDGEMENTS

REFERENCES

1. NOAA - Earth System Research Laboratory. www.esrl.noaa.gov.

2. Sohrabi, M., Riazi, M., Jamiolahmady, M., Kechut, N.I., Ireland, S., Robertson, G., "Carbonated Water Injection (CWI) – A Productive Way of Using CO_2 for Oil Recovery and CO_2 Storage", *Energy Procedia* (2011) **4**, 2192-2199.

3. Shakiba, M., Ayatollabi, S., Riazi, M., "Investigation of oil recovery and CO_2 storage during secondary and tertiary injection of carbonated water in an Iranian carbonate oil reservoir", *Journal of Petroleum Science & Engineering*, (2016) **137**, 134-143.

4. Hasanvand, M.Z., Ahmadi, M.A., Shadizadeh, S.R., "Geological Storage of Carbon Dioxide by Injection of Carbonated Water in an Iranian Oil Reservoir: A Case Study", *Journal of Petroleum Science & Engineering*, (2013) **111**, 170-177.

5. Burton, M., Bryant, S.L., "Eliminating Buoyant Migration of Sequestered CO_2 Through Surface Dissolution: Implementation Costs and Technical Challenges", SPE 110650, presented at the SPE 2009 ATCE, Anaheim, California, Nov. 11–14.

6. Hoefner, M.L., Fogler, H.S., "Pore evolution and channel formation during flow and reaction in porous media". *AIChE Journal*, (1988) **34** (1), 45–54.

7. Svec, R.K., Grigg, R.B., "Physical effects of WAG fluids on carbonate core plugs", SPE 71496, presented at the SPE 2001 ATCE, New Orleans, LA, Sept. 30-3.

8. Grigg, R.B., Svec, R.K., "Co-injeted CO2-brine interactions with Indiana Limestone", SCA 2003-19, presented at the 2003 Int. Symposium of the Society of Core Analysts, Pau, France, Sept. 21-24.

9. Zekri, A.Y., Shedid, S.A., Almehaided, R.A., "Investigation of supercritical carbon dioxide, asphaltic crude oil and formation brine interactions in carbonate formations". *J. Petrol. Sci. Eng*., (2009) **69**, 63–70.

10. Luquot, L., Gouze, P., "Experimental determination of porosity and permeability changes induced by injection of CO_2 into carbonate rocks". *Chemical Geology*, (2009) **265**, 148–159.

11. Luhmann, A.J., Kong, X., Tutolo, B.M., Garapati, N., Bagley, B.C., Saar, M.O., Seyfried, W.E.J., "Experimental dissolution of dolomite by CO_2-charged brine at 100°C and 150 bar: Evolution of porosity, permeability, and reactive surface area", *Chemical Geology*, (2014) **380**, 145-160.

12. Grigg, R.B., Svec, R. K., Lichtner, P.C., Carey, W., Lesher, C.E., "CO_2/Brine/Carbonate Rock Interactions: Dissolution and Precipitation", presented at the 4° Annual Conference. on Carbon Capture & Sequestration, Alexandria, May 2-5, 2005.

13. Grigg, R. B.: "Long-term CO_2 Storage: Using Petroleum Industry Experience". *Carbon Dioxide Capture for Storage in Deep Geologic Formations*, volume 2, Elsevier. Chapter 11, (2005), 853–865.

14. Rogers, J.D., Grigg, R.B., "A literature Analysis of the WAG Abnormalities in the CO2 Process", SPE 59329, presented at the 2000 SPE/DOE Improved Oil Recovery Conference, Tulsa, Oklahoma, April 3-5.

15. Duan, Z., Sun, R. Zhu, C., Chou, I.M., "An improved model for calculation of CO_2 solubility in aqueous solutions containing Na^+, K^+, Ca_2^+, Mg_2^+, CL^-, and SO_4^{2-}", *Marine Chemistry*, (2006) **98**, 131-139.

16. Vargas, J.; Pagotto, P. C.; Santos, R.; Trevisan, O. V., "Determination of Dispersion Coefficient in Carbonate Rock using Computed Tomography by Matching in Situ Concentration Curves", presented at the: 2013 Int. Symposium of the Society of Core Analysts, Napa, California, USA, Sept. 16-19.

IMPACT OF CO$_2$ ON THE COMPLEX ELECTRICAL CON-
DUCTIVITY OF CARBONATE ROCKS
UNDER RESERVOIR CONDITIONS

Jana H. Börner[1], Volker Herdegen[2], Edith Müller-Huber[3], Klaus Spitzer[1]

[1] Technical University Bergakademie Freiberg, Institute of Geophysics and Geoinformatics, Freiberg, Germany
[2] Technical University Bergakademie Freiberg, Institute of Thermal, Environmental and Natural Products Process Engineering, Freiberg, Germany
[3] Technical University Berlin, Institute of Applied Geosciences, Department of Applied Geophysics, Berlin, Germany

ABSTRACT

Carbonate rocks provide great challenges to geophysics and reservoir engineering due to their extremely heterogeneous pore space and the reactive nature of the carbonate rock matrix. The presence of a reactive gas such as CO$_2$ in the pore space of a carbonate rock acts on the electrical conductivity mainly through three effects: 1. the resistive gas reduces the water saturation thereby decreasing bulk conductivity; 2. the gas simultaneously dissolves in the pore water thereby changing its ion content and the pH; 3. the CO$_2$-rich pore water interacts with the reactive carbonate matrix, which results in mineral dissolution, precipitation, and/or pH buffering.

We systematically investigate these effects under reservoir conditions in the laboratory using the spectral induced polarization (SIP) method. This method is accompanied by measurements of the nuclear magnetic resonance (NMR) under normal conditions. Several types of carbonate rocks are investigated under normal conditions and during exposure to CO$_2$ aiming at temperatures up to 80°C and pressures up to 30 MPa. We use both cores and crushed samples of varying particle size. Systematic investigations of the SIP of (non-reactive) quartz sand under reservoir conditions serve as a reference.

The different carbonate types show significant variation in their SIP response (i.e., the frequency dependent complex electrical conductivity) depending on salinity, porosity, pore-space heterogeneity and – in the case of crushed samples – the organization of particles in the packing. The NMR response shows a strong difference between the amount of free and capillary bound water in the samples at the same time.

Our approach reduces the complexity of the entire system and lets us differentiate between electro-chemical interactions and pore-space controlled processes. We aim at a systematic quantification of these processes in terms of their electrical manifestation and the derivation of a model description. The combined approach of SIP and NMR allows for the assessment of monitoring options with electrical methods in carbonate reservoirs.

INTRODUCTION

Carbonate reservoirs have come into focus since they host huge resources of oil and natural gas. Consequently, they are also targets for enhanced oil recovery (EOR) and carbon dioxide sequestration techniques. Carbonates, however, provide great challenges due to their extremely heterogeneous pore space and the reactive nature of the carbonate rock matrix. Electromagnetic methods can be of great value for monitoring fluids since they are sensitive to the pore content and provide information on the electrical properties of large rock volumes. Nevertheless, the petrophysical knowledge of the electrical properties of carbonates, which is an essential basis of monitoring, is still rather poor. We therefore carry out investigations on the electrical properties of carbonate rocks with the focus on understanding the impact of chemical interaction (e.g. pH-buffering and dissolution of carbonate matrix) on the spectral complex conductivity. In order to stringently relate our observations to said chemical interaction effects, we work with crushed carbonate samples. This has several advantages: controlled destruction of the heterogeneous pore space, enlarged interfaces for interaction, increased permeability.

In a first step, we have to understand the relation between the properties of core and crushed samples so we are able to transfer our observations to the behaviour of the solid core material. We therefore systematically investigate the electrical properties of different carbonates with very low porosity, high porosity and with both vuggy and microporosity at different states of crushing. In the second step, the electrical properties of representative crushed samples are going to be measured under pressure during exposure to CO_2.
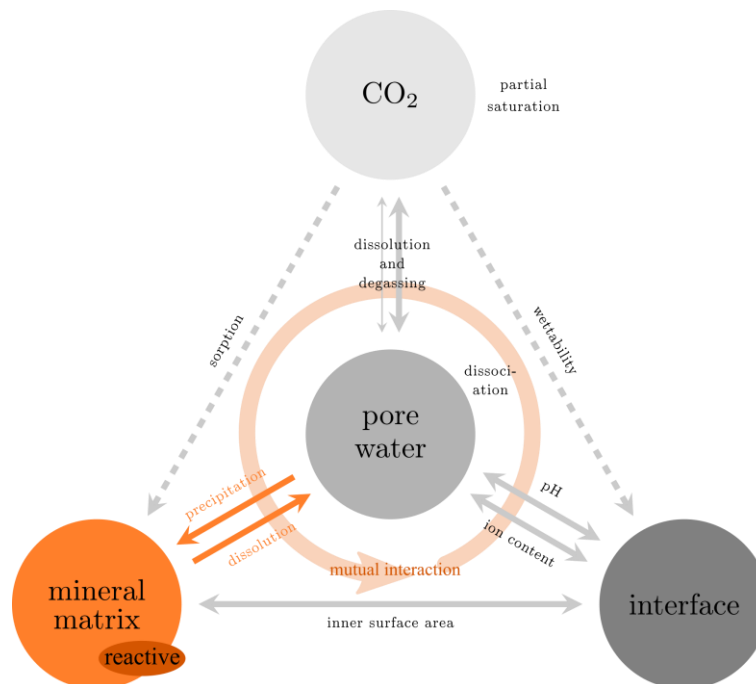
Fig. 1: Schematic representation of the phases and processes acting on the electrical rock properties during interaction between CO_2 and water-bearing rocks (after [8],[6]). Processes, which are of particular interest in the case of reactive rocks, are marked in orange.

THEORY

Electrical conductivity of water-bearing rocks

The electrical rock conductivity in general is a complex and frequency-dependent quantity and originates from both electrolytic and interface conduction mechanisms [1]:

$$\sigma^*(\omega) = \sigma'(\omega) + \boldsymbol{i}\sigma''(\omega) \tag{1}$$

Electrolytic conductivity depends on pore space characteristics, saturation and pore water conductivity [2]. Interface conductivity depends on grain roughness (i.e. inner surface area), pH and weakly also on salinity (e.g. [3]). It depends less strongly on water saturation than the electrolytic conductivity (e.g. [4]). A decrease in pH causes a decrease in σ'' [5]. Mainly based on [2] and [4], σ^* at a fixed frequency may be described by:

$$\sigma' = S_{\mathrm{w}}^n \Phi^m \sigma_{\mathrm{w}} + S_{\mathrm{w}}^k \sigma'_{\mathrm{if},S_{\mathrm{w}}=1} \tag{2}$$

$$\sigma'' = S_{\mathrm{w}}^k \sigma''_{\mathrm{if},S_{\mathrm{w}}=1} \tag{3}$$

where S_{w} denotes water saturation, Φ is porosity, m is the cementation exponent, n and k are the real and imaginary part saturation exponent, respectively, and $\sigma'_{\mathrm{if},S_{\mathrm{w}}=1}$ and $\sigma''_{\mathrm{if},S_{\mathrm{w}}=1}$ denote the real and imaginary part, respectively, of interface conductivity at full saturation.

Effect of CO₂ on rock conductivity

The presence of the reactive gas carbon dioxide (CO_2) in pore space gives rise to a network of physical and chemical processes (Fig. 1, [6]). All these processes act on σ^*. First of all, CO_2 is forced into the pore space of the storage formation. A connected flowing phase is formed due to the pressure gradient. When no pressure gradient is applied, the non-wetting CO_2 forms bubbles in the pore centers. Character and efficiency of the phase replacement depend on pressure, temperature, CO_2 mass flow and pore space characteristics, such as porosity, inner surface area, pore connectivity and shape. The combination of all these parameters results in variations of capillary pressure as well as absolute and relative permeability. During flow, chemical interaction between gas and pore water take place. Also, water dissolves in the CO_2. This may lead to drying out of connate interface water. During injection, CO_2 partially replaces the pore water of the storage formation and consequently reduces rock conductivity σ^* (cf. Eqs 2, 3). The main task of electromagnetic monitoring techniques is to correctly reconstruct $S_{\mathrm{CO2}} = 1 - S_{\mathrm{w}}$ from conductivity measurements.

CO_2 is highly soluble in water. The amount of carbon dioxide, which is dissolved in a pore water with known sodium chloride (NaCl) content at thermodynamic equilibrium, is a function of pressure, temperature and salinity. During flow the thermodynamic equilibrium is slightly disturbed. A low flow velocity and resting phases between periods of flow reduce the potential impact of this disturbance. A small portion of the dissolved CO_2 forms carbonic acid, which is unstable and dissociates into protons, hydrocarbonate and carbonate

ions. These ions occur in addition to anions and cations of dissociated salts. Consequently, they act on the pore water conductivity σ_w. As a result of the dissociation, the pH decreases as well (computed with PHREEQC: ~3.0), when no buffering occurs. Static dissolution experiments on the un-buffered system demonstrated an increase in pore water conductivity with pressure due to the additional ions from dissociation for low-saline water. For solutions with > 5.8 g/l NaCl, a conductivity decrease was observed that is due to a decrease in ion mobility, which dominates the electrolyte conductivity at high salinities despite the added charge carriers (for details see [7]). The effect of CO_2 dissolution and dissociation on pore water conductivity σ_w may be predicted for all salinities based on physicochemical properties by the following model [7]:

$$\sigma_w^{norm}(p, T, c_{NaCl}) = \frac{\sigma_w}{\sigma_w^0} = \frac{1}{\sigma_w^0} \sum_{i=1}^{2} [\Lambda_i \gamma_i \alpha_i c_i] \tag{4}$$

Here, σ_w denotes the electrolyte conductivity with CO_2, σ_w^0 is the initial electrolyte conductivity. Λ denotes molar conductivity, γ is the activity coefficient, α is the degree of dissociation and c is concentration. The activity coefficients γ_i of NaCl and dissociated CO_2 are exponential functions and depend on the concentrations of all dissolved components. A purely empirical formulation to describe σ_w^{norm} is also available (for details see [7]).

The impact of chemical interaction on the three-phase system of CO_2–electrolyte–sand may be deduced from the flow experiments (for experimental details see [8]). Chemical interaction may be quantified by comparing the complex conductivity under pressure to the complex conductivity after depressurization at the end of the flow experiments. For all pressures and temperatures in the case of the un-buffered system, σ' reflects the salinity regime predicted by our models (Eq. 4). At the same time σ'' increases stably. The effect may be described by a constant factor σ_{if}^{norm} as a good approximation. These observations are due to the change in pH from acidic back to near neutral during degassing.

Besides the impact of CO_2 on the pore water, the low pH environment due to dissolution and dissociation may trigger changes of the rock matrix, which would result in an increased inner surface area, and consequently affect the imaginary part of conductivity σ'' [8]. In the special case of the inert quartz sand, the surfaces are not affected by the CO_2 or the low pH. In the case of a buffering system including carbonate rocks, we expect a different behaviour.

Summarizing, the electrical rock conductivity during interaction between rock, water and CO_2 may be described by the following model [8]:

$$\sigma^*(p, T, c_{NaCl} = S_w^n \Phi^m \sigma_w^{norm} \sigma_w + S_w^k X \sigma_{if}^{norm} \sigma'_{if,S_w=1} + i S_w^k X \sigma_{if}^{norm} \sigma''_{if,S_w=1} \tag{5}$$

The formulation is valid for the frequency range between 0.1 Hz and 100 Hz. The quantity X covers changes in the inner surface area. Note that in case of strong mineral dissolution the porosity might change as well and parameters might influence each other.
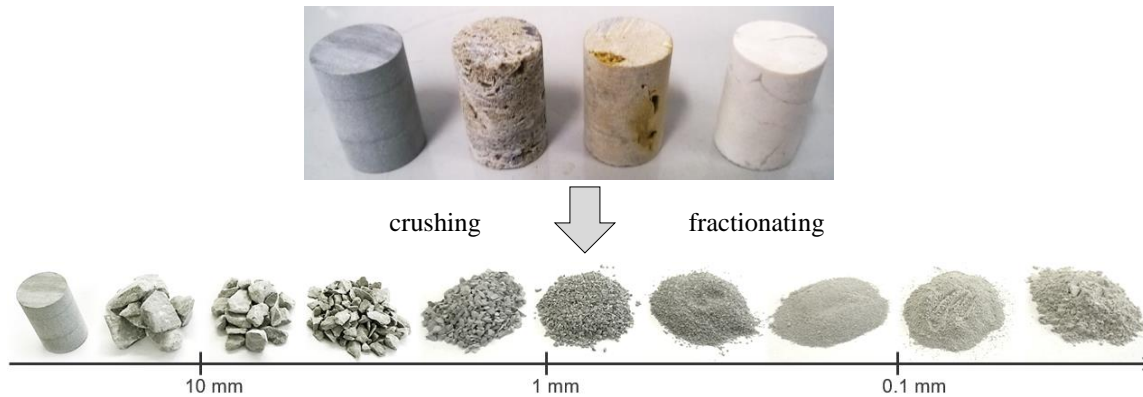
Fig. 2: Photographs of the investigated carbonate rocks. Top: cores (diameter: 2cm) of mud-dominated micritic Wellenkalk, grain-dominated oomoldic Schaumkalk, micritic Madiger Kalk with macro-pores and dense Jurakalk consisting of 99.9% pure calcit (from left to right). Bottom: crushed fractions of Wellenkalk with varying particle size.

MATERIALS AND METHODS

In order to investigate the electrical properties of carbonate rocks, four carbonates with different characteristics are considered (Fig. 2). The dense micritic Wellenkalk (top of Fig. 2, left-most core) is characterized by a crystalline, homogeneous structure and low porosity. The oomoldic Schaumkalk (second core in Fig. 2) shows high porosity and mollusc shells are macroscopically visible. The third carbonate – a micritic Madiger Kalk – is related to the Wellenkalk, but contains additional macro-pores, which increase its average porosity to almost that of the Schaumkalk. The right-most core in Fig. 2 shows a very-low porous Jurakalk, which consists of almost pure calcite and serves as a reference substance, therefore. These carbonate rocks were crushed into nine fractions of varying particle size ranging from <0.063 mm to >10mm particle diameter (see Fig. 2, bottom).

The properties of the resulting particle-size fractions are not necessarily the same as those of a natural unconsolidated rock. All properties have to be understood as a superposition of an intra-particle (dominated by original carbonate structure) and an inter-particle (dominated by packing) response (see Fig. 3). Fig. 3 shows this for porosity and inner surface area. Depending on particle size, the considered property and the properties of the original carbonate rock, the intra- or inter-particle contribution governs the bulk property. For repeatability reasons, the high-pressure and temperature experiments under CO_2 are going to be carried out with a particle size fraction, which is dominated by the packing properties in order to eliminate the influence of the carbonate matrix heterogeneity.
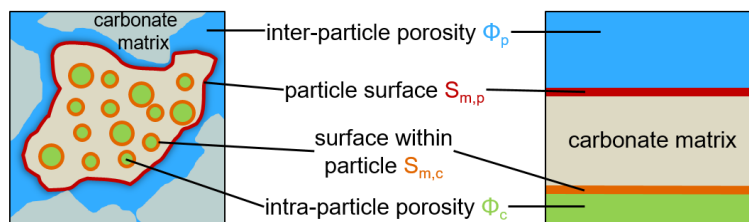
Fig. 3: Porosity and inner surface area components in a crushed sample.
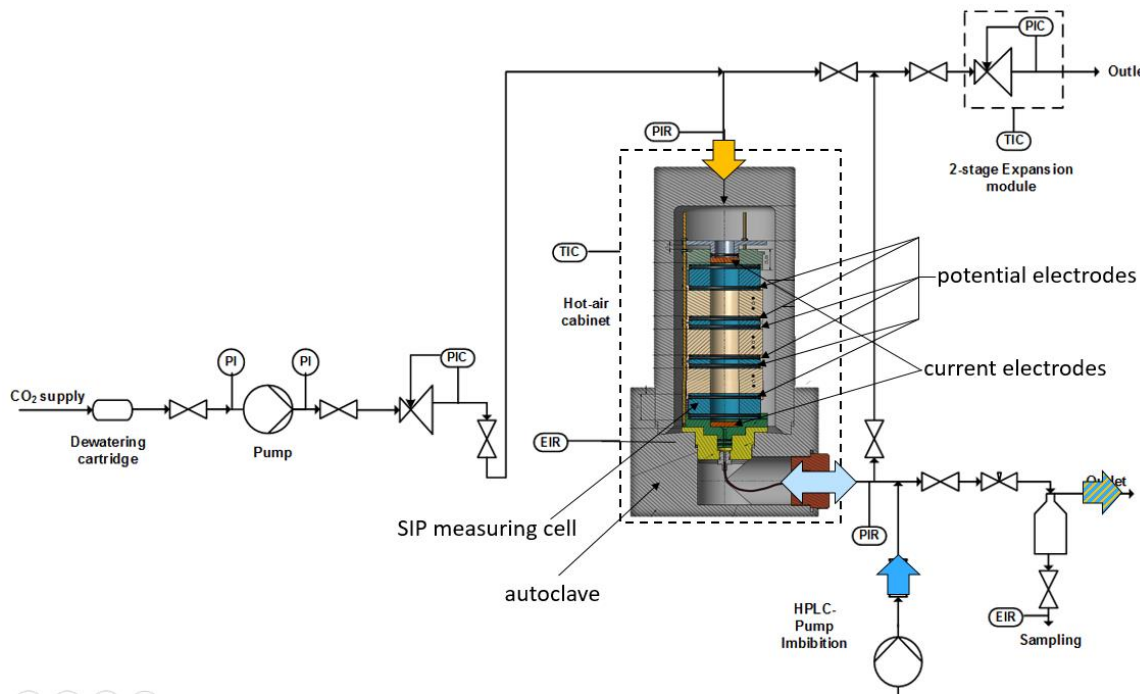
Fig. 4: Laboratory set-up for SIP-measurements at elevated pressure and temperature (based on [7,8]).

The laboratory set-up for measuring the spectral complex conductivity in a time-lapse manner during exposure to and flow-through by CO_2 at elevated pressure and temperature is shown in Fig. 4. It is based on the apparatus described in [7,8] and is now equipped with a new SIP measuring cell and the possibility to both drain and flush the sample. Systematic investigations of the electrical properties of the crushed samples were carried out at normal conditions.

NMR measurements were carried out at ambient pressure with a standard CPMG sequence at a constant temperature of 19°C. In a well-established processing procedure, the envelope of the decaying signal was transformed into a T_2 relaxation time distribution, which allows for evaluating the water and surface properties of the samples. Both fully water saturated and gravitatively drained samples were investigated.

RESULTS

The NMR results for all fractions of crushed Wellenkalk are shown in Fig. 5. Qualitatively speaking, all investigated carbonates exhibit the same behaviour. At large particle diameters, a T_2 peak representing the free water between the particles dominates the NMR response. As the particles get smaller, their specific inner surface ($S_{m,p}$ in Fig. 3) increases and the amount of capillary bound water increases as well. This results in a decreasing magnitude of the free-water peak and the evolving of a peak at shorter T_2 times, which finally dominates the whole response at very small particle sizes. This interpretation is supported by the measurements on drained samples (lower left panel): the free-water peak vanishes whereas the capillary-bound water peak for small particles remains stable.
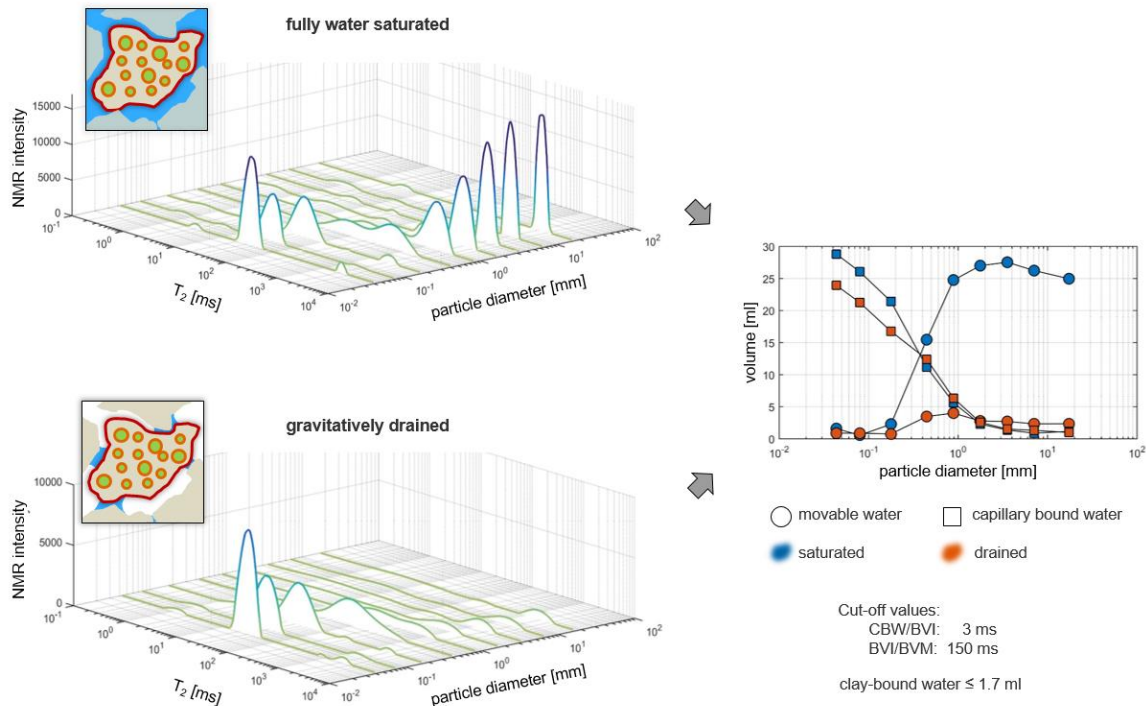
Fig. 5: NMR results for all fractions of crushed Wellenkalk. T_2 relaxation time distributions vs. particle size for the fully water-saturated samples (top left panel) and the gravitatively drained samples (bottom left panel)

The SIP response for all four carbonates is plotted in Fig. 6. Measurements on core samples (left column) demonstrate the variability of carbonate rocks. Although all cores have been saturated with similar salinities (appr. 0.07 S/m; variations in salinity only originate from the natural equilibrium of the rocks with their pore-filling fluid) the real part conductivity varies significantly, which is due to the differences in porosity. The imaginary conductivity also shows strong variations. Especially, the dense and clean Jurakalk (violet markers) shows very low imaginary conductivity. Stronger polarization in the other carbonates might also be due to the existence of minor clay content.

The right-hand side column in Fig. 6 gives the SIP response of one fraction of crushed carbonates for all four rocks. It is obvious that at this particle size (0.63 – 1.25 mm) the behavior of the carbonates in terms of real conductivity is already homogenized. However, the imaginary conductivity is still very different between the rock types, even new features appear in the frequency response (c.f. Wellenkalk, blue markers). The clean Jurakalk still is the carbonate with the lowest imaginary conductivity.

These first results show that the crushing has to be handled carefully and the carbonates need to be crushed to a sufficient extend to show a homogeneous frequency response. Comparisons between the SIP responses from all fractions for one carbonate reveal systematic changes in the electrical properties.
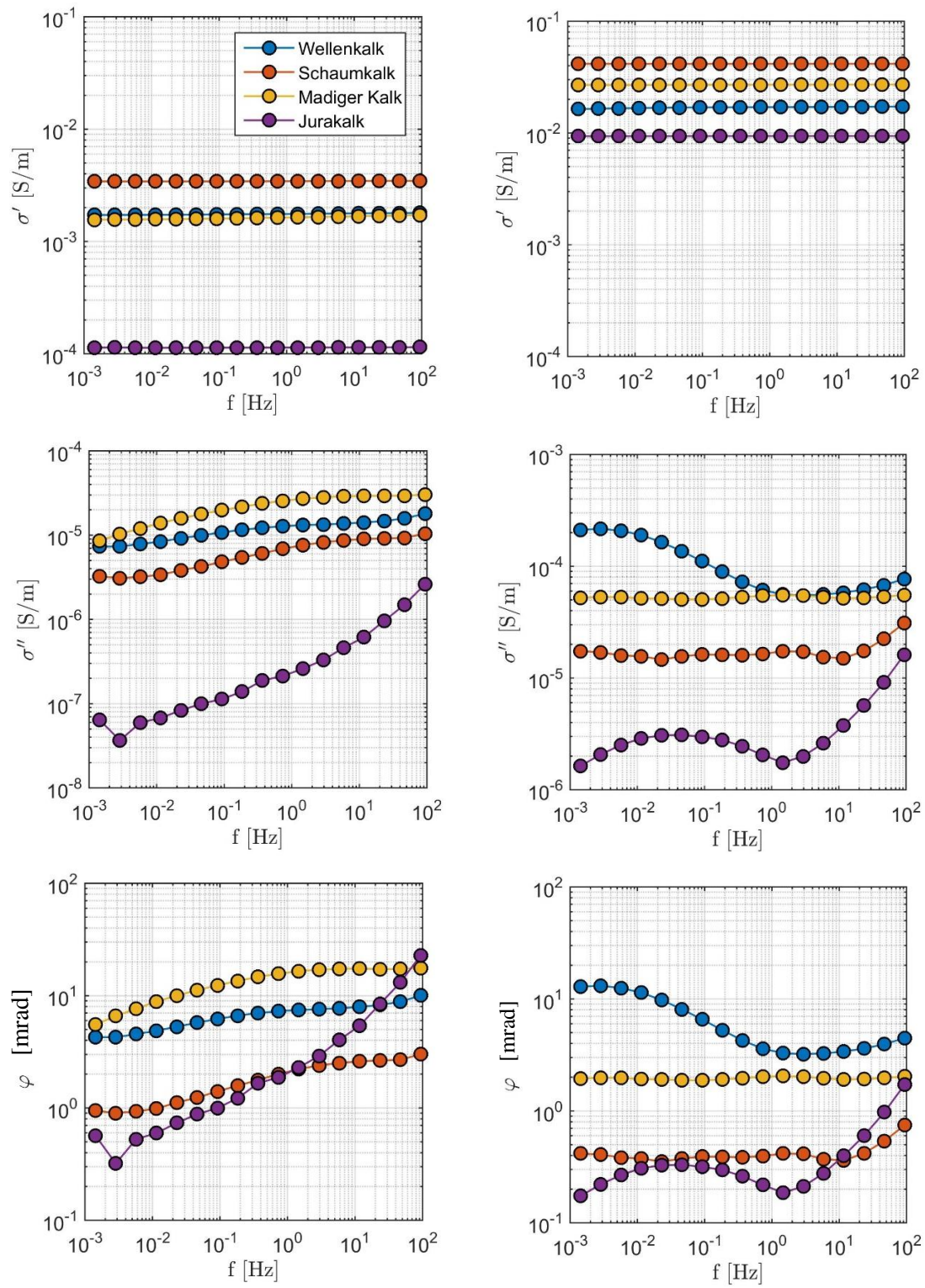
Fig. 6: Complex conductivity of the cores (left column) and a crushed sample (right column, particle size 0.63 – 1.25 mm) in terms of real and imaginary conductivity and phase shift (from top to bottom).

CONCLUSIONS

Carbonate rocks provide great challenges to petrophysics due to their heterogeneous pore space and the reactive nature of the carbonate matrix. Using measurements on both cores and crushed carbonate samples, we investigate the complex electrical properties of carbonate rocks at both normal and reservoir conditions. First results of this work in progress demonstrate the variability of carbonate rocks and the effects of crushing on carbonate properties. Systematic crushing of the solid materials allows for controlling porosity (demonstrated by SIP) and inner surface area (demonstrated by NMR).

Next steps are the completion of the SIP measurements and accompanying mineralogical analyses at normal conditions to gain a full understanding of the properties of crushed samples. In the near future, time-lapse measurements at elevated pressure and temperature during interaction between carbonate matrix, CO_2-rich saline pore water and free CO_2 phase are going to be carried out. This work will contribute to our general understanding of carbonate reservoirs and to the development of a laboratory approach to study the impact of chemical interaction on electrical rock properties.

ACKNOWLEDGEMENTS

REFERENCES

1. Olhoeft, G.R., 1979. *Electrical properties, initial report of the petrophysics laboratory*. Circular 789, U.S. Geological Survey.
2. Archie, G. E., 1942: *The electrical resistivity log as an aid in determining some reservoir characteristics*. Trans. Americ. Inst. Mineral. Met. 146, S. 54–62.
3. Revil, A. and Skold, M., 2011. *Salinity dependence of spectral induced polarization in sands and sandstones*. Geophys. J. Int. 187: pp. 813–824.
4. Vinegar, H.J. and Waxman, M.H., 1984. *Induced polarization of shaly sands*. Geophysics 49: pp. 1267–1287.
5. Skold, M.; Revil, A. and Vaudelet, P., 2011. *The pH dependence of spectral induced polarization of silica sands: Experiment and modeling*. Geophysical Research Letters 38. L12304.
6. Börner, J.H.; Herdegen, V.; Repke, J.U. & Spitzer, K., 2013. *The impact of CO_2 on the electrical properties of water bearing porous media - laboratory experiments with respect to carbon capture and storage*. Geoph. Prosp. 61: pp. 446-460.
7. Börner, J.H.; Herdegen, V.; Repke, J.U. and Spitzer, K., 2015. *The electrical conductivity of CO2–bearing pore waters at elevated pressure and temperature: a laboratory study and its implications in CO2 storage monitoring and leakage detection*. Geophys. J. Int. 203: pp. 1072–1084.
8. Börner, J.H., Herdegen, V., Repke, J.-U. and Spitzer, K., 2017. *Spectral induced polarization of the three-phase system CO_2 - brine - sand under reservoir conditions*. Geophysical Journal International. 208 (1): 289 - 305.

PORE-SCALE OBSERVATIONS OF THE EFFECT OF SURFACE TREATED NANOPARTICLES ON DRAINAGE PROCESSES

Roy Wung[1], David A. DiCarlo[1], Steven L. Bryant[2], and Pradeep Bhattad[3]
1 Department of Petroleum Engineering, The University of Texas at Austin, Austin, TX
2 Departments of Chemical and Petroleum Engineering, University of Calgary, Calgary, Canada
3 Materials & Structural Analysis, Thermo Fisher Scientific, Houston, TX

ABSTRACT

In this study we observe, using pore scale X-ray micro-CT imaging and advanced petrophysical analysis, how surface treated silica nanoparticles improve sweep efficiency of n-octane in drainage corefloods. Specifically, upon injection of n-octane into a brine saturated core, preferential flow paths are observed and attributed to both viscous instability and rock heterogeneity; when the displaced phase contains a modest volume of nanoparticles, the same preferential flow paths are suppressed resulting in higher overall octane sweep efficiency. Grain analysis on microCT images of the core confirms that the flow paths are governed by pore scale heterogeneity. We argue nanoparticle stabilized non-wetting droplets are formed during the displacement, and work to block pores in high permeability regions and divert flow to low permeability regions thus improving overall volumetric sweep efficiency.

INTRODUCTION

Immiscible displacements of a wetting fluid by a less viscous non-wetting fluid within a porous medium often results in the injected fluid moving in preferential flow paths and with poor sweep efficiency. These preferential paths, or fingers, occur because of viscous instability, and are exacerbated by any natural heterogeneity in the medium. This problem is ubiquitous through many subsurface displacement processes.

For example, in gas EOR, poor sweep efficiency and early breakthrough of injected gas results in sub-optimal incremental oil production and unnecessary gas cycling. In geologic carbon sequestration, CO_2 storage volumes and security are not maximized when CO_2 takes preferential flow paths within saline aquifers. Other examples include water injection in oil-wet reservoirs and leakoff of energized fracture fluids into natural fractures.

To this end, many solutions have been offered to remediate this problem. Theoretically, the simplest physical way is by viscosifying the invading fluid through the addition of additives – this is done often in the oil patch by adding polymer to water floods. However

there are no effective viscosifiers for gases and other non-aqueous phase liquids. Instead, additives added to the invading aqueous phase can cause the invading fluid to foam or emulsify when in contact with non-aqueous phase. Thus increasing the invading fluid's effective viscosity by increasing the fluid-fluid interface area in the porous media and adds resistance to the flow.

Most of the additives suggested have been surfactants, but recently it has been shown that, when suitable, surface-treated nanoparticles are added to the brine, the resultant CO_2/brine mixture can foam. It has been conclusively determined that foaming occurs when two fluids are co-injected through a porous medium (Aroonsri, 2013; Espinosa, 2010). This occurs for a range of fluid mixture qualities, temperatures, pressures and nanoparticle concentrations. However, foaming during co-injection only occurs above a threshold velocity, which may be difficult to achieve in a reservoir far from the injection site.

An alternatively proposed mechanism to co-injection for foam generation has been drainage displacements, in which a non-wetting phase such as CO_2 or oil displaces brine initially resident in the core. When nanoparticle laden brine is used in such experiments, the displacement pattern has been shown to change from preferential to more piston-like where the CO_2 invades a much larger percentage of the core (Aminzadeh, 2013). This same effect is also seen with low-pressure CO_2 analogs like n-octane (DiCarlo, 2011).

While data such as increased pressure drop, later breakthrough time, and regions of intermediate fluid density in mm-resolution CT images during displacements with nanoparticles suggest in-situ foam/emulsion generation, studies to date have not conclusively proven this increased efficiency is due to generation of foam or emulsion. Thus while these results are very encouraging on the use of nanoparticles ameliorating the low-viscosity effects of CO_2 and other non-wetting phases, the exact physics of how the nanoparticles affect the flow is still in question.

In this work, we report pore-scale evidence of the effect of nanoparticles on drainage displacements. We use n-octane to displace brine with and without nanoparticles in a Boise sandstone core. Spatial distributions of residual brine are measured using micro-CT at the end of each experiment. The 15 μm resolution of the scanning is fine enough to determine the filling of individual pores (regions not seen with larger scale scanning), and we determine how the spatial pore size distribution affects the pore filling with and without nanoparticles. This gives us key insights on the effect of nanoparticles on the displacement physics and how this can increase the core-scale sweep efficiency of injecting a non-wetting phase.

MATERIALS AND METHODS
One cylindrical Boise sandstone core (15.2 cm length, 2.5 cm diameter) was the porous media of choice for the experiments performed because of its availability, low clay content and moderate heterogeneity. The porosity and permeability were 30% and 3.8 D, respectively. The core was confined in a custom epoxy coreholder and fitted with flow

fittings. X-ray microCT imaging on the middle section of the epoxy confined core performed using Heliscan microCT (Thermo Fisher Scientific) and the imaging settings were energy 120kV, target current 90µA, and image resolution 15.7µm/voxel.

n-Octane was chosen as an experimentally convenient non-wetting phase. The wetting phase was either a synthetic brine of 0.3M NaI solution in deionized water (the control case) or a 0.3M NaI in deionized water dispersion containing 5 wt% of silica nanoparticles (the nanoparticle case). NaI was added as a dopant to the wetting phase to increase the X-ray attenuation contrast with the non-wetting phase consisting of pure n-Octane. The nanoparticles, EOR-5XS from Nissan Chemical USA, consisted of a silica core 5-30 nm in diameter with a proprietary surface coating to prevent aggregation. These nanoparticles stabilize CO_2-in-brine foams at a range of conditions (Aroonsri, 2013; Worthen, 2013).

For the control experiment, the core was first vacuumed and saturated with the control brine. Next, with the core oriented horizontally, n-octane was injected to displace the aqueous phase at a flow rate of 0.60 cm^3/min (2.4 PV/hour) for 4+ PV to achieve residual water saturation. Throughout the drainage process, pressure drop was measured and recorded from the core inlet to the core outlet. Water cut was also recorded using a fraction collector. Micro-CT image of the same middle section of the core was acquired in the saturated state prior to drainage and after the end of drainage step.

3D micro-CT images of the sample were taken in the following states:

Step   Core state
1.   Dry
2.   Saturated with control brine
3.   Residual control brine after drainage with octane
4.   Core was cleaned and dried to reset to the original dry state
5.   Saturated with brine containing nanoparticle dispersion
6.   Residual aqueous phase after drainage with octane

3D microCT images were first registered to bring all five images in a perfect geometric alignment using VoxelPerfect algorithm [Latham et al. 2008]. This allowed for voxel by voxel subtraction of the reference dry image from other images in step 2-4 and the resulting difference shows the 3D distribution of NaI containing brine. The difference images were used to quantify porosity from the fully saturated images and residual saturation at the end of drainage by segmenting the difference image as by a "total connected porosity" segmentation technique [Ghous et. al., 2007]. From these images, we are able to determine how the presence of nanoparticles affects the pore scale spatial distributions of residual water following drainage processes. 3D visualization, grains segmentation and grain size distribution analysis was performed using PerGeos.

RESULTS

Figure 1a shows the overall pressure drop history as a function of injected n-octane pore volume for both the control (blue) and nanoparticle (red) experiments. For both curves, the

pressure drop increases initially because of multi-phase flow in the core, followed by a decrease in pressure with increased n-octane saturation. The pressure drop recorded during the nanoparticle experiment was up to 2.5 times greater than the control case, with the largest difference occurring at the breakthrough of injected n-octane at the core exit.

Figure 1b shows the core-average brine saturation history as a function of injected n-octane pore volume for both the control (blue) and nanoparticle (red) experiments. n-octane arrival at the core exit is indicated on the curve by the deviation from the unit slope. The core-average saturation asymptotically approaches the residual brine saturation value. In the control experiment, n-octane shows early breakthrough, around 0.48PV and reaches a core-average residual brine saturation of 41%. In the nanoparticles case, n-octane breakthrough is delayed to 0.56PV and residual brine saturation is decreased to 31%.
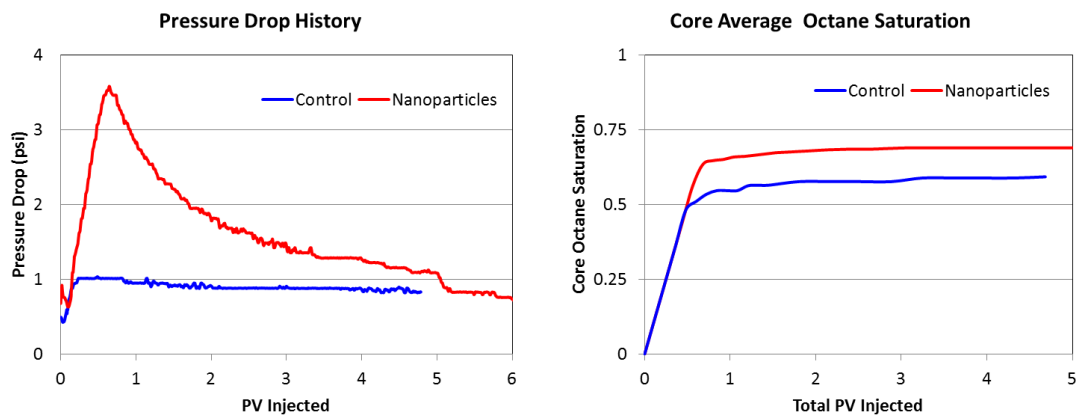
Figure 1a: Pressure drop versus PV of octane injected. Flow switched from brine to octane at PV=0

Figure 1b: Core averaged octane saturation versus PV of octane injected.

Figure 2a shows the core with the region scanned. Figure 2b shows a 45mm tall section of the core imaged with microCT at 4 different states. The 3D images in dry, saturated, and drained states are registered, and only a longitudinal cross section is shown here. From the dry image we can see the pores in darker color and grains in various lighter shades as a function of mineral density, chemical composition and mixture of phases (e.g. edge of pore and mineral) finer than the voxel resolution. Figure 2b shows the images after drainage of control brine. n-octane swept regions can be seen in darker shades and unswept or partially swept regions can be seen in lighter colors as they still retain NaI doped brine. In comparison, the after drainage image in nanoparticle dispersed brine case shows more n-octane swept region.
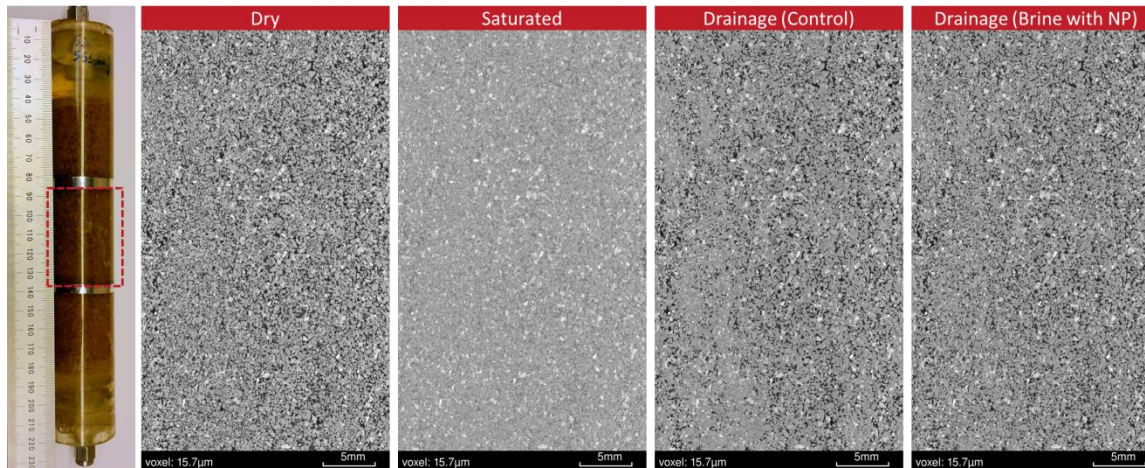
Figure 2a (left): Core with region scanned. Figure 2b (right): Micro-CT images of core at different core flooding states

To quantify the amount of brine present at the end of two drainage processes, the dry image was subtracted from the drained images. Figure 3a shows the resulting difference image, wherein any unchanged voxels compared to the dry image, such as solid grains, get subtracted; while the changes in the pores get highlighted. Hence the coloration in these images ranges from 0% brine saturation at a voxel (black) to a 100% brine filled voxel (white) with grayscale represented weighted sub-voxel saturation. Figure 4 shows the same data in 3D, showing distribution of residual saturation follows along the tight laminations. Overall saturation calculated from micro-CT images was lower than the experimental observation. This could be due to the imaging and analysis was performed only on the middle 1/3rd region away form end zone, while the weight measurement in experimental results would account for the brine saturation in the entire core holder.
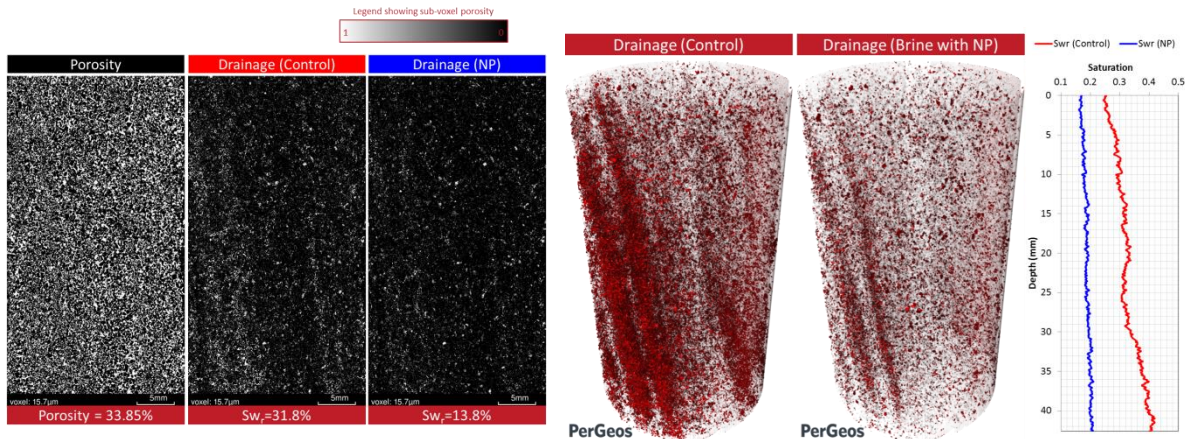
Figure 3: Longitudinal cross section from 3D microCT images showing difference images (a) porosity, (b) residual saturation in control and (c) residual saturation in NP.

Figure 4: 3D view of pores filled with brine after drainage. The brine is shown in red in this figure.

The distribution of residual brine as seen in Figures 3 and 4 suggests that the displacement front of n-octane is not uniform, but rather bypasses regions of pore space. In particular, brine saturations persist in channels on the left side of the image oriented in the direction of flow. This results in a larger saturation of residual water in the left portion of the figure. Within the left side, there are streaks of high and low residual water saturation, potentially indicative of heterogeneity and layering of different grain types. Compared to the control experiment, the overall residual water saturation is lower and distributed more uniformly, indicating much less bypassing of wetting phase during drainage. Figure 3 and 4 suggests that the presence of nanoparticles increases overall octane saturation by increasing the number of octane filled pores.
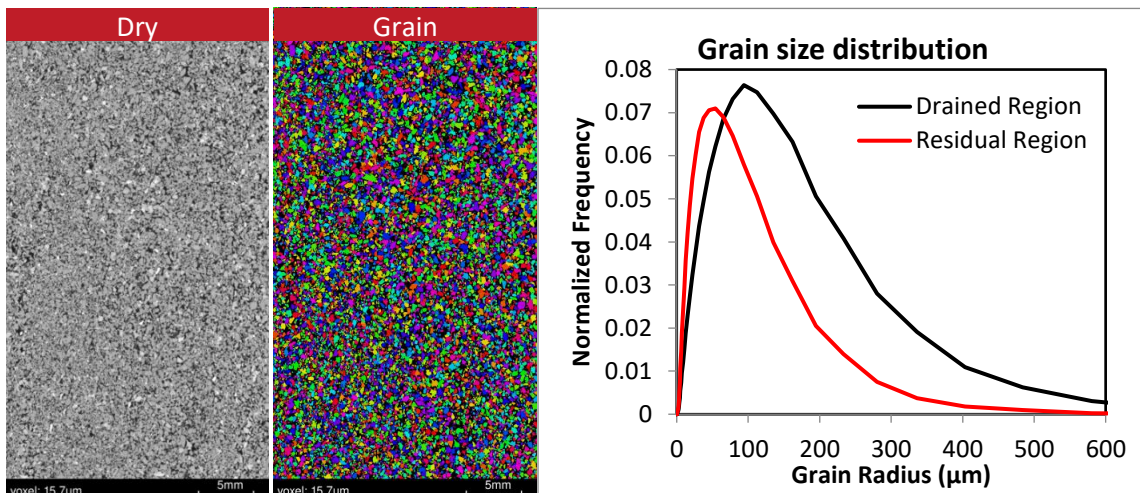
Figure 5: Cross section from 3D grains segmented image showing lamination with finer grains dominating region where residual saturation was observed after the drainage in the control case without nanoparticles and coarser grains dominating drained region.

Saturation profiles along the height of the core were calculated by average saturation in each horizontal cross section from 3D cylindrical image and the residual water saturation profiles confirm the above qualitative observations. The control experiment (red) shows a positive saturation gradient, with an inlet residual water saturation of 25% and outlet saturation of 41%, as expected from a displacement dominated by preferential flow. In contrast, the nanoparticle experiment (blue) saturation profile is lower and relatively constant, indicative of a uniform displacement. Therefore, for the core subsection under microCT inspection, the improvements in n-octane conformance control in the presence of nanoparticle dispersion results in a lower core-average residual water saturation of 19% compared to the control case of 33%.

These pore scale micro-CT results can be compared to earlier experiments performed with a macro mm resolution, modified medical CT scanner. It was shown in DiCarlo et al (2011) that an n-octane displacement front in the presence of nanoparticles is more spatially uniform with a later breakthrough when compared to a control displacement without nanoparticles. The main limitation of the earlier experiments, however, was the inability to

correlate core scale fluid displacements with pore scale properties due to the relatively coarse resolution of the CT scanner.

DISCUSSION

The results of the drainage experiments with and without nanoparticles can be summarized as follows:

1. Higher pressure drop and better sweep efficiency was observed during injection of n-octane into a nanoparticle dispersion saturated core, compared to the control case.

2. Following n-octane injection, micro-CT imaging shows less preferential flow, higher core volume swept by n-octane, and lower residual brine saturation when nanoparticles are present.

3. At the resolution of 15.7μm/voxel, it is difficult to comment of the presence of an intermediate emulsion phase. Further investigation at higher resolution will be performed as next part of this study.

4. Grain size distribution calculated from 3D image were split into two parts, the drained region and region showing residual saturation in the control case. This was achieved by using the results of control case as mask. The region showing residual saturation in the control case has smaller grains, and thus smaller pores and lower permeability, on average than the drained region.

Results 1 and 2 are consistent with previous observations described by DiCarlo et al. and Aminzadeh et al. Results 3 and 4 are novel findings that substantiate and provide deeper understanding of Results 1 and 2.

In particular, the micro CT images presented here show, as one wold expect, the pore scale heterogeneity controls the preferential flow paths in control case, where no nanoparticles are present. More importantly, Figure 4 is positive confirmation that nanoparticles divert flow of non-wetting fluid from an area of large grain and pores into a region of smaller pores and lower permeability previously inaccessible. These observations provide insight to the potential mechanisms by which nanoparticle affect flow patterns during drainage displacements.

A simple working hypothesis involves the physics of pore filling. When a non-wetting phase invades a pore saturated with wetting fluid, it progresses until the fluid-fluid interface attains a critical curvature at the smallest radius. Any additional advancement of the invading non-wetting fluid disrupts the configurational stability of the two-phase interface, and an instantaneous decrease in local capillary pressure during this process creates disconnected droplets of non-wetting fluid advancing to the next pore (Roof, 1970). This is known as Roof snap-off. Normally, as each new invading fluid droplet is created, they coalesce and saturate the pore before invading the adjacent pore. In the presence of nanoparticles, however, the subsequent non-wetting droplets are armored by the surrounding nanoparticles during Roof snap-off events, which prevent coalescence and leave separated droplets in the pore (Binks and Horozov, 2006).

One question is whether enough droplets form to make an actual emulsion with lamellae spanning the pores. Previous experiments imaged at the mm scale by DiCarlo et al (2011) and Aminzadeh et al (2013) showed regions of intermediate density when nanoparticles are present; this can either be an artifact of the relatively poor visual resolution, or suggest the in-situ formation of a separate intermediate saturation phase (i.e. an emulsion).

In actuality, Result 3 does not preclude emulsions. Any emulsion lamellae, consisting of a film of nanoparticle dispersion with a thickness of 10s of nm, would be too small to be seen even at this enhanced resolution (~15µm/voxel). If lamellae are present but not visible, an emulsion phase would appear as octane. To confirm the presence of emulsion, in future study, we will perform similar experiments at ~1µm/voxel with higher concentration of NaI. At this resolution, we will not be able to observe films directly (sub-voxel sized features); however grayscale change within the pore would suggest the presence of an intermediate phase.

However, what has been clearly demonstrated is the efficacy of nanoparticles to address preferential flow due to viscous instability in heterogeneous rocks. As found in result 4, the spatial variation in grain sizes correlates to the preferential flow paths observed in the control experiment. Those same flow paths were inhibited during the nanoparticle experiment, resulting in higher contact area between octane and brine. This provides positive confirmation that the mechanism by which nanoparticles improve immiscible displacements during drainage processes is a function of pore scale heterogeneity. Again, whether the exact mechanism is from pore blocking by individual droplets or the viscosification of n-octane through in-situ emulsion generation, this has yet to be determined.

It should be noted that how a small difference in grain size lead to a large improvement in flow pattern (See Figure-5). Differences in grain sizes and level of heterogeneity occur naturally in geologic media and often vary across many orders of magnitude, which begs the question as to what extent can nanoparticles effectively improve subsurface displacement processes? Future work will be conducted with unconventional rocks or rocks with larger permeability contrast (e.g., with a fracture).

CONCLUSION

A pair of drainage experiments in a sandstone core were performed to measure the sweep efficiency of n-octane following injection. 3D micro-CT scanning is used for a comprehensive petrophysical analysis of the core to correlate pore scale properties with core scale flow patterns.

When surface treated silica nanoparticles are present in the resident brine, we observe a higher pressure drop, later breakthrough, and lower residual brine saturation. Through micro-CT scanning, we visualize improved n-octane volumetric sweep efficiency. An analysis of core grain sizes indicates that the n-octane flow path was dictated by grain size. In the absence of nanoparticles, n-octane flows in a region of large grains and bypasses

regions of smaller pores. With nanoparticles, n-octane sweep was enhanced to reach more areas previously bypassed characterized by small grains and pores. This is attributed to the in-situ generation of octane-in-brine droplets during pore scale Roof-snap off events, which work to block pores, increase local pressure, and divert flow to low permeability regions.

The observations noted in this paper have significant implications on a variety of subsurface displacement processes, including EOR, CO_2 sequestration, and water injection in oil wet reservoirs. With a deeper petrophysical understanding of this phenomenon of nanoparticle enhanced volumetric sweep efficiency, we can greatly improve oil production from gas EOR, CO_2 storage capacity for geologic sequestration, and other similar subsurface fluid displacement processes.

ACKNOWLEDGEMENTS

REFERENCES
1. Aminzadeh, B., D. Chung, X. Zhang, S. Bryant, C. Huh, D. DiCarlo. (2013). Influence of Surface-treated Nanoparticles on Displacement Patterns during CO_2 Injection. Paper SPE 166302
2. Aroonsri, A., Worthen, A. J., Hariz, T., Johnston, K. P., Huh, C., & Bryant, S. L. (2013, September 30). Conditions for Generating Nanoparticle-Stabilized CO_2 Foams in Fracture and Matrix Flow. SPE. doi:10.2118/166319-MS
3. Binks, B., and T. Horozov. (2006). Colloidal Particles at Fluid Interfaces: an Introduction, in Colloidal Particles at Liquid Interfaces, pp. 1-74, Cambridge Univ. Press, Cambridge, U.K.
4. DiCarlo, D., B. Aminzadeh, M. Roberts, D. Chung, S. Bryant. (2011, December 2011). Mobility Control though Spontaneous Formation of Nanoparticle Stabilized Emulsions. Geophysical Research Letters, Vol. 38, L24404
5. Ghous, A., Senden, T. J., Sok, R. M., Sheppard, A. P., Pinczewski, V. W., Knackstedt, M., A., (2007). 3D characterisation of microporosity in carbonate cores. in *SPWLA Middle East Regional Symposium.*
6. Latham, S. J., Varslot, T., Sheppard, A. P. (2008). Image registration: enhancing and calibrating X-ray micro-CT imaging, pp. 1-12, Proc. of SCA, Abu Dhabi
7. Roof, J. G. (1970), Snap-off of oil droplets in water-wet pores, SPE J., 10, 85–90.
8. Worthen, A. J., Bagaria, H. G., Chen, Y., Bryant, S. L., Huh, C., and Johnston, K. P., (2013). Nanoparticle-stabilized carbon dioxide-in-water foams with fine texture, J. Colloid Interface Sci, v. 391, p. 142-151.

ROCK STRENGTH PREDICTION DURING CORING OPERATION

Dee Moronkeji, Raul Villegas, Richard Shouse and Umesh Prasad
Baker Hughes, Houston, TX, USA

This paper was prepared for presentation at the International Symposium of the Society of Core Analysts held in Vienna, Austria, 27 August – 1 September 2017

ABSTRACT

Coring operations have become more challenging as tougher conditions are encountered more frequently. Hole stability, rock strength, temperature, depth, mud weight and other parameters directly affect core recoveries and quality. It is therefore important to have reliable information during the pre-planning phase. Rock strength and mechanical specific energy (MSE) can help to improve coring system and core bit selection to aim towards a better recovery and higher core quality for more representative tests.

There are different factors that can affect drilling efficiency and core recovered. Some of these factors are fixed and cannot be changed such as lithology, rock strength and downhole insitu stresses. The factors that are variable and can be optimized are drilling processes and parameters. To optimize the drilling process and overall core recovery, the variable factors have to be analyzed. Gstalder and Raynal [1] noted however that drillability of rocks cannot be defined absolutely or using a single test because of the many variables during drilling. The main purpose of this study is to validate the analytical predictive strength model used as input to aid in coring technology selection and compare to strength measurements in the laboratory. Analytical rock strength is derived from acoustic and bulk density data in real-time in order to do a coring analysis. Unconfined compressive strength (UCS) and indirect tensile strength (BTS) were measured in the laboratory for three different lithologies and cement to determine the rock strength. The measured laboratory UCS correlates very well to the analytical predicted UCS from our model for low to medium strength rocks, giving high confidence in our prediction to optimize the drilling process for better core recovery. Unique realtime downhole measurements from a specific formation can also be used to estimate MSE and the output used for the planning stage of coring operations. The total energy required to remove a unit volume of rock is the MSE. Parameters such as weight on bit (WOB), torque, rate of penetration (ROP) and rotation per minute (RPM) can be controlled during drilling to help minimize MSE to improve efficiency. This study is an effort to characterize strength in different lithologies and use this knowledge in planning coring operations in increasingly difficult environments and to improve the drilling efficiency, optimize performance and reduce cost per foot with minimized non-productive time (NPT).

INTRODUCTION

Reliable knowledge of rock strength is important for successful coring operations especially in areas where no previous coring knowledge is available. Therefore rock strength estimation from logs becomes very vital and must use formation specific empirical strength correlations to guide in obtaining intact core samples. Complicating this rock strength empirical correlation are the dependence of rock strength on mineralogy and microstructure of the rock. Khaksar et al. [2] discussed in detail the importance of using multiple variables, as using a single variable alone might not sufficiently capture the rock strength. We have made an attempt to use different coring parameters and rock mechanical properties estimated from logs and laboratory measurements to look at trends that can guide in optimizing coring efficiency. The coring operation was conducted at the Baker Experimental Test Area (BETA) well located in Okmulgee County, Oklahoma. Logging information was available during the drilling process previously done in the well in the Glenpool field and recently in 2016 when the whole cores were obtained in the sandstone, shale and in the basement granite. The well had previously been cemented with light gray oilfield cement at the shallow depths between 400-462 ft. and this was also cored and tested. The sandstone, shale and sandy shale formations were cored between 490-521 ft. as shown in the lithology in Figure 1 and the granite from the basement rock was cored from 5385-5388 ft. The predominant rock type cored in this well is shale. Figure 2 shows a set of four samples prepared from the whole core in each lithology tested.

CORING OPERATION

Parameters such as lithology, porosity, rock structure (fracture or consolidated) and rock strength are key inputs needed for successful coring operation using the best coring technology selection available.

All of these parameters are taken into consideration during the planning phase of a coring operation to make the best selection for core bit, coring technology and barrel length.

If proper selection is made, core recovery (core recovered/core cut) and core efficiency (core recovered/barrel length) will be optimized. Time spent on a coring operation is directly related to barrel length, the bigger the length the more time that will be required for every stage of the coring operation (making-up, coring downhole, breaking-out and recovering the core). UCS, lithology and formation properties play a key role to decide the most suitable barrel length to improve core efficiencies.

UCS is particularly useful for core bit selection to optimize core quality and ROP. Predicting reliable UCS can help in selection of different features such as:

1. Cutter size: Appropriate cutter size selection for the UCS range of the target formation will help to improve core quality by delivering a smooth cutting action to reduce reactive torque and vibrations that may cause induced fractures. New generation cutters provide high wear and impact resistant PDC cutters which is important for extended coring runs.
2. Blade count: Although the main objective in a coring operation is to acquire high quality samples, ROP plays an important role on rig time and is always desired to

be as high as possible without compromising quality. Normally the harder the formation, the bigger the blade count in a PDC core bit. Efficient cuttings removal brings higher ROP and is normally easier to achieve efficient removal with a low blade count. This is why it is important to look into new generation core bits that incorporate the latest technology, new matrix materials (core bit body) improvement to reduce erosion, CFD (Computational Fluid Dynamics) analysis to optimized blade count and next generation cutters to find the right balance between durability and ROP.

3. Gauge Pads: Plays an important role to minimize torsional and lateral vibrations to help deliver a high quality core. Gauge protection materials need to be taken into consideration as well, a high UCS formation would normally require premium protection to perform at its best for a longer period of time.

ROCK MECHANICAL PROPERTIES (RMP)

Acoustic log data for the determination of formation elastic properties has been widely used due to its known physical relationships, Coates and Denoo [3]. A direct calculation of elastic properties (Young's Modulus, Shear Modulus, Bulk Modulus and Poisson's ratio) based on physical relationships to the direct measurement of formation density and acoustic wave velocities exists.

To calibrate the log-derived rock mechanical properties (RMP), testing consisting of unconfined triaxial tests for static elastic properties and rock strength, X-Ray diffraction (XRD) to identify and quantify minerals present in the samples and indirect tensile strength (BTS) for rock strength. Compressional and shear wave ultrasonic velocity measurements as a function of hydrostatic stress testing for dynamic elastic properties determination were also conducted. All the samples were tested as received with the bulk density estimated from the physical dimensions and weight. Almost all the available log data correlations to rock strength are typically derived from acoustic wave velocities, porosity and formation density, Chang et. al. [4] and Zoback, M. [5]. The compressional slowness (DTC) and shear slowness (DTS) gives a good correlation to UCS. It should also be noted that DTS is less affected by formation fluid (gas) than compressional slowness (DTC). Mason [6] also showed an excellent correlation between shear velocity and UCS and then developed a bit selection method based on DTS from log data. When high quality processed DTS is available, it gives a better correlation to UCS. Irrespective of the rock type it is obvious that the trend obtained is UCS decreasing with increase in acoustic slowness with either DTC or DTS.

A proprietary correlation is used to estimate the strength based on acoustic slowness and gives a good match both on the DTC and DTS for the shale lithology but seems to under predict the strength in the sandstone as shown in Figure 3. The proprietary correlation is the DTC_UCSLOG and DTS_UCSLOG in Figure 3. In this case, the acoustic slowness relationship with the laboratory measured strength for the sandstone and granite seems to be better predicted by Freyburg [7] correlation. It should be noted however that the Freyburg [7] correlation is based on the compression velocity. The relationship between laboratory measured UCS and ROP is shown in Figure 4 with the ROP increasing with

lower strength. The RPM was kept constant throughout the coring process and as expected there is lower ROP and higher strength in the sandstone and granite samples, while the shale and cement samples exhibited higher ROP and lower strength. Curry et al. [8] showed that penetration rate is sensitive to both borehole pressure and formation fluid as well. The laboratory measured results of the triaxial and ultrasonic tests are shown in Table 1. Correlation of UCS with Young's modulus (Stiffness) shows the correlation as expected in Figure 5 with low to medium strength region for cement and shale, and high strength region for sandstones and granite (Coates and Denoo [3]). Correlation between dynamic Young's modulus (Ultrasonic laboratory testing) to static Young's modulus (Triaxial laboratory testing) on cement, shale and granite is shown in Figure 6. It shows a good correlation with the dynamic values higher than the static values as expected, however only three ultrasonic tests were available, no ultrasonic measurements were done on the sandstone sample.

The similar strength in the sandstone and granite shown in Table 1 might be due to the mineralogical composition between the two rock samples. The XRD shows the sandstone to be predominately quartz (90%) whereas the granite consists predominately of feldspar (54%), quartz (29%) and chlorite (10%). The low strength in the granite might be due to the presence of chlorite, Yatabe et al. [9] found the presence of weak clay minerals like chlorite and smectite to lower strength. Correlation between Young's modulus and ROP is shown in Figure 7, showing increase in ROP with decrease in Young's modulus, implying as expected that stiffer rock is harder to core.

XRD was conducted only on six samples, four shale samples and one each of sandstone and granite. Consequently, the grain modulus was estimated from the mineralogical composition of each rock type tested and its relationship to ROP is shown in Figure 8. The correlation between Grain modulus and ROP shows a good trend with lower grain modulus corresponding to increase in ROP. The use of wireline mineralogical logs for weight and volume percent of the mineralogical composition of the rock might come in handy due to the findings in Figure 8 and may be used to estimate ROP during coring process. This relationship needs to be explored more with a larger dataset.

For QA/QC, the bulk density is also plotted with UCS and Indirect tensile strength in Figures 9 and 10 showing increase in strength as expected in both plots as formation bulk density increases. The ratio of indirect tensile strength to UCS seems low in this formation, as low as 3-5 times the UCS in the three lithologies.

MECHANICAL SPECIFIC ENERGY (MSE)
Teale proposed the concept of Mechanical Specific Energy (MSE) in the 60's and discovered that minimizing MSE would maximize drilling and result in maximum rate of penetration (Teale [10]). The total energy required to remove a unit volume of rock is the MSE. Parameters such as weight on bit (WOB), torque, rate of penetration (ROP) and rotation per minute (RPM) can be controlled during drilling to help minimize MSE to improve efficiency.

Pessier and Fear [11] showed that when specific energy is approximately equal to the UCS of a rock, then the minimum specific energy has been reached. This principle holds in oil

and gas drilling under confining pressure. The efficiency hardly reaches 35% and under ideal conditions it reaches the UCS if drilling is efficient.

Minimizing MSE will therefore improve drilling efficiency as shown in equation (1). Pessier and Fear [11] also developed a bit specific coefficient (μ) to express torque as a function of WOB as shown in equation (2).

$$MSE = WOB \left(\frac{1}{B_A} + \frac{13.33\mu * RPM}{B_D * ROP} \right) \tag{1}$$

$$\mu = 36 \frac{T}{B_D * WOB} \tag{2}$$

MSE was calculated based on the drilling and coring surface data in the different lithology and correlated to ROP. MSE correlation to ROP during drilling of the well is shown in Figure 11, note that drilling data was only available for shale and sandstone. MSE is high at low ROP and decrease as ROP increases. MSE seems to be higher in shale and therefore reducing drilling efficiency as compared to the sandstone, this could be due to the mineralogy of the shale and it has also been shown by Pessier and Fear [11] that higher sand content increases ROP and reduces specific energy. Hamrick [12] also showed that if rocks are broken into pieces smaller than necessary, this would lead to more energy expenditure than required. It should also be noted that in the 60 ft. of data analyzed in Figure 11, it is predominantly a shale to sandy–shale lithology and only ~14ft. of sandstone layer. MSE correlation to ROP during the coring operation is shown in Figure 12 and covers the four samples cored in this well. Similar trend is obtained as during drilling.

Average rate of penetration, unconfined compressive strength and static Young's modulus is shown in Table 2 for cement, shale, sandstone and granite. Even though the strength is not significantly different between the sandstone and granite, the average ROP significantly drops in the granite. The very low ROP in the granite might also be due to the bit available for this coring which is not the main choice for this type of hard formation but was used so as to be able to make comparison between the lithology. As explained previously also, the presence of chlorite in the granite might have caused the lower strength but the presence of feldspar and quartz still made it significantly difficult to core with this bit even with lower strength than usual for a granite.

CONCLUSION

The use of log based rock mechanical properties can help to determine coring parameters as both strength (UCS) and stiffness (Young's modulus) correlates well with ROP.

The log predicted UCS based on DTS correlates well with the laboratory measurement as the maximum UCS predicted during the coring was 3500 psi and 14000 psi, respectively for shale and granite. However additional empirical correlation was needed for the sandstone, this might be due to few sandstone cored and tested. Grain modulus seems to show a good correlation with ROP, however we have limited data and this needs to be further investigated as a parameter to predict ROP through wireline mineralogical logging or XRD analysis when core samples are available. Figure 11 showed that when MSE

decreased in the deeper shale, ROP increased. Drilling efficiency can be optimized by changing parameters such as WOB and RPM, so as to increase the ROP. Unique realtime downhole measurements from specific formations will be explored further in future work to estimate MSE based on the initial trends observed in this study.

NOMENCLATURE
B_A = Cross sectional area of bit (in^2)
B_D = Bit Diameter (in)
MSE = Mechanical Specific Energy (psi)
WOB = Weight On Bit (lbf)
ROP = Rate of Penetration (ft/hr)
RPM = Rotations Per Minute (rev/min)
Torque = Rotational torque (ft-lbf)
μ = Bit Specific Coefficient of Sliding Friction
BTS = Indirect tensile strength

ACKNOWLEDGEMENTS

REFERENCES
1.   Gstalder, S. and Raynal, J., "Measurement of Some Mechanical Properties of Rocks and Their Relationship to Rock Drillability," *SPE Petroleum transactions, SPE 1463*, (August 1966).
2.   Khaksar, A. et al., "Rock Strength from Core and Logs: Where we Stand and Ways to Go," SPE 121972 Presented at the SPE EUROPEC/EAGE Annual Conference and Exhibition held in Amsterdam, The Netherlands, (June 8-11, 2009).
3.   Coates, G.R. and Denoo, S.A., "Mechanical Properties Program Using Borehole Analysis and Mohr's Circle," SPWLA Twenty-Second Annual Logging Symposium, (June 23-26, 1981).
4.   Chang, C., Zoback, M.D. and Khaksar, A., "Empirical Relations between Rock Strength and Physical Properties in Sedimentary Rocks," *Journal of Petroleum Science & Engineering,* (2006) **vol. 51**, 223-237.
5.   Zoback, M.D., *Reservoir Geomechanics*, Cambridge University Press, New York, (2008), 107-118.
6.   Mason, K.L., "Three-Cone Bit Selection with Sonic Logs," *SPE Drilling Engineering,* (June 1987), 135-142.
7.   Freyburg, E., "Der Untere und mittlere Buntsandstein SW-Thuringen in seinen gesteinstechnicschen Eigenschaften," Ber. Dtsch. Ges. Geol. Wiss., A; Berlin 176, 911-919.

8.   Curry, D., Fear, M., Govzitch, A. and Aghazada, L., "Technical Limit Specific Energy-An Index to Facilitate Drilling Performance Evaluation", Paper SPE/IADC 92318 presented at the SPE/IADC Drilling Conference, Amsterdam, The Netherlands, (February 23-25, 2005).

9.   Yatabe R., Yagi N., Yokota K. and Bhandary N.P., "Influence of expansive chlorite on the strength of weathered Green Rock at Mikabu Belt of Japan," Proceedings of International Conference on Geotechnical and Geological Engineering, Melbourne, Australia, (November 19-24, 2000).

10.   Teale R., "The Concept of Specific Energy in Rock Drilling," *International Journal of Rock Mechanics and Mining Sciences & Geomechanics Abstracts* 2, (March 1965), no. 1, 57–73.

11.   Pessier, R.C. and Fear, M.J., "Quantifying Common Drilling Problems with Mechanical Specific Energy and a Bit-Specific Coefficient of Sliding Friction," SPE 24584 presented at the SPE 67th Annual Technical Conference and Exhibition, Washington, DC, (October 4-7, 1992).

12.   Hamrick, T.R., "Optimization of Operating Parameters for Minimum Mechanical Specific Energy in Drilling," *Dissertation submitted to the College of Engineering and Mineral Resources at West Virginia University* in partial fulfillment of the requirements for the degree of Doctor of Philosophy, Mechanical Engineering, (2011).

Table 1: Triaxial and Ultrasonic laboratory Test Results

Lithology	Triaxial (Static)							Ultrasonic (Dynamic)					
	Bulk Density	Unconfined compressive strength	Poisson's Ratio	Young's Modulus	Shear Modulus	Bulk Modulus	Lame's Constant	Compressional slowness	Shear slowness	Poisson's Ratio	Young's Modulus	Shear Modulus	Bulk Modulus
	DEN	UCS	v	E	G	K_b	λ	DTC	DTS	vd	Ed	G	K
	g/cc	psi		Mpsi	Mpsi	Mpsi	Mpsi	us/ft	us/ft		Mpsi	Mpsi	Mpsi
Cement	1.73	2421.5	0.12	1.16	0.52	0.51	0.17						
	1.66	1741.5	0.09	0.91	0.42	0.37	0.09						
	1.72	1421.0	0.09	0.88	0.40	0.36	0.09						
	1.71	1589.2	0.13	1.15	0.51	0.52	0.18						
	1.67	1930.5	0.10	1.06	0.48	0.44	0.12						
	1.81	2217.6	0.22	1.01	0.41	0.61	0.34						
	1.81	2234.5	0.13	1.00	0.44	0.45	0.16						
	1.77	2463.6	0.11	1.25	0.56	0.53	0.16						
	1.73	1628.4	0.12	1.03	0.46	0.45	0.14						
	1.78	1666.1	0.07	0.90	0.42	0.35	0.07	136.0	251.00	0.29	1.02	0.40	0.81
Shale	2.51	3206.0	0.11	0.76	0.34	0.33	0.10	167.0	312.00	0.30	0.89	0.34	0.74
	2.49	3859.9	0.06	1.00	0.47	0.38	0.06						
	2.49	3030.5	0.10	1.04	0.47	0.43	0.12						
	2.43	3037.8	0.02	0.98	0.48	0.34	0.02						
Sandstone	2.62	13718.5	0.07	4.78	2.23	1.87	0.38						
	2.48	10421.2	0.09	3.44	1.58	1.39	0.34						
	2.61	12406.2	0.05	4.25	2.03	1.58	0.22						
Granite	2.74	12325.0	0.09	5.40	2.48	2.19	0.54						
	2.65	12309.1	0.12	6.02	2.68	2.66	0.88						
	2.65	10722.8	0.11	6.95	3.12	3.00	0.92						
	2.62	13505.3	0.16	7.12	3.07	3.50	1.46						
	2.63	14040.4	0.14	6.55	2.88	3.01	1.09						
	-	13881.0	0.29	2.69	1.04	2.13	1.44	91.0	163.00	0.28	3.42	1.34	2.59

Table 2: Average Coring Data and Rock Properties in the Samples

Lithology	Avg. ROP	Avg. UCS	Avg. Static Young's Modulus
	Ft./hr.	psi	Mpsi
Cement	129	1919	1.04

Shale	65	3365	0.95
Sandstone	58	12182	4.16
Granite	0.5	13773	6.83
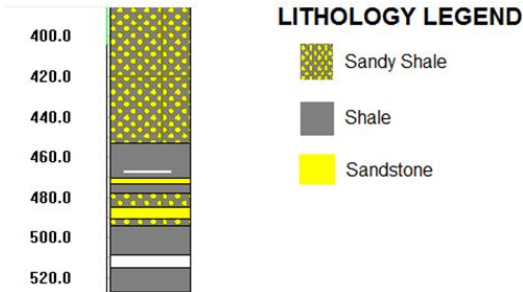
Figure 1: Lithology and Depth of Rocks Cored
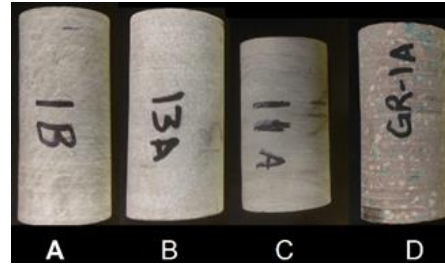
Figure 2: (A) Cement (B) Sandstone (C) Shale and (D) Basement Granite
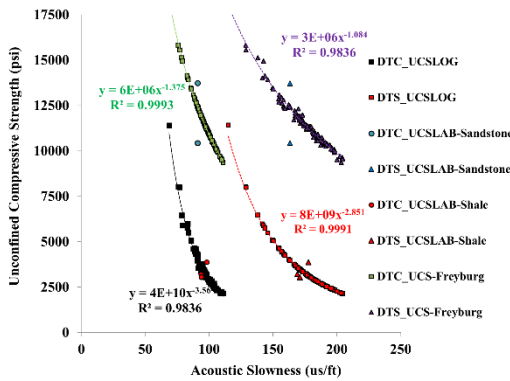
Figure 3: Unconfined Compressive Strength and Acoustic Slowness
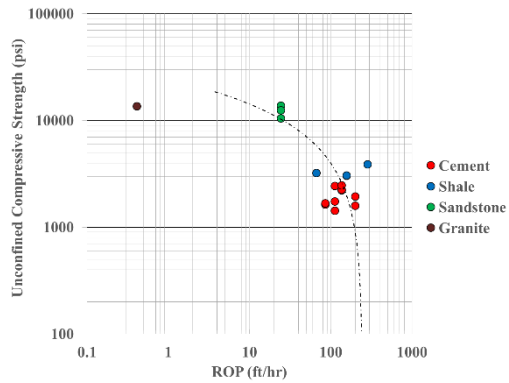
Figure 4: Laboratory Measured Unconfined Compressive Strength and Rate of Penetration during Coring
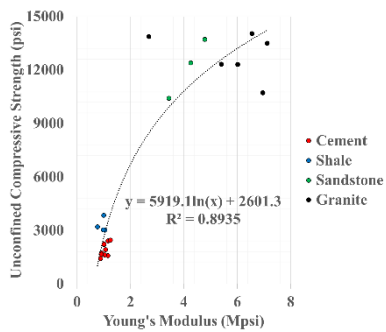
Figure 5: Unconfined Compressive Strength and Young's Modulus Correlation
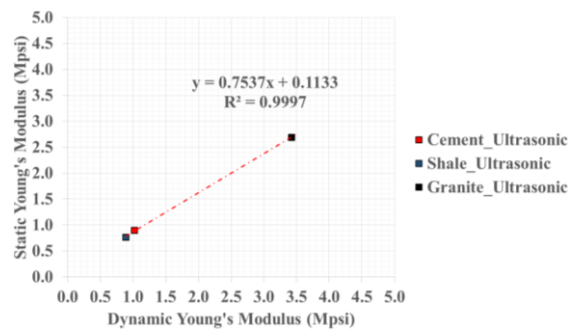
Figure 6: Dynamic to Static Young's Modulus Correlation
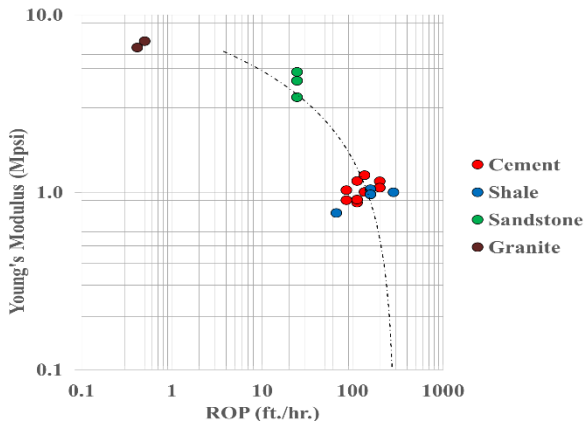
Figure 7: Young's Modulus and Rate of Penetration
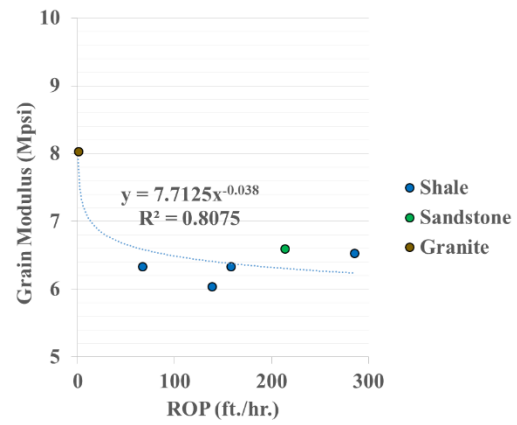
Figure 8: Grain Modulus and Rate of Penetration
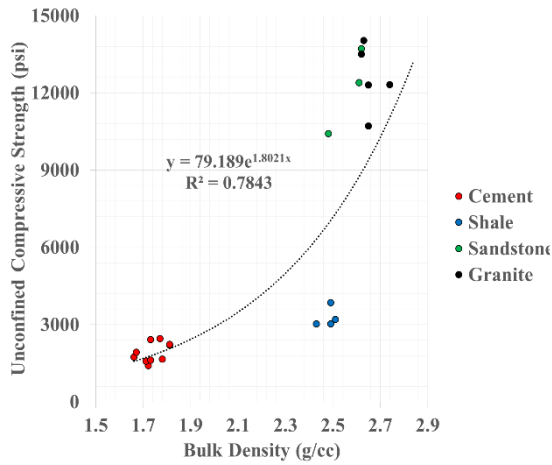
Figure 9: Unconfined Compressive Strength and Bulk Density Correlation
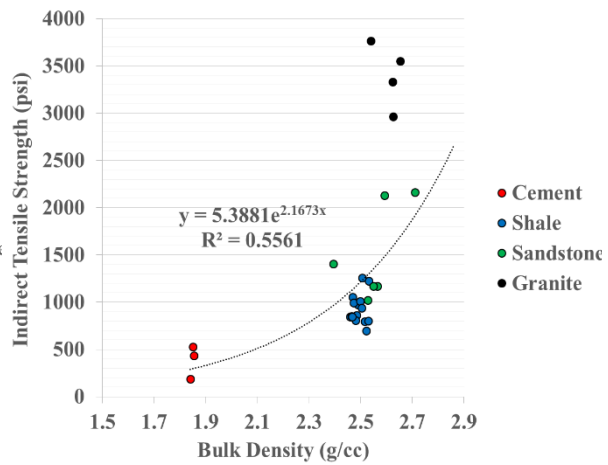
Figure 10: Indirect Tensile Strength and Bulk Density Correlation
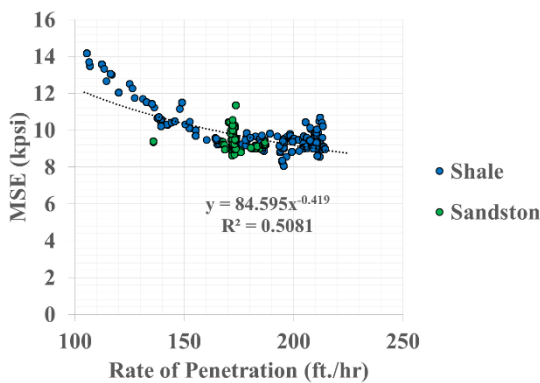
Figure 11: MSE Change with Rate of Penetration (ROP) in Shale and Sandstone during Drilling
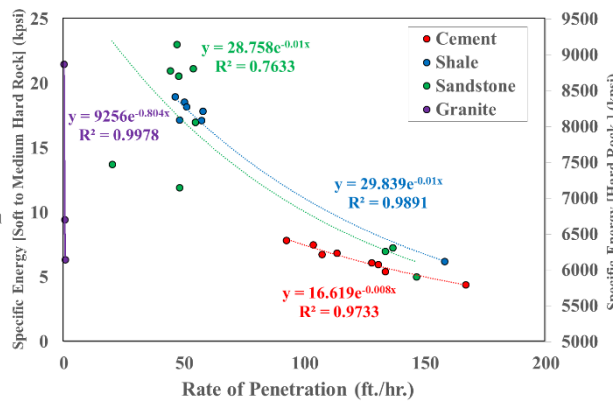
Figure 12: MSE Change with Rate of Penetration (ROP) during Coring Operation

APPLICATION OF CORE ANALYSIS TECHNIQUES FOR TIGHT ROCKS FOR THE INVESTIGATION OF BOREHOLE CEMENT

Marisa B. Rydzy, James Heathman, Chad Broussard, Jorge Patino,
Nours Elmetni, Aaron Dhaemers, and Matthias Appel
Shell International Exploration and Production, Houston, TX

ABSTRACT

In this study, we performed water and gas permeability measurements on borehole cement using core analysis techniques that had previously been applied to nano-porous rocks, such as shale and tight sand. A series of plug-sized samples produced from five different cement mixtures were subjected to water and gas permeability measurements, nuclear magnetic resonance (NMR) spectroscopy, mercury injection capillary pressure (MICP) tests, and micro x-ray computed tomography (MXCT) scans. The water permeability of all cement plugs fell in the low nano-Darcy range. The difference in permeability among cement types was small but consistent and appeared to be primarily a function average pore size (calculated as weighted average) as indicated by MICP (and NMR). Results from time-dependent water permeability and NMR measurements showed a decrease in permeability and pore size as cement continued to cure. MXCT images of the tested plugs revealed the presence of bubbles within the cement. With the help of basic digital rocks analysis technology, we were able to quantify the size and amount of the bubbles and calculate a bubble size distribution for each imaged sample. Overall, the bubbles did not contribute significantly to the cement porosity (less than 1 porosity unit). Other than introducing a certain degree of heterogeneity, the isolated void spaces appeared not to affect the fluid flow. Gas permeabilities were measured after the samples had been dried. The resulting permeability values were higher than the ones measured with water by orders of magnitude which was likely due to drying-induced fractures and gas slippage.

INTRODUCTION

The main purpose of borehole cement is to provide a hydraulic seal between casing and formation (Nelson, 1990) over the lifetime of a well. The permeability of cement not only characterizes its effectiveness as a sealant but also provides a measure of durability

(Manmohan and Metha, 1981; Bathia and Mindness, 1989). The pore structure of cement depends on variety factors, including the composition of the cement mixture (class, water-cement ratio, additives), as well as setting time and temperature (e.g. Goto and Roy, 1981; Talabani and Hareland, 1995; Atahan et al., 2009). Cement represents physically and chemically complex nano-porous system. Portland cement represents the most common type of hydraulic cement and is primarily composed of finely powdered tricalcium silicate, dicalcium silicate, tricalcium aluminate, and tricalcium aluminoferrite, as well as small amounts of gypsum (Michaux et al., 1990). Depending on the fraction of each of these compounds Portland cement is divided into 8 groups (Classes A-H; Nelson, 1983). When the cement components are mixed with water, a chemical reaction between compounds and water occurs (a.k.a. hydration), whereby an unstable, supersaturated solution is formed from which new solids precipitate and grow into the water-filled pore space. As cement hardens (sets, cures, or ages), its compressive strength increases while porosity and permeability decline (e.g. Powers, 1956; Michaux et al. 1990).

A number of studies have been dedicated to the investigation of Portland cement permeability. The very first cement permeability results that were published, had been obtained from gas flow experiments on dried cement plugs (Coleman and Corrigan, 1940). Morgan and Dumbauld (1952), questioned the approach as drying of set cement was (and still is) believed to alter its physical and chemical properties. They recognized that permeability measurements on cement needed to be conducted with water, which became the standard approach in the following years. Subsequent publications presented results from water permeability measurements of cement as functions of cement-water ratio, curing time and temperature, cement fineness, pore size distribution, and content of a variety of additives (e.g. Manmohan and Metha, 1981; Nyame and Illston, 1981; Banthia and Mindness, 1989; Talabani and Hareland, 1995; Ai et al., 2001; Vichit-Vadakan and Scherer, 2002, 2003; Ye, 2005, and many more). With the advance of computational capabilities in recent years, pore-network models and simulations have become the focus of cement permeability studies (Zalzale et al., 2010; Hu and Stroeven, 2011; Wong et al., 2012). Interestingly, the simulation results best corresponded with gas permeabilities measured in dried cement plugs, which may have prompted a resurgence of this measurement approach as the most recent cement permeability measurements have been conducted with gas (Wong et al., 2009; Zhang et al., 2014; LeMinous et al., 2017). Overall, published cement permeability results vary widely and range over several orders of magnitude from nd to md range. Aside, from the effect of compositional differences and curing time/conditions, a number of other reasons have been proposed to explain the wide data spread, including delayed hydration, fines migration, or variation in water saturation (Zalzale et al. 2010). In addition, some inconsistency can surely be attributed to the differences in measurement procedures and data quality.

In this study, we tested a series of cement plugs formed from a number of different cement mixtures. The main focus on the study were on water (and gas) permeability measurements that were conducted with experimental setups that had previously been used to measure ultra-low permeabilities in nano-porous rocks, such as shales. The objective of the study at hand was to compare permeabilities of different cement types and to observe the time-dependency of their permeability response. Micro X-ray computed tomography images of the plugs, NMR T2 spectra, and pore-size distribution curves from mercury injection capillary pressure tests were also acquired to aid in the interpretation of the permeability data.

SAMPLES AND EXPERIMENTAL PROCEDURES

We tested plugs that had been prepared from 5 different Portland cement mixtures (API classes H, A, or G with a variety of different additives, **Table 1**) according to API RP 10B-2 specifications. The cement slurries had been poured into 2.54-cm diameter cylindrical molds and allowed to cure for 1 week. The resulting cement plugs were cut/trimmed to a length of about 2.54 cm and weighed. The amount of free water in the cement plugs was determined based on T2 measurements with a 2 MHz nuclear magnetic resonance (NMR) spectrometer. **Table 1** provides an overview of the different cement types tested as well as a summary of cement plug properties, such as the average plug density, volume fraction of unbound water (NMR-Phi), and the logarithmic average of the relaxation time (Log Mean T2). The latter is loosely related to the average pore size. All values listed in **Table 1** represent an average of results from tests on at least 8 cement plugs. Water permeability measurements were performed on 2-4 plugs per cement type.

Table 1: Overview of cement samples and their average properties (W/C mass ratio of water and cement)

Cement	Description	W/C	Strength	ρ, g/cc	ϕ_{NMR}, %	Mean T2
C-1	Class H	0.39	5150 psi	2.00±0.04	0.328±0.001	0.481±0.021
C-3	Class H + KCl +dead-burnt manganese oxide	0.36	5179 psi	2.09±0.04	0.358±0.011	0.343±0.008
C-4	Class H +dead-burnt manganese oxide+ SBR latex	0.23	5592 psi	2.08±0.06	0.272±0.004	0.282±0.005
C-5	Class A + KCl + silica flour	0.59	3271 psi	1.92±0.07	0.472±0.017	0.516±0.009
C-7	Class G + KCl	0.46	4399 psi	1.98±0.01	0.340±0.008	0.389±0.006

The permeability measurements were conducted using Hassler-type flow cell (Hassler, 1944). The liquid permeameter systems had been designed, constructed, and previously employed for permeability measurements in nano-porous rocks, such as shales (Rydzy et al. 2016). The water permeabilities were measured with DI-water under an effective stress of 4.5 MPa (650 psi) using the steady-state technique. Inlet and outlet pore pressure were set to 6.9 MPa (1000 psi) and 0.7 MPa (100 psi), respectively, resulting in a pressure differential of 6.2 MPa (900 psi) across the plug. The injected water volume was recorded as function of time. From the resulting flow rate, the pressure differential, sample length

and diameter, as well as the water viscosity (1 cP at 30°C), the permeability was calculated using Darcy's Law (e.g. Peters 2012).

In addition to the water permeability testing, we performed gas permeability measurements on dried cement plugs. (The experimental setup is described in Rydzy et al., 2016). The dried cement plugs were subjected to pulse-decay tests under varying effective stresses (from 3.4 to 24.1 MPa or 500-3500 psi in increments of 3.4 MPa or 500 psi). Following the permeability measurements, we acquired micro X-ray CT (MXCT) images of the cement plugs and generated bubble size distribution curves based on the MXCT images using the 3D Object Counter Function in the open source image analysis software IMAGEJ (https://imagej.nih.gov/ij/). The process is shown in **Figure 1**. We also acquired mercury injection capillary pressure (MICP) curves of crushed dried cement particles (particle size between 0.5 and 2.38 mm) from which we calculated weighted pore-throat size averages (**Figure 2**). The MICP measurements were conducted after the samples had been exposed to atmosphere for over 2-4 months. Directly prior to the MICP measurements the plugs had been dried under vacuum at 80°F for about 2 days.
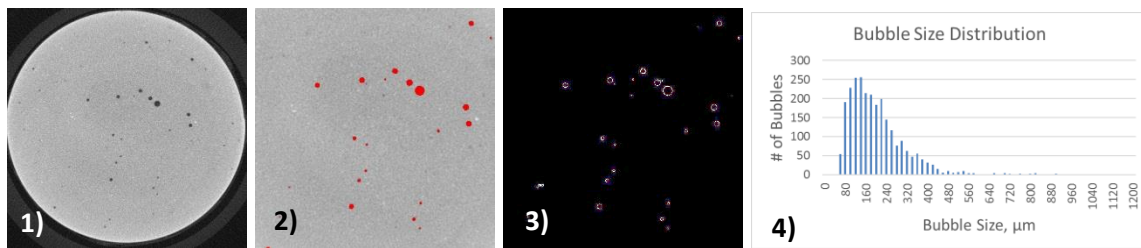
Figure 1: Process of determining a bubble size distribution: the original image (1) was loaded into IMAGEJ and cut into an 800x800x800 pixel3 image volume. A 3D mean filter was applied before the image was segmented (2). The 3D Object Counter Plugin was then run on the segmented image (3). The program data output could then be used to generate a bubble size distribution for the respective plug (4).

RESULTS AND DISCUSSION

After a fast initial hydration reaction, unreacted cement compounds end up being enclosed by a layer of impermeable precipitate. The hydration reaction then becomes diffusion controlled and slows down significantly. Hydration continues with decreasing speed for as long as water and anhydrous compounds are present. This process can take an infinite amount of time. According to Michaux et al. (1990), complete hydration is never attained. As cement sets, its porosity, pore sizes, and permeability continue to decrease. The decrease in these physical properties over time could be observed in results of the water permeability measurements (**Figure 3**).
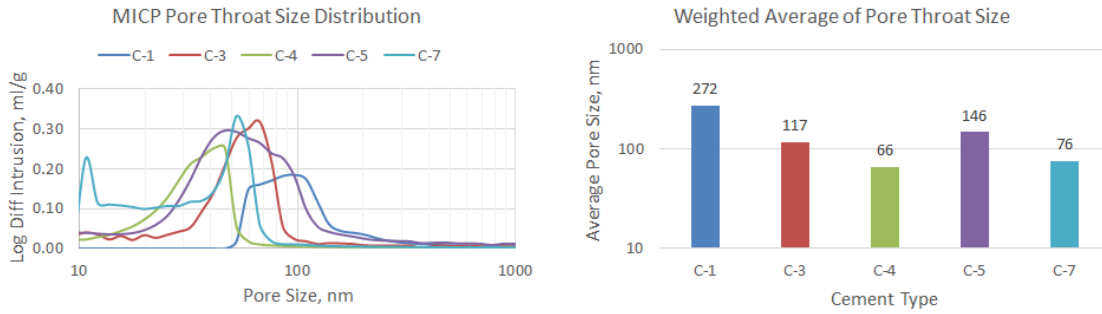
Figure 2: Mercury injection capillary pressure (MICP) pore-throat size distributions obtained for dried cement particles (particle size: 0.5-2.38 mm, left) and the weighted pore throat size average calculated from the MICP data (right)

The water permeability of all samples, except the Cement 4 (C-4) plugs, had been measured over the course of 11 days (**Figure 3**). With the exception of Cement 1 (C-1) all cements had been allowed to set for 10 to 13 days before they were subjected to the water permeability tests. Overall, the water permeability of all samples fell in the low nano-Darcy range with values between 0.5 and 10 nd. The permeability of C-1 plugs was higher than the permeability of all other cements despite the extended setting period. Backward extrapolation of its permeability-time trend approximates a permeability of around 200 nd for the 10th day of curing. **Figure 3** also shows the water permeability of all tested cement plugs averaged over all 11 test days. Even though the difference between permeabilities for different cement types was rather small, the results were consistent among plugs from the same cement batch.
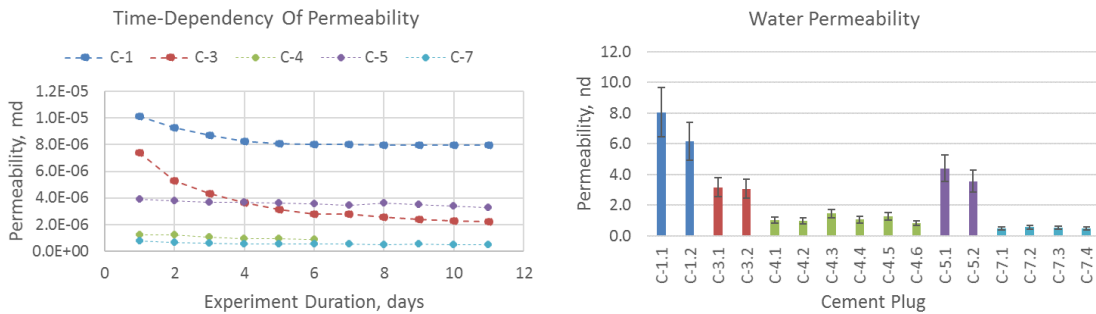
Figure 3: Decrease in water permeability over time (for clarity, only results for 1 plug per batch are shown) and water permeability of all plugs average over all 11 test days

Figure 4 shows the water permeability as a function of NMR-derived porosity, the pore size proxy Log Mean T2, and the MICP-derived weighted average of the pore-throat size distribution. Due to the time-sensitive nature of the results, the permeability values plotted against the NMR data were the ones recorded on the first day of testing as the NMR measurements were performed prior to the water permeability measurements. The MICP

measurements were performed after the permeability was measured. Consequently, the permeability values recorded on the last day of testing were plotted against the weighted average of the pore-throat size distribution. Early discussions regarding fluid flow in cement revolved around the question whether it was porosity, pore size distribution, or pore threshold diameter that determined the cement permeability (Goto and Roy, 1981). The results shown in **Figure 4** clearly indicate that porosity and pore size have little effect on the water permeability overall. A clear correlation, however, was found between the weighted average of the pore-throat diameter distribution (for pore throats smaller than 1000 nm) and the cement permeability measured with water.
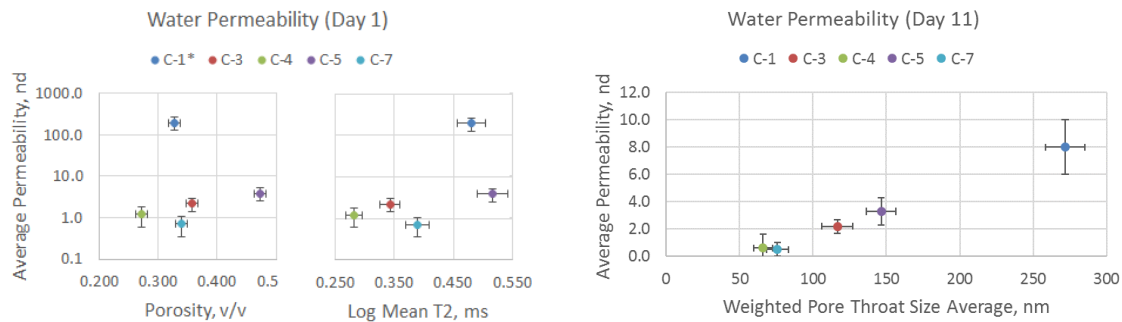
Figure 4: Average water permeability depicted as function of porosity, logarithmic average of the relative pore-size proxy T2, and weighted average of the pore-throat diameter distribution.

After the water-permeability measurements, we dried 4 additional plugs from 2 different cement types (C-1 and C-4), and subsequently performed unstressed helium porosimetry and stressed gas permeability measurements on them. The results are shown in **Figure 5**. The gas permeability values are significantly higher than the corresponding water permeability measurements by several orders of magnitude. At 500 psi effective stress, we obtained permeabilities of $2 \cdot 10^5$ nd and $4.5 \cdot 10^5$ nd for C-1 and C-4 plugs, respectively. These results were typical for gas permeabilities measured in dried Portland cement samples which have been reported as 10^{-17}-10^{-19} m^2 (Wong et al. 2009; Zhang and Talman, 2014; Le-Minous et al. 2017), which corresponds to 10^5-10^7 nd. One reason for the elevated permeability values can be attributed to gas slippage (Klinkenberg, 1941), as the measurements were conducted at an average pore pressure of only 0.7 MPa (100 psi). Gas slippage alone was unlikely to account for the elevated permeability values. Many authors of previous studies suggested that micro-cracks were created by the drying process (e.g. Morgan and Dumbauld, 1952; Talabani and Hareland, 1995; Wong et al. 2009). If micro-cracks were responsible for the increased permeability, it could be assumed, based on the stress-permeability trend, that the plugs of the C-4 cement contained more cracks than the plugs of C1-cement. The C-4 plugs exhibit a much stronger stress-dependency than the C1-plugs (**Figure 5**), despite its compressional strength being higher (**Table 1**).
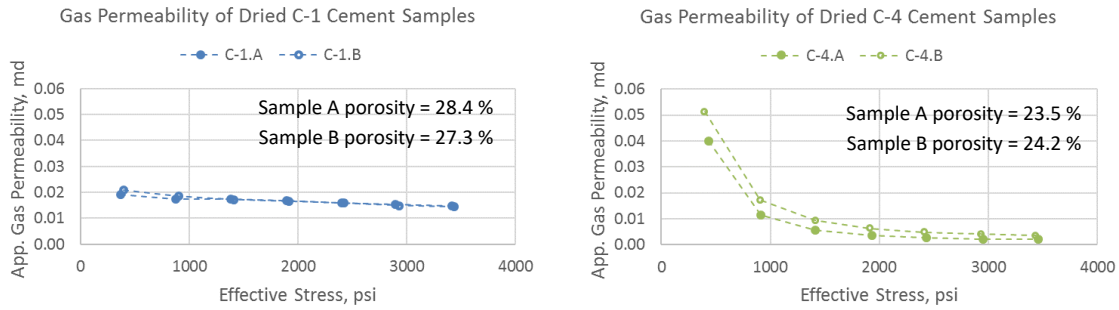
Figures 5: Results of gas permeability measurements on dried cement plugs

Following the permeability measurements, we acquired MXCT scans of the cement plugs to investigate the degree of heterogeneity in the samples. The MXCT images (**Figure 6**) show that isolated spherical void spaces (bubbles) are randomly spread throughout the samples. Quantitative analysis confirmed that number of bubbles, the volume occupied by them, and their size distribution varied between cement types. For example, C-4 plugs exhibited a large number (>10,000) of relatively small bubbles (average bubble size = 123 µm), while C-5 and C-7 plugs contained less bubbles (in the 1000s) of much larger size (average bubble size around 190 µm). Cements C-1 and C-3 contained the least amount of bubbles (in the 10s, with average bubble size of around 180 µm). The volume occupied by bubbles on average only contributed 0.2 to a maximum of 1% (1 porosity unit) to the overall porosity of the cement. As the permeability was primarily a function of the pore throat size distribution and bubbles occurred mostly isolated, we concluded that the effect of the presence of bubbles could be assumed negligible.
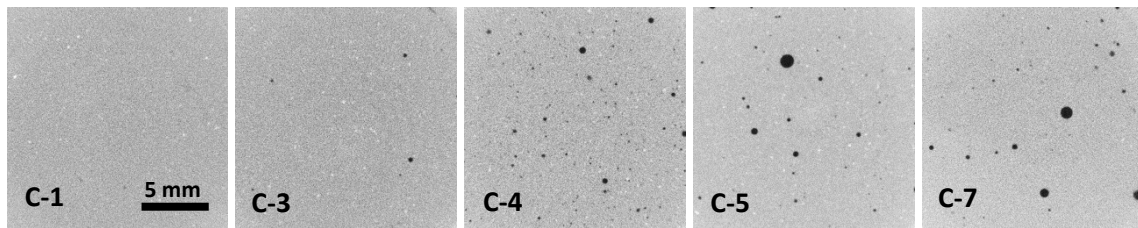
Figure 6: MXCT images (16 mm x 16 mm, pixel length = 20 µm) of cement plugs.

CONCLUSIONS

In this paper, we presented observations and results from core analysis measurements on different types of borehole cement. It was shown that water and gas permeability measurement techniques that had previously been developed for nano-porous rocks, such as shale and tight sand, could be successfully applied to test the nano-porous cement samples. NMR was also shown to be a useful tool for the characterization of the cement plugs as it provided porosity data and some information regarding the relative pore size of the cements. Using MXCT and basic digital rocks analysis techniques we quantitatively

analyzed the larger void spaces (bubbles) in the cement plugs. Results for gas and water permeability, porosities, Log Mean T2, and pore-throat size distribution were consistent among cement plugs stemming from the same batch. It was shown that water permeability was primarily a function of the pore throat size distribution and the curing time. Log Mean T2, and the presence of bubbles in the cement plugs appeared to have little effect on the outcome of the permeability results. As for the way forward:

- Time-dependent NMR measurements could provide additional insight into the effect of the setting process on the pore structure of cement. Note that in between tests the cement plugs would have to be stored in water at a constant temperature to prevent partial drying of the sample and to allow for consistent cement setting kinetics.

- As the bubbles introduce a certain degree of heterogeneity, their presence could theoretically be responsible for the small variation in permeability observed among the plugs of the same cement type. To tests this hypothesis a relatively large number of samples (e.g. ≥4) would have to be tested and imaged to be statistically representative.

- The gas permeability behavior of dried samples under stress may provide insight on how much the cement may have fractured during the drying process. This could be confirmed through higher-resolution imaging of the dried samples.

REFERENCES

Ai, H., Young, J. F., & Scherer, G. W. (2001). Thermal expansion kinetics: method to measure permeability of cementitious materials: II, application to hardened cement pastes. Journal of the American Ceramic Society, 84(2), 385-91.

Atahan, H. N., Oktar, O. N., & Taşdemir, M. A. (2009). Effects of water–cement ratio and curing time on the critical pore width of hardened cement paste. Construction and Building Materials, 23(3), 1196-1200.

Banthia, N., & Mindess, S. (1989). Water permeability of cement paste. Cement and Concrete Research, 19(5), 727-736.

Coleman, J. R., & Corrigan, G. L. (1941). Fineness and water-cement ratio in relation to volume and permeability of cement. Transactions of the AIME, 142(01), 205-215.

Dewaele, P. J., Reardon, E. J., & Dayal, R. (1991). Permeability and porosity changes associated with cement grout carbonation. Cement and concrete research, 21(4), 441-454.

Goto, S., & Roy, D. M. (1981). Diffusion of ions through hardened cement pastes. Cement and Concrete Research, 11(5-6), 751-757.Hearn, N., Hooton, R. D., & Mills, R. H. (1994). Pore structure and permeability. In Significance of tests and properties of Concrete and Concrete-Making Materials. ASTM International.

Hassler, G.L., 1944. Method and apparatus for permeability measurements. US2345935 A.

Hu, J. and Stroeven, P., 2011. Application of image analysis to assessing critical pore size for permeability prediction of cement paste. Image Analysis & Stereology, 22(2), pp.97-103.

Klinkenberg, L. (1941). The permeability of porous media to liquids and gases. Drilling and Production Practice. American Petroleum Institute.

LeMinous, J.C., Mutti, D., Bouvet, A., Massie, I., Xiao, E., & Schnell, E. (2017), Permeability Study of API Class G and B Cements considering Seawater and WBM Contamination, SPE/IADC-184613-MS

Li, S., & Roy, D. M. (1986). Investigation of relations between porosity, pore structure, and C1− diffusion of fly ash and blended cement pastes. Cement and Concrete Research, 16(5), 749-759.

Luping, T., & Nilsson, L. O. (1992). A study of the quantitative relationship between permeability and pore size distribution of hardened cement pastes. Cement and concrete research, 22(4), 541-550.

Manmohan, D., & Mehta, P. K. (1981). Influence of pozzolanic, slag, and chemical admixtures on pore size distribution and permeability of hardened cement pastes. Cement, Concrete and Aggregates, 3(1), 63-67.

Michaux, M., Nelson, E. B., & Vidick, B. (1990). 2 Chemistry and Characterization of Portland Cement. Developments in Petroleum Science, 28, 2-1.Morgan, B. E., & Dumbauld, G. K. (1952). Measurement of the Permeability of Set Cement. Journal of Petroleum Technology, 4(06), 16-10.

Nelson, E. B. (Ed.). (1990). Well cementing (Vol. 28). Newnes.

Nyame, B. K., & Illston, J. M. (1981). Relationships between permeability and pore structure of hardened cement paste. Magazine of Concrete Research, 33(116), 139-146.

Peters, E. J. (2012). Advanced Petrophysics: Volume 1: Geology, Porosity, Absolute Permeability, Heterogeneity and Geostatistics. Live Oak Book Co, Austin, Texas.

Powers, T. C. (1958). Structure and physical properties of hardened Portland cement paste. Journal of the American Ceramic Society, 41(1), 1-6. WILEY

Vichit-Vadakan, W., & Scherer, G. W. (2002). Measuring Permeability of Rigid Materials by a Beam-Bending Method: III, Cement Paste. Journal of the American Ceramic Society, 85(6), 1537-1544.

Vichit-Vadakan, W., & Scherer, G. W. (2003). Measuring permeability and stress relaxation of young cement paste by beam bending. Cement and Concrete Research, 33(12), 1925-1932.

Wong, H. S., Zobel, M., Buenfeld, N. R., & Zimmerman, R. W. (2009). Influence of the interfacial transition zone and microcracking on the diffusivity, permeability and sorptivity of cement-based materials after drying. Mag. Concr. Res, 61(8), 571-589.

Wong, H. S., Zimmerman, R. W., & Buenfeld, N. R. (2012). Estimating the permeability of cement pastes and mortars using image analysis and effective medium theory. Cement and Concrete Research, 42(2), 476-483.

Ye, G. (2005). Percolation of capillary pores in hardening cement pastes. Cement and concrete research, 35(1), 167-176.

Zalzale, M., McDonald, P. J., & Scrivener, K. L. (2013). A 3D lattice Boltzmann effective media study: understanding the role of CSH and water saturation on the permeability of cement paste. Modelling and Simulation in Materials Science and Engineering, 21(8), 085016.

A SIMULATION STUDY OF LOW CONCENTRATION SURFACTANT ENHANCED WATER ALTERNATING GAS FLOODING

Perekaboere Ivy Sagbana, Sarkodie Kwame, Farzin Vajihi, Diaz Pedro, Ali Soleiman

Department of Petroleum Engineering, London South Bank University

This paper was prepared for presentation at the International Symposium of the Society of Core Analysts held in Vienna, Austria, 27 August – 1 September 2017

ABSTRACT

A large amount of oil still remains trapped in the reservoir after primary and secondary means of oil recovery. Gases which have been injected either in a miscible or immiscible state with the oil have problems of gravity segregation, viscous fingering, and channelling.

In this paper, a new method has been proposed known as surfactant enhanced water alternating gas flooding (SWAG) were a slug of low concentration surfactant is injected into the reservoir and then followed by a gas and then water slug. The results from this method will be compared to conventional water alternating gas flooding (WAG), water flooding and gas flooding.

Eclipse reservoir simulator was used to evaluate the performance of this method. The data used to build the model used for simulation was obtained from laboratory experiments. The results obtained shows that oil recovery improved significantly when low concentration surfactant was injected before water alternating gas flooding and increasing surfactant concentration will improve oil recovery until a peak concentration is reached and any further increase does not affect oil production. Water cut was delayed for surfactant enhanced WAG when compared to water flooding, water alternating gas flooding and gas flooding.

INTRODUCTION

The petroleum industry today is focusing on improving oil recovery factor (RF) from oilfields as well as keeping an economic oil rate during production. This is because it is becoming increasingly difficult to discover new fields (Muggeridge et al, 2013).

Due to the decline in oil production and large amounts of oil remaining trapped in the reservoir after applying the common enhanced oil recovery techniques, it is reasonable to use methods that are profitable to improve oil recovery (Salehi et al, 2013). Gas injection is known to be the second largest enhanced oil recovery technique. However, the high gas mobility and low density decreases the sweep efficiency of gas injection thus affecting oil recovery. The low sweep efficiency in gas injection occurs as a result

of the injected gas rising to the top of reservoir. This leads to oil overriding due to early gas breakthrough and viscous instability (Renkema and Rossen, 2007).

The WAG injection has been proposed as a method to improve sweep efficiency of gas injection. This is done mainly by using the water to control the mobility of the displacement and to stabilise the front. The WAG injection process combines the improved displacement efficiency of the gas flooding with an improved macroscopic sweep by water injection. Despite the satisfying results of injecting water and gas alternately, the reduction of oil-gas contact in the presence of water decreases the effectiveness of WAG (Syahputra et al, 2000). Several studies have also reviewed the problems associated with a WAG injection process and discussed that the main issue is the water-blocking phenomena (Rao et al, 2004). The water isolates the residual oil from coming in contact with gas.

Salehi et al (2013) conducted surfactant alternating gas flooding (SAG) experiment in their study in other to create foam to overcome the water blocking effect experienced during WAG. They studied the effect of SAG ratio on oil recovery and compared their results to conventional waterflooding, gas flooding and WAG. Their results showed that oil recovery in SAG is related to the SAG ratio and recovery factor for SAG was higher compared to WAG, waterflooding and gas flooding.

Adbi et al (2014) examined the improvement of oil recovery during waterflooding and WAG in the presence of alsphatene depositions on a rock using non-ionic surfactant. This study was conducted because the presence of asphaltene in oil reduces recovery factor during production. Their results showed an incremental oil recovery when non-ionic surfactant was introduced into the injection water for WAG compared to the absence of surfactant.

Majidae et al (2014) conducted an experimental and numerical study of chemically enhanced WAG (CWAG). A new technique was developed which involves the injection of alkaline, surfactant and polymer additive as a chemical slug during WAG process to minimise water-blocking effect by interfacial tension reduction and improving mobility ratio with the polymer. Their results showed that CWAG achieved 26.6% more than twice the oil recovery from conventional WAG.

Harsen et al (1995) performed numerical simulations to study surfactant effect on WAG process in a heterogeneous reservoir. They concluded the foam created during surfactant interaction with gas blocks the highly permeable region in the reservoir. The advantages of this method over WAG are the reduction of gas-oil ratio and diversion of water which ultimately leads to increase oil recovery rate.

Memon et al (2016) investigated the impact of foaming surfactant in WAG flooding using CO_2 gas and different surfactant blends in displacement experiments. They discussed that increase in oil recovery when surfactant is present in WAG is as a result of the control of CO_2 mobility by the surfactant which was able to create a stable foam.

The different works published in the literature have shown that surfactant can improve the efficacy of WAG. In this study, the objective is to demonstrate the oil recovery potential of low concentration surfactant enhanced water alternating gas flooding and compare the recovery to other conventional recovery methods numerically.

METHODOLOGY

The approach employed for this black oil simulation study, was to validate the effectiveness of a low concentration Surfactant enhanced water alternating gas (SWAG) recovery method. The data used to run the simulation for water flooding, gas flooding, water alternating gas flooding and surfactant enhanced water alternating gas flooding were obtained from laboratory experiments. The surfactant used was alcohol alkoxy sulfate. The performance comparisons of different EOR methods which are SWAG, WAG, water, gas flooding was conducted using Eclipse simulation software. The comparative analysis of each recovery method was based on:

1) Oil Recovery,
2) Water Cut, and
3) Pressure decline

Grid description

A simple box model of 10 x 1 x 1 was used for the simulation. The reservoir rock is assumed to be sandstone and homogeneous. The rock property is a representative of the core sample used for core flooding experiments to obtain relative permeability curves. The laboratory units' option in Eclipse software was used to run the simulation. Rock and fluid properties are detailed in the Tables 1 and 2 and were specified in the 'PROPS' section. Time step used was 60 x 0.01 which gave a total simulation time of 1.8 hours. The model consists of one injection well and one producer well which were completed in the first and tenth blocks of the model.

Table 1: Rock Properties

Porosity	0.18
Perm X, Y, Z	100 x 100 x 75 (mD)
Reservoir size	10 x 2 x 3 (cm)

Table 2: Fluid properties

Oil viscosity	20 cp
Water viscosity	1.01cp
Oil density	0.926 g/cc
Water density	1.00 g/cc
Initial pressure	350 Atm

Relative permeability (Rel perm) curves

Relative permeability (rel perms) of gas, oil, surfactant and water derived from core flooding experiments were inputted in the PROPS section of the eclipse data file for SWAG, WAG, water flooding and gas flooding simulations. Figures 1, 2 gives the rel perm curves with associated capillary pressure for water and surfactant flooding while Figure 3 shows the rel perm curves for gas flooding. The rel perm used for water alternating gas flooding was the combination of the gas/oil and water/oil rel perm curves used for water flooding and gas flooding. While for SWAG, a combination of surfactant/oil and gas/oil rel perms were used for the simulation.

The surfactant model

Surfactant phase is introduced using the SURFACT keyword in the RUNSPEC section for the simulation of SWAG. The combination of two phase surfactant/ oil and gas/oil relative permeability curves were inputted into the PROPS section. This curve showed a reduction in the residual oil saturation due to a reduction in water oil capillary pressure trend when compared to that from other recovery methods. The Trend between surfactant concentrations and surface tension between oil and water was derived from lab experiments and inputted using The SURFST keyword. The concentration range used was between 0.001 – 0.5 g/scc with a corresponding surface tension range of 7 – 7.93469E-06 cp (as defined in Eclipse).
The capillary de-saturation function describes the transition between immiscible and miscible conditions as a function of capillary number (Eclipse, 2015). SURFCAPD keyword is used to account for this effect.

Some of the key assumptions made for this model are as follows:

1) Black oil model
2) No surfactant absorption into rock was considered
3) Isothermal conditions

Recovery methods control strategies

The control strategy is defined in the SCHEDULE, WCONINJE, where the pressure or flow rate conditions are set. The injection well is mandated to open or shut when certain conditions have been reached. For each recovery method, the flowing schemes were employed:

Water flooding – A continuous water injection scheme was initiated in the simulation for the whole simulation time step, with a maximum rate of 10 cc/hr as liquid rate limit.

Gas flooding - Based on the economic limit, a gas volume rate was imposed on the injection well for the time of simulation. The gas injection limit was 100 cubic centimetre (cc)/hr.

WAG - The scheme involved in this scenario involved the injection of water and then gas and water finally over mid time steps of 0.6 hours each. The injection limit was based on injection rates of water and gas as used in the laboratory core flooding experiment.

Low concentration surfactant enhanced WAG (L.C SWAG) -The scheme involved injection of low concentration surfactant slug followed by gas flooding and then water only water injection. Using the black oil model (ECLIPSE 100) calculations are based on a mixture property of water and concentration of surfactant used for the simulation.

RESULTS AND DISCUSSIONS

Figure 4 presents the diagram of the synthetic reservoir model. Oil recovery factor for low concentration surfactant enhanced WAG was compared with water flooding, gas flooding, water alternating gas flooding in Figure 5. The results showed that surfactant enhanced WAG gave the highest oil recovery (FOE) of 58 % when compared to the other methods. Gas flooding yielded the least recovery of 37%. The poor performance of gas flooding was due to inefficient sweep of oil by gas through the reservoir. The FOE for the water flooding was 48 % and 47% was derived from the WAG. The benefit of surfactant enhanced WAG over the other recovery methods is the mechanism in which this method utilises to improve oil recovery. The mechanisms involved are lowering water/oil interfacial tension by the surfactant and reduction of gas mobility when the gas interacts with the surfactant.

Figure 6 presents water cut for each enhanced oil recovery process. The water flooding compared to the WAG method saw an increase in water cut at the end of the simulation (95%) and thus might be of concern for operators on issues of early water treatment and handling which obviously would come at a cost. Furthermore, the WAG method gives a trade-off between water handling and gas injection; for this reason, the WAG method was combined with low conc. Surfactant flooding. Surfactant enhanced WAG gave a delayed water production at time 0.4 hours this shows an indication of better field management and reduced cost on handling water and even gas injected.

The pressure decline of each recovery method is considered and illustrated in Figure 7. Gas flooding method presented the least decline in pressure and thus a poor FOE

realisation over the period of 2 hours. The surfactant enhanced WAG presented significant declining pressure differentials indicating excellent FOE of 58% compared to WAG and water flooding which also showed significant decline as well. Adding to the efficiency of surfactant enhanced WAG over the WAG, water flooding and gas flooding, it can be reiterated with a higher-end simulation reservoir pressure of 179 Atms combined with delayed water cut was achieved.

Figure 8 presents the range of recoveries for SWAG, WAG, water flooding and gas flooding where the range represents the difference between the highest and lowest recoveries. The chart shows the best performance of SWAG as compared to the other recovery mechanisms. SWAG had the highest recovery range at 55% and lowest recovery at 15% followed by water flooding with 46% maximum recovery and 15% minimum recovery and then WAG with 45% maximum and 15% minimum recovery. Gas flooding had the lowest maximum recovery at 30% and minimum recovery at 5%.

Figure 9 shows the effect of surfactant concentration on SWAG. The result shows that oil recovery increased up to an optimum concentration of 0.03g/cc. The maximum oil recovery was achieved at 0.03g/cc and further increase in surfactant concentration does not affect the recovery rate.

CONCLUSIONS AND RECOMMENDATIONS

The performance comparisons between EOR methods of low concentration SWAG, WAG, water flooding and gas flooding was conducted to evaluate the efficiency of this proposed method. The conclusions made from this study are:

1) The low concentration surfactant enhanced WAG seems most suitable for a medium viscosity reservoir producing better performance compared to conventional WAG, waterflooding and gas flooding.
2) Oil recovery improved in surfactant enhanced WAG and water cut was delayed when compared WAG.
3) Oil recovery in surfactant enhanced WAG can be affected by surfactant concentration. There is a maximum concentration after which increase in surfactant concentration does not affect oil recovery.
4) The efficiency of surfactant enhanced WAG is attributed to the surfactant reduction of water/oil interfacial tension and gas trapping.

REFERENCES

1) Abdi, M., Moradi, S., Habibniya, B., and Kord, S., (2014) Improving oil recovery during water injection and WAG processes in asphaltenic oil reservoir by using non-ionic surfactants. *International Journal of Science and Emerging Technologies,* pp302.

2) Eclipse (2015). Simulation Software Manuals. Schlumberger.

3) Hanssen, J.E., Surguchev, L.M., Svorstøl, I. and Blaker, T., 1995. SAGA injection: a new combination IOR process for stratified reservoirs. *Geological Society, London, Special Publications*, *84*(1), pp.111-123.

4) Majidaie, S., Khanifar, A., Onur, M., and Tan, I., (2012) a simulation study of chemically enhanced water alternating gas (CWAG) injection. *Society of Petroleum Engineers,* pp 1-9.

5) Muggeridge, A., Cockin, A., Webb, K., Frampton, H., Collins, I., Moulds, T., and Salino, P., (2013) Recovery rates, enhanced oil recovery and technological limits. *Philosophical Transactions of the Royal Society of Mathematical, Physical and Engineering Science Publication.*

6) Rao, D.N., Ayirala, S.C., Abe, A.A., and Xu, W., (2006) Impact of low cost dilute surfactants on wettability and relative permeability, *Society of Petroleum Engineers,* pp1-14.

7) Renkema, W.J., Rossen, W.R., (2007) Success of SAG foam processes in heterogeneous reservoirs. *SPE Annual Technical Conference and Exhibition California, U.S.A.,* pp. 11-14.

8) Salehi, M., Safarzadeh, M., Sahraei, E., and Alireza., (2013) Experimental study of surfactant–alternating-gas injection versus water-alternating-gas and waterflooding enhanced oil recovery methods. *Society of Petroleum Engineers Journal*, pp1-13.

9) Syahputra, A., Tsau, J., and Grigg, R., (2000) Laboratory Evaluation of Using Lignosulfonate and Surfactant Mixture in CO2 Flooding, Society of Petroleum Engineers Journal, pp 1-9.

10) Sharma, A., Rao, D.N., (2008) Scaled physical model experiments to characterize the gas-assisted gravity drainage EOR Process. *SPE/DOE symposium on improved oil recovery, Tulsa, Oklahoma, USA*.

FIGURES
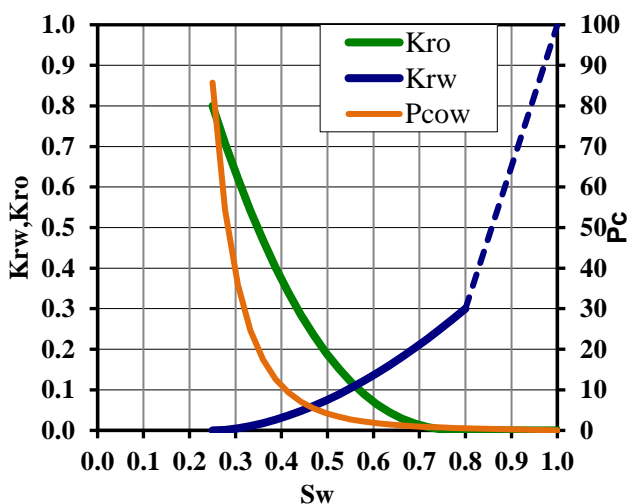
Figure 1: water/oil relative permeability and capillary pressure curves
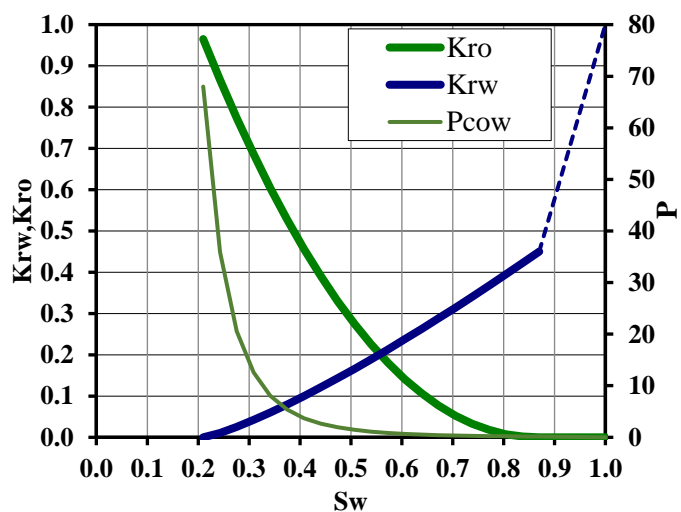
Figure 2: Surfactant/oil relative permeability and capillary pressure curves
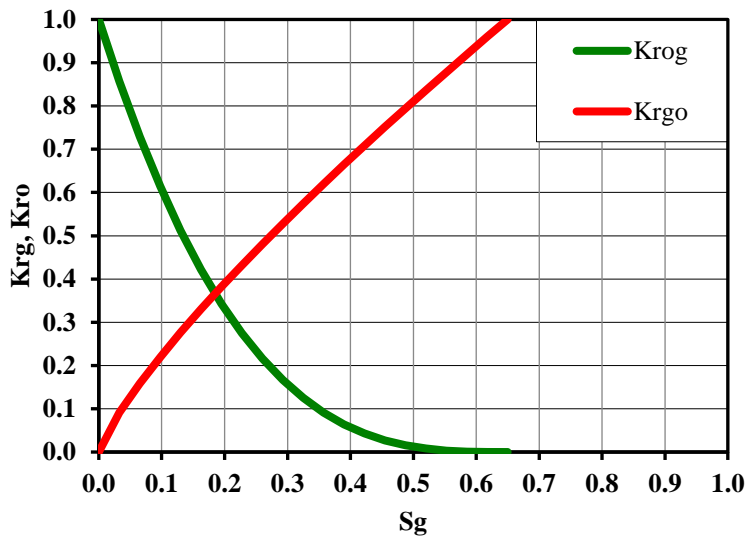
Figure 3: Gas/oil relative permeability curves
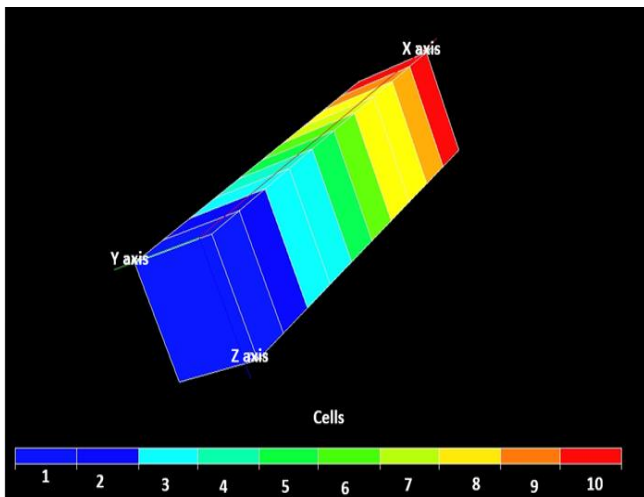
Figure 4: Reservoir model
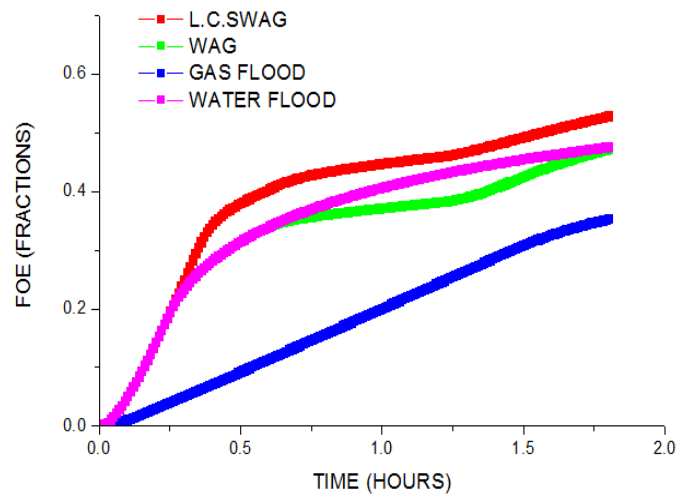
Figure 5: Comparison of oil recoveries for WAG, SWAG, water flooding and gas flooding
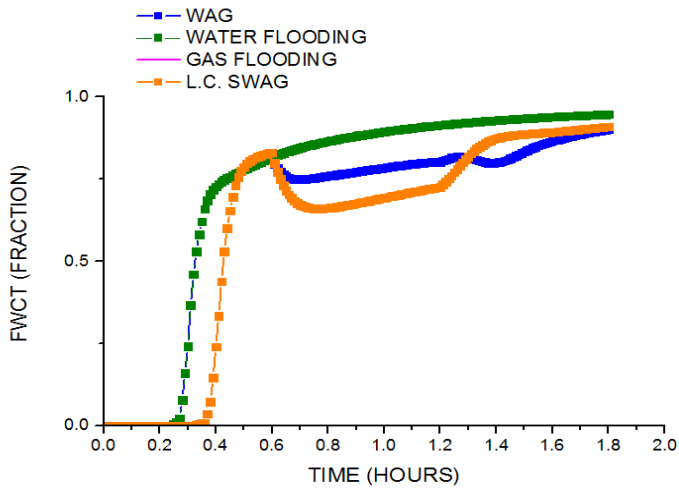
Figure 6: Water cut comparison for WAG, SWAG, water flooding and gas flooding
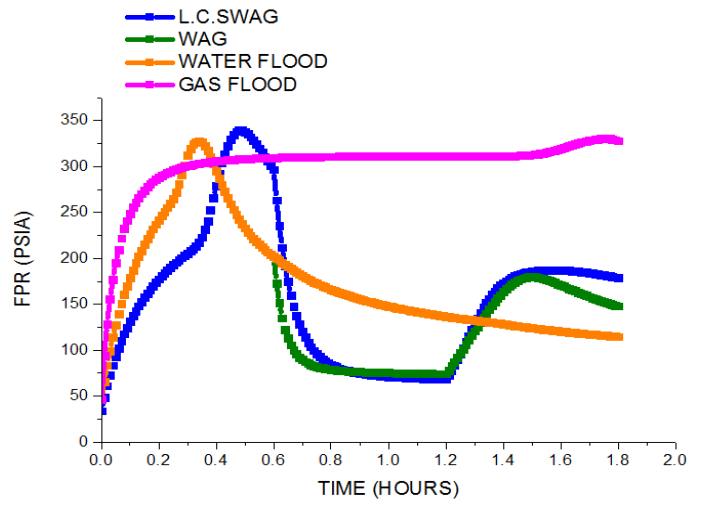
Figure 7: Pressure decline for SWAG, WAG, water flooding and gas flooding
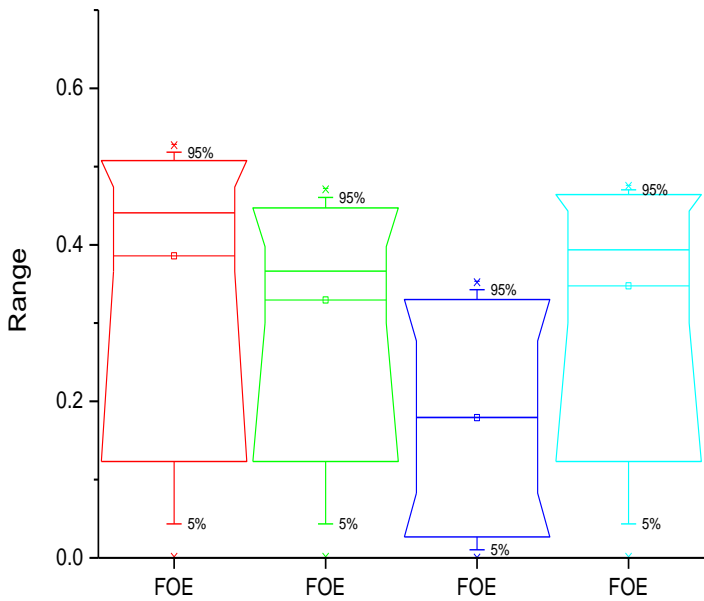
Figure 8: Range of oil recoveries for Swag, WAG, water flooding and gas flooding
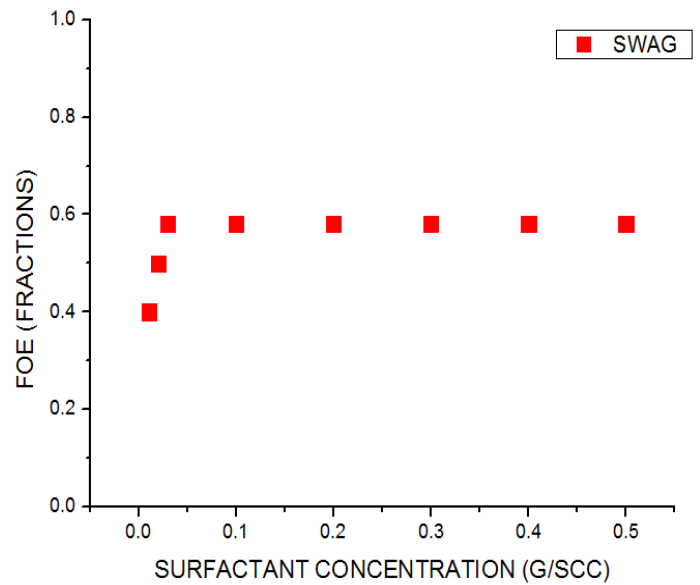
Figure 9: Effect of surfactant concentration on SWAG

Effect of Low Salinity Water Injection on Capillary Pressure and Wettability in Carbonates

Farzin Vajihi, Pedro Diaz, Ivy Sagbana, Hassan Zabihi, Arash Farhadi, Saham Sherhani
London South Bank University

ABSTRACT

In the past decade, much attention has been pointed toward Low Salinity Water Injection (LSWI) as an efficient oil recovery technique. Despite compelling laboratory evidence of LSWI and smart water potential, the underlying mechanisms causing the incremental oil recovery in carbonate rocks are still controversial. Several studies have indicated that wettability alteration is the primary mechanism for LSWI. However, high temperature was required to observe this wettability alteration in majority of cases. This paper presents the effect of LSWI and smart water on the wettability of limestone at ambient conditions at the laboratory scale.

An ultra-centrifuge was used to measure the capillary pressure curve prior and after LSWI on four limestone core samples at ambient conditions. The end point from the imbibition capillary pressure data were used to calculate incremental oil recovery. U.S. Bureau of Mines (USBM) method was deployed to calculate wettability of the limestone core samples from forced drainage and imbibition capillary pressure curve. The effect of brine salinity and ionic composition was investigated by diluting seawater and altering concentration of sodium chloride (NaCl) and sulphate (SO_4^{2-}).

The result from imbibition capillary pressure data indicated a reduction in residual oil saturation as the salinity was reduced. Twenty times diluted seawater enriched with four times sulphate lead to an incremental oil recovery of 7% compared to twenty times diluted seawater. Moreover, depletion of NaCl in the low salinity brine enriched with sulphate lead to 1.6% additional oil recovery. Reducing salinity of the injected brine resulted in a more water-wet condition. The highest wettability index alteration towards water-wet condition was observed when sulphate was spiked in low salinity brine. The result obtained in this work provided direct evidence that LSWI could change the wetting condition of the rock toward a more water-wet state. It was concluded LSWI could be an effective oil recovery technique, which could be improved by altering ionic composition of the brine on limestone core samples.

INTRODUCTION

Low salinity water injection is an emerging oil recovery technique. The chemistry of injected water can be reformed by dilution (i.e. LSWI) or selectively modifying the concentration of individual ions (i.e. Smart Water) presented in the brine. Majority of the researchers have reported a positive response to LSWI and wettability alteration is believed to be the primary reason for incremental oil recovery in carbonate cores [1, 4 and 10].

Yousef et al. [9] conducted coreflooding experiments to study the effect of LSWI on oil recovery and wettability alteration for carbonate rocks at reservoir conditions. The incremental oil recovery by injection of diluted seawater was up to 18% of the OOIP. Putervold et al. [6] investigated the concentration ratio between NaCl and SO_4^{2-} in the injection brine that is required to improve oil recovery in chalk core sample. The results suggest 90% depletion of NaCl and enrichment of sulphate concentration by 3-4 times in the brine was required in order to achieve maximum oil recovery. A successful design of waterflooding to alter the wettability of the carbonate rock depends on optimum salinity and ionic concentration of the injected brine. However, very limited attention has been given to effect of salinity and ionic composition of injected water on capillary pressure.

Capillary pressure (P_c) data are vital in modelling heterogeneous carbonate reservoirs. In general, capillary pressure data from drainage process is used to determine Original Oil in Place (OOIP) and imbibition capillary pressure is used to design recovery characteristic of hydrocarbons in secondary and tertiary flooding [5]. Webb et al. [8] investigated the effect of formation water free of sulphate and seawater with high concentration of sulphate on capillary pressure curves and oil recovery of carbonate core samples at reservoir condition. An incremental oil recovery of 15% was observed when seawater was injected compared to formation water in forced imbibition test. Wang and Alvarado [7] investigated the effect of low salinity brine on capillary pressure hysteresis using an improved quasi-static porous plate method at 30°C. The core samples were not aged in this work to reduce the possibility of wettability alteration and isolate the effect of interfacial viscoelasticity caused by LSWI. Results indicated less hysteresis and an incremental oil recovery 15% OOIP for low salinity compared to high salinity.

This paper presents effect of salinity and ionic composition of the injected water on capillary pressure and wettability at ambient condition by deploying multi-speed centrifuge technique which has not been used previously in this field.

EXPERIMENTAL PROCEDURES

Material

Various laboratory tests were conducted to select Indiana limestone outcrop core plugs with similar petrophysical properties. This includes routine core analysis such as porosity, gas permeability, and dimensions measurements. X-ray Diffraction (XRD) analysis indicated the mineralogy of the rock is composed of 98wt% calcite. The petrophysical properties of the limestone core samples are presented in Table 1. Dead crude oil from

North Sea was mixed with heptane in ratio of 60:40, respectively. The Total Acid Number (TAN) of the synthetic oil was 0.18 mg KOH/g measured by ASTM D-664 method. The oil properties used in this work are presented in Table 2.

Synthetic brine was prepared in laboratory from distilled water reagent grade chemical. Four types of brines were prepared I) formation water, II) seawater, and III) diluted seawater, and IV) seawater selectively modified ionic composition. Table 3 indicates the formulation of the brines used in this work. In this paper, formation water is referred as FW and seawater (SW), ten times diluted seawater (0.1xSW), ten times diluted seawater doped with 4 times sulphate ($0.1xSWx4SO_4^{2-}$) and ten times diluted seawater depleted in sodium chloride (0.1xSWx0NaCl).

Description of Equipment and Procedures

A refrigerated centrifuge apparatus was used in this work to measure both forced drainage and imbibition capillary pressure curves at ambient condition. A schematic diagram of the centrifuge forced drainage and imbibition is provided in Figure 1. The average saturation detected by the centrifuge camera was used to measure the local capillary pressure at the inlet of the core sample. Three different interpretation methods I) Hassler-Brunner, II) Forbes Continuous, and III) Forbes + Spline were used in multi-speed centrifuge experiment to convert the average capillary pressure curve to local capillary pressure curve.

Core preparation

To minimise the wettability alteration of the rock, core samples were injected with distilled water to remove any dissolvable sulphate. Toluene and methanol were used to clean the core plugs before drying in oven. Then, the core samples were saturated with formation brine using vacuum pump and centrifuge. Primary drainage P_c experiment was conducted using the centrifuge to measure the irreducible water saturation. Forced imbibition and secondary drainage experiments were performed to measure the capillary pressure curve for high salinity FW which was followed by low salinity imbibition and drainage P_c curve. The purpose of this experiment was to evaluate effect of LSWI and smart water on wettability. The experiment was conducted at ambient conditions and the core samples were not aged after the primary drainage which minimised the possibility of wettability alteration in the core samples.

RESULTS AND DISCUSSION
Salinity Effect

The experimental results indicated an increase in oil recovery as the salinity of the imbibing brine is reduced. The highest oil recovery and wettability alteration is observed using twenty times diluted seawater in secondary flooding mode. The results are comparable with previous experimental work by Yousef et al. [9]. Figure 2 shows that the oil recovery and

wettability are not a linear function of salinity and more than 95% reduction in salinity is required to obtain reasonable oil recovery. The irreducible water saturation (S_{wi}) was increased as the S_{wi} is a function of wettability and pore-size distribution. It worth mentioning that the experimental work presented here were performed at ambient conditions to minimise the wettability alteration. Majority of research has reported positive effect of LSWI in carbonates at high pressure and temperature. This is due to the increase in reactivity of potential determining ions (Ca^{2+}, Mg^{2+}, and SO_4^{2-}) at higher temperature [4, 9 and 10]. Knowing the effect of temperature, additional oil recovery and further change in wetting condition toward a more water wet state can be expected.

Non-active Ions and Sulphate

Twenty times diluted SW spiked with 2 and 4 times sulphate and depleted in NaCl was used as the imbibing fluid to determine the capillary pressure curve, oil recovery and wettability index. The results presented in Figure 5 and 6 indicate a reduction in residual oil saturation as the sulphate was increased. This confirms that SO_4^{2-} can lead to an expansion of EDL even at low temperature (24°C). Depletion of NaCl had less effect on oil recovery compared to SO_4^{2-}. An incremental oil recovery of 7% and 1.6% was obtained when 4 times sulphate was added and NaCl was depleted in low salinity water, respectively.

Non active ions (Na^+, Cl^-) are not part of the inner Stern layer in Electrical Double Layer (EDL), which can lead to reducing the influence of potential determine ions [2]. High affinity of sulphate toward the rock surface leads to adsorption of calcium due to reduced electrostatic repulsion. Removal of NaCl from imbibing fluid provides better access for calcium and magnesium ions in double layer to get closer to surface of the rock which leads to expansion of EDL. However, the incremental oil recovery obtained after depletion of NaCl did not have any effect on wettability. Wang and Alvarado [7] reported the incremental oil recovery is due to interfacial viscoelasticity which leads to suppression of snap-off and continuity of oil recovery.

CONCLUSIONS

Significant incremental oil recovery has been reported by reducing salinity, NaCl, and increasing SO_4^{2-} at reservoir condition. In this paper the effect of salinity, non-active salt, and SO_4^{2-} on oil recovery and wettability at ambient condition has been investigated. Low salinity water and sulphate enriched brine successfully improved the wettability and oil recovery of limestone rock at ambient conditions. Marginal oil recovery was observed by depletion of NaCl but the wetting condition was not changed. The incremental oil recovery achieved by depletion of NaCl was result of liquid-liquid interaction and not wettability alteration. In summary:

- The capillary pressure data confirms that both LSWI and smart water are able to modify wettability of the limestone core samples from a mix-wet state toward a more water-wet state.

- Forced imbibition tests by centrifuge indicated an incremental oil recovery up to 8% by modifying the ionic concentration and salinity of the SW.
- The increase in oil recovery is not a linear function of salinity. Over 95% of SW`s total dissolved salts were removed prior to any noticeable incremental oil recovery.
- Increasing concentration of SO_4^{2-} by 2-4 times altered the wettability toward water-wet condition. Whereas, depletion of NaCl resulted in reducing the residual oil saturation but had no effect on wettability.

ACKNOWLEDGEMENTS

REFERENCES

1. Austad, T., Shariatpanahi, S.F., Strand, S., Black, C.J.J., Webb, K.J., 2012. *"Conditions for a low-salinity enhanced oil recovery (EOR) effect in carbonate oil reservoirs".* Energy Fuels 26 (1), 569–575.
2. Fathi, J.S., Austad, T., Strand, S. 2012. *"Water-Based Enhanced Oil Recovery (EOR) by Smart Water In Carbonate Reservoirs".* Paper SPE 154570, Presented at the SPE EOR Conference at Oil and Gas West Asia, Muscat, Oman, 16-18 April.
3. Fernø,, M.A., Grønsdal, R.J., Nyheim, A.M., Berge, M., and Graue, A., 2011. *"Use of Sulfate for Water Based Enhanced Oil Recovery during Spontaneous Imbibition in Chalk".* Paper Energy & Fuels, 25(4): 1697-1706.
4. Gupta, R., Griffin, S., Willingham, T.W., Casico, M.L., Shyeh, J.J., Harris, C.R. 2011. *"Enhanced Waterflood for Middle East Carbonate Cores – Impact of Injection Water Composition".* Paper SPE 142668 presented at SPE Middle East Oil and Gas Show and Conference, 25-28 September, Manama, Bahrain.
5. Masalmeh, S.K., Jing, X.D., 2006. *"Capillary Pressure Characteristics of Carbonate Reservoirs: Relationship between Drainage and Imbibition Curves".* Paper SCA2006-16 Presented at the SCA International Symposium, Trondheim, Norway, 12 – 16 September
6. Puntervold, T., Strand, S., Ellouz, R., Austad, T., 2015. *"Modified Seawater as a Smart EOR Fluid in Chalk".* Journal of Petroleum Science and Engineering 133, 440-443.
7. Wang, X. and Alvarado, V., 2016. "*April. Effects of Low-Salinity Waterflooding on Capillary Pressure Hysteresis".* Paper SPE-179562 Presented at SPE Improved Oil Recovery Conference, Tulsa, Oklahoma, USA, 11-13 April.
8. Webb, K.J., Black, C.J.J., and Tjetland, G., 2005. *"A Laboratory Study Investigating Methods for Improving Oil Recovery in Carbonates".* Paper SPE 10506, SPE International Petroleum Technology Conference, Doha, Qatar, 21 – 23 November
9. Yousef, A.A., Al-Saleh, S., Al-Kaabi, A.O., and Al-Jawfi, M.S. 2010. "*Laboratory Investigation of Novel Oil Recovery Method for Carbonate Reservoirs*". Paper

CSUG/SPE 137634, presented at the Canadian Unconventional Resources & International Petroleum Conference, Calgary, Alberta, Canada, 19-21 October.

10. Zhang, P., Tweheyo, M.T., Austad, T., 2007. *"Wettability alteration and improved oil recovery by spontaneous imbibition of seawater into chalk: Impact of the potential determining ions: Ca^{2+}, Mg^{2+} and SO_4^{2-}"*. Colloids Surf. A: Physicochem. Eng. Asp. 301, 199–208.

Table 1: Indication of core samples petrophysical properties

Sample	Length (Inch)	Diameter (Inch)	Gas Perm. (mD)	Porosity (%)
L1	4	1	60	17.2
L2	4	1	75	19
L3	4	1	72	18.7
L4	4	1	54	16.9

Table 2: Oil Properties

Oil	Density (g/cm³) at 20°C	Viscosity (cp) at 20°C	TAN (mg KOH/g)
Synthetic Oil	0.862	18	0.18

Table 3: Indication of brine formulation

Salts(g/l) Brine	NaCl	CaCl₂.2H₂O	KCl	MgCl₂.6H₂O	Na₂SO₄	NaHCO₃	Total Dissolved Salts (TDS), g/l
Formation Water (FW)	67.56	14.7	0.52	4.47	0	0.34	87.59
Seawater (SW)	26.30	1.91	0.75	9.15	3.41	0.17	41.68

Seawater diluted 10 times (0.1xSW)	2.63	0.19	0.07	0.91	0.34	0.02	4.17
Seawater diluted 20 times (0.05xSW)	1.31	0.10	0.04	0.46	0.17	0.01	2.08
20Xdiluted SeawaterX2times Sulphate (0.05xSWx2SO$_4^{-2}$)	1.31	0.10	0.04	0.46	0.34	0.01	2.25
20Xdiluted SeawaterX4times Sulphate (0.05xSWx4SO$_4^{-2}$)	1.31	0.10	0.04	0.46	0.68	0.01	2.60
20Xdiluted SeawaterX2times SulphateX0NaCl (0.05xSWx2SO$_4^{-2}$x0NaCl)	0.00	0.10	0.04	0.46	0.34	0.01	0.94
20Xdiluted SeawaterX4times SulphateX0NaCl (0.05xSWx4SO$_4^{-2}$x0NaCl)	0.00	0.10	0.04	0.46	0.68	0.01	1.28
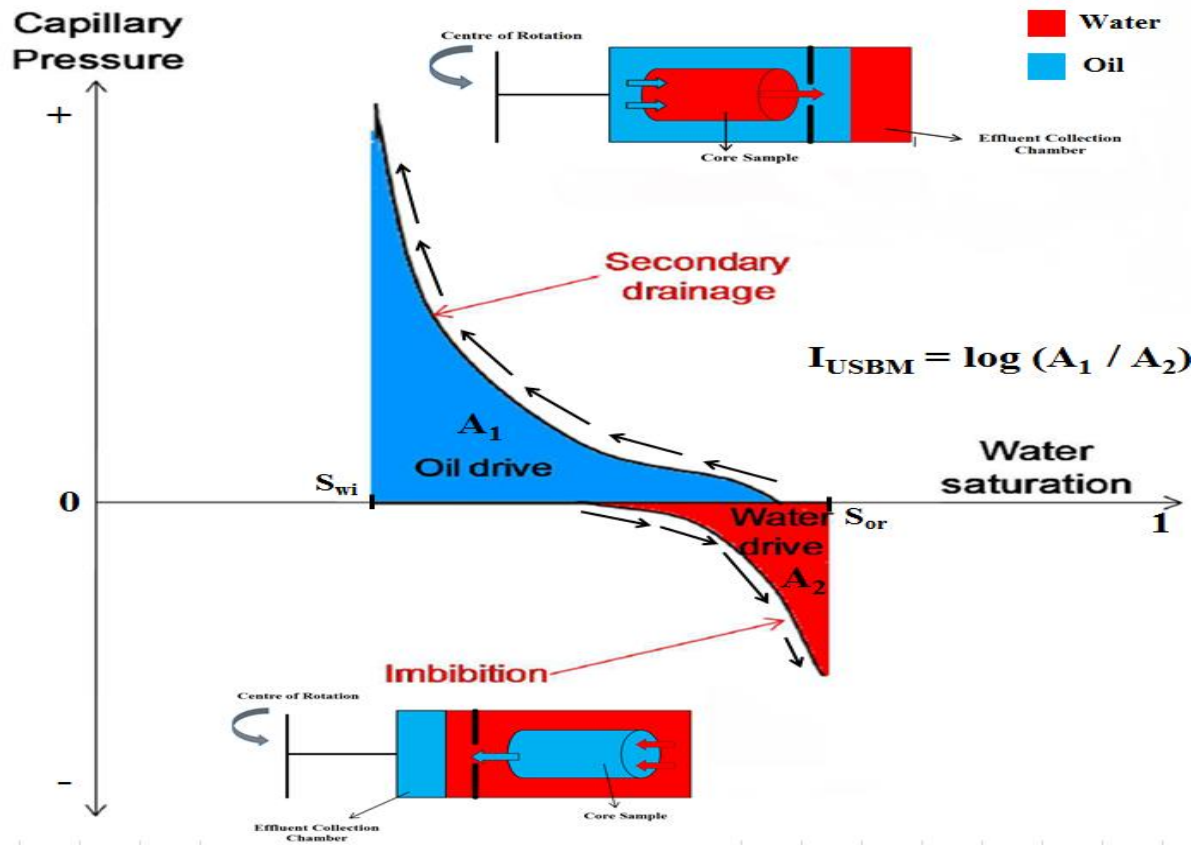
Figure 1: Indication of Centrifuge core holder setup, forced drainage and imbibition cycle
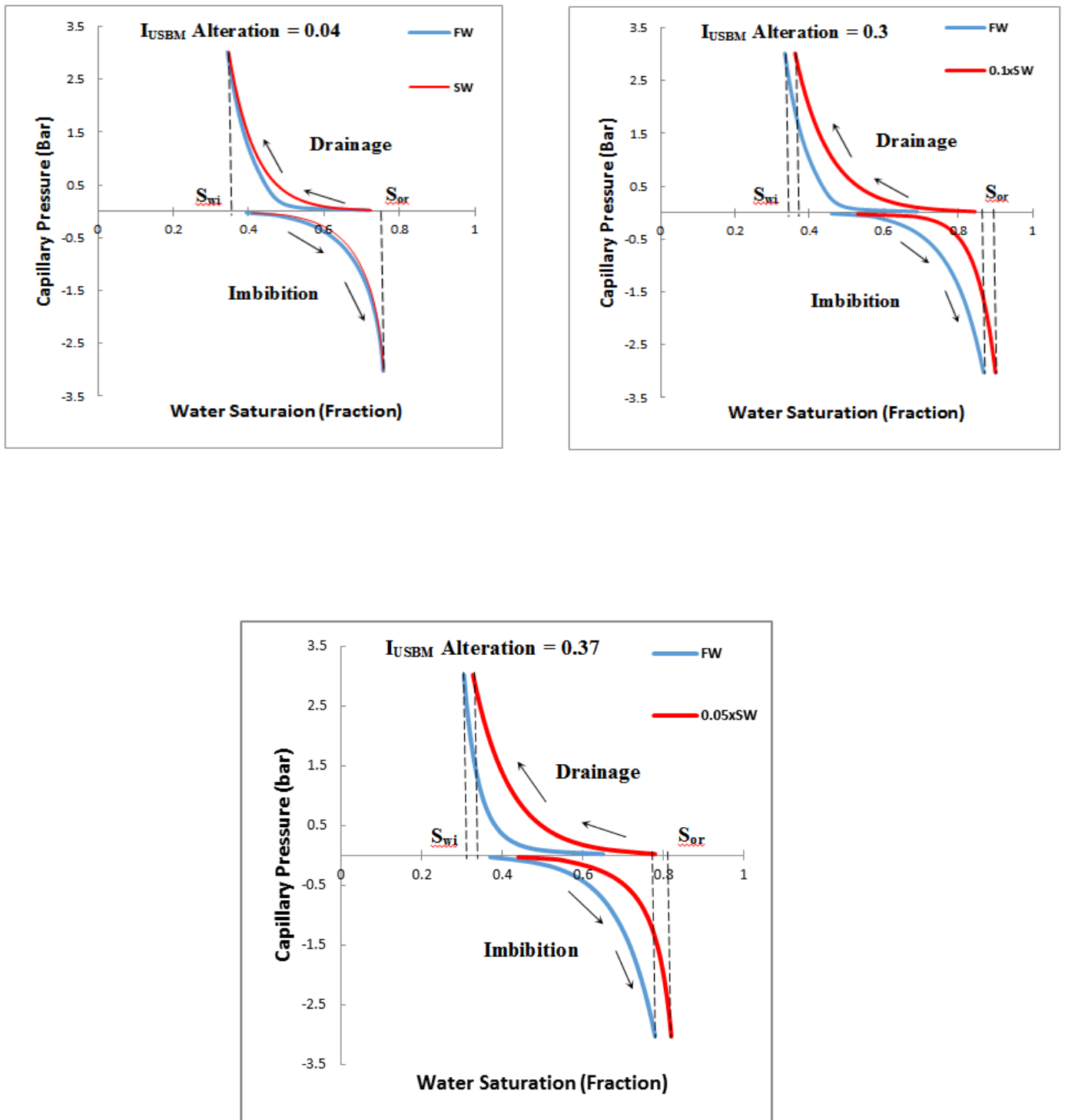
Figure 4: Formation Water and twenty times diluted Seawater capillary pressure curve for Limestone 4
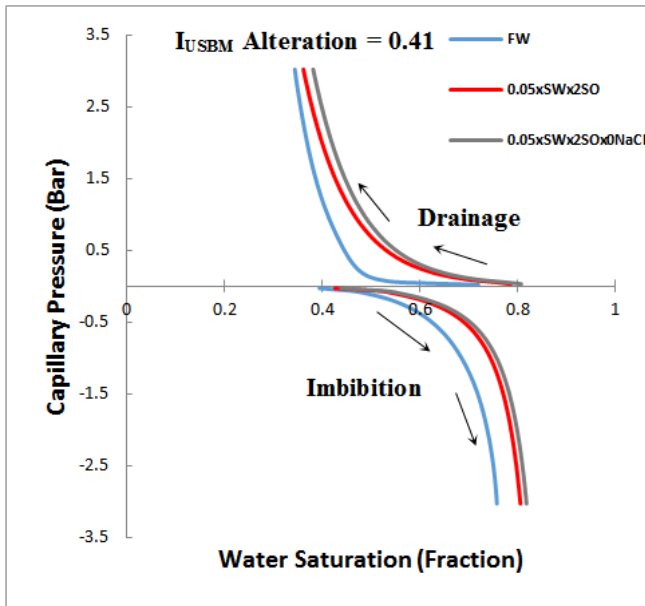
Figure 5: Formation Water, twenty times diluted Seawater enriched with twice sulphate with/without sodium chloride capillary pressure curve for Limestone 1
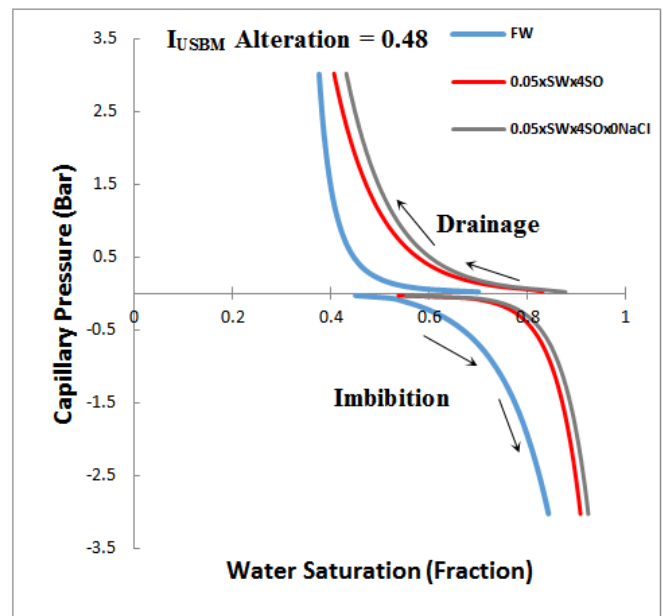
Figure 6: Formation Water, twenty times diluted Seawater enriched with four times sulphate with/without sodium chloride capillary pressure curve for Limestone 2

EXPERIMENTAL INVESTIGATION OF FACTORS AFFECTING LABORATORY MEASURED RELATIVE PERMEABILITY CURVES AND EOR

Sami M. Aboujafar
Libyan Petroleum Institute, Tripoli - Libya

This paper was prepared for presentation at the International Symposium of the Society of Core Analysts held in Vienna, Austria, 27 August – 1 September 2017

ABSTRACT
Relative permeability curves are a fundamental input to reservoir models which provide the only way to predict the subsurface fluid flow behaviour. There is still much controversy surrounding the factors affecting the measurement of relative permeability curves in the laboratory, and to achieve an optimum enhanced oil recovery mechanism in petroleum reservoirs, we need a better understanding of the flow characteristics, which is greatly affected by fluid-rock and fluid-fluid interactions. These interactions directly control rock wettability, capillary pressure and relative permeability curves.

This study deals with different laboratory experiments in order to investigate the possible effects of several factors, including fluid system properties, rock types and measurement conditions and/or procedures, on the measurement of relative permeability, displacement efficiency and therefore the enhanced oil recovery applications and the practical significance of these factors. Laboratory core-floods and centrifuge experiments were conducted on sandstone and carbonate cores to assure a measurement of valid flow behaviour. Drainage and imbibition relative permeabilities in two phase system were measured and handled. Sensitivity analysis for fluid properties, lithology types and measurement conditions were done by using a core-flood simulator with history matching to properly account for capillary pressure effects and to establish the validity of different scenarios of measurements by the technique used and then study the flow behaviour with the investigated parameters.

Results were compared with previously achieved investigations. There was a correlation between fluid system properties, residual saturations and relative permeability end points. Remaining oil saturations from laboratory measurements might be too high due to experimental procedures and capillary end effect .The effect of wettability was also observed and discussed, since, in most cases, residual oil saturations were increased and relative permeability to water was decreased as the samples tend to be water wet. The laboratory investigations of relative permeability curves should be conducted at conditions as closely as possible to reservoir conditions in order to achieve reliable and accurate results. An improved oil recovery can be achieved by controlling the composition and properties of the fluid system and their reactions with the geological system.

INTRODUCTION

Relative permeability curves are fundamental for the analysis of reservoir problems. They are directly related to various production procedures during the field development. During the measurement of relative permeability curves, there are many challenges which must be taken into account such as the effects of changes in fluid properties at reservoir conditions and heterogeneity in the reservoir. Laboratory core experiments are the main tool for studying these properties for scientific and practical applications.

In laboratory flow tests, it is necessary to simulate in the experiments all the factors of importance which influence the flow in the reservoir to assure a measurement of valid flow behaviour. These factors have been studied by many investigators and may include; wettability characteristics of the system, reservoir temperature and pressure, fluid properties such as viscosity, density and salinity, fluid flow rate, interfacial tension. These factors also have an effect on residual saturations, displacement efficiency and enhanced oil recovery.

Previously, it has been shown that brine salinity can be very important in water flooding process. Laboratory tests indicated that residual oil saturation obtained at the end of water flood test depends on the salinity and/or viscosity of the brine used. There are many published data in the literature showing that water flood recovery is dependent on the composition, especially the salinity, of the injection brine. Jadhunandan and Morrow (1995) and Yildiz and Morrow (1996) published papers on the influence of brine composition on oil recovery. The effect of oil viscosity and viscosity ratio on relative permeability curves have been investigated and studied extensively by many authors including Leverett, Tzimas et al, Dong and Dullien. Wettability of the system has a significant effect on relative permeability and oil recovery. A water-wet system will exhibit greater primary oil recovery, but the relationship between primary recovery and wettability has not been developed. Emery et al., Kyte et al and Donaldson et al. studied the wettability of core samples. The results showed that as the system becomes more oil-wet, less oil is recovered at any given amount of injected water.

Laboratory procedures such as flow rates can significantly affect relative permeability curves. At sufficiently low flow rates, microscopic flow behaviour should always be capillary dominated if the system has a strong wetting preference. The effect of interfacial tension can also be significant. If the experimental flow rate is high and the interfacial tension is small, the capillary forces become less significant and slugs of both fluids may begin to flow through the same network of pores.

This work's objectives were to study and investigate the probable effect of several parameters on water-oil relative permeability curves and residual oil saturations. Comparisons of different measurement conditions and lithology types were also made.

EXPERIMENTAL PROCEDURES

In this study, water flooding and centrifuge methods were used to measure relative permeability curves. In addition to that, wettability tests (USBM and/or Amott/Harvey)

were conducted using core materials with different lithology types taken from different reservoirs. These core materials have a wide permeability range from less than one mD to more than 500 mD. The porosity range was between 5 % and 34 %. Different types of fluids were used to conduct these tests. A wide range of oil viscosities, from 1 to more than 30 cp, were used in these experiments. Oil/water viscosity ratio was in the range of 1 to 30. Several brine salinities ranging from 8,000 ppm to 230,000 ppm were also used.

One of the objectives of this study was to evaluate the effect of reservoir fluid properties on relative permeability curves and residual saturations. A sensitivity analysis of several reservoir fluid types was made at different measurement conditions (ambient and reservoir conditions). The water phase was brine with more than ten different concentrations. For the oil phase, a range of different properties were used. Before conducting the relative permeability tests, it was essential for the core samples to be at representative conditions, initial water saturations, which match the height above the oil water contact in the reservoir. Initial water saturations were achieved by oil flood at different flow rates using different kinds of oils.

Having the samples at initial water saturations, these samples were placed in a relative permeability measurements apparatus. The measurement conditions were set as required and monitored. The obtained data were used to calculate relative permeability curves using a two-phase 1D black-oil simulation model with history matching. This software is used for analyzing single SCAL experiments as well as several SCAL experiments simultaneously. In addition to that, samples with different lithologies were selected to perform centrifuge capillary pressure in two different cycles (drainage and imbibition). The selected samples were placed in Beckman Ultracentrifuge vessels under oil or water and the conditions were set as required and the obtained data were processed.

The wettability of the samples was measured by two methods; Amott/Harvey and USBM techniques. In the case of USBM method, multi-point imbibition and drainage curves to end point saturations were performed by centrifuging and the area under the curves were used to calculate the USBM wettability index. For the Amott/Harvey method, two spontaneous imbibition measurements and two forced displacement measurements were conducted. The Amott water index, Iw, and the Amott oil index, Io, were calculated and combined to give the Amott–Harvey index which describes the wettability of the rock.

The procedures covered oil-water experiments. Both imbibition and drainage cycles were handled and a comparison of a variety of flow properties was made. Other factors which may have an impact on relative permeability curves such as IFT and flow rates were taken into account and examined. The data analysis and interpretation were performed by a 1-D core flood simulator where different scenarios of core flooding with different phases of reservoir fluids can be performed through simulation and/or estimation. Simulation is forward simulations of a multi-phase flow experiment, while estimation utilizes an optimization routine to history match the experimental data obtained in the laboratory. Several correlations were used and tested for their validity to history match the

experimental data. This was done through a sensitivity analysis of several cases. These correlations are summarized in Table 1. The selected correlation in each case depends on the type of the experiment that is being analysed. Figure 1 shows an example of history match of oil production and pressure drop and the generated relative permeability curves for one of the studied samples (carbonate sample).

RESULTS AND DISCUSSION

In this section, the results and the interpretation of the data which were obtained from the experimental work will be introduced. The selected samples for this study were taken from different hydrocarbon basins including sandstone and carbonate rocks. These samples represent different formations covering a variety of depositional environments such as fluvial channel, distributary channel, shelf and reef. The datasets are also a mixed suite of rock fabrics and composition. The petrophysical properties, routine core analysis, (porosity, air permeability and grain density) were measured for all of the samples. The statistical analysis of these properties showed that the samples have a porosity range from 5 % to 34 % and a permeability to air range from 0.234 to 551.0 mD.

Core-flood Analyses and Interpretation

About eleven oils and fourteen brine salinities were used to investigate the effect of fluid properties and measurement conditions on relative permeability curves and residual oil saturations. These properties include oil viscosity and density, brine salinity/density and viscosity, IFT and temperature. The properties of these fluids and the main results of residual and initial saturations, as an average for each reservoir, are given in Table 2.

The experimental results from relative permeability tests in this work are also included in Table 2. This table shows the average endpoint saturations of oil and water. Oil and water permeabilities at the endpoints are also listed for each reservoir. The water relative permeabilities at residual oil saturations were plotted as a function of oil/water viscosity ratio for different salinity values in Figure 2. This figure shows a relation between Krw@Sor and oil to water viscosity ratio. In this figure the multiple dots for each color represent samples with same oil/water viscosity ratio, so each color represent a group of samples with specific oil/water ratio. It can be seen that as the oil viscosity (or higher oil/water viscosity ratio) increases, the Krw@Sor decreases. In the viscosity ratio range from 1 to 10 most of the samples gave high krw@sor, on the other hand when viscosity ratio becomes more than 10 most of the samples gave low krw@sor. The general trend of this figure was compared with other published data and there was a similar trend. The effect of oil viscosity on residual oil saturations is shown in Figure 3. This figure shows that as the oil viscosity increases, residual oil saturations increases. Several values for the oil viscosity have been used to study their effect on Sor, these oil viscosities were used with different brine salinities, so for each group of samples, represented with different color, a specific oil and brine were used. In the case of lowest oil viscosity, six samples were used some of them showed an increased Sor with high oil viscosity and others showed a decrease in Sor, this can be due to the nature of the rock samples (sample heterogeneity), wettability

and the interaction between the two fluids and the rock. These results were in a good agreement with other published data. The effect of oil and water viscosities was also investigated by a 3D plot as shown in Figure 4. In this figure the average value of residual oil saturation, Sor, for each reservoir were plotted against oil and water viscosities. From this figure it can be seen that, residual oil saturations increases with increasing both oil and water viscosities. However, the effect of oil viscosity is more obvious on residual oil saturations than water viscosity. Figure 5 shows a relationship between residual oil saturations and the mobility ratio. In this figure, although there is a spread in the data, the residual oil saturations, both from centrifuge and flooding experiments, were increased when the mobility ratio is increased. The reason why there was no clear trend in this figure might be due to the assumptions of stable displacement front in conventional water flood theory which might not be applicable in all cases especially in the case of heavy oil reservoirs.

The effect of reservoir conditions was also investigated. Figures 6 and 7 show how the fractional flow curves changed and/or shifted by changing the temperature. The measurements were conducted at three different temperatures, 25, 45 & 75 C°, for high and low salinity brines. These figures show that the effect of temperature is not consistent in both salinity cases, it was obvious that this effect can be significant on some samples and can be neglected on others. The low salinity brine clearly shifts the fractional flow curve to the right, while in the case of high salinity brine the water fractional curves at 45 C° and 75 C° shifted to opposite directions relative to 25 C° curve. These observations can be attributed to the associated lithology of the samples and the interactions between the fluid system and the rock.

Centrifuge Capillary Pressure
In general, the residual oil values from centrifuge tests are lower compared to flooding experiments. In the case of high viscosity, it would be difficult to achieve the residual oil saturations which were achieved by centrifuge in a water flood test because the differences in the displacement mechanism. The capillary and gravity forces control the residual oil from centrifuge, while viscous forces are not important. During a water flood, fingering and by passing the oil phase could cause a higher residual oil. From the laboratory measurements it was noticed that water relative permeability at S_{or} decreases with increasing residual oil, as expected, and becomes very low for high S_{or}. Also the flow rate used in the lab should be carefully designed to achieve accurate results and to minimise any possible errors in the initial and residual saturations.

USBM & Amott/Harvey Wettability
The other parameter which has an influence on relative permeability and residual saturations is wettability. The effects of wettability on residual oil saturations for the studied reservoirs are shown in Figures 8 and 9. Figure 8 shows that, for USBM wettability indexes ranging between 0.0 and 0.6, residual oils were varied from 0.20 to 0.60. In general, the data indicates that, $S_{or}@K_{rw}$ increases and $K_{rw}@S_{or}$ decreases as the system changes from zero USBM wettability index (intermediate wet) towards water wet. This observation was

similar to Amott/Harvey index shown in Figure 9. In both cases shown in Figures 8 and 9 there is an indication that residual oil saturation is usually low when the core samples have neutral wettability, which is neither water-wet nor oil-wet. On the other hand, residual oil saturation tends to be high at strongly water wet conditions.

Calculation of Relative Permeability Curves by History Matching

In order to get a good relative permeability results, history matching of the experimental data through a number of forward simulations were made. This was performed on the data obtained from the lab using a commercial 1D core flooding simulator. An example of the history matching of oil production, pressure drop and the generated relative permeability curves for one of the studied samples is shown in Figure 1. This figure shows a comparison of the relative permeability curves for different fluid systems. This figure shows that the fluid properties such as viscosity and salinity have an influence on oil-water relative permeability curves and residual saturations.

The general trend is that, with increasing oil viscosity, residual oil saturation increases while irreducible water saturation decreases. Both oil and water relative permeability curves shift to lower values with increasing oil viscosity. These observations were more obvious in the case of high $\mu o/\mu w$ ratio and less when the viscosity of the two fluids gets close to each other ($\mu o/\mu w=1$). Also, it was observed that the salinity has a little effect and sometimes this can be neglected on the irreducible water saturations.

In this work different correlations were used to history match the laboratory data. The most used ones were Corey and LET for relative permeability and Skjaeveland and LET for capillary pressure. These correlations, listed in Table 1, were used to obtain the real endpoints from the laboratory measured data. It was observed that, residual oil saturations from laboratory measurements are higher than the history match data. On the other hand, the $K_{rw}@S_{or}$ values from laboratory measurements are lower.

The Effect of Different Parameters on Oil Recovery

In this study, the effect of many parameters on the recovery of crude oil during water flooding was investigated. Sensitivity analyses of fractional flow curves were made and compared as shown in Figures 10 and 11. These figures show two examples of these analyses. In these investigations different properties were used for the fluid system to generate different values of the mobility ratio between the existing fluids in the reservoir. Figure 10 shows an example of the effect of brine salinity on residual fluids and oil recovery. This figure shows a relationship between three different values of brine salinity and residual oil saturation. From this figure it can be seen that residual oil saturations generally decreases when low salinity brine is used. This is due to the fact that the interaction between low salinity brine and the rock samples depends on the composition of the fluid system (water and oil) and in general low salinity brines when injected into the samples work to change the initial wettability of the rock to more water wet wettability and this results in an increased oil recovery and less residual oil saturations.

Another investigation is shown in Figure 11. This figure compares three different cases of the fractional flow curves and how they are affected and shifted by changing the properties

of both oil and water. From this figure it can be seen that the efficiency of a water flood depends greatly on the mobility ratio of the displacing fluid to the displaced fluid, the lower this ratio the more efficient the displacement. This means that ultimate recovery efficiency will be obtained if the ratio is so low that the fractional flow curve has no inflection point. Also it can be seen that the effect of oil viscosity on these curves and thus on the drive mechanism is more obvious in the case of low salinity system. In general, it can be said that fractional flow curves are very sensitive to many parameters and a great care should always be taken when studying these curves.

CONCLUSION
The main results can be summarized as follows:
- When the oil viscosity increases, residual oil saturations generally increase and relative permeability to water decreases.
- Generally the end point water relative permeability data do not vary significantly with salinity variations.
- At the same injection flow rate and with the same water phase, relative permeabilities were a function of oil viscosity in the oil viscosity range studied.
- Generally, residual oil saturations were decreased when low salinity brine was used.
- The effect of wettability was clearly observed. In most cases, residual oil saturations were increased and relative permeability to water was decreased as the samples tend to be water wet and/or strongly water wet. On the other hand, residual oil saturations usually low, when the core samples have neutral wettability.
- Water fractional flow curves and thus oil recovery were affected by many parameters including the properties of the fluid/rock system and measurement conditions.
- The effect of oil viscosity on water fractional flow curves was more significant in the case of low salinity systems.
- The effect of temperature on water fractional flow curves was not consistent in the cases of low and high salinity systems.
- Laboratory investigations of relative permeability curves should be conducted at conditions as closely as possible to reservoir conditions.
- Residual oil saturations obtained from laboratory measurements can be higher than the real values. This depends on the measurements conditions and procedures.
- An improved oil recovery can be achieved by controlling the composition and properties of the fluid system and their reactions with the geological system.

With the results from these investigations, a complete picture of the relationship between different flow parameters and relative permeability curves can be developed and applied.

REFERENCES
1. Abrams, A. "The Influence of Fluid Viscosity, Interfacial Tension, and Flow Velocity on Residual Oil Saturation Left by Water flood", 1975, SPE 5050.
2. Akin, S., Castanier, L.M., and Brigham, W.E. "Effect of Temperature on Heavy-Oil/Water Relative Permeabilities", 1998, *SPE Annual Technical Conference and*

Exhibition, New Orleans, Louisiana, 27-30 September 1998. SPE-49021-MS.

3. Geffen, T.M., Owens, W.W., Parrish, D.R. et al. "Experimental Investigation of Factors Affecting Laboratory Relative Permeability Measurements", 1951, *Journal of PetroleumTechnology* 3 (4): 99-110. SPE-951099-G.

4. Hyung Tae Kwak, Gigi Zhang, and Songhua Chen, "The Effects of Salt Type and Salinity on Formation Water Viscosity and NMR Responses", 2005, Paper SCA 2005-51, Proceedings, *SCA International Symposium, Toronto, Canada*, 21-25 August 2005

5. Jadhunandan, P.P. and Morrow, N.R. "Effect of Wettability on Water flood Recovery for Crude-Oil/Brine/Rock System", 1995, *SPE Formation Evaluation* 10 (1): 40–46. SPE-22597-PA

6. Land, C.S. "Comparison of Calculated With Experimental Imbibition Relative Permeability", 1971, SPE J. 11 (4): 419–425. SPE-3360-PA.

7. McCaffery, F.G. and Bennion, D.W. "The Effect of Wettability on Two-Phase Relative Permeability", 1974, *Journal of Petroleum Tech.*13 (4). PETSOC-74-04-04.

8. Odeh, A. S. "Effect of Viscosity Ratio on Relative Permeability", 1959, Trans. AIME.

9. Sandberg, C. R., Gournay, L. S. and Sippel, R. F. "The Effect of Fluid Flow Rate and Viscosity on Laboratory Determination of Oil/Water Relative Permeability", 1958.

Table 1. Different Correlations Used for Relative Permeability and Capillary Pressure Calculations.

Relative Permeability	Capillary Pressure
Corey	Skjaeveland
Chierici	Burdine
Burdine	Bentsen and Anli
Sigmund – McCaffery	LET – Primary & Secondary Drainage
LET	LET – Imbibition

Table 2. Summary of Fluid Properties and Experimental Results

Reservoir No	Brine Salinity, ppm	Viscosity of Oil, cp	Viscosity of Brine, cp	μ_o/μ_w	Average S_{wi},%	Average S_{or},%	Average K_o @ S_{wi}, mD	Average K_w @ S_{or}, mD
1	8000	6.850	0.922	7.431	20.365	43.210	20.401	13.120
2	9000	7.120	0.855	8.327	12.040	41.625	20.410	13.120
3	12000	12.12	1.023	11.85	17.971	37.848	103.64	29.771
4	22000	3.583	0.918	3.903	22.978	22.948	4.9190	1.7475
5	60000	1.691	1.111	1.522	18.010	22.221	23.440	4.3320
6	85000	32.00	1.172	27.31	12.454	34.456	207.50	56.698
7	110000	1.867	1.263	1.478	18.450	25.338	11.509	5.1605
8	115000	1.500	1.090	1.376	30.520	46.722	1.7255	0.5015
9	120000	3.516	1.116	3.151	25.525	34.598	10.618	1.0285
10	160000	1.876	1.271	1.476	19.550	28.877	9.5540	7.4320
11	168000	4.696	1.290	3.642	18.658	30.275	3.5470	0.6480
12	180000	4.697	1.350	3.479	9.2800	31.504	1.7180	0.5011
13	208000	1.500	1.470	1.022	44.950	36.255	0.0450	0.0066
14	220000	3.583	1.891	1.895	22.978	22.948	2.4510	0.5300
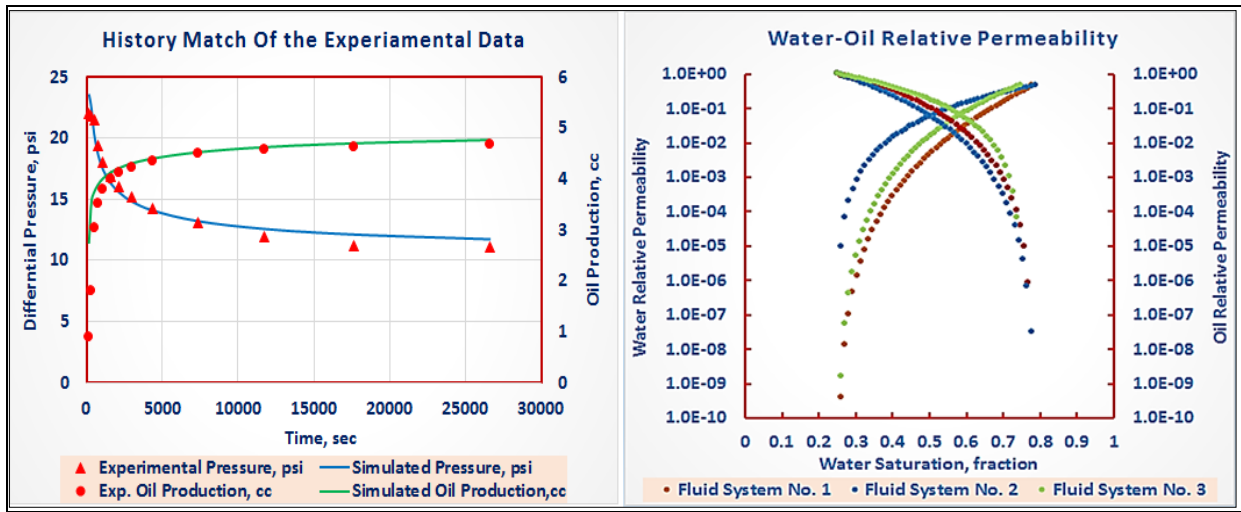
Figure 1. Sensitivity Analysis of Relative Permeability Curves for a Carbonate Sample.
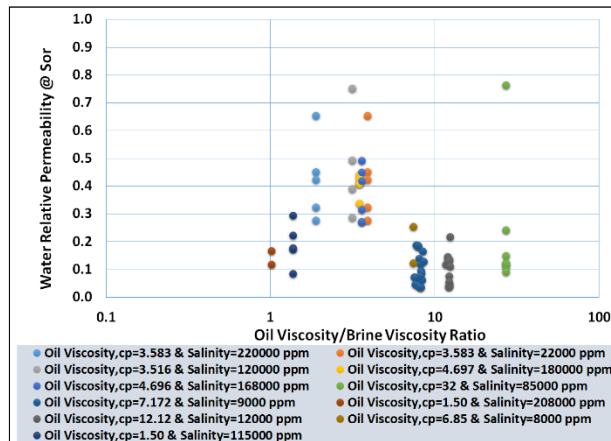
Figure 2. Water Relative Permeability Vs Oil/Water Viscosity Ratio
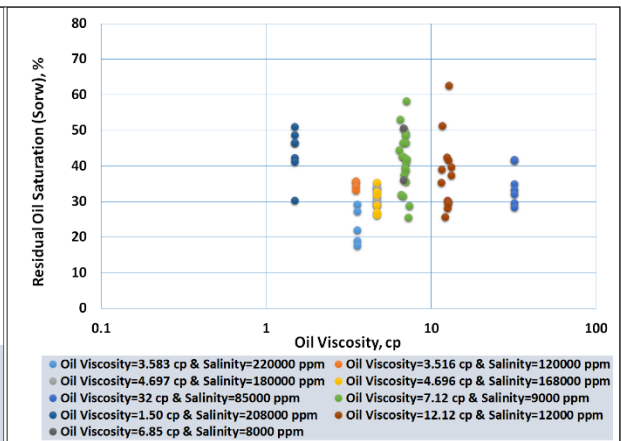
Figure 3. Residual Oil Saturation Vs Oil Viscosity
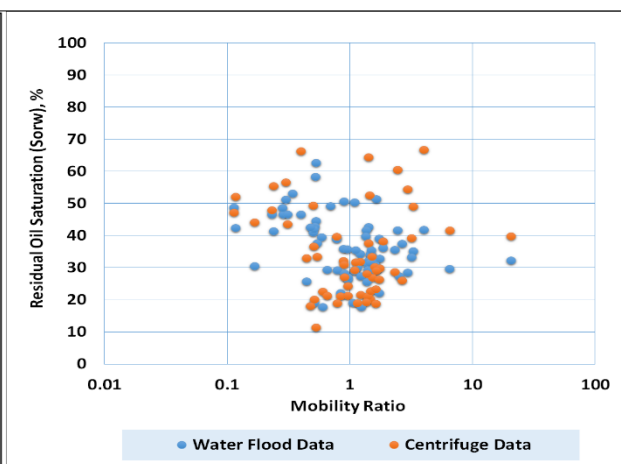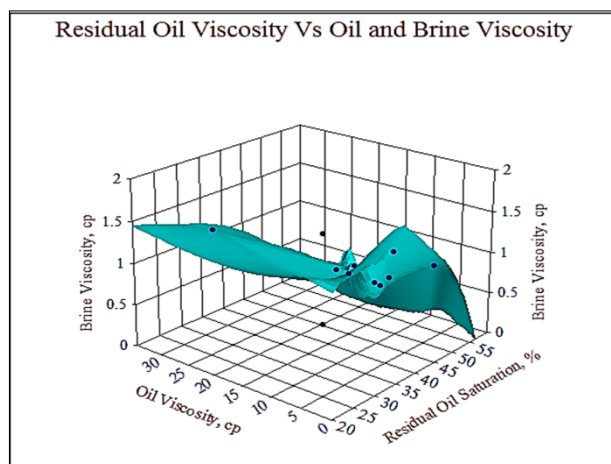
Figure 4. Residual Oil Saturation Vs Oil and Water Viscosity
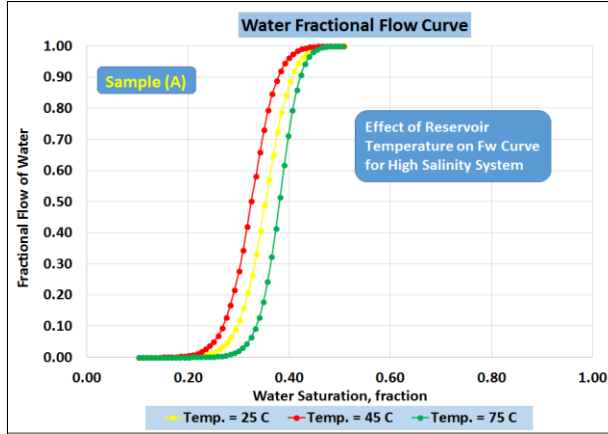
Figure 5. Residual Oil Saturation as A Function of Mobility Ratio
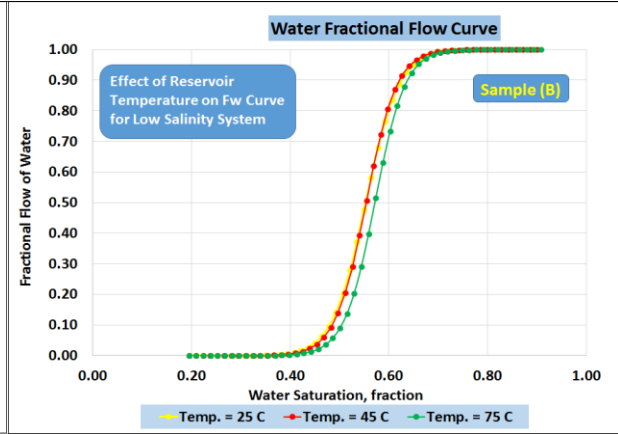
Figures 6 & 7. The effect of Reservoir Temperature on Water Fractional Flow Curves for High Salinity and Low Salinity Systems
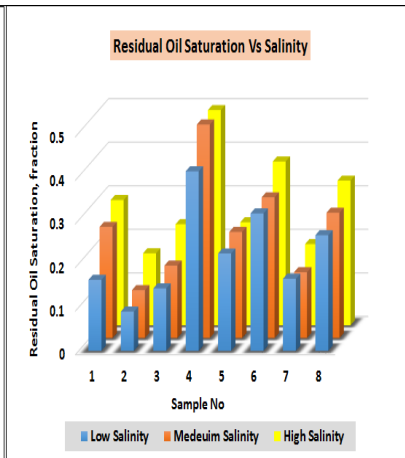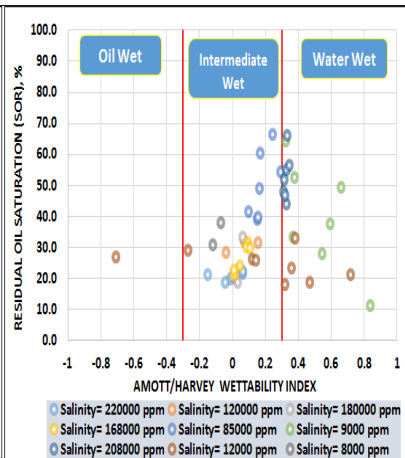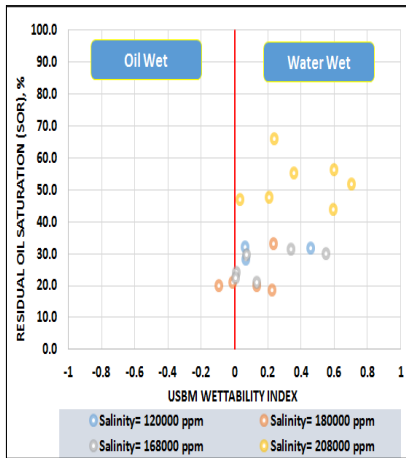
Figures 8 & 9. Sor vs USBM & Amott/Harvey Indexes.

Figure 10. Effect of Salinity on Residual Oil Saturation.
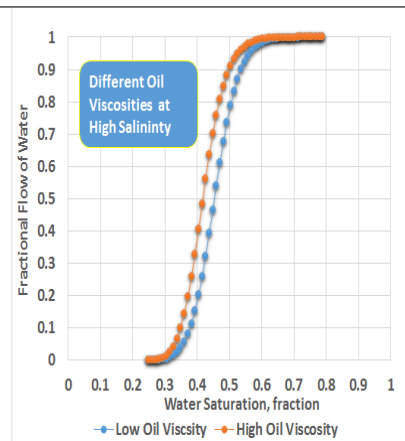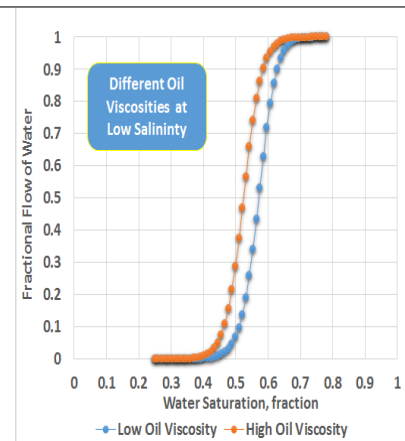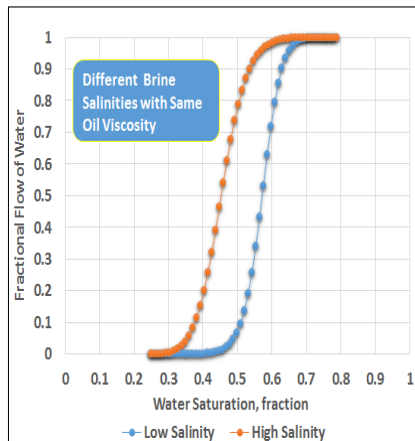
Figure 11. Effect of Fluid Properties on Water Fractional Flow Curves; Different Brine Salinities with Same Oil Viscosity, Different Oil Viscosities @ Low Salinity and Different Oil Viscosities @ High Salinity.

EOR BY ALKALI FLOODING IN THE VIENNA BASIN: FIRST EXPERIMENTAL RESULTS OF ALKALI/MINERAL REACTIONS IN RESERVOIR ROCKS

Wolfgang Hujer[1]; Verena Leitenmüller[2], Kenny Walrond[2]
[1]OMV UPSTREAM TECH Center&Lab, [2]Department of Petroleum and Geothermal Recovery, Mining University Leoben

This paper was prepared for presentation at the International Symposium of the Society of Core Analysts held in Vienna, Austria, 27 August -1 September 2017

ABSTRACT

The alkali/mineral reactions in Nordhorn sandstone, dolomite and reservoir sandstones from the Vienna Basin have been analysed by static tests using steel autoclaves and plastic bottles to gain first insights into potential dissolution and precipitation within the reservoir during alkali-polymer flooding. The interaction of the rocks with NaOH, KOH, Na_2CO_3 and K_2CO_3 at 60°C and pH values between 11.1 and 13.8 has been tested. Duration of the tests was 26 days for autoclaves and 54 days for plastic bottles. Weak dissolution and precipitation of silica crusts have been observed for the Nordhorn sandstone with NaOH in autoclave tests but not in bottle tests. Dolomite shows strong reactions with NaOH and KOH in all tests resulting in precipitation of Mg-hydroxides and calcite. Weak reactions have been observed for tests with Na_2CO_3 and K_2CO_3. Reservoir sandstones of the Vienna Basin are predominately characterized by high amounts of detrital quartz and dolomite. Strong dissolution of grains and precipitation of calcium-silicates occurred in tests with NaOH and KOH resulting in cementation of pore space. Only weak reactions on detrital dolomite have been observed in tests with Na_2CO_3 and K_2CO_3. Further tests are in preparation to analyze changes in pH and the chemical composition of alkaline solutions during alkali/rock interaction to determine the usability of above listed alkaline solutions for alkali-polymer flooding.

INTRODUCTION

The Neogene of the Vienna Basin hosts several mature oil and gas fields that are produced since the 1940's. The applicability of several EOR methods including alkali-polymer flooding within selected reservoir horizons is currently under investigation. The plan is to inject a pre-flush with low-salinity water, followed by an alkaline solution to generate in-situ soaps for mobilizing the crude oil. Afterwards, the injection of a polymer solution follows to enhance the fluid viscosity and support displacement of chemicals. The selection of the alkali solution that should be used for flooding is strongly depending on interaction of alkaline solutions with minerals in reservoir rocks. Interactions between alkali solutions and formation rocks can cause dissolution of existing minerals, precipitation of new

minerals and therefore result in permeability changes and reduce effectiveness of alkaline solutions [1, 2]. These effects can cause severe problems during injection of alkaline solution thus having a strong potential influence on the economics of alkali-polymer flooding. To obtain better understanding of rock-alkali reactions; a first test series of static tests using steel autoclaves and plastic bottles have been performed. Alkali solutions used for the tests are NaOH, KOH, Na_2CO_3 and K_2CO_3. Rocks used for testing are Nordhorn sandstone, dolomite and reservoir sandstone samples from the formation selected as candidate for alkali-polymer flooding.

EXPERIMENTAL SET-UP

Two experimental set-ups have been used concomitantly due to time-constraints. For the first set-up, steel autoclaves that are normally used for corrosion inhibit testing on coupons have been used. The steel autoclaves have been cleaned to remove any rust. A Nordhorn sandstone sample and a dolomite sample have been used for testing. Both samples were broken into 1-2 cm sized pieces to increase the available surface for reaction and a sample piece was put into an autoclave. The autoclaves have been evacuated and afterwards filled with ~100 ml sodium-hydroxide solution [15 g_{NaOH}/1L synthetic brine (synthetic brine = 22.09 g/L NaCl)]. The NaCl concentration refers to the chloride content in the water from the water treatment plant that would be used together with the alkali solution. The pH of the solution was 13.8. The reason for the high concentration and pH was to create some extreme scenario for mineral dissolution and precipitation. Finally, nitrogen gas was used to apply a pressure of ~10 bar. The autoclaves have been stored in a drying cabinet at 60°C (reservoir temperature) for 26 days.

For the second test set-up, polypropylene bottles have been used. The second test set-up included Nordhorn sandstone, dolomite and reservoir sandstone samples (oil removed). Each rock type has been tested with sodium-hydroxide solution, potassium-hydroxide solution, K_2CO_3 and Na_2CO_3 solution. The concentration of the individual solutions was always [15 g alkali/1L synthetic brine (synthetic brine = 22.09 g/L NaCl)]. The pH of the solutions ranges from 11.30 to 13.54. Each bottle was filled with ~250 ml of solution. A plastic foil was applied on top of the plastic bottles to reduce evaporation. The bottles were then stored in a drying cabinet at 60°C for 54 days. All samples have been cleaned with hot methanol after testing to remove salt crusts.

All samples as well as untreated samples of every lithology have been analyzed using a LEO 1450 EP SEM with an attached EDX system.

Sample Descriptions
<u>Nordhorn Sandstone</u>
The sample can be described as fine-medium-grained, porous sandstone that consists of quartz (96.6%), potassium feldspar (0.9%) and kaolinite (2.5%). The quartz grains exhibit well developed quartz cement overgrowths (plate 1a). The kaolinite is present as cement in pore space and as replacement within potassium feldspar. Under the SEM, the kaolinite

exhibits a well-developed booklet structure (plate1b). Pore space consists predominately of primary interparticle pores.

Dolomite

The sample can be described as bluish-greyish dolosparite with trace amounts of calcite present. The sample belongs to the so-called "Hauptdolomit" geological unit; a Triassic dolomite that has sourced the detrital dolomite grains present in the reservoir sandstone samples. SEM images of the untested sample show that it consists of well-developed dolomite rhombohedra with some open intercrystalline pore space (plate 3a).

Reservoir Sandstone

The sample can be described as medium-coarse-grained, moderately to well sorted litharenite (plate 5a, 5b). The mineralogical composition comprises mainly quartz (~46%) and detrital dolomite (~36%), ferroan dolomite cement (~6%), feldspars (~4%), crystalline rock fragments (~2%) detrital limestone (~4%), detrital clay coats on grains (~1%) and calcite cement (~1%). Pore space consists predominately of primary interparticle pores.

RESULTS

Autoclave Tests

Nordhorn Sandstone with NaOH, 1.5% Brine, pH 13.8

The quartz cement surfaces show discontinuous, poorly crystalized encrusting's (plate 2a) that consist of Si and O based on SEM-EDX analyses. Those crusts are interpreted as amorphous silica crusts that precipitated on the quartz cement surfaces. Similar crusts are also observed on kaolinite cement crystals (plate 2b). Furthermore, the edges of the kaolinite crystals show evidence for dissolution.

Dolomite with NaOH, 1.5% Brine, pH 13.8

Macroscopically, the surface of the tested sample exhibits a whitish staining. The SEM analyses reveal that the dolomite rhombohedra are covered by multiple layers of newly formed mineral that exhibits a webby ("honey-comb") texture (plate 3b). The size of individual crystals is <1 micron. EDX analyses show the presence of C, O, Mg, Ca and Fe but these results are strongly influenced by the dolomite below. Based on the texture, this newly formed mineral is interpreted as Mg-hydroxide (interpreted as brucite).

The Mg-hydroxide layers are overgrown by round-shaped to elongated crystals that occur either isolated or as aggregates (plate 3b). The crystal surfaces are smooth and round-shaped. Size of crystals is <10 microns. EDX analyses show the presence of calcium and phosphor. The latter could be sourced from the dolomite sample although it has not been detected by EDX analyses before. These crystals are interpreted as calcium-phosphates.

The third newly formed mineral consists of well-developed, prismatic-shaped crystals that overgrow both the webby Mg-hydroxides and the Ca-phosphates. The size of the crystals ranges in the tenths of microns. Based on EDX analyses, those minerals comprise calcium (Ca), carbon (C) and oxygen (O) and are interpreted as calcite.

Bottle Tests
Dolomite Sample with NaOH, 1.5% Brine, pH 13.54
The dolomite rhombohedra are strongly dissolved and almost not recognizable anymore. The complete sample is covered by micrometer-sized micro-pores. The dissolution also created secondary macro-pores (plate 4a). Columnar calcite crystals have been observed but no brucite coatings are present.
Dolomite sample with KOH, 1.5% Brine, pH 13.39
The dolomite rhombohedra show strong dissolution resulting in abundant, ~1 micron-sized dissolution pores (plate 4b). Furthermore, two new mineral phases have formed. The first one comprises 2-4 microns long, prismatic-shaped crystals cover the dolomite surface. Based on EDX-analyses they consist of Mg, Ca and O and probably represent a magnesium-hydroxide. Tiny calcite crystals are present between the prismatic-shaped crystals. The second phase consists of columnar-shaped, ~10 microns long crystals. EDX-analyses show Ca, C and O thus the crystals are interpreted as calcite.
Dolomite sample with Na_2CO_3, 1.5% Brine, pH 11.41
The rhombohedra show only weak dissolution that is mainly evidenced by flaking of several micrometer-sized plates from the crystal surface.
Dolomite sample with K2CO3, 1.5% Brine, pH 11.30
The dolomite rhombohedra show no signs of dissolution.

Nordhorn Sandstone with NaOH, 1.5% Brine, pH 13.4
Only traces of silicate crusts have been observed on few quartz cement surfaces.
Nordhorn Sandstone with KOH, 1.5%Bbrine, pH 13.2
The sample shows very weakly developed dissolution pits on quartz cement surfaces. No changes have been observed on kaolinite cement crystals.
Nordhorn Sandstone with Na_2CO_3, 1.5% Brine, pH 11.41
Neither dissolution nor precipitation of new mineral phases has been observed.
Nordhorn Sandstone with K_2CO_3, 1.5% Brine, pH 11.30
Quartz cement surfaces show minor dissolution and very localized precipitation of calcium-silicates has been observed.

Reservoir Sandstone Sample with NaOH, 1.5% brine, pH 13.4
Macroscopically, the sample is more cemented after cleaning than before the testing. Quartz grains show dissolution evidenced by depressions on grain surfaces that are bounded by crusts (plate 6b). Detrital dolomite and dolomite cement rhombohedra are strongly dissolved and partly not recognizable anymore. Furthermore, crystals that resemble brucite in texture and composition have developed. The same crusts found on quartz grains are also present. These crusts additionally form pore-bridging cement between grains (plate 6a). Based on EDX analyses, these crusts consist of Si, Ca, C and O and are interpreted as poorly crystallized to amorphous calcium-silicates.

Reservoir Sandstone Sample with KOH, 1.5% brine, pH 13.2

The detrital dolomite and dolomite cement rhombohedra are strongly dissolved; minerals resembling brucite have formed (plate 7b). Quartz and other siliciclastic grains exhibit dissolution in form of depression on grain surfaces that are bounded by irregular-shaped, poorly crystallized crusts. These crusts consist of Ca, Si, C and O thus being interpreted as calcium-silicates. Overall, the dissolution and precipitation (plate 7a) is less pervasive compared to reservoir rock samples exposed to NaOH.

<u>Reservoir Sandstone Sample with Na2CO3, 1.5% brine, pH 11.41</u>
Detrital dolomite and dolomite cement show 1-2 microns-sized mineral flakes with a platy- to ragged-shaped texture. Based on EDX-analyses, these crystals comprise of Ca, Mg, C and O. The crystal texture and the chemical composition point to a magnesium-hydroxide (?brucite). Quartz grains and other siliciclastic grains show now dissolution or precipitation of new minerals.

<u>Reservoir Sandstone Sample with K2CO3, 1.5% brine, pH 11.30</u>
The rhombohedra of detrital dolomite and dolomite cement are characterized by very thin, rough layer that could represent an overgrowth by irregular-shaped, very fine crystals (probably poorly developed magnesium-hydroxide). The quartz grains and other silicate do not show any dissolution.

DISCUSSION
Autoclave Tests
<u>Nordhorn Sandstone Sample</u>
The Nordhorn sandstone sample showed only weak dissolution and precipitation after 26 days of testing at 60°C. It was expected that more dissolution would have been observed due to the high pH of 13.8, especially as the solubility of silica increases strongly at pH >7.5 [3]. The observed weak dissolution and precipitation of amorphous silica crusts on quartz grains and cement could be explained by two factors; temperature and chemical stability of quartz cement. Strong reaction of quartz with strongly basic NaOH solution was observed at 80°C after 8 days [4] whereas the same works report almost no reaction at 23°C after 265 days of testing. Temperature was considered as a key parameter for quartz solubility. Based on our results, it could be imaginable that a temperature of 60°C was too low for stronger reactions. The other factor could be the chemical stability of quartz cement as this cement had time to precipitate under chemical equilibrium in the subsurface resulting in well-ordered crystals. The diagenetic kaolinite present also only showed weak reactions which was unexpected as kaolinite is considered to be very reactive with NaOH [1], even at room temperature [5]. A reason could be that these experiments have been conducted on powdered or disintegrated samples whereas the kaolinite cement in our study consisted of well crystallized booklets. The observed crusts on quartz and kaolinite cement surfaces were interpreted as amorphous silica crusts. Such crusts precipitate after reaching equilibrium with the solution [4]. The observed low volumes indicated that this equilibrium most likely was achieved near before the end of the tests.
<u>Dolomite Sample</u>

The dolomite sample reacted strongly with the NaOH solution which was in good agreement with published data [4]. The presence of brucite and calcite could be explained by the following chemical formula after [6].

$$CaMg(CO_3)_2 + 2MOH \rightarrow Mg(OH) + CaCO_3 + M_2CO_3 \text{ where } M=Na, K, \qquad (1)$$

The reasons for precipitation of phosphate minerals are still under investigation. Alkali carbonate crystals were not been found during SEM analyses. Based on the observed crystal structure, brucite would increase micro-porosity and most likely affect wettability if formed within the reservoir.

Bottle Tests

Nordhorn Sandstone Samples

The Nordhorn sandstone samples showed no to very localized weak dissolution and precipitation of new minerals. Interesting to note is that the bottle test sample exposed to NaOH showed less alterations than the autoclave sample. This could be explained by the larger amount of liquids within the bottles which needed longer to achieve equilibrium and maybe also by ambient pressure conditions.

Dolomite Samples

The dolomite samples showed strong reactions both with NaOH and KOH solutions. The dolomite rhombohedra were strongly dissolved and abundant new micro-pores were generated. Calcite had precipitated in both tests whereas Mg-hydroxides had only been observed in the KOH test. Weak dissolution was observed in the Na2CO3 test. The precipitation of radial ("star-like") iron-rich crystals is still under investigation. Almost no reaction was observed in the K2CO3 test

Reservoir Sandstone Sample

The reservoir sandstone had been strongly altered by NaOH solution. The detrital dolomite and dolomite cement showed the same alteration as observed in the dolomite sample tests. Furthermore, the siliciclastic grains were strongly dissolved. The dissolved material had precipitated as amorphous calcium-silicate crusts. The sample exposed to KOH showed similar dissolution and precipitation features but the alterations were less intensive than compared to NaOH. The sample exposed to the Na2CO3 solution showed minor precipitation of Mg-hydroxides on dolomite rhombohedra whereas the siliciclastic grains remained mainly untouched. A similar but even weaker developed precipitation had been observed in the tests with K2CO3 solution. Again the quartz grains were untouched. The test results for Na2CO3 and K2CO3 solution could be explained by the high reactivity of dolomite towards alkaline solutions [4].

CONCLUSION

A series of static tests using steel autoclaves and plastic bottles to obtain first insights into rock-alkali interactions have been conducted. Based on the test results, the following conclusions can be made:

1) The reaction between rock samples and alkaline solutions can be tested both with steel autoclaves and plastic bottles.
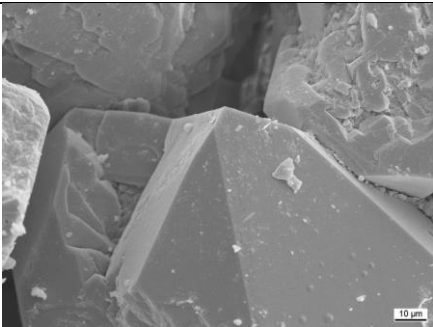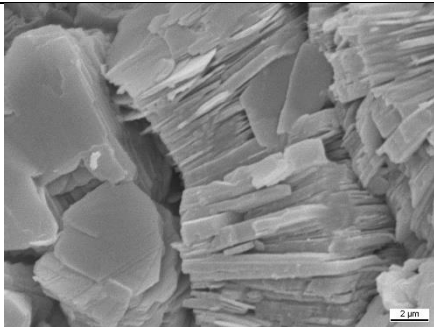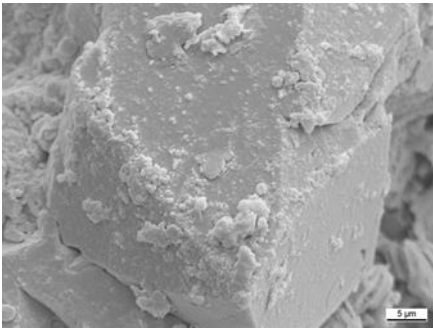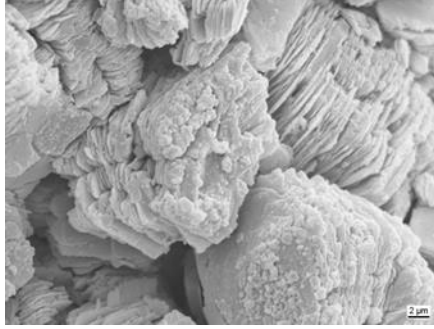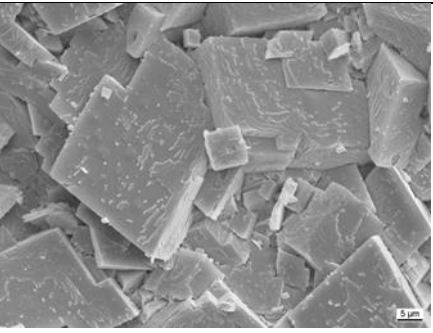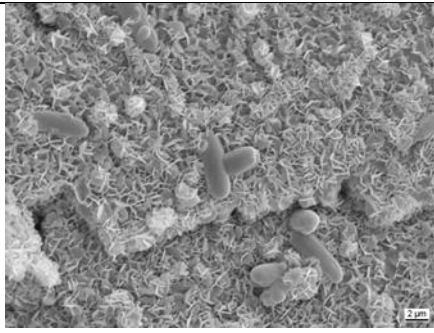
2) Temperature is a key factor for quartz solubility in alkaline solutions. The 60°C in the test set-up resulted in less reaction than the 80°C used in published test results [4].

3) The differences in reaction of quartz grains in Nordhorn sandstone between autoclave and plastic bottle tests are related to higher amount of liquid in the latter and probably also higher pressure conditions in the autoclaves.

4) Dolomite is a highly reactive mineral phase in contact with alkaline solutions, especially NaOH and KOH but also Na_2CO_3 and K_2CO_3. Dedolomitization results in precipitation of micro-porous brucite and calcite and creation of abundant dissolution pores.

5) Reservoir sandstones characterized by abundant detrital quartz and dolomite react with NaOH and KOH resulting in grain dissolution and precipitation of brucite and calcium silicates. This precipitates will have a negative influence on reservoir properties and therefore injectivity. Further testing would be necessary to evaluate the usability of NaOH and KOH for alkali-polymer flooding in the Vienna basin.

6) The weak reactions of reservoir sandstones with Na_2CO_3 and K_2CO_3 solutions compared to NaOH and KOH argue for the use of those solutions for alkali-flooding

7) Additional tests are in preparation to analyze changes of pH and the chemistry of different alkaline solution during contact with reservoir rock samples over time. These tests will also include potential gravel-pack materials (sand, carbolite, glass spheres).

ACKNOWLEDGEMENTS

REFERENCES

1. Mohnot, S. M., J. H. Bae, W. L. Foley,"A Study of Mineral/Alkali reactions", *Society of Petroleum Engineers*, (1987), **SPE13032**, pages 653-663.
2. Southwick, J. G., Solubility of Silica in Alkaline Solutions: Implication for Alkaline Flooding", (1985), **SPE12771**, pages 857-864.
3. Iller, R. K., "*The Chemistry of Silica: Solubility, Polymerization, Colloid and Surface Properties and Biochemistry*", J. Wiley and Sons, New York, 1979, pages 866.
4. Coquette, M., M. A. Berube, J. Locat, "Behavior of Common Rock-Forming Minerals in a Strongly Basic NaOH-Solution", *Canadian Mineralogist* (1991), **vol. 29**, pages 163-173.
5. Carroll, D., H. C. Starkey, "Reactivity of Clay Minerals with Acids and Alkalies", *Clays and Clay Minerals* (1971), **vol. 19**, pages 312-333.
6. Hadley, D. W. "Alkali Reactivity of Carbonate Rocks", *Highway Research Board*, (1964), **vol 40**, pages 1-20

Plate 1a. Quartz Cement, NH Sandstone	Plate 1b. Kaolinite Cement, NH Sandstone
Plate 2a. Quartz Cement, NH Sandstone, after NaOH Autoclave Test	Plate 2b. Kaolinite Cement, NH Sandstone, after NaOH Autoclave test
Plate 3a: Dolomite Sample Surface	Plate 3b: Dolomite Sample Surface after NaOH auotclave test
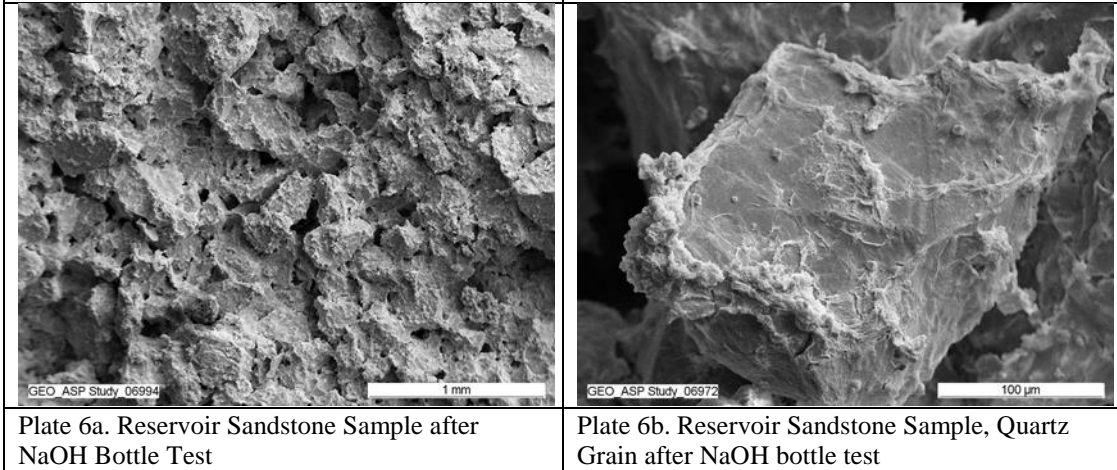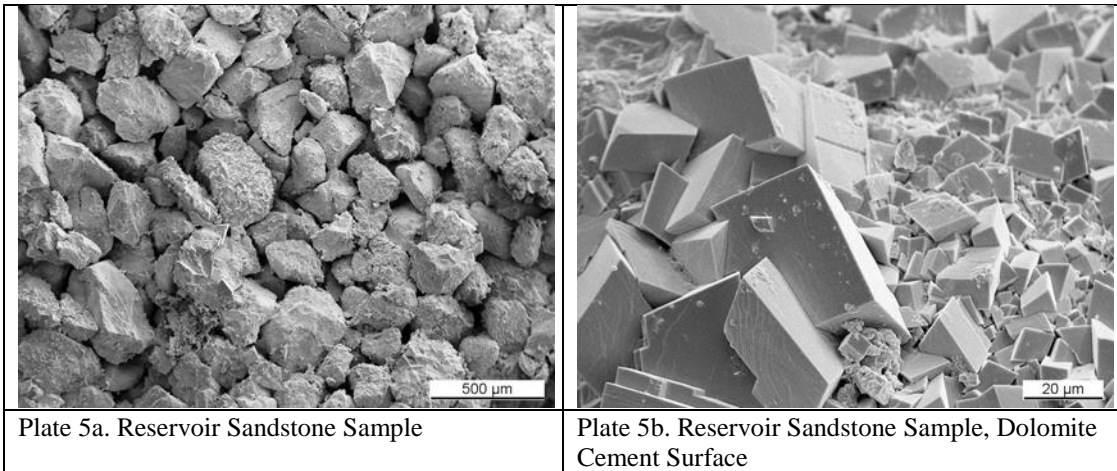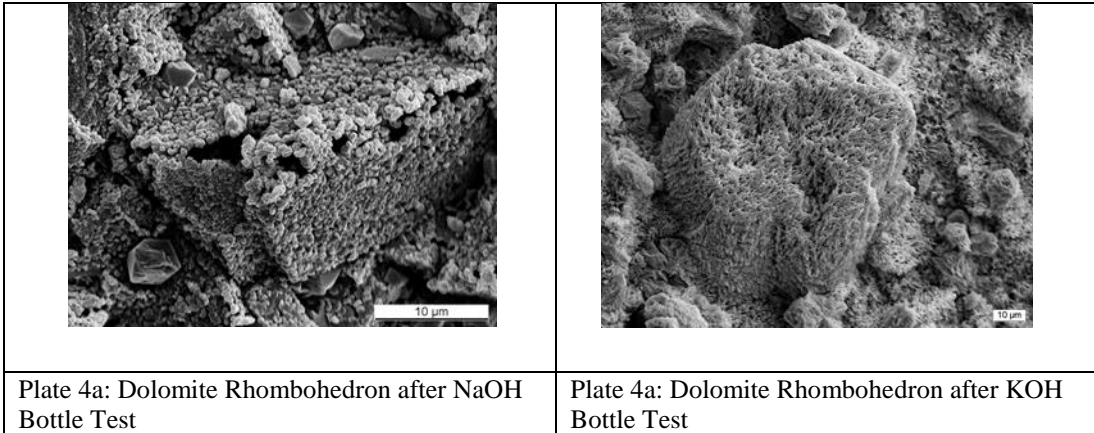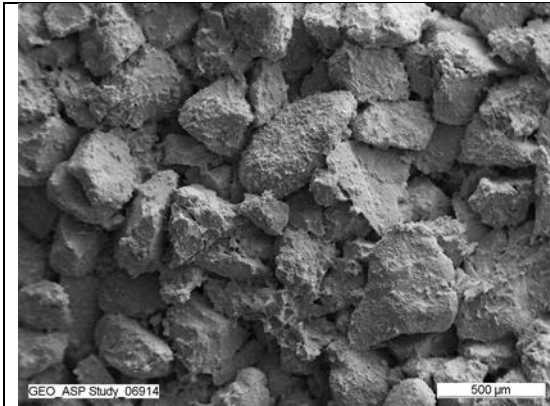
| Plate 4a: Dolomite Rhombohedron after NaOH Bottle Test | Plate 4a: Dolomite Rhombohedron after KOH Bottle Test |

| Plate 5a. Reservoir Sandstone Sample | Plate 5b. Reservoir Sandstone Sample, Dolomite Cement Surface |
| Plate 6a. Reservoir Sandstone Sample after NaOH Bottle Test | Plate 6b. Reservoir Sandstone Sample, Quartz Grain after NaOH bottle test |

| Plate 7a. Reservoir Sandstone Sample after KOH Bottle Test | Plate 7b. Reservoir Sandstone Sample, Dolomite Cement Surface after KOH Bottle Test |
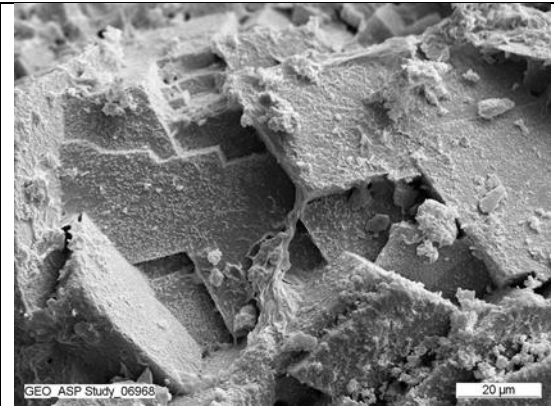
ON THE RISK OF PERMEABILITY ALTERATION BY SALT PRECIPITATION: AN EXPERIMENTAL INVESTIGATION USING X-RAY RADIOGRAPHY

Souhail Youssef[1], Yannick Peysson[1], Olivier Lopez[2], Jostein Alvestad[2], Christin Weierholt Strandli[2], Øivind Fevang[2]

[1]IFP Energie nouvelles, Rueil-Malmaison, France

[2]STATOIL ASA, Trondheim, Norway

This paper was prepared for presentation at the International Symposium of the Society of Core Analysts held in Vienna, Austria 27 August - 1 September 2017

ABSTRACT

We have experimentally investigated the effect of drying a brine saturated porous medium by gas injection and assessed the resulting salt precipitation on permeability. State of the art equipment designed for high throughput coreflood experimentation was used to capture the dynamics of salt migration. Experiments, where nitrogen gas was injected at an imposed pressure in a brine-saturated core, were monitored by X-ray radiography to visualize the evolution of local saturation and salt concentration as well as salt precipitation. Results show that salt precipitation results from the interplay of different parameters, namely pressure gradient, brine concentration, capillary forces and vapor partial pressure. Experimental observations indicate that in the case of dry gas injection, salt precipitates systematically but permeability alteration is observed only if a capillary contact is maintained with the brine. However, in the case of humid gas injection, presence of brine can inhibit dry-out if an equilibrium is reached between salt concentration and partial vapor pressure.

INTRODUCTION

In the field of natural gas production as well as gas storage in aquifer, salt deposition is considered as a potential risk for gas wells. In Northern Germany, field evidences of mainly halite precipitation have been reported during gas production [1]. A synthetic review of gas well productivity impairment by salt plugging can be found in [2]. Injection of a gas phase through a water saturated porous medium can reduce the water saturation not only by displacement mechanisms but also by evaporation mechanisms. To understand the phenomena of drying induced by gas production, Mahadevan *et al.* [3] did an extensive experimental and theoretical study to show that injection of vapor saturated gas (i.e., humid gas) in a rock sample can induce drying [3-4]. The origin of the drying is that the water mole fraction in the gas phase at equilibrium depends on pressure. In the context of gas storage in aquifer, experiments have been conducted by [5-6] injecting dry gas in brine saturated sandstone samples with different salt concentrations in the brine. They showed that the drying rate is proportional to the gas velocity and that any dissolved salt in the water can be transported by capillary flows induced by drying and can even accumulate near the injection surface. The permeability can then be reduced by pore clogging. They

conclude that all of these mechanisms must be included in models to calculate the near wellbore permeability and porosity changes with time, to correctly determine well injectivity.

In this study, we present a comprehensive experimental investigation of the effect of gas flow in a sandstone sample initially saturated with water or brine. Five experiments have been conducted on a small Bentheimer sandstone sample using different experimental conditions i.e. dry or humid gas, deionized water or brine, with and without capillary contact, in order to highlight the effects of drying by gas injection and salt precipitation on permeability impairment.

MATERIAL AND METHODS

Experiments were conducted on a Bentheimer sandstone of 1 cm in diameter and 2 cm in length with a porosity of 23% and a permeability of 1350 mD. To perform the different experiments, we have used nitrogen, deionized water and a 100 g/l KBr brine. KBr salt was chosen as it has a high electronic density allowing a good X-ray contrast with water. The solubility limit of KBr in water at 20°C is 560 g/l.

The experimental set-up used in this study is shown in Figure 1. Nitrogen was injected at a constant pressure using a downstream pressure regulator. Its flow rate was monitored by a Coriolis mass flow meter. A humidifier canister was used to saturate the gas. Brine solution was injected using an Isco Pump. The different lines were connected to an X-ray transparent hassler type cell equipped from each side with three connections (inlet, outlet and static line for the pressure transducer). A data acquisition system was used to monitor the pressure, mass flow and temperature. Finally, the set-up was installed in a dedicated radiography facility equipment for in-situ saturation monitoring.

During fluid injection, the sample was imaged using an X-ray radiograph equipment. The system consists of an X-ray source, a flat panel and a data processing unit for computation, visualization and data analysis. The radiographs were captured with a resolution a 20 µm at a rate of one frame per second. Radiographs were then cropped to show only the sample (see zone 1 in Figure 1). The stack of images was processed to monitor water saturation and salt concentration evolution during gas injection [7]. Indeed image gray levels are proportional to the transmitted X-ray intensity which is defined by the Beer Lambert's law in the case of a multicomponent material as:

$$I_t = I_o\, e^{-(\mu_{bt}\, X_b + \mu_g\, X_g) + \alpha}$$

where I_o and I_t are respectively the incident and the transmitted X-ray intensity, μ_{bt} and μ_g are respectively the brine and the gas attenuation coefficients, X_w and X_g are respectively the brine and the gas portions in the linear path of the X-ray and α is the attenuation of the structure. Considering two references states, 100% brine saturated and dry images the above equation can be written as:

$$I_b = I_o\, e^{-\mu_{b0}\, X + \alpha} \qquad , \quad I_g = I_o\, e^{-\mu_g\, X + \alpha}$$

where X is the linear path of the X-ray that corresponds to the total porosity and μ_{b0} is the initial brine attenuation coefficient.

By construction we obtain $\qquad\qquad X_b + X_g = X$

Afterward, normalizing the X-ray intensity I_t by both the 100% brine and the dry case, and considering $\mu_b \gg \mu_g$ we obtain:

$$\frac{\ln\left(\frac{I_b}{I_0}\right) - \ln\left(\frac{I_t}{I_0}\right)}{\ln\left(\frac{I_b}{I_0}\right) - \ln\left(\frac{I_g}{I_0}\right)} = \frac{-\mu_{b0}X + \mu_{bt}X_b}{-\mu_{b0}\,X}$$

When salt concentration is constant, $\mu_{bt} = \mu_{b0}$ and $\frac{X-X_b}{X} = S_g$, where S_g is the gas saturation. If the salt concentration changes, μ_{bt} will vary with an upper limit equal to the KBr attenuation coefficients. If we normalize the X-ray transmitted intensities (i.e. relative X-ray absorption) by the mean intensity of a dry sample with precipitated salt, we can assess qualitatively the variation of salt quantity compared to the initial distribution.
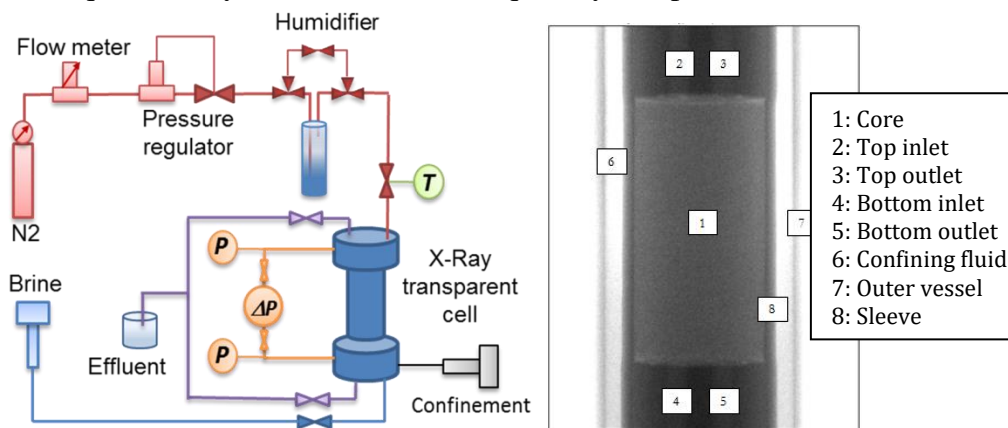
Figure 1: Experimental set-up and a radiograph showing the sample shape and the basic components of the Hassler injection cell.

RESULTS AND DISCUSSION

As pointed out in the introduction, drying and salt precipitation result from the interplay of different parameters. To un-correlate the effect of these parameters, we have conducted a number of experiments that map the parameter domain by varying the gas humidity, salt content and boundary condition (with and without capillary contact). In the following, we discuss the impact of these parameters.

Effect of gas humidity

To study the effect of gas relative humidity, we have conducted two experiments where we have injected dry gas and humid gas, respectively, in a sample initially saturated with deionized water (Experiments 1 and 2). The inlet relative gas pressure was set to 100 mbar. The pressure drop was chosen to be above the entry pressure of 70 mbar and corresponds to a pressure gradient of 5 bar/m which is representative of near well bore pressure gradient. Figure 2 and Figure 4 show the evolution of the mean gas saturation within the sample as well as the mass flow rate of the gas. Four regimes can be distinguished: between 0 and 10 min, the gas drains the sample till a mean residual water saturation of 30% to 40%. Next we observe a smooth increase in the gas saturation and the flow rate until the gas saturation

reaches around 74% (70 min for dry case and 120 min for the humid case). Following this, we note an increase in the gas flow rate as well as in the gas saturation. This change in the drying rate corresponds in the case of dry gas to the advent of a discontinuity and a sharp front on the saturation profile (see Figure 3). In the case of wet gas, profiles (see Figure 5) exhibit a decrease in the water saturation at the outlet of the sample till a uniform saturation is reached all along the sample. The final stage, in the two cases, corresponds to the dry state.

The comparison between experiments 1 and 2 shows clearly the difference between dry gas and humid gas drying effects. Whereas with dry gas it took two hours to dry out the sample, it took ten hours to dry out the sample with humid gas. However, the major difference is observed in the saturation profiles. In the case of dry gas, the drying front propagates from the inlet toward the outlet while in the case of humid gas drying took place first at the outlet and then propagates to the inlet. The two first order mechanisms involved in those cases are most likely an instantaneous phase equilibrium between gas and water coupled with a capillary equilibrium generated by the gas flow and the water saturation. In the dry gas experiment, drying is activated immediately at the entrance of the sample. However in the case of humid gas, water vaporization is due the pressure drop (i.e., gas expansion) along the sample that allows the gas to uptake more vapor as suggested by [4]. In the two cases, capillary forces helps to redistribute water to compensate for the water under-saturation.
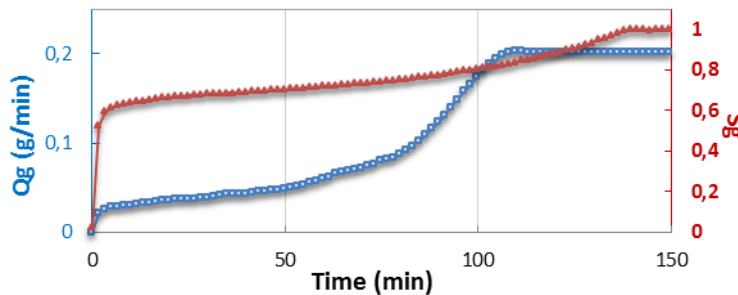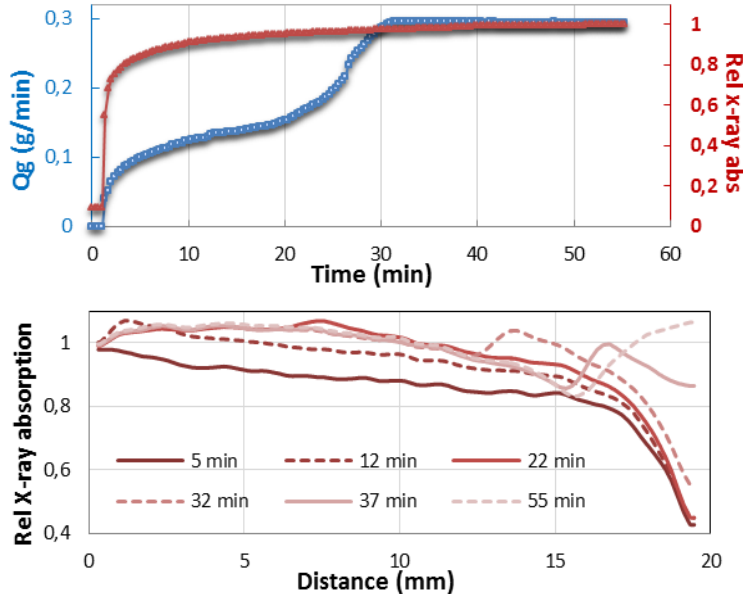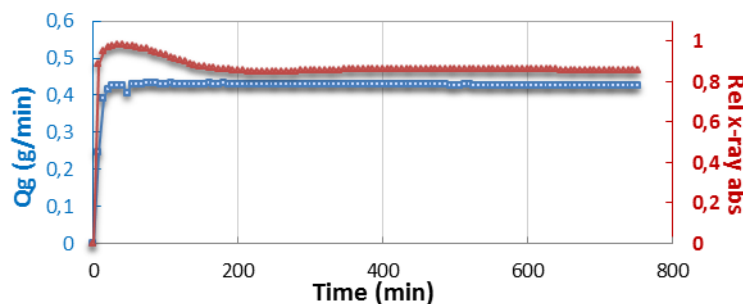

Figure 2: Experiment 1- Gas saturation (red curve) and mass flow rate (blue curve) evolution as a function of time for **dry gas** injection in sample initially saturated with **deionized water**.
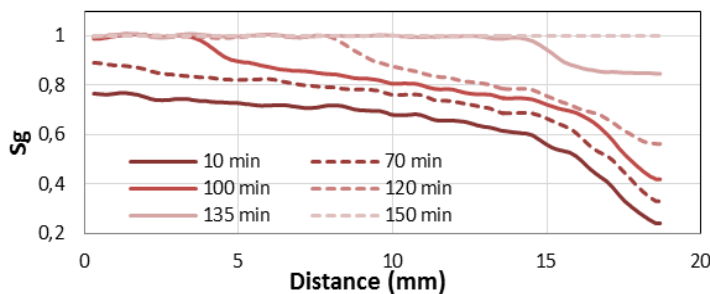
Figure 3: Experiment 1- Evolution of gas saturation profile as a function of time for **dry gas** injection in sample initially saturated with **deionized water** (gas is injected from left).
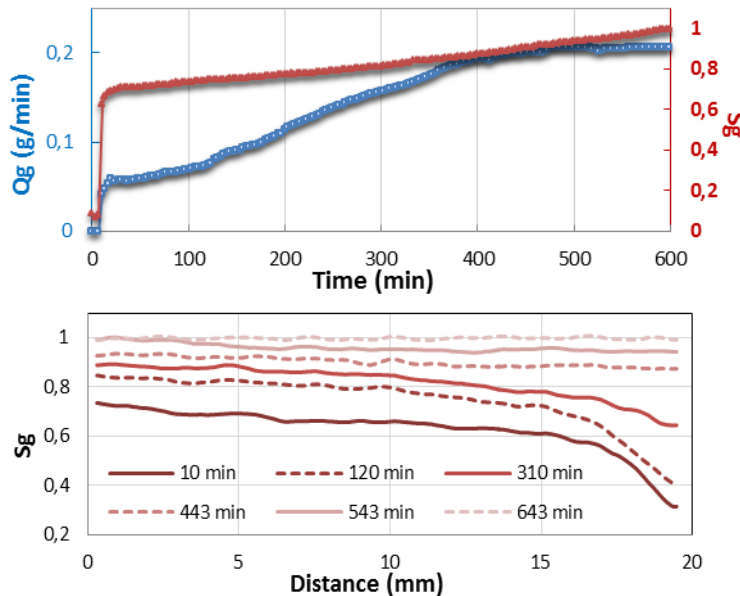
Figure 4: Experiment 2- Gas saturation (red curve) and mass flow rate (blue curve) evolution as a function of time for **humid gas** injection in sample initially saturated with **deionized water**.
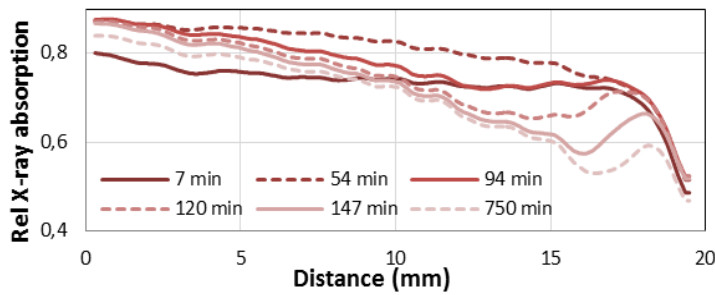

Figure 5: Experiment 2- Evolution of gas saturation profile as a function of time for **humid gas** injection in sample initially saturated with **deionized water** (gas is injected from left).

Effect of salt

In the following experiments, we have injected dry (experiment 3) and humid gas (experiment 4) in a sample initially saturated with a 100g/l KBr brine. Figure 6 and Figure 8 show the evolution of the gas flow rate as a function of time as well as the relative X-ray absorption that was normalized by the finale stage of experiment 3. In the case of dry gas, the flow rate exhibits the same behavior as for the two first experiments. The final flow rate did not show any evidence of permeability alteration due to salt precipitation.

The profiles for the dry gas injection case show a more complex behavior (see Figure 7). The profiles can be interpreted qualitatively as the relative variation in salt quantities (i.e., a relative X-ray absorption above one means a decrease in salt quantity whereas below one means an increase in salt quantity compared to the initial distribution). Thus, we can observe that the salt quantity decreases slightly by the inlet while it increases at a specific location situated 5 mm from the outlet, which corresponds to the location of the capillary end effect. This behavior can be explained by the competition between drying and capillary rise. As drying decreases first the saturation on the side of the inlet as shown by the first experiment, capillary forces tend to equilibrate the saturation by displacing brine toward the inlet. Consequently, the salt concentration increases locally, and once it reaches the solubility limit, it precipitates. However, salt precipitation did not affect the permeability. This is probably due to the low quantity of salt initially present in the sample that represents less than 1% of the pore volume.
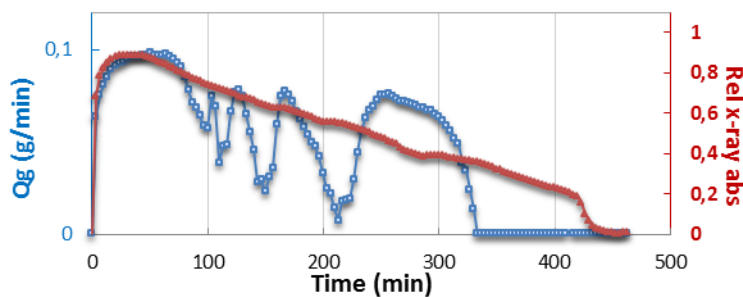
Figure 6: Experiment 3-X-ray relative absorption (red curve) and gas mass flow rate (blue curve) evolution as a function of time for **dry gas** injection in sample initially saturated with 100 g/l KBr **brine**.
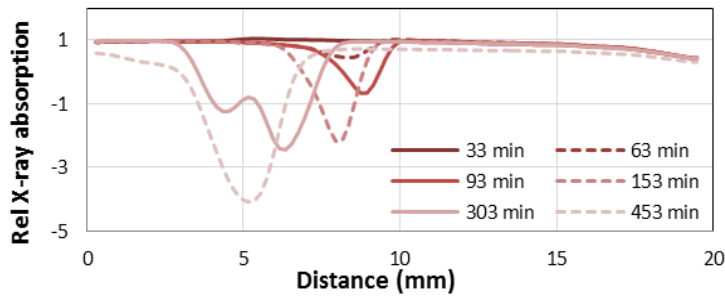
.

Figure 7: Experiment 3-Evolution of X-ray relative absorption profile as a function of time for **dry gas** injection in sample initially saturated with 100 g/l KBr **brine** (gas is injected from left).

In the case of humid gas injection, the flow rate increases rapidly during the drainage phase before it stabilizes at almost a constant value and remains constant for more than 12 hours. The relative permeability to gas was estimated to 50%, suggesting that the sample had not dried out. The dependency of the water vapor pressure to the salt concentration explains the fact that the sample did not dry out completely. The profiles along the sample, as shown in Figure 9, indicate a variation in the local concentration of the salt that reaches a steady configuration. We can observe a concentration gradient at 750 min that is driven by the equilibrium between the pressure drop, brine salinity and water vapor pressure. In this case, the presence of salt inhibits the drying due to the pressure drop. Clearly the pressure gradient is not high enough to compensate for the reduction in the vapor pressure due to the increase in salt concentration.

Figure 8: Experiment 4-X-ray relative absorption (red curve) and gas mass flow rate (blue curve) evolution as a function of time for **humid gas** injection in sample initially saturated with 100 g/l KBr **brine**.

Figure 9: Experiment 4- Evolution of X-ray relative absorption profile as a function of time for **humid gas** injection in sample initially saturated with 100 g/l KBr **brine** (gas is injected from left).

Capillary effect

To investigate the capillary effect, dry gas was injected in a sample initially saturated with a 100g/l KBr brine while contact with brine was maintained by sweeping the bottom face of the sample. Figure 10 shows the evolution of the gas flow rate and the relative X-ray absorption as a function of time. In this case, we observe a completely different behavior than in the previous cases. After an initial increase due to drainage, the gas flow rate experiences successive decline and rise cycles with increasing amplitude before it reaches zero after six hours of injection. The relative X-ray absorption shows a constant decrease which corresponds to an increase of the sample density. This observation suggests an accumulation of additional salt within the sample that is supplied by the brine in contact with the bottom face of the sample.

The profiles illustrated in Figure 11 give more insight into the mechanisms that take place during this experiment. We observe first a local decrease in the relative X-ray attenuation at 8 mm from the inlet at 63 min that suggests an increase in salt concentration. The advent of this salt strip is correlated with a decrease in the gas flow rate and corresponds most probably to salt precipitation that alters permeability to gas. We observe then an alternation of dilutions and precipitation corresponding respectively to the increase and the decline of the gas flow rate with an intensification of the relative X-ray attenuation along the salt strip. Finally, we observe a displacement of the salt strip during the successive cycles of dilution precipitation toward the inlet of the sample. At the end of the experiment the salt strip is located 5 mm far from the inlet.

Figure 10: Experiment 5- X-ray relative absorption (red curve) and gas mass flow rate (blue curve) evolution as a function of time for **dry gas** injection in sample initially saturated with 100 g/l KBr **brine** and with **capillary contact**.

Figure 11: Experiment 5- Evolution of X-ray relative absorption profile as a function of time for **dry gas** injection in sample initially saturated with 100 g/l KBr **brine** and with **capillary contact** (gas is injected from left).

The observed phenomena can be explained by the competition between drying and capillary rise. Indeed, the gas flow dries out the sample, which is manifested by a decrease in the water saturation. However, as we have an active capillary contact, capillary suction compensates for the decrease of water saturation to maintain a capillary equilibrium, which in turn leads to an increase of local salt concentration. At one point the salt concentration is sufficiently high to precipitate salt and altering the gas permeability. As the gas flow rate declines, the capillary rise becomes predominant, allowing the dilution of the precipitated salt and a regeneration of the gas permeability. The alternation of this instable equilibrium leads to an increase of the precipitated salt after each stage till a point of no return is reached where the volume of precipitated salt is sufficiently high to stop the gas flow and the capillary suction.

CONCLUSIONS

In this study, we have shown the importance and interplay of different parameters that govern brine drying and salt precipitation. These parameters include: gas relative humidity, pressure drop, brine concentration, capillary forces and vapor partial pressure.

In the case of dry gas injection in a sample saturated with brine, the water is dried out near the inlet of the sample and will lead to pore plugging if there is sufficient capillary induced flow of brine into the area/location in the plug where the drying effect is strongest. The pore plugging will completely block or strongly reduce the rock permeability.

In the case of humid gas injection in a sample saturated with deionized water, the pressure drop along the core induces an increase in the water content in the gas phase towards the outflow end of the core, allowing evaporation of water at the outlet of the sample. However, if the sample is saturated with brine, the increase in local concentration of brine at the outflow end (caused by evaporation due to the pressure drop) reduces the vapor pressure of the water. This, in turn, inhibits dry-out, as the pressure drop is insufficient to evaporate more water, and one is left with a high salinity brine at the outflow end of the core.

We have demonstrated that dry gas injection combined with a capillary water contact can trigger salt precipitation and possibly blocking of the pore space. These experiments establish the basis for simulation models that can be used to integrate the different physical phenomena that take place during water displacement, evaporation and possibly precipitation.

REFERENCES

1. Kleinitz W., Dietzsch G., Köhler M. (2003) Halite scale formation in gas-producing wells; *Trans. IChemE*, 81(A), pp352-358.
2. Aquilina, P. (2012) Impairment of Gas Well Productivity by Salt Plugging: A Review of Mechanisms, Modeling, Monitoring Methods, and Remediation Techniques, paper SPE 158480 prepared for presentation at the SPE Annual Technical Conference and Exhibition, San Antonio, Tx, 8-10 October.
3. Mahadevan J., Sharma M.M., Yortsos Y.C. (2006) Flow-Through Drying of Porous Media; *AiChE Jounral* ; 52(7); pp2367-2380
4. Mahadevan J., Sharma M.M., Yortsos Y.C. (2007) Water removal from porous media by gas injection: experiments and simulation; *Trans.Porous Media*; 66; pp287-309
5. Peysson Y., Bazin B., Magnier C. Kohler E., Youssef S. (2011) Permeability alteration due to salt precipitation driven by drying in the context of CO_2 injection, *Energy Proceedia* (4) p4387-43941
6. Peysson Y., André L, Azaroual M. (2013) Well injectivity during CO_2 storage operations in deep saline aquifers 1: Experimental investigation of drying effects, salt precipitation and capillary forces, *Int. Journal of Greenhouse Gas Control*, 22, pp 291-300
7. Youssef S., Mascle M., Peysson Y., Olga Vizika O. (2017) CAL-X: an X-Ray Radiography tool for high throughput coreflood experimentation. Applications in the EOR context. To be presented at Int. Sym. of the Society of Core Analyst Vienna, Austria

Visualization Investigation of the Mechanisms of Higher Quality Heavy Oil Recovery by Dense CO₂ Injection

Seyyed Mehdi Seyyedsar and Mehran Sohrabi
Heriot-Watt University, United Kingdom

This paper was prepared for presentation at the International Symposium of the Society of Core Analysts held in Vienna, Austria, 27 August – 1 September 2017

ABSTRACT

The efficiency of primary recovery from heavy oil reservoirs is low due to their nature of high oil viscosities and low dissolved gas contents. Because of a substantial reduction in the oil viscosity, CO_2 injection would be a potential solution to enhance recovery from heavy oil reservoirs. Many heavy oil reservoirs are shallow and likely to have a low temperature. Under the conditions of those reservoirs, CO_2 would be a dense liquid or supercritical fluid. Another benefit of dense CO_2 injection could be a favorable improvement in the physical properties of the recovered oil. It appears that the mechanism of extraction of light and intermediate components of the oil by CO_2 causes the changes in the properties of recovered oil. To identify the processes that affect the physical properties of heavy oil, the contact between CO_2 and heavy oil was visually investigated under reservoir conditions. In addition, several experiments were performed using a transparent micromodel setup to understand the impact of the extraction of oil components on the flow in porous media.

As CO_2 contacts the oil, the extraction of hydrocarbons, mostly methane at the beginning, from the oil starts immediately. The extraction of hydrocarbons by CO_2 initially leads to a sudden swelling of the oil mainly because of the liberation of the dissolved gas from the oil. Consequently, an accumulation of the light and intermediate compounds of the oil takes place in the oil phase, near the interface of the oil and CO_2. The results of the direct visualization of the flow reveal that the contact of CO_2 and heavy oil results in the formation of a different oil-rich phase. This light and less viscous oil-rich phase has a relatively lighter color than the oil in contact with CO_2 and it is significantly mobile in pore spaces.

INTRODUCTION

Heavy oils, because they constitute one of the largest reserves of fossil fuels on earth, are considered an alternative source in propping up the rising demand for oil. Heavy oil is defined as a dense (low API gravity) oil and is generally known for its high viscosity and limited mobility in porous media (Meyer, et al., 2003). Because the techniques of primary production mainly rely on natural forces within oil reservoirs, the efficiency of primary recovery by pressure depletion in heavy oil reservoirs is generally low.

Carbon dioxide is of great interest for enhancing oil recovery because of its characteristics such as high solubility in oil and oil viscosity reduction. A remarkable decrease in oil viscosity by CO_2 dissolution, in particular, for viscous oils have been reported in the literature (Miller, et al., 1981) (Klins, 1984). CO_2 dissolution in oil would also result in oil swelling which increases oil volume (saturation) in porous media and hence improves the relative permeability for oil. Another mechanism usually associated with CO_2 injection for oil recovery is the extraction of light and intermediate components of oil by the injected CO_2. However, this process is mainly considered as an active mechanism of recovery when the reservoir oil is a light oil.

The results of our coreflood investigations have shown that the concentration of light and intermediate components in the oil recovered by liquid CO_2 or supercritical CO_2 injection is higher than that of the original heavy oil in the core. Furthermore, it was observed that the oil recovered by dense CO_2 injection has a significantly lower viscosity than the original oil in the rock (Seyyedsar, et al., 2016). At first glance, the in-situ alteration of the properties of heavy oil by CO_2 would be related to the impacts of the mechanism of extraction of oil compounds by CO_2. However, the process of extraction is a slow process, in particular in porous media. That is, it is believed that the process of extraction occurs under certain conditions of temperature and pressure. Another crucial factor controlling the strength of extraction by CO_2 is the ratio of the volume of CO_2 to the volume of oil. Investigations have shown that decreasing the ratio of CO_2 to oil to a smaller ratio (but still above that required to saturate the oil) reduces the amount of oil extracted. However, the pressure at which the extraction begins remains unchanged indicating that the density of CO_2 is the dominant factor determining the extraction behavior of CO_2 (Menzie, et al., 1963) (Holm, et al., 1974).

Given the above, the oil used in the investigations regard to the extraction had usually the characteristics of the conventional (light) oil. It recurs in the literature that small hydrocarbon molecules are extracted more efficiently into a CO_2-rich phase than are large ones. For example, (Orr, et al., 1987) measured compositions of CO_2-rich and oil-rich phases. Their data confirm that small molecules partition preferentially over large molecules into a CO_2-rich phase. Thus, a combination of the mass transfer between CO_2 and heavy oil as well as the flow of CO_2 and the oil in porous media are likely to be the main reasons of the in-situ improvement of the properties of heavy oil by CO_2.

In this study, direct visualization approach was employed to investigate the contact and flow of CO_2 and heavy oil under reservoir conditions. A setup was designed to evaluate the impacts of the mechanism of extraction on the properties of heavy oil. Several experiments were performed and repeated using a transparent micromodel system to visually observe the underlying mechanisms of flow of CO_2 and heavy oil. In addition, further analysis of the fluids in the coreflood experiments was performed to evaluate the impact of CO_2 on various properties of heavy oil in porous media.

Observations, Results, and Discussion

The oil that was used in our coreflood experiments (Crude 'C') is a stock-tank oil sample and is characterized as extra-heavy oil. First, a visualization setup was used to observe the

contact of CO_2 with heavy oil under reservoir conditions. Around 0.4 cm^3 of the crude oil 'J' was poured into the container using a syringe. Care was taken to ensure that no air was trapped within the oil and also to have a flat level of oil in the container. After isolating the cell, the heater was switched on and set at 28° C. Later, methane was introduced to the system and the pressure at a controlled rate increased to the test pressure. The oil in the container was only accessible from the top end of the container. It was observed that the level of oil started rising after having contact with methane due to the dissolution and diffusion of methane into the dead oil. This swelling of the oil was relatively rapid at early times of the contact of methane with the oil. The images captured during this process clearly show the swelling of the oil, Figure 1.
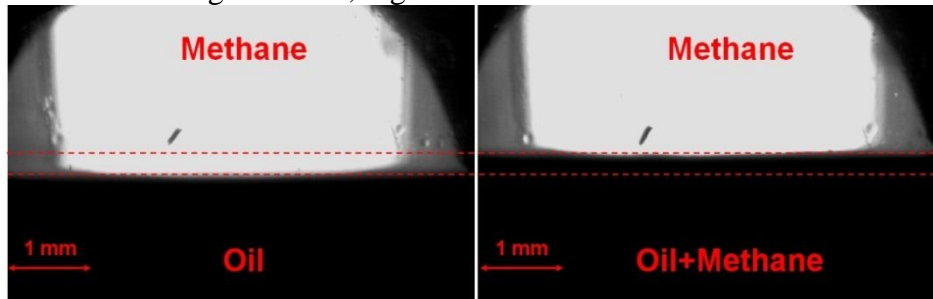
Figure 1: Level of oil in the container before the contact with methane (left) and after equilibrium with methane (right).

When the oil in the container was fully saturated with methane, CO_2 was introduced to the system from the bottom of the chamber and methane was removed from the top of the cell at constant pressure. The procedure was performed at a slow and controlled rate to ensure complete displacement of methane by CO_2 and to ensure that the pressure of the system remained constant during this displacement. This was continued until the time that CO_2 displaced methane from the chamber. Then, the chamber was kept connected to the CO_2 cell until the end of the run. It was observed that once the CO_2 contacted the oil in the container, extraction of hydrocarbons, mostly methane at the beginning, from the oil started instantly, as evidenced in Figure 2. The contact between CO_2 and the oil in the container caused to the extraction of light and intermediate components of the oil from the interface. It was seen that this phenomenon initially led to a sudden swelling of the oil mainly due to the liberation of dissolved methane from the oil. The liberation of methane and other hydrocarbon components from the oil was continued as time went on which indicates that CO_2 had also affected the oil below the surface. The process of extraction of hydrocarbon continued although the speed of it decreased dramatically after a complete liberation of light components of the oil such as methane. The similar behavior was also observed in the coreflood experiments where the liberation of methane from the oil increased the core pressure during the shut-in periods (Seyyedsar, et al., 2015).

Eventually, more hydrocarbon components were extracted from the oil by CO_2 and the level of the oil went below the original level of oil before the contact with CO_2 started. Figure 3 shows that the volume of oil in the container has decreased significantly after around 10 days of contact between oil and CO_2. At this stage, to be able to record the level of the oil in the container, the height of the camera was lowered.

A behavior similar to what was described above was also observed when the oil was dead (no dissolved hydrocarbon gas) albeit to a lesser extent, in particular at the beginning of the contact between CO_2 and dead oil, since the oil did not have solution gas (methane). In the dead oil again it was observed that the extraction of oil components continued and a significant volume of oil was gone into the CO_2-rich phase. After completing each test, the pressure of the system was decreased slightly at constant temperature and it was observed that the volume of oil was slightly decreased due to the liberation of dissolved CO_2 from the oil. Moreover, it was observed that a small amount of greasy-nature liquid was left at the bottom of the chamber after decreasing the pressure to the ambient conditions which is believed to be the extracted hydrocarbons in the CO_2-rich phase.
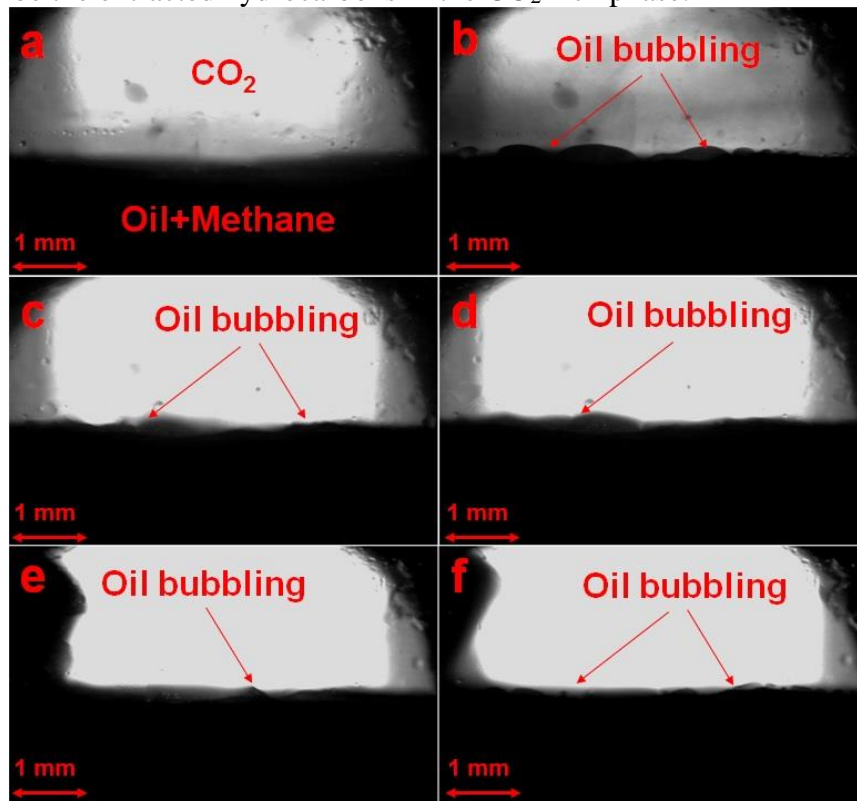
Figure 2: Extraction of oil components by CO_2 (a) first contact, (b) 1 minute, (c) 4 minutes, (d) 10 minutes, (e) 20 minutes, (f) 100 minutes after the first contact.
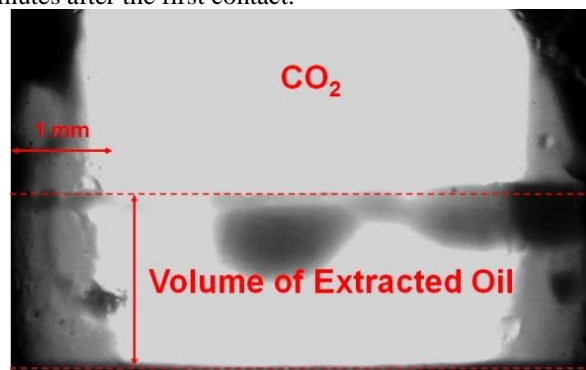
Figure 3: Shrinkage of oil volume due to the extraction of hydrocarbon components by CO_2, after 10 days.

The composition of the remaining oil after the extended contact of oil and CO_2 was analyzed and compared to the composition of the original dead oil, Figure 4. As shown, all the components up to C_{10} were completely extracted from the original oil by CO_2. Moreover, the concentration of the intermediate components up to C_{23} was reduced significantly in the remaining oil whereas the amount of the heavier components remained unchanged or changed little. The changes in the composition of the oil because of the extraction accounts for a decrease around 29% of the mass of the original oil but it was seen that that is even higher in terms of volume of oil under reservoir conditions.
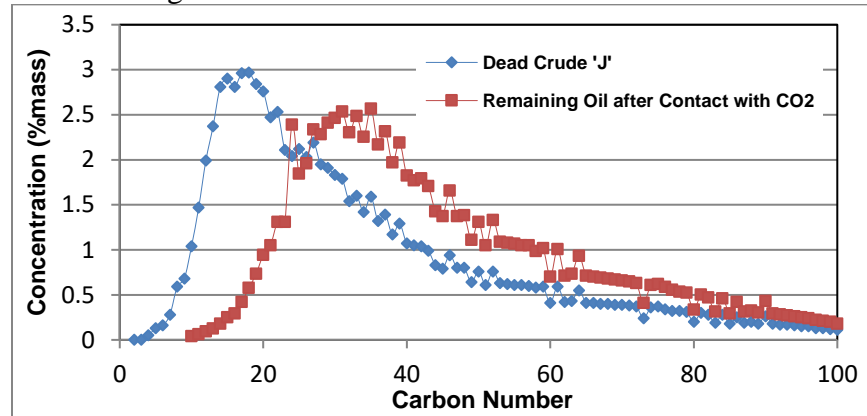
Figure 4: Compositional analysis of crude 'J' and the remaining oil after contact with (liquid) CO_2.

In a porous medium, the components extracted by the CO_2-rich phase could be easily displaced and recovered at the production outlet because of the high mobility of the carrying phase. The remaining oil that has lost a significant fraction of its light and intermediate compounds is heavier than it was before the contact with CO_2 and hence, it would have higher viscosity and density than the original oil. However, CO_2 dissolution in the remaining oil would reduce its viscosity and density and the oil can also be displaced toward the production outlet by the displacing fluid. The same procedure, which was conducted for the contact of liquid CO_2 and live heavy oil, was followed for a test under the conditions of our coreflood experiments at which CO_2 was a supercritical fluid. Similar behavior was observed during early times of the contact of CO_2 and oil.

The compositional analysis of the produced oil during the coreflood experiments revealed that from the early time of injection of CO_2 into the core, relatively higher quality oil was recovered (Seyyedsar, et al., 2016). It was shown that the speed of the mechanism of extraction decreases significantly after the sudden extraction of relatively light components (mainly methane) from the oil at early times of the process, albeit it is a continuous process. The speed of this process would further decrease in porous media due to several reasons such as the presence of water and the formation heterogeneities. Moreover, other parameters such as oil composition and oil viscosity can affect the process of extraction of hydrocarbons by CO_2. The oil used in the coreflood experiments (crude 'C') had a higher viscosity than the oil used in the visual contact experiments (crude 'J'). Also, crude 'C' has a lower concentration of light and intermediate components than crude 'J'. These factors, therefore, would have decreased the speed of the extraction of hydrocarbon compounds by CO_2 in the coreflood experiments.

An indication of oils recovered due to the extraction in fluids flow processes is their lighter color compared with that of the original oil (Holm, et al., 1974). Therefore, if the extraction mechanism was stronger in the coreflood experiments, it could have been expected to observe two different types of oils (in terms of color, viscosity, etc.) in the production outlet but that was not the case in our experiments. The produced oil in the coreflood tests was a relatively homogeneous black oil. Moreover, no considerable condensate accumulation was observed in the wet-gas-meter system during the coreflood tests. The same dead crude oil, that was used to prepare live oil for the coreflood tests, was used to prepare CO_2-saturated oil for viscosity measurements. Whilst the volume of CO_2 in the rocking cell was significant compared to the volume of oil, no considerable condensate (oil) production was also observed during removing the gas cap from the CO_2-saturated oil. The other active mechanism during the period of CO_2 injection which could potentially alter the composition of recovered oil was CO_2 dissolution and diffusion in the oil. It was shown that the dissolution of CO_2 in heavy oil results in oil swelling as well as significant reduction in the oil viscosity. Consequently, the oil saturated with CO_2 will have higher mobility than the original oil and it will also travel faster in porous media. To evaluate these phenomena and also to understand their effects on the process of oil recovery, direct visualization of the flow of CO_2 and heavy oil using a transparent micromodel was performed under the similar conditions of the coreflood experiments that CO_2 was a liquid fluid. Initially, the micromodel was fully saturated with brine and then crude oil 'J' was injected through the micromodel to establish initial water and oil distributions.

Having established the initial water and oil distributions, CO_2 was injected at 0.01 *cm³/hr* through the micromodel from the bottom end of the model. Figure 5 shows a section of the micromodel before the breakthrough of CO_2. Although several branches can be seen around the stream of CO_2, only one main finger was generated in the model. Moreover, it was observed that parts of the oil which were in direct contact with CO_2 became lighter in color due to the dissolution of CO_2 in the oil.
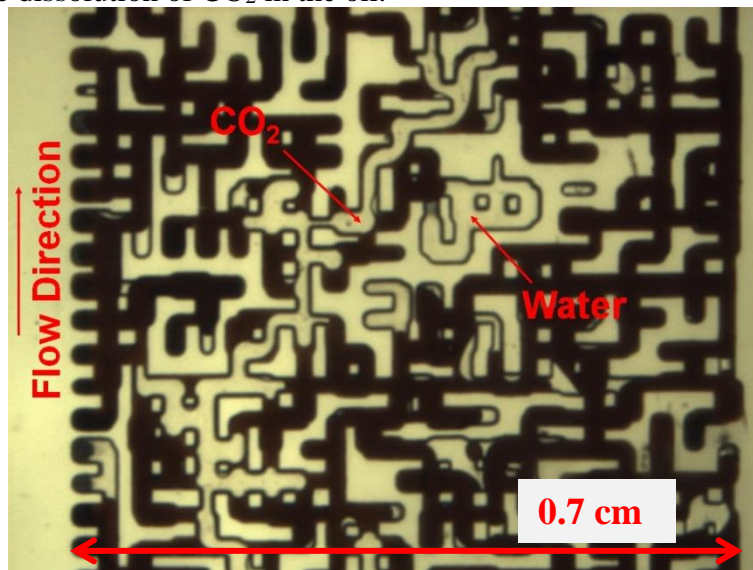
Figure 5: A magnified section of the micromodel before the breakthrough of CO_2.

After the breakthrough, oil production continued, at relatively low rates, mainly because of viscous forces and the dissolution of CO_2 in the oil and the resultant oil swelling and oil viscosity reduction. It is shown in Figure 6 that formation of a new phase with a light color in the CO_2-rich stream was observed. Although this new phase could not travel in the porous medium as fast the stream of CO_2, it was seen that this phase is significantly mobile. At first glance, this can be related to the mechanism of extraction of oil compounds by CO_2. However, the extracted compounds are essentially miscible with CO_2 and the extraction generally occurs in all parts of the interface between oil and CO_2. In addition, it was observed that this new phase was formed as a result of CO_2 and oil contact in the flow paths of CO_2. It is, therefore, believed that this new phase is a fraction of the oil in contact with CO_2 which has significantly low viscosity and probably it is rich in light and intermediate components of the oil which can explain the high mobility of this phase in pore spaces. It was shown that dense (liquid) CO_2 can extract heavy oil components. As soon as CO_2 contacts the oil in the micromodel, light and intermediate compounds of the oil are attracted by the CO_2-rich phase. Therefore, an accumulation of these components would take place in the oil phase, near the interface of oil and CO_2. That is, the similar process occurred during the period of CO_2 injection in the micromodel and hence, the displaced oil by the flow of CO_2 had a higher concentration of the light and intermediate components than the original oil in place. It is, in general, considered that when dense CO_2 is injected into an oil reservoir, three hydrocarbon phases may exist at high CO_2 concentrations. These three phases include a vapor phase, an oil-rich phase, and a CO_2-rich phase. The results of our coreflood experiments, in which dense CO_2 was injected in intermittent fashion (Seyyedsar, et al., 2015), and the visualization experiments also confirmed that at least three phases could appear in pore spaces when dense CO_2 contacts the oil. Here, it was shown that a second oil-rich phase also forms in porous media during immiscible dense CO_2 injection for oil recovery which contributes to higher quality oil production.
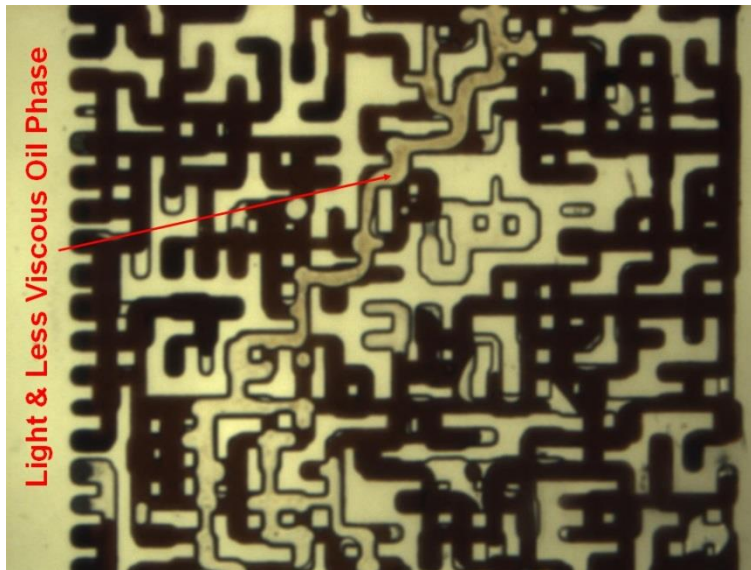
Figure 6: The same magnified section of the micromodel after a short time after the breakthrough.

Figure 7 depicts a sequence of images showing the formation of the light and less viscous oil phase as a result of the contact between the oil and CO_2. A small layer of the surface of the oil is removed and displaced by the flow of CO_2 (Figure 7a). That part of the oil has a higher concentration of the light and intermediate components than the original oil in the micromodel due to the extraction strength of dense CO_2. Hence, the light and less viscous oil phase has a high mobility and it is displaced fast (Figure 7b-f). Figure 7g-h shows that this process takes place at various locations in the porous system. However, the fact that the light and less viscous oil phase is formed in the main path of CO_2 confirms that the contact between the oil and CO_2 contributes to this process.

In another experiment, water was injected into the micromodel after the period of CO_2 injection. The tertiary waterflood was continued until there was virtually no free CO_2 in porous media, Figure 8. Three different types of oil in term of color can be seen in the image; first, the dark color oil which was the oil in direct contact with the injected CO_2 and water. The extraction of components of the oil during the period of CO_2 injection led to a darker color of the oil in the micromodel. Second, the light color oil is the fraction of oil which was not in direct contact with the flowing stream of secondary CO_2. Thus, the extraction of hydrocarbon compounds by CO_2 was not significant. The third oil type is the light and less viscous oil phase which was trapped due to the topology of the micromodel.

CONCLUSION

The results of our coreflood experiments had shown that the injection of dense CO_2 for heavy oil recovery results in higher quality oil production in addition to improving the recovery factor. In this study, to identify the mechanisms leading to the higher quality oil production, several static and dynamic fluids contact experiments were performed in micro-scale. Based on the observations and results of the experiments reported here, the following conclusions are drawn:

- As soon as dense CO_2 contacts heavy oil, extraction of hydrocarbons from the oil starts. The extraction of hydrocarbons to the CO_2-rich phase happens from the interface of the oil and CO_2.
- As a result of CO_2 and heavy oil contact in the flow paths of CO_2, the formation of an oil-rich phase in the CO_2-rich stream was observed. This oil-rich phase has a relatively lighter color than the oil in contact with CO_2 and it is significantly mobile in porous media. The light color oil in the stream of CO_2 has a higher concentration of light and intermediate components as well as a lower viscosity than the original oil in pore spaces.

ACKNOWLEDGEMENTS

Figure 7: A sequence of images taken every 2 minutes from the same magnified section of the micromodel after the breakthrough. The formation of a light color oil phase in the CO_2-rich stream is happening due to the contact and flow of CO_2 and the oil (arrows indicate points of interest).
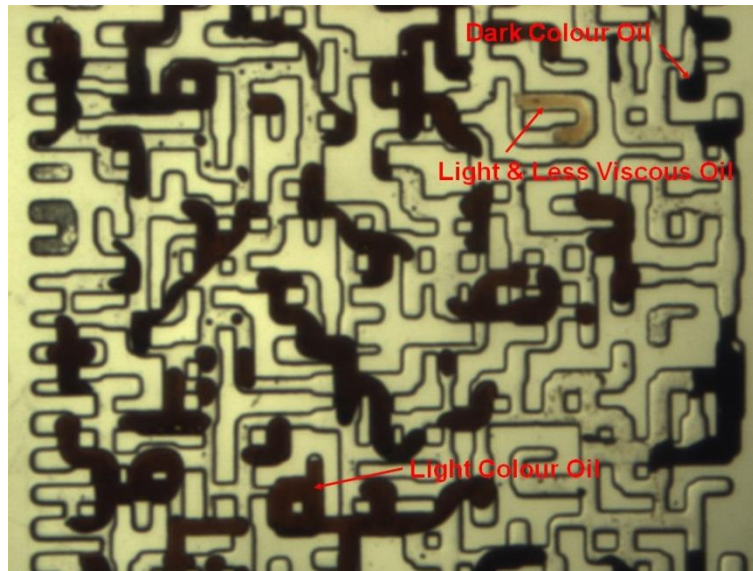
Figure 8: A magnified section of the micromodel after the extended period of tertiary waterflood.

REFERENCES

1. Meyer, R.F, Attanasi, E.D. *Heavy Oil and Natural Bitumen--Strategic Petroleum Resources*. U.S. Geological Survey: Virginia, 2003.
2. Miller, J.S., Jones, R.A. *A Laboratory Study to Determine Physical Characteristics of Heavy Oil After CO2 Saturation*. SPE/DOE Enhanced Oil Recovery Symposium, Tulsa, Oklahoma, 5-8 April 1981.
3. Klins, M.A. *Carbon Dioxide Flooding: Basic Mechanisms and Project Design*. D. Reidel Publishing Company: Boston, 1984.
4. Seyyedsar, S.M., Farzaneh, S.A., Sohrabi, M. Experimental Investigation of Tertiary CO2 Injection for Heavy Oil Recovery. *Journal of Natural Gas Science and Engineering*, 2016, 34, 1205-1214.
5. Menzie, D.E., Nielsen, R.F. A Study of the Vaporization of Crude Oil by Carbon Dioxide Repressuring. *Journal of Petroleum Technology*, 1963, 15, 1247-1252.
6. Holm, L.W., Josendal, V.A. Mechanisms of Oil Displacement by Carbon Dioxide. *Journal of Canadian Petroleum Technology*, 1974, 26, 1427-1438.
7. Orr, F.M., Silva, M.K. Effect of Oil Composition on Minimum Miscibility Pressure-Part 2: Correlation. *SPE Reservoir Engineering*, 1987, 2, 479-491.
8. Seyyedsar, S.M., Farzaneh, S.A., Sohrabi, M. *Enhanced Heavy Oil Recovery by Intermittent CO2 Injection*. SPE Annual Technical Conference and Exhibition, Houston, Texas, 28-30 September 2015.

EXPLICIT CONTINUUM-SCALE MODELING OF WATER-BASED IOR/EOR MECHANISMS

Kata Kurgyis[1], Bernd Flemisch[2], Rainer Helmig[2] and Holger Ott[1]
[1]Department Petroleum Engineering, Montanuniversität Leoben, 8700 Leoben Austria
[2]Institut für Wasser- und Umweltsystemmodellierung, Universität Stuttgart, 70569 Stuttgart, Germany
This paper was prepared for presentation at the International Symposium of the Society of Core Analysts held in Vienna, Austria, 27 August – 1 September 2017

ABSTRACT

In this paper, we discuss first steps towards an explicit numerical description of water-based chemical IOR/EOR processes on the continuum scale. Low-salinity-water and alkaline flooding belong to this family of water based methods. The mechanism governing additional oil production during low-salinity-water flooding is believed to be a combination of several physicochemical processes like multicomponent ion exchange and double layer expansion. These processes are captured in a complexed mechanistic model implemented in the open-source flow and transport simulator DuMu^x. Explicit description, in this context, means to implement the change of wetting properties due to the composition of the injected water by a set of chemical processes linked to concentrations and the concentrations to measured and interpolated flow properties such as relative permeability and capillary pressure saturation functions. The developed models are intended to be used for the design and interpretation of core-flood experiments, and will serve as a basis for upscaling.

INTRODUCTION

Many studies indicate that recovery of crude oil by water flooding (in secondary and tertiary recovery mode) can often be improved by simple and cost effective means through modifying the ionic composition of the injection water. Low salinity water flooding (LSWF) and alkaline flooding belong to this family of low-cost, water-based improved oil recovery (IOR) and enhanced oil recovery (EOR) methods. The recovery mechanisms of both deviate: while low saline water flooding modifies the wetting state of the reservoir as a result of reactions between constituents of the injected water and mineral-fluid interfaces, in alkaline flooding, surface active components are generated in-situ by contacting alkali solutions with specific crude oil components such as fatty acids, lowering interfacial tension between brine and crude. Nevertheless, both methods are not independent of each other and deserve a common investigation, however, in the present study, we primarily focus on LSWF.

The mechanisms governing low salinity effects are believed to be a combination of several physicochemical processes as in double layer expansion (DLE), multicomponent ion exchange (MIE), fine migration, emulsification and salting out among others. DLE and

MIE are the two most quoted phenomena extensively investigated in the past decades. Researchers investigated DLE on pore scale during LSWF and managed to accurately simulate the impact of electrical double layer on ionic diffusion behavior adjacent to a charged surface [1]. In another study [2], mass transfer equilibrium reactions characterizing ion exchange processes emerging during core flooding with diluted brine which was further confirmed by experimental evidence by a difference reported between divalent ion concentration of the injected brine and that of the effluent [3]. Their work has been further developed by several researchers [4, 5] through proposing equilibrium and kinetic reactions models to describe MIE during LSWF.

Additional recovery through the mobilization of fine particles is discussed controversially among researchers. Partial stripping of mixed wet particles alongside incremental oil recovery was reported as core flooding experiments had been executed with chemically modified injection water [6]. On the other hand, during a different study no fines migration or permeability reduction has been observed, although numerous core flood experiments were performed by LSWF [4]. The same conclusion can be derived based on studies inspecting alkaline like behavior of LSWF: results published by Lager et al. [4] indicate that despite the observed alkaline like behavior (water-in-oil emulsification, interfacial tension reduction) due to carbonate dissolution and cation exchange in several studies [7, 8], local pH increase in all probability is not the cause of incremental oil recovery.

Surface electrical potentials are responsible for wetting properties. Charged mineral surfaces are screened to a certain extend by dissolved ions of the aqueous phase forming an electrical double layer resulting in an effective electrical surface potential (zeta-potential). Lowering the ionic strength of the solvent, results in higher zeta potential yielding to an increase in the thickness of the double layer. If the double layer of two, similarly charged surfaces overlap, repulsive forces dominate over attractive forces, promoting desorption over adsorption. Under reservoir conditions, double layers form on the pore wall as a result of the charged mineral surfaces and the brine – crude oil interface caused by accumulation of polar organic components at the interface. Lowering the ion concentration of the brine yields a reduction in the ionic strength and gives rise to overlapping double layers. Therefore, electrical double layer expansion and as a consequence, desorption of polar organic compounds is a consequence of the interaction of Van der Waals forces in the crude oil – brine – rock system. [9]

Other than to double layer expansion, divalent ions contribute to multi-component ion exchange simultaneously. Polar organic compounds adsorb to charged solid surfaces by virtue of indirect bonds functioning as ion or ligand bridges. Upon injecting water with reduced divalent ion concentration, adsorbed carboxylic aggregates are stripped from the pore wall as ion and ligand bridging, and ion exchange processes emerge. [10]

STRATEGY

The objective of the here presented research is to develop the numerical capability for an explicit description of low-saline water flooding processes on the continuum scale. In this context, explicit description means that the change of wetting properties is linked to measured and interpolated flow properties. The developed model will be used for design and interpretation of core flood experiments and will serve as a basis for upscaling from the continuum-scale to field scale applications.

For these purposes, the relevant chemical mechanisms governing LSWF are coupled in a complex mechanistic model based on the work of Kuznetsov et al. [11]. In this work the physicochemical processes causing a change in the wetting state are described by a set of chemical reactions. Due to the complexity of the proposed mechanistic model, it is decomposed into three, superimposed problems in a manner that in each sub-model a new feature is introduced as shown in Figure 1.
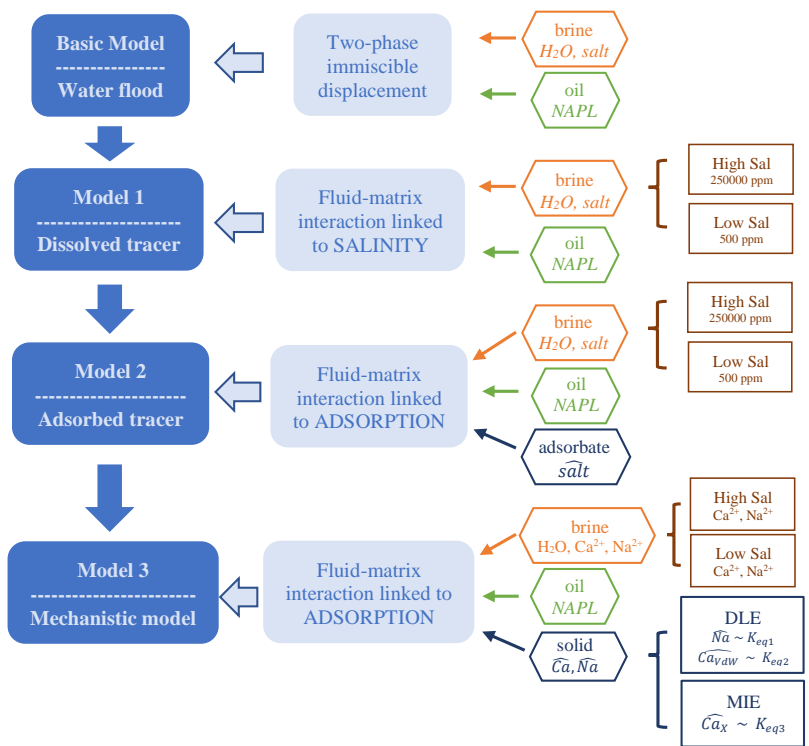
Figure 1: Strategy of the mechanistic model construction

Model 1: Dissolved saline tracer

A core sample saturated with oil and brine is flooded with chemically modified water characterized by a lower salinity of the injection water with respect to the initial brine phase. Due to the change in the total dissolved solids in the brine phase, the thermodynamic equilibrium between the crude oil, brine and rock is disturbed resulting in a new wetting state expressed by modified relative permeability and the capillary pressure saturation function.
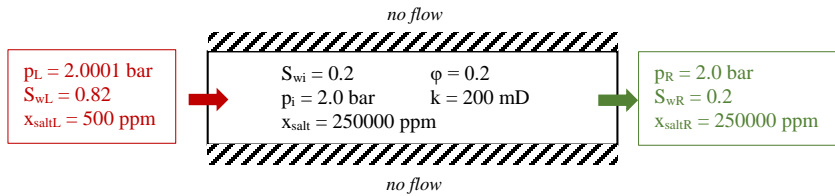
Figure 2: Basic model description

The first phenomenological model is illustrated in Figure 2. The salinity of the brine is specified as a primary variable. The relation between salinity and the wetting state (alteration) is established by a linear interpolation of fluid properties as function of salinity.
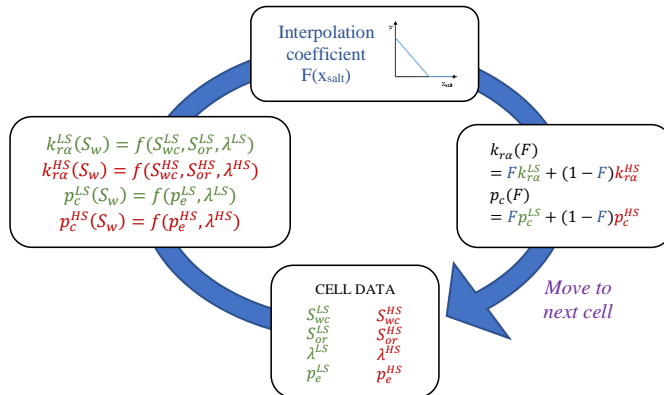
Figure 3: Interpolation scheme applied in the phenomenological models

Figure 3 demonstrates the interpolation workflow: relative permeability and capillary pressure data is provided as function of water saturation corresponding to the high saline water initially saturating the core and to the injected low saline water. As the low saline water imbibes into the core, the in-situ high saline water is displaced and maybe diluted leading to a variation of brine salinity in the simulation domain. At a given location, an interpolation coefficient is determined that defines the relative contribution of the two-phase flow properties corresponding to low and high salinity representing the flow properties at the actual salinity. Linear interpolation means the adaptation of this coefficient

into equation (1) – (3), which is executed in every cell and each time step during the simulation:

$$k_{rw}(S_w) = F(x_{salt})k_{rw}^{LS}(S_w) + \left(1 - F(x_{salt})\right)k_{rw}^{HS}(S_w) \tag{1}$$

$$k_{ro}(S_w) = F(x_{salt})k_{ro}^{LS}(S_w) + \left(1 - F(x_{salt})\right)k_{ro}^{HS}(S_w) \tag{2}$$

$$p_c(S_w) = F(x_{salt})p_c^{LS}(S_w) + \left(1 - F(x_{salt})\right)p_c^{HS}(S_w) \tag{3}$$

Model 2: Adsorbed saline tracer

As the next step, adsorption is introduced by relating the wettability alteration to the total amount of adsorbed ion concentration. As low saline water enters the pore, polar hydrocarbon components bound to the rock surface desorb as ions dissolved in the brine adsorb to the mineral surface. Desorption of organic components, and hence, the concentration of adsorbed organic components, is proportional to the concentration of inorganic ions adsorbing from the aqueous phase. In the present model, the source of adsorption is not studied at this stage; therefore, the process is controlled by an isotherm coefficient relating the concentration of salt ions dissolved in brine to the adsorbate concentration. As a result of coupling adsorption with the low salinity displacement, it is necessary to adjust the interpolation function. For this adsorbed tracer model, the interpolation coefficient correlates with the adsorbate concentration.

Model 3: Mechanistic model

In the next development phase, the mechanisms acting behind the organic component desorption were analyzed. At this stage, low saline effects are assumed to result from the double layer expansion and multi-component ion exchange. On this account, the number of salt components in the brine phase is increased: instead of a single salt component, monovalent ions are represented by Na^+ compound, whereas divalent ions are denoted as Ca^{2+} component.

$$Na^+ + \hat{S} \rightleftharpoons \widehat{Na} \qquad \sim K_{eq1} \tag{4}$$

$$Ca^{2+} + 2\hat{S} \rightleftharpoons \widehat{Ca_{VdW}} \qquad \sim K_{eq2} \tag{5}$$

$$Ca^{2+} + \hat{S} \rightleftharpoons \widehat{Ca_X} \qquad \sim K_{eq3} \tag{6}$$
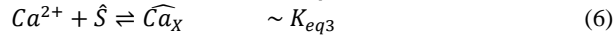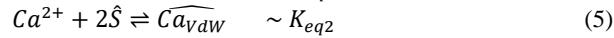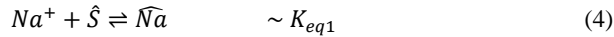
The adsorption of monovalent and divalent ions is described by equilibrium reactions given in equation (4) – (6) between the dissolved ions (Na^+, Ca^{2+}) and the solid surface ($\hat{S}$) resulting in adsorbed monovalent ($\widehat{Na}$) and divalent ($\widehat{Ca_{VdW}}$, $\widehat{Ca_X}$) ions. These chemical reactions are linked to the wetting properties through the total adsorbate concentration which determines the interpolation coefficient used to adjust multi-phase flow properties. The relative contribution of multi-valent ions to DLE and MIE [12], in addition to the impact of these two mechanisms on each other [13] are incorporated by an adjustment in the equilibrium constant of the chemical reactions capturing these phenomena.

Implementation

The introduced model concept was implemented into the numerical framework of the open-source porous media flow and transport simulator DuMu^X. DuMu^X can be applied to multi-phase, -component, -scale and -physics fluid flow problems using continuum mechanical approaches. This software is a module of DUNE (Distributed and Unified Numerics Environment) that consists of several grid management, finite element shape function and iterative solver libraries resulting in fast computational performance, yet high flexibility and adaptivity [14].

The work presented here is based on a coupled, fully implicit 2-phase-N-component (2pnc) model capable to handle the number of components present in the fluid system with high flexibility, and solution-dependent flow properties. One of the extended versions of the 2pnc model coupling mineralization and evaporation processes to porous media flow providing a good foundation to realize organic compound ad- and desorption processes as well [15].

RESULTS

In the following section, simulation results are illustrated for the complex mechanistic model (Model 3), as during the development phase, Model 1 and 2 produced nearly identical results as Model 3.

Figure 4a illustrates saturation profiles for a secondary water flood scenario, when low saline water is injected into a core at connate water saturation. Simulation results (blue curve) were compared with analytical solution (red curve) based on the Buckley-Leverett fractional flow theory. The numerical results show a smearing out effect on the shock fronts leading to slight deviation from the analytical solution which is caused by numerical dispersion. This dispersion is amplified as a consequence of the linear interpretation implementation that is well illustrated in Figure 4a as one may observe more significant smearing out on the low saline shock front than on the high saline shock front. Since flow properties are functions of salinity, the salinity change across the core (green curve) has a severe impact on the flow profile: a gradual change in salinity results in high dispersion on the low saline shock front.

Figure 4b demonstrates the water and oil relative permeability curves for the high saline (dashed lines) and low saline water (dotted lines). The solid lines represent the relative permeability of Model 3 including the linear interpolation symbolized by the shift from the high saline permeability curve to the low saline lines. In the analytical solution, high saline flow properties change to low saline flow properties along a linear trend as a result of the abrupt change in the salinity on the interface of low saline and high saline water. In contrast to this, variation in the salinity and as a consequence, in the adsorbate concentration is a gradual change caused by a mixing zone between the high saline and low saline water.

The relative contribution of the dissolved ions to the different adsorption mechanisms are represented by the adsorbate concentration curves shown in Figure 4c. As all reactions are assumed to be in equilibrium, the initial adsorbate concentration values, which strongly

depends on the brine ionic composition, must be specified under equilibrium conditions. These values are not easy to measure and have a strong dependency on the equilibrium constants and the total surface site available for the ions to react. Currently the surface site is a prescribed value, thus providing a good foundation for further development by linking this value to pore surface area per volume ratio and shape factors characterizing the oil-brine-mineral contact area.
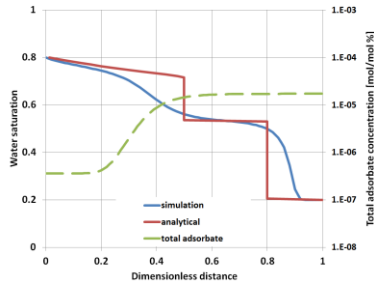

Figure 4a: Secondary water flood simulation from Model 3 compared with analytical solution
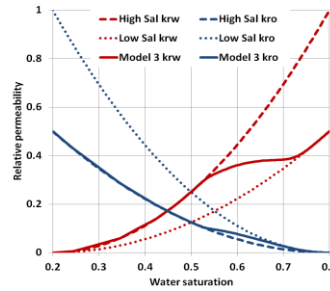
Figure 4b: Transition of relative permeability curves in secondary water flood
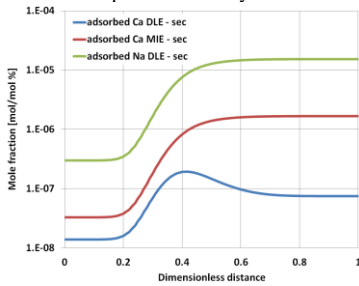
Figure 4c: Adsorbed ion concentrations expressed in mole fraction in secondary water flood
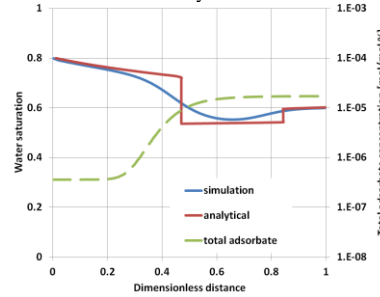
Figure 4d: Tertiary water flood simulation from Model 3 compared with analytical solution

A tertiary recovery scenario was also simulated in order to evaluate the capability of the implemented model. In this case, a core with higher initial water saturation than connate water is flooded with the low saline water (Figure 4d). Similarly to the secondary water flood scenario, deviation between the analytical and the numerical results were observed due to the previously mentioned smearing out effect. Contrary to the secondary water flood scenario, where shock front heights determined by the simulation are identical to the analytical solution, in the case of the tertiary recovery, a difference was noted between the manner how oil bank forms based on the simulation and the analytical solution. Based on the Buckley-Leverett solution, oil bank height is constant, whereas in the model, oil bank height increases over time yielding to underestimation of the oil bank height at early simulation time, and overestimation at later simulation time caused by the fact that in case

of the analytical solution, constant injection rate is assumed, whereas in the simulation, due to current code limitations, constant pressure difference is applied over the core.

Low salinity water flood is believed to cause economical increase in the recovery factor, only in cases where significant shift in the wettability condition is achieved. Literature states an optimum salinity value for this in a range of 4000 – 5000 ppm. [11, 16] This effect is accounted for by an optimal adsorbate concentration (or salinity in the earlier models) in the interpolation function, where adsorption rate is the fastest. Related to the interpolation function, it means that low salinity effects are enhanced if adsorbate concentration (salinity) is at this optimum value or below. Figure 5a shows the saturation profile for the same secondary low salinity water flood scenario with different linear interpolation function definition. In one case, a linear interpolation is applied neglecting this optimal salinity value (blue line): amplified smearing out effect on the low saline shock front. In the second case, where an interpolation considering this optimal value is used (Figure 5b – red line), the smearing out of the low saline water front is weakened, an oil bank forms and a spreading wave forms between the oil bank and the high saline water shock front.
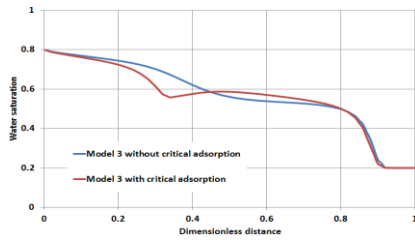
Figure 5a: Secondary water flood in Model 3   Figure 5b: Interpolation function
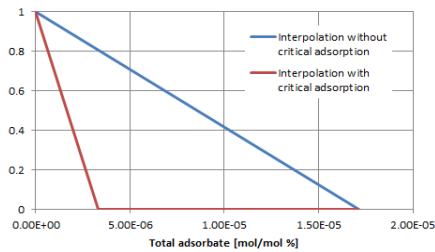
CONCLUSION

In the presented work a complex mechanistic model is proposed that implements low salinity effect by correlating the change in the wetting conditions with salinity controlled flow properties. The obtained simulation results are in good agreement with analytical solution. Deviations are caused by numerical dispersion. The simulation model exhibits high sensitivity to the captured phenomena as well as to the realization of the interpolation function.

A combination of experimental research and the explicit numerical description could provide essential information on the equilibrium constants, total surface site concentration and finally to the interpolation function, leading to an accurate model description for LSWF.

REFERENCES

1. Joekar Niasar, V., Mahani, H., "Nonmonotonic Pressure Field Induced by Ionic Diffusion in Charged Thin Films" *Industrial & Engineering Chemistry Research*, (2016) **55**(21), 6227-6235

2. Hill, H.J., "Cation exchange in Chemical Flooding: Part 3 – Experimental", *SPE Journal*, (1978) **18**(6), 445-457
3. Valocchie, A.J., Street, R.L. and Roberts, P.V., "Transport of ion exchanging solutes in groundwater: Chromatographic theory and field simulation" *Water Resources Research*, (1981) **17**(5), 1517-1527
4. Lager, A., Webb, K.J., Black, C.J.J., Singleton, M., Sorbie, K.S., "Low Salinity Oil Recovery – An Experimental Investigation" *Petrophysics*, (2008) **49**, 28-35
5. Suijkerbuijk, B.M.J.M, Kuipers, H.P.C.E., Al-Quarshubi, E.C.M. et al. "The Development of a Workflow to Improve Predictive Capability of Low Saline Response" presented at the *International Petroleum Technology Conference* in Beijing, China, 26-28 March 2013
6. Tang, G.-Q. and Morrow, N.R., "Influence of brine composition and fines migration on crude oil/brine/rock interactions and oil recovery" *Journal of Petroleum Science and Engineering*, (1999) **24**, 99-111
7. Al-Attar, H.H., Mahmoud, M.Y., Zekri, A.Y., Almehaideb, R., Ghannam, M.T., "The Impact of LoSalTM on Oil Recovery from a Selected Carbonate Reservoir in Abu Dhabi – An Experimental Approach", *SPE* (2013) SPE-164331-MS
8. Yousef, A.A., Al-Saleh, S.M., Al-Jawfi, M., "New Recovery Method for Carbonate Reservoirs through Tuning the Injection Water Salinity – Smart Water Flooding" *SPE* (2011) SPE143550-MS
9. Lee, S.Y., Webb, K.J., Wang, X. et al., "Low Salinity Oil Recovery – Increasing Understanding of the Underlying Mechanisms" *SPE* (2010) SPE-129722-MS
10. Ligthelm, D.J., Gronsveld, J., van der Linde, H.A. et al., "Novel Waterflooding Strategy by Manipulation of Injection Brine Composition", *SPE* (2009) SPE-119835-MS
11. Kuznetsov, D., Cotterill, S., Giddins, M.A., Blunt, M.J. "Low-Salinity Waterflood Simulation: Mechanistic and Phenomenological Models" *SPE* (2015) SPE-174615-MS
12. Arnarson, T.S., and Keil, R.G., "Mechanisms of pore water organic matter adsorption to montmorillonite", *Marine Chemistry*, (2000) **71**, 309-320
13. Mahani, H., Berg, S., Illic, D., Bartels, W.-B., Joekar Niasar, V., "Kinetics of Low-Salinity-Flooding Effect" *SPE* (2015) SPE-165255-MS
14. Flemisch, B., Darcis, M., Helmig, R. et al., "DuMuX: DUNE for multi-{phase, component, scale, physics,…} flow and transport in porous media" *Advances in Water Resources*, (2011) **34**, 1102-1112
15. Jambhekar, V.A., Helmig, R., Schröder, N., Shokri, N., "Free-Flow-Porous-Media Coupling for Evaporation-Driven Transport and Precipitation of Salt and Soil" *Transport in Porous Media*, (2015) **110**(2), 251-280
16. Austad, T., Rezazidoust, A., Puntervold, T., „Chemical Mechanism of Low Salinity Water Flooding in Sandstone Reservoirs" *SPE* (2010) SPE-129767-MS

Pore-Level Study of the Effect of Miscibility and Wettability on Oil Recovery during Gas Assisted Gravity Drainage

H. Khorshidian, L.A. James, and S.D. Butt

Memorial University of Newfoundland

ABSTRACT
The effect of the gas-oil interfacial tension and wettability on the performance of gas assisted gravity drainage (GAGD) process was investigated at the pore-level to explore conditions leading to high oil recoveries. This work extends the previous investigation of GAGD parameters, i.e., the contribution of film flow and wettability, that we presented in 2015 and 2016. GAGD experiments were conducted in a new micromodel with an improved capillary continuity to reflect mechanisms of oil recovery effectively. The result of the experiment showed that the heterogeneities of the porous medium causes the gas-front to bypass oil in small pores surrounded by large pores. The subsequent drainage of bypassed pores was possible where the gas-oil capillary pressure was sufficiently increased due to a reduction in the hydrostatic pressure of oil. The strong hydraulic continuity of oil in an oil-wet porous medium compared to a water-wet porous medium contributed to a low residual oil saturation under immiscible conditions. In water-wet micromodels, a near-complete oil recovery was obtained under miscible conditions as no interface between oil and gas was formed, and no oil was bypassed when the miscible displacement is developed.

INTRODUCTION
Gas Assisted Gravity Drainage (GAGD) is an effective method of oil recovery influenced by the reservoir rock and fluids' properties, such as the state of wettability [1, 2], heterogeneities [3, 4], and interfacial tension between the fluids [5, 6]. During GAGD, the entry of gas into an oil-occupied pore occurs when the gas-oil capillary pressure is sufficiently increased. [7]. The capillary pressure between two phases is directly proportional to their interfacial tension and inversely proportional to the pore size. Therefore, the gas-oil capillary pressure in larger pores is lower so drainage of oil initially begins from larger pores [8]. The gas-front may bypass smaller oil-occupied pores that are surrounded by larger pores [4]. In gas-invaded zones, thick films of oil may be retained in fine capillaries of a porous medium formed around the rock grains and on their rough surfaces. In the gravity drainage, these fine capillaries provide the wetting phase with continuous paths to maintain strong hydraulic continuity linking the bypassed pores to pores at lower elevations [9]. Under such conditions, the hydrostatic pressure of oil in bypassed pores decreases at higher elevations from the gas-front. Therefore, the local gas-oil capillary pressure in a bypassed pore at greater elevations can be higher than the gas-oil capillary pressure in the gas-front when a hydraulic communication between the bypassed pore and gas-front is maintained [10]. The fine capillaries of a porous medium,

depending on their length and geometry, contribute to a limited increase of the gas-oil capillary pressure beyond which the hydraulic continuity of oil is terminated [10, 11].

The reduction of the gas-oil interfacial tension decreases the gas-oil capillary pressure at the gas-oil interface. Therefore, a better GAGD performance might be expected with a reduction in capillary forces allowing gravitational forces to drain the liquid more easily. However, the injection of a rich gas may also reduce the gas-oil differential density dissolving in oil.

In GAGD, the stability of the gas-front, in addition to heterogeneities of the porous medium, is controlled by the gas-oil interfacial tension. The gas-front normally bypasses oil when gas-oil interfaces in larger pores (leading zones) surround gas-oil interfaces in smaller pores (trailing zones). Fig. 1 schematically shows drainage of oil by gas in a porous medium containing large and small pores. When the viscous forces are negligible, the minimum vertical distance (D_{min}) between the leading and trailing gas-oil interfaces prior to the bypass of oil can be calculated by Eq. 1,

$$D_{min} = \frac{P_{cgo}^{T} - P_{cgo}^{L}}{\Delta\rho_{go}g} \tag{1}$$

where P_{cgo}^{T} and P_{cgo}^{L} are the gas-oil capillary pressure in the trailing and leading zones respectively, and $\Delta\rho_{go}$ is the gas-oil differential density. In a system with a fixed pore size distribution, decreasing the gas-oil interfacial tension lowers variations of gas-oil capillary pressure in various pore sizes (numerator in Eq. 1). Therefore, a reduction of the gas-oil interfacial tension and an increase of the gas-oil differential density can stabilize the gas-front and eventually reduce the size of a bypassed zone (Fig. 1c).

A further reduction of the gas-oil interfacial tension may lead to miscible oil displacement conditions depending on oil and gas composition, temperature and injection pressure [12]. Under miscible conditions, in addition to a direct oil displacement, the extraction of oil by gas and swelling of oil volume are the main mechanisms of the oil recovery [13, 14].

In our previous work, the effect of wettability on the GAGD performance was studied in a micromodel with poor capillary continuity. In this work, a new micromodel with improved capillary continuity has been developed to investigate the effect the gas-oil interfacial tension on the GAGD performance under oil-wet and water-wet conditions to identify the effect of wettability on residual oil saturations varying the gas-oil interfacial tensions.

EXPERIMENTAL DETAILS

A new pore network micromodel with an improved capillary continuity was fabricated bonding two acrylic (Plexiglas®) plates containing coarse pores and fine capillaries. The coarse pore network (Fig. 2) is made by repeating a designed pattern (Fig. 3) containing pore sizes in the range of 150 - 1300 μm. The designed pore network was etched by CO_2 laser on an acrylic plate, and the depth of etching was in the range of 140 - 160 μm. Another plate of the micromodel was scratched with a grit 60 sandpaper to form fine capillaries covering the coarse pore network from the top port to the bottom port. The porosity of the designed pattern is 0.48, and the pore volume (PV) of the micromodel is 0.940 ± 0.005 ml. The pore sizes of the micromodel are one order of magnitude larger than the pore sizes in

a sandstone. The magnification of the pore structure reduces the capillary forces compared to the gravitational forces. This helps us to study the interaction of capillary and gravitational forces in a system with limited height. In addition, fluid saturations are quantified via image analysis and error due to resolution is less relative to larger pores. The fluid saturations in the micromodel were calculated using an in-house developed image analysis methodology that evaluates the colour of pixels (red: oil and blue: water) in the recorded pictures during an experiment. The fluid saturation and recovery factor can be calculated with respect to the total number of pixels (with red, blue and white colours) and micromodel porosity. The associated uncertainty with the calculated saturations is ±2%.

The wettability of the micromodel was varied from a strongly oil-wet condition to a strongly water-wet condition as described in the previous work [10]. Fig. 3a and Fig. 3c show images of the repeated pattern in the oil-wet and water-wet micromodels, respectively (note films of the wetting phase in narrow fine capillaries).

GAGD tests were conducted at 24°C injecting CO_2 and C_3H_8 (99% purity) under fixed pressure (4.0 bars in immiscible tests and 8.4 bars in a miscible test) from the top port of the micromodel. A precision piston pump (Quizix 20K series) was used to produce fluids from the bottom port of the micromodel at a constant rate (0.1 ml/hr in immiscible tests and 0.3 ml/hr in a miscible test). The initial oil and water saturations under the oil-wet condition is established by injecting 5 PV water (blue dyed) into a fully oil-occupied micromodel at a flow rate of 5 ml/min followed by injecting 10 PV of oil (red dyed Varsol™ without dissolved gas) at a flow rate of 5 ml/min to establish a low water saturation. Under water-wet conditions, the fully water-occupied micromodel is flooded by 10 PV of oil at a flow rate of 5 ml/min.

Table 1 shows the interfacial tension between test fluids at the corresponding conditions measured with VINCI IFT 700 apparatus. Table 2 also shows the composition of oil (Varsol™) measured with Agilent 7890 distillation system. In addition, equilibrium swelling of oil volume when contacted by C_3H_8 and CO_2 was measured at test conditions (4.0 bars and 24°C). The volume of oil in equilibrium with C_3H_8 was increased by 32 ± 1%, but no significant swelling of oil was observed with CO_2. The density of live oil containing C_3H_8 at equilibrium was measured at 0.705 ± 0.001 g/ml using Anton Paar DMA-HPM density apparatus.

RESULTS & DISCUSSION

The GAGD experimental results are presented in Table 3 showing the variation of fluids' saturation and ultimate oil recoveries. Fig. 4 and Fig. 5 show the micromodel images during GAGD tests performed with CO_2 in the oil-wet and water-wet micromodels, respectively. In both wettability conditions, the bypass of oil with the gas-front occurred in pores where a higher gas-oil capillary pressure must be overcome compared to their neighboring pores (e.g. smaller pores surrounded by larger pores). The average residual oil saturation in GAGD tests performed using CO_2 at the time of the gas-breakthrough was 0.31 PV ± 1.4% in the oil-wet micromodel, and 0.35 PV ± 1.4% in the water-wet micromodel. The average residual oil saturation after 2 PV production (total test duration: 19 hrs) was 0.21 PV ± 1.4% and 0.31 PV ± 1.4% in oil-wet and water-wet conditions, respectively. Similar results were obtained when experiments were repeated but with varied bypassed residual oil zones.

The difference in the initial positioning of the water saturation was the major source of variation in results of repeated experiments.

In the oil-wet micromodel, additional recovery from initially bypassed pores was obtained after the gas-breakthrough via film flow mechanism [10]. The fine capillaries maintained the hydraulic continuity of oil between zones at different elevations and provided a continuous path for the flow of oil. Therefore, a low residual oil saturation was obtained due to an effective increase of the gas-oil capillary pressure at higher elevations. Fig. 6a shows the ultimate state of the residual oil saturation in the oil-wet micromodel. In addition to small pores and around the solid grains, the residual oil was also found in the pores with entries blocked by water. Under such conditions (Fig. 6a), the cumulative capillary pressure required to simultaneously displace the gas-water and water-oil interfaces is high, and may lead to the retention of oil depending the size of the pore and geometry of local fine capillaries.

Fig. 6b shows the ultimate residual oil in the water-wet micromodel that is retained in larger pores than in the oil-wet micromodel. Under water-wet conditions, paths of the oil drainage in certain regions was blocked by the presence of water in smaller pores. In addition, the presence of water around the solid grains and corners of the fine capillaries restricted the hydraulic continuity of oil for an effective increase of the gas-oil capillary pressure. Consequently, the flow of oil in the form of thick films in water-wet media is restricted and resulted in a slight reduction of the residual oil saturation (0.04 PV) after approximately 15 hrs of production post gas-breakthrough.

The central region of the pore network contains wide channels forming a larger scale of heterogeneity, i.e., fracture. During GAGD, the leading edge of the gas-front was formed in wide channels causing the bypass of oil in the matrices. Under oil-wet conditions, the bypassed oil was subsequently recovered from the matrix because of the strong hydraulic continuity of oil. However, in the water-wet micromodel, the subsequent drainage of the bypassed oil from matrices was low due to weak hydraulic continuity oil.

The immiscible GAGD experiments were also performed with C_3H_8 (pressure: 4.0 bar, production rate: 0.1 ml/hr) to study the influence of a reduced gas-oil interfacial tension on GAGD performance. Figs. 7a & 7b. show the oil-wet and water-wet micromodels after 2 PV production, respectively. The ultimate residual oil saturation under oil-wet conditions was similar for both gas types. Under the water-wet condition, the variation of the gas type resulted in a slight reduction (0.03 PV) of the residual oil saturation.

In the oil-wet micromodel, because of strong hydraulic continuity of oil, the oil saturation in bypassed zones was effectively reduced when the vertical distance between these zones and the outlet port is sufficiently increased. Ultimately, the residual oil was retained in regions where hydraulic continuity of oil was terminated due to the geometric constraints of fine capillaries. In the water-wet micromodel, reducing the size of bypassed zones, with the reduction of the gas-oil interfacial tension to gas-oil differential density ratio, could decrease of the ultimate residual oil saturation particularly in zones where the hydraulic continuity of oil to lower elevations was not maintained. The injection of C_3H_8 instead of CO_2 improved the ultimate oil recovery factor due to swelling of the residual oil volume. However, this mechanism may become ineffective in a reservoir containing live oil.

An additional GAGD test was performed in a water-wet micromodel by injecting C_3H_8 at 8.4 bars to develop a miscible oil displacement (Fig. 8). The miscible gas injection, stabilized by gravity, resulted in an oil recovery factor of more than 99%. The small volume of the unrecovered oil was found in zones surrounded by water. In a miscible displacement, a region of swelled oil containing a high concentration of dissolved gas was developed between the gas and oil. A fully-developed transition zone formed with no interface with gas on top and oil on bottom. Consequently, a high recovery of oil was obtained by eliminating capillarity. The miscible oil displacement was gravity stable with the lowest density of gas being on top and increasing in the direction of gravity.

The GAGD experimental results in micromodels with improved capillary continuity showed that high oil recovery is obtained under oil-wet conditions. Under water-wet conditions, the positive influence of the gravitational force on the immiscible displacement of oil is limited by the presence of water. Miscible gas-oil displacement is very effective in obtaining very high recovery under all conditions including water-wet conditions.

CONCLUSIONS

During immiscible GAGD processes, heterogeneities of porous media caused the gas-front to bypass oil in smaller pores surrounded by larger pores. Under oil-wet conditions, the strong hydraulic communication of oil contributed to an additional oil recovery from initially bypassed regions where the gas-oil capillary pressure was effectively increased. However, under water-wet conditions, the presence of residual water in smaller pores and around the solid grains restricted the flow of oil from bypassed zones, and residual oil was retained at higher saturations. A reduction in the ratio of the gas-oil interfacial tension and gas-oil differential density slightly improved the GAGD performance in the water-wet micromodel. Very high oil recovery can be obtained with the displacement of oil under miscible conditions eliminating the capillarity at gas-oil interfaces in a heterogeneous porous medium.

Future Works

The cumulative oil-water capillary pressure that must be overcome for the simultaneous displacements of oil-water interfaces can be lowered in porous media with intermediate wetting conditions. In future works, the performance GAGD in slightly oil-wet and water-wet conditions will be evaluated and compared with the presented results.

ACKNOWLEDGEMENTS

REFERENCES

1.   Vizika, O. and J. Lombard, *Wettability and spreading: two key parameters in oil recovery with three-phase gravity drainage.* SPE Reservoir Engineering, 1996. **11**(01): p. 54-60.
2.   Caubit, C., H. Bertin, and G. Hamon. Three-phase flow in porous media: wettability effect on residual saturations during gravity drainage and tertiary waterflood.

presented in part at SPE Annual Technical Conference and Exhibition held in Houston Texas, USA, September 2004.

3.   Parsaei, R. and I. Chatzis, *Experimental investigation of production characteristics of the gravity-assisted inert gas injection (GAIGI) process for recovery of waterflood residual oil: effects of wettability heterogeneity.* Energy & Fuels, 2011. **25**(5): p. 2089-2099.

4.   Catalan, L.J., F.A. Dullien, and I. Chatzis, *The effects of wettability and heterogeneities on the recovery of waterflood residual oil with low pressure inert gas injection assisted by gravity drainage.* SPE Advanced Technology Series, 1994. **2**(02): p. 140-149.

5.   Blunt, M., D. Zhou, and D. Fenwick, *Three-phase flow and gravity drainage in porous media.* Transport in porous media, 1995. **20**(1-2): p. 77-103.

6.   Rao, D., *Gas injection EOR-A new meaning in the new millennium.* Journal of Canadian Petroleum Technology, 2001. **40**(02).

7.   Dullien, F.A., *Porous media: fluid transport and pore structure.* Academic Press, Waterloo, Ontario, Canada, 2nd Edition, 1992, Chapter 2, 128-158.

8.   Lenormand, R., *Liquids in porous media.* Journal of Physics: Condensed Matter, 1990. **2**(S): p. SA79.

9.   Dullien, F.A., C. Zarcone, I.F. Macdonald, A. Collins, and R.D. Bochard, *The effects of surface roughness on the capillary pressure curves and the heights of capillary rise in glass bead packs.* Journal of Colloid and Interface Science, 1989. **127**(2): p. 362-372.

10.   Khorshidian, H., L. James, and S. Butt, The Role of Film Flow and Wettability in Immiscible Gas Assisted Gravity Drainage, *presented in part at the International Symposium of the Society of Core Analysts Colorado, USA, August 2016.*

11.   Piri, M. and M.J. Blunt, *Three-phase threshold capillary pressures in noncircular capillary tubes with different wettabilities including contact angle hysteresis.* Physical Review E, 2004. **70**(6): p. 061603.

12.   Helfferich, F.G., *Theory of multicomponent, multiphase displacement in porous media.* Society of Petroleum Engineers Journal, 1981. **21**(01): p. 51-62.

13.   Bahralolom, I.M. and F.M. Orr Jr, *Solubility and extraction in multiple-contact miscible displacements: comparison of N2 and CO2 flow visualization experiments.* SPE Reservoir Engineering, 1988. **3**(01): p. 213-219.

14.   Campbell, B.T. and F.M. Orr Jr, *Flow visualization for co2/crude-oil displacements.* Society of Petroleum Engineers Journal, 1985. **25**(05): p. 665-678.

(a) Leading and Trailing zones in Gas-Front   (b) Prior to Bypass of Smaller Pore   (c) After Bypass of Oil in Smaller Pore
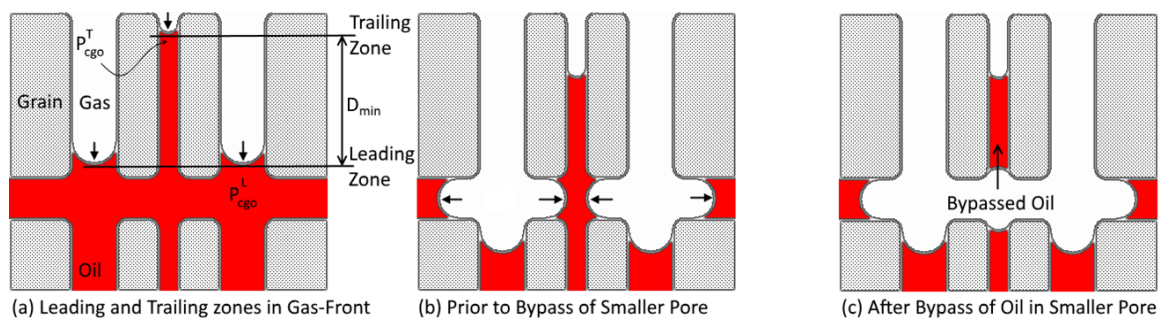
Fig. 1: Schematic representation of the bypass of oil with leading zones in the gas-front
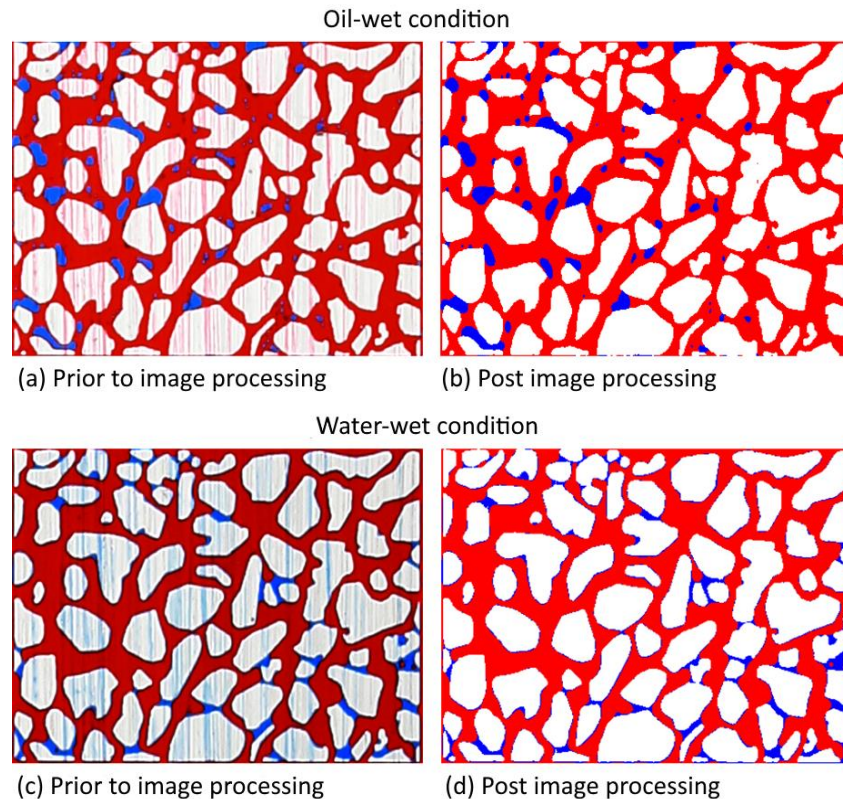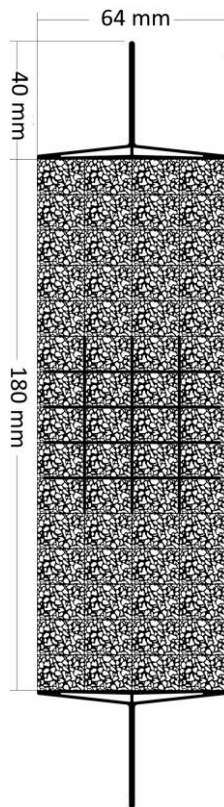
Fig. 2: Designed pore network of micromodel

Fig. 3: The repeated pattern of micromodel prior and after image processing (red: oil - blue: water, pattern size: (16×12 mm)

Table 1: Interfacial tensions between fluids under experiment conditions

Bulk Fluid	Drop Fluid	Pressure (bar)	IFT (mN/m)
C_3H_8	Water	4.0	63.4±1.2
C_3H_8	Water	8.4	47.3±1.2
C_3H_8	Oil	4.0	15.8±0.2
C_3H_8	Oil	8.4	Miscible
CO_2	Water	4.0	71.3±1.8
CO_2	Oil	4.0	21.8±0.3
Varsol	Water	4.0	31.5±0.8

Table 2: Composition of Varsol™ oil

Component	Composition (wt%)
C8	1%
C9	8%
C10	27%
C11	38%
C12	25%
C13	2%
Sum	100%

Table 3: Summary of experimental results (uncertainty of calculated saturations: ±2%)

Wettability	Oil-wet				Water-wet				
Injected Gas	CO_2		C_3H_8		CO_2		C_3H_8		Miscible
Replication	1	2	1	2	1	2	1	2	1
Initial Oil Saturation (PV)	0.91	0.86	0.84	0.79	0.83	0.74	0.75	0.75	0.76
Initial Water Saturation (PV)	0.09	0.14	0.16	0.21	0.17	0.26	0.25	0.25	0.24
Oil Saturation at Breakthrough (PV)	0.30	0.31	NA	0.28	0.36	0.34	0.33	0.33	NA
Water Saturation at Breakthrough	0.09	0.14	NA	0.21	0.17	0.26	0.25	0.25	NA
Ultimate Oil Saturation (PV)	0.23	0.19	0.20	0.21	0.32	0.30	0.29	0.27	< 0.01
Ultimate Water Saturation (PV)	0.07	0.11	0.13	0.20	0.17	0.24	0.24	0.25	0.24
Ultimate Oil Recovery Factor (%	76%	78%	84%	82%	61%	59%	74%	76%	> 99%

NA: Data Not Available   * IOIP: Initial Oil in Place

(a) Prior to gas injection
   So=0.91 Sw=0.09

(b) Prior to gas-breakthrough
   So=0.67 Sw=0.09

(c) Gas-breakthrough time
   So=0.30 Sw=0.09

(d) Post gas-breakthrough
   So=0.23 Sw=0.07
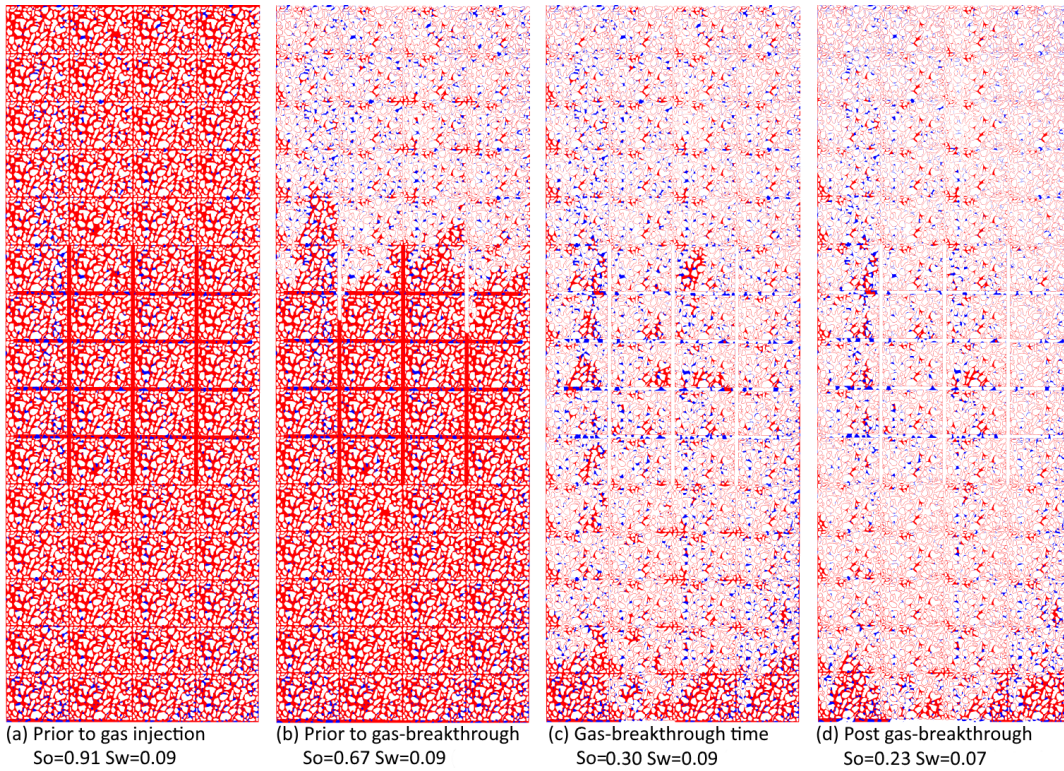
Fig. 4: Immiscible GAGD experiment performed with CO_2 in oil-wet conditions (processed image, red: oil – blue: water)

(a) Prior to Gas Injection
   So=0.83 Sw=0.17

(b) Prior to Gas-Breakthrough
   S=0.65 Sw=0.17

(c) Gas-Breakthrough Time
   So=0.36 Sw=0.17

(d) Post Gas-Breakthrough
   So=0.32 Sw=0.17
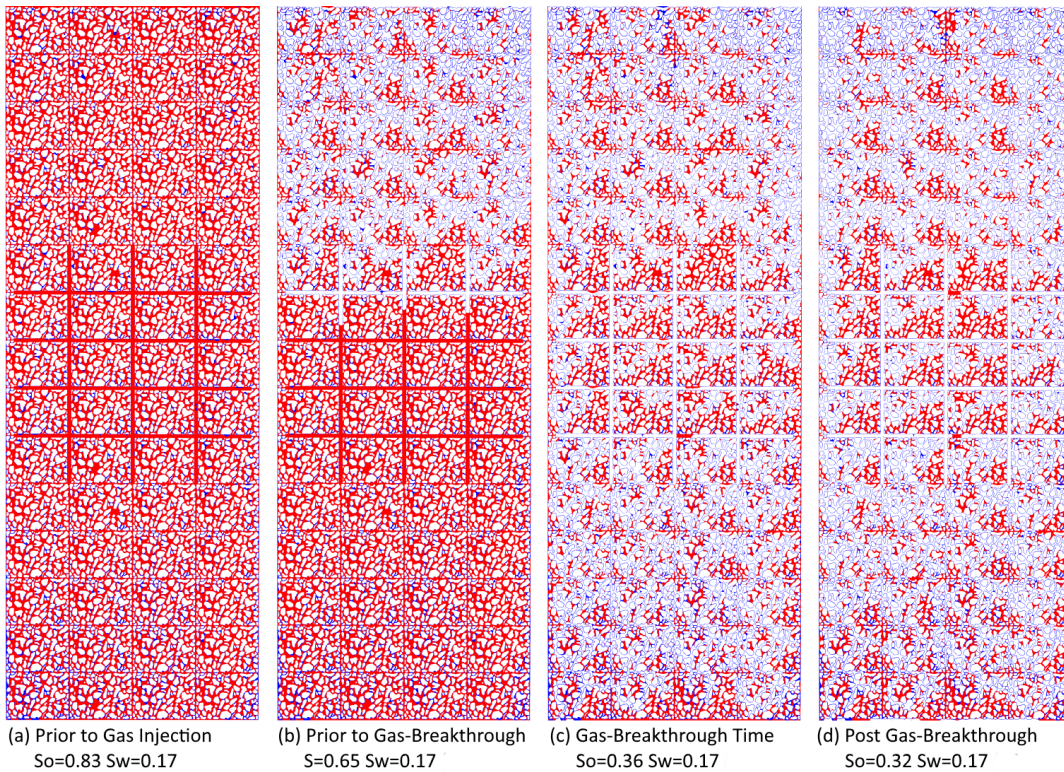
Fig. 5: Immiscible GAGD experiment performed with CO_2 in water-wet conditions (processed images, red: oil – blue: water)
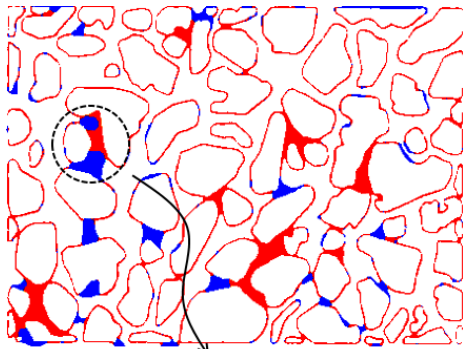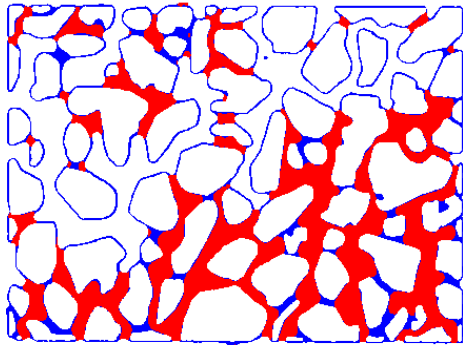
Fig. 6: Residual oil (red) and water (blue) in oil-wet and water-wet conditions (processed images)
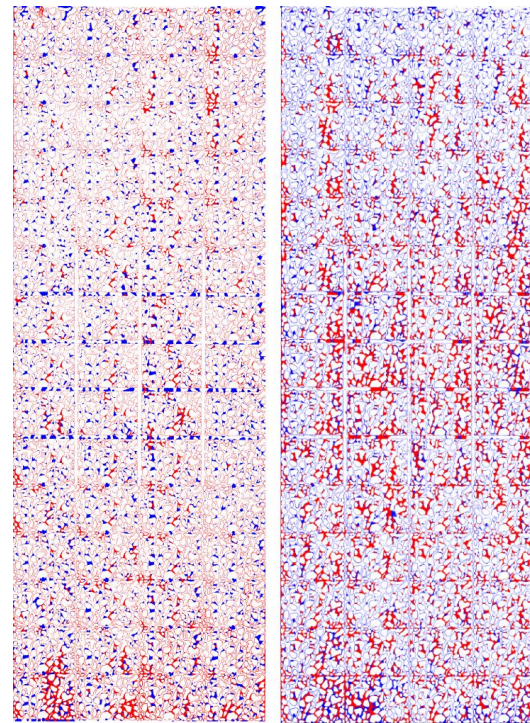
Fig. 7: Immiscible GAGD performed with C₃H₈ in oil-wet and water-wet conditions (processed images, red: oil, blue: water)
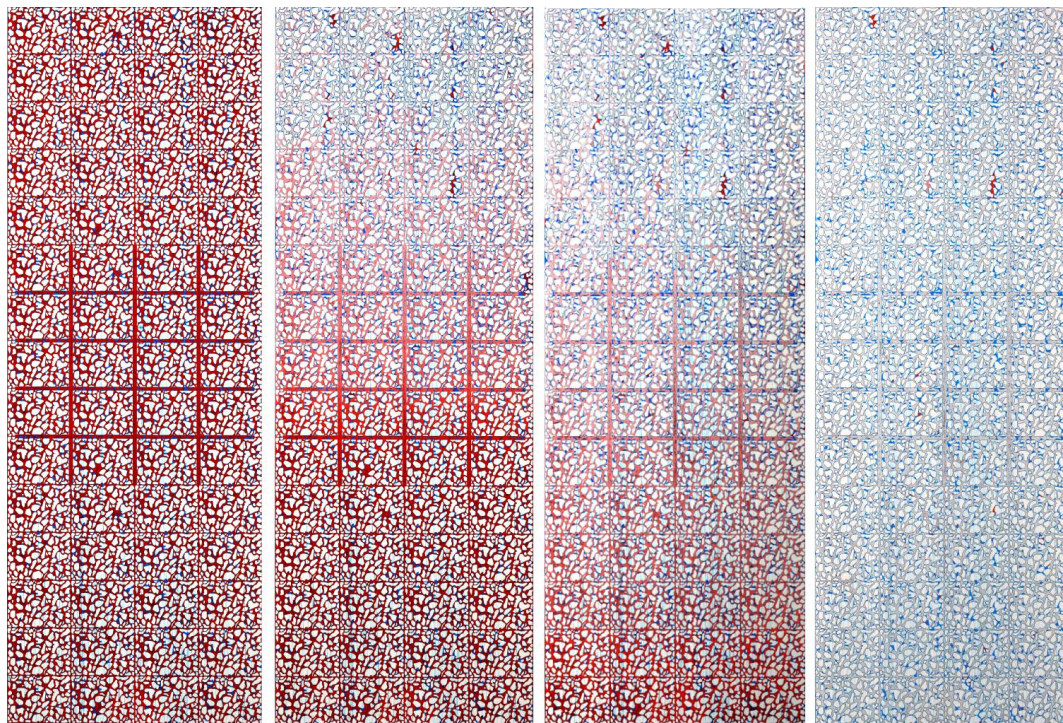
Fig. 8: Miscible GAGD experiment performed with C₃H₈ in water-wet conditions (unprocessed images, red: oil – blue: water – pink: oil with dissolved gas)

Investigation of Water Flooding and Carbonated Water Injection (CWI) in a Fractured Porous Media

Sedigheh Mahdavi, L.A. James
Memorial University of Newfoundland, St. John's, NL, Canada

ABSTRACT

Carbonated water injection (CWI) for enhanced oil recovery (EOR) has been investigated in several studies. Vertical and horizontal displacements are affected by heterogeneity especially fractures in porous media. This work is part of a comprehensive study on how the fracture geometry affects the performance of carbonated water injection in presence of gravity. It is motivated from previous work where we observed increased recovery using CWI compared to water flooding in homogenous media.

In this study, a fractured porous medium was fabricated in a glass micromodel for medium pressure (ambient to 1000 psi (6.89 MPa) experiments. Simple water flooding and CWI were performed in a fractured medium with vertical fractures at 305 psi (2.1 MPa) and 69.8°F (21°C). This study analyzes the effects of CWI on sweep efficiency and pore scale recovery. The results show that CWI is more effective in fracture oil recovery, trapped oil extraction than simple water flooding in vertically oriented fractured porous media. CWI displaces oil in the entire micromodel as well as around fractures, whereas in water flooding, water is not being able to distribute evenly in porous media and recover oil in narrow pores, throats and fractures. We observed better sweep efficiency in the lower part of the porous media when vertical fractures were present. The mechanistic study of macroscale displacement revealed that reduced oil viscosity controls the oil displacement in fractures. Fracture-matrix interaction was enhanced under CWI. Fractures were observed to conduct the oil extensively. The effect of gravity was verified by performing CWI injection in vertically oriented fractured micromodel. A quantitative analysis confirmed higher performance of CWI than water flooding in the presence of gravity by an additional 10.8% compared to water flooding.

INTRODUCTION

Gas injection is a potential method to improve sweep efficiency [Cotter 1962, Holm and Josendal 1974]. The challenge with every CO_2-based EOR process is to increase both micro and macro scale displacement efficiencies. The oil swelling and partial miscibility phenomenon still plays an important role in an immiscible CO_2 injection where sufficient CO_2 transfers to the oil phase swelling the oil helping reconnect immobilized oil ganglia. Reducing the oil viscosity and increasing oil swelling are two active mechanisms in CO_2

injection. [Khatib et al. 1981]. The solubility of CO_2 in both water and oil phases is a function of both pressure and temperature although it is a stronger function of pressure.. CO_2 is more soluble in oil than other gases [Klins and Farouq 1982]. The main challenge for a successful CO_2 injection process is related to the CO_2 density and viscosity, which cause poor volumetric sweep efficiency [Wellington and Vinegar 1985]. In general, the high viscosity contrast between the gas and oil results in highly unfavorable mobility, and the high density difference between the gas and the oil results in gravity segregation. Consequently, CO_2 injection often results in poor sweep efficiency [Green and Wilhite 1998]. Poor sweep efficiency is common in a fractured porous medium. Low displacing fluid viscosity can cause the fluid to flow through high-permeability zones bypassing oil in neighbouring matrix zones. Fractures cause premature breakthrough and an unstable frontal displacement which leads to poor overall recovery [Laroche et al. 1999]. In gas injection processes, gas and oil interactions are promoted by fractures more than in conventional reservoirs. However, high gas mobility compared to water and oil cause by-passed oil and gravity override [Van Dijkum and Walker 1991]. A challenge with continuous CO_2 injection, water alternating gas injection (WAG), and simultaneous WAG (SWAG) is that the sweep efficiency is still poor [Kulkarni and Rao 2005; Rangel-German and Kovsec, 2006]. Solvent injection in homogeneous and especially heterogeneous porous media results in very low residual oil saturation [Er 2007]. CWI is suggested as a possible alternative method.

Several studies have been performed on the efficiency of CWI since 1951 [Martin 1951; Perez et al. 1992; Dong et al. 2011]. CWI is an alternative injection method that requires less CO_2 compared to continuous CO_2 injection. Hence, this process is attractive for reservoirs with limited access to CO_2 such as remote offshore fields. Riazi et al. [2011] performed a series of homogeneous micromodel studies at 2000 psia (13.7 MPa) and 100 °F (38°C). They recorded 6-8% additional oil recovery for secondary and tertiary CWI compared to water flooding. Sohrabi et al. [2012] investigated the effect of CWI on core scale oil recovery where they achieved an additional 24% recovery. Mosavat and Torabi [2014, 2017] conducted a series of homogeneous micromodel and sand-pack studies. They believed that the main oil trapping mechanism was wettability trapping. Compared to water flooding, secondary and tertiary CWI recovered 9.4% and 7.3% additional oil, respectively. We previously [Mahdavi et al. 2016] investigated the effect of CWI in a homogeneous glass micromodel at 305 psia (2.1 MPa) and 69.8 °F (21°C) in the presence of gravity. The effect of gravity was observed in both water flooding and secondary CWI. Better oil redistribution and fewer by-passed oil zones were detected in CWI compared to water flooding in the presence of gravity. Residual oil approached 50% for CWI compared to 64% in water flooding. Seyyedi et al. [2017] conducted a series of tests: micromodel, slimtube and coreflooding experiments using live oil at 2500 psia (17 MPa) and 100 °F (38°C). The compositional analysis on each contact period showed that a new gas phase is formed plus the live oil (CH_4 + stock tank oil) and carbonated phase. At the early stage, the new phase has less CH_4 and CO_2 content; later the contact made the new gas phase rich in CO_2 resulting in 24% additional oil recovery compared to water flooding. According to the literature there is no reported comparative studies of CWI in heterogeneous fractured

porous media in the presence of gravity. In this study, we examine CWI in heterogeneous media in the presence of gravity.

EXPERIMENTAL PROCEDURE

Fluids Characterization- The fluids in this study are oil (29.8 °API) from offshore Canada, deionized water (DI) and pure CO_2 supplied by Praxair (99.8% purity). We measured and calculated all the physical properties at 305 psia (2.1 MPa) and 21°C (69.8 °F). The viscosity of the oil (6.8 cP) and DI (0.997 cP) was measured using a Cambridge VISCOlab PVT high pressure viscometer. The density of the oil (0.877 g/cm^3) and DI water (0.997 g/cm^3) was measured using an Anton Paar densitometer. A high-resolution camera (Canon EOS 6D, 100 mm focal length) was used to take pictures of the CWI process and the images were analyzed using in-house image analysis software. To differentiate between the fluids, the water was dyed blue using methylene blue while the CW was colorless, and the oil was dark brown. The carbonated water was prepared by mixing CO_2 with deionized water for 48 hours to reach the equilibrium. The solubility of CO_2, in DI was calculated using CMG-WINPROP^{TM}. The calculated solubility of CO_2 in oil and DI water was 0.021 $^{g\,CO_2}/_{kg\,oil}$ and 0.014 $^{g\,CO_2}/_{kg\,water}$, respectively.

Porous Medium Characterization- A heterogeneous micromodel (20 cm $\times$ 3.5 cm) with fractures was designed and fabricated. A close-up image of the fully oil saturated micromodel is shown in Figure 1. Experiments including water flooding and secondary CWI were performed in both horizontal (laying flat, no gravity) and vertical (on edge, with gravity) orientations.

Matrix and Fracture Characterization- A matrix pattern was prepared using a thin section of a sandstone rock sampled from an offshore oil reservoir and drawn in Corel DRAW X7. We etched four vertical fractures perpendicular to fluid flow (Figure 1). The overall length (the vertical distance between top and bottom) and aperture of each fracture is 1.29 and 0.1 cm, respectively. Using image analysis, the porosity of the micromodel was determined to be 38%. The etched depth of the micromodel varied between 60 – 70 μm measured using scanning electron microscopy (SEM). The water steady state permeability was determined to be 400 D for the overall micromodel.
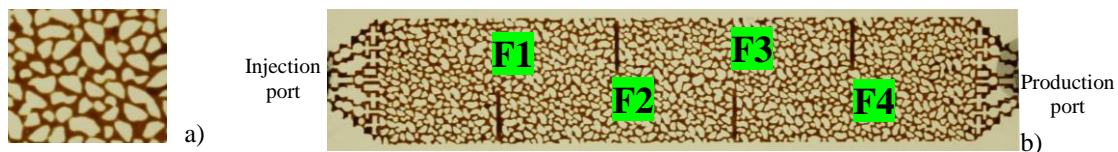
Figure 1: Schematic of fractured micromodel with fractures (denoted F) perpendicular to flow), a) a close-up and b) whole micromodel

Experimental Procedure-The experimental setup consists of a Quizix 20K pump, accumulators, pressure transducers, and imaging system. Before each test, the micromodel was first cleaned using solvents (i.e. toluene, acetone and water) and dried with air then fully saturated with oil. The experimental conditions were set at a pressure of 305 psi (2.1 MPa) and a temperature of 21°C (69.8 °F). Water or carbonated water (depending on

experiment) was injected at a rate of 0.0024 cc/min to satisfy the capillary number in the range of 10^{-7}. Some of the experiments were conducted twice for repeatability.

RESULTS and DISCUSSION
Comparison of WF and CWI with Gravity
The water flooding (WF) and CWI scenarios were conducted in two different orientations: with and without gravity. The displacement pattern, matrix-fracture interaction, residual oil saturation and pore scale phenomena were recorded. Figure 2 shows a series of some of the vertical WF and CWI experiments under gravity effect at different injected pore volumes. Water enters the micromodel (Figure 2a) and then moves downward due to the gravity effect to fill the fracture 1 (F1) whereas, the CW front (z-x direction) moves forward slower than the water front. Moreover, CW is distributed more evenly in z-direction (Figure 2a') than water (Figure 2a). By comparing to the oil displacement pattern in Figures 2b and 2b' at 0.05 PV, it is observed that in proximity to the fracture, the water fingers towards the fracture (F3).

Breakthrough occurred in WF and CWI at 0.24 and 0.37 PV injection, respectively, which is shown in Figure 2c and 2c'. The fluid distribution in the fracture and the matrix was more evenly distributed in CWI than water flooding prior to breakthrough (Figure 2c and 2c'). The oil displacement in the lower part of the micromodel was more complete and homogenous in CWI than WF. Water could reach to the upper fracture F2 (Figure 2c) and displace the oil in the fracture which did not happen in the case of CWI in Figure 2c'. However, comparing the residual oil saturation upstream (to the left) of fracture F2 in Figures 2d and 2d', we observe better sweep efficiency for the carbonated water (CWI) than water (WF) and there was a large by-passed zone behind the fracture F2.

2a) WF-V
9.2% recovery
at 0.05 PV

2a') CWI-V
14.9% recovery
at 0.05 PV

2b) WF-V
22.9% recovery
at 0.17 PV

2b') CWI-V
24.1% recovery
at 0.17 PV

2c) WF-V
25.2% recovery
at 0.24 PV (BT)

2c') CWI-V
38.1% recovery
at 0.37 PV (BT)

2d) WF-V
38.8% recovery
at 7 PV
38.8%

2d') CWI-V
48.9% recovery
at 7 PV
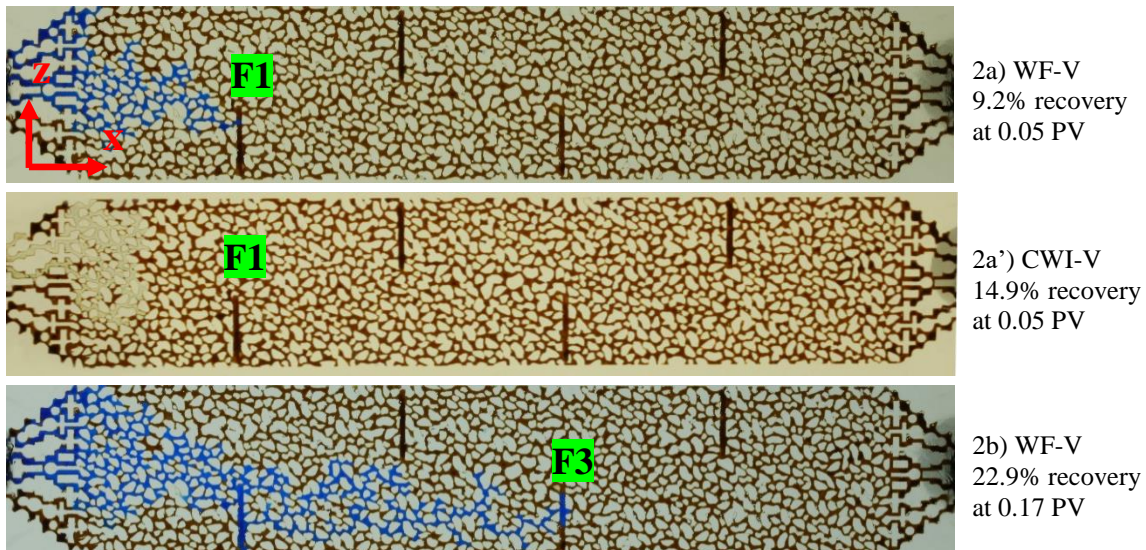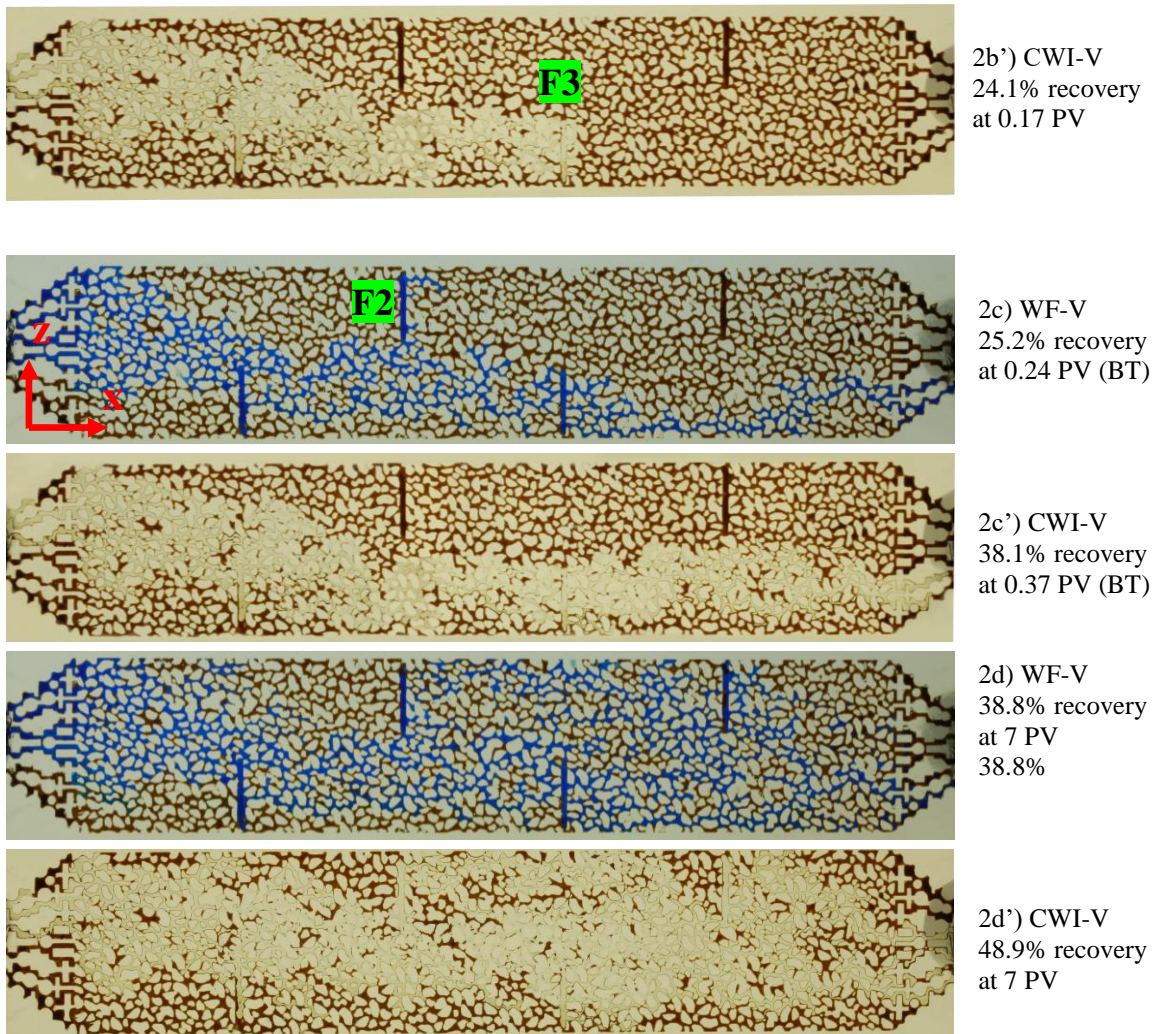
Figure 2: Comparison of WF and CWI in the presence of gravity (vertical orientation)

By continuing injection to ~ 7 PV (Figures 2d and 2d'), CWI indicates that the CW phase is able to sweep the remaining oil in the upper fractures and matrix over a large area. The trapped oil in WF is mostly oil banks, especially in the upper part and close to the production port (right side of the figures). In contrast to waterflooding, CWI traps oil mostly in pore spaces. Recovery factor changes 25.2% and 38.1% from breakthrough to 38.6% and 49.7% for water flooding and CWI, respectively (average of two replicates).

Comparison of WF and CWI without Gravity

The performance of CWI and WF were examined without the effect of gravity in a fractured micromodel (Figure 3's series). We observed that, initially water and CW have similar displacement patterns (Figures 3a and 3a'). However, water appears to exhibit viscous fingering behaviour more than CWI. In CWI, the CW distribution and displacement patterns among the fractures and matrix are more homogeneous (Figures 3b

and 3b') due to the modified mobility of CW. The mobility control is the dominant mechanism in CWI before breakthrough.

3a) WF-H 3.0% recovery at 0.05 PV

3a') CWI-H 5.4% recovery at 0.05 PV

3b) WF-H 14.9% recovery at 0.17 PV

3b') CWI-H 12.9% recovery at 0.17 PV
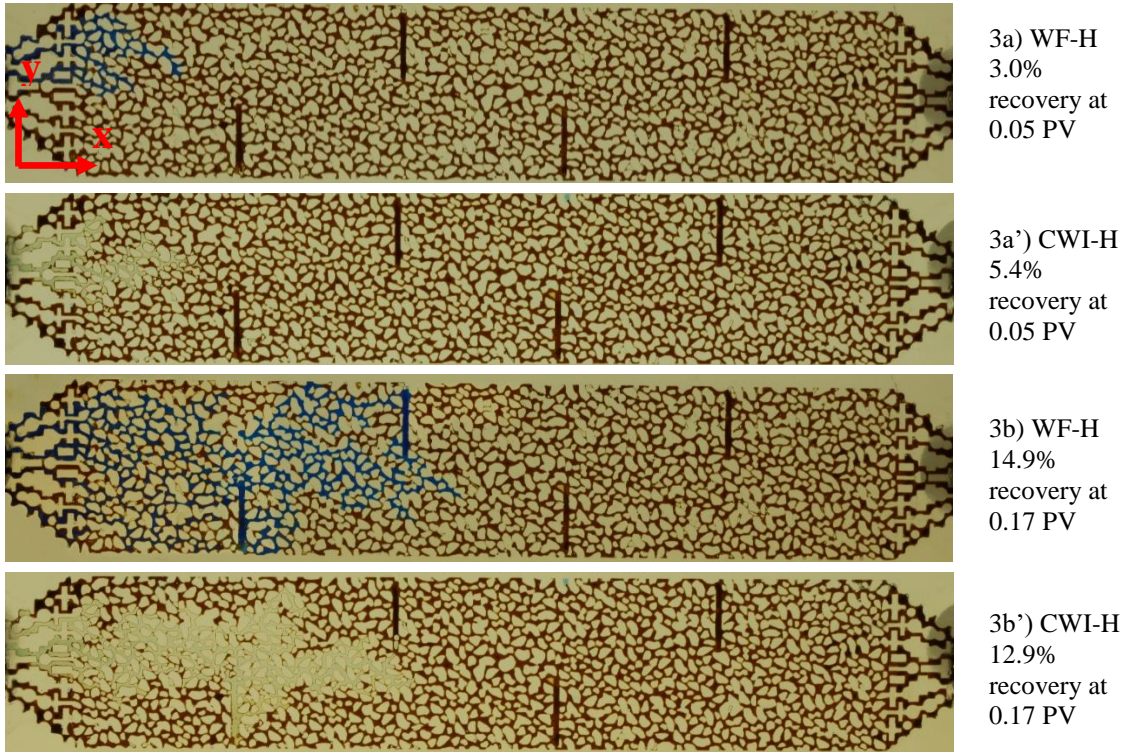
Breakthrough happens in WF and CWI at 0.1 PV and 0.13 PV, respectively. The oil displacement pattern is more homogeneous in CWI than WF. However, there is not much difference in oil recovery in WF and CWI prior to breakthrough (Figures 3c and 3c') due to effect of fractures and flow distribution. The viscous fingering is more pronounced near the production port for WF compared to CWI (Figure 3c and 3c' at right side), i.e. the flood front moves in a more stable manner in the case of CWI.

3c) WF-H 38.6% recovery at 0.35 PV (BT)

3c') CWI-H 40.0% recovery at 0.44 PV (BT)

3d) WF-H 43.7% recovery at 7 PV

3d') CWI-H 57.0% recovery at 7 PV
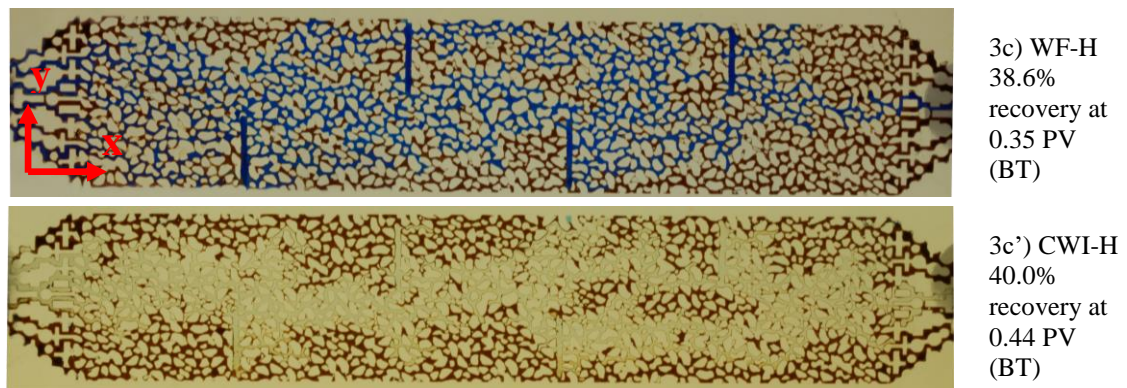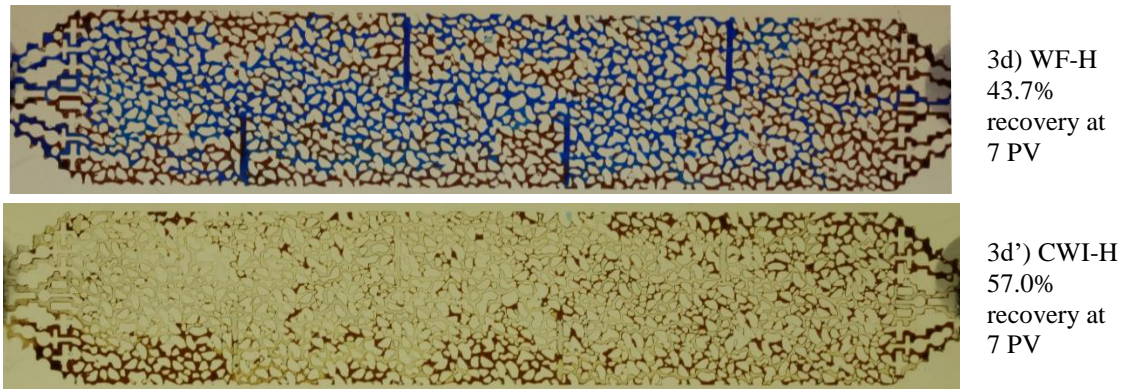
Figure 4: Comparison of WF and CWI without gravity

Overall, CWI has a more effective, stable frontal displacement and pore scale recovery in presence of fractures perpendicular to the flow. After breakthrough, the residual oil decreases more with CWI. At 7 PV (Figures 3d and 3d') it is clear that CWI has better sweep and pore scale recovery efficiency compared to WF.

Fracture Conduction

It was found that fractures (highlighted by the green lines) play an important role in oil displacement in a fractured porous media (Figure 5). It is shown that the fractures play a role in collecting and transporting oil mostly via film flow. Fluid flow moves towards the fractures being more permeable. The water or carbonated water and oil move from matrix pores upstream of the fracture into the fracture and outward into the matrix again downstream of the fracture. The oil from different pores appears to accumulate in the fracture entering the porous matrix again (Figure 5 a-c and Figure 5 d-h).

(a)   (b)   (c)   (d)

(e)   (f)   (g)   (h)
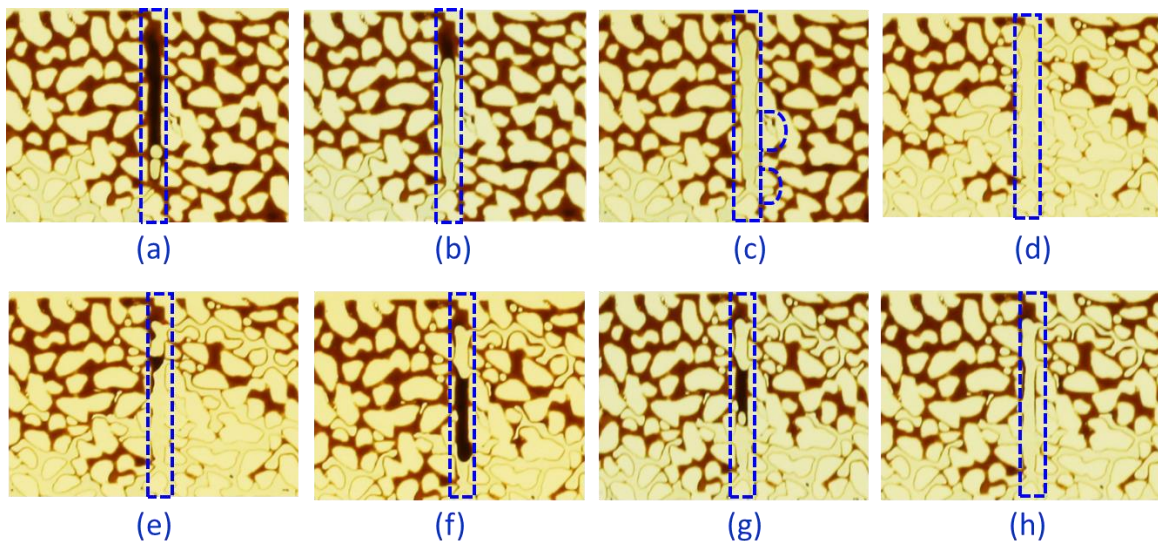
Figure 5: Sequence of fracture oil conduction

Recovery Analysis

Figure 6 shows the recovery factor versus injected pore volume. As shown the higher recovery is achieved when gravity is not present (micromodel is horizontal). Ultimate oil recovery at 7 PV injection was 57.1% for CWI in the horizontal micromodel compared to 43.7% recovery from WF without the effect of gravity. After breakthrough, CWI recovered more oil than WF in the horizontal models (40.0% recovery at breakthrough to 57.1% at 7 PV for CWI and 38.6 % recovery at breakthrough to 43.7% at 7 PV for WF). In the presence of gravity, we see similar phenomena in that recovery at breakthrough is substantially higher for CWI compared to WF.

Recovery from the vertical micromodel with fractures at breakthrough and 7 PV injection is on average 38.6% and 49.7%, respectively using CWI. Waterflooding recovery was 25.2% and 38.8% at breakthrough and 7 PV water injected. Mahdavi and James [2016] reported an average of 15.3% recovery at breakthrough and 52.5% recovery at 7 PV injected for CWI using a homogenous micromodel (no fractures) with similar permeability. The ultimate recovery is similar but there is a large difference in recovery at breakthrough. Water flooding from the vertical homogenous model recovered 25.7% and 36.2% at breakthrough and 7 PV injected, respectively [Mahdavi and James, 2016]. The comparable waterflooding recovery results between the homogenous micromodel and the micromodel with fractures indicates our ability to compare recovery results between the different micromodels. The fractures do not seem to increase sweep efficiency for the water flooding case. What we see is higher recovery at breakthrough using CWI in a fractured micromodel compared to waterflooding and even CWI in a homogeneous micromodel. These differences may be attributed to primarily better vertical sweep efficiency when fractures are present. The transfer of CO_2 from the water to the oil swells the oil and possible developing miscibility may contribute to the increased production observed using CWI compared to WF.
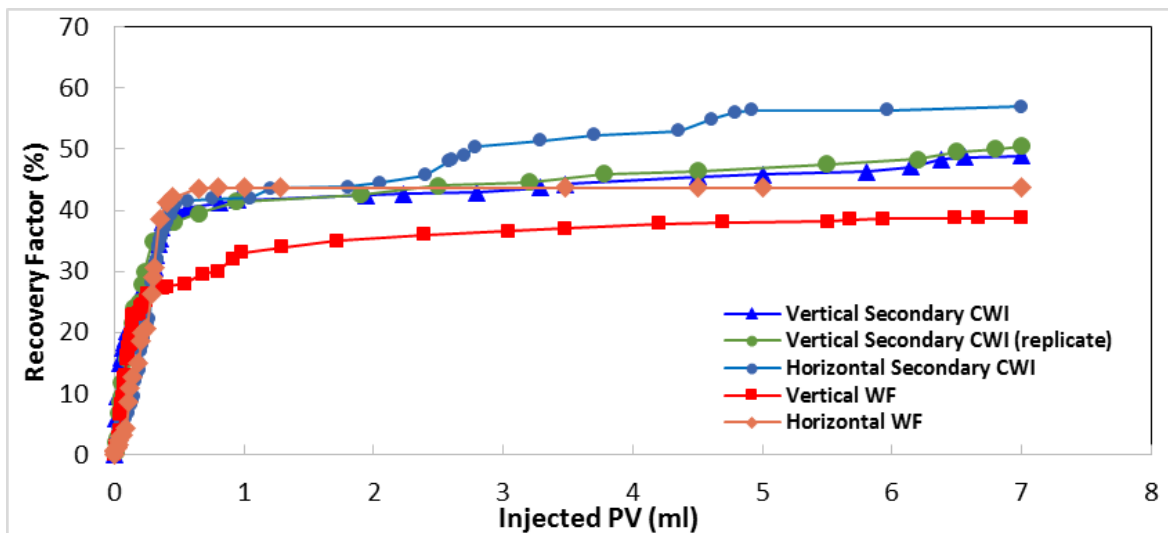
Figure 6: Oil recovery factor in different scenarios as a function of injected pore volume

CONCLUSION

Based on the pore scale fractured micromodel experiments, the effect of gravity was verified in presence of fractures. We observed that vertically oriented fractures aids in the distribution of the carbonated water in the micromodel increasing vertical sweep efficiency. Water flooding exhibited earlier breakthrough compared to CWI under similar conditions. CWI produces more oil after breakthrough. Horizontal carbonated water phase sweeps a larger area and results in less residual oil saturation after breakthrough. Pore scale events such as fracture conduction and oil entrapment were observed in both water flooding and CWI. However, fracture conduction and pore scale sweep efficiency was more pronounced in CWI. It is believed that CO_2 transferred from the water to the oil and partial miscibility may be reasons for better recovery efficiency from carbonated water compared to water alone.

ACKNOWLEDGEMENTS

REFERENCES

Cotter, W.H., "Twenty-Three Years of Gas Injection into A Highly Under Saturated Crude Reservoir", Journal of Petroleum Technology 14 (4), 361-365. SPE-82-PA, 1962.

Dong, Y., Ishizawa, C., Lewis, Ed, and Dindoruk, B., "Carbonated Water Flood: What We Observed in Sand pack Experiments", International Symposium of the Society of Core Analysts, Austin, Texas, USA, 18-21 September, SCA2011-34, 2011.

Er, V., T. Babadagli, Visual Investigations on the Oil Recovery and Sequestration Potential of CO_2 in Naturally Fractured Oil Reservoirs, 8th Canadian International Petroleum Conference (CIPC), Calgary, Alberta, Canada, 12-14 June, 2007.

Green, D.W., Willhite, G.P., "Enhanced Oil Recovery", Society of Petroleum Engineers, 1998.

Holm, L.W, V.A. Josendal, 1974, "Mechanisms of Oil Displacement by Carbon Dioxide", SPE-4736-PA, Journal of Petroleum Technology, 1974.

Khatib A.K. and R.C. Earlougher, "CO_2 Injection as an Immiscible Application for Enhanced Recovery in Heavy Oil Reservoirs", SPE 9928, California Regional Meeting in Bakersfield, USA, March 25-26, 1981.

Kilns M.A., A.M. Farouq Ali, "Heavy Oil Production by Carbon Dioxide Injection", Journal of Canadian Petroleum Technology (JCPT), pp 64-72, 82-05-06 PETSOC, 1982.

Kulkarni, M.M. and D.N. Rao, "Experimental Investigation of Miscible Secondary Gas Injection", SPE 95975, SPE Annual Conference and Exhibition, Dallas, 9-12 October 2005.

Laroche, C., Vizika, O., Kalaydjian, F., "Wettability Heterogeneities in Gas Injection; Experiments and Modeling". Petroleum Geoscience, Vol.5(1), pp.65-6. 1999.

Mahdavi, S. and L.A. James, "Pore Scale Investigation of CWI with and without Gravity", SCA2016-037, SCA Conference, Colorado, USA, 16-21 August 2016.

Martin, J.W., "Additional Oil Production Through Flooding with Carbonated Water. Producers Monthly, pp 13-15, 1951.

Mosavat, N., Torabi, F., "Experimental Evaluation of the Performance of CWI under Various Operating Conditions in Light Oil Systems", Fuel, 123, 274-284, 2014.

Mosavat, N. and Torabi, F., "Micro-optical Analysis of Carbonated Water Injection in Irregular and Heterogeneous Pore Geometry", Fuel 175, 191–2016.

Perez, J.M., Poston, S.W., and Sharif Q. J., Carbonated Water Imbibition Flooding: An Enhanced Oil Recovery Process for Fractured Reservoirs, Paper SPE 24164, SPE/DOE 8th symposium on Enhanced Oil Recovery, Tulsa, Oklahoma, USA, April 22–24, 1992.

Rangel-German, E.R. and A. R. Kovscek, "A Micromodel Investigation of Two-Phase Matrix-Fracture Transfer Mechanisms", Water Resources Research, 42, W03401, 2006.

Riazi, M., Sohrabi, M, Jamiolahmady, M., "Experimental Study of Pore-Scale Mechanisms of Carbonated Water Injection", Journal of Transport in Porous Media, 86:73–86, 2011.

Sohrabi, M., Nor Idah Kechut, Riazi, M., Jamiolahmady, M., Ireland, S., Robertson, G., "Coreflooding Studies to Investigate the Potential of CWI as an Injection Strategy for Improved Oil Recovery", Transport Porous Media Journal, 91:101–121, 2012.

van Dijkum, C.E. and T. Walker, "Fractured Reservoir Simulation and Field Development, Natih Field, Oman", SPE 22917, 66th Annual Technical Conference and Exhibition, Dallas, TX, USA, October 6-9, 1991.

Wellington, S.L. and H.J. Vinegar, CT Studies of Surfactant-Induced CO_2 Mobility Control, SPE 14393, 60th Annual Technical Conference and Exhibition, Las Vages, NV September 22-25, 1985.

EXPERIMENTAL AND NUMERICAL INVESTIGATION OF DISPERSION IN A DUAL PERMEABILITY POROUS MEDIUM DURING MISCIBLE DISPLACEMENT

Saeid Eskandari, L.A. James

Department of Engineering and Applied Science, Memorial University of Newfoundland

ABSTRACT

This study presents an analytical and experimental investigation of the mixing and spreading process in a dual permeability porous medium during the miscible displacement process. The coupled two-dimensional model of high and low permeability zones that are horizontally parallel is assumed, and the interaction between two zones is manipulated by imposing the continuity of concentrations at the interface between the two zones. The mathematical model of governing equations, considering the longitudinal and transverse dispersion has been developed for each region. The equations in following have been coupled considering the continuity of concentrations and mass fluxes along the boundary of high and low permeability regions. To testify the model, the experimental study has been conducted using a two-dimensional glass micromodel, dyed and clear water and a new image processing technique. A series of miscible displacements has been implemented and taken images at known time steps have been processed using a uniquely developed image processing tool to measure the dispersion coefficients in each region at different time steps. In the following, the validity of the mathematical analysis has been tested with the experimental results. The results of this study provide a deeper understanding of the mixing process during miscible displacement, the importance of longitudinal and transverse dispersion in high and low permeability zones with different heights and the effect of injection velocity in the development of mixing zone over time.

INTRODUCTION

Miscible and near-miscible displacement processes are increasingly feasible methods for the recovery of oil from depleted reservoirs as an enhanced oil recovery (EOR) process. However, a fundamental understanding of the dependency of transport phenomenon on porous media properties and their indirect impact on oil recovery efficiency is lacking. Moreover, it is believed that miscibility may repeatedly develop and break down in a reservoir due to dispersion arising from reservoir heterogeneity and therefore the effectiveness of miscible processes as an EOR method are complicated by the heterogeneity of a porous medium. Dispersion is a transport mechanism of a substance or conserved property by a fluid due to the fluid's bulk motion [1]. A distinction is commonly

made between dispersion occurring in the flow direction, longitudinal (D_L), or perpendicular to it, transverse (D_T).

The advection-diffusion equation (ADE), mass conservation law, has been commonly used [2] to describe solute dispersion in two-dimensional porous media:

$$D_L \frac{\partial^2 C}{\partial x^2} + D_T \frac{\partial^2 C}{\partial y^2} - \upsilon_x \frac{\partial C}{\partial x} - \upsilon_y \frac{\partial C}{\partial y} = \frac{\partial C}{\partial t} \qquad (1)$$

where C is the solute concentration, t is time, υ_x and υ_y are the components of flow velocity, and D_L and D_T are the hydrodynamic longitudinal and transverse dispersion coefficients, respectively. The mathematical approach to modeling dispersion regularly focused on applying the partial differential equation referred to as the advection-dispersion (Eq. 1) from continuum mechanics. The dispersion mechanism is mainly characterized by contributions of molecular diffusion and mechanical dispersion expressed as a function of the Peclet number. Many mathematical studies including imperial correlations have been done. Taylor [3] (1954) described the principles of solute transport in porous media. He envisioned the porous media as a bundle of capillaries and viscous fluid flowing through a tube of circular cross section. Taylor defined dispersion D ($m^2 s^{-1}$) as:

$$D = \frac{a^2 \upsilon^2}{48 D_m} \qquad (2)$$

where v is the velocity ($m s^{-1}$), D_m is the molecular diffusion ($m^2 s^{-1}$), and a is the tube radius (m). This study also showed that the proposed model was valid under the condition that Peclet number is within the range of $6.9 \ll$ Pe $\ll \frac{4l}{a}$ [4]. Aris (1956) removed the restriction imposed on some of the parameters at the expense of describing the distribution of the solute in terms of its moment in the direction of flow. Aris also showed that the rate of growth of the variance is proportional to the sum of molecular diffusion and Taylor dispersion [5]. There are also some studies started with Barenblatt [6] (1960) called dual permeability approach. The dual-permeability porous medium involves two regions with different hydraulic and discursively transport properties. The term dual-permeability indicates that fluid flows in two distinct regions that one region may represent a higher permeability space with faster flow and second domain with lower permeability and therefore slower flow in the rock matrix. Other studies after, (e.g. dye tracer studies by Cislerova et al. [7], 1990; Villholth et al. [8], 1998; and Larsson et al. [9], 1999) have used this approach to investigate the miscibility development and interaction between two domains. However, most studies used probabilistic methodologies, and have not considered the analytical solutions. Leij et al. [10], in 2012, considering this lack, presented a mathematical model for dispersion development in a dual-permeability medium using analytical approach by solving Laplace transformation and matrix decomposition. The study illustrates the difference in travel time for the two regions and shows the difference in fluid velocities.

On the other hand, mixing processes that occur during miscible injection have been studied at different scales, from a laboratory to field scale, using various experimental approaches.

One of the initial leading studies was published by Brigham et al. [11] in 1961 describes the result of experiments on miscible displacement in different porous media. Both glass bead packs and natural cores were used to represent a porous medium. Since the required experimental parameters were not directly measurable, appropriate assumptions were made to obtain such values by Brigham. After analyzing the error function, he proposed Eq. 3 to calculate the longitudinal dispersion.

$$D_L = \frac{1}{t}\left(\frac{x_{90} - x_{10}}{3.625}\right)^2 \tag{3}$$

The variables are time t (s) and x_{10} is defined as the distance to the point of 10 percent displacing fluid and x_{90} is the distance to the point of 90 percent displacing fluid. However, Brigham related the dispersion coefficient to the error function by drawing the best straight line through the values of U (the error function parameter). The modified equation based on this method is given in Eq. 4 and 5.

$$D_L = \frac{1}{t}\left(\frac{x_{90} - x_{10}}{3.625}\right)^2 \tag{4}$$

$$U = \frac{V_p - V}{\sqrt{V}} \tag{5}$$

The parameters include the pore volume V_p of the porous medium (cm^3) and the volume of the recovered fluid at any time, V (cm^3). For transverse dispersion, Grane and Gardner [12] (1961) carried out a set of experiments in homogeneous porous media to study the influence of fluid flow velocity and pore structure properties on transverse dispersion. They observed that by increasing the difference in density the mechanical dispersion significantly decreased and therefore density difference has a significant effect. Perkins and Johnston [4] (1963) performed experimental investigations using the Brigham method. Perkins and Johnston studied the impact of various parameters including density contrast and pore geometry. Fried and Combarnous [13] (1971) published the result of the extensive laboratory experiments performed to investigate the influence of the increase in velocity on dispersion in porous media. Most of the later experimental studies applied the same methodology to refine the understanding of longitudinal and transverse mixing and effective parameters by directly considering the physical mechanisms governing solute transport. The current study uses an analytical solution for miscible displacement in a dual-permeability two-dimensional porous medium. A new experimental approach is applied to validate the analytical results.

MODEL DESCRIPTION
We assume a two-dimensional porous medium as in Fig. 1, consisting of high permeability (1) and low permeability (2) regions combined in one glass etched pore network micromodel. In this model, inlet pressure (P_1) and outlet pressure (P_2) are constant. The high permeability region is very low in width (w) (assumed 1D) and region 2 is higher in width (W) and considered two-dimensional (w $\ll$ W). It is assumed that for y = 0, v = v_{x1},

for y > 0, v(x, y) = (v_{x2}, v_{y2}). The concentration in region 1 (y = 0) is assumed C(x, y) and in region 2 is assumed C^*(x, y). Initial conditions for $\forall$x,y is C(x, 0) = C^*(x, y, 0) = 0 and boundary conditions are assumed as Eq. 6.
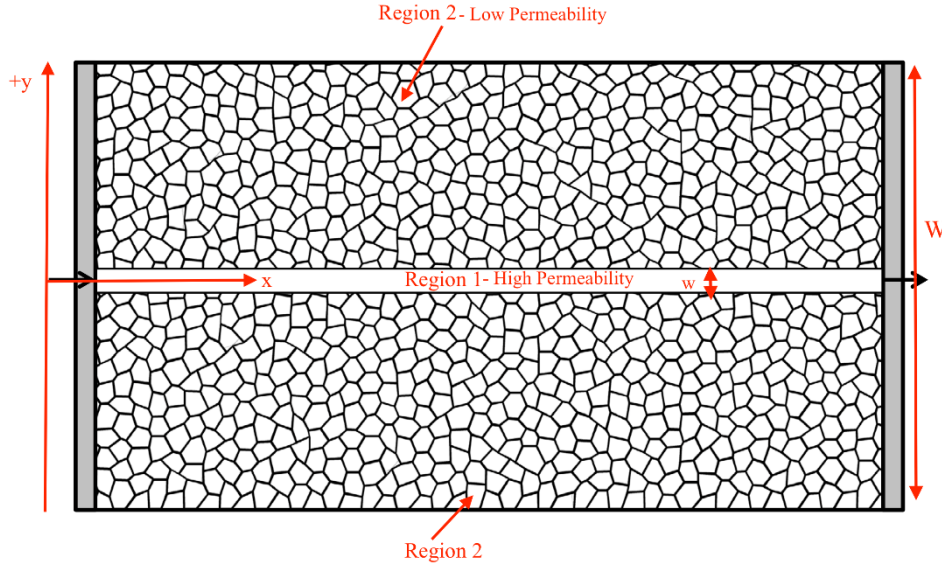
Figure 1. Assumed dual-permeability porous medium

$$\begin{cases} \forall t \Rightarrow C(0,t) = C_0 \\ \forall t \Rightarrow C^*(0,t) = 0 \\ \forall x, t \Rightarrow lim_{\Delta y \to 0} C^*(x, \Delta y, t) = C(x,t) \end{cases} \quad (6)$$

Dominant velocity is in x-direction and only in high-permeability region and advection in low-permeability region is neglected. Considering the advection-diffusion equation (Eq. 1) in each region, the equations below are assumed:

$$y = 0: \frac{\partial C}{\partial t} + \upsilon \frac{\partial C}{\partial x} - D_{x1} \frac{\partial^2 C}{\partial x^2} = -q(x,t)$$

$$y > 0: \frac{\partial C^*}{\partial t} - \upsilon_{x2} \frac{\partial C^*}{\partial x} - \upsilon_{y2} \frac{\partial C^*}{\partial y} - D_{x2} \frac{\partial^2 C^*}{\partial x^2} - D_y \frac{\partial^2 C^*}{\partial y^2} = q(x,t)$$

$$\forall t, x \text{ and } y = 0: q(x, t) = D_y lim_{\Delta y \to 0} \frac{C^*(x, \Delta y, t) - C(x,t)}{\Delta y} \quad (7)$$

$$\forall t, x \text{ and } y > 0: q(x, y, t) = 0$$

The model examines single phase flow (clear water injected into dyed water where the fluids are the same viscosity and we have single phase flow. When an increased concentration C_i^n enters the first cell, due to the fluid velocity in the x-direction, concentration distribution in the entire system reforms. To keep it simple, we assumed that

the concentration in each cell has a single value. We need to solve for the concentration in the ith cell at time step n (C_i^n), depending on time and transport properties.

EXPERIMENTAL PROCEDURE

Micromodel flooding experiments are conducted to evaluate the validity of the obtained mathematical model and gain a deeper understanding of miscible displacements in a 2D medium. To avoid the effect of density difference in driving dispersion, clear and dyed water are used as a displacing and displaced water, respectively. The experimental apparatus include a syringe and hand pump, micromodel holder, burette, graduated cylinder, weighing paper, moisture trap, digital camera connected to computer with appropriate lens, pressure transducers, a mass balance, pressure gauges, temperature transducers, a temperature gauge, tubing, valves, Swagelok® fittings (tees, caps, plugs, nuts, ferrules, tube adapters, connectors, and a pressure relief valve), and tools.
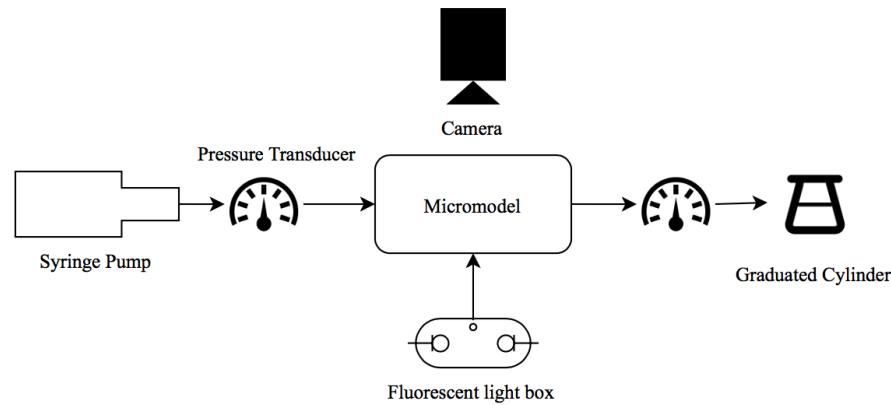
Figure 2. Experimental Setup Schematic

Fig. 2 shows the schematic of the experimental set up. Table 1 shows the micromodel properties. The micromodel is placed between two frames with a port at each end (injection and production). A syringe pump (Cole-Pamer dual syringe pump RS-232) is used to inject the water. Injection of dyed water and full saturation of micro model associated with image processing is needed to calculate the porosity and absolute permeability. Miscible displacement tests were conducted, an image processing technique developed to find the concentration profile, and the longitudinal and transverse dispersion coefficients were calculated.

Table 1. Properties of the dual-permeability micromodel

K_1	56 D	$\emptyset_1$	0.52	L_1	32 cm	W_1	0.5 cm
K_2	18 D	$\emptyset_2$	0.39	L_2	32 cm	W_2	6.0 cm

During the miscible displacement tests, we have single phase flow and we do not have a distinct interface between the displacing and displaced fluids. Clear water is injected into coloured/dyed water. However, a mixing zone exists between the pure displacing fluid and the displaced fluid. The scaled concentration in the mixing zone ranges from zero (clear

displacing fluid) to 100 (pure displaced fluid, red). Images taken during the miscible injection at known times are used to approximate the concentration profile. The most challenging part is distinguishing the concentration based on colour gradient (clear to red) and this requests robust calibration of color intensity and image processing. To relate the different colors to corresponding concentrations, several images were taken to obtain a unique correlation on a per pixel basis. After extracting the concentration profile, the
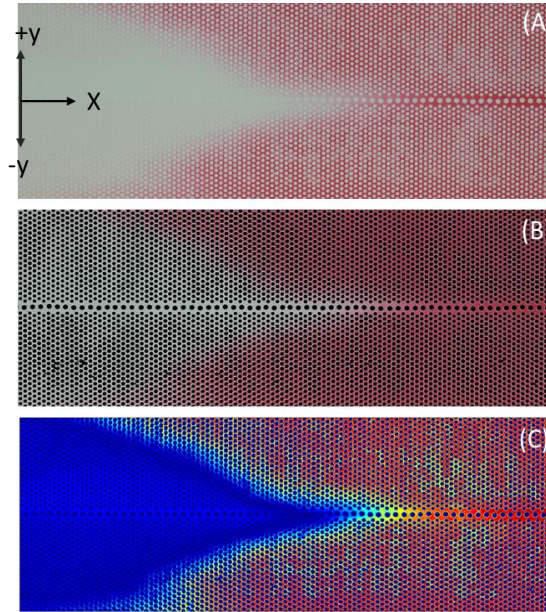
Figure 3. Image processing technique

longitudinal and transverse dispersion will be estimated by fitting the experimentally measured transient solute concentration profiles with the aid of the Bayesian estimator to an analytic solution of Eq. 1. The cropped raw image (A), selected-analyzed mask image (B) and processed image (C) is illustrated in Fig. 3.

RESULTS AND DISCUSSION
To study the dispersion in a dual-permeability porous medium using experimental and numerical investigations the following results have been accomplished.

Experimental Observations
During the experiment, we observed a developing mixing zone over time. As Fig. 4 shows, the mixing zone in high permeability region is caused by longitudinal dispersion, and in lower permeability porous medium longitudinal and transverse dispersion are coupled. From the Taylor Eq. 2, two factors affect miscible displacement: advection and dispersion, especially in the case of lower injection rate. Comparing the longitudinal dispersion in each region shows that dispersion is greater in the porous medium region. This may be caused by a presence of dominant flow velocity and lower height of the region 1. As shown in Fig.

4, in the high permeability zone (channel), the fluid advances from left to right at a higher rate than in the low permeability porous medium.
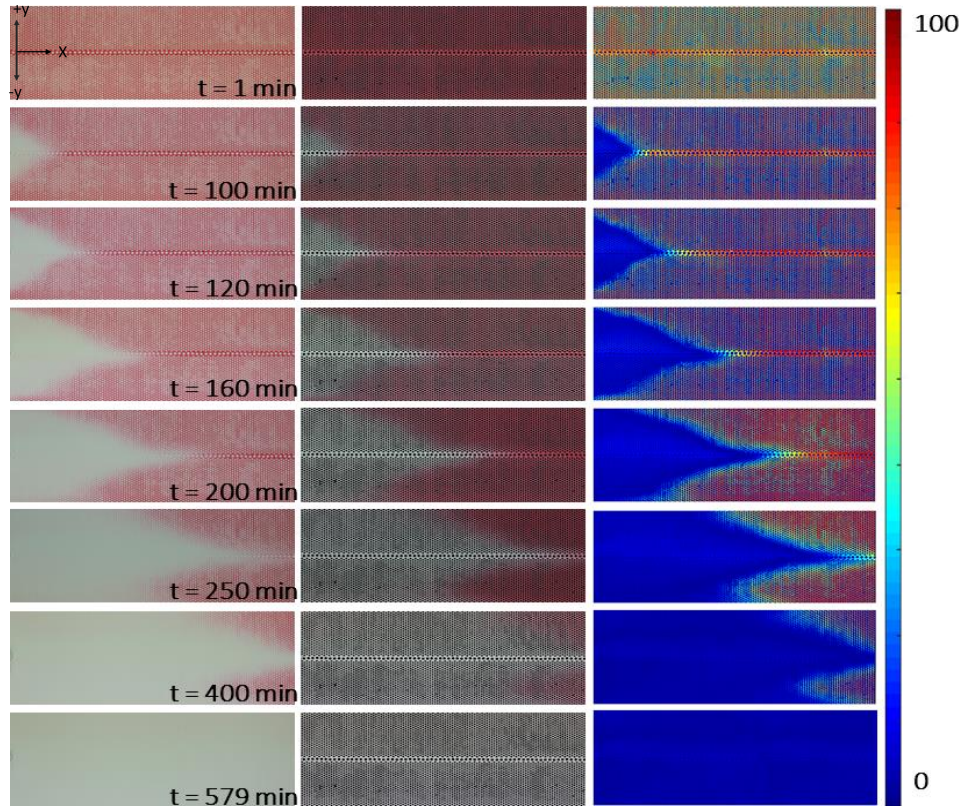
Figure 4. Miscible displacement progress over time

Analytical Solution

Eq. 7, presents the assumed mathematical model for miscible displacement in the dual-permeability medium with defined assumptions. The set of equations is solved using first and second order upwind scheme. In high permeability region, due to very low height for the medium, advection and longitudinal dispersion terms have been considered, and in the lower permeability medium, advection, longitudinal and transverse dispersion have been assumed. Although both regions have longitudinal dispersion terms, the longitudinal coefficient in high permeability region is considered 20 times larger than the lower permeability zone. Table 2 shows the assumed parameters and coefficients for the set of equations. The assumptions appear reasonable in circumstances of the relatively smaller contribution of dispersion terms to spreading of displacing fluid when there is a clear difference in velocity between the two regions. Fig. 5 shows that the predicted longitudinal and transverse dispersion coefficients in the low permeability region in Table 2 are in a good agreement with the experimental results. This leads to same dispersion coefficients in both component in low permeability region in the absence of a dominant velocity.

Table 2. Assumed parameters and coefficients for the set of equations

$\upsilon_x\ (^m/_s)$	$\upsilon_{x2}(^m/_s)$	$\upsilon_{y2}(^m/_s)$	$D_{x1}(^{m^2}/_s)$	$D_{x2}(^{m^2}/_s)$	$D_y(^{m^2}/_s)$
3×10^{-5}	1.5×10^{-6}	2×10^{-6}	2×10^{-6}	1×10^{-7}	1×10^{-7}

Model Validation

The simulation results are used to find the displacement process in both regions over time. Fig. 5 illustrates the miscible displacement flooding in the same dual permeability pattern as the one used in the micro model experiment.
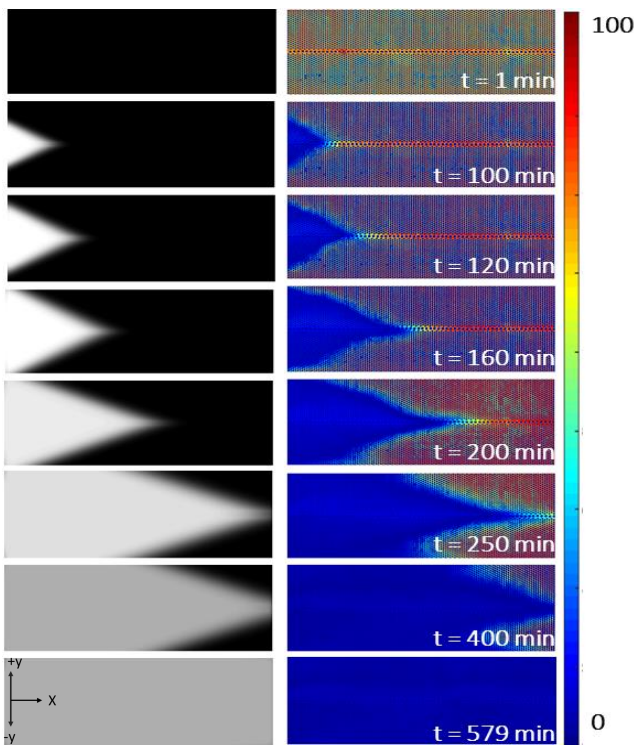
Figure 5. Mathematical vs experimental results of miscible displacement progress over time
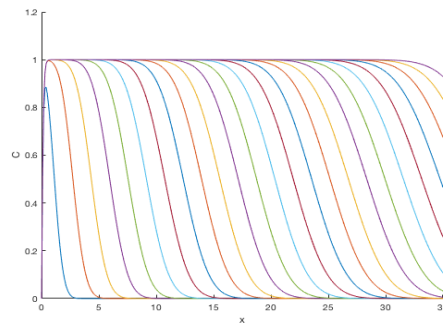
*Figure 6. Concentration profile of displacing fluid versus x-directio*n
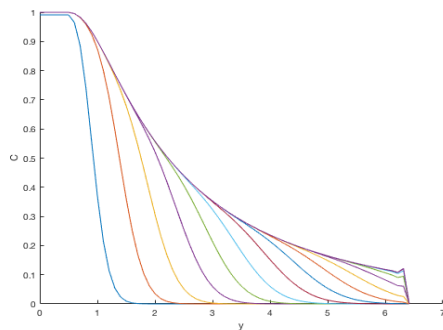
Figure 7. Concentration profile of displacing fluid versus y-direction

Fig. 6 and 7 shows the concentration profile versus positions in the x and y-directions for different times. Fig. 6, showing the concentration profile in the direction of displacement indicates a convection dominated mass transfer whereas Fig. 7 showing the concentration profile in the y-direction. The shape of the concentration profile is indicative of conduction dominated mass transfer. The analytical solution indicates a solid agreement with experimental images. If a more viscous miscible fluid was injected we would likely see the convective terms reduced due to the more viscous flow but conductive mass transfer should not be affected.

CONCLUSIONS

Experimental results showed that the mathematical models fit the miscible displacement concentration profiles obtained from miscible tests. Experimental results illustrated some typical mixing zones that are larger in high permeability zone than lower permeability region. This observation also, concludes higher longitudinal dispersion coefficient in high permeability region. Despite the significantly dominant longitudinal dispersion in high permeability zone, in the low permeability region, longitudinal and transverse dispersion coefficients are in same order of magnitude which indicates the effect of the presence of dominant velocity in the x-direction on the amplitude of the longitudinal dispersion. The simulation and experimental results show that the longitudinal and transverse dispersion in low permeability region are in the same order of magnitude. This is most likely caused by the absence of dominant velocity in the region.

ACKNOWLEDGEMENTS

REFERENCES

[1] M. Sahimi, Flow and Transport in Porous Media and Fractured Rock, Newblock VCH, 1995.

[2] J. Bear, Dynamics of Fluids in Porous Media, Elsevier, 1972.

[3] G. Taylor, "Conditions under which dispersion of a solute in a stream of a solvent can be used to be measured molecular diffusion," *Royal society of London ,* 1957.

[4] K. P. a. C. Johnston, "A review of diffusion and dispersion in porous media," *AIME,* 1963.

[5] R. Aris, "On the dispersion of a solute in a fluid flowing through a tube," *The royal society of London,* vol. 235, no. 1200, 1956.

[6] I. z. a. I. K. G. Barenblatt, "basic concepts in the theory of seepage of homogeneous liquids in fissured rocks," *Journal of applied mathematics,* vol. 24, 1960.

[7] J. S. a. T. V. M. Cislerova, "Changes of steady stae infiltration rate in recurrent ponded infitration experiments," *Journal of hydrology,* 1990.

[8] K. J. a. J. F. K. Villholth, "Flow and transport processes in a macroporous subsurface-drained glacial till soil I:field investigations," *Journal of hydrology,* 1998.

[9] E. H. B. K. O. a. M. T. N. Larsson, "Progressive increase of the mutated mitochondrial DNA fraction in Kearns-Sayre syndrome," *Pediatr. Res.,* 1990.

[10] N. T. M. F. a. A. S. F. Leij, "Solute transport in dual-permeability porous media," *Water resources research,* 2012.

[11] P. R. a. J. D. W. Brigham, "Experiments on mixing during miscible displacement in porous media," *Society of petroleum engineering,* 1961.

[12] F. G. a. G. Gardner, "Measurements of transverse dispersion in granular media," *Journal of chemical engineering,* 1969.

[13] J. F. a. M. Combarnous, Dispersion in Porous Media. Advances in Hydroscience, NewYork: Academic press, 1971.

INVESTIGATION OF CO- AND COUNTER CURRENT FLOW BEHAVIOR IN CARBONATE ROCK CORES

Pouyan Ahmadi[1], Masoud Riazi[1], Mohammad Reza Malayeri[1]

[1]EOR Research Center, School of Chemical and Petroleum Engineering, Shiraz University, I.R. Iran

This paper is prepared for presentation at the International Symposium of the Society of Core Analysts held in Vienna, Austria, 27 August – 1 September 2017

ABSTRACT

Imbibition constitutes a key recovery mechanism in oil carbonate reservoirs – its manipulation can potentially improve oil recovery in water flooding as an Enhanced Oil Recovery (EOR) process. In this study, six carbonate cores were investigated with porosity and permeability of 18% and 32 mD, respectively. In each case, three types of faces in contact with brine were considered i) one open face (OOF) ii) two open faces (TOF) iii) one open face and another face isolated from brine with a special tube that allows collection of the co-current produced oil during the imbibition test (OOCO). These arrangements were used to investigate ionic solution effects on the amount of co- and counter-current produced oil and to evaluate the effect of currents on each other when the lateral surface of cores is coated and one or two faces are contacted with brine. The results showed that generally during Smart Sea Water (SSW) injection with respect to 5times diluted Sea Water Brine with distilled water (5dSW,) total recovery increased as more ions were activated in wettability alteration and IFT reduction. In OOF cores, oil recovery was also about 10% more than OOCO, perhaps due to elimination of co-current flow in OOF. The amount of oil recovery increased by 15% in SSW in TOF cases because of simultaneously co- and counter-current oil flow production at the two faces of the cores. For OOCO counter-current oil production was smaller than OOF and TOF cases at the other face, because the end face is isolated from brine which allows produced oil to go across it and accumulate in the tube. Overall, the oil production of the six cores in different types of brine were ranked as follows:
TOF-SSW > OOE-SSW > TOF-5dSW > OOF-5dSW = OOCO-SSW > OOCO-5dSW

INTRODUCTION

The world's oil reserves are overwhelmingly held in carbonate reservoirs - their recovery has been the subject of many investigations. This type of oil reservoir is characterized by two types of porous medium namely i) matrix blocks and ii) natural fractures. EOR methods for fractured reservoirs are usually designed to facilitate the transmission between matrix and fractures. One such method for enhanced oil recovery from carbonate reservoirs is low salinity water imbibition which is aimed at altering wettability from oil-wet to neutral or water-wet conditions. Should a block matrix be surrounded by water that exists in the fractures then two types of imbibition are expected to occur. 1) co-current and 2) counter-current imbibition. When water enters the carbonate block matrix, oil can be produced either in the same direction (co-current) or opposite direction (counter-current) (see Figures 1 and 2). The amount of oil production due to these

mechanisms would depend on block matrix length, oil/water viscosity ratio, type of ions that exist in the brine, crude oil chemistry, and reservoir pressure and temperature conditions.
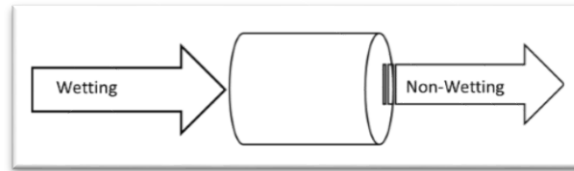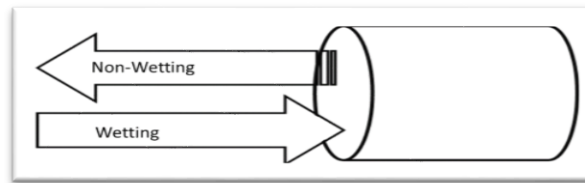

Figure 1: Co-current imbibition

Figure 2: Counter-current imbibition

Many factors such as wettability, viscosity [1], interfacial tension [2], oil composition, injection fluids properties are known to influence counter-current imbibition [3]. In addition, the interaction between fluid and porous media depends on pore shape, matrix permeability, relative permeability and boundary conditions, which would, in turn, determine the rate of imbibition and oil recovery [4]. At the beginning of the imbibition process, the counter-current imbibition always prevails. The oil/water mobility ratio determines how counter-current continues which, in turn, depends on wetting phase viscosity. If brine mobility is high, then the counter-current continues, otherwise it stops and instead co-current imbibition begins to produce oil [5]. The surfaces where oil is produced as droplets determine the capillary back pressure (CBP) at the open face. CBP was mentioned by Parsons and Chaney (1966), but it is usually ignored in co- and counter-imbibition [6]. During the imbibition process large oil droplets would usually stick to the open face of the core. In this process if the radius of curvature of oil droplets is much higher than pore radius, then they would only produce small back pressures. Snap off phenomenon could also happen for strongly water wet conditions near the faces that are in contact with the wetting phase, resulting in coalescence of large droplets on the outside of the core [7].

The present study investigates the ability of brine composition to increase the amount of counter-current and co-current produced oil, which feeds into the fractures and is expected to increase oil recovery.

EXPERIMENTAL SET UP AND PROCEDURE
In an imbibition process, two important parameters, interfacial tension and wettability, can be profoundly affected and controlled by the composition of the injecting fluid. Low salinity water and smart water (containing SO_4^{2-}, Ca^{2+} and Mg^{2+} ions) at the oil/brine and rock/brine interfaces, cause low interfacial tension and more water wetness, respectively. Accordingly, in the present investigation, 5-times diluted seawater and also seawater with manipulated sulfate, calcium and magnesium ions were used. 5-times diluted sea water showed to perform the best among dilution experiments and the IFT and contact angle are represented in figure 3. For ion concentration

manipulation EOR the one with 3 times sulfate, calcium and 6 times magnesium was the best and the results are shown in figure 4.
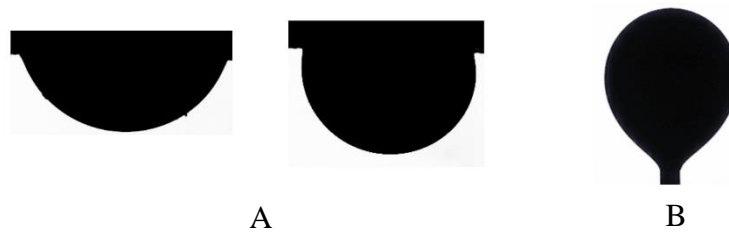

A   B

Figure 3: 5 diluted seawater A) change of contact angle in a calcite thin section (from 125 to 78) B) pendant drop IFT measurement (11.1 mN/m)

A   B

Figure4**:** SW-3S-C-6M A) change of contact angle in a calcite thin section (from 129 to 30) B) pendant drop IFT measurement (8.3 mN/m)

After determining the best wettability and IFT between diluted sea water samples and optimum salinity of seawater as smart seawater (SSW), their effects on the amount of produced oil during co-current and counter-current imbibition were investigated.

Core preparation
The outcrop block of a carbonate formation has been considered and many plugs were taken from it, thereafter among all cores, six cores with similar permeability and porosity selected. The carbonate cores' petrophysical properties are provided in Table 1.

Table 1: Petrophysical properties of investigated carbonate cores.

Brine-condition-core NO	Porosity %	Permeability (mD)	Length (mm)	Diameter (mm)
SSW- OOF-1	17.4	32	67	38.1
SSW-TOF-2	18.3	31	67	38.1
SSW-OOCO-3	19.0	33	67	38.1
5dSW-OOF-4	16.9	29	67	38.1
5dSW-TOF-5	17.9	32	67	38.1
5dSW-OOCO-6	18.0	30	67	38.1

As a first step, these cores were saturated with formation brine, then initially maintained for 14 days at 75°C to achieve original positive carbonate surface charge as it would exist at the reservoir conditions. Then oil flooding was started until the saturation of formation brine in cores reached to about 0.2 cc for which the fluid saturation is given in Table 2. Once this is done then the saturated cores were further maintained for 40 days at 2500 psi and 75°C. After the accomplishment of this aging process, the matured cores were categorized in two groups

1) 5dSW is mutual wetting phase imbibition brine and three cores were coated with tubes and epoxy resin as: i) first core-one open face (OOF) ii) second core-two open faces (TOF) iii) third core-one open face and another face isolated from brine with a special tube that would be able to collect the co-current produced oil during imbibition test (OOCO) as depicted in figure 5.
2) SSW is mutual wetting phase imbibition brine and three cores as: i) first core-one open face (OOF) ii) second core-two open faces (TOF) iii) third core-one open face and another face isolated from brine with a special tube that would be able to collect the co-current produced oil during imbibition test (OOCO) as depicted in figure 5.

Table 2: Fluid saturation volume

Core NO	pore volume (cc)	FW Volume (cc)	Oil Volume (cc)
1	13.28	2.6	10.68
2	13.97	2.7	11.27
3	14.50	2.9	11.60
4	12.90	2.6	10.30
5	13.66	2.7	10.96
6	13.74	2.8	10.94
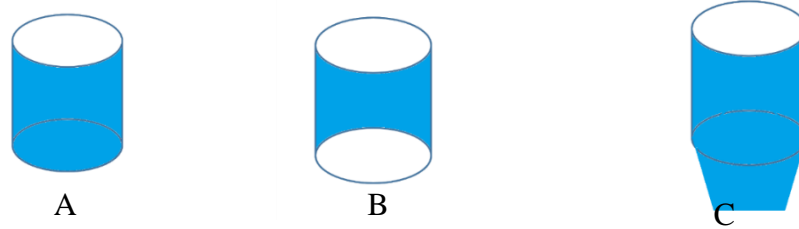
Figure 5: blue color shows the lateral surfaces and faces that coated with epoxy resin.
A) OOF   B) TOF   C) OOCO

Table 3: recovery factor during SSW and 5dSW imbibition.

%RF$_{(Brine)}$ Time (hrs.)	RF$_{(SSW- OOF-1)}$	RF$_{(SSW-TOF-2)}$	RF$_{(SSW-OOCO-3)}$	RF$_{(5dSW-OOF-4)}$	RF$_{(5dSW-TOF-5)}$	RF$_{(5dSW-OOCO-6)}$
4	14.98	22.18	7.76	5.48	9.12	2.91
12	18.73	24.84	9.48	8.23	16.42	4.85
48	21.54	29.28	12.07	11.88	26.46	6.80
72	25.28	32.83	12.93	14.63	23.72	8.74
96	29.03	37.27	14.66	14.63	27.37	8.74
120	29.03	38.15	14.66	14.63	27.37	8.74
144	29.03	38.15	14.66	14.63	27.37	8.74
168	29.03	38.15	14.66	14.63	27.37	8.74
192	29.03	38.15	14.66	14.63	27.37	8.74
216	29.03	38.15	14.66	14.63	27.37	8.74
240	29.03	38.15	14.66	14.63	27.37	8.74
264	29.03	38.15	14.66	14.63	27.37	8.74
288	29.03	38.15	14.66	14.63	27.37	8.74
312	29.03	38.15	14.66	14.63	27.37	8.74

RESULTS AND DISCUSSION

Two groups of cores were submerged in Amott cells. The cells were filled with the synthetic brines to the same level to eliminate gravity effects and were kept at a constant temperature of 75°C. Then, at specified time intervals, the amount of produced oil was recorded. Table3 presents the oil recovery versus time for SSW and 5dSW for co- and counter-current imbibition.

For all brines that were used in these experiments, viscosity was almost equal to distilled water due to the low level of total dissolved solids (TDS). Thus all resistances against entrance of the brines into the cores were in the oil phase, and all flow was due to capillary pressures. Due to optimum wettability alteration in SSW, capillary pressure is stronger than what was in 5dSW imbibition.

More oil recovery in TOF cores was due to the existence of co-current and counter-current imbibition at two faces simultaneously (Figures 6 and 7). By entrance prevention of brine from one face (OOF) co-current imbibition will be eliminated and hence oil will be produced by a

counter-current imbibition process. On the contrary, when the other face is allowed to co-currently produce oil (in a special condition without contact with brine) the amount of counter-current oil production will be reduced. The reason is that when co-current imbibition is allowed (OOCO) to the cores, then the amount of fluid resistance between oil and brine for co-current imbibition is lower than OOF (when only counter-current happened). This is because after a while of counter-current imbibition, the fluid front will be displaced thus i) fluid volumes that have to be replaced and displaced will be increased and ii) capillary pressure would not have enough force to imbibe the brine and eject the oil outside the cores at the same face.

Movement of an oil-water front in imbibition process is known to be piston like. Important factors with positive and negative impacts on oil productions are trapping of oil drops in the water invaded zone due to porous nature of the medium, interlayer friction, mixed wettability conditions which are categorized as factors that hinder the upward movement of oil drops and decrease oil production; however, bouancy force and capillary pressure are those which facilitate oil production.

One important issue is the competition between the oil interlayer frictions as an obstacle against the oil flow and capillary pressure as a booster in progress of imbibition process. As the process goes forth and the front descends in the core, interlayer friction increases because of a longer path ahead of the oil droplet than before while capillary pressure increases duo to more water wetness condition behind the front; however, increase in these two opposing factors is unequal and capillary pressure which imbibes the brine and ejects the oil out of the core seems not to be high enough
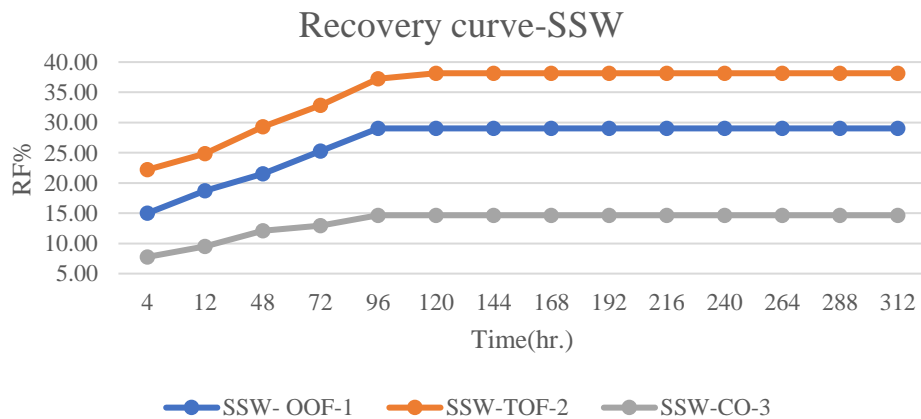
Recovery curve-SSW

Figure 6: Recovery curve of SSW-OOF-1, SSW-TOF-2, SSW-CO-3
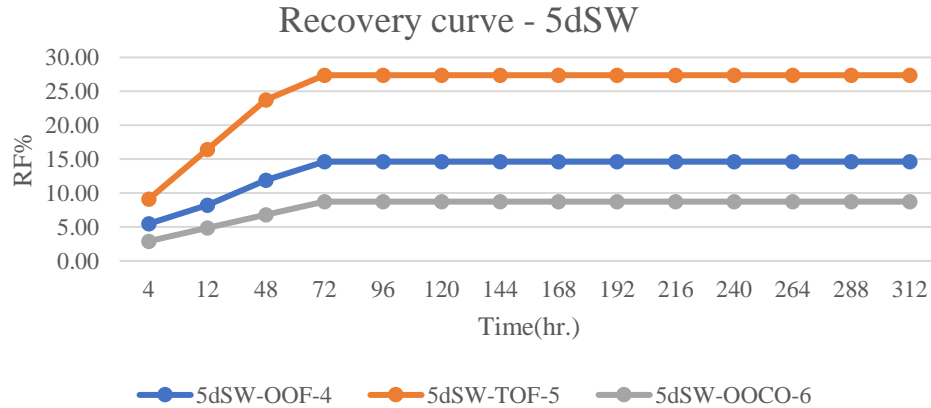
Figure7: Recovery curve of 5dSW-OOF-4, 5dSW-TOF-5, 5dSW-OOCO-6

CONCLUSIONS

- Generally speaking, for SSW with respect to 5dSW, the total recovery increased as optimum ions were used as a result of wettability alteration and IFT reduction.

- when lateral surface of cores is coated and
  i)One face is in contact with brine and the other face is isolated, only counter current will be happening. OOC
  ii)Two faces are in contact with brine, at two faces co-current and counter current will be happening. TOF
  iii)One open face is in contact with brine (Counter-current imbibition) and another face isolated from brine with a special tube that allows collection of the co-current produced oil during the imbibition test, co-current imbibition will weaken the counter current imbibition from the side that is in contact with brine. OOCO

- Wettability alteration to more water wetness increased capillary pressure and improved co- and counter-current imbibition processes.

- Fluids interlayer friction (Resistance against of flow) in competition with capillary pressure, determine whether co-current or counter-current imbibition or both will occur.

- Due to elimination of co-current flow in OOF, the amount of counter-current oil recovery increased but total production typically decreases.

- For OOCO though due to opening of one face without contact with brine, counter-current oil production was much lower at the open face.

- Based on the experimental findings, the oil production of the six cores in different types of brine can be ranked as follows:
  TOF-SSW > OOE-SSW > TOF-5dSW > OOF-5dSW = OOCO-SSW > OOCO-5dSW

ACKNOWLEDGEMENTS

REFERENCES

[1] Ma, S., X. Zhang, and N. R. Morrow. "Influence of fluid viscosity on mass transfer between rock matrix and fractures." *Journal of Canadian Petroleum Technology* 38.07 (1999).

[2] Ma, S. M., X. Zhang, and N. R. Morrow X Zhou "Characterization of wettability from spontaneous imbibition measurements." *Journal of Canadian Petroleum Technology* 38.13 (1999).

[3] Behbahani, H. S., Di Donato, G., & Blunt, M. J. Simulation of counter-current imbibition in water-wet fractured reservoirs. *Journal of Petroleum Science and Engineering*, *50*(1), 21-39. (2006).

[4] Mattax, Calvin C., and J. R. Kyte. "Imbibition oil recovery from fractured, water-drive reservoir." *Society of Petroleum Engineers Journal* 2.02 (1962).

[5] Bell, J.M., Cameron, F.K.: The flow of liquids through capillary spaces. *J. Phys. Chem*. 10, 658–674 (1906).

[6] Li, Y., Ruth, D., Mason, G., Morrow, N.R.: Pressures acting in counter-current spontaneous imbibition. *J.Petrol. Sci. Eng*. 52(1–4), 87–99 (2006).

[7] Å Haugen, MA Fernø, G Mason, NR Morrow "The effect of viscosity on relative permeabilities derived from spontaneous imbibition tests." *Transport in Porous Media* 106.2 (2015).

An integrated workflow for MICP integration, pore typing and saturation height modeling – Poster # 62

Philippe Rabiller (Rabiller Geo-Consulting)

This paper was prepared for a presentation at the International Symposium of the Society of Core Analysts held in Vienna, Austria, 27 August – 1 September 2017.

ABSTRACT

Improving the integration and interpretation of MICP with other petrophysical and geological data is crucial to increase the efficiency and the reliability of: pore typing, saturation-height modeling and evaluation of the cap-rocks efficiency. In this view, the workflow and the modular suite of processes, illustrated here, were specifically designed for a seamless integration of Capillary Pressure data with logs and core data. They were successfully field tested (> 4000 MICP) in varied geological settings. They drastically minimize the user bias because they do not impose any predefined interpretative model of MICP curves such as "Thomeer's hyperbola" or "Gaussian fitting functions" while allowing the integration of the results of such models.

A regular re-sampling of the saturation data as a function of the pressure is the first step of the processes. It is followed by an automated (and editable) conformance correction and detection of "features of interest" in the drainage pore throat size distribution (PSD) curves, e.g.: picking of the Katz & Thompson Threshold and Entry Pressure. The regular resampling allows displaying the data in the classic layouts and X-plots views, with other logs. It makes possible all the subsequent processes, particularly the varied permeability models and the use of clustering, data prediction and histogram up-scaling techniques. By means of the latter techniques, a PSD log, regularly sampled with depth, can be created over the entire logged intervals of cored and un-cored wells and the predicted PSD can be up-scaled from plug to log or bed scale. In the final steps, the saturation, at any depth increment above Free Water Level, is computed by simply reversing the method used to derive PSD from MICP saturation curves and using the Pc equating the buoyancy forces at this depth increment; other methods can be used as well.

INTRODUCTION

The workflow presented here was developed for a seamless integration of MICP data with logs and core data with the aim to simplify the tasks of geoscientists, by letting them visualize, along with all logs and core data, their MICP data and use them for saturation height modeling, evaluation of rock sealing efficiency and, in first place, for pore typing and facies characterization. Indeed, unless MICP data are visualized and integrated with all available information, the characterization of rocks in terms of the relationship between porosity, permeability and texture is incomplete and the subsequent inferences based on rock facies and properties, are lacking the accuracy so much needed. Thus, the workflow is designed so as to:

➢ Maximize the possibilities to save, process, visualize (on depth display and X-plot) and edit the MICP data together with logs and core data into a single "host" software.

➢ Integrate the varied methods published on MICP processing and benefit from all.
➢ Benefit of cluster analysis and data prediction techniques.
➢ Minimize the user bias and the need for expertise.

So far, this workflow has been used well over 4000 MICP samples, of varied vintage, in varied formations from varied basins. Given the format of this paper, only the most important and innovative functionalities applied to drainage curves are illustrated.

DESCRIPTION OF THE WORKFLOW

Figure 1 summarizes the workflow, described below.

Stage 1: Creating the Saturation Array Log.

Stage 1 is carried in single well mode. Labs format the MICP data as spreadsheets, where mercury saturation is listed by irregular steps of injection pressure. Those data may be of varied vintage and varied range of pressure with varied and irregular pressure increments. Their integration requires that, in a first step, they are collated, well by well, into spreadsheets, where the lines are ordered by increasing depth and the pressure and saturation values are listed in columns indexed in the order of the pressure increment. The first column must list the depth of each sample.

Presenting the MICP data into a standard format suitable for display (Figure 2) and process, in single or multi-well modes, is achieved by "binning" the Hg saturation values into an array log whose bins are regular intervals of the logarithm of Pc. By default, the array log is 240 bins and covers the 100,000 psi to 0.1 psi pressure range, i.e.: pore throat (PT) radius from 0.001092µm to 1092 µm. Bins with "missing" values are filled by linear interpolation and the saturation curve is smoothed by an adjustable sliding window. The possibility is offered to evaluate the effect of binning and smoothing. With the default options, this effect is negligible and independent of the Pore Throat Radius (PTR).

Stage 2: Conformance Correction and Picking of Entry Pressure

The surface effects are corrected in 2 steps. In a first step, the pressure at conformance is picked by an algorithmic analysis of the shape of the saturation and PSD curves, considered jointly. The conformance correction is kept sufficiently mild so as to optimize the algorithmic picking of the entry pressure, performed in the second step, along the criteria illustrated by Katz & Thompson [1]. The output of each step is comprised of 2 QC indexes flagging those samples which do not fit the predefined quality criteria of the picking, in which case the user may discard the sample(s) or graphically edit their correction, before applying the corrections to the whole set of data. Permeability is very sensitive to the largest pore throats of the PSD; thus, if conformance and entry pressure corrections are wanting, a poor match between the measured and modeled permeability should invite to re-examine the corrections applied and iterate this stage.

Stage 3: Analysis of the Shape of the PSD Curve.

The 3rd stage, is devoted to the detection of the "features of interest" in the shape of the PSD. The flowchart in Figure 1 shows that this stage is performed twice:
➢ On the original PSD and in single-well mode, during the "plug scale" stage,

➢ On the Predicted and Up-scaled PSD, in multi-well mode, before performing saturation height modeling.

The primary "features of interest" of the PSD curves, shown in track 4 of figure 2, are their local minima, maxima and inflexion points. They are picked by searching for the "zero crossing", of the 1st, 2nd and 3rd order piecewise derivatives. The number and position of such features help quantifying the complexity of the porous network.

There are 2 very important features, namely:
➢ the Katz & Thompson Threshold which is "*the inflection point of the [saturation] curve [..]at which the mercury first forms a cluster spanning the sample [as established] by continuously monitoring the electrical resistance across the sample and determining the pressure where electrical continuity is made*".
➢ the apex of the Thomeer's hyperbola which, as summarized by Pittman [2] is "*the position on the mercury injection curve that represents a continuous, well-interconnected pore system through the rock. [...Swanson] noted that at this point, "the mercury saturation expressed as percent of bulk volume is indicative of **that portion of the space effectively contributing to fluid flow**.*"

The second feature is picked by an algorithmic implementation of the trial solutions proposed by Katz & Thompson [1], Pittman [2], Walls & Amaefule [3] and Nokken & Hooton [4]. The track 9 of figure 2 illustrates the fact that the result of the trial solution for "maximal electrical conductance" corresponds exactly with the results of the picking of the other trial solutions. Not only this is a good indication that the tabulation technique is not distorting the data, but because the PSD and the "electrical maximal conductance" trial solution share the same array format, the latter trial solution simplifies the picking of the same feature on the Up-scaled PSD. This second feature is used to partition the PSD in 2 parts: the part which doesn't contribute to the permeability and the part which actually does contribute to permeability and hence to the production through permeability mechanism. This partition is a key element of a new version of the Purcell model.

Stage 4: Purcell-PSKT Permeability Modeling.
The 4th stage is devoted to the characterization, at plug scale, of the porosity/permeability relationships. To that purpose, the Purcell equation is implemented along 3 modalities:
➢ the first modality, is the classic form of the Purcell equation [5].
➢ In the second modality, the Purcell equation is applied to each term of the suite of the PTR subsets formed by incrementing the first subset by 1 element of the PSD: $PTR_{[a]}$, $PTR_{[a \to (a+1)]}$, $PTR_{[a \to (a+2)]}$, $PTR_{[a \to (a+3)]}$, ….., $PTR_{[a \to (n)]}$ Where "a" is the first (smallest radius) element of the PSD array log, with a significant value, and "n" is the last one (corresponding to "entry pressure").
➢ The third modality, termed "Purcell-PSKT" model, is similar to the second but the first term of the suite of PTR subsets is the PSD element which corresponds to the apex of the Thomeer's hyperbola. Thus, by taking into account only the PTR subset which actually contribute to the permeability the Purcell-PSKT model honors the results of Pittmann [2], Swanson [6], Katz & Thompson [1], Walls & Amaefule [3].

Not only the Purcell-PSKT model predicts the permeability better than the Purcell model proper [7], but most importantly, it allows generalizing to any complex porous network, the use of the FZI method, introduced by Amaefule and his co-workers [8], which postulates that the porosity is "effective" in terms of permeability. In this conceptual framework, the validity of the derivation of PHI_Z by the Purcell-PSKT model is verified by using the Darcy and Poiseuille equations in the way proposed by Amaefule for the FZI theory: if the Darcy and Poiseuille equations are honored then a straight line must appears when X-plotting FZI (X axis) versus the ratio r_{mh}/PHI_Z, where "r_{mh}" is the Mean Hydraulic Radius. Consequently, PHI_Z should be used, instead of total porosity PHI_T, in the equations proposed by Leverett [9] or Amaefule & al.[8] to predict S_w from P_c.

The 2nd part of the 4th stage, is devoted to porosity typing: the PSD and the distribution of the contribution of each PTR to the permeability are "binned" into array logs whose bins are regular increments of increasing porosity and are grouped into 5 editable classes defined by their PTR range of radius (µm), namely: Nano: $(r < 0.1)$, Micro: $(0.1 < r < 0.5)$, Meso: $(0.5 < r < 2)$, Macro: $(2 < r < 10)$ and Mega: $(r > 10)$. Two such array logs are created: one for PHI_T, the other for PHI_Z, as shown in tracks 8 & 9 of Figure 3; they ease the comparisons of MICP data with descriptions of core, fine scale core data and thin sections, other logs and borehole imagery logs which mostly respond to porosity.

Stage 5: Application of Up-Scaling, Clustering and Prediction Techniques
In the view of defining RRT, a 3 step approach is proposed, whose application to the evaluation of the sealing efficiency of rocks was previously illustrated [10; 11]. It is based on the use of:
➢ "Multi Resolution Graph Based Clustering" (MRGC) and "Coarse to Fine Self Organized Map Ordering" (CFSOM) [12; 13] for the grouping of MICP data into Reservoir Rock Types (RRT). The result of such clustering is illustrated by Figure 4.
➢ "k-Nearest Neighbor" (k-NN) modeling for prediction, of the PSD, RRT, permeability, PHI_Z and FZI. This method allows carrying simultaneously, the predictions of all those predict and testing both the validity of its results and the applicability of the prediction model [14]. By predicting the actual PSD, with the appropriate predictors, a PSD log regularly sampled with depth, is generated over the whole logged intervals, even in un-cored wells. The use of k-NN modeling in this field of work is reported, for example, by Theologou and his co-workers [15].
➢ Histogram Up-scaling method, [16] which is used in the following way to account for the heterogeneities between plug scale and log scale. Let's consider a depth increment "A" in the logged interval of a well; "A" being characterized by a set of log readings (its coordinates in the n-dimensional log space) and by a real or a predicted PSD. By means of the k-NN method, the "k" depth increments most similar to "A", i.e.: its "k" nearest neighbors in the log space, can be retrieved together with their PSD (real or predicted) and presented by order of increasing distance from "A" in the log space, i.e.: by decreasing similarity with "A". By optimizing a threshold on this distance it is possible to select the PSD of only those depth increments whose log readings are considered sufficiently similar to "A". The selected PSD may be similar and hence it

may be inferred that they belong to some facies homogeneous at log scale; if they differ significantly then the facies they belong to is heterogeneous; how much they differ is quantifiable. In both cases, a summation and volume weighted averaging allows up-scaling the selected PSD for they are scalar variables.

Eventually the stages 3 and 4 described above should be iterated on the up-scaled predicted PSD which is used in stage 6 as input for Saturation/Height Modeling.

Stage 6: Saturation Height modeling.

The figure 5 illustrates how Saturation Height Modeling is performed by reversing the method used to derive PSD and applying it onto the up-scaled PSD, regularly sampled with depth. The input required are:

➢   the density (constant or variable with field conditions), of hydrocarbon(s) and brine
➢   the Hc/brine IFT and contact angle (constant or variable with field conditions).

In a first step, for each depth increment of the entire logged interval, the array log of "Saturation vs Pc" is computed by piecewise integration of the up-scaled PSD. Then, ΔP_c developed by buoyancy forces at each depth increment is computed for any given position, or for a suite of regularly incremented positions, of the FWL. Finally, ΔP_c is used to scan and test the "Saturation vs Pc" array log so as to: retrieve the saturation, compute a dynamic permeability cut off, and estimate the volume of Hc which can be mobilized by permeability mechanism [7]. The superimposition of a Pc_{field} scale onto the PSD, permeability and saturation arrays logs in the graphic display of the output relies on the Pc/radius equivalence, for any couple of fluids whose IFT and contact angle are specified for lab and field conditions.

CONCLUSIONS.

The figures illustrating the workflow evidence the feasibility to load and format the MICP data, process them and display all the results in the conventional Depth and X-plot views of the petrophysical software commercially available. A seamless integration of MICP with other logs and core data and the use of clustering and prediction techniques are thus made possible.

The implementation of the trial solutions proposed by Katz & Thompson, Pittmann, Walls & Amaefule provides an accurate estimation of the porosity (PHI_Z) effectively contributing to the permeability, either from actual PSD or from the up-scaled PSD.

The new "Purcell-PSKT" model, specifically designed to combine the results of Katz & Thompson, Pittman, Walls & Amaefule with the Purcell equation, provides a better prediction of permeability than the Purcell model proper; thus, it gives a greater confidence in the picking of the "entry pressure". The Purcell-PSKT model allows the generalization of the FZI method to a complex porous network and the validity of its derivation of PHI_Z is corroborated by the same techniques proposed for the FZI method. By using PHI_Z instead of PHI_T, the Leverett and FZI theories should prove more effective to predict S_w as a function of Pc.

Saturation height modeling is greatly simplified by simply reversing the method used to derive PSD from the MICP saturation curves.

REFERENCES

1. Katz, A.J., A.H.,Thompson : "Prediction of Rock Electrical Conductivity from Mercury Injection Measurements"; Journal of Geophysical Research, Jan. 1987, Vol. 92, No.B1, 599-607.
2. Pittman, E.D. : "Relationship of Porosity and Permeability to Various Parameters Derived from Mercury Injection Capillary Pressure Curves for Sandstone," AAPG Bull., 1992, vol. 76, No. 2; 191-198.
3. Walls, J.D. & J.O., Amaefule : "Capillary Pressure and Permeability Relationships in Tight Gas Sands," ; 1985; paper SPE 13879.
4. Nokken M. R. & R. D. Hooton: "Using Pore Parameters to Estimate Permeability or Conductivity of Concrete"; Materials and Structures; 2006; DOI 10.1617/s11527-006-9212-y.
5. Purcell, W.R.: "Capillary Pressures-Their Measurement Using Mercury and the Calculation of Permeability"; 1949, Trans. AIME, 186, 39-48.
6. Swanson, B. F.; "A simple correlation between permeabilities and mercury capillary pressures"; 1981; Journal of Petroleum Technology, Dec., p. 2488-2504.
7. Rabiller, Ph.; "Combining porosimetry and Purcell permeability modeling to calibrate FZI and define a dynamic permeability cut off. Poster#26"; 2017; International Symposium of the Society of Core Analysts.
8. Amaefule J. O.; M. Altunbay M., D. Tiab; D. G. Kersey; D. K. Keelan, "Enhanced Reservoir Description: Using Core and Log Data to Identify Hydraulic (Flow) Units and Predict Permeability in Uncored Intervals/Wells"; 1993; paper SPE 26436.
9. Leverett M. C.; "Capillary Behavior in Porous Solids"; 1941; Transactions Of The American Institute Of Mining And Metallurgical Engineers; Volume 142; 152-168.
10. David Z. Tang, Ph. Rabiller, A. Bakhiet, G. Gregory, P. Lawrence, A. Samsudin, W. Tan; "Well-log Electrofacies Prediction of Middle and Upper Jurassic Carbonates, Saudi Arabia: A Case Study for Exploration Applications"; 2012; Geoarabia.
11. Rabiller, Ph.; "Integration of MICP Data with Logs, as a Means to Improve Reservoir and Seal Characterization"; 2017; Search and Discovery Article #42013.
12. YE, S-J., Ph. Rabiller; "A New Tool for Electro-Facies Analysis: Multi-Resolution Graph-Based Clustering"; 2000; SPWLA 41st annual symposium; paper PP; 1-14
13. YE, S.J. & Ph. Rabiller; "Automated facies Ordering"; 2005; Petrophysics; Vol. 46, n° 6; 409-423
14. Rabiller, Ph. ; P. Boles; N.H. Dewhirst; : "Facimage™ Modeling as a Substitute for Gas Content from Core Desorption and for Real Time Facies Analysis."; 2013; URTeC symposium (Denver); ID: 1580723
15. Theologou, P.; M. Skalisnski; R.K., Mallan; "An MICP based Pore typing workflow-Core scale to log scale" , paper L ; 2015; SPWLA, 56th Annual Symposium.
16. Rabiller, Ph.; J.P., Leduc; S.J., YE : "The iterative use of clustering and modeling to improve permeability prediction."; 2001; SPWLA 42nd annual symposium; paper E.
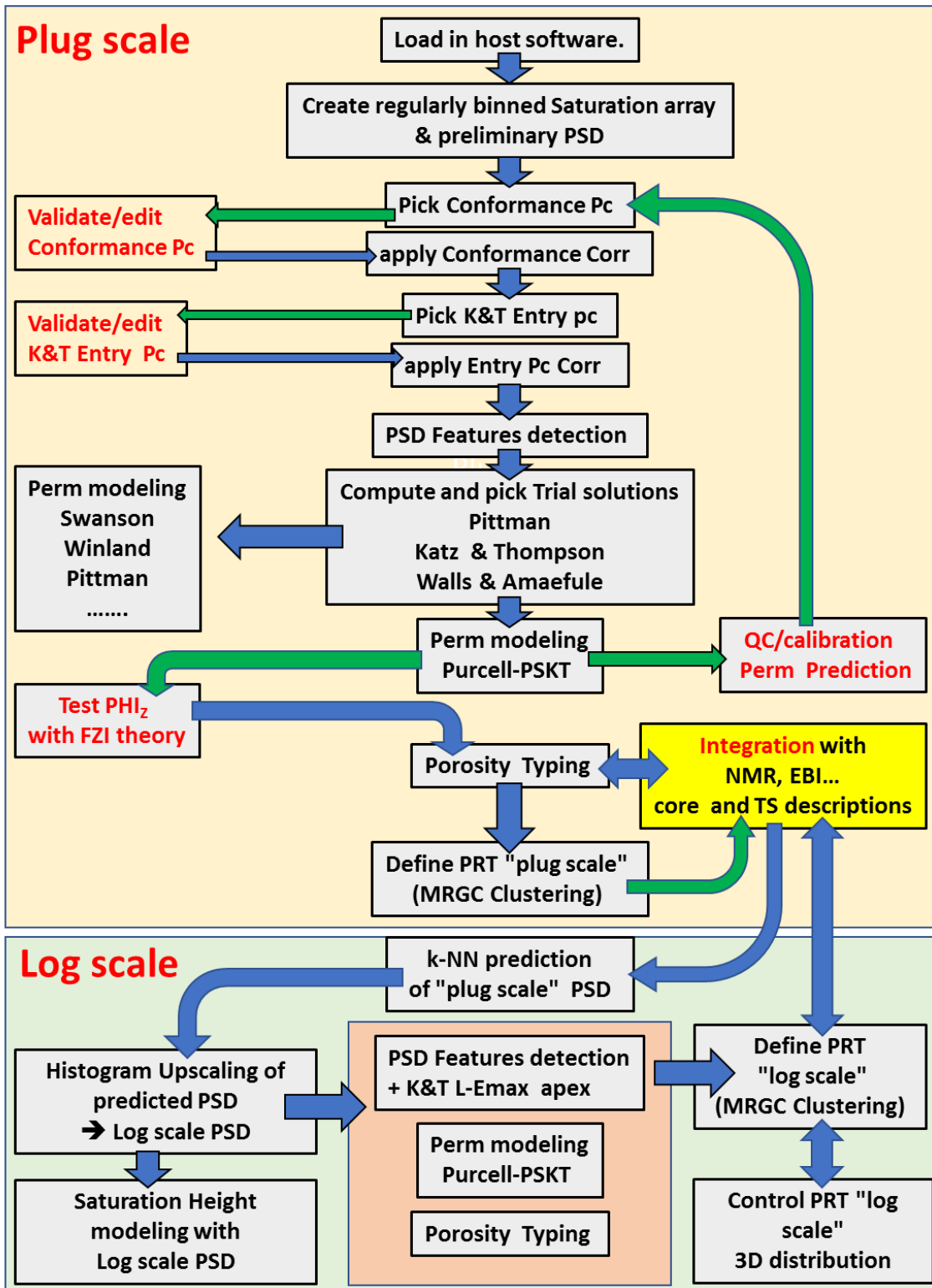
Figure 1 : Diagram of the workflow.
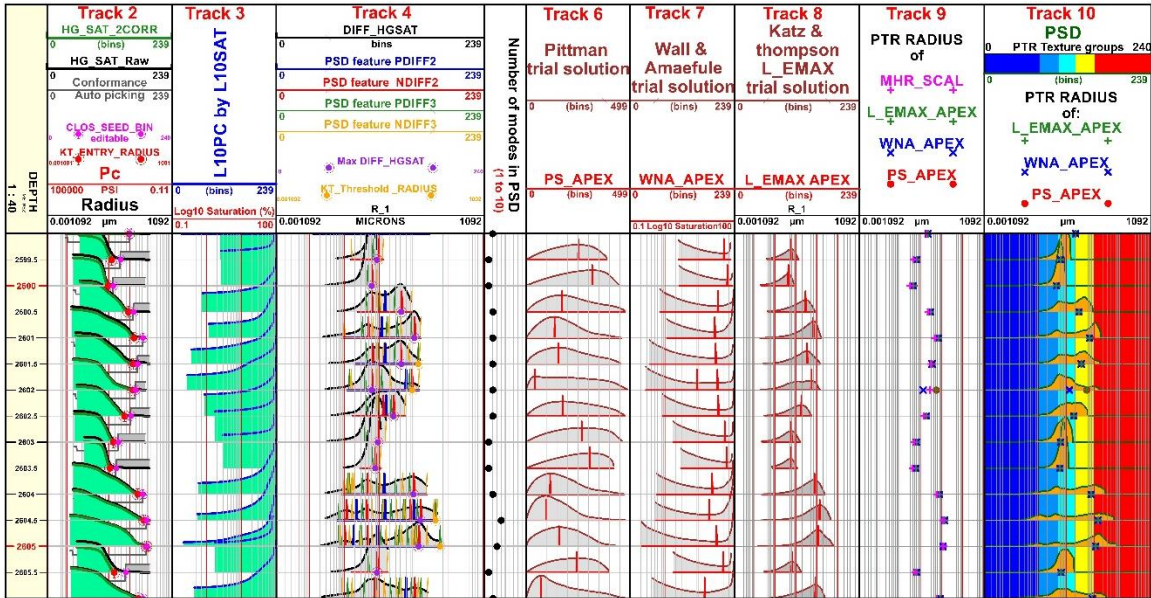
Figure 2 : The 2nd and 3rd tracks show the saturation displayed into a standard format suitable for any process. Conformance Correction and Picking of Entry Pressure are shown on 2nd track. The detection of the "features of interest" in the structure of the MICP data and the result of trial solutions are shown, respectively, in tracks 4, 6, 7, 8, 9.
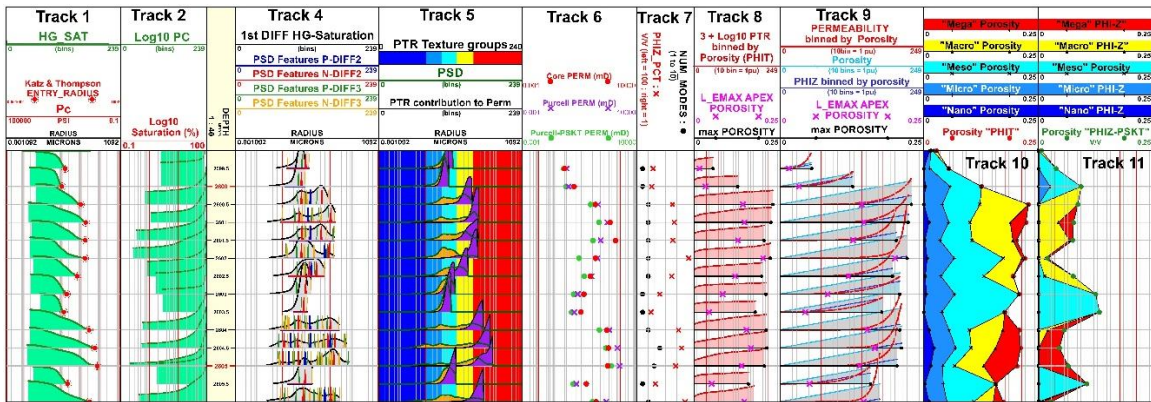
Figure 3: Track 5 shows the "contribution of PTR to permeability" superimposed to PSD, thus illustrating the fact that only largest PTR classes contribute to permeability. Core permeability and the results of permeability modeling are shown on track 6. The complexity of the porous network is illustrated by the PSD features (track 4), the number of modes and the ratio PHI_Z/PHI_T (track 7). On tracks 9 to 11, the PSD and contribution of PTR to permeability are "binned" by porosity and thus the contribution of each PTR groups to porosity (either PHI_T : track 10 or PHI_Z : track 11) is graphically illustrated for easier comparisons with descriptions of thin sections.
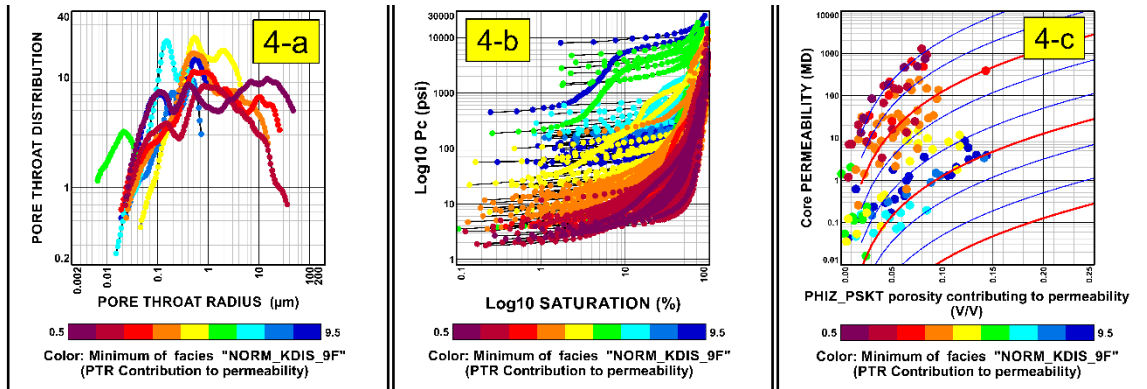
Figures 4a to c illustrate the application of MRGC clustering to MICP data and more specifically to "PTR contribution to permeability" which provides the most interesting classification in terms of pressure (Height) vs Saturation (4b) because it is PHI$_Z$, which controls the flow. X-plot 4a displays only the "kernel" of each facies. Clustering PSD provides insights on porous network texture, however PSD "facies" are less significant in terms of dynamic flow properties for flow is not controlled by PHI$_T$. The X-axis of the FZI plot (4c) is PHI$_Z$, note the good fit between facies and FZI curves.
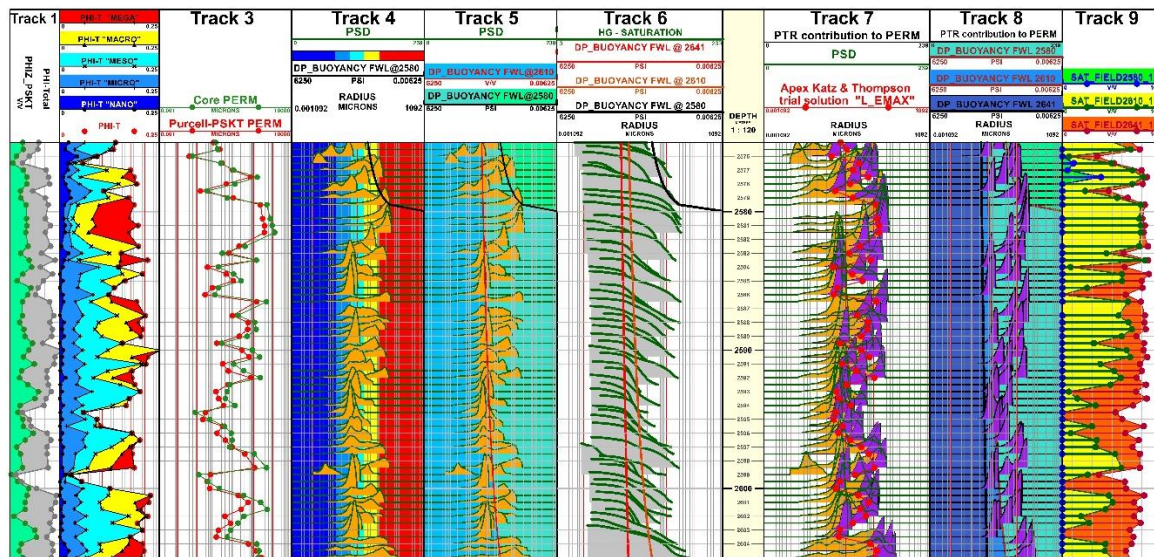
Figure 5: Saturation Height modeling. The rightmost track displays the saturation for 3 positions of the FWL. The saturation is obtained by equating the buoyancy force and the capillary pressure. Because saturation is sampled as a function of Pc, retrieving saturation for any position of FWL is made simple and accurate. The tracks 8 & 9 illustrate the fact that the most important reservoir characteristic is the distribution of the pore volume accessible by those pore throats which actually control the permeability. The tracks 4 & 5 & 8 illustrate the fact that a "static" description of pore network "texture" (track 4) is insufficient to explain fluid storage and flow, hence the importance of partitioning them by the PTR corresponding to Δp buoyancy (track 5).

THE USE OF PARAMAGNETIC DOPANTS IN OPTIMISING THE ACCURACY OF CRITICAL AND RESIDUAL OIL SATURATION DETERMINATION

Phil Mitchell, Lukasz Gromala and Mahmood Siddiqui

Engineering and Technology Services, Saudi Arabia

This paper was prepared for presentation at the International Symposium of the Society of Core Analysts held in Vienna, Austria, 27 August – 1 September, 2017.

ABSTRACT

The use of paramagnetic dopants to alter the relaxation characteristics of reservoir fluids is well established in downhole procedures such as the log-inject-log method for determining remaining oil saturation with NMR (Nuclear magnetic resonance) logging tools.

However, in the laboratory under controlled conditions much of the effort expended in recent decades has been research to reduce uncertainty in surface relaxivity with the goal of determining fluid saturations in oil zones as well as estimates of permeability from logging tools.

Benchtop spectrometers are now affordable and are rapidly becoming a standard tool in most SCAL (Special core analysis) laboratories for numerous purposes including basic characterisation as well as rapid capillary pressure determination (in conjunction with centrifuge) among others.   There is however, relatively little published work on the use of paramagnetic dopants to improve the practical determination of water and oil saturation – whose NMR T_2 profiles in reservoir rocks typically overlap – as a tool to optimise end-point saturations for advanced studies by centrifuge or relative permeability waterflood studies.

This paper offers some practical insights into how NMR T_2 (spin-spin relaxation time) profiles determined using paramagnetic dopants with judicious care to separate oil and water signal can not only provide important quality assurance but even become the definitive measure of saturation at crucial points in the saturation range during displacement studies. This is particularly true if detecting small changes in saturation is an experimental objective. Comparisons with established methods such as Dean-Stark and retort extraction are also presented to demonstrate the underused potential of NMR spectrometers as a practical laboratory tool for fluid saturation determination.

INTRODUCTION

The accurate determination of residual oil saturation after some displacement experiment is a continuous challenge in the SCAL laboratory. Increasingly in recent times redundancy in the form of an independent cross-check of this parameter is mandated by clients as part of a rigorous quality control procedure. A non-destructive method to confirm final oil saturation is clearly preferable in this regard. The use of laboratory NMR spectrometers has yet to acquire a routine status in SCAL laboratories despite decades of research aimed at distinguishing between oil and water during NMR relaxation experiments both in the laboratory [1] and in operational environments [2].

In the case studies discussed in this paper, we chose to use Manganese as a paramagnetic dopant to separate the oil and water in the measure T_2 distributions, which was added to the aqueous phase in the form of $MnCl_2$.

This paper focuses on two case studies, both carbonate core samples originating from Middle-East hydrocarbon producing formations, with somewhat differing objectives but in each case accurate final oil saturation being required to achieve the ultimate goal.

Case 1 – Residual Oil Zone (Between current and original gas-oil contact)

Samples were cut and preserved at rigsite from core drilled with low-invasion technology from a depth zone believed to capture the original and current gas-oil contact in a field which has been under production for around a decade. The objective was to preserve samples and transfer them to the laboratory to enable determination of residual oil saturation in this zone to aid in recovery estimates from a gas cap expansion mechanism.

Case 2 – Critical Oil Saturation (In oil-water transition zone)

A set of samples were taken and preserved at original oil saturation at rigsite in similar fashion to Case 1 with the objective of establishing critical oil saturation in the well – the threshold point in the oil-water transition zone where the oil first becomes mobile when moving from the water zone to the hydrocarbon zone. The final oil saturation was compared with the value determined by direct extraction (by retort) for quality assurance purposes.

EXPERIMENTAL PROCEDURES

NMR T_2 (transverse relaxation) decay measurements were made using an Oxford Instruments Maran Ultra spectrometer with 75mm probe operating at 35 ^{o}C and 2.2 MHz frequency. The typical CPMG (Carr-Purcell-Meiboom-Gill) sequence was used with an inter-echo spacing 0.4ms, 1024 echos and sufficient scans to attain a SNR (Signal to noise ratio) of at least 50. All samples were either soaked or flushed in brine solutions containing $MnCl_2$. The system response with increasing dopant levels was investigated in order to achieve an optimal level of dopant to attain the study objectives. A typical carbonate sample showing the transformation of the T_2 distribution as a function of increasing dopant levels in the 100% water saturated state is given in Figure 1. The same sample was then flushed to high initial oil saturation prior to being flooded to residual oil. The sample was then flushed with increasing strength of dopant (without mobilising oil) to show the resulting transformation of the brine T_2 distribution in the presence of a constant remaining oil saturation. The result is displayed in Figure 2.

Case 1 – Residual Oil Zone (Between current and original gas-oil contact)

A total of eight samples were selected for study originating from the depth range in the well covering the interval between the original and current gas-oil contact and a short distance into the oil zone. The current gas-oil contact in the well was independently qualitatively determined from log data. The selected samples were pressure-saturated with undoped brine to remove any air. This provided a base T_2 distribution to measure total porosity. The samples were then submerged in a concentrated solution of manganese chloride and the T_2 distribution measured again after several hours of soaking and then after a period of two days to observe the transient effect of the dopant. The samples were then subjected to Dean-Stark extraction [3] to compare residual oil determination by the two methods.

Case 2 – Critical Oil Saturation (In oil-water transition zone)
The transition zone samples had T_2 distributions measured in the "as-received" state. They were then immersed in concentrated manganese chloride solution and the T_2 distribution re-measured. Finally, they were flushed to produce any recoverable oil with a weaker solution (2g/l) of manganese chloride in order to retain signal in the aqueous phase and therefore derive total porosity as well as the saturations of the two aqueous and oleic phases present. The samples were then extracted by the retort method [3] as an independent quality assurance procedure to confirm final residual oil saturation.

RESULTS AND DISCUSSION

Case 1 – Residual Oil Zone (Between current and original gas-oil contact)
Table 1 shows residual oil saturation calculated from both the NMR data and by Dean-Stark extraction. Figure 3 shows a typical NMR response (Sample 3) before and after soaking in 1M Manganese-doped brine solution. The NMR-derived residual oil saturation was calculated by taking the ratio of the area under the peak associated with residual oil (above 10 ms relaxation time). The agreement between Dean-Stark-derived saturation and NMR is generally good and the position of the current gas-oil contact is unequivocal and independently qualitatively confirmed by wireline data.

Case 2 – Critical Oil Saturation (In oil-water transition zone)
A summary of the results for this zone is given in Table 2. The objective in this zone was to determine oil saturation before and after flushing. The initial oil saturations were derived from the 100g/l doped case and the final oil saturations from the 2g/l doped experiment. The latter also yielded total porosity. The native-state experiment was not used quantitatively in the calculations but serves to illustrate that prior to doping, the two phases cannot be distinguished in the measured T_2 distribution. The distributions after flushing yield bimodal distributions, with the shorter relaxation time mode (water) invariably larger than the peak at higher relaxation times (oil) since after flushing the samples are at residual oil saturation. Examples plots are given in Figures 4 & 5 showing the shallowest and deepest samples tested.

A plot of initial versus final oil saturation for the whole population in this zone is given in Figure 6. All samples exhibited some mobilisation of oil except the deepest sample whose initial oil saturation was low and evidently below the critical value. The linear extrapolation (black dotted line) on the plot gives a pessimistic indication of critical oil saturation since the true relation is essentially asymptotic to the equivalence (solid) line. The extrapolated value of 0.057 is only a little higher than the sole sub-critical example in the population (0.044) so the critical saturation clearly lies in a very narrow range somewhere in the region of 0.05. The NMR determinations were intended to be as accurate as possible in order to

detect small changes in saturation before and after flushing. Quality assurance of these data is similarly demanding so consideration was given as to whether retort or Dean-Stark final extraction would be the more accurate for this purpose. Accordingly, we subjected a significant population of samples spanning water volumes between around 0.5 ml to 4ml. The volume of water within the samples was known very accurately because they were artificially prepared with gravimetric determination of the added water to an accuracy of 0.01g. A comparison plot is given in Figure 7 with an equivalence line demonstrating the considerably better performance of the retort method, at least in our laboratory. Systematic water loss resulting in underestimation of water saturation is a perennial cause for concern in the Dean-Stark extraction method, especially for low water volumes as is demonstrated in the comparison plot.

CONCLUSIONS

1. The method described in this paper provides an important quality assurance procedure for final saturation confirmation for a variety of SCAL procedures.

2. The procedure is non-destructive and therefore minimises or eliminates potential conflicts with other testing objectives.

3. The method can be tuned to very high accuracy if required to detect small changes in fluid saturation or when small or low porosity samples are being tested.

REFERENCES

1. Horkowitz J., Hartman D.E, Clerke E.A, Coates G.R. "Residual oil saturation measurements in carbonates with pulsed NMR logs", (**1998**).

2. Dunn K.-J, Bergman D.J, LaTorraca G.A.: "Nuclear Magnetic Resonance: Petrophysical and Logging Applications", Handbook of Geophysical Exploration, Seismic Exploration, Volume 32, (2002).

3. API Recommended Practice 40, "Recommended Practices for Core Analysis, Second Edition", *American Petroleum Institute*, 1220 L Street, N.W., Washington, D.C.20005, (**1998**).
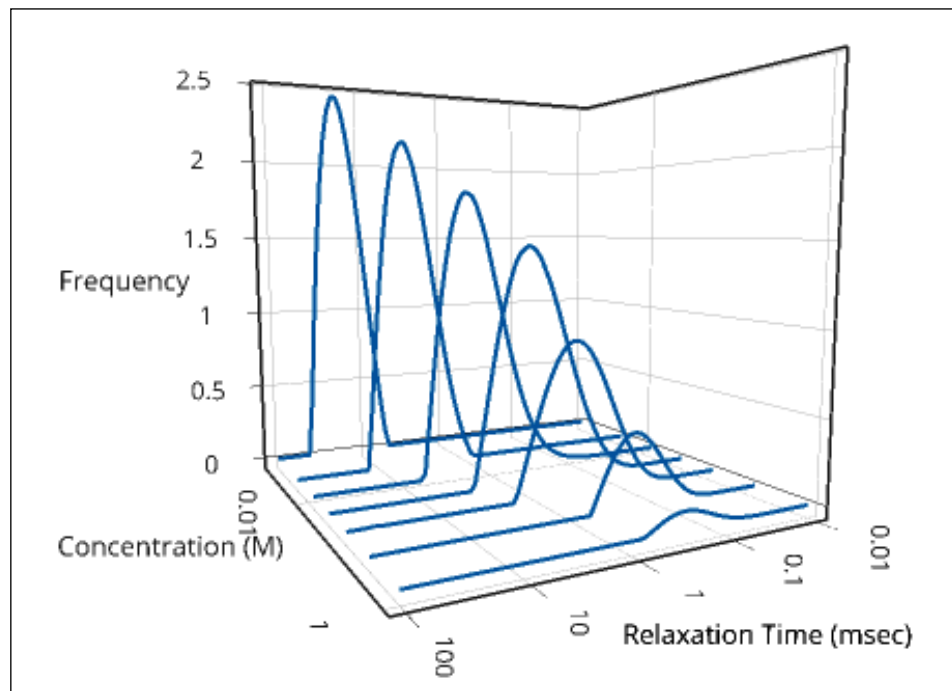
Figure 1 - Effect of increasing Mn^{2+} dopant concentration on NMR T_2 distribution

.
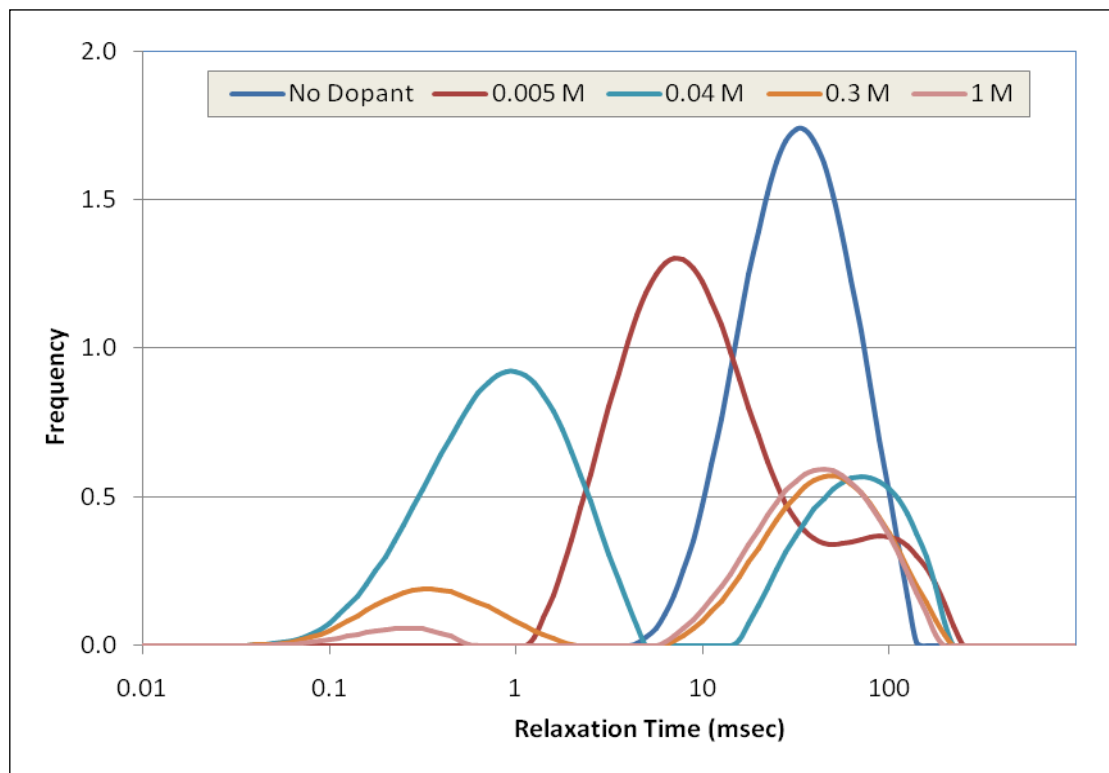
Figure 2 – Separation of brine and oil peaks (oil peak around 30 msec) with increasing Mn^{2+} dopant concentration

Table 1 - Residual Oil Saturation Comparison between NMR and Dean-Stark

Sample	NMR Porosity	NMR Sor	D&S Sor	Zone
	frac	frac	frac	
1	0.223	0.105	0.118	Residual Oil
2	0.195	0.215	0.256	Residual Oil
3	0.235	0.326	0.377	Residual Oil
4	0.173	0.310	0.328	Residual Oil
5	0.217	0.412	0.446	Oil Zone
6	0.172	0.551	0.546	Oil Zone
7	0.229	0.512	0.573	Oil Zone
8	0.214	0.637	0.580	Oil Zone
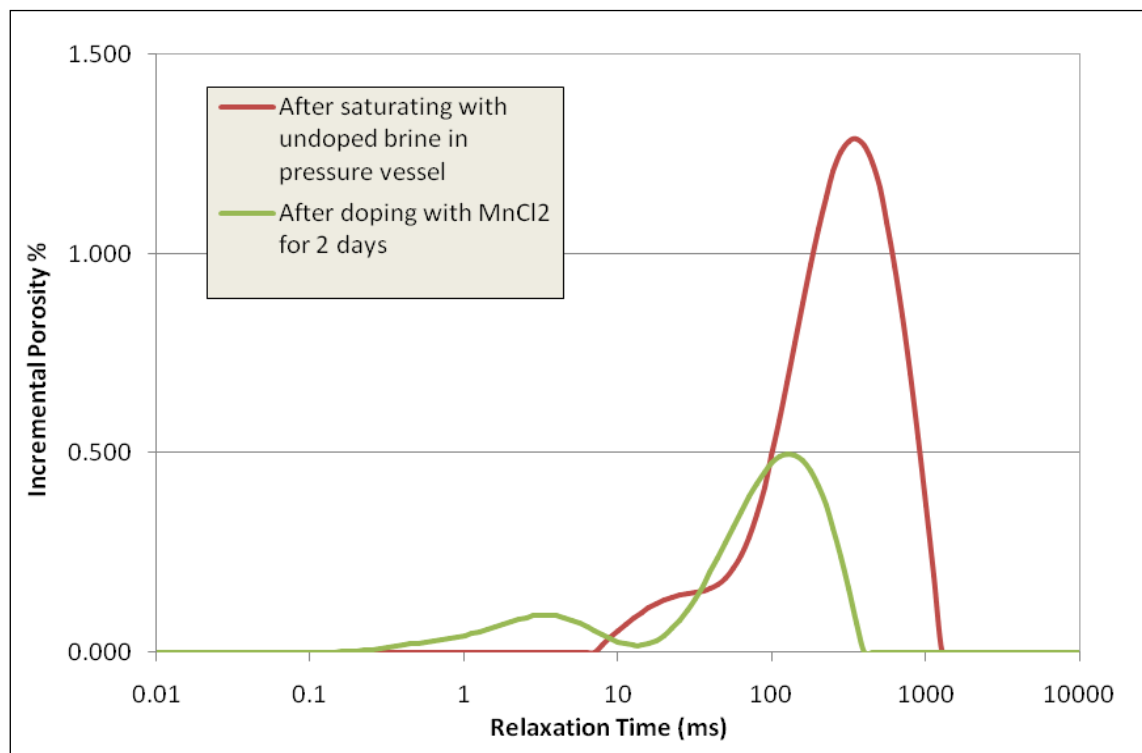
Figure 3 - NMR T_2 distribution in sample 3 before and after Mn^{2+} doping

Table 2 – NMR T2 Data Summary (Transition Zone)

Sample	Depth	NMR Porosity	NMR Soi	NMR Sor	D&S Sor
	D. ft	frac	frac	frac	frac
128	4992.45	0.237	0.542	0.246	0.238
134	4995.55	0.223	0.450	0.256	0.244
140	4998.55	0.256	0.407	0.203	0.176
146	5001.45	0.225	0.477	0.175	0.177
152	5004.25	0.228	0.471	0.239	0.249
158	5007.55	0.212	0.430	0.237	0.225
164	5010.65	0.212	0.480	0.255	0.261
170	5013.65	0.229	0.436	0.216	0.218
176	5016.55	0.215	0.355	0.220	0.226
182	5019.55	0.220	0.520	0.213	frac
188	5022.55	0.189	0.296	0.234	0.228
194	5025.65	0.231	0.375	0.255	0.263
200	5028.55	0.233	0.344	0.214	frac
212	5034.55	0.232	0.366	0.214	0.223
218	5037.45	0.239	0.320	0.222	0.222
224	5040.45	0.236	0.397	0.212	0.217
230	5043.55	0.258	0.415	0.216	0.218
236	5046.45	0.210	0.173	0.138	0.137
248	5052.65	0.218	0.297	0.222	frac
254	5055.65	0.217	0.250	0.188	0.194
260	5058.55	0.250	0.225	0.187	frac
272	5064.55	0.215	0.210	0.152	0.150
278	5067.55	0.209	0.044	0.041	0.049
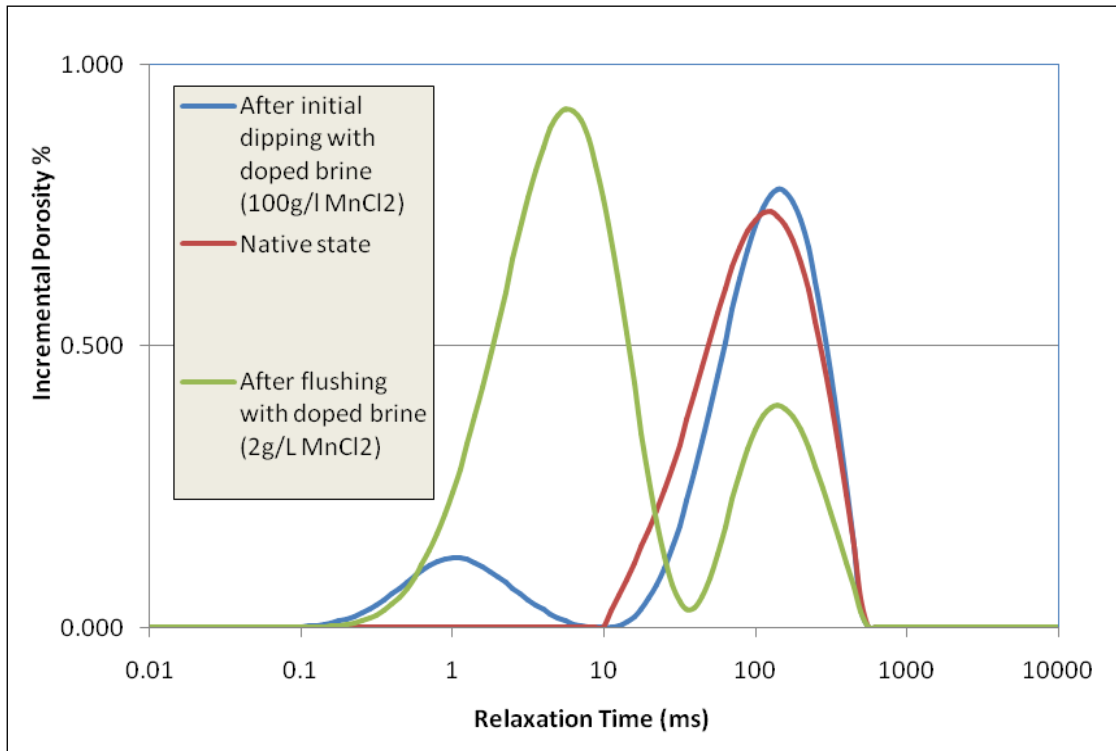
Figure 4 - Top of the oil zone before and after flushing with Mn^{2+} doped brine
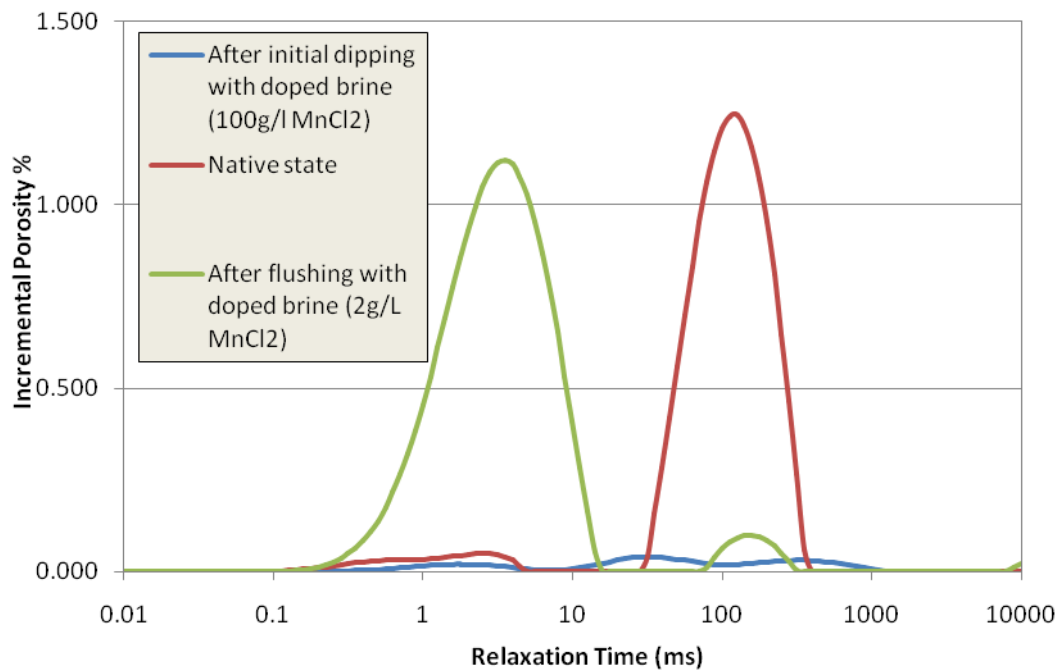
Figure 5 - Base of the transition zone before and after flushing with Mn^{2+} doped brine
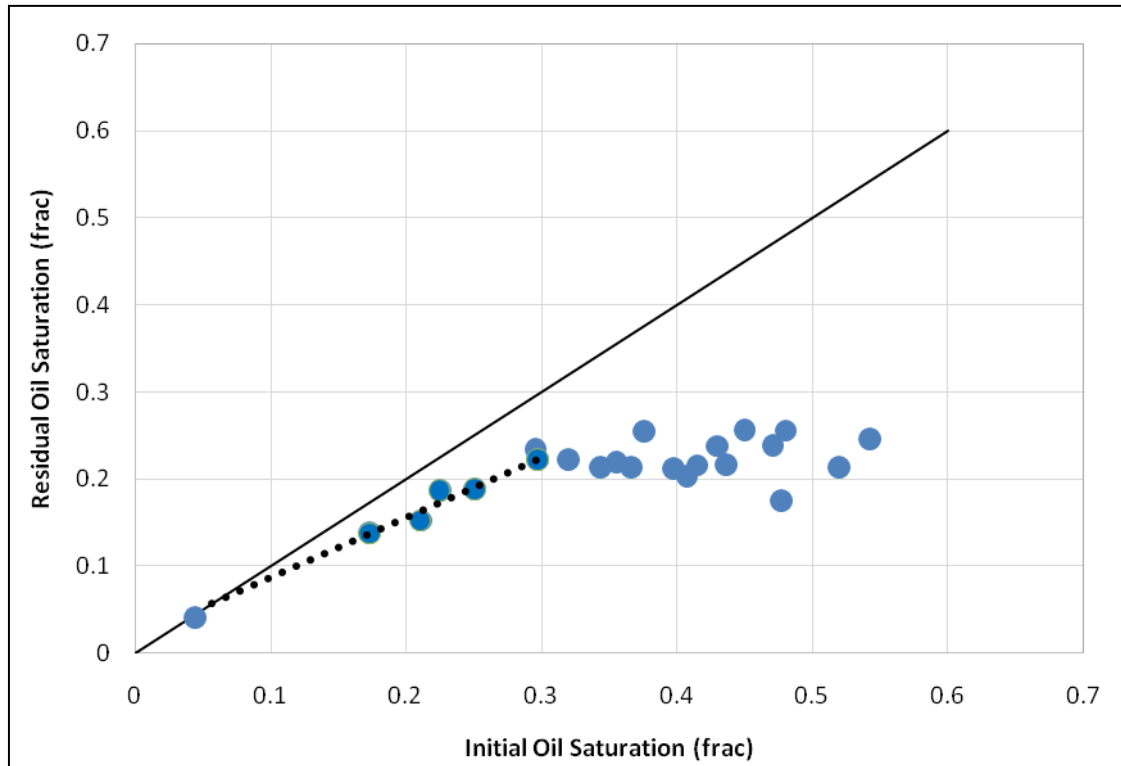
Figure 6 - Initial versus Residual Oil Saturation in Transition Zone
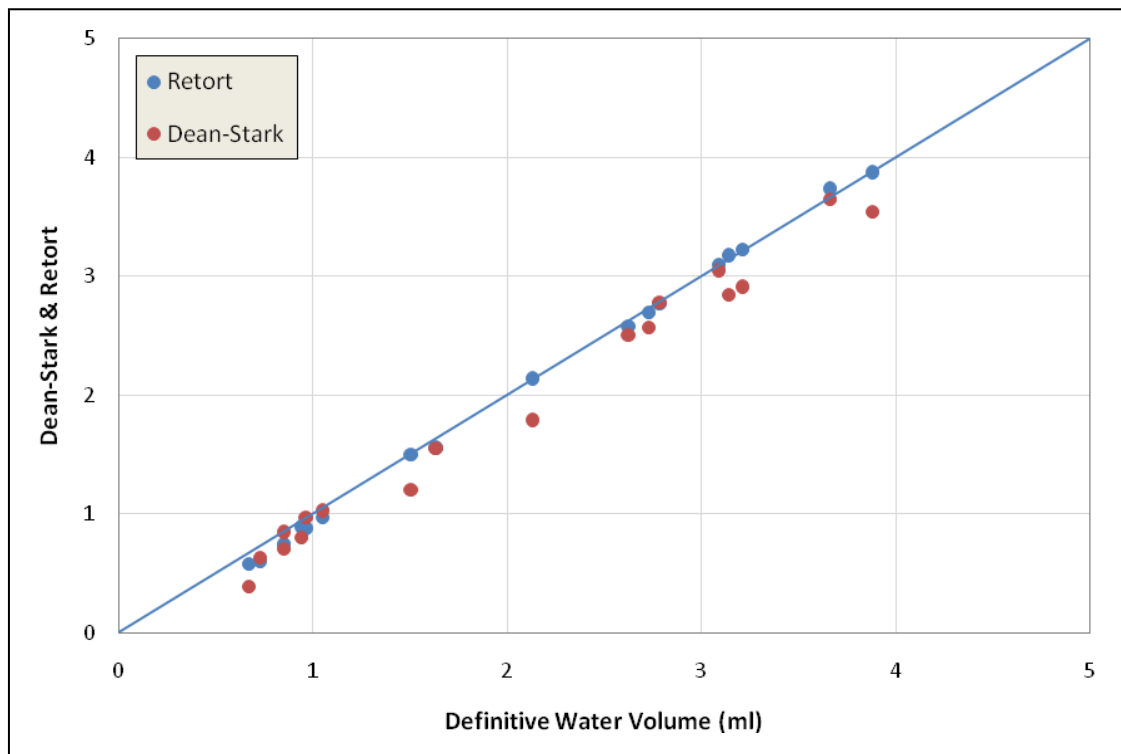
Figure 7 - Comparison between Dean-Stark and Retort water extractions

REVISITING NMR CORE-LOG CALIBRATION

Wim Looyestijn, Xiangmin Zhang, Albert Hebing

PanTerra Geoconsultants B.V., The Netherlands

ABSTRACT

Historically, NMR (nuclear magnetic resonance) measurements are used to partition the water-filled pore space into bound water and free fluid. In practice, however, this is a gross oversimplification of reality. The T2-cutoff that is used in this process is calibrated by comparing fully saturated and desaturated plug samples. Since the desaturation is done at one particular capillary pressure, the result is strictly speaking valid for that pressure only, i.e. at just one height in the reservoir. Repeating the calibration at various desaturation pressures is impractical.

We show, with practical examples, how this fundamental shortcoming can be overcome. First, we compare NMR data with MICP capcurves, and show that conversion of NMR data into capcurves for a given lithological unit can reliably done with one set of fixed parameters. Second, we show that having one calibration point, the NMR response at any other desaturation pressure can be simulated faithfully. This enables the construction of a height-dependent T2-cutoff, yielding the correct connate water saturation at any desired height.

The benefit of this approach is that NMR logs can be interpreted independent of other logs, and thus provide verification of the, often complicated, resistivity interpretation. The concepts of the methods are not new, but consistent and practical workflows are still lacking. We demonstrate our workflow/methods for a sandstone reservoir, and validate the result against standard log analysis data.

INTRODUCTION

Traditionally, the T2-distribution, measured by NMR on a water-saturated sample, is divided into two parts: the (total) bound water, TBW, and the free fluid index, FFI. The split is made at a certain T2 value, called the TBW cutoff, or FFI cutoff, or T2-cutoff. In connection with NMR logs, we prefer the name TBW cutoff, because TBW can be computed in most cases, whereas FFI might be affected by the presence of hydrocarbons and/or acquisition parameter settings.

The concept of TBW/FFI is a simplification because what is "bound" water depends on the capillary pressure, i.e. on the height above FWL. The optimal procedure is to calibrate the cutoff against saturations obtained at a representative pressure in the reservoir. In reality,

this is not always feasible, but errors may occur if this is not realised. Repeating the calibration at various desaturation pressures is possible, but impractical and is rarely done. Fortunately, two corrective approaches are available: (i) convert the NMR response to a (pseudo) cap curve, and (ii) adjust the T2-distribution to the required saturation (pressure) by modeling. These are described further below. We demonstrate the methodology using data from a recent study on a sandstone reservoir; the method is applicable to any data set.

Bound water T2-cutoff and permeability

The standard method of finding the TBW cut-off on individual samples is by finding the T2 value where the cumulative Sw=1 distribution matches the water volume of the desaturated sample. This method is graphically shown in Figure 1.The green arrow indicates where the desaturated water volume intersects the cumulative Sw=1 distribution. For the present study we found little variation in cutoff, so it is allowed to take the average value. This happened to be 32 ms, which is the same value as the global default for sandstone. Other sandstones may have a somewhat higher or lower cutoff. Carbonates typically have a much higher cutoff, but the concept often fails [Looyestijn and Steiner, 2012].

Since the desaturation on the present samples was done at 500 psi (air/brine, by centrifuge), this cutoff is valid far away from the FWL.

Permeability is usually predicted by either of two empirical formulas [Dunn et al, 2002], each having a porosity factor and a pore size factor, either the ratio FFI/TBW or the T_{2mean}.

$$K_{Coates} = A \, (POR/10)^B \, (FFI/TBW)^C \qquad\qquad \text{Equation 1}$$

$$K_{SDR} \quad = a \, (POR/100)^b \, T_{2mean}^c \qquad\qquad \text{Equation 2}$$

with POR in % and T_{2mean} in ms, and K in mD. The three parameters in each formula may be optimized using core NMR and permeability data. Care should be taken that the same TBW cutoff is used for the core and the NMR log.

Both permeability predictions work equally well; however, the presence of hydrocarbons will affect T_{2mean}, and thus the predicted permeability. In contrast, TBW is not affected (unless in heavier oil), and will give a more robust permeability in hydrocarbon intervals. These complications can be addressed by calibration at (simulated) in-situ conditions [Looyestijn and Steiner, 2012]. Gas will reduce FFI (and T_{2mean}), but not TBW; the equations need to be used with a gas-corrected (cross-plot) porosity, PORX, and FFI computed as PORX-TWB.
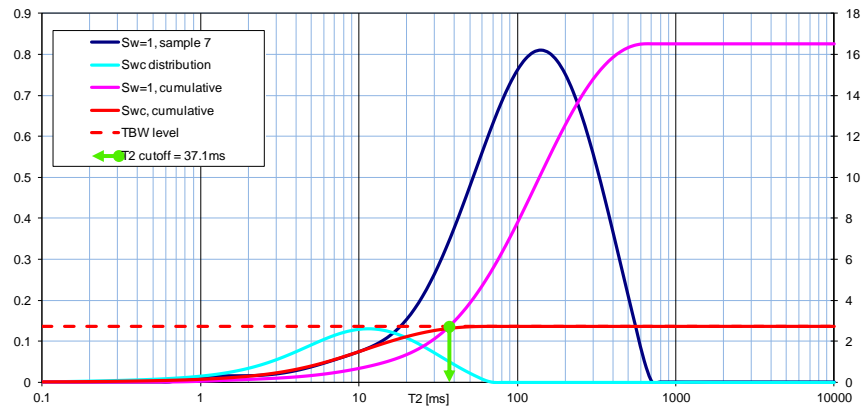
Figure 1   Derivation of TBW cutoff for sample 7

Conversion of NMR to capcurve

The approach taken in the previous section basically interrogates the T2-distribution at one particular desaturation pressure. This can be generalized. The NMR to capcurve conversion assumes a relationship between pore body size (NMR: T2 ~ R) and pore throat size (Pc ~ 1/r). Lumping all parameters together in a single parameter, κ, the relationship becomes [Looyestijn et al, 1999]:

$$P_{c,i} \; = \; \kappa \; / \; T_{2,i} \quad \text{or} \quad \kappa \; = \; P_c(S_w) \; T_2\,(S_w) \qquad\qquad \text{Equation 3}$$

The value for κ varies somewhat for different sandstones; the common range is 2 to 8 psi.s for Hg-air capcurve pressure. In the simplest form, κ is a constant, i.e. κ has the same value for all S_w. This implies a constant ratio between pore body size, R, and pore throat size, r, for all pore sizes. In most rocks, however, it has been found that κ starts off at a constant value, but increases towards the smaller pores, i.e. the shorter T2 and higher Pc. One such relationship is described in [Looyestijn et al, 1999], but many other functional relationships may be proposed.

We illustrate the concept using the form that is implemented in the software of Interactive Petrophysics (IP):

$$P_{c,i} = \frac{10^A}{T_{2,i}^B} \qquad\qquad \text{Equation 4}$$

For B=1 this defaults to a constant ratio, i.e. Pc and T2 are strictly inversely proportional as given by eq.3 with κ as a constant.

The result for two arbitrary individual samples from a recent study is shown in Figure 2 and 3. It can be seen that the NMR distribution (top left) is smoother than the MICP poresize distribution (bottom left); however this difference is not apparent in the capcurves (bottom right). The κ curve in the second figure (top right) is obtained by reading off the NMR and the MICP data as a function of Sw. It shows that the value of κ varies with T2, and that a simple formula cannot precisely describe κ over the entire range of T2. However,

κ is reasonably flat over the range between roughly 3 and 300 ms, corresponding to approximately 500 to 2 m above the FWL. This is typically found in most rocks.

There are several reasons why the conversion is not perfect. The overlay of the MICP and pseudo NMR-capcurve (bottom left), shows that the NMR curve is smoother than the MICP curve. This is partly the reason of the observed Sw-dependence of κ. Furthermore, NMR does not really measure pore size, but rather the volume/surface ratio, and MICP does not measure pore throat size distribution, but rather that of the volumes accessible through throats. Finally, MICP is usually not done on the same sample as NMR, but on a trim end. The rock in this example is fairly clean, and clay effects do not play a significant role. In general, however, appropriate corrections to the MICP data need to be considered.

Although not fully correct over the entire range, the NMR-cap curve (bottom right) will give a good value for Sw over most of the reservoir, but may be off in the lower part of the transition zone; in particular, it may fail to predict the correct entry pressure.

Individual samples will have different A and B values. If the variations are small, the average values may be used, or, better, all samples should be matched with a single set of A and B. If the variations are large, the sample set needs to be broken up in two or more groups.
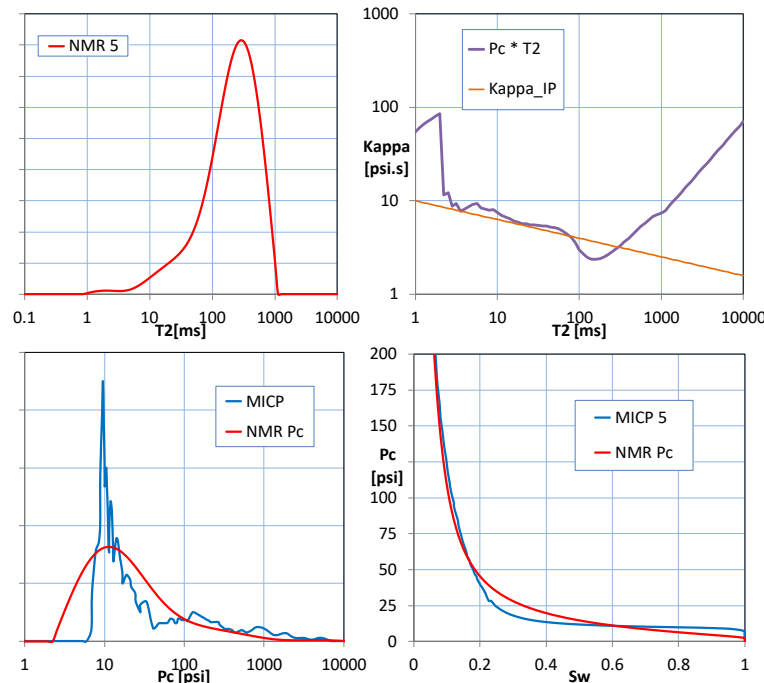
Figure 2   NMR - Pc calibration for sample 5. Pressure is for Hg-air systems.
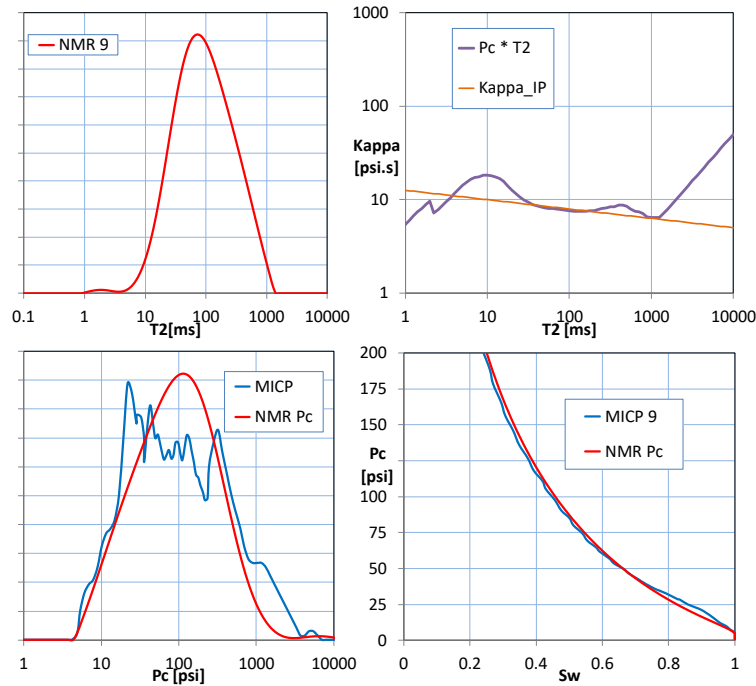
Figure 3   NMR - Pc calibration for sample 9. Pressure is for Hg-air systems.

Modeling NMR response at any desaturation

The desaturation process is modeled [Looyestijn and Hofman, 2005] by a gradual decrease of the signal amplitude as a function of T2, i.e. starting from the largest T2 (largest pores). The mechanism is shown below.
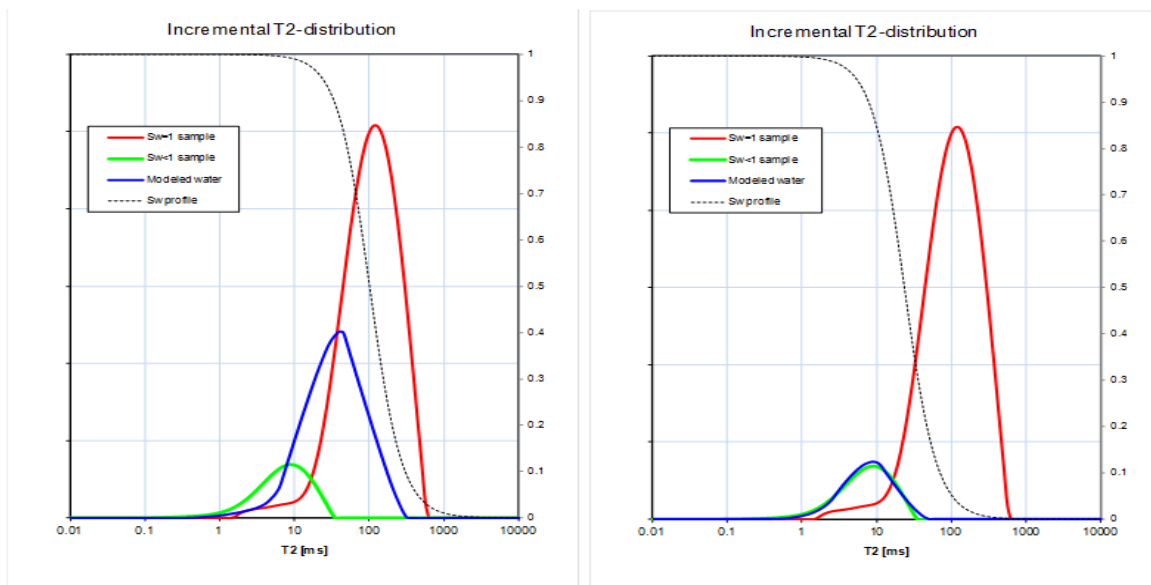
Figure 4   Desaturation modeling: (left) at intermediate saturation, and (right) matching actual experiment

The desaturation profile (black dotted line) gives the water fraction as a function of T2, and thus of pore size. The model accounts for the fact that a certain fraction of pores is only partly desaturated. The residual water is still wetting the pore surface, but the volume has reduced. This results not only in a reduced amplitude, but also in a shorter T2. Consequently, while the long T2 components disappear with increasing desaturation, there is a small increase at short T2. This is observed in all samples in this study.

The desaturation profile is then moved over the T2 axis until the experimental saturation is reached; the observation that the actual T2 position of the distribution agrees with the observed one validates the correctness of the modeling.

Predicted T2-distribution @ Pc

Sample: 2   Porosity: 15.2   %

	Pc [psi]	T2,mid [ms]	TBW [% BV]	Swi [% PV]	T2cutoff [ms]
Experimental	500	25	1.1	7.5	24.6
Modeled	400	32	1.9	12.6	42.4
	300	43	2.5	16.7	57.3
	200	68	3.6	24.2	85.0
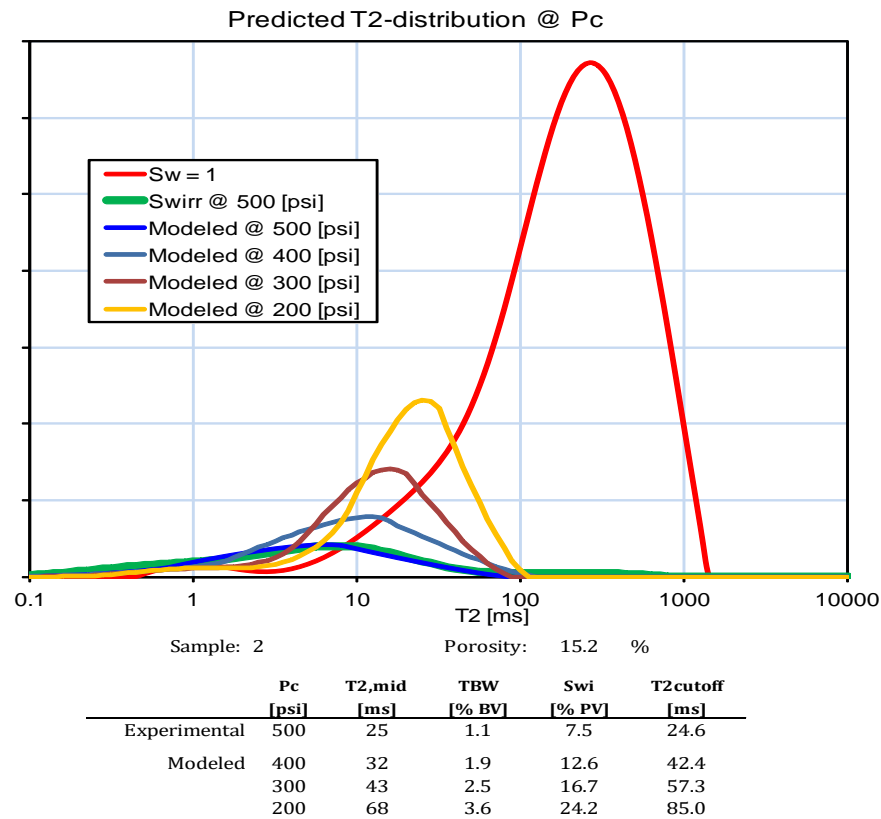
Figure 5   Predicted T2-distribution at experimental conditions and other [Hg-air] pressures for sample 2

Because this experimental measurement is fully predicted by the model, other experimental conditions may now be modeled with confidence. Here, the T2-distribution is predicted for three lower pressures. The corresponding position of the desaturation profile was computed by shifting its mid-point, $T_{2,mid}$, using the relationship between Pc and T2 as defined by eq. 2; this yields (or, when using eq. 1, the same with B=1):

$$\tilde{T}_{2,mid} \; = \; T_{2,mid} \left(P_c \Big/ \tilde{P}_c \right)^{1/B}$$

Equation 3

The corresponding T2-cutoffs are computed in the traditional manner, i.e. by finding the T2 value for which the cumulative T2-distribution (Sw=1) equals the desaturated water volume.

An arbitrary example is shown in Figure 5. The modeling perfectly predicts the response of the desaturated sample. Notice that there is a reasonable agreement between the mid-point of the desaturation profile, $T_{2,mid}$, and the T2-cutoff. This is usually found in all rock types. The relationship between Pc and T2-cutoff can now be used to calculate bound water (TBW) as a function of height above FWL. In fact, this is not really different from using the NMR-cap curve that was discussed in the previous section.

Hydrocarbon correction of NMR log data

Rigorous correction of the NMR log for hydrocarbon effects is not possible, because the part of that contains hydrocarbons could have had almost any shape. However, a reasonably good approximation is possible [Looyestijn et al. 1999]. The underlying principle is that the unknown FFI part must be such that the Coates and SDR permeabilities are equal.

An example is shown in Figure 6. Here the NMR response is simulated for a gas interval and subsequent invasion of OBM filtrate. The NMR porosity is too low because the remaining gas has a low hydrogen index. The simulated response (pink curve) clearly differs from the response that would be obtained if the interval were water bearing because the filtrate has a longer relaxation time than the water that it replaces. The reconstructed distribution (dotted curve) is not perfect, but much closer.
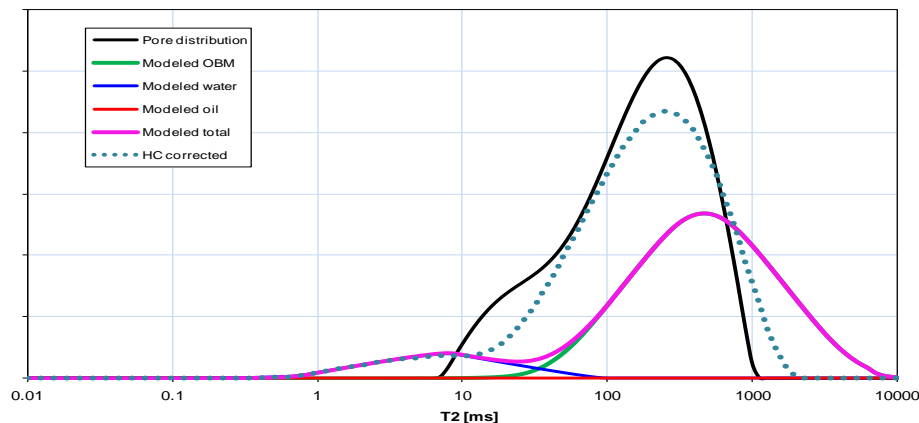
Figure 6   Simulated NMR response in a gas zone with OBM filtrate invasion and reconstructed Sw=1 response

Laboratory versus reservoir conditions

There are several effects that may cause the NMR log to differ from core measurements [for example, Looyestijn and Steiner, 2012]. The most important one is the presence of hydrocarbons, as mentioned in the previous section. Other effects are related to wettability, but that does not impact on the capcurve conversion. Similarly, temperature effects on surface relaxivity are small, if any.

Interpretation of NMR log

The result of the core calibration was applied to the NMR log, taken in the same well, using the approach implemented in Interactive Petrophysics (IP). The well was drilled with oil-base mud in a gas-bearing sandstone. Track-3 shows the NMR log with the default CBW cutoff at 3 ms, and the TBW cutoff at 33 ms. Track-4 shows the hydrocarbon-corrected T2-distribution.
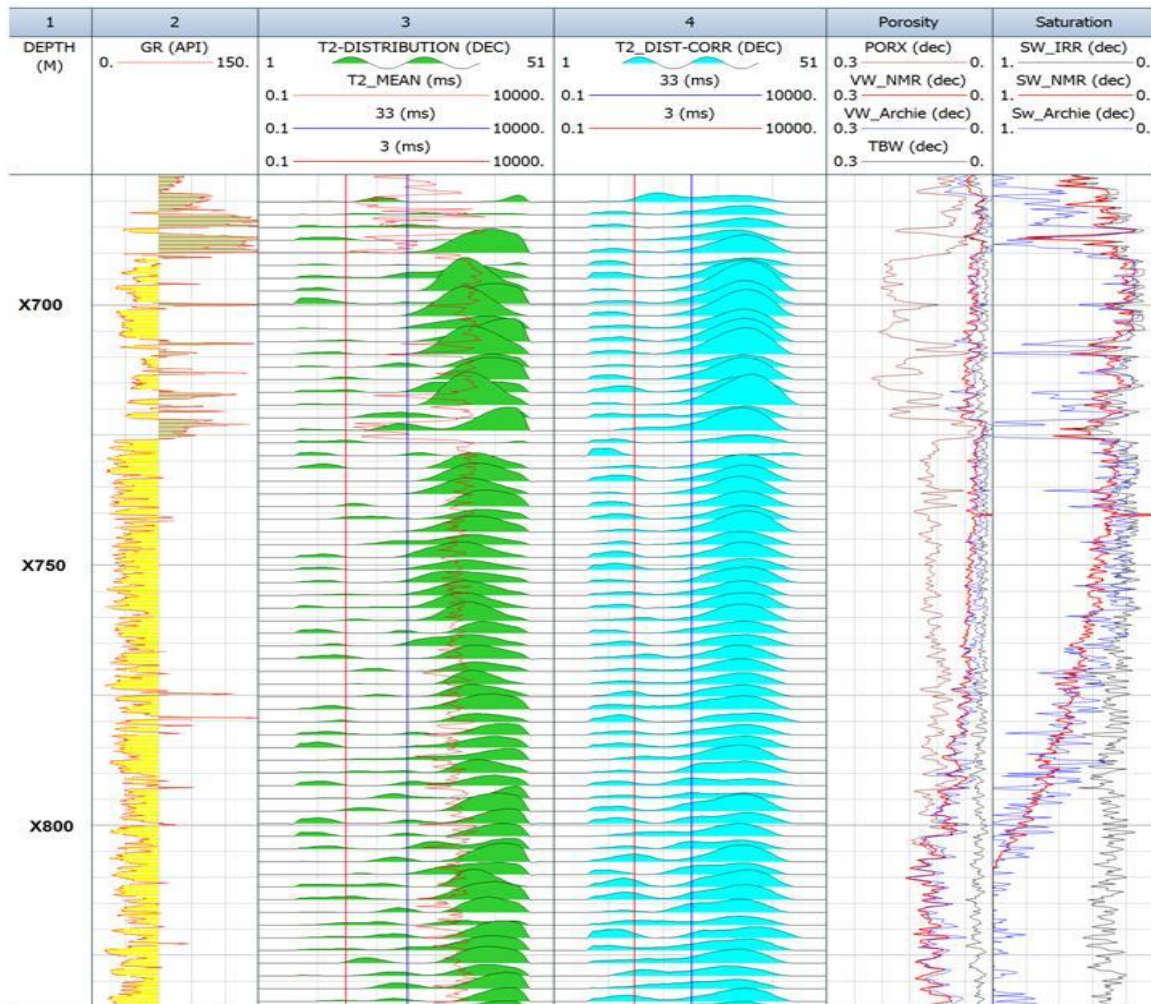
Figure 7   Interpretation of NMR log.

The value of TBW, computed with this cutoff, is shown in track-5, where it is compared against the water volume, Vw_Archie, computed by the Archie method using a combination of density, neutron and resistivity logs. PORX is the gas-corrected density-neutron cross-plot porosity. Track-6 shows the corresponding water saturations, and indicates a gas-water contact at x805 m. SW_IRR (=TBW/PORX) does not follow the transition zone and remains more or less constant. The saturation profile for the NMR

capcurve, SW_NMR, correctly describes the transition zone, assuming the FWL at x810 m. Note that the scatter is much less than in Sw_Archie; this is because the latter is obtained by combining logs that probe different rock volumes, whereas SW_NMR is measured by a single log.

CONCLUSION

We demonstrated that the desaturated NMR response on core samples can faithfully be reproduced by modeling. As a consequence, this allows the prediction of the NMR interpretation parameters, such as T2-cutoff for bound water, at any other desaturation pressure, i.e. at any desired height above the FWL.

As a further step, the NMR log was converted into a cap curve log, using a conversion calibrated against MICP on the available core plugs.

Application of the NMR-cap curve shows a matching saturation profile with the resistivity derived saturation, with an indication of the FWL. Since these two interpretations are completely independent, they form a strong validation of the saturation levels.

The NMR-derived saturation profile shows less scatter than the traditional profile, because the latter combines a number of logs with very different measurement volumes.

ACKNOWLEDGEMENTS

REFERENCES
1. Looyestijn, W.J, Volokitin, Y., Slijkerman, W.F.J., and Hofman, J., 1999, *A Practical Approach to Obtain Primary Drainage Capillary Pressure Curves from NMR Core and Log Data*, SCA9924; also published in Petrophysics (2001), volume 42, 4.3.
2. Looyestijn, W.J. and Hofman, J.P., 2005, *Wettability Index Determination by Nuclear Magnetic Resonance,* SPE 93624, presented at the MEOS, Bahrain, March 2005. Published in SPEREE April 2006, pp 146 – 153.
3. Looyestijn W.J. and Steiner S., 2012, *New approach to interpretation of NMR logs in chalks*, SPWLA 53rd Annual Symposium, Cartagena, Colombia, paper HH, published in Petrophysics, April 2013.
4. Interactive Petrophysics, 2013, *User Manual*. Synergy Software Ltd.
5. Dunn, K-J., Bergman, D.J. and Latorraca, G.A., 2002, *Nuclear Magnetic Resonance, Petrophysical and Logging Applications*, Pergamon, ISBN 0-08-043880-6.

ENHANCED SPATIAL RESOLUTION OF MAGNETIC RESONANCE MEASUREMENT AND APPLICATION TO WHOLE CORE SHALE

Jin-Hong Chen[1], Yang Zhao[1], Daniel T. Georgi[1], Mohammad Delshad[1], and Qiushi Sun[1], and Hyung Kwak[2]

[1]Aramco Research Center – Houston; [2]Saudi Aramco EXPEC Advanced Research Center

ABSTRACT

Low field Nuclear Magnetic Resonance (NMR) has been widely used in laboratories for fluids and small core plug analysis to provide more accurate petrophysical measurements and for calibration of borehole log data. One fundamental limiting factor of NMR application for whole core or well logging is that the spatial resolution is limited by the length of the *rf*-coil. In addition, the end effects of finite coil length can compromise the accuracy of NMR measurement when the core is longer than the coil. Pulsed field gradient (PFG) technology may be used for slice selection in the laboratory; however, PFG-based method does not work well for rocks with short relaxation time, for example shales and other tight rocks, because the NMR signal decays significantly during the application of PFGs.

Herein we propose a method that provides high spatial resolution NMR measurement using the response map of the *rf*-coil coupled with a data acquisition and processing protocol that step-wise moves the *rf*-coil or the studied subject with equal increments of the desired spatial resolution. The main advantages of this method are that it:

- Provides a measurement of fluid content and images with any desired spatial resolution that is not limited by the length of the *rf*-coil or antenna used in the measurement. This can be especially useful in laboratory applications for samples longer than the coil and in well-logging where the studied objects are always much longer than the tool's antenna.
- Eliminates end effects from the finite length of the *rf*-coil.
- Enable acquisition of high-spatial resolution NMR relaxation data for samples with short relaxation times.
- Delineates sample heterogeneity facilitating the upscaling of NMR-based petrophysical properties.

We applied this method to acquire high-spatial resolution NMR measurement on shale whole cores.

INTRODUCTION

Horizontal drilling and hydraulic fracturing has revolutionized hydrocarbon production from unconventional shale and other tight reservoirs; however, the hydrocarbon storage and transport mechanisms remain poorly understood for these reservoirs. This understanding is important for predicting and optimizing production.

Low field (2 MHz) NMR has proved to be a powerful technology for estimating reservoir fluid contents and characterizing fluid transport properties. It has been widely used in laboratories for fluids and small core plug analysis to provide more accurate petrophysical measurements and for calibration of field log data. However, it has rarely been used on whole core samples. This is probably because in conventional whole cores, fluids would largely be expelled while cores are extracted from downhole. This is not the case for cores taken from unconventional source rocks, with nD permeability where the native fluids (except for gas) largely remain in the rock. Thus, estimating fluid content and characterizing fluid-solid interaction using NMR should reveal important information about the shale reservoirs that may not be available by any other method.
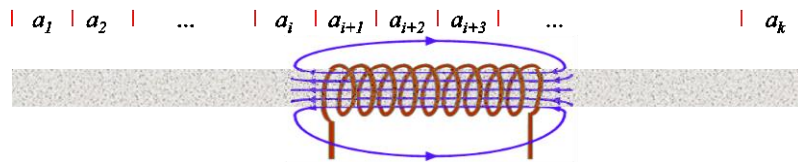
Fig. 1: Illustration of a long sample in a short *rf*-coil while the required resolution is smaller than the coil.

One fundamental limiting factor of NMR application for long whole cores or for well logging is that the spatial resolution is limited by the length of the radio-frequency (*rf*) coil. The length is a few inches for laboratory instrument and a few inches to a few feet for well-logging tools. In typical NMR measurements the length of sample is shorter than that of coil. In this case, the length of coil is assumed to be infinite, which ensures the *rf* field strength and measurement sensitivity across the sample is homogenous. For NMR measurements on long samples or essentially log applications where the sample is longer than the *rf*-coil, one must consider the end effect of a finite coil for accurate measurement. **Fig. 1** illustrates a long sample within the *rf* magnetic field generated by a solenoid coil. On top of the figure, the labeled signal along the core has a smaller spatial resolution than the coil length. **Fig. 1** shows two problems for a conventional NMR measurement: first, the best resolution that can be achieved in a simple experiment would be approximately the length of the *rf*-coil, which can be much larger than the required resolution. Second, the measurement is not accurate because the measured signal includes signal from the two ends of the coil which have much different detection sensitivity comparing to the homogeneous central part within the coil.

A solution to these problems to obtain high spatial resolution NMR measurement is to use PFG technology for slice selection, which is widely used in medical magnetic resonance imaging (MRI). However, high quality PFG can significantly increases the cost of the NMR instruments. In addition, it cannot be used to quantitatively analyze materials with short transverse relaxation times, T_2, because the signal decays to a very small value during the application of PFG. Many tight rocks, such as shales, tight sandstones, and tight carbonates, have T_2 components of 1 ms or less. For example, if a PFG with length 0.6 ms is used, after a pair of PFG the signal with 1 ms T_2 decays to exp(-1.2/1) = 0.3. In this case, 70% signal is lost and more will be lost if longer PFG is used or the T_2 is shorter.

In this paper, we describe a method that
- Provides NMR measurement with any desired spatial resolution that is not limited by the length of the *rf*-coil or antenna used in the measurement. This can be especially useful in laboratory applications for samples longer than the coil and in well-logging where the studied objects is always much longer than the tool antenna.
- Eliminates end effects from the finite length of the *rf*-coil.
- Enables acquisition of high spatial resolution NMR relaxation data for samples with short relaxations

The developed technique was used to log 35 whole shale cores (4 inches in diameter and a foot long) from two Middle East wells and to acquire T_2 spectra and fluid content with one inch spatial resolution along the cores using an NMR spectrometer with a four-inch long *rf-coil*.

METHOD

$$S_1 = r_1 a_1$$

$$S_2 = r_1 a_2 + r_2 a_1$$

$$S_3 = r_1 a_3 + r_2 a_2 + r_3 a_1$$

$$S_i = r_1 a_i + r_2 a_{i-1} + r_3 a_{i-2} + ... + r_n a_{i-n+1}$$
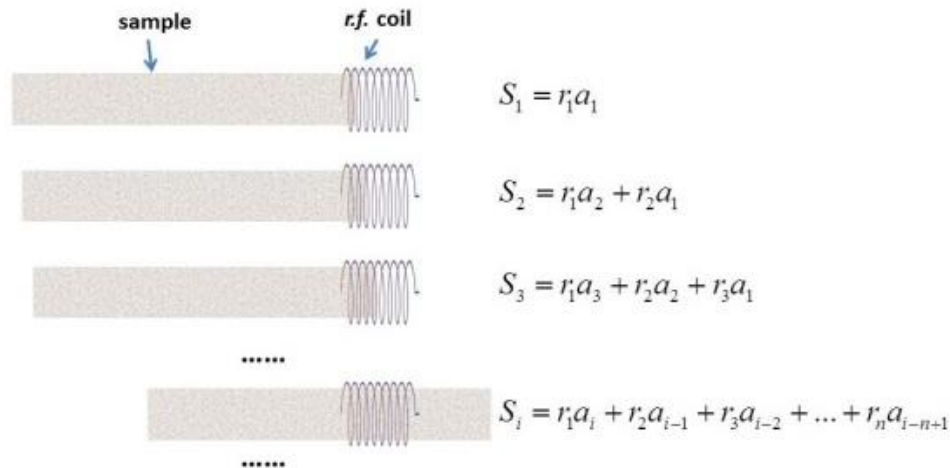
Fig. 2: Illustration of the data acquisition by step wisely moving the sample through the coil. The equations show the acquired signal at each step.

Mathematic description of general method The fluid content of the whole core can be expressed as $\{a_1, a_2, a_3, ..., a_k\}$, as showed in **Fig. 1**. The total length of the core is then

$k \times l$ where l is the spatial resolution and k is the number of sections the sample has. Our method requires a response map of the *rf*-coil with spatial resolution equal to or a fraction of the desired resolution l. This can be experimentally measured or calculated if the shape of the coil is known.

The method also needs to acquire the NMR data for the long coil stepwise with steps equal to or less than the spatial resolution l. The stepwise data acquisition can be achieved in two ways: (1), moving a sample though the *rf*-coil. This is normally done in the laboratory when the sample is longer than the *rf*-coil. **Fig. 2** shows how this stepwise passing of sample through a coil. (2), moving the *rf*-coil along the measurement subject. This is a typical data acquisition procedure in logging where the logging tool moves along the wellbore from bottom to top.

For both data acquisition methods, the detected signal at step i can be expressed as:

$$S_i = r_1 a_i + r_2 a_{i-1} + r_3 a_{i-2} + r_4 a_{i-3} + \cdots + r_n a_{i-n+1} \tag{1}$$

$\{r_1, r_2, r_3, \ldots, r_n\}$ represents the one dimensional response map of the *rf*-coil. It is convenient to express Eq. (1) in matrix form as

$$S = RA \tag{2}$$

with

$$S = \begin{bmatrix} s_1 \\ s_2 \\ \vdots \\ \\ \\ \\ \\ \\ \\ s_{k+n-1} \end{bmatrix} \tag{3}$$

$$R = \begin{bmatrix} r_1 & & & & & & & & & \\ r_2 & r_1 & & & & & 0 & & & \\ r_3 & r_2 & r_1 & & & & & & & \\ & & & \ddots & & & & & & \\ & & & & r_n & \cdots & r_3 & r_2 & r_1 & \\ & & & & & & & & \ddots & \\ & & & & & & & r_n & r_{n-1} & r_{n-2} \\ & & 0 & & & & & & r_n & r_{n-1} \\ & & & & & & & & & r_n \end{bmatrix} \tag{4}$$

$$A = \begin{bmatrix} a_1 \\ a_2 \\ \vdots \\ \\ \\ \\ \\ \\ a_k \end{bmatrix} \tag{5}$$

Matrix S is the measured NMR signal from the spectrometer which contains coil end effects, and, thus, has a spatial resolution slightly larger than the length of the *rf*-coil. Matrix R is the response matrix and is determined by *rf*-coil and also the way the NMR data acquisition was carried out. Matrix A is the desired NMR signal along the sample with high spatial resolution.

A is obtained by solving Eq. (2). Note that the dimension of S, R, and A are $(k+n-1) \times 1$, $(k+n) \times k$, and $k \times 1$, respectively; therefore, obtaining A is an over-determined problem because the dimension of S is larger than A.

To solve Eq. (2), we convert Eq. (2) to:
$$R'S = (R'R)A \tag{6}$$
where R' is the transpose of matrix R. In Eq. (6), $R'R$ is a $k \times k$ matrix and $R'S$ is a $k \times 1$ matrix. Then:
$$A = (R'R)^{-1}R'S \tag{7}$$
where $(R'R)^{-1}$ is the inverse of $R'R$. All the terms on the right of Eq. (7) are know: matrix S is the measured NMR signal using the stepwise approach and matrix R represents the response function constructed as Eq. (4) using the *rf*-coil response map. Thus, evaluating the right side of Eq. (7) gives us A: the NMR signal with spatial resolution predetermined as l.

For a typical CPMG echo train data, each acquired signal, S_i, includes m echoes. Both S and A are matrixes, which can be expressed as;

$$S = \begin{bmatrix} s_{1,1} & \cdots & s_{1,m} \\ \vdots & \ddots & \vdots \\ s_{k+n-1,1} & \cdots & s_{k+n-1,m} \end{bmatrix} \tag{8}$$

$$A = \begin{bmatrix} a_{1,1} & \cdots & a_{1,m} \\ \vdots & \ddots & \vdots \\ a_{k,1} & \cdots & a_{k,m} \end{bmatrix} \tag{9}$$

Each row in *A* represents the echo train with full intensity and free of *rf*-coil end effects. Inversion of each echo train in *A* produce NMR T_2 spectra along the long sample.

Computation programs were coded with Matlab to solve Eq. (7) using a general linear least squares method for singular value decomposition. Inversion program of the echo trains in *A* was also coded with Matlab to obtain the NMR T_2 spectra.

NMR measurement An NMR spectrometer from Ecotek Corp was used for data acquisition. It operates at 1.83 MHz with probe diameter 108 mm allowing the 4-inch full-diameter cores to be pushed through as illustrated in **Fig. 3**. The *rf*-coil located in the middle of the magnet was approximately 4 inches long, and, thus, could not 'see' the whole one foot long whole core in one single measurement.

The NMR signal was acquired using CPMG [1, 2] pulse sequence. The echo time, *TE*, was 0.17 ms (milliseconds) and inter-scan delay was 500 ms.

Fig. 3: Illustration of a whole core in Teflon shrink-wrap in the spectrometer probe. The large gray box encloses the magnet and *rf*-coil. A separate box on the left contains the control console and the *rf* amplifier.

A series of data acquisitions were made, beginning with the top of the core flush against the start of the sensitive window of the *rf* probe. This way, the initial scan should always be a noise signal. NMR acquisitions are continued along the length of the core by pushing it manually through the 4-inch probe, one inch at a time. The acquisition continued until the core completely passes through the sensitive window, once again ending in a pure noise signal. For a foot long core to pass through the 4-inch probe, it required 17 acquisitions.

To measure the response map of the *rf*-coil with resolution equal to 1 inch, a disk-shaped polycarbonate standard was prepared. The inner diameter and thickness were approximately 3.68 and 0.94 inches, respectively. It was filled with double-distilled water doped with $CuSO_4$ with a concentration of approximately 215 ppm to shorten the water T_2 to 70 ms. This standard contained 178.2 g of water (approximately 178.2 ml) at room condition. To map out the *rf*-coil response, the standard sample was place into the coil and manually pushed through the magnet one inch at a time. The NMR CPMG echo was acquired at each step.

The standard sample also served to calibrate the fluid content in the whole core samples. The percent fluid content in the rock is calculated as:

$$p_{Fluid} = r \frac{M_0^{core} / V^{core}}{M_0^{w} / V^{w}} \times 100\% \qquad (10)$$

where r is the measured response factor at the position in the coil, M_0^{w} and V^{w} are the measured NMR signal and volume for the standard water sample, and M_0^{core} and V^{core} are the measured NMR signal and volume for the core sample.

RESULTS AND DISCUSSION
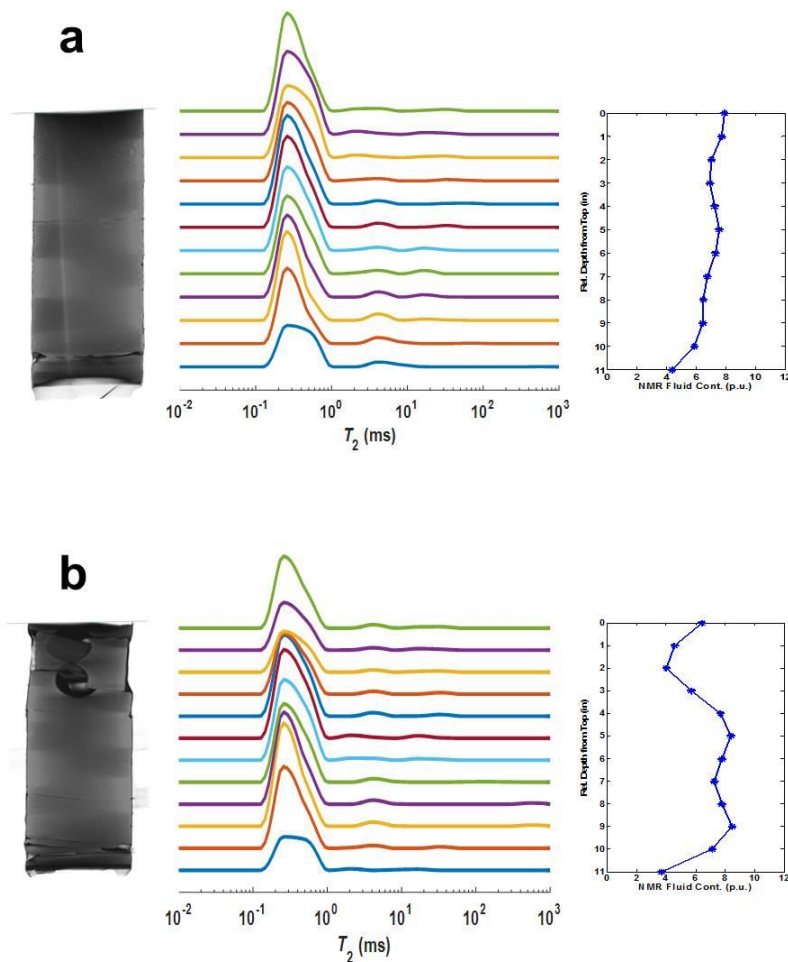
Fig. 4: CT image, NMR measured fluid content and NMR T_2 spectrum of every inch along two one-foot long whole cores (a) and (b) measured with the 4 inch long *rf*-coil. From left to right for the two samples are: slice of CT image, T_2 spectra, and fluid content from the T_2 measurement.

Response map of rf-coil The response map of the *rf*-coil represents the detection sensitivity at each position for the coil. It is determined by both the excitation of the nuclear spins by

the *rf* pulse from the coil and detection of the current generated by the excited nuclear spin. Table 1 lists the acquired relative signal intensity at each relative position inside the probe measured using the standard sample for the NMR spectrometer used in this test. The relative signal intensity provides the coil response curve. The data shows that the coil response is quite uniform in the middle of the coil and falls off quickly at the two ends of the coil. It can be seen that fluids at positions 1 and 5 contribute less than half of the full signal. At positions 0 and 6 fluids contribute very little to the detected signal and will be neglected hereafter. This response map is unique and can be varied for different spectrometers and different coils for the same spectrometer.

Table 1 - Acquired NMR signal intensity of the standard sample in the coil

Relative Position	0	1	2	3	4	5	6
Relative Signal Intensity r	0.01	0.35	1.00	0.98	0.98	0.49	0.05
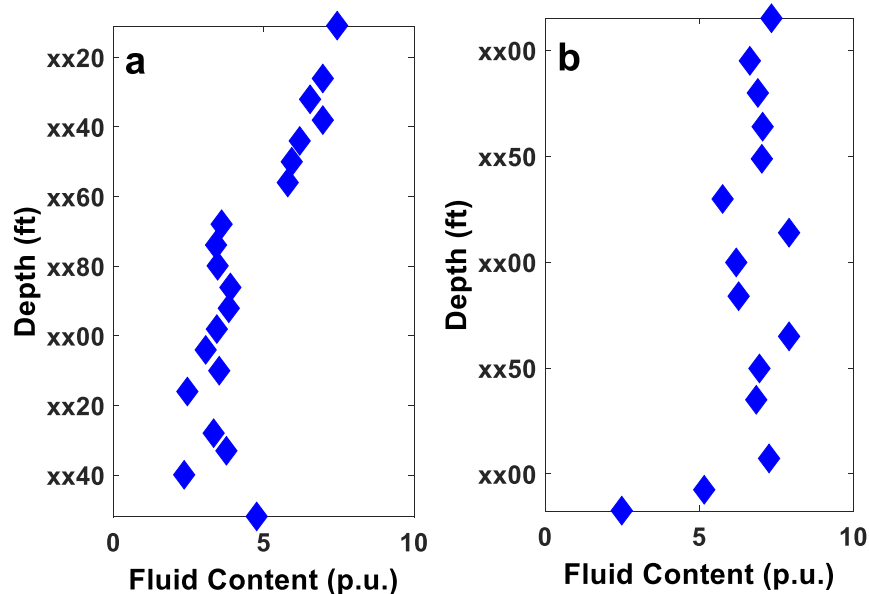
Fig. 5: NMR measured fluid contents for the 35 whole cores from two wells acquired at different depth.

High spatial resolution NMR Fig. 4 shows representative NMR results for two whole cores (a) and (b) using the stepwisely acquired data. On the left is the slice images taken from the whole core CT, showing that the whole core broke off at several places; in addition, two plugs were drilled before our measurements from the core (b). The middle column is the T_2 spectrum for each inch of the whole core and the last column shows the summation of the T_2 spectrum which is the total fluid content for each inch of the core. The variation of the NMR measured fluid content in the right column over the one foot long core is consistent with the integrity of the cores which is more obvious for sample (b). This strongly suggests that the NMR result of one inch spatial resolution is quite accurate. As a result, we have achieved 1 inch spatial resolution from 12 inch length whole core sample using a 4 inches long *rf*-coil by the proposed method.

The NMR T_2 spectra show that the main T_2 peak are largely at the same value, indicating the pore system over each inch of the sample are relatively similar through whole core sample. It is also interesting to note that the NMR T_2 peak is 'smeared' at the locations where the whole core is not intact.

Fig. 5 shows the NMR measured fluid content for the 35 whole cores from two wells (a) and (b). Each point in the plot represents the average fluid content from 12 NMR spectra over the 1foot long whole core. The results suggest that in the studied part well (a) has two distinct zones separated at XX60 ft while well (b) might have some layered structure in the middle of the studied zone. On well (b), there could be some large changes at the bottom of the studied zone in the formation.

All the cores studied here were from a shale gas reservoir and have been kept in the laboratory for more than a year. The original gas should have bled off and the NMR measured fluid in the cores can only be water. The data shows the water content is quite high, approximately 8 p.u. in the top zone of well (a) and most of the zone in well (b).

CONCLUSION

A method has been developed that can acquire NMR data with spatial resolution higher than the length of the *rf*-coil which has usually been considered as the limit of the spatial resolution without using gradients. In addition, this method can acquire accurate data by eliminating the end effects of the *rf*-coil. More importantly, it only uses hard pulses and does not require the application of gradient pulses, which enables the acquisition of NMR data on samples with very short relaxation times. We have successfully demonstrated the current method on shale whole cores to acquire NMR T_2 spectra with 1inch spatial resolution using a 4 inches *rf*-coil. The NMR whole core logging method in this work can be used as a non-destructive tool to estimate fluid content in whole cores at well-sites or at core handling facilities.

ACKNOWLEDHEMENT

REFERENCE

[1] Carr HY, Purcell EM. Effects of Diffusion on Free Precession in Nuclear Magnetic Resonance Experiments. *Physical Review*. 1954;94:630-8.
[2] Meiboom S, Gill D. Modified Spin-Echo Method for Measuring Nuclear Relaxation Times. *Review of Scientific Instruments*. 1958;29:688-91.

How to Obtain Primary Drainage Capillary Pressure Curves Using NMR T2 Distributions in a Heterogeneous Carbonate Reservoir

Fabian Brandimarte, QGC; Martin Eriksson, KPO; Adam Moss, AKM Geoconsulting

ABSTRACT

Nuclear Magnetic Resonance (NMR) derived T_2 distributions have long been recognised as providing valuable information about pore size and fluid distribution in reservoir rocks. Conversional methods for deriving water saturation from T_2 distributions use the T_2 cut-off method, this determines the bound fluid saturation. The T_2 cut-off method models water saturation at a theoretical irreducible water saturation, it does not account for transition zone water saturations.

The fully brine-saturated sample T_2 distribution can be thought of as a 'pseudo' pore-size distribution. This property has been used by researchers to convert T_2 distributions to capillary pressure curves. Single conversion factor/scaling factors have been used, but this assumes that the pore space has a single surface relaxivity value and resembles a bundle of capillary tubes. Methods using variable scaling factors have been published. A variable scaling factor takes account of variable surface relaxivity throughout the pore space and the existence of pore body restrictions/throats. All previous published studies have been on sandstone reservoir rocks

This work investigates the use of core calibrated variable scaling factors to derive capillary pressure curves from log NMR T_2 distributions in a heterogeneous carbonate reservoir. The resulting capillary pressure curves are used to predict water saturation in a hydrocarbon column hundreds of metres thick.

The variable scaling factor functions are obtained using mercury injection primary drainage capillary pressure curves and brine-saturated T_2 distributions from plug samples. We discuss methods for evaluating heterogeneity at the plug scale and assessing the validity of the derived scaling factor functions in highly heterogeneous carbonate rocks. The scaling factor functions can be used to convert the NMR log data to modelled mercury injection curve at every depth interval. The resulting capillary pressure curves are converted to reservoir conditions using special core analysis and fluid property data. Knowing the height above free water level, the water saturation at each depth can be estimated. The resulting water saturation is compared with the NMR log T_2 cut-off water saturation and log water saturation from resistivity based models. Recommendations are made on sample selection strategies and special core analysis data required to obtain accurate water saturations using this methodology in heterogeneous carbonate reservoirs.

INTRODUCTION

Nuclear Magnetic Resonance (NMR) measurements have been used extensively to characterise reservoir rock pore geometry using logging and lab based NMR spectrometers [1]. NMR can be used to model permeability, free fluid and bound volumes. The sensitive of the NMR measurement to pore-size distribution potentially enables capillary pressure to be modelled from NMR data. Several workers have proposed methods to derive drainage capillary pressure vs saturation curves from NMR data [2-4]. This paper demonstrates how to use core plug capillary pressure and NMR T2 data to obtain modelled capillary pressure curves from NMR logs in a heterogeneous carbonate reservoir.

NMR THEORY

In simple terms in NMR we are measuring the relaxation behaviour of hydrogen nuclei [5]. In this study, we measure the T$_2$ relaxation of the hydrogen nuclei. In most porous rock systems, there will be a continuous range of pore sizes, rather than several discrete sizes. In fully brine saturated rocks each pore-size has a distinctive T$_2$ value. The NMR response to one pore-size will have a characteristic T$_2$ value and signal amplitude proportional to the amount of fluid contained in pores of that size. For examples within this paper a CPMG sequence (Carr-Purcell-Meiboom-Gill) is used to measure NMR T$_2$ distributions of core plugs and in the NMR log.

In a water-wet rock, relaxation of hydrogen protons in the water occupying the smallest pores occurs, because of interaction with the pore surfaces. Part of the T$_2$ distribution relates to water in pores which could be displaced by hydrocarbons and part relates to capillary-bound water. The T$_2$ cut-off method is often used to define capillary bound water volumes, the defaults for carbonates is 100ms. Using a T$_2$ cut-off value to define capillary bound water for NMR logs will assume that all rocks are at an irreducible water saturation and does not account for a transition zone. Therefore, to use NMR logs to accurately define water saturations it is beneficial to convert the NMR T$_2$ distributions to capillary pressure curves and calculate the saturation at each given height above the free water level.

MERCURY INJECTION VS NMR

Mercury injection utilises the very high interfacial tension between mercury and air to produce capillary pressure data up to extremely high capillary pressure and obtain low wetting phase saturations. Details on mercury injection theory and experimentation can be found in Shafer & Neasham (2000) [6]. Mercury injection capillary pressure (MICP) curves can be converted to a pore size distribution by rearranging the Washburn equation, Equation 1.

$$r = \frac{-C\ 2\sigma cos\theta}{Pc_{MICP}}$$

(1)

Where: r = Pore radius (microns), Pc$_{MICP}$ = Mercury injection capillary pressure (psia), σ = Mercury/air interfacial tension (485 dynes/cm), θ = Contact angle between the mercury/air interface & the rock (130º), C = A unit conversion factor

The NMR T_2 distributions are not 'anchored' to any points of reference, it can be 'calibrated' to the distribution of pore throat radii data using a scaling factor, Equation 2.

$$Scaling\ Factor = \frac{-C\ 2\sigma cos\theta}{Pc_{MICP} \times T_2} \tag{2}$$

Using a single scaling factor assumes that a linear relationship exists between pore throat radius and pore body size. Also, the NMR is recorded on the entire plug whereas the MICP data is measured on a plug trim. The MICP may not be representative of the plug, especially if there are small scale heterogeneities within a plug. Figure 1 shows a sandstone example in which a single scaling factor works well. Figure 2 shows a vuggy carbonate sample example. The pore-space of this vuggy carbonate sample has pores arranged such that small pores 'shield' larger pores. Hence the mercury injection derived pore size distribution is unimodal & the T_2 distribution is multi modal. The example in Figure 2, illustrates why a scaling factor function is required for complex pore systems such as vuggy carbonates.

THE DATA SET

The dataset used for this study includes: 16 plug samples with high pressure MICP curves and NMR T_2 measurements at 100% brine saturation. The plug samples are all from a carbonate reservoir. Figure 3 shows the ambient Klinkenberg gas permeability against ambient helium porosity for the clean dry plug samples. Samples from this reservoir are known to be heterogeneous and can contain large vugs. To evaluate the degree of heterogeneity the absolute percentage difference between the helium porosity of the MICP trim and total NMR porosity of the plug was calculated, Figure 4. Samples with large differences are likely to be those in which heterogeneity on the plug scale is high. This means that a mercury injection 'trim' cut from the plug may not be representative of the whole plug. Every plug in this study was imaged using CT scanning. Inspection of the CT scan images confirmed that plugs with small differences in the two porosity values appear to be reasonably homogeneous, Sample 16, Figure 5. Plugs with large differences in porosity between plug & trim are were confirmed to be heterogenous from their CT scan images, Sample 3, Figure 5. Only plugs with an absolute difference of less that 20% between trim and plug porosity are used to calibrate the global scaling factor model. The well was logged using the Schlumberger MRX tool.

CONSTRUCTING THE GOLBAL SCALING FACTOR MODEL

Figure 6 shows the workflow used in this study. All mercury injection and NMR measurements were at zero confining stress (ambient), therefore both NMR and mercury injection curves were stress corrected using the Juhasz method in Equations 3a, 3b and 4.

$$Pc(res) = Pc \times \left[\frac{\emptyset_{res}}{\emptyset_{lab}}\right]^{-0.5} \tag{3a}$$

$$T2(res) = T2 \times \left[\frac{\emptyset_{res}}{\emptyset_{lab}}\right]^{-0.5} \tag{3b}$$

Where: Pc = Capillary pressure at zero confining stress (psia), Pc(res) = Capillary pressure at reservoir equivalent confining stress (psia), T2 = T_2 relaxation time at zero confining stress (mS), T2(res) = T_2 relaxation time at reservoir equivalent confining stress (psia), Φres = Porosity at reservoir equivalent confining stress (fraction), Φlab = Porosity at zero confining stress (fraction)

$$Snw(res) = Snw \times \left[\frac{\emptyset_{res}}{\emptyset_{lab}} \right] \tag{4}$$

Where: Snw = Non wetting phase saturation at zero confining stress (fraction), Snw(res) = Non wetting phase saturation at reservoir equivalent confining stress (fraction)

Previous studies proposed using a single scaling factor to convert T_2 distributions to capillary pressure curves, this study uses a scaling factor for every saturation point. Thus 'forcing' the T_2 distribution to match the capillary pressure curve, Figure 7. The scaling factor for each saturation point is the multiplier needed to convert the T_2 time to the equivalent capillary pressure. Doing this accounts for the varying degree of pore-shielding and surface relaxivity that occurs within the pore-space over the whole range of pore sizes. A scaling factor versus saturation function is defined for each sample, Figure 8.   A global scaling factor relationship can be obtained by calculating the best fit scaling factor for each saturation unit using all samples. This data set produced a polynomial relationship. There is a larger variation in scaling factors at saturations greater than 0.6. This corresponds to larger pores and indicates that for these samples surface relaxivity & pore-shielding is variable in these larger pores.

The global scaling factor relationship has been applied to the stress converted T_2 distributions for each plug. Figure 9 shows a comparison of the modelled capillary pressure curve with the measured mercury injection capillary pressure curve for Sample 4. For the set of sixteen samples over 80% had a root mean squared error of saturation prediction of less than eight saturation units, Figure 10. Capillary pressure curves derived from the global scaling factor funct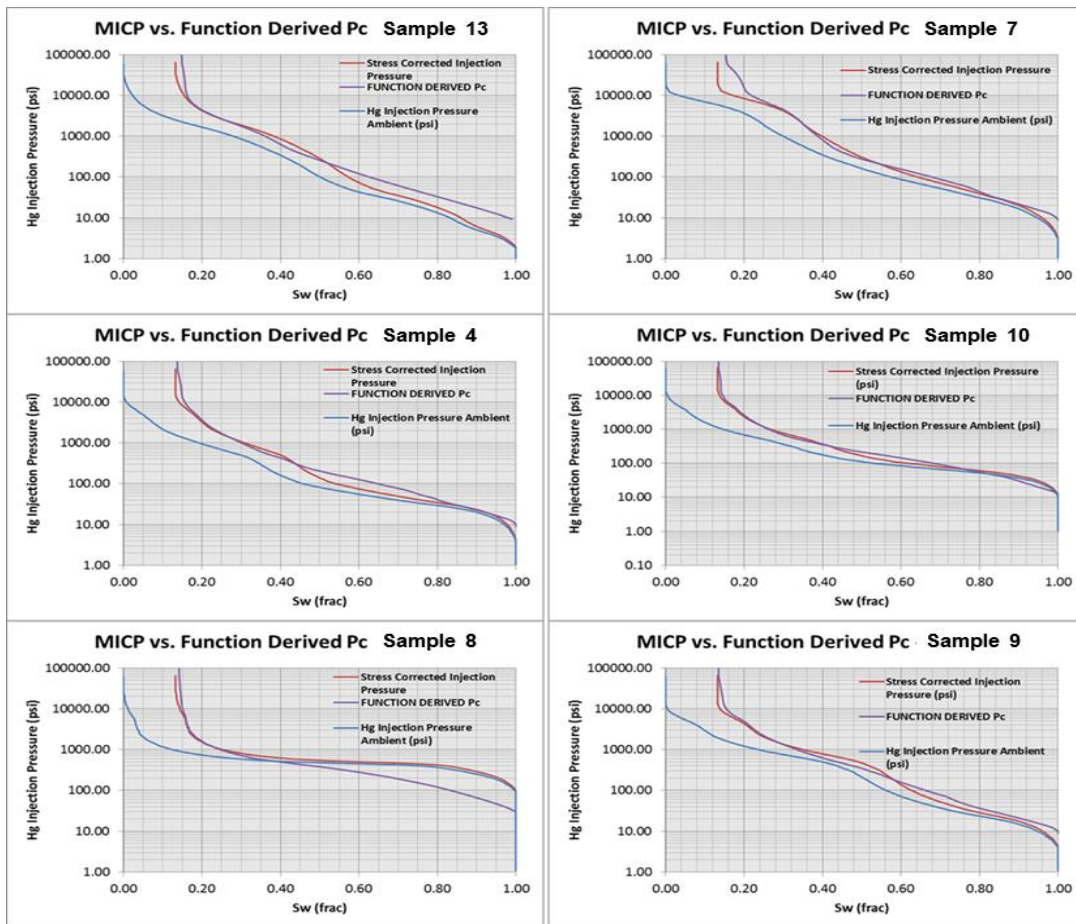ion are compared with the stress corrected mercury injection curves for six of the plug samples in Figure 11. The match between modelled and measured capillary pressure is excellent for some samples and not quite so good for others, this variation in fit is due to the use of the global scaling factor model/equation from Figure 8. For the limited sample set available the global scaling factor relationship is reasonably successful.

APPLICATION OF THE GOLBAL SCALING FACTOR MODEL
The global scaling factor relationship has been used to model capillary pressure curves and predict water saturations using NMR log data from a 400m section of the carbonate reservoir well. In the MRX NMR log the T_2 bins that represent the smallest depth of investigation where used as these will measure rocks that have been most effected by drilling mud filtrate invasion, i.e. have the smallest gas effect. To model water saturation the following are required: depth of free water level (FWL), brine density, hydrocarbon density, water-hydrocarbon interfacial tension and water-hydrocarbon-rock contact angle. The calculation of the capillary pressure versus depth profile was further complicated in

this well because it has a gas leg. The results of applying the global scaling factor model to the NMR log data are shown in Figure 12, Track 4. The resulting water saturation clearly shows a transition zone water saturation for at least 100m above the free water level. The transition zone water saturation is not seen using the default 100ms T_2 cut-off for carbonates and a SCAL optimised 173ms T_2 cut-off, Tracks 5 & 6. Figure 12 also shows the Archie resistivity model water saturations using core calibrate values for the Archie cementation & saturation exponents. The global scaling factor model water saturations are similar to the Archie values over the whole section, including the transition zone.

CONCLUSION
A variable scaling factor model has been derived using core NMR and capillary pressure data. This is used to convert the NMR log data to modelled mercury injection curve at every depth interval. The resulting capillary pressure curves are used to estimate water saturation at each depth. The resulting water saturation compared well with log water saturation from resistivity based models. This model can be used in future wells in the field, which have NMR logs, to obtain a rapid fluid saturation versus depth profile.

ACKNOWLEDGEMENTS
The authors thank the KPO partners for permission to publish this study.

REFERENCES
1. Walsgrove, T., Stromberg, S., Lowden, B. and Basan, P., 1997, "Intergration of Nuclear Magnetic Resonance Core Analysis and Nuclear Magnetic Resonance Logs: An Example from the North Sea, UK. *SPWLA 38th Annual Logging Symposium*, 15-18 June 1997.

2. Marschall, D., Gardner, J.S., Mardon, D., Coates, G.R., "Method for Correlating NMR Relaxometry and Mercury Injection Data", Paper SCA1995-11, *Proc. Int. Symposium of Society of Core Analysts,* (1995).

3. Lowden, B.D., and Porter, M.J., "T2 Relaxation Time Versus Mercury Injection Capillary Pressure: Implication for NMR Logging and Reservoir Characterization" Paper SPE 50607, *SPE European Petroleum Conference, The Hague, (1998), Oct. 20-22.*

4. Volokitin, Y., Looyestijn, W.J., Slijkerman, W.F.J., Hofman. J.P., "A Practical Approach to Obtain Primary Drainage Capillary Pressure Curves from NMR Core and Log Data", Paper SCA1999-25, *Proc. Int. Symposium of Society of Core Analysts,* (1999).

5. Coates, G., Xiao, L., and Prammer, M., *NMR Logging Principles & Applications,* Halliburton Energy Services, 1999.

6. Shafer, J. and Neasham, J., "Mercury Porosimetry Protocol for Rapid Determination of Petrophysical and Reservoir Quality Properties", *Paper SCA2000-21, Proc. Int. Symposium of Society of Core Analysts,* (2000).
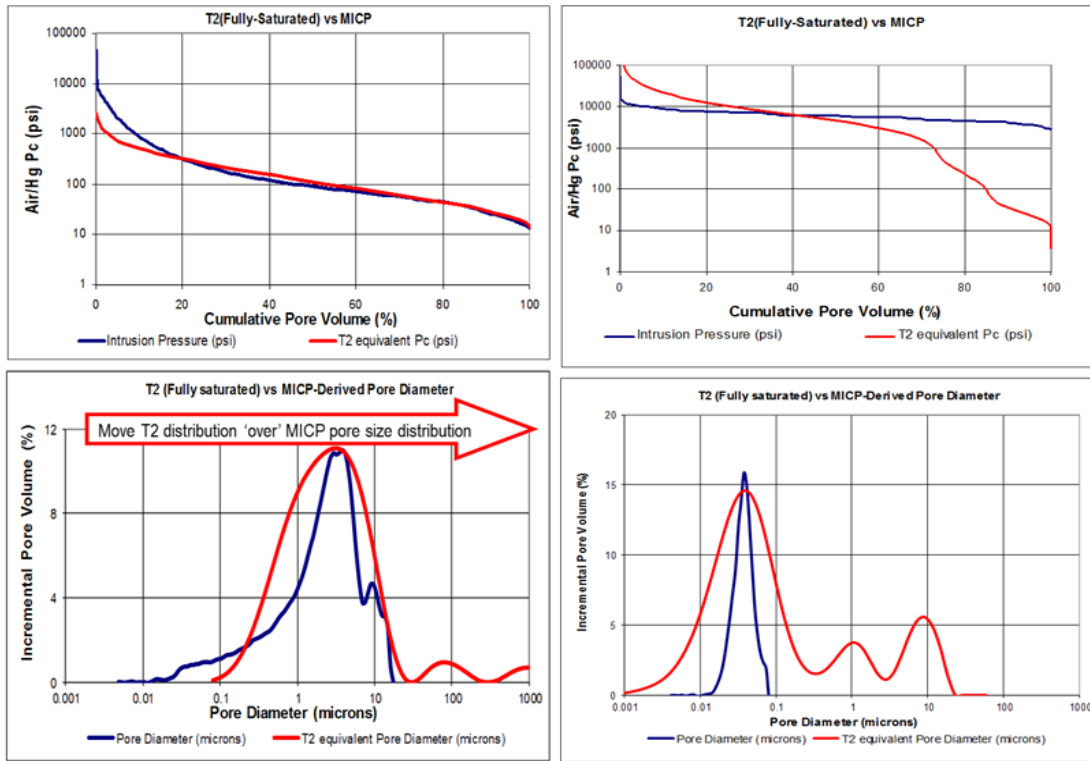
Figure 1: Comparison of a sandstone T_2 distribution and mercury injection primary drainage capillary pressure curves using a single scaling factor. Ka = 0.8 mD, Porosity = 19.67%, Scaling factor = 0.8 microns/ms

Figure 2: Comparison of a carbonate T_2 distribution and mercury injection primary drainage capillary pressure curves using a single scaling factor, showing the effect of pore shielding by smaller pores. Ka = 0.01 mD, Porosity = 4.6%, Scaling factor = 0.006 microns/ms
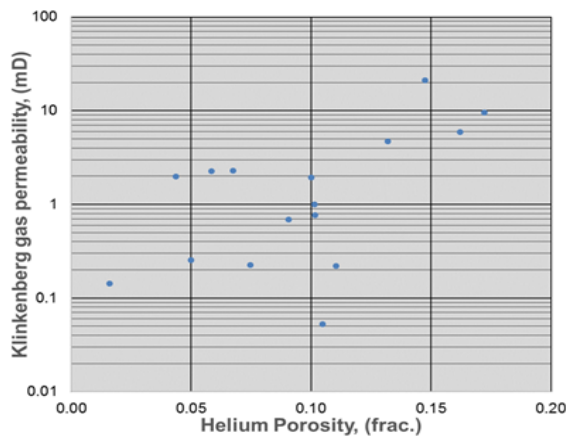
Figure 3: Ambient Klinkenberg gas permeability against ambient helium porosity for the clean dry plug samples.
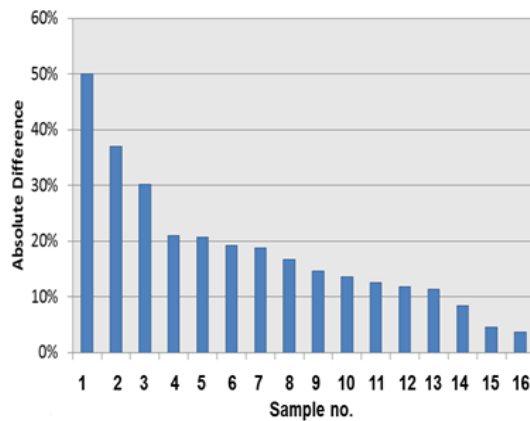
Figure 4: Absolute percentage difference between the helium porosity of the mercury injection trim and total porosity of the plug measured using NMR.
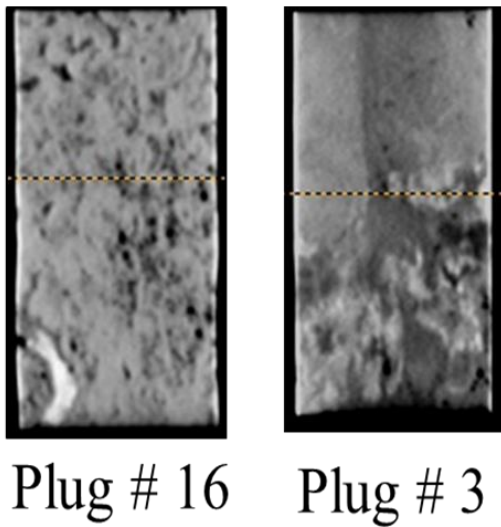
Figure 5: CT scan images of plug sample 16 (reasonably homogeneous) & plug 3 (heterogeneous)
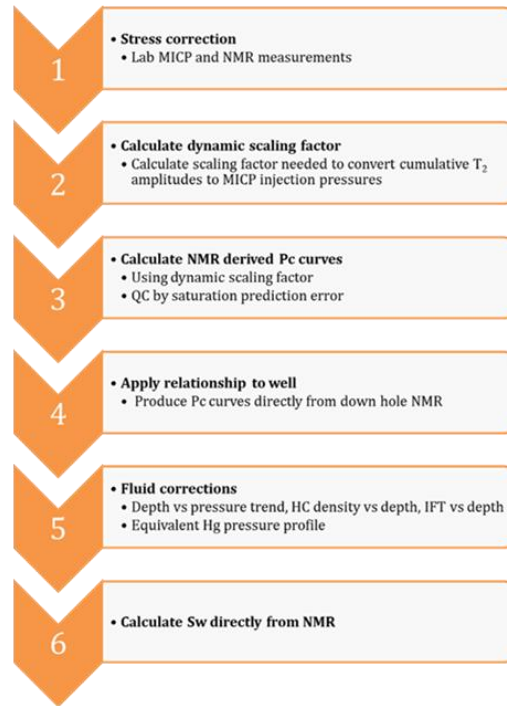
Figure 6: NMR derived capillary pressure workflow
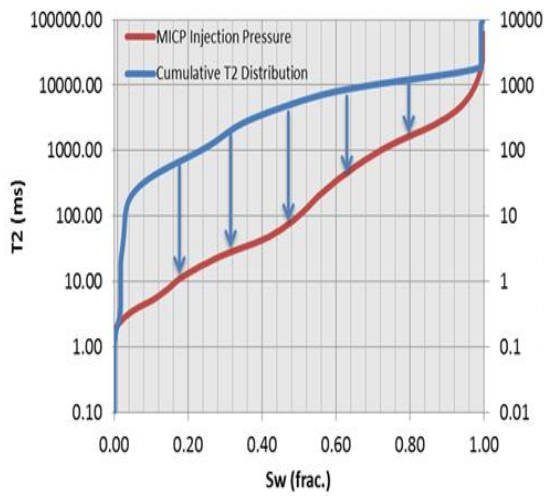
Figure 7: This plot demonstrates that it is possible to convert each T_2 time to a given capillary pressure.
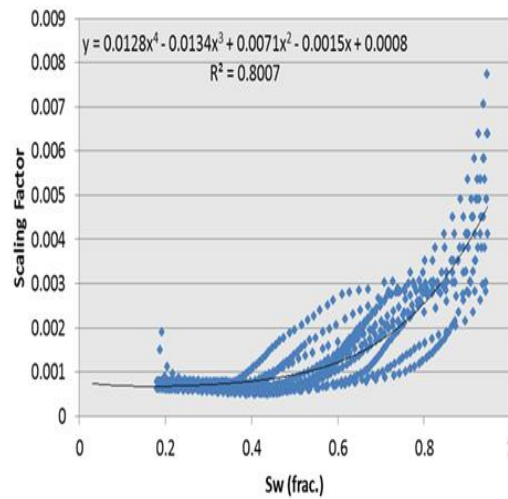
Figure 8: The scaling factor versus water saturation with a global polynomial regression, porosity outliers removed.
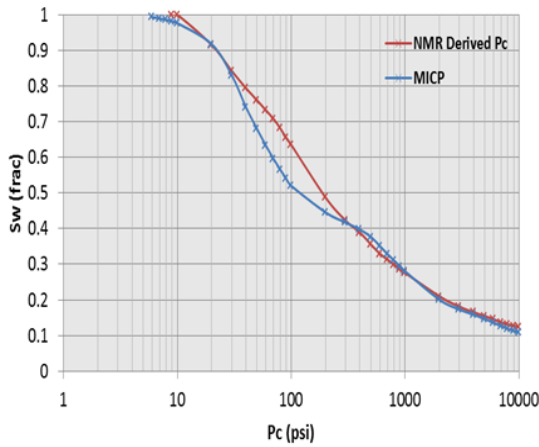
Figure 9: Comparison of the mercury injection capillary pressure curve and the NMR global function derived capillary pressure curve for sample 4.
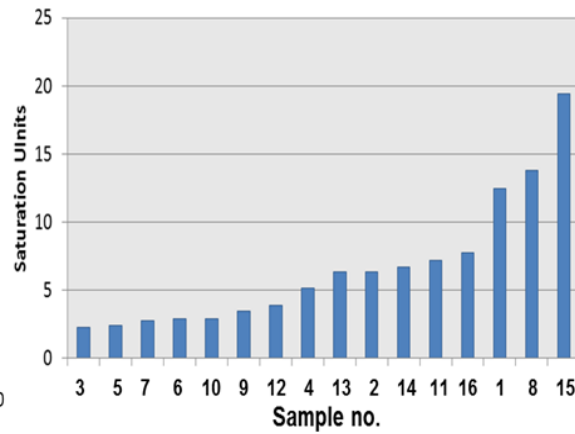
Figure 10: Root mean squared error of saturation predictions for all samples.

Figure 11: Capillary pressure curves derived from the global scaling factor function (purple curves) compared with the stress corrected mercury injection curves (red curves). The original ambient mercury injection curves are plotted in light blue.
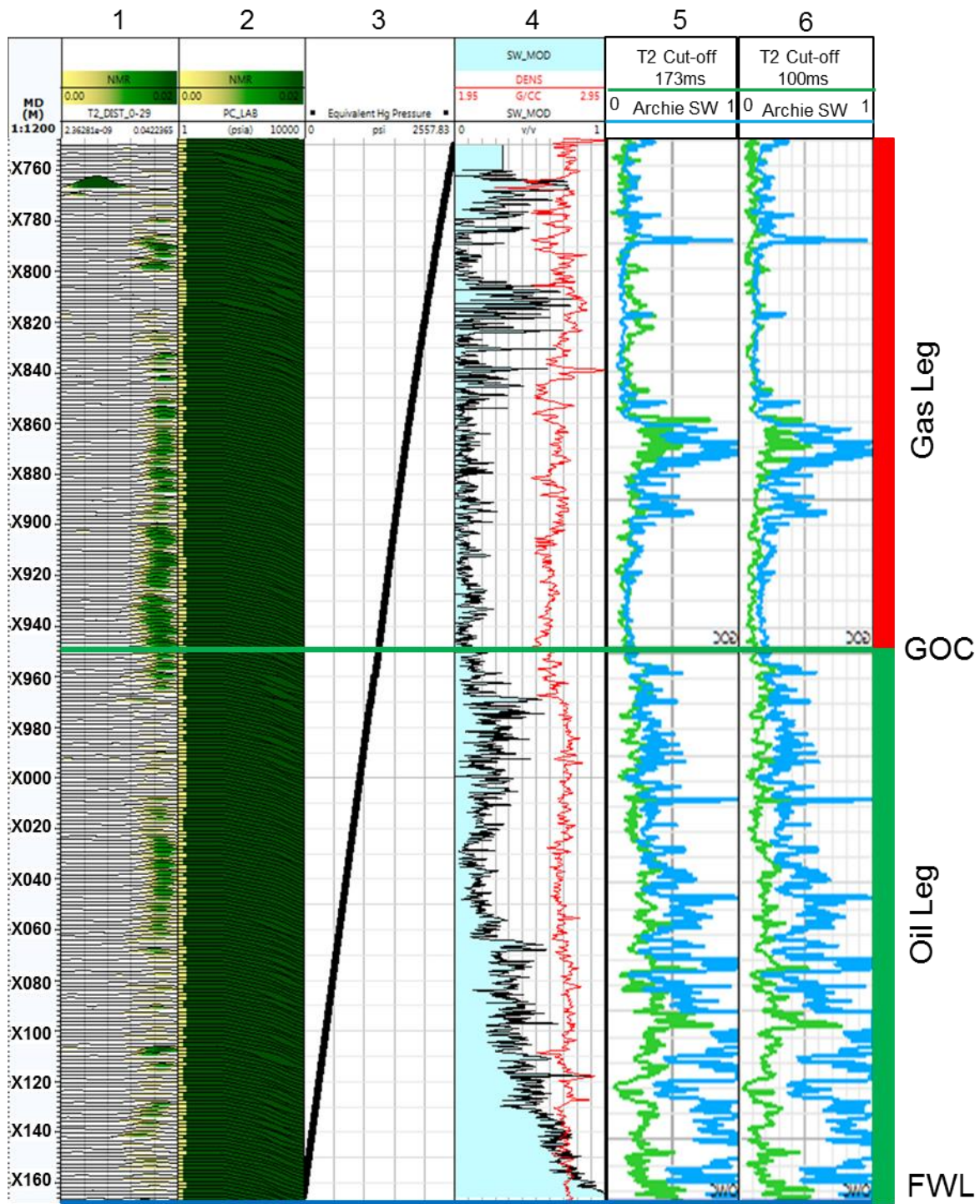
Figure 12: Final water saturation log (Track 4, shaded blue) derived using the NMR log & the global scaling factor model. Tracks 5 & 6 show the comparison of the Archie resistivity model water saturation (light blue) and water saturation from the NMR log with a SCAL optimised 173ms T2 cut-off & the default carbonate T2 cut-off of 100ms (green) respectively.

How to use Infrared Spectroscopy Mineralogy Data to Calibrate Logs.

Dr Adam K Moss – AKM Geoconsulting & Dr Gavin Hunt – Spectra-Map Ltd

This paper was prepared for presentation at the International Symposium of the Society of Core Analysts held in Vienna, Austria, 27 August – 1 September 2017

ABSTRACT

Over the last decade, hyperspectral infrared spectroscopy has become recognised as a useful technique for quantifying mineral content in core, plugs and cuttings. Mineral abundance can be defined on a sub-millimetre level. These fine scale data are extremely valuable for both geologists and core analysts. This paper aims to provide methodologies to use these high resolution mineral data to help calibrate common log interpretation models.

Log interpretation models all include constant parameters that relate to some property of the rock being tested. For example, to obtain shale volumes from gamma logs requires an estimate of the gamma response in both 'clean' sand and high shale content rocks. The log interpreter will make an educated guess as to the value of these parameters based on all available information. Knowledge of the rocks mineralogy greatly enhances the selection of these parameters. Awareness of minerals spatial distribution allows the log interpreter to vary/zone these parameters throughout the logged section.

Examples from reservoir sections will be shown to illustrate methods to calibrate a number of log interpretation models including, shale volume from gamma logs, density log porosity models and clay bound water from NMR. The fine scale mineralogy data are also used to evaluate mineralogical controls on permeability.

INTRODUCTION

Short Wave Infrared (SWIR) Imaging Reflectance spectrometry is a semi-quantitative mineral logging technique that can rapidly analyse core, cuttings or any other material without the need for sample preparation. Detailed descriptions of infrared spectroscopy theory and measurements can be found in Clark (1999) [1] & Hunt (2014) [2].

SWIR reflectance spectroscopy is a non-destructive, molecular-vibrational analytical technique that measures the absorption and reflection of infrared light at narrow and discreet wavelengths off a sample surface, Figure 1. Many minerals have their diagnostic molecular (overtone) vibrations in the SWIR; the most common vibrations are associated with subtle changes between the hydroxyl and cation molecular bonds common to the clays and phyllosilicates [1].

Detailed mineral information about the polytype and crystallinity of clays, such as illite, smectite, chlorite, kaolin polymorphs and crystallinity, Figure 2, can be identified by this technique. Other identifiable minerals include, micas, carbonates, sulphates, borates and also hydrocarbons from core and cuttings. The only constraint is that the mineral must have a diagnostic spectral reflectance signature within the 1.3-2.5 micron spectral range that the SWIR instrument operates. So, tectosilicates, such as quartz and feldspars cannot be uniquely identified. SWIR Reflectance spectroscopy does not provide whole-rock data and is therefore a semi-quantitative technique. Increased accuracy and precision in mineral quantification can be achieved using other data to calibrate, such as XRD or point count, but these data are also considered to be semi-quantitative.

Spectra-Map's SpecCam infrared imaging spectrometer acquires automated, high-throughput mineral information from drill core, cuttings, chips, plugs or hand samples. Round, half cut and biscuit cut core can all be measured. Logging is non-contact and non-invasive so no sample preparation is required. It collects high spatial resolution scan lines at regular intervals - consisting of 140 * 0.5mm square pixels – to create an infrared image over the core, Figure 3. Typically, 46,000 sample (pixel) points are acquired from a metre of core using the system.

Accurate modal percentage values can be derived from the SpecCam due to the large number of data points collected. To get a more accurate modal percentage value, the abundance of a mineral in a pixel spectrum is used to calibrate the results. Using modal counts by this method produce very accurate modal percentages, like those returned by other methods, such as XRD or petrology.

The spatially continuous data from SWIR reflectance spectroscopy allows us to determine trends that point sampling techniques, such as XRD, are unable to gauge. This makes SWIR reflectance spectroscopy of core potentially very useful for 'calibrating' log interpretation models.

Data Set
Block 21/16 is located on the Western Platform of the Central North Sea. Well 21/16-2 targeted the oil bearing Upper Jurassic Fulmar Formation. The base of the Fulmar sand and shale formation shows a deformed zone and rests unconformably on anhydrite, dolomite and halite of the Permian Zechstein Group.

Slabbed and resonated 'biscuit' slice core totalling 64.5m in length was available for the study. Thirty-five routine core analysis plugs were also available for testing. The previous operator included all the drilling, logging, core analysis and petrophysical reports in the data set. The core was scanned using the infrared imaging spectrometer at a resolution of one core width line scan per 3mm. The measured spectra were deconvoluted to determine core mineralogy and the modal percentage of each mineral calculated. Figure 4 shows the resulting data for part of core 3.

Shale Volume from Gamma Logs
Gamma log data can be used to estimate the volume of shale in a formation. This method assumes that the majority gamma rays are emitted from clays and fine grained sediments. The gamma log response from shales can be extremely variable. Therefore, the method relies on defining a formation specific minimum gamma value, that would be representative of a clean sand, and a maximum gamma value that defines a rock of a hundred percent shale [3]. Equation 1 defines the model:

Equation 1:

$$Vsh* = \frac{GR\ value\ (\log) - GR(\min)}{GR\ (\max) - GR(\min)}$$

Where: *Vsh* = Shale/clay volume (fraction)*
                  GR value (log) = Log gamma value (API)
                  GR (max) = 100% shale (API)
                  GR (min) = 0% shale (API)

In this study, we assume that the terms clay and shale are interchangeable. This is a reasonable assumption because in most clastic formations the minerals that are gamma emitters are predominantly clays. The shale/clay volumes obtained using Equation 1 can be considered to represent an upper bound for shale/clay volumes [3]. A more realistic shale/clay volume is obtained by using the non-linear relationship defined in Equation 2:

Equation 2:

$$Vsh = 0.33\ (2^{2Vsh*} - 1)$$

Where: *Vsh = Shale/clay volume (fraction)*
                  Vsh* = Shale/clay volume from Equation 1 (fraction)

Equations 1 and 2 are combined and the gamma minimum and maximum values at each depth obtained. This is done by using Excel Solver (optimiser) to determine the variable values needed to match the volume of shale/clay from Equation 2 with the total clay volume measured by the core spectroscopy, Figure 5. Note that the 0.5mm resolution spectroscopy total clay volumes are averaged over a 6 inch (15.24cm) moving average to convert the spectroscopy data to a similar measurement 'window' as the gamma log. The clay content is higher in the upper half of the core, above 7115ft, this corresponds to the Fulmar Formation. The carbonate rich Zechstein Formation is below 7115ft. The optimised gamma minimum & maximum values for the gamma shale/clay model are shown in Figures 6.

The operator reported that they used a gamma minimum value of 35 API and a maximum of 115 API. From the range of values seen in Figure 6 the use of single values for gamma minimum and maximum is inadequate to model the shale/clay volume over these formations. Knowing the optimised gamma minimum and maximum at each depth allows the log interpreter to use different values for each parameter on a zone by zone basis and hence obtain a more accurate shale/clay volume than single values for the whole formation.

Porosity from Density Logs

The density log measures the bulk density of a formation. This includes all the mineral grains and fluid. If the density of the mineral grains and fluid are known an estimate of porosity can be made using Equation 3 [3].

Equation 3:

$$\phi = \frac{\rho_{ma} - \rho_b}{\rho_{ma} - \rho_f}$$

Where: ϕ = *Total porosity*
          ρ_{ma} = *Grain (matrix) density (g/cc)*
          ρ_b = *Bulk (log) density (g/cc)*
          ρ_f = *Fluid density (g/cc)*

Note that the porosity calculated in Equation 3 is total porosity. The grain/matrix density parameter in Equation 3 is usually estimated by plotting core plug grain density against porosity and extrapolating to porosity equals zero. Figure 7 shows these plots for the limited number of available core plugs from the Fulmar and Zechstein Formations. Grain density values of 2.74g/cc and 2.96g/cc respectively are obtained.

The mineralogy data from the core spectroscopy scanner can be used to calculate grain/matrix density at each 3mm interval. A grain density for each mineral is defined and the relative proportion of each used to calculate average grain density at each depth. Because the spectroscopy core scanner does not detect quartz or feldspar we assume a grain density (2.65g/cc) for these 'undetected' minerals and include these minerals in the density calculation. The calculated and core plug grain density is plotted in Figure 8A. The calculated grain density match the plug values well in the Fulmar Formation (7087-7115ft) and Upper Zechstein (7115-7138ft). Below 7138ft the Zechstein is thought to contain high density anhydrite. Anhydrite was not one of the minerals included in the library of mineral spectra during deconvolution, hence it was not detected. The resulting calculated grain density below 7138ft is too low.

The spectrometer derived grain density has been used to calculate porosity using the density log and Equation 3. The operator quoted a fluid density of 0.64g/cc over the zone of interest. The resulting porosity is compared with the plug porosity in Figure 8B. The 'standard' density log porosity is also calculated using the grain density values from Figure 7. The spectrometer based density log porosity matches the plug porosity much better than the 'standard' density log porosity in most zones apart from between 7125-7135ft. Three QEMSCAN mineralogy data points from this zone are available, they contain more plagioclase feldspar than any other part of the core. The grain density of plagioclase ranges from 2.61 to 2.765g/cc. Plagioclase is one of the minerals not detected by this spectroscopy core scanner. Therefore, the assumed grain density of 2.65g/cc for the undetected minerals may need to be revised for this zone. Increasing the grain density of the undetected minerals in this zone would increase the calculated density log porosity closer to the measured plug values. More investigation into the mineralogy of this zone is required.

Clay Bound Water Volume from NMR
Definition of clay bound water volumes is vital to know when defining total and effective porosity. Clay bound water (CBW) volumes can be obtained from NMR data by applying a clay bound water T_2 cut-off. The standard clay bound water T_2 cut-off for clastic rocks is 3ms [4]. The clay bound water T_2 cut-off can be obtained for individual core plugs by inspection of the humidity oven dried sample T_2 distributions. These data are available for three Zechstein Formation plugs, Figure 9. These three plugs where also scanned in the infrared imaging spectrometer and mineralogy content obtained. The basic properties and clay volumes for the plugs are listed in Table 1. We can calculate a clay bound water volume if we know both the clay volume and the clay porosity. For the purposes of this workflow illustration we assumed a clay porosity of 20%. The calculated clay bound water volumes are reported in Table 1. These values are then used to estimate the clay bound water T_2 cut-off using the 'sum of amplitudes' method detailed in Moss & Jing (2001) [5], Table 1. The clay bound water T_2 cut-off are also plotted on Figure 9. The estimated clay bound water T_2 cut-off values define the clay bound water for these plugs reasonably well.

Plug	Depth (ft)	Helium Porosity (pu)	NMR Porosity (pu)	Klinkenberg Permeability (mD)	Humidity Oven Dried Water Saturation (%)	Spectroscopy Clay Volume (%)	Clay Bound Water Estimate (assume clay porosity = 20%) (%)	Clay Bound Water (CBW) T2 Cut-off (ms)
46	7121.0	7.87	7.78	0.36	13.95	2.59	6.654	4.47
50	7124.9	21.74	22.09	31.00	2.78	8.08	7.314	2.28
74	7149.1	4.45	3.58	0.01	15.17	12.39	69.265	5.62

Table 1: NMR plug data

Linking Mineralogy and Permeability
In many clastic formations clay and cement type and volume have a large effect on permeability. High resolution mineralogy data such as that produced by the infrared imaging spectrometer can be used to evaluate the mineralogical controls on permeability. A 21.5ft section of core had plug calibrated mini-permeability measurements made at 1cm intervals. A comparison of the calibrated mini-permeability data and the spectrometer derived mineralogy can be seen in Figure 10. An increase in total clay content corresponds to a reduction in permeability between 7099ft and 7108ft, Figure 10A. Between 7108ft and 7115ft permeability increases by fours orders of magnitude with very little variation in clay content. In this zone, no mineralogical controls on permeability could be found. The permeability increase is probably due to grain size/textural variation. The Zechstein Formation begins at 7115ft, below this depth dolomite controls permeability, Figure 10B.

The infrared imaging spectrometer can also detect solid and liquid hydrocarbon. Figure 10C shows the percentage of pixels that produced a hydrocarbon spectra versus depth. The hydrocarbon parameter appears to relate to permeability, although the link is weak. This effect could be due to increased hydrocarbon saturation in high permeability zones and or increased oil based mud filtrate in higher permeability rocks. Regardless of the cause the hydrocarbon parameter could be used as a useful proxy for permeability. This is an area of ongoing research.

CONCLUSIONS

Infrared imaging spectrometer measurements on core produce spatially continuous mineral data. Workflows have been developed to use these data to help calibrate log interpretation models and evaluate mineralogical controls on permeability. Spatially continuous mineral data of this type are invaluable to both geologist and petrophysicist.

ACKNOWLEDGEMENTS

REFERENCES

1. Clark, R. N., Chapter 1: Spectroscopy of Rocks and Minerals, and Principles of Spectroscopy, in *Manual of Remote Sensing, Volume 3, Remote Sensing for the Earth Sciences*, (A.N. Rencz, ed.) John Wiley and Sons, New York, p 3- 58, 1999.

2. Hunt, G., "The application of IR spectroscopy for real time mineralogical analyses of core and cuttings," Paper SCA2014-50, *Proc. International Symposium of Society of Core Analysts, (2014).*

3. Rider, M., *The Geological Interpretation of Well Logs*, Whittles Publishing, 2000.

4. Coates, G., Xiao, L., and Prammer, M., *NMR Logging Principles & Applications,* Halliburton Energy Services, 1999.

5. Moss, A. K. and Jing, X. D., "An investigation into the effect of clay type, volume and distribution on NMR measurements in sandstones," Paper SCA2001-29, *Proc. International Symposium of Society of Core Analysts, (2001).*
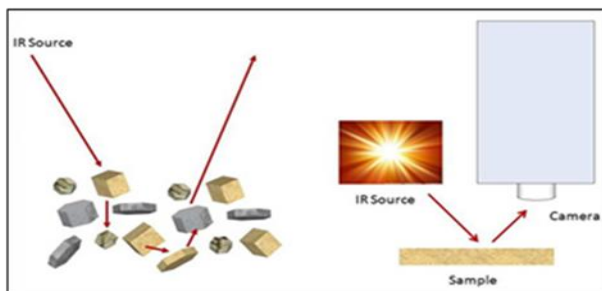
Figure 1: Reflectance spectroscopy light pathway
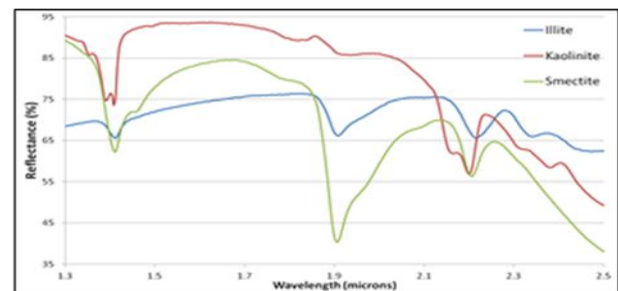
Figure 2: Example mineral reflectance spectra
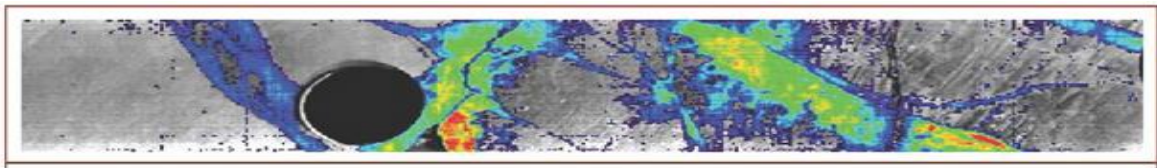
Figure 3: A section of core colour coded to show the presence and amount of chlorite infill in sandstone, against a greyscale IR background image.
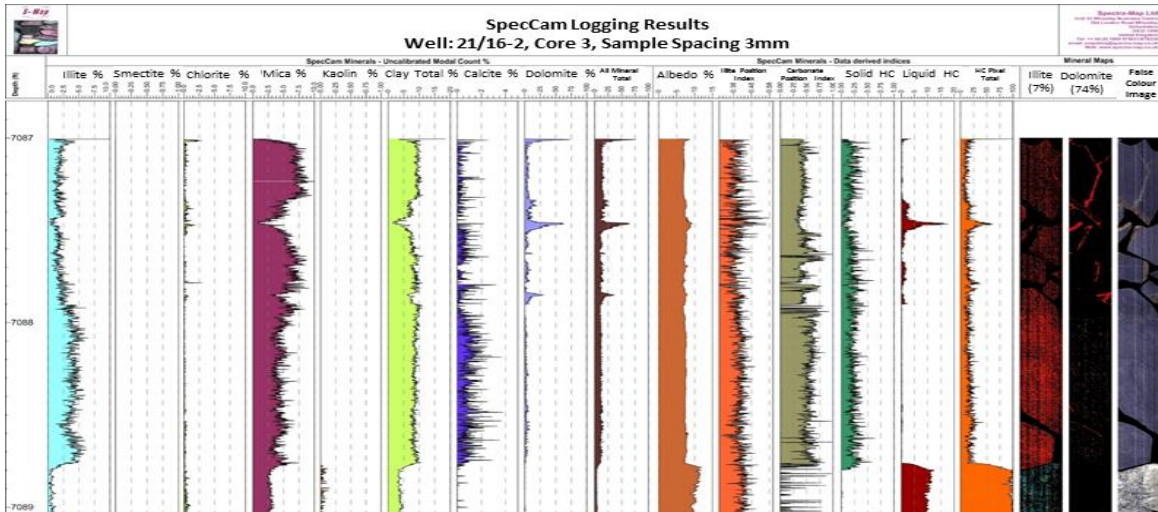
Figure 4: SpecCam infrared core logging results for well 21/16-2, core 3
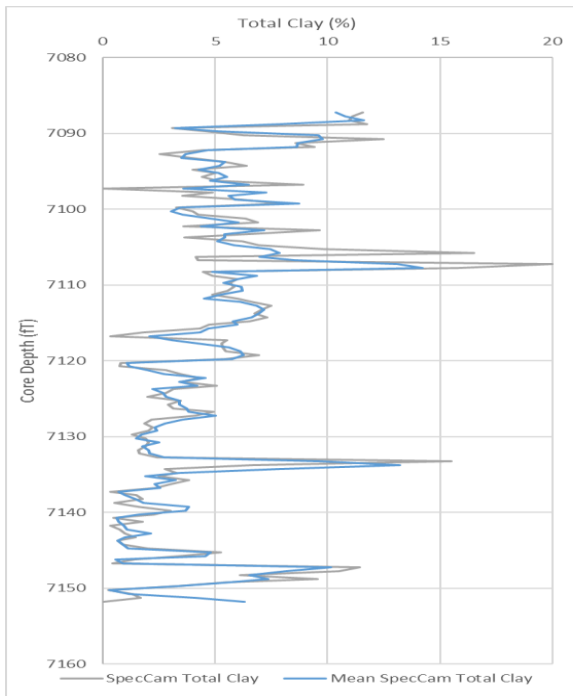
Figure 5: Spectrometer total clay volume versus depth
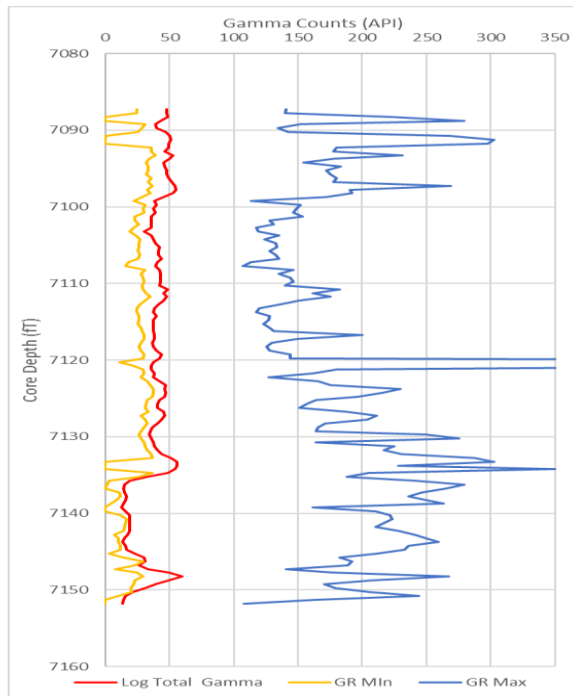
Figure 6: Total gamma log & optimised gamma min & max values versus depth for the non-linear gamma
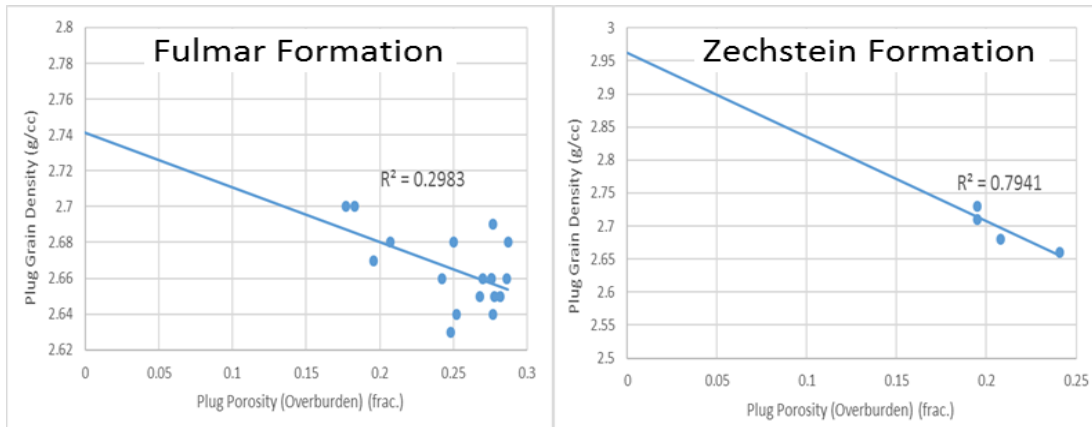
Figure 7: Plug grain density versus porosity for the Fulmar and Zechstein formations
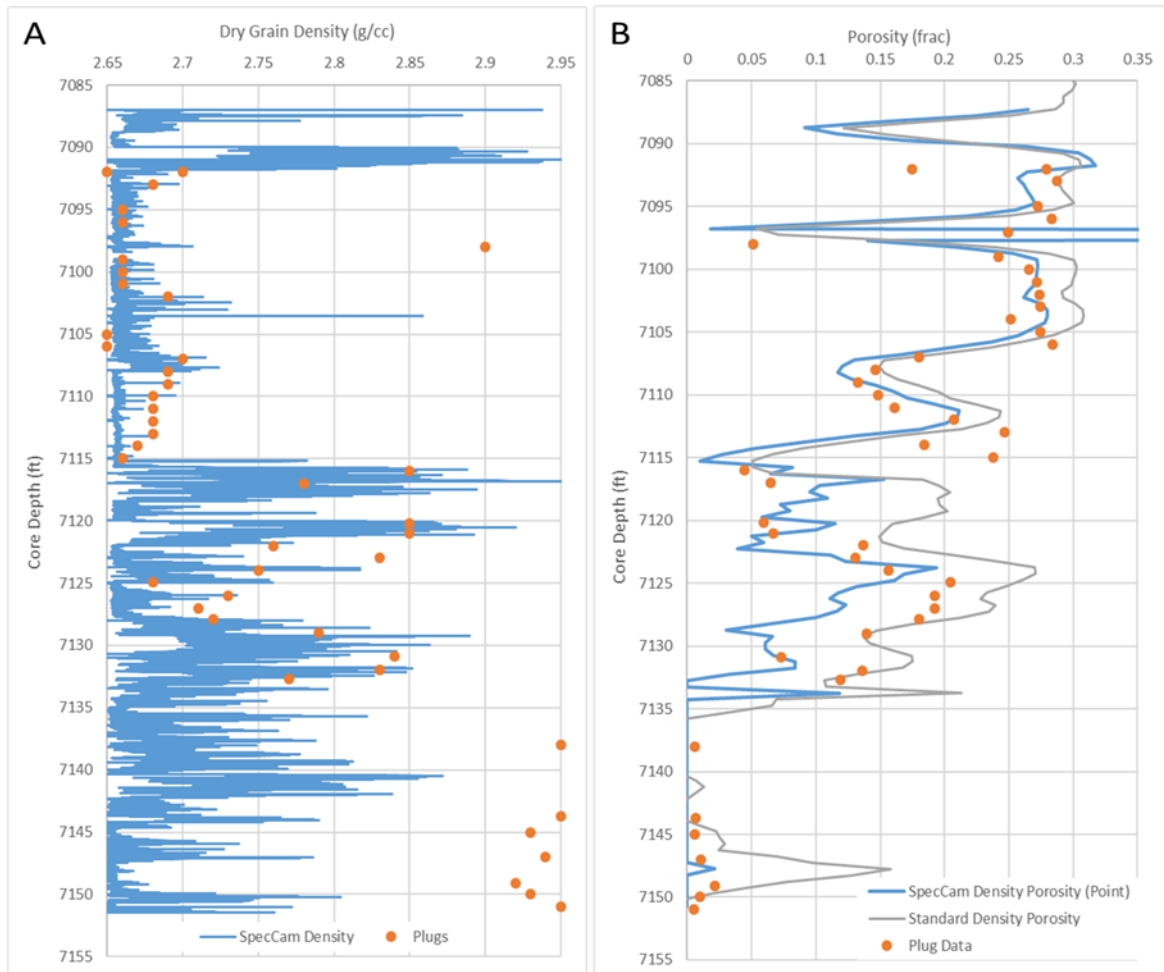
Figure 8A: Spectrometer mineralogy modelled and core plug grain density versus depth

Figure 8B: Density log and core plug porosity versus depth
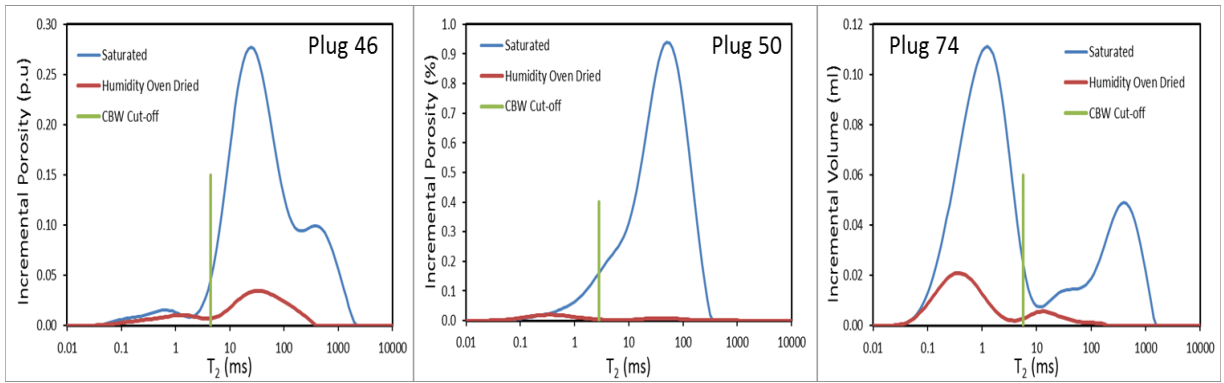
Figure 9: NMR T$_2$ distribution plots for three Zechstein Formation core plugs.
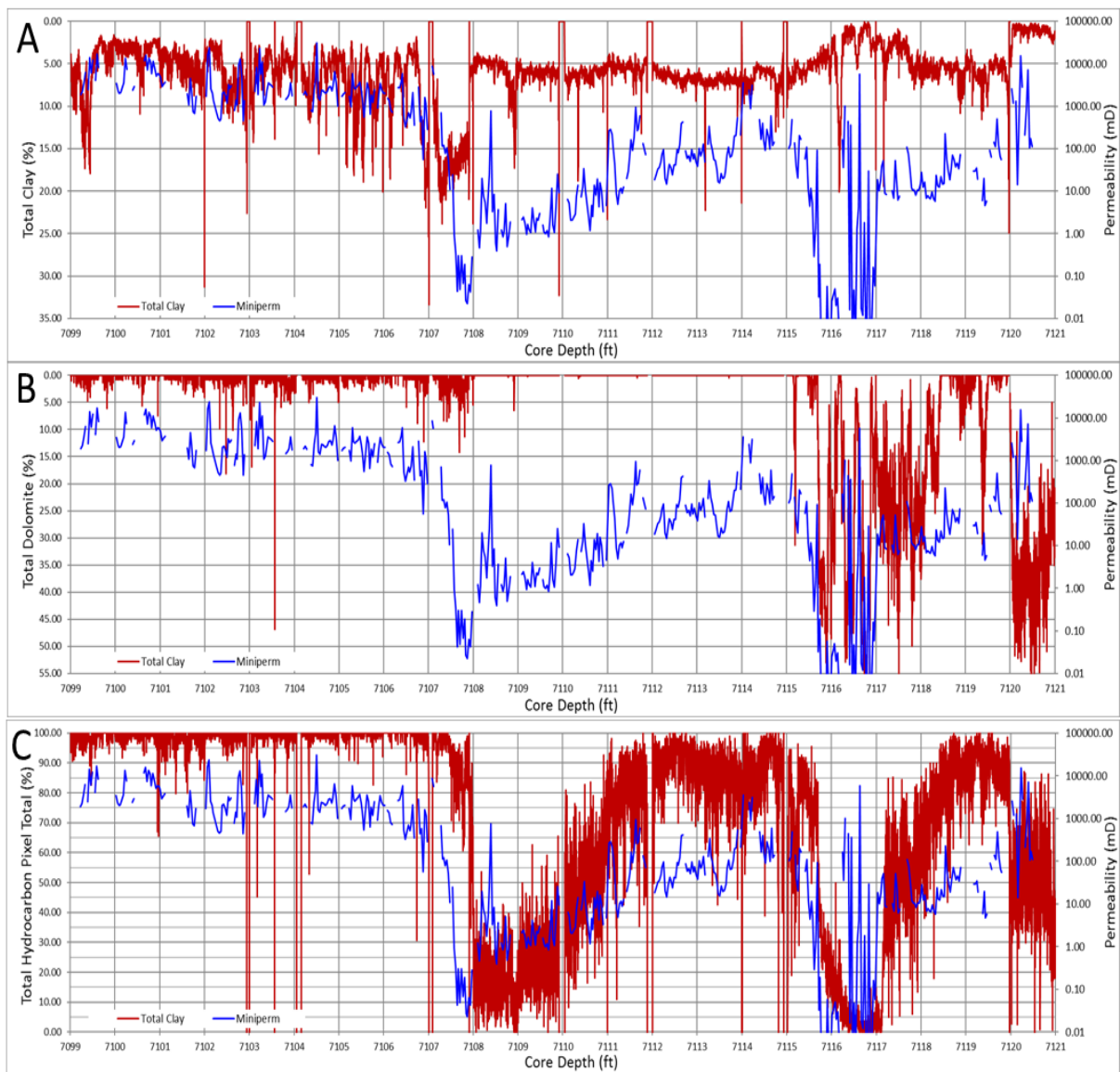
Figure 10: Permeability, mineralogy and hydrocarbon total versus depth.

Low Permeability Rocks:
Validation of Routine Core Properties

F. Pairoys[1], P. Gramin[2], W. Xu[1]
[1]Schlumberger, [2]BP

This paper was prepared for presentation at the International Symposium of the Society of Core Analysts in Vienna, Austria, 27 August- 1 September, 2017

ABSTRACT

There are several industry-accepted methods to obtain gas permeability of core plugs. The most commonly used method is the steady-state method. This method allows correction for Klinkenberg gas slippage and Forchheimer inertial effects. Alternatively, gas permeability is determined by the use of unsteady-state approaches, which include pressure falloff and pulse-decay methods. As the pulse-decay method is dedicated to permeability in the low range only, it is not discussed in this paper.

When comparing steady-state and pressure falloff approaches, the pressure falloff method is of interest because it offers shorter turnaround time and the ability to determine gas slippage-corrected permeability values in a single measurement. Another advantage of the method is that porosity and permeability measurements can be executed in one single automated run using specific apparatus. As a consequence, both measurements are completed by using the same gas, which is helium. At low permeability, while the apparent permeability measured with helium is higher relative to nitrogen apparent permeability, once it is corrected for gas slippage, both helium and nitrogen Klinkenberg permeability values should converge.

In this study, a set of various outcrop samples with known porosity and Klinkenberg permeability were investigated with the different measurement methods. The reference permeabilities were determined via four-point steady-state gas permeability with nitrogen. The same samples were then tested using the pressure falloff technique with injection of helium. Based on the Thomas and Pugh acceptance criteria, the helium Klinkenberg permeability was compared to the reference nitrogen steady-state Klinkenberg permeability. If the majority of the data results showed good agreement between the two methods, the helium permeability values for low permeability samples (< 1 mD) were found to be outside of the acceptance criteria. Re-measuring the sub-set of "out-of-acceptance-criteria" samples with nitrogen, the pressure falloff Klinkenberg permeability values decreased, falling within acceptable accuracy boundaries, but always slightly larger than the nitrogen steady-state reference values. According to the observations and in the frame of understanding the permeability difference, several hypotheses for further investigations are discussed.

INTRODUCTION

Reservoir porosity and permeability are parameters of importance in petroleum engineering. While porosity describes the reservoir storage capacity, permeability quantifies the ability of a rock to allow a fluid to pass through it.

Since 1856 when Darcy [1] defined fluid conductivity of a porous material in his famous technical report, permeability has become one of the most studied rock properties. In his study, Darcy states that flow rate is directly proportional to the pressure gradient, which is described by the Stokes' equation at the pore scale. But the viscous flows or Stokes' flows are a limited case. At higher flux for instance, i.e. when the dimensionless Reynolds' number becomes greater than 1, the inertial energy dissipation induced by the molecule accelerations in the tortuous porous network leads to higher pressure gradient than the one predicted by Darcy's law, as shown by Forchheimer [2]. The Forchheimer inertial resistance is very pronounced in high-permeability samples, but almost negligible in low-permeability samples. Unlike for inertial flow, the gas slippage effect known as the Klinkenberg effect [3] occurs in samples of low permeability. This effect becomes significant when pore size is comparable to the mean free path of the flowing gas, which depends solely on pore pressure in case of isothermal gas flow. Muskat [4] was the first to report that a significant discrepancy between gas permeability and water permeability can occur during experiments on the same sample. Klinkenberg showed that this difference was due to the invalidity of Darcy's law in a certain range of pressure. This phenomenon can be more or less pronounced according to the type of gas and the type of experimental tests - steady-state or unsteady-state approach.

The primary objective of this paper was to demonstrate that Klinkenberg permeability values derived from the unsteady-state pressure falloff and the steady-state method are equivalent for samples with permeability ranging from 10,000 mD down to 0.001 mD. Using 18 core plugs of various rock types, the reference Klinkenberg permeability (determined via the four-point steady-state method using nitrogen) were compared with permeability values obtained from the pressure falloff method using helium. Helium is traditionally the preferred gas when using the pressure falloff method because pore volume can be initially determined in the same apparatus, and both porosity and permeability can be measured during a single automated run. Helium and nitrogen Klinkenberg permeability values agree to each other for samples with Klinkenberg permeability greater than 1 mD, despite use of different measurement methods. This does not apply for samples of permeability less than 1 mD. All samples with Klinkenberg permeability below 1 mD were re-measured with nitrogen using the pressure falloff technique. Results of this testing led to further ongoing investigations based on several hypotheses that are provided in this paper.

BACKGROUND

Assuming an isotropic porous medium with unidirectional and horizontal flow and isothermal condition, the original Darcy's law for compressible gas corrected for inertial effect is described by Equation 1:

$$\frac{P_1^2 - P_2^2}{2P_q L} = \frac{\mu V}{K_g} + \beta \rho V^2 \tag{1}$$

where P_1 and P_2 are the upstream and downstream pressures, respectively, P_q is the pressure at which the gas flow rate is measured, L is the length of the porous material, μ is the gas viscosity, V is the gas velocity, K_g is the gas permeability, β is the inertial factor, and ρ is the gas density.

Even when inertial effects are taken into account, the gas permeability is still dependent on the mean free path of the flowing gas, due to the gas slippage phenomenon. Klinkenberg noted that mean free path λ of gas is inversely proportional to gas pressure P:

$$\frac{4c\lambda}{r} = \frac{b}{P} \tag{2}$$

where the constant c is slightly less than 1 [2] and b is referred to as the gas slippage factor, partly a rock property and partly a gas property. Experimentally, this has an effect on the measured apparent measured permeability and leads to a relation between the Klinkenberg corrected permeability K_{inf} at high pressure, which is equivalent to the liquid permeability, and the apparent gas permeability K_g:

$$K_g = K_{inf}\left(1 + \frac{4c\lambda}{r}\right) \tag{3}$$

Combining equations (2) and (3), the Klinkenberg relationship is obtained:

$$K_g = K_{inf}\left(1 + \frac{b}{P}\right) \tag{4}$$

Klinkenberg demonstrated that the equivalent liquid permeability K_{inf} could be extrapolated by plotting gas permeability against inverse mean pressure, the intersection of the slope extrapolated to infinite mean pressure results in the gas slippage-corrected permeability. This method is known as the common steady-state method. It requires several measurements at varying mean pressure (four-points in this study). For low-permeability rocks, this test can be time consuming, as it requires long time to achieve pressure equilibrium (relaxation time is proportional to the square of the sample size).

Other unsteady-state methods based on the analysis of the transient pressure signal are also

available and are known as pulse decay or pressure falloff methods. The pulse decay method is not discussed in this paper as it is dedicated to permeability range from 10 ηD to 0.1 mD only. The pressure falloff method, capable of measuring permeability in the range between 0.001 mD and 10 D, is characterized as an upstream gas reservoir that is brought to constant pressure (about 200 psi for this study). The pressured gas is then released to one end of the sample and vented to atmospheric pressure at the other end of the sample. The transient pressure signal is recorded versus time. A single pressure transducer is needed to record the pressure decrease in the upstream reservoir. The main advantages of pressure falloff over steady-state method is the considerable reduction in test duration since one single transient pressure signal is required to obtain the Klinkenberg permeability, the slippage factor b and the inertial factor β.

The equations and iterative scheme used to describe the pressure falloff method are quite complicated in comparison to the steady-state method. We refer you to the paper by Jones [6] and the Recommended Practice 40 published by the American Petroleum Institute, API RP40 [5] for a detailed description of the iterative workflow.

EXPERIMENTAL PROTOCOL

The reference measurements were performed on eighteen core plugs of different rock types. They were tested for porosity and nitrogen steady-state Klinkenberg permeability using 4-point measurements. Bulk volume was determined by the summation of ambient grain volume and pore volume obtained at 800 psi confining pressure using Boyle's law. Porosity was calculated from the calculated bulk volume and pore volume. Finally, the steady-state nitrogen Klinkenberg permeability was measured at the same 800 psi confining pressure.

A second series of measurements was then performed on the same 18 samples using the pressure falloff system. Both pore volume and Klinkenberg permeability were measured using helium at 800 psi confining pressure. Data results were then compared to the reference measurements from the first series.

Each measurement was then validated against the experienced-based acceptance criteria from Thomas and Pugh [7] as indicated in Table 1. As there is no acceptance criteria for permeability values less than 0.01 mD, a relative error of ± 35% was used.

Table 1: Core properties and data accuracy acceptance criteria applied.

Parameter Measured	Experience-based criteria	Statistically derived criteria
Core Porosity	± 0.5 p.u.	± 0.5 p.u.
Gas Permeability (from Thomas and Pugh [7])	< 0.01 mD: N/A, ± 35% in this paper 0.01 … 0.1 mD: ± 30 % 0.1 … 1 mD: ± 25% 1 … 50 mD: ± 15% 50 … 1,000 mD: ± 15%	< 0.01 mD: N/A 0.01 … 0.1 mD: ± 21% 0.1 … 1 mD: ± 21% 1 … 50 mD: ± 13% 50 … 1,000 mD: ± 8%

Note that quality assurance and quality controls were daily performed on the equipment: these included pore volume measurement of metallic cylinders with inner holes of different

diameters, and permeability measurements of sintered metallic standards covering a wide range of helium permeability. Every fifth sample was rerun for porosity and permeability repeatability. An automatic leak test was also performed while measuring pore volume and permeability to helium, as both properties are measured during a single automated run.

EXPERIMENTAL RESULTS

Porosity ϕ was first determined on eighteen samples of different rock types. Porosity values were found to be within the acceptance boundaries (Figure 1).
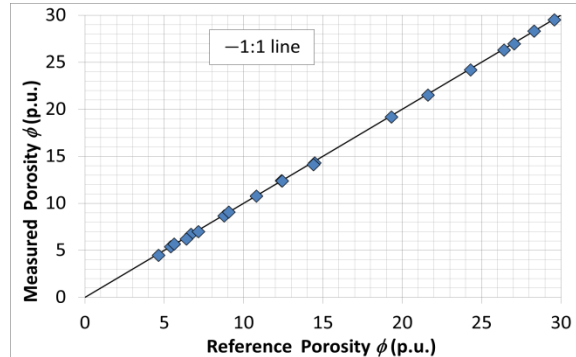
Figure 1: Cross-plots of reference data versus measured data for porosity.

Porosity data results are not discussed in the following results section: the quality of data did not raise any concerns to question further observations.

The unsteady-state pressure falloff Klinkenberg permeability was then measured on the same eighteen samples using helium at 800 psi of confining pressure.

Figure 2 presents the helium Klinkenberg permeability cross-plot between steady-state $K_{inf}[N_2\text{-ss}]$ reference values (X axis) and pressure falloff $K_{inf}[H_e\text{-pf}]$ measured values (Y axis). The Klinkenberg permeability relative errors and the acceptance criteria (Table 1) are also plotted.
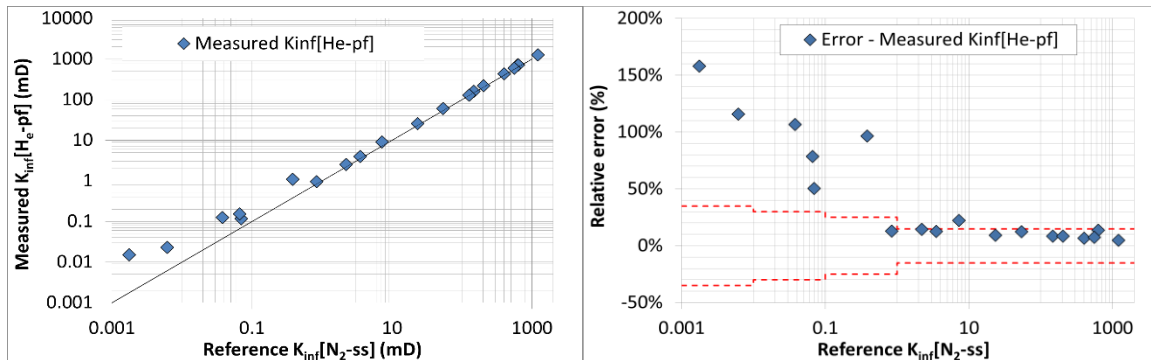
Figure 2: Cross-plots of helium Klinkenberg permeability vs. reference permeability (left) and associated plot showing data in relation to accuracy acceptance (right).

When measured with helium, the pressure falloff Klinkenberg permeability K_{inf}[He-pf] values for the majority of samples with less than 1 mD permeability fall outside of the defined accuracy limits, demonstrating higher permeability values relative to reference values. The trend shows increasing relative error as sample permeability decreases.

All out-of-acceptance-criteria samples were rerun using nitrogen. Figure 3 on the left presents the cross-plot of measured pressure falloff K_{inf}[N_2-pf]-K_{inf}[H_e-pf] (Y axis) and reference steady-state K_{inf}[N_2-ss] values (X axis). The associated Klinkenberg permeability errors based on Table 1 are also plotted on the right side of Figure 3.
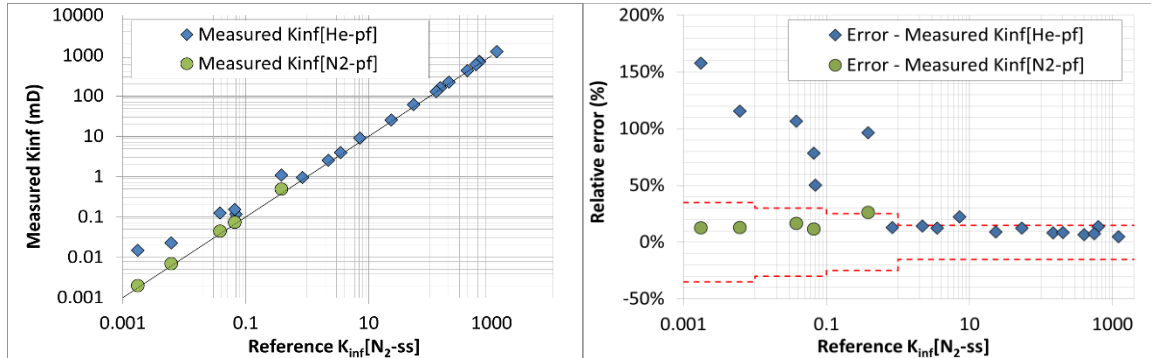
Figure 3: Klinkenberg permeability cross-plot and acceptance criteria plot (including five samples re-measured with nitrogen).

The re-measured nitrogen Klinkenberg permeability values decreased, plotting within the acceptable accuracy boundaries. These data show that pressure falloff Klinkenberg permeability is higher when using helium vs. nitrogen, especially in the range of 0.001 to 1 mD (K_{inf}[H_e-pf] > K_{inf}[N_2-pf]. Figure 3 also shows a slight but consistent overestimation of the nitrogen Klinkenberg-corrected permeability when using the pressure falloff method compared to the nitrogen Klinkenberg permeability using the steady-state approach (K_{inf}[N_2-pf] > K_{inf}[N_2-ss]).

DISCUSSION

This section is focused on summarizing the experimental observations and providing the possible reasons of the permeability difference on samples with Klinkenberg permeability less than 1 mD. The main observations from the study are:

-    Observation 1, K_{inf}[N_2-pf] > K_{inf}[N_2-ss]

The use of nitrogen and the pressure falloff method to measure Klinkenberg permeability K_{inf}[N_2-pf] of low-permeability samples (<1 mD) resulted in overestimated values with respect to nitrogen steady-state permeability K_{inf}[N_2-ss]. The discrepancy increased systematically with decreasing permeability. This was also observed by Rushing *et al.* [8].

-    Observation 2, K_{inf}[H_e-pf] > K_{inf}[N_2-pf]

In the low permeability samples, the use of helium in the pressure falloff method resulted in helium Klinkenberg permeability K_{inf}[He-pf] values that were higher than the nitrogen Klinkenberg permeability K_{inf}[N_2-pf] values, with the difference again increasing as

permeability decreased. Rushing *et al.* [8] reported the different observation while using the steady-state approach measured with back pressure (K_{inf}[H_e-ss] ~ K_{inf}[N_2-ss]).

The following discussion provides hypotheses for further investigations.

- Hypothesis for K_{inf}[N_2-pf] > K_{inf}[N_2-ss]:

The use of two different methods and models could explain the observed permeability discrepancy. According to Rushing *et al.* [8], observation 1) could be attributed to fundamental problem with the unsteady-state methodology. Lenormand *et al.* [10] suggested that the overestimation of permeability during the transient experiments, compared to the steady-state approach, could be due to the analytical integration process and the non-linear relationship between the uniform apparent gas permeability and the average pressure.

Another idea for future investigation is to test different flow regimes and related temperature variations. If the isothermal condition is violated, the balance between gas heat capacity, thermal diffusivity, adiabatic expansion, and the Joule-Thomson effect, according to the selected gas should be investigated, especially at the low permeability range (<1 mD) while applying several hundred psi of pressure release during the pressure falloff tests.

Gas molecule adsorption is another effect potentially contributing to lower the nitrogen Klinkenberg permeability under assumed isothermal conditions. Nitrogen adsorption onto the rock surface during the long term steady-state measurement could be more pronounced compared to a short time nitrogen exposure during the pressure falloff measurements.

- Hypothesis for K_{inf}[H_e-pf] > K_{inf}[N_2-pf]

Below 1 mD permeability, gas slippage effect is known to be more pronounced for helium than for nitrogen when measuring the apparent gas permeability. For the intrinsic Klinkenberg permeability, this should not be an issue [8]. Nevertheless, a consistently higher helium Klinkenberg permeability during pressure falloff tests is observed in this study. A possible "leakage" was discarded since the experimental system successfully passed the leak tests before and after each measurement.

While the iterative scheme used to solve the pressure falloff permeability can perhaps lead to this deviation, the nitrogen adsorption effect can also explain the reduction of permeability with pore size reduction due to nitrogen adsorption.

CONCLUSIONS AND RECOMMENDATIONS

Eighteen core plugs were tested for porosity and Klinkenberg permeability using the pressure falloff method. Data results were then compared with reference values established via numerous measurements and the steady-state approach for Klinkenberg permeability. Laboratory errors were calculated for each parameter. The measurement error was compared with accuracy criteria. Despite porosity data falling within the acceptance criteria, helium Klinkenberg permeability showed deviations exceeding the defined criteria in the low permeability range. The samples outside of the criteria acceptance limits were

re-measured for pressure falloff Klinkenberg permeability using nitrogen. All non-acceptable values significantly decreased and plotted within the defined accuracy boundaries. Nevertheless, nitrogen pressure falloff Klinkenberg permeability was found to be consistently greater than the steady-state reference values. Reasons for the discrepancies are discussed in the paper. Although a lot of experimental studies have already been performed in the past by different laboratories and research institutions, additional works need to be done to understand the permeability differences. For instance, a new gas transport model which will include an adsorption parameter is currently being tested: gas adsorption phenomenon is suspected to contribute to lower the nitrogen Klinkenberg permeability under assumed isothermal conditions especially in the low permeability range. The influence of the rock type on the observed effect will also be a subject of future investigation.

ACKNOWLEDGMENTS

REFERENCES

1. Darcy, H.: "Les Fontaines Publiques de la Ville de Dijon", Victor Dalmont, Paris, 1856
2. Forchheimer, P.: "Wasserbewegung durch Boden", Zeits. ver Deutsh Ing., **48**, 1731
3. Klinkenberg, L.J.: "The Permeability of Porous Media to Liquids and Gases", Drilling and Production Practice, 200-213, 1941
4. Muskat, M.: "The Flow of Homogeneous Fluids Through Porous Media", NY McGraw-Hill, 1937
5. Recommend Practices for Core Analysis, Report RP 40, 2nd edition, Exploration and Production Dept., American Petroleum Institute, 1998
6. Jones, S.C.: "A Rapid Accurate Unsteady-State Klinkenberg Permeameter", SPE Journal, 383-397, 1972
7. Thomas, D.C., Pugh, V.J.: "A Statistical Analysis of the Accuracy and Reproducibility of Standard Core Analysis", The Society of Core Analysts, SCA1989-8701, 1989
8. Rushing, J.A., Newsham, K.E., Lasswell, P.M., Cox, J.C., Blasingame, T.A.: "Klinkenberg-Corrected Permeability Measurements in Tight Gas Sands: Steady-State Versus Unsteady-State Techniques", SPE 89867, ATCE, Houston, 2004
9. Schaff S.A., Chambre P.L.: "Flow of Rarefied Gases", Princeton University Press, 1961
10. Lenormand, R., Bauget, F., Ringot, G.: "Permeability Measurement on Small Rock Samples", SCA2010-32, Halifax, Nova Scotia, Canada, 2010

A new and modular laboratory core holder for high-precision measurements with low frequency impedance spectroscopy on natural rocks

Matthias Halisch[1], Thomas Grelle[1], Sarah Hupfer[1], Jan-Thorsten Blanke[1], Carlos Lehne[1]

[1] Leibniz Institute for Applied Geophysics (LIAG), Dept. 5 Petrophysics & Borehole Geophysics, Stilleweg 2, D-30655 Hannover, Germany

ABSTRACT

Investigating complex electrical properties of natural rocks and soils by using spectral induced polarization (SIP, i.e. "low frequency impedance spectroscopy, typically from 1 mHz up to 100 kHz) is of high research interest for all pore space and boundary surface specific processes and properties between the matrix and the pore fluid. The deduction of hydraulic and pore space related structural properties, as well as the correlation of SIP-data with CAL and SCAL data is recently in the focus of research. In the past ten years, especially the development of new measurement equipment has greatly improved the quality of the results. Nevertheless, no uniform standards and technical requirements exist for adequate core holders for the determination of SIP related parameters. Furthermore, most of the core holders do not take different materials (unconsolidated, consolidated) or different core geometries (diameter, length, cross-section shape) into account. Within the department Petrophysics and Borehole Geophysics of the Leibniz Institute for Applied Geophysics (LIAG), a new and modular core holder for measuring complex electrical properties has been developed, in order to address the mentioned needs and functionalities. In addition, the core holder is characterized by a significantly reduced residual noise, so that also rock materials, which feature low frequency phase effects (such as Fontainebleau or Nivelsteiner Sandstone), can be investigated with high measurement accuracy and excellent reproducibility. The core holder is currently pending for patent and already commercially available for interested working groups.

INTRODUCTION

Spectral Induced Polarization (SIP) measurements (i.e. "low frequency" impedance spectroscopy, typically conducted in a frequency range from 1 mHz up to 100 kHz) are used in many different ways to characterize natural rocks and soils. Main foci of interest are the enhanced characterization of the causes of polarization effects in sedimentary rocks. The interactions between the matrix-fluid-system and within the electrical double layer as well as the correlation with petrophysical parameters, such as specific surface area, permeability, and pore radii distribution as derived from mercury intrusion capillary pressure data are considered. A variety of polarization models, either grain based or pore based, have been developed over the past years to describe the polarization effects of

sedimentary rocks [e.g.: 1; 2; 3; 4; 5; 6; 7]. The electric resistivity, as well as electric conductivity are both described as complex quantity values. As explained by [8], complex conductivity (σ^*) of a rock sample is determined by measuring the magnitude of conductivity ($|\sigma|$) as well as the phase shift (φ), relative to a reference resistor. The real (σ') and imaginary (σ'') part of σ^*, which represent the ohmic conduction and polarization charge transport mechanisms, respectively, are directly determined from impedance measurements. The phase shift thereby is defined as:

$$\varphi = \arctan(\sigma''/\sigma') \approx \sigma''/\sigma' \text{ (for } \varphi < 100 \text{ mrad)}, \qquad (E1)$$

which is by convention defined as a positive value in conductivity space. Generally, complex conductivity models are based on two contributing conductivity terms, as denoted amongst others by [9]:

$$\sigma^* = \sigma_{el} + \sigma^*_{surf}. \qquad (E2)$$

The first term (σ_{el}) represents the conductivity of the electrolyte filled interconnected pore space, whereas the second term (σ^*_{surf}) reflects conduction and polarization within the Electrical Double Layer (EDL) of the interconnected pore (matrix) surface, respectively. In addition, also electromagnetic coupling effects at frequencies > 1 kHz, which are caused by inductive and capacitive reciprocities, need to be taken into account for impedance spectroscopy (IS) measurements [10]. Because of this, SIP-measurements are mostly performed in between frequencies of 1 mHz to 1 kHz or even lower (100 Hz). The SIP method itself has developed from classic frequency domain IP, and takes both, electric resistivity as well as phase shift into account. This method has become a potentially good tool for the enhanced characterization of rocks as well as of soils, due to the dependence of the measurements on the internal surface area (S_{por}) of the investigated materials [e.g.: 11]. Additionally, strong efforts have been taken into account to predict permeability by using SIP method [12; 13;].

Hence, it is favorable to study a wide frequency range with SIP-measurements, in order to cover the majority of IP related parameters, effects and processes. Nevertheless, most of the SIP devices produce accurate and reliable data only within a limited frequency range. These issues have been addressed by the manufactures, which have been improving their equipment consequently over the last years [14]. Unfortunately, the type of electrode system used leads to restrictive limitations, even if the electronics of the instrumentation fulfills state of the art demands [15]. For 2-electrode systems, the electric coupling between sample and electrodes may cause transfer impedance effects, which furthermore cause frequency dependent disturbances on a wide frequency range (from 1 mHz up to the kHz domain). For 4-electrode setups, electromagnetic coupling, especially between connection wires, also lead to frequency dependent errors, typically above frequencies of 100 Hz to 1 kHz. Besides these instrumental influences, specific core holder effects, such as coupling issues of the sample-electrode system, self-polarization effects of the electrode material, leakage currents alongside the core surface and evaporation of the saturating fluid have severe impact upon the quality of SIP data. Taking this as motivation, the concept for the new core holder was created accordingly.

CONCEPT

According to these challenges, the sample holder needs to be constructed completely out of non-polarizable and brine-resistant material (i.e. free of any metal), including non-polarizable potential and non-oxidizing (i.e. electro-chemically inert) current electrodes. Besides these technical requirements, more universal demands exist and need to be addressed as best as possible. Hence, such a core holder should be easy to handle, as far as possible maintenance free, compactly designed and able to fit different core sizes without changing the entire measurement setup. Figure 1 showcases a schematic exploded assembly drawing of the general concept and design of the SIP core holder.
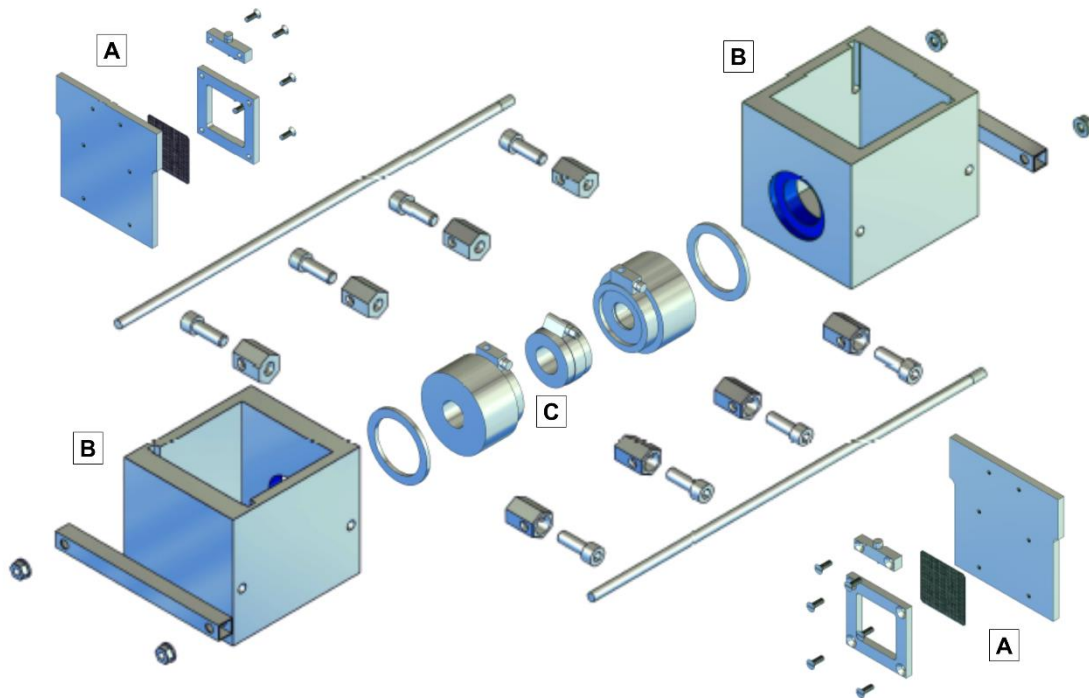
Figure 1: Schematic exploded assembly drawing of the core holder / cell for SIP measurements. (A): current electrode holder with platinum net electrodes; (B): acrylic glass electrolyte reservoirs; (C): potential electrode adapter for silver chloride ring-electrodes and core holder sleeve.

The SIP core holder is basically made out of three main modules: the current electrodes (A), the electrolyte (brine) reservoirs (B), and the core sleeve with the potential electrode adapters (C). The current electrodes are made out 8 x 8 cm of platinum net, with a mesh aperture of 125 µm to guarantee a highly uniform distributed current density along the medial core holder axis. The electrode holders are made out of acrylic glass and can be connected to the power generator with a 2 mm socket plug. The assembled current electrodes are raked into a guide rail, located at the edge of the electrolyte reservoirs (B). The reservoir tanks are connected with two guide rails on each side, which allows to adjust the electrode distance flexibly, depending upon the length of the core plug. Main part of the SIP cell is the sample sleeve (C), including two adapter for the potential electrodes, which are made as a ring-electrodes. Thus we can achieve the best possible signal-to-noise

ratio as well as the best possible coupling towards the sample material and the saturation fluid, respectively. This module can be easily replaced to address a variety of plug lengths and diameters (length: 30 mm to 80 mm; diameter: 20 mm to 45 mm). The electrodes are made out of silver wire (99.9 % purity; diameter 0.4 mm), which can be chlorinated in order to prevent polarization effects on the electrode surface. For this, the electrode can be connected to a power supply by using the 2 mm socket plug, which usually is used to measure the potential signal. Then, the adapter module is placed in a vessel filled with hydrochloric acid and a small alternating potential is applied (1 – 2 V for about 5 – 10 minutes). By doing this, the silver is electrochemically oxidized:

Oxidation: $2\,Ag + 2\,HCl \rightarrow 2\,AgCl + 2H^{+} + 2\,e^{-}$ (E3)
Reduction: $2\,H^{+} + 2\,e^{-} \rightarrow H_2$ (E4)
Total: $2\,Ag + 2\,HCl \rightarrow 2\,AgCl + H_2$ (E5)
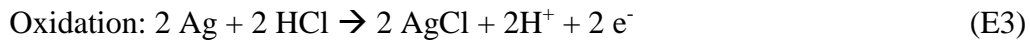
This chloride layer depletes over time and several measurements, and hence needs to be reproduced occasionally. By experience, every 5 samples this procedure needs to be repeated. Additionally, the sample is placed in a chemically inert silica rubber sleeve, which is tightened with a small hose clamp. By doing this, the rubber adapts towards the sample surface and prevents creeping currents alongside the skin surface. Furthermore, this sleeve seals the entire potential electrode module towards saturation fluid leakages, as soon as the reservoir tanks are clutched along the guide rails. Figure 2 shows the core holder as side face view. The position of the electrodes and of the sample are highlighted.
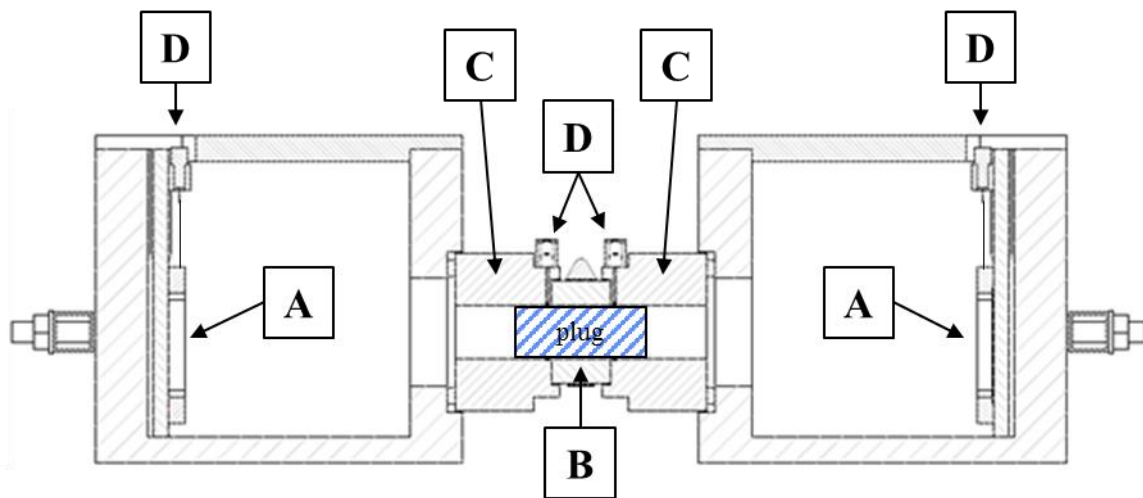
Figure 2: Schematic side view of the SIP sample cell. The current electrodes (A) are located in the electrolyte reservoirs. The sample is fixed within the silica rubber sleeve (B), which his fixed by the potential electrode adapters (C). Current as well as electric potential can be measured by 2 mm socket plugs (D).

RESULTS & DISCUSSION

For testing of the new sample cell, a simple experiment has been conducted. The main goal of this improved cell was to reduce the "noise", i.e. measuring errors caused by coupling, creeping currents and self-polarization of the electrodes, to the largest possible extent. Hence, a non-polarizable reference material should be used, in this specific case, a sodium-chloride solution with approximately 100 mS/m specific conductivity. In an ideal case, the measured phase shift should be equal to zero. A small round robin test between three different institutions (LIAG, Bundesanstalt für Materialforschung und –prüfung = BAM, Bundesanstalt für Geowissenschaften und Rohstoffe = BGR, and Clausthal University of Technology = TUC) has been performed to achieve independent results for different 4-electrode SIP core holders. The results for the phase shift measurement for a frequency range from 1 mHz to 100 kHz (according to equation E1) are presented in figure 3.
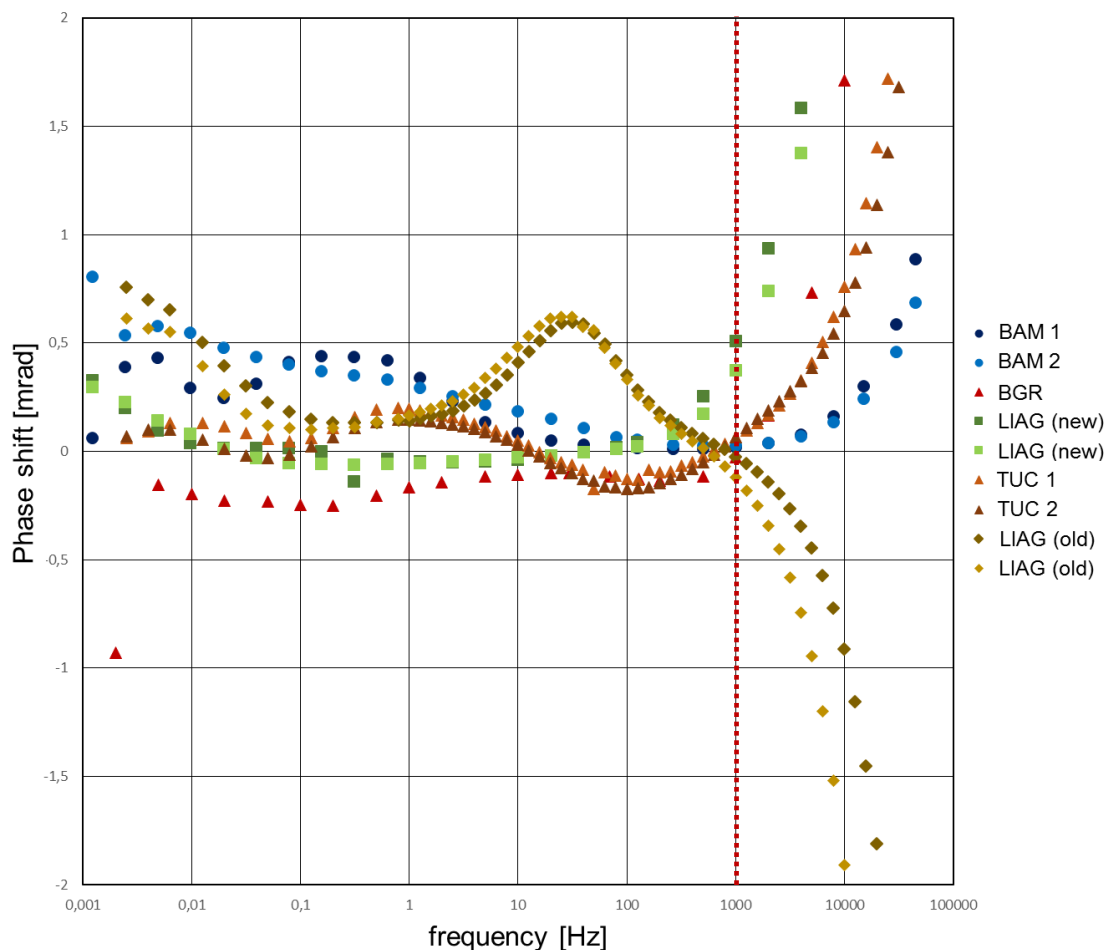
Figure 3: Representation of the results of the phase shift measurements on sodium-chloride solution with a specific conductivity of approximately 100 mS/m for the small round robin test amongst three different institutions (LIAG, BAM and TUC). The dashed red line indicates the threshold frequency, from which upwards electro-magnetic coupling effects dominate the measurements.

As showcased, all three core holders feature low to very low "noise-effects" (± 0.5 to 1 mrad). For frequency ranges > 1 kHz, electro-magnetic coupling effects dominate the results, and hence should be neglected. The new LIAG SIP core cell features the overall lowest "noise-level" (< 0.25 mrad) for all of the used cells, closely followed by the TUC (< 0.5 mrad) and the BAM (< 1 mrad) core holder. For comparison, the old LIAG core holder (also a 4-electrode core holder, but with non-optimized electrode configuration and platinum electrode material) has been measured as well (brownish diamonds), showcasing the most pronounced noise (phase maximum around 20 Hz) for all of the investigated cells.

SUMMARY & CONCLUSIONS

For this paper, the authors have showcased the motivation and the concept for the development of a new core holder for high-precision spectral induced polarization measurements on natural rocks (figure 4). The modular construction enables flexible handling of different sample sizes and geometries, combined with high user-friendliness and low maintenance efforts. The results of the round robin test have shown, that the LIAG cell has pushed the edge of "low-noise" SIP core holders a little bit further, featuring the lowest phase shift of all investigated cells. Hence, this new setup is particularly suitable for investigating rocks that feature low phase effects such as the Fontainebleau Sandstone as presented in [16, this SCA proceedings] with high accuracy and with high reliability.
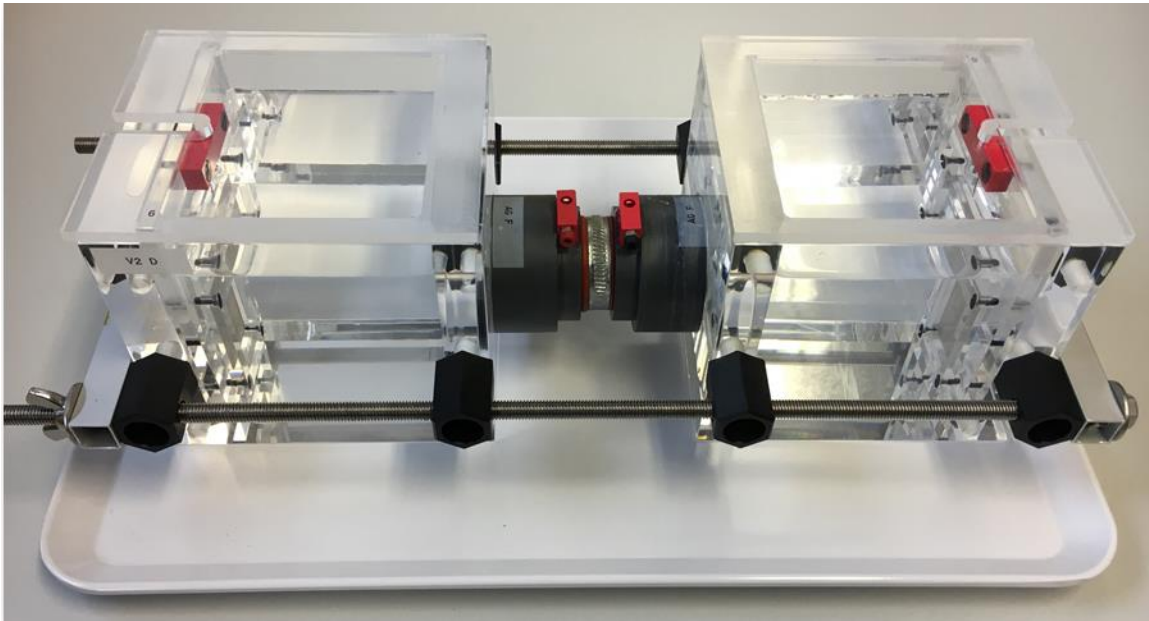
Figure 4: The actual version (Mk. II) of the LIAG 4-electrode core holder and measuring cell for high-precision SIP-measurements.

OUTLOOK

The ongoing development and improvement of this type core holder for spectral induced polarization measurements is one main task for the Petrophysics working group at the LIAG. Consequently, the current version of this core holder has been registered for patent, and the successful announcement is expected to arrive soon. Already now, the SIP cell is commercially available at the LIAG. In a next development step, this core holder is being adopted and re-configured (e.g. the potential electrode layout) for measuring the complex electrical properties of unconsolidated material (soils, unconsolidated sands and clayey materials). Additionally, this core holder will be prepared to fit the requirements to measure NMR spectra without removing the sample material from the SIP sample holder (i.e. no metal parts are allowed to be placed inside of the NMR magnet). Furthermore, the parallel measurement of the streaming potential as well as the application of overburden stress (tri-axial, up to 300 bar, i.e. approx. 4400 psi) are under development.

Acknowledgements

REFERENCES

1. Schwarz G. 1962. A theory of low-frequency dispersion of colloidal particles in electrolyte solution. *Journal of Physical Chemistry* 66, 2636-2642, doi:10.1021/j100818a067.
2. Scott J.B.T. and Barker R.D. 2005. Characterization of sandstone by electrical spectroscopy for stratigraphical and hydrogeological investigations. *Quarterly Journal of Engineering Geology and Hydrogeology* 38, 143-154.
3. Tarasov A. and Titov K. 2007. Relaxation time distribution from time domain induced polarization measurements. *Geophysical Journal International* 170, 31-43, 10.1111/j.1365-246X.2007.03376.x.
4. Kruschwitz S., Binley A., Lesmes D. and Elshenawy A. 2010. Textural controls on low frequency electrical spectra of porous media. *Geophysics* 75, WA113-WA123, doi:10.1190/1.3479835.
5. Weller A., Slater L., Nordsiek S. and Ntarlagiannis D. 2010. On the estimation of specific surface per unit pore volume from induced polarization: a robust empirical relation fits multiple data sets. *Geophysics* 75, No.4, p.WA105-WA112
6. Revil A., Koch K. and Hollinger K. 2012. Is the grain size or the characteristic pore size that controls the induced polarization relaxation time of clean sands and sandstones. *Water Resources Research* 48, W05602, doi:10.1029/2011WR011561
7. Weller A. and Slater L. 2015. Induced polarization dependence on pore space geometry: empirical observations and mechanistic predictions. *Journal of Applied Geophysics* 123, 310-315 doi:10.1016/j.appgeo.2015.09.002.
8. Weller A. and Slater L. 2012. Salinity dependence of complex conductivity of unconsolidated and consolidated materials: comparisons with electrical double layer models. *Geophysics* 77, No.5, p. D185-D198

9. Vinegar H.J. and Waxman M.H. 1984. Induced Polarization of shaly sands. *Geophysics* 49, p. 1267-1287

10. Marshall D.J. and Madden T.R. 1959. Induced polarization, a study of its causes. *Geophysics* 24, p. 790-816

11. Börner F.D., Schopper J.R., and Weller A. 1996. Evaluation of transport and storage properties in the soil and groundwater zone from induced polarization measurements. *Geophysical Prospecting* 44, p.583 ff

12. Revil A. and Florsch N. 2010. Determination of permeability from spectral induced polarization in granular media. *Geophysical Journal International* 181, No.3, p.1480-1498

13. Weller A., Nordsiek S., and Debschuetz W. 2010. Estimating permeability of sandstone samples by nuclear magnetic resonance and spectral induced polarization. *Geophysics* 75, No.4, p. E215-E226

14. Zimmermann E., Kemna A., Berwix J., Glaas W., Münch H. and Huisman J. 2008. A high-accuracy impedance spectrometer for measuring sediments with low polarizability. *Meas. Sci. Technol*. 19 (10), 105603.

15. Volkmann J., and Klitzsch N. 2015. Wideband impedance spectroscopy from 1 mHz to 10 MHz by combination of four- and two-electrode methods. *Journal of Applied Geophysics*, 114 (2015), 191-201, http://dx.doi.org/10.1016/j.japgeo.2015.01.012.

16. Halisch M., Kruschwitz S., Weller A., Mensching B. and Gürlich L. 2017. Maximizing the core value – joint investigations with special emphasis on complex electrical conductivity give new insights into Fontainebleau Sandstone. *Society of Core Analysts (SCA) International Symposium*, Vienna, Austria, SCA2017-053

LOW SALINITY WATER FLOODING IN CARBONATE ROCKS – DISSOLUTION EFFECT

M. Altahir, M. Yu, F. Hussain,

The University of New South Wales, Sydney, NSW, Australia

ABSTRACT

Low Salinity Water flooding in carbonate rocks has emerged recently as a new research trend and a promising method to increase oil recovery. Wettability alteration of mixed wet carbonates to more water-wet is thought to be the main mechanisms controlling the increase in oil recovery. There is very limited data available on dissolution effect during low salinity water flooding. This paper presents a simple experimental approach to investigate carbonate dissolution during single phase low salinity water injection.

We used a low permeability (0.5 mDarcy) limestone core from an oilfield located in Iraq. The core was fully saturated with seawater (TDS = 44,580 mg/l). We then injected seawater, 3 times diluted sea water, 6 times diluted seawater and deionized water. Pressure drop across the core was monitored and produced water samples were collected continuously. The results show increases in Ca^{+2} ion concentration and in pH in the effluent which indicate limestone dissolution. The effluent pH increased up to 9 which can potentially increase oil recovery due to wettability alteration or alkaline effect. Scanning Electron Microscope (SEM) images of the inlet and outlet of the core indicate that dissolution can release carbonate fines which are then trapped near the core outlet. In spite of fines migration, we did not notice a significant change in core permeability and this can be attributed to the simultaneous effect of both dissolution and fines migration.

INTRODUCTION

A number of laboratory and field studies show the effectiveness of low salinity waterflooding to improve oil recovery [1-5]. Various mechanisms have been identified for low salinity flooding [6-8]. However, most of these mechanisms are associated with low salinity water flooding in sandstones. For carbonate rocks, wettability alteration is thought to be the major mechanism [6]. The wettability alteration mechanism is usually associated with ionic exchange associated with SO_4^{2-}, Mg^{2+} and Ca^{2+} ions.

Yousef, Al-Saleh [1] achieved 19% total incremental oil by injecting seawater with sequentially reducing the salinity. They also observed a decrease in pressure drop across

the composite core. This change in pressure drop was attributed to change in pore geometry due to limestone rock dissolution which was enhanced the connectivity of micro-pores in the cores. Mahani, Keya [9] concluded that LSWF can exists without any dissolution and it is primarily driven by surface charge change by conducting zeta potential and contact angle measurements on limestone core.

Chandrasekhar and Mohanty [10] argued that Mg^{2+} and SO_4^{2-} are the main potential determining ions which change wettability. The sea water containing Ca^{2+} ion in the absence of Mg^{2+} and SO_4^{2-} was unable to change wettability of the rock. They concluded that dissolution and multi-ion exchange are the main mechanisms behind incremental oil recovery. In this paper we describe an innovative approach to investigate dissolution and dissolution induced fines migration. First, discuss the experimental facility and rock characterization. Then the results of a single phase experiments are presented. SEM images are used to show dissolution effect.

EXPERIMENTAL PROCEDURE

Rock and fluids systems

We used reservoir heterogeneous limestone core from an Iraqi oil field. From the XRD and XRF results, the core consists of 96.6% Limestone and 3.4% Dolomite with no clay. The SEM images of the cores did not show any fractures. The core initially has the dimensions of 65 mm length and 2.55 mm diameter. Due to sample length limitation of the Scanning Electron Microscope instrument, we cut the core to half. Scanning Electron Microscope (SEM) images were taken for the inlet and the outlet of the composite core. SEM images of before and after experiment flooding were taken for comparison purposes and to study the potential of dissolution on changing the rock geometry. We use synthetic sea water (SW) in the experiment (TDS = 44,580). Before the experiment the cores were fully saturated with the SW.

The composite cores were mounted in the coreholder at 50 deg C. We used filter paper at the inlet and outlet to make sure no fines comes out of the core in the effluent. So, any incremental ions concentration in the effluent only represents dissolution. An injection rate of 0.1 cc/min was maintained during the experiment. Initially sea water was injected followed by 3x diluted, 6x diluted and deionized water. For each of the four injection concentration, at least 15 pore volumes (PV) were injected. Pressure drop across the composite cores was recorded continuously. The produced brine samples were collected at the outlet and pH was measured immediately to minimise interaction with atmospheric CO_2. Then ionic chromatography was run on all of the effluent samples to quantify produced anions and cations concentrations. After the flow experiment SEM images were taken again for the inlet and outlet of the core plugs.

RESULTS

Permeability and Ionic Concentrations

Figure 1 shows the measured permeability results. There is no significant change in permeability during the experiment. However, during the de-ionized water injection, the permeability changes slightly from 0.55 mD to 0.60 mD. This could be attributed to pores enlargement due to dissolution of carbonate in de-ionized water. To further confirm dissolution we conducted ion chromatography and inductively coupled plasma optical emission spectrometry (ICP-OES) analysis on the produced water samples. All the cations' and anions' concentrations were measured with an uncertainty of 0.1 mg/l and 1.0 mg/l, respectively. The concentration of Ca^{2+} is given in Figure 2. Figure 3 shows the total dissolved solids (TDS) concentration. There is no significant difference between the injected and produced TDS profile except the deionized water injection. During the de-ionized water injection, TDS produced is 20-30 mg/l compared to 0 mg/l injected. During this phase, Ca^{2+} show increased concentration further supporting the dissolution of calcite. The equation of the dissolution is:

$$CaCO_3 + H_2O \leftrightarrow Ca^{+2} + HCO_3^- + OH^- \tag{1}$$

Equations-1 shows that the dissolution should increase the pH of the produced solution. pH measurements of the produced water samples (Figure 4) show an increase of pH to 9.5 during de-ionized water injection. Such high pH values can cause alkaline effect which may increase oil recovery during two-phase displacements. For higher salinity injection phases SW, 3x diluted and 6x diluted; pH values increase up to 8.

SEM images and Fines migration

We imaged 40 subsections of the injection and production faces of the composite core. These subsections included one or multiple pores. All of the images show fines migration. The suggested mechanism of these fines migration is dissolution. The dissolution effect breaks the bond between the grain and the rock surface which leads to fines mobilization and subsequent blockage. Fines migration in sandstones have been studied in a number of previous studies [5, 11-14]. Fines migration can improve volumetric sweep efficiency and hence oil recovery by partially or fully blocking the high permeability channels. Our SEM images show that such mechanism can exist in carbonate rocks Figure 5. Unlike previous sandstone studies[5, 6], we did not observe any permeability drop during the flow experiment (Figure 1). This is probably due to the coexistence of dissolution and fines migration. Fines migration and subsequent blockage causes permeability to drop but dissolution causes permeability to increase.
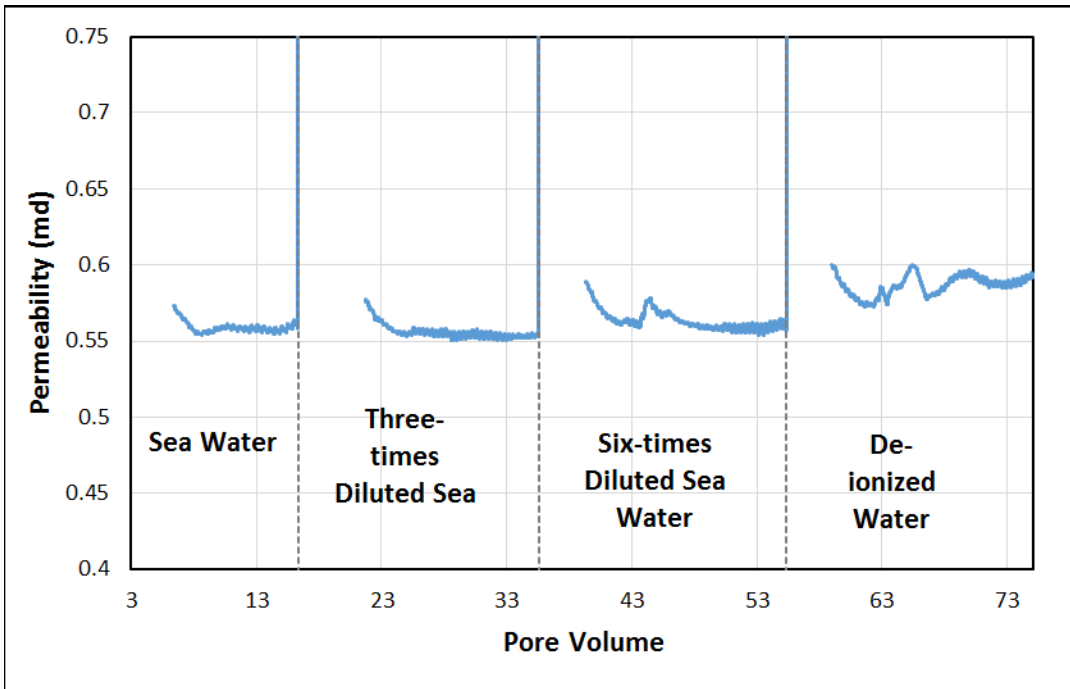
Figure 1: Laboratory measurements of permeability
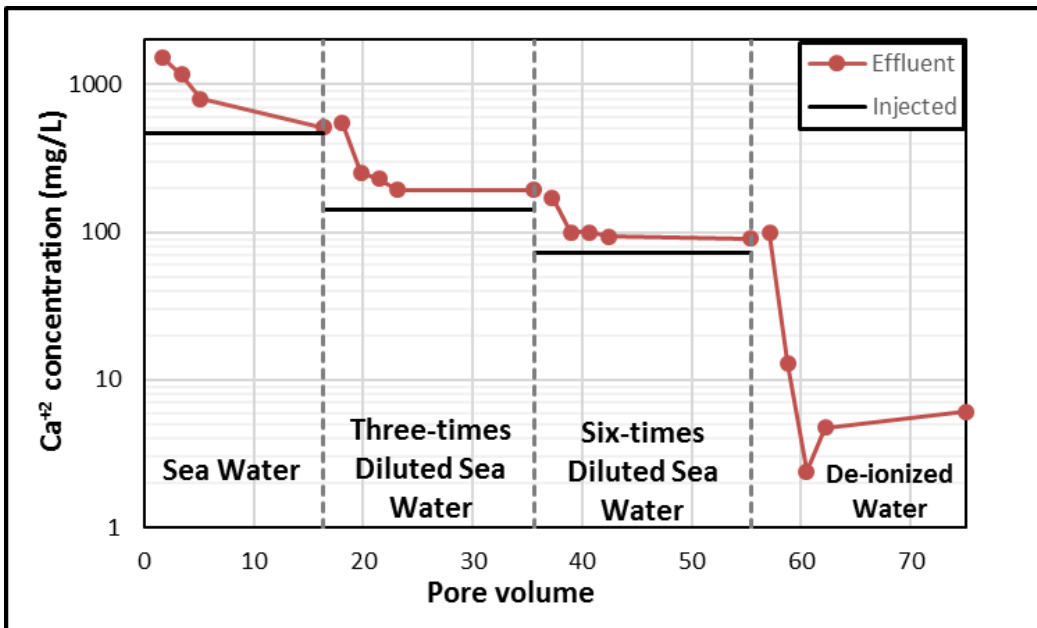
Figure 2: Ca^{2+} concentration of produced water samples
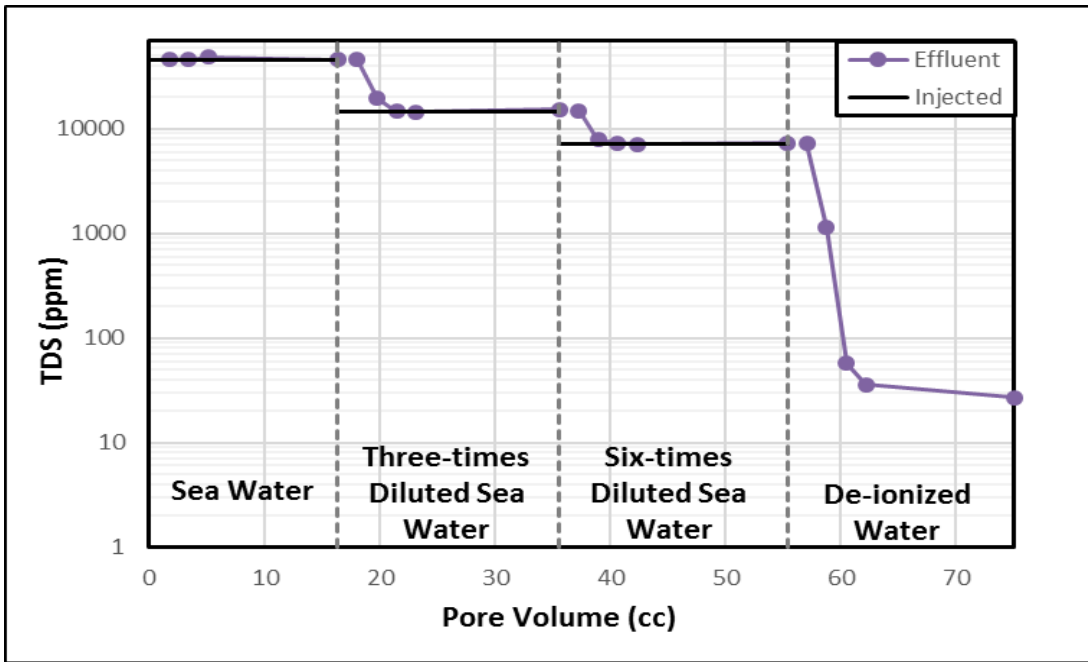
Figure 3: Total concentration of produced water samples
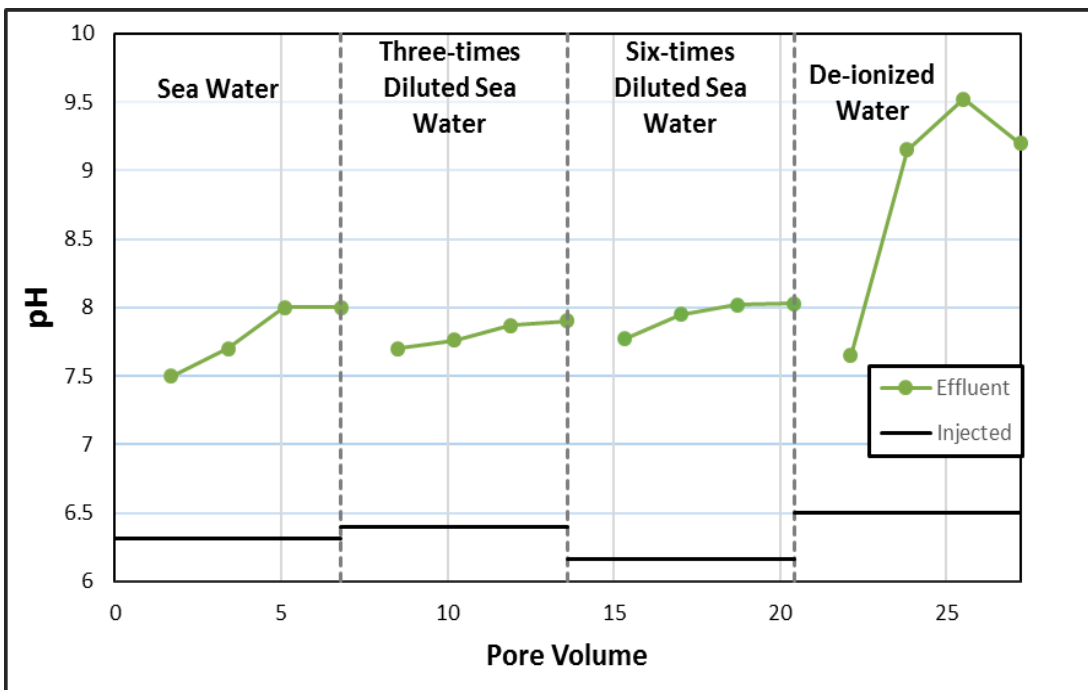
Figure 4: pH of produced water samples
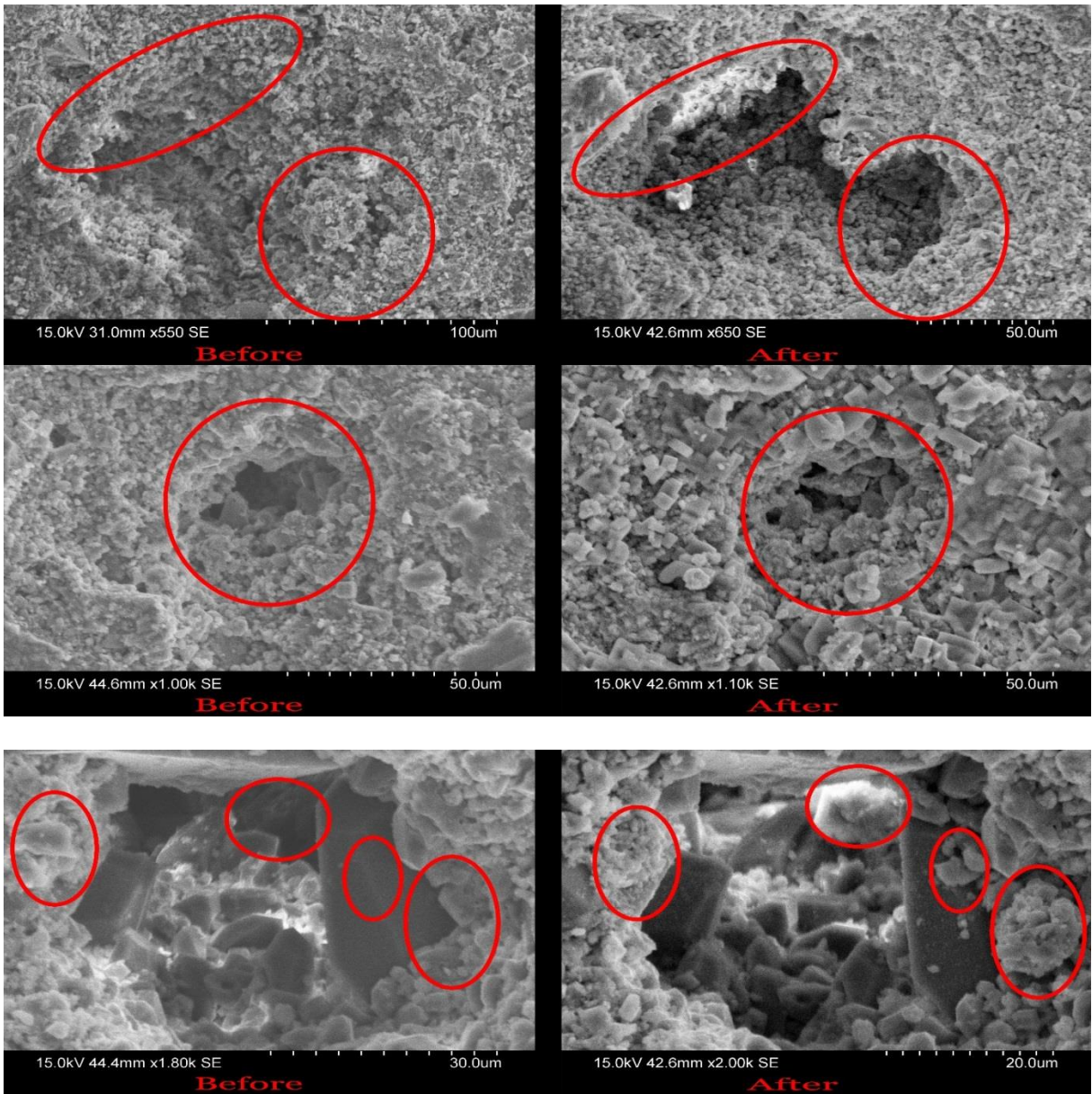
Figure 5: SEM images of the core before and after injection – pore enlargement and fines migration

4. Conclusions

We present a single phase experiment to investigate dissolution and fines migration mechanisms in carbonate rocks. An integrated core and fines characterization approached was adopted to investigate dissolution and fines migration effects.

- Increase in the produced Ca^{+2} ions concentration show dissolution effects.
- SEM images of the rock showed considerable fines migration which is most likely induced by dissolution. The dissolution and dissolution induced fines migration can result in pore enlargement or partial or complete pore blockage.
- Despite fines blockage, no significant change in the pressure drop was observed. The increase in pressure drop due to fines migration and the decrease in pressure drop due to dissolution can compensate each other.
- An increase in pH was observed which further supports dissolution of carbonate. During de-ionized water injection pH increased to 9.5. Such a high pH increase can affect oil recovery due to alkaline effect or wettability alteration. Rock dissolution, pH change and fines migration may significantly affect oil recovery from carbonate rocks.

Reference

1. Yousef, A.A., et al., *Laboratory investigation of the impact of injection-water salinity and ionic content on oil recovery from carbonate reservoirs.* SPE Reservoir Evaluation & Engineering, 2011. **14**(05): p. 578-593.
2. Yousef, A.A., et al. *Smartwater flooding: industry's first field test in carbonate reservoirs.* in *SPE Annual Technical Conference and Exhibition, San Antonio, Texas.* 2012.
3. Zahid, A., A.A. Shapiro, and A. Skauge. *Experimental studies of low salinity water flooding carbonate: A new promising approach.* in *SPE EOR Conference at Oil and Gas West Asia.* 2012. Society of Petroleum Engineers.
4. Al-Shalabi, E.W., K. Sepehrnoori, and G. Pope. *Geochemical interpretation of low salinity water injection in carbonate oil reservoirs.* in *SPE Improved Oil Recovery Symposium.* 2014. Society of Petroleum Engineers.
5. Zeinijahromi, A., et al., *Effect of fines migration on oil–water relative permeability during two-phase flow in porous media.* Fuel, 2016. **176**: p. 222-236.

6.   Al-Shalabi, E.W. and K. Sepehrnoori, *A comprehensive review of low salinity/engineered water injections and their applications in sandstone and carbonate rocks.* Journal of Petroleum Science and Engineering, 2016. **139**: p. 137-161.
7.   Dang, C., et al. *Modeling and Optimization of Low Salinity Waterflood*. in *SPE Reservoir Simulation Symposium*. 2015. Society of Petroleum Engineers.
8.   Sheng, J., *Critical review of low-salinity waterflooding.* Journal of Petroleum Science and Engineering, 2014. **120**: p. 216-224.
9.   Mahani, H., et al. *Driving Mechanism of Low Salinity Flooding in Carbonate Rocks*. in *EUROPEC 2015*. 2015. Society of Petroleum Engineers.
10.   Chandrasekhar, S. and K. Mohanty. *Wettability Alteration with Brine Composition in High Temperature Carbonate. Paper SPE 166280*. in *SPE Annual Technical Conference and Exhibition, New Orleans, Louisiana, USA*. 2013.
11.   Bedrikovetsky, P., et al. *Porous media deposition damage from injection of water with particles*. in *ECMOR VIII-8th European Conference on the Mathematics of Oil Recovery*. 2002. Freiberg Germany.
12.   Nguyen, T.K.P., A. Zeinijahromi, and P. Bedrikovetsky, *Fines-migration-assisted improved gas recovery during gas field depletion.* Journal of Petroleum Science and Engineering, 2013. **109**: p. 26-37.
13.   Zeinijahromi, A., T.K.P. Nguyen, and P. Bedrikovetsky, *Mathematical Model for Fines-Migration-Assisted Waterflooding With Induced Formation Damage*. Spe Journal, 2013. **18**(3): p. 518-533.
14.   Oliveira, M.A., et al., *Slow migration of mobilised fines during flow in reservoir rocks: Laboratory study.* Journal of Petroleum Science and Engineering, 2014. **122**: p. 534-541.

Low-Salinity Waterflood with non-Polar Oil: the effects of fines migration excluding the wettability alteration effects

M. Yu[a], F. Hussain[a], P. Bedrikovetsky[b]

a The University of New South Wales, Sydney, NSW, Australia
b The University of Adelaide, Adelaide, SA, Australia

ABSTRACT

Numerous controversial results on the effect of fines migration on oil recovery with low salinity (LS) waterflood have been reported. However, the current mathematical models do not allow separating the effects of wettability alteration and fines migration from coreflooding tests. We perform LS flooding for non-polar oils, where the rock remains fully water-wet independently of salinity, so the effects can be attributed to fines mobilization and straining only.

Robust characterization of the rock sample and injected and produced fluids allows us to identify and evaluate fines migrations mechanism. Experiments are performed on Berea (400 mDarcy) sandstone. Before the experiments, the plugs are characterized using XRD, XRF, SEM imaging. Then, the first plug is subjected to single-phase water injection with varying salinities from 4 to 0 mass% NaCl. The second sister plugs are used to perform oil drainage and subsequent high salinity (4 g/L) water flooding. Then the oil drainage experiment is repeated and finally low salinity waterflooding is performed. During each experiment, pressure drop across the plugs, fluids' production rate, breakthrough salinities and fines concentrations are measured continuously. Elemental analysis is run on the produced fluids to see if there are any dissolution effects. Next, the fines are separated from the produced fluids from both plugs and SEM-EDX analysis used to identify the composition of the collected fines. Finally, post-experiment SEM are taken. These SEM are registered with the images taken before the experiments to visualize any fines migration. Single phase experiments show at least an order of magnitude drop in permeability. Two-phase experiment show 50% reduction in water permeability and 5% increase in the oil recovery.

INTRODUCTION

Low-salinity effect (LSE) has been found by many researchers that additional amount of oil can be recovered by switching from injecting high-salinity water to low-salinity water [1-3]. There are multiple mechanisms taking place jointly during LSE. An initial mixed-wet condition is always formed when polar compound is present in oil [4-6]. Polar compounds in oil can be adsorbed on clay particles so clay will be oil-wet. Mixed-wet

condition is formed when quartz adsorbs water, while clay adsorbs oil [2]. In such case, LSE can increase the percentage of mobile oil. Wettability alteration is considered the main mechanism affecting oil recovery [7] while fines migration has been a controversial topic.

Fines migration, as one of many proposed mechanisms for LSE, explains that fines particles are mobilised when torque balance exerted on these particles is broken during alteration of salinity [8]. These particles then travel in the suspension and some of them will be strained by narrow flow channels that have smaller diameters than particle size. Such pore blockage firstly occurs in high-swept zone, thus redirects water into less-swept zone, therefore, more water is forced to flush low-swept zone than before. Re-distribution of flow channel can increase local swept efficiency thus contribute to improved ultimate recovery. This is also called fines migration and straining.

To model fines migration and straining, Bedrikovetsky, Siqueira [9] proposed a maximum retention function model. Maximum retention model only considers changes in flow conditions that can make particles roll again, such as weakening of electrostatic force due to changing of salinity. To integrate with this model, wettability change should be deactivated. In this paper, we performed a set of low-salinity waterflooding experiments by using paraffinic non-polar oil. So, the results are limited to fines mobilisation and straining only.

EXPERIMENT PROCEDURE

1. ROCK AND FLUID CHARACTERISATION
1.1 Rock and fluid properties
Berea sandstone was selected (porosity 22.6%, Initial permeability = 340 mD). One plug (Berea-1: L = 3.6 cm, D = 2.6 cm) was used for single-phase test with a purpose of confirming fines migration and its impact on permeability. Another plug (Berea-2: L = 3.6 cm, D = 2.6 cm) was used for two-phase test. **Error! Reference source not found.**.

Soltrol 130 (an isoparaffin solvent) was used to prevent occurrence of wettability alteration. The absence of polar-components in soltrol will prevent the formation of initial mixed-wet condition [2].Brines of 8 different salinities (4%, 3%, 2%, 1%, 0.5%, 0.25% and 0 % in mass concentration) were prepared by using de-ionized water.

1.2 Mineral identification
10 gram of Berea core was milled and dried. The powder was analyzed under X-ray diffraction and fluorescence to qualify and quantify existing minerals. Mineralogy of Berea core is presented in
Table *1*.

Table 1 Mineral composition and percentage of Berea sandstone

Mineral Name	Composition (%wt)
Quartz	84.80 ±8.9
Kaolinite	6.11 ±0.48
Muscovite	4.90 ±0.3
Microcline	4.18 ±0.33

1.3 Pore scale imaging

Scanning Microscope Images were taken on both injection and production sides of Berea-1. Both injection and production faces of the plug were coated with carbon to enhance electron conductivity. SEM 3400I facility at UNSW Australia was used for imaging. Images were taken at 50 different locations on both injection and production faces of the core plug.

2. CORE FLOODING TEST

Both plugs were pre-saturated with 4% (mass concentration) NaCl brine. Wet weight and dry weight were measured to determine pore volume gravimetrically. The experiment was performed at 25ºC. The core outlet was open to atmospheric pressure. Initial permeabilities were firstly measured by injecting the same 4% brine at a constant rate. Experiment schematic is shown in **Error! Reference source not found.**.
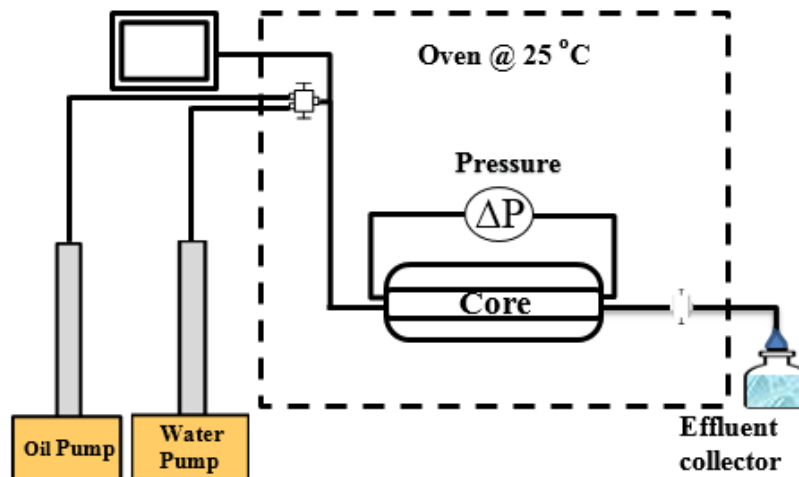
Fig 1 Schematic presentation of experimental apparatus.

2.1 Single-phase coreflooding with stepwise reduced salinity

Berea-1 plug was subjected to a continuous waterflood (0.25 *ml/min*) with the sequential salinity reduction. The entire process took 3138 pore volumes and 8 stages, starting with 4% brine and ending with de-ironized water. Permeability drop with respect to salinity reduction is showed in **Error! Reference source not found.**. Water samples were collected in small vials with caps for particle concentration and type analyses.
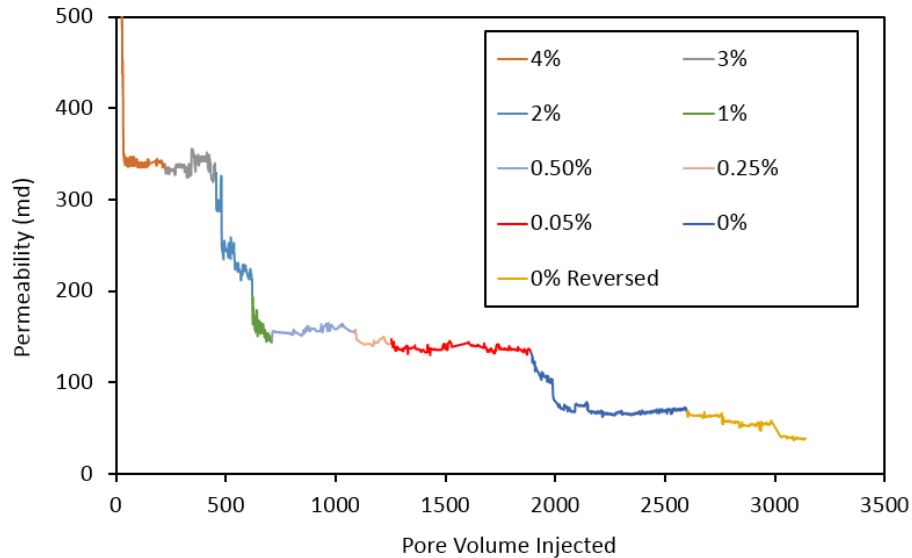
Fig 2 Permeability drop for Berea_1P plug. First permeability drop was noted at 2% NaCl brine. 1% NaCl brine and fresh water also caused permeability reduction

2.2 Two phase waterflooding

4% brine was injected to measure core`s absolute permeability. In the first step, Soltrol was injected at 5cc/min into brine saturated plug to produce connate water saturation (S_{wi}). When steady-state conditions were achieved, the experiment was stopped. In the second step, 4% brine was injected at a rate of 0.25 cc/min to mimic high-salinity waterflooding. This produced residual oil saturation ($S_{or-high}$). Water samples were collected during high salinity water flooding.

Next, same oil was injected at 5 cc/min to re-produce irreducible water saturation (S_{wi}). Values of S_{wi} and k_{ro} were compared with first drainage step (Table 2). Finally, de-ionized water was injected to mimic low-salinity flooding and produce residual oil saturation (S_{or-low}). Pressure and production data were recorded continuously. The values of S_{wi} and k_{rowi} are similar in both oil injection stages, suggesting that same oil saturation was achieved before the high-salinity and low-salinity waterfloods (Table 2).

Table 2 end-point saturation, relative permeability and core exponent

	Stage	S_{wi}	$K_{ro}(S_{wi})$	S_{or}	$K_{rw}(S_{or})$
Berea-2	High-salinity injection	0.311	0.66	0.385	0.09
	Low-salinity injection	0.314	0.66	0.362	0.05

3. POST EXPERIMENT CHARACTERIZATION

After core flooding, cores were dried and SEM imaging was repeated. Spectrex PC-2000 Laser Particle Counter was used to quantify particles suspended in each produced water sample. A special filter membrane device was used to filter particles suspended in water samples. According to our known mineralogy information, polytetrafluoroethylene (PTFE) membrane was selected because PTFE material only contains carbon(C) and florin(F) elements that are not included in both sandstones. The filtration method adopted in this paper is described in details by Guo, Hussain [10].

4. RESULTS

4.1 SINGLE-PHASE RESULTS

The permeability profile of Berea plug and Obernkirchener plug is shown in **Error! Reference source not found.**. There is an order of magnitude permeability drop from 4% brine injection to de-ionized water injection. **Error! Reference source not found.** shows the particle concentration of Berea_1P plug along with pore volume injected. The first sample shows significantly high concentration of particles. In general, particle production seems to be associated with permeability drop. As described above, all four stages that showed permeability drop (2%, 1%, fresh water and fresh water reversed flow) showed particle concentration. Conductivity plot shows the reduction of concentration of sodium ion, which can be further interpreted as the reduction of salinity.

Particles released from the core was filtered on PTFE membranes and then identified by Energy Dispersive Spectrum (EDS) technique. The particles were mainly quartz and kaolinite. Quartz were relatively larger in terms of size that it was usually visible under 500-micron scale. By contrast, kaolinite particles were so small that they were only visible under 10-micron scale. A statistics analysis (**Error! Reference source not found.**) shows that for Berea-1 plug, quartz was produced in each stage, while the boost of kaolinite production is only during fresh water injection.

Error! Reference source not found. shows the initial condition of a pore at the inlet face before water flooding. A few fines are highlighted by red circles which disappeared after water flooding. **Error! Reference source not found.** shows migration of a big chunk of clay near the exit of an existing pore after experiment. This may block the pore and force water to flow through another pore.
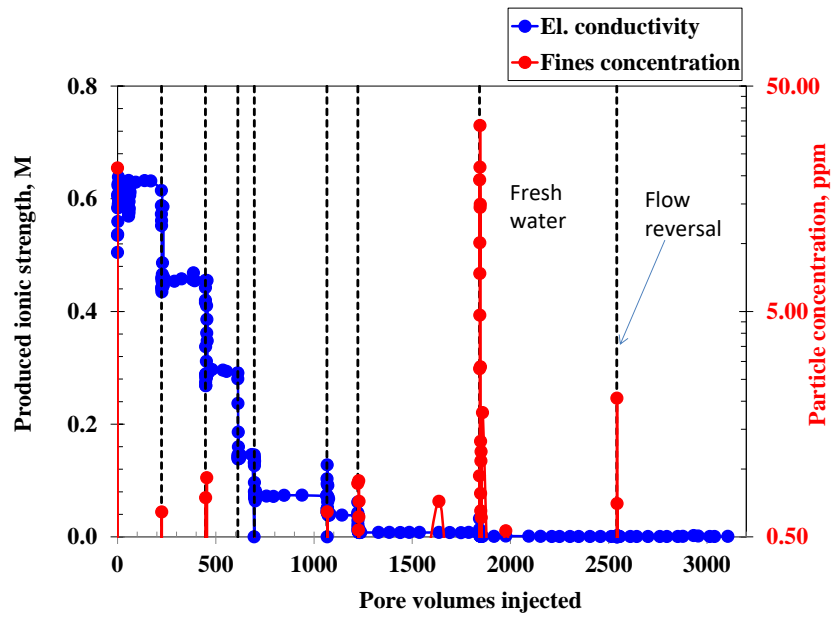
Fig 3 Result of particle concentration- a large number of particles were produced during fresh water flooding. Reversed flow can re-mobilize strained fines during previous stages.
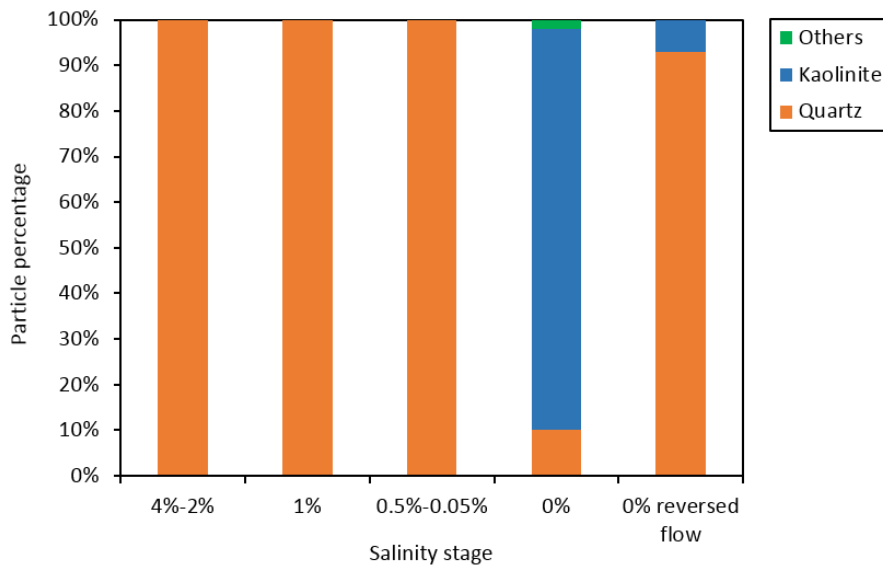
Fig 4 Percentage of produced quartz, kaolinite from SEM/EDS analysis.
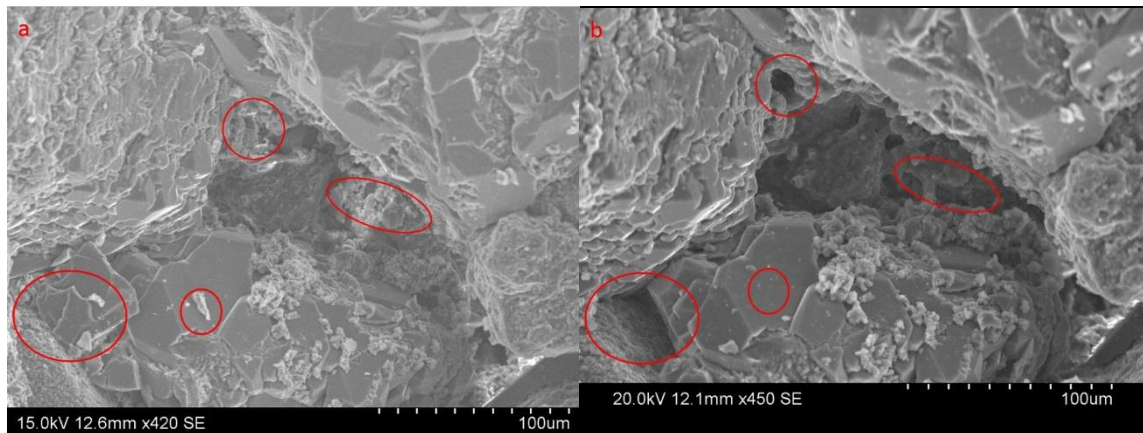
Fig 5 shows fines in four locations on inlet face are initially attached on grain surfaces (a) and migration of these fines after water flooding created extra pore volume (b).
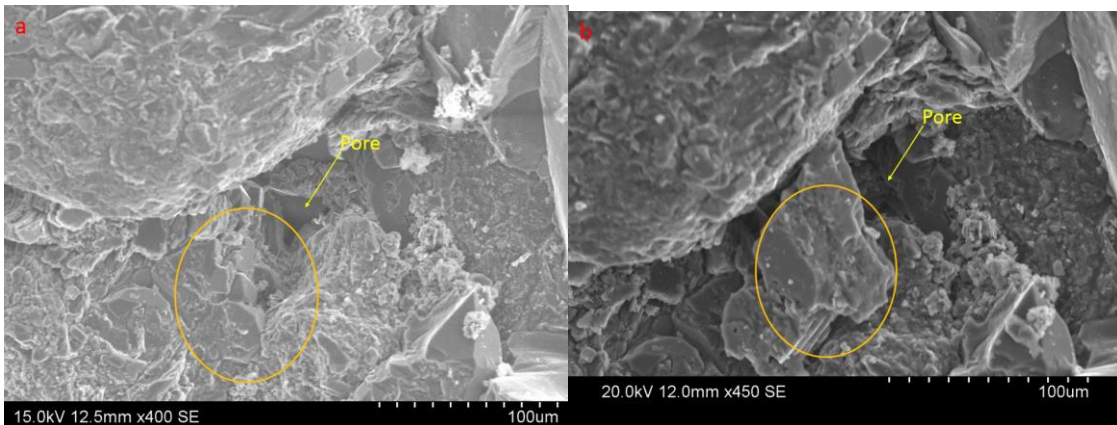
Fig 6 shows one position near a pore on outlet face before water injection (a) and a big chunk of particles migrated and blocked the outlet of this pore(b).

4.2 TWO-PHASE RESULTS

Cumulative oil production curve for high-salinity and low-salinity injections is shown in **Error! Reference source not found.**. Oil recovery in low-salinity water flooding is 2.5% more than high salinity flooding. Pressure drop for Berea sandstone increased from 3.5psi for high-salinity injection to 6 psi for low-salinity injection which was used to measure end point water permeability (Table 2**Error! Reference source not found.**). The results show that water permeability was reduced to half after low salinity water injection.

Error! Reference source not found. Error! Reference source not found.shows the number of fines produced with high salinity water were negligible compared with that with low salinity water. Also, concentration graph shows that fines production occurs in early stage of low-salinity injection. EDS results (**Error! Reference source not found.**) for two phase flow test matches single phase flow results where clay is mobilized only during low salinity water flooding. High concentration of particles, mainly kaolinite is produced near

low-salinity water break through (**Error! Reference source not found.** and **Error! Reference source not found.**). The quantity of particles on membranes may somewhat represent their quantity in water.
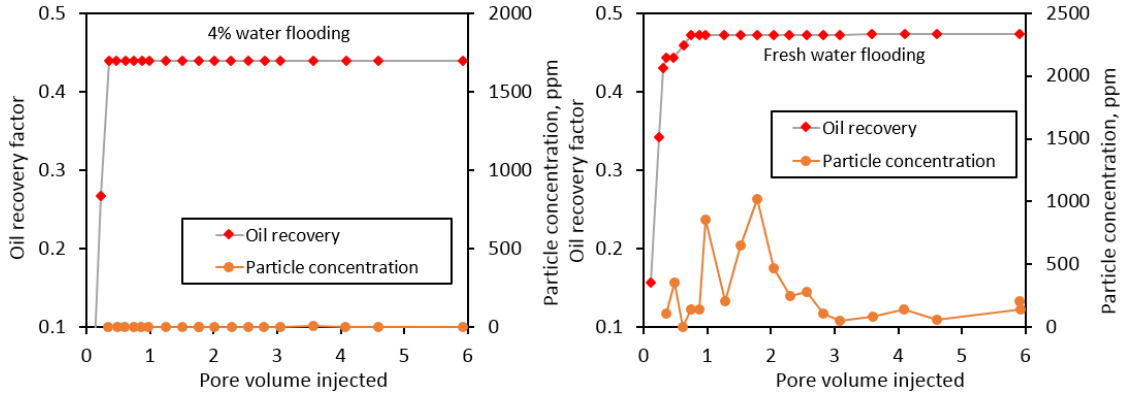
Fig 7 Oil recovery and particle concentration from effluent for both high-salinity water and fresh water
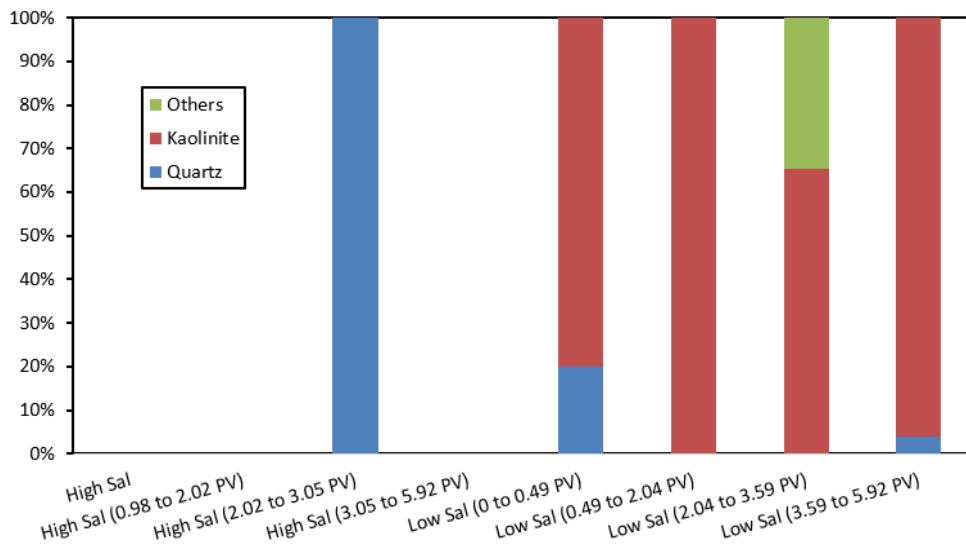
Fig 8 Percentage of different type of particle identified under SEM/EDS.

CONCLUSION

Wettability alteration was avoided by using non-polar oil. SEM images and particle identification give direct evidence of fines migration. This correlates well with the data on fines concentration, which is significant during fresh water flooding and negligible during HS flooding. The core contains no swelling clays; hence water swelling effect is excluded. Fines production is found to be associated with absolute permeability reduction for single-phase experiment (10 times) and water relative permeability reduction for water-oil displacement experiment (2 times). The produced fine particles during our test are mostly

kaolinite. There is also some decrease in residual oil saturation (almost 3%) during the LS waterflood in comparison with the high-salinity waterflood. As there is no wettability alteration, improved recovery was due to fines migration induced flow diversion.

Reference

1. Yildiz, H.O. and N.R. Morrow, *Effect of brine composition on recovery of Moutray crude oil by waterflooding.* Journal of Petroleum science and Engineering, 1996. **14**(3-4): p. 159-168.
2. Tang, G.-Q. and N.R. Morrow, *Influence of brine composition and fines migration on crude oil/brine/rock interactions and oil recovery.* Journal of Petroleum Science and Engineering, 1999. **24**(2): p. 99-111.
3. Fogden, A., et al., *Mobilization of fine particles during flooding of sandstones and possible relations to enhanced oil recovery.* Energy & Fuels, 2011. **25**(4): p. 1605-1616.
4. Buckley, J., K. Takamura, and N. Morrow, *Influence of electrical surface charges on the wetting properties of crude oils.* SPE Reservoir Engineering, 1989. **4**(03): p. 332-340.
5. Fogden, A. and E.V. Lebedeva, *Changes in Wettability State Due to Waterfloodin.* Petrophysics, 2012. **53**(06): p. 420-429.
6. Sharma, M. and P. Filoco, *Effect of brine salinity and crude-oil properties on oil recovery and residual saturations.* SPE Journal, 1998. **5**(03): p. 293-300.
7. Al-Shalabi, E.W. and K. Sepehrnoori, *A comprehensive review of low salinity/engineered water injections and their applications in sandstone and carbonate rocks.* Journal of Petroleum Science and Engineering, 2016. **139**: p. 137-161.
8. Hussain, F., et al., *An experimental study of improved oil recovery through fines-assisted waterflooding.* Journal of Petroleum Science and Engineering, 2013. **109**: p. 187-197.
9. Bedrikovetsky, P., et al., *Modified particle detachment model for colloidal transport in porous media.* Transport in porous media, 2011. **86**(2): p. 353-383.
10. Guo, Z., F. Hussain, and Y. Cinar, *Permeability variation associated with fines production from anthracite coal during water injection.* International Journal of Coal Geology, 2015. **147**: p. 46-57.

CORRELATION BETWEEN CORE LINEAR X-RAY AND WIRELINE BULK DENSITY IN TWO CLASTIC RESERVOIRS: AN EXAMPLE OF CORE-LOG INTEGRATION

Yu Jin and David K. Potter

Department of Physics, and Department of Earth and Atmospheric Sciences, University of Alberta, Edmonton, Canada

This paper was prepared for presentation at the International Symposium of the Society of Core Analysts held in Vienna, Austria, 27 August -1 September, 2017

ABSTRACT

Linear X-ray measurements on core samples potentially provide a rapid means of obtaining a high resolution quantitative density profile. We tested this on slabbed core from two shoreface clastic reservoirs in the North Sea by comparing the linear X-ray results with wireline bulk density data over the same depth matched intervals. A linear X-ray scanner system produced inverted images on an electronic image intensifier. The digital images were composed of pixels of different grayscale. These grayscale values are referred to as "luminance" values. Low luminance values represent low penetrability of X-rays (i.e., high attenuation of X-rays, and therefore high density core) and are seen as dark pixels on the images, whilst high luminance values represent high penetrability of X-rays (low density core) and are seen as light pixels on the images. Luminance values were taken at high resolution along the slabbed core. The results were compared with the wireline bulk density data. A key result was that when the luminance data was averaged (by a simple smoothing technique) over the same vertical intervals that each wireline bulk density measurement was made (about 1 to 2 feet), the luminance and bulk density data showed a good correlation. Both the smoothed luminance and wireline bulk density exhibited similar profiles with depth in the intervals studied from the two clastic reservoirs, and crossplots quantitatively demonstrated the good correlations. As expected the correlations were worse if the luminance data was smoothed over an interval that did not correspond to the vertical interval of each wireline bulk density measurement. The strong correspondence between appropriately smoothed luminance and wireline bulk density data over identical intervals gives us confidence that the raw (unsmoothed) high resolution point luminance data offers a rapid, non-destructive means of obtaining a high resolution density profile on slabbed or whole core. The luminance data and X-ray images readily pin-pointed thin naturally cemented higher density dendritic barite filled fracture veins within the quartz sandstone that were not easily seen from standard visible light core images. Other features, such as thin clay laminae, were also better defined from the linear X-ray data than from visible light images.

INTRODUCTION
Some previous studies have indicated the potential of linear X-ray measurements for characterizing sedimentary structures [1,2] and high resolution density variations [3] in whole core and slabbed core samples. The latter study by Duncan et al [3] compared the grayscale of digital linear X-ray images (which they termed "luminance" values) of core with the wireline bulk density data from the same intervals. The present paper compares luminance data from the digital linear X-ray images on core with the corresponding wireline bulk density log data on sections of slabbed core from two different clastic reservoirs. We first compared raw single point luminance readings against the corresponding wireline bulk density log readings, and then compared smoothed luminance data that was averaged over the same vertical interval as each wireline bulk density log reading. The main purpose was to compare the luminance and wireline bulk density data over the same vertical scale of measurement, to see if this improves the correlations between the two types of measurement (compared to correlations between the wireline bulk density data and single point luminance measurements).

SAMPLES AND METHODS
Two clastic reservoir sections from the North Sea were studied: (i) a 24ft long quartz sandstone shoreface facies with barite filled fracture veins from Well 2, and (ii) a 36ft long quartz sandstone shoreface facies with clay laminae from Well 8, which also contained an upper small calcite dogger interval, and a lower micaceous sandstone. A linear X-ray scanner was used to create inverted images of the slabbed core on an electronic image intensifier. The images were picked up by a charge coupled device (CCD) camera and digitized. Point luminance values (the grayscale of the images at a particular point <0.1 inch in diameter) were taken directly from the digital X-ray images in real time during the scanning. Low luminance values representing low penetrability of X-rays (i.e., high attenuation of X-rays, and therefore high density core) were seen as dark pixels on the images, whilst high luminance values representing high penetrability of X-rays (low density core) were seen as light pixels on the images.

The luminance values were compared with the corresponding wireline bulk density values for the same sections after first depth matching the core against the log depths. The wireline bulk density log values were first compared to the nearest raw single point luminance values. We then compared the wireline bulk density log values with smoothed luminance data points that were averaged over vertical distances comparable to that of a typical wireline bulk density log reading.

RESULTS AND DISCUSSION
Figure 1 (top) shows linear X-ray images of the 24 foot section in Well 2. The black areas are barite (some barite filled fracture veins are particularly evident). The grey areas are quartz, and the "holes" are where core plugs have been taken. **Figure 1 (bottom)** shows linear X-ray images of a 12 foot section (of the 36 feet that was imaged) in Well 8. Inclined clay laminae can clearly be seen within the otherwise homogeneous quartz.

Figure 2 shows plots of wireline bulk density and luminance with depth for the 24 foot interval in Well 2. The top two plots are the wireline bulk density values (taken every half foot) and the raw high resolution luminance values (taken about every 3 inches). The raw luminance data exhibits far more variation than the wireline density profile, and reflects the higher resolution of the core X-ray measurements. The bottom two plots of **Figure 2** show smoothed luminance data that has been averaged vertically over 1 foot (5 point average) and 1.5 feet (7 point average) respectively. These smoothed luminance curves show a much closer correspondence to the wireline bulk density profile, since each smoothed luminance value represents an average over an approximately similar vertical interval to each wireline bulk density log reading. From these curves it appears that the luminance averaging over 1.5 feet (7 point average) is closest to the wireline bulk density profile.

A more quantitative test of the correlations of the Well 2 data is shown in the crossplots of **Figure 3**. The top crossplot is merely the wireline bulk density data plotted against each corresponding nearest single point raw luminance value. It is apparent that the regression coefficient is quite low with $R^2 = 0.37$. Significantly, however, when the wireline bulk density is plotted against the smoothed luminance data the correlations are much better. The regression coefficient $R^2 = 0.58$ for luminance data averaged vertically over 1 foot (5 point average, **Figure 3 middle**), and $R^2 = 0.63$ for luminance data averaged vertically over 1.5 feet (7 point average, **Figure 3 bottom**). All crossplots showed the expected inverse correlation of higher bulk density corresponding with lower luminance. We determined the regression coefficients for luminance data averaged vertically over several other spacings. For example, averaging over 2 feet vertically gave $R^2 = 0.60$. The maximum R^2 value was for the 1.5 feet vertical averaging shown in **Figure 3 bottom**. This might suggest that the wireline bulk density log was actually averaging vertically close to 1.5 feet.

Figure 4 shows plots of wireline bulk density and luminance with depth for the 36 foot interval in Well 8. The top two plots are the wireline bulk density values (taken every half foot) and the raw high resolution luminance values (taken in this case at very high resolution about every 0.8 inches). The higher resolution raw luminance data exhibits substantially more variation than the wireline density profile. The bottom two plots of **Figure 4** show smoothed luminance data that has been averaged vertically over 1 foot (17 point average in this case due to the high resolution of measurement) and 2 feet (31 point average) respectively. These smoothed luminance curves again show a fairly close correspondence to the wireline bulk density profile, since each smoothed luminance value represents an average over an approximately similar vertical interval to the wireline bulk density log.

Figure 5 shows crossplots of wireline bulk density versus luminance for Well 8. The top crossplot merely gives the wireline bulk density plotted against the nearest single point raw luminance value. The regression coefficient is quite low with $R^2 = 0.43$. Again significantly, however, when the wireline bulk density is plotted against the smoothed luminance data the correlations are much better. The regression coefficient $R^2 = 0.64$ for

luminance data averaged vertically over 1 foot (17 point average, **Figure 5 middle**), and $R^2 = 0.68$ for luminance data averaged vertically over 2 feet (31 point average, **Figure 5 bottom**). We determined the regression coefficients for luminance data averaged vertically over several other spacings, and the maximum R^2 value was for the 2 feet vertical averaging shown in **Figure 3 bottom**. This might suggest that for Well 8 the wireline bulk density log may actually be averaging vertically close to 2 feet. However, all the R^2 values for luminance averaged vertically between 1.5 and 2 feet were very close ($R^2 = 0.678$ for 1.5 feet vertical averaging and $R^2 = 0.683$ for 2 feet vertical averaging, with intermediate R^2 values for averaging between 1.5 and 2 feet).

CONCLUSIONS

1. The results from the two clastic reservoirs studied showed an inverse correlation between the grayscale of linear X-ray images (the "luminance") on core and the wireline bulk density. As the bulk density increases the luminance decreases.

2. The best correlations between luminance and wireline bulk density occurred when the smoothed (i.e., averaged) luminance vertical interval was between 1 and 2 feet, which we believe closely corresponded to the vertical interval over which the wireline bulk density log averages each reading.

3. The good correlation between wireline bulk density and luminance that is averaged over the same vertical interval gives us confidence that the raw point luminance values taken at small scale vertical spacings are giving an accurate profile of the high resolution density variations.

4. The linear X-ray images and luminance values readily picked out higher density barite filled fracture veins in one of the reservoirs, and clay laminae in the other reservoir, that were much more difficult to see from visual observations alone.

ACKNOWLEDGEMENTS

REFERENCES

1. Algeo, T. J., Phillips, M., Jaminski, J. and Fenwick, M. 1994. High resolution X-radiography of laminated sediment cores. Journal of Sedimentary Research A: Sedimentary Petrology and Processes, **A64**, 665-668.

2. Rigsby, C. A., Zierenberg, R. A. & Baker, P. A. 1994. Sedimentary and diagenetic structures and textures in turbiditic and hemiturbiditic strata as revealed by whole-core X-radiography; Middle Valley, northern Juan de Fuca Ridge. Proceedings, Scientific Results, ODP leg 139, 105-111.

3. Duncan, A. R., Dean, G. and Collie, D. A. L. 1998. Quantitative density measurements from X-ray radiometry In: Harvey, P. K. & Lovell, M. A. (eds) Core-Log Integration, Geological Society, London, Special Publications, **136**, 17-24.
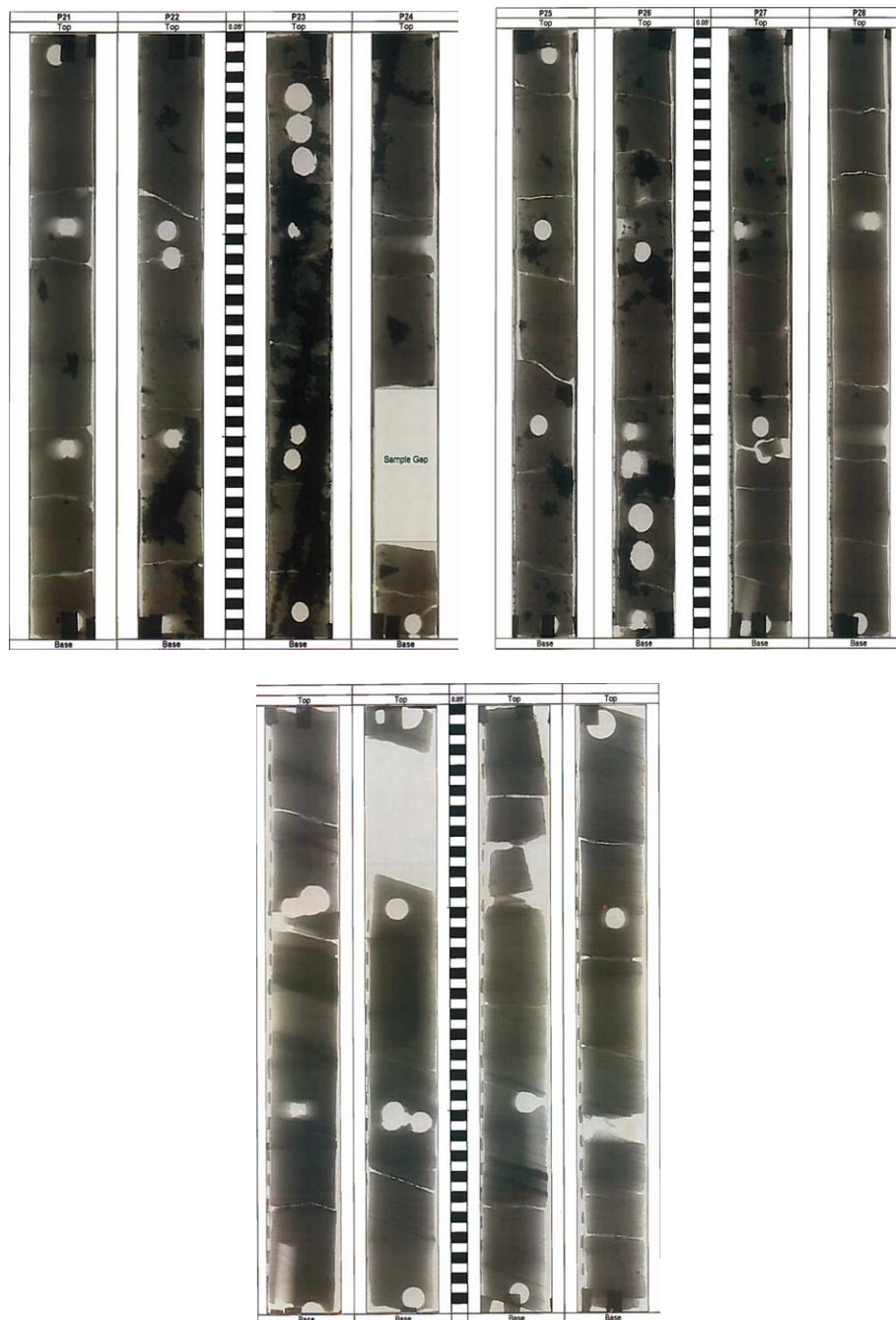
Figure 1. Top: Linear X-ray images of the 24 foot section in Well 2. The black areas are barite (particularly evident in the barite filled fracture veins of the 3rd section from the left). The grey areas are quartz, and the "holes" are where core plugs have been taken. **Bottom:** Linear X-ray images of a 12 foot section in Well 8 (a further 24 feet was also imaged, but not shown here due to available space). Inclined clay laminae can be seen (e.g., towards the base of the 3rd section from the left).
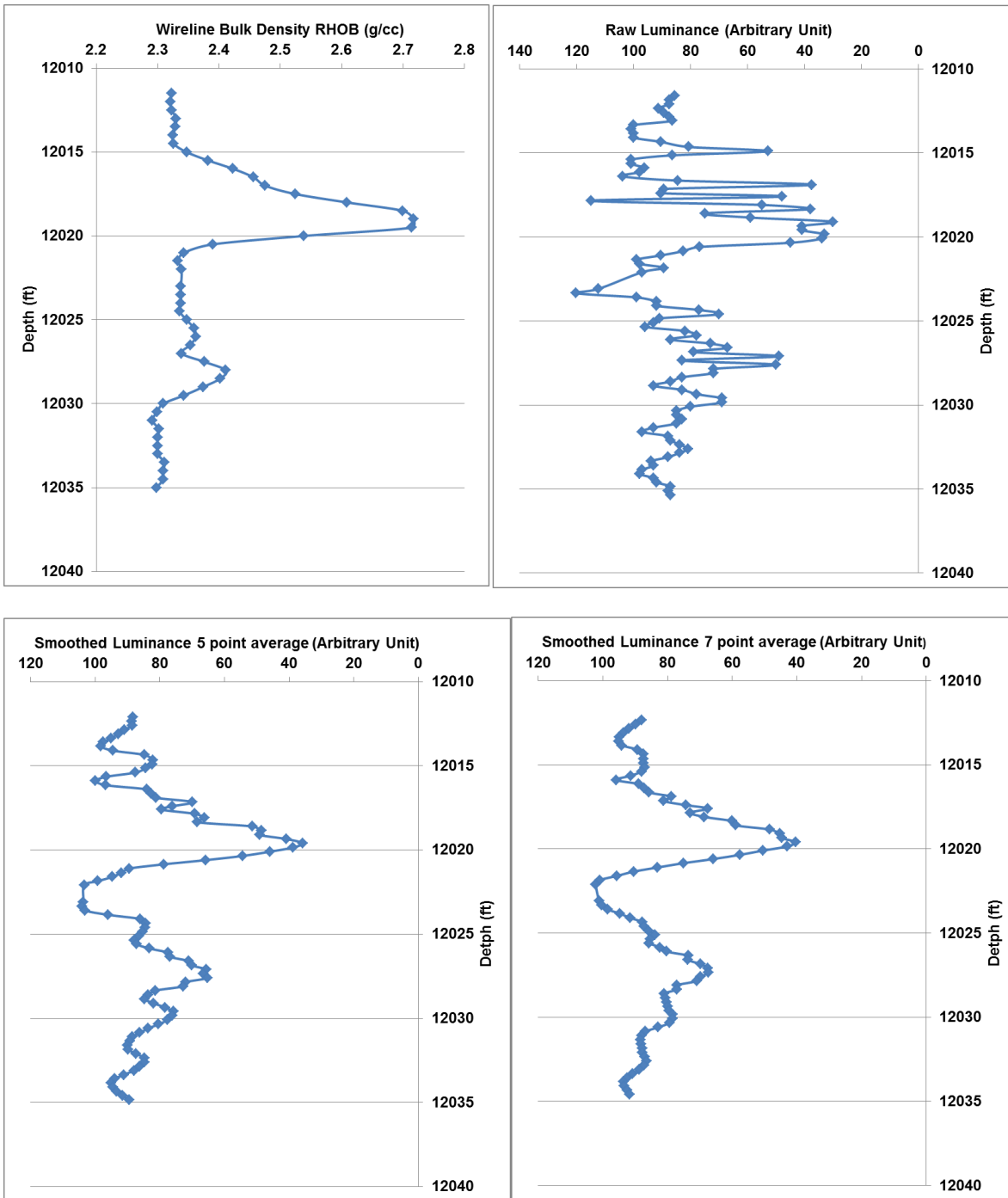
Figure 2. Plots with depth for Well 2. **Top left:** Wireline bulk density. The high value at 12,018-12,020 ft is due to the barite filled fracture veins. **Top right:** Raw high resolution luminance values (at approximately 3 inch vertical spacing). **Bottom left:** Smoothed luminance 5 point average (averaged over 1 foot vertically). **Bottom right:** Smoothed luminance 7 point average (averaged over 1.5 feet vertically).
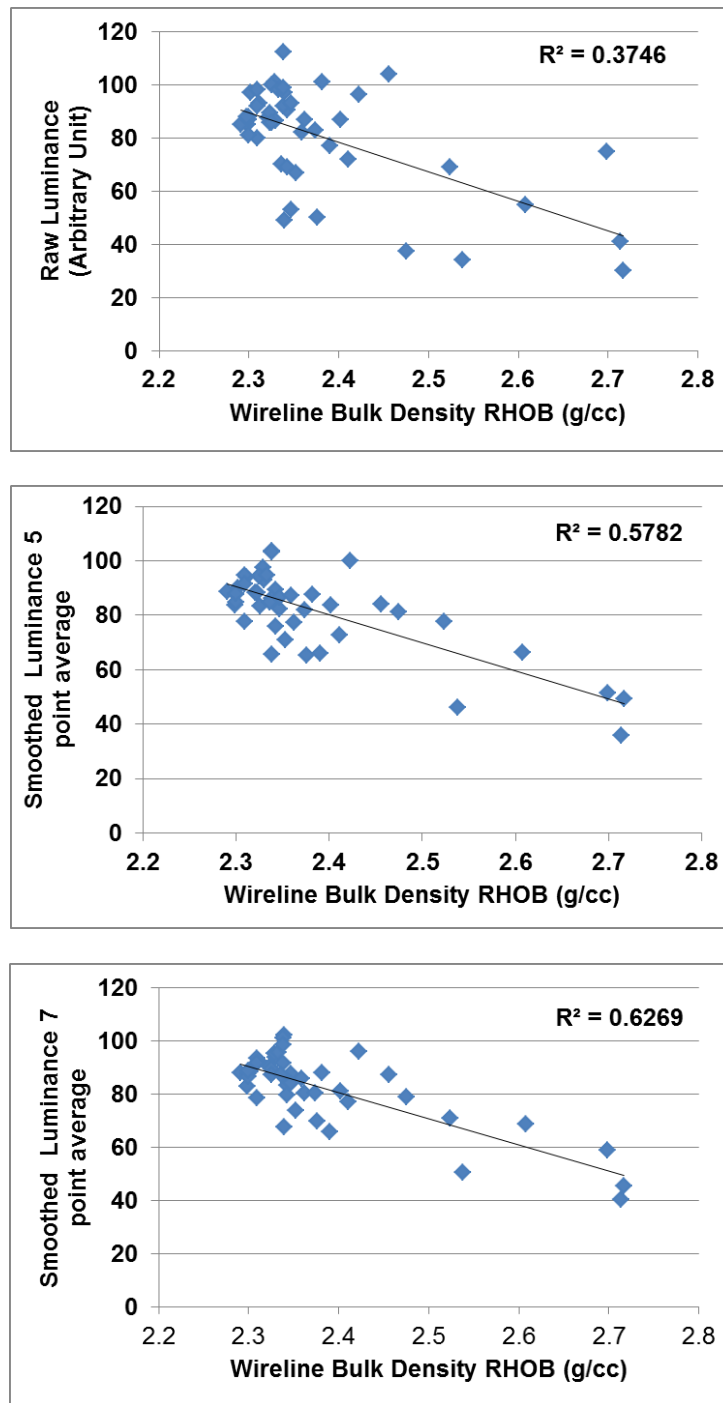
Figure 3. Crossplots for Well 2 of wireline bulk density versus (i) **Top:** Raw single point luminance at the nearest depths to the corresponding wireline bulk density readings, (ii) **Middle:** Smoothed luminance 5 point average (averaged over 1 foot vertically), and (iii) **Bottom:** Smoothed luminance 7 point average (averaged over 1.5 feet vertically).
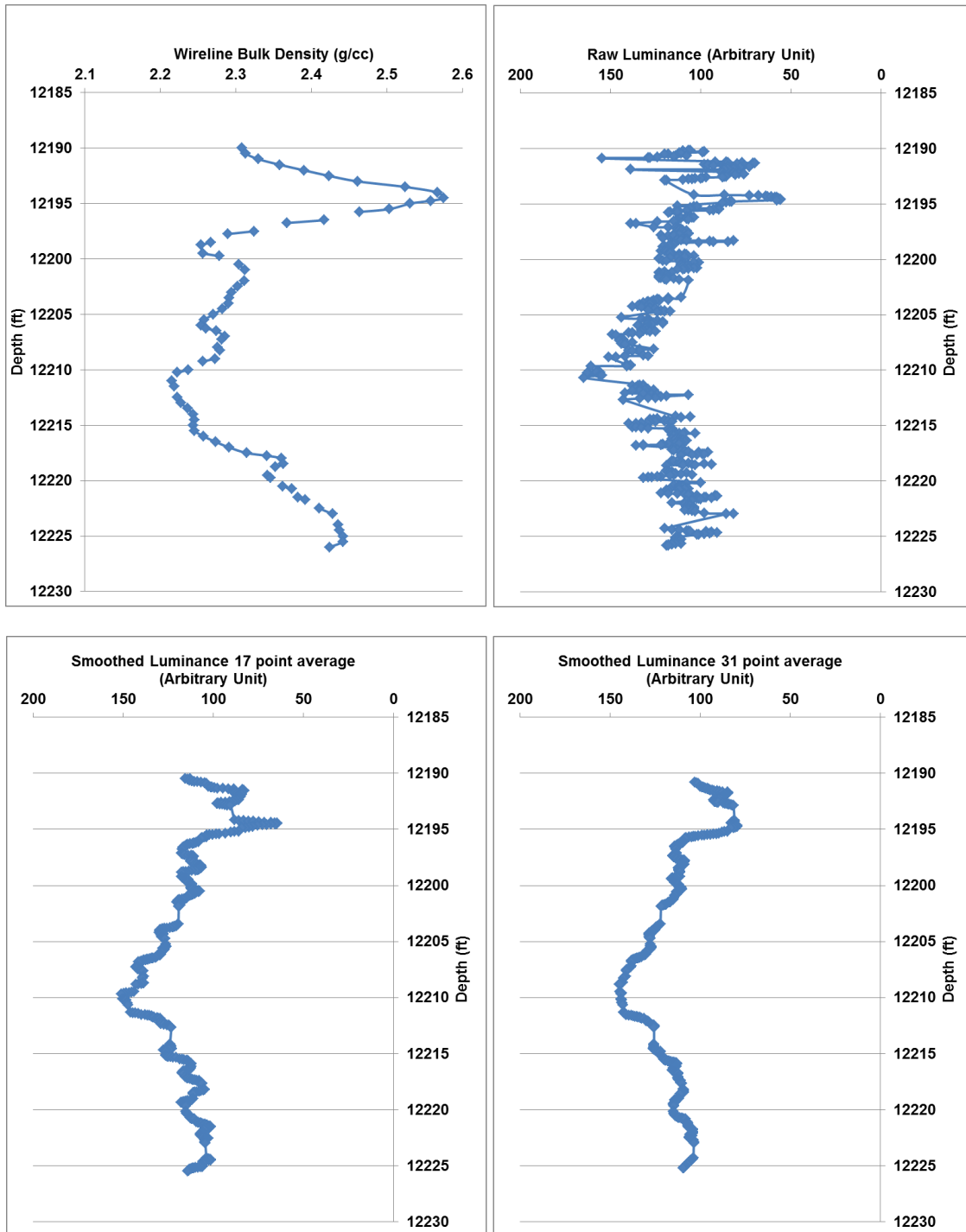
Figure 4. Plots with depth for Well 8. **Top left:** Wireline bulk density. The high value at 12,195 ft is due to a calcite dogger. **Top right:** Raw high resolution luminance values (at approximately 0.8 inch vertical spacing). **Bottom left:** Smoothed luminance 17 point average (averaged over 1 foot vertically). **Bottom right:** Smoothed luminance 31 point average (averaged over 2 feet vertically).
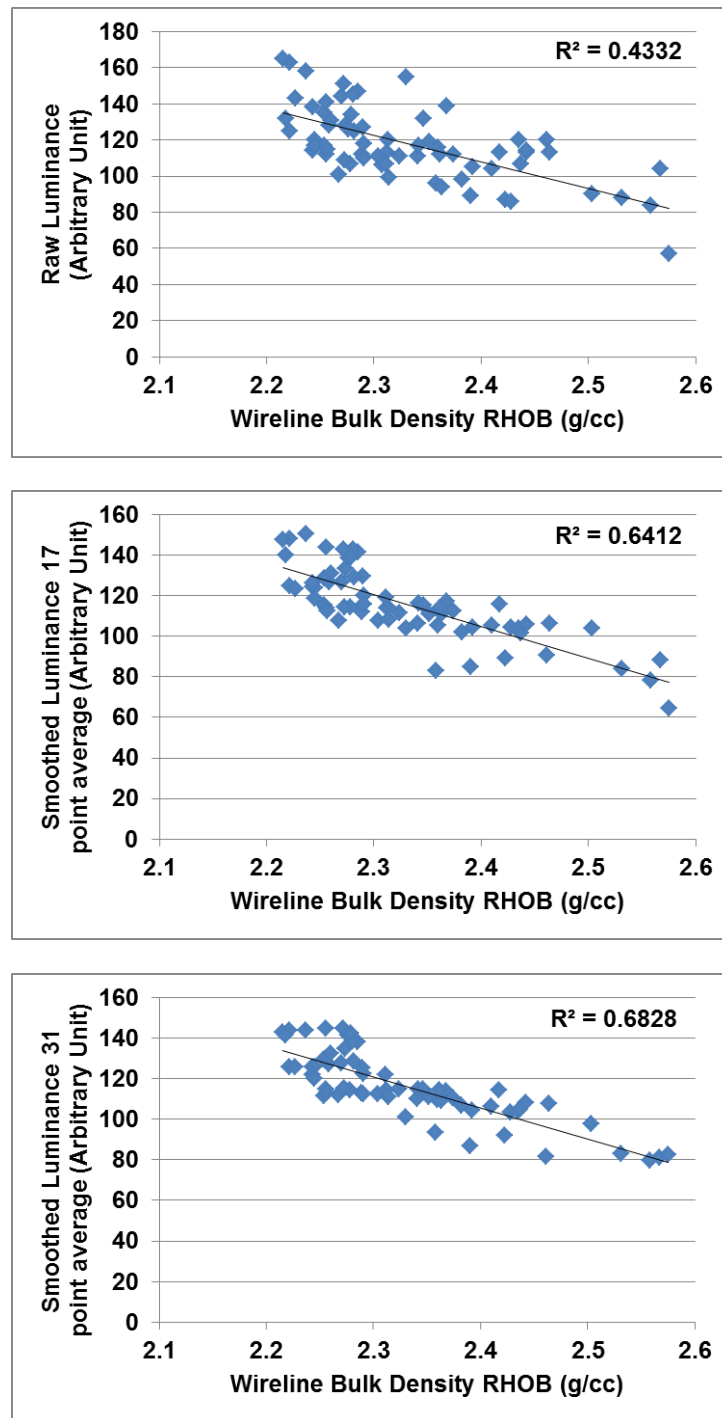
Figure 5. Crossplots for Well 8 of wireline bulk density versus (i) **Top:** Raw single point luminance at the nearest depths to the corresponding wireline bulk density readings, (ii) **Middle:** Smoothed luminance 17 point average (averaged over 1 foot vertically), and (iii) **Bottom:** Smoothed luminance 31 point average (averaged over 2 feet vertically).

Rock visualization using micro-CT scanner and X-ray transparent triaxial apparatus

M. Soldal[1], H. D. Wilkinson[1], I. Viken[1] and G. Sauvin[1].
The Norwegian Geotechnical Institute, Sognsveien 72, 0806 Oslo, Norway.

This paper was prepared for presentation at the International Symposium of the Society of Core Analysts held in Vienna, Austria, 27 August -1 September 2017

ABSTRACT

The macroscopic deformation and failure of rocks under compression is typically an gradual process of damage accumulation, crack formation and finally failure. Most often failure is accompanied by localization of deformation, which influence the stress distribution within the rock, and reduces its mechanical performance. Localization of strain in rock samples mechanically tested in the lab, can often take place unnoticed by deformation sensors. In this study a recently developed X-ray transparent triaxial test setup for rock testing inside a Computed Tomography (CT) scanner is utilized for the first time. Two different sandstones are scanned at progressively increasing shear stresses, enabling visualization of deformation taking place inside the sample as it is loaded to macroscopic failure.

INTRODUCTION

Experimental geomechanical investigation of rock deformation under varying stresses typically deals with global measurements of changing sample dimensions. However, most geomaterials exhibit strain localization into narrow zones when stressed, which may or may not be detectable using traditional deformation measurements. Strain localization under shear stress application typically indicates that failure is imminent [8], and the behaviour of bands with localized deformation can strongly influence the macroscopic response of the rock specimens, and should be investigated [3].

Various experimental measuring techniques have already been utilized in efforts to capture strain localization (e.g. acoustic techniques, microscopy, photogrammetry and multiple local strain measurements). One inherent challenge is that the necessary resolution and volume of interest can change rapidly, from the sample scale to narrow bands of strain

localization [4] and the measuring technique should capture all. One powerful tool for accessing the interior of rock samples and characterizing the density distribution within in a non-destructive manner is X-ray imaging. A given number of 2D projections of the sample in interest captured at various angles are used to reconstruct 3D volumes in X-ray Computed Tomography (CT). The CT volumes show the three-dimensional distribution of the sample's X-ray linear attenuation coefficient, which is closely related to the density [9].

Several intriguing studies of the onset of deformation localization as seen in a CT scanner are already available (e.g. [2,5, 7 and 8]). Most of them consider relatively small samples under low stresses. Others have shown deformational trends on more competent rocks by CT imaging samples prior to and after they are subjected to high shear stresses (e.g. [3]).

In this study, a newly developed X-ray transparent triaxial apparatus is utilized to isotropically consolidate (effective stress 5 MPa) and then shear 1.5" diameter samples. The apparatus enables 4D visualization of rock damage during destructive tests (i.e. during application of shear stresses). Here we describe the experimental equipment and present some results from drained triaxial tests on two different sandstones.

MATERIAL AND METHOD

CT scanner

A Nikon Metrology XT H 225 LC industrial CT scanner with a 225 kV micro-focus X-ray tube and a 4.2 Megapixels detector panel is used for imaging. The spot size of the X-ray beam is typically 3 µm. During a CT scan the object in interest rests on a manipulator table that rotates 360 degrees around its longitudinal axis. During this rotation, a specific number of 2D projections are collected and later turned into a 3D volume using some back-projection algorithms.

Optimization of settings to employ during CT acquisition can be a time-consuming task. The overall trade-off in this study is between time and image quality. Number of projections, frames to average, exposure time etc are all parameters that can enhance the signal to noise ratio, but also at the same time increase the acquisition time.

Artefacts in CT data can affect the result considerably. Most pronounced in this study are the ring artefacts. Ring artefacts are caused by defective pixel elements and show up as rings in the reconstructed CT volumes. The option of minimizing ring artefacts given by the acquisition software undertakes a process of shifting the projection images a specific number of pixels when collecting the CT data. As a result, the total acquisition time is significantly increased and it was decided to rather remove the ring artefacts in the image post processing. A method similar to that of Sijbers was utilized for this purpose [1], and an example of ring artefact removal is given in Figure 1.

Tracking the deformation field within the scanned rock volume as stress varies, involves several processing steps. Using both an in-house developed Matlab code and third-party Matlab code, the process consists of firstly defining a region of interest within the volume and a center of rotation. Afterwards the volume is processed and among other things, the ring artefacts are removed. The process of finding the displacement field involves subdividing the CT volumes iteratively into finer and finer sub-volumes, and for every refinement, the sub-volumes are phase-correlated to find the relative offset.
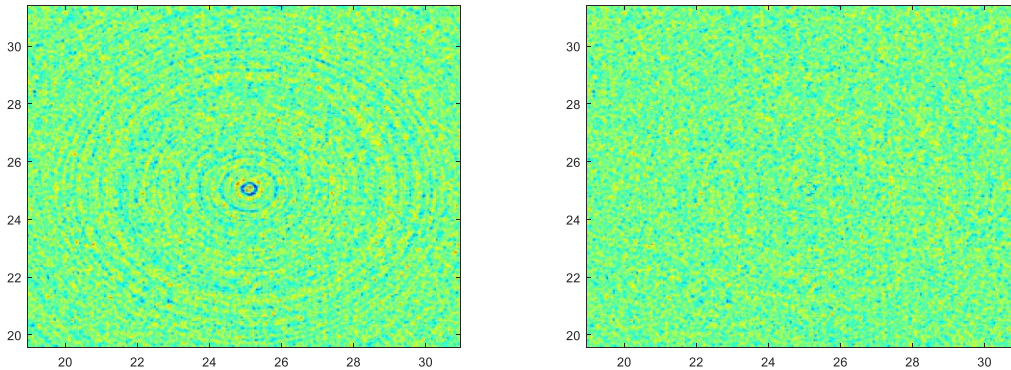
Figure 1: Color coded horizontal cross section of a CT scanned sandstone before (left) and after (right) ring artefact removal.

For each CT scan 3000 projections is collected, each taken using an exposure time of 1000ms. The time it takes to complete one scan is approximately 50 minutes, and the resulting voxel resolution is 45 μm.

Triaxial apparatus

The main challenge in designing the triaxial apparatus was the need for both X-ray transparency and sufficient system strength and stiffness. Our triaxial apparatus is self-compensating, meaning that there is no need for steel bars disturbing the X-rays to hold the top and bottom parts together and that the tensional axial forces are sustained by the cell body (see Figure 2). The cell body is mainly made up of winded carbonfiber with titanium end caps out of view for the CT image. In addition, an aluminum liner on the inside of the carbonfiber cylinder is absorbing some of the forces acting on the cell body. The axial force (up to 100 kN) is hydraulic applied through a piston connected to the bottom of the sample and controlled by a pressure controller. The top cap is equipped with bayonet fittings and securely attached to the titanium end piece. The top and bottom pieces have pore pressure inlets connected to pressure controllers, and stacked piezo ceramic elements for acoustic P, S1 and S2 measurements. The rock sample is enclosed in a rubber membrane which is surrounded by hydraulic oil enabling application of confining pressure using yet another pressure controller. Radial deformation is measured as the change in diameter at mid-height by a cantilever connected to the membrane. Axial deformation is measured by two LVDTs fixed to the top and bottom pieces.
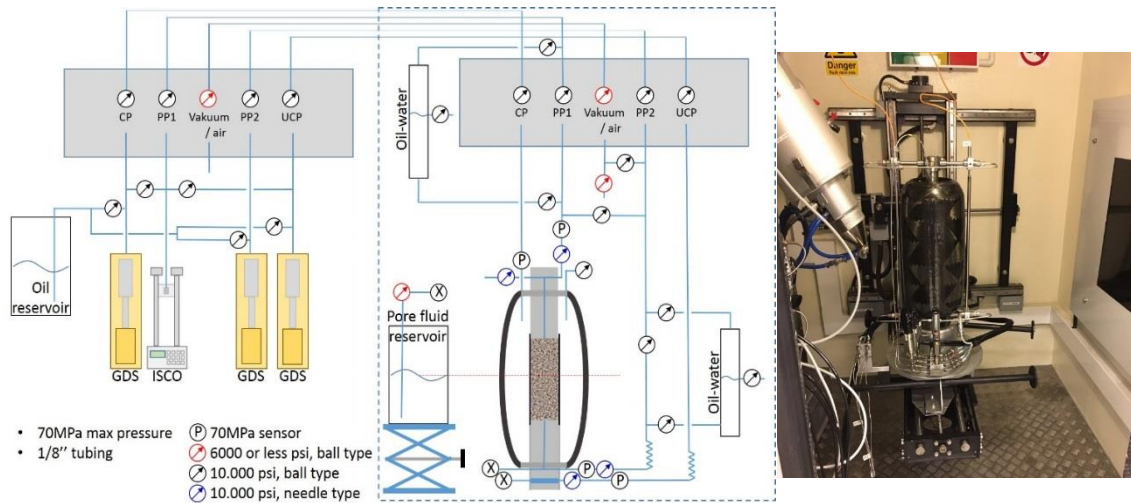
Figure 2: Schematics of the triaxial setup (left). The parts inside the dotted square are placed inside the CT cabinet, whereas the rest of the system is outside. To the right is an image of the X-ray transparent triaxial cell placed on the rotating manipulator table inside the cabinet.

On the X-rays' journey from the X-ray tube to the detector panel, they consequently have to pass through carbonfiber, aluminum, hydraulic oil, rubber membrane and rock sample. As the latter is the only object of interest, the rest are merely acting as filters causing an increased X-ray energy demand.

To accommodate the 360 degrees rotation of the triaxial apparatus during CT acquisition, flexible tubings are installed which can tolerate the rotation even at high pressures. As pressure controllers are located outside the CT cabinet and pressure drop in tubings are a function of their length, special care is taken to locate pressure transducers as close to the rock sample as possible.

Material

In this study, we give the results from two drained triaxial tests on two different sandstones (Figure 3). They were selected to represent different properties in terms of porosity, strength and deformation characteristics. Sample number 1 is a moderately layered sandstone with a porosity around 20 %, and it was drilled parallel with layering. Sample number 2 is a much weaker sandstone with a porosity of about 60 %. Both samples are approximately 38 mm in diameter and twice the diameter in height.

Figure 3: Sample number 1 (left) and sample number 2 (right) before triaxial testing.

Experimental procedure

After weighing and measuring the samples' diameters and heights, they are inserted into the triaxial cell. The piston and the top piece are brought in contact with the sample and the isotropic stress is increased to 1.0 MPa. Sample number 1 is saturated with brine at this effective stress and the backpressure is increased to 1 MPa. Sample number 2 is tested in dry conditions. Both samples are loaded isotropically to an effective stress of 5 MPa. This stress level serve as the reference level for further strains during the application of shear stresses.

Next, the effective vertical stress is increased in steps under drained conditions, while the horizontal effective stress is kept constant. After each step, the sample is allowed some time to stabilize before the CT acquisition begins. As progressively more shear stress and resulting strain is applied to the samples, it becomes impractical to ensure sample stabilization prior to CT acquisition. Most likely, this results in some image distortions in the later CT scans as the sample is deforming during CT scanning. Shear stress in increased until the sample fails or until further axial deformation can potentially damage the rubber membrane. Throughout the entire tests, all pressures and deformations are recorded.

RESULTS

Plots of shear stress versus axial strain for the two samples are given in Figure 4, together with the relative time for the CT acquisitions. Axial strain is given as the deformation recorded by the LVDTs divided by the initial sample height at the start of shearing and positive strain indicates compression. Sample number 1 displayed a relatively brittle behaviour, whereas sample number 2 displayed apparent strain hardening and did not lose its ability to withstand increasing shear stress. The reduction in shear stress in Figure 4 is from axial unloading to isotropic stress conditions before the final CT scan.
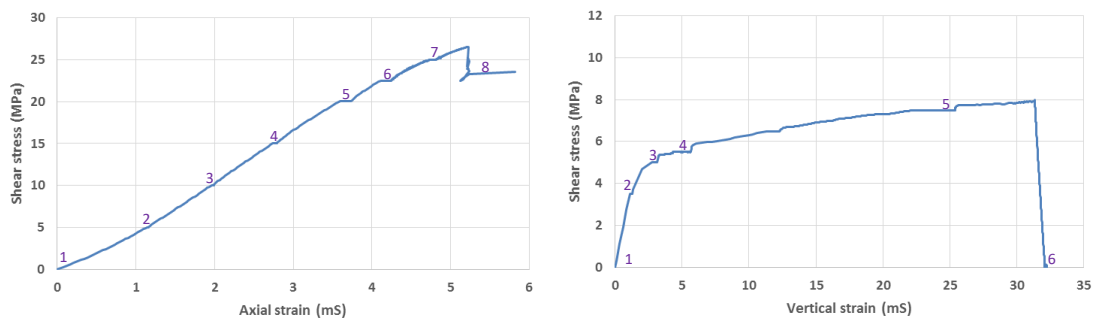
Figure 4: Axial strain versus shear stress for sample number 1 and 2. Numbers in purple indicate the relative timing of the CT scans.

Figure 5 shows the middle vertical cross section of sample 1 after it failed (left). The middle and right plots in fig 5 show the vertical displacement relative to the isotropic stress level before shearing. The displacement vectors indicate a downward movement of the upper right side of the failure plane.
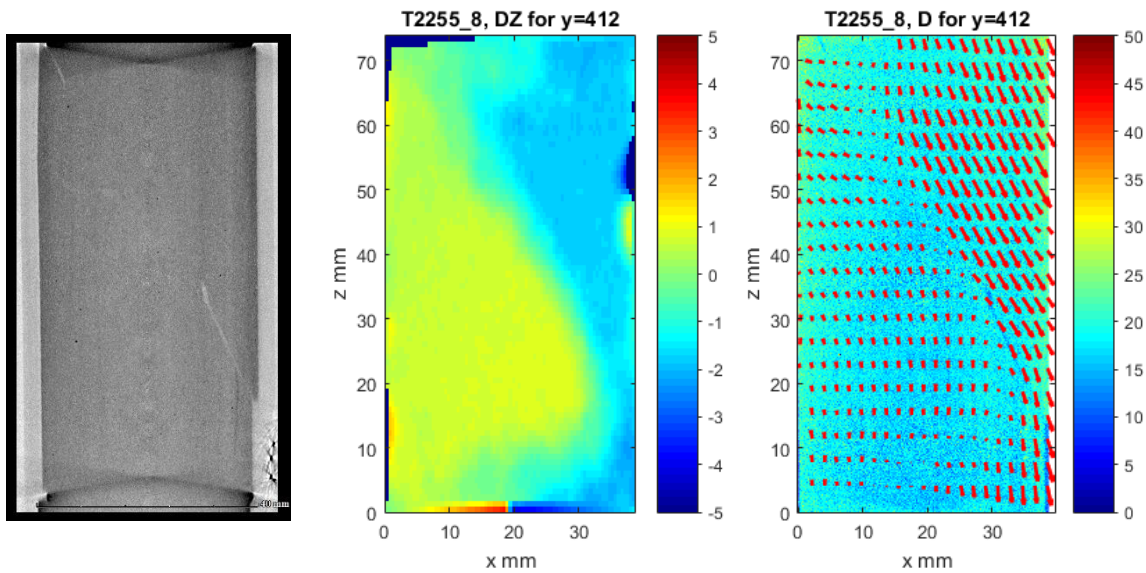
Figure 5: The central cross section of sample number 1 after macroscopic failure (left), the calculated relative displacement (middle) and the displacement vectors in the longitudinal axis (right). The processed volume is downscaled 4^3 times relative to the CT volume, and the displacement vectors are not to scale.

Sample 2 experienced compaction without ever forming a clear shear plane. The radial deformation sensor indicated only minor radial dilatation for sample 2 (approximately 1 mS). However, the CT images clearly show the occurrence of radial expansion in the lower 30 % or so of the sample (i.e. along diameters not recorded by the deformation sensor). Figure 6 shows the radial strain distribution along the middle vertical cross section from the CT scans. It is calculated from the reconstructed volumes' change in diameter with increasing shear stress.
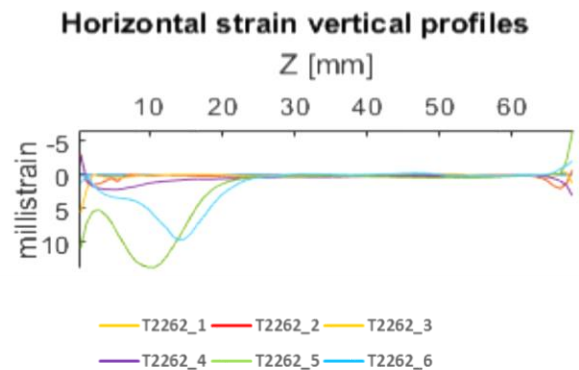
Figure 6: Radial strain calculated along the same vertical profile for the 6 CT scans of sample 2.

The central vertical cross sections from four CT scans for sample number 2 are given in Figure 7 (scans 3-6). The lower part of figure 7 shows the relative vertical displacement vectors for the same CT scans. With progressively increasing shear stress, the vertical deformation follows the radial deformation trend and concentrates in the lower region of the sample.
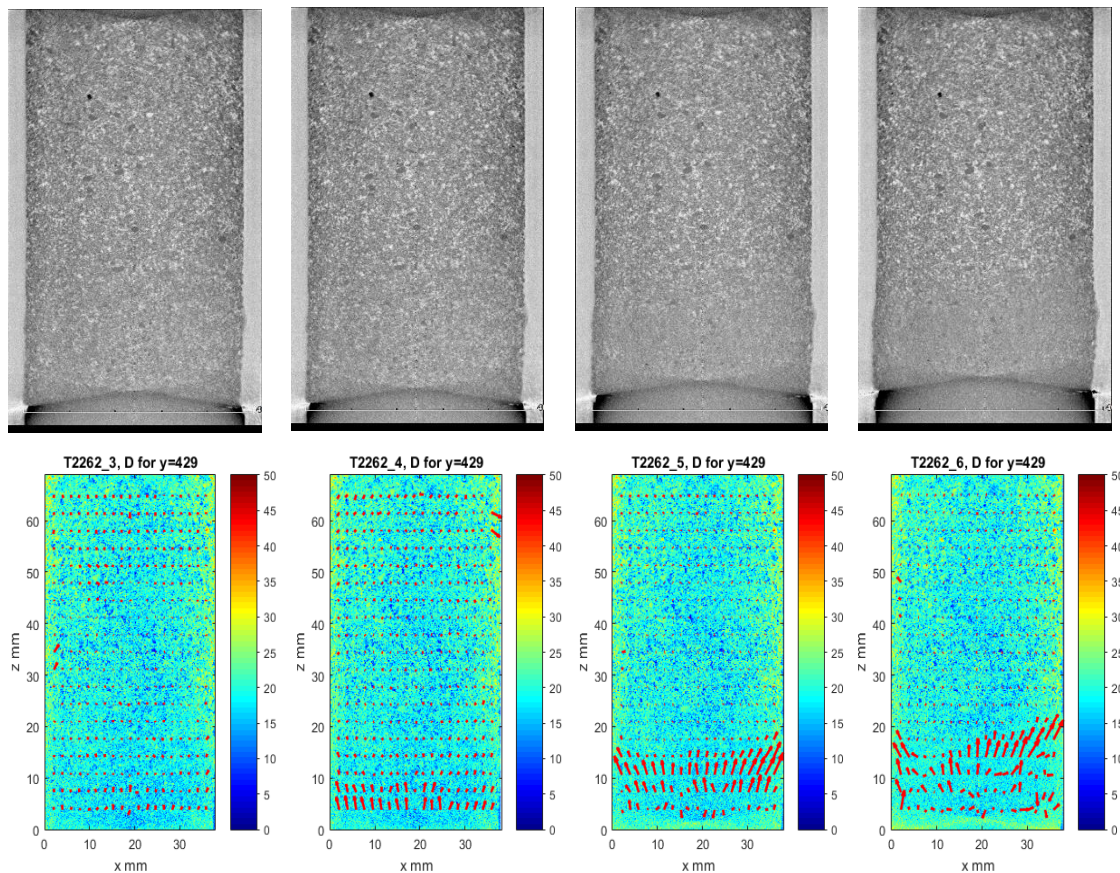
Figure 7: Vertical cross sections of CT scan 3-6 of sample 2 (top). The lower plot shows the calculated vertical displacement vectors in approximately the same cross sections.

CONCLUSION

Triaxial testing of normally sized samples under realistic reservoir conditions inside an industrial CT scanner inherently creates challenges in terms of image quality. Noise issues have to be adressed, and the material making up the triaxial cell body will absorb significant portions of the X-ray energy. Consequently, the exposure time and total acquisition time is increased. Even so, the opportunity of glancing into the rock interior as it deforms can increase the understanding of strain localization and distribution. In this study, with only preliminary data treatment of the first experiments in a new setup, we have seen that the

CT images can reveal deformation information not readily available using more traditional deformation sensors.

Experimental plans include coupling measurement of changes in geophysical properties (electrical and acoustic) directly to rock damage. Furthermore, the triaxial apparatus will be used to study fluid flow and porosity development under anisotropic stress conditions in various rocks. By combining measurements of changes in geophysical properties with detailed mapping of fluid saturation, the aim is to contribute to relevant rock models [1].

REFERENCES

[1] Alemu, B. L., Aker, E., Soldal, M., Johnsen, Ø. and Aagard, P. Effect of sub-core scale heterogeneities on acoustic and electrical properties of a reservoir rock: a CO2 flooding experiment of brine saturated sandstone in a computed tomography scanner. *Geophysical Prospecting*, (2013) **61**, 235-250.

[2] Alikarami, R. and Torabi, A. Micro-texture and petrophysical properties of dilation and compaction shear bands in sand. *Geomechanics for Energy and the Environment*, (2015) **3**, 1-10.

[3] Bèsuelle, P., Desrues, J. and Raynaud, S. Experimental characterisation of the localisation phenomenon inside a Vosges sandstone in a triaxial cell. *International Journal of Rock Mechanics & Mining Sciences*, (2000) **37**, 1223-1237.

[4] Bèsuelle, P., Viggiani, G., Lenoir, N., Desrues, J. and Bornert, M. X-ray Micro CT for Studying Strain Localization in Clay Rocks under Triaxial Compression in *Advances in X-ray Tomography for Geomaterials*, ISTE, London (2006), 35-52.

[5] Desrues, J. and Viggiani, G. Strain localization in sand: an overview of the experimental results obtained in Grenoble using stereophotogrammetry. *International Journal for Numerical and Analytical Methods in Geomechanics*, (2004) **28**, 279–321.

[6] David, C., Menèndez, B. and Mengus, J. Influence of mechanical damage on fluid flow patterns investigated using CT scanning imaging and acoustic emissions techniques. *Geophysical Research Letters*, (2008) **35**, L16313.

[7] Higo, Y. Oka, F., Kimoto, S., Sanagawa, T. and Matsushima, Y. Study of strain localization and microstructural changes in partially saturated sand during triaxial tests using microfocus X-ray CT. *Soils and Foundations*, (2011) **51**, 95–111.

[8] Higo, Y., Oka, F., Sato, T., Matsushima, Y. and Kimoto, S. Investigation of localized deformation in partially saturated sand under triaxial compression using

microfocus X-ray CT with digital image correlation. *Soils and Foundations*, (2013) **53**, 181-198.

[9] Louis, L., Wong, T. and Baud, P. "Imaging strain localization by X-ray radiography and digitial image correlation: Deformation bands in Rotbach sandstone. *Journal of Structural Geology*, (2007) **29**, 129-140.

[10] Sijbers, J. and Postnov, A. Reduction of ring artefacts in high resolution micro-CT reconstructions. Physics in Medicine and Biology, (2004) 49, 247-253.

USING LOW FREQUENCY ELECTRICAL IMPEDANCE SPECTROSCOPY FOR AN ENHANCED PORE SPACE CHARACTERIZATION AND ASSESSMENT OF CARBONATES

Sarah Hupfer[1], Matthias Halisch[1], Andreas Weller[2]

[1]Leibniz Institute for Applied Geophysics, Dept. 5 Petrophysics & Borehole   Geophysics, Stilleweg 2, D-30655 Hannover, Germany

[2]Clausthal University of Technology, Institute of Geophysics, Arnold-Sommerfeld-Straße 1, D-38678, Clausthal-Zellerfeld, Germany

This paper was prepared for presentation at the International Symposium of the Society of Core Analysts held in Vienna, Austria, 27 August -1 September 2017

ABSTRACT

This study investigates the complex electrical conductivity of carbonate samples using low frequency electrical impedance spectroscopy. The analysis is conducted in combination with petrophysical, mineralogical and geochemical measurements. We show that Spectral Induced Polarization (SIP) is a useful tool to obtain detailed information about rock properties and pore space characterization. Rock parameters like permeability, pore-size and specific surface area can be estimated. So far only sandstones or sandy materials were investigated in detail by laboratory SIP measurements. Several robust empirical relationships have been found that combine IP signals and petrophysical parameters, especially hydraulical properties. Nevertheless, only few and incomplete investigations about SIP on carbonates exist in literature.

For our study different types of carbonates were analyzed with laboratory SIP experiments. Rock properties like grain density, porosity, permeability and surface area were determined by routine core analysis. Geochemistry and mineralogy were used to differentiate the carbonate types of carbonates. First results of the SIP-measurements showed polarization effects for all different types. With respect to the frequency dependence, four different types of polarization behavior were observed in the spectra of the imaginary part of conductivity: a constant quadrature conductivity, a constant slope, a combination of both and a maximum type have been be identified. Each behavior can be assigned to the specific carbonate type.

A comparison between SIP data and the petrophysical parameter of the sample set showed that it is very challenging to find a clear correlation between polarization effects and any petrophysical parameter for carbonate rocks, in comparison to sandstones. Nevertheless, these data indicates that the surface conductivity controls the conduction and polarization mechanism. The linear gradient of this relation leads to an estimation of the formation factor of carbonates. Furthermore, the investigation of the dissolution behaviour of

carbonate rock will be focused on the estimation of the impact on polarization effects that result from varying pore space.

INTRODUCTION

Impedance spectroscopy (IS) or spectral induced polarization (SIP) is used for a wide range of applications within geophysics. As well as characterization of hydraulic properties of shallow aquifers, IP measurements can improve the reliability of permeability prediction from geoelectric measurements [1, 2, 3]. The method is mainly controlled by the lithological properties of the rock, and the polarization is related to the surface conductivity and the surface area of the interconnected pore network [4, 5, 6]. Laboratory SIP measurements can provide pore radii distribution [7, 8], a simplified description of the pore space geometry and improve the prediction of a formation factor [9].

The electrical conductivity is described as complex quantity. The real part of the complex electrical conductivity (σ^*) represents the ohmic conduction (σ') while the imaginary part represents the polarization phenomena (σ'').

$$\sigma^* = \sigma' + i\sigma'', \qquad [E1]$$

with i= $\sqrt{(-1)}$ being the imaginary unit. Most models of σ^* for a porous material at low frequencies assume a parallel circuit consisting of two conduction terms:

$$\sigma^* = \sigma_{el} + \sigma^*_{surf}, \qquad [E2]$$

with σ_{el} representing an electrolyte contribution via conduction and with σ^*_{surf} being a mineral surface contribution through conduction and polarization within the electrical double layer of the pore surface. Polarization is solely associated with the surface conductivity at low frequencies (<1 kHz). For a fully saturated material the complex electrical conductivity can be separated in the following way:

$$\sigma' = 1/F * \sigma_w + \sigma'_{surf} \text{ [E3]} \qquad and \qquad \sigma'' = \sigma''_{surf}, \qquad [E4]$$

where F is the electrical formation factor and σ_w is the fluid conductivity.

Originally, the formation factor was defined as the ratio between σ_w and the electrical conductivity (σ_0) of a fully-saturated porous rock on the condition that electrical conductivity is purely ionic and only via the pore fluid:

$$F = \sigma_w/\sigma_0. \qquad [E6]$$

For low salinity measurements an additional conduction mechanism (σ^*_{surf}) occurs, which is taken into account using a complex term. SIP can be used to determine this term and correct the formation factor for low salinity measurements.

A preliminary investigation was conducted on clay-rich carbonate samples from the Tushka area in Egypt using SIP [10] and with focus on fractal dimension [8]. The SIP measurements showed polarization effects and a strong relationship between σ_{surf} and σ'', which is comparable to sandstones. But a correlation between σ'' and S_{por} was not observed. Those results were used as the basis for an extended and more systematic study on carbonate rocks. One goal is to improve the SIP data processing for a better correlation and prediction of petrophysical parameters from SIP data. The complex electrical properties were investigated using SIP in combination with petrophysical, mineralogical and geochemical measurements. We want to extend the carbonate data basis and compare these results with existing relationships and the better known polarization behavior of sandstones. Additionally we want to improve the prediction of petrophysical parameters from SIP.

SAMPLES & METHODOLOGY

This systematic study includes the four different carbonate types: Indiana Limestone (ILS), Silurian Dolomite (DOL), Leuders (LK) and Edwards Brown Carbonate (EBK), which were classified as biogenous sediments. Sample sets of each carbonate type show a broad range of petrophysical parameter (Tab. 1). All petrophysical measurements following protocols related to core and scal analysis RP40 [11]. Imaging methods such as scanning electron microscopy (SEM) and x-ray computer tomography (μ-CT) were used to obtain a qualitative image to differentiate the carbonate types and to describe the pore space (Fig. 1).

The LK has a very fine crystalline calcium carbonate matrix with small recrystallization structures. The samples contain also a small amount of iron hydroxide, which can be seen as a white coloured material in Fig. 1 a. The DOL carbonate consists of large crystals with some dissolution structures (Fig. 1 b). The matrix is homogeneous with more than 90% dolomite. The ILS contains almost exclusively calcium carbonate (Fig. 1 c). Aggregates with calcites shells can be seen, which recrystallize towards the pore. The matrix of the EBK is fine-grained and consists of idiomorphic rhombohedral-shaped crystals (Fig. 1 d). Some of them show cavities inside. Cementation can be noticed on the crystal surfaces but does not occur in larger pores. Kaolinite was identified in some samples, but is of minor importance because of its negligible amount. The four samples used are clay-poor carbonates.

Table 1: Range of petrophysical parameter of the carbonate sample sets.

SIP measurements were conducted at a constant temperature of 20°C using $CaCl_2^-$ as fluid with a constant conductivity of 100 mS/m. The used measurement cell is described in [12, this SCA proceedings]. A frequency range of 2 mHz to 100 Hz was used for this analysis.

		ILS	DOL	LK	EBK
φ	Min	17.01	9.76	10.76	18.60
[%]	Max	19.91	17.62	20.93	41.64
K	Min	161.64	4.79	0.08	23.06
[mD]	Max	290.23	260.58	4.41	273.80
Spor	Min	2.66	0.10	9.67	13.39
[1/μm]	Max	4.80	24.77	2.93	31.60
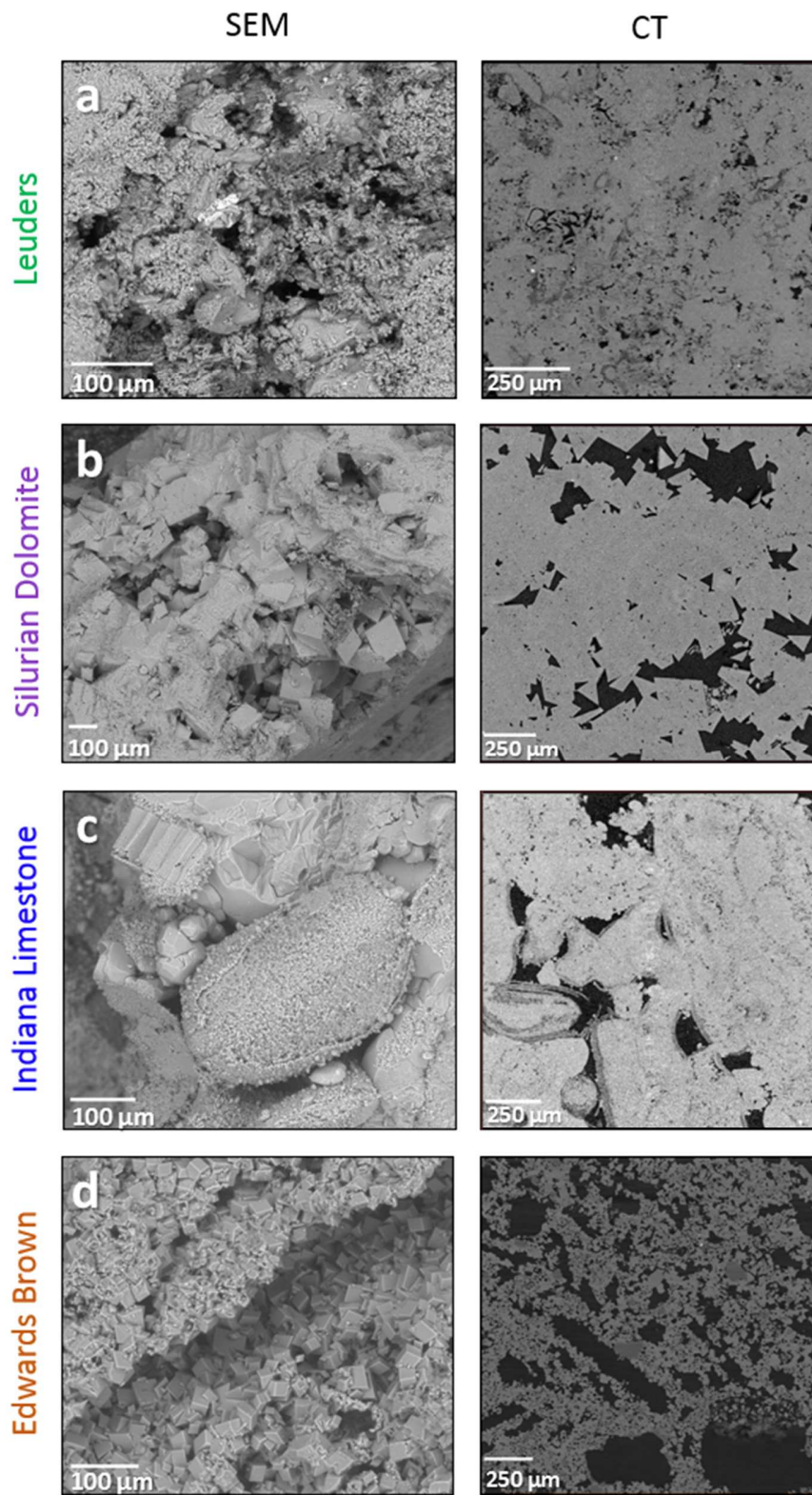
Figure 1:
Left: SEM images.
Right CT images.
a) Leuders
b) Silurian dolomite
c) Indiana Limestone
d) Edwards Brown
Carbonate

RESULTS

The real and imaginary part of the conductivity are displayed in Figure 2 using one characteristic curve for each carbonate type. The real part is influenced by the conductivity of the saturating fluid and thus depends on the porosity of the samples. The EBK, with a porosity of 40%, shows the highest value about 11 mS/m, whereas the other three samples with porosities of less than 20% show significantly lower conductivities ranging between 2-6 mS/m. The behavior of the imaginary part of the conductivity is different for all carbonate types exhibiting a constant quadrature conductivity (ILS), a constant slope (DOL), a combination of both (LK), and a maximum type (EBK) with a peak frequency of 0.2 Hz. Each polarization behavior can be assigned to a specific carbonate type and is reproducible for the whole sample set. This observation is in contrast to the Tushka carbonates of the preliminary study, where the specific curve types occur randomly within the sample set and do not correlate with the microfacies association.
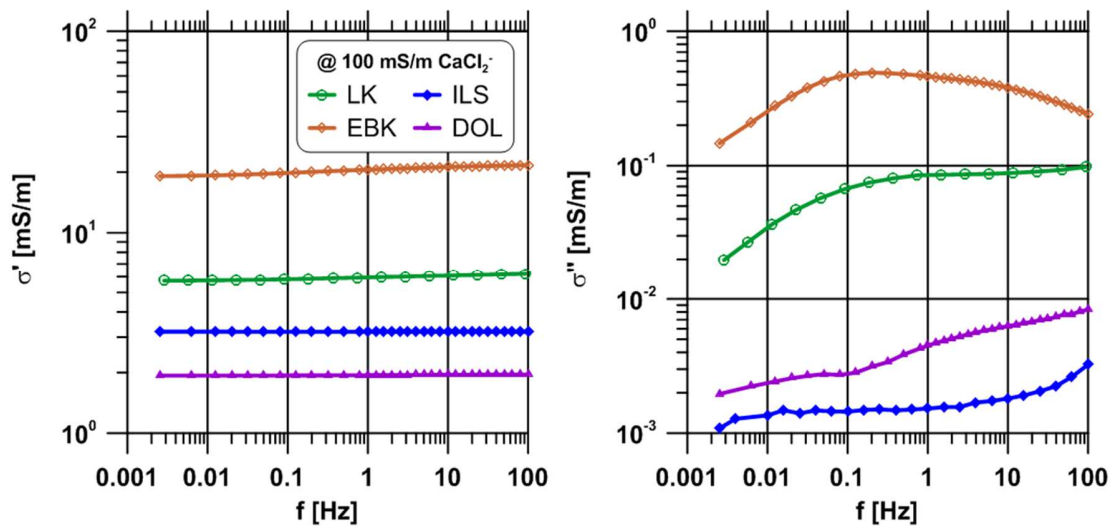
Figure 2: Exemplified results of the SIP measurements of the carbonate sample sets. Left: Conductivity spectra. Right: Spectra of the imaginary part of the conductivity.

Figure 3 shows the relationship of the surface area per unit pore volume (Spor) with the imaginary part of conductivity at 1 Hz in comparison with the Tushka carbonates [10] and the relationship to sandstones [6]. The carbonate types with higher polarization effects (EBK, LK) sustain the correlation with sandstones very well, whereas ILS and DOL data with lower polarization effects indicate no clear correlation. ILS show a similar shift towards a higher surface area without being shifted towards higher conductivity values like the Tushka carbonates. No significant change for imaginary conductivity with increasing surface area can be observed for the DOL type.

The relationship between σ'' and σ'_{surf} is shown in Figure 4, including the data of the Tushka carbonates and the correlation for these carbonates and the sandstones as well.
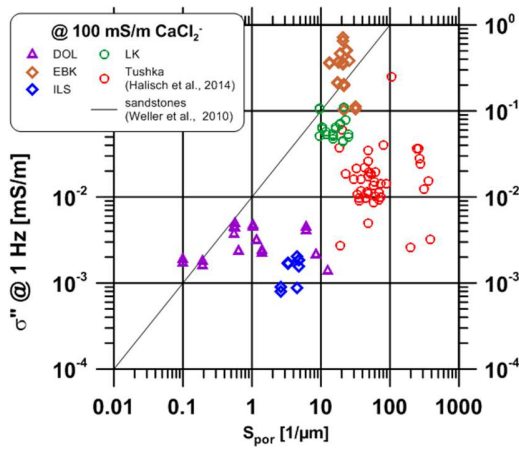
Figure 3: σ" (@1 Hz) and S$_{por}$ relationship for the investigated carbonate samples and including the Tushka carbonates in comparison to the sandstone fit.
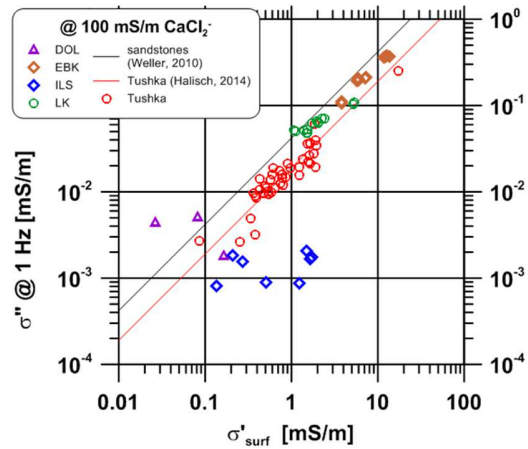
Figure 4: Crossplot between σ" (@1 Hz) and σ'$_{surf}$ for the investigated samples and the Tushka carbonates. Additional the fits for Tushka carbonates and sandstones are plotted.

The ratio of the two surface conductivities corresponds to the linear gradient l, which can explain the data

$$l = \sigma''_{surf} / \sigma'_{surf} \quad \text{with} \quad \sigma'' = \sigma''_{surf.} \qquad [E7]$$

The gradient for sandstones is 0.042 and for the Tushka carbonates 0.019 with a coefficient of determination R^2 of 0.911 and 0.853, respectively. In comparison, the carbonate types in this study show a gradient of l=0.029 (R^2=0.98). The fit of the correlations for all carbonate types (this study and Tushka carbonates) lead to a value of 0.025 (R^2=0.93). The two samples sets with higher polarization effects (EBK, LK) follow the trend very well, whereas the DOL and ILS exhibit larger deviations from the given trend. Thus, the observations show clearly that the surface conductivity controls the bulk conductivity and the polarization mechanism.

For experiments with a single salinity of the saturating brine, it is only possible to get an apparent F (F') with equation [E6] due to the complex behavior of the conductivity. Archie's Law relates F to the interconnected porosity (ϕ).

$$F = \phi^{-m}, \qquad [E8]$$

where m is the cementation coefficient. The cementation coefficient is unknown for the used carbonates types. One possibility to determine F using SIP measurements is to vary the salinity of the pore fluid, but this method is time consuming and impracticable for field measurements. A method which uses only one single salinity measurement can provide a

predicted formation factor. According to [5], the predicted formation factor is determined by

$$F_P = \sigma_w / (\sigma' - \sigma'_{surf}) = \sigma_w / (\sigma' - \sigma''/l), \quad [E9]$$

whereas the gradient l is known from fitting the relationship between σ'' and σ'_{surf}.
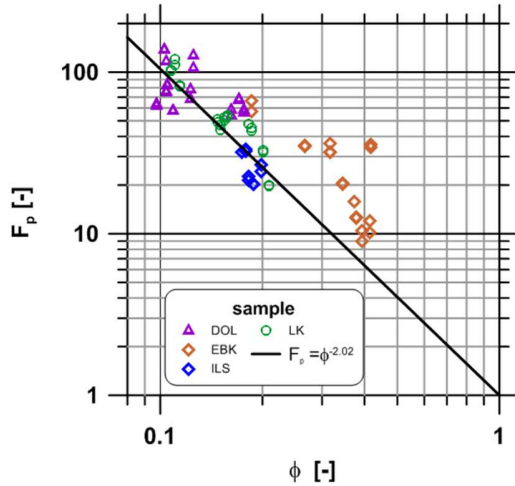
Figure 5: Formation factor calculated from [E9] plotted against porosity for the studied carbonates.
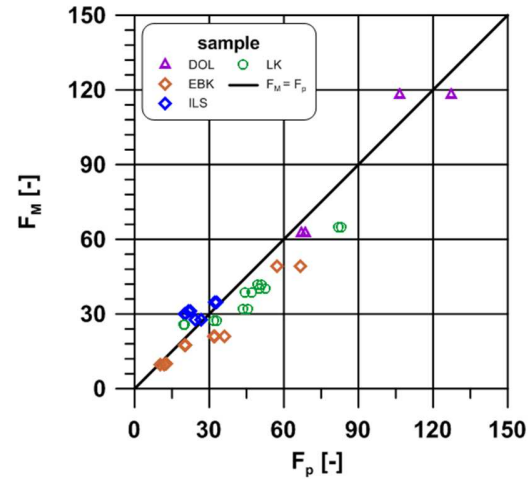
Figure 6: Crossplot of F_P versus F_M. Average deviation between F_p and F_M is 0.096.

Figure 5 shows the results of the calculated F_P in relation to the porosity ϕ. A fit with [E8] provides a cementation exponent of 2.02 for the studied carbonates. The crossplot of F_M versus F_p is shown in Figure 6. F_M is the formation factor determined at very high salinities with a two-electrode measurement and could also be referred to as true formation factor. The comparison of these different determined formation factors offers a good consistency. Considering all samples, the average deviation between F_M and F_p reaches d=0.096.

CONCLUSIONS & OUTLOOK

We have investigated four different carbonate sample sets, which showed significant differences in CT and SEM images. Four different types of polarization curves were observed in the spectra of imaginary part of conductivity. Each carbonate type can be attributed to a characteristic curve type. The carbonates with higher polarization effects ($\sigma'' > 10^{-2}$ mS/m) fit the existing relationships for sandstones much better than the types with lower polarization effects. Nevertheless, this data set satisfies a single linear relationship $\sigma'' = l * \sigma'_{surf}$ with l = 0.029. The estimation of the gradient l is helpful in conjunction with an IP measurement to improve petrophysical interpretation from resistivity and IP measurements. The gradient l leads to a reliable prediction of formation factors of carbonate rocks. This prediction is useful in well logging and in hydrogeophysics.

To improve the understanding of polarization phenomena of carbonates, we have carried out multi-salinity measurements, determination of cation exchange capacity and 3D imaging. Additionally, the dissolution behavior of carbonates to quantify the influence on the polarization effects resulting from changes of the pore space will be investigated.

REFERENCES

[1]   Revil, A. and Florsch, N. 2010. *Determination of permeability from spectral induced polarization in granular media.* Geophysical Journal International, Vol.**181**, No.3, p.1480-1498.

[2]   Weller, A., Nordsiek, S. and Debschuetz, W. 2010. *Estimating permeability of sandstone samples by nuclear magnetic resonance and spectral induced polarization.* In: Geophysics, Vol.**75**, No.4, p. E215-E226.

[3]   Weller, A., Kassab, M.A., Debschuetz, W. and Sattler, C.D. 2014. *Permeability prediction of four Egyptian sandstone formations.* Arabian Journal of Geoscience, Vol.**7**, No.12, p.5171-5183. DOI 10.1007/s12517-03-1188-7.

[4]   Börner, F.D. and Schön, J.H. 1991. *A relation between the quadrature component of electrical conductivity and the specific surface area of sedimentary rocks.* Log Analyst, Vol.**32**, p.612–613.

[5]   Börner, F. D., Schopper, J. R. and Weller, A. 1996. *Evaluation of transport and storage properties in the soil and groundwater zone from induced polarization measurements*: Geophysical Prospecting, Vol.**44**, p.583–601.

[6]   Weller, A., Slater, L., Nordsiek, S. and Ntarlagiannis, D. 2010. *On the estimation of specific surface per unitpore volume from induced polarization: a robust empirical relation fits multiple data sets.* Geophysics, Vol.**75**, No.4, p.WA105-WA112.

[7]   Revil, A., Koch, K. and Hollinger, K. 2012. *Is it the grain size or the characteristic pore size that controls the induced polarization relaxation time of clean sands and sandstones?*: Water Resources Research, Vol.**48**, No.5, W05602, doi:10.1029/2011WR011561.

[8]   Weller, A., Ding, Y., Zhang, Z., Kassab M. and Halisch, M. 2016. *Fractal dimension of pore space in carbonate samples from Tushka area (Egypt).* International Symposium of the Society of Core Analysts, paper SCA2016-079.

[9]   Weller, A., Slater, L. and Nordsiek, S. 2013. *On the relationship between induced polarization and surface conductivity: Implications for petrophysical interpretation of electrical measurements.* Geophysics, Vol.**78**, No.5, D315-D325.

[10]   Halisch, M., Weller, A. and Kassab, M. A. 2014. *Impedance Spectroscopy on Carbonates.* International Symposium of the Society of Core Analysts, paper SCA2014-039.

[11]   RP40, American Petroleum Institute. 1998. *Recommended practices for core analysis*.

[12]   Halisch, M., Grelle, T., Hupfer, S., Blanke, J.-T. and Lehne, C. 2016. *A new and modular laboratory core holder for high-precision measurements with low frequency impedance spectroscopy on natural rocks.* International Symposium of the Society of Core Analysts, paper SCA2017-021.

STUDY OF DRILL CUTTINGS POROSITY FOR FORMATION EVALUATION

S. T. Dang, M. M. Rolke, C. H. Sondergeld and C. S. Rai
Mewbourne School of Petroleum and Geological Engineering
University of Oklahoma

ABSTRACT

Petrophysical measurements on drill cuttings have an economic appeal especially in unconventional formation evaluation. Drill cuttings are readily available, a byproduct of drilling, and can potentially provide a variety of reservoir quality parameters, such as total organic carbon, porosity, mineralogy, thermal maturity, pore structure and habit, mechanical elastic properties, etc. While log and core data are only available for a limited number of wells, drill cuttings are available for all wells. Therefore, the determination of porosity using drill cuttings can provide a more spatially detailed representation of a formation, which is critical because shale plays can be both vertically and laterally heterogeneous. Porosity is a primary variable controlling hydrocarbon storage of within a formation. There are multiple laboratory methods to directly measure porosity in cores — Low Pressure Pycnometer (LPP), High Pressure Pycnometer (HPP), Nuclear Magnetic Resonance (NMR), Mercury Injection (MICP), etc. A challenge arises when porosity is obtained from drill cuttings due to the inability to directly measure bulk volume of a sample. This study presents the application of a new methodology to measure the porosity from drilling cuttings.

Conventional approaches to calculate porosity require measuring two of three variables namely pore, grain or bulk volume. Our approach uses measures of high-pressure pycnometer grain density on dry drilling cuttings; volume of oil occupying pore space is quantified by NMR measurements.

Initial results on 3 tight sands and 27 shale samples show the new approach is promising for the estimation of porosity. 90% of the cutting porosities made on tight sands and shales are within 1.5% p.u. of the core porosities. This error is believed to be due to sample loss during the saturation process or excess oil on the surface of the cuttings.

INTRODUCTION

Petrophysical characterization is critical to a successful exploration program. Logging While Drilling (LWD) is a routine practice, in which reservoir properties are estimated from combinations of different log responses in real-time. These parameters later will be compared to core data, which are generally accepted as more reliable. However, core acquisition is costly and is limited to very few wells.

The workflow to determine petrophysical properties for unconventional reservoirs is more complicated and uncertain than the conventional counterpart. Shale is typically heterogeneous (Ross and Bustin, 2008[1]; Nobakht et al., 2013[2]), therefore, more spatially detailed reservoir description is essential, especially in evaluating completion efficacy (Prioul et al., 2016[3] and Cipolla et al., 2011[4]). Drill cuttings are available as a byproduct of the drilling process. Different drill bits can provide different qualities of cuttings; however, when cuttings larger than 1 mm (20 mesh size) are available, they can be a cost-effective alternative to various reservoir characterizations. While some routine core analyses, such as organic richness (TOC), mineralogy (from X-Ray Diffraction or FTIR, Ballard, 2007[5]; Sondergeld and Rai, 1993[6]), or producibility (from Rock-Eval® or SRA®), are quite easily performed on cuttings, porosity and mechanical properties are difficult to measure (Dang et al., 2017[7]). This is due to the irregularity of cutting shape and the miniature scale of cuttings.

In this study, we focus on proposing a new method that help to reasonably estimate cutting porosity, as well as addressing difficulties while measuring this parameter.

EXPERIMENTAL APPROACH

There are two major approaches to porosity measurements: first, is the measurement of bulk volume and grain volume (Eq. 1), and second, is the measurement of bulk density and grain density (Eq. 2). The first method requires good control on sample mass conservation (Karastathis, 2007[8]). The last approach usually suffers from a large uncertainty in the estimated bulk density due to presence of residual fluids. Common to both approached is the measurement of bulk volume. These concerns make the estimation of cutting porosity challenging.

$$\emptyset = \frac{V_{bulk} - V_{grain}}{V_{bulk}} \dots\dots\dots\dots\dots\dots\dots\dots\dots\dots\dots \text{ (1)}$$

$$\emptyset = \frac{\rho_{grain} - \rho_{bulk}}{\rho_{grain} - \rho_{fluid}} \dots\dots\dots\dots\dots\dots\dots\dots\dots\dots\dots \text{ (2)}$$

Attempts to measure the bulk volume of cuttings through the injection of fluids, such as mercury, oil or water into a known volume pycnometer containing cutting samples were not successful due to the variable wettability of cuttings. Mercury injection suffers from a

large and unknown conformance effect (Bailey, 2009[9]), which limits bulk volume determination. **Fig.1** shows bulk volume measured by MICP after low pressure (20 psi) injection for cutting samples (1-2mm); the results are underestimated, compared to the true bulk volume. True bulk volume of cuttings is calculated from the bulk volume estimated from a rock plug (from which the cuttings are generated), then normalize cuttings' weight to plug's weight. With a small injection pressure, oil or water can help to overcome conformance effect on cutting surface. However, for tight rocks having small capillary tubing size, even under low pressure, the intrusion of wetting phase can happen. Unfortunately, organic rich shales typically include both water-wet and oil-wet flow paths (Odusina et al., 2011[10]). Some previous studies also proposed using powder pycnometer to measure solid volume of cuttings, these measurements have to reply of the consistency of powder packing, and cutting surface roughness (Meazza et al., 1996[11], Egermann et al., 2006[12]
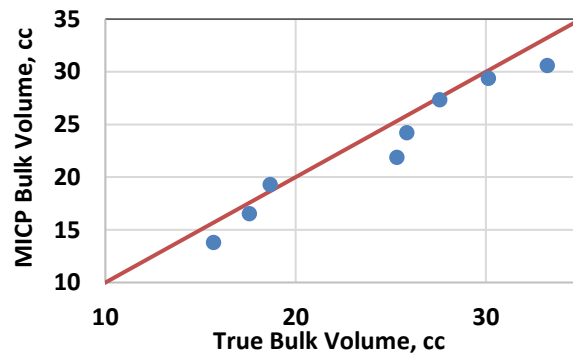
Fig. 1 Comparison between true bulk volume and bulk volume measured by mercury Injection for rock cutting samples. Because of conformance effect, MICP generally underestimates bulk volume. The error ranges from 2.5% to 12%.

To overcome the challenge of measuring bulk volume for cutting samples, we propose the following approach (**Equations 3-7**). First, cuttings are prepared by sieving above 1mm (20 mesh), dried at 100°C for 24 hours; this protocol was determined through thermogravimetric analyses (TGA) (Sondhi and Solano, 2009[13]). 100°C is efficient to remove surface or free water. Clay-bound water requires higher temperature to be eliminated. Therefore, the porosity estimated from this study, should be considered as effective porosity. The drying step is critical to accurately estimate sample mass (m_{bulk}) and rock grain density (ρ_{grain}). Grain density is estimated, using high-pressure pycnometer (HPP), with He as the purge gas and pressure of 250 psi. Drill cuttings are collected in a Teflon (PTFE) filter mesh bag (**Fig. 2**) for the saturation with dodecane (ρ=0.75 g/cc). We saturate for 24 hours at a constant hydrostatic pressure of 7000 psi, after which, the samples are assumed to be 100% saturated. Shale generally includes reactive clays (O'Brien and Chenevert, 1973[14]), so, dodecane is selected as the injected fluid, instead of brine.

Applying simple oil-gas capillary pressure conversion, 7000 psi is considered high enough to saturate pores having throats larger than 1 nm. The difference of NMR T2 volume or sample mass between dry and saturated cuttings include oil fraction injected in pore space (V_{oil}) and oil fraction coating on the cuttings 'surface. NMR spectra run on saturated cuttings allowed us to differentiate these two oil fractions.

Detailed derivation for the equation used for this approach:

$$\phi = V_{oil} / V_{bulk} \dots\dots\dots\dots\dots\dots\dots\dots\dots\dots\dots\dots(3)$$

$$V_{bulk} = m_{bulk} / \rho_{bulk} \dots\dots\dots\dots\dots\dots\dots\dots\dots\dots\dots..(4)$$

$$V_{bulk} = m_{bulk} / (\rho_{grain} \times (1- \phi)) \dots\dots\dots\dots\dots\dots\dots\dots\dots.(5)$$

Substituting V_{bulk} from Eq. 5 to Eq. 3, we have:

$$\phi = V_{oil} / (m_{bulk} / (\rho_{grain} \times (1- \phi))) \dots\dots\dots\dots\dots\dots\dots..(6)$$

Solving Eq. 6 for porosity, ϕ:

$$\phi = V_{oil} \times \rho_{grain} / (V_{oil} \times \rho_{grain} + m_{bulk}) \dots\dots\dots\dots\dots\dots\dots.(7)$$

Fig. 2 Cutting samples were sieved, then collected in PTFE filter mesh bag, ready for the saturation process.

Protocols to measure m_{bulk} and ρ_{grain} have been well established (Karastathis, 2007), the accuracy of porosity calculated from this method, depends on how V_{oil} is quantified. T2 distribution for both dry and saturated cutting samples were acquired using the benchtop Oxford Geospec2™ instrument with operating frequency of 12 MHz, and echo spacing of

114μs (**Fig. 3**). The difference in mass before and after saturation was also recorded. **Fig. 4** shows the good agreement between the oil volumes measured by mass difference and NMR gain. NMR volume gain include oil fraction injected in pore space and oil fraction coating on the cuttings' surface
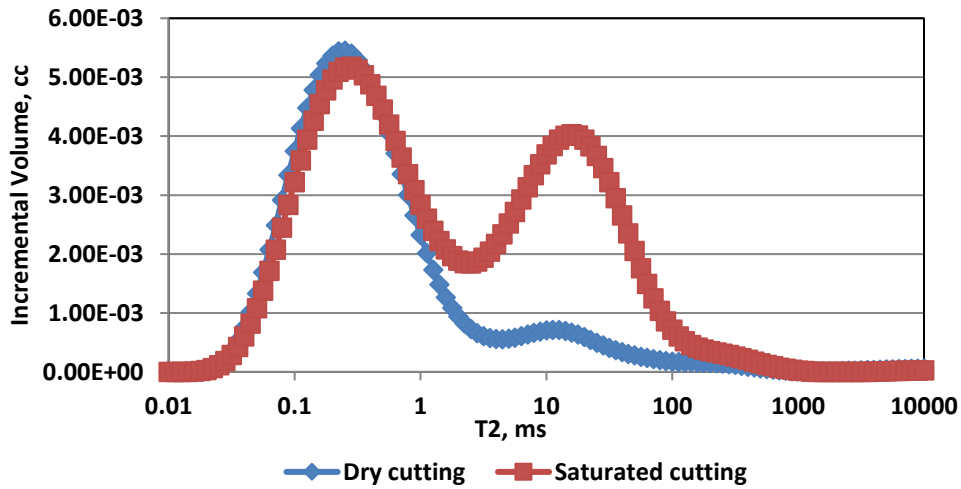
Fig. 3 NMR T2 distribution for a Barnett cutting sample before and after saturation. 'Dry cutting' NMR signal shows the existence of clay-bound water with T2 less than 1ms. The porosity estimated from this study should be considered as effective porosity, not total porosity. Note the increase of NMR T2 peak at 10-50 ms due to the injection of dodecane.
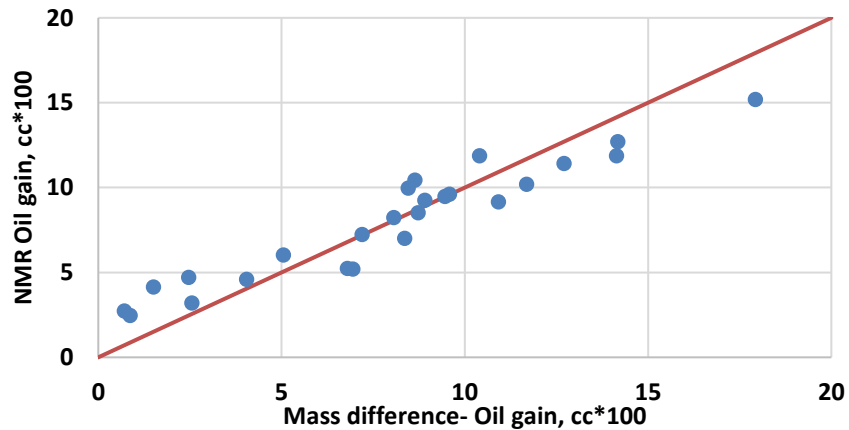
Fig. 4 Injected dodecane volume measured by two different methods: mass gain versus NMR volume gain. NMR volume gain include oil fraction injected in void space and oil fraction coating on the cuttings' surface. Note the error range of mass measures is about 5×10^{-4} g, equivalent to 7×10^{-4} cc; the error range of NMR measures is about 5×10^{-2} g

For the same mass, 1-2mm (10-20 mesh) cuttings have an average surface area 20-40 times more than a core plug. This leads to the overestimation of V_{oil} due to the extra layer of

dodecane coating on the cutting surface, which is supposed not to be included in the porosity calculation. Mass difference between dry and wet cuttings cannot exclude this unwanted oil fraction from calculation. However, by setting a T2 cutoff at 70 ms, we can identify the amount of oil actually occupying pore spaces (see **Fig. 5**). In this study, we propose using the difference in NMR before and after saturation with T2 relaxation times less than 70 ms to better estimate of porosity.
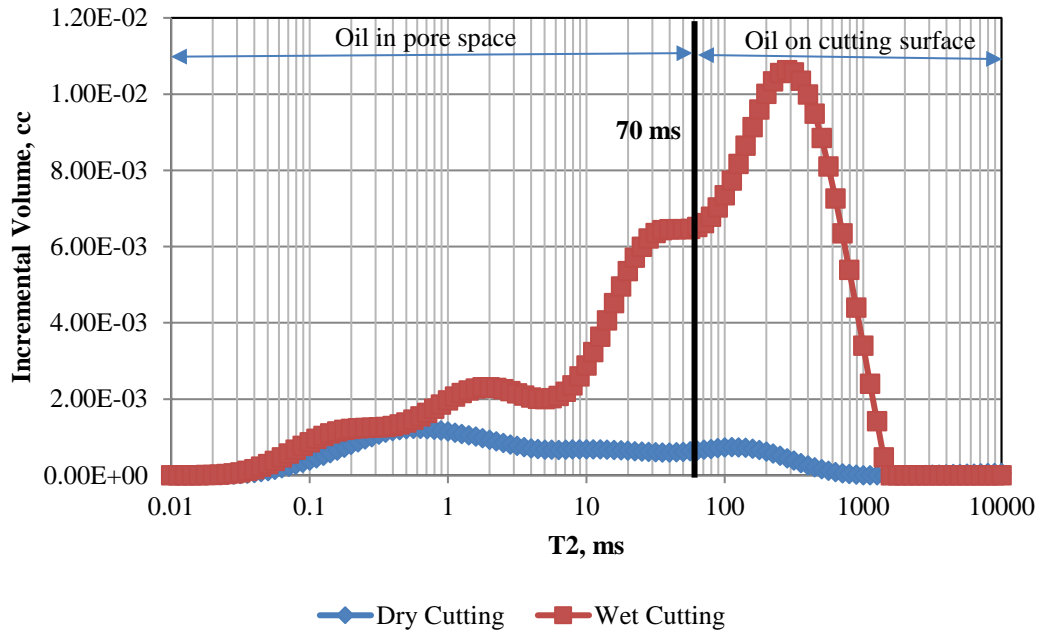
Fig. 5: The increase in NMR T2 amplitude due to the dodecane saturation of cutting samples. T2 cutoff of 70 ms is used to distinguish the volume of oil injected into pore space and the volume of oil coating on the surface of cuttings.

EXPERIMENTS AND SAMPLES

Three outcrop sand and 27 shale samples were selected to test this method. 1" ×1" plugs were attained for each of these samples. While shale samples would be subjected to crushed helium porosity measurement (Karastathis, 2007), sand samples porosity were measured by the combination of high pressure helium pycnometer test (HPP) and T2 NMR. High pressure He pycnometer test allows estimation of air occupying the void space; T2 NMR allows to estimation of liquid occupied void space.

By crushing and sieving, we also create cutting samples with mesh size above 20 mesh (>1-2mm). The purpose is to compare the results from traditional core porosity test and this new protocol for cutting porosity.
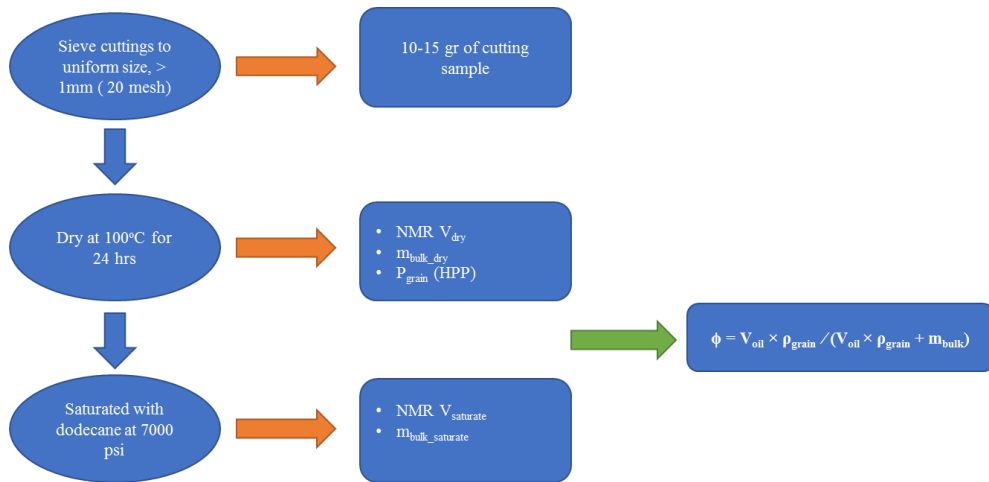
Fig. 6 Flow charts for the proposed new method of cuttings analysis.

RESULTS

We performed conventional core porosity tests along with the proposed method on cuttings for total 30 samples. Porosity for the core measurements range from 1 to 19 p.u with a controlled error of 0.5-1 p.u. **Fig. 7** shows the comparison between results on cutting and core samples. 90% of the cutting porosities are within 1.5%. of the core porosities. The results confirm that the proposed method can be used to estimate cutting porosity with a reasonable range of error. Note the cutting size will impact the quality of the test, sample size above 20 mesh (> 1mm) is recommended.
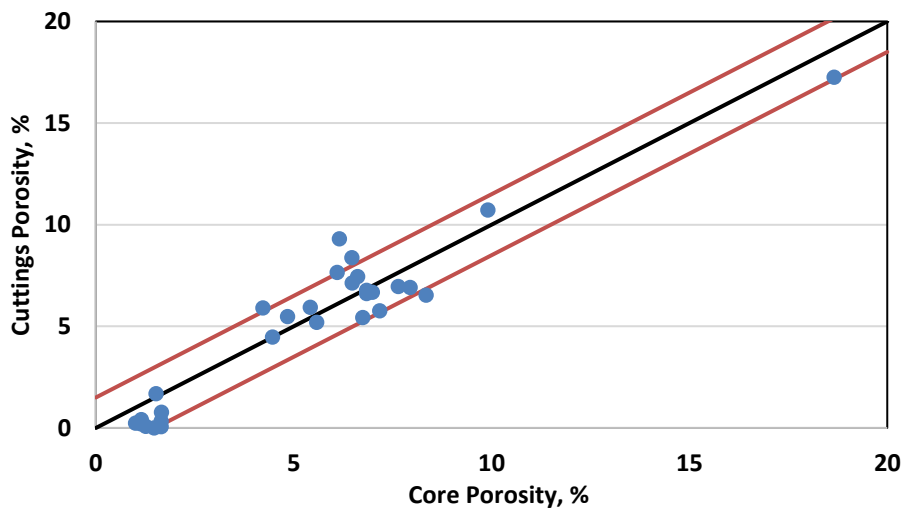
Fig. 7: Comparison of core porosity using conventional methods (standard error of 0.5-1 p.u) versus with cutting porosity (propagated error of 1-1.5 p.u) measured by proposed method in this study. 90% of the cutting porosities are within 1.5 p.u.

CONCLUSIONS

Despite the depth-registration issue, petrophysical characterization on cuttings is promising because of its cost efficiency and availability. This helps to study the heterogeneity of shale formations in both horizontal and vertical scales. In shale, heterogeneity governs both storage and success in completion. This study introduce a new workflow to quantify cutting porosity, which is one of the most difficult reservoir properties to be measured from cuttings. The results show that estimated cutting porosity agrees well with measured porosity from core, with a reasonable error range.

REFERENCES

1. Ross, D., and M. R. Bustin, Impact of shale heterogeneity upon gas storage potential and deliverability: examples from Jurassic and Devonian- Mississippian shale gas reservoirs, CSP/CSEG/CWLS Geo-convention, (2008)
2. Nobakht, M., R. Ambrose, C. R. Clarkson, J. Youngblood, and R. Adams, Effect of completion heterogeneity in a horizontal well with multiple fractures on the long-term forecast in shale gas reservoirs, *Journal of Canadian Petroleum Technology*, (2013)
3. Prioul, R., M. Frydman, and J. Caniggia, Estimating anisotropy mechanical properties and stress based on measurements on cuttings for competition quality: methodology and case study in Vaca Muerta, (2016) SPE-180969-MS
4. Cipolla, C., R. Lewis, S. Maxwell, and M. Mack, Appraising unconventional resource plays: Separating reservoir quality from completion effectiveness, (2001) IPTC 14677.
5. Ballard, B. D., Quantitative Mineralogy of Reservoir Rocks Using Fourier Transform Infrared Spectroscopy. Society of Petroleum Engineers, (2007) doi:10.2118/113023-STU
6. Sondergeld, C. H., and C. S. Rai, A new exploration tool: quantitative core characterization, *Pure and Applied Geophysics* , (1993), 141: 249-268
7. Dang, S., T, I. Gupta, A. Chakravarty, P. Bhoumick, S. Taneja, C. H. Sondergeld, and C. S. Rai, Recovering Elastic Properties from Rock Fragments, *Petrophysics journal*, (2017), Vol. 58, 3: 270-280
8. Karastathis, A., Petrophysical measurements on tight gas shale, Master thesis, (2007), University of Oklahoma.
9. Bailey, S., Closure and compressibility corrections to capillary pressure data, Denver Well Logging Society Fall Workshop at Colorado School of Mines, (2009)
10. Odusina, E., C. H. Sondergeld, and C. S. Rai, An NMR study on shale wettability. Canadian Unconventional Resources Conference, (2011) SPE 147371
11. Meazza O., M. Della Martera, and A. Lyne, Porosity from cuttings: options and answers, SCA #9606, Society of Core Analysts, Montpellier, France, (1996)

12. Egermann, P., N, Doerler, M. Fleury, J. Behot, F. Deflandre, and R. Lenormand, Petrophysical measurements from drill cuttings: an added value for the reservoir characterization process, (2006) SPE 88684
13. Sondhi, N., and L. Soleno, Application of thermogravimetric- Fourier transform infrared spectroscopy analysis in determining heating protocol for porosity measurement in shale, SPWLA symposium, (2009)
14. O'Brien, D. E., and M. E. Chenevert, Stabilizing sensitive shales with inhibited potassium-based drilling fluids. *Journal of Petroleum Technology*, (1973), 255, 1089–110

LINKING MINERAL REACTIVE SURFACE AREA WITH ITS DISTRIBUTION AND PORE GEOMETRY

Ma Jin[1], Duncan Webster[2], Xiang-Zhao Kong[1*], Martin O. Saar[1]

[1]Geothermal Energy & Geofluids Group, Department of Earth Sciences, ETH-Zürich, CH-8092, Switzerland, [2]SCANCO Medical, Bruettisellen Switzerland

This paper was prepared for presentation at the International Symposium of the Society of Core Analysts held in Vienna, Austria, 27 August – 1 September 2017

ABSTRACT

Fluid-rock interactions play an important role in geological and geo-engineering processes, such as chemical stimulation of enhanced geothermal systems and carbon capture, utilization, and storage (CCUS). However, involved reactions are highly dependent on the accessible reactive surface area of minerals which is difficult to quantify. In particular, it is difficult to quantify the surface area of each reacting mineral within whole rock samples, due to the typically heterogeneous distribution of minerals and pores. In this study, we perform detailed laboratory analyses on sandstone samples from deep geothermal sites in Lithuania, in an effort to better quantify reactive surface areas.

We measure specific surface area (SSA) of whole rock samples using a gas adsorption method (BET) with N_2 at a temperature of 77.3 K. We also quantify the samples' porosity and pore size distribution (PSD), using Helium gas pycnometry and Hg porosimetry, respectively. Rock compositions are determined by a combination of X-ray fluorescence (XRF) and quantitative scanning electron microscopy (SEM) - Energy-dispersive X-ray spectroscopy (EDS), which are later geometrically mapped onto 2D images, derived from SEM- Backscattered electrons (BSE, resolution:1.2 µm) and 3D images derived from Micro Computed Tomography (Resolution of 9.5 µm). These digital-mineral maps are then correlated with BET-determined SSA as well as whole-rock porosity and PSD. Porosity and PSD are also analyzed using both 2D and 3D images. It is anticipated that these analyses will provide an in-depth understanding of rock sample chemistry for subsequent hydrothermal-reactive-flow-through experiments on whole-rock samples at elevated pressures and temperatures.

1. INTRODUCTION

Fluid-rock reaction is an important process involved in many geological and geo-engineering systems such as enhanced geothermal systems (EGS) (Althaus and Edmunds, 1987; Pandey et al., 2015) and carbon capture, utilization, and storage (CCUS) (Xu et al., 2003; Guas, 2010). These reactions lead to mineral dissolution and precipitation which may cause changes of reservoir porosity and permeability (Cai et al., 2009; Nogues et al., 2013). Unfavorable fluid-rock reactions can make sustainable reservoir operations challenging. For example, mineral precipitation can lead to a dramatic reduction of the reservoir permeability by several orders of magnitude (Cheshire et al., 2017; Yasuhara et al., 2017) and, consequently, a significant decrease in reservoir productivity/injectivity

during EGS and CCUS. On the other hand, favorable fluid-rock reactions can increase the reservoir permeability by dissolving minerals. For CCUS, such dissolution reactions could facilitate long-term CO_2 mineral trapping (Voskov et al., 2017). However, an increase in reservoir permeability could also cause fluid-pathway "short-circuiting" and lower heat exchange efficiencies in geothermal reservoirs (Feng et al., 2016).

Due to the complexity of coupled fluid flow and fluid-rock reactions, it is well recognized that reactive transport modelling is a powerful approach to predict reservoir operation performances (Beckingham et al., 2016). However, the accuracy of these models depends on reliable measurements of mineral geochemical parameters, among which mineral reactive surface area is the critical one, as it is often poorly constrained in a multi-mineral system (Bourg et al., 2015).

In this study, reactive surface area of individual minerals in sandstone samples is determined by a series of laboratory analyses. A combined method of X-ray fluorescence (XRF), powder X-ray diffraction (XRD), and scanning electron microscope (SEM) - energy dispersive X-ray spectroscopy (EDS) was employed to identify rock compositions. High-resolution SEM - backscatter electron detector (BSE) and SEM-EDS images were analysed to estimate porosity and pore-size distribution (PSD), which were also measured and confirmed by Helium gas pycnometry and mercury porosimetry, respectively. Furthermore, mineral distributions were digitally mapped and reactive surface area of individual minerals was determined. The calculated surface areas were then calibrated, using roughness correction and normalization, to the measurements employing the BET gas absorption method. We also perform 3D micro-CT imaging of a whole-core sample for further analyses of pore connectivity, porosity, and PSD.

2. MATERIALS AND METHODS

2.1 Rock samples

The rock samples used in this study are sandstone, from a depth of 954.6 m in a geothermal well, Vydmantai-1, at the southeast end of the Baltic Sea of Lithuania. The Vydmantai-1 well was drilled in 1989 to a depth of 2564 m (Rasteniene et al, 2005). Transmitted light microscopy observations show that these sandstone samples are well-rounded, fine to very fine grains (sizes of 65μm - 250μm), composed of quartz, feldspar, mica, and a carbonate mineral.

Sandstone specimens were prepared as cylinders, thin sections, and chips for various analyses (see also Sections 2.2 and 2.3). A cylindrical rock specimen with a diameter of 25.4 mm and a length of 39.0 mm was cut for 3D micro-CT imaging, porosity measurements. Later, we will conduct reactive flow-through experiments with the rock cores. A 35 μm-thick thin section with a size of 11.37 mm x 8.34 mm was sliced for microscopy measurements, such as SEM-BSE imaging and SEM-EDS element mapping.

2.2 Porosity and pore size distribution (PSD)

The pore volume of the cylindrical specimen was measured using the Micromeritics AccuPyc II 1340 Pycnometer in the Rock Deformation Laboratory at ETH Zurich. The pore volume was confirmed after 16 purges of Helium at a temperature of 25.14°C. Then

the specimen porosity was obtained as the ratio between the measured pore volume and the total specimen volume. Pore (or throat) size distribution was obtained by Mercury intrusion porosimetry. This PSD measurement was carried out at a temperature of 22.6°C and a maximum pressure of 400 MPa using the Porotec Pascal 140 and 440 (with a detectable size range of 2 nm-100 μm in diameter) in the IGT Claylab at ETH Zurich.

Independent analysis of porosity and PSD of the 35 μm-thick thin section was also performed using various image-processing techniques. The thin section was continuously scanned in 10 x 10 windows using a Jeol JSM-6390 LA SEM together with a BSE in the Electron Microscopy Lab at ETH Zurich. The scanning was performed at an electron accelerating voltage of 15 keV at a working distance of 10 mm to obtain a 1.2 μm-resolution. These 10 x 10 grayscale SEM-BSE coherent images were then stitched using ImageJ to generate a full image of 9474 x 6947 pixel^2, as shown in Figure 1a. Figure 1b shows the corresponding binary image (pores in black and solid in white) using a threshold of 70 on a scale of 0 to 255 (black to white, see the inset with a gray-scale histogram at the top right). This binary image was then used for porosity, PSD, and SSA analyses (see Section 2.4). According to the principle of stereology (Weibel, 1969), the 2D area density mm^2/mm^2 is equivalent to the 3D volume density mm^3/mm^3. The sample porosity can thus be approximated by the 2D areal density mm^2/mm^2 and obtained using image processing. PSD was analysed using the Xlib plugin of ImageJ with a continuous PSD calculation. Its basic principle is that pore space is segmented and measured with circles.

Micro-computed tomography was employed to obtain a 3D geometric representation of the core sample, performed by Scanco Medical AG, Brüttisellen. Cross-section images with 9.5 μm-resolution were acquired using energy of 130 kV and a current of 61 μA. The number of projections was 2000 and the integration time was 3.74 s. Collected images were reconstructed and PSD was analysed using Scanco Medical's Proprietary software (Hilderbrand et al, 1997).

2.3 Mineralogy analysis

Rock compositions were determined using a combination of different techniques, including XRF, XRD, SEM element mapping, and SEM quantitative chemical analysis. To ensure representative measurements, 24.4 g of the sandstone sample was crushed into fine powder for both XRF and XRD analyses.

The XRF analysis was performed using an XRF spectrometer (WD-XRF, PANalytical AXIOS) in the high-pressure Lab at ETH Zurich. During the XRF measurement, 1.5 g of the crushed powder was mixed with Lithium-Tetraborate at a ratio of 1:5 using a Claisse M4® fluxer. The mixture was processed for loss on ignition (LOI) at 1050°C for 2 hours and then melted at 1080°C using the PANalytical Eagon 2 fusion instrument. Weight percentages of 10 major oxides (SiO_2, TiO_2, Al_2O_3, Fe_2O_3, MnO, MgO, CaO, Na_2O, K_2O, P_2O_5) and of 21 trace elements (S, Sc, V, Cr, Co, Ni, Cu, Zn, Ga, Rb, Sr, Y, Zr, Nb, Ba, La, Ce, Nd, Pb, Th, U) were measured during the XRF test. The results were calibrated with ca. 30 certified international standards with emphasis on igneous and metamorphic rock compositions.

The XRD analysis was performed with a Powder X-ray Diffractometer (Bruker AXS D8 Advance) and a Lynxeye superspeed detector in the high-pressure lab at ETH Zurich. The spectrum was analysed using ICDD PDF-2 (Version 4.15.3.4) with the Database Version 2.1502. Crystalline mineral phases were identified as quartz, dolomite, K-feldspar (orthoclase), muscovite, kaolinite and ilmanite. However, XRD analysis is semi-quantitative. To obtain quantitative mineral composition in weight percentage, we need to combine the XRD-XRF results. Taking typical densities of identified minerals (The engineering toolbox: http://www.engineeringtoolbox.com/mineral-density-d_1555.html), we summarize mineral volume fractions in Table 1. Here mineral chemical formulas were confirmed with both XRD and quantitative SEM analysis.

The quantitative SEM analysis was carried out with the Jeol JSM-6390 LA SEM and a EDS system, Thermo Fisher NORAN NSS7, in the high-pressure lab. Elements were mapped on the SEM image with a pixel resolution of 2.4 μm using a 30 mm^2 Silicon-drift detector (SDD). The element-wise pixels were registered according to element X-ray spectra at 20 sec x 50 frames (1000 counts). Similarly, the same area of the thin section as the BSE analysis (11.37mm x 8.34 mm) was continuously scanned with 5 x 5 windows. The resultant 25 coherent images were again stitched using ImageJ to produce a full image of 4737 x 3474 pixel^2, as shown in Figure 2. We then overlay all element images to generate a combined SEM-EDS image of mineral distribution. To estimate the chemical formula of individual minerals, we calibrated the X-ray beam current using a Farady-cup, determined element ratios on several spots, and integrated the previous XRD results to produce an average chemical formula, as summarized in Table 1.

2.4 Surface area analysis

Mass-specific surface areas (SSA) of rock samples were measured using a gas adsorption method based on the Brunauer–Emmett–Teller (BET) theory. The measurements were conducted using a surface area analyser, Quantachrome Autosorb 1MP, in the Claylab at ETH Zurich. Before BET measurements, small pieces of rock samples (in total 3.6 g) were vacuumed at 150°C for about 15 hours. During the BET measurements, we employed a 5-point method and nitrogen as the adsorption gas at a temperature of 77.3 K.

Perimeter density (μm/μm^2) in thin section, i.e., the ratio between solid perimeter and solid area, was also independently obtained from the binary image (from the 1.2 μm SEM-BSE image) shown in Figure 1b. Based on the principle of stereology (Weibel, 1969), SSA (m^2/g) was then the product of a bias correction factor of $4/\pi$, bulk rock density (measured as 2.11 g/cm^3), and perimeter density. Because of the resolution difference between the BET measurement and SEM imaging, a roughness correction factor (Table 2) needs to be applied to match these two independent SSA measurements.

In this study, however, we are more interested in obtaining the SSA of individual minerals, in particular the SSA of individual minerals exposed to pore space, which we define as the accessible surface area. In principle, the global surface area is the sum of individual mineral accessible surface areas. To obtain the accessible surface area of individual minerals from the SEM-EDS image, we first calculated the perimeter density of individual minerals and then excluded the contact surface area between mineral grains. However, because of the

lower resolution (2.4 μm) and the limitation of the counting method employed on the SEM-EDS image, we need to down-scale the SEM-EDS image to the SEM-BSE image size, such that we take advantage of the high-resolution SEM-BSE image as well as the constrain of the BET measurement. To do that, it is necessary to apply a scaling factor (SF) to account for the differences between the two binary images, i.e., between the SEM-BSE and SEM-EDS images. To estimate this SF, minerals were grouped into three types: (i) minerals with fully filled grains, such as quartz, dolomite, K-feldspar, and ilmanite; (ii) minerals with partially filled grains, such as muscovite; (iii) minerals with poorly filled grains, such as Kaolinite. For each group, we selected 5-10 typical locations and calculated area fractions and perimeters of individual minerals for the two binary images. The SF was estimated using ratios of area fractions and of perimeters, as listed in Table 2. The volume fractions, listed in Table 1, were then obtained based on the principle of stereology (Weibel, 1969). After applying the roughness correction, the perimeter density and the accessible perimeter density of individual minerals was obtained. Similar to the above approach to obtain SSA, the accessible SSA of individual minerals was calculated according to the principle of stereology (Weibel, 1969). The difference is that, instead of using bulk solid density, we use individual mineral densities (Table 1) to calculate the SSA and the accessible surface area of individual minerals. The results are listed in Table 2.

3. RESULTS AND DISCUSSION

3.1 Porosity and PSD

We measured the diameter and the length of the cylindrical rock sample with a Vernier calliper. From the measured diameter of 25.4±0.1 mm and the measured length of 39.0±0.1 mm, we obtained a sample volume of 19.7±0.1 ml. The sample solid volume of 15.441±0.004 ml was measured with a Helium pycnometer. We calculated a porosity of 21.9±0.4 %.

Figure 3 shows PSD from mercury intrusion measurements and from calculations on SEM image and 3D CT data. We smoothed the mercury porosimetry raw data (gray solid line) with a 10-ponit running averaging filter (to obtain the blue solid line). The mercury porosimetry results show a peak at a pore (throat) size of 15 μm in the range of 0.01 – 100 μm. SEM image analysis shows a peak at a pore size of 30 μm in the range of 1.2 – 80 μm. In addition to image resolution issues, the discrepancies between the curves is very likely introduced by the difference in measuring principles employed by these two methods, i.e., the mercury injection method better reflects the pore throat size, while the image analysis method is more sensitive to the total pore area. The PSD results are also partially confirmed by the 3D micro CT analysis. Due to the limitation of current computational resources, the resolution of the 3D CT image was up-scaled to 19.5 μm. For this resolution, most pores have been filtered-out so that only ~16% (relatively large) pores remain. The PSD from 3D CT data for pores bigger than 39 μm is shown as a black, dashed line in Figure 3, showing that the results from the analysis of 3D CT data match well with results from the analysis of 2D SEM data. This strongly suggests that the stereological method, used in this study, is valid. However, further analysis of smaller pore sizes is required.

3.2 Specific surface areas (SSA)

The bulk mass-specific surface area (SSA) of 1.447 m^2/g was determined by BET measurements, employing a 5-point-constrained line with a correlation coefficient of 0.99995. The stereological analysis of the SEM-BSE image (Figure 1b) yields a bulk SSA value of 0.031 m^2/g. After applying a resolution correction to the SEM-EDS image, the relative difference of the perimeter density, compared to the BSE image, was reduced from 40.0% to 2.9%, so that the stereological analysis yields a bulk SSA value of 0.032 m^2/g. After the roughness correction for individual minerals with their own scaling factors (SFs), shown in Table 2, the SSA of individual minerals is at a reasonable value, compared to literature values. The bulk SSA, i.e., the overall accessible SSA of all minerals, is then calculated as 1.441 m^2/g. This agrees well with the bulk BET measurement (1.447 m^2/g). The volume fractions calculated from the extracted mineral maps are in very good agreement with the XRD and XRF results (Table 1). The accessible surface areas and their proportion before and after the correction are listed in Table 2. This suggests that the clay mineral kaolinite contributes more than 85% to the accessible surface area.

Our results suggest that lower and upper bounds for the accessible surface area could be determined, using the resolution correction and the roughness correction, respectively. We suggest that the resolution correction alone leads to an underestimation of the accessible surface area, resulting in a lower bound. In contrast, the roughness correction likely results in an overestimation of the accessible surface area, which would constitute an upper bound. We also note that the mineral accessible surface area, as defined in this paper (i.e., the surface area exposed to the pore space), does not account for the effective in-situ fluid accessibility during fluid flow. Therefore, further analyses of the accessible surface area are needed for our later flow-through experiments and pore-scale, reactive fluid flow simulations.

CONCLUSION

We have quantified the porosity and the PSD of rock samples, employing Helium pycnometry and Hg porosimetry, respectively. Rock compositions were determined by a combination of XRF, XRD, and SEM-EDS, which are later geometrically mapped onto 2D images, derived from SEM-BSE images. The stereological method used in this study is validated by comparing the mineral volume fraction, porosity, and PSD results from image processing and from laboratory measurements. Normalization of stereological specific surface area (SSA) to BET measurements of SSA yields roughness corrections of individual minerals. Our results indicate that image processing, combined with laboratory analyses, is a promising method to quantify a porous medium's reactive surface area.

ACKNOWLEDGEMENTS

REFERENCES

1. Althaus, E, Edmunds, W.M., 1987, Geochemical research in relation to hot dry rock geothermal systems. Geothermics: 16, 451-458.
2. Beckingham, L.E., Mitnick, E.H., Steefel, C.L., et al., 2016, Evaluation of mineral reactive surface area estimates for prediction of reactivity of a multi-mineral sediment. Geochimica et Cosmochimica Acta: 188, 310-329.
3. Cai, R., Lindquist, W.B., Um, W., et al., 2009, Tomographic analysis of reactive flow induced pore structure changes in column experiments. Advances in Water Resources: 32, 1396–1403.
4. Cheshire, M.C., Stack, A.G., Carey, J.W., et al., 2017, Wellbore Cement Porosity Evolution in Response to Mineral Alteration during CO2 Flooding. Environmental Science & Technology: 51, 692-698.
5. Feng, G.H., Xu, T.F., Zhu, H.X., 2016, Dynamics of fluid and heat flow in a CO2-based injection-production geothermal system. Journal of Groundwater Science and Engineering: 4, 377-388.
6. Gaus, I., 2010, Role and impact of CO2–rock interactions during CO2 storage in sedimentary rocks. International Journal of Greenhouse Gas Control: 4, 73–89.
7. Hildebrand, T., Ruegsegger, P., 1997, A new method for the model-independent assessment of thickness in three-dimensional images. Journal of Microscopy: 185, 67–75.
8. Landrot, G., Ajo-Franklin, J.B., Yang, L., et al., 2012, Measurement of accessible reactive surface area in a sandstone, with application to CO2 mineralization. Chemical Geology: 318-319, 113-125.
9. Li, L., Peters, C.A., Celia, M.A., 2006, Upscaling geochemical reaction rates using pore-scale network modelling. Advances in Water Resources: 29, 1351–1370.
10. Luhmann, A.J., Kong, X.Z., Tutolo, B.M., et al., 2014, Experimental dissolution of dolomite by CO2-charged brine at 100 °C and 150 bar: Evolution of porosity, permeability, and reactive surface area. Chemical Geology: 380, 145-160.
11. Nogues, J.P., Fitts, J.P., Celia, M.A., et al., 2013, Permeability evolution due to dissolution and precipitation of carbonates using reactive transport modeling in pore networks. Water Resources Research: 49, 6006-6021.
12. Pandey, S.N., Chaudhuri, A., Rajaram, H., et al., 2015, Fracture transmissivity evolution due to silica dissolution/precipitation during geothermal heat extraction. Geothermics: 57, 111–126.
13. Peters, C.A., 2009, Accessibilities of reactive minerals in consolidated sedimentary rock: An imaging study of three sandstones. Chemical Geology: 265, 198-208.
14. Rasteniene, V., Puronas, V., 2005, Geothermal Atlas of Lithuania. Proceedings World Geothermal Congress 2005, Antalya, Turkey.
15. Voskov, D.V., Henley, H., Lucia, A., 2017, Fully compositional multi-scale reservoir simulation of various CO2 sequestration mechanisms. Computers & Chemical Engineering: 96, 183-195.
16. Weibel, E.R., 1969, Stereological Principles for Morphometry in Electron Microscopic Cytology. International Review of Cytology: 26, 235-302.

17. Xu, T.F., Apps, J.A., Pruess, K., 2003, Reactive geochemical transport simulation to study mineral trapping for CO2 disposal in deep arenaceous formations. Journal of Geophysical Research-Solid Earth: 108, Issue B2.

18. Yasuhara, H., Kinoshita, N., Lee, D.S., 2017, Evolution of mechanical and hydraulic properties in sandstone induced by simulated mineral trapping of CO2 geo-sequestration. International Journal of Greenhouse Gas Control: 56, 155-164.
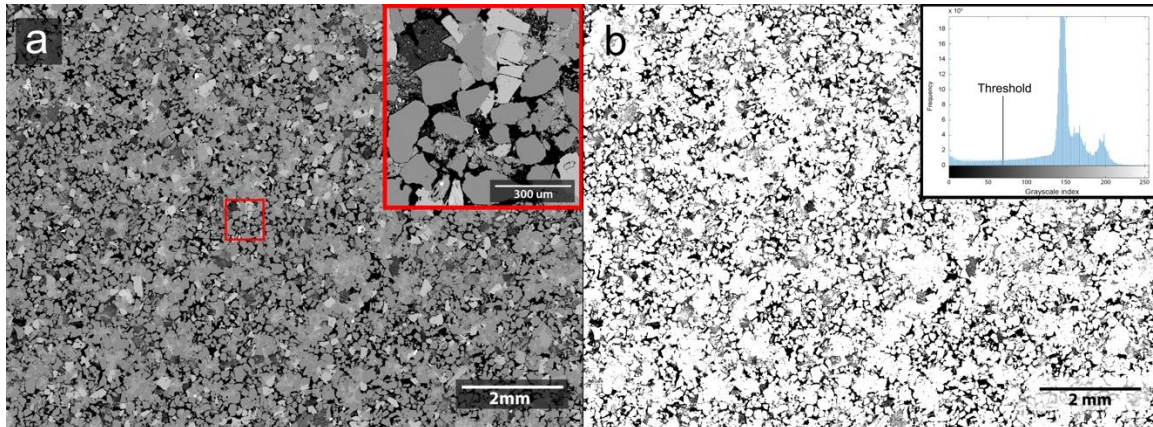
Figure 1: Analysis of the SEM-BSE image: (a) grayscale SEM-BSE image with a resolution of 1.2 μm, enlarged by a factor of 5 (inset in the right-upper corner) of the red square; (b) the corresponding binary image (black represents pores and white represents solid) with the inset showing a gray-value histogram and the applied threshold.
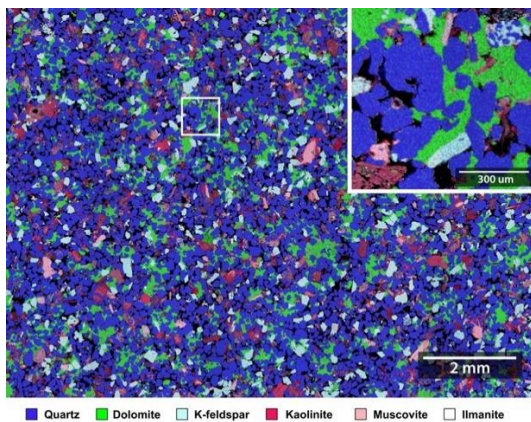
Figure 2: Mineral distribution of the SEM-EDS image with a resolution of 2.4 μm. Minerals are colour-coded as indicated at the bottom of the image.
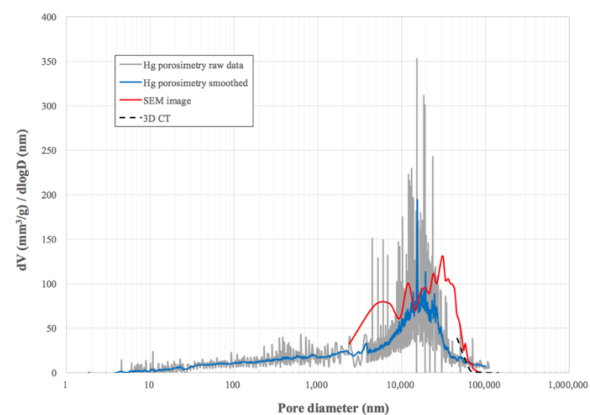
Figure 3: Comparison of PSDs obtained from mercury intrusion porosimetry, SEM image analysis, and analysis of 3D CT data.

Table 1: Minerals and their chemical formula, identified using a combined XRF+XRD method and SEM image processing. The mineral densities are from the engineering toolbox: http://www.engineeringtoolbox.com/mineral-density-d_1555.html

Mineral	Average chemical formula	Density g/cm³	XRF+XRD vol.%	SEM vol. %
Quartz (Qtz)	SiO_2	2.62	47.65	45.53
Dolomite (Dol)	$CaMg_{0.77}Fe_{0.23}(CO3)_2$	2.84	12.36	12.22
K-feldspar (Ksp)	$KAlSiO_3$	2.56	11.82	9.93
Muscovite (Mu)	$K_{0.85}Na_{0.15}Al_2(AlSi_3O_{10})(OH)_2$	2.82	5.38	4.76
Kaolinite (Kln)	$Al_{1.9}Si_{2.1}O_5(OH)_4$	2.60	0.91	5.64
Ilmanite (Ilm)	$Fe_2Ti_5O_{12}$	4.72	0.23	0.27

Table 2: Scaling corrections for mineral area fractions (AF), perimeter densities (PD), and specific surface areas (SSA), based on SEM-BSE image analysis and literature BET values: quartz (Tester et al., 1993; Navarre-Sitchler et al., 2013), dolomite (Pokrovsky et al., 2005; Zhang et al., 2014; Zhang et al., 2015), K-feldspar (Stillings and Bratley, 1995; Richter et al., 2016), muscovite (Lin and Clemency, 1981; Kalinowski and Schweda, 1996; Richter et al., 2016), kaolinite (Wieland and Stumm, 1992; Devidal et al., 1997; Dawodu and Akpomie, 2014; Hai et al., 2015; Tan et al., 2017). Mineral abbreviations are listed in Table 1.

	Pore	Qtz	Dol	Ksp	Mu	Kln	Ilm	Total
EDS AF %	21.64	44.82	12.03	9.77	4.88	6.29	0.27	99.7
EDS accessible PD µm/µm²		18382.6	1605.5	2181	1767.8	6875.4	242.1	31054.5
Resolution correction based on BSE image (BSE PD: 51567.3 µm /µm²)								
SF applied to AF		1.02	1.02	1.02	0.98	0.9	1.02	
Res. corrected AF %	21.65	45.53	12.22	9.93	4.76	5.64	0.27	100
SF applied to PD		1.3	1.3	1.3	1.94	2.98	1.3	
Res. corrected accessible PD µm /µm²		23897.4	2087.2	2835.3	3429.5	20488.8	314.7	53052.9
Roughness correction based on literature BET values of pure mineral (our bulk BET result: 1.447 m²/g)								
Res. corrected accessible SSA m²/g		0.040	0.037	0.039	0.089	0.230	0.052	0.03
Accessible SSA proportion %		45.05	3.93	5.34	6.47	38.62	0.59	
SSA from BET (Lit.)		0.02-0.55	0.07-1.96	0.08-0.25	0.66-5.53	13.2-78.0		
SF applied to SSA		5	50	5	50	100	25	
Rou. corrected accessible SSA m²/g		0.20	1.87	0.19	4.47	23.04	1.29	1.441
Accessible SSA proportion %		5.00	4.37	0.59	3.59	85.79	0.66	

Resolving the Link between Porosity and Permeability in Carbonate Pore Systems

Moustafa R Dernaika and Gary G Sinclair, Ingrain Inc - Abu Dhabi

This paper was prepared for presentation at the International Symposium of the Society of Core Analysts held in Vienna, Austria, 27 August – 1 September 2017

ABSTRACT

In carbonate reservoirs, permeability prediction from porosity alone is often difficult due to complex pore systems leading to poor porosity-permeability relationships. The main objective of this paper is to resolve the porosity-permeability relationships by understanding the effects of rock texture, pore type as well as compaction/dissolution. Over 500 core plugs were studied from 5 different carbonate reservoirs across the Middle East. The data set available included laboratory-measured Helium porosity and gas permeability. The textures of the samples were analyzed in thin-section photomicrographs and were classified as grainy, muddy and mixed. The pore types were defined as interparticle, intercrystalline, moldic, intraparticle and vuggy. The texture information was plotted in the porosity-permeability domain. Clear trends were seen in the data improving the relationships between porosity and permeability. Different textures gave distinct porosity-permeability trends. The extent of the trend was controlled by the degree of compaction and dissolution. Conclusive relationships between permeability and textural rock properties were clearly found in carbonates, which can provide better permeability predictions from porosity. Rock texture was the main parameter important for the understanding of the porosity and permeability characteristics of the studied carbonate reservoirs.

INTRODUCTION

Core laboratory measurements can have a major impact on the reservoir modeling process [1] but often yield unrepresentative results that raise questions about the effectiveness of the core data in the reservoir model and its calibration. This is partly related to the lack of understanding of reservoir heterogeneity and to the unrepresentative selection of plug samples. Hence, the petrophysical data that is obtained is often left unexplained and with no possibility to link macroscopic measurements to fundamental microscopic properties and geological heterogeneities in the core [2].

As common carbonates have complex and multimodal pore systems, variation of permeability at single porosity can be very large (three to five orders of magnitude). This leads to poor porosity-permeability relationships [3] and imposes a challenge in classifying carbonates into rock types for proper permeability prediction. The porosity-permeability relationships can be resolved by additional information about the pore system, which is mainly related to the rock microstructure (texture) being grainy, muddy or mixed. The microstructure information can be obtained from thin-section photomicrographs. The

microstructure (or micro-texture) of the rock has significant pore geometrical properties regarding flow of liquids through the core and thus largely define absolute permeability.

In this study, plug samples were selected to represent statistical distribution of porosity and textures in the cores. The porosity was initially derived from dual energy CT scanning [4] while the different textures were identified in the core X-ray CT images (see figure 1). The microstructure information of the plugs was confirmed from thin-section photomicrographs, and was plotted in the porosity-permeability domain. Samples with grainy microstructure gave high permeability whereas muddy samples showed lower permeability for the same porosity. The porosity and permeability data were fitted into unique trends based on the micro-textural analysis. The different trends were mainly controlled by the different rock microstructures whereas the extent of the trend was due to different diagenesis processes (e.g. cementation and compaction).

PERMEABILITY AND TEXTURE

Carbonate rocks can be geologically categorised based on their microstructures or textures. The microstructure and texture are used interchangeably to describe the rock content, which can basically be identified from a thin-section photomicrograph. Carbonate structures may be classified as grainy, muddy or mixed [5]. Grainy carbonate contains grains only. Muddy carbonate contains matrix only (mud). Mixed carbonate contains both grains and matrix. In this perspective, the Dunham [6] classifications of grainstone and rudstone, for instance, fall into the grainy class, while the mudstone and wackstone would fall into the muddy classification. Floatstone and packstone may be defined as mixed. In all these classes, the presence of cement and the effect of compaction/dissolution can be noticed. The aim of this texture-based classification is to realize the effects of grain size distribution and amount of micrite matrix on the flow characteristics in a porous carbonate. The understanding of these parameters can help establish a sound basis for potential correlations between microscopic and macroscopic properties. Such correlations in the porosity-permeability domain can greatly enhance the ability to predict permeability from porosity and texture. Figure 2 gives an overview of the effects of rock texture on permeability. Within the grainy texture, porosity and permeability can vary with grain size, grain compaction and presence of cement. Sample #1 has the lowest poroperm data because of cementation and compaction. Sample #2 has the highest permeability, which is the result of large grains and their uniform size distribution. Its porosity is moderate because of the large grains. Sample #3 has moderate permeability and high porosity because of the smaller grain sizes. The mixed texture samples have lower permeability values over the same porosity range. This is caused by the micrite content in the samples that maintain good porosity but lower permeability because of its small particle sizes and associated small pores. In the grainy samples the flow is mainly controlled by the interparticle porosity within the grainy structure, whereas, in the mixed samples, the flow is controlled by both the grainy and muddy structures, and is supressed by the intercrystalline porosity within the muddy structure. This explains the drop in permeability for the mixed samples at the same porosity. The muddy texture samples have the lowest permeability values over the same porosity range. This is obviously caused by the fact that permeability is only

controlled by the intercrystalline porosity within the small micrite particles in the muddy structure.

TEXTURE-BASED POROSITY-PERMEABILITY RELATIONSHIPS
Five carbonate reservoir cores (A, B, C, D & E) were evaluated to understand the porosity-permeability relationships. Each cored interval ranged from 300 to over 500 feet, and some of the cores represented more than one formation. The cores were mainly limestone with highly varying porosity (~5% to 30%) and permeability (~0.01 mD to 1000 mD). One and a half inch (1.5") diameter plug samples were statistically selected to represent all the cored intervals. Figure 3 to figure 7 present the conventionally measured helium porosity and gas permeability data on the selected plugs. The porosity and permeability data for each plug were associated with the sample texture that was identified from the corresponding thin-section photomicrograph. Figure 3 shows two distinct porosity-permeability trends from the analysed core in reservoir A. The textures of the samples were classified as grainy and muddy. No mixed texture was detected in the core. The grainy texture was dolomite while the muddy texture was calcite. Both textures revealed a rather large porosity range, which was the result of different degrees of leaching and compaction. The different textures had clear effects on the porosity-permeability relationships as well as on the capillary pressure (Pc) curves. The grainy samples showed higher permeability range with lower entry pressures. Figure 4 shows two distinct porosity-permeability trends from the analysed core in reservoir B. The textures of the samples were classified as grainy and mixed. No muddy texture was detected in the core. The grainy texture was oolitic grainstone while the mixed texture contained micrite matrix within the grainy structure. The different textures had clear effects on the porosity-permeability relationships as well as on the capillary pressure curves. The mixed samples gave lower permeability trend caused by the micrite matrix. The grainy samples had high porosity while the mixed samples gave large porosity range, which was the result of different porous micrite fractions in the samples. Figure 5 presents core data from a tight formation in reservoir C. The samples showed mixed structure with single porosity-permeability trend. Large porosity and Pc variations were caused by different degrees of compaction and cementation. Only few samples were analysed because of the poor physical condition of the core. Figure 6 shows texture-based poroperm relationships with unique average Pc curves from each trend in reservoir D. Five different trends were obtained: Grainy texture 1 (grainstone cemented), grainy texture 2 (rudstone cemented), grainy texture 3 (grainstone highly cemented), mixed texture 4 (packstone) and muddy texture 5 (wackstone cemented). The reservoir was well cemented, which had negative impact on the porosity of the samples. Figure 7 depicts different poroperm trends with unique average Pc curves in reservoir E. Four different trends were identified: Grainy with highest porosity and permeability, mixed with highest porosity range and lower permeability, leached muddy texture with lower permeability and large porosity range that is caused by different dissolution degrees, and muddy cemented texture, which gave the least porosity/permeability values.

DISCUSSION

The analysed samples and their porosity-permeability relationships are believed to be representative to the reservoir properties. This was possible by applying statistical sample selection [4,7,8] based on high-resolution dual energy CT imaging of the entire cores. In all the five reservoirs, it was possible to establish relationships between porosity and permeability in accordance to textural variation. The grainy, mixed and muddy textures seem to be the main controlling parameters in this relationship. Figure 8 plots all the reservoir poroperm data from figure 3 to figure 7. We can see distinct porosity-permeability trends in relation to the three identified textures. This result is very interesting and confirms the strong relationship that exists between permeability and rock texture. It is important to note that the often seen poroperm data cloud is not obtained in any of the analysed cores. All the poroperm data characteristics were classified and understood based on the rock textures. Although the rock microstructure appears to be the main control of flow we should also notice the effects of the porosity type. For instance, a muddy carbonate may have 'touching vug' porosity with a very high permeability.

Textural variations are best seen in thin-section photomicrographs but they can also be noticed in X-ray CT images (as in figure 1). This would allow plugging locations to be initially selected in the reservoir cores based on different CT textures. This would then provide the link between the plug poroperm trends and the different textures in the cores enabling permeability to be upscaled (from the porosity log) to the entire whole core intervals; this application was demonstrated in [7]. CT images can detect different textures while thin-sections confirm the geological contents. The different textures can be incorporated in reservoir rock typing as fundamental geological features of carbonate rocks. Grainy samples tend to show higher permeability and lower entry capillary pressures. If core CT images are not available, textures can be derived from facies analysis from core description. This texture-based technique can be implemented in logs if a reservoir facies model is established, which can correlate log response to facies in uncored wells.

CONCLUSIONS

Representative samples were analysed from five different carbonate reservoirs in the Middle East. The sample's textures were identified from thin-section photomicrographs and were plotted in the porosity-permeability domain. Conclusive relationships between permeability and textural rock properties were clearly found in carbonates, which can provide better permeability predictions from porosity. The following can be concluded from the results in this study,

1. Three different textures (grainy, muddy & mixed) were identified in the reservoirs.
2. Distinct porosity-permeability trends were obtained for the different textures.
3. The extent of the trend was controlled by compaction, cementation and dissolution.
4. Similar textures within the different reservoirs gave similar permeability range.
5. Prediction of permeability is possible from porosity and rock texture.
6. The different rock textures gave distinct capillary pressure curves. This would make textural analysis a fundamental tool for rock typing.

ACKNOWLEDGEMENTS

The authors wish to acknowledge Ingrain management for the permission to publish the results of this research study. Bashar Mansour, Yasir Naseer Uddin and Mauricio Contreras are acknowledged for the experimental work, and Osama Al Jallad for the discussions on the geology of the rocks.

REFERENCES

1. Masalmeh, S.K. and Jing, X.D.: "The Importance of Special Core Analysis in Modelling Remaining Oil Saturation in Carbonate Fields", SCA-2008-03 presented at the SCA 2008 conference, Reviewed Proc. International Symposium of the Society of Core Analysts Abu Dhabi, October (2008).
2. Dernaika, M., Kalam, Z., Skjaeveland, S., (2014), "Understanding Imbibition Data in Complex Carbonate Rock Types," paper SCA2014-59 presented at the International Symposium of the Society of Core Analysts held in Avignon, France, 8-11 September, 2014
3. Buiting, J.J.M., Clerke, E.A. (2013) "Permeability from porosimetry measurements: Derivation for a tortuous and fractal tubular bundle" J Petrol Sci Eng, http://dx.doi.org/10.1016/j.petrol.2013.04.016i
4. Dernaika, M. R., Naseer Uddin, Y., Koronfol, S., Al Jallad, O., Sinclair, G., (2015) "Multi-Scale Rock Analysis for Improved Characterization of Complex Carbonates" SCA2015 paper presented at the International Symposium of the Society of Core Analysts held in St. John's, Newfoundland and Labrador, Canada, 16-21 August.
5. Mousavi, M., Prodanovic, M. and Jacobi, D.: "New Classification of Carbonate Rocks for Process-Based Pore-Scale Modeling", SPE Journal (April 2013), SPE 163073.
6. Dunham R.J. 1962. Classification of Carbonate Rocks According to Depositional Texture. In Classification of Carbonate Rocks: A Symposium. American Association of Petroleum Geologists Memoir 1, ed. W.E. Ham, 108-121. Tulsa, Oklahoma: AAPG.
7. Dernaika, M. R., Mansour, B., Gonzalez, D., Koronfol, S., Mahgoub, F., AlJallad, O., Contreras, M. (2017) "Upscaled Permeability and Rock Types in a Heterogeneous Carbonate Core from the Middle East" SPE-185991-MS presented at the SPE Reservoir Characterisation and Simulation Conference and Exhibition in Abu Dhabi, UAE, 8—10 May.
8. Al-Owihan, H., Al-Wadi, M., Thakur, S., Behbehani, S., Al-Jabari, N., Dernaika, M. and Koronfol, S., (2014), "Advanced Rock Characterization by Dual-Energy CT Imaging: A Novel Method for Complex Reservoir Evaluation" paper IPTC 17625 presented at the International Petroleum Technology Conference held in Doha, Qatar, 20–22 January.
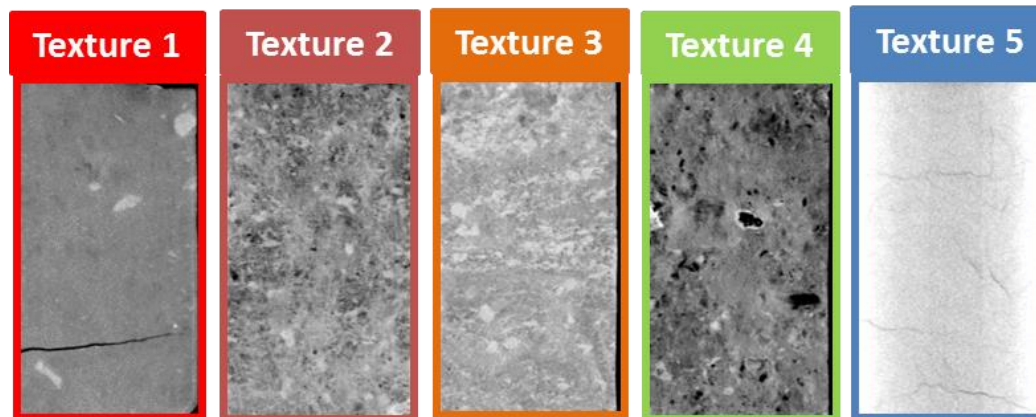
Figure 1 Example CT textures that can be identified in full-diameter 4-inch core
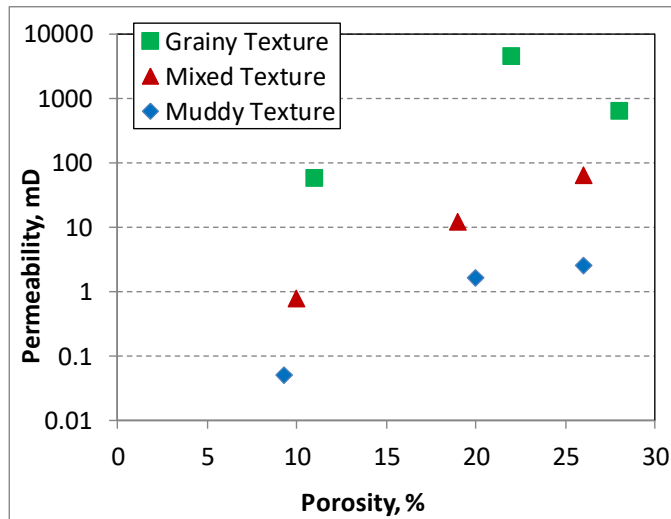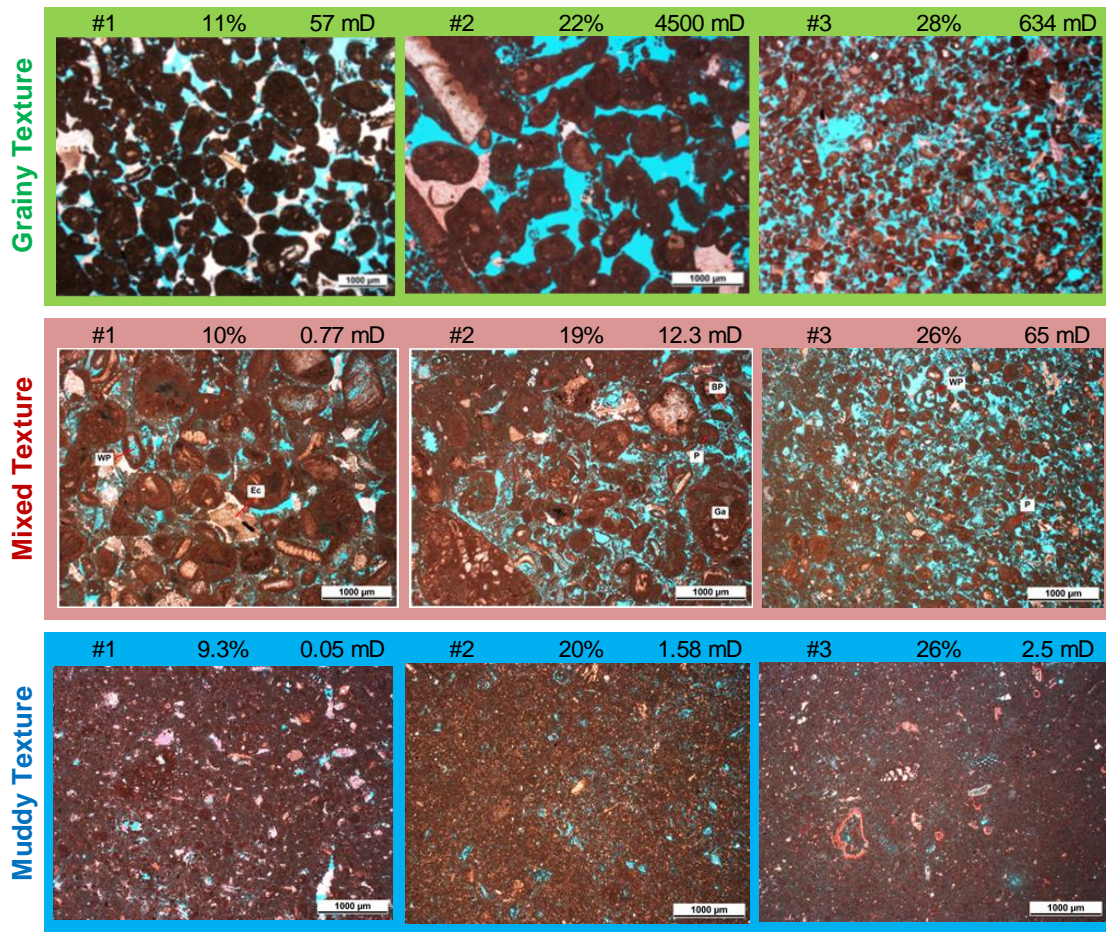
Figure 2 Permeability variation with rock texture/structure. Each sample is represented by its number, thin-section photomicrograph, porosity and permeability. Over the same porosity range, grainy samples tend to give the highest permeability values, while the muddy samples show the lowest permeability values. The mixed samples fall in between the grainy and the muddy samples in the poroperm plot.
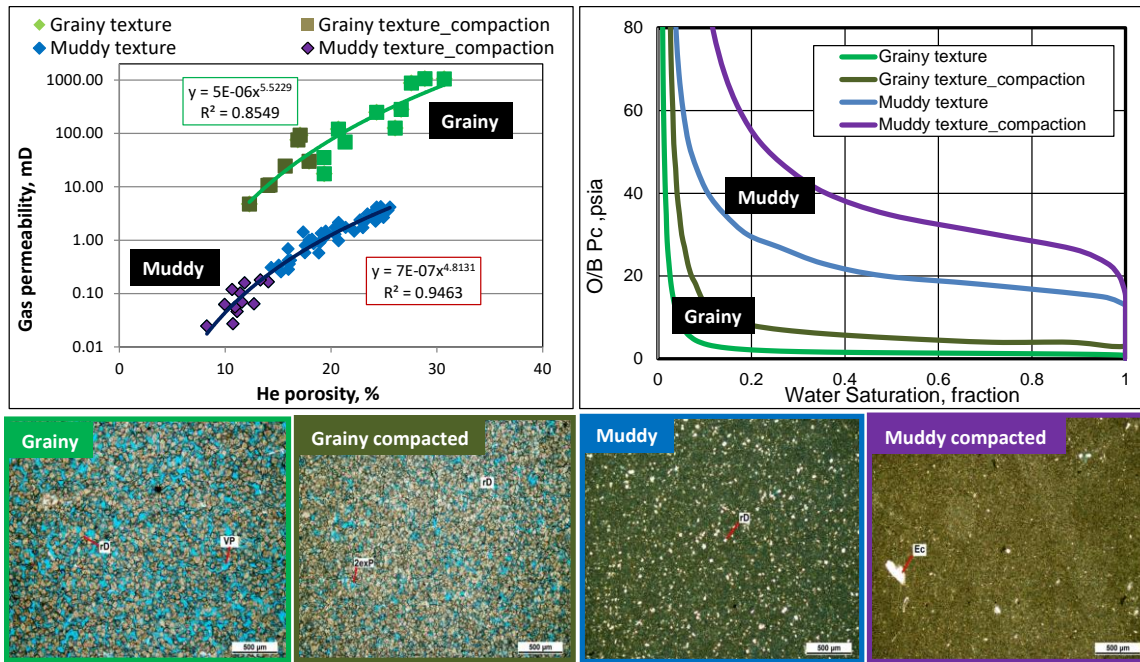
Figure 3 Grainy and muddy textures in reservoir A. Distinct poroperm trends with unique Pc curves
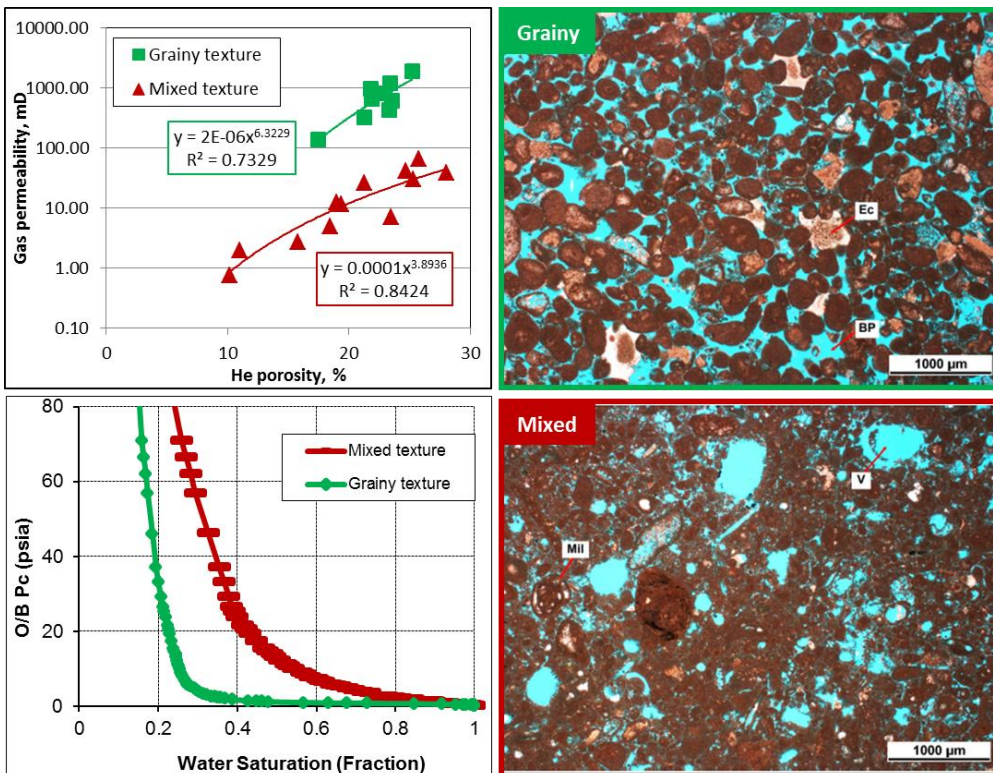
Figure 4 Grainy and mixed textures in reservoir B. Distinct poroperm trends with unique Pc curves. The thin-section photomicrographs and the Pc curves are shown for the average porosity samples.
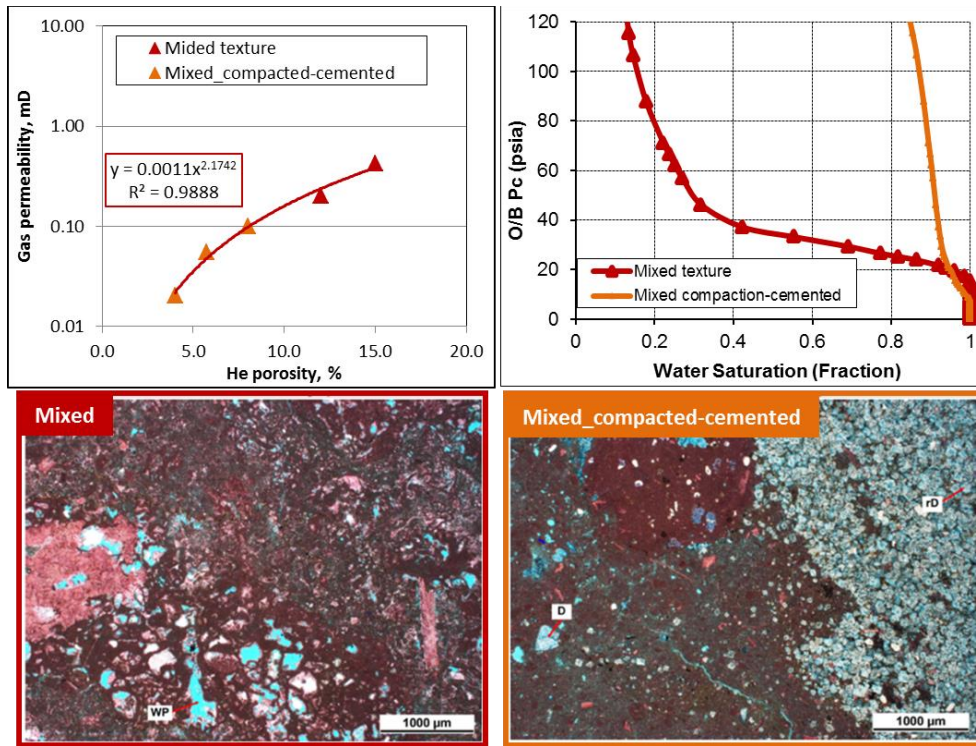
Figure 5 Mixed textures in reservoir C. Single poroperm trend with varying porosity and Pc curves caused by different degrees of compaction and cementation.
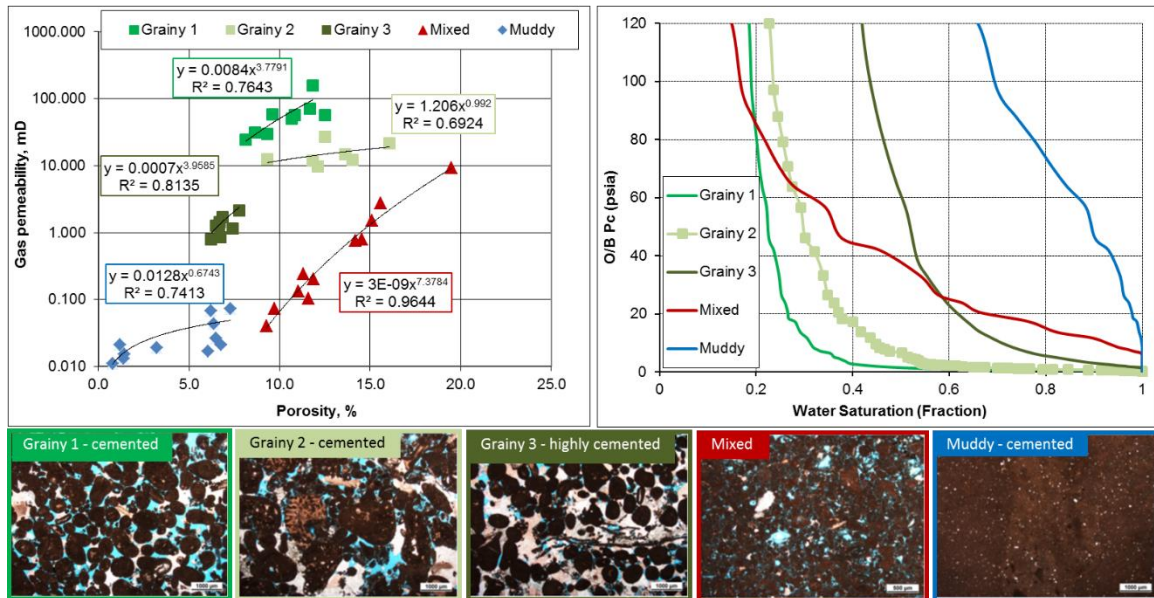
Figure 6 Texture-based poroperm trends with unique average Pc curves in reservoir D. Grainy texture 1 (grainstone cemented), grainy texture 2 (rudstone cemented), grainy texture 3 (grainstone highly cemented), mixed texture (packstone), muddy texture (wackestone cemented).
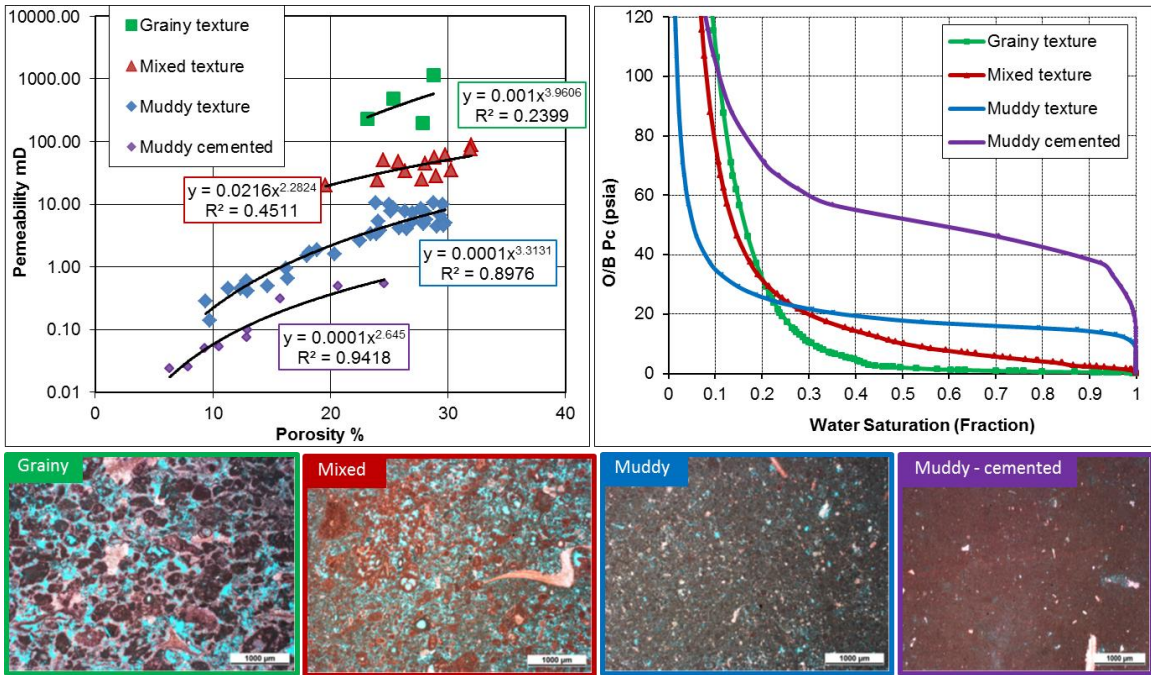
Figure 7 Texture-based poroperm trends with unique average Pc curves in reservoir E.
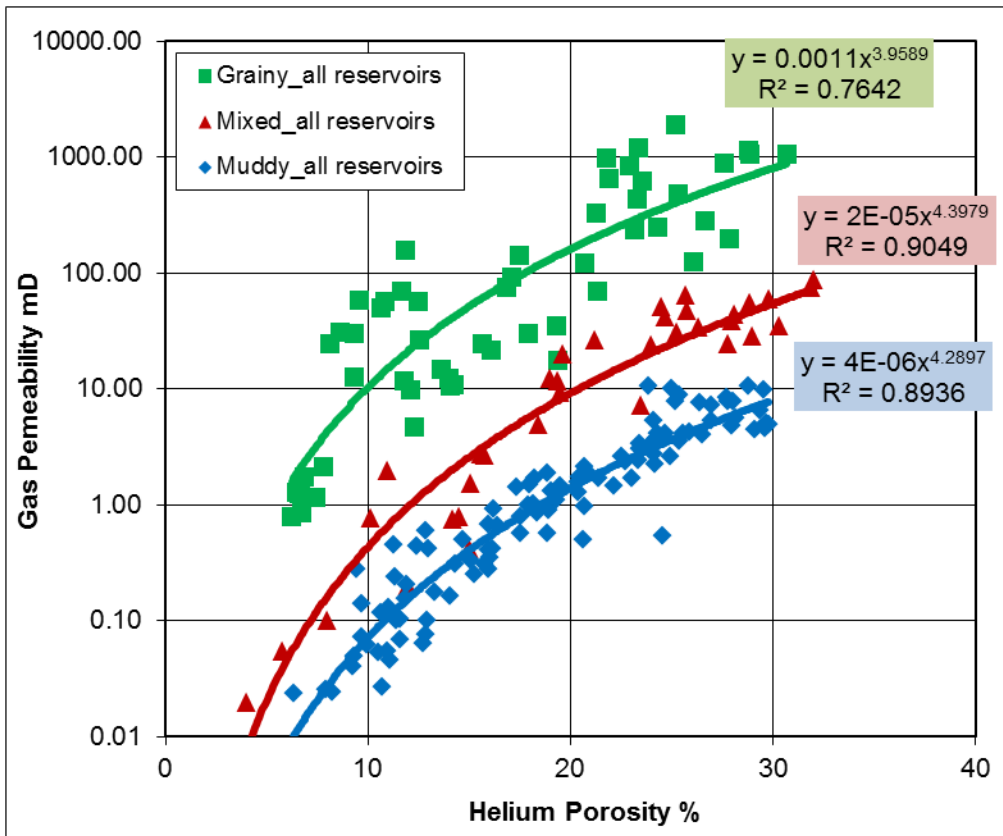
Figure 8 Texture-based poroperm trends for all samples in the five different reservoirs (A, B, C, D & E)

Dielectric and Acoustic Properties with a
Single Laboratory Instrument

Matthew Josh

CSIRO Energy, 26 Dick Perry ave, Kensington, WA 6151, Australia

This paper was prepared for presentation at the International Symposium of the Society of Core Analysts held in Vienna, Austria, 27 August – 1 September 2017

ABSTRACT

Electrical and acoustic petrophysical models derived from laboratory testing of rock samples are two of the principal methods for estimating the key reservoir properties (porosity, fluid permeability, fluid type, saturation and mineralogy) from borehole logs. The current generation of multi-frequency dielectric logging tools, which have appeared in the petroleum industry in the last decade, have led to a resurgence in all aspects of rock electrical properties, not limited to simply the low frequency conductivity, but including both real and imaginary components of dielectric permittivity and covering a broad spectrum of frequencies. This is due partly to the desire to use dielectric mixing rules to determine rock saturation, which is more easily achieved at approximately 1 GHz, and because dielectric permittivity strongly correlates with specific surface area and cation exchange capacity in the vicinity of 20 – 100 MHz. A novel laboratory petrophysical instrument has been developed which integrates both swept frequency dielectric analysis with P-wave velocity, on thin samples typically 8 mm thick, so that a single small sample can be machined and hydrated then analysed to provide both properties simultaneously. The instrument was able to resolve P-wave transit time in a Teflon sample less than 1 mm thickness, and was further validated with a number of non-porous engineering materials including sapphire, plexiglass and quartz. When applied to porous geological samples including Fontainebleau sandstone and Berea sandstone the real relative dielectric permittivity increased from approximately 4 when the sample was baked dry to approximately 6.8 (Fontainebleau) and 12 (Berea) when the sample was vacuum saturated with DI water. Simultaneously the P-wave velocity in both sandstones was higher in the saturated case.

INTRODUCTION

Acoustic and dielectric properties are two of the fundamental rock parameters which are exploited by the petroleum industry for evaluating reservoirs. During exploration, acoustic properties are integral to the application of surface seismic and likewise electrical properties are integral to CSEM. These same petrophysical parameters are also used during drilling and production to provide more targeted information about the extent of the reserves in-place and provide input to production related decision making. Clearly each of these activities are founded on a substantial background in laboratory based rock properties determination, which is used to create the rock physics models which relate the ultimate reservoir parameters: porosity, mineralogy, fluid permeability, saturation and fluid type to

the petrophysical properties which can be measured from the surface or borehole. Numerous examples of this can be found in the petroleum industry and related literature **(Archie, 1941; Mazzagatti et al., 1983; Myers, 1991; Seleznev et al., 2011; Sen and Chew, 1983, Shen et al., 1987)**. The most widely used and recognised example is Archie's law,

$$R_t = a\phi^{-m} S_w^{-n} R_w \qquad (1)$$

which relates the resistivity of the rock (R_t) to the porosity (ϕ), saturation (S_w), tortuosity factor (a) and brine resistivity (R_w) via a pair of simple exponents (Archie parameters, m, the cementation exponent and n, the saturation exponent), which need to be evaluated for the particular field or formation being investigated **(Ellis and Singer, 2007)**. Archie's law has been a staple of the petroleum industry ever since its publication. However, difficulties in estimating porosity from resistivity created by variations in formation salinity, have led to later advancements in high frequency dielectric logging, because dielectric permittivity is less affected by salinity. This has been complimented by alternative dielectric mixing models such as the complex refractive index method (CRIM, **Birchak et al., 1974):**

$$\sqrt{\varepsilon_{eff}} = \phi S_w \sqrt{\varepsilon_{rw}} + \phi(1 - S_w)\sqrt{\varepsilon_h} + (1 - \phi)\sqrt{\varepsilon_{ma}} \qquad (2)$$

where ε_{eff} is the effective dielectric permittivity of the formation and ε_{ma} and ε_{rw} are the rock matrix and pore fluid dielectric permittivities respectively and ε_h is the dielectric permittivity of gas. CRIM is often used with the current generation of high frequency dielectric logging tools to quantify, porosity and pore fluid type **(Seleznev et al., 2011).** Similarly, the rock acoustic properties, including the compressional (primary or P-) wave **(Gassmann, 1951)** are derived from elastic theory,

$$V_p = \sqrt{\frac{K + \frac{4}{3}\mu}{\rho}} \qquad (3)$$

where P-wave velocity, V_p, is related to the bulk modulus (K), shear modulus (μ) and the rock bulk density (ρ) and each of these properties is also affected by the porosity, pore fluid type and saturation. Rocks present a range of challenges that are less significant in other fields of materials research, even when it is possible to obtain intact, representative and reasonably homogenous samples. For example engineering materials such as glass and polymers are often characterised by their consistency regardless of their origin and do not change significantly with time or other regular laboratory environmental factors. Rocks however, continually rehydrate and equilibrate with humidity and temperature and one of the challenges which confronts laboratory petrophysics is the consistency of any given sample during multiphysics tests. This is compounded by the requirement of specific sample geometries for different tests. A relatively short (~ < 10 mm) sample used for parallel plate dielectric analysis is preferred to avoid fringing field capacitance compared with the relatively long (~ 60 mm) sample used for acoustic analysis chosen to insure adequate wavelengths within the sample and achieve acceptable resolution.

A new laboratory instrument is presented, which addresses the requirement to test rock samples with consistent hydration and under stable and repeatable laboratory conditions

by achieving P-wave velocity measurement and dielectric measurement simultaneously on a short sample of < 10 mm. This was achieved by the design and manufacturing of the world's first integrated dielectric electrode assembly containing piezo-transducers, with a frequency high enough to achieve satisfactory acoustic analysis in a < 10 mm sample. The instrument has been validated using a number of engineering materials and rock samples.

INSTRUMENT PRINCIPLES

The instrument was developed from the principles of a regular parallel plate capacitor which is commonly used in dielectric standards **(Von Hippel, 1954)** and has been used regularly in laboratory petrophysics **(Keysight 5989-2589EN, Mazzagatti et al., 1983; Shen et al., 1987)**. This style of instrument has the advantage of a relatively large volume of investigation compared with end-loaded coaxial transmission line instruments **(Stuchly and Stuchly, 1980)** and a convenient sample geometry compared with through-loaded airline instruments **(Nicholson and Ross, 1970; Keysight App Note 5989-2589EN).** A parallel plate dielectric instrument can perform beyond 100 MHz, which covers much of the frequency range of the current state of the art in multi-frequency dielectric logging tools. Parallel plate dielectric cells produce a uniform and parallel electric field which provides the advantage of allowing anisotropy analysis, which is not available with either end-loaded or airline coaxial measurement. They use large electrode surfaces which are similar and compatible with acoustic platen geometries and this has made possible the integration of piezo-ceramic componentry to create a fully integrated dielectric and acoustic platen (Figure 1a), which allows both measurements to be made simultaneously. The instrument is attached to two separate external circuits (highlighted in orange and blue, Figure 1a) to achieve the simultaneous measurement. An impedance analyser (Agilent 4294a, Figure 1b) determines the equivalent parallel capacitance (C_p) and resistance (R_p) (Figure 1c) between the guarded and unguarded electrodes which is then converted into the real and imaginary dielectric permittivity and conductivity via:

$$\varepsilon^* = \varepsilon_0 \times \varepsilon_r^* = \varepsilon_0 \times (\varepsilon'_r + j\varepsilon''_r) \qquad (4)$$

$$\varepsilon'_r = \frac{C_p d}{\varepsilon_0 A} \qquad (5)$$

$$\sigma_{equivalent} = \frac{d}{R_p A} \qquad (6)$$

$$\varepsilon''_{requivalent} = \frac{d}{2 \times \pi \times f \times \varepsilon_0 \times R_p \times A} \qquad (7)$$

where A, is the area of the capacitor plates, d is the thickness of the sample, ε_0 is the permittivity of free space, ε^*_r is the complex relative permittivity of the sample and σ is the conductivity of the sample.
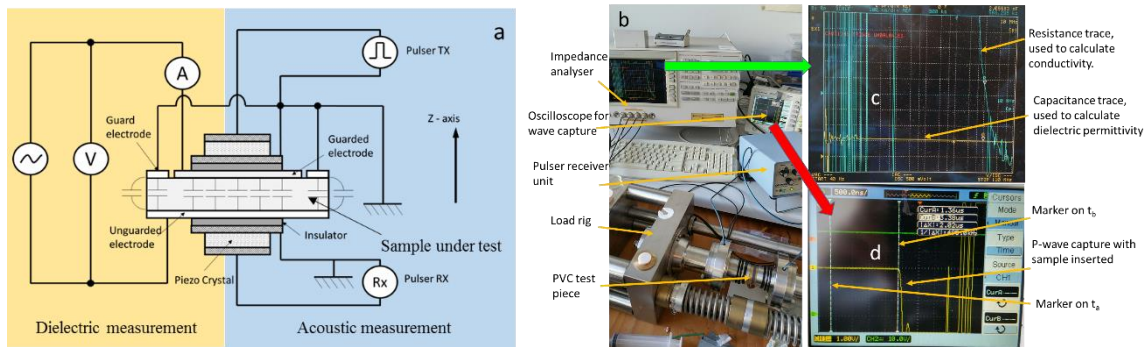
Figure 1: a) The circuit schematic of the instrument including both external circuits (orange background) the conventional three terminal connected parallel plate dielectric cell and (blue background) the conventional pulser-receiver configuration which drives and detects signal through the matched piezo-crystal pair. The P-wave propagates in the same direction as the electric field is oriented. b) The instrument can generate both electrical and acoustic data sets simultaneously. A polymer sample (grey PVC) is inserted into the instrument in the foreground and the two traces visible on two separate instruments are being saved simultaneously and provided in the breakout data. c) the dielectric trace and d) the acoustic trace.

The instrument is simultaneously connected to an ultrasonic pulser receiver unit (Olympus 5077PR, Figure 1b), which is used to drive the piezo-ceramic crystals housed within the transducer platens. A high voltage, typically 100 – 400 V, drives one of the transducer pairs whilst the other is connected through the pulser-receiver unit to an oscilloscope to capture the received waveform (Figure 1d).
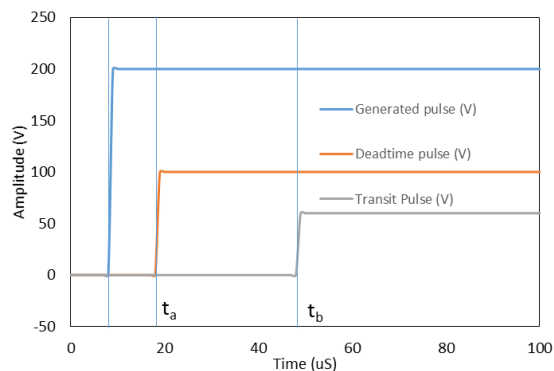
Figure 2: Sketch of the captured acoustic waveforms. (blue) The generated (transmitted) pulse, (orange) the deadtime pulse detected at the receiver (at time t_a) when the transducers are connected together without a sample. (grey) Transit pulse detected at the receiver (at time t_b) when the sample is inserted between the transducers.

Separate calibration processes are required for the two instrument measurement functions. The dielectric function is calibrated using short, open and load test pieces to remove the series and parallel stray impedances of the cell when connected to the impedance analyser. The acoustic measurement is calibrated by directly coupling the transducers together and capturing a waveform of the so-called *deadtime* pulse and recording the deadtime (Figure 2), t_a, which is related to cable lengths, transducer geometry and internal electronics of the pulser-receiver unit. Then the sample under test is inserted between the transducers and a new waveform is captured at time t_b. The transit time of the pulse through the sample is

calculated along with the velocity (P-wave) and the number of wavelengths interacting with the sample using,

$$Transit\ time = t_b - t_a \qquad (8)$$

$$P - wave\ velocity = \frac{d}{Transit\ time} = \frac{d}{t_b - t_a} \qquad (9)$$

$$Number\ of\ wavelengths = n = f \times (t_b - t_a) \qquad (10)$$

where f, is the transducer frequency and d is the thickness. Accepted rules of thumb in acoustic analysis **(ASTM Designation D2845 – 00, 2000)** dictate that approximately 10 wavelengths should interact with the sample to allow sufficient resolution of the P-wave arrival "picks" and typically for a $f = 1$ MHz instrument the preferred minimum sample length is approximately 20 – 30 mm. For this instrument dielectric analysis requires a sample that is less than 10 mm thick and so a piezo-crystal operating at $f = 4.6$ MHz (nominally 4.0 MHz, but measured otherwise) was used to create a shorter wavelength. The dielectric–acoustic platens are mounted into a large stainless steel housing which can be inserted into a uniaxial load cell. This ensures that a reliable acoustic connection is made between the sample and the platens and that series impedance is not affected by an airgap. Samples must cover no less than diameter 25 mm, determined by the diameter of the guarded electrode. The sample can have any shape, such as a rectangular tile or a rough cut piece of rock from core, so long as it has precision cut parallel faces with a tolerance of 30 µm determined by a small amount of play built into the instrument. Many engineering materials such as glass are already manufactured to these specifications and need only be prepared into a sample small enough to be manageable Table 1.

RESULTS

A selection of samples were prepared and measured to validate and demonstrate the instrument. These included *polymers*, Plexiglass (Perspex/Acrylic or PMMA) and Teflon in multiple thicknesses; *ceramics*, quartz and sapphire, which has an ultra-high P-wave velocity; *metals*, aluminium 6061-T6 and stainless steel 316, which were not useful as dielectric standards, but have well accepted acoustic properties; and *geological samples* Fontainebleau sandstone and Berea sandstone in different states of saturation.

Table 1: A table of engineering materials and geological samples investigated in this study, included a number of common reference materials, glasses and polymers along with two selected geological materials in different states of saturation. The metal samples are too conductive for the instruments range of sensitivity.

	Sample thickness (mm)	P-wave travel time (nS)	P-wave velocity, Vp (m/s)	Number of wavelengths	Capacitance at 10 MHz (pF)	Resistance at 10 MHz (Ω)	Real relative dielectric permittivity, εr at 10 MHz	Conductivity at 10 MHz (S/m)
TeflonA	0.25	160	1563	0.736	26.028	4.53E+00	2.03	1.52E-13
TeflonB	0.50	360	1389	1.656	12.897	5.04E+00	2.01	2.73E-13
TeflonC	1.99	1400	1421	6.440	3.429	2.13E+01	2.12	2.57E-13
TeflonD	4.99	3560	1402	16.376	1.349	1.81E+02	2.10	7.60E-14
PlexiglassPerspex	4.88	180	2711	8.280	1.82	7.23E+05	2.76	1.86E-05
C-cut Sapphire	5.25	460	11413	2.116	7.56	4.67E+05	12.35	3.10E-05
Quartz	3.19	520	6135	2.392	3.98	1.59E+06	3.96	5.52E-06
Aluminium (6061-T6)	4.98	820	6073	3.772	N/A	Very Low	N/A	Very High
Stainless Steel (316)	5.00	900	5556	4.140	N/A	Very Low	N/A	Very High
Dry Berea	7.70	2.84	2711	13.064	1.83	7.58E+04	4.38	2.80E-04
Wet Berea	7.70	2.38	3235	10.948	6.36	2.36E+03	15.24	8.98E-03
Dry Fontainebleau	9.84	3.74	2631	17.204	1.31	1.65E+06	4.02	1.65E-05
Wet Fontainebleau	9.84	2.30	4278	10.580	2.36	3.57E+04	7.21	7.60E-04

For all of the geological samples tested, more than 10 wavelengths interacted with the sample. In thin polymer samples (including the 0.25 mm thick Teflon) or in ultra-high speed materials such as sapphire, it is evident that the number of wavelengths interacting with the sample was substantially less than 10, however these materials do not fall within the intended scope-of-purpose of the instrument. As a comparison, the measured P-wave velocity of the plexiglass is 2711 m/s compared with the published value of 2750 m/s **(www.signal-processing.com/table.php),** and C-cut sapphire measures 11413 m/s compared with published values of 11100 m/s **(www.signal-processing.com/table.php)** and 11913 m/s **(Adavnced NDT)**. Measured and published values for P-wave velocity are consistent for the entire sample collection. The P-wave velocity in Berea sandstone has increased from 2711 m/s to 3235 m/s from dry to saturated, compared with Fontainebleau sandstone increasing from 2631 to 4278 m/s. i.e. Fontainebleau sandstone demonstrates a much bigger change with saturation even though it is less than ½ as porous. The Berea sandstone had a porosity of $\phi_{pycn} = 20.5$ % from helium pycnometery and $\phi_{mass} = 19.60$ % from the vacuum saturated mass. The Fontainebleau sandstone had a porosity of $\phi_{pycn} = 8.80$ % from helium pycnometery and $\phi_{mass} = 8.85$ % from vacuum saturated mass. The complex dielectric permittivity in the geological samples significantly increased after they were saturated. The measured complex relative permittivity of Fontainebleau sandstone increased from $\varepsilon^*_r = 4.072 + 0.0596j$ to $\varepsilon^*_r = 6.865 + 0.1746j$ at 100 MHz. Using values determined in the laboratory, $\varepsilon^*_{rw} = 81 + 0.467j$ (deionised, DI, water), $\varepsilon^*_{ma} = 3.96 + 0.0204j$ (quartz sample provided) and $\varepsilon^*_h = 1$ (air), CRIM estimates a sample complex relative permittivity of $\varepsilon^*_{eff} = 6.796 + 0.0363j$ which increases to $\varepsilon^*_{eff} = 6.797 + 0.268j$ if $\varepsilon^*_{rw} = 81 + 5.9j$ (i.e. brine is used rather than DI). This would be consistent with a formation brine of approximately 0.1 g/l NaCl. Measured Berea has increased from $\varepsilon^*_r = 4.033 + 0.2308j$ to $\varepsilon^*_r = 12.00+2.661j$ at 100 MHz where CRIM estimates $\varepsilon^*_{eff} = 11.744 + 0.0644j$ using DI water and $\varepsilon^*_{eff} = 11.864 + 2.661j$ when $\varepsilon^*_{rw} = 81 + 34.05j$, which is consistent with a formation brine of approximately 0.5g/l. These small increases in water imaginary permittivity can be accounted for by a small amount of salt residue within the rock samples. The increase observed in the real relative dielectric permittivity of the dry to saturated sandstones is nearly perfectly estimated by CRIM indicating there is no evidence for interaction between the constituents, which would be more common at lower frequencies or if clay content was significant.

The transit time through the different thicknesses of Teflon sample are perfectly correlated with the thickness of the sample (Figure 3) consistent with equation 9 and a gradient corresponding to a P-wave velocity of 1372 m/s, which matches published values of 1400 m/s **(NPL)** and 1372 m/s **(Adv. NDT).** More surprising is that the 0.25 mm thickness sample is resolvable from the 0.5 mm thick sample and both are consistent with the global trend which has a correlation coefficient of $R^2 = 0.9999$. This suggests that although the sample is extremely thin for the frequency of measurement (i.e. less than 1 wavelength within the sample) the resolution appears to be sufficient, although this is not recommended **(ASTM Designation D2845 – 00, 2000)**.
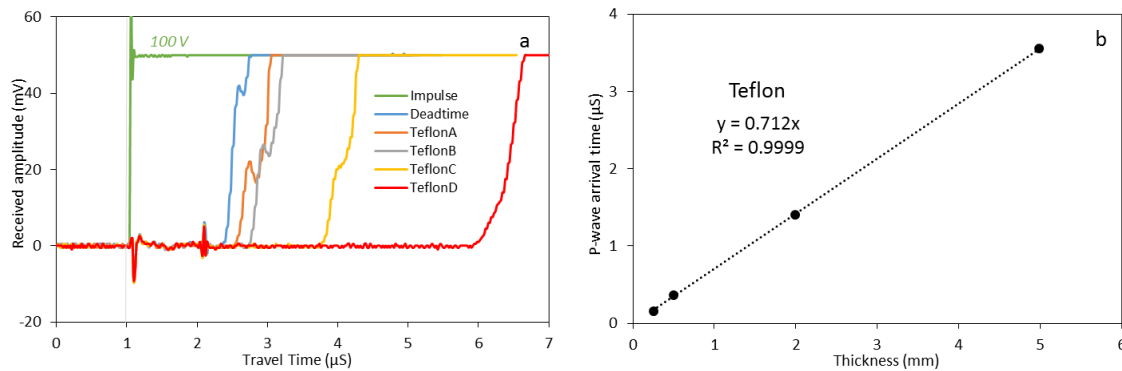
Figure 3: a) P-wave captures through the 4 different Teflon samples with different thicknesses. The waveforms are overlaid along with the driving pulse and the deadtime pulse created when no sample is inserted between the platens. The arrival time of the front edge of the P-wave increases with the thickness of the sample. b) The arrival time of the P-wave correlates ($R^2 = 0.9999$) nearly perfectly with the thickness of the Teflon sample; in addition, the 0.25 mm and 0.5 mm thick samples are consistent with the thicker samples indicating that thin samples do not appear to be a problem for this instrument.

The capacitance of the Teflon loaded cell also varies inversely with the thickness of the sample (Table 1), exhibiting a correlation coefficient of $R^2 = 0.9999$, which is consistent with equation 5 above.
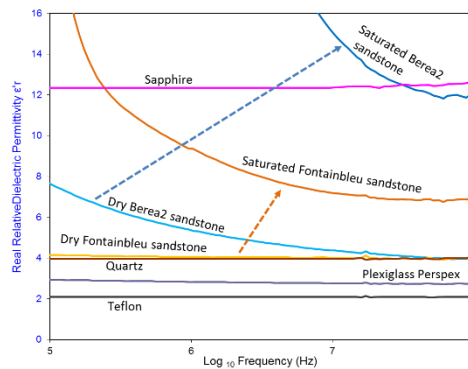
Figure 4: Dielectric frequency response of the polymers, ceramics and saturated geological samples. The geological samples both increase in dielectric permittivity after being saturated. Dry Fontainebleau sandstone has an almost identical dielectric permittivity to that of a synthetic single crystalline quartz sample.

The polymers and ceramics that were measured generally exhibit no change in dielectric permittivity as the frequency is increased (Figure 4), whereas the geological samples generally exhibit a reduction in dielectric permittivity with increasing frequency i.e. they are dispersive. This is one reason why *"multi-frequency"* is the state of the art in dielectric logging in the petroleum industry. Dielectric permittivity of clay bearing rocks is largely determined by the cation exchange capacity **(Myers, 1991)**, and subsequent investigations **(Leung and Steiger, 1992; Josh, 2014),** demonstrate that the three properties CEC, SSA and dielectric permittivity, usually vary together, in an essentially linear relationship with as much as 90 % correlation. However, this correlation generally appears to weaken slightly as the frequency is increased above 100 MHz because the longer scale polarisation mechanisms begin to "turn-off" **(Guéguen and Palciauskas, 1994; Sen and Chew, 1983)**. Polymers and ceramics, however do not exhibit this phenomenon, they are mostly non-

dispersive. For example sapphire has a real dielectric permittivity of $\varepsilon'_r = \sim 12.35$ **(c.f. 11.1 Harman et al., 1994)** and quartz $\varepsilon'_r = \sim 3.95$ **(c.f 3.78, Von Hippel, 1954)**. Plexiglass has a real dielectric permittivity of $\varepsilon'_r = \sim 2.83$ at 1 MHz which reduces to $\varepsilon'_r = 2.74$ at 100 MHz **(c.f. 2.76 at 1 MHz and ~2.69 at 100 MHz, Von Hippel, 1954)** and is more dispersive than many other polymers. Fontainebleau sandstone is a nearly pure quartz content, low porosity sandstone, consisting of very fine quartz grains highly cemented together. It's dry state dielectric properties nearly perfectly match that of quartz, however the dielectric permittivity of the Fontainebleau sandstone is very slightly dispersive, probably because of a surficial contribution caused by a small content of water incorporated into the quartz cement **(French and Worden, 2013)** and possibly additional water adsorbed from the atmosphere.

CONCLUSION

The use of electrical and acoustic logging in the petroleum industry has always required corresponding laboratory measurements on core samples to provide calibration and to establish the essential physical models (e.g. Archie's Law). The appraisal of conventional and unconventional reservoirs relies on proper quantification of basic rock parameters such as mineralogy, organic matter content, porosity, fluid permeability and fluid type and saturation, which are only indirectly determined from the downhole measurements. Well calibrated cross-property relationships then allow borehole measurements such as electrical properties including dielectric permittivity; acoustic properties and other physical measurement, to be used to estimate the properties of interest.

The development of a combined dielectric and acoustic instrument allows both permittivity and velocity to be measured simultaneously on a single sample, so that the data sets have guaranteed equivalence/correspondence. This was achieved through the design, development and testing of a novel electrical and acoustic platen customised to the short samples that are typically used in dielectric analysis. The instrument has been demonstrated successfully and reproduces the published values for a range of engineering samples, polymers and ceramics. It has also been shown to achieve consistent results on well characterised geological sample standards including Fontainebleau and Berea sandstones.

ACKNOWLEDGEMENTS

I would like to acknowledge Stuart Dahl, Tony Siggins, Rod Banks and Greg Lupton for instrumentation and componentry, Maxim Lebedev, Joel Sarout, Alexy Yurikov and Claudio Delle Piane, Wayne Murray, Dave Walton for technical assistance. David Dewhurst, Tobias Müller, Marina Pervukhina, Ben Clennell and Emma Josh, for editing.

REFERENCES

Archie, G. E., 1941, The electrical resistivity log as an aid in determining some reservoir characteristics, Trans. AIME, vol. 146, October.
ASTM Designation D2845 – 00, 2000, Standard test method for laboratory determination if pulse velocities and ultrasonic elastic constants of rock.

Birchak, J. R., C. G. Gardner, J. E. Hipp and J. M. Victor, 1974, High dielectric constant microwave probes for sensing soil moisture: Proceedings of the IE, vol.62, no.1, pp.93,98, January. doi: 10.1109/PROC.1974.9388.

Ellis, D. V. and J. M. Singer, 2007, Well Logging for Earth Scientists, Springer, The Netherlands.

French, M. W. and R. H. Worden, 2013, Orientation of microcrystalline quartz in the Fontainebleau formation, Paris basin and why it preserves porosity, Sedimentary geology, vol. 284 – 285, pp. 149 – 158.

Gassmann, F., 1951, Über die Elastizität poröser Medien. Viertel. Naturforsch. Ges. Zürich, vol. 96, pp. 1 – 23.

Guéguen, Y., and Palciauskas, V., 1994, Introduction to the Physics of Rocks, Princeton University Press, 392 pp.

Harman, A. K., S. Ninomiya, and S. Adachi, (1994). Optical constants of sapphire (alpha-Al2O3) single crystals. Journal of Applied Physics. vol. 76, no. 12, pp. 8032–8036.

Josh, M., 2014, Dielectric permittivity: A petrophysical parameter for shales, Petrophysics, vol. 55, no. 4, pp 319 – 332, August.

Josh, M., B. Clennell, and T. Siggins, 2009, Practical broadband dielectric measurement of geological samples: 50th SPWLA Ann. Logging Symp., Woodlands Texas, June 21-24.

Keysight App. note 5989-2589EN, Basics of measuring the dielectric properties of materials.

Leung P. K., and R. P. Steiger, 1992, Dielectric constant measurements: A new, rapid method to characterize shale at the wellsite: IADC/SPE Drilling Conference paper no. IADC/SPE 23887, New Orleans, USA. pp. 401-408, February.

Mazzagatti, R. P., D. J. Dowling, J. C. Sims, A. E Bussian and R. S. Simpson, 1983, Laboratory measurement of dielectric constant near 20 MHz, SPE 12097 at the 56th Ann. technical conference and exhibition, San Francisco, October 5-8.

Myers, M. T., 1991, A saturation interpretation model for the dielectric constant of shaly sands: International symposium, Society of Core Analysts: SCA Conference paper number 9118, San Antonio, USA.

Nicholson, A. M. and G. F. Ross, 1970, Measurement of the intrinsic properties of materials by time-domain techniques, IEEE trans. instrumentation and measurement, vol. IM – 19, no. 4, November.

Olympus, 5077PR user's manual, 2000.

Seleznev, N. V., R. L. Kleinberg, M. M. Herron, M. Machlus, A. E. Pomerantz, S. L.

Sen, P. N. and W. C. Chew, 1983, The frequency dependent dielectric and conductivity response of sedimentary rocks, Journal of microwave power, vol. 18, no. 1, pp 95 – 105.

Shen, L. C., H. Marouni, Y. X. Zhang and X. D Shi, 1987, Analysis of the parallel-disc sample holder for dielectric permittivity measurement, IEEE trans. geoscience and remote sensing, vol. GE – 25, no. 5, September.

Stuchly, M. A. and S. S. Stuchly, 1980, Coaxial line reflection methods for measuring dielectric properties of biological substances at radio and microwave frequencies – A review, IEEE trans. instrumentation and measurement, vol. IM – 29, no. 3, September.

Von Hippel, A. R., 1954, Dielectric Materials and their Applications: The Technology Press of M.I.T., United States of America.

Effectively combining NMR measurements and capillary pressure saturation data: A new joint inversion approach

Thomas Hiller and Norbert Klitzsch

Institute for Applied Geophysics and Geothermal Energy, RWTH Aachen, Mathieustr. 10, 52074 Aachen, Germany

This paper was prepared for presentation at the International Symposium of the Society of Core Analysts held in Vienna, Austria, 27 August – 1 September 2017

ABSTRACT

Nuclear magnetic resonance (NMR) relaxation measurements are a well established laboratory and bore-hole method to characterize the storage and transport properties of rocks due to its direct sensitivity to the corresponding pore fluid content (water / oil) and pore sizes. Thereby, the correct estimation of these properties depends strongly on the underlying pore model. Commonly, cylindrical capillaries or spherical pores are assumed for interpreting NMR relaxation data. However, for deducing the size of these pores and thus the pore size distribution (PSD) from the NMR relaxation time distribution a calibration of the NMR data is necessary. Here, we present a novel joint inversion approach of NMR relaxation and capillary pressure saturation (CPS) data based on an angular pore model. This inversion (1) omits the need for the aforementioned calibration and can therewith be used to directly determine the PSD of the sample; (2) accounts for residual water by taking advantage of the angular pore model and (3) can determine the shape of the angular pores by using NMR data measured at both the drainage and the imbibition branch. We show the applicability of the joint inversion approach with angular pores on different synthetic and experimental data sets.

INTRODUCTION

Multi-phase fluid flow through porous media plays an important role in many geoscientific and geotechnical applications and is therefore subject to a broad range of research projects. Especially in the context of reservoir characterization (be it water or hydrocarbon reservoirs), the determination of petrophysical parameters like e.g. porosity and permeability is of utmost importance. These parameters are then further used to characterize the transport and storage properties of rocks or soils e.g. the ability to conduct fluids through its pore space and are the basis of a profound reservoir evaluation.

Among other methods, NMR has been proven to be a viable tool in order to directly or indirectly determine these petrophysical parameters. With its direct sensitivity to hydrogen protons, NMR can be used to noninvasively determine water content. Furthermore, the NMR relaxation behavior is directly related to the surface-to-volume ratio of the pore space and can therefore be used to determine the corresponding PSD. However, the link between NMR relaxation times and pore sizes, generally involves a calibration procedure via the surface relaxivity ρ_s which itself is a sample dependent parameter [1, 2].

If the pore space contains water and air, only the water contributes to the NMR signal. Several attempts have been made to derive transport properties directly from NMR measurements [3-5]. This works sufficiently well, e.g., for sediments and conventional reservoirs but has limitations when a considerable amount of clay minerals is present or the pore space is very heterogeneous, like e.g. in carbonate rocks [6]. Additionally, also a non-uniform distribution of surface relaxivities within a rock may strongly influence the NMR signal and simple NMR-permeability relationships break down (e.g. [7]).

One way to account for a heterogeneous pore space is to consider angular pores. They can be used to explain the typical shift in relaxation time distributions to smaller relaxation times when draining an initially fully saturated sample [8]. In this work we employ angular pores to the joint inversion approach proposed by [9]. This joint inversion combines NMR and CPS data at different levels of saturation to directly invert for the PSD and surface relaxivity ρ_s. Furthermore, we present a method that allows to additionally invert for the cross-sectional shape of our angular pore model by using NMR data from the CPS hysteresis (drainage and imbibition) simultaneously. We like to point out that our employed pore model of a capillary bundle is still a strong simplification of the real pore space. Especially when considering the advancement that has been made in recent years to study two-phase fluid flow processes on the pore scale. However, the presented method allows for a fast and reliable estimation of macroscopic transport processes on the sample scale.

BASICS OF NMR RELAXATION

The NMR relaxation mechanism results from the interaction of a porous medium with its pore-filling fluid (usually water) containing a detectable amount of Hydrogen protons H^+. In most laboratory and well-logging applications, the Hydrogen protons are aligned with a strong static magnetic field **B**. The characteristic precession frequency of protons around this static magnetic field is called Larmor frequency $\omega_L = \gamma_H \mathbf{B}_0$ and solely depends on the strength of $\mathbf{B}_0$ and the gyromagnetic ratio γ_H of Hydrogen. A NMR relaxation measurement is started by applying an energizing electromagnetic pulse with the corresponding devices' Larmor frequency and thus tipping away all Hydrogen protons from their equilibrium state. After the pulse is switched off, the protons can relax back into their equilibrium state. The relaxation process is described by the macroscopic phenomenological Bloch equations with their corresponding solutions

$$M_z(t) = \mathbf{M}_0 \left[1 - e^{-\frac{t}{T_1}} \right]$$
$$M_{xy}(t) = \mathbf{M}_0 e^{\frac{-t}{T_2}} \tag{1}$$

where $\mathbf{M}_0$ is the equilibrium magnetization and M_z and M_{xy} are the longitudinal and transversal magnetization, respectively. Here, we only focus on the transversal magnetization and its corresponding relaxation constant T_2. The NMR relaxation process is a superposition of three independent mechanisms [4, 5]. The bulk relaxation T_b of the pore fluid, the surface relaxation T_s due to the interaction of pore fluid and rock matrix and diffusional relaxation T_d (only for transversal relaxation) caused by magnetic field gradients. If we assume the fast diffusion regime, which is reasonable for natural porous

media under consideration, the surface relaxation dominates and diffusional relaxation can safely be neglected. Then, the transversal relaxation time T_2 is given by

$$\frac{1}{T_2} = \frac{1}{T_{2,\mathrm{b}}} + \frac{1}{T_{2,\mathrm{s}}} = \frac{1}{T_{2,\mathrm{b}}} + \rho_\mathrm{s}\frac{S}{V}, \tag{2}$$

where ρ_s is the surface relaxivity and S/V the surface-to-volume ratio of the porous medium. Generally, one can deduce the following straightforward relationship from equation 2: the larger the pore the longer is the relaxation time T_2 and vice versa. To calculate a multi-exponential NMR relaxation signal, equations 1 and 2 can readily be combined

$$\frac{M_{\mathrm{xy}}(t)}{\mathbf{M}_0} = \sum_i \frac{V_i}{V_0} e^{\frac{-t}{T_{2,i}}} = \sum_i \frac{V_i}{V_0} e^{-t\left(\frac{1}{T_{2,\mathrm{b}}}+\rho_\mathrm{s}\frac{S_i}{V_i}\right)}, \tag{3}$$

with V_0 being the total water-filled pore volume. S_i and V_i denote the individual surface area and volume of pore class i relaxing with the characteristic relaxation time $T_{2,i}$. From equation 3 one can see that at full saturation the magnetization $\mathbf{M}_0$ is proportional to the total pore volume V_0 and hence relates signal strength to water content of the saturated sample. This enables NMR to be a direct method to determine the water content of a given sample and to deduce from this i.e. also the porosity.

JOINT INVERSION WITH ANGULAR PORES

[9] has introduced a joint inversion approach that allows to combine several NMR measurements at different levels of saturation, e.g. during a drainage process. By using the Young-Laplace relation

$$p \propto \frac{1}{R} \tag{4}$$

as a constraint, where p is pressure and R the radius of a cylindrical pore, and equation 3, he could directly infer from the joint inversion the surface relaxivity ρ_s and hence, the PSD.

We extend this approach so that pores with a triangular cross-section can also be considered. In the case of full saturation, the NMR signal of a single angular pore depends only on its volume (amplitude) and total surface-to-volume ratio (relaxation time). In contrast to cylindrical pores, angular pores are not completely desaturated but water remains in the pore corners. Thus, the partially saturated pores contribute to the NMR signal too. The radius R in equation 4 corresponds to the radius of the arc menisci R_{AM} in the corner of a partially filled angular pore (cf. Figure 1). From geometrical relations based on the works of [10, 11] it is possible to deduce the partial saturation of an angular pore based on the applied pressure. Similar to equation 3 one can calculate a NMR relaxation signal for a single angular pore after [8]

$$\frac{M_{\mathrm{xy}}(t)}{\mathbf{M}_0} = \sum_c \frac{V_c}{V_{\Delta 0}} e^{-t\left(\frac{1}{T_{2,\mathrm{b}}}+\rho_\mathrm{s}\frac{S_c}{V_c}\right)}, \tag{5}$$

where c is the corner index, $V_{\Delta 0}$ the volume of the single angular pore and S_c and V_c the surface and volume of the corresponding corner, respectively. The above relations for angular pores can be combined with the joint inversion approach from [9]

$$\mathbf{d} = \mathbf{Gm}, \tag{6}$$

where $\mathbf{d} = \left[M_{\mathrm{xy}}(t)/\mathbf{M}_0\right]_n$ is the data vector holding all n NMR signals, $\mathbf{m} = V_i/V_0$ is the model vector representing the PSD and $\mathbf{G}$ is the forward operator that describes the relationship between model and data (equation 5). For different pressure steps p_n the entries of

$$\mathbf{G}_i(\rho_s, p_n) = \begin{cases} \sum\limits_i e^{-t\left(\frac{1}{T_{2,\mathrm{b}}} + \rho_s \frac{S_i}{V_i}\right)} & p_n < p_{\mathrm{crit},i} \\ \sum\limits_i \sum\limits_c \frac{V_{c,i}}{V_{\Delta 0}} e^{-t\left(\frac{1}{T_{2,\mathrm{b}}} + \rho_s \frac{S_{c,i}}{V_{c,i}}\right)} & p_n \geq p_{\mathrm{crit},i} \end{cases}, \tag{7}$$

depend on the critical pressure p_{crit} of the corresponding pore size class i. If the pressure is smaller than the critical pressure $p_n < p_{\mathrm{crit},i}$ the pore class i is fully saturated. If, on the contrary, the pressure is larger than the critical pressure $p_n \geq p_{\mathrm{crit},i}$ pore class i is partially saturated and the contributions of the three corners c need to be considered. Note that, in the case of cylindrical pores $\mathbf{G}_i(\rho_s, p_n \geq p_{\mathrm{crit},i}) = 0$, the entries of the forward operator are zero due to the full-empty characteristic [9]. The non-linear system of equations in equation 6 can now be solved for $\mathbf{m}$ and ρ_s simultaneously by applying, e.g., a regularized (damped) Levenberg-Marquardt algorithm [9,12, 13]. To all inversions presented in this work a first-order smoothness constraint was employed [14] and the inversion is regularized so that the final NMR data misfit is of the same order as the data noise.

First, we use a synthetic model with a cross-sectional shape of $[90°, 60°, 30°]$ and surface relaxivity $\rho_s = 10\ \mu\mathrm{ms}^{-1}$ to demonstrate the joint inversion with angular pores (Figure 2). T_2 NMR signals are calculated at four different levels of saturation and superposed by 0.5% Gaussian noise to simulate a signal-to-noise ratio (SNR) of 200, which is a reasonable value for laboratory NMR measurements (Figure 2c). In each sub-panel of Figure 2 the red lines indicate the corresponding fits or inverted model, respectively. Combining these four signals and applying an angular inversion model yields an almost perfect fit to the forward model (Figure 2a) with an inverted surface relaxivity of $\rho_s = 10.02\ \mu\mathrm{ms}^{-1}$. The CPS-curve fit also agrees nicely with the forward model (Figure 2b).

APPLICATION TO REAL DATA
Now we apply our joint inversion approach to two different laboratory samples (Figure 3). The first one is a sintered borosilicate, generally used as filter material, with a very homogeneous grain and pore structure and a porosity of $\Phi \approx 0.3$ (Figure 3a). The measured intrinsic gas permeability is $k_{\mathrm{int(gas)}} = 7\mathrm{d}$. The second one is a coarse-grained sandstone from a tight gas reservoir with a porosity of $\Phi \approx 0.1$ (Figure 3b). The measured

intrinsic gas permeability is $k_{\text{int(gas)}} = 10\mu d$, which is more than four orders of magnitude smaller compared to the borosilicate sample.

Example 1 – Sintered Borosilicate
Figure 4 shows the joint inversion applied to NMR data acquired on a sintered borosilicate sample during a drainage experiment. [9] already used this data set to initially present the joint inversion with cylindrical pores. One particular drawback of a cylindrical pore model, when applied to real data, is its inability to account for residual water in pore crevices, which was also reported by [9]. We use seven NMR signals (Figure 4c) measured at decreasing saturations from 100% (black) to 7% (yellow). In contrast to the cylindrical pore model presented in [9], the joint inversion with angular pores gives a unimodal PSD (Figure 4a) with a peak at $x \approx 2\text{x}10^{-5}$m and therewith fits much better to the Mercury Injection Capillary Pressure (MICP) data. Note, that MICP data generally yields pore throat sizes and not pore sizes due to the non-wetting character of mercury. Considering the very narrow MICP distribution and the slight shift of the NMR PSD mode to larger values compared to the MICP data, the two data sets agree very well with each other. Finally, also the fitted CPS-curve matches the experimental data nicely (Figure 3b).

Example 2 – Tight Gas Sandstone
Figure 5 shows the inversion result for the tight gas reservoir sandstone. The sample was installed in a high-pressure flow cell with a confining pressure of $p_{\text{conf}} = 15$ MPa and continuously drained with nitrogen gas and increasing differential pressures up to $\Delta p = 2.5$ MPa [15]. The inherent differences between these two samples is strongly reflected in the measured NMR signals. Note that the time axis of Figure 5c is in log-scale to better distinguish between the individual signals especially at partial saturation. Also the applied drainage pressures are an order of magnitude larger compared to the borosilicate sample. The inverted PSD shows a slight trimodal character with the major peak (mode) at $x \approx 3\text{x}10^{-7}$m.

As a cross check, we estimate the permeability of the inverted PSD for both samples by a simple Kozeny-Carman-type [16] relation

$$k_{\text{NMR}} = \frac{\Phi R_{\text{lgm}}^2}{8\tau},\tag{8}$$

with porosity Φ and R_{lgm} equal to the logarithmic mean radius of the PSD. We assume tortuosity $\tau = 1$ because we have no information about it. Thus, we may overestimate the permeability. We obtain $k_{\text{NMR}} = 5.9d$ and $k_{\text{NMR}} = 33\mu d$ as permeabilities for the borosilicate and sandstone sample, respectively. Even though our permeability estimation may be strongly simplified and considering the quite simple pore model of a capillary bundle, the derived values are exceptionally close to the measured data.

USING THE JOINT INVERSION TO DETERMINE PORE SHAPE
Additional to PSD and surface relaxivity, the shape of the angular pore can be determined by the introduced inversion approach, if NMR data during drainage and imbibition are considered. This is due to the drainage and imbibition hysteresis of angular pores, which

solely depends on their shape [8, 11]. Figure 6 demonstrates this exemplary for a synthetic model with a cross-sectional shape of $[90°, 80°, 10°]$ and a surface relaxivity of $\rho_s = 10\ \mu ms^{-1}$. Figure 6a-c shows the joint inversion result if only drainage data is used. Although the inverted surface relaxivity $\rho_s = 10.6\ \mu ms^{-1}$ is close to the given value, the inverted angular shape is far off $[90°, 59.5°, 30.5°]$. Due to the deviation in the inverted shape (Figure 6a) also the fitted imbibition branch of the CPS-curves does not fit with the forward model (Figure 6b). In Figure 6d-f the NMR signal at 50% saturation is taken from the imbibition branch. Now, not only the surface relaxivity $\rho_s = 9.9\ \mu ms^{-1}$ fits well to the forward model but also the inverted angular shape $[90°, 79.9°, 10.1°]$ and, hence, the CPS-curves.

We tested this approach for triangular shapes ranging from $[90°, 89°, 1°]$ to $[90°, 45°, 45°]$ and found exceptionally well fits, especially for very acute triangular shapes up to $[90°, 65°, 25°]$. For less acute triangular shapes the difference in the inverted shape is generally off by $\approx 5°$. This however, is to be expected due to the decreasing hysteresis for less acute triangles [17].

SUMMARY
We presented a joint inversion approach for NMR data at different water saturations using an angular pore-bundle model. This joint inversion provides the PSD and surface relaxivity of the studied samples. The implementation of angular pores allows the consideration of residual water in pore crevices and hence considerably improves the robustness of the method. Additionally, it is also possible to estimate the permeability of the measured samples even though the applied pore model (capillary bundle) is a strong simplification of a real porous medium. We have also shown that we can additionally invert for the shape of the angular pores when both, the drainage and imbibition branches of a CPS hysteresis are used. So far the latter was shown for synthetic data only because of lacking NMR data at the imbibition path.

ACKNOWLEDGEMENTS

REFERENCES
1. Torrey, H.C., "Bloch Equation with Diffusion Terms", *Physical Review*, (1956) **104**, 563-565
2. Brownstein, K.R. and Tarr, C.E., "Importance of classical diffusion in NMR studies of water in biological cells", *Physical Review A*, (1979) **19**, 2446
3. Kenyon, W.E., "Petrophysical Principles of Applications of NMR Logging", *The Log Analyst*, (1997) **38**, 21-43
4. Coates, G.R., Xiao, L. and Prammer, M.G., *NMR logging: principles and applications*, Gulf Professional Publishing, 1999
5. Dunn, K.-J., Bergman, D.J. and LaTorraca, G.A., *Nuclear magnetic resonance: petrophysical and logging applications*, Handbook of Geophysical Exploration Vol. 32, Elsevier, 2002

6. Westphal, H., Surholt, I., Kiesl, C., Thern, H.F. and Kruspe, T. „NMR Measurements in Carbonate Rocks: Problems and an Approach to a Solution", *pure and applied geophysics*, (2005),**162**, 549-570

7. Costabel, S. and Yaramanci, U., "Estimation of water retention parameters from nuclear magnetic resonance relaxation time distributions", *Water Resources Research*, (2013), **49**, 2068-2079

8. Mohnke, O., Jorand, R., Nordlund, C. and Klitzsch, N., „Understanding NMR relaxometry of partially water saturated rocks", *Hydrology and Earth System Sciences*, (2015), **19**, 2763-2773

9. Mohnke, O., "Jointly deriving NMR surface relaxivity and pore size distributions by NMR relaxation experiments on partially desaturated rocks", *Water Resources Research*, (2014), *50*, 5309-5321

10. Mason, G. and Morrow, N.R., "Capillary behavior of a perfectly wetting liquid in irregular triangular tubes", *Journal of Colloid and Interface Science*, (1991), **141**, 262-274

11. Tuller, M, Or, D. and Dudley, L.M., "Adsorption and capillary condensation in porous media: Liquid retention and interfacial configurations in angular pores", *Water Resources Research*, (1999), **35**, 1949-1964

12. Levenberg, K., "A method for the solution of certain problems in least-squares", *Quarterly of Applied Mathematics*, (1944), **2**, 164-168

13. Marquardt, D.W., "An Algorithm for Least-Squares Estimation of Nonlinear Parameters", *Journal* of the *Society* for *Industrial* and *Applied Mathematics*, (1963), **11**, 431-441

14. Aster, R.C., Borchers, B. And Thurber, C.H., *Parameter Estimation and Inverse Problems*, Academic Press, 2013

15. Hoder, G., *Monitoring of Two-Phase Fluid Flow Experiments by NMR*, MSc thesis, RWTH Aachen University, 2016

16. Carman, P.C., *Flow of gases through porous media*, Academic Press, New York, 1956

17. Hiller, T. and Klitzsch, N. *Joint Inversion of NMR and desaturation data using an angular pore model*, 76. General Assembly of the German Geophysical Society, 2016
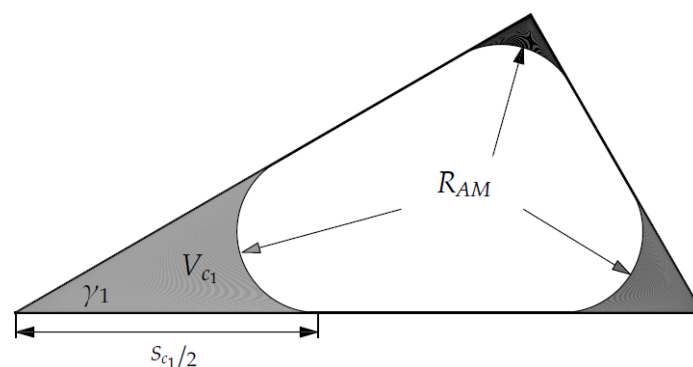
Figure 1. Cross-section of a triangular pore (water-gray, air-white). The pressure dependent radius of the arc menisci is the same in every corner of a triangle irrespective of the individual corner angle γ. S_c and V_c are the surface and volume of the corresponding corner and determine the individual relaxation time T_2 after equation 5.
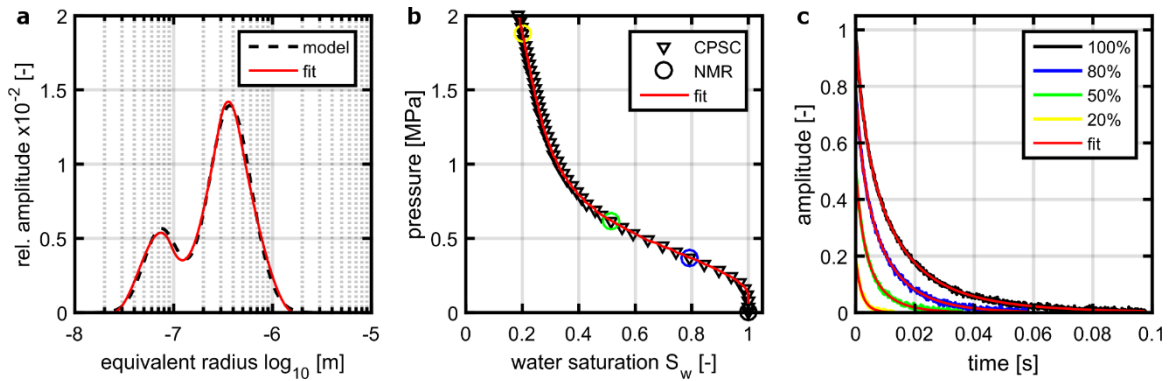
Figure 2 a: forward model with cross-sectional shape [90°,60°,30°] and $\rho_s = 10\ \mu ms^{-1}$ (dashed black line) b: corresponding CPS curve (black downward triangles), color-coded are the saturation levels where a NMR signal was calculated (circles) c: NMR signals (with 0.5% Gaussian noise) at the corresponding saturation levels (from black – full saturation to yellow – 20% saturation); in all three sub-panels the red lines show the inversion results, the inverted surface relaxivity is $\rho_s = 10.02\ \mu ms^{-1}$.
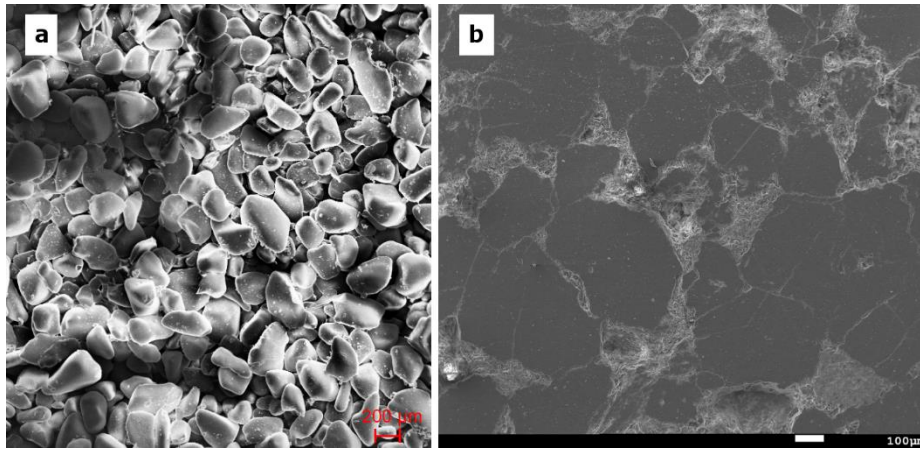
Figure 3 SEM images of the two samples used in this study a: sintered borosilicate with a quite homogeneous grain size structure. The red scale refers to 200μm b: tight sandstone with coarse-grained structure and irregular angular pores.
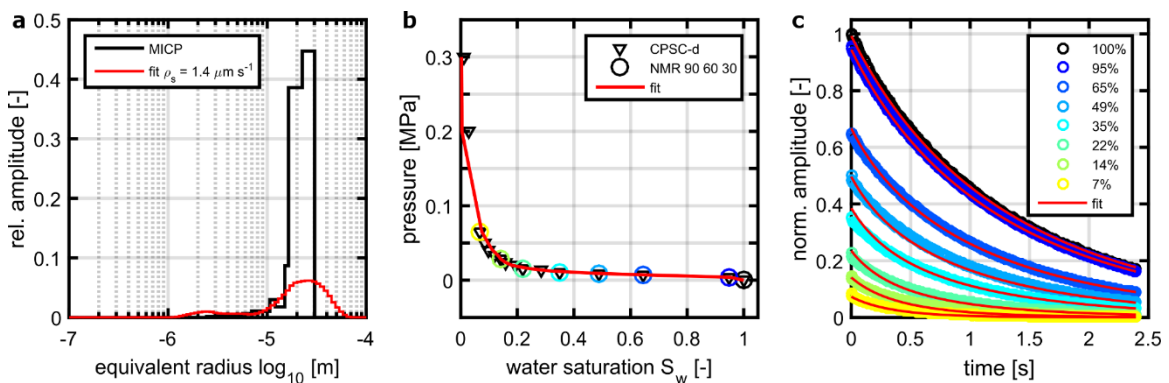
Figure 4 Joint inversion results of the NMR data set for a sintered borosilicate sample measured at decreasing levels of saturation and using an angular pore [90°,45°,45°] a: Mercury Injection Capillary Pressure (MICP) curve (black) b: corresponding CPS curve (black downward triangles); color-coded are the saturation levels where a NMR signal was measured (circles); Note that the full saturation signal (O – 100%) was measured at 0 Pa and is plotted here at 1x10³ Pa for visualization purposes only. c: NMR signals at the corresponding saturation levels (from black – full saturation to yellow – 7% saturation); in all three sub-panels the red lines show the inversion results, the inverted surface relaxivity is $\rho_s = 1.4\ \mu ms^{-1}$.
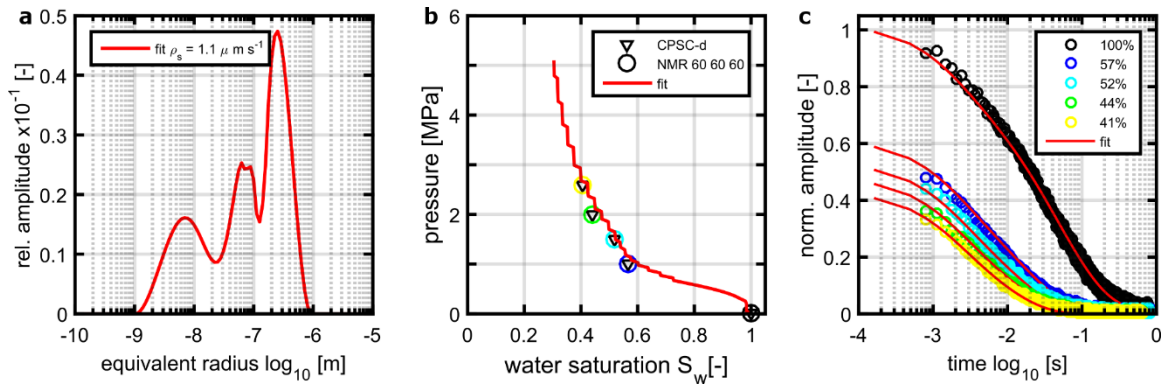
Figure 5 Joint inversion results of the NMR data set for a tight sandstone sample measured at decreasing levels of saturation and using an angular pore model [60°,60°,60°] a: inverted PSD (red) b: corresponding CPS curve (black downward triangles), color-coded are the saturation levels where a NMR signal was measured (circles) c: NMR signals at the corresponding saturation levels (from black – full saturation to yellow – 41% saturation); in all three sub-panels the red lines show the inversion results, the inverted surface relaxivity is $\rho_s = 1.1\ \mu\mathrm{ms}^{-1}$.
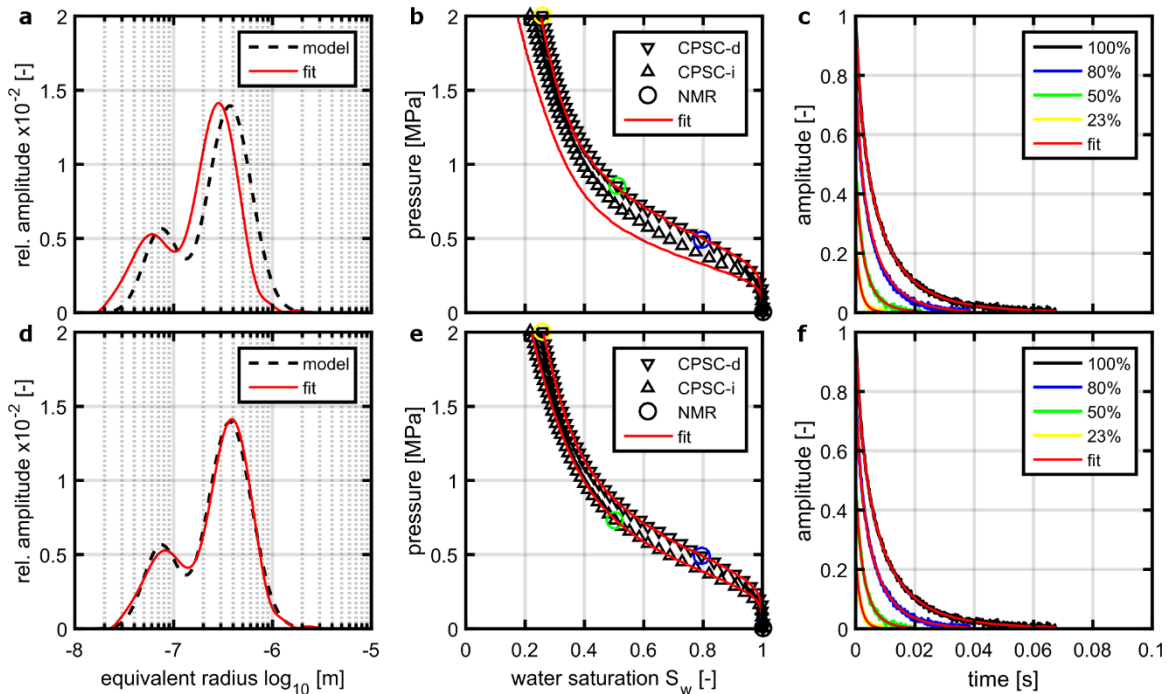
Figure 6 Joint inversion for surface relaxivity ρ_s and pore shape angle α when using synthetic NMR signals either only during drainage (a-c) or during drainage and imbibition (d-f); a+d: forward model with cross-sectional shape [90°,80°,10°] and surface relaxivity $\rho_s = 10\ \mu\mathrm{ms}^{-1}$ (dashed black line) b+e: corresponding CPS curve (black downward triangles – drainage, black upward triangles - imbibition), color-coded are the saturation levels where a NMR signal was calculated (circles) c+f: NMR signals (with 0.5% Gaussian noise) at the corresponding saturation levels (from black – full saturation to yellow – 23 % saturation); in all six sub-panels show the inversion results; when using drainage only the inverted angle and surface relaxivity are $\alpha_{\mathrm{inv}} = 30.5°$ and $\rho_s = 10.6\ \mu\mathrm{ms}^{-1}$ (a-c); when using drainage and imbibitions the inverted angle and surface relaxivity are $\alpha_{\mathrm{inv}} = 10.1°$ and $\rho_s = 9.9\ \mu\mathrm{ms}^{-1}$ (d-f).

Towards a better understanding of electrical relaxation

Sabine Kruschwitz[1], Matthias Halisch[2], Carsten Prinz[3], Andreas Weller[4], Mike Müller-Petke[2], Raphael Dlugosch[2]

[1] Bundesanstalt für Materialforschung und –prüfung, Unter den Eichen 87, 12205 Berlin and Technische Universität Berlin, Gustav-Meyer-Allee 25, 13355 Berlin, Germany
[2] Leibniz Institute for Applied Geophysics (LIAG), Stilleweg 2, 30655 Hannover, Germany
[3] Bundesanstalt für Materialforschung und –prüfung, Unter den Eichen 87, 12205 Berlin, Germany
[4] Clausthal University of Technology, Institute of Geophysics, Arnold-Sommerfeld-Straße 1, 38678 Clausthal-Zellerfeld, Germany

This paper was prepared for presentation at the International Symposium of the Society of Core Analysts held in Vienna, Austria, 27 August – 1 September 2017

ABSTRACT

Other than commonly assumed the relaxation times observed in the electrical low-frequency range (1 mHz – 40 kHz) of natural porous media like sandstones and tuff stones cannot be directly related to the dominant (modal) pore throat sizes, measured (e.g.) with mercury intrusion porosimetry (MIP). Working with a great variety of sandstones from very different origins and featuring great variations in textural and chemical compositions as well as in geometrical pore space properties, it was observed that particularly samples with narrow pore throats were characterized by long (low-frequency) relaxations. These, however, can (following the current theories) be rather explained by long "characteristic length scales" in these media or low diffusion coefficients along the electrical double layer. However, there is no straightforward way (or single approved method) of getting reliable numbers for properties such as the lengths of pore throats, the diameter and length of the wide pores and their respective distributions. Consequently we follow a multi-methodical approach and combine the benefits of MIP, micro-computed tomography (µ-CT) and nuclear magnetic resonance (NMR) to achieve much deeper insight due to the different resolutions and sensitivities to either pore constrictions (throats) or wide pores. This helps us to understand, whether the observed electrical relaxation phenomena actually depend on geometric length scales or rather on other properties such as chemical composition, clay content, clay type or cation exchange capacity. In this paper, we showcase selected results of a systematic study of a total of 16 sandstones and three tuffs. Findings and the particular advantage of the used method combination are discussed and shown in detail for a representative sample selection.

INTRODUCTION

Many recent approaches in geophysics and hydrogeophysics try to use the characteristic relaxation time of electrical low-frequency or so called spectral induced polarization (SIP) measurements to derive information on properties such as hydraulic properties (Börner et

al. 1996, Hördt et al. 2009, Weller et al. 2016), effective permeability (e.g. Binley et al. 2005; Weller et al. 2015) or pore size distribution (Revil and Florsch 2010; Florsch et al. 2014). Based on the theory of Schwartz (1962), who related the low-frequency dispersion of colloidal particles in electrolytes to the particle sizes of the grains, it has been intensively discussed amongst geophysicists, how to interpret and relate relaxation phenomena in electrolyte saturated solid matter, i.e. porous natural rocks such as sandstones, tuffs, limestones etc. Some researchers reported on power-law relationships between the electrical relaxation time and the modal pore throat size measured with MIP for their samples (e.g. Scott and Barker 2003; Kruschwitz et al. 2010, Titov et al. 2010). Others argued that rather the length of narrow pore constrictions determine the polarization and hence, relaxation properties. This so called membrane polarization theory has also been implemented in recent numerical modelling approaches (Bücker and Hördt 2013a and 2013b). Kruschwitz et al. 2016 studied this highly debated relationship between the electrical relaxation time τ and the modal pore throat size compiling the largest and most diverse data set as yet. Including published and unpublished sources they worked with geological materials from very different areas with a wide variation of dominant pore throat sizes, specific surface areas, porosities and permeabilities. Their aim was to systematically study the question of what is the characteristic textural length scale controlling low-frequency relaxation and hence the frequency of the peak phase.

In conclusion Kruschwitz et al. 2016 could divide the large group of samples into three groups as illustrated in Fig. 1. The graph shows the measured SIP relaxation times τ_{peak} as a function of dominant (model) pore throat size D_{dom} determined with MIP. In this graph we can distinguish three groups of samples. The first group ("type 1" samples) simply follow the "predicted" behavior and feature relaxation times that might be controlled by the modal pore throat sizes of the samples. A representatives of type 1 samples is for example Bentheimer sandstone. The second group ("type 2" samples) consists of rocks, that likewise seem to follow the predicted $\tau_{peak} \sim D_{dom}$ relationship, but at the same time show a low-frequency relaxation (large τ_{peak} values), that cannot be explained by the very small pore throat sizes measured with MIP. A representative of this type 2 samples is Langenauer sandstone. These materials show a so-called "double-peak" SIP behavior, because they show two separate relaxation processes in the SIP data and accordingly are addressed by two τ_{peak} values, whereas their pore spaces are characterized by only one dominant pore throat size in the MIP. For these samples as well as for those belonging to the third group ("type 3" samples), which do not follow the predicted $\tau_{peak} \sim D_{dom}$ relationship at all, but show very slow SIP relaxation processes even though the dominant pore throat sizes are mostly smaller than 5 µm. These findings raised anew and rather desperately the question what is really controlling the low-frequency relaxation time in porous solid media. From a theoretical, electrochemical point of view it should rather be the lengths of pores, not the diameter. The reason why still a dependency on the pore throat diameters was observed (for type 1 and party type 2 samples) could be that for these materials the pore throat lengths are relatively equal in size compared to their diameters.

This requires though, that we characterize the pore systems in much more detail than it has been done with MIP so far. Only a better comprehension of the characteristic length scales present in a pore space will help to understand what is causing the measured SIP relaxation phenomena. For Langenauer sandstone for example we would expect (additionally to the pore throat size) a second characteristic length of about 20 – 150 µm to explain the high relaxation time of ca. 5.3 s (marked in Fig. 1). In this study we follow a multi-methodical approach and apply µ-CT and NMR on the majority of the same samples as shown above. As all these methods are sensitive to other pore space properties and have different resolutions which is beneficial to fully leverage their potential by combining them.
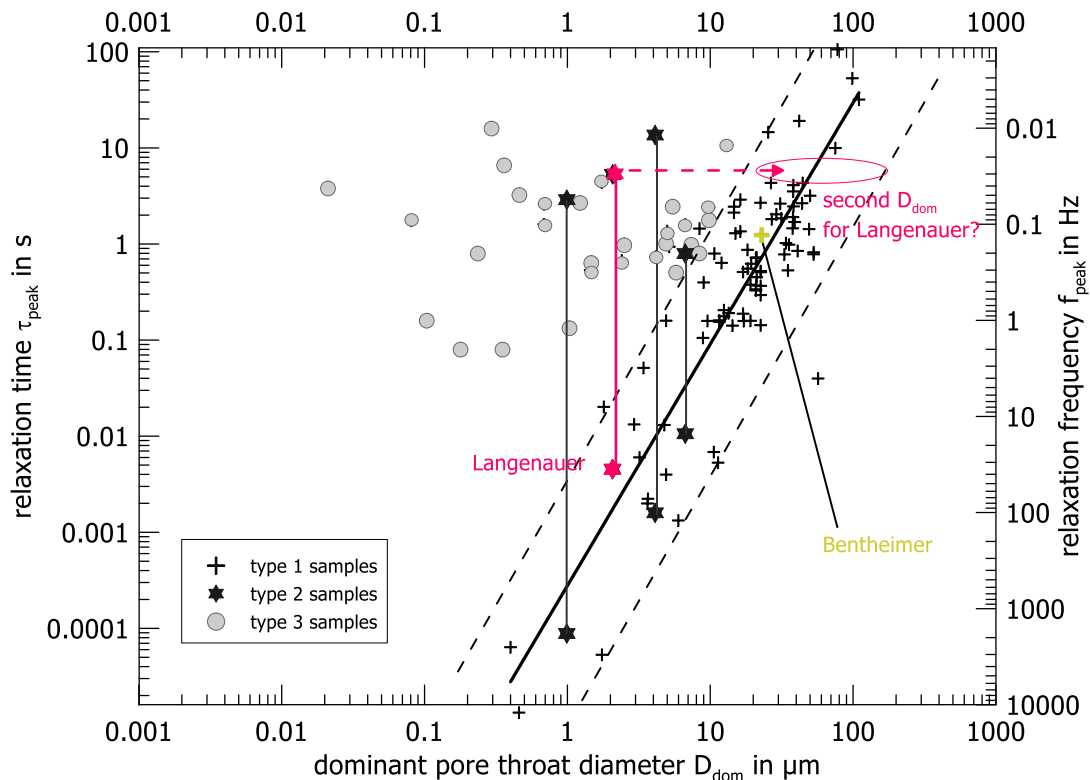
Figure 1: Characteristic relaxation times τ_{peak} from SIP versus dominant modal pore throat size D_{dom} determined with MIP (modified after Kruschwitz et al. 2016).

SAMPLES & METHODOLOGY

For our comparison of the pore space characteristics, two different rocks have been selected for presentation in this paper: Bentheimer sandstone and Langenauer sandstone (marked in Fig. 1). Bentheimer sandstone is a Berea type sandstone that has been used and described in many previous petrophysical studies. The shallow-marine material was deposited during the Early Cretaceous and is quarried near Bad Bentheim and Gildehaus, Germany. It is a fine to medium grained sandstone of white to yellowish or light red color. Bonding is mostly due to grain-grain cohesion (Dubelaar and Nijland, 2014). Langenauer sandstone (sometimes referred to as Dlugopole oder Wünschelburger sandstone) originates from the

Upper Cretaceous, and recent outcrops can be found in the vicinity of Dlugopole, a few kilometers south of Wroclaw, Poland. It is a medium grained, white-yellowish sandstone. Scanning electron microscopy images for both materials are shown in figure 2, also indicating the presence of caolinite as dominant clay mineral (10.5 vol.-% for the Bentheimer, and 8.5 vol.-% for the Langenauer sandstone, according to quantitative X-ray diffraction analysis).
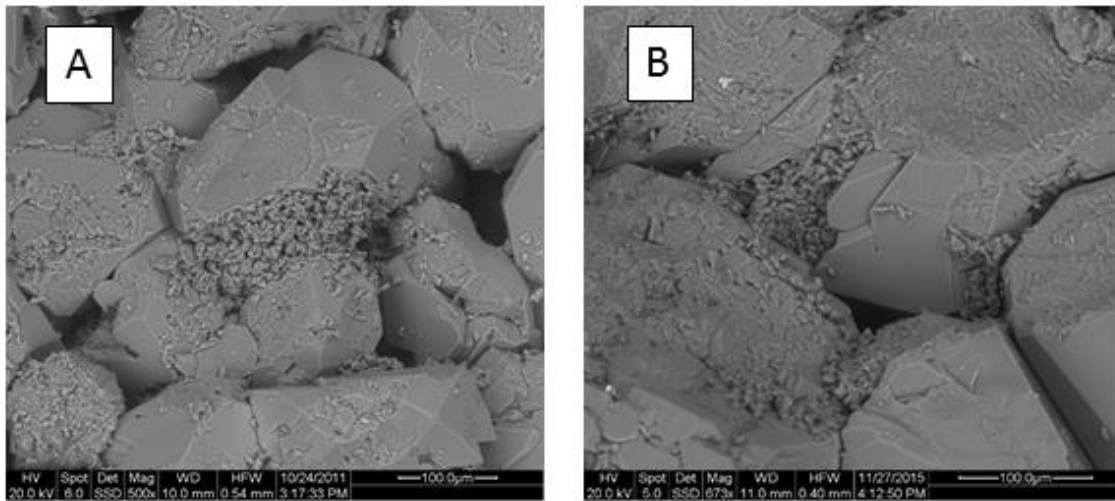
Figure 2: SEM images of Bentheimer sandstone (A) and Langenauer sandstone (B).

Mercury intrusion porosimetry measurements were conducted using an AutoPore III from Micromeritics. The pressure range of the AutoPore system from 0.004 - 400 MPa corresponds to pore sizes of ca. 400 µm down to 3.6 nm. The cumulative intruded mercury volume versus pressure curves were converted to a differential intrusion (in ml/g) versus pore diameter (in µm) assuming cylindrical pores using the Washburn equation. The dominant pore throat sizes are the modal pore throat sizes and were calculated from the maximum value in the differential intrusion over pressure curves. The µ-CT imaging has been performed with a nanotom 180 S (GE Sensing & Inspection Technologies), a high-resolution X-ray CT system. The minimum focal spot size is 0.6 µm, which is optimal for pore structure analyses of small cylindrical samples with diameters of 1 mm at a length of 5-10 mm. Voxel resolutions of 1.25 – 2.0 µm could be achieved. The digital image analysis (DIA) workflow has been extensively described by Schmitt et al. (2016) and Halisch et al. (2016). The NMR measurements were carried out with a Magritek Core Analyzer (Magritek, Wellington, New Zealand) operating at a Lamor frequency of 2 MHz. We use a CPMG pulse sequence with an echo spacing of 200 µs and the built-in cooling/heating system ensures a constant sample temperature between 21°C and 22°C during the measurements. The porosity of the fully saturated samples (for NMR and SIP the very same samples could be used) has been determined by calibration with a bulk water sample of known dimension. The smooth relaxation time distributions are derived using a common multi-exponential approach. A regularization parameter is used to weigh the minimum structure in the relaxation time distribution and the minimum

residual between the measured data and model response (e.g., Whittall et al., 1991). A pore size distribution is finally calculated assuming fast-diffusion and cylindrical pores as (Brownstein and Tarr, 1979):

$$d = 4\rho T_2 \tag{1}$$

with d being the pore size, ρ the surface relaxivity, and T_2 the transverse relaxation time. The SIP measurements were carried out in the laboratory using a SIP-ZEL device (Zimmermann, 2008). The system allows for two simultaneous 4-point measurements over a frequency range from 1 mHz to 45 kHz. The measurements were carried out at 27 logarithmically equidistant steps in the frequency range. The sample holder used has been manufactured at BAM and has been described elsewhere, for example in Kruschwitz (2008). A spectrum of measured electrical impedances is obtained and usually recorded either as magnitude $|\rho|$ and phase ϕ, or as real (ρ') and imaginary (ρ'') part of the resistivity respectively. All samples in this study show a peak relaxation behavior, which means that the phase or more precisely the imaginary part of the resistivity exhibits a clear maximum at a certain frequency. Like in other studies we work with the peak relaxation time τ_{peak}, which is $1/(2\pi f_{peak})$, with f_{peak} being the frequency, where the quadrature resistivity is maximal.

RESULTS

For the purpose of clarity we chose a common representation of the results of all methods in one diagram. We plot pore volume distributions and systematically regard the fractions of porosity (here added together from large to small pore sizes) that are covered in each part of the curves. In case of µ-CT we use the volumes of the equivalent diameter distributions. In the following we summarize our observations for two investigated sandstones.

Bentheimer sandstone (sample Bh5, Fig. 3):

The MIP displays a narrow unimodal distribution of pore throats with a dominant size around 39 µm. For the µ-CT the maximum resolution was a voxel size of 1.75 µm. The biggest part of the total porosity contained in pore with an equivalent diameter of ca. 125 µm. Using a surface relaxivity of 37.5 µm/s the NMR T2 spectrum covers reasonably well the equivalent diameter volume curves as calculated in the DIA, its maximum appears then at ca. 85 µm. Adding together the porosities that the methods capture from the wide pores to the small pores (thresholds Φ given in Fig. 3 on top), we find that MIP clearly cannot see the wider pore fractions that are recorded in the DIA. In a regular pore throat-pore body system this is to be expected as the MIP always addresses the pore body volumes to the respective throats sizes that provide entry to them. This is why the porosities with MIP and µ-CT are significantly different for pores $\geq$ 45 µm, but tend to be more in the same range for pores $\geq$ 10 µm. The NMR seems to be influenced by both the wider pores and the smaller throats. The total porosities determined by NMR and MIP are with ca. 23% in good agreement, gravimetrically we determined 23.3%. When we use the equivalent diameter and NMR distributions to calculate from their arithmetic mean a proxy characteristic length scale for the wide pores we get about 105 µm. This results in a pore throat to pore body ratio of ca. 1:2.7. It should be noticed that the position of the NMR

spectrum and hence the surface relaxivity ρ has been chosen so that it fits and mostly covers the frequency distribution of the equivalent pore diameters determined by µ-CT. It is conceivable that NMR is more strongly influenced by the larger pores and should be shifted further right in this diagram covering more the width, breadth or even length distributions (compare Zhang et al. 2017). Similar analysis of further samples will help to improve our knowledge of how to correlate these distributions.
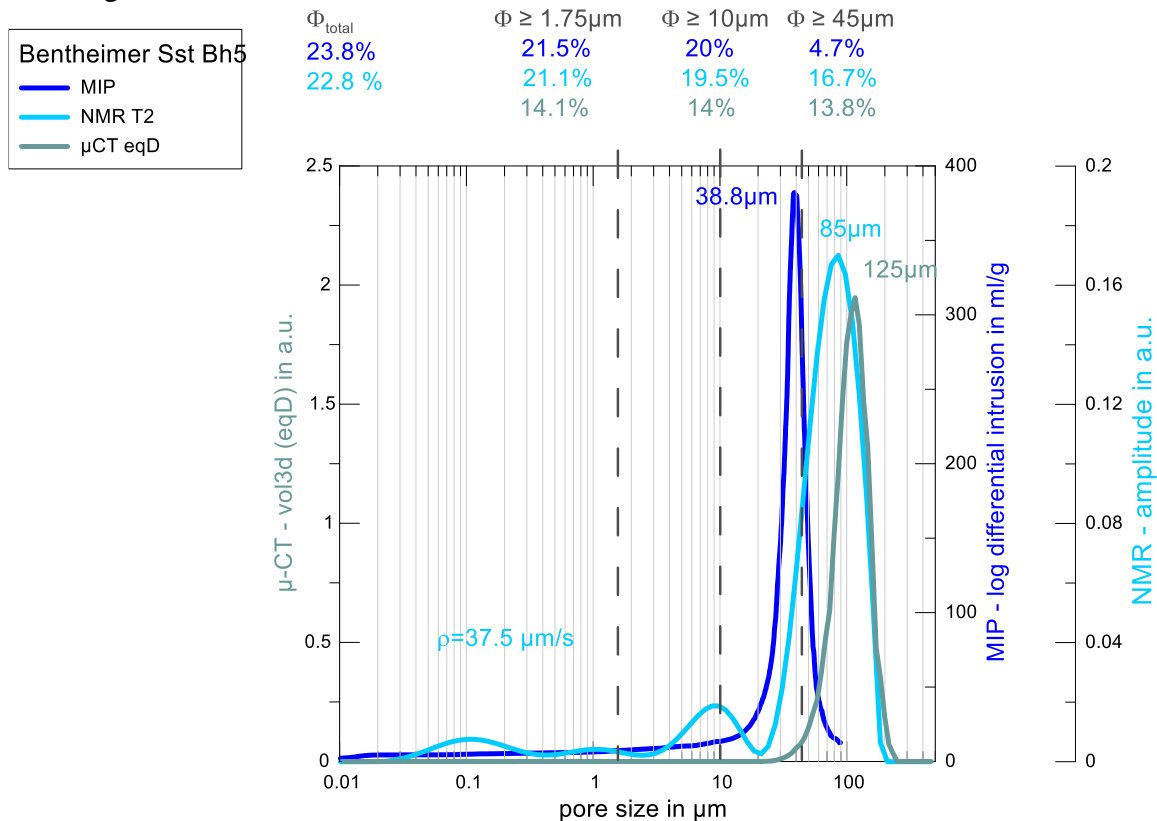
Figure 3: Bentheimer sandstone, pore size distributions as determined with MIP (dark blue), NMR (light blue) and µ-CT equivalent diameter (green) and cumulative porosities for three different pore fractions.

Langenauer sandstone (Fig. 4):
Similar to Bentheimer sandstone also Langenauer sandstone has a uni-modal MIP pore size distribution, here with a peak at ca. 2 µm. The µ-CT curve however identifies big pores in the range around 75 µm. The porosity identified for pores ≥ 8 µm is 6.9%, which is much higher than what is seen with MIP for this pore size. The NMR T2 spectrum indicates a bi-modal distribution supporting both the µ-CT and MIP data well when a surface relaxivity of 30 µm/s is assumed. Looking at the porosities, NMR identifies with 5.8% slightly more volume in the wide pore region (pore size ≥ 8µm) as compared to the pore throat region (pore sizes between 1.25 and 8 µm), where additional porosity of 3.8% are detected. More clearly than for the Bentheimer sandstone the NMR signal seems to be influenced by both the wide and the small throats. The total porosities of 12% (MIP) and 12.1% (NMR) correspond well to the 11.7% measured gravimetrically. Calculating with a mean value of 60 µm (mean of NMR and µ-CT peaks) for the wide pores, the pore throat to body ratio

for Langenauer sandstone is about 1:30. Compared to the Bentheimer sandstone Langenauer sandstone has a more heterogeneous pore system that is clearly dominated by two very different length scales. A wide pore size of around 60 µm convincingly explains the low frequency relaxation in SIP (compare Fig. 1).
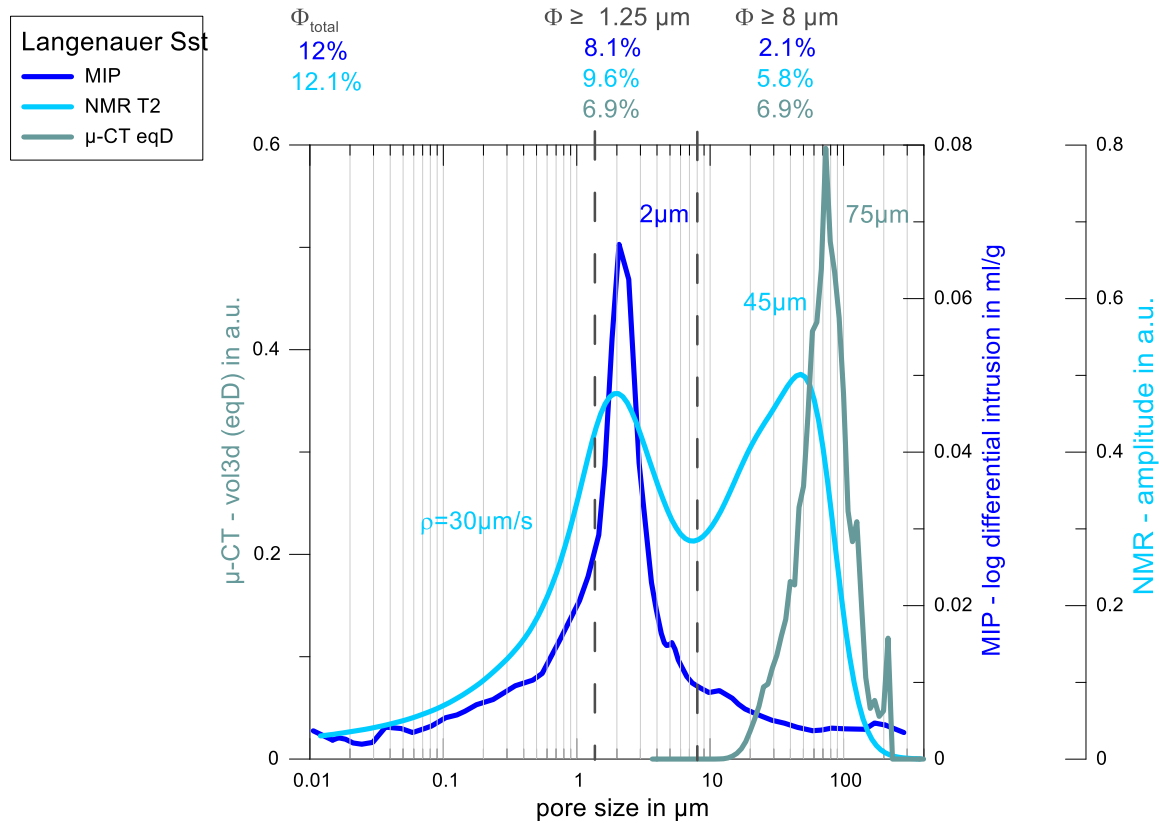
Figure 4: Langenauer sandstone, pore size distributions as determined with MIP (dark blue), NMR (light blue) and µ-CT equivalent diameter (green) together with cumulative porosities for three different pore fractions.

CONCLUSION

In this paper we present an important contribution towards a better understanding of SIP relaxation phenomena due to an enhanced characterization of complex pore systems in solid media using MIP, µ-CT and NMR. Samples with fairly uniform pore geometries are observed to follow the predicted power law relationship of SIP relaxation time τ_{peak} and dominant pore throat size D_{dom} as determined with MIP. In these uniform pore spaces the size ratios of pore throats to pore bodies are moderate, here ca. 1:3 for Bentheimer sandstone. Samples where two SIP relaxation processes are observed seem to be characterized by more extreme ratios of throat to body sizes. For the investigated Langenauer sandstone we get a ratio ca. 1:30. Presumably one relaxation can be attributed to the so-called active zone in the pore throat and another one to the length of the pore body.

REFERENCES

1. Börner, F., J. Schopper, and A. Weller, "Evaluation of transport and storage properties in the soil and groundwater zone from induced polarization measurements", *Geophysical Prospecting (1996)*, **44(4)**, 583-601.
2. Hördt, A., R. Blaschek, F. Binot, A. Druiventak, A. Kemna, P. Kreye, and N. Zisser, "Case histories of hydraulic conductivity estimation with induced polarization at the field scale", *Near Surface Geophysics (2009)*, **7 (5-6)**, 529-545.
3. Weller, A., Z. Zhang, L. Slater, S. Kruschwitz, and M. Halisch, "Induced polarization and pore radius — A discussion", *Geophysics (2016)*, **81(5)**, D519-D526.
4. Binley, A., L. Slater, M. Fukes, and G. Cassiani, "Relationship between spectral induced polarization and hydraulic properties of saturated and unsaturated sandstone", *Water Resources Research (2005)*, **41**, W12417.
5. Weller, A., L. Slater, A. Binley, S. Nordsiek, and A. Xu, "Permeability prediction based on induced polarization: Insights from measurements on sandstone and unconsolidated samples spanning a wide permeability range", *Geophysics (2015)*, **80 (2)**, D161-D173.
6. Revil, A. and N. Florsch, "Determination of permeability from spectral induced polarization in granular media", *Geophysical Journal International (2010)*, **181**, 1480–1498.
7. Florsch, N., A. Revil, and C. Camerlynck, "Inversion of generalized relaxation time distributions with optimized damping parameter", *Journal of Applied Geophysics (2014)*, **109**, 119-132.
8. Scott, J., and R.D. Barker, "Determining pore throat size in Permo- Triassic sandstones from low-frequency electrical spectroscopy*". Geophysical Research Letters (2003),* **30**, 1450–1453.
9. Kruschwitz, S., A. Binley, D. Lesmes, and A. Elshenawy, "Textural controls on low frequency electrical spectra of porous media", *Geophysics (2010)*, **75 (4)**, WA113–WA123.
10. Titov, K., A. Tarasov, Y. Ilyin, N. Seleznev, and A. Boyd, "Relationships between induced polarization relaxation time and hydraulic properties of sandstone", *Geophysical Journal International (2010)*, **180**, 1095–1106.
11. Bücker, M., and A. Hördt, "Long and narrow pore models for membrane polarization", *Geophysics (2013a)*, **78 (6)**, E299 – E314.
12. Bücker M., and A. Hördt, "Analytical modelling of membrane polarization with explicit parametrization of pore radii and the electrical double layer", *Geophysical Journal International (2013b)*, **94**, 804-813.
13. Kruschwitz, S., C. Prinz, and A. Zimathies, "A Study into the correlation of dominant pore throat size and SIP relaxation frequency", *Journal of Applied Geophysics (2016)*, **135**, 375-386.
14. Dubelaar, W.C., and T.G. Nijland, "The Bentheim Sandstone: geology, petrophysics, varieties and its use as dimension stone", in: Lollino, G., Giordan, D., Marunteanu, C., Christaras, B., Yoshinori, I., Margottini, C. (Eds.), *Engineering Geology for Society and Territory (2014)*, **vol. 8**, Springer International Publishing, Switzerland, 557-563.

15. Schmitt, M., M. Halisch, C. Müller, and C.P. Fernandes, "Classification and quantification of pore shapes in sandstone reservoir rocks with 3D X-ray micro-computed tomography", *Solid Earth (2016)*, **7**, 285-300.

16. Halisch, M., M. Schmitt, and C.P. Fernandes, "Pore Shapes and Pore Geometry of Reservoirs Rocks from µ-CT Imaging and Digital Image Analysis", Proceedings of the Annual Symposium of the Society of Core Analysts (2016), Snowmass, Colorado, USA, SCA2016-093.

17. Whittall, K. P., M.J. Bronskill, and R.M. Henkelman, "Investigation of analysis techniques for complicated NMR relaxation data", *Journal of Magnetic Resonance (1991)*, **95**, 221–234.

18. Brownstein, K. R., and C.E. Tarr, "Importance of classical diffusion in NMR studies of water in biological cells", *Physical Review A (1979)*, American Physical Society, **19 (6)**, 2446-2453.

19. Zimmermann, E., A. Kemna, J. Berwix, W. Glaas, H. Münch, and J. Huisman, "A high accuracy impedance spectrometer for measuring sediments with low polarizability", *Meas. Sci. Technol. (2008)*, **19 (10)**, 105603.

20. Kruschwitz, S., "Assessment of the Complex Resistivity Behavior of Salt Affected Building Materials", Dissertation. Federal Institute for Materials Research and Testing (2008), Berlin, Germany.

21. Zhang, Z., S. Kruschwitz, A. Weller, M. Halisch, and C. Prinz, "Enhanced pore space analysis by use of µ-CT, MIP, NMR, and SIP", Proceedings of the Annual Symposium of the Society of Core Analysts (2017), Vienna, Austria (SCA2017-083).

Combining porosimetry and Purcell permeability modeling to calibrate FZI and define a dynamic permeability cut off.

Philippe Rabiller (Rabiller Geo-Consulting)

ABSTRACT

An integrated algorithmic workflow is proposed for the interpretation of MICP experiments. By combining, among other features, the detection of local minima, maxima and inflexion points of the distribution of Pore Throat Size (PSD) and the permeability modeling of the latter by Purcell method, it introduces new possibilities to calibrate RCA poro-perm on MICP and thus to improve the reliability of the FZI method and the definition of a dynamic permeability cut off. Saturation/height modeling is also part of this workflow which, to date, has been used over 4000 MICP measurements in complex carbonates of varied geological settings.

Because the Purcell's method for permeability modeling quantifies the contribution of each class of pore throat size to the permeability, the set of those classes which actually controls the fluid flow can be accurately delineated, even if the PSD does not exhibit clearly individuated subsets, and characterized by its lower and upper (entry pressure) limits, its equivalent pore throat radius, the radius of the pore throat class contributing most to permeability and the fraction (PHI$_Z$) of the effective porosity involved. The entry pressure is defined according to the experimental results of Katz and Thompson (1987) and, so far, the observations support the idea that a good approximation of the lower limit of this subset is the Mean Hydraulic Radius (MHR) which roughly corresponds to the apex of the trial solutions proposed by Pittman or Walls and Amaefule. We show that, in formation exhibiting complex porous network, PHI$_Z$ should be used for the computation of "true" RQI and FZI, instead of the effective porosity which inevitably results in degrading FZI. The impact of the change of porosity values is illustrated and its relationship with the complexity of PSD curve shape is examined in terms of texture. We expose how the calibration of RCA poro-perm on SCAL porosimetry allows retrieving the true RQI from RCA poro-perm and its associated PHI$_Z$ value and how a dynamic permeability cut off can be defined.

INTRODUCTION

The FZI method, first introduced by J. Amaefule [1] is a familiar way to use RCA Poro-Perm measurements for reservoir characterization and for computing Sw. Reservoir Rock Type (RRT) can be defined on the basis of the position of their points, on X-Plots view, along the FZI function. However, the use of MICP data reveals pitfalls which can be encountered in the application of FZI method; it also explains their origin and offer the

possibility to avoid them, in which case the use of FZI method could be further extended by computing the FZI from continuous profiles of porosity and permeability.

 The permeability is driven by the subset of pore throats exhibiting the largest radiuses and Purcell permeability modeling clearly shows that this subset of largest pore throat is not necessarily giving access to the whole pore volume (PHI_T) but rather only to a variable fraction of it. Subsequently, the FZI method reliably describes the relationship between porosity and permeability only in formations where this subset of largest pore throat gives access to about the same fraction of PHI_T while it fails to do so in formations for which only a fraction, variable from sample to sample, of PHI_T contributes to the permeability. The failure is due to the fact that, in the second case, the FZI computation is performed by means of parameters which do not pertain to the same volume of the porous network of the plug. Thus, to ensure a reliable application of the FZI method, it is critical to insert a calibration step, based on reference MICP, meant at estimating the fraction of the porosity which is accessed through the subset of those pore throats contributing to the permeability. The acronym "PHI_Z" is used here to refer to this fraction of the pore volume. We describe ways to

➢ accurately computes PHI_Z, from SCAL data, by combining porosimetry and a specific implementation of the Purcell permeability model,
➢ derive PHI_Z and the true RQI and FZI from "RCA" measurements,
➢ predict the calibrated RQI and permeability in heterogeneous facies,
➢ derive a dynamic permeability cut off.

WORKFLOW AND FUNDAMENTALS OF THE METHOD.

As stated by Amaefule [1] and his co-workers, the FZI method implies that the porosity is effective in terms of permeability, i.e.: instead of PHI_T, "PHI_Z" must be used. PHI_Z is not measured in the lab, and less so by RCA, yet both the application of the Purcell model and the observations carried by several researchers [2-4], to cite only a few of those who published recently, indicate that in complex porous network, PHI_Z may significantly differ from PHI_T. It is shown here, that PHI_Z is derivable from MICP, which allows the calibration of PHI_Z from RCA porosity, and that, a good relationship is found between the "true" RQI and MHR (Mean Hydraulic Radius), as explained in the FZI theory, and the Entry Pressure. In this project, the computation of PHI_Z, is but a part of a larger workflow [5] dedicated to the MICP interpretation and the Saturation Height modeling.

In a first stage the "true" PHI_Z, RQI and FZI are computed, which imposes:
➢ the computation of the PSD (Pore Throat Size Distribution) from the Saturation and Pressure curves, the application of the necessary conformance correction and the determination of the entry pressure.
➢ The delimitation of the lower limit of the subset of those largest pore throats contributing to the permeability.
➢ The derivation of Permeability and PHI_Z by means of a specific implementation of the Purcell model, called "Purcell-PSKT" model. RQI_{true} and FZI_{true} are then computed using Permeability and PHI_Z.
In a second stage, a method is proposed to derive PHI_Z from RCA;

In a third stage a method is exposed to create a dynamic permeability cut-off by predicting MHR, derived from RQI, over un-cored intervals.

DERIVING PHIZ AND FZI FROM MICP
Picking the Minimum Pore Throat Radius of PHI$_Z$.
The minimum Pore Throat Radius of the PTR classes comprising PHI$_Z$ is algorithmically picked by means of the trial solutions, illustrated in figure 1, proposed by: Katz & Thompson [6], Pittmann [7], Walls & Amaefule [11]. It is worth noting that, the trial solution proposed by Walls & Amaefule [11], is intended for low permeability rocks.

Pittman [7] summarizes how the minimum Pore Throat Radius is defined by Swanson [8] who "*established the position on the mercury injection curve that represents a continuous, well-interconnected pore system through the rock",* noted that at this point, *"the mercury saturation expressed as percent of bulk volume is indicative of that portion of the space effectively contributing to fluid flow"* and *"determined that on a mercury injection curve, this point corresponded to the apex of the hyperbola of a log-log plot".* Acknowledging that "*for some samples, the inflection point was vague and difficult to determine*", Pittman proposed "*A plot of Hg saturation/capillary pressure versus Hg saturation, as a means of determining the apex of Thomeer's hyperbola*". All those authors have discussed the physical meaning of their methods in the light of a well-established theoretical background. Comisky & al. [9] provide with a most interesting review of those methods and expose that the Purcell model provides the best estimate of permeability. D. S. Schechter [10] proves the validity of the Walls & Amaefule method to determine the Swanson's parameter. It is striking that the picking of the Katz & Thompson trial solution for "maximal electrical conductance" provides exactly the same results than the picking of the Pittman or Walls & Amaefule trial solutions, these are illustrated by figures 2a & 2b. Thus, because of the convergence of the results and because it shares the same scale than the PSD, the Katz & Thompson trial solution can be used to confidently pick the PSD curves, particularly after their upscaling.

The Purcell-PSKT Model.
The computation of PHI$_Z$, "*the fractional pore volume connected to the largest pore throat system which actually controls the fluid transport*", relies on a new implementation of the Purcell model: the Purcell-PSKT model, specifically designed to integrate the findings of Pittmann, Swanson, Katz & Thompson, Walls & Amaefule. In this implementation, the Purcell equation is applied to each term of the suite of the PTR subsets formed by incrementing the first subset of this suite by 1 element of the PSD array log: PTR$_{[a]}$, PTR $_{[a \to (a+1)]}$, PTR $_{[a \to (a+2)]}$, PTR $_{[a \to (a+3)]}$, …, PTR $_{[a \to (n)]}$, where
➢ "n" is the element of the PSD array log which corresponds to "entry pressure"
➢ "a", which is defined in the previous step, is the PSD element corresponding to the point at which *"the mercury saturation expressed as percent of bulk volume is indicative of that portion of the space effectively contributing to fluid flow".*

The permeability at each increment is computed using the porosity of the specific subset of pore throat of this increment without any adjustment of the lithological factor. Thus, only the PTR subset actually contributing to the permeability is characterized both in terms of Permeability and in terms of porosity (PHI$_Z$), by the Purcell-PSKT model. RQI$_{true}$ and FZI$_{true}$ are then derived. The figures 3 exemplify that the Purcell PSKT model achieves a better prediction of the permeability than does the classic Purcell model.

Validation of the "True" FZI, RQI and PHI$_Z$.
Amaefule & al. [1] propose a graphic method to test the FZI method: they show that, on the plot of the ratio (MHR/PHI) versus FZI, a straight line whose slope is the Kozeny constant (Kc) is formed by the data points and "*provides corroborative evidence of the soundness of the theory*", because such result complies with Poiseuille and Darcy laws. In this project, the same test is proposed to check the validity and the accuracy of RQI$_{true}$ and FZI$_{true}$ provided by the Purcell-PSKT model: on Figure 4a, the ratio (MHR$_{true}$/PHI$_Z$) is plotted versus FZI$_{true}$ and for ease of comparison, it is divided by the value proposed by Amaefule & al. for Kc; because all the data points are aligned along the first diagonal, it can be concluded that PHI$_Z$, as derived by the Purcell-PSKT model, honors the fundamentals of the FZI theory. This is not the case in Figure 4b, where PHI$_T$ is used instead of PHI$_Z$ and FZI$_{RCA}$ instead of FZI$_{true}$: a "cloud" appears instead of a straight line.

The X-plot proposed by Amaefule & al. can be rearranged so that PHI$_Z$ is on the Y axis and the product (FZI$_{PHI\_Z}$ * Kc) is plotted on the X axis (Figure 4c). Because a good relationship between MHR and RQI is postulated by the FZI theory and is revealed by the SCAL measurements, then this plot provides a simple means to visualize if a set of RCA measurements honors the FZI theory, in which case, the data points fall on a line. Should a cloud be observed, then the RCA samples do not honor the FZI theory and the scatter of the cloud visualizes (and ranks) the variability of the ratio PHI$_Z$/PHI$_T$. An additional benefit of the derivation of RQI$_{true-RCA}$ and FZI$_{true-RCA}$ is that the Entry Radius can be estimated from the RCA by means of the good relationship observed between RQI$_{true}$ and Entry Radius measured on SCAL data.

ESTIMATION OF PHI$_Z$, RQI$_{TRUE}$ AND FZI$_{TRUE}$ FROM "RCA".
The principle of an algorithmic procedure used for estimating PHI$_Z$ from RCA measurements is illustrated Figures 5a & 5b, using 7 wells and 481 points. It relies on the calibration of the RQI$_{RCA}$ computed from RCA porosity and permeability against the RQI$_{PHI\_Z}$ computed from PHI$_Z$ and permeability obtained by means of the Purcell-PSKT.

➢ In a first step the trend RQI$_{PHI\_Z}$ vs. permeability (ordinate) is manually picked; it is desirable to pick an upper and a lower trend so as to account for the natural variability of the samples.

➢ In a second step the trend is "transferred" on a X-plot displaying the RQI$_{rca}$ vs. permeability (ordinate). For a given permeability, the calibrated RQI is the ordinate of the corresponding point of the trend RQI$_{PHI\_Z}$ vs. permeability. If a lower and a upper trends are defined then the lower and upper boundaries of RQI$_{RCA}$ are defined.

Once the calibrated RQI is obtained the PHI$_Z$ is defined. Further, as it was shown previously, the correlation between RQI$_{PHI-Z}$, MHR and Entry radius can be used to estimate those parameters from RCA. The capability of this algorithmic procedure to retain the natural variability observed in samples is somehow hampered by the very process of defining a trend on which it is based. For a greater accuracy and efficiency, the author prefers to apply k-NN data prediction techniques to PHI$_Z$ and the other parameters describing the set of pore throat truly contributing to permeability.

DERIVING A DYNAMIC PERMEABILITY CUT-OFF

MHR is the Pore Throat Radius below which the contribution to permeability of any PTR subset is negligible. MHR can be retrieved from RQI$_{RCA}$, or predicted directly from RQI$_{true}$ by means of k-NN modeling (in very much the same way as porosity and permeability are predicted) and used to define a dynamic cut-off of the permeability in field conditions. To that purpose, MHR is displayed on a track honoring the convention used for PSD, (i.e.: log$_{10}$ scale of radius (µm)) and by superimposing, with a scale compatible for the radius (using the field/lab conversion) the value of P$_c$ field conditions, computed for the any given HAFWL, the facies which may contribute to production by permeability mechanism, and those which may not, are identified. The principle of the algorithmic procedure, which consists in converting Pc into PTR radius, is illustrated by Figure 6. If the multiple k-NN predictions method is used to predict MHR, then those multiple predictions can be displayed as an array binned with the conventions defined above for PSD; thus the range of variation of MHR at each depth increment is visualized, and the most probable value together with the extrema and percentiles of interest are easily picked algorithmically, in very much the same way as it was shown for PSD.

CONCLUSIONS.

The Purcell-PSKT model, developed in this project, integrates the results of Katz & Thompson[6], Pittman [7], Walls & Amaefule [11] within the Purcell model [12]. It provides a better prediction of permeability than the Purcell model.

By providing a measure of PHI$_Z$, "*the fraction of porosity that effectively contributes to the permeability*", the Purcell-PSKT model allows generalizing to any complex porous network, the use of the FZI method, which in turn is used to prove the validity of the derivation of PHI$_Z$ by the Purcell-PSKT model.

An algorithmic method, graphically illustrated, is proposed to

➢ derive RQI and FZI from RCA data. Based on the FZI theory, this method relies on the calibration on the RQI$_{true}$ and FZI$_{true}$ computed from SCAL data.
➢ Derive MHR and Entry pressure from RCA data
➢ Create a dynamic permeability cut-off allowing, for any HAFWL, to flag only those facies which may contribute to production by permeability mechanism.

By deriving PHIZ from RCA it is anticipated that the applicability of the FZI and the Leverett methods to compute S$_w$ will be not restricted to the sole facies sampled for SCAL and their application will provide more accurate and reliable results.

REFERENCES

1. Amaefule J. O.; M. Altunbay M., D. Tiab; D. G. Kersey; D. K. Keelan, "Enhanced Reservoir Description: Using Core and Log Data to Identify Hydraulic (Flow) Units and Predict Permeability in Uncored Intervals/Wells"; 1993; paper SPE 26436.
2. Buiting, J.J.M., Clerke, E.A.; "Permeability from porosimetry measurements : Derivation for a tortuous and fractal tubular bundle"; 2013; Journal of Petroleum Science and Engineering, Volume 108, Pages 267–278
3. Journal of Sedimentary Research, 2015, v. 85, 1197–1212 Kaczmarek, S. E.; S. M. Fullmer; F. J. Hasiuk; "A universal classification scheme for the microcrystals that host limestone microporosity"; 2015; Journal of Sedimentary Research; v. 85, 1197–1212.
4. Stanley, R.; Guidry, S.; Al-Ansi, H.; "Microporosity spatial modeling in a giant carbonate reservoir"; 2015; IPTC-18327-MS
5. Rabiller, Ph.; "An integrated workflow for MICP integration, pore typing and saturation height modeling – Poster # 37"; 2017; International Symposium of the Society of Core Analysts.
6. Katz, A.J., A.H., Thompson : "Prediction of Rock Electrical Conductivity from Mercury Injection Measurements"; Journal of Geophysical Research, Jan. 1987, Vol. 92, No.B1, 599-607.
7. Pittman, E.D. ; "Relationship of Porosity and Permeability to Various Parameters Derived from Mercury Injection Capillary Pressure Curves for Sandstone," AAPG Bull., 1992, vol. 76, No. 2; 191-198.
8. Swanson, B. F.; "A simple correlation between permeabilities and mercury capillary pressures"; 1981; Journal of Petroleum Technology, Dec., p. 2488-2504.
9. Comisky, J.T.; K.E. Newsham; J.A. Rushing; T.A. Blasingame, :" A Comparative Study of Capillary-Pressure-Based Empirical Models for Estimating Absolute Permeability in Tight Gas Sands"; 2006; SPE paper 110050; 1-18.
10. Schechter, D. S.; "Advanced Reservoir Characterization and Evaluation of C02 Gravity Drainage in the Naturally Fractured Sprayberry Trend Area"; Quarterly Report, January 1 - March 31, 1998; Contract No.: DE-FC22-95BC14942.
11. Walls, J.D. & J.O., Amaefule : "Capillary Pressure and Permeability Relationships in Tight Gas Sands," ; 1985; paper SPE 13879.
12. Purcell, W.R.: "Capillary Pressures-Their Measurement Using Mercury and the Calculation of Permeability"; 1949; Trans. AIME, 186, 39-48.
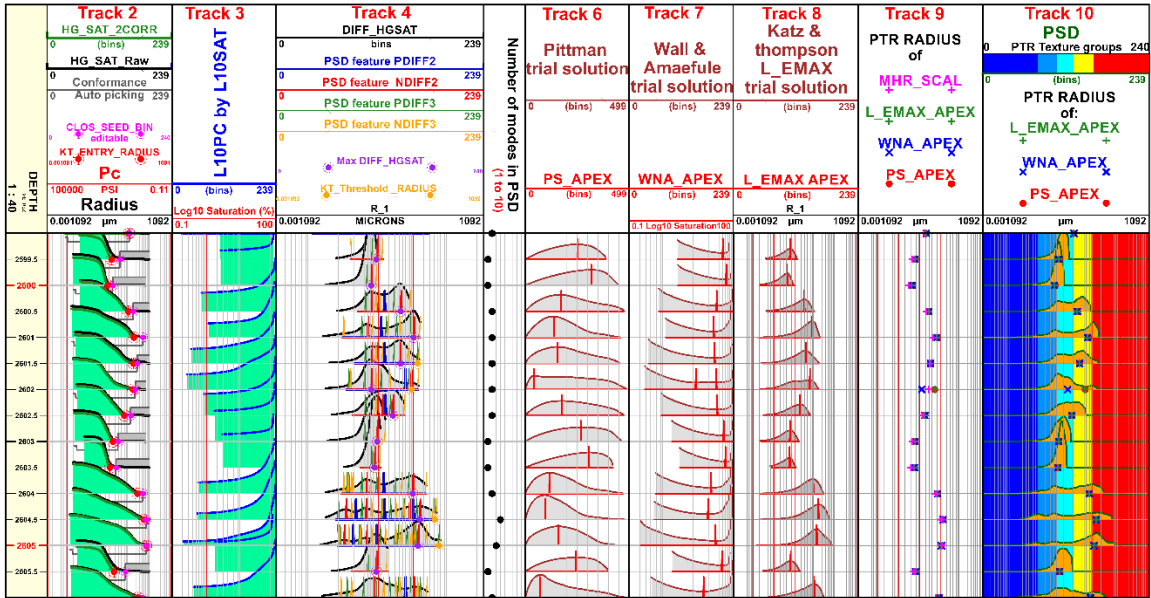
Figure1: The minimum Pore Throat radius of the PTR classes forming PHI$_Z$ is algorithmically picked by means of the trial solutions proposed by: Katz & Thompson [1987], Pittmann [1992], Walls & Amaefule [1985]. The fourth track illustrates the picking of the varied "features" of the PSD curves. Note, on track 9, the strong correlation between MHR and the apex of the varied trial solutions.
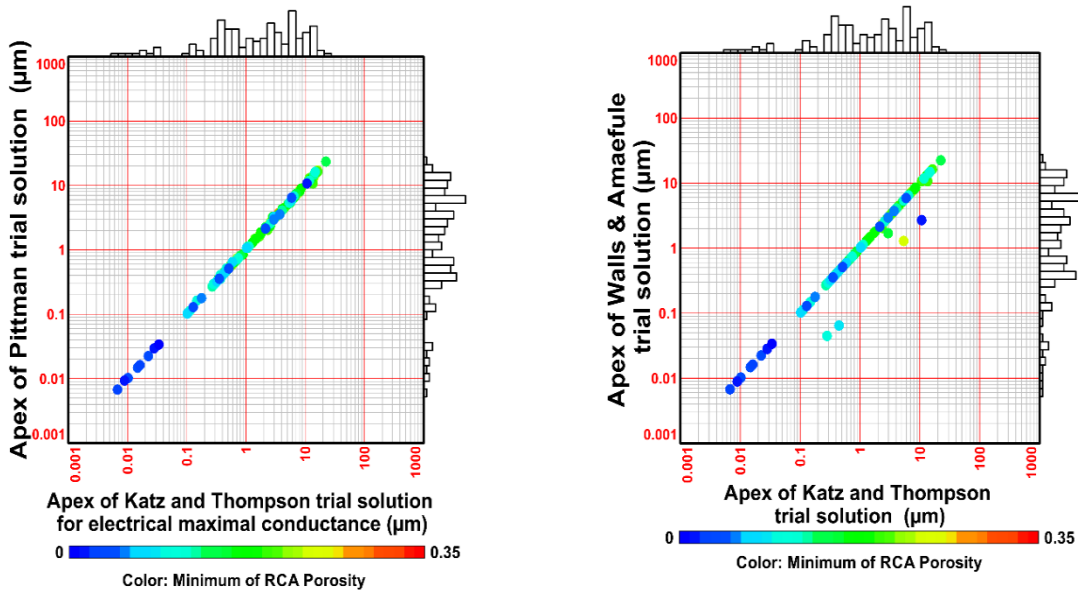
Figures 2a & 2b: The trial solutions proposed by Pittman [1992], Walls & Amaefule [1985], and Katz & Thompson [1987] ("maximal electrical conductance") provides exactly the same results and thus the latter simplifies the picking of the hyperbola apex on the upscaled PSD curves, as it eliminates the need to generate a trial solution.
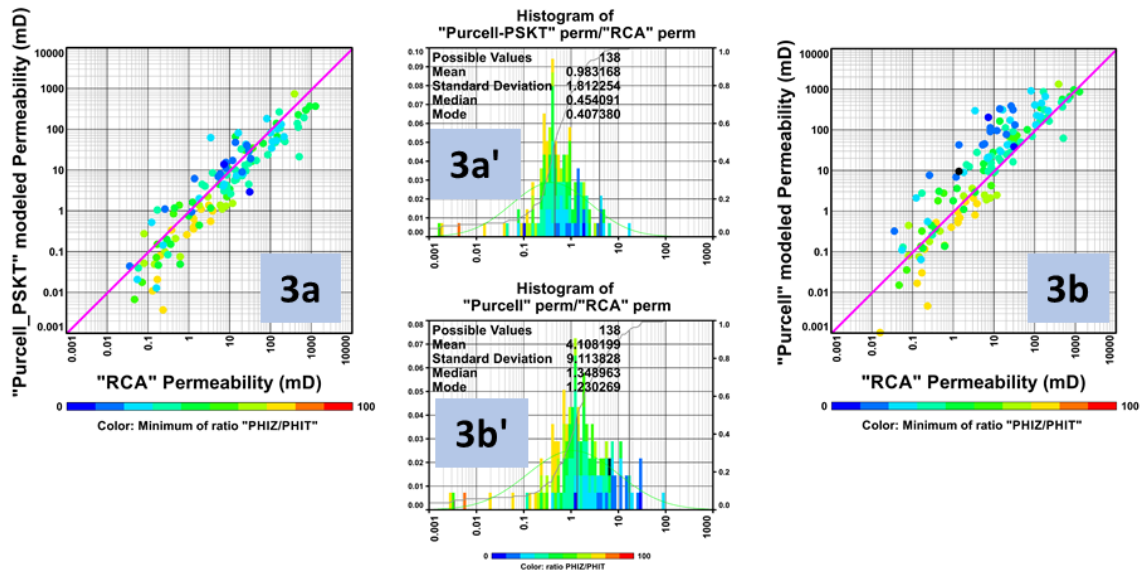
Figures 3a to 3b': To avoid any bias, the conformance and the Entry pressure were left un-edited. The Purcell-PSKT model provides a better prediction of the permeability than the Purcell model proper. It is naturally less sensitive to the complexity of the porous network shown by the color code controlled by the ratio PHI_Z/PH_T.
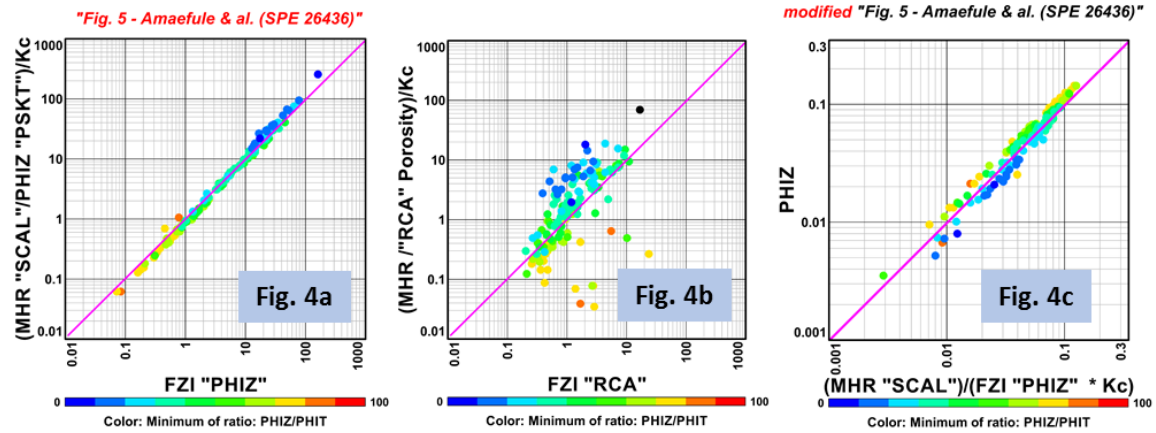
Figure 4a: The ratio (MHR_{true}/PHI_Z) divided by the Kozeny constant, is plotted versus FZI_{true} (i.e.: FZI for "PHI_Z"). The straight line in the center of the plot (4a) validates the derivation of PHI_Z by the Purcell-PSKT model. Figure 4b: If a "cloud" appears instead of a line, when PHI_T is used instead of PHI_Z and FZI_{RCA} instead of FZI_{true}, then it must be concluded that the RCA data does not honor the foundations of the FZI theory and thus they need to be calibrated. Figure 4c: The plot proposed by Amaefule & al. is rearranged so that PHI_Z is on the Y axis and the product ($FZI_{PHI\_Z} * Kc$) is plotted on the X axis. As in the original X-plot, a straight line is observed if FZI theory is honored.
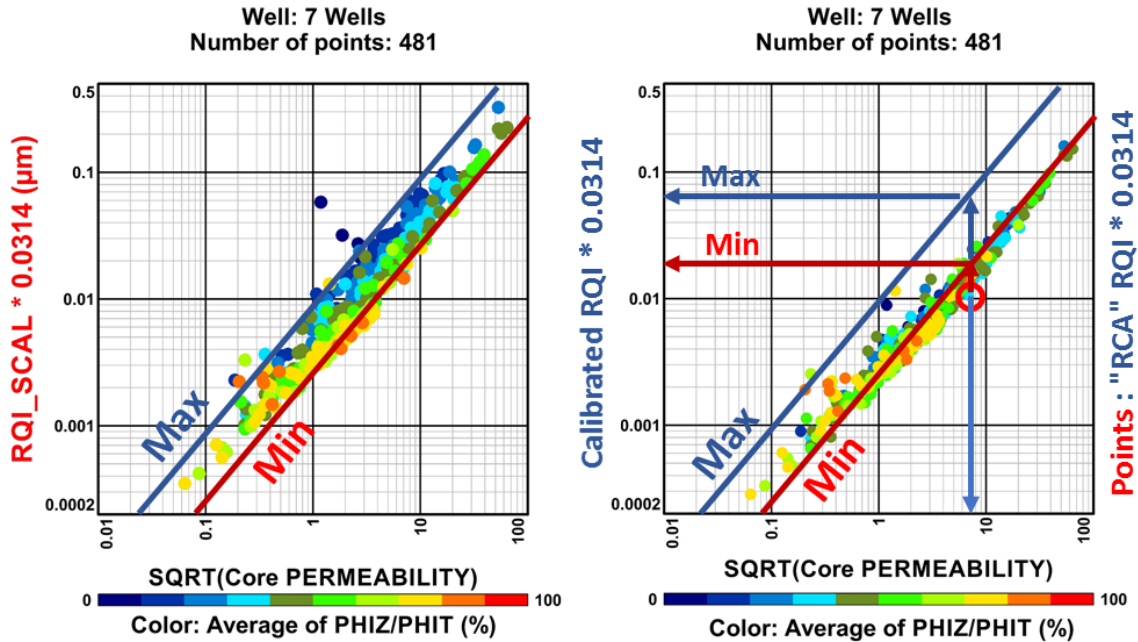
Figures 5a & 5b schematize the principle of an algorithmic procedure used for estimating PHI$_Z$ from RCA measurements. The calibration trends are picked on SCAL data.
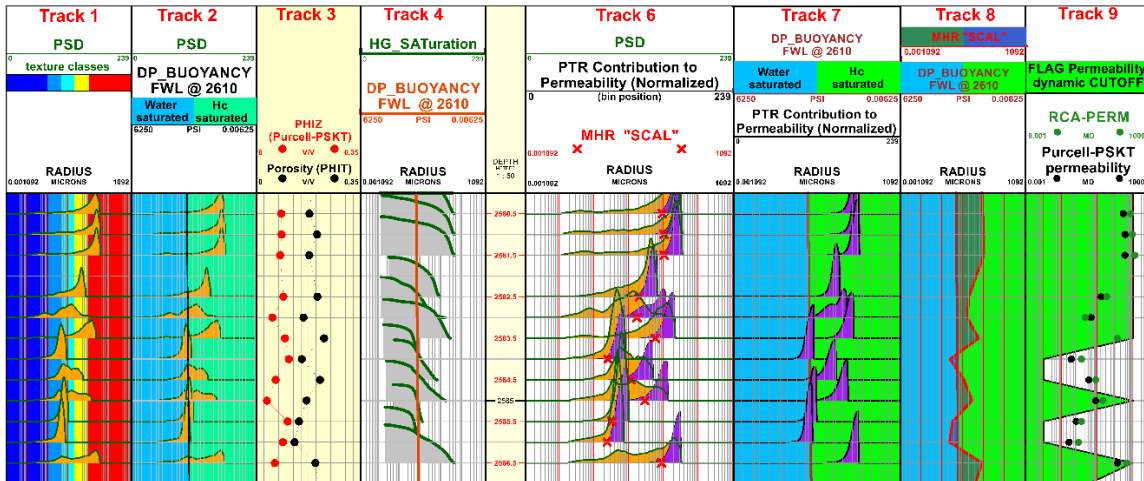
Figure 6: Track 6 shows PSD (orange) and the contribution (purple) of each PTR class to permeability superimposed together with MHR; it clearly illustrates that only the largest PTR contribute to permeability. The track 7 displays the Pc "Field" superimposed to the contribution of each PTR class to permeability and thus allows to determine the fluids moved by the permeability mechanisms in this Pc conditions. The principle of the algorithmic procedure, to determine a dynamic cut off for permeability is illustrated by tracks 8 and 9. The MHR Radius is converted into Pc Field conditions and compared to Pc defined from Hc Buoyancy to create the cut off.

ANALYSING FLOW IN ROCKS BY COMBINED POSITRON EMISSION TOMOGRAPHY AND COMPUTED TOMOGRAPHY IMAGING

Yibing Hu[1], Ryan. T. Armstrong[1], Tzong-tyng Hung[2], Brendan Lee[2], Igor Shikhov[1], and Peyman Mostaghimi[1]

[1]School of Petroleum Engineering, The University of New South Wales, NSW 2052, Australia

[2]Biological Resources Imaging Laboratory, Mark Wainwright Analytical Centre, The University of New South Wales, NSW 2052, Australia

ABSTRACT
Combined Positron Emission Tomography (PET) and micro-Computed Tomography (micro-CT) provides an unprecedented imaging method to visualise and study fluid flow in porous media by continuous monitoring of tracer labelled fluid distribution in the pore space. We employ this method for understanding complex displacement processes in core samples to evaluate and visualise fluid flow. A flow cell to hold core samples and distribute the fluid has been designed and mounted within the PET-CT scanner. Each sample is imaged with micro-CT scanner and then moved into the PET chamber. Reservoir fluid labelled by radioisotope, [^{18}F]-FluoroDeoxyGlucose (18F-FDG) is injected by a syringe pump with pre-set rate and then continuous imaging is conducted by PET. The ^{18}F-FDG decays and emits positrons whose annihilation produces gamma rays. Image reconstruction and segmentation is applied for visualisation and simulation. The spatial fluid saturation is displayed by processing normalized radiation intensity values and the detection of the labelled flow phase. The tracer distribution illustrates the fluid pathways. The 3D flow displacement procedure is displayed, and the flow mechanisms are studied by analysing flow and core structure data acquired from the PET and CT scanners. The developed imaging method provides a unique opportunity to determine the pathway of fluid flow in porous media and offers detailed information on the fluid transport processes.

INTRODUCTION
This work reports a qualitative study on a fluid displacement experiment using combined PET and micro-CT imaging techniques. Micro-CT is a powerful tool for studying reservoir rock properties in 3D [1] and is recently used for visualising dynamic flow in rocks [2]. Schembre and Kovscek [3] measured dynamic relative permeability from CT monitored spontaneous imbibition experiments on Berea sandstone and diatomite cores. They used CT imaging to collect the saturation profile for their calculation and the method showed good reliability in measurement of relative permeability curve. Berg et al. [2] studied multiphase flow drainage and imbibition in sandstones and limestones using fast dynamic micro-CT. They imaged real-time pore-scale fluid displacement, and observed drainage Haines jump events and imbibition snap-off events. However, micro-CT dynamic imaging has the drawback of limited temporal resolution and sample size.

An alternative method to visualise dynamic flow processes in porous media is using PET. High-resolution PET combined with micro-CT can be applied for the qualitative and quantitative

study of flow and to image the fluid distribution and front progress in 4D. Ferno et al. [4] applied the combined PET and CT imaging of the saturation processes in sandstones and chalks for visualisation of fluid displacement and gas injection within the core sample. They used ^{22}Na ($t_{1/2} \approx 2.6$ years) and calculated the spatial fluid saturation based on the CT number and time-averaged radiation intensity ratio from PET. The activity profile and fluid front were acquired and plotted against imaging time and core length, thus comparing the signal-to-noise ratio of PET and CT. Pini et al. [5] investigated the small-scale heterogeneity of Berea sandstones by implementing micro-CT and PET scanning. They described spatial and temporal progression of NaHCO$_3$ solution labelled with ^{11}C. They studied the radioactivity advection-dispersion transport by analysing tracer activity and decay by measuring residence-time and tracer mass balance. The comparative study of concentration profiles as a function of time or distance from the tracer transport imaging and 1D "streamtube" model for tracer spread showed similarity in the tracer plume movement and. Zahasky and Benson [6] used micro-CT and PET to verify the fluid saturation in a Berea core. They calculated the flow saturation, estimated the average capillary pressure, and derived voxel permeability equation.

This work reports results from a qualitative study on fluid displacement experiments using combined PET and micro-CT imaging techniques. It investigates combined PET and micro-CT imaging of fluid movement labelled by the radioactive tracer ^{18}F-FDG. The results of PET imaging are compared with micro-scale numerical simulation for flow distribution and permeability estimation.

METHODOLOGY

PET Imaging

The Inveon MicroPET-CT scanner (Siemens) used in this work is capable of providing three dimensional micro-CT and micro-PET images of samples. The system has a variable focus X-ray source and a detector of 2048×3096 pixels. The Inveon micro-PET is equipped with an LSO detector for fast scintillation decay time, highlight output and effective atomic number. The micro-CT imaging resolution is 0.425 mm and the PET camera resolution is 0.776 mm. The PET camera captures positron-emitting radioisotope radiation and generates the dataset of the distribution of radioactivity. ^{18}F –FDG is used in this work as it has proved to be effective for the imaging of fractured reservoir rocks [7,8].

The radioisotope is diluted by the injection fluid, and injected into the matrix by an NE-1050 syringe pump. The decaying isotope will emit low energy positrons (in MeV range) which can travel in surrounding media a distance in the order of millimetres. The positive charge of the positron can attract an electron and lead to annihilation, generating two photons with 511 keV of energy. The photons are emitted in the form of gamma rays in opposite directions (180^0 to each other) and detected in coincidence. The detectors are made of lutetium oxyorthosilicate crystals and arranged in a circle. The detector can define their line of response (LOR), thereby reconstructing the tomographic image of isotope distribution from a dataset of LORs. The reconstructed 2D images can be stacked to make 3D images and coupled with temporal information to generate 4D dataset.

Experiment Design

As Figure 1 shows, sample A is made of Sigma-Aldrich borosilicate glass beads of 6 mm diameter packed in a polycarbonate tube of 25 mm in diameter. Sample B is an artificially fractured Bentheimer sandstone core of 25 mm in diameter and 50 mm in length. Sample C is a Bentheimer sandstone core of 25 mm in diameter and 55 mm in length. Porosity of each sample is calculated on segmented micro-CT images using software Mango and the images are

pre-processed by Unsharp Mask, Neighbourhood Filter and Converging Active Contours Segmentation [9]. The samples are dried in the vacuum drying oven and sealed in the flow cells. The flow cell is made of polycarbonate tubes and sealed with araldite plug. It is designed and duplicated to contain the samples, distribute fluid from the syringe pump through the core into the collection vessel and test the flowing characteristics. The connection PEEK (polyether ether ketone) tubing is fitted with soft silicon tubing and the fitting points are sealed with thermoplastic to prevent leakage. The flow cell connected to the collection vessel with outlet tubing is placed in the scanner for the initial micro-CT scan. While the micro-CT scan is being performed, we prepare the radioactive substance behind the L-Block (Lead shields). 30-60 MBq of ^{18}F-FDG was diluted in 50 ml water and drawn into a syringe. At the rear of the instrument where the micro-PET imaging component resides, the syringe is loaded on the pre-programmed pump and attached to the inlet tubing. The PET image is acquired for 30-70 minutes.

Figure 1. (left) sample A: glass beads pack (37 % in porosity); (middle) sample B: fractured sandstone (18.44 % in porosity); (right) sample C: sandstone (16.28 % in porosity).

Permeability Calculation

The permeability of the three samples is estimated using two methods. For sample A, the permeability is related to packing mechanism, particle size and compactness of packing. For granular packing, the permeability can be estimated by the Kozeny-Carman Equation [10,11]:

$$k = \frac{d^2\varepsilon^3}{36K_0\tau^2(1-\varepsilon)^2} \qquad (1)$$

where d is the average diameter of the glass spheres, ε is the total porosity, $K_0\tau^2$ is the Kozeny's coefficient and can be assumed as 4.2-5.0 for granular packs with porosity range from 0.36 to 0.4 (this sample is 0.37) [11].

For sample B and C, Finite Element Method (FEM) was employed for flow simulation and rock permeability calculation via the GeoDict package [12]. To calculate absolute permeability of the rock samples, we use the Left Identity Right (LIR) solver for the Navier-Stokes equations with periodic boundary condition [13]. To calculate permeability of the entire core samples, we take subsections with a range of porosity values from the micro-CT images and fit the porosity and simulated permeability value to a linear relationship [14]. The absolute permeability from the simulation is used to plot a 3D map of voxel permeability to demonstrate the heterogeneity of the core. The permeability is influenced by the image resolution and number of voxels capturing flow pathways [15]. The samples considered in this paper have high permeability and large pore sizes that are well captured by the micro-CT image. For low-permeability samples, in range of mD and below, image registration and calibration can be employed to improve the quality of images and resolve small pore sizes [15].

Voxel Permeability 3D map

Using the PET imaging results, we are able to visualise flow distribution and migration in the cores and combine them with micro-CT images to demonstrate the heterogeneity of the sample. Voxel permeability map is created by averaging the properties from high resolution CT images to make PET voxel sized subsection and coupling it with PET imaging results. In each voxel of the PET image, the permeability can be calculated on the micro-CT images as [6]:

$$k_i = \phi_i \frac{1}{\overline{P_c}^2} \left[\sigma_{w/nw} \cos\theta_{w/nw} J(\mathrm{S}_{w,i}) \right]^2 \qquad (2)$$

where k_i is the voxel permeability, ϕ_i is the voxel porosity (from CT images), $\overline{P_c}$ is the average capillary pressure of the slice, $\sigma_{w/nw}$ is the surface tension, $\cos\theta_{w/nw}$ is the contact angle and $J(\mathrm{S}_{w,i})$ is the J-Leverett function. The J - Leverett function can be derived as [6]:

$$J(\mathrm{S}_{w,i}) = \frac{P_c(\mathrm{S}_{w,i})}{\sigma_{w/nw} \cos\theta_{w/nw}} \sqrt{\frac{k_c}{\phi_c}} \qquad (3)$$

where $P_c(\mathrm{S}_{w,i})$ is the voxel capillary pressure, k_c is the sample permeability and ϕ_c is the sample porosity.

We can derive, from the above equations, the voxel permeability for the PET and micro-CT images:

$$k_i = \phi_i \frac{1}{\overline{P_c}^2} \left[P_c(\mathrm{S}_{w,i}) \sqrt{\frac{k_c}{\phi_c}} \right]^2 \qquad (4)$$

The capillary pressure curve is simulated on the micro-CT images using the Pore Morphology Method [16]. The distribution of the fluid is determined by estimating the pore space accessible to the non-wetting phase (NWP) using Young- Laplace equation for a spherical interface. Each sphere works as a probe to make new pore space accessible and the probe locations are included in the NWP portion of the total space. Voxel saturation is obtained by normalizing the intensity value of the PET images. For each voxel of the PET, we calculate voxel porosity based on the micro-CT images and by combining it with the capillary pressure value, we obtain the permeability using Equation 4.

RESULTS
Fluid Saturation Process
The experiment parameters are included in the table below:

Table 1. PET experiment parameters

Sample	Flow Rate (ml/min)	Injected Volume (ml)	Pore Volume (ml)	Dose (Mbq)
Glass beads (A)	0.5	15	11.4	33.7
Fractured sandstone (B)	0.1	7	6.2	40.2
Sandstone (C)	0.1	6	5.6	60.0

Glass Beads Pack
Figure 2 is the CT image from PET-CT scan and it shows the packing of the glass beads. The saturation process (Figure 3) of the sample shows gravity dominated flow in large pores as the fluid fills the sample from bottom to top with a relatively even surface. Another phenomenon from the comparison between PET and CT images is that the radioactivity may exaggerate the saturation of fluid, as one can observe from the PET images that the concave areas are larger than the individual beads.
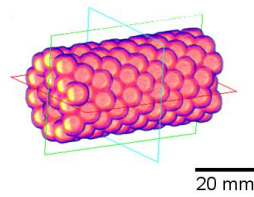
Figure 2. PET-CT image of the sample A.
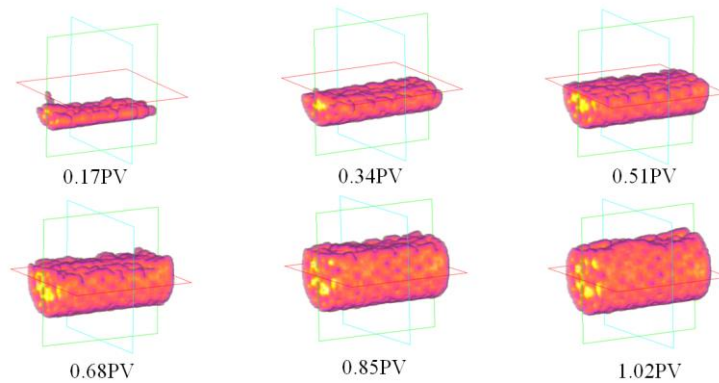
Figure 3. PET images of fluid saturation in sample A.

Fractured Sandstone

Figure 4 shows the PET-CT image of the sample. A low porosity region can be observed in the middle of PET-CT image, which could be the micro-pore region below the resolution.
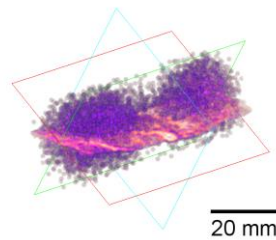
Figure 4. PET-CT image of fractured sample B.

Figure 5 shows the saturation process with PET imaging. Gravity affected flow can be observed before 0.6 PV as the activity propagates below the fracture. The fluid fills the bottom half of the sample in a capillary dominated flow pattern. At 0.6 PV, the fluid saturated zone starts to grow from both ends to meet in the middle where the low porosity zone.
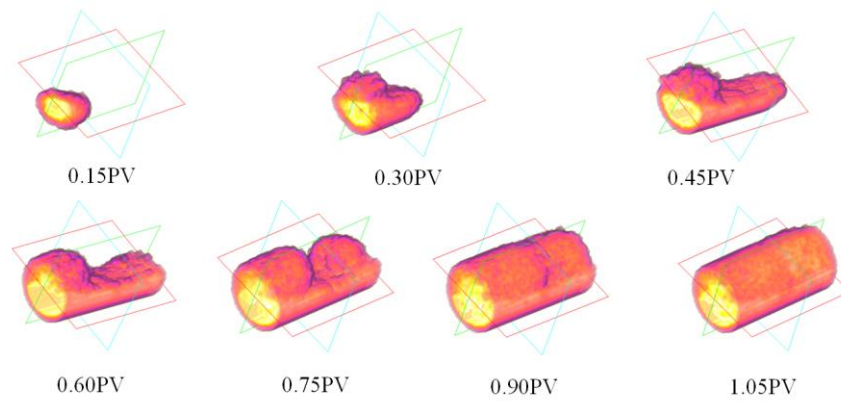
Figure 5. PET images of fluid saturation in sample B.

Sandstone

Figure 6 is the PET-CT of sample C. Figure 7 shows a diffusion flow phenomenon at the front as the flow is dominated by capillary force. The flow at 0.17 PV forms a smaller cylindrical fluid distribution and then diffuses to fill the entire section. After 0.51 PV, individual boluses can be detected at the rear of the saturated zone, which shows a higher flow rate than the uniform front.
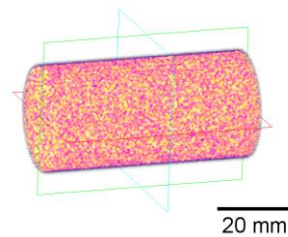
Figure 6. PET-CT image of sample C.
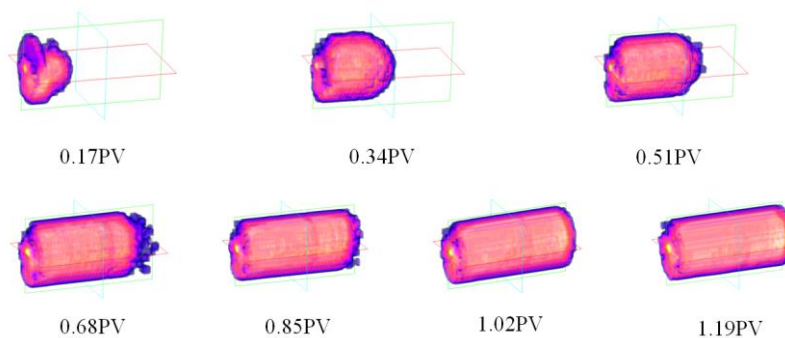
Figure 7. PET images of fluid saturation in sample C.

Permeability

Absolute permeability in the injection direction of the three samples measured with the methods described above is listed in the table below:

Table 2. Absolute permeability measurements

Sample	Permeability (mD)	Method	Porosity
Glass beads (A)	2.58×10^5	Kozeny-Carman	37%
Fractured sandstone (B)	4565	FEM simulation	18.44%
Sandstone (C)	1236	FEM simulation	16.28%

Figure 8 presents the FEM simulation results of the fractured sandstone. The velocity field of the artificial fracture shows similarity with the PET flow imaging with regard to the low flow rate (porosity) zone. The pressure field shows the pressure drop from injection end to the collection end. Contrary to the simulation results, the PET flow image shows that the fluid accumulates at the rear of the sample and builds pressure before entering the collection tube.
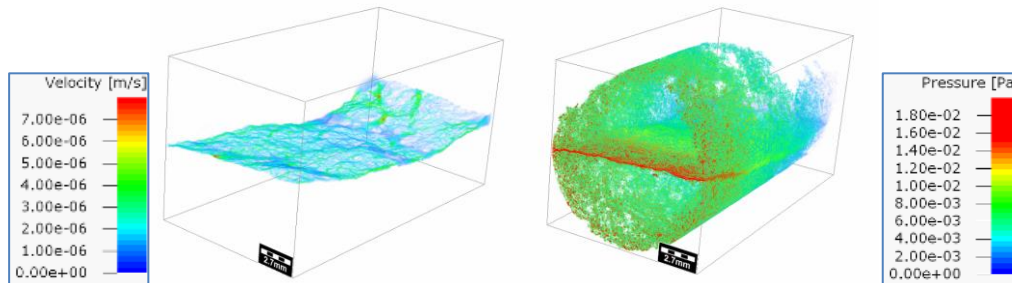
Figure 8. (left) velocity field of artificial fracture; (right) pressure field of fractured sandstone.

Voxel 3D map

Figure 9 is the slice averaged voxel porosity and saturation map of sample C. The voxel porosity map is created by resampling the micro-CT image to the resolution of the PET image. The voxel saturation map is generated by using the method explained for voxel saturation in Equation 4. Low values are on the edge and it can be the result of limited time for diffusion.
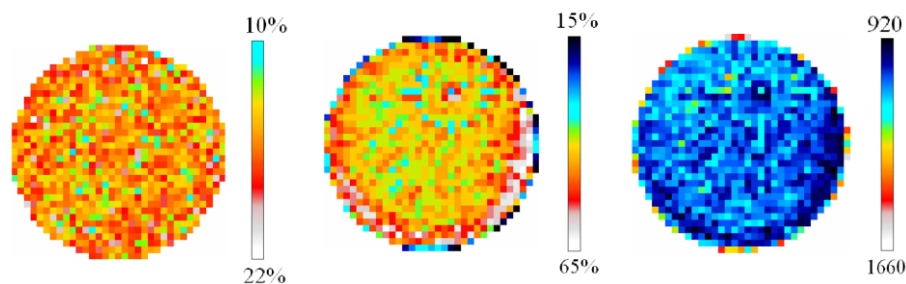
Figure 9. (left) voxel porosity map, highlighting the pore space heterogeneity in the direction parallel to the axis; (middle) voxel saturation map, lowest values on the boundary (possibly caused by short diffusion time); (right) voxel permeability map (mD).

The voxel permeability map (Figure 9) is the result of applying Equation 4 on the porosity and saturation maps and averaging. The voxel permeability ranges from 920 mD to 1660 mD and Figure 9 shows a relatively low permeability region on the bottom half of the sample.

CONCLUSION AND FUTURE WORKS

This work combines PET imaging and micro-CT imaging to describe flow in porous media. The qualitative study by high resolution PET imaging visualises the fluid distribution and propagation through different cores. Numerical simulations were performed to obtain permeability maps. Below conclusions can be drawn from this study:

1. The combination of high resolution PET imaging and micro-CT imaging shows great potential in study of flow in porous media.

2. PET imaging is capable of capturing the saturation process and 3D spatial fluid distribution in cores. The dominating flow displacement pattern can be observed from the dynamic PET images.

3. Voxel-averaged maps based on high resolution micro-CT and PET dynamic imaging exhibit the structural heterogeneity of the samples.

In the future studies, the voxel-averaged map can be involved in the larger scale simulators to simulate the front progression of the injection phase. Vertical set up can help to eliminate the gravity affection and this needs further design of the apparatus.

Reference

1. Mostaghimi, P., Armstrong, R.T., Gerami, A., Warkaini, M.E., Ramandi, H.L. and Pinczewski, V., "Micro-CT imaging and microfluidics for understanding flow in coal seam reservoirs," In *International Symposium of the Society of Core Analysts, Newfoundland, Canada.* (2015). SCA2015-051.
2. Berg, S., Armstrong, R., Ott, H., Georgiadis, A., Klapp, S. A., Schwing, A., Neiteler, R., Brussee, N., Makurat, A., Leu, L. and Enzmann, F., "Multiphase flow in porous rock imaged under dynamic flow conditions with fast X-ray computed microtomography," *Petrophysics*, (2014)**55,** 4, 304–312.
3. Schembre, J. M., & Kovscek, a. R., "Direct Measurement of Dynamic Relative Permeability from CT Monitored Spontaneous Imbibition Experiments," *Proceedings of SPE Annual Technical Conference and Exhibition.* (2001). SPE-71484
4. Ferno, M., Gauteplass, J., Hauge, L. P., Abell, G. E., Adamsen, T. C. H., & Graue, A., "Combined positron emission tomography and computed tomography to visualise and quantify fluid flow in sedimentary rocks," *Water Resources Research*, (2015) **51,** 9, 7811–7819.
5. Pini, R., Vandehey, N. T., Druhan, J., & Neil, J. P. O., "Quantifying solute spreading and mixing in reservoir rocks using 3D PET imaging," *Journal of Fluid Mechanics*, (2016) **796,** 558–587.
6. Zahasky, C., & Benson, S. M., "Phase Saturation Validation and Tracer Transport Quantification Using Micropet in a Heterogeneous Sandstone Core," *the International Symposium of the Society of Core Analysts, Snowmass, Colorado, USA.* (2016), SCA2016-028.
7. Mau, M., Dusterhoft, R., Rickman, R., Gibson, R., Energy, H., Buffler, A., Heerden, M. Van., "Dynamic Imaging of Fluid Mobility in Low-Permeability Matrices Using Positron Emission Tomography," *Unconventional Resources Technology Conference, Denver, Colorado, USA.* (2013), 1–10.
8. Mau, M., Dusterhoft, R., Rickman, R., Gibson, R., Buffler, A., Heerden, M. Van, & Town, C., "Dynamic 3D Imaging of Fluid Mobility in Natural Fractures Using High-resolution Positron Emission Tomography," *International Petroleum Technology Conference, Doha, Qatar.* (2014), IPTC 17478.
9. Averdunk, H., "Mango User Guide," (2004,2005), Applied Mathematics, ANU.
10. Bear, J., *Dynamics of Fluids in Porous Media*, Dover Publications, Inc., New York, (1972), 112–167.
11. Dias, R. P., "Permeability analysis in bisized porous media : Wall effect between particles of different size," *Journal of Hydrology*, (2008) **349,** 470–474.
12. Jaganathan, S., Tafreshi, H. V., & Pourdeyhimi, B., "A Case Study of Realistic Two-Scale Modeling of Water Permeability in Fibrous Media," *Separation Science and Technology*, (2008) **43,** 8, 1901–1916.

13. Cheng, L., Wiegmann, A., Planas, B., "FlowDict2015 Reference," (2016).
14. Nelson, P.H., "Permeability-Porosity Relationships in Sedimentary Rocks," *The Log Analyst*. (1994), 38-62.
15. Mostaghimi, P., Armstrong, R.T., Gerami, A., Hu, Y., Jing, Y., Kamali, F., Liu, M., Liu, Z., Lu, X., Ramandi, H.L., Zamani, A., Zhang, Y., "Cleat-scale characterisation of coal: an overview," *Journal of Natural Gas Science and Engineering*, (2017) **39**, 143-160.
16. Hilpert, M. and Miller, C. "Pore-morphology-based simulation of drainage in totally wetting porous media," *Advances Water Resources*, (2001) **24**, 243 – 255.

Prediction of Relative Permeability and Capillary Pressure using Digital Rock Physics: Case Study on two Giant Middle Eastern Carbonate Reservoirs.

Kamel Zahaf[1], Thierry F. Lecoq[1], Badar S. AL Badi[1], Sven Roth.[2], Hu Dong[2] and Martin J. Blunt[2,3]

[1]ADMA-OPCO [2]iRock Technologies [3]Imperial College London

ABSTRACT

Carbonate reservoir rocks are often highly complex, exhibiting extreme heterogeneity in the size, shape, connectivity and wettability of the pore space. In turn this variability strongly impacts the behavior of the capillary pressure and relative permeability and hence the oil recovery. Special core analysis cannot describe or separate these effects since the measurements are limited in the number of samples that can be handled, as well as the displacement cycles and wettabilities that can be considered.

We study 16 samples from two large Middle Eastern carbonate reservoirs (both limestones and dolomites). Static and dynamic properties of these rocks were determined through a combination of nano to cm scale sample selection and imaging to capture micro-porosity, macro-porosity and vugs, and multi-scale generalized network modeling and upscaling to capture the four orders of magnitude variation in pore size. The pore-scale distribution of contact angle was tuned to match one set of waterflood capillary pressure curves, which indicated mixed-wet characteristics with a tendency to be weakly oil-wet. On benchmark samples, the measured waterflood relative permeability was compared successfully to the predicted results.

Samples with the widest range of connected pore sizes – principally the limestones with a mix of micro-, macro- and vuggy-porosity – tended to display oil-wet type waterflood behavior, implying poor recovery, whereas the dolomite samples with a more restricted range of pore size showed mixed-wet characteristics in their flow response with more favorable recoveries. This study shows the value of digital rock technology, which aids the identification of multiphase flow rock types and quantifies how the pore size distribution, connectivity, mineralogy and wettability impact local displacement efficiency.

INTRODUCTION

Digital Rock Physics (DRP) or pore-scale modeling has received considerable attention in recent years as a complimentary and integral technology to laboratory measurement for the prediction of reservoir properties, for which the right laboratory measurements are difficult to perform or require long measurement times [1].

In network modeling the void space of a rock is represented at the microscopic scale. The topology of the pore space is determined using the maximal ball algorithm to extract

pore networks from macro- and microporosity [2]. The network extraction algorithm outputs a robust network suitable for computation of multiphase fluid displacement.

Multiphase flow properties are simulated based on the pore-scale modeling technology pioneered by Imperial College and adopted by iRock Technologies [3]. The displacement of one phase by another is computed semi-analytically on the pore space, using expressions for threshold capillary pressures derived for different pore and throat shapes and sizes. Contact angles are assigned to the network elements to reproduce any available wettability measurements. A multi-scale approach is employed, where networks are generated from images of different resolution and then combined and upscaled to make predictions for the full core.

DIGITAL ROCK PHYSICS (DRP) WORKFLOW

Step I: Core selection and characterization

Core characterization involved visual description, plug overview X-ray scanning, **E**valuation of **M**inerals, **SCAN**ning electron microscopy (**QEMSCAN**), Backscattered Electrons, (BSE) derived porosity and pore-size distribution. All this information lead to the micro-CT and nano-CT subsampling plan. Heterogeneity and variability in the sample plug will dictate the strategy of sampling.

Step II: Rock model construction

Prior to any simulations, the 3D X-ray images were processed and segmented. The processing includes image enhancement (noise reduction) and cropping the volume into a three-dimensional rock model. A quality control at this step is needed to validate pore size distribution and porosity of the digital rock model with laboratory data before proceeding with data acquisition, described later. Once the model is validated, rock properties are then calculated.

Step III: Upscaling and multiphase flow modeling

The goal of upscaling is to average properties from pore-scale network modeling to the whole core plug, where different regions may have different properties.

The imaging of rock samples and upscaling of the results are performed using a proprietary three-stage approach [2]. The basis of the method is to construct a generalized network model of the rock rather than being an explicit representation of large "pores" connected by "throats" as in traditional pore-network modelling approaches, we instead consider interconnected elements. These elements may indeed be real pores and throats, or could represent an averaged behavior of a region of micro-porosity. In this way we can construct a network at any scale, representing features spanning many orders of magnitude in scale. The wettability constrained to SCAL data is obtained from the lab to predict waterflood capillary pressure and relative permeability.

ROCK CHARACTERIZATION

Carbonate reservoirs are complex in their structure and pore geometries, and often display heterogeneity at all length scales [4], as is the case in this study. Core samples from two

Middle Eastern offshore carbonate fields A and B were used in this study. Table 1 below provides a summary of the 16 samples. Dolomitic and calcitic samples were carefully selected covering wide permeability and pore-type ranges.

Table 1. Core description and summary results.

WELL	Plug_No	Plug description	DRP		CCA_Lab	
			φ total	K (mD)	φ total	K (mD)
A	3	Biomoldic dolostone, the darker anhydrite patches are scattered within the lighter dolomite matrix; visible pores are only present in the dolomite material. Two recrystallized fractures roughly parallel to each other are observed	0.1771	1	0.178	4
A	15	Dolostone, part of the core is more vuggy then the other parts, but there is no apparent 'bedding'. Some mm- to cm-scale anhydrite patches are observed	0.216	185	0.23	228
A	18	Dolomudstone, the rock is homogeneous, and has a fine-grained texture. There are few visible pores. The sample has small breaks filled with epoxy.	0.2798	72	0.304	73
A	19	Dolomudstone, the sample is oil stained and black in color. The rock appears homogeneous, and has a fine texture.	0.2083	15	0.2283	22
A	23	Dolomudstone, homogenous with visible vugs. A set of recrystallized fractures (dark lines) roughly parallel to the long axis of the core plug are observed.	0.1743	45	0.176	56
A	30	Dolomudstone, visible pores are up to ~0.5-1 mm in diameter. The sample has a strong oil smell. The cutting surface after core cleaning shows subtle layering/burrows	0.2038	58	0.214	50
A	33	Dolomudstone, the rock is characterized by alternating porous (vugs up to ~1 mm) 'layers' and cemented 'layers' showing no visible pores.	0.1809	70	0.18	58
A	40	Vuggy, bioclastic packstone, vugs up to ~1 mm in diameter; the sample contains abundant bioclasts and anhydrite patches. Some large vugs are associated with anhydrite dissolution.	0.2084	55	0.2059	68
A	48	Mud-dominated packstone, abundant vugs up to ~1 mm in diameter; the sample contains abundant bioclasts, primarily algal, foram, and bivalve in origin.	0.2098	26	0.21	25
A	113H	Dolostone, the rock is relatively homogeneous with primarily intercrystalline pores. Abundant calcite cement and anhydrite patches are scattered in the rock sample	0.173	306	0.176	347
A	127H	Dolostone, the rock show abundant vugs that are up to 0.5-1 mm in diameter and are unevenly distributed (no apparent bedding). Some anhydrite patches are observed.	0.2754	677	0.28	524
B	8	Wackestone, the rock contains abundant bioclasts (primarily foram) and large vugs up to several mm in diameter	0.2887	37	0.291	45
B	69	Wackestone, fossiliferous with shell fragments up to ~5 mm long, abundant vugs up to ~0.5 mm in diameter.	0.2935	4.7	0.289	11.5
B	291	Mud-dominated packstone, abundant vugs that are up to 0.5-1 mm in diameter. There are a few clasts (with the largest one ~12×7 mm) that can be observed on core plug surface.	0.1664	13	0.159	15
B	329	Dolomudstone, the rock is relative homogeneous, and has a fine texture. A fracture (mechanical in nature) cuts through one end of the core plug obliquely.	0.2059	17	0.202	12.9
B	351	Packstone, the rock has abundant vugs that are up to ~1 mm in diameter. There are a few holes/breaks on the core plug surface that were filled with epoxy	0.2079	20	0.215	29

All the plugs were imaged; see Figure **1**, with a voxel size of approximately 40 μm. This overview scan provided information about the heterogeneity of the core plug and served as the sample volume to upscale all properties acquired at the pore scale.
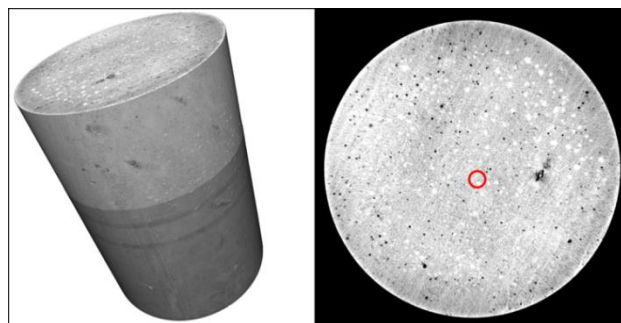
Figure 1. Plug MCT images and plug heterogeneity assessment (sample A_19).

Figure 2 shows a high-resolution BSE mosaic image**.** BSE mosaics are images of a large area at nanometer resolution, acquired with a scanning electron microscope. Two sets of images were taken per sample: one overview image of the entire plug surface with a pixel size of 488 nm, and additional representative sub-areas of approximately 2×2 mm imaged

at a pixel size of 48.8 nm. The resulting images were used to extract pore-size distributions (from nm to cm) to characterize the pore space of the samples and to quality control the MICP and NMR measurements.

Large area BSE image. Image dimension 15.0 x 16.3 mm; pixel size is 488 nm.

Sub-area BSE image. Image dimension 2.2 x 2.1 mm; pixel size is 48.8 nm.
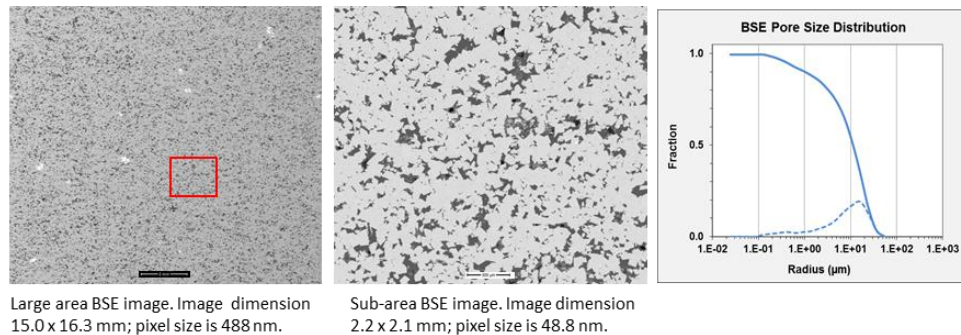
Figure 2. BSE images and BSE-derived pore size distribution.

The overview micro-CT, QEMSCAN and BSE images data were used to construct a sub-sampling strategy. As carbonate reservoirs are very complex, sub-sample strategy may differ from sample to sample in number and resolution.

POROSITY AND PERMEABILITY PREDICTIONS

Pore system analysis and permeability for the 11 samples from well A are summarized in Table 1. Seven of them are pure dolomitic, two are dolomite-dominated but contain different amounts of calcite nodules (sample A_15: 90% dolomite/7% calcite; sample A_113H: 80% dolomite/20% calcite). Two other samples are primarily calcitic with admixture of dolomite (A-40 and A_48).

Three of the samples were high permeability (k > 100 mD) with no microporosity and some vugs (samples A_113H, A_127H and A_15). Three other samples also contained no micro-porosity, but overall had smaller, less well-connected pores with permeability in the range 15-72 mD: samples A_18, A_19 Figure 2 and A_23. The remaining five samples contained microporosity with lower permeabilities from 26 –70 mD with one sample, A_3, with a much lower predicted permeability of 1 mD.

Five samples from well B (Table 1) were investigated. All samples are calcitic, except for the dolosiltstone sample B_329, which contains a mineral mixture of 75% dolomite and 25% calcite. Dolomite builds the framework of this rock, while microcrystalline calcite minerals occupy and reduce the pore space. The samples have intermediate permeability in the range 4.7 –37 mD. Two samples contain only macro-porosity and some vugs: B_291 and B_329. The lowest permeability sample is almost all micro-pores, the mud-to wackestone B_69. The remaining two samples (wackestone B_8 and packstone B_351).

Figure 3 shows the porosity partitioning for four samples. Limestone samples are made of micro-macro and vuggy porosity, while the dolomites have more restricted range of pore size. At this stage, it is important to understand the rock architecture of the pore system and thus the connectivity between them. Later we will show the impact on the

multiphase flow behavior and recovery. Figure 3 shows that the DRP predictions of porosity and permeability compare well with the measurements, Table 1.
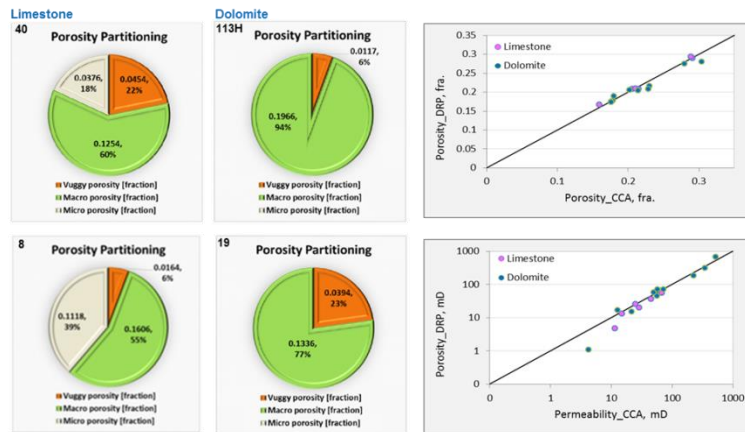
Figure 3. (a) Porosity partitioning based on image segmentation (b) Porosity and permeability predictions against laboratory measurements.

PORE THROAT DISTRIBUTION (MICP) CALIBRATION

The objective of this step is to calibrate the 3D pore networks using trim MICP. First, the pore throat distribution was derived from DRP then compared blindly to the MICP results (Figure 4). Where there are discrepancies, different sub-volumes were selected to produce DRP models to capture the small-scale heterogeneity and upscaled to provide a better match to the data. In summary, a realistic network topology combined with network properties tuned to experimental data such as MICP is sufficient to predict single and multiphase properties.
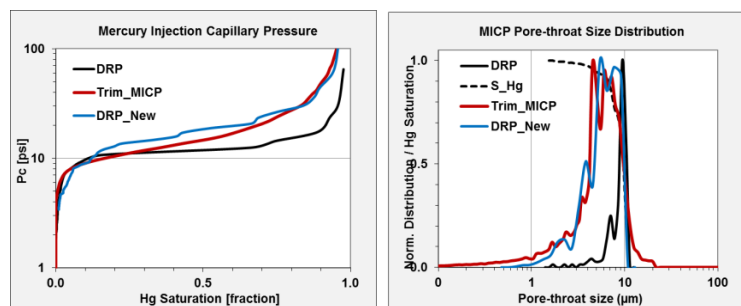
Figure 4. Sample A_15: Mercury injection capillary pressure (left) and pore throat distribution (right) comparison before and after updating to capture small-scale heterogeneity.

SIMULATION OF WATERFLOODING
Capillary pressure prediction

The up-scaled simulated primary drainage capillary pressure was compared with the measured laboratory data, see Figure 5. The contact angles in the simulations were adjusted to match the laboratory waterflood capillary pressure measured on one sample (A-30). In this case, we assume a weakly oil-wet condition with around 60% of the pore space oil-wet with an average contact angle of 135°.
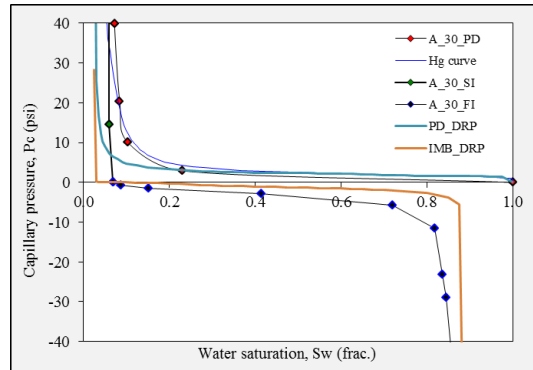
Figure 5. Sample A_30-Comparison of the measured primary drainage and imbibition capillary pressure.

Primary drainage relative permeability prediction

Figure 6 shows the predicted primary drainage relative permeability for both dolomite and limestone samples. In general, dolomite samples with a unimodal pore-size distribution (for instance, sample B_329, Figure 7) have a poor connectivity of the oil phase. In contrast, the limestone samples have a more connected pore system with higher oil relative permeabilities (for instance, sample B_351, Figure 7).
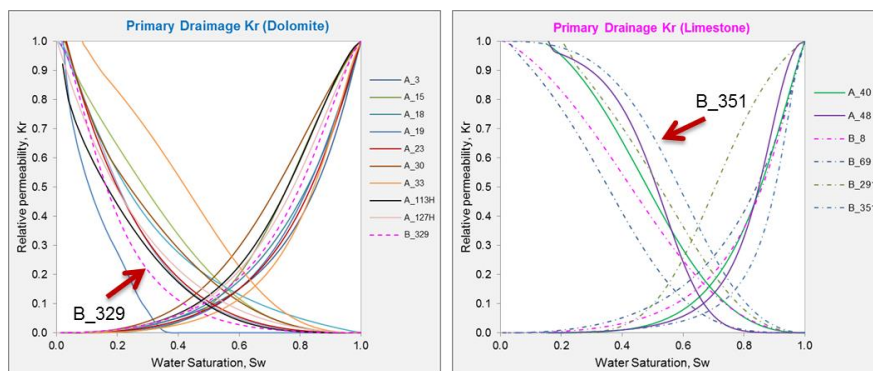
Figure 6. Primary Drainage relative permeability: dolomite (left) and limestone (right).
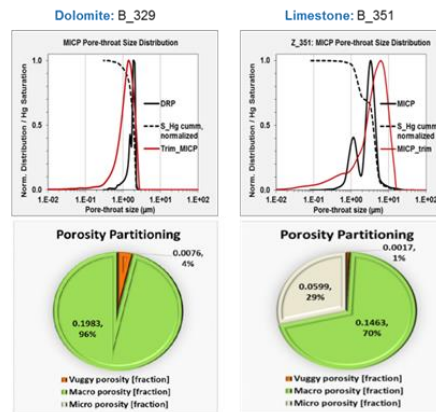
Figure 7. Pore throat distribution and porosity portioning showing the impact of pore type distribution on primary drainage relative permeability.

Prediction of waterflood relative permeability
The principal control on waterflood relative permeability is the connectivity of the phases in the pore space, governed by wettability (the contact angles) and pore structure. A rough indicator of waterflood recovery efficiency is not necessarily the theoretical residual saturation, but the water saturation where the oil and water relative permeability curves cross –the higher the value, the better the likely local recovery from waterflooding. Figure 8 compares the predicted and measured waterflood relative permeability curves for two samples B_69 (limestone) and A_19 (dolomite).

1- Overall the shape of the predicted relative permeability, particularly the oil relative permeability, is captured compared to the measured laboratory relative permeability which means the overall pore type system is well captured in the 3D pore network.
2- The predicted water relative permeability end point did not match the measured data: this could be due either to a poor characterization of wettability, or the true end-point not being measured in the experiments.

Figure 9 shows the predicted waterflood relative permeability for all the samples. We see two types of behaviour: classical oil-wet for the limestone samples (with the corss-over saturation marked by the red arrow) and mixed –wet for the dolomite samples (green arrow).

Oil-wet type behavior
For the limestone*s*, the saturation at which the waterflood relative permeability curves cross is less than 0.5, implying poor recovery. The oil relative permeability is lower for waterflooding than for primary drainage, as the oil now fills the smaller pores, while water in the larger pores, and has a higher relative permeability. This behavior is also seen for cores taken from the giant Ghawar field in Saudia Arabia [5]. Our samples have a mix of micro, macro and vuggy porosity with a very high oil relative permeability in primary

drainage, Figure 6. This implies that there is a well-connected pathway of larger pores: these, largely oil-wet regions fill with water during waterflooding, leading to high water relative permeabilities, extreme relative permeability hysteresis, early water breakthrough and poor recoveries.
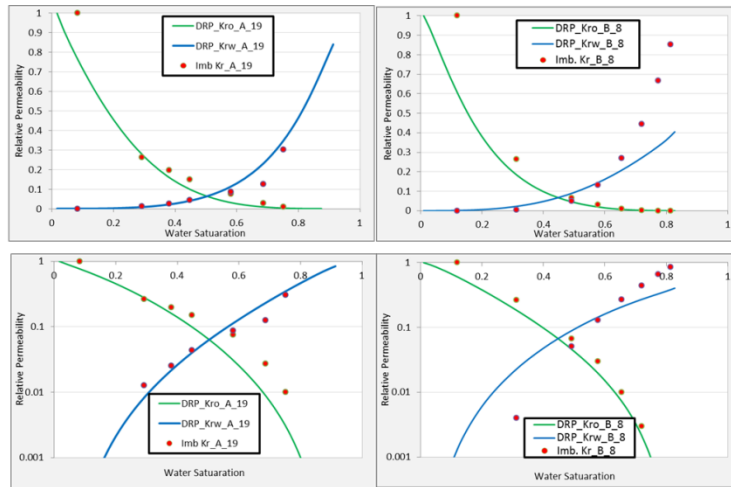
Figure 8. Waterflood relative permeability, comparing measured (points) and predicted (lines) data: and dolomite (left, A_19) and limestone (right, B_8)
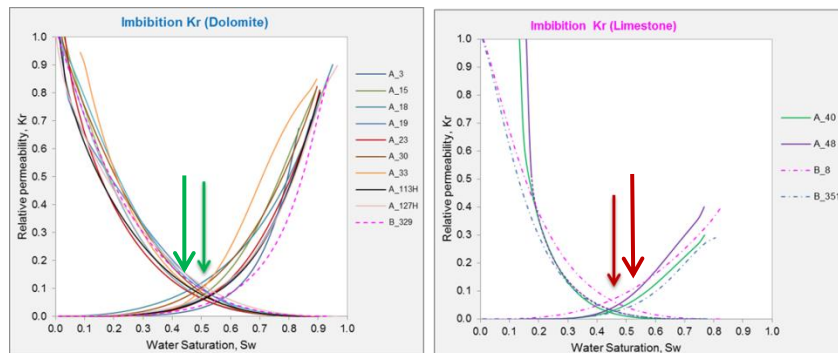
Figure 9. Waterflood relative permeability; dolomite (left) and limestone (right). The arrows indicate the cross-over saturation which is a guide to recovery: green is favorable while red is less favorable.

Mixed-wet type behavior

For the dolomites, we see higher cross-over saturations and very low waterflood water relative permeability, implying that during waterflooding the water can have a low connectivity at low saturation as there is no clear path of large oil-wet pores through the samples. This behavior has been seen experimentally from other cores from Abu Dhabi [6]. For samples A_113H, A_117H, A_19 and A_23, we see a cross-over saturation of greater than 0.5 and waterflood water relative permeabilities that can lie below those for primary drainage. In the wettability sensitivities and scanning curves, optimal recovery is generally for a mixed-wet, or at least not completely oil-wet state, and for intermediate

initial saturations, where the connectivity of the water is most restricted. These samples tend to have the highest permeability with a well-connected pore space, but without huge extremes in pore size and no micro-porosity. It is not possible for the water to occupy a preferential channel of much larger pores during waterflooding.

CONCLUSIONS

- A realistic multi-scale network topology with properties tuned to experimental data allows a robust prediction of multiphase flow properties.
- The DRP models were able to match measured relative permeability data.
- This analysis allowed the interpretation of the flow behavior and local displacement efficiency. Dolomites with a relatively narrow range of pore size gave favorable waterflood recoveries under mixed-wet or weakly oil-wet conditions. This is because – at the pore scale – the water remains poorly connected during waterflooding. In contrast the limestones, with a wider range of pore size and a pathway of connected larger pores displayed extreme relative permeability hysteresis between primary drainage and waterflooding with high water relative permeability during waterflooding. Here water rapidly connects across the pore space, leading to unfavorable local displacement.
- DRP is a useful complement to SCAL and enables the confident and robust assignment of rock types based on multiphase flow and recovery characteristics.
- Future work could extend this study, and use *in situ* measurements of contact angle to assign wettability.

ACKNOWLEDGMENTS

REFERENCES

1. Masalmeh, X. K., X. Jing, S. Roth, C. Wang, H. Dong, "Towards Predicting Multi-Phase Flow in Porous Media Using Digital Rock Physics: Workflow to Test the Predictive Capability of Pore-Scale Modeling" *SPE*-177572-MS (2015).
2. Dong H. and M. J. Blunt, "Pore-network extraction from micro-computerized-tomography images" *Physical Review E*, (2009), **80**, 3, 036307.
3. Valvatne, P.H. and Blunt, M.J, "Predictive Pore Scale-Modeling of two-phase flow in mixed-wet media", *Water Resources Research*, (2004), **40**, W07406, doi: 10.1029/2003WR002627.
4. Natarajan D., Naveen K., Verma T., Abdul Salam, and Ibrahim Al Sammak, Kuwait Oil Co; Koronfol S., Dernaika M., The WJ. 'Computation of Relative Permeability Curves in Middle Eastern Carbonates Usung Digital Rock Physiscs" IPTC-18211-MS (2014).
5. Okasha, T. M., J. J. Funk, and Rashidi, H. 2007. Fifty years of wettability measurements in the Arab-D carbonate reservoir. In: SPE 105114, proceedings of the SPE Middle East Oil and Gas Show and Conference, Manama, Kingdom of Bahrain.
6. Dernaika, M. R., Basioni, M. A., Dawoud, A. M., Kalam, M. Z., and Skjaeveland, S. M. 2013. Variations in Bounding and Scanning Relative Permeability Curves With Different Carbonate Rock Type. SPE Reservoir Evaluation & Engineering, 16(3), 265-280.

Pore-Scale Saturation, Temperature, Pressure and Velocity Characterization of SAGD Process

Sahand Etemad[1], Arash Behrang[1], Apostolos Kantzas[1,2]
1. University of Calgary, Calgary, AB, Canada
2. PERM Inc. TIPM Laboratory, Calgary, AB, Canada

ABSTRACT

In this paper, pore-scale phenomena in SAGD such as steam propagation and fingering as well as entrapment of oil behind the swept zone are visualized and evaluated. Using saturation, temperature, velocity and pressure profiles at the steam chamber edge and throughout the media, the interconnectivity of each parameter is discussed.

For this goal, a 2-D glass micromodel was reconstructed, binarized and meshed in COMSOL. Then the digital 2-D micromodel was fed into OpenFOAM, which is the open source CFD package of choice in this work. The mass and momentum conservation equations are used to model the fluid dynamic. For tackling the phase change, i.e. steam condensation and evaporation on the interface, within the simulation, the Lee phase change model was added to the pre-defined Volume of Fluid (VOF) based solver, compressibleMultiphaseInterFoam. The Lee model assumes that mass is transferred at a constant pressure due to temperature difference. For each phase in the multi-region model, sets of mass conservation, Navier-Stokes momentum and energy equations under non-isothermal conditions are solved simultaneously.

The results show connection between temperature, pressure, velocity and flow (saturation) profile. Sharp temperature gradient between steam and oil phase was observed, pressure profile throughout the medium shows pressure buildup behind the steam-oil interface, downward flowing of condensate and heated oil as well as upward and sideways propagation of steam was observed through flow streams and velocity profile component. Heat propagation within the media and viscosity reduction was investigated. Oil entrapment behind the swept zone as well as steam chamber growth is demonstrated and finally effect of steam additives on sweep efficiency and recovery factor was reported.

INTRODUCTION

The increasing universal demand for energy and the decreasing conventional oil resources are the motivation for the study of heavy oil recovery. Total discovered bitumen in place is 4512 billion barrels worldwide which goes up to 5505 billion barrels with an additional 993 billion prospective barrels of natural bitumen recourses (Meyer *et al.*, 2007). This source of energy has high viscosity and density and because of that primary recovery methods are not sufficient for production. The enhanced oil recovery methods can be classified into thermal and/or solvent displacements, chemical, polymer flooding, micellar flooding and microbial methods (Hart, 2014). In thermal methods, oil viscosity will

decrease several orders of magnitude by increasing the formation temperature (Butler *et al*., 1981). Typical thermal recovery methods can be classified into steam flooding, cyclic steam stimulation (CSS) and steam-assisted gravity drainage (SAGD) (Butler, 1997; Butler *et al*., 1981). SAGD, has a high recovery factor and relatively low environmental footprint and is widely used. However, pore-scale phenomena have to be investigated deeply as they lead to a better understanding of macroscopic observations in the field, (Al-Bahlani and Babadagli, 2009)

In SAGD, Figure 1, steam is injected into upper horizontal well, propagates vertically at the beginning and then flows toward the perimeter of the created steam chamber. This process can be described in the following stages: Continuous steam injection into the chamber, chamber growth upward and sideways, condensation of the steam on the interface between oil and steam and downward flow of the heated oil and condensate to the production well.

There are many uncertainties such as steam condensation on the interface, oil recovery, pressure distribution, fluid flow on the chamber and transition zone between oil and steam phases. Better understanding of the temperature, pressure, velocity and flow profiles is necessary for SAGD improvement. The SAGD process has been visually investigated both experimentally and through numerical simulation. Because of experimental complexities such as setting the boundary and initial conditions and continuous measurements throughout the medium, there is more attention toward numerical simulations to model SAGD at the grain level (Al-Bahlani and Babadagli, 2009) Simulation of SAGD in OpenFoam (Andersen, 2011) adding the phase change model to it, enables us to keep track of the velocity, pressure and temperature profile continually throughout the medium, steam chamber geometry.

In this work, SAGD is evaluated in a micromodel through numerical simulation and by visualizing flow, temperature, pressure and velocity profile. For this propose, a 2D micromodel with 390×390 μm dimensions and square shaped grains was reconstructed and fed into the OpenFoam. Full T, P, V and optical mapping of the SAGD recovery experiment is performed.

(a)   (b)
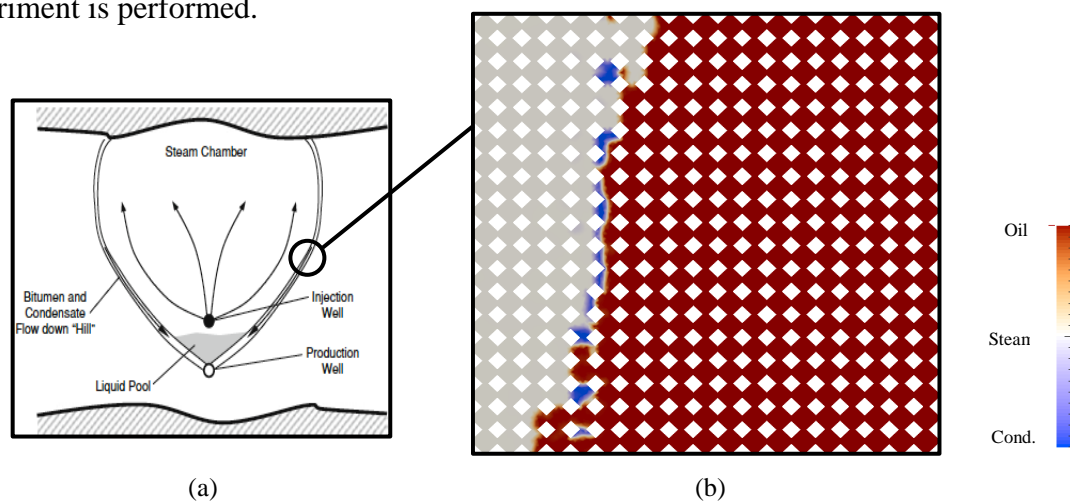
Figure 1: SAGD, Field scale (Yang and Gates, 2009) (a), Pore Scale (b)

METHODOLOGY

Lagrangian and Eulerian methods are two popular methods for fluid flow simulation. The limitation for Lagrangian methods is the restriction to simple cases (Lee *et al*., 2015). Therefore, for simulating complex geometries of the pore, methods based on Eulerian viewpoints will be used, Figure 2. For tackling two phase flow and capture the interface between phases, Volume of Fluid Method (VOF) and Level-Set (LS) methods are used. They are based on Eulerian point of view (Hirt and Nichols, 1981) (Osher and Sethian, 1988) (Peng *et al*., 1999). The LS method can capture complex interfaces but the drawback is the mass loss when solving the advection equation (Kartuzova and Kassemi, 2011) (Wang *et al*., 2008). In the VOF method, energy, momentum and mass equation is solved for each and every phase simultaneously (Hirt and Nichols, 1981). Sum of the volume fractions for all phases in a cell is equal to one, Figure 3. VOF is an interface tracking method and which is widely used in phase change problems. It is mass conservative (Hirt and Nichols, 1981) (Sussman and Puckett, 2000). As we can see from Figure 3, α (volume fraction), of each phase has a value between 0 and 1.
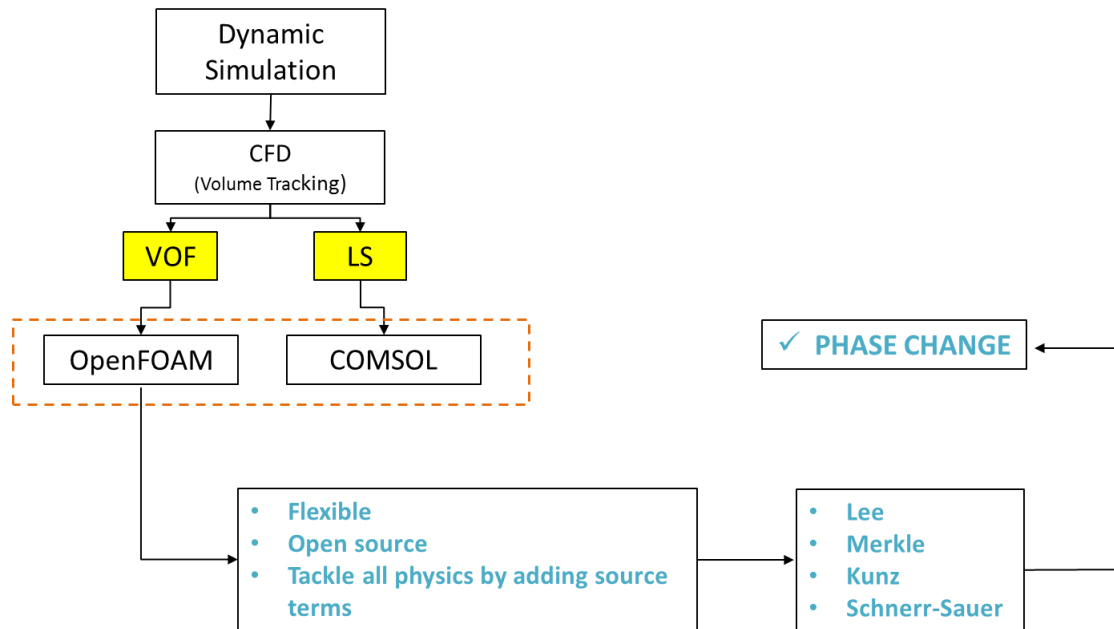
Figure 2: Pore level Modeling VOF method

"compressibleMultiphaseInterphasechangeFoam" is the solver we used for SAGD simulation in this work and is based on VOF method to compute the conservation equations for oil, condensate and vapor (Gueyffier *et al*., 1999). A single momentum equation is solved for three phases and the properties of the mixture are calculated based on the VOF method. Governing equations to model fluid flow and heat transfer in condensation/evaporation phenomena are mass, momentum and energy conservation. The governing equations are as follows:
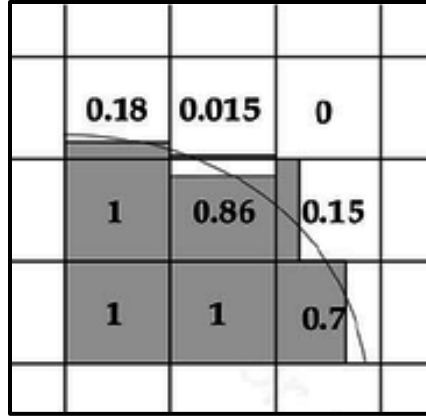
Figure 3: Schematic of alpha value in the cells close to the interface (VOF) (Martinez *et al.*, 2006)

$$\sum_{i=oil,water,steam} \alpha_i = 1 \tag{1}$$

$$\alpha_{oil} = \frac{oil\ volume}{total\ cell\ volume} \quad \alpha_{steam} = \frac{steam\ volume}{total\ cell\ volume} \quad \alpha_{water} = \frac{water\ volume}{total\ cell\ volume} \tag{2}$$

The continuity equation for each phase (Kartuzova and Kassemi, 2011):

$$\frac{\partial(\alpha_i\rho_i)}{\partial t} + \underbrace{\nabla \cdot [\alpha_i\rho_i\vec{u}]}_{flux\ of\ fluid} = S_{\alpha_i}, \quad i = oil, water, steam \tag{3}$$

Where ρ, u and t are density, velocity and time, respectively. S_i is interfacial mass transfer:

$$S_{\alpha_l} = \dot{m}_i \cdot A_i \tag{4}$$
$$S_{\alpha_v} = \dot{m}_i \cdot A_i \tag{5}$$
And
$$A_i = |\nabla\alpha| \tag{6}$$

Where A_i is the interfacial area density vector and $\dot{m}_i$ is mass flux vector which can be determined based on the proper phase change model, and α volume fraction of the primary phase (Schmidt and Grigull, 1989). In order to tackle phase change, we use LEE phase change model (Lee *et al.*, 2015).

We use averaging for measuring properties of the mixture fluid in order to solve momentum and energy equation at the same time for mixture (Piro and Maki, 2013):

$$\rho = \sum_{i=oil,water,steam} \rho_i\alpha_i \tag{7}$$
$$\mu = \sum_{i=oil,water,steam} \mu_i\alpha_i \tag{8}$$

Momentum equation:

$$\underbrace{\overbrace{\frac{\partial(\rho\vec{u})}{\partial t}}^{Inertia\ per\ volume}}_{Variation} + \underbrace{\nabla.(\rho\vec{u}\vec{u})}_{Convection} = \overbrace{\underbrace{-\nabla P}_{Internal\ force} + \underbrace{\nabla.[\mu(\nabla\vec{u}+\nabla\vec{u}^T)]}_{Diffusion}}^{Divergenve\ of\ stress} + \underbrace{\rho\vec{g}}_{External\ force} +$$

$$\underbrace{\vec{F}}_{Volume\ force} \tag{9}$$

F is defined as follows:

$$F = \left[\sigma\kappa\boldsymbol{n} + \frac{d\sigma}{dT}\left(\sigma T - \boldsymbol{n}(\boldsymbol{n}.\nabla T)\right)\right]|\nabla\alpha|\frac{2\rho}{\rho_1+\rho_2} \tag{10}$$

Where $\kappa = -\nabla.\boldsymbol{n}$ and σ are the curvature and surface tension terms, respectively.

Energy equation:

$$\frac{\partial(\rho C_p T)}{\partial t} + \nabla.\left(\underbrace{\vec{\boldsymbol{v}}(\rho E + P)}_{Flux\ of\ energy}\right) = \nabla.\left(\underbrace{k_{eff}\nabla T}_{Energy\ transfer\ due\ to\ conduction}\right) +$$

$$\underbrace{Q}_{volumetric\ heat\ sources} \tag{11}$$

Where Q is the volumetric heat sources, k_{eff} is the thermal conductivity term given by:

$$k_{eff} = \sum_{i=oil,water,steam} k_{eff_i}\alpha_i \tag{12}$$

Using these equations, a new solver is developed in OpenFOAM solver in order to address the phase change problem.

The Lee phase change model (Lee *et al*., 2015) was implemented into the solver "multiphasecmpressibleinterFoam" which is a VOF-based solver of the OpenFOAM package to take phase change into account in presence of steam, oil and condensate. This model assumes that phase change happens in constant pressure because of temperature gradient.

$$S_{\alpha_v} = -S_{\alpha_l} = r_l\alpha_l\rho_l\frac{T-T_{sat}}{T_{sat}} \quad T > T_{sat} \quad \text{evaporation process} \tag{13}$$

$$S_{\alpha_l} = -S_{\alpha_v} = r_v\alpha_v\rho_v\frac{T_{sat}-T}{T_{sat}} \quad T < T_{sat} \quad \text{condensation process} \tag{14}$$

where S_{α_v} and S_{α_l} are the interfacial mass transfer rates for vaporization and condensation respectively. r denotes the mass transfer intensity factor with unit s^{-1}. The r value is recommended to be as such to keep interfacial temperature close to saturation temperature, i.e. consistency between temperature and saturation profile. Researchers have used a very wide range of values for r, flow regime, geometry, mesh size and time steps. (Alizadehdakhel *et al*., 2010; De Schepper *et al*., 2009; Wu *et al*., 2007) (Goodson *et al*., 2010; Yang *et al*., 2008). We sat $r_v = r_l = 1000$ to get T_i (interface temperature) close to T_{sat}.

RESULTS

In this section, we will demonstrate saturation, temperature, velocity and pressure mapping throughout the geometry and in different time-steps. Analysis of the results and discussion of the correlation among all parameters, P, $\vec{V}$, T and α will follow.

Figure 4 shows snapshots for the simulation. Saturation, Temperature, Velocity and Pressure profiles in 9 different time steps (early stage to steam chamber development) are demonstrated in figure 4(a), 4(b), 4(c) and 4(d) respectively.
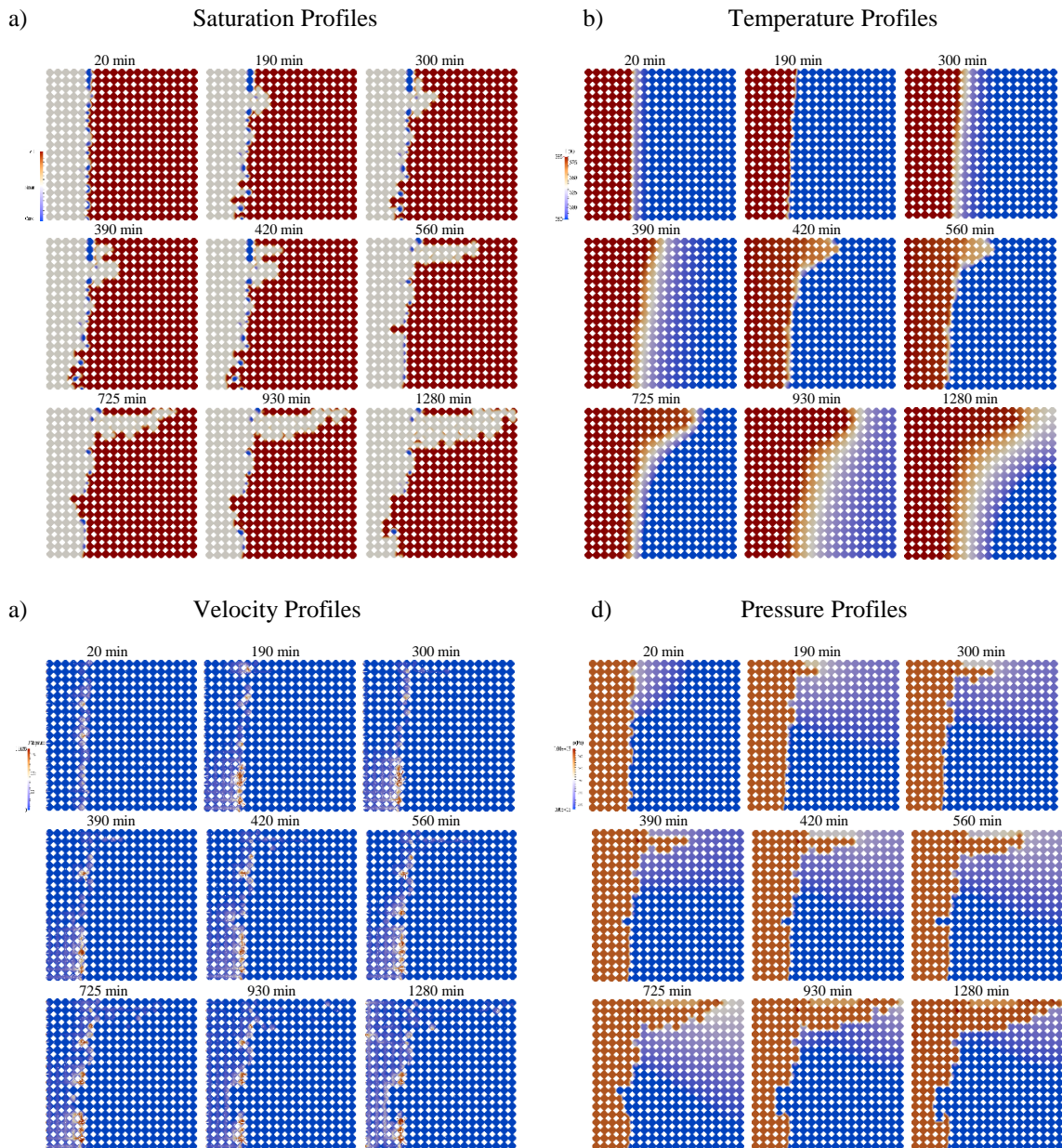
Figure 4: Saturation (a), Temperature (b), Velocity (c) and Pressure(d) profiles

The geometry was used in this work is a 2D reconstructed micromodel with square shaped grains which is based on the lab experiment, (Mohammadzadeh *et al*., 2010).

In this set of simulations, the system is initially saturated with steam at 385 K and oil in 280 K. The micromodel is supplied with steam from the left-hand side of the geometry and oil, condensate and steam production is from the bottom face. The system is at atmospheric pressure and $T_{sat} = 373\ K$.

Figure 4(a) is the saturation profile during the simulation in 9 different time-steps. As we can see, steam drains the oil out with a piston like trend at the beginning, from the beginning of the simulation until 190 min, later fingering of steam toward the right end of the geometry will be dominant, sideways propagation of the steam. Condensate with blue colour is generated on the interface between oil and steam. Oil is trapped locally in the swept zone. A blocking effect of the condensate on sweep efficiency of steam is observed. As we can see from the last three time-steps, steam is bypassing the lower part of the geometry because the condensate is blocking the steam from further propagation. We also observe local revaporization of the generated condensate. An example will be vaporizing the condensate phase partially from minute 420 to 560. In the real field, we have overburden heat loss because of the grains cooling down the steam, in these sets of simulations, the grains are not meshed and we do not have heat diffusion from the steam into the grains. Infinite amount of cold bitumen in the surrounding area in filed scale will results in more condensate generation while we have insulated boundaries for temperature here. We also have not included heat loss into the system. In the real experiment or field scale, the sealed faces are not fully insulated and lead to more condensation of steam.

Regarding steam chamber growth and steam phase fingering into the bitumen phase, upwards and sideways propagation of steam in real field data were observed (Ito and Ipek, 2005). In a sand pack experiments, steam fingering rather than a piston like propagation was observed as steam chamber grows (Butler and Dargie, 1994). Others (Sasaki *et al*., 2001) showed steam fingering in their 2D experimental model. The results of our simulation are consistent with these experiments as steam is propagating from the top of the micromodel and fingers towards the right end.

In terms of residual oil in the steam chamber behind the swept zone, Mohammadzadeh *et al.* (Mohammadzadeh *et al*., 2010) showed oil phase trapped behind the steam front in their 2D SAGD experiment on micromodel. Residual oil saturation inside the steam chamber is too low to be moved by steam phase, (Butler and Dargie, 1994). The results of our simulations show oil entrapment behind in the steam chamber which is immobile because of low saturation which agrees with the experimental data.

In Figure 4(b), the snapshots of temperature profile correspond to the previous 9 saturations have been demonstrated. High temperature steam with red color in the picture is cooling down on the interface, (white colour) and will be condensed. The reason will be the direct contact of steam with the oil phase which is in 280 K temperature. We see sharp temperature reduction on the interface. There is consistency between temperature and saturation profile as we compare the results from Figure 4(a) and 4(b). The interconnectivity will be having temperature close to the saturation temperature at the interface. As the simulation continues, high temperature is propagating from the top which is the steam fingering region. Condensate is generated on the interface which is the

transition zone where the temperature lays in between the steam and oil temperature, white colour on the temperature map.

Gates *et al.* showed temperature and saturation profiles of steam chamber from a simulation (Gates *et al.*, 2005). Syed *et al.* mapped temperature profiles continuously through their micromodel using infrared camera in an experimental work (Syed *et al.*, 2016). Mohammadzadeh *et al.* installed several thermocouples throughout their geometry and monitored temperature distribution (Mohammadzadeh *et al.*, 2010). The conclusion was that the temperature profiles match the saturation profiles where temperature at the interface is close to saturation temperature. As we observe in the results section, temperature profile in our simulation is consistent with the saturation profile which agrees with the experimental observations above.

We also showed the results for velocity profile throughout the media in Figure 4(c). Initial steam injection velocity is $10^{-4} \frac{m}{s}$. Based on the velocity profile, the high velocity regions will be on the interface where droplets of condensate are generated and there is high convection velocity because of temperature difference, red colour on the velocity profile. Arrows show the directions of flow. Condensate and oil have downward flow and steam is propagating sideways, upward and downwards. The magnitude of the arrows represents the magnitude of the velocity. Due to higher viscosity for oil, the arrows are smaller in this region meaning the mobility toward production is lower in comparison to condensate and steam phases. As we go further from the steam, high temp region, the velocity vector will be smaller as the effect of temperature will be smaller. This will lead to smaller viscosity reduction and less mobility. When steam starts fingering from the top, the velocity vectors in this region will go higher in number and magnitude meaning that velocity toward the right end goes higher. Figure 5 shows a closer look of the velocity vectors in vicinity of the interface where the convection velocity between the phases with different temperatures is noticeable. In the steam phase on left side, there is propagation of steam in all directions and oil is getting mobilized only in vicinity of the steam phase and toward the production, bottom face. Figure 6 is a zoom-out view of the velocity vectors overlapping the saturation profile. Propagation of steam as well as convection velocity at the interface is noticeable.

Velocity profiles in our simulations show the flow of heated oil in the vicinity of the steam-oil interface. Away from the steam chamber, velocity vectors disappear, which means that oil will stay immobile. This is consistent with Butler's hypothesis that due to water condensation on the interface between steam and oil, major oil flow happens on the steam chamber because of interfacial tension support between oil and condensate as well as imbibition phenomena, (Butler and Dargie, 1994).
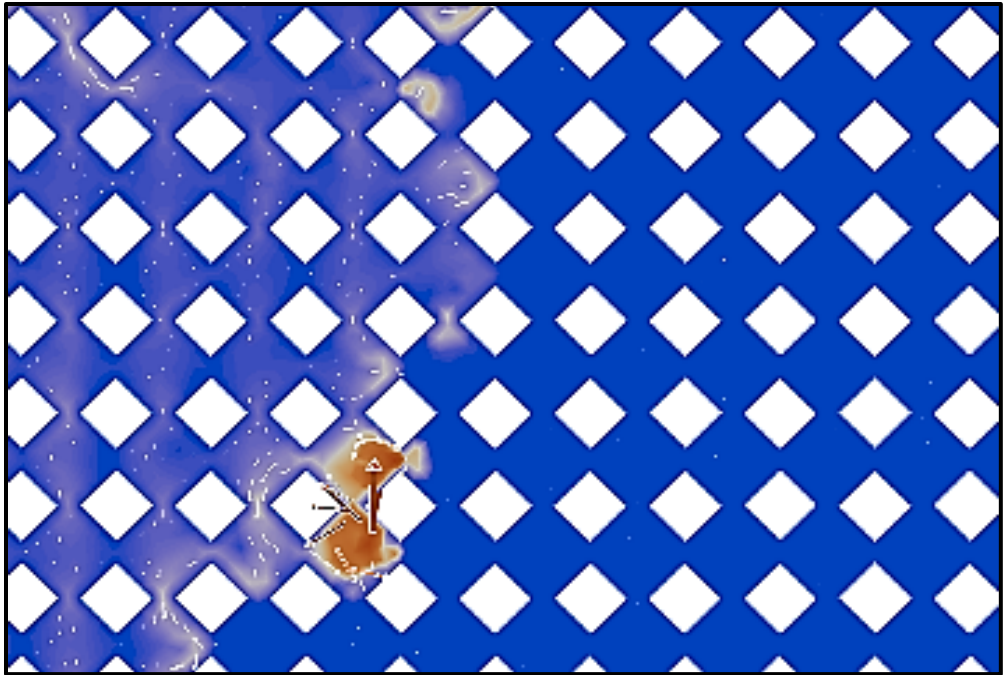
Figure 5: Zoom in view for the velocity vectors in vicinity of the interface
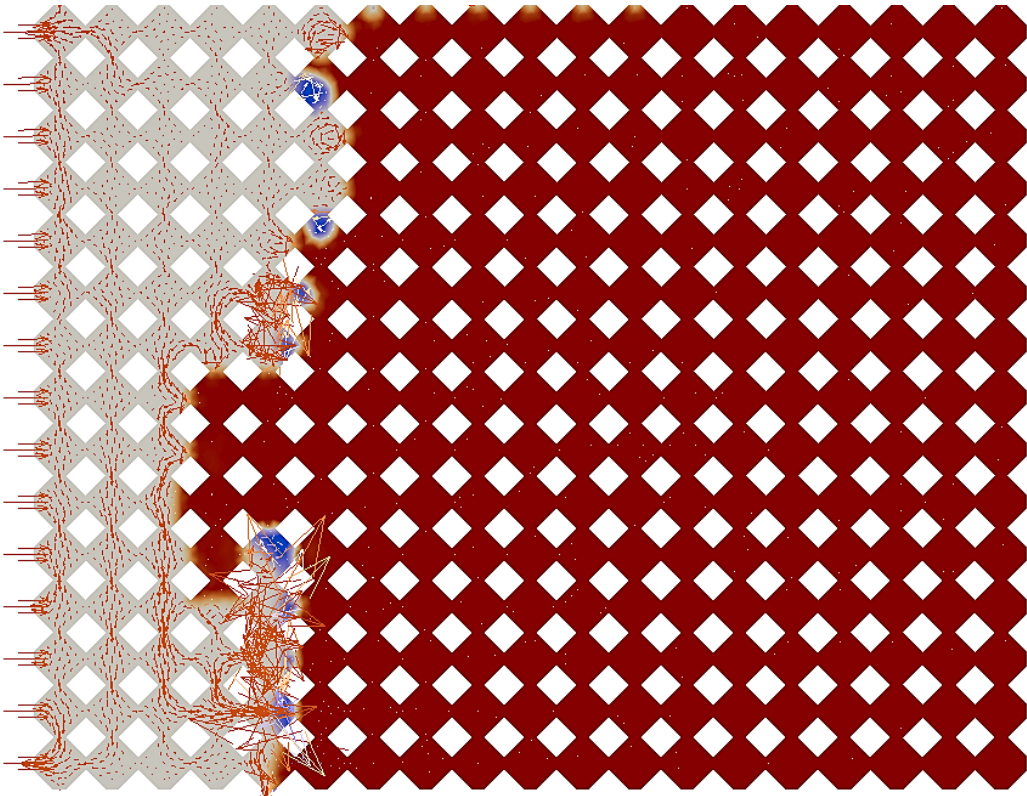
Figure 6: Zoom out view for the velocity vectors overlapping the saturation profile

Finally, Figure 4(d) shows the pressure profile during the simulation and is corresponds to the 9 time steps in saturation, temperature and velocity profiles. Pressure builds up behind the interface between oil and steam, 1.01 bar. The reason is the oil with higher viscosity which is blocking the steam from further proceeding until the pressure goes up and it has enough energy to pushes the oil toward the production site. System is initially sat to atmospheric pressure. During simulation, there is 200 Pa pressure difference between the oil and steam phases in maximum which is because of pressure buildup in the steam phase. Pressure profile is matched to the saturation and temperature profiles meaning that high pressure region is the steam region which is propagating from the top and has higher temperature respectively.

CONCLUSION

SAGD simulation was conducted and saturation, temperature, pressure and velocity profiles were analyzed. It was concluded that steam is fingering from the top, condensate is generated on the interface, pressure builds up behind the swept zone and velocity is higher on the interface and lower in the oil region. Velocity, pressure, temperature and saturation profiles match with each other meaning that there is a sharp temperature, pressure and velocity gradient between oil and steam phases. Blocking effect of generated condensate as well as the re-vaporization of the condensate was observed. The velocity magnitude reported to be higher on the interface because of convection velocity due to high temperature gradient and condensation with higher density and lower viscosity in comparison to the oil.

Finally, it is critical to investigate effect of different parameters on SAGD performance and find and optimum state for the procedure. Effects of different mineralogy, injection rate, steam temperature and the understanding of SAGD thermodynamics to reduce heat losses in the process are priorities for future work. Running Solvent-SAGD simulation to reduce oil-water IFT for higher sweep efficiency as well as for improving heat efficiency will be another important task in the future.

ACKNOWLEDGEMENTS

REFERENCES

Al-Bahlani, A.-M., and T. Babadagli, 2009, SAGD laboratory experimental and numerical simulation studies: A review of current status and future issues: Journal of Petroleum Science and Engineering, v. 68, p. 135-150.
Alizadehdakhel, A., M. Rahimi, and A. A. Alsairafi, 2010, CFD modeling of flow and heat transfer in a thermosyphon: International Communications in Heat and Mass Transfer, **v. 37**, p. 312-318.

Andersen, M., Jarpner C, et al. 2011, A interphaseChangeFoam tutorial: Chalmers University of Technology, URL: http://www.openfoam.org/.

Butler, R., 1997, Thermal recovery of oil and bitumen, publ: GravDrain Inc.(2nd printing), Calgary, Alberta, 528pp.

Butler, R., G. McNab, and H. Lo, 1981, Theoretical studies on the gravity drainage of heavy oil during in‑situ steam heating: The Canadian journal of chemical engineering, **v. 59**, p. 455-460.

Butler, R. M., and B. Dargie, 1994, Horizontal wells for the recovery of oil, gas, and bitumen, Petroleum Socitey Monograph Number 2, Canadian Institute of Mining Metallurgy and Petroleum, University of Calgary.

De Schepper, S. C., G. J. Heynderickx, and G. B. Marin, 2009, Modeling the evaporation of a hydrocarbon feedstock in the convection section of a steam cracker: Computers & Chemical Engineering, **v. 33**, p. 122-132.

Gates, I. D., J. Kenny, I. L. Hernandez-Hdez, and G. L. Bunio, 2005, Steam injection strategy and energetics of steam-assisted gravity drainage: SPE International Thermal Operations and Heavy Oil Symposium.

Goodson, K., A. Rogacs, M. David, and C. Fang, 2010, Volume of fluid simulation of boiling two-phase flow in a vapor-venting microchannel: Frontiers in Heat and Mass Transfer (FHMT), **v. 1**.

Gueyffier, D., J. Li, A. Nadim, R. Scardovelli, and S. Zaleski, 1999, Volume-of-fluid interface tracking with smoothed surface stress methods for three-dimensional flows: Journal of Computational physics, **v. 152**, p. 423-456.

Hart, A., 2014, A review of technologies for transporting heavy crude oil and bitumen via pipelines: Journal of Petroleum Exploration and Production Technology, **v. 4**, p. 327-336.

Hirt, C. W., and B. D. Nichols, 1981, Volume of fluid (VOF) method for the dynamics of free boundaries: Journal of computational physics, **v. 39**, p. 201-225.

Ito, Y., and G. Ipek, 2005, Steam fingering phenomenon during SAGD process: SPE 97729 International Thermal Operations and Heavy Oil Symposium, Calgary, Nov. 1-3.

Kartuzova, O., and M. Kassemi, 2011, Modeling interfacial turbulent heat transfer during ventless pressurization of a large scale cryogenic storage tank in microgravity: 47th AIAA/ASME/SAE/ASEE Joint Propulsion Conference & Exhibit, p. 6037.

Lee, H., C. R. Kharangate, N. Mascarenhas, I. Park, and I. Mudawar, 2015, Experimental and computational investigation of vertical downflow condensation: International Journal of Heat and Mass Transfer, **v. 85**, p. 865-879.

Martinez, J., X. Chesneau, and B. Zeghmati, 2006, A new curvature technique calculation for surface tension contribution in PLIC-VOF method: Computational Mechanics, **v. 37**, p. 182-193.

Meyer, R. F., E. D. Attanasi, and P. A. Freeman, 2007, Heavy oil and natural bitumen resources in geological basins of the world: Open-File Report 2007–1084, US Geological Survey, Washington, DC. pubs.usgs.gov/of/2007/1084/ (accessed November 29, 2010).

Mohammadzadeh, O., N. Rezaei, and I. Chatzis, 2010, Pore-Level Investigation of Heavy Oil and Bitumen Recovery Using Solvent− Aided Steam Assisted Gravity Drainage (SA-SAGD) Process: Energy & Fuels, **v. 24**, p. 6327-6345.

Osher, S., and J. A. Sethian, 1988, Fronts propagating with curvature-dependent speed: algorithms based on Hamilton-Jacobi formulations: Journal of computational physics, **v. 79**, p. 12-49.

Peng, D., B. Merriman, S. Osher, H. Zhao, and M. Kang, 1999, A PDE-based fast local level set method: Journal of computational physics, **v. 155**, p. 410-438.

Piro, D. J., and K. J. Maki, 2013, An adaptive interface compression method for water entry and exit: Technical Report 2013-350, University of Michigan, Department of Naval Architecture and Marine Engineering. URL: http://deepblue.lib.umich.edu/handle/2027.42/97021.

Sasaki, K., S. Akibayashi, N. Yazawa, Q. Doan, and S. Ali, 2001, Experimental modelling of the steam-assisted gravity drainage process enhancing SAGD performance with periodic stimulation of the horizontal producer: SPE Jour, p. 189-197.

Schmidt, E., and U. Grigull, 1989, Properties of water and steam in SI-units: Springer, Berlin. Edition 4.

Sussman, M., and E. G. Puckett, 2000, A coupled level set and volume-of-fluid method for computing 3D and axisymmetric incompressible two-phase flows: Journal of Computational Physics, **v. 162**, p. 301-337.

Syed, A. H., N. Mosavat, J. Riordon, P. Lele, Z. Qi, M. Kim, H. Fadaei, A. Guerrero, and D. Sinton, 2016, A combined method for pore-scale optical and thermal characterization of SAGD: Journal of Petroleum Science and Engineering, **v. 146**, p. 866-873.

Wang, Z., J. Yang, and F. Stern, 2008, Comparison of particle level set and CLSVOF methods for interfacial flows: 46th AIAA Aerospace Sciences Meeting and Exhibit, Reno, Nevada.

Wu, H., X. Peng, P. Ye, and Y. E. Gong, 2007, Simulation of refrigerant flow boiling in serpentine tubes: International Journal of Heat and Mass Transfer, **v. 50**, p. 1186-1195.

Yang, X., and I. D. Gates, 2009, Design of hybrid steam-in situ combustion bitumen recovery processes: Natural resources research, **v. 18**, p. 213-233.

Yang, Z., X. Peng, and P. Ye, 2008, Numerical and experimental investigation of two phase flow during boiling in a coiled tube: International Journal of Heat and Mass Transfer, **v. 51**, p. 1003-1016.

Fluid Topology in Drainage and Imbibition: Pore Scale Imaging by Synchrotron Tomography

Hamid Hosseinzade Khanamiri, Ole Torsæter, Georg J. B. Voss

PoreLab Research Center, Department of Geoscience and Petroleum, Norwegian University of Science and Technology (NTNU), 7491 Trondheim, Norway

ABSTRACT

Recent works on the enhanced oil recovery (EOR) by injection of low salinity surfactant (LSS) have shown that the efficiency of LSS can be sensitive to subtle changes in ionic composition. Different compositions can result in different interfacial tension (IFT), relative permeability, wettability and mobilization of residual oil. A flooding experiment including drainage and imbibition by water and LSS was performed on water-wet Berea sandstone. The 3-dimensional (3D) pore scale changes of the fluid configuration were captured under flow using fast X-ray tomography. The connectivity (Euler characteristic) was calculated separately for ganglia and for connected pathways of the wetting and nonwetting phases to give more insight of their impact on topology of the water and oil phases. The results showed that the topology of a fluid mainly depended on the topology of the corresponding ganglia and was less sensitive to topology of the corresponding connected pathway. The ganglia and the whole phase (ganglia plus connected pathway) showed hysteresis in the topology in imbibition and drainage for both wetting and nonwetting phases. The connected pathways however had insignificant hysteresis in imbibition and drainage, i.e. the hysteresis in topology of a phase was likely to be caused by the ganglia. Furthermore, we hypothesized that the ratio of the Euler characteristic of the connected pathways of wetting and of nonwetting phases could be used as a descriptor of the wetting change.

INTRODUCTION

In two-phase flow in porous media, nonwetting fluid moves either as a connected pathway or as a group of disconnected clusters (ganglia) which break up and coalesce (Avraam and Payatakes, 1995). The phenomenon where the disconnected clusters of the nonwetting phase are mobile is known as the ganglion dynamics. Synchrotron tomography has helped to understand better behavior of flowing fluids. Youssef et al. (2014) found that mean ganglia size and largest cluster size depend on capillary number. Rücker et al. (2015) observed that ganglion dynamics occurred at length scale equivalent to oil clusters length. Therefore, an intermediate flow regime between pore and Darcy scale is expected. Berg et al. (2015) showed that at the onset of oil mobilization, oil clusters break off as opposed to moving in the form of a single large cluster. One of the major challenges has been to find

a parameter which helps quantifying the dynamic microscopic changes. In this regard, Herring et al. (2013) used Euler characteristic (χ) to describe the connectivity of the oil clusters where χ is defined as:

$$\chi = N - L + O \tag{1}$$

In this equation, N is the number of isolated clusters of a fluid phase, L is the number of redundant connections within all clusters, and O is the number of cavities. A negative value of χ indicates higher connectivity while a positive value indicates fragmented fluid. χ is dimensionless; however it is usually normalized with the total volume of the system (bulk volume) for convenience. We have reported the normalized values in mm^{-3} unit. Schlüter et al. (2016) believed that the connectivity had been ignored in characterization of two-phase flow. Avraam and Payatakes (1995) observed a dependency of relative permeabilities on changes in microscopic flow regimes when the flow regime changes from ganglion dynamics to connected pathway. Relative permeability depends on pore scale fluid configuration which in turn, depends on the connectivity (Armstrong et al. 2017). Overall, recent advances seem to be promising for better understanding of two-phase flow.

In this work, we examined the drainage and imbibition in a water wet Berea sandstone sample. The connectivity was calculated for both water and oil phases. In addition, the connectivity of the oil and water ganglia, and of the oil and water connected pathways were calculated separately. The evolution of ganglia and connected pathways topology revealed their effect on the connectivity of the whole phases and on the origins of connectivity hysteresis.

MATERIALS AND METHODS

Material. The core sample was a Berea sandstone (D=4mm, L≈10mm) extracted from a parent plug which had a permeability and porosity of 270mD and 15.2%, respectively. There was no aging before the experiment. The composition of the brines is given in Table 1. The core was initially saturated with high salinity water (HSW). The ionic strength of low salinity water (LSW) was 10 times lower than that of the HSW. LSW-N contains only NaCl and LSW-NC contains both NaCl and CaCl$_2$ in the solution. The low salinity surfactant (LSS) solutions were prepared by dissolving 0.5 wt% surfactant in the LSW-N and LSW-NC. LSS-N and LSS-NC are the surfactant solutions which were prepared using LSW-N and LSW-NC brines, respectively. The surfactant is a blend of alkylbenzene sulfonates with a chain length distribution of C$_{15}$-C$_{18}$ (Khanamiri et al. 2016a, b). Detailed properties of the surfactant can be found in the aforementioned references. The oil phase was a mixture of 90% by volume crude oil and 10% 1-Iododecane. 1-Idododecane enhances the contrast of oil and water phases. The oil phase was used in a previous study by Khanamiri et al. (2016b) where the crude oil properties were also documented. IFT of the mixed oil with the HSW, LSS-N, LSS-NC were 5.3, 0.1 and 0.03mN/m, respectively at room temperature.

Injection and imaging. The experiment was conducted at ambient conditions in the *TOMCAT* beamline at the *Swiss Light Source*. Details of the injection steps are listed in

Table 2. The core sample was 100% saturated with HSW (Table 1) before starting the experiment. Drainage was performed at two different flow rates. Waterflooding was done by HSW at two different flow rates. Low salinity surfactant (LSS) was then injected in four different steps denoted by LSS1-NC, LSS2-N, LSS3-NC and LSS4-N. LSS-N is the LSS with NaCl only and the LSS-NC is the one with both NaCl and $CaCl_2$ (See Table 1). The X-ray tomography was performed during the injections. The imaging in one scan took about 18 sec and the time interval between two scans was approximately two minutes. The pixel size of the projections was 3.25μm and the vertical field of view for camera was 2866μm. The number of scans per injection step is shown in the last column of Table 2.

Table 1: composition of the brines and surfactant solutions

Brine	NaCl [g/l]	$CaCl_2.2H_2O$ [g/l]	$MgCl_2.6H_2O$ [g/l]	$^*M^{2+}/M^+$	ionic strength [mol/l]
HSW	29.250	2.210	0.305	0.033	0.5561
LSW-N	3.25	-	-	0	0.0556
LSW-NC	3.202	0.0404	-	0.005	0.0556
LSS-N	0.5 wt% surfactant dissolved in LSW-N				
LSS-NC	0.5 wt% surfactant dissolved in LSW-NC				

$^*M^{2+}/M^+$ is the molar ratio of divalent to monovalent cations.

Table 2: details of injection and image acquisition

injection step	injection	flow rate (ml/min)	duration (≈min)	*PVI	scan No.
1	Oil injection 1	0.004	35	7	1-18
2	Oil injection 2	0.04	10	20	19-23
3	HSW1	0.004	15	3	24-31
4	HSW2	0.008	15	6	32-39
5	LSS1-NC	0.008	20	8	40-49
6	LSS2-N	0.008	20	8	50-58
7	LSS3-NC	0.008	20	8	59-69
8	LSS4-N	0.008	20	8	70-81

***PVI** was the injected volume in terms of number of pore volume of the whole core. The pore volume of the core with 10mm length was roughly 0.02ml.

Image Processing. The reconstruction of 3D tomographic data sets from 2D projections was obtained during the injection experiment using *ImageJ*. The analyzed height was 2447μm and the analyzed volume was about 964 million voxels in each model. The images were denoised by an anisotropic diffusion filtering (Tschmperlé and Deriche 2005) which is an effective denoising technique that preserves edges. The filtering was implemented in *Xlib* plugin (Münch 2015) of *ImageJ*. Statistical Region Merging (Nock and Nielsen 2004) was used for segmentation. Afterwards, the moment-preserving thresholding (Tsai 1985) was used to segment the water phase and the *Default* thresholding method in *ImageJ* was used to extract the pore volume. The oil phase was then obtained by subtracting the water images from pore volume images. As a cleaning cut-off, any object smaller than 3^3 voxel was removed from the 3D models. The largest cluster in each 3D data set of oil was assumed to be the oil connected pathway and the rest of the clusters were considered the oil ganglia. Water phase was also treated in the same manner. The 3D size analysis of oil clusters was obtained in *CTAn*. The phase volume and Euler characteristic were calculated using *BoneJ* plugin (Doube et al. 2010) in *ImageJ*.

RESULTS AND DISCUSSION

The largest oil cluster was considered the oil connected pathway and the rest of the clusters were assumed to be the oil ganglia. The same assumption was made for the water phase. The total phase is therefore the summation of the connected pathway and ganglia. χ_{oT}, χ_{oG}

and χ_{oP} are the Euler characteristic of the total oil phase, oil ganglia and oil connected pathway, respectively. χ_{wT}, χ_{wG} and χ_{wP} denote the Euler characteristic of the total water phase, water ganglia and water connected pathway, respectively. The temporal resolution was 2 *min*.

Source of topological hysteresis in imbibition and drainage. The Euler characteristics of the total oil phase (χ_{oT}) vs S_w at high salinity water (HSW) injection is different from that at drainage, as shown in Figure 1. Therefore χ_{oT} might have a hysteretic behavior at drainage and imbibition processes. χ_o for the pathway and ganglia of the oil phase were calculated and plotted separately to investigate the effect of ganglion dynamics and connected pathway on the hysteresis of the oil phase connectivity. As shown in Figure 1, hysteresis is apparent in χ_{oG} of the oil ganglia vs water saturation. χ_{oG} is similar to χ_{oT}. However, the connected pathway does not show hysteresis in drainage and imbibition; i.e. cause of the hysteresis in χ_{oT} for the total oil phase is the ganglia part of the phase. In the case of the wetting phase (water), χ_{wG} and χ_{wT} are also similar. Although the data seem more scattered, it still seems that there is also some hysteresis in χ_w between drainage and imbibition for the water ganglia (χ_{wG}) and the total water phase (χ_{wT}). Similar to the oil connected pathway, the water connected pathway has nearly no hysteresis in drainage and imbibition. Therefore, the hysteresis in connectivity (topology) of both the wetting and nonwetting phases in drainage and imbibition could be caused by the ganglia part of each phase. The creation or breakage of redundant connections is likely to be the main cause of topology change in the connected pathways. On the other hand, a broader range of events including snap-off, Hains jumps, redundant connections and coalescence change the topology of the ganglia. As a result, the topology of the ganglia resembles that of the total phase where all possible events collaborate in changing the topology (See Figure 1).

Euler characteristic of the nonwetting and wetting phases. The ranges of χ for the wetting and nonwetting phases are slightly different. The redundant connections of the connected pathway could be more stable in the wetting phase i.e. they may not break easily as they have strong contact with the rock grains. Therefore, further creation or disappearance of the redundant connections could be minimized. On the other hand, connected pathway in the nonwetting phase (oil) most likely creates connections frequently with the numerous clusters of the oil ganglia. In other words, topology of water connected pathway could evolve mainly by *film flow/film expansion* while topology of oil connected pathway could evolve mainly by *jump-and-coalescence*. These changes could explain that larger topological variations in the nonwetting connected pathway occur than in the wetting connected pathway (See Figure 1).

Euler characteristic is an additive function. This means that adding χ_{oP} to χ_{oG} results in χ_{oT}; and adding χ_{wP} to χ_{wG} results in χ_{wT}. χ_{oP} and χ_{wP} are both negative, with χ_{oP} representing larger absolute values. Figure 1 shows also that χ_{oG} is larger than χ_{wG} ($S_w \approx 0.51–0.73$). Therefore χ_{oT}, on average, is larger than χ_{wT}; and nonwetting phase is in general more disconnected than the wetting phase ($S_w \approx 0.51–0.73$). However, the nonwetting phase is slightly more connected when $S_w < 0.51$.
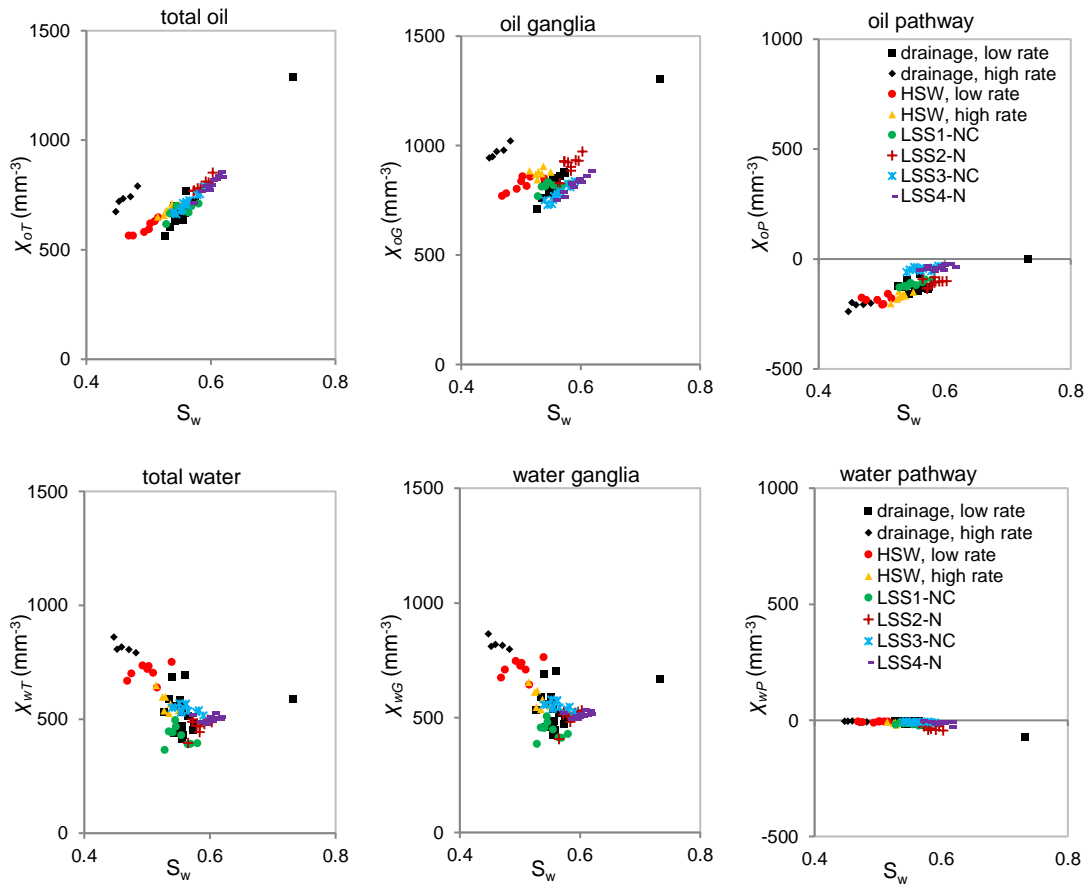
Figure 1: Euler characteristic of water and oil phases for the total phase (ganglia plus connected pathway), ganglia and connected pathway.

<u>Pore geometry and topology of the wetting connected pathway.</u> As mentioned in previous section, the total water phase is more connected than the total oil phase in the S_w interval of 0.51–0.73. It is also clear that the connected water pathway has near-zero negative χ_{wP} values while the connected pathway of the oil phase has higher connectivity. This may be caused by the presence of water in smaller pores and channels where oil phase is usually not present. Therefore, water could be trapped and isolated in smaller pores where the nonwetting oil phase would usually have little or no access. In other words, the topology of the wetting connected pathway may be dictated by the geometry of the porous media which is fixed and static. This discussion implies that it is a possibility to link the topological changes of the wetting connected pathway (χ_{wP}) to the possible wettability changes. The reason could be that topology of the connected pathway of water due to its affinity to rock may not change much unless the affinity itself has changed. This is discussed in detail later. On the other hand, it also suggests that the topology of the nonwetting phase is mainly affected by the process (drainage, imbibition, Figure 1) and the dynamics (rate changes, Figure 1) because it may be less affected by pore geometry compared to the wetting phase. Therefore, the topology of the nonwetting phase may describe the process better than that of the wetting phase can. For this reason, the recent

works have mainly focused on the topology of the nonwetting phase to study the pore scale phenomena (Schlüter et al. 2016, Rücker et al. 2015, Armstrong et al. 2016).
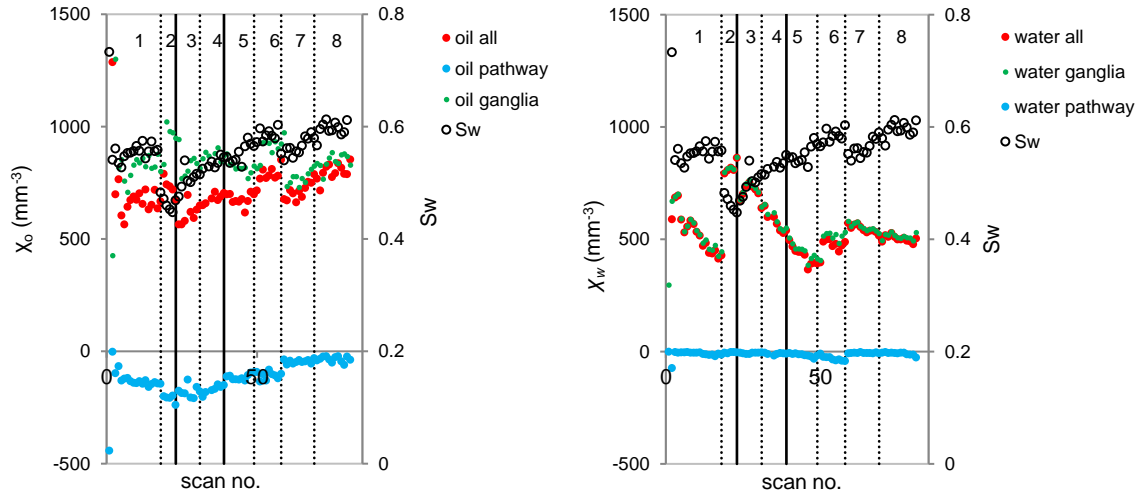
Figure 2: Evolution of χ for oil (*left*) and water (*right*) phases for the whole phase (all), ganglia and connected pathway; χ (*left vertical axis*) is shown by red, green and blue circles. S_w (*right vertical axis*) is shown by open circles. The numbers 1-8 represent the injection steps mentioned in **Table 2**.

<u>Euler characteristic vs time and its reproducibility.</u> Here, the evolution of topology and S_w vs time is discussed. The difference between χ_{wG} and χ_{wT} is insignificant while there is some difference between χ_{oG} and χ_{oT} (Figure 2). The connected pathway of oil becomes closer to the threshold of major fragmentation ($\chi_{oP}=0$) at the start of injection step 7 (third surfactant injection, LSS3-NC) and continues flowing under similar condition in steps 7 and 8 (LSS3-NC and LSS4-N); simultaneously χ_{oG} approaches χ_{oT}.

There is a reduction in S_w at injection step 7 (LSS3-NC), due to oil mobilization upstream of field of view of camera. S_w in step 7 is similar to that in step 5 (See Figure 2). S_w profiles of steps 6 and 8 are also similar. Therefore, it became possible to observe the changes in topology when the S_w history is repeated in surfactant injection. Figure 1 and Figure 2 show that χ_{oT} (oil phase) is almost reproducible in the mentioned injection steps and χ_{oG} (oil ganglia) have minor similarity in these two periods. On the other hand, χ_{wT} (water phase) and χ_{wG} (water ganglia) are different both in value and in trend. For the total nonwetting phase, Schlüter et al. (2016) also stated that the topology depends mainly on the process, not on the system history. The main reason would be the stronger dependency of the wetting phase connected pathway topology on the pore geometry and/or wetting and less dependency of nonwetting phase topology on those parameters, as discussed in the previous section. In case of the connected pathways, χ is not reproducible before and after invasion of upstream oil in neither of the water and oil phases.

<u>IFT, wetting and ionic composition.</u> Here, the implication of surfactant and ionic composition is discussed. Figure 3 shows no immediate change in number of oil clusters after switching to surfactant injection in step 5 (IFT 0.03mN/m). However, the number of

oil clusters almost in the middle of step 5 starts to increase. This could be a sign of oil solubilization by the surfactant. As shown in Figure 2 and Figure 3, χ_o for the total oil phase, oil ganglia and connected pathway of oil level off in step 5 for a short time after which they start increasing when the number of oil clusters starts increasing. Switching the surfactant injection to step 6 (IFT 0.1mN/m) with NaCl as the only salt in the injected solution causes a sharp increase in the number of oil clusters, χ_{oT} and χ_{oG}. Time resolution of 2 *min* is not sufficient to resolve the dynamics seconds after the composition change, but the outcome of the composition change is visible in the mentioned parameters. Smooth increase in S_w (See Figure 2) suggests that the observed behavior in step 6 is probably not due to possible oil mobilization upstream out of the field of view of the camera. The sharp increase in the number of oil clusters and χ_{oT} by switching from LSS-NC (IFT 0.03mN/m) to LSS-N (IFT 0.1mN/m) is also accompanied by a sharp increase in the χ_{wT} and χ_{wG} (See Figure 2 and Figure 3). An opposite behavior was observed for the connected pathway of the water phase. The increase in χ_w is the most obvious change for the connected pathway of water since start of the entire experiment. The change in the topology of the rather stable connected water pathway can be a result of the possible change in the wettability. Step 6 (LSS2-N) is the first step in the entire imbibition without CaCl$_2$ in the injected solution. In a previous work with the same rock type/oil/brine/surfactant system at similar wetting conditions of strongly water wet (Khanamiri et al. 2016b), we observed that low salinity surfactant with only NaCl (LSS-N) changed the wetting to less water wet more than the surfactant solution with both sodium and calcium cations did (LSS-NC). It seems that the ratio of Euler characteristic in the connected pathways of water and oil (χ_{wP}/χ_{oP}) could be used to qualitatively track changes of wettability (See Figure 4). Before surfactant injection, χ_{wP}/χ_{oP} is between 0 and 0.1. Afterwards it starts to variate sharply in surfactant injections with different ionic compositions.
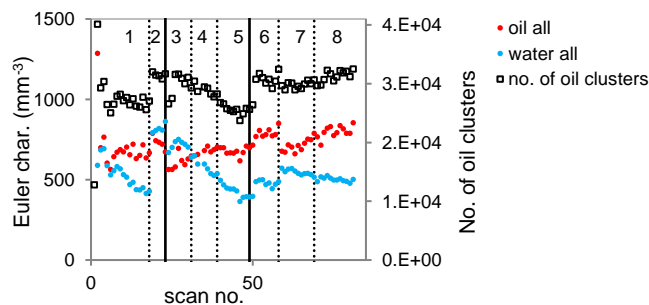
Figure 3: Changes in no. of oil clusters (*black markers/right vertical axis*) are similar to changes in χ_{wT}.

The hypothesis of using χ_{wP}/χ_{oP} to describe the wetting change should be examined by further experiments. The major observation is that changing the ionic composition in the surfactant injection does change the connectivity of the oil and water phases. Bartels et al. (2017a) found that the wetting changes in low salinity water injection led to the fragmentation and reconnection of oil in different pores. In another work, Bartels et al. (2017b) believed that the disconnection and reconnection of oil are characteristic of the ganglion dynamics. However, it is not possible to decide if the fragmentation/connection is driven by ganglion dynamics, the possible wetting change or both. We believe that the

topology of connected pathways, particularly in wetting phase, largely depends on the pore geometry and wetting. Since the pore geometry is fixed, the changes in topology of the connected pathways could be due to the wetting change.
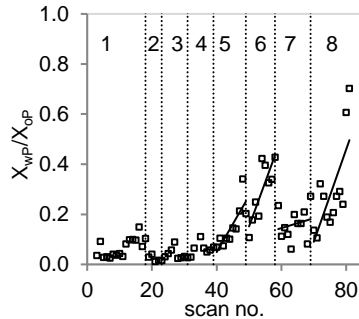
Figure 4: Ratio of the Euler characteristic for connected pathways of water and oil (χ_{wP}/χ_{oP}) vs time varies with varying ionic composition of the injected surfactant (steps 5-8). Four trend lines indicate the sharper changes at steps 6 & 8 (only NaCl) than at steps 5 & 7 (both NaCl & CaCl$_2$). This could be a sign of wetting change.

CONCLUSIONS

In an unsteady state two-phase immiscible flow experiment and by analyzing topology of the ganglia and connected pathways separately, we learned the following.

- The pore scale topology of fluids in two-phase displacement may be determined mainly by the topology of the ganglia, and appears less affected by the topology of the connected pathways.
- The ganglia and the whole phase (ganglia plus connected pathway) show hysteresis in the topology in imbibition and drainage for both wetting and nonwetting phases. The connected pathways of both wetting and nonwetting phases show however insignificant hysteresis in the topology in drainage and the imbibition. Therefore, the hysteresis is likely to be caused by the ganglia part of the phases.
- The topology change in the wetting connected pathway (χ_{wP}) seems to be dictated by the pore geometry and the wetting changes. The topology of the connected pathway of the wetting phase due to its affinity to rock may not change much unless the affinity itself (wettability) has changed.
- Less dependency of the nonwetting phase topology on the pore geometry makes the nonwetting phase topology a suitable criterion to study the displacement process (reported also by Schlüter et al. 2016).
- The ratio of the Euler characteristic for connected pathways of wetting (water) and nonwetting (oil) phases seems to be a descriptor of the wetting change.

ACKNOWLEDGEMENT

REFERENCES

1. Armstrong, RT, JE McClure, MA Berrill, M Rücker, S Schlüter, S Berg, "Beyond Darcy's law: The role of phase topology and ganglion dynamics for two-fluid flow," Physical Review E, (2016) 94, 043113, 1–10.
2. Armstrong, RT, JE McClure, MA Berrill, M Rücker, S Schlüter, S, Berg, "Flow Regimes During Immiscible Displacement," Petrophysics, (2017) Feb, 58 (1), 10–18.
3. Avraam, DG, AC Payatakes, "Flow regimes and relative permeabilities during steady-state two-phase flow in porous media," J. Fluid Mech., (1995) 293, 207–236.
4. Bartels, WB, H Mahani, S Berg, R Menezes, JA van der Hoeven, A Fadili, "Oil Configuration Under High-Salinity and Low-Salinity Conditions at Pore Scale: A Parametric Investigation by Use of a Single-Channel Micromodel," Society of Petroleum Engineers (SPE), SPE Journal (2017a) Feb.
5. Bartels, WB, M Rücker, S Berg, H Mahani, A Georgiadis, A Fadili, N Brussee, A Coorn, H van der Linde, C Hinz, A Jacob, C Wagner, S Henkel, F Enzmann, A Bonnin, M Stampanoni, H Ott, M Blunt, SM Hassanizadeh, "Fast X-Ray Micro-CT Study of the Impact of Brine Salinity on the Pore-Scale Fluid Distribution During Waterflooding," Petrophysics, (2017b) Feb, 58 (1), 36–47.
6. Berg, S, RT Armstrong, A Georgiadis, H Ott, A Schwing, R Neiteler, N Brussee, A Makurat, M Rücker, L Leu, M Wolf, F Khan, F Enzmann, M Kersten, "Onset of Oil Mobilization and Nonwetting-Phase Cluster-Size Distribution," Petrophysics, (2015) Feb, 56 (1), 15–22.
7. Doube, M, MM Kłosowski, I Arganda-Carreras, F Cordeliéres, RP Dougherty, J Jackson, B Schmid, JR Hutchinson, SJ Shefelbine, "BoneJ: Free and extensible bone image analysis in ImageJ," Bone, (2010) 47:1076–9.
8. Herring, AL, EJ Harper, L Andersson, A Sheppard, BK Bay, D Wildenschild, "Effect of fluid topology on residual nonwetting phase trapping: Implications for geologic CO_2 sequestration," Adv. Water Resour. (2013) 62, 47–58.
9. Khanamiri, HH, M Nourani, T Tichelkamp, JÅ Stensen, G Øye, O Torsæter, "Low salinity surfactant EOR with a new surfactant blend: effect of calcium cations," *Energy & Fuels*, (2016a) 30 (2), 984–991.
10. Khanamiri, HH, O Torsæter, JÅ Stensen, "Effect of Calcium in Pore Scale Oil Trapping by Low-Salinity Water and Surfactant Enhanced Oil Recovery at Strongly Water-Wet Conditions: In Situ Imaging by X-ray Microtomography," *Energy & Fuels*, (2016b) *30* (10), 8114–8124.
11. Münch, B; Xlib, http://imagej.net/Xlib, 2015.
12. Nock, R, F Nielsen, "Statistical Region Merging," IEEE Trans. Pattern Anal. Mach. Intell. (2004) 26 (11): 1452–1458.
13. Rücker, M, S Berg, RT Armstrong, A Georgiadis, H Ott, A Schwing, R Neiteler, N Brussee, A Makurat, L Leu, M Wolf, F Khan, F Enzmann, M Kersten, "From connected pathway flow to ganglion dynamics," Geophys. Res. Lett. (2015) 42, 3888–3894.
14. Schlüter, S, S Berg, M Rücker, RT Armstrong, HJ Vogel, R Hilfer, D Wildenschild, "Pore-scale displacement mechanisms as a source of hysteresis for two-phase flow in porous media," Water Resour. Res. (2016), 52, 2194–2205.
15. Tsai, W, "Moment-preserving thresholding: a new approach," Computer Vision, Graphics, and Image Processing, (1985) 29: 377–393.
16. Tschmperlé, D, R Deriche, "Vector-Valued Image Regularization with PDE's: A Common Framework for Different Applications," IEEE Trans. Pat. Anal. Mach, Intell. (2005) 27 (4): 506–517.
17. Youssef, S, E Rosenberg, H Deschamps, R Oughanem, E Maire, R Moks, "Oil ganglia dynamics in natural porous media during surfactant flooding captured by ultra-fast x-Ray microtomography," International Symposium of the Society of Core Analysts, SCA2014-23, Sep (2014), Avignon, France.

Enhanced pore space analysis by use of μ-CT, MIP, NMR, and SIP

Zeyu Zhang [(1)] [(2)], Sabine Kruschwitz [(2)] [(3)], Andreas Weller [(4)], Matthias Halisch [(5)],
Carsten Prinz[(2)]

[(1)] Southwest Petroleum University, School of Geoscience and Technology, Chengdu, China
[(2)] Federal Institute for Material Research and Testing (BAM), D-12205 Berlin, Germany
[(3)] Berlin University of Technology, Institute of Civil Engineering, 13355 Berlin, Germany
[(4)] Clausthal University of Technology, Institute of Geophysics, D-38678 Clausthal-Zellerfeld, Germany
[(5)] Leibniz Institute for Applied Geophysics (LIAG), D-30655 Hannover, Germany

This paper was prepared for presentation at the International Symposium of the Society of Core Analysts held in Vienna, Austria, 27 August – 1 September 2017

ABSTRACT

We investigate the pore space of rock samples with respect to different petrophysical parameters using various methods, which provide data upon pore size distributions, including micro computed tomography (μ-CT), mercury intrusion porosimetry (MIP), nuclear magnetic resonance (NMR), and spectral induced polarization (SIP). The resulting cumulative distributions of pore volume as a function of pore size are compared. Considering that the methods differ with regard to their limits of resolution, a multiple length scale characterization of the pore space geometry is proposed, that is based on a combination of the results from all of these methods. The findings of this approach are compared and discussed by using Bentheimer sandstone. Additionally, we compare the potential of SIP to provide a pore size distribution with other commonly used methods (MIP, NMR). The limits of resolution of SIP depend on the usable frequency range (between 0.002 and 100 Hz). The methods with similar resolution show a similar behavior of the cumulative pore volume distribution in the overlapping pore size range. The methods μ-CT and NMR provide the pore body size while MIP and SIP characterize the pore throat size. Using this difference, the average pore body to throat ratio is determined to be about three for the Bentheimer sandstone.

Our study shows that a good agreement between the pore radii distributions can only be achieved if the curves are adjusted considering the resolution and pore volume in the relevant range of pore radii. The MIP curve with the widest range in resolution should be used as reference

INTRODUCTION

The transport and storage properties of reservoir rocks are determined by the size and arrangement of the pores. Different methods have been developed to determine the pore size distribution of rocks. These methods are based on different physical principles. Therefore, it can be expected that the methods recognize different geometries and sizes. The pore size ranges in which the methods are most sensitive are necessarily different [1].The authors of the report [2] state that no experimental method provides the absolute value of parameters such as porosity, pore size, surface area, and surface roughness. The selection of a method of characterization has to consider the type of material and the parameter of interest. A variety of studies has been performed to compare the different experiments with different aims, for example comparing capillary pressure method and NMR [3]. This study presents an approach to describe and quantify the pore space geometry of Bentheimer sandstone using methods with different resolution. One sample is investigated by µ-CT, MIP, NMR, and SIP. The resulting pore size distributions are compared.

METHODOLOGY

The experimental methods include mercury intrusion porosimetry (MIP) [4], nuclear magnetic resonance (NMR) [5], micro computed tomography (µ-CT) [6], and spectral induced polarization (SIP) [7].

µ-CT can only resolve the part of the pore space with pore sizes larger than the resolution of the µ-CT image. Considering a voxel size of 1.75 µm of the µ-CT image and a minimum extension of pores of two voxels in one direction that can be separated by the algorithm, a minimum pore size of 3.5 µm (or minimum pore radius 1.75 µm) has to be regarded as effective resolution limit of µ-CT. Therefore, the pore volume determined by µ-CT ignores the pore space with radii smaller than 1.75 µm. For this study, a GE nanotom X-ray µ-CT has been used. For pore network separation, a combination of manual thresholding and watershed algorithms is applied to achieve the qualitatively best separated pore space. Additionally, separation results have been cross checked with SEM data. More details on this digital image analysis workflow can be found in [8].

From MIP method, the entry sizes of pores and cavities can be determined according to the Washburn-equation [9]:

$$r = -\frac{2 \cdot \gamma \cdot \cos\theta}{p},$$ (1)

with r being the pore throat radius, $\gamma = 0.48$ N/m the surface tension of mercury, $\theta = 140°$ the contact angle, and p the pressure. The MIP experiments have been conducted with the PASCAL 140/440 instruments from Thermo Fisher [10], which covered a pressure range between 0.015 and 400 MPa corresponding to a pore radius range from 1.8 nm to 55 µm. The resulting pore volume is regarded to be the total pore volume that is used to calculate the porosity of the sample.

From NMR, considering the capillary tube model with straight cylindrical pores of uniform radius r, we get the following relationship [3]:

$$r = 2\rho T_2 , \tag{2}$$

with ρ being the surface relaxivity, and T_2 the transverse relaxation time. The signal amplitude at a given relaxation time corresponds to the pore volume related to the pore radius determined by equation 2. The NMR experiments have been performed with a Magritek Rock Core Analyzer equipment operating at a Larmor frequency of 2 MHz at room temperature (~ 20°C) and ambient pressure. After drying at 35°C for more than 48 hours in vacuum, the sample is fully saturated with low conductivity brine. NMR measurements can be calibrated to get the porosity of the sample. The early time relaxation signal corresponds to the total water content. The range of pore radii depends on the value of surface relaxivity.

Another approach to derive a pore size distribution is based on the SIP method. Debye decomposition [11] is used to determine the electrical relaxation time distribution as well as the total chargeability from complex conductivity spectra. To transform the relaxation time distribution into a pore size distribution, we use the approach proposed by [12] and applied by [13] for the Stern layer polarization model:

$$r = \sqrt{2\tau D_{(+)}} , \tag{3}$$

with $D_{(+)}$ being the diffusion coefficient of the counter-ions in the Stern layer and τ being the relaxation time. Originally, this equation describes the relation between the radius of spherical particles in an electrolyte solution and the resulting relaxation time. Though it remains discussible whether the radius of spherical grains can be simply replaced by the pore radius [14], we generally follow this approach. Additionally, we assume a constant diffusion coefficient $D_{(+)} = 3.8 \times 10^{-12}$ m²/s as proposed by [15]. With the pore radius r calculated from relaxation time τ, we compile a curve showing the cumulative volume fraction as a function of pore radius. The signal amplitude at a given relaxation time corresponds to the pore volume related to the pore radius determined by equation 3.

SIP spectra were recorded using a four-electrode sample holder as described by [16]. The complex conductivity spectra were acquired with the impedance spectrometer ZEL-SIP04 [17] in the frequency range between 0.002 and 100 Hz under ambient conditions at a constant temperature of about 20 °C. The sample was fully saturated with a sodium-chloride solution with a conductivity of 100 mS/m. At least two measurements were performed for the sample to verify the repeatability. The SIP method resolves only a range of pore radii that depends on the diffusion coefficient. Using $D_{(+)} = 3.8 \times 10^{-12}$ m²/s in equation 3, we get a range of pore radii between 0.1 and 25 µm.

SAMPLE MATERIAL

This study investigated a Bentheimer sandstone sample BH5-2. Being exposed in outcrops just east of the Dutch-German border in the vicinity of Bad Bentheim, the shallow-marine Bentheimer Sandstone was deposited during the Early Cretaceous and forms an important reservoir rock for petroleum [18]. The sample investigated in our study is characterized by a porosity of 23 %, a permeability of 425 mD and a specific internal surface of 0.3 m²/g. Figure 1 showcases an SEM (A) image, as well as a 2D CT slice of the material (B) and a 3D view upon the pore system (C).
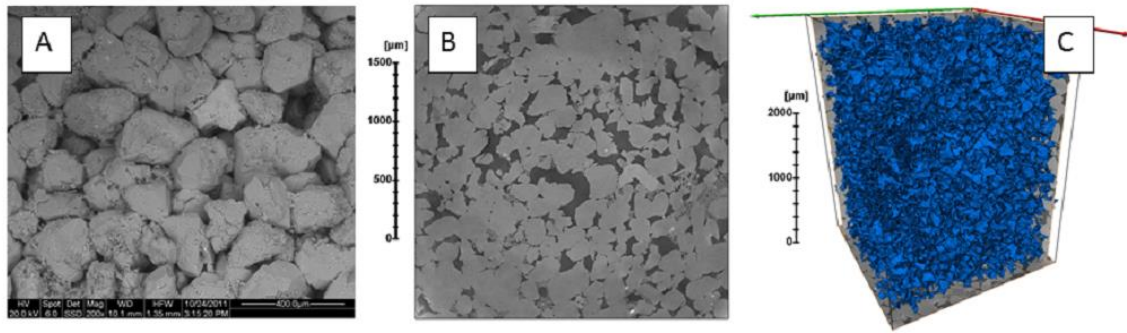
Figure 1: SEM (A) and 2D (B) and 3D (C) CT views upon the minerals and pore structure of the investigated sample of Bentheimer sandstone.

RESULTS AND DISCUSSION

The pore radius distribution is described by the relationship between the parameter V_c and the pore radius r, which is presented in a double logarithmic plot showing the relation log (V_c) versus log(r) following the procedure described in [19]. V_c represents the cumulative volume fraction of pores with radii less than r, which is expressed by

$$V_c = \frac{V(<r)}{V},$$

(4)

with V being the total pore volume, and $V(<r)$ the cumulative volume of pores with radii less than r.

The MIP curve gets a fixed position in the plot shown in Figure 2. It covers the widest range of pore radii and the full range of V_c. All other curves have to be adjusted considering the limits of the range of pore radii. The μ-CT curve uses the absolute pore radii determined by the image processing algorithm. The maximum of the μ-CT curve corresponds to $V_c = 1$ because no larger pore size has been detected by other methods. The fractional porosity of the sample as determined by MIP reaches 0.238. The porosity determined by μ-CT reaches only 0.184 (Table 1). This value corresponds to a fraction of 0.773 of the porosity determined by MIP. Therefore, the minimum of the μ-CT curve at the pore radius of 1.75 μm has been adjusted at $V_c = 1 - 0.773 = 0.227$. We observe a strong shift of the μ-CT curve to larger pore radii in comparison with MIP. This shift can be explained by the different pore geometries sensed by the two methods. MIP records the pore throat radius

that is the entry radius to fill the pores with mercury. Although MIP might not represent the true distribution of pore throats due to the restricted accessibility to the pores, the dominant pore radius of Bentheimer sandstone is relatively large so that this problem is of minor importance for this sample. The μ-CT method provides the average pore radius calculated from the equivalent pore diameter which is larger than the pore throat radius and corresponds to the average pore body radius. Considering the median pore radius at $V_c = 0.5$ for the two methods, we get a ratio of about three between the pore body and pore throat radius of the investigated Bentheimer sandstone sample.
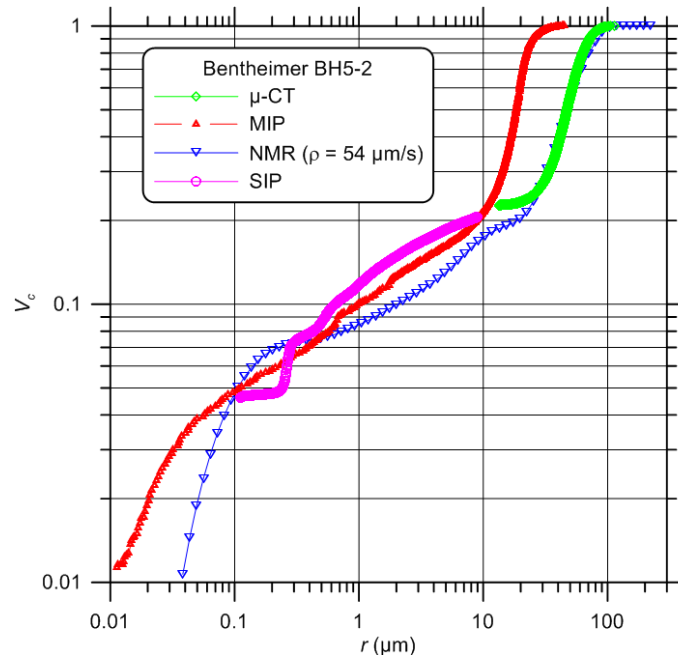
Figure 2: The comparison of V_c-r curves determined from μ-CT, MIP, NMR and SIP for sample BH5-2.

The NMR method is sensitive to the pore body radius, too. Therefore, we expect a similar $V_c - r$ - curve for NMR and μ-CT for the larger pore radii. If we assume a coincidence of the two curves at $V_c = 0.5$ we get a surface relaxivity of $\rho = 54$ µm/s.

The relaxation time distribution derived from SIP is attributed to a range of pore radii between 0.1 and 10 µm. We assume that the IP signals are caused by the ion-selected active zones in the narrow pores that are comparable with the pore throats. Therefore, we take the values of V_c at the minimum and maximum radius from the MIP curve. This procedure results in fair agreement between SIP and MIP curves in the relevant range of pore radii. In comparison with MIP, a slight overestimation of V_c is observed for pore radii larger than 0.3 µm.

The slope (s) of the curve log (V_c) versus log (r) is related to the fractal dimension D of the pore volume ($D = 3 -s$) [3]. We observe a varying slope in the investigated range of pore radii. The only range of more or less constant slope, which extends from pore radius 0.1 µm to 10 µm, corresponds to a fractal dimension $D = 2.678$ from MIP or $D = 2.618$ from SIP.

The measured porosity values as well as the ranges of pore radii of the used methods are compiled in Table 1. Different methods are characterized by different resolution, and the resulting porosities depend on the resolution.

Table 1: Measured porosity and pore radii range of sample BH5-2.

Methods	*r_min*	*r_max*	recognized porosity
	µm	µm	%
µ-CT	1.1	114	18.4
MIP	0.002	45	23.8
NMR	0.001	324	22.8
SIP	0.1	10	

CONCLUSIONS

The pore size distribution of Bentheimer sandstone can be determined by various methods (MIP, µ-CT, NMR, SIP) with different resolutions. The dominant pore throat radius of Bentheimer sandstone determined by MIP is about 14 µm. The µ-CT indicates a dominant pore body radius of about 47 µm. Because of the missing resolution for pore radii smaller than 1.75 µm, µ-CT underestimates the pore volume and porosity. NMR and µ-CT provide a similar pore radius distribution for larger pores if a surface relaxivity of 54 µm/s is selected. Only a restricted range of pore radii (0.1 µm to 10 µm) can be resolved by SIP. The methods µ-CT and NMR indicate the distribution of pore body radii, while MIP and SIP represent the distribution of pore throat radii. Comparing the two distributions, an average ratio between the radii of pore body to pore throat of about three has been determined for the investigated sample of Bentheimer sandstone. The $V_c - r$ curves has proved to be suitable for a comparison of the pore radii distribution resulting from the different methods. Our study shows that a good agreement between the pore radii distributions can only be achieved if the curves are adjusted considering the resolution and pore volume in the relevant range of pore radii. The MIP curve with the widest range in resolution should be used as reference.

ACKNOWLEDGEMENTS

REFERENCES

1. Meyer, K., P. Klobes, and B. Röhl-Kuhn, 1997, *Certification of reference material with special emphasis on porous solids*: Crystal Research and Technol., **32**, 173-183.
2. Rouquerol, J., D. Avnir, D. C. W. Fairbridge, D. H. Everett, J. H. Haynes, N. Pernicone, J. D. F. Ramsay, K. S. W. Sing, and K. K. Unger, 1994, *Recommendations for the characterization of porous solids (Technical Report)*: Pure and Appl. Chem., **66**, 1739-1758.
3. Zhang, Z., and A. Weller, 2014, *Fractal dimension of pore space geometry of an Eocene sandstone formation*: Geophysics, **79**, D377-387. doi:10.1190/GEO2014-0143.1.
4. Rübner, K., and D. Hoffmann, 2006, *Characterization of mineral building materials by mercury-intrusion porosimetry*: Particle and Particle Systems Characterization, **23**, 20-28.
5. Weller, A., S. Nordsiek, and W. Debschütz, 2010, *Estimating permeability of sandstone samples by nuclear magnetic resonance and spectral-induced polarization*: Geophysics, **75**, E215 – E226. doi: 10.1190/1.3507304.
6. Schmitt, M., M. Halisch, C. Müller, and C. P. Fernandes, 2015, *Classification and quantification of pore shapes in sandstone reservoir rocks with 3-D X-ray micro-computed tomography*, Solid Earth Discuss., **7**, 3441-3479. doi:10.5194/sed-7-3441-2015.
7. Kruschwitz, S. F., A. Binley, D. Lesmes, and A. Elshenawy, 2010, *Textural controls on low-frequency electrical spectra of porous media*: Geophysics, **75**, 4, WA113–WA123.
8. Halisch, M., Schmitt, M., and Fernandes, Celso Peres, 2016, *Pore Shapes and Pore Geometry of Reservoirs Rocks from µ-CT Imaging and Digital Image Analysis*: Proceedings of the Annual Symposium of the SCA 2016, Snowmass, Colorado, USA, SCA2016-093.
9. Washburn, E. W., 1921, *The dynamics of capillary flow*: Physical Review, **17**, 3, 273-283.
10. Mancuso, C., C. Jommi, and F. D'Onza, 2012, *Unsaturated Soils: Research and Applications*, Volume 1, 123-130. doi: 10.1007/978-3-642-31116-1, ISBN: 978-3-642-31115-4 (Print).
11. Nordsiek, S., and A. Weller, 2008, *A new approach to fitting induced-polarization spectra*: Geophysics, **73**, 6, F235-F245. doi: 10.1190/1.2987412.
12. Schwarz, G., 1962, *A theory of the low-frequency dielectric dispersion of colloidal particles in electrolyte solution*: Journal of Physical Chemistry, **66**, 2636-2642. doi: 10.1021/j100818a067.
13. Revil, A., K. Koch, and K. Holliger, 2012, *Is it the grain size or the characteristic pore size that controls the induced polarization relaxation time of clean sands and sandstones?*: Water Resources Research, **48**, W05602. doi: 10.1029/2011WR011561.

14. Weller, A., Z. Zhang, L. Slater, S. Kruschwitz, and M. Halisch, 2016, *Induced polarization and pore radius – a discussion*: Geophysics, **81**, 5, D519-526. doi:10.1190/GEO2016-0135.1.

15. Revil, A., 2013, *Effective conductivity and permittivity of unsaturated porous materials in the frequency range 1 mHz-1GHz*: Water Resources Research, **49**, 306-327. doi: 10.1029/2012WR012700.

16. Schleifer, N., A. Weller, S. Schneider, and A. Junge, 2002, *Investigation of a Bronze Age plankway by spectral induced polarization*: Archeological Prospection, 9, 243–253. doi: 10.1002/arp.194.

17. Zimmermann, E., A. Kemna, J. Berwix, W. Glaas, and H. Vereecken., 2008, *EIT measurement system with high phase accuracy for the imaging of spectral induced polarization properties of soils and sediments*: Measurement Science and Technology, **19**, 9, 094010. doi: 10.1088/0957-0233/19/9/094010.

18. Dubelaar, W.C., and T. G. Nijland, 2015, *The Bentheim Sandstone: geology, petrophysics, varieties and its use as dimension stone*. In: Lollino, G., Giordan, D., Marunteanu, C., Christaras, B., Yoshinori, I., Margottini, C. (Eds.), *Engineering Geology for Society and Territory*, Springer International Publishing, Switzerland, **8**, 557-563.

19. Weller A., Y. Ding, Z. Zhang, M. Kassab, and M. Halisch, 2016, *Fractal dimension of pore space in carbonate samples from Tushka Area (Egypt)*: Proceedings of the Annual Symposium of the SCA 2016, Snowmass, Colorado, USA, SCA2016-085.

Measuring Methane Adsorption in Shales Using NMR

M.J. Dick[1], C. Muir[1], D. Veselinovic[1], and D. Green[1]

[1]*Green Imaging Technologies, Fredericton, NB, Canada*

ABSTRACT

Despite the downturn in oil and gas prices, shale reservoir production continues and is expected to grow as prices normalize. The total gas in place is a measure of the total natural gas content in a shale which consists of both free gas in the porous spaces of the shales and adsorbed gas on the surface of the shale matrix. The total gas in place is dependent on the pore pressure and temperature and is vital to the profitable development of a shale reservoir. Traditionally, gas isotherms are measured by exposing the core to helium and methane at ever increasing pressure while tracking the volume of gas absorbed and adsorbed. These experiments involve destruction of the core and provide no information on the pore size distribution.

Free gas can be distinguished from adsorbed gas using NMR T_2 distributions and thus the total gas in place can be determined using NMR. This proves advantageous as the NMR analysis can be completed without destruction of the shale core while providing pore size distributions.

In this work, we present a method for measuring absorbed gas, adsorbed gas and total gas content in shales using NMR. T_2 measurements were taken over time after the introduction of methane to both a sandstone and a shale. Methane absorption was observed in both rocks, while adsorption was only observed in the shale. T_1-T_2 maps acquired in the shale show that methane enters both organic and inorganic pores at similar rates.

INTRODUCTION

Shales are an important source of natural gas. Gas in shales can be absorbed as free gas in the pore network or adsorbed on the surface of the organic material. Gas storage in shales is characterized by plots of the quantity of adsorbed gas, free gas and/or total sorbed gas at different pressures called isotherms [1].

The quantity of free and adsorbed gas is traditionally measured volumetrically using a system of two cells, a reference cell and a sample cell, which are separated by a valve. A crushed rock sample is placed in the sample cell. The reference cell is filled with a gas at a known pressure. The valve is opened and the gas from the reference cell expands into the sample cell and the pressures in the two cells equalize. The procedure is performed first with a non-adsorbing gas, such as helium, to determine the void volume, or free gas content, in the rock sample via the difference in temperature and pressure before and after

opening of the valve between the two cells. The system is then vacuumed to remove the gas, the reference cell is filled with an adsorbing gas and the procedure is repeated. When the valve is opened and the adsorbing gas expands into the sample cell it will fill the void volume and adsorb on the sample. Therefore, the amount of adsorption can be calculated by subtracting the free gas content. The expansion of the gases is repeated at numerous pressures to generate isotherms. The disadvantages of this traditional method are that the sample is destroyed for the measurement, and no information is acquired on the size of the pores occupied by the gas.

NMR can be used to generate gas isotherms. The advantages of NMR measurements are that the samples will remain intact and the measurements will provide information on the samples' pore size distributions. Measuring gas in shales is challenging with NMR due to the low hydrogen index of gas and the small pore volume of shales, both of which result in low NMR signal. However, with recent advances in NMR hardware, gas measurements in shales are possible. In this study we set out to use NMR to generate isotherms by distinguishing the amount of free gas and adsorbed gas in a rock. This paper presents our initial results of the measurement of total gas in place in a shale.

EXPERIMENTAL

A shale core plug and a sandstone core plug were chosen for the study. The characteristic information on each rock studied is shown in Table 1. Each core sample was confined hydrostatically by fluorinert to a pressure of 2500 psi in an Oxford Instruments P5 overburden NMR probe [2] in an Oxford Instruments GeoSpec 2-75 rock core analyzer [3]. The samples were evacuated with a vacuum pump, then as received or dry T_2 measurements were taken before the introduction of methane. Methane was then introduced to the samples at 2000 psi. T_2 measurements were acquired at 2 minute intervals for the first hour, then at 15 minute intervals for the following 3 hours, then at 60 minute intervals for the remainder of the experiment in the sandstone and the shale. These T_2 measurements were employed to retrieve the total gas content present in each rock as a function of time. T_1-T_2 maps were also acquired with and without methane for the shale. Acquisition parameters for the T_2 measurements and T_1-T_2 maps are shown in Table 2. Data acquisition and analysis of the T_2 and T_1-T_2 data was achieved via Green Imaging Technologies software [4]. Pore volumes were determined using NMR volumes from T_2 measurements for both the shale and sandstone. To fully saturate the rocks, the shale was pressure saturated with brine at 10 000 psi in a pressure cell for three days while, the sandstone was brine saturated in a vacuum saturation apparatus.

RESULTS

As mentioned above, the gas absorption/adsorption characteristics were studied for a shale (Eagle Ford 1) and a sandstone (Carbon Tan 1). These rocks were chosen due to the

expected difference in their gas absorption/adsorption characteristics. The higher surface to volume ratio of the pores in the shale coupled with its higher organic content should make the shale much more likely to exhibit adsorption of methane. The presence of organic content in the shale (as received) was confirmed prior to the methane absorption/adsorption experiment using T_1-T_2 NMR maps recorded at different temperatures (Figure 1). Organic content is visible in the T_1-T_2 maps as intensity off diagonal at each temperature. The significant increase in intensity observed in the 70ºC data reflects the organic content liquefying with temperature and as a result its T_1 becoming longer bringing more intensity into the scale of the map. This increases the observed NMR porosity of the shale.

The first set of gas experiments were to record a series of T_2 scans as a function of time for both the sandstone and the shale. These scans provided the total gas content in each rock as a function of time. Specifically, the upper panel of Figure 2 shows the volume of methane (@ 2000 PSI) for both rocks as a function of time. From this data, it is clear that there is a difference in behaviour for each rock. At first both rocks are very quickly filled with a volume of methane. For the sandstone, it is filled to approximately its pore volume via absorption. For the shale, it is filled to 75% of its pore volume via absorption. This absorption is most likely occurring in the small fractures and larger pores. After this initial absorption, the sandstone shows no more appreciable increase in volume. Conversely, the shale shows an increase in gas content over a period of several hours. After approximately 1.5 hours the shale has been filled to its pore volume via absorption. The shale continues to take on approximately another 35% of a pore volume due to adsorption over a period of several hours. This yields a final gas content consisting of approximately 65% absorbed gas and 35% adsorbed gas which is consistent for shales with methane pressure around 2000 PSI [5].

The lower panel of Figure 2 shows the total gas content (adsorbed and absorbed) of both the shale and the sandstone. In order to retrieve the total gas content, the volume of methane (scm^3) at 2000 PSI (Figure 2 – upper panel) was converted to the volume of methane at standard temperature and pressure (15ºC and 1 atm) using the ideal gas equation. The converted volume was then divided by the bulk volume of each rock yielding a total gas content in units of scm^3/cm^3. For the shale, a total gas content of approximately 8 scm^3/cm^3 was observed and this is consistent with other shales [5].

One of the main goals of this work was to see if NMR could be used to distinguish adsorbed gas from absorbed gas. Figure 3 shows a comparison of two background subtracted T_2 spectra taken at different times as the shale was being filled with methane. The peaks in the spectra represent the different pore networks in the shale. The red spectrum was taken a few minutes after the introduction of methane into the rock where absorption dominates. The blue spectrum was taken several hours after the introduction of methane where both absorption and adsorption are occurring. The increase in observed methane volume when going from the red trace to the blue trace seems to be occurring in both pore networks equally. There is no distinction between absorption and adsorption. This is not unexpected as the adsorbed methane could have a T_2 very similar to the absorbed methane in the pores of this shale. In addition, the adsorbed and absorbed methane are likely in fast exchange

with one another making distinguishing between them impossible. The ability to distinguish between adsorbed and absorbed methane may be dependent on the shale being studied. Other shales may have pore networks where conditions exist where adsorption could be distinguished from adsorption. Gu et al. have reported seeing differences in T_2 spectra due to adsorption vs. adsorption of methane in a shale [6].

Figure 4 shows a T_1-T_2 map of shale Eagle Ford 1 taken a few hours after the introduction of methane. If the map in Figure 4 is compared to the map in the left-hand panel of Figure 1 (as received), conclusions about where the methane has gone once it entered the shale can be drawn. The long tail in the map at T_2 values greater than 1 ms corresponds to methane filling into the large inorganic pores of the shale. Conversely, the increase in intensity overlapped with the organic content observed ($T_2 < 1$ ms) in the left-hand panel of Figure 1 corresponds to methane entering the smaller organic pores of the shale. The methane seems to be filling all the pores equally within a few hours of methane being introduced into the rock.

CONCLUSION

A method has been presented for using NMR to measure absorption, adsorption and total gas content in shales. T_2 measurements were taken over time after the introduction of methane to both a sandstone and a shale. Methane absorption was observed in both rocks, while adsorption was only observed in the shale. T_1-T_2 maps were also acquired in the shale. They showed that methane filled both the inorganic pores and organic pores equally. This agrees with changes in the T_2 spectra of the shale. T_2 peaks originating from inorganic and organic pores grow at equal rates after the introduction of methane. No distinction was made between adsorbed and absorbed methane in the shale. This is likely due to fast exchange between the absorbed and adsorbed gas. Additionally, the absorbed and adsorbed gas could have very similar T_2 values.

FUTURE WORK

This paper summarizes the preliminary results of our investigation looking into using NMR to measure gas adsorption and absorption. As the investigation is preliminary, there is still a significant amount of work to complete. First, we will repeat the experiment on the shale sample, acquiring T_2 measurements at shorter intervals initially to get more data relating to absorption. We will then run the experiment for a week to determine whether more methane is adsorbed at later times. We will also acquire T_1-T_2 maps during this longer experiment to see if any changes in the maps over time could be used to distinguish absorption from adsorption. The ultimate goal of the work is to generate a gas isotherm using NMR, so we will repeat the experiment in the shale at several different pressures to generate the isotherm. Finally, we will acquire T_2 measurements on shales of different origins to investigate how the isotherms may vary with shale type.

REFERENCES

1. Alexander, T., Baihly, J., Boyer, C., Clark, B., Waters, G., Jochen, V., Le Calvez, J., Lewis R., Miller, C. K., Thaeler, J. and Toelle, B. E., "Shale Gas Revolution," *Oilfield Review,* (2011), **23**, 3, 40-55.

2. P5 Overburden Probe User Manual, Version 1, Oxford Instruments, Green Imaging Technologies.

3. Geo-Spec 2-75 User Manual, Version 1.8, Oxford Instruments.

4. GIT Systems and LithoMetrix User Manual, Revision 1.9, Green Imaging Technologies

5. Lu, X.-C., Li, F.-C., and Watson, A. T., "Adsorption measurements in Devonian shales," *Fuel*, (1995), **74**, 4, 599-603.

6. Gu, Z., Liu, W., Sun, W., Hu, Z., "NMR Response of Methane in Gas Shale," *Unconventional Resources Technology Conference*, August 1-3 2016, URTeC 2438441.

Tables and Figures

Core Sample	Sandstone (Carbon Tan 1)	Shale (Eagle Ford 1)
Origin	Utah, USA	Eagle Ford, Texas, USA
Core Diameter (cm)	2.51	3.81
Core Length (cm)	5.08	4.79
Bulk Volume (mL)	25.14	54.61
Dry Core Mass (g)	55.54	129.16
Pore Volume (mL)	4.10	2.60
Porosity (p.u.)	16.3	4.76

Table 1. Properties of rock samples.

Measurement	T_2	T_1-T_2
Recycle delay (ms)	750	1000
Tau (µs)	50	50
Number of Echoes	5000	5000
Number of Steps	N/A	30
Filter Width (kHz)	125	125
90º Pulse Length (µs)	7.5	7.4
180º Pulse Length (µs)	15.2	15.0

Table 2. Acquisition parameters for T_2 and T_1-T_2 measurements of sandstone (Carbon Tan 1) and shale (Eagle Ford-1).
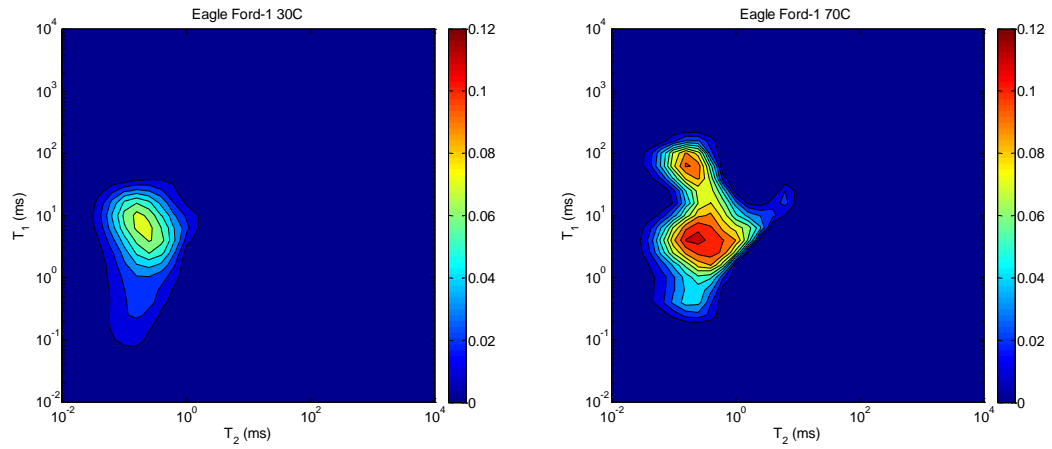
Figure 1. T_1-T_2 NMR maps for the as received shale sample (Eagle Ford 1) tested taken at 30ºC and 70ºC.
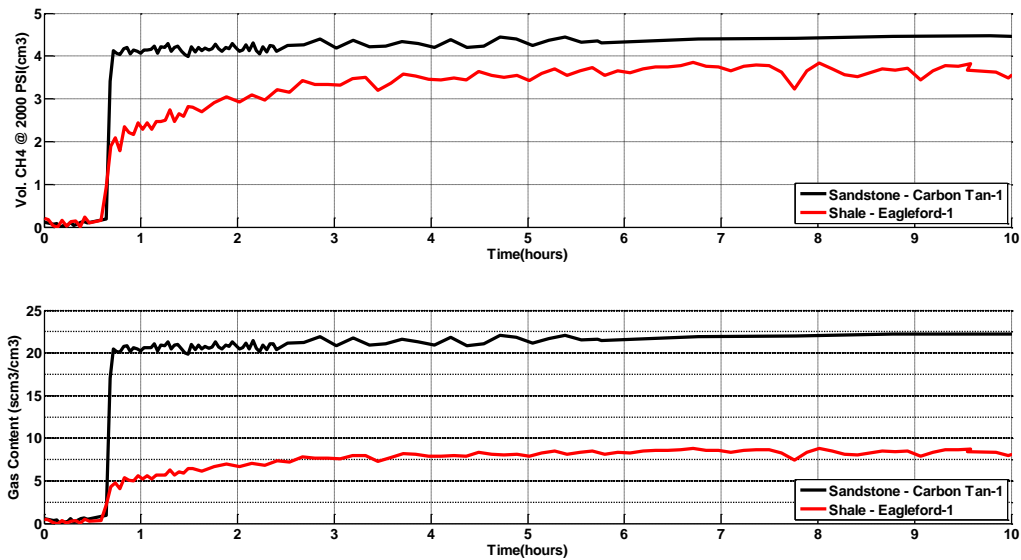
Figure 2. Volume of methane and total gas content as a function of time for shale sample (Eagle Ford 1).
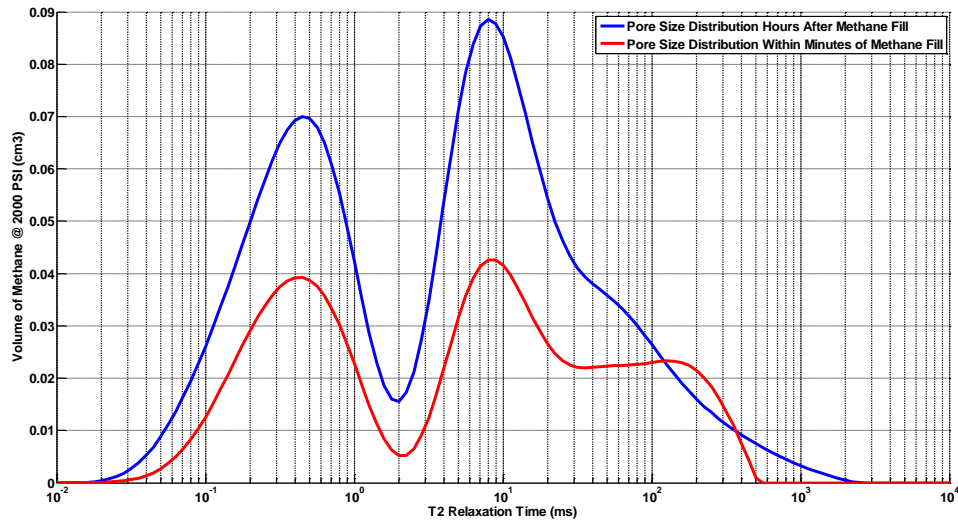
Figure 3. Background subtracted T$_2$ spectra measured after introduction of methane to shale sample (Eagle Ford -1).
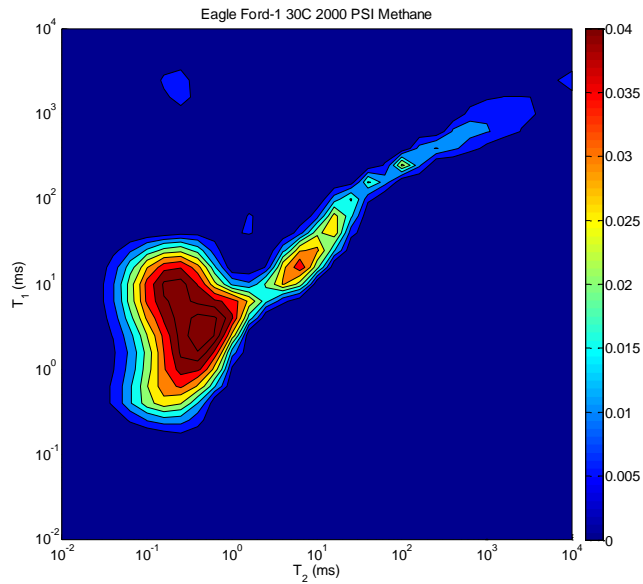
Figure 4. T$_1$-T$_2$ map recorded several hours after introduction of methane to shale sample (Eagle Ford -1).

A ROBUST INTEGRATION BETWEEN GEOCHEMISTRY AND ADVANCED DIGITAL CORE ANALYSIS METHODS TO GENERATE HIGH-RESOLUTION POROSITY-PERMEABILITY LOGS: A CASE STUDY ON A MAJOR UNCONVENTIONAL PLAY IN MIDDLE EAST

Adnan Al-Shamali, P.K.Mishra, Naveen K. Verma and Riyad Quttainah [1],
Osama Al Jallad, Avrami Grader, Joel Walls, Safouh Kornfol and Anyela Morcote [2].
[1] Kuwait Oil Company, [2] Ingrain Inc.

ABSTRACT

In Kuwait, the unconventional source and reservoir rock represented by Najmah Formation is characterized by a complex diagenetic history and depositional variability. This complexity makes the conventional evaluation methods alone insufficient to determine porosity and permeability logs accurately. A major goal of this study was to produce high-resolution porosity-permeability logs for Najmah Formation using advanced digital analysis and geochemistry measurements.

Sixty (60) feet of continuous core were analyzed from an oil field in South West Kuwait. The analysis started with dual-energy x-ray CT scanning of full-diameter whole core and core gamma logging. Plug litho-samples were selected to represent the varying porosity and organic matter content along the entire core length. Two-dimensional Scanning Electron Microscopy (2D SEM) and three-dimensional Focused Ion Beam (3D FIB-SEM) images were acquired and analyzed to accurately determine the kerogen content and porosity. Matrix permeability was directly computed from the 3D FIB-SEM images using the Lattice Boltzmann method. The SEM porosity was calibrated by determining the amount of movable hydrocarbons at in-situ reservoir conditions based on geochemical analyses (XRF, XRD and LECO), pyrolysis indices, Pressure-Volume-Temperature (PVT) data and desorption and adsorption isotherm experiments.

The digitally obtained porosity and permeability data showed a unique trend that was used to produce permeability at the core level. The integration between digital analysis and geochemistry data increased the estimated porosity and confirmed higher mobile hydrocarbon in the reservoir in comparison with the measured data at the surface. This produced a new porosity-permeability trend that was more representative of the reservoir conditions and caused a significant increase in the rock permeability.

The integration between the digital SEM analysis and the geochemical measurements was key in estimating in-situ porosity and permeability characteristics of the tight formation

under study. Moreover, this analysis provided an important tool for obtaining different high-resolution porosity and permeability logs based on various porosity considerations (effective, organic, inorganic, clay). This would lead to increase certainty of reservoir properties by quantifying sensitivities of TOC, porosity, and permeability and their impact on volume of mobile hydrocarbons thus increasing the net pay in the main reservoir interval.

INTRODUCTION

The Najmah Formation (Callovian-Oxfordian) was deposited in Gotnia intra-shelf basin which developed within the Arabian Plate during Mid-Jurassic and Late Mid-Jurassic period [3], [12], [9]. It is mainly composed of tight, organic matter rich argillaceous and bituminous lime mudstone interbedded with oncoidal and bioclastic packstone [3], [12], [10]. Petrophysically, it is characterized by average matrix porosity ranging from 2 to 6% and low permeability ranging from 0.01 to 1.5 mD, thus it is considered as unconventional play [9].

Its Mid-unit was deposited under anoxic/euxinic outer ramp conditions which lead to preserving large quantities of kerogen type II within its matrix. Consequently, it became one of the best hydrocarbon source rock in Jurassic section in Kuwait and the Middle East [3], [9]. Besides to its important role as a source rock, it is also acting as a reservoir and seal rocks with significant light oil production from fractured carbonate limestone intervals in Kuwait [3], [9].

Najmah Formation is also highly heterogeneous laterally and vertically due to the variability of its depositional environments (inner ramp to starved basin) and diagenetic alteration [12], [10]. Further, literature emphasized that heterogeneity of the shale rocks is observable at multiple scales starting from core up to nano-scales. Such heterogeneity was found to be the main controlling factor on the type of pores, texture of the rock and porosity versus permeability relations within the Middle East shale rocks [2], [7]. Accordingly, the conventional methods alone will not be sufficient to characterize shales and identify their sweet spots.

Additionally, within the oil window, part of this preserved organic carbon will be converted into movable crude oil and non-movable bitumen under subsurface conditions [4]. However, in standard logging analysis methods, the non-moveable oil and remaining kerogen are calculated as potential moveable oil [4]. Consequently, the derived logging data (e.g. porosity and permeability logs) from mature source rocks will be overestimated and successively will affect the estimated original oil in place (OOIP) and yield unreliable field development and production plans. This has been recognized in the open-hole porosity log recorded in Najmah source rock under investigation.

Therefore, this study aims at presenting a solution to accurately characterize the source rocks of Lower Mid- and Lower Najmah Formation through an advanced integrative workflow combining digital analysis and geochemistry measurements to generate high resolution porosity-permeability logs. These logs can support estimating an accurate (OOIP) and yield reliable field development and production plans.

METHODOLOGY

Sixty (60) feet of continuous whole cores were imaged at a resolution of 0.5 mm/voxel by Dual Energy (DE) X-ray CT scanning technique [15], [1], [7] to produce high resolution effective atomic number (Zeff) and bulk density (Rhob) logs with data point every 0.5 mm. Later, the whole cores underwent core gamma measurements. These produced logs were used to select plug samples representing the varying porosity and organic matter content along the entire core length. Afterward, detailed geochemical lab analyses represented by XRD, EDS, XRF and pyrolysis were used to determine the extracted core plugs mineralogical composition, total organic carbon (TOC) content, kerogen types and its degree of maturation. Also, Mercury Injection Capillary Pressure (MICP) analysis was performed on all extracted samples to obtain the size distribution of pore throats (PTSD). This will help in determining the optimum resolution needed to resolve the pore systems hosted within the shale samples.

Successively, two-dimensional Scanning Electron Microscopy (2D SEM) and three-dimensional Focused Ion Beam (3D FIB-SEM) images were acquired at resolutions ranging from (10 to 5 nm/voxel). Both 2D and 3D SEM images were segmented digitally by separating pore spaces from inorganic matrix grains and organic matters to determine their kerogen content and porosity at pore level. Also, the segmented 3D FIB-SEM images were used to compute the absolute permeability using the Lattice Boltzmann method [14], [6].

Finally, the quantified SEM porosities and permeabilities were calibrated digitally by removing the amount of movable hydrocarbons at in-situ reservoir conditions based on geochemical data, PVT data and adsorption isotherm experiments. This lead to generate a calibrated porosity versus permeability trend which helped in upscaling the porosity and permeability at the core level and hence generating high-resolution porosity and permeability logs.

RESULTS AND DISCUSSION

DE and Spectral Core Gamma

DE and Core Gamma data provide early visibility into the critical properties of the whole core through continuous high-resolution rock property logs. These logs help in determining the organic matter rich sweet spots for the sample selection. Also, the acquired gray and color-scale images give quick insight on the sedimentary structure and fabric of the rocks as well as their porosity types.

DE gray-scale images illustrate that these cores are highly heterogeneous with alternating layers of laminated and massive limestones (Figure1). The laminated layers are more dominant in the top portion of the cores and have more porosity compared to the massive layer which is more dominant in the bottom portion of the cores.

Zeff (reflects mineralogy) and Rhob (reflects porosity) logs (Figure 1) confirm these observations and they reflect the abundancy of porosity as well as dolomite (Zeff$_{Dol}$=13.8) and clay minerals in the top portion of the core. On the other hand, they showed that the bottom portion of the core is more calcitic (Zeff$_{cal}$=15.7) and has less porosity. The core-

measured total GR from spectral gamma scanning is the black curve labeled SGR (Figure 4). It shows that the top part of the core is highly radioactive (average about 300 API), which is due to the existence and richness of organic matter and clay minerals [13], [5]. However, the bottom part is less radioactive (average about 100 API) which indicates lower organic matter and clay mineral contents. The brown curve labeled GRwoU is the gamma without uranium and is used to estimate clay content. The red dashed curves are from well log data and generally agree with core data, although they do not show the fine scale layers. One exception is that the well log PEFZ curve is shifted far to the right (higher values) probably because of barite mud effects on the logging tool response. By integrating both of spectral gamma and DE logs, 28 plugs were selected to represent the variations in mineralogy and porosity to characterize them geochemically and petrophysically.
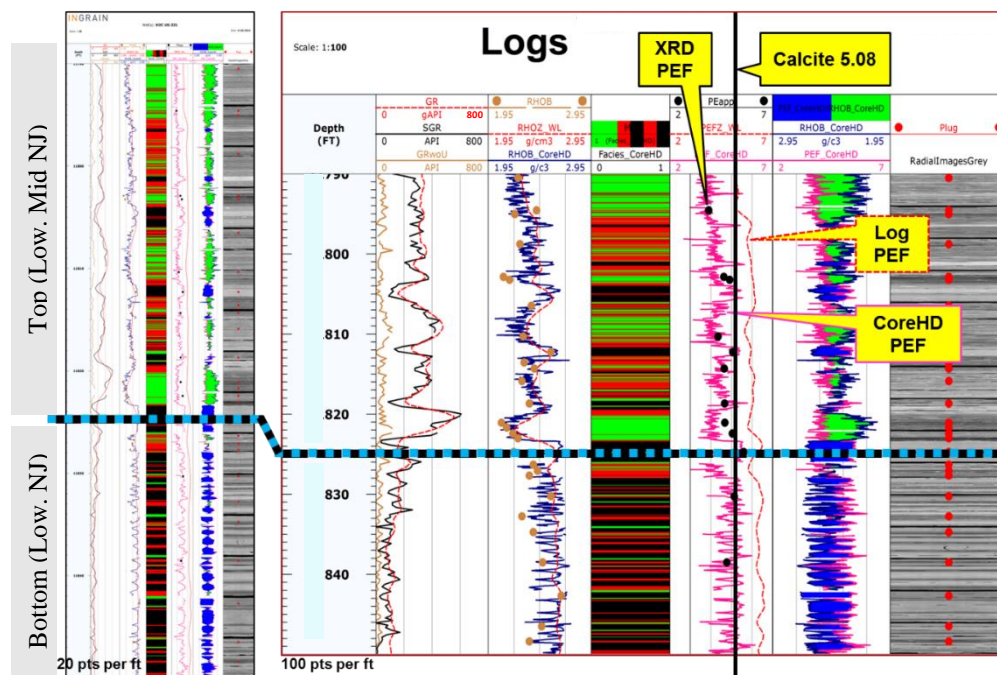
Figure 1: Spectral Gamma, Zeff and Rhob logs obtained from gamma logging and DE XCT scanning, respectively. The logs show a variation in organic matter content, mineralogical composition and porosity distribution in Najmah cores from top to bottom.

Geochemical analysis

All extracted plugs were analyzed geochemically for the purpose of quantifying their mineralogical composition and organic matter maturation and types. XRD results showed that calcite minerals are the most abundant minerals (64% in these rocks) which agrees with DE Zeff log data. The most dominant clay minerals in Najmah rock is illite with an average of 15 wt%, mainly concentrated in top portion of Najmah Formation. The organic matter within these rock samples was also characterized using LECO-TOC and Rock-Eval tests. Both tests showed that the top portion of Najmah has a high TOC content almost equal to 9 wt.% while the bottom portion has less TOC content almost equal to 5 wt.% on average which is in line with the spectral core gamma and DE logs. Additionally, the

pyrolysis analysis showed that the rock has a significant amount of crude oil "S_1" (7 mg HC/g rock in average) and non-moveable oil and solid kerogen "S_2" equal to 26 mg HC/g rock in average which indicates that this source rock has very good quality [11]. Also, they showed that the kerogen has Type II with 439°C in average Tmax which indicates marine depositional environment and mature kerogen [11]. The Hydrogen Index (HI) is averaging at 337 which indicate mature kerogen that transformed to oil [11]. The Vitrine Reflectance "Ro" is ranging between 0.6 and 0.8 which indicates predominance of crude oil in the rock, early maturity of kerogen and existence of the rock in the oil zone [11].

Digital Rock Analysis

With assistance from the MICP derived PTSD (Figure7), the pore systems of these rocks were resolved at resolution 5 to 15 nm using 2D-SEM and 3D FIB-SEM microscopy (Figure2).
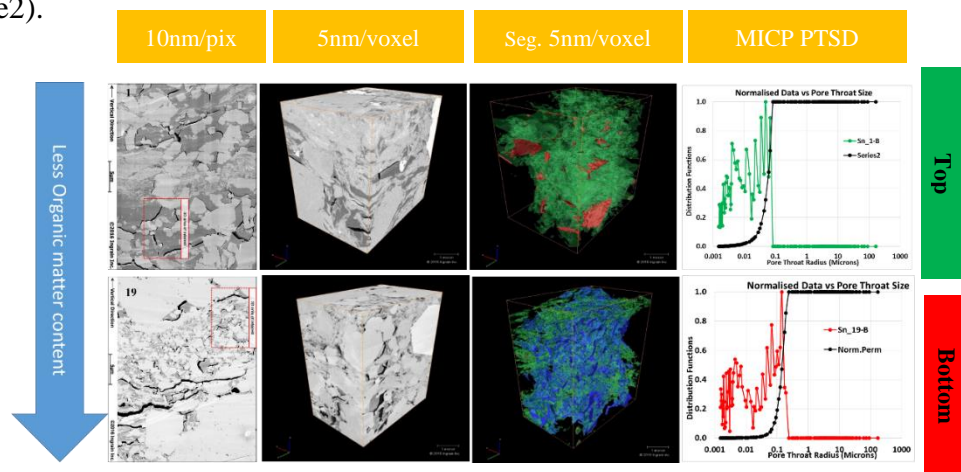
Figure 2: An example of a 3D volume and MICP analysis for SampleS #1 and 19. Green: represents organic matter. Blue: represents connected porosity, Red: represents disconnected porosity in this specific volume.

2D SEM and 3D FIB-SEM images and segmentation results showed that most of the porosity in these samples are hosted within the organic matter with average porosity equal to 5 vol. % (Figure 3b). Most of these organic pores appear to be fracture type which is dominant in the shale source rock located within oil window as illustrated in Figure (7) (Driskill et al., 2013). SEM derived TOC is in line with the measured LECO derived TOC (Figure 3a). Also, the TOC derived from SEM images showed higher average organic matter "OM" content in the top portion of Najmah core (Avg.= 22 vol.%) than its bottom portion (Avg.= 13 vol.%). This coming in line with the gamma logs, LECO test and Rock-Eval analysis.

On the other hand, the computed absolute permeabilities on Najmah samples showed a relatively high connectivity values ranging from 41 to 20017 nD. By plotting the 3D porosity versus the computed permeability, a distinct trend was obtained (Figure 3c).
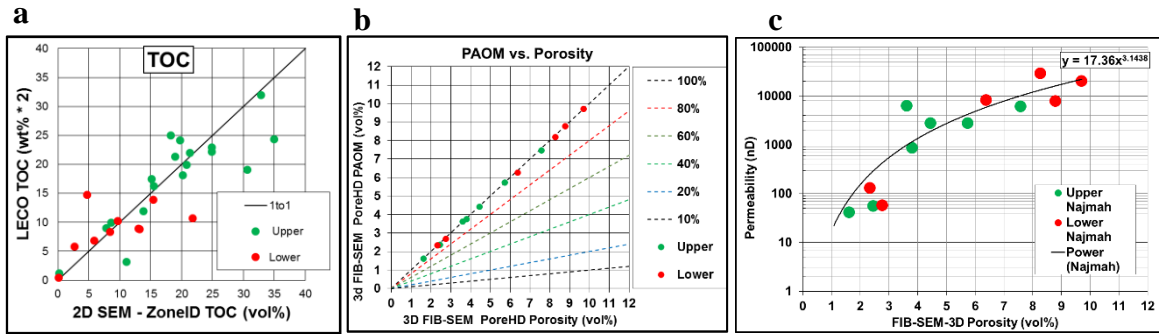
Figure 3: a) a cross plot shows the relation between the TOC quantified from SEM images and LECO TOC test. b) cross-plot shows that the majority of porosity in Najmah shale is hosted within organic matters. c) a cross-plot shows the relation between computed porosity and permeabilities in Najmah Formation

Poroperm Upscaling to Core-Scale

Porosity Correction

The main objective of this study is to generate high-resolution porosity and permeability logs for Najmah source rock using the porosity-permeability trend obtained from SEM analysis, DE derived porosity log and geochemistry data. However, the porosity defined by the 2D SEM and the 3D FIB-SEM represents the detectable effective porosity. It does not include the porosity in the clays which must be added to the effective porosity in order to be compared with the open-hole logs. A method for estimating clay-bound water (CBW) porosity has been presented by Walls, et al 2016 [16]. This method uses published data for the porosity of four pure clay minerals including illite. The apparent clay porosity for pure illite is 0.09. If we assume that essentially all of the clay in Najmah is illite (which is supported by XRD and XRF data), then the clay associated porosity is 0.15 times 0.09 or 0.014 (fractional volume). Hence, 1.4% additional porosity was added to the quantified SEM effective porosities to correct them. Additionally, the pyrolysis analysis showed that Najmah source rock is existing within the oil window in which significant volumes of kerogen has transformed to producible light "S_1" and non-producible heavy oil "x fraction of S_2". Also, the Langmuir adsorption experiment conducted on Najmah cores by Kuwait Oil Company (KOC) showed that methane was dissolved in the oil which covers the organic matter rather than adsorbed on the organic matter surfaces. Thus, the volume of porosities occupied by S_1 and x fraction of S_2 should be added to the effective porosity besides to clay porosity. Accordingly, both of Langmuir adsorption experiment, Gas Oil Ratio (GOR) and oil density derived from PVT test, and pyrolysis indices (S_1 and S_2) were integrated to calculate the amount of gas in solution – mimicking the Langmuir isotherm experiments (Figure 4). The calculations showed that if ($S_1+0.4*S_2$) are used (at each plug location that LECO-SRA was measured in the laboratory) a reasonable correlation between dissolved gas and the Langmuir results is obtained (Figure 4). Consequently, the equivalent volumes of S_1 and $0.4*S_2$ were considered as an actual part of porosity besides to 1.4% porosity hosted within the clay minerals.
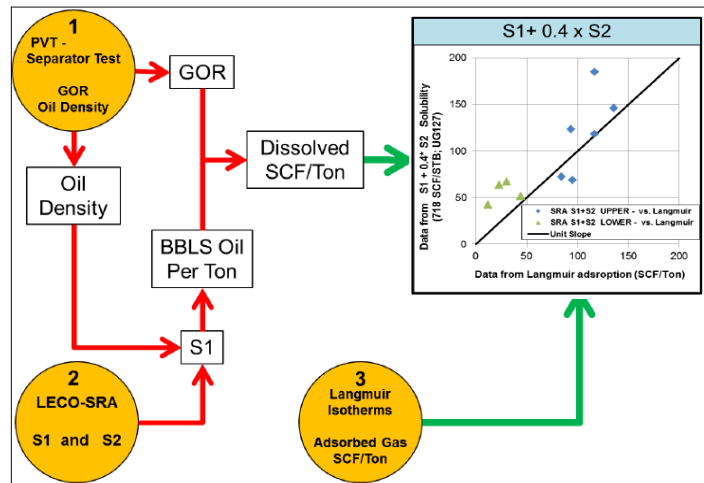
Figure 4: Workflow for computing solution gas content in SCF/Ton and the corresponding comparison between gas solubility data and Langmuir adsorption data ($S_1+0.4*S_2$).

After adding these porosities to the effective porosities derived from SEM (5% on average), the porosities of the samples derived from upper Najmah as well as DE derived porosity log have approximately doubled, reaching 10% on average (Figure 5). Even though the porosity of top Najmah has increased, it's still lower than the open-hole log density-porosity (25% in average). Such relatively high value of porosity wasn't observed in MICP, He and DE derived porosity measurements which are averaging 5%, similar to SEM derived porosities. This phenomenon is attributed to calculating the non-moveable oil and remaining kerogen in standard logging analysis methods as potential moveable oil [4]. By applying the corrections described above, the resultant porosity log matched reasonably well with the wireline density-porosity. The lower Najmah porosities have also increased slightly reaching to 7.5% on average which is close to the open-hole log. This is expected because of the low concentration of organic matter and crude oil towards the bottom of the Najmah Formation which resulted in more reliable logging data.
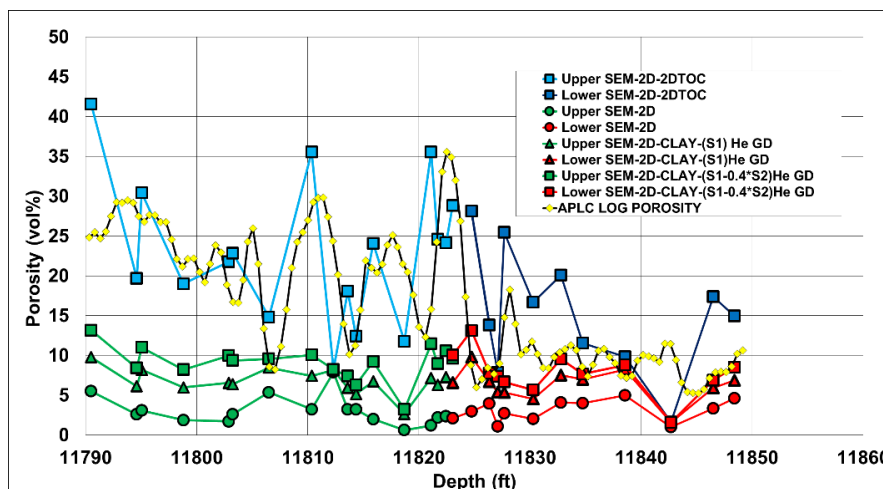
Figure 5: Estimates of total porosity which includes effective porosity, clay porosity, S1, and part of S2. Red and green circles: Effective porosity. Red and green squares: Total porosity (Effective porosity + clay porosity + S1 + 0.4*S2). The black curve with yellow dots represents the computed wireline density-porosity log. The blue curve with squares represents the plug sample total porosity plus organic material.

Porosity-Permeability Correlation Correction and Upscaling

Since effective SEM porosities of the 28 samples increased two times after applying (S1+0.4*S2+CBW) correction, the absolute permeability increased as well. Therefore, the initial 3D porosity-permeability trend obtained through DRA required correction also. Consequently, the same volume of producible TOC (residual oil (S1) + 0.4*S2) added previously was eroded digitally from the solid organic content of each 3D FIB-SEM volume and the permeability was recomputed using Lattice Boltzmann (LBM) method. The resulting new porosity-permeability trend was generated (Figure 6a), and together with the corrected DE derived porosity log, was used to generate a high-resolution permeability log at core scale (Figure 6b). The generated permeability logs showed that permeability increased by a factor of 5X to 20X. This new computed porosity-permeability trend should better represent in-situ conditions, where a significant fraction of the organic matter imaged at the surface is likely mobile and producible at reservoir temperature and pressure.
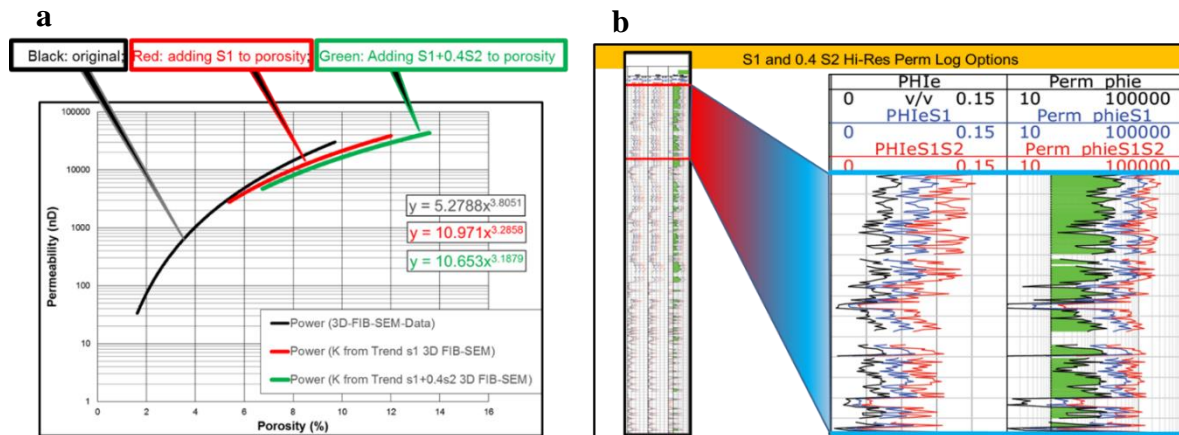
Figure 6: a) Green curve: Porosity-permeability correlation generated by eroding the producible organic matter from 3D FIB volume of each sample individually. b) High resolution porosity and permeability logs calculated after removing the S1+0.4*S2+Clay porosity from effective porosity.

SUMMARY and CONCLUSIONS

1- The integration between the digital SEM analysis and the geochemical measurements was key in estimating in-situ porosity and permeability characteristics of the tight formation under study.

2- This link provides the constraints for adjusting the distribution and balance of organic porosity and organic matter and yields different poro-perm scenarios and improved reservoir characterization which leads to:

    a. Higher accuracy in determining reservoir properties for improved quantification of reserves and productivity.

    b. Increase certainty of reservoir properties by quantifying sensitivities of TOC, porosity, and permeability and their impact on volume of mobile hydrocarbons thus increasing the net pay in the main reservoir interval.

ACKNOWLEDGEMENTS

REFERENCES

1. *Al-Owihan, H., Al-Wadi, M., Thakur, S., Behbehani, S., Al-Jabari, N., Dernaika, M., & Koronfol, S. (2014). Advanced Rock Characterization by Dual Energy CT Imaging: A Novel Method in Complex Reservoir Evaluation. International Petroleum Technology Conference. doi:10.2523/iptc-17625-ms*

2. *Almarzooq, A., Alghamdi, T., Koronfol, S., Dernaika, M., & Walls, J. (2014). Shale Gas Characterization and Property Determination by Digital Rock Physics. SPE Saudi Arabia Section Technical Symposium and Exhibition. doi:10.2118/172840-ms.*

3. *Alsharhan, A. S., & Nairn, A. E. (2003). Sedimentary basins and petroleum geology of the Middle East. Amsterdam: Elsevier.*

4. *Asquith, G. B. (2015). OOIP Utilizing GEOCHEM [ECS] Data, Triple Combo Data Only, and Pyrolysis S1 Data, Permian Wolfcamp "A" and "B" Shales, Midland Basin, Texas. AAPG Search and Discovery , article# 110207.*

5. *Bigelow, E. L. (1992). Introduction to Wireline log analysis. Houston: Western Atlas International.*

6. *De Prisco, G., Toelke, J., & Dernaika, M. (2012). Computation of relative permeability functions in 3D digital rocks by a fractional flow approach using the lattice Boltzmann method. SCA, 36. Aberdeen, Scotland.*

7. *Dernaika, M., Jallad, O. A., Koronfol, S., Suhrer, M., Walls, J., & Matar, S. (2015). Petrophyscial and Fluid Flow Properties of a Tight Carbonate Source Rock Using Digital Rock Physics. Proceedings of the 3rd Unconventional Resources Technology Conference. doi:10.15530/urtec-2015-2154815.*

8. *Driskill, B., Walls, J., Sinclair, S. W., & DeVito, J. (2013). Applications of SEM Imaging to Reservoir Characterization in the Eagle Ford Shale, South Texas, USA. AAPG Memoir , 102, 115-136.*

9. *Khan, B., Nohut, O., Steene, M. V., Ghneej, A. A., & Ajmi, A. A. (2014). Petrophysical Evaluation of Unconventional Najmah Formation of Kuwait - A Case Study. Proceedings 76th EAGE Conference and Exhibition 2014. doi:10.3997/2214-4609.20141390.*

10. *Khan, D., & Al-Ajmi, M. (2016). Depositional architecture of the Gotnia basin during Oxfordian in southern part of Kuwait. International Conference and Exhibition, Barcelona, Spain, 3-6 April 2016. doi:10.1190/ice2016-6459957.1*

11. *McCarthy, K., Rojas, K., Niemann, M., Palmowski, D., Peters, K., & Stankiewicz, A. (2011). Basic Petroleum Geochemistry for Source Rock Evaluation. Schlumberger Oil Review , 23(2), 32-43.*

12. *Ray, D. S., Al-Shammeli, A., Al-Khamees, W., Fuchs, M., & Groen, V. D. (2013). Depositional and Diagenetic Sedimentological Model of Najmah-Sargelu Formation, Umm Gudair, Kuwait. International Petroleum Technology Conference. doi:10.2523/iptc-17117-ms.*

13. *Russell, W. L. (1944). The Total Gamma Ray Activity Of Sedimentary Rocks As Indicated By Geiger Counter Determinations. Geophysics, 9(2), 180-216. doi:10.1190/1.1445076.*

14. *Tölke, J., Prisco, G. D., & Mu, Y. (2013). A lattice Boltzmann method for immiscible two-phase Stokes flow with a local collision operator. Computers & Mathematics with Applications, 65(6), 864-881. doi:10.1016/j.camwa.2012.05.018.*

15. *Walls, J., & Armbruster, M. (2012). Shale Reservoir Evaluation Improved by Dual Energy X-Ray CT Imaging. Journal of Petroleum Technology, 64(11), 28-32. doi:10.2118/1112-0028-jpt*

16. *Walls, J., D. Buller, A. Morcote, M.L. Everts, B. Guzman, Integration of Whole Core, Drill Cuttings, and Well Log Data for Improved Characterization in the Wolfcamp Formation, Unconventional Resources Technology Conference (URTeC) DOI 10.15530-urtec-2016-2461526*

EFFECT OF MICROFRACTURE ON ULTRATIGHT MATRIX PERMEABILITY

G. Leśniak, P. Such, R. Cicha-Szot

Instytut Nafty i Gazu - Państwowy Instytut Badawczy, Kraków, Poland

ABSTRACT

Measurements of reservoir rock permeability have been executed in the oil industry for several decades. Depending on the type of permeability, oil and gas reservoirs can be divided into those with pore reservoirs, pore – fracture reservoirs and fracture reservoirs. In practice, pore and fracture permeability is observed in all unconventional reservoirs with varying proportions of either type. Natural microfracture systems increasing the permeability of the rock matrix are also recorded in shale rocks. In this paper anomalous results of permeability for rock samples from shale formations have been analysed. Observations with the use of SEM and petrographic microscope allow us to distinguish microfractures generated as a result of decompression of rocks (change of stress) and natural ones. The fractures generated as a result of core decompression are usually associated with very fine laminations with a material of different grain size composition comparing with rock matrix (smaller or larger grains), or with clay laminations within mudstones (author's microscopic observations). It has been concluded that the microfracture systems present in the examined rocks are the reason for anomalous values of permeability measured by the Pulse-Decay method. Dependences of overburden pressure on fracture permeability have been analysed. Simulative research performed for plug-type core samples allowed us to obtain permeability values in a function of the microfractures width. Finally, dependence of reservoir conditions on fracture width as well as on porosity was examined.

Key words: anomalous permeability, shale rocks, microfracture width.

INTRODUCTION

Measurements of permeability of reservoir rocks have been performed in the oil industry for over 100 years. At that time, the measurement methodology was changed, and in addition to steady state measurement (flow measurement), measurements were made in unsteady state (Pulse Decay method).

All natural reservoirs of crude oil and natural gas, taking into account the type of permeability, can be divided in porous reservoirs, porous-fracture reservoirs and fracture ones. In practice, all unconventional fields are dominated by porous-fracture permeability (with variable proportions of both types). Also in the shale complexes, natural fracture systems and microfracture are observed. These fracture systems aid a permeability of the

rock matrix. The problem is to determine the real width of the microfractures under the reservoir conditions. It is necessary to perform flow simulation. In conventional reservoir, width of microfracture can be evaluated on the basis of comparison of the permeability obtained from the well test and the results obtained for the rock matrix as well as the descriptions of fractures and microfracture distribution. The methodology developed for a conventional reservoir [5,6,7,15] was applied to calculate the width of microfractures in the shale.

In the literature on shale gas permeability measurements, the values of gas permeability ranges from a few to several hundred nano Darcy for the rock matrix (the rock matrix is understood as a skeleton and cements) [2, 3]. The distribution of results is connected with the mineral composition and the petrographic type of shale (mudstones, claystone's, siltstones). For typical claystones, permeability value level covers the range from several to twenty nD, for siltstones it may reach the level of several hundred nD. In fact, we rarely deal with pure petrographic types of rocks. Generally they are mixtures of claystones mudstones, siltstones or claystones with a thicker detrital fraction scattered in the rock matrix.

The permeability (regardless of the applied method) is related to the system of connected pores. If this system is built from the pores of a small number of connections, then even a large number of pores will not bring about high permeability (eg pumice). The matrix permeability values for shale rock should be related to the porosity types present in the analyzed samples. In the case of pores occurring exclusively in organic matter (in most samples pores are insulated), the matrix permeability value should be relatively low (several nD). If there are mixed pores (OM-Pores, InterP Pores, ItraP Pores, Fig.1) in the sample, then we can expect the matrix permeability to be much higher (up to several hundred nD).
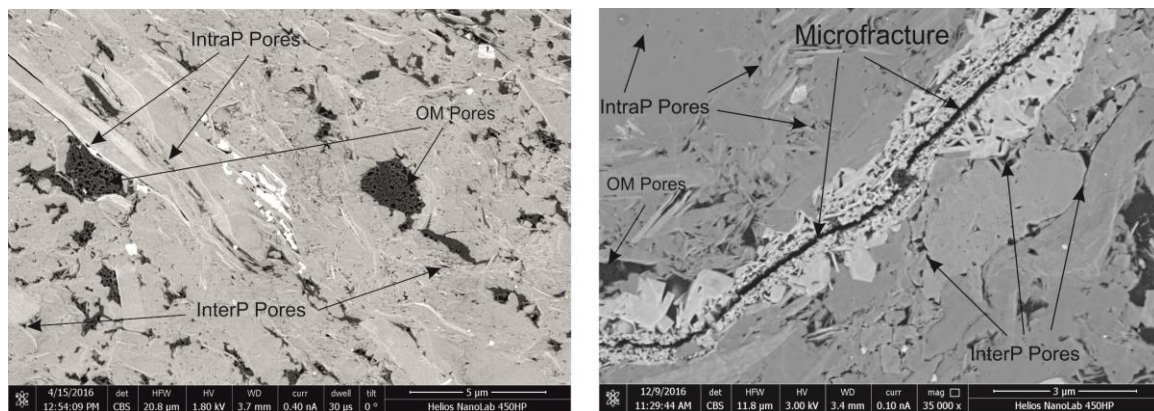
Figure 1 Typical pore space in shale from Baltic Basin

Silurian and Ordovician shales from the Baltic basin have a different mineral composition compared to the most famous and most commonly described shales (Barnet, Marcellus, etc.). Mineral composition of the Baltic basin shales is dominated by clay minerals (from 40 to 60%) from the illite and chlorite groups. The mineral composition is complemented by quartz, feldspars, carbonates (calcite, dolomite, ankerite) and muscovite, biotite and iron

sulphides (pyrite and marcasite). It seems that for such a high content of minerals developed in the form of plaques, the compaction should lead to a creation of numerous pores (InterP Pores, IntraP Pores) as a result of a bending of mineral plaques or their delamination. Of course, this leads to the creation of numerous relatively well- linked pores. It should be assumed that the permeability of the rock matrix of the analyzed shales may be higher than the values reported for US shales. The anomalous high permeability values obtained for a large number of investigated shale samples stimulated the search for the causes of this situation.

RESEARCH STUDY

The problem encountered during the selection of shale samples for permeability measurements is that the sample is cut in the form of a cylinder of 2.54 cm in diameter and 4 cm in length, which is often unfeasible. This is caused by typically shale cleavage and the presence of microfractures. Observations in the petrographic microscope allows us to divide the microfractures resulting from the expansion of the rock after pulling to the surface (change of stress) and the system of natural microfractures (Fig. 2). The fracture resulting from the expansion of the core are associated with very fine laminations with different granulometric material from the rock matrix (smaller or larger grains) or clay laminates within the mudstones.
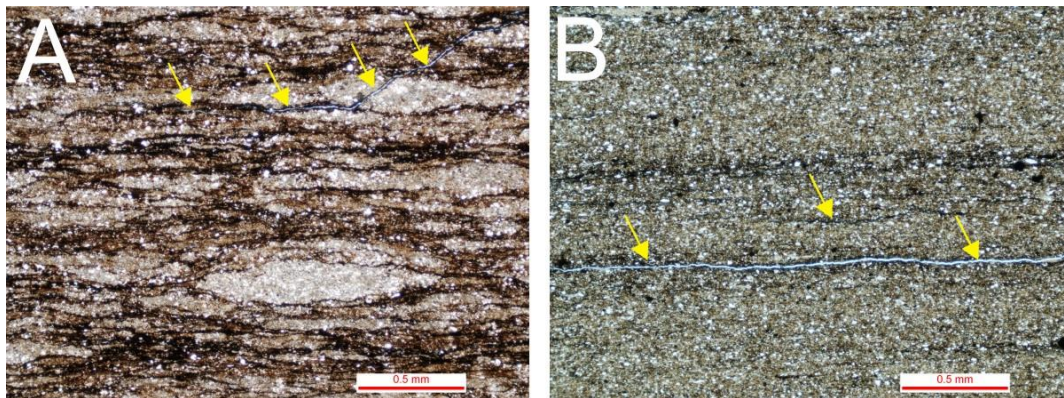
Figure 2 Foto A – natural microfractures, B - microfractures generated by decompression

The research procedure was as follows:
- preparation of plug samples,
- permeability measurement - Pulse Decay (PDP-250) ,
- 3D imaging - X-ray microtomography (CT) – resolution 10-12 μm,
- 2D X-ray imaging (RTG)
- selection of samples in which we deal with the microfracture permeability (based on permeability measurements and 3D and 2D imaging),
- calculation of width of microfractures based on permeability measurements

48 samples of the Baltic basin shale cores were selected for the study. The results are shown in Figure 3 and 4.

The range of obtained permeability researches cover the range from 3.8 mD to 0.4 nD (that is, six orders of magnitude). Samples with permeability above 1 mD (no 19 and 29) were

recognized as the samples with fractures formed during their preparation. For the rest of samples the base question is: are the obtained permeability values only connected with rock matrix or also with microfractures? Assuming that the value of 0.4 nD is the lowest permeability of the rock matrix, and taking into account permeability of the rock matrix (according to available publications) [2,3,14] can be up to 1.3 μD, we should accept that all measurements of permeability values greater than 0.0013 mD (1.3 μD) should be connected with the existence of the microfracture system present in the samples.
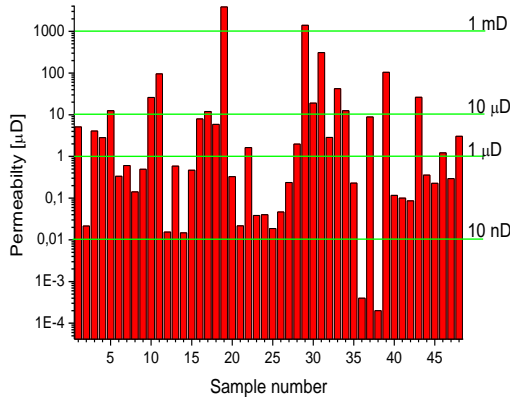
Fig.3 Histogram of permeability distribution
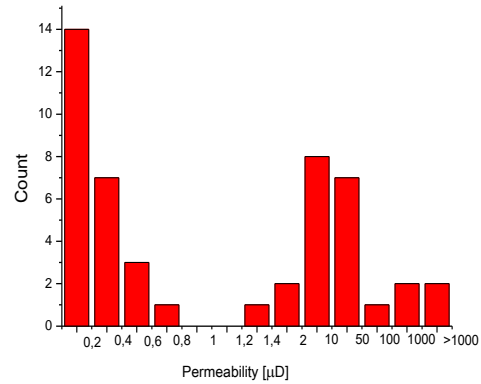
Fig. 4 Frequency diagram distribution of permeability

In order to examine the effect of effective stress on permeability and microfracture width for samples with macroscopically visible microfractures permeability measurements at different confining pressure were performed [16]. The results are shown in Figure 5 and Table 1.

Table 1 Measurement of permeability in different confining pressure for fractures sample

Confining pressure [psi]	Permeability [μD]	With of fracture [μm]
2000	0.0688	2.496
3000	0.0364	2.017
4000	0.0286	1.860
5000	0.0236	1.744
6000	0.0225	1.715
7000	0.0221	1.705
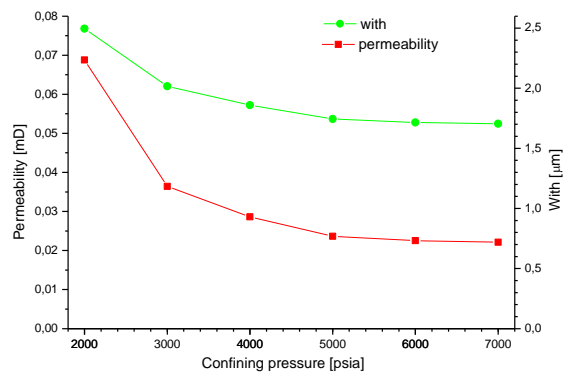
Figure 5 Relationship between confining pressure permeability and with of fracture

CALCULATIONS OF WIDTH OF MICROFRATURES

Analyses of microfracture permeability for classical reservoir rocks (dolomites, sandstones) are performed by the "random traverses" method with the use of a polarization microscope and polished thin section. This method consists in random placing of segments of the length L on a tested thin section and counting the number of intersections of each

segment with microfractures [9,10,13]. The width of the microfracture is an important value determined during microscopic measurements. It is one of the values used to calculate the fracture permeability and porosity values. Measurement of the width is carried out for each observed microfracture. It is based on the measurement of the width of the microfracture at several points. The value of the width of microfracture is assumed to be the average of all measurements for a given thin section. However, we should bear in mind that these measurements are performed on expanded samples. In the previous studies for shale rock, values ranging from 0.005 to 0.008 mm were accepted for calculations.

In our analysis, it was decided to reverse the problem and, calculate the actual width of the microfracture on the basis of measured permeability.

A formula for calculating the microfracture permeability is (1) [1,7,8]:

$$k = \frac{C\pi}{2L} \frac{b_l^3}{k_l} \sum_{i=1}^{m_l} n_i \qquad (1)$$

where:

k - microfracture permeability

ml - the number of field of view applied to the thin section number l,

n - number of intersection fractures with section ml, each length L,

b - width of the microfracture

kl - number of test section applied to the sample

C - factor of random system, resulting from unit conversions (mm per cm)

After transforming the formula for microfracture permeability in order to calculate width (b) we obtain (2)

$$b = \sqrt[3]{\frac{k \times k_l \times 2L}{\pi \times C \times \sum_{i=1}^{m_i} n_i}} \qquad (2)$$

The obtained results represent only permeability of the microfracure network.

The permeability measurements using plugs, give theoretically both permeabilities: that of the rock matrix and the microfracture network permeability. Of course, if there are microfracure passing through the whole sample, practically only microfracture permeability is measured (the gas always flows through the places with the smallest possible flow resistance).

Therefore, two cases should be considered. Case 1: microfracture system are present in the sample, but fractures are not connected to each other and do not pass through the entire sample. For this reason, the permeability value of the rock matrix should be subtracted from the permeability of the sample when calculating the width of the microfractures.

The second case - there are microfracture networks in the sample and they pass through the whole sample, so it can be assumed that the value of the measured permeability depends only on microfracture permeability (we do not measure the permeability of the matrix during the measurement).

In order to correctly estimate the permeability of the rock matrix, it was assumed that the micro fractures were not responsible for the permeability value below 0.6 μD [2,3,14]. For all measurements, the permeability frequency distribution was computed (Figure 4). In

Figure 4, we clearly see the frequency distribution of permeability values into two sets from 0.3 to 604 nD and above 1.2 µD. Based on the results of all analyzes the value of 0.6 µD was arbitrarily assumed as the maximum permeability of the rock matrix.

For all samples, 3D imaging in X-ray tomography (CT) and X-ray imaging (2D), in multiple planes were performed [11,12]. On this basis, samples with potential micro fractures or laminations forming from detrital material as pseudo fracture (both methods allow capture areas / laminas with reduced density) were selected (Fig. 6).

The samples with values of permeability greater than 1.2 µD include micro fractures or fine laminations forming pseudo microfracure rocks. In the samples with a permeability lower than 600 nD also fine microfractures or lamination occur but they do not cross the entire sample (based on data shown on Fig. 3 two groups of sample can be distinguished – one with microfractures which goes through whole length of the sample, the second with microfractures which goes through a part of the sample).
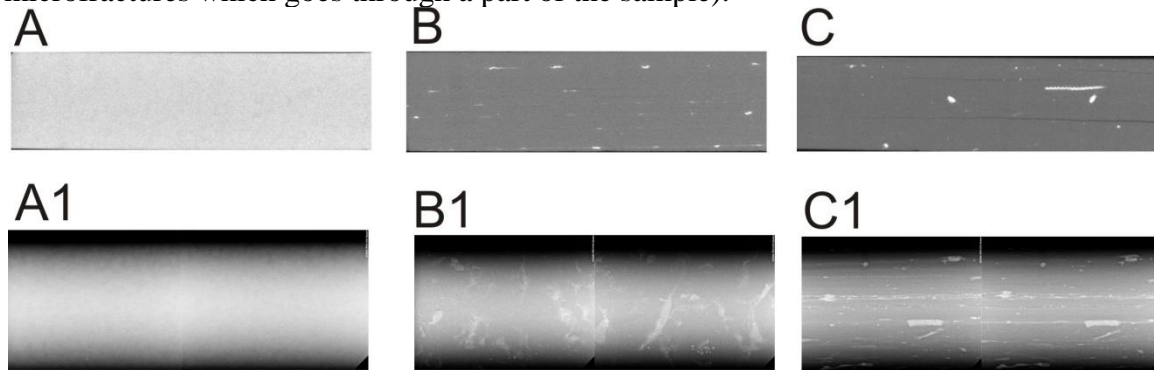
Fig. 6 Imaging in CT (A, B, C) and RTG (A1, A2, A3) A, A1 – sample without microfractures and lamination;
B, B1 – sample with microfracture and lamination (do not cross the entire sample);
C, C1 – sample with microfracture (crossed the sample)

There were only five in the whole set of analyzed samples, which can be described as having no microfractures or lamination in them. It can be assumed that for these samples only the permeability of the rock matrix was measured. The maximum permeability value is 295.3 nD. On this basis, the permeability of the rock matrix for further calculations was accepted as 300 nD.

In his work Heller [4] reports the results of permeability of the rock matrix for shale on the level of several to several dozen nD and on the level of several up to several dozen µD.

The permeability of the matrix at µD level is explained by lamination / stratification of carbonates. In the samples analyzed by Heller the sum of clay minerals varied from 5 to 52%. The permeability results at µD level were obtained for samples with the total clay mineral content of less than 25%.

In the samples analyzed in this article, the average content of clay minerals is 44 to 64%. These samples also exhibit significantly lower quartz content. It should be assumed that the real permeability of the rock matrix will be less than 1 µD.

In the studies executed for shale gas prospecting in Poland, the matrix permeability of the shale was accepted from 200 to several hundred nD. Adopting the 300 nD value for the calculation is a safe variant at this stage of the study.

Table 2 Results of calculations of width of microfracure

Sample number	k-measured [mD]	k-km [mD]	number of microfratures	width of microfracture [μm]	number of microfratures	width of microfracture [μm]
sample of permeability > 1.2 μD						
49	0.0012184	0.0012184	1	1.035	4	0.652
23	0.0016281	0.0016281	1	1.140	4	0.718
29	0.0019714	0.0019714	1	1.215	4	0.765
4	0.0028218	0.0028218	1	1.369	4	0.862
33	0.0028655	0.0028655	1	1.376	4	0.867
52	0.0030537	0.0030537	1	1.409	4	0.888
3	0.0040748	0.0040748	1	1.549	4	0.976
1	0.0051350	0.0051350	1	1.687	4	1.063
17	0.0079767	0.0079767	1	1.935	4	1.219
38	0.0088810	0.0088810	1	2.028	4	1.277
18	0.0120271	0.0120271	1	2.252	4	1.419
6	0.0124535	0.0124535	1	2.257	4	1.422
35	0.0125460	0.0125460	1	2.257	4	1.422
31	0.0189670	0.0189670	1	2.594	4	1.634
11	0.0259657	0.0259657	1	2.903	4	1.829
46	0.0262357	0.0262357	1	2.894	4	1.823
32	0.0310969	0.0310969	1	3.054	4	1.924
34	0.0422202	0.0422202	1	3.405	4	2.145
12	0.0960610	0.0960610	1	4.508	4	2.840
42	0.1045971	0.1045971	1	4.638	4	2.921
30	1.3920000	1.3920000	1	10.990	4	6.923
20	3.8649000	3.8649000	1	15.201	4	9.576
sample of permeability > 300 nD						
21	0.0003270	0.0000270	1	0.291	4	0.183
7	0.0003350	0.0000350	1	0.317	4	0.200
47	0.0003578	0.0000578	1	0.375	4	0.236
16	0.0004657	0.0001657	1	0.532	4	0.335
10	0.0004935	0.0001935	1	0.560	4	0.353
14	0.0005838	0.0002838	1	0.637	4	0.401
8	0.0006048	0.0003048	1	0.652	4	0.411

Calculation of width of microfracture was carried out in two variants. For the samples with permeability greater than 1.2 μD, the width of microfracture was calculated for the full permeability value for one and four microfractures in the sample.

For these samples it was assumed that the flow from which the permeability is calculated is related only to the microfracture permeability while the permeability of the rock matrix is negligible. For the samples with permeability lower than 600 nD, calculation of the width

of microfracture was made for the permeability value reduced by the permeability of the rock matrix. The results are shown in Table 2.

Based on observations of 3D imaging in CT and 2D in RTG, it was found that in the analyzed samples we can certainly deal with one microfracture passing through the entire sample [11]. Sometimes it develops into a system of two or more connected microfractures. Therefore, the calculations are presented for 1 and 4 microfractures, treating the second case as a microfracture system. The calculations assume:

- one field of view with an L value equal to the sample diameter (2.54 cm diameter)
- one intersection with a microfracture,
- four intersections with microfractures,
- permeability for a particular sample,
- C-factor (random system) -171000- resulting from unit conversions (mm per cm).

The obtained results of the width of microfractures (for one microfracture, Tab.2) range from 1.035 to 15.201 μm. This width can be compared with the average pore size in classic sandstone reservoirs. For the four microfractures in the sample, these values range from 0.652 to 9.576 μm. In the case of the samples with permeability of less than 600 nD for one microfracture, the width is from 0.291 to 0.652 μm, and for 4 microfractures from 0.183 to 0.411 μm.

It should be noted that the change in the number of microfractures in a sample does not alter the calculated of width of microfractures in the same way. Also, the differences of the width of microfractures – if we ignore the permeability values of the rock matrix - do not change drastically. The variation in the width of microfractures is approximately 40%.

CONCLUSION

Studies have shown that the "anomalous" values of permeability in shale rocks correspond to microfracture systems. Therefore, it is important to put more emphasis on the correct determination of permeability of the rock matrix (without microfractures).

The impact of microfracture parameters on the permeability of shale under reservoir conditions was analyzed. The width existing microfractures was calculated..

The permeability value over which microfracture samples (matrix permeability) should be expected in the specimen samples of shale rock was estimated.

ACKNOWLEDGEMENTS

REFERENCES

1. Aguilera R., 1980. Naturally Fractured Reservoirs. PennWell Publ. Comp., Tulsa, 1–703
2. Apaydin O., 2012. New coupling considerations between matrix and multiscale natural fractures in unconventional resource reservoirs. PhD thesis, Colorado School of Mines

3. Cho Y., Apaydin O.G., Ozkan E., 2013. Pressure-dependent natural fracture permeability in shale and its effect on shale-gas well production. SPE Reservoir Evaluation & Engineering (216-228)

4. Heller R., Vermylen J., Zoback M., 2014 Experimental investigation of matrix permeability of gas shales" AAPG Bulletin v. 98 no 5, (975-995)

5. Leśniak G., 1992, "Mikroszczelinowatość wapieni wizenu z otworu Nosówka 2"Nafta-Gaz, nr.7-8 (165-168)

6. Leśniak G., Darłak B., 1995, Laboratory investigation of petrophysical properties of fractured and vugged rocks" Modern exploration and improved oil and gas recovery methods. Kraków, 12-15 wrzesień 1995, (203-204)

7. Leśniak G., Darłak B.,1994, Próba kompleksowego przedstawienia parametrów fizycznych złóż szczelinowych na przykładzie wapieni wizenu z odwiertu Nosówka-8. Nafta-Gaz nr. 8 (277-283)

8. Nelson R.A., 1985. Geologic Analysis of Naturally Fractured Reservoirs. Gulf Publ. Comp., Houston, 1–320.

9. Paduszyński J., 1965 Szacowanie gęstości mikroszczelin metodą trawersów losowych, Nafta, 8.

10. Romm E.S., 1970 Usowierszeństwowanie metoda szlifów dla opriedielienia paramietrow trieścinowatości. Tr. WNIGRI, 290.

11. Rydzy M. B., Patino J., Elmenti N., Appel M., 2016. Stressed permeability in shales: effect of matrix compressibility and fractures – a step towards measuring matrix permeability in fractured shale samples. SCA2016-027

12. Chhatre S. S., Braun E. M., Sinha S., Determan M. D., Passey Q. R., Zirkle T. E., Wood A. C., Boros J. A., Berry D. W., Leonardi S. A., Kudva R. A., 2014. Steady state stress dependent permeability measurements of tight oil bearing rock. SCA2014-012

13. Smechov J.M. (red): Treščinovatost' gornych porod i treščinnovye kollektory. Trudy WNIGRI, 193, 1-120, Leningrad 1962

14. Subrata Roy, Reni Raju, Chuang H.F., Cruden B.A., Meyyappan M. 2003: Modeling gas flow through microchannels and nanopores", Journ of Applied Physics, vol 93, no8 (4870 - 4879)

15. Such P., Leśniak G., 2003, Complex Correlation for Chracterisation of Transport System in Fracture Rocks Proceedings of 12 th. Improved Oil Recovery Symposium, Kazań 2002 (502-505)

16. Such P., Dudek L., Mroczkowska – Szerszeń M,, Cicha-Szot R., 2015 The influence of reservoir conditions on filtration parameters of shale rocks. Nafta-Gaz no 11 (25-29)

A COMPARATIVE STUDY OF SHALE PORE STRUCTURE ANALYSIS

R. Cicha-Szot, P. Budak, G. Leśniak, P. Such,
Instytut Nafty i Gazu - Państwowy Instytut Badawczy, Kraków, Poland

ABSTRACT

One of the challenges of economically exploiting shale gas reservoirs is proper estimation of gas flow rate. To achieve this goal, better understanding of pore structure and flow paths in fine grained rocks is needed. The nano to micrometer scales of pore systems requires more complex analysis and application of different techniques to understand pore changes in shale systems. Except for pore size analysis using scanning electron microscopy, in this study mercury intrusion capillary pressure (MICP), nitrogen adsorption and Klinkenberg gas slippage analysis are considered to evaluate pore size. Gas slippage measures the pores most responsible for fluid flow and can be applied at levels of stress comparable to those experienced during reservoir production. However, pore size and pressure restricts the slippage effect, which is not visible in every rock. In this study, slippage was measured on plugs oriented parallel to bedding. All samples were pre-stressed at reservoir conditions (σ_{eff}~33 MPa). Due to the high heterogeneity of the analyzed shale samples, Klinkenberg permeability, SEM, MICP and nitrogen adsorption analysis were performed on the same plug to obtain the most adequate and coherent pore size results.

Theoretical calculations of average pore diameter derived from slippage data collected in this study for samples with high clay content and low carbonate content yielded lower diameters than estimates from MICP data. Pore size evaluated with MICP and Klinkenberg gave similar results for samples with existing microfractures. Although similar pore diameters might be distinguished on SEM images, detailed pore size analysis using FIB-SEM showed very different results when evaluated with gas slippage.

INTRODUCTION

Permeability is one of the parameters in the evaluation of shale play and the finding of production sweet spots. Pore space geometry and mineral composition influence hydrocarbon production through wettability, capillarity and all phenomena which may occur in nanometer scale pores such as diffusion, condensation etc. [1]. Moreover, fluid flow in shales occurs not only in the mineral matrix, but also in connected organic matter and in natural and induced microfractures. The latter are crucial in estimating permeability because they provide less resistance to flow than nano-sized pores. In recent years, several physical flow models have been proposed to estimate shale permeability; however, all these models require effective pore diameter as an input parameter. Techniques applied to characterize pore systems in conventional reservoir rocks such as mercury intrusion, low pressure gas adsorption or scanning electron microscopy may provide general information

about pore size distribution in shales; however, because of shale ductility and different stress conditions, it might not be sufficient to adequately characterizing pore systems in shales. Moreover, the high pressures applied during mercury intrusion capillary pressure analysis may alter nanopore space.

Slippage measurements for analyzing shale pore structures make it possible to obtain pore sizes in stressed samples. Moreover, such a technique characterizes only the part of the pore system that is responsible for fluid flow. Very few studies have been published that include gas slippage measurement on stressed shale samples [2,3]; however, these studies were performed on mudstones or siltstones, whereas Central European shale formations are mainly claystones, which are more prone to deformation of pore space with effective stress.

In this study, stress-dependent unsteady-state gas permeability measurements were performed. Analysis of Klinkenberg gas slippage effect in comparison with other pore structure characterization techniques is presented.

SAMPLES AND METHODS

The comparison of pore structure analysis was conducted using a series of 10 samples with different fabrics and compositions which represent silurian and ordovician shale formations from the Baltic Basin. The average mineralogical composition of these shale samples is: quartz (21.6 – 43.2 %), minerals from the illite muskovite group (25.9 – 37.75 %), carbonate represented by calcite, dolomite and ankerite (25.9 – 37.8 %), chlorites (3.7 – 13.2 %), plagioclase (2.7 – 5.8%), feldspar (0.7 – 5.2 %), minerals from the illite/smectite group (1.2-7.7%). Mineral composition of samples determined by X-ray diffraction (XRD) is shown in Table 1.

Table 1. Mineral composition of selected samples

Sample ID	Quartz	Total carbonate	Total clay	Pl	F-K	P	Mr
	[%]	[%]	[%]	[%]	[%]	[%]	[%]
3	25.1	16.3	47.0	5.1	2.1	4.4	-
8	21.6	18.1	47.8	4.4	1.5	4.2	2.4
11	23.4	1.3	57.5	4.6	0.9	7.9	3.6
14	25.4	1.4	60.9	5.8	1.9	3.0	1.6
19	28.4	7.1	51.9	4.3	2.5	4.2	1.7
29	26.9	10.7	54.4	3.2	1.7	2.6	0.5
32	34.8	1.8	46.3	5.2	5.2	5.2	1.5
42	26.7	3.1	57.6	4.0	3.2	3.0	2.4
47	31.4	2.8	51.6	4.2	2.9	5.5	1.6
48	29.0	1.8	57.7	4.1	2.7	3.4	1.3

Pl-plagioclase, F-K – potassium feldspar, C- carbonates, P – pyrite, Mr- marcasite,

Stress-dependent unsteady state nitrogen permeability measurements were performed on 1-inch diameter plugs using the pressure pulse decay method. Plugs were run at a range of simple effective stresses defined as the difference between confining pressure and pore pressure. All samples were tested at an effective stress of 33MPa, which imitates reservoir conditions of shale formations in the Baltic Basin. Additionally, to determine the impact

of pore pressure decrease on effective pore diameter, two samples (32 and 42) were subjected to stress of 4.8, 8.2 and 19.9 MPa. The samples were left for 24 hours at each new simple effective stress to allow them to equilibrate at the new stress condition. Klinkenberg plots were generated by plotting permeability versus the inverse of mean pore pressure. Derived from the slope of linear fit of permeability vs inverted pore pressure crossplot, Klinkenberg's slippage parameter was used to calculate pore size assuming slit-shaped and tube-shaped pores.

Prior to permeability testing, the plugs were imaged with a micro X-ray CT scanner and radiography to characterize density and distribution of fractures and distinguish laminations which may affect permeability. In turn, after the permeability measurements, the plugs were crushed and destructive analyses were performed including petrographic analysis (on polished thin sections), scanning electron microscopy (SEM and FIB-SEM), mercury intrusion, low-pressure adsorption, XRD and Rock-Eval analysis.

Petrographic analyses of thin sections and SEM analyses of ion polished sections were performed on mirrored surfaces of the plug (circular cross-section) to characterize the structure and texture of the analyzed shale samples as well as the distribution of natural and induced microfractures. SEM analysis was conducted on a Helios NanoLab 450HP (FEI).

For comparison with pore size obtained by slippage measurements, pore structures were characterized by mercury intrusion (MICP) with Micromeritics AutoPore IV and low pressure nitrogen adsorption at 77K using a TRISTAR apparatus. Pore size distributions were calculated from adsorption data using the Barett, Joyner, Halenda (BJH) method and FAAS correction.

This experimental program minimized the effect of heterogeneity of shale formation, thus providing more comparable data.

Table 2 Porosity, surface area, TOC and permeability of samples analyzed in this study

Sample ID	Total porosity[*]	Open porosity[*]	Specific surface area	BET surface area[**]	TOC	Permeability
	[%]	[%]	[m^2/g]	[m^2/g]	[%]	10^{-15} [m^2]
3	13.15	1.64	1.65	10.56	0.96	0.004075
8	11.16	3.03	2.84	13.02	1.19	0.000605
11	14.59	3.59	1.56	7.96	1.98	0.025966
14	16.12	0.48	0.17	7.67	2.15	0.000584
19	14.57	1.81	2.01	5.63	1.8	0.005894
29	18.57	1.65	1.71	10.98	0.57	0.001971
32	16.20	5.27	5.15	5.84	1.62	0.031097
42	12.59	3.95	2.32	4.32	4.5	0.104597
47	13.16	3.72	4.15	6.46	3.54	0.000358
48	14.98	0.94	0.68	3.27	3.7	0.000228

[*]unstressed porosity; [**]from N$_2$ adsorption data

RESULTS AND DISCUSSION

Complex non-destructive characterization of samples prior to permeability measurements is crucial to estimate the matrix permeability of shale samples [4]. Micro X-ray computed tomography (MXCT) and radiography showed a network of natural and/or induced microfractures (image resolution ~6μm) in all analyzed samples. In most cases, the microfractures are not parallel to lamination or are partially filled with pyrite or calcite, which suggests a natural origin of such microfractures (MXCT image of sample 14 and 42 - Table 3). Moreover, in samples 11 and 14 laminations with thicker detrital material can be distinguished. None of the distinguished microfractures runs through whole sample (length of the samples is ca. 2.3 inches), thus flow-through the samples is affected by the effective pore throats of the matrix. The samples show different structures and, as a result, various pore space geometries; for example, samples 3 and 8 can be classified as clayey-silt micro heterolites (Table 4).

Table 3 MXCT and RTG images of investigated core samples (Part 1)
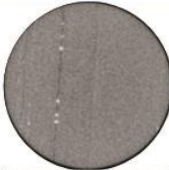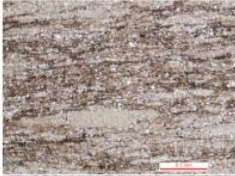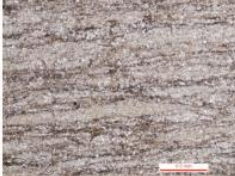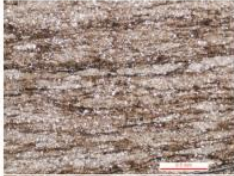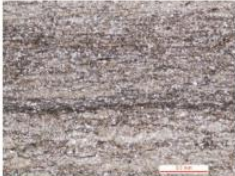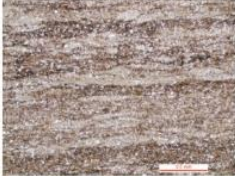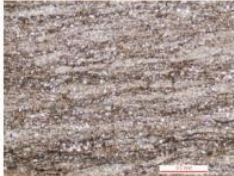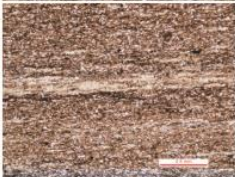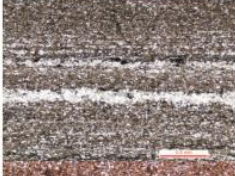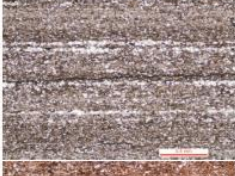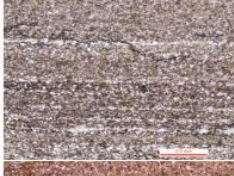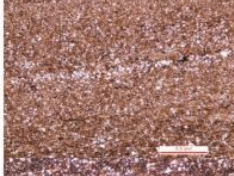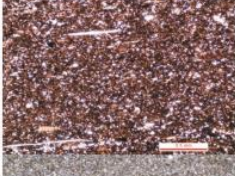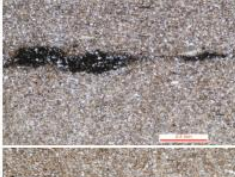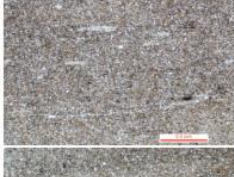
Table 3 MXCT and RTG images of investigated core samples (Part 2)

Pore size distribution for each sample determined using MICP and low pressure adsorption are presented on Figure 1. For samples 11, 14, 47 and 48, effective pore diameter calculated from Klinkenberg is lower due to specific mineral composition consisting of over 50% clay content; also, 5-11% of pyrite and ca. 2% of carbonates may fill up natural microfractures. Moreover, for these samples, relatively high TOC content (2-3.7%) and permeability in the range of several hundreds of nanodarcy were observed. An exception is sample 11, which has permeability in the microdarcy range, probably due to laminations with thicker detrital material and microfractures visible on MXCT, which may affect this permeability value. The remaining samples, which have higher quartz and/or carbonate content, show Klinkenberg pore diameters similar to the dominating pore diameters from MICP or nitrogen adsorption. Such consistency of results may be related to several effects, such as less susceptibility to compression or the occurrence of a specific network of microfractures.

Table 4. Thin sections of selected shale samples

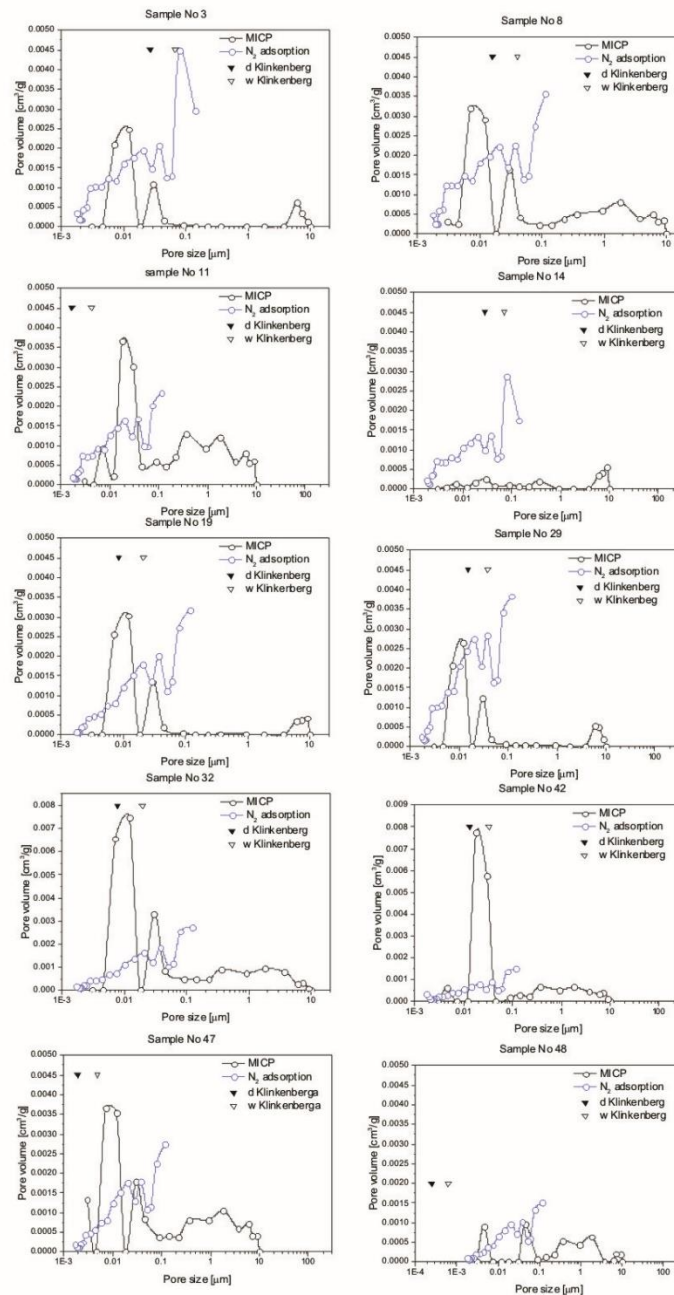| Sample ID	Thin section
3	
8	
11	
14	
32	
42	
47	
48	

Figure 1. MICP and low pressure nitrogen adsorption data. Triangle points show pore sizes calculated according to Klinkenberg at reservoir conditions of the Baltic Basin shale formations. d – diameter of tube shaped pores, w – width of slit shaped pores.

Samples 3, 8, 19 and 29 have very similar pore size distribution curves with high content of micropores and nanopores that can be seen only with nitrogen adsorption; this may suggest deformation of pores formed from clay sheets or pores in organic matter caused by high mercury injection pressure. The most pronounced effect is seen in sample 29, which consists of 54% clay minerals and is characterized by a high BET surface area (over 10

m^2/g). Generally, for samples with domination of nano sized pores observed in MICP, pore diameter at 75% mercury saturation might be assumed as the effective pore diameter that determines flow. In turn, in samples with extremely low open porosity (0.48% - sample 14), effective pore diameter is close to the dominant pore size diameter estimated from nitrogen adsorption data.

In samples 32 and 42, which have very dense low range distribution of microfractures and a bigger microfracture that is clearly seen in MXCT, similar values of Klinkenberg and MICP diameter might be due to the principles of MICP analysis, which sees microfractures as pore throats and, thus, increases the value of effective pore size diameter.

Although, microfractures and pores with diameters in the nanometer range are quite often seen on SEM images, average microfracture widths for samples 32 and 42 (calculated from SEM in an unstressed state) are 3 and 2 times wider, respectively (Table 5). Moreover, more detailed SEM analysis and calculation of average pore diameters using FIB-SEM data showed larger values; this suggests that SEM images of unstressed pores are not geometrically representative of pore structures in the subsurface and cannot be considered during permeability estimation of shale reservoirs.

Table 5 Comparison of slit-shaped pore size and tube-shaped pore size from SEM and Klinkenberg

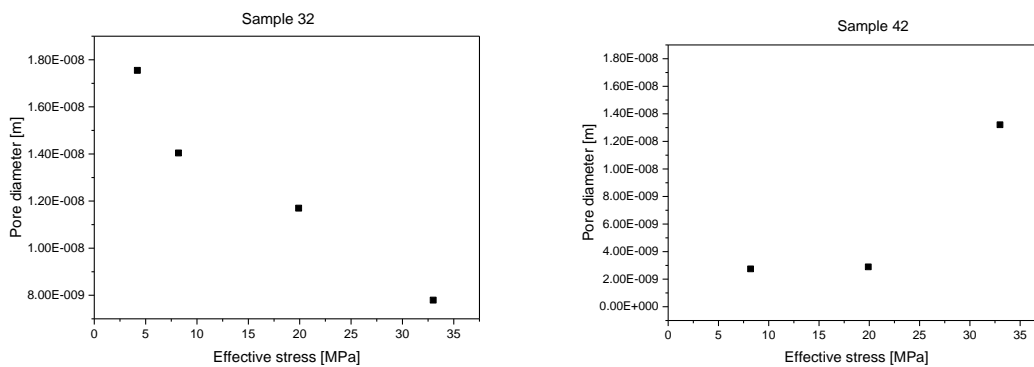| Sample ID	Pore width Klinkenberg	Pore width SEM	Pore diameter Klinkenberg	Pore diameter FIBSEM (median)
	[m]	[m]	[m]	[m]
8	$4.05 \cdot 10^{-8}$	$11.98 \cdot 10^{-8}$	$1.61 \cdot 10^{-8}$	$1.00 \cdot 10^{-7}$
32	$2.35 \cdot 10^{-8}$	$7.21 \cdot 10^{-8}$	$9.39 \cdot 10^{-9}$	$2.50 \cdot 10^{-8}$
42	$3.31 \cdot 10^{-8}$	$7.58 \cdot 10^{-8}$	$1.32 \cdot 10^{-8}$	$1.53 \cdot 10^{-8}$

Figure 2. Pore diameter at different stress states presented for selected samples

Tests at different stress conditions were performed on samples 32 and 42; for sample 32, an increase in effective stress caused a decrease in effective pore size. Such a trend is very intuitive and is expected behavior of a reservoir during hydrocarbon production. However, for some samples increasing effective stress caused the opposite results, as shown in Fig.2 (sample 42). This is attributed to the fact that smaller pores, which are most responsible for

slippage, are cut off from the flow at high effective stress, therefore the slippage effect decreases and the effective pore size increases. A similar decrease in slippage was previously reported for Eagle Ford Shales.

In order to provide proper estimation of permeability in reservoir conditions, the effect of temperature needs to be taken into account. Temperature significantly affects gas density and the mean free path of gas molecules, thus resulting in lower permeability. For the tested samples, there was a change in permeability of one order of magnitude. Moreover, slippage is negatively correlated with permeability and, thus, significantly reduces estimated effective pore diameter.

CONCLUSION

In order to provide more accurate estimation of clay rich shale permeability, additional pore characterization using Klinkenberg slippage is needed on an existing well-characterized plug. Pore size distribution obtained by conventional analysis performed in unstressed conditions may lead to significant errors. However, as has been shown in the paper, microfractures may reduce the effect of stress in rocks with specific mineral composition and pore space structure; thus, dominant pore diameter might be included in estimations of permeability. Initially, it seemed that SEM image analysis produced similar pore diameter measurements as Klinkenberg slippage. However, more detailed analysis showed a large discrepancy between the results. Moreover, for production simulation, correction related to reservoir temperature needs to be considered (as with other reservoir conditions, temperature is naturally included in permeability Pulse Decay measurements).

ACKNOWLEDGEMENTS

REFERENCES

1. Akkutlu I., Didar B., "Pore size dependence of fluid phase behaviour and properties in organic-rich shale reservoirs", *SPE 1640099* SPE International Symposium on Oilfield chemistry, 8-10 April, The Woodlands, USA
2. Cui A., Wust R., Nassichuk B., Glover K., Brezovski R., Twemlow C., "A nearly complete characterization of permeability to hydrocarbon gas and liquid for unconventional reservoirs: a challenge to conventional thinking", *SPE 168730*, Unconventional Resources Technology Conference, 12-14 August, Denver, USA
3. Heller R., Vermylen J., Zoback M., "Experimental investigation of matric permeability of gas shales", *AAPG Bulletin*, **98**, 975-995
4. Rydzy M., Patino J., Elmetni N., Appel M., "Stressed permeability in shales: effect of matrix compressibility and fractures – a step towards measuring matrix permeability in fractured shale samples", *SCA2016-027*, 21-26 August, Snowmass, CO, USA

ELECTRICAL PROPERTIES OF BLACK SCHIST FROM THE HIMALAYAS OF CENTRAL NEPAL

Jana H. Börner[1], Frédéric Girault[2], Frédéric Perrier[2], Mukunda Bhattarai[3],
Lok Bijaya Adhikari[3], Klaus Spitzer[1]

[1] Technical University Bergakademie Freiberg, Institute of Geophysics and
Geoinformatics, Freiberg, Germany
[2] Institut de Physique du Globe de Paris, Sorbonne Paris Cité, Univ. Paris Diderot,
CNRS, Paris, France
[3] Department of Mines and Geology, Lainchaur, Kathmandu

ABSTRACT

Our study is focused on rocks from a shear zone located in the Himalayas of central Nepal,
60 km north of Kathmandu. The whole region was heavily affected by the deadly Mw7.8
Gorkha earthquake in 2015. The shear zone is associated with outcrops of black schist and
large CO_2 discharges with a metamorphic isotopic signature.

We analyzed the frequency-dependent, complex, electrical conductivity of the black schist
and an old augen gneiss, both collected in the shear zone. The electrical conductivity of
both cores and crushed material was measured. Cores were drilled parallel and
perpendicular to the natural foliation in order to investigate local electrical anisotropy.

We carried out laboratory measurements of the complex electrical conductivity, thereby
focusing on anisotropy, salinity dependence and the impact of carbon dioxide on the
electrical properties. The augen gneiss shows the expected low polarizability and moderate
conductivity, which is dominated by the pore-filling brine. It shows a weak anisotropy. By
contrast, the black schist possesses extraordinary high polarizability and, consequently, a
high conductivity. Its anisotropy is very pronounced.

Understanding the anomalous conductivity of the Himalayan black schists provides
valuable information, which might help to interpret the results of deep crustal MT surveys
and reveal the nature of the Himalayan orogeny. Furthermore, understanding the physics
of conductive phases in metamorphous rocks in the presence of CO_2 opens important new
perspectives in numerous applications.

INTRODUCTION

The Himalayan Range, frequently affected by large earthquakes, results from the collision of the Indian plate with Eurasia. The tectonic process essentially takes place along a single subhorizontal fault, the Main Himalayan Thrust (MHT). The MHT exhibits a ramp, which blocks all motion, except during large earthquakes. The so called Main Central Thrust (MCT) shear zone is located approximately 60 km north to Kathmandu (Nepal). It belongs to the Lesser Himalayan Sequence (LHS). The MCT places high-grade metamorphic rocks of the Greater Himalayan Sequence, located northward, over low-grade metamorphic rocks of the LHS (see Fig. 1).
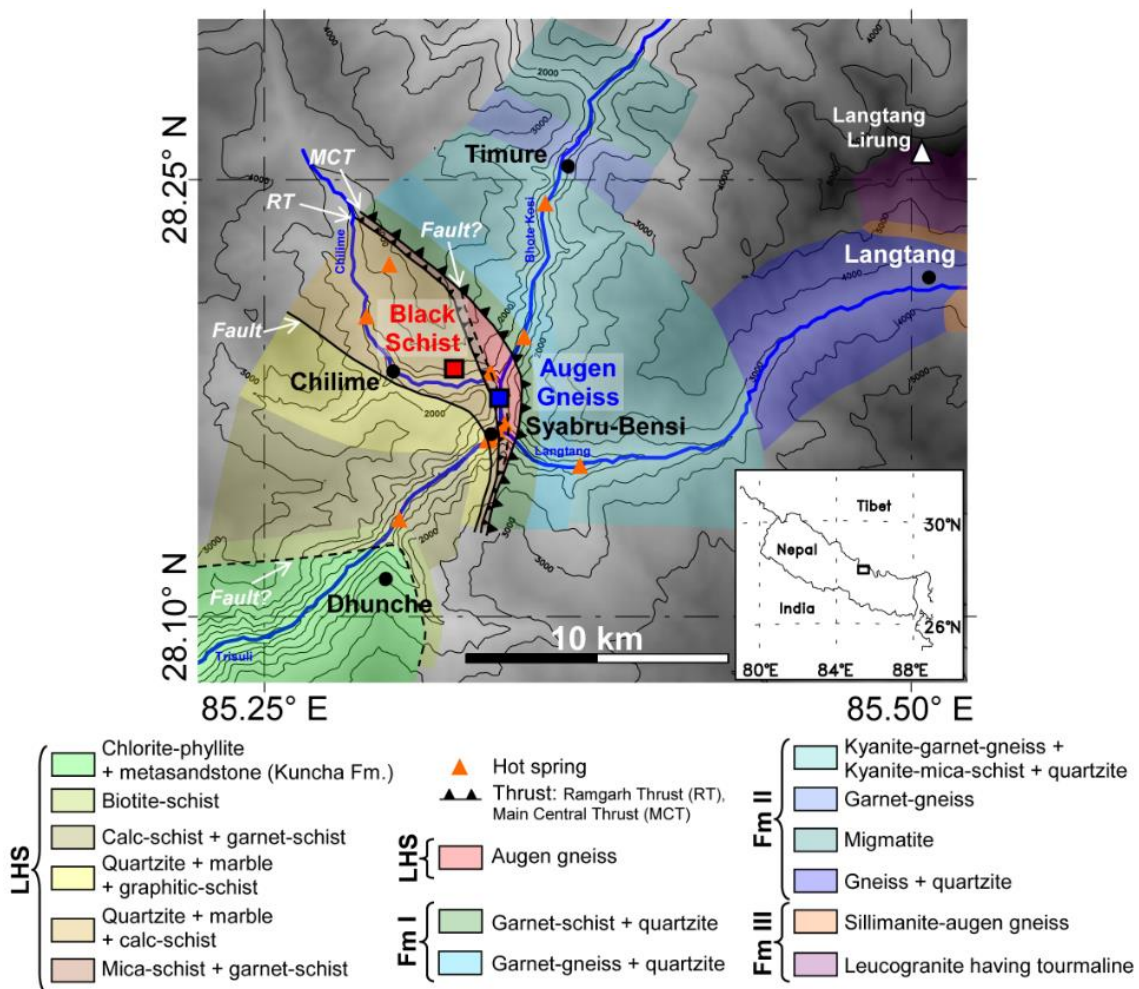

Fig. 1: Geological map of the upper Trisuli and Langtang valleys (central Nepal) showing the sampling locations in the Lesser Himalayan Sequence (LHS). The inset shows the sampling area in Nepal. (geology taken from various sources, see [1] and references therein, courtesy of Laurent Bollinger).

Two decades ago, a magnetotelluric (MT) sounding profile perpendicular to the MHT and MCT revealed a conductive zone associated with seismic activity at a depth of 10 to 15 km (e.g. [2]). Appart from recent investigations, which aim at the reproducibility and numerical stability of said anomaly, different explanatory approaches are available to explain the presence of a deep conductive zone. The zone might be associated either with the presence of highly conductive brines or with the increased occurrence of conductive phases such as graphitic mineralization (e.g. [3]).

More recently, large CO_2 discharges with a metamorphic isotopic signature were discovered [4], and studied in detail on the surface near the location of the conductivity anomaly. The combined observations suggest that carbon, indeed, could account for the observed mid-crustal conductor or at least play an important role in the crustal conductivity structure of the area.

To evaluate this possibility, we analyzed the electrical conductivity of Himalayan rock samples collected in the CO_2 degassing area north of Kathmandu, in the region affected by the deadly Mw7.8 2015 earthquake. We investigated two characteristic rock types of the MCT shear zone: a coarse-grained, quartz-feldspar-biotite-muscovite-tourmaline augen gneiss, and a biotite-rich, black mica-schist. We carried out laboratory measurements of the complex electrical conductivity of the Himalayan rocks, thereby focusing on anisotropy and salinity dependence. Understanding the anomalous conductivity of the Himalayan black schist may provide valuable information, which might help to enhance both the interpretation of deep crustal geophysical surveys and our understanding of the Himalayan orogeny.

MATERIALS AND METHODS

The Himalayan sequences are dominated by high- and low-grade metamorphic rocks. We investigated two characteristic rock types of the Main Central Thrust (MCT) shear zone. The focus of the laboratory study was on the electrical properties of a biotite-rich, black mica schist, which contains 4 to 8% of graphite. For comparison, we also investigated a quartz-feldspar-biotite-muscovite-tourmaline augen gneiss, which is common in the area of interest.

The electrical properties of the rocks were investigated by laboratory measurements of the complex and frequency-dependent electrical conductivity σ (spectral induced polarization method, SIP). The experimental set-up, which is capable of measuring the SIP response under both normal and reservoir conditions, is described in [5]. The resulting conductivity data contains information on both electrolytic conduction (σ_{el}) and polarization effects (σ_{surf}):

$$\sigma^*(\omega) = \sigma_{el} + \sigma_{surf}^*(\omega) \qquad (1)$$

Here, ω denotes angular frequency and the asterisk marks complex quantities. The two conduction mechanisms occur simultaneously and form the bulk conductivity, which may

be described by a real and an imaginary part (σ' and σ'', respectively) or by a magnitude and phase shift ($|\sigma|$ and φ, respectively). Both formulations are equivalent to one another:

$$\begin{aligned}
\sigma^*(\omega) &= \sigma'(\omega) + i\sigma''(\omega) \\
&= |\sigma^*| \cdot e^{i\varphi} \\
&= \left[\sigma_{el} + \sigma'_{if}(\omega)\right] + i\sigma''_{if}(\omega)
\end{aligned} \qquad (2)$$

We used core samples, drilled both parallel and perpendicular to the natural foliation of the rocks, as well as crushed samples. The supplementation of our investigations by crushed samples allows for a better understanding of the conduction mechanisms within the rock and for an efficient realization of multi-salinity experiments of rocks, which are very low-porous in their consolidated state. In addition, measurements on black schist – quartz sand mixtures were carried out in order to investigate the mass fraction of black schist, which is necessary to dominate the bulk properties. Exemplary experiments in a CO_2 atmosphere at elevated pressure were conducted to assess the impact of CO_2 on the SIP response of the investigated rocks.
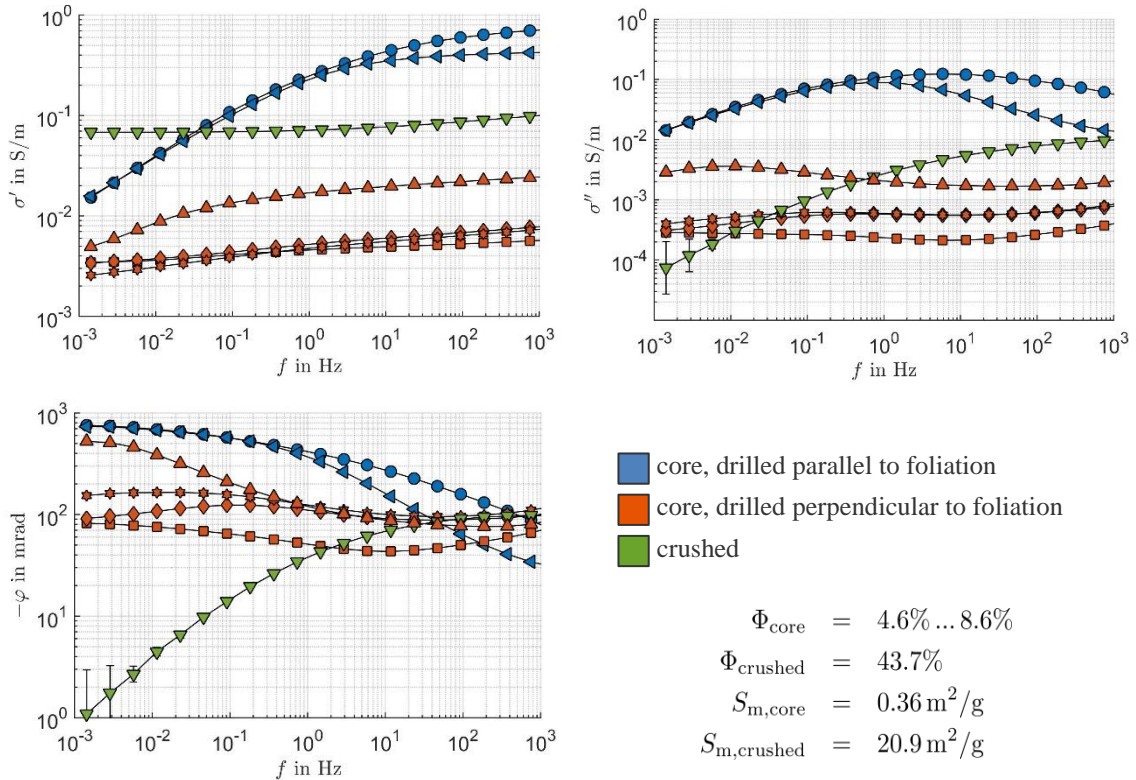

Fig. 2: Frequency-dependent complex conductivity of the black schist in terms of real part conductivity (top left), imaginary conductivity (top right) and phase shift (bottom left). All samples were saturated with a NaCl solution with a conductivity σ_w=0.1 S/m. The porosity Φ and the specific inner surface area of both cores and crushed material are given in the bottom right panel.

RESULTS

The black schist investigated in the laboratory shows highly anomalous electrical properties. The conductivity data of various cores and the crushed samples in shown in Fig. 2. Generally, the black schist is very conductive given its low porosity. At the same time it is extremely high polarizable, which shows up in the high imaginary conductivity and phase shift.

Conductivity is strongly dependent on frequency, which means that a black schist formation may appear differently at different frequencies (and therefore depths after inversion) of electromagnetic surveys such as MT or CSEM (controlled source electromagnetics). The very pronounced polarization and surface conduction is probably due to the presence of graphite.

A crushing of the sample causes an averaging of both real and imaginary conductivity at high frequencies. At the same time, the low frequency response is lost due to crushing. This implies, that a large part of the electrical conduction is associated with the texture of the solid core material, which is destroyed during crushing. Measurements on black schist – quartz sand mixtures demonstrated that already rather low mass fractions (appr. 25%) of black schist can dominate the bulk properties of the whole material.

$$\Phi_{core} = 1.9\% \dots 2.6\%$$
$$\Phi_{crushed} = 38.1\%$$
$$S_{m,core} = 0.34\,m^2/g$$
$$S_{m,crushed} = 2.2\,m^2/g$$

core, drilled parallel to foliation
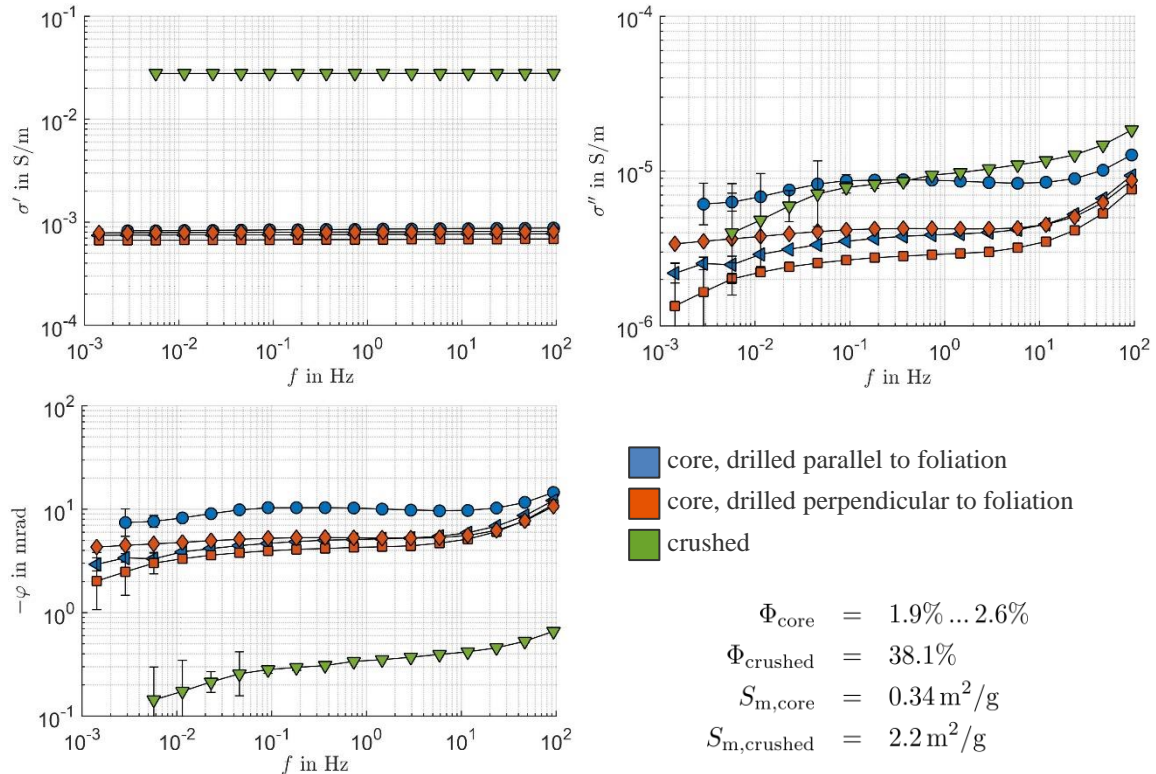core, drilled perpendicular to foliation
crushed

Fig. 3: Frequency-dependent complex conductivity of the augen gneiss in terms of real part conductivity (top left), imaginary conductivity (top right) and phase shift (bottom left). All samples were saturated with a NaCl solution with a conductivity σ_w=0.1 S/m. The porosity Φ and the specific inner surface area of both cores and crushed material are given in the bottom right panel.

The anisotropy of the black schist is very pronounced for both real & imaginary conductivity (factor 50 at 1Hz). Depending on the direction of the foliation both magnitude and frequency characteristics of the conductivity components change significantly. This means that black schist structures may show a strongly directional conductivity during geophysical imaging.

The measurements of the black schist indicate that the graphite is arranged according to the foliation without forming connected bands. If connected bands were present, this would show up as a strong ohmic (i.e. real-valued, frequency-independent) conductivity contribution. Since the polarization effects dominate the black schist properties, the graphite seems to be disseminated and only loosely aligned along with the foliation.

For comparison, the abundant augen gneiss was investigated, the results are plotted in Fig. 3. Compared to the black schist, the augen gneiss shows –as expected – a low conductivity, which is dominated by electrolytic processes. Its imaginary conductivity is small and the frequency dependence is weak, which indicates that polarization effects are moderate. It is also evident, that the crushing procedure has only little effect on the imaginary conductivity. This observation leads to the conclusion that the polarization effects present in the augen gneiss are driven by bulk volume effects and do not depend on the texture of the solid material.

Despite the macroscopically visible foliation, the electrical anisotropy of the augen gneiss is rather weak. Although a small tendency to higher conductivity and polarization along the foliation may be seen, it is in the same range as the individual variety of the core properties and cannot be considered significant. Except for a potential large scale fracture anisotropy, the gneiss may be considered as isotropic from the electrical point of view.
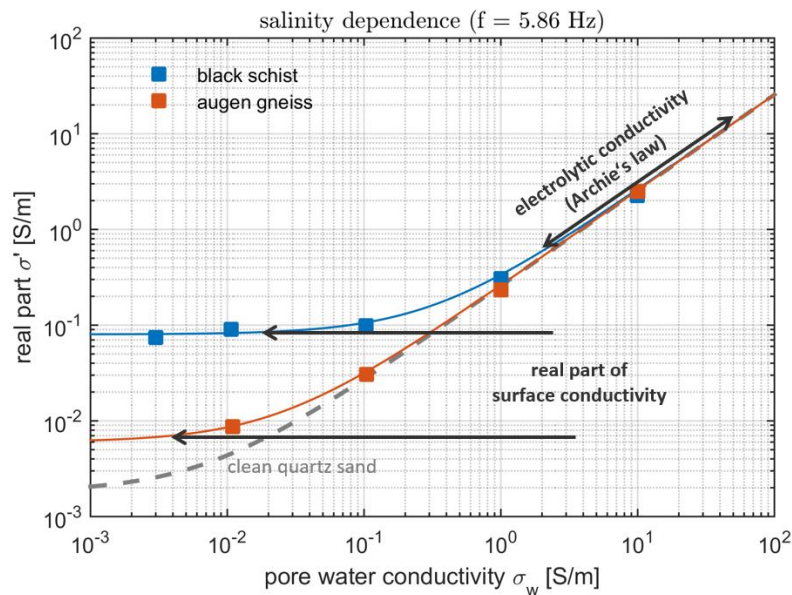

Fig. 4: Salinity dependence of real part conductivity derived from multi-salinity experiments on crushed samples. The Archie region and the real part of the surface conductivity (cf. Eq. 2) are indicated [6,7].

The dominance of electrolytic conduction in the augen gneiss implies that inferring brine conductivity from electrical measurements (for known porosity and temperature) should be well possible. To further investigate the relationship between water conductivity (i.e. salinity) and conductivity we carried out multi-salinity measurements on crushed samples of both black schist and augen gneiss.

The results are shown in Fig. 4 in terms of the real conductivity at 5.86 Hz. The curve of a typical clean quartz sand is shown for comparison. The slope of the curves at high water conductivities represent the formation factor whereas the intercept with the y-axis (appears as horizontal asymptote at low water conductivities) is the real part of surface conductivity.

The investigations show, that both black schist and augen gneiss have a comparable formation factor, which is due to the similar porosity and particle size of the crushed samples. The real part of the surface conductivity is however very different for both rocks. The augen gneiss exhibits a low surface conductivity - as found in the complex conductivity as well – and is mainly dominated by the Archie behaviour. As expected, it is well possible to relate water and bulk conductivity.

On the other hand the black schist shows an extremely high real surface conductivity, which dominates bulk conductivity over a wide range of salinities. In presence of the black schist, a high formation conductivity might consequently be misinterpreted in terms of brine conductivity if the surface conduction and polarization effects are not taken into account.

Exemplary experiments with the water-saturated, crushed rocks under CO_2 at 5MPa hydrostatic pressure for 5.5 to 7 days demonstrated the change in electrical properties due to the interaction of the rocks with CO_2. The real conductivity strongly increased for both rocks due to CO_2 dissolution and dissociation and the heavy mineral dissolution starting under pressure. The imaginary conductivity in- or decreases due to CO2 depending on pH-variation and mineral dissolution [5,8]. The strong reaction of the real conductivity causes a decrease in phase shift in all cases.

CONCLUSION

The investigated rocks possess anomalous and highly indicative electrical properties. The black schist is highly conductive also at low salinities or mass fractions due to the dominating surface conduction. This implies that black schist formations could appear as conductive anomalies in large scale MT surveys. Such high conductivity might be misinterpreted as brines, when the surface conduction is neglected. The strong anisotropy and frequency dependence has to be considered for black schist formations. The complex conductivity measurements suggest that the graphite is disseminated within the black schist but with a preferred orientation along the natural foliation.

The augen gneiss on the other hand is characterized by a strong domination of electrolytic conduction and low surface conduction. Consequently, gneiss formations are more sensitive to changes in formation brine salinity and effects of surface conduction are probably negligible on a large scale. The laboratory evaluation will enhance our

understanding of the anomalous conductivity of the Himalayan rocks and will provide valuable information, which might help to reveal the nature of the Himalayan high conductivity zone.

ACKNOWLEDGEMENTS

REFERENCES

1. Girault, F. & Perrier, F., *Measuring effective radium concentration with large numbers of samples. Part I – experimental method and uncertainties*, Journal of Environmental Radioactivity, Volume 113, November 2012, Pages 177-188.
2. Lemonnier, C., Marquis, G., Perrier, F., Avouac, J.-P., Chitrakar, G., Kafle, B., Sapkota, S., Gautam, U., Tiwari, D., & Bano, M., 1999. *Electrical structure of the Himalaya of Central Nepal: high conductivity around mid-crustal ramp along the MHT*, Geophysical Research Letters, 26, 3261–3264.
3. Groppo, C., Rolfo, F., Castelli, D. & Connolly, J. A. D., 2013. *Metamorphic CO_2 production from calc-silicate rocks via garnet-forming reactions in the CFAS–H_2O–CO_2 system*, Contrib. Mineral. Petrol., 166, 1655-1675.
4. Girault, F., Bollinger, L., Bhattarai, M., Koirala, B., France-Lanord, C., Rajaure, S., Gaillardet, J., Fort, M., Sapkota, S., & Perrier, F., 2014. *Large-scale organization of carbon dioxide discharge in the Nepal Himalayas*, Geophysical Research Letters, 41, 6358–6366.
5. Börner, J.H., Herdegen, V., Repke, J.-U. and Spitzer, K., 2017. *Spectral induced polarization of the three-phase system CO_2 - brine - sand under reservoir conditions*. Geophysical Journal International. 208 (1): 289 - 305.
6. Archie, G. E. (1942): *The electrical resistivity log as an aid in determining some reservoir characteristics*. Trans. Americ. Inst. Mineral. Met. 146, S. 54–62.
7. Waxman, M. H. & L. J. M. Smits (1968): *Electrical conductivities in oil-bearing shaly sands*. In: Society of Petroleum Engineers Journal 8, S. 107–122.
8. Börner, J.H., Herdegen, V., Repke, J.-U. and Spitzer, K., 2015. *The electrical conductivity of CO_2–bearing pore waters at elevated pressure and temperature: A laboratory study and its implications in CO_2 storage monitoring and leakage detection*. Geophysical Journal International. 203 (2): 1072 - 1084.

IMPROVED CHARACTERIZATION OF UNCONVENTIONAL RESERVOIRS BY ANISOTROPY OF MAGNETIC SUSCEPTIBILITY

Norbert Schleifer[1], Nina Gegenhuber[2] and Robert Scholger[2]

(1) Wintershall Holding GmbH, Central Laboratory, Germany; (2) Montanuniversität Leoben, Chair of Applied Geophysics, Austria

ABSTRACT

The re-evaluation of the legacy data of two Rotliegend gas-wells within the Northern German basin required a routine core analysis program which was designed including the non-destructive measurement of the anisotropy of the magnetic susceptibility (AMS).

The main objective of this approach was to see whether the depositional environment of the sedimentary rocks can be correlated with the degree of magnetic anisotropy. The study should further clarify whether adding rock magnetic properties to a core analysis program leads to an improved understanding of unconventional reservoir rock.

The program covered basic petrophysical parameters as porosity, gas-permeability and grain density, but also ultrasonic velocity (shear and compressional wave) and internal surface area (S_{por}). Magnetic Properties were measured at the Paleomagnetic Laboratory of the MU Leoben. Advanced magnetic methods were included to identify the iron minerals dominating the magnetic properties and the orientation of its remanent (permanent) magnetization. Results show that environments which represent low energetic deposits can be identified by low porosities and permeabilities, but also by a high magnetic susceptibility and an anisotropy characterized by a shape parameter ranging from positive to negative values. On the other hand, higher energetic depositional environments as dunes and sandflats are characterized by high porosities and permeabilities as well as low magnetic susceptibility and a positive shape parameter.

In contrast to the other petrophysical parameters the AMS shape parameter of distinct facies show differences between investigated wells and within single members of the Rotliegend Waste Zone. The abundance and orientation of minerals with higher magnetic susceptibility, e.g. iron minerals, clays, is obviously correlated to certain depositional environments and has also an impact on the key petrophysical parameters porosity and permeability.

INTRODUCTION

Around 2010 it was decided to re-evaluate the tight gas-potential of the sandstones of the so-called "Rotliegend waste zone" in the Northern German Basin. The Rotliegend is of

Permian age. The "Waste Zone" is defined by five members of the Hannover formation below the Zechstein formation and above the conventionally produced Wustrow Member. Samples for this study come from the Bahnsen, Niendorf and Munster members. Thickness of the "Waste Zone" can reach up to 125 m as in the fairway north of Hannover. The RWZ consists of Sabkha sediments (Neuendorf et al., 2005) deposited in the vicinity of a salt lake dominated by silts and clays with sands associated mainly with thick silt deposits. As the size of the salt lake varied throughout time depositional environments with different energetic levels are present. Samples from two wells RWZ 1(B) and RWZ 2(D) were investigated for this study covering a variety of depositional environments. These facies and their characteristics are listed in Table 1. Core description and facies definition along the cores is based on gamma-ray well log cut-offs. Some zones remain "undefined" in terms of facies category.

ROUTINE CORE ANALYSIS PROGRAM

After reviewing the available legacy data it became clear that laboratory techniques in the 1970's were limited to permeability measurements above 0.1 mD. The new measurements covered 58 plugs from well RWZ 1(B) and 131 plugs from well RWZ 2(D). Plug diameter and height is 30 mm.

Precipitated salt while storage was removed by immersion in 2%-KCl brine. Conductivity of the brine was monitored until no further increase was observed.

The program covered the following measurements.

- Steady state air-permeability
- Porosity and grain density using Archimedes principle
- Specific pore surface area S_{por} by N_2-adsorption using BET method
- Ultrasonic velocity of compressional V_p and shear waves V_s

Experiments

Steady State Air-Permeability

Air-permeability is measured by a steady-state setup using atmospheric flow mode. Confining pressure is set to 400 psi. Each measurement was repeated three times. Klinkenberg permeability is calculated based on the equation by Riekmann, 1970,

$K_a = K_L/(1+0.5*K_L^{-0.37}/P_m)$
with

K_a: apparent permeability, K_L: Klinkenberg permeability, P_m: mean pressure

Porosity and Grain Density

Archimedes principle using isopropyl-alcohol was applied to measure porosity and permeability. Cleaned samples were dried at 80°C and weighted. 100% saturation was achieved by immersion of the samples under vacuum pressure. Samples stayed immersed till the weighting cycle was finished.

Specific Pore Surface area (S_{por})

The measurement of S_{por} was run on 30 selected samples at the Chair of Mineral Processing at MUL. A Test requires 10g of sample material. Samples were heated at 200 °C up to 4 hours to establish constant dry weight. Weight changes were monitored. A Flowsorb 2300© Micromeritics™ instrument was used. Surface area in units m^2/g was determined by nitrogen adsorption as well as desorption using BET method.

Ultrasonic velocity of compressional V_p and shear waves V_s

Ultrasonic velocities were determined at ambient conditions without confining stress on dry samples. Compressional (V_p) and shear wave (V_s) velocity probes were used with a frequency of 1 MHz (Gegenhuber & Schön, 2014). Wave propagation was along the cylindrical axis of the plugs.

ANISOTROPY OF MAGNETIC SUSCEPTIBILITY (AMS)

Magnetic susceptibility k_m describes the behaviour of a material in a magnetic field (Thompson & Oldfield, 1986) and is a non-destructive method. Sediments and sedimentary rocks show low magnetic susceptibilities compared to other rock types like volcanic or metamorphic rocks. Abundant minerals as quartz, calcite and kaolinite show diamagnetic behavior resulting in negative values. Abundance of paramagnetic minerals in contrast increase k_m, e.g. illite, micas and siderite, chlorite. Examples for the application of the method in core analysis are given by Potter, 2007 and Potter et al., 2011. As other petrophysical parameters like permeability and ultrasonic velocity, K_m is a directional dependent parameter. During sedimentation magnetic minerals can be aligned along a preferential direction or within a plane. This process is influenced by particle size and shape, dynamics of the depositional environment, direction of the current magnetic field and post-sedimentary processes. The resulting anisotropy of magnetic susceptibility (AMS) is characterized by an ellipsoid, whose axes are defined by maximum susceptibility (k_{max}), intermediate susceptibility (k_{int}) and minimum susceptibility (k_{min}). Several parameters are defined to the shape and degree of anisotropy (Table 3). The main anisotropy parameter referred to in this paper, is shape parameter T. In general a positive T close to 1 characterizes an oblate shaped ellipsoid. Low energetic environments or depositional environments without predominant flow direction should show this AMS behaviour. Deposits with a dominant flow direction within a bedding plane also result in a flat ellipsoid but the dominant flow direction should be represented by a $k_{max} > k_{int}$ within the bedding plane if the remanence carriers are dominantly multidomain magnetite (Potter

& Stephenson, 1988). This results in a lower positive shape parameter T. Negative T values are assigned to prolate shaped ellipsoid. This means that there is a dominant flow direction but no alignment within a bedding plane ($k_{max} > k_{int}$, $k_{int} \sim k_{min}$). Shape parameters close to zero represent no pronounced AMS with a $k_{max} \sim k_{int} \sim k_{min}$. All measurements were carried out with a AGICO MFK 1 Multifunctional Kappabridge.

NATURAL REMANENT MAGNETIZATION

The natural remanent magnetization (NRM) (Thompson&Oldfield, 1986) is defined as the magnetization of a rock which is also present without an external magnetic field. Titanium-iron oxides are the main carriers of this magnetization. There are several processes whereby an NRM can be created, e.g. cooling of rocks below the Curie-temperature (thermoremanent magnetization) in the Earth's magnetic field leads to the alignment of mineral domains and the resulting NRM records the prevailing Earth's magnetic field direction (assuming the sample is not very anisotropic).

In the Paleomagnetic laboratory of MUL the paleomagnetic field is investigated by a 2G Cryogenic Magnetometer Modell 760-4K. Carriers of NRM can be investigated by stepwise destroying the NRM by heating up to the Curie temperature or by applying strong alternating magnetic fields (AF). Achieving a saturated isothermal remanent magnetization (SIRM) aligning all the magnetic domains along a strong applied field also gives insight into the abundant iron minerals. The ratio of remanent magnetization to induced magnetization is called the Remanence-factor or Königsberger Factor Q. The induced magnetization is calculated multiplying K_m with the average Earth's magnetic field strength (50 µT).

RESULTS

The distribution of the depositional environments within the porosity-permeability cross-plot are shown in Figure 1. A maximum porosity of 19.3 % and a maximum permeability of 140.5 mD are found in well RWZ1 (B). Most of the samples from well RWZ2 (D) lie below 10% porosity and have a Klinkenberg permeability K_L between 0.001 to 10 mD. Samples from low energetic depositional environments like pond/lake, aeolian mudflat and low energetic fluvial deposit tend to have lower porosities and permeabilities. The sandflat deposits cannot be discriminated and show a distribution above 1% porosity and between 0.01 and 100 mD. Aeolian dune (base) show intermediate values.

Looking at the susceptibility (K_m) and shape parameter (T) cross-plots, depositional environments can be distinguished (Fig. 2). In well RWZ 1(B) high susceptibility ($100*10^{-6}$ SI $<K_m< 1000*10^{-6}$ SI) is associated to samples from low energetic fluvial deposits, pond/lake and aeolian mudflat. Shape parameters of this samples vary between positive and negative values. Aeolian dune (base), dry, damp and wet sandflat samples have low to intermediate K_m but are characterized by T values mainly above 0.5. In well RWZ 2 (D) no clear discrimination of the depositional environment is possible based solely on K_m. However again dry, damp and wet sandflat samples are associated to high T values. In contrast to well RWZ 1 (B) pond/lake samples have only positive T values and aeolian dune (base) samples show T values around zero. Samples from low energetic fluvial

deposits can be found with positive as well as negative T values, with the majority in the positive range.

Comparing the magnetic carriers within each well and facies (Table 3) one can see that despite aeolian mudflat, pond/lake and low energetic fluvial deposit samples in well RWZ 1(B) magnetite is the dominant iron mineral and in well RWZ 2(D) hematite is the dominant iron mineral. Correlations with other petrophysical parameters as compressional wave velocity V_p and specific surface area S_{por} measured via nitrogen adsorption are shown in Figure 3. High velocities and susceptibilities are associated with aeolian mudflat, pond/lake and low energetic fluvial deposits. Velocities below 4000 m/s and susceptibilities below $250*10^{-6}$ SI are associated with sandflat deposits as well as aeolian dune (base). Adsorption S_{por} versus K_m show a different distribution. Aeolian mudflat, pond/lake and low energetic fluvial deposit have highest values ($S_{por} > 1$ m^2/g; $K_m > 100*10^{-6}$ SI). Dry and amp sandflat together with aeolian dune (base) show lowest values (S_{por} a 0.1-1 m^2/g; $K_m < 100*10^{-6}$ SI).

Wet sandflat samples are in the same S_{por} range but show Km values above $100*10^{-6}$ SI.

Compiling the results of petrophysical measurements facies dependent parameters can be found. An example is given in Table 4. Within Niendorf member of well RWZ2 (D) correlations could be found allowing to distinguish between the four depositional environments: Aeolian mudflat, dry, damp and wet sandflats. Parameters leading to this discrimination are K_m, NRM, Shape parameter T, porosity and permeability. Figure 4 shows a depth plot of these parameters within the Niendorf member of RWZ2 (D).

DISCUSSION

The conventional porosity-permeability cross-plots show the expected distribution with clay rich facies as pond/lake and aeolian mudflat having lowest values (Fig.1). Facies with no or less clay, as aeolian dune (base) and dry sandflat show highest porosity and permeability. As their clay content lie in a narrow range the damp and wet sandflat as well as the low energetic fluvial deposits show a wider range of permeability even higher than the dry sandflat facies. S_{por} is a parameter which is dominated by clay content. In Figure 3 the sandflat facies have overlapping S_{por} which explains the wide variation of permeability within these facies. Aeolian dune (base) show a tendency towards higher S_{por} which might be explained by a higher fraction of finer sand grains. Although the fluvial deposits are distributed in the lower permeability range their S_{por} is comparable with sandflats and aeolian dune (base). The impact of grain size and grain contacts is measured by compressional wave velocity V_p (Fig. 3). Aeolian dune (base) and sandflats show lowest velocities based on larger grain sizes and higher porosities compared to clay rich facies. Magnetic susceptibility supports this discrimination. In well RWZ 1(B) pond/lake, aeolian mudflat and low energetic fluvial deposits are characterized by high susceptibility and shape parameters varying between -0.5 and 1 (Fig. 2, left). Fluvial deposits in well RWZ 2(D) show a different behavior. They have a lower K_m but a tendency towards positive T values (Fig. 2, right). Permeability and porosity values of this facies are also higher in well RWZ 2(D). Although less abundant, a better alignment of hematite, as magnetic carrier (Table 3) seems to exist in this well.

The AMS of the investigated environmental deposits shows differences between the two wells which do not become obvious when looking at the conventional porosity-permeability correlation. Aeolian dune (base) samples show distinct positive T values in well RWZ 1(B) but values close to zero in well RWZ 2 (D). The same shift towards lower values can be observed within the sandflat and aeolian mudflat facies. In contrast pond/lake and low energetic fluvial deposit samples show a trend towards more positive T values. The impact of magnetic carriers and their domain state on AMS in this study has not been fully understood yet (Potter & Stephenson, 1988), however the different distributions of the shape parameters within the two wells might be an indication for that.

Acidization or mobilization of iron minerals (Gaupp&Schöner, 2008) might be another reason for weaker foliation in the lower energetic deposits than in the higher energetic deposits. A magnetic overprint by the coring process could be identified in both wells with a stronger impact on samples of well RWZ 2(D). The example of well RWZ 2(D), Niendorf member (Table 4, Fig. 4) shows that depositional environments are distinguishable by using a compilation of the petrophysical parameters K_m, NRM, T, porosity and permeability. The facies aeolian mudflat and damp sandflat also show that their shape parameter can change from positive to negative values within a Rotliegend member of a single well.

CONCLUSIONS

The study shows that implementation of AMS leads to an improved petrophysical discrimination of depositional environments compared to conventional porosity-permeability cross-plots. All samples included in the study show a measurable and distinct anisotropy. As the method is cheap and non-destructive it can be easily included in conventional core analysis workflows. Interpretation of the results however need additional rock magnetic studies to identify the magnetic carriers and to understand post-sedimentary impacts on magnetic anisotropy. AMS response of depositional environments and main magnetic carrier change between two wells of same stratigraphy. Even within a single well and within a single Rotliegend member same depositional environments defined by core description appear different in their AMS response.

NOMENCLATURE

AF: Alternating magnetic field.
AMS: Anisotropy of magnetic susceptibility
BET: Interpretation of nitrogen adsorption/desorption data (Brunauer et al., 1938).
K_a: apparent (measured) permeability
K_L: Klinkenberg corrected permeability.
K_m: (Mean) magnetic suceptibility.
K_{max}, K_{int}, K_{min}: maximum, intermediate and minimum susceptibility.
NRM: Natural remanent magnetization
P_m: Mean Pressure
Q: Remanence Factor, Königsberger Factor.
SIRM: saturated remanent magnetization.
Spor: Specific surface area in m^2/g measured by nitrogen adsorption.
V_p, V_s: Ultrasonic compressional and shear wave velocities (m/s).

ACKNOWLEDGEMENT

REFERENCES

1. *Brunauer, S.; Emmett, P. H.; Teller, E. (1938):* Adsorption of Gases in Multimolecular Layers. Journal of the American Chemical Society. Vol. 60, No. 2, pp. 309–319.

2. *Gaupp, R. & Schöner, R. (2008):* Intra-reservoir generation of organic acids and late stage enhanced porosity in sandstone. AAPG Annual Conference. Article #40373.

3. *Gegenhuber, N. & Schön, J. (2014):* Thermal Conductivity Estimation from Elastic-Wave Velocity—Application of a Petrographic-Coded Model. Petrophysics, Vol. 55, No. 1, pp. 51–56.

4. *Neuendorf, K.; Mehl, J. and Jackson, J. (2005):* Glossary of Geology 5th edition. American Geological Institute.

5. *Potter, D. K. and Stephenson, A. (1988):* Single domain particles in rocks and magnetic fabric analysis. Geophysical Research Letters, 15, 1097-1100.

6. *Potter, D. K. (2007):* Magnetic susceptibility as a rapid, non-destructive technique for improved petrophysical parameter prediction. Petrophysics, Vol. **48**, No. 3), pp. 191-201.

7. *Potter, D. K., Ali, A., Imhmed, S. and Schleifer, N. (2011).* Quantifying the effects of core cleaning, core flooding and fines migration using sensitive magnetic techniques: implications for permeability determination and formation damage. Petrophysics, Vol. **52**, No. 6, pp. 444-451.

8. *Riekmann, M. (1970):* Untersuchung von Turbulenzerscheinungen beim Fließen von Gasen durch Speichergesteine unter Berücksichtigung der Gleitströmung. Erdöl-Erdgas-Zeitschrift, Jg. 86, pp. 36-51.

9. *Thompson R. and Oldfield, F. (1986):* Environmental Magnetism: London, Allen & Unwin, 277 p.

Table 1: Depositional environments (facies) investigated in the study.	
Facies:	Classification
Aeolian dune (base)	Well bedded, fine to coarse sand deposits with upward increasing dip angles. Bases consist of sandstones with angels of 5-15° increasing upward to more than 15°. cross-bedding. Variation of sediments depend on wind velocity.
Aeolian mudflat	Wavy laminated claystones with lenses of siltstone, clay content > 50%, periodical subaerial deposition, sand and silt were blown into the clay deposit
Damp sandflat	Aeolian sands temporarily deposited under aquatic conditions, adhesive bound clay possible, clay content < 20%
Dry sandflat	No clay, maximum dip angle 5%
Wet sandflat	Aeolian sands deposited under wet conditions, clay/silt content 20 to 50%, clasts of clay deposited by high energetic flow.
Low energetic fluvial deposit	Low energetic, shallow braided stream channel system and sheetflood sediments. Fine grained to coarser sediments.
Pond/lake	Silt with high clay content (>95%), sand inclusions, lamination, low energetic deposit

Table 2: Definition of anisotropy parameters used in the study.				
Parameter	Equation	Oblate (disc)	Prolate (cigar)	Neutral
Mean susceptibility	$K_m=(k_{max}+k_{int}+k_{min})/3$	$k_{max} \sim k_{int} > k_{min}$	$k_{max}>k_{int}\sim k_{min}$	$K_{int}=(k_{min}*k_{max})/2$
Foliation F	$F = k_{int}/k_{min}$	high	low	F=L
Lineation L	$L = k_{max}/k_{int}$	low	high	L=F
Shape Parameter T	$T = (\ln (L) - \ln (F))/ (\ln(L)+ \ln (F))$	$0<T\leq1$	$-1\leq T<0$	T=0
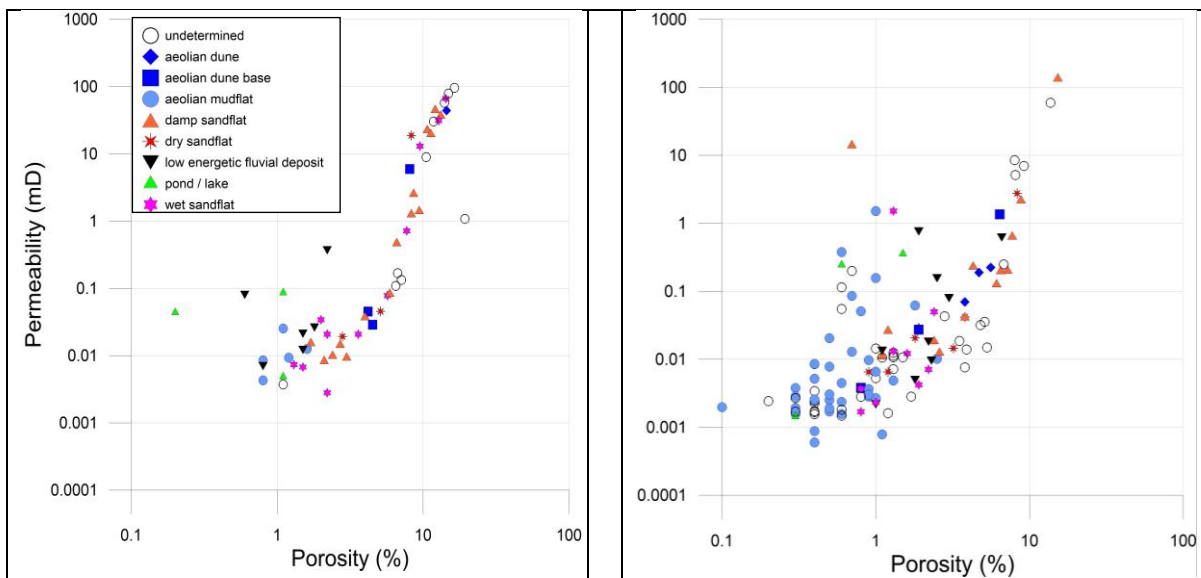
Figure 1: Double-logarithmic porosity-permeability cross-plots for the wells RWZ 1(B) (left); RWZ 2(D) (right) with indication of depositional environment.
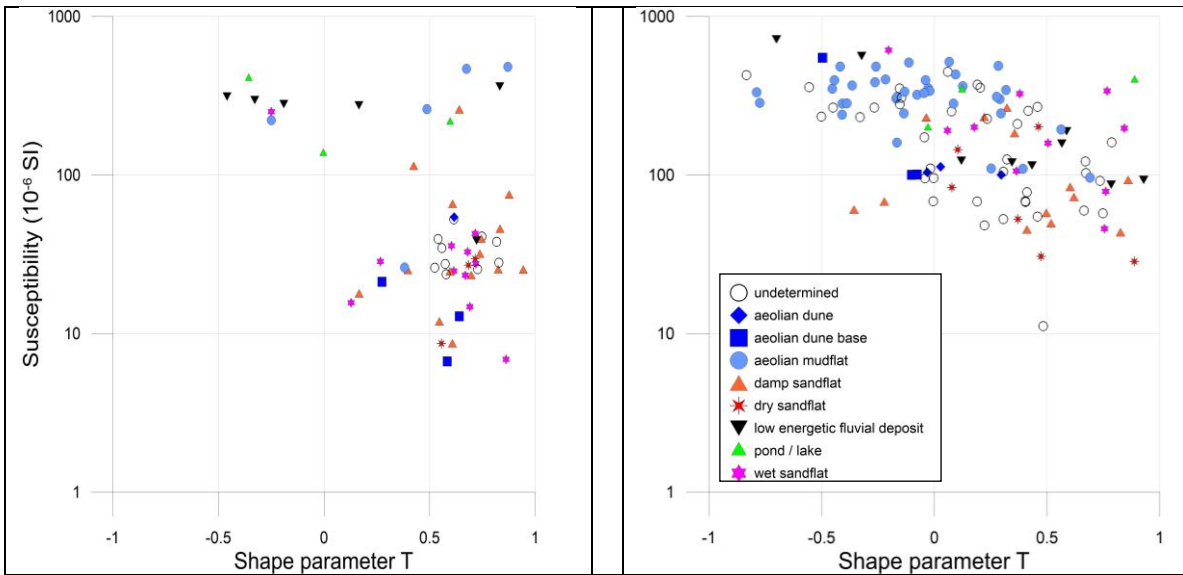
Figure 2: Shape Parameter T versus K_m for the wells RWZ 1(B) (left); RWZ 2 (D) (right) with indication of depositional environment.
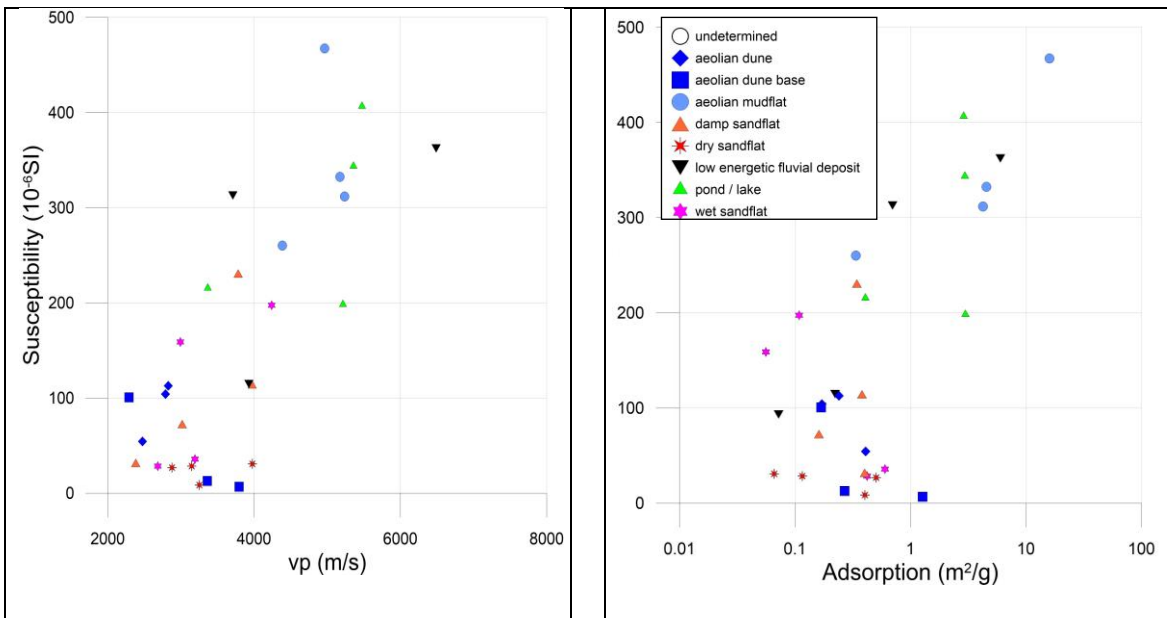

Figure 3: Cross-plots of K_m versus Vp (left) and adsorption S_{por} (right) with indication of depositional environment.

Table 3: Carriers of NRM within the depositional environments:		
Facies	**Well RWZ1 (B)**	**Well RWZ2 (D)**
Aeolian dune (base)	Magnetite	Hematite
Aeolian mudflat	Magnetite, hematite	Hematite
Wet sandflat	Magnetite	Hematite
Damp sandflat	Magnetite	Hematite
Dry sandflat	Magnetite	Magnetite
Low energetic fluvial deposit	Hematite	Hematite
Pond/lake	Hematite	Hematite

Table 4: Facies dependent petrophysical parameters within well RWZ2 (D) Niendorf member.			
Aeolian mudflat	*Dry sandflat*	*Damp sandflat*	*Wet sandflat*
high K_m	low to intermediate K_m	low Km	low Km
high NRM	low to intermediate NRM	low NRM	low NRM
$-0.5 < T < 0.75$	$T > 0$	$-0.5 < T < 1$	$T > 0$
low porosity	high porosity	intermediate to high porosity	low porosity
low permeability	high permeability	intermediate to high permeability	low permeability
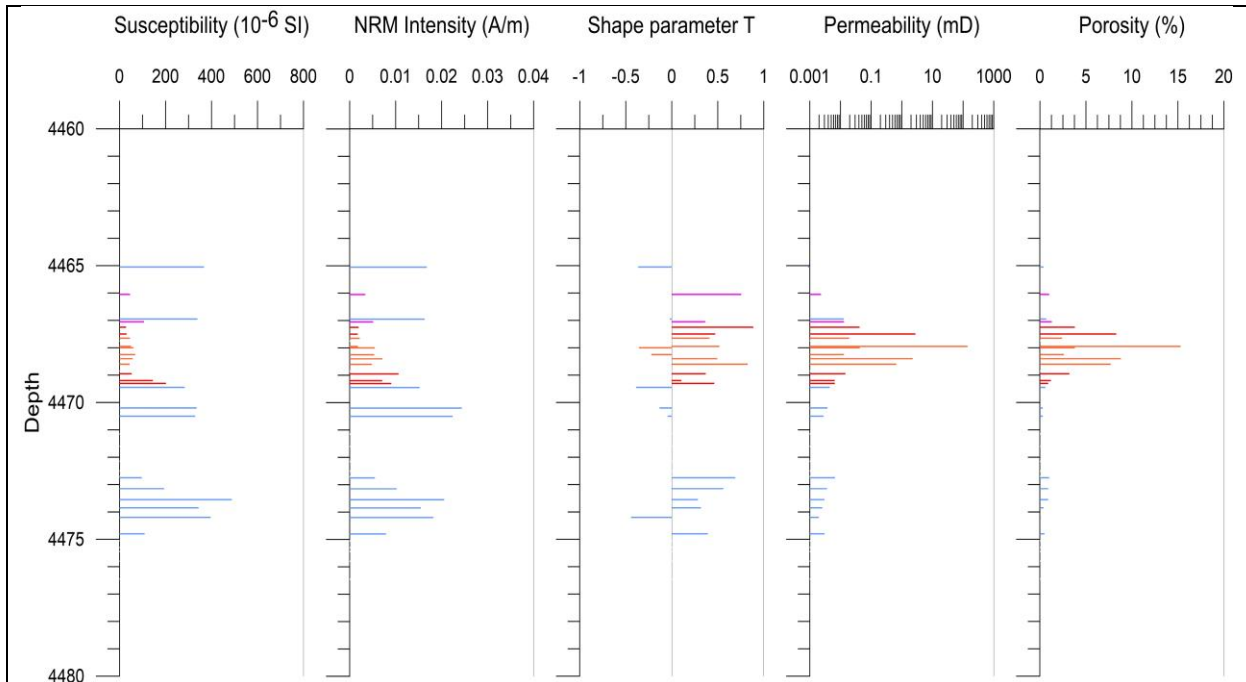
Figure 4: Depth plot of petrophysical parameters of well RWZ 2 (D), Niendorf member. Blue: Aeolian mudflat; Red: Dry sandflat; Orange: Damp Sandflat; Pink: Wet Sandflat (see also Table 4).

ANISOTROPIES OF ELECTRICAL CONDUCTIVITY AND MAGNETIC SUSCEPTIBILITY IN HORN RIVER GROUP SHALES: INSIGHTS INTO ROCK AND PORE FABRICS

[1]Vivian T. Ebufegha and [1,2]David K. Potter

[1]Department of Physics, and [2]Department of Earth and Atmospheric Sciences, University of Alberta, Edmonton, Canada

This paper was prepared for presentation at the International Symposium of the Society of Core Analysts held in Vienna, Austria, 27 August -1 September, 2017

ABSTRACT

Combined anisotropy of electrical conductivity (AEC) and anisotropy of magnetic susceptibility (AMS) measurements provide valuable insights into the rock fabric and 3D orientation of pore spaces in shales. We describe a novel method of determining the 3D anisotropy of electrical conductivity derived from 18 directional resistance measurements (which are then converted to conductivity) made on each shale core sample. Thirty-three initially cubic shale samples were each trimmed and polished into 18 sided samples to facilitate the directional measurements. The samples were from the Horn River Group, British Columbia, Canada. The multifaceted samples were saturated with potassium chloride (KCl) prior to the resistance measurements. The results indicated that these Horn River Group samples were not well described by the usually assumed transversely isotropic model that is often applied to shales. Instead we found that a full 3D anisotropic characterization provided a much better description of their anisotropic properties. Moreover, we found that conductivity varied by up to 17% in the bedding plane, which would not have been expected from the conventional transverse isotropic model. Good correlations were found between the directional resistivities (derived from the resistance measurements) and illite clay content derived from low temperature magnetic susceptibility measurements. Significantly, we also found a good correlation between the percent AEC from our full 3D results and porosity in clay rich samples. This correlation with porosity was not apparent when the same samples were treated as being transversely isotropic. The AEC principal axes suggested that the pores are mainly oblate with that oblateness being closely parallel to the bedding plane. The AEC results were compared with low field anisotropy of magnetic susceptibility (AMS). The AMS was determined by making directional magnetic susceptibility measurements in exactly the same 18 orientations as the directional resistance measurements used to derive the AEC principal anisotropy axes. This allowed a direct comparison between the AMS and AEC principal anisotropy axes. The results indicated that the orientations of the principal AMS and AEC axes were quite similar (although the magnitudes were somewhat different). Since the AMS reflects the anisotropy of the rock matrix minerals, the results indicated that the rock matrix fabric (from the AMS results) tended to be in a similar orientation to the pore fabric (from the AEC results).

INTRODUCTION

Shales have long been known to be electrically anisotropic [1,2]. Recently, however, interest in the accurate interpretation of resistivity data for fluid saturation computations and subsurface structure mapping have led to renewed interest in the study of their electrical anisotropy [3-6]. Since shales typically consist of alternating organic-clay rich and silty intervals, most studies have traditionally treated them as being transversely isotropic with a vertical axis of symmetry [7,8]. In such a model each layer in the laminated sequence is treated like an isotropic medium and an independent resistor. A given sample or section of shale thus consists of a set of resistors, each with resistivity ρ_i. The bulk electrical resistivity is assumed not to vary in the horizontal plane and the degree of electrical anisotropy, λ, is calculated as:

$$\lambda = \rho_v / \rho_h \;\; = \;\; \sigma_h / \sigma_v \tag{1}$$

where ρ_v is the transverse resistivity (resistivity normal to the lamination plane), ρ_h is the longitudinal (lamination parallel) resistivity, σ_v is the transverse conductivity, and σ_h is the longitudinal conductivity.

The majority of the few available studies on electrical anisotropy in mudrocks determine the degree of electrical anisotropy from wireline log derived resistivities. The vertical resolution of standard induction logging tools is between 2ft and 6ft [4]. At such macroscopic scales electrical anisotropy due to microstructural fabric elements like grain alignment, microfractures or pore distribution are difficult to resolve. Higher resolution laboratory techniques traditionally measure horizontal and vertical resistivities in cubic samples or core plugs. Resistivities are either measured in one cubic sample or on two cylindrical core plugs taken perpendicular and parallel to the bedding plane. Since at least nine directional resistivities are needed to determine the six coefficients of the 3D resistivity (and hence also conductivity) tensor, the petrofabric implications of electrical anisotropy cannot be fully understood with only two directional resistivities (or conductivities). In the present paper, a novel method of determining the anisotropy of electrical conductivity (AEC) from 18 directional resistance measurements (which are then converted to resistivity and conductivity) on each sample is presented. The primary goals were to: (i) identify the petrofabric elements that control electrical anisotropy in shales of the Horn River Basin, (ii) define the 3D orientations and magnitudes of the AEC principal axes, and compare with low field anisotropy of magnetic susceptibility (AMS), and (iii) to test the suitability of the traditional transverse isotropic model of electrical conductivity anisotropy in shales on a core plug scale.

SAMPLES AND METHODS

Sample Preparation

33 cubic shale samples from the Imperial Komie well in British Columbia, Canada, were trimmed and polished into 18 sided samples (**Figure 1, top**). 9 samples were from the Muskwa, 17 from the Otter Park and 7 from the Evie formations. The samples were oven dried at 40ºC for 48 hours to remove water held in pore spaces prior to saturating with 20

weight % potassium chloride (KCl) solution. To ensure full saturation, the samples were fully immersed in the electrolyte for one week before taking resistance measurements.

Anisotropy of Electrical Conductivity (AEC) and Comparison with Anisotropy of Magnetic Susceptibility (AMS) in Multifaceted Shale Samples

Determination of the anisotropy of electrical conductivity (AEC) first involved electrical resistance being measured in at least 9 axes for each sample. For each of the Horn River Group samples saturated in the KCl solution, electrical resistance was measured in the 9 axes shown in **Figure 1 (middle)**. In each axis, two determinations of resistance were measured in opposite directions of current flow and were averaged to determine the electrical resistance in that axis. Therefore 9 directional resistances were produced from 18 measured electrical resistances. **Figure 1 (bottom)** shows a schematic of the set-up used to measure electrical resistance. A potential drop of 10V was applied across a circuit consisting of a resistor of known resistance in series with a Horn River Group sample whose resistance was unknown. The voltage was applied by an AFG320 function generator connected to the sample via Ag-AgCl disc electrodes attached to opposite faces of the sample in the direction of current flow. The voltage drop across the sample and test resistors were measured using a Tektronix TD3054B digital oscilloscope. Electrical resistance in each sample direction was calculated as follows:

$$R_{sample} = \{R_{test}\ (V_1 - V_2)\}\ /\ V_2 \qquad\qquad (2)$$

where R_{sample} is the resistance of the sample, R_{test} is the resistance of the test resistor, V_1 is the voltage drop across the sample and V_2 is the voltage drop across the test resistor. The 9 directional resistances were converted to electrical resistivities using the method described in Ebufegha [9] and then converted to conductivity (by taking the reciprocal of each resistivity value), and the 9 conductivity values were then used to calculate the anisotropy of electrical conductivity (AEC). The same 9 measurement axes that were used for determining electrical resistance were also used here for determining anisotropy of magnetic susceptibility (AMS) using a Bartington MS2B low field magnetic susceptibility sensor and the method described by Ebufegha and Potter [10]. Having identical measurement axes meant that the magnetic anisotropy could be directly compared with the electrical anisotropy.

RESULTS AND DISCUSSION

The full 3D anisotropy of electrical conductivity (AEC) results indicated that the Horn River Group samples studied were not transversely isotropic. The results showed conductivity variations in the bedding plane of 0.1% to 17%. The percent AEC (defined as $100(\sigma_1 - \sigma_2)\ /\ \sigma_3$ where σ_1, σ_2 and σ_3 are the max, int and min conductivities) is shown in **Figure 2 (left hand profile),** and varies between 65% and 107% in the Evie formation and between 73% and 180% in the Muskwa and Otter Park formations. In all three formations, maximum and intermediate electrical conductivities were closely parallel to the bedding plane and minimum electrical conductivity closely perpendicular to it. Using the traditional (transversely isotropic) model, however, the % σ_h/σ_v overestimated the anisotropy by a

factor of 1.4 to 12.9 in the different formations (**Figure 2, right hand profile**) compared to our full 3D AEC results. The variation in % σ_h/σ_v ranged from 140% to 390% in the Evie, and between 157% and 1557% in the Muskwa and Otter Park.

Current flow in the Horn River Group shales is mainly by surface conductance through the electrical double layer of clay minerals. A moderate to strong correlation (R^2 ranging from 0.5 to 0.76) between the concentration of illite (which we determined from low temperature magnetic susceptibility measurements [11]) and electrical resistivity (and therefore conductivity) was observed in all nine measurement axes [9]. Although clay content was the primary control on conductivity of Horn River Group shales, its correlation with the anisotropy of electrical conductivity was poor (R^2 was only 0.073 for the samples studied). A good correlation was instead observed between anisotropy of electrical conductivity and porosity. **Figure 3 (top)** shows porosities cross-plotted against % anisotropy of electrical conductivity (AEC) values obtained from our full 3D electrical anisotropy approach (derived from the 18 directional resistance measurements) in the clay rich Lower Muskwa and Otter Park formations. A clear correlation is observed with $R^2 = 0.70$. (Note that the porosities were derived from density log measurements, with a correction for organic matter, and only samples with total organic carbon, TOC, data were used for this purpose). In contrast **Figure 3 (bottom)** shows that the % σ_h/σ_v values (assuming the samples are transversely isotropic) for the same samples did not show any strong correlation with porosity ($R^2 = 0.15$).

The Horn River Group shales are significantly more electrically anisotropic than they are magnetically anisotropic. Their AEC values are between 65% and 180% while their AMS values range from 0% to 35%. No direct correlation is observed between percent AEC and percent AMS. A relationship was, however, observed between the AEC and AMS principal axes orientations. Samples with normal magnetic fabric [10] at room temperature (maximum AMS axis parallel to the bedding plane and minimum AMS axis normal to it) have minimum AMS axis orientations that show a similar profile with depth as their minimum AEC axes (**Figure 4 A**). Both the AMS and AEC minimum axes are steeply inclined and normal to the bedding plane. The steep inclinations mean that the declinations are less well defined and show more scatter (as would be expected)**.** Samples with inverse magnetic fabric [10] at room temperature (minimum AMS axis parallel to the bedding plane and maximum AMS axis normal to it, due to the presence of stable single domain ferrimagnetic particles) have maximum AMS axis orientations that show a similar profile with depth as their minimum AEC axes (**Figure 4 B**). The results suggest that preferred mineral or matrix alignments (from the AMS orientations) and the pore space alignments (from the AEC orientations) are essentially in the same orientations.

CONCLUSIONS
1. The Horn River Group shales from the Imperial Komie well are not transversely isotropic with respect to electrical conductivity, contrary to the traditional model. When transverse isotropy is assumed, the relationship between porosity and percent anisotropy of electrical conductivity is not obvious. Including the full 3D variation of electrical conductivity in anisotropy determination yields a clear correlation with porosity.

2. Clays are the primary control on electrical conductivity in the shale samples studied, while porosity is the primary control on the anisotropy of electrical conductivity. In clay rich rocks the concentration and spatial arrangement of clay minerals significantly affects the electrical conductivity. Since the pore saturating fluid is not the only control on electrical conductivity, saturation calculations that do not account for clay conductivity and its anisotropy may be erroneous.

3. The orientations of the principal AMS and AEC axes are quite similar, and indicate that both the mineral and pore space alignments are closely parallel to the bedding plane.

ACKNOWLEDGEMENTS

REFERENCES

1. Mousseau, R. J. and Trump, R. P., 1967. Measurement of electrical anisotropy of clay-like materials. *Journal of Applied Physics*, **38** (11), 4375 - 4379.
2. Chemali, R., Gianzero, S. and Su, S. M., 1987. The effect of shale anisotropy on focused   resistivity devices. SPWLA 28th Annual Logging Symposium.
3. Klein, J. D., Martin, P. R. and Allen, D. F., 1997. The petrophysics of electrically anisotropic reservoirs. *The Log Analyst*, **38**, 25-36.
4. Clavaud, J. B., 2008. Electrical anisotropy of shale: the effect of compaction. *Petrophysics*, **49** (3), 243-260.
5. Bachrach, R., 2011. Elastic and resistivity anisotropy of shale during compaction and diagenesis: Joint effective medium modeling and field observations. *Geophysics*, **76** (6), E175- 186.
6. Ellis, M., Ruiz, F., Nanduri, S., Keirstead, R., Azizov, I., Frenkel, M. and MacGregor, L., 2011. Importance of anisotropic rock physics modelling in integrated seismic CSEM interpretation. *First Break*, **29**, 87-95.
7. Tsvankin, I., 1997. Anisotropy parameters and P-wave velocities for orthorhombic media. *Geophysics*, **62** (4), 1292-1309.
8. Saeidi, O., Rasouli, V., Vaneghi, R. G., Gholami, R. and Torabi, S. R., 2014. A modified failure criterion for transversely isotropic rocks. *Geoscience Frontiers*, **5**, 215-225.
9. Ebufegha, V. T., 2016. Anisotropy of mudrocks: Quantifying controls and fabric implications in the Horn River Basin. PhD Thesis, University of Alberta, pp.185.
10. Ebufegha, V. T. and Potter, D. K., 2014. A comparison of quantitative techniques for determining the 3D anisotropy of shale samples: application to Horn River Basin shales, British Columbia, Canada. In *Proceedings of the 2014 International Symposium of the Society of Core Analysts, 8-11 September 2014*, Avignon, France. Paper SCA2014-011 (12 pages).
11. Ebufegha, V. T. and Potter, D. K., 2016. Quantifying shale mineralogy and anisotropy from low temperature magnetic susceptibility measurements. In *Proceedings of the 2016 International Symposium of the Society of Core Analysts, 21-26 August 2016*, Snowmass, Colorado, USA. Paper SCA2016-033 (12 pages).
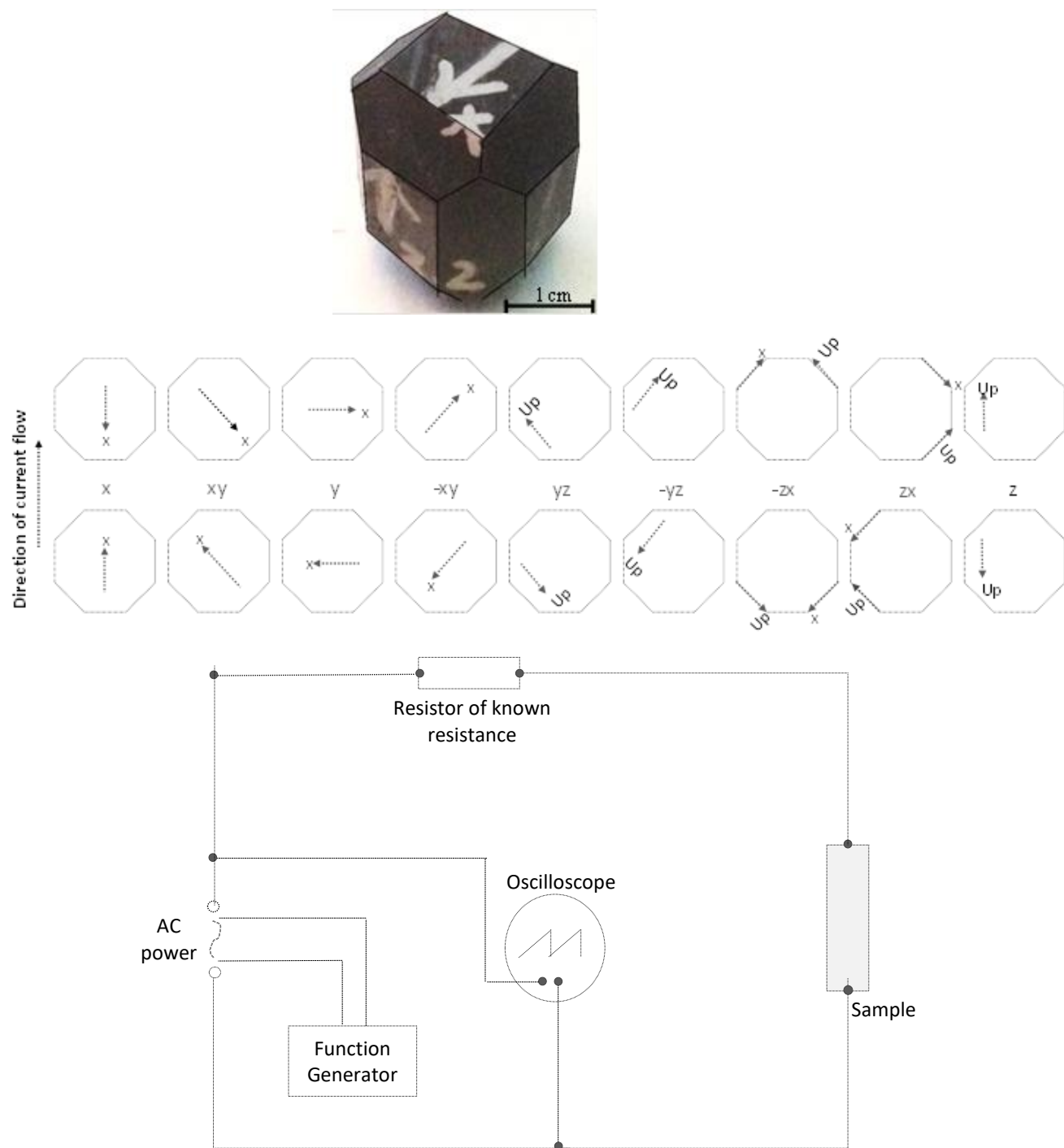
Figure 1. Top: One of the 18 sided samples that allow resistance measurements to be made in 9 different sample axes. **Middle:** Schematic of the 18 measurement directions along 9 different sample axes. **Bottom:** Schematic of the experimental set-up for resistance measurements.
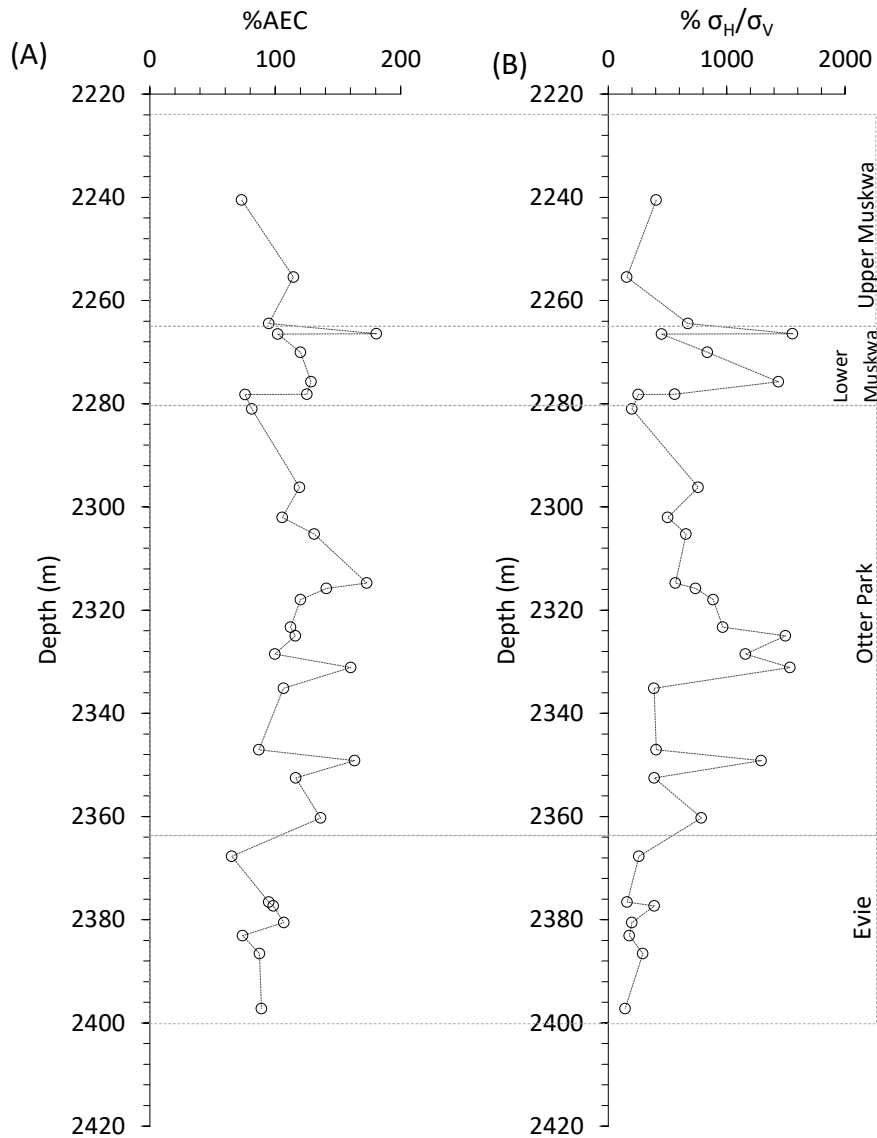
Figure 2. (A) Percent 3D anisotropy of electrical conductivity (AEC) derived from the 18 resistance measurements in the directions shown in the middle schematic of **Figure 1**. (B) Percent conductivity parallel to the lamination plane to that perpendicular to the lamination plane (% σ_h / σ_v) using the traditional two conductivity (transversely isotropic) model. Note that this model significantly overestimates anisotropy compared to the full 3D measured anisotropy shown in (A).
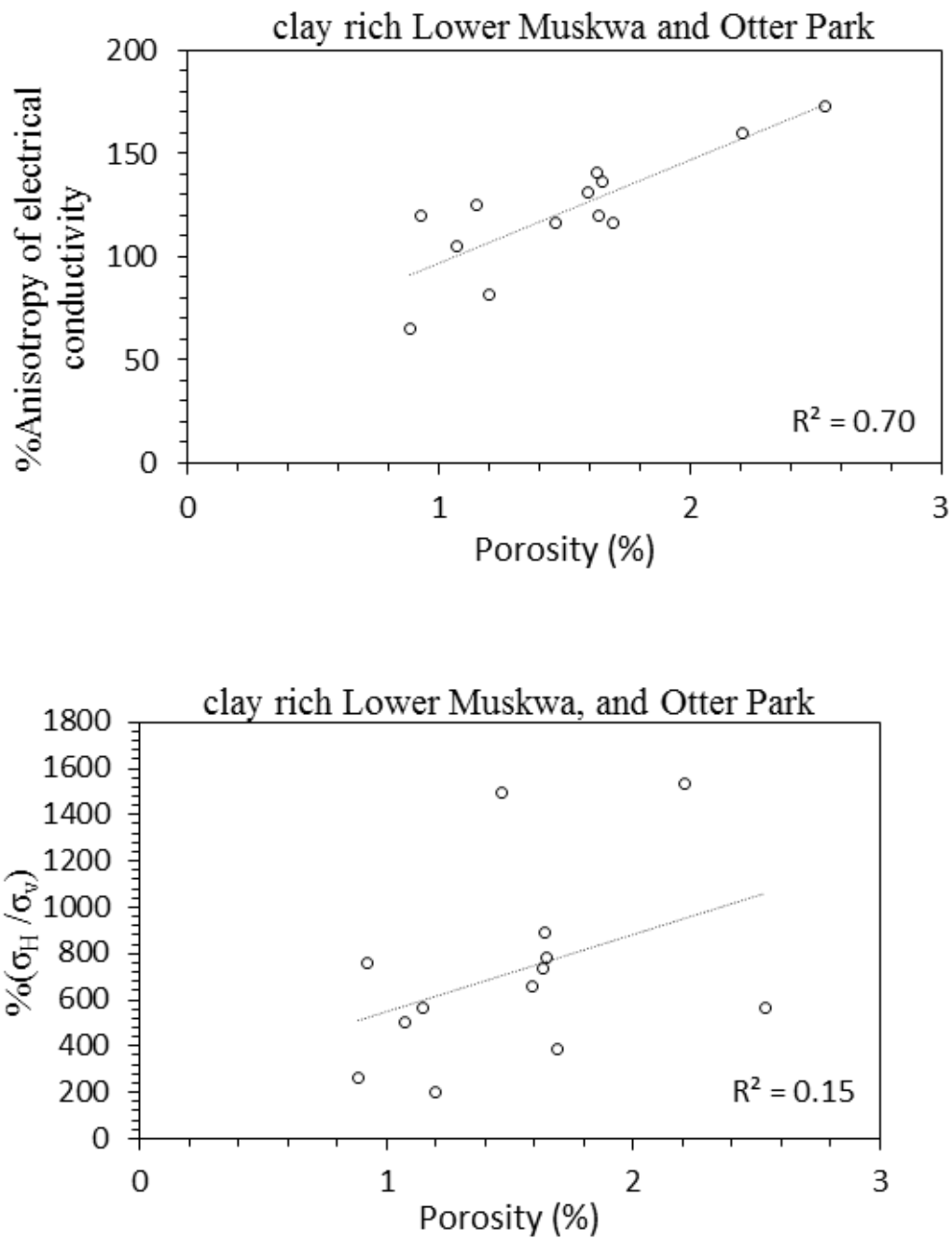
Figure 3. Top: Crossplot of porosity versus percent 3D anisotropy of electrical conductivity (AEC) derived from the 18 resistance measurements. **Bottom:** Crossplot of porosity versus percent conductivity parallel to the lamination plane to that perpendicular to the lamination plane (% σ_h / σ_v) using the traditional two conductivity (transversely isotropic) model.
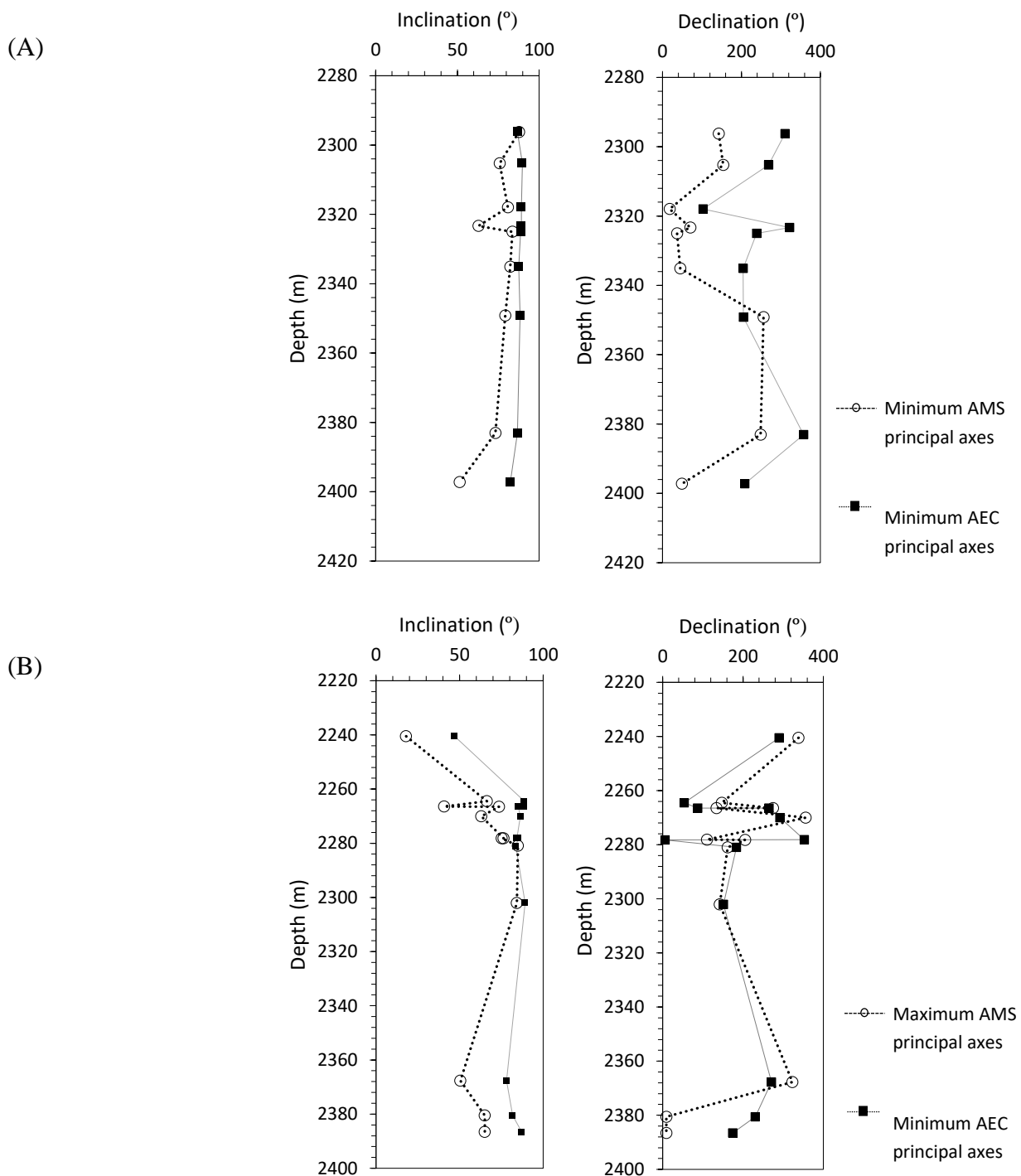
Figure 4. Variation with depth of the orientations (inclination and declination) of the principal anisotropy axes. (A) minimum anisotropy of magnetic susceptibility (AMS) axes and minimum anisotropy of electrical conductivity (AEC) axes for samples with normal magnetic fabrics. (B) maximum AMS axes and minimum AEC axes for samples with inverse magnetic fabrics.

WATER PERMEABILITY MEASUREMENTS ON HYDRATE-SATURATED SANDSTONE CORES WITH IMMOBILE GAS

Stian Almenningen and Geir Ersland
Department of Physics and Technology, University of Bergen

ABSTRACT

Water permeability values for hydrate-bearing sandstone cores are presented and compared with existing theoretical flow models for water through hydrate-filled sediments. Differential pressure has been measured from constant flow injection of brine into Bentheim sandstone cores presaturated with methane hydrate and the permeability is calculated based on Darcy's law. Initial water saturation prior to hydrate formation has been ranging between 0.72 and 0.95, aimed at mimicking the natural hydrate growth process from dissolved methane in water and keeping the potential final gas saturation low and immobile. The results show that the permeability is decreasing towards zero at a hydrate saturation of around 0.50 when hydrate formation has been initiated with some free gas (approximately 0.20-0.30) in the core. In this case, the growth process is believed to start at the gas/water interface that exists throughout the pore network. Hydrate formation from a completely water saturated core resulted in a hydrate saturation of only 0.19 but the corresponding permeability was nearly zero. Heterogeneous hydrate growth at the end surfaces of the core is assumed to account for this observation. Theoretical permeability models are also reviewed and compared with the findings of this study. Accurate predictions of water permeability in hydrate sediments are important to assess production of methane gas from hydrate deposits. The presented permeability values can be used to calibrate reservoir simulators and will enhance the knowledge of flow potential in hydrate reservoirs.

INTRODUCTION

Natural gas hydrates are one promising energy resource that can contribute to the world's future energy demand, acting as a gap between conventional fossil fuels (coal and oil) and completely renewable energy sources. Production of hydrates yields methane gas which has a low carbon footprint compared to coal and oil, and one proposed production method gives an additional environmental effect by allowing injected CO_2 to be stored in the formation as methane gas is harvested [1]. The energy potential is huge as even extraction of only the most promising hydrate deposits (arctic sandstones under existing infrastructure) will give 10's of TCF surplus of methane gas to the global energy market [2].

As with production of conventional gas and oil, mining of methane hydrates rely on sufficient permeability to permit flow of liberated gas and water. Gas hydrates are also of interest as a sealing mechanism related to CO_2 storage in saline aquifers [3]. In either way, knowledge of permeability alteration in response to hydrate saturation is important to assess the potential of production or sealing.

Some experimental studies have previously been published on permeability in hydrate-saturated porous media: effective gas permeability measurements [4-9], effective water permeability measurements [7, 10-12], and two-phase flow [13-15]. Noticeable differences in relative permeability to water ($k_{rw} \approx 0.1$ at $S_H = 0.45$ and residual gas [11], $k_{rw} \approx 0.02$ at $S_H = 0.09$ and residual gas [10], and $k_{rw} \approx 0.004$ at $S_H = 0.07$ and residual gas [15]), shows the importance of phase distribution on permeability and that extensive permeability measurements are needed to calibrate permeability models.

This study is a continuation of the work presented in Almenningen *et al.* [9] where effective permeability to gas was measured in sandstone containing hydrate and immobile water. A critical gas saturation of 0.34-0.38 was identified where the gas permeability dropped from mD to µD range (S_H ranging from 0.37 to 0.61). Effective permeability to water has been measured in this study for the same range of hydrate saturation and with immobile gas. The aim of this experimental work is to identify the equivalent critical saturation of water and also to provide experimental values needed to validate permeability correlations.

Review of Permeability Models
A comprehensive review of permeability models applicable to hydrate-saturated porous media is previously given by Kleinberg *et al.* [12]. This section will provide a to-the-point overview of available permeability correlations mainly built on the work provided by Kleinberg *et al.* [12]. The models are later used to evaluate the permeability values found in this experimental study.

One of the simplest way to model flow through porous media is by assuming that flow conduits consist of straight cylindrical channels with constant cross-sectional area. The Poiseuille's equation describes flow through circular tubes and the permeability of a media consisting of *n* tubes becomes:

$$k = \frac{n\pi r^4}{8A} = \frac{\Phi r^2}{8},$$ (1)

where *r* [m] is the radius of the tubes, *A* [m^2] is the cross-sectional area of the media and *Φ* [fraction] is the porosity of the media. The reduction in permeability with hydrate saturation will then depend on how the hydrate distributes within the pores. If hydrate coats the cylindrical walls with a uniform layer the permeability reduces to:

$$k = \frac{\phi r^2 (1-S_H)^2}{8} \implies k_{rw} = (1-S_H)^2, \tag{2}$$

where S_H [fraction] is the hydrate saturation and k_{rw} [fraction] is the relative permeability to water. If hydrate is located in the center of the cylindrical pores and grows radially outwards, the permeability relation becomes:

$$k = \frac{\phi r^2}{8}\left(1 - S_H^2 - \frac{(1-S_H)^2}{\log\left(\frac{1}{S_H^{0.5}}\right)}\right) \implies k_{rw} = 1 - S_H^2 + \frac{2(1-S_H)^2}{\log S_H}. \tag{3}$$

These permeability correlations for grain-coating and pore-filling hydrate growth are rigorous but lack realism in their assumptions. The pore network of authentic rocks consists of tortuous channels where the actual flow path is longer than the length of the medium. Pores are also varying in size and shape, and the wetting properties of the solid grains will influence on where hydrate forms in the pore space. Kleinberg *et al.* [12] tried to derive more realistic permeability relations, starting from a Kozeny equation of permeability and introducing the relation between saturation changes and electrical properties from the work of Hearst *et al.* [16] and Spangenberg [17]. The relative permeability of water, when hydrate coats grains, becomes:

$$k_{rw} = (1 - S_H)^{n+1}, \tag{4}$$

and for hydrate growing in the center of pores, the relative permeability becomes:

$$k_{rw} = \frac{(1-S_H)^{n+2}}{\left(1+S_H^{0.5}\right)^2}, \tag{5}$$

where n is the saturation exponent from Archie's relations. This exponent is not easy to obtain as it will change during hydrate growth [17], and the derivation of the equations is also neglecting the change in the cementation exponent m during hydrate growth. A generalization of Equation 2 that is widely used to compare with experimental data originates from Masuda *et al.* [18]:

$$k_{rw} = (1 - S_H)^N, \tag{6}$$

where N acts as a fitting parameter. Masuda *et al.* [18] chose $N = 10$ and 15 to account for hydrate growth in pore throats, but a variety of values have been found by fitting the equation to experimental data: $N = 3\text{-}5$ [4], $N = 8\text{-}9$ [5], $N = 7.7\text{-}9.4$ [19], and $N = 38$ [10].

Another permeability relation that is also based on a Kozeny equation, and that is developed by modelling of a 2D pore network containing different hydrate distributions, is [20]:

$$k_{rw} = \frac{(1-S_H)^3}{(1+2S_H)^2}. \tag{7}$$

This equation takes into account the change in tortuosity and specific surface area due to hydrate formation.

The reservoir simulator TOUGH+HYDRATE v1.5 reduces the absolute permeability during hydrate growth according to the reduction in porosity and the user can then choose from many different relative permeability correlations, such as Corey's [21] and Grant's curves [22]. The absolute permeability reduction is given by:

$$\frac{k}{k_0} = \left(\frac{\phi - \phi_c}{\phi_0 - \phi_c}\right)^n, \tag{8}$$

where the subscript *0* denotes reference state and Φ_c is a non-zero critical porosity where the permeability *k* is zero. The exponent *n* is reported to be in the range from 2 to 3 but can also be as large as *n* = 10 or more, depending on how hydrate grows in the pore space (Moridis and Pruess [23], and references therein).

Equations 2-7 are applicable if hydrate forms from water saturated with methane gas (one phase, two components). If a gas phase is present after hydrate formation, two-phase flow models should be applied to model the relative permeability of water and gas under the influence of solid hydrates. Equations 2-7 can nonetheless be used for water flow if the residual gas present after hydrate formation is assumed immobile. However, the measured water permeability will then be expected to be lower than predicted by Equations 2-7 because of the extra flow restriction offered by the stationary gas phase.

EXPERIMENTAL PROCEDURE

Cylindrical Bentheim sandstone cores (length ≈ 15 cm and diameter ≈ 5 cm) were used as porous medium. They have fairly constant porosity and absolute permeability of 0.22-0.24 and 0.9-1.1 D, respectively. Every core was saturated to a predefined value (ranging from 0.72 to 0.95) with brine and then mounted into the rubber sleeve inside the core holder. Salinity values of 0.1, 1.0, 2.0, 2.5, 3.0, 3.5 and 4.0 wt% NaCl were used to customize the final hydrate saturation. All pump lines and tubes were purged under vacuum before filling the pump with methane gas (>99.5%). The core was pressurized to 8.3 MPa from both ends and the overburden pressure was applied to the sleeve by pressurized oil (3 MPa above pore pressure). Hydrate formation was initiated by circulation of antifreeze through a cooling jacket that surrounds the core holder and that reduced the temperature to a constant 4°C for all tests. Hydrate growth was finalized when the consumption of methane gas stopped, and permeability measurements were performed by injecting brine (same salinity as the initial brine saturating the core) from one side of the core. Another pump containing the same brine

was connected to the other side of the core and was set to hold a constant pressure of 8.3 MPa. Differential pressure was monitored and recorded as the pressure drop stabilized across the core during constant volume rate injection. The permeability of each hydrate-saturated core was calculated by Darcy's law. Temperature sensors placed at the inlet and outlet core ends were used to monitor the temperature evolution during injection. The injected water was not pre-cooled, but low injection rates (< 0.03 mL/min) assured no temperature increase and corresponding hydrate dissociation during permeability measurements. The reader is referred to Almenningen *et al.* [9] for details of the experimental set-up.

RESULTS AND DISCUSSION

A total of nine flow experiments were conducted to investigate the water permeability of hydrate-saturated sandstone cores. High initial brine saturations varying between 0.72 and 0.95, together with salinities ranging between 0.1 and 4.0 wt% NaCl, resulted in final hydrate saturations between 0.19 and 0.60 (Table 1). The residual gas saturation after hydrate formation did not exceed 0.18 and the gas phase was considered immobile during water flow. No produced methane gas was observed in the production pump for all experiments.

The water permeability followed an increasing trend with increasing water saturation but remained low for all saturations of water (Figure 1). The maximum permeability was observed to be in the order of 100-200 µD at the highest water saturation of approximately 0.55, which corresponds to a relative permeability in the order of 0.0001. This shows the major impact of hydrates on permeability and is also reflected in the critical water saturation where permeability dropped to zero. Measurable permeability values were not obtained at water saturations lower than 0.40, while the critical water saturation for regular two phase flow (water and gas) is lower than 0.20 for Bentheim sandstone [24].

The objective to create hydrate from one phase (dissolved methane in water) by saturating the cores completely with brine was not achieved. Upon cooling of the core, no injection of gas followed as it would do during hydrate growth due to up-concentration of gas in the hydrate phase. The best attempt of creating hydrate from high initial brine saturation was accomplished during experiment 2 ($S_{wi} = 0.95$). However, the final hydrate saturation became only 0.19 as hydrate growth initiated at the gas/water interface in both core ends. Further growth diminished when the solid hydrate film blocked for methane transport inwards in the core into the water phase. Consequently, the resulting permeability became close to zero despite the low hydrate saturation. The possibility of additional hydrate formation from dissolved methane inside the core cannot be ruled out as the experiment was conducted without *in situ* monitoring and information about growth characteristics relied solemnly on pressure communication with the pump.

Permeability measurements have traditionally been used in conjunction with ultrasonic and electrical measurements to estimate hydrate growth habit. Either pore-filling or pore-coating growth are suggested by comparing experimental values to the predictions of Equations 3 (or 5) and 2 (or 4), respectively. Some studies indicate pore-filling hydrate growth [5, 7, 12, 15], while other point to a shift from pore-coating to pore-filling hydrate growth as the hydrate saturation reaches a certain value [4, 11]. A hybrid modelling approach has also been developed which consists of a weighted combination of Equations 4 and 5 [25]. The permeability measured in this study is not comparable to the predictions of Equations 2-5 nor 7. Only Equations 6 and 8 can match the experimental values; with $N = 14$ and $n = 7$, respectively, giving the best fit (Figure 2). The findings imply that the assumption of either pore-filling or pore-coating hydrate growth is too simplistic and that the permeability evolution is highly influenced by heterogeneous growth. Hydrate occupying pore throats close to the core ends may explain the observed low permeability in this study. Building of permeability correlations should therefore be assisted with *in situ* monitoring of hydrate distribution to account for effects originating from different preparation methods and experimental procedures.

CONCLUSIONS

Effective permeability to water was measured for nine cylindrical sandstone cores filled with methane hydrate saturations ranging between 0.19-0.60 and immobile gas. The effective permeability to water was consistently low for all combinations of saturation, decreasing from an upper level of 100-200 µD and down to zero permeability at a water saturation of approximately 0.40. For comparison, the absolute permeability of the cores was 0.9-1.1 D. The measured permeability values were order of magnitudes lower than what was predicted by existing permeability correlations with fixed parameters. Only equations containing fitting parameters could simulate the experimental results.

REFERENCES

1. Graue, A., B. Kvamme, B. Baldwin, J. Stevens, J.J. Howard, E. Aspenes, G. Ersland, J. Husebø and D. Zornes, "MRI Visualization of Spontaneous Methane Production From Hydrates in Sandstone Core Plugs When Exposed to CO2". *SPE Journal,* (2008) **13**(2): p. 146-152.
2. Boswell, R. and T.S. Collett, "The Gas Hydrates Resource Pyramid". *Fire in the Ice* (The National Energy Technology Laboratory Methane Hydrate Newsletter), (2006) **Fall**: p. 5-7.
3. Kvamme, B., A. Graue, T. Buanes, T. Kuznetsova and G. Ersland, "Storage of CO2 in natural gas hydrate reservoirs and the effect of hydrate as an extra sealing in cold aquifers". *International Journal of Greenhouse Gas Control*, (2007) **1**(2): p. 236-246.

4. Kumar, A., B. Maini, P.R. Bishnoi, M. Clarke, O. Zatsepina and S. Srinivasan, "Experimental determination of permeability in the presence of hydrates and its effect on the dissociation characteristics of gas hydrates in porous media". *Journal of Petroleum Science and Engineering*, (2010) **70**(1–2): p. 114-122.

5. Liang, H., Y. Song, Y. Chen and Y. Liu, "The Measurement of Permeability of Porous Media with Methane Hydrate". *Petroleum Science and Technology*, (2011) **29**(1): p. 79-87.

6. Chuvilin, E., S. Grebenkin and E. Tkacheva, "CHANGE OF GAS PERMEABILITY OF GAS-SATURATED SEDIMENTS DURING HYDRATE FORMATION AND FREEZING", in *Proceedings of the 8th International Conference on Gas Hydrates*, (2014), Beijing, China.

7. Kneafsey, T.J., Y. Seol, A. Gupta and L. Tomutsa, "Permeability of Laboratory-Formed Methane-Hydrate-Bearing Sand: Measurements and Observations Using X-Ray Computed Tomography". *SPE Journal*, (2011) **16**(1): p. 78-94.

8. Ersland, G., J. Husebø, A. Graue, B. Kvamme, B. Baldwin, J. Howard and J. Stevens, "Measurements of Gas Permeability and Non-Darcy Flow in Gas-Water-Hydrate Systems", in *Proceedings of the 6th International Conference on Gas Hydrates*, (2008), Vancouver, Canada.

9. Almenningen, S., H. Juliussen and G. Ersland. "Permeability measurements on hydrate-bearing sandstone cores with excess water", in *The 30th International Symposium of the Society of Core Analysts*, (2016), Snowmass, Colorado.

10. Li, B., X.S. Li, G. Li, J.L. Jia and J.C. Feng, "Measurements of Water Permeability in Unconsolidated Porous Media with Methane Hydrate Formation". *Energies*, (2013) **6**(7): p. 3622-3636.

11. Delli, M.L. and J.L.H. Grozic, "Experimental determination of permeability of porous media in the presence of gas hydrates". *Journal of Petroleum Science and Engineering*, (2014) **120**: p. 1-9.

12. Kleinberg, R.L., C. Flaum, D.D. Griffin, P.G. Brewer, G.E. Malby, E.T. Peltzer and J.P. Yesinowski, "Deep sea NMR: Methane hydrate growth habit in porous media and its relationship to hydraulic permeability, deposit accumulation, and submarine slope stability". *JOURNAL OF GEOPHYSICAL RESEARCH*, (2003) **108**(B10): p. 1-17.

13. Johnson, A., S. Patil and A. Dandekar, "Experimental investigation of gas-water relative permeability for gas-hydrate-bearing sediments from the Mount Elbert Gas Hydrate Stratigraphic Test Well, Alaska North Slope". *Marine and Petroleum Geology*, (2011) **28**(2): p. 419-426.

14. Ahn, T., J. Lee, D.G. Huh and J.M. Kang, "Experimental Study on Two-phase Flow in Artificial Hydrate-bearing Sediments". *Geosystem Engineering*, (2005) **8**(4): p. 101-104.

15. Jaiswal, N.J., A. Dandekar, S. Patil, R.B. Hunter and T.S. Collett, "Relative Permeability Measurements of Gas-water-hydrate Systems". *Natural gas hydrates - Energy resource potential and associated geologic hazards: AAPG Memoir*, (2009) **89**: p. 723-733.

16. Hearst, J.R., P.H. Nelson and F.L. Paillet, *Well Logging for Physical Properties*. (2000) New York: McGraw-Hill.

17. Spangenberg, E., "Modeling of the influence of gas hydrate content on the electrical properties of porous sediments". *Journal of Geophysical Research: Solid Earth*, (2001) **106**(B4): p. 6535-6548.
18. Masuda, Y., S. Naganawa, S. Ando and K. Sato, "Numerical calculation of gas production performance from reservoirs containing natural gas hydrates", in *Annual Technical Conference*, (1997), San Antonio, Texas.
19. Konno, Y., Y. Jin, T. Uchiumi and J. Nagao, "Multiple-pressure-tapped core holder combined with X-ray computed tomography scanning for gas–water permeability measurements of methane-hydrate-bearing sediments". *Review of Scientific Instruments,* (2013) **84**(6): p. 064501.
20. Dai, S. and Y. Seol, "Water permeability in hydrate-bearing sediments: A pore-scale study". *Geophysical Research Letters*, (2014) **41**(12): p. 4176-4184.
21. Corey, A.T., "The Interrelation Between Gas and Oil Relative Permeabilities". *Producers Monthly*, (1954) November: p. 38-41.
22. Grant, M.A., "Permeability Reduction Factors at Wairakei", paper 77-HT-52, in *AICHE-ASME Heat Transfer Conference*, (1977), Salt Lake City, Utah.
23. Moridis, G.J. and K. Pruess, "User's Manual of the Tough+ Core Code v1.5: A General-Purpose Simulator of Non-Isothermal Flow and Transport Through Porous and Fractured Media", Report LBNL-6871E, Lawrence Berkeley National Laboratory, Berkeley, California, (2014).
24. Teige, G.M.G., W.L.H. Thomas, C. Hermanrud, P.E. Øren, L. Rennan, O.B. Wilson and H.M.N. Bolås, "Relative permeability to wetting-phase water in oil reservoirs". *Journal of Geophysical Research: Solid Earth*, (2006) **111**(B12): p. 1-20.
25. Delli, M.L. and J.L.H. Grozic, "Prediction Performance of Permeability Models in Gas-Hydrate-Bearing Sands". *SPE Journal*, (2013) **18**(2).

Table 1. List of all experiments with related saturations and permeability values. Margins of error reflect equipment uncertainties.

Experiment ID	S_{wi} ±0.01	Salinity [wt% NaCl]	S_{wf} ±0.02	S_H ±0.02	S_g ±0.02	K [μD]
1	0.78	0.1	0.30	0.60	0.10	0
2	0.95	0.1	0.80	0.19	0.01	1.1 ±0.7
3	0.80	2.0	0.43	0.47	0.10	17 ±2
4	0.74	2.5	0.41	0.41	0.18	3.9 ±0.2
5	0.80	3.0	0.46	0.44	0.10	26 ±3
6	0.79	3.5	0.55	0.32	0.13	108 ±16
7	0.80	3.5	0.51	0.37	0.12	62 ±9
8	0.80	3.5	0.52	0.36	0.12	176 ±37
9	0.72	4.0	0.35	0.48	0.17	0
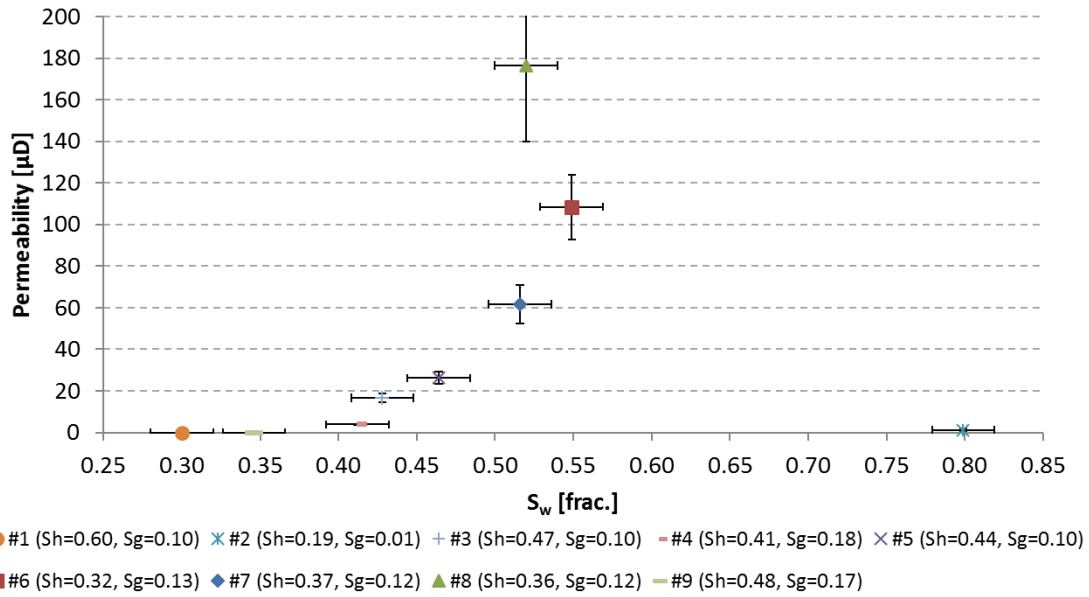
Figure 1. Water permeability after hydrate formation. Experiment 2 had close to zero permeability, despite having a high final water saturation, because of heterogeneous hydrate accumulation at the core ends. Margins of error reflect equipment uncertainties.
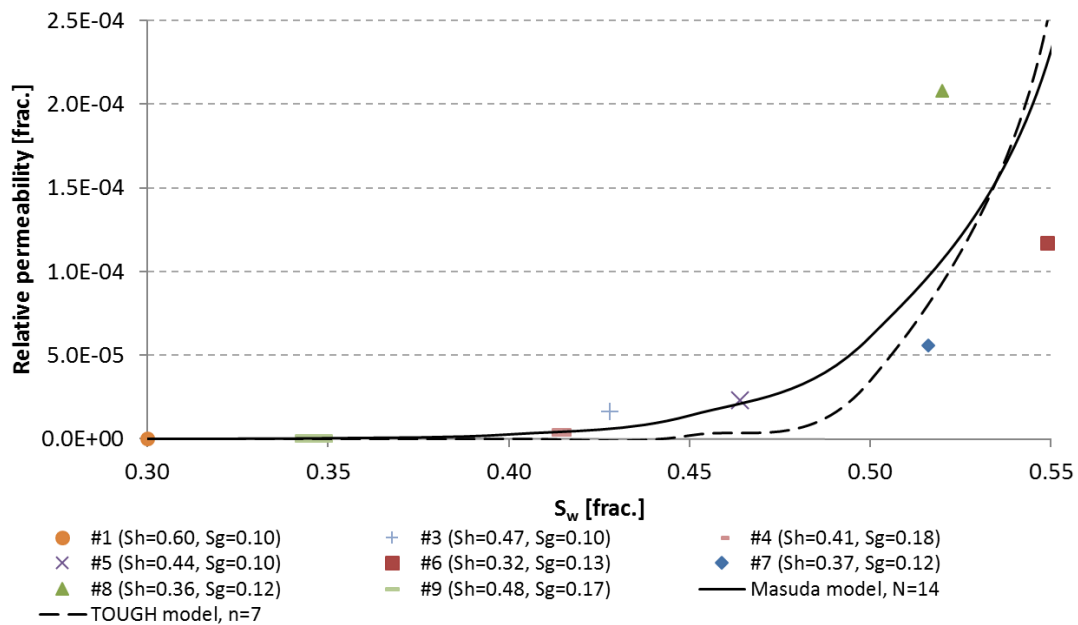

Figure 2. Comparison between experimentally obtained values of relative permeability to water and theoretical permeability values. Experiment 2 has been excluded from the graph because of heterogeneous hydrate growth. Only the models of Masuda and TOUGH+HYDRATE predicted permeability values comparable to experimental data, with a best fit achieved with $N = 14$ and $n = 7$, respectively.

CHARACTERIZATION OF MICRO-PORES IN ORGANIC-RICH UNCONVENTIONAL RESERVOIR ROCKS

Elizabeth Krukowski, Robert Krumm, and James Howard
Premier Oilfield Laboratories

ABSTRACT

Physical measurements of pore-size distributions in many unconventional reservoir rocks are hampered by a combination of very small features that push the limits of many measurement techniques and the challenges associated with removing residual liquids from the pores. Organic-rich reservoir rocks that act both as source and producer are especially difficult to analyze because of the residual liquids, hydrocarbons and formation water that are trapped in the smallest pores. A combination of low-pressure gas adsorption and differential thermal analysis measurements are used to quantify the proportion and distribution of pores in the micro-scale (less than 5 nm). Pore-size estimation with conventional low-pressure gas adsorption using N_2 has a lower limit of several nanometers, but is severely affected by the presence of organic carbon. The use of CO_2 as the absorbent gas improves the size range down to 0.5 nm. Solvent extraction on small chips of sample was successful in removing small amounts of residual water and hydrocarbon that increased the total pore volume by approximately 10-20% compared to as-received samples. That volume increase was dominated by the very smallest pores, less than 5 nm, as measured with CO_2 adsorption. Thermal analysis measurements verified the loss of water and light hydrocarbons from the extracted samples, while the more complex kerogen that decomposed at higher temperatures was less affected by the extraction. The solvent extraction step removed oil from the solid organic matter and opened very small pores in the sample. The combination of results indicated that a majority of pores in these organic-rich samples fell in the 100-500 nm range and that only a small proportion were true micropores. While extraction of residual hydrocarbons opened up a number of very small pores, their contribution to the overall pore volume was small.

INTRODUCTION

Porosity in fine-grain organic-rich shale occurs as a variety of types and sizes, including intergranular pores associated with the mineral matrix and intraparticle pores found in the solid organic matter [1]. The nature of these pores is important not only for understanding storage capacity of the reservoir, but the connectivity amongst the different types of pores affects fluid flow properties. Porosity in shale and kerogen is widely observed with Scanning Electron Microscopy (SEM) with high-resolution detailed images that are used to classify and characterize pore types (Figure 1). These images are the standard for assessing pores in unconventional, very low-permeability reservoir rocks. As

unconventional reservoirs become increasingly vital for oil production, a more quantitative approach becomes necessary to develop viable models.

The analysis of low-pressure gas adsorption measurements allows quantitative insight into pores ranging from 1 to 500 nm [2-7]. Analysis of standard adsorption curves yields a specific surface area, average pore diameter, pore volume and a pore-size distribution (PSD). Nitrogen gas adsorption is a standard analytical tool for porous materials, especially ones with simple networks of sub-micron sized pores [5]. Recent studies have extended the use of low-pressure gas adsorption measurements on more complex fine-grain geological materials to investigate pore size distributions [3]. Based on the type of isotherms and the gas adsorption, a clearer picture of the pore networks within shale was created [3]. Other studies focused on small improvements in technique to minimize and avoid errors related to low pressure gas adsorption analysis in order to address the evaluation of pores in complex geological materials [8,9].Oversampling data points at very low relative pressures generated a more detailed view of the micropore and mesoporous regions.

Standard core preparation involves extracting a sample with toluene and/or chloroform to remove fluids, especially residual water and oil, prior to testing. Measurements on the "as received" samples versus the post-extraction samples illustrated changes in the pore structures [2]. This study analyzed porosity evolution through the use of sequential solvents of chloroform and two combined solvents with higher polarities. This enhanced evolution showed a recovery of pore systems with each cleaning. The highest recovery of pore space resulted from extracted high maturity samples. Combining N_2 and CO_2 gas adsorption data allows a complete picture of the PSD from 0.5-500 nm [3]. The adsorption of CO_2 has advantages over N_2 when probing nanometer sized pores in organic matter due to the nature of interactions with the carbon surface [10]. These earlier studies often reported Type II isotherms, in large part because only the adsorption curve was acquired. The hysteresis from the desorption often distinguishes Types II and IV and is a necessary component for a complete interpretation (Figure 2).

Many of the previous studies on shale used samples that were size-separated to include all material less than a given maximum size [2-7]. This study focused on shale samples that were sieved to a diameter between 90 and 32 µm. By having a lower limit on the particle size, it ensured that we were looking at pore systems within the shale and not individual particles.

A combination of low pressure gas adsorption and differential scanning calorimetry/thermal gravimetric analysis (DSC/TGA) present the combined tools capable of yielding quantitative data. Thermal analysis generally does not reveal much information about pores and pore volume, but it is useful to characterize different components of a sample. A properly executed thermal gravimetric analysis of an organic-rich shale sample can provide quantitative information on the amounts of residual water and oil in the pore system, kerogen and other organic matter, and even mineral types and abundances. [13]

Quantitative results on the porosity in shale require a combination of techniques to solve the challenge these fine-grained rocks present. These challenges include a highly variable mineralogy that presents surfaces of wildly different adsorption properties along with the difficulties in removing residual liquids from these surfaces prior to testing.

METHODOLOGY

The samples used in the study came from a carbonate-rich unconventional reservoir characterized by variable amounts of clay minerals and organic matter. The samples were first crushed and sieved to a range of 90 to 32 µm before separating into two aliquots. The first aliquot was treated as in the "as-received" state with residual liquids present. The second aliquot was subjected to toluene extraction to remove residual water and oil. The range in crushed-rock particle size was large enough to capture the small pore systems present in the shale while also reducing the enhanced surface area effect associated with very small, sub-micron, particles. Samples from both aliquots were dried overnight at 150 °C. Several grams of the dried samples were degassed under vacuum at 70 °C for ~12 hours in the measurement tube. Samples were then analyzed by nitrogen adsorption at -196 °C and/or by carbon dioxide adsorption at 0 °C (ASAP 2020, Micromeritics). The data acquisition parameter file oversampled the very low relative pressure regions to ensure high resolution in the micropore and mesopore regions. Surface areas were calculated from the slope of the adsorption curve between 0.1-0.3 relative pressure with the Brunauer-Emmet-Teller (B.E.T) model. Pore-size distributions were calculated from the N_2 adsorption data with the Barrett-Joyner-Halenda (BJH) method and a Density Functional Theory (DFT) model for both N_2 and CO_2 data [11,12.]

A much smaller sample, 30-50 mg, of ground and dried shale from both the as-received and extracted workflow was used for thermal analysis (SenSys Evo, Setaram). The instrument monitored simultaneously weight loss as a function of temperature (Thermal Gravimetric Analysis, TGA) and heat flux (Differential Scanning Calorimetry, DSC). The thermal program for these samples started with an initial increase from room temperature by 3 °C/min to 300 °C where temperature was held for 2 hours, before a second ramping up to 820 °C by 3 °C/min. The samples were then cooled and discarded.

RESULTS

The N_2 adsorption and desorption curves for "as-received" samples are characterized by low initial adsorbed volumes followed by a significant volume increase at higher partial pressures (Figure 3). The presence of hysteresis associated with the desorption stage indicates a Type IV adsorption model, in contrast to the Type II adsorption described for shale in the literature [3].

In contrast, the solvent extracted samples have N_2 adsorption curves that suggest quasi-Type I behavior with rapid volume increases at the lowest partial pressures (Figure 4). This observation of a shift in the adsorption curve was seen in other porosity evolution experiments that used different solvents [2]. The desorption curves of the extracted samples do show hysteresis, thereby these samples are not true Type I materials. The CO_2

adsorption covers a limited range of partial pressures up to 0.03 because it was measured at 0°C and not colder temperatures (Figure 3). Even with the limited total pore volume the CO_2 sensed more surface area than the N_2 adsorption.

The carbonate and clay mineral-rich shale used in this study showed a positive correlation between surface area and pore volume (Figure 5). This correlation is not seen in other conventional rock types such as sandstones and carbonates. Despite the small particle size of these shale samples, the actual pore systems are several orders of magnitude smaller and can be filled with condensing gas during adsorption. In contrast, the sandstone pore networks are seldom preserved during sample preparation, where particle size greatly affects the measured surface areas. In the case of fine-grain shale samples the gas adsorption senses both internal and external surface areas, with emphasis on the internal surface area associated with the pores. The CO_2 adsorption curve senses an equivalent surface area at a fraction of the pore volume as it probes the smaller, organic-rich pores in these samples.

The total pore volume measured by N_2 gas adsorption reflects the percentage of pores that fall within the range of size sensed by the gas condensation or pore filling. This set of samples was defined by two lithofacies, one whose N_2 gas pore volume matched the pore volume measured by standard He porosimetry on an extracted sample and a second facies whose He-based pore volume was greater than the N_2-volume (Figure 6). Facies 1 has a narrower range of pore sizes that is captured entirely by the N_2 adsorption curve while Facies 2 has pores larger than the maximum size captured in the N_2 data. A comparison of these two measurements provides a quick estimate of the proportion of meso- and macro-pores found in fine-grain unconventional reservoir rocks.

Pore size distributions generated from gas adsorption and desorption curves were limited in the range they covered. Nitrogen adsorption yields a pore size distribution that starts at several nanometers up to 300-400 nanometers. The pore-size distribution calculated from the DFT model with the N_2 adsorption data indicates a broad range of pores in the 30 to 100 nm range with a small contribution around 2 nm (Figure 5). In the lower range, 1-10 nm, the error in the calculated PSD is much higher than in the mesopore region [8,9]. The addition of CO_2 adsorption on the same sample allowed for an extension of the pore size distribution down to 0.5 nm [3,10] (Figure 7). Combining nitrogen and carbon dioxide allows for a complete view of the sample from micropores to mesopores. The conversion of the adsorption curves to pore-size distributions enhances the interpretation of additional micropores being developed by solvent extraction (Figure 8). While the extraction process increased the total pore volume by 20%, those new pores were dominated by less than 5 nm pores associated with organic matter in these samples.

The DSC/TGA measurements confirmed the absence of water and light hydrocarbons in the post extraction samples compared to the "as received" (Figure 9). The as received sample shows more water and light hydrocarbons coming off the sample in the 200-500°C range (Figure 10). Post Extraction removed much of the water and light hydrocarbons

shown by smaller weight loss in the sample in the 200-500° C range. These curves overlapped between 600-800°C as similar amount of carbonate minerals decomposed from both samples equally.

CONCLUSIONS

The majority of the pores sensed by the N_2 adsorption fell into a broad distribution of sizes that ranged between100-500 nm. For many of these samples there was not a distinct pore size that might be used to distinguish lithofacies. Different lithofacies did not exhibit significant differences in pore size distributions nor average pore size, though they did have different total pore volumes. The limitation of the adsorption method for pore size distribution measurement was highlighted by Toluene extraction created a new population of micropores ($< 5nm$) with a very narrow range of sizes, most likely associated with the organic matter. The solvent extraction increased the porosity of the sample by 10-20%, either through removal of residual liquids or creation of new porosity in the solid organic matter. The DSC/TGA data confirmed water and light hydrocarbons were lost through the extraction process.

REFERENCES

1. Loucks, R., Reed., R., Ruppel, S., and Jarvie, D., "Morphology, genesis and distribution of nanometer-scale pores in siliceous mudstones of the Mississippian Barnett shale", J. Sed. Research, (2009), 79, 848-861.
2. Zargari S., K. Canter, M. Prasad, "Porosity evolution in oil-prone source rocks," *Fuel*, (2015) **153**, 110-117.
3. Clarkson C., N. Solano, R. Bustin, A. Bustin, G. Chalmers, L. He, Y. Melnichenko, A. Radlinski, T. Blach. "Pore structure characterization of North American shale gas reservoirs using USANS/SANS, gas adsorption and mercury intrusion," *Fuel*, (2013), **103**, 606-616.
4. Labani M., R. Rezaee, A. Saeedi, A. Hinai. "Evaluation of pore size spectrum of gas shale reservoirs using low pressure nitrogen adsorption, gas expansion and mercury porosimetry: A case study from the Perth and Canning Basins, Western Australia," *Journal of Petroleum Science and Engineering*, (2013), **112**, 7-16.
5. Sing, K. "The use of nitrogen adsorption for the characterisation of porous materials," *Colloids and Surfaces A: Physiochemical an Engineering Aspects*, (2001), 187-188.
6. Chalmers G.R., R.M. Bustin, I.M. Power, "Characterization of gas shale pore systems by porosimetry, pycnometry, surface area, and field emission scanning electron microscopy/transmission electron microscopy image analyses: Examples from the Barnett, Woodford, Haynesville, Marcellus, and Doig units," *AAPG Bulletin*, (2012), **96**, 1099-1119.
7. Mastalerz M., A. Schimmelmann, A. Drobniak, Y. Chen. "Porosity of Devonian and Mississippian New Albany Shale across a maturation gradient: Insights from organic petrology, gas adsorption, and mercury intrusion," *AAPG Bulletin*, (2013), **97**, 10, 1621-1643.

8. De Lange M., T. Vlugt, J. Gascon, F. Kapteijn, "Adsorptive characterization of porous solids: Error analysis guides the way," *Microporous and Mesoporous Materials*, (2014), **200**, 199-215.
9. Groen J., L. Peffer, J. Perez-Ramirez, "Pore size determination in modified micro- and mesoporous materials. Pitfalls and limitations in gas adsorption data analysis," *Microporous and Mesoporous Materials*, (2003), **60**, 1-17. Marsh, H., and Reinoso, F., *Activated Carbon*, (2006) Elsevier Scientific, 554pp.
10. Landers J., G. Gor, A. Neimark, "Density functional theory methods for characterization of porous materials," *Colloids and Surfaces A: Physicochemical and Engineering Aspects* (2013), **437**, 3-32.
11. Webb, P. and Orr,C., *Analytical Methods in Fine Particle Technology*, (1997), Micromeritics Instrument Corp., 325 pp.
12. Kok, M., "Thermal investigation of Seyitomer oil shale,"Thermochimica Acta (2001), **369**, 149-155.

FIGURES
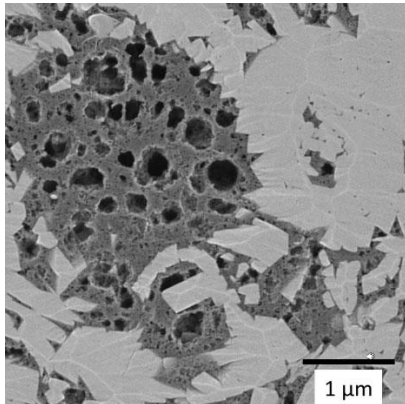
https://www.fei.com/products/dualbeam/helios-nanolab-660-for-oil-and-gas/
Figure 1. SEM image from FEI showing differences in porosity in organic matter versus matrix material.
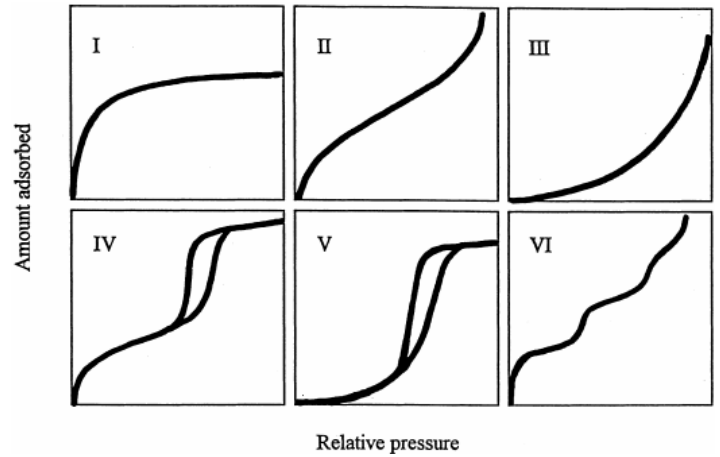
Figure 2. IUPAC Classification of gas adsorption / desorption isotherms.
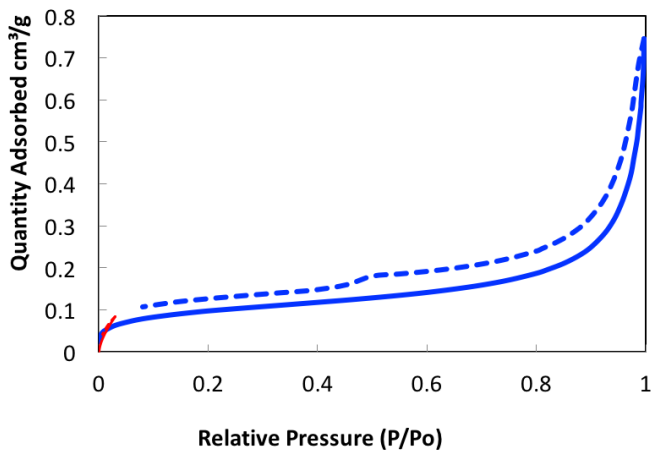
Figure 3. Adsorption-Desorption curves for N_2 (Blue) and CO_2 (red) for single sample in "as-received" state. Solid blue curve is N_2 adsorption and dashed-blue line is N_2 desorption. Note the limited range of partial pressures measured with the CO_2 adsorption test.
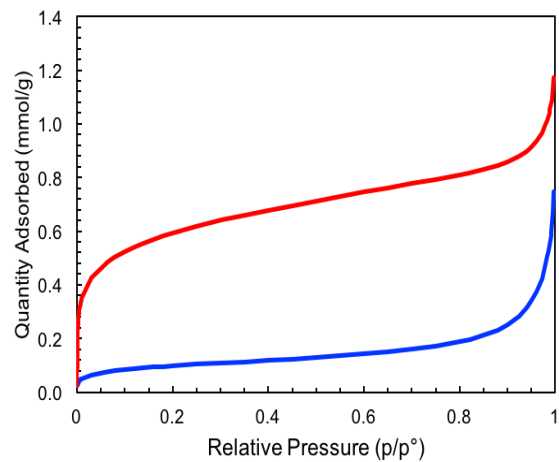
Figure 4. N_2 adsorption curve for sample in "as-received" state (blue) and after solvent extraction with toluene (red). The significant increase in the volume of smallest pores (lowest partial pressures) is reflected in the increase in total pore volume (P/Po=0.99).
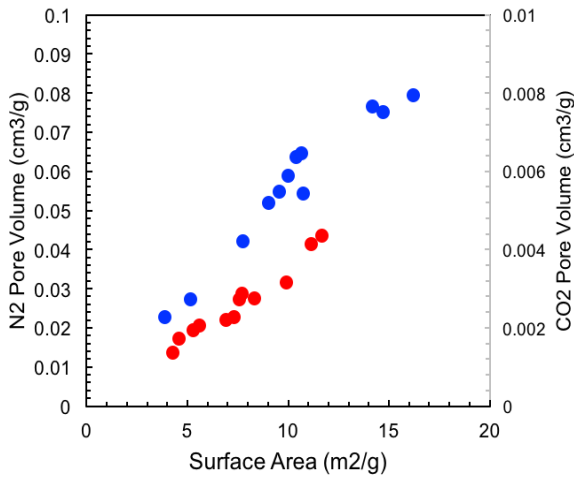
Figure 5. Pore volume correlation with Surface Area for N2 and CO2 adsorption measurements. Note the order of magnitude difference in pore volume scale for the different gases. This positive correlation is not observed for other coarser-grain rock samples..
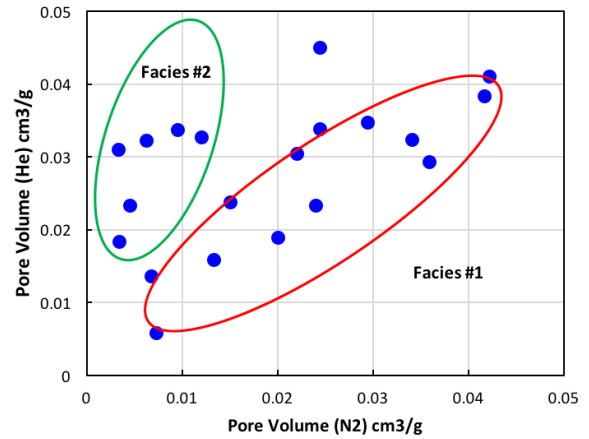
Figure 6. Comparison of pore volume measured by N2 gas adsorption and standard He-porosimeter on cleaned crushed rock samples. Facies #1 has a 1:1 correspondence that indicates all of the pores in the sample are filled at maximum partial pressure for N2, and therefore less than 400 nm. Facies #2 has a larger pore volume measured with He that indicates some of the pores in these samples are larger than the maximum pore diameter sensed by N2 adsorption.
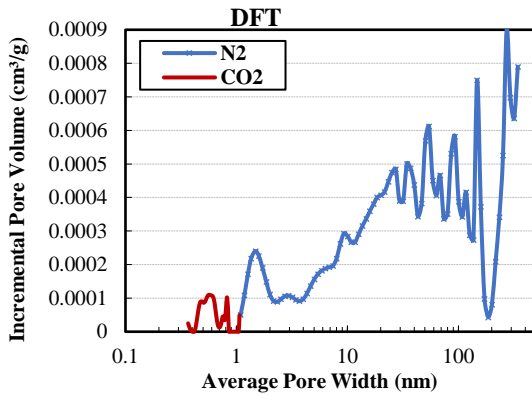
Figure 7. Combined Pore Size Distribution of CO_2 and N_2. CO_2 shows pores sizes down to 0.5 nm and combined with N_2 we can see from micropore to mesopore range.
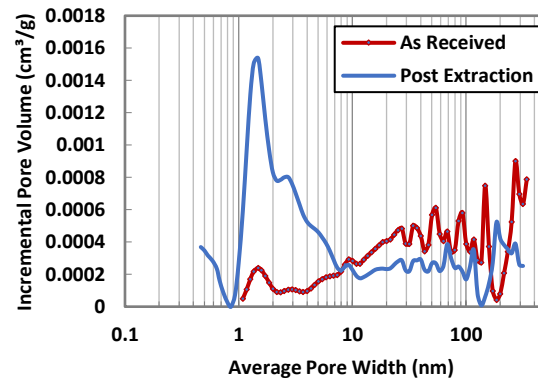
Figure 8. Pore Width plotted versus Pore Volume shows the difference between a sample before and after cleaning as seen in Figure 4. Post cleaning with toluene shows a dramatic increase in microporosity, but little change in mesopore and macropore volumes.
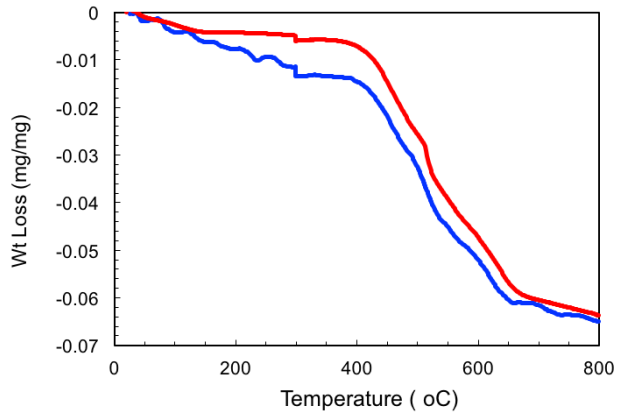
Figure 9. TGA curves for organic and clay-mineral rich "as-received shale (blue) and solvent extracted (red). The larger weight loss between 100 and 425oC for the as-received sample indicates the presence of water and light hydrocarbons that were mostly removed by the extraction process. Carbonates decompose at temperatures above 550oC and are not affected by extraction.
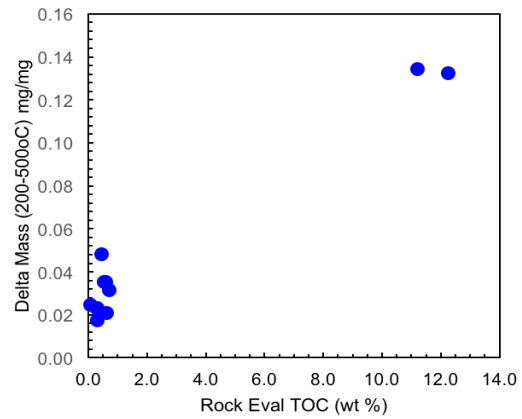
Figure 10. TGA weight loss between 200 and 500oC compared to TOC weight percent from RockEval. Two organic-rich samples obscure the trend between the two properties at lower TOC values.

PERMEABILITY REDUCTION AND WATER IMBIBITION IN UNPROPPED FRACTURES IN CARBONATE-RICH SHALE

Robert L. Krumm, and James J. Howard
Premier Oilfield Labs

ABSTRACT

Hydraulic fracturing of ultra-low permeability reservoir rock has revolutionized hydrocarbon production in the 21st century. High pressure completion fluids can imbibe into the rock matrix and alter geomechanical properties of the rock proximal to the fracture face. Imbibition of the fracture fluid can damage the formation reducing effective permeability but it can also improve hydrocarbon recovery near the hydraulic fracture. The geomechanical fluid sensitivities may result in rock softening thereby reducing fracture permeability and potentially resealing unpropped fractures over time.

A procedure was developed to investigate fracture face fluid sensitivities and quantify the amount of fluid imbibing into the fracture face. This workflow uses micro-CT and contrast agents to visualize the extent of imbibition, low field T_2 NMR to quantify saturation changes, and steady state liquid permeability measurements to investigate changes in the fracture permeability. This paper outlines the workflow for this procedure and experimental results of fluid/rock interactions are presented for brine on unpropped oil-saturated carbonate rich shale. The results show reductions in fracture permeability, and in some instances, the observed permeability diminishing to near the matrix permeability indicating a closed fracture. The results also show rapid countercurrent imbibition through the fracture face and average oil recovery by imbibition ranging from 31-46%.

INTRODUCTION

Ultra-low permeability hydrocarbon bearing reservoirs, such as the Marcellus source-rock play, have proven to be immense opportunities for production of oil and natural gas. In the United States, ultra-low permeability formations accounted for the majority of oil and natural gas production growth for the last decade. In all of these plays, hydraulic fracturing of horizontal wells was the critical technology making these formations economically viable.

During the hydraulic fracturing process, a portion of the fracturing fluid enters the formation via leakoff [1]. Some of the leakoff fluid mixes with formation fluids and is

produced as flowback water. Mixing is usually evidenced by changes in ionic concentrations of the produced water with time. It is often observed in some unconventional plays like the Eagle Ford that only a fraction of the fracturing fluid is recovered [2] meaning a portion of the fluid becomes trapped in the rock [3]. There are multiple driving forces that cause water to imbibe into the rock matrix: capillary action [4], osmotic flow [5], and hydration of clay minerals [6]. This paper focuses on systems with water-based completion fluids and hydrocarbon-saturated formations.

Water imbibition in ultra-low permeability reservoir rock has seen increased attention in recent years because of potential positive and negative effects it could have on recovery. For example, if the hydraulic treatment is performed with a water-based fluid and the formation initially contains mostly oil and gas, the water-based fluid will move into the rock matrix while oil and/or gas will enter the fracture, so that countercurrent imbibition increases the recovery of hydrocarbons [7]. Imbibition can potentially reduce hydrocarbon recovery by changing relative permeability near the fracture face. Roychaudhuri et al.[8] were one of the first to specifically investigate shale imbibition from a hydraulic fracture face. Roychaudhury et al.[9] showed that countercurrent imbibition rates in shale are a function of clay content and wettability.

Conductivity of the hydraulic fractures is important for the overall performance of a well. Completion fluids can have deleterious effects on the geomechanical properties of the rock which can result in reduced fracture conductivity [10]. Water-based fracture fluid influenced reductions in fracture conductivity were observed in propped and unpropped samples [11]. The reductions in fracture permeability were attributed to multiple causes; softening of the rock causing compaction and more proppant embedment, relative permeability alterations, and swelling of clay minerals. Kakkar [11] performed tests on unpropped fractured Eagle Ford core samples and showed how different completions fluids caused reductions in unpropped fracture perms with basic (pH > 7) solutions creating the greatest decrease. Kakkar also found that high clay content samples showed greater decreases in fracture permeability with increasing effective stress, suggesting that higher clay content samples exhibited greater fluid sensitivity. Zhang et al. [12] performed a propped-fracture fluid sensitivity study using Barnett shale in an API conductivity cell. Zhang et al. showed an 88% permanent decrease in fracture conductivity after brine was flowed through the fracture. They attributed the decrease in conductivity to the rock softening that allowed more proppant embedment.

This paper focuses on the worst-case scenario; unpropped fractures exposed to brine. Fractures were induced in cores with a shearing load frame and micro-Computed Tomography (micro-CT) was used to characterize the fractures. Steady-state permeability to decane measurements were done before and after breaking samples and changes in fracture conductivity upon exposure to brine were recorded over time. NMR T_2

measurements were used to monitor changes in saturation and micro-CT was used to visualize invaded areas after the test.

EXPERIMENTAL

Samples
Carbonate rich shale samples were used in this study. Plugs (2.54cm dia.) were cut from core, wrapped in cellophane and aluminum foil, and were preserved with a coating of wax. The trim ends of the samples were used for XRD mineralogy.

Fluids
Decane represented the oil phase in all experiments because its NMR hydrogen index is nearly the same as water. Brines doped with 50wt. % potassium iodide (KI) were used for the aqueous phase; the potassium iodide serves as the contrasting agent for CT scans. CT contrast tests with plugs saturated with different concentrations of KI brine were done beforehand and it was determined that high KI concentrations were necessary to provide sufficient contrast to visualize imbibition in shale. The small pores are beneath the resolution limits of the micro-CT used and given the relatively low porosity of these samples, more mineral is captured per unit voxel than fluid. With most minerals having greater X-ray attenuation than either brine or oil, compounded with the unlikeliness the imbibing fluid progresses as a continuous phase, large amounts of contrast agents were necessary to notice any appreciable differences in the images.

All brines were made with D_2O to eliminate the possibility of misinterpretation of the NMR T_2 distribution. The NMR instrument used for these measurements does not detect D_2O, therefore the amount of oil displaced from the sample was determined by the overall reduction in NMR signal intensity and confirmed with mass balance.

Workflow
All samples began the workflow with micro-CT screening with the broken or cracked samples being rejected (Figure 1). The micro-CT used was a Zeiss model 510 Versa with an auto loading stage. Samples were scanned at a resolution of 58µm/voxel at 140KeV/10W. This lower resolution scan was chosen to better cover the entire region of fractures and imbibed areas in the core plugs.

Acceptable samples were then dried in a vacuum oven for 24 hours at 80°C. Drying the samples was done in lieu of harsher solvent extractions to minimize the possibility of damaging the samples. After drying, the samples were checked with an NMR T_2 measurement to determine liquid content. The target signal volume for the dried samples is less than 0.2ml. If an average core plug is 2.54cm dia. by approximately 5cm long and is assumed to have a porosity of 8%, the total pore volume of the sample is roughly 2ml. Therefore drying to a residual signal of 0.2ml represents removing approximately 90% of

the native liquids. If the samples contained more than 0.2ml, they were returned to the drying oven for another 24h and the process was repeated until the samples were sufficiently dry, usually 48-72h total.

After drying, samples were pressure saturated with decane at 138 bar and 66°C. NMR T_2 measurements were acquired with a low-field spectrometer (GeoSpec2, Oxford Instruments) using standard data acquisition and processing methods (GITSystems Advanced, Green Imaging Technology).

Accurate measurement of matrix permeability in ultra-low permeability reservoir rock was a critical part of this investigation because without knowing the matrix permeability, it is impossible to determine if a fracture has closed. Permeability in unconventional reservoir rock can be measured by multiple methods; crushed rock permeability, pulse decay, and steady state[13]. The requirement for small particle size meant crushed rock methods were unsuitable. Pulse-decay permeability was an acceptable technique but was ruled out because interpretation of the data is not as straight forward as steady state methods. Further, since fracture permeability measurements were done steady state, it made sense to have a commensurate measurement for matrix permeability.

Steady state permeability measurements provided baseline matrix permeability. Decane was flowed through the plugs at very slow rates and the differential pressure was recorded. Core plugs were loaded into a heat-jacketed core holder. Chandler Engineering Q5000 syringe pumps controlled the flow of decane, typically less than 0.1ml/hr. The pumps were housed in a thermally controlled cabinet to mitigate the effects of temperature fluctuations in the room. Constant back pressure on the plugs of 35Bar was supplied by an accumulator. The net overburden pressure was maintained at 172Bar. Steady state permeability measurements were done at 66°C in order to help liberate residual waxes from the sample. Measurements were performed at multiple flow rates, two or more, and linear regression provided the permeability according to the Darcy equation and the methods outlined by McPhee at al.[14]

After the steady state measurements, the samples were dried at ambient conditions since plugs needed to be reasonably dry before they were fractured. The plugs were shrunk wrapped in Teflon and fractured in a load frame using offset plates to shear the plug. This method for shearing plugs usually created one continuous fracture longitudinally through the plug, the ideal fracture for this type of experiment. Shearing the plugs provided a fracture surface profile that was more representative of the fractures in the subsurface and far superior for these types of experiments compared with tensile failure fractures or saw cuts. Another micro-CT scan was done on the plugs ensuring fracture conformity; heavily fractured samples were rejected. Fractured plugs, still in their Teflon wrapper, were once again pressure saturated with decane.

The fracture permeability system was essentially identical to that used for the steady state decane permeability measurements except this system had larger capacity pumps. Back pressure was 35Bar, net overburden was 172Bar, and temperature 66°C. Fractured samples were loaded into the cells, in their Teflon wrappers, and decane was flowed through the crack at multiple steady rates to measure the fracture permeability. This was very similar to the steady state permeability to decane measurements with the exception that steady state pressure differential was now attained in hours not days. After the baseline fracture permeability was measured with decane, fluid flow was then changed to KI doped brine.

Unpropped fracture permeability to KI brine was measured over several days until steady state pressure drop was achieved. After KI brine flow, the samples were removed from their respective core holders and final NMR T_2 measurement was done. The volume of decane displaced from the plug was the difference in signal before/after the imbibition test. Micro-CT was done to get an idea of the extent of imbibition into the rock and examine the extent of changes to the fracture.

RESULTS AND DUSCUSSION

Porosities as measured by NMR T_2 relaxation ranged from 9.2% to 13.0% with values clustering around 10% (Table 1). XRD analysis on the samples provided the clay and carbonate content. Two different samples types were represented in this study, one that is high carbonate / low clay, the other low carbonate / high clay.

Table 1: Tabulated results for selected shale samples. SSK stands for Steady State Permeability.

Sample ID	XRD Carbonate	XRD Clay	Φ (p.u.)	Matrix SSK_{oil} (nD)	Fracture SSK_{oil} (nD)	Fracture SSK_{water} (nD)	% Oil Displaced
1	22.5	50.4	9.2	25.5	415.5	31.1	46
2	21.9	52.1	13.0	54.4	40266.7	3755.5	31
3	43.8	25.1	9.8	102.2	25004.3	504.6	33
4	42.2	29.1	10.2	63.4	3608.0	78.8	41

All the permeabilities of the measured sample were within one order of magnitude ranging from about 10-100 nD (Table 1). The steady state permeability measurements were performed at multiple rates and took about one week to complete.

After measuring matrix permeability, the plug samples were allowed to dry and were then sheared using offset plates a load frame. Micro-CT was used to analyze the fractures and verify that there was a single fracture in each sample extending from one end of the plug to the other. The two broken halves were pressure saturated with decane and reassembled in a core holder with no proppant or offset to keep the fracture open.

Fracture permeability was measured at steady state with decane at multiple rates over one day. Each flow rate reached steady state in about an hour. This paper does not address the relationship between increasing net confining stress and unpropped fracture permeability; net confining stress was maintained constant at 172Bar. Fracture permeability was independent of rock type.

The liquid flowing through the fracture was changed from decane to 50% KI in D_2O brine and pressure drop recorded over time. Changing the fluid in the fracture caused a significant decrease in the measured permeability. In two of the experiments, the fracture permeability decreased nearly to matrix permeability values signifying near total closure of the fracture. Micro-CT examination after the flow-through experiment was unable to identify the fractures that were created in samples 1 and 4 meaning the fracture aperture was reduced to less than the resolution of the micro-CT, 58µm. The rate that the fractures lost permeability was rapid and steady state was reached in a matter of a few days. There are two possible explanations for the loss of permeability when the fracture was exposed to water: 1) the fracture surface softened allowing the two halves to fuse, or 2) mineral dissolution of the contact points of the rock-rock interface caused the fracture aperture to shrink. Because of the quick decreases in fracture permeability, the former is more likely.

Micro-CT was able to identify regions within the plug samples that were infiltrated with the KI doped brine. Obtaining micro-CT images with noticeable fluid boundaries was difficult with two of the other samples not showing any. It was found that the brine rapidly dispersed nearly homogenously throughout these samples and immediate transfer of the sample to the micro-CT after the flow measurement was critical; reducing the total time the samples were exposed to the KI brine was also important for the same reasons. The left image in Figure 2 shows Sample 4 after fracturing and before fracture permeability measurements with decane and KI doped brine. The fracture in this sample is a hairline crack along bedding extending the entire length of the plug. After flowing decane and brine through the crack, the fracture is indistinguishable from the KI brine infiltrated matrix. The image on the right in Figure 2 is the same distance along the plug. The bright striations in the image on the right are regions infiltrated by KI brine. All tomograms were collected using the same acquisition parameters. There is noticeably more X-ray beam hardening, i.e. brightness along the edge of the sample, after exposure to the KI brine signifying a change in the density of the sample.

NMR T_2 relaxation measurements were done on the samples before and after the fracture flow-through measurements. The NMR measurement does not sense the D_2O that was used to make the brine, therefore, the change in saturations in the plug was determined by the loss of total signal intensity comparing NMR before and after flow-through measurements. The amount of oil displaced by brine imbibition is summarized in Table 1Table 1. Samples that had greater oil displacement were also the ones where the fracture permeability decreased to near matrix permeability; there was a greater pore pressure gradient across the length of these samples allowing the brine to overcome some of the

capillary pressure restrictions. The exposure of the rock to the brine was only a few days and the speed and magnitude the saturations changed exceeded expectations.

CONCLUSIONS

This paper presents a new workflow for determining fracture fluid sensitivities. Novel to this workflow was the determination of the matrix permeability as a baseline comparison for fracture permeability, a new technique based on shear that created fractures with profiles more representative of those in the subsurface, and the use of micro-CT to image the extent of imbibition from the fracture face. The results of this exploratory study found that fracture face fluid sensitivity could adversely affect productivity and may allow unpropped fractures to seal. Several key observations were:

- Unpropped fracture permeability was reduced in all samples when exposed to brine. This is likely the result of the brine changing the mechanical properties of the shale. The shale softened and the two sides of the fracture annealed. Two of the four samples showed a near complete sealing of the fracture.
- Countercurrent imbibition into the fracture face occured quickly over the course of the experiment (2-3 days) with the invading brine displacing 31-46% of the original oil in the sample. The samples used were initially fully oil saturated. Samples that saw the largest amount of oil displacement also had the largest pressure gradients.
- Micro-CT can be used with an appropriate contrast agent like potassium iodide to image the infiltrated zones. The dispersion of the brine into the sample matrix occurs rapidly over the course of 2-3 days.

REFERENCES

1. Barree, R. D., & Mukherjee, H., "Determination of Pressure Dependent Leakoff and Its Effect on Fracture Geometry", *SPE Annual Technical Conference and Exhibition*. (1996) Denver, Colorado.
2. Cheng, Y., "Impact of Water Dynamics in Fractures on the Performance of Hydraulically Fractured Wells in Gas-Shale Reservoirs", *Journal of Canadian Petroleum Technology*, (2012)**51**,2, 143–151.
3. Roychaudhuri, B., Tsotsis, T. T., & Jessen, K., "An experimental investigation of spontaneous imbibition in gas shales", *Journal of Petroleum Science and Engineering*, (2013)**111**, 87-97.
4. Ren, W., Li, G., Tian, S., Sheng, M., & Geng, L., "Analytical modelling of hysteretic constitutive relations governing spontaneous imbibition of fracturing fluid in shale", *Journal of Natural Gas Science and Engineering*, (2016)**34**, 925–933.
5. Wang, F., & Pan, Z., "Numerical simulation of chemical potential dominated fracturing fluid flowback in hydraulically fractured shale gas reservoirs", *Petroleum Exploration and Development*, (2016)**43**,6, 1060–1066.
6. Xu, M., & Dehghanpour, H., "Advances in Understanding Wettability of Gas Shales", *Energy & Fuels*, (2014)**28**,7, 4362–4375.

7.   Takahashi, S., & Kovscek, A. R., "Spontaneous countercurrent imbibition and forced displacement characteristics of low-permeability, siliceous shale rocks", *Journal of Petroleum Science and Engineering*, (2010)*71*,1, 47–55.
8.   Roychaudhuri, B., Tsotsis, T. T., & Jessen, K., "An Experimental and Numerical Investigation of Spontaneous Imbibition in Gas Shales", *SPE Annual Technical Conference and Exhibition*. (2011) Denver, Colorado.
9.   Roychaudhuri, B., Tsotsis, T. T., & Jessen, K., "An experimental investigation of spontaneous imbibition in gas shales", *Journal of Petroleum Science and Engineering*, (2013)*111*, 87–97.
10.   Zhou, T., Zhang, S., Yang, L., Ma, X., Zou, Y., & Lin, H., "Experimental investigation on fracture surface strength softening induced by fracturing fluid imbibition and its impacts on flow conductivity in shale reservoirs", *Journal of Natural Gas Science and Engineering*, (2016)*36*, 893–905.
11.   Pratik Kakkar, *Experimental Study of the Effect of Stress and Fluid Sensitivity on Propped and Un-propped Fracture Conductivity in Preserved Reservoir Shale*. University of Texas, Austin.
12.   Zhang, J., Ouyang, L., Hill, A. D., & Zhu, D., "Experimental and Numerical Studies of Reduced Fracture Conductivity due to Proppant Embedment in Shale Reservoirs", *SPE Annual Technical Conference and Exhibition*. (2014) Amsterdam, Netherlands.
13.   Sinha, S., Braun, E. M., Determan, M. D., Passey, Q. R., Leonardi, S. A., Boros, J. A., … Kudva, R. A., "Steady-State Permeability Measurements on Intact Shale Samples at Reservoir Conditions - Effect of Stress, Temperature, Pressure, and Type of Gas", *SPE Middle East Oil and Gas Show and Conference*. (2013) Manama, Bahrain.
14.   McPhee, C., Reed, J., & Zubizarreta, I., "Core Analysis: A Best Practice Guide", *Developments in Petroleum Science*, (2015)*64*.
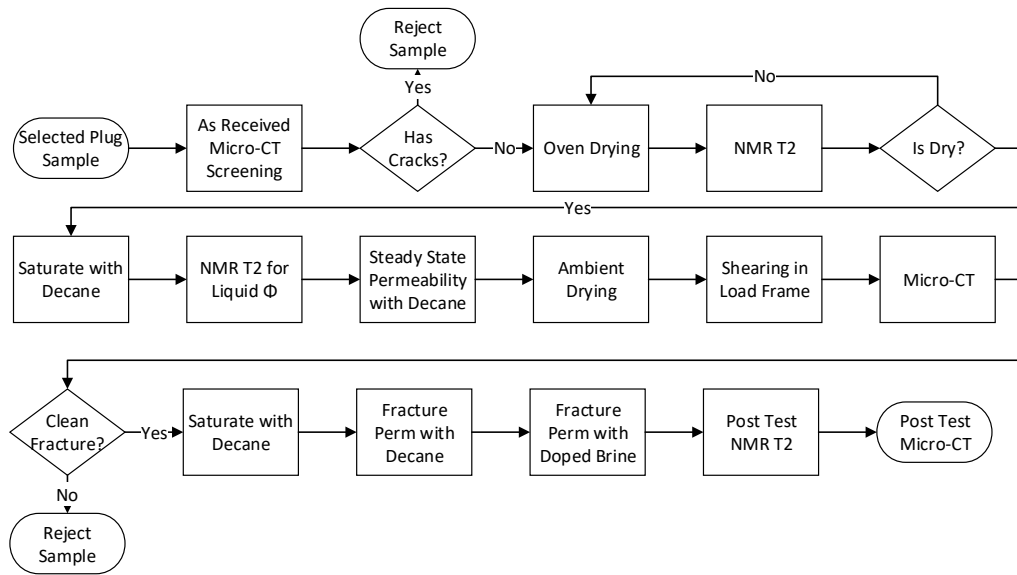
Figure 1: Workflow used for determining the effect of brine imbibition on fracture permeability.
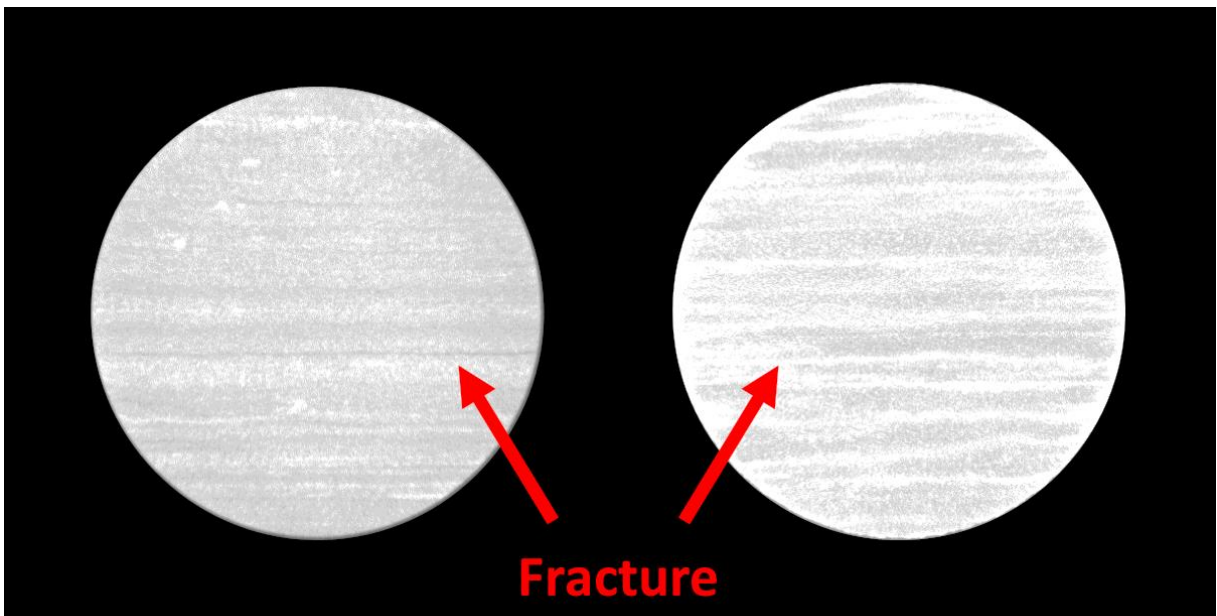
Figure 2: (left) Micro-CT tomogram of a fractured core plug 4V before fracture permeability measurement. (right) Micro-CT of the same core plug after fracture permeability measurement with decane and potassium iodine doped brine. The light colored striations in the sample are regions where the brine infiltrated. There is also a more pronounced beam hardening artifact signifying more X-ray attenuation around the edges of the plug. The fracture in this example completely sealed when exposed to brine. The resolution of both images is 58µm/voxel.

SHALE GAS FORMATIONS IN POLAND – NEW EVALUATION METHODS FOR PROCESSING AND QUANTITATIVE INTERPRETATION USING COMPUTED X-RAY TOMOGRAPHY

*Krakowska P., *Puskarczyk E., **Jędrychowski M., ***Madejski P., *Habrat M.
*AGH University of Science and Technology in Krakow (Poland), Faculty of Geology, Geophysics and Environmental Protection
**AGH University of Science and Technology in Krakow (Poland), Faculty of Physics and Applied Computer Science
***EDF Polska SA, Research and Development in Krakow (Poland)

ABSTRACT

Computed X-ray tomography (CT) is a non-invasive method of rock analysis and provides many parameter results of shale gas formations. Samples from Silurian shale gas deposits from different regions of Poland were presented in a comparative study. Qualitative and quantitative analysis of pyrite and pore space was carried out using 2D slices and 3D models from nanotomography results as a new evaluation method. Petrophysical and mineralogical laboratory measurement results were also compared to the results obtained from CT. Evaluation of pyrite content and pore space heterogeneity offers insights about possible reservoir and geomechanical properties of shale gas deposits in Poland.

INTRODUCTION

Unconventional oil and gas deposits in Poland are spread along a belt from the north-west to the south-east edge of Poland [1]. Hydrocarbons are accumulated in the Silurian and Ordovician formations [2, 3]. Knowledge of physical and chemical parameters of shale gas deposits brings us closer to effective hydrocarbons exploration. Moreover, proper estimation of parameters may explain why hydraulic fracturing is not conducted in a controlled manner in shale gas deposits in Poland. Heterogeneity of pore space and mineral distribution in shales plays an important role. Detailed characterization of shale heterogeneity suggests the best propositions for exploration. Pyrite, as a heavy mineral, significantly influences the mechanical properties of the rock [4]. Pores and pore channels shape also affect the reservoir and mechanical properties. Hence, the techniques of 2D and 3D rock visualization should be taken into account in sophisticated analysis.

Computed X-ray tomography (CT) is a non-invasive method of rock analysis [5, 6] and provides many parameter results of shale gas formations [7, 8]. Exemplary samples from Silurian shale gas deposits from different regions (north-west and south-east Poland) were presented and also the objects of the comparison. Qualitative and quantitative analysis of pyrite and pore space was carried out using 2D slices and 3D models from nanotomography results as a new evaluation method. Furthermore, petrophysical and mineralogical laboratory measurement results were also compared to the results obtained from CT.

DATA SET AND METHOD

Data set comprised of samples of Silurian shale gas deposits. Samples 5, 6 and 22 were taken from a well located on the Lublin Synclinorium, south-east Poland, while sample 872 represents the shale from a well situated in the Peribaltic Syneclise, in the north-west Poland. Sample 5, 6 and 22 are from 2385.4, 2385.8, 2500.5 m depth, respectively, while 872 – from 3546 m.

The main laboratory technique, used in the analysis presented in this paper, was the computed X-ray nanotomography. Nanotom S 180n General Electric Sensing & Inspection Technologies at the Faculty of Physics and Computer Sciences, AGH UST in Krakow (Poland), is equipped with a 57-W X-ray tube. The maximum work voltage of the tube is 180 kV. Images are recorded by the Hamamatsu 2300×2300 pixel 2D detector (Ham C 7942CA-02). The maximum spatial resolution is about 500 nm. The reconstruction of measured objects was carried out using the Feldkamp algorithm for the cone beam X-ray CT. All the data was subjected to a filtering process using a 3D median filter.

Mineral composition was derived by XRD method (Table 1). Total porosity and density was estimated using a helium pycnometer. The effective porosity of 872 sample was determined by mercury porosimetry. For the samples 5, 6 and 22, Tight Rock Analysis (TRA) was conducted in Terra Tek Schlumberger Reservoir Laboratory [9, 10]. Permeability of all samples was measured using a pressure decay permeability method (Terra Tek). TRA pressure decay permeability testing was carried out on crushed shale samples at "as received" conditions. A crushed 12/20 mesh sample was weighed out to 30g and then exposed to helium gas in the reference cell. The rate at which the helium gas diffuses into the particles was monitored. No net overburden stress was applied on the sample.

P- and S-wave velocity, measured in the Laboratory of Petrophysics at Faculty of Geology, Geophysics and Environmental Protection AGH UST in Krakow (Poland), was investigated to obtain information about elastic properties.

RESULTS

The results of XRD analysis contributed the information about the mineral composition (Table 1). In comparison to the sample 872, increase in clay mineral content is significant

in samples 5, 6 and 22, from 17% for 872 to 46% in sample 22. These results are also reflected in quartz content. Sample 22 included more pyrite than sample 872. The conclusion from these exemplary samples is as follows: geomechanical properties of shale gas reservoirs improve to the north Poland. Total porosity obtained from helium pycnometer and CT results differ because of the different measurement resolution (Table 2). Sample 22 has better reservoir parameters (e.g., higher porosity, permeability) than sample 872.

Pyrite is quite a common mineral in shale deposits. Pyrite can mainly be found in the shapes of framboids or euhedral crystals [11]. The orientation of pyrite in shale influences significantly the mechanical properties of the rock, e.g. causing uncontrolled hydraulic fracturing. The CT measurement results offered insight into the amount and orientation of pyrite in the shale samples. Pyrite content derived from the CT results is close to these obtained from XRD analysis (Table 1). Estimation of pyrite content is a new evaluation method based on CT measurement results.

2D slices from CT measurements are presented in Figure 1-4. The most bright elements represent pyrite, the most dark – pores. Figures 1-3 show 2D slices of samples 5, 6 and 22, respectively, while Figure 4 – sample 872. Samples 5, 6 and 22 differ in pyrite and pores orientation from sample 872. Pyrite predominates in the thin laminae in samples 5, 6 and 22, as opposed to the dispersed form in sample 872. In sample 5 (Figure 1) it is clear that the pyrite is developed in the form of elongated forms, while in sample 872 more spherical.

3D visualizations for samples 5, 6, 22 and 872 are presented in Figures 5-8. A transparent colour of pyrite indicates forms with volume less than 8 μm^3, red – more than 10000 μm^3. Pyrite in forms larger than 10000 μm^3 occurs sporadically. The P and S-wave velocities also indicate the weak elastic properties in samples from Lublin Synclinorium. Figure 8 shows the distribution of pyrite diameters from CT results (Table 2). The most detected pyrites have a diameter in the range of 10-20 μm in the all samples (Figure 11). Also, the diameters below 10 μm are common.

Pore space is shown in Figure 9 and 10. Pore space of sample 5 is similar to the samples 6 and 22. Sample 872 has very low porosity in the CT results – only 0.2%. Additionally, the microcrack is visible in sample 6 (green object in Figure 9). Most probably, the microcrack was naturally formed as a result of stress regime in the formation connected with the pyrite laminae appearance (e.g. lack of continuity). Moreover, microcracks are also visible in Figure 12, which resulted in increase the quantity of objects with pore diameters above 200 μm. Generally, microcracks cause increase in porosity and pore space heterogeneity.

Pore space is developed in some laminae. That is why pores are visible only in one direction and in consolidated volume (not in whole 3D visualization). The greatest amount of pores have diameters less than 10 μm (Figure 12). From the analysis of pore space distribution, samples from the Lublin Synclinorium indicate better reservoir properties. The increase in

porosity and heterogeneity of pore space distribution reduces the geomechanical properties (e.g. decrease in compressive strength, Young modulus, increase in Poissons ratio).

CONCLUSIONS

Computed X-ray tomography is a powerful tool in petrophysical analysis of rocks. Several samples from unconventional oil and gas deposits from Poland were investigated using CT results. The conclusions are as follows:

- A new evaluation method of pyrite content estimation was presented.
- Pyrite content derived from CT results was comparable to these from XRD results.
- Pyrite occurrence and orientation in shale samples differ depending on well location.
- Pyrite in laminae was detected in samples from the south-east Poland, while in dispersed form in the whole sample from north-west Poland.
- Better reservoir parameters were identified in shale samples from south-east Poland.
- The most pyrite diameters were in the range of 10-20 µm, pores – less than 10 µm (range of micro and nanopores).

This paper presents the preliminary results of the project. The goal of the project is to analyse CT results of the tight, low porosity and low permeability shales, sandstones, limestones and dolomites, and to create and develop the software to process and interpret the CT result for the geological and petrophysical purposes (poROSE – Porous Materials Examination Software). Furtermore, project task is to analyse fluid flow in Polish tight rock.

ACKNOWLEDGEMENTS

REFERENCES

1. Porębski, S.J., Prugar, W., Zacharski, J., "Silurian shales of the East European Platform in Poland: some exploration problems", *Geological Review*, (2013) **61**, 8, 468-477.
2. Kotarba, M .J., "Geology, ecology and petroleum of the lower Paleozoic strata in the Polish part of the Baltic region", *Geological Quarterly*, (2012) **54**, 2, 103-108.

3. Poprawa P., "Shale gas potential of the Lower Palaeozoic complex in the Baltic and Lublin-Podlasie basins (Poland)", *Geological Review*, (2010) **58**, 3, 226-249.

4. Zhang, Ch., Dong, D., Wang, Y., Guan, Q., "Brittleness evaluation of the Upper Ordovician Wufeng–Lower Silurian Longmaxi shale in Southern Sichuan Basin, China", *Energy Exporation & Exploitation* Special Issue: Chinese Petroleum, (2017) **0(0)**, 1-14.

5. Jarzyna, J., Krakowska, P., Puskarczyk E., Wawrzyniak-Guz, K., Bielecki, J., Tkocz, K., Tarasiuk, J., Wroński, S., Dohnalik, M., "X-ray computed microtomography – a useful tool for petrophysical properties determination", *Computational Geosciences*, (2016) **20**, 5, 1155-1167.

6. Krakowska, P., Dohnalik, M., Jarzyna, J., Wawrzyniak-Guz, K., "Computed X-ray microtomography as the useful tool in petrophysics: a case study of tight carbonates Modryn formation from Poland", *Journal of Natural Gas Science and Engineering*, (2016) **31**, 67-75.

7. Josh, M., Esteban, L., Delle Piane, C., Sarout, J., Dewhurst, D.N., Clennell, M.B., "Laboratory characterization of shale properties", *Journal of Petroleum Science and Engineering*, (2012) **88-89**, 107-124.

8. Tang, X., Jiang, Z., Jiang, S. and Li, Z., "Heterogeneous nanoporosity of the Silurian Longmaxi Formation shale gas reservoir in the Sichuan Basin using the QEMSCAN, FIB-SEM, and nano-CT methods", *Marine and Petroleum Geology*, (2016) **78**, 99-109.

9. Handwerger, D., Suarez-Rivera, R., Vaughn, K., Keller, J., "Improved Petrophysical Core Measurements on Tight Shale Reservoirs Using Retort and Crushed Samples", SPE Annual Technical Conference and Exhibition, 30 October-2 November, Denver, Colorado, USA, (2011) SPE 147456, 1-19.

10. Suarez-Rivera, R., Chertov, M., Willberg, D., Green, S., Keller, J., "Understanding Permeability Measurements in Tight Shales Promotes Enhanced Determination of Reservoir Quality", SPE Canadian Unconventional Resources Conference, 30 October-1 November, Calgary, Alberta, Canada, (2012) SPE 162816, 1-13.

11. Cárdenesa, V., Merinerob, R., De Boevera, W., Rubio-Ordóñezc, A., Dewanckelea, J., Cnuddea, J.P., Booned, M., Van Hoorebeked, L., Cnuddea, V., "Characterization of micropyrite populations in low-grade metamorphic slate: A study using high-resolution X-ray tomography", *Palaeogeography, Palaeoclimatology, Palaeoecology*, (2016) **441**, 4, 924-935.

Table 1. Selected mineral content from XRD and CT results. Symbols: P CT – pyrite from CT results, P XRD – pyrite from XRD results, Q – quartz, F – feldspars, C – calcite, D – dolomite, Sc – sum of clay minerals

Sample	P CT [%]	P XRD [%]	Q [%]	F [%]	C [%]	D [%]	Sc [%]
5	1.2	-	-	-	-	-	-
6	1.8	-	-	-	-	-	-
22	2.1	2	24	11	14	3	46
872	0.3	<1	46	21	10	3	17

Table 2. Petrophysical parameters. Symbols: BD – bulk density, GD – grain density, Φeff – effective porosity, Φtot – total porosity from pycnometer, Φtot – total porosity from CT results, K – absolute permeability, Vp – P-wave velocity, Vs – S-wave velocity

Sample	BD [g/cc]	GD [g/cc]	Φeff [%]	Φtot [%]	Φtot CT [%]	K [nD]	Vp [m/s]	Vs [m/s]
22	2.668	2.729	3.20	4.16	2.4	198	4061	1658
872	2.623	2.709	0.77	3.15	0.2	47	5054	2751
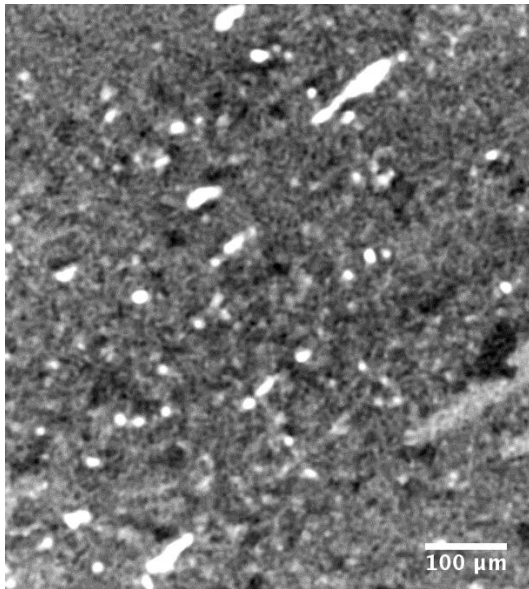
Figure 1. 2D slice of shale sample no. 5. White elements – pyrite, black – pores
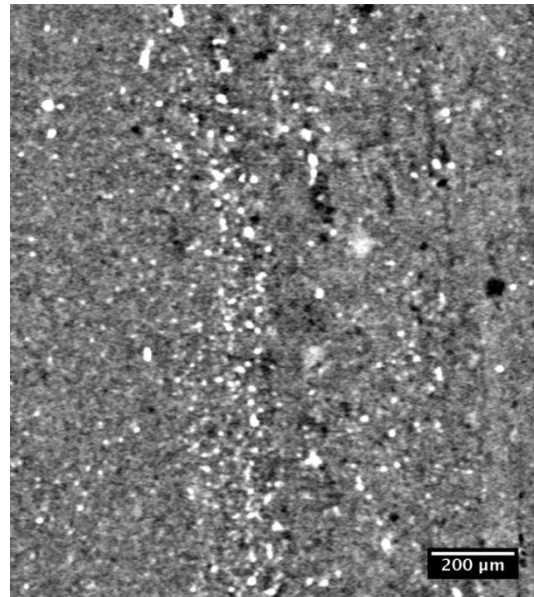
Figure 2. 2D slice of shale sample no. 6. White elements – pyrite, black – pores
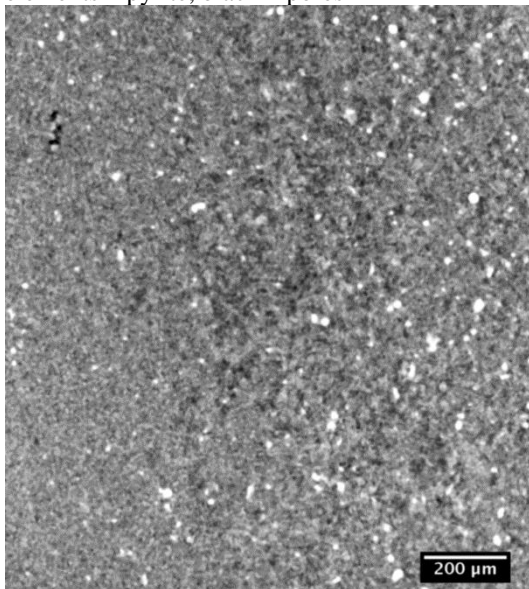
Figure 3. 2D slice of shale sample no. 22. White elements – pyrite, black – pores
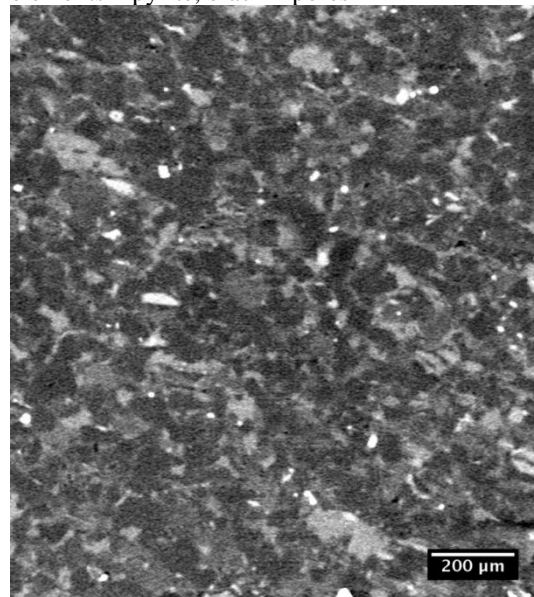
Figure 4. 2D slice of shale sample no. 872. White elements – pyrite, black – pores
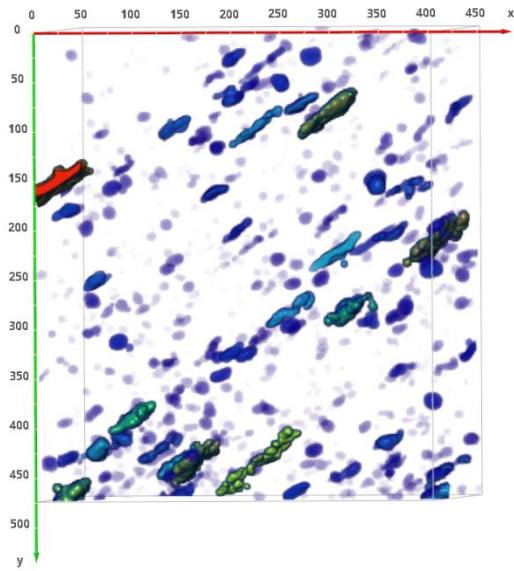
Figure 5. 3D visualization of pyrite in shale sample no. 5. Colour: transparent – less than 8 μm^3, red – more than 10000 μm^3
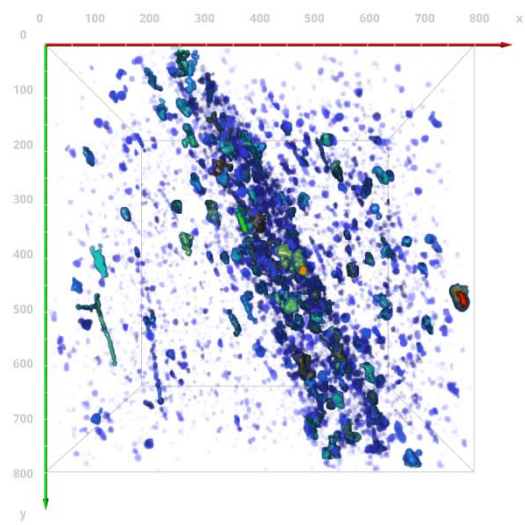
Figure 6. 3D visualization of pyrite in shale sample no. 6. Colour: transparent – less than 8 μm^3, red – more than 10000 μm^3
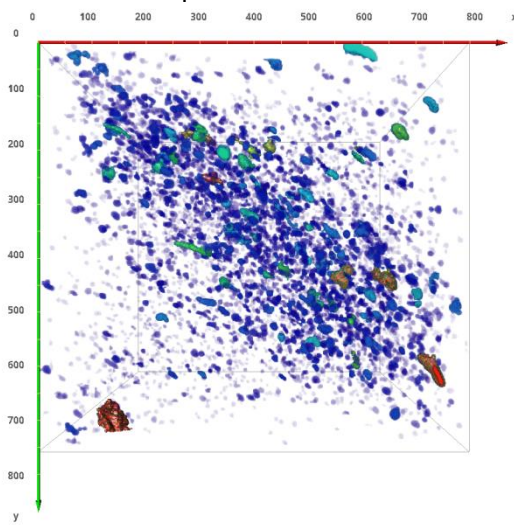
Figure 7. 3D visualization of pyrite in shale sample no. 22. Colour: transparent – less than 8 μm^3, red – more than 10000 μm^3
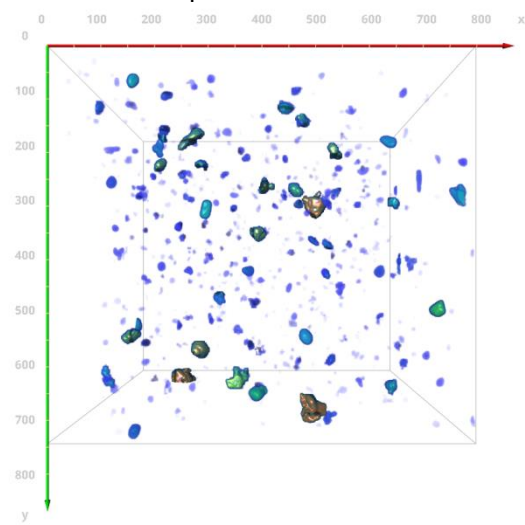
Figure 8. 3D visualization of pyrite in shale sample no. 872. Colour: transparent – less than 8 μm^3, red – more than 10000 μm^3
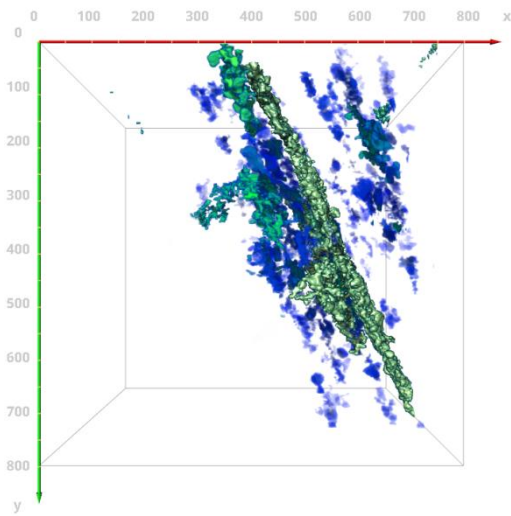
Figure 9. 3D visualization of pore space in shale sample no. 6. Colour: transparent – less than 8 μm^3, red – more than 800000 μm^3
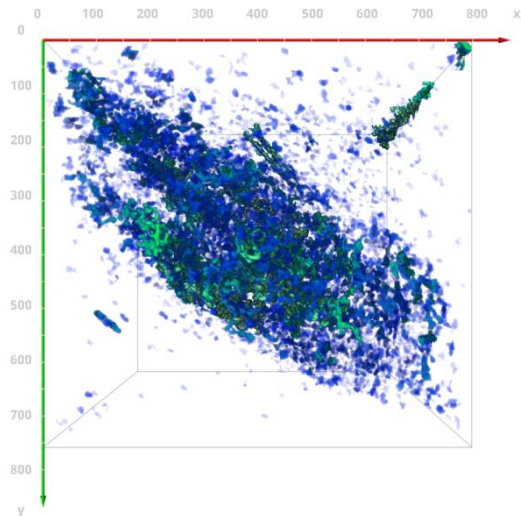
Figure 10. 3D visualization of pore space in shale sample no. 22. Colour: transparent – less than 8 μm^3, red – more than 100000 μm^3
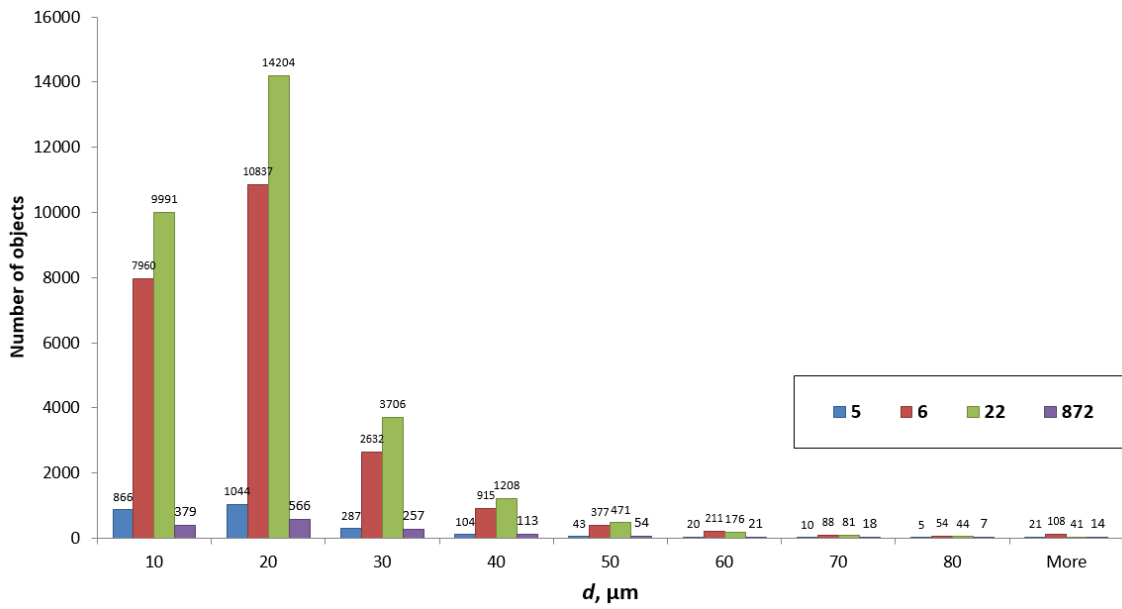
Figure 11. Distribution of pyrite diameter d for the all samples detected by CT results
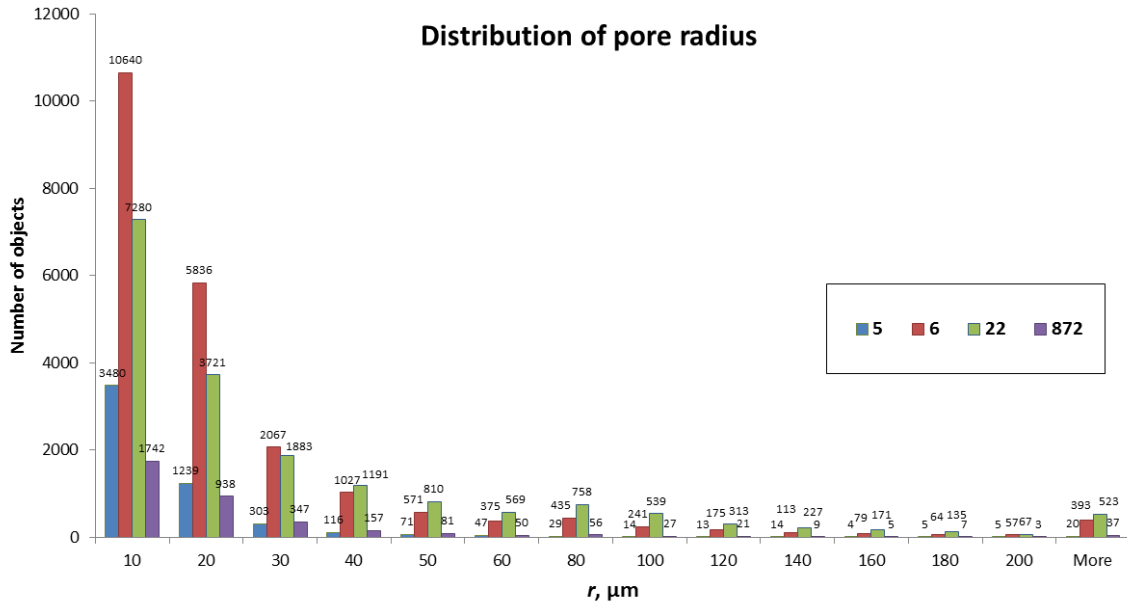
Figure 12. Distribution of pore diameter *r* for the all samples detected by CT results

SUCCESS, PITFALLS AND LIMITATIONS IN THE CHEMOSTRATIGRAPHIC ANALYSIS OF BRINE-RICH CORES: THREE FORKS FORMATION, NORTH DAKOTA

Harry Rowe[1], Evan Sivil[2], Austin Morrell[1], Pukar Mainali[1], Jarred Garza[1]

[1]Premier Oilfield Laboratories, Houston, TX
[2]Bureau of Economic Geology, University of Texas at Austin, Austin, TX

ABSTRACT

The Three Forks Formation (Devonian, Williston Basin, ND) is difficult to analyze for facies-scale chemostratigraphic variability due to the overwhelming concentrations of brines emanating from the rock which coat the surface of the core. The brine coating impacts the surface-sensitive X-ray fluorescence (XRF) analysis typically undertaken by 1) creating a layer that attenuates X-ray energies from the low-energy emitters (e.g., Mg, Al, Si, and P, S, K, and Ca), and 2) impacting the inter-element corrections established for non-brine-bearing mudrocks. Tremendous care was taken to wash and immediately analyze a cored Three Forks succession for the purposes of removing/minimizing brine contributions, and consequently, develop a high-quality chemostratigraphic record of change from the economically important succession of strata.

The rocks were soaked with water and rinsed multiple times before scanning for major and trace elements. It was observed that brine would quickly build up on the surface of the rocks, thus the rocks were scanned under incipient dryness, and an evaluation of the brine contamination was made by monitoring the chlorine peak on the X-ray fluorescence software. Raw counts data for the chlorine were evaluated, and samples were reanalyzed until deemed "clean" of chlorine or the overwhelming inter-element effects of chlorine. The chemostratigraphic results reveal that significant stratigraphic variations in %Al (clay proxy), %Mg (dolomite proxy), %S (sulfate proxy), and Si/Th (quartz/clay proxy) occur and can be used to break up the succession. Trace element signatures (Sr, Ba, Mn), and elemental ratios also help refine the traceability of the stratigraphic record by defining marker horizons/zones. The chemostratigraphic evaluation will focus on understanding stratigraphic variations in the distribution of clay-dolomite-sulfate-quartz, and developing a chemofacies model with the potential to use across large portions of the Williston Basin.

INTRODUCTION

The Williston Basin (North Dakota, Montana, and southern Canada) initially developed as

an inter-cratonic sag during the Cambrian, but evolved throughout the Phanerozoic Eon (Figure 1). Strata of the Three Forks Formation were interpreted to represent deposition in sabkha, tidal flat, and shallow marine environments that were intermittently connected to the Panthalassic Ocean [1-5]. The Three Forks Formation was deposited conformably above the Late Devonian Birdbear Formation, and lays unconformably below the Devonian-Mississippian-aged Bakken Formation, Williston Basin, North America (Figure 2). The spatial extent of the Three Forks and related units is shown in Figure 1B.

The purposes of the study are to demonstrate 1) common analytical pitfalls associated with a brine-laden succession of rock, and 2) how bulk elemental chemostratigraphy can be utilized to develop an understanding of stratal subdivisions and the changes in paleoenvironments that they represent. Most importantly, the development of a highly-resolved (facies-scale) chemostratigraphic/chemofacies framework for any stratigraphic succession creates a structure upon which other, less resolving analyses can be tied and interpreted. For instance, the linkages between strata and the parameters that govern production (e.g., porosity, permeability) may be further interpreted in the context of changing chemofacies, which are a function of facies-specific differences in mineralogy, depositional conditions, and diagenesis.
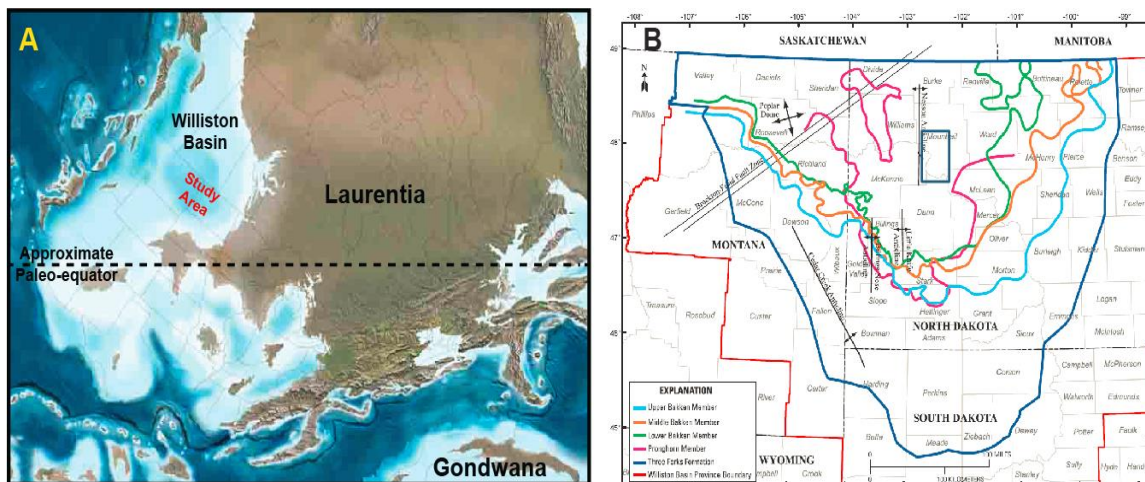

Figure 1: A) Paleogeographic map of Late Devonian North America (Laurentia), with the Williston Basin located on the western edge of the continent, at tropical to subtropical latitudes [6]. B) Lateral extent of the Three Forks Formation (dark blue boundary) in the context of overlying related units of Late Devonian and earliest Mississippian age [7]. The dark blue rectangle in southwestern Mountrail County, ND, marks the general location of the study core.

Linkages between the chemostratigraphic framework and productivity parameters are not explored for the presented core, as the study of the core by the operator is ongoing. However, recent work on the Three Forks suggests that a direct linkage between mineralogy (mainly dolomite) and porosity is lacking, and instead, porosity development is more tightly linked with changes in maturity across the basin. Maximum porosities are reported to be ~12%-15% [8-9], but another recent work presented limited data on facies-

specific samples that showed a range of 1.2 to 8.0% porosity and broad permeability range of 11 to 2585nD [10].

METHODS

A 257-foot thick succession of Three Forks was cored in southwestern Mountrail County, North Dakota, USA. The lower Three Forks contact with the Birdbear Formation was estimated to be 2 feet below the bottom of the core, and the upper Three Forks contact with the Bakken was recovered, providing an almost complete record of Three Forks deposition. The exact core name and location is not provided, as they are proprietary; however, the detailed geochemical workflow is defined.

Geochemistry: Energy-Dispersive X-ray Fluorescence (ED-XRF)

ED-XRF spectra were generated using Bruker Tracer IV spectrometers. Two instruments were used--one for major element analysis plus Ba, V, and Cr, the second for trace element analysis. The major elements were analyzed at 15kV and 35µA with a helium flow system (DeWitt Systems) that enhanced the X-ray signal of low-energy emitters, like Mg and Al. Trace elements were analyzed at 40kV and 11µA using a Ti-Al energy filter. Prior to analysis the slabbed core face was pre-scrubbed with a wet rag, and labeled every three inches with small Avery labels (#5412). Immediately before major element analysis, the sample was dunked in warm tap water and scrubbed multiple times with a hard plastic brush, then dried. Major element analysis was undertaken for 60 seconds; however, if the accumulation of each raw X–ray spectrum indicated an abundance of chlorine (denoted by an energy peak immediately to the left of the Rh-Lα peak), then the analysis was stopped, the sample was re-scrubbed and re-dried, and reanalyzed until the chlorine peak was absent or barely above baseline.

Before trace element analysis the core slab face was dunked and lightly scrubbed with a wet towel, then dried and analyzed. It was deemed imperative that the major element analysis occur before trace analysis in order to confirm that the original brine film was removed, but it was also important for trace analysis to quickly follow major element analysis so that minimal brine accumulation occurred on the surface of the cleaned sample. A total of 1016 major and trace analyses were undertaken in the Three Forks, accompanied by 14 analyses of the overlying lowermost Bakken (Pronghorn Mbr). Raw x-ray spectra were subsequently calibrated using a suite of reference materials [11-12]

Hierarchical Cluster Analysis (HCA), Elemental Characteristics of Clusters, and Chemofacies Assignment

In data mining, hierarchical clustering is a method of sample grouping which seeks to build a hierarchy of sample groups usually presented in terms of a sample dendrogram, demonstrating sample ranking by similarity. In order to decide which sample groups (*clusters*) should be combined (for agglomerative), or where a cluster should be split (for divisive), a measure of dissimilarity between sets of observations is required [12-16]. This

measure is achieved by use of an appropriate metric (a measure of distance between pairs of observations). The primary goal of HCA is to partition a multivariate data set into meaningful groups--in the present case these groups may be considered *chemofacies*. The primary outcome of HCA is a number of clusters that maximize the sample similarity within each cluster and maximize the sample differences between clusters. In a vertical succession characterized by discrete lithologies, the inter-cluster differences are well-defined; however, in many mudstone lithologies, the inter-cluster differences are smeared because the lithologies fall along a spectrum of geochemical composition (e.g., limestone--muddy limestone--limey mudstone--mudstone).
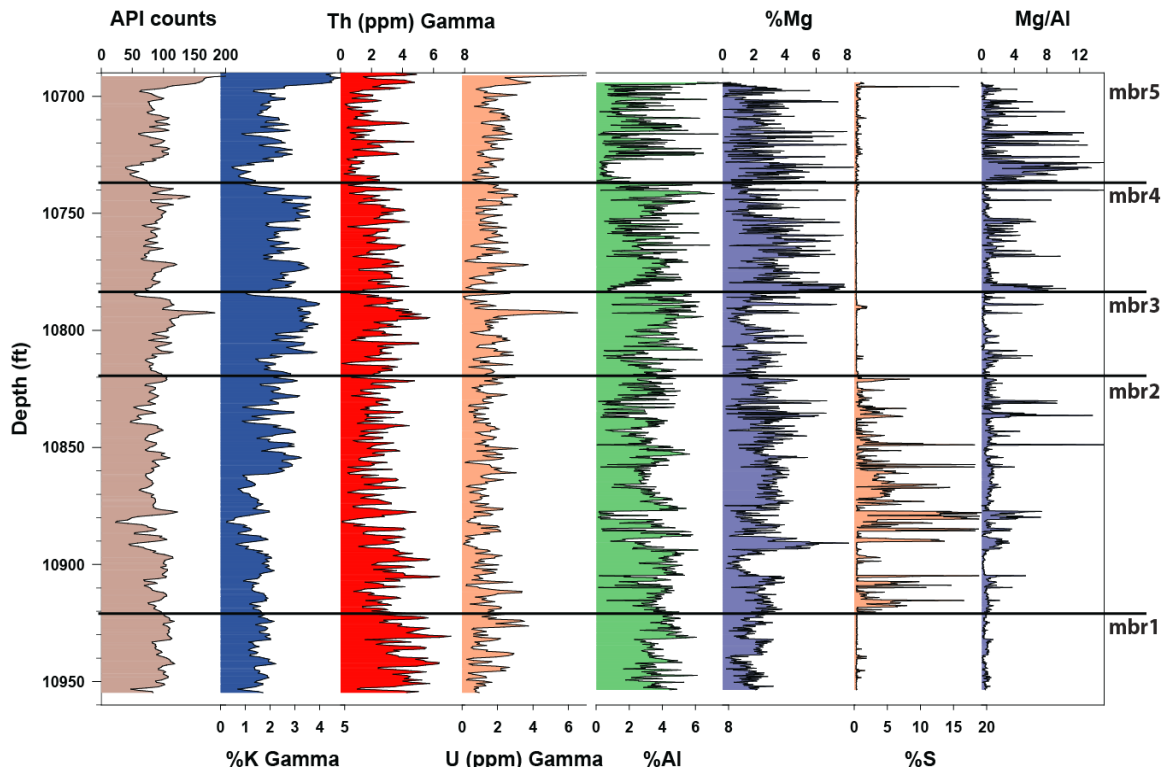
Figure 2: Spectral gamma ray logs (API, %K, Th, U) and bulk elemental (%Al, %Mg, %S, Mg/Al) chemostratigraphic results for the well and the study core, respectively. The %Al is used as a proxy for clay content. The %Mg is used as a proxy for dolomite content. Calcium cannot be used as effectively as a dolomite proxy because intervals of calcite- and anhydrite-bearing strata occur within the Three Forks succession. The %S content is used as an anhydrite proxy. Finally, the Mg/Al ratio can largely be used as a dolomite/clay proxy, as these two minerals dominate the bulk mineralogy of the Three Forks Formation. Subdivision of the Three Forks succession, using "member" terminology, is based on the initial occurrence of anhydrite (mbr1-mbr-2) near the bottom of the succession (~10,920 ft), the large-scale decrease in anhydrite content (mbr2-mbr3) around 10,820 ft, the abrupt increase in dolomite (mbr-3-mbr-4) at ~10,780 ft, and another abrupt increase in dolomite (mbr4-mbr5) at ~10,738 ft. The hiatus between the upper Three Forks and the overlying Pronghorn/Lower Bakken is marked by a one-inch-thick pyrite-rich interval characterized by sulfur values >15% and arsenic values >3,000 ppm.

RESULTS

Large-scale changes in the geochemical characteristics of the Three Forks Formation are observed in Figure 2. The dominant mineral components of the sedimentary succession are

detritals (clay and quartz), dolomite, and anhydrite, which are proxied by %Al and %Si, %Mg, and %S, respectively. Pulses of anhydrite and dolomite reflect the oscillatory nature of the depositional system. Furthermore, changes in the trace element composition (Zr/Ti, Sr, Ba) and the Fe/Ti demonstrate additional signatures that help subdivide the succession (Figure 3). The HCA and elemental ranking within each cluster (specifics not shown) lead to the generation of eleven chemofacies assignments whose nomenclature were affirmed through evaluation of their location in bi-plots of key major elements (Figure 4A-C). For instance, chemofacies samples termed "quartz-arenaceous Dolomite" fall along the high-%Si/low-%Al trend, while the "Dominant Detrital" chemofacies samples plot in the high-%Si/high-%Al region of the graph (Figure 4A). Similarly, samples belonging to the "Anhydrite" chemofacies plot in the high-%Ca/high-%S region of Figure 4C.
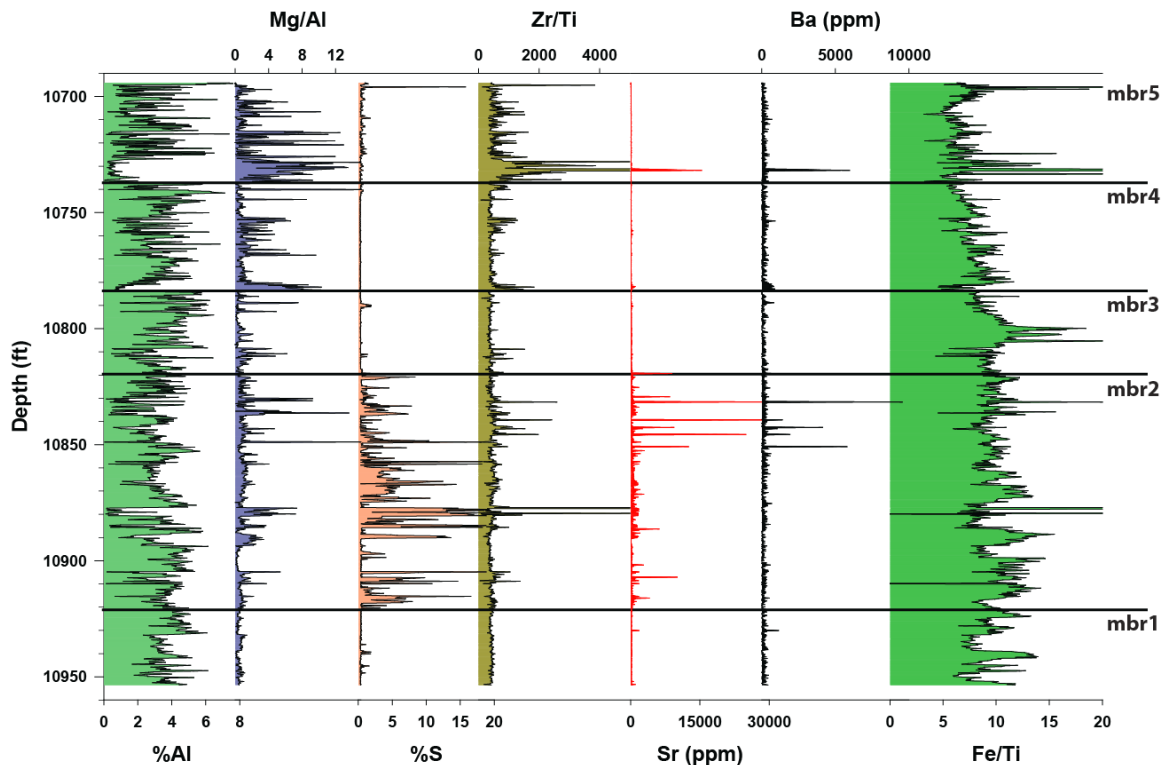
Figure 3: Additional chemostratigaphic signatures defined in the context of the clay-, dolomite-, and anhydrite-defined members. The Zr/Ti ratio reveals abrupt changes in detrital characteristics throughout mbr2, at the base and in the middle of mbr4, and throughout mbr5. This ratio may indicate changes in relative grain size, as Ti is often associated with clays, and Zr with zircons. The Sr and Ba records define abrupt, large-scale changes in their content increase upward throughout mbr2, and a single punctuated interval near the base of mbr5. It is possible that the Sr is a signature of Sr enrichment in dolomite and or calcite, but it could also exist in the anhydrite, strontianite, and/or celestine phase. The Ba content is most-likely preserved in barite, but may inhabit a carbonate phase. The significance of the shift in Fe/Ti in the middle of mbr3 is uncertain, however, it signals a protracted decrease in the iron content to the basin relative to other detrital content, as proxied by Ti. The same signature is observed with Al in the denominator.
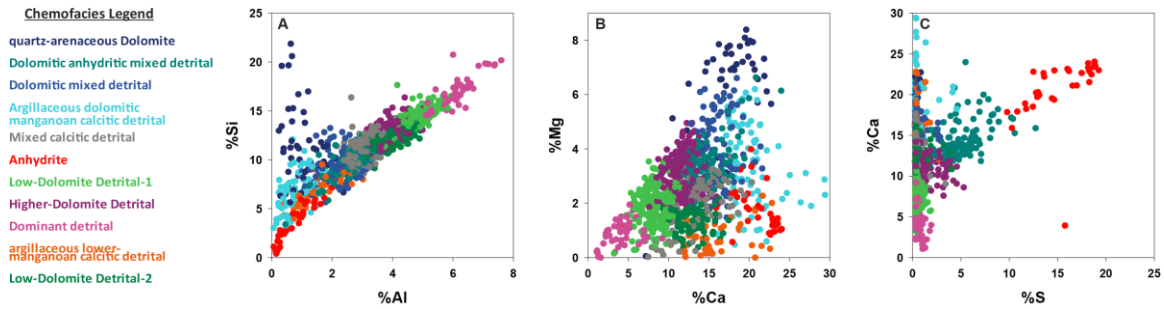
Figure 4: Bi-plots of elements color-coded by chemofacies assignment. A) %Al vs %Si, indicating %clay vs. %silica (clay and quartz) variability. B) %Ca vs. %Mg, largely a function of anhydrite and dolomite variability. C) %S vs. %Ca, demonstrating anhydrite-rich trend (red and dark cyan samples).

The stratigraphic expression of the eleven chemofacies defined through HCA and elemental ranking within each cluster are demonstrated (Figure 5A) in the context of proxies for dolomite and anhydrite (Figure 5B). A well-defined evolution from detrital, low-dolomite deposition, to higher dolomite and ultimately higher anhydrite deposition, culminating in maximum anhydrite deposition at ~10, 880 feet is observed. The overlying succession reveals a complex oscillation between dolomite-rich and dolomite-poor strata, culminating in detrital-rich strata deposition immediately below the overlying Pronghorn unit. Starting from the bottom of Figure 5, the overall evolution of chemofacies can be viewed as tracing the progression of the system from detrital to dolomitic/detrital, to dolomitic-anhydritic, and ultimately to a system that oscillated between dolomite-rich and –poor deposition. Further investigation will be focused on better defining the evolving nature of the depositional system and the potential forcing mechanisms (climate, sea level, connectivity to the global ocean) that shaped its evolution.

CONCLUSION

Using a rigorous, labor-intensive approach that relies on interpretation of raw X-ray spectral lines, brine-laden drill core can be cleaned sufficiently to generate a high-quality chemostratigraphic record from the Three Forks Formation. Major elemental trends (Mg, Al, S) define previously-characterized members/units, and potentially provide additional resolution for further refinement. For instance, the upper Three Forks (above anhydrite) is characterized by more dolomite-mudstone cycles than previously defined. Spikes in Sr, Ba, Zr, and other trace elements may be correlated locally or across large parts of the Williston Basin. Chemofacies analysis (grouping of elemental information) may provide a more complex but useful way of defining facies heterogeneity in the Three Forks, and is particularly useful when coupled with traditional core description and lithofacies assignments. Chemofacies trends may indicate the need for refinement of the paleoenvironmental model, which has traditionally been described as evaporitic to nearshore deposition, dominated by sabkha-like depositional conditions.
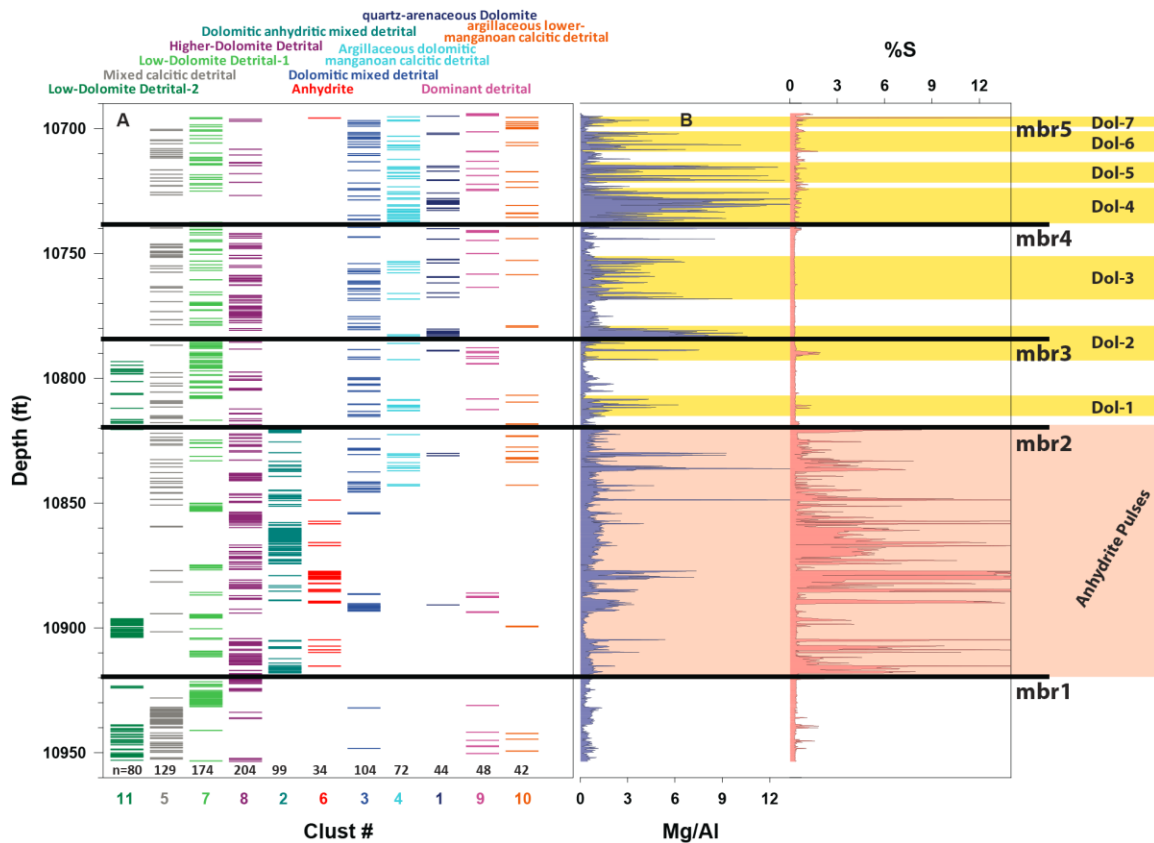
Figure 5: A) Stratigraphic display of chemofacies assignments derived from HCA and evaluation of elemental characteristics defined in HCA. B) Chemofacies in "A" are defined in the context of major mineralogical shifts in the dolomite/clay (Mg/Al) proxy, and anhydrite (%S) proxy. Note dominance of "Dolomitic anhydritic mixed detrital" and "Anhydrite" chemofacies assignments in mbr2 (pink shading). Also note multiple dolomite-rich zones (Dol-1 through Dol-7) in the upper Three Forks (yellow shading).

ACKNOWLEDGEMENTS

REFERENCES

1. Berwick, B. R., 2008, Depositional environment, mineralogy, and sequence stratigraphy of the Late Devonian Sanish Member (Upper Three Forks), Williston Basin, North Dakota: Master's Thesis, Colorado School of Mines, 263 p.
2. Berwick, B. R., and M. L. Hendricks, 2011, Depositional Lithofacies of the Upper Devonian Three Forks Formation and the Grassy Butte Member of the Lower Bakken Shale in theWilliston Basin, in J. W. Robinson, J. A. LeFever, and S. B. Gaswirth, eds., The Bakken–Three Forks petroleum system in the Williston Basin: Denver, Colorado, Rocky Mountain Association of Geologists, p. 159–172.
3. Bottjer, R. J., R. H. Sterling, A. D. Grau, and P. A. Dea, 2011, Stratigraphic relationships and reservoir quality at the Three Forks-Bakken unconformity, Williston Basin, North Dakota, in J. W. Robinson, J. A. LeFever, and S. B. Gaswirth, eds., The Bakken–Three Forks petroleum system in the Williston Basin: Denver, Colorado, Rocky Mountain Association of Geologists, p. 173–228.
4. LeFever, J. A., R. D. LeFever, and S. H. Nordeng, 2011, Revised nomenclature for the Bakken Formation (Mississippian-Devonian), North Dakota, in J. W. Robinson, J. A. LeFever, and S. B. Gaswirth, eds., The Bakken–Three Forks petroleum system in the Williston Basin: Denver, Colorado, Rocky Mountain Association of Geologists, p. 11–26.
5. Robinson, J. W., LeFever, J. A., and S. B. Gaswirth, 2011, Reference List for the Bakken and Three Forks Formations in the Williston Basin, in J. W. Robinson, J. A. LeFever, and S. B. Gaswirth, eds., The Bakken–Three Forks petroleum system in the Williston Basin: Denver, Colorado, Rocky Mountain Association of Geologists, p. 428-437.
6. Blakey, R., 2013, Key Time Slices of North American Geologic History, CD-ROM.
7. Gaswirth, S. B., and K. R. Marra, 2015, U.S. Geological Survey 2013 assessment of undiscovered resources in the Bakken and Three Forks Formations of the U.S. Williston Basin Province. AAPG Bulletin 99, 639-660.
8. Kolte, K., 2014, Diagenesis, composition and porosity of the upper Three Forks formation, Williston Basin, North Dakota and Montana, M.S. Thesis, Colorado State University, 73pp.
9. Nekhorosheva, V. V., 2011, Stratigraphy, diagenesis and fracture characterization of the upper Devonian Three Forks formation in Montana, Wyoming, and South Dakota, M.S. Thesis, Colorado School of Mines, 114pp.
10. Baah, D. S., 2015, Nano-petrophysics study of the Three Forks formation in the Williston Basin, North Dakota, U.S.A., M.S. Thesis, University of Texas at Arlington, 68pp.

11. Rowe, H., Hughes, N., and Robinson, K., 2012. The quantification and application of handheld energy-dispersive x-ray fluorescence (ED-XRF) in mudrock chemostratigraphy and geochemistry. Chemical Geology, 324–325, 122–131.
12. Rowe, H. D., Wang, X., Fan, B., Zhang, T., Ruppel, S. C., Milliken, K. L., Loucks, R., Shen, Y., Zhang, J., Liang, Q., and Sivil, E., 2017, Chemostratigraphic insights into fluvio-lacustrine deposition, Yanchang Formation, Upper Triassic, Ordos Basin, China: Interpretation 5, SF149-SF165
13. Templ, M., 2003. Cluster Analysis applied to Geochemical Data. Diploma Thesis, Vienna, University of Technology, Vienna, Austria, 137pp.
14. Templ et al., 2008. Cluster analysis applied to regional geochemical data: Problems and possibilities. Applied Geochemistry 23, 2198-2213.
15. Turner, B.W., Tréanton, J.A., Slatt, R.M., 2016. The use of chemostratigraphy to refine ambiguous sequence stratigraphic correlations in marine mudrocks. An example from the Woodford Shale, Oklahoma, USA. J. Geol. Soc. Lond. 173, 854-868.
16. Phillips, Nestor D., 1991, Refined Subsidence Analyses as a Means to Constrain Late Cenozoic Fault Movement, Ventura Basin, California. MS Thesis, The University of Texas at Austin.

Experimental Study of Wettability Alteration in Carbonate Fractured Porous Media using Computed Tomography

Luis Oliveira Pires, Osvair Vidar Trevisan
University of Campinas

Abstract

Oil recovery from naturally fractured reservoirs is mainly controlled by water spontaneous imbibition into matrix blocks. However, imbibition rate and ultimate recovery value are mostly affected by wettability of the reservoir rocks and their pore structure. The present paper focuses on the study of wettability alteration of matrix blocks in fractured porous media, for a more favorable condition to water spontaneous imbibition. Further the research aims to investigate the mechanisms involved in the transfer of fluids at the matrix-fracture boundary.

Several experiments were carried out at bench scale involving coreflooding of outcrop dolomite with brines of designed salinity. The rock samples were carefully prepared to exhibit fractures of controlled geometry and storage/flow parameters as well as to bear oil as the preferred wetting fluid.

Injection of synthetic brines with different compositions was carried out at a constant injection rate. In addition to the evaluation of the produced fluids, Computed Tomography (CT) scans were performed along the tests to study the distribution of water saturation in matrix media.

Oil recovery in fractured reservoirs occurs at a much slower rate than in conventional reservoirs. It was observed that at the beginning of brine injection there was a rapid oil recovery, corresponding to the stored oil in the fracture, which is followed by a recovery at constant rate, but considerably at a much slower pace. This occurs because the oil recovery is dependent upon of water imbibition within the matrix, to promote the oil displacement in the direction of the fractures. As the samples were aged, their wettability was mixed/oil-wet, and the low affinity between matrix and brine led to a lower spontaneous imbibition rate. Moreover, it was observed that by injecting designed salinity brines there was an increase in the oil recovery at the secondary recovery stage, and in the imbibition rate into the matrix.

Introduction

Fractured porous media flow presents great challenges and among them the difficulty in flow prediction, mainly by the high conductivity of fractures and the reduced sweep efficiency. In addition, oil recovery from carbonates is influenced by the porous surface

affinity to adsorb carboxylic groups of oil, which sets the wettability towards preferential to oil [1].

Some studies have shown that carbonate surfaces with wettability preferential to oil when in contact with designed salinity brines promote oil desorption from the porous surface [2 and 3]. There are several theories which explain the possible mechanisms that allow the oil recovery increase, among them the multi-component ion exchange and the calcite dissolution models stand out [4 and 5].

The main focus of this paper is on oil recovery by the injection of design salinity brines. The purpose is to evaluate how the mechanisms of brine imbibition into the rock matrix is affected when of the injection of water at different salinities.

Experimental Methodology
Rocks and Fluids

In the present study, dolomite outcrops from Silurian formation, originated from Thornton formation (Illinois, United States) were used. Gas porosity was measured using an UltraPore 300 Porosimeter from CoreLab Instruments without overburden pressure and gas permeability was measured on an UltraPerm 500 Permeabilimeter from CoreLab Instruments using an overburden pressure of 600 psi.

Two different injection sequences were studied: DFD1.1 (Sequence 1) - primary recovery injecting formation water (FW), secondary recovery with the injection of seawater (SW), and tertiary recovery with injection of seawater 20 times diluted (SW20d); and DFD1.2 (Sequence 2) - primary recovery with injection of seawater (SW) and secondary recovery with injection of seawater depleted of sodium chloride (SW0NaCl). The composition of each brine is presented in Table 1.

The oil used in the experiments is from a Brazilian pre-salt field with a density of 0,9 g/cm^3 and a viscosity of 11,3 cp at 70 °C.

Preparation of samples

At each experiment a composite set of 3 samples placed in series was used. The preparation of the samples consisted of an initial cleaning phase with toluene and methanol followed by the basic petrophysical characterization. An artificial fracture was then induced through a longitudinal bore with a 4 mm diameter. The fracture was filled with sand and at the inlet and outlet faces a small piece of metal screen was placed to trap sand in the fracture. Porosity and permeability of the fractured samples were determined.

One of the major difficulties in the study of fractured porous media in the laboratory scale is to use samples with a uniformly distributed initial water saturation. In order to overcome this difficulty, the evaporation method was to used to render a controlled initial saturation condition, as proposed by Springer (2003) [6]. An initial water saturation (Swi) of 10%

was adopted. To achieve the initial water saturation was necessary to use a brine with a 10 times higher concentration than the original brine (FW10d ~ 1.924.200 ppm instead of FW ~ 192.420 ppm). After brine saturation, samples were placed in a desiccator and its mass controlled to reach 10% water saturation. This method assumes that there is no precipitation of brine and that there is an uniform redistribution of water in the sample. Oil saturation was realized by vacuuming the core samples to a level higher than water evaporation pressure so to admit the oil. Samples were pressurized up to 3.000 psi for 24 hours. A dynamic aging process was performed at 90 °C for 20 days and consisted of periodic injections of 2 porous volumes using a flow rate of 0,01 mL/min.

There is a difference in the preparation of samples DFD1.2 and DFD1.2. The inlet face of first core and the outlet face of last core of DFD1.2, samples were sealed with epoxy to ensure that flow is forced through the fracture.

Experimental apparatus

The experimental apparatus consisted of an injection system, a core holder, a backpressure, a collector for produced fluids and a bypass system, as outlined in Figure 1. Experiments were performed at 70 °C and at 600 psi, controlled by a backpressure.

The injection rate used was 0,05 cm³/min. The low injection rate, correspondent to half of the injection rate used in several displacement experiments presented in literature, is considered to warrant that the dominant flow mechanism is the spontaneous imbibition into the matrix. So, fluid flow is governed by capillary and not by viscous forces. CT scans were regularly performed to evaluate the variation of the fluid saturation over time and at the end of 30 days the injection brine was replaced by a brine with different composition.

Computed Tomography

Computed tomography was used to determine porosity and fluid saturation along the core during brine injection. The determination of porosity of the sample requires that it be totally saturated with two different fluids, since the scan measures the density of the material based on a measurement unit (voxel). Initially samples were vacuumed and a CT scan was performed, then the sample was saturated with FW10d brine and a new tomography was performed. From the difference between these two CT scans it was possible to estimate the average porosity of each slice (ϕ^{voxel}) spaced by 1,8 mm, according to Equation 1.

$$\phi^{voxel} = \frac{CT_{WS} - CT_{DS}}{CT_W - CT_A} \qquad\qquad 1$$

In the above equation, CT_{WS} and CT_{DS} correspond to the average CT of each voxel saturated saturated with FW10d brine and vacuumed, respectively, and CT_W and CT_A correspond to CT number of FW10d brine and of air, respectively. The water saturation of each voxel (S_W^{voxel}) can be determined according to Equation 2.

$$S_W^{voxel} = \frac{CT_{WF} - CT_{OS}}{\phi^{voxel}(CT_W - CT_O)} \qquad\qquad 2$$

Where CT_{WF} is the average water injection CT, CT_{OS} is the average CT number of the core saturated with oil, and CT_O is the oil CT number.

Results

Porosity distribution

Porosity profiles of samples allow to observe the heterogeneity of the rock sample. As the main focus of the study is the matrix, a MATLAB routine was used to eliminate the area correspondent to the fracture, and therefore to determine the average CT number corresponding only to the matrix media. Porosity profiles of the total core, the matrix only and of the fracture of DFD1.1 and DFD1.2 experiments are shown in Figure 2 and Figure 3, respectively. From these figures it can be seen that porosity profiles of matrices are practically the same as that of the total core, indicating the small contribution of the fracture to the porosity of the fractured rock.

Oil recovery

In DFD1.1 experiment the injection sequence was: FW, followed by SW and finally by SW20d. The evolution of the average water saturation of the sample matrix over the duration of the test is shown in Figure 4. Initially there was a high oil production rate, because all the oil present in the fracture was instantaneously produced, then oil production rate decreases, corresponding to the production of oil originated from the matrix. The increase in water saturation indicates that water was filling the matrix while the oil was moving from matrix to fracture, and produced from there. Figure 4 represents the increase of water saturation in the matrix, and, at the same time, represents oil production from matrix to fracture.

FW injection should not promote any change in rock wettability since there was an ionic balance previously established between the rock, the oil and FW brine. It was observed that 29,9% of original oil in place (OOIP) had been recovered at the end of 30 days and at the end the oil production reached a plateau. On the other hand, the following injection of SW, with a very different ionic composition, in particular ions with potential for the wettability alteration (sulfate, calcium and magnesium), promoted an considerable increase in the oil recovery rate, indicating an alteration of the matrix wettability. Wettability alteration is followed by oil desorption of the porous matrix and, as presented in Figure 4, resulted in a slight increase in oil recovery from the begging of SW injection. The incremental oil recovery value was 31,4% of OOIP. A constant of oil production rate is evident throughout the SW injection. For the injection of SW20d, however, oil recovery did not increase so significantly, and 12,6% of additional OOIP was recovered.

In the DFD1.2 experiment the injection sequence used was: SW followed by SW0NaCl. The volume of oil recovered at the end of 30 days of SW injection was approximately 32,5% of the OOIP, which was not very different from the oil recovery observed with the FW injection in the DFD1.1 test. The difference is that in the DFD1.2 test the recovery rate

remained practically constant over time. SW0NaCl injection showed a significant increase in recovery of about additional 40 % OOIP, as shown in Figure 5.

Although the DFD1.1 experiment last for a longer duration, the brines used in the DFD1.2 carried more potential to alter rock wettability, which may explain the same final oil recovery in less time. Nonetheless, the whole process is very slow and oil production was at a steady low rate for 1440 hours (60 days) before reaching a plateau.

It is important to note that the recovery increments are not instantaneous. Time is necessary for the spontaneous imbibition of the new injected brine into the matrix, and for the interaction of this brine with oil and the rock surface. Only after that the dislodged oil is produced.

Water Spontaneous Imbibition into matrix media

At the beginning of injection, the oil present in the fracture was produced almost instantaneously, which corresponds to a very short water breakthrough time. Brine spontaneous imbibition into matrix is a relatively slower mechanism. The oil near the fracture-matrix boundary is first produced, and as the brine penetrates the matrix, oil that is at greater distances from the fracture will migrate towards it.

Brine imbibition occurred from the center of the samples (fracture) to the borders. Figure 6 and Figure 7 shows matrix water saturation along the length of samples over time. It is clear that there was an increase in water saturation of the matrix of the samples throughout the duration of the water injections.

Influence of boundary conditions

One of the major differences between DFD1.1 and DFD1.2 was that the inlet and outlet faces of DFD1.2 cores were partially sealed. The effects of such difference can be seen in Figure 6 and Figure 7. In DFD1.1 the formation of a water front is clear at the inlet face near brine injection. In spite of the high permeability of the fracture, the capillarity of the sample at the inlet face allowed the brine to flow not only through the fracture but also across the face of the matrix block. For this reason the water saturation was higher in the matrix region near the inlet face. The border effect diminishes as the flow moves towards the fracture while going deeper across the sample length. This higher saturation in the inlet face may be responsible for the higher oil production at the begging of the primary recovery of DFD1.1 test, compared with DFD1.2.

In the DFD1.2 test, as the inlet and outlet faces of the composite core were sealed, injected brine was forced to penetrate only through the fracture. Thus, the brine imbibition into the matrix only occurs across the matrix-fracture interface. Therefore, water saturation was observed to be more evenly distributed throughout the length of the samples, with changes in time occurring radially. It is worthwhile noticing that the recovery in the DFD 1.2 test was slightly higher, although the core ends were sealed, which corroborates that the brines

used in the test had a greater efficiency in altering the matrix wettability, given that the samples had same capillary properties originally.

Conclusions

The present study showed that the used designed salinity brines in fractured carbonate media allowed an additional oil recovery as brine penetrates into matrix media. This oil increase was accompanied by an increase in oil recovery rate. Thus, there was not only a higher final oil recovery but also an anticipated production.

As the brine penetrates into the matrix, not only it displaces movable oil towards the fracture, but also its composition is able to desorb oil from matrix surface, and consequently, alter its wettability towards a more water-wet condition. The wettability alteration will allow higher brine imbibition into the matrix, and more oil recovery will be recovered.

By using computed tomography is possible to see water saturation variation as the injected brine in the fracture penetrates into the matrix blocks, and to study mass transference between matrix-fracture interface. As brine imbibition through matrix blocks is a slow process, as it could be seen in the presented experiments, the proposed apparatus was able to replicate spontaneous imbibition mechanism. Also, imbibition was strongly influenced by its boundary conditions. High matrix capillarity allow brine imbibition in every faces where matrix was directly exposed to brine. In addition, viscous forces did not have great contribution on oil recovery process.

Acknowledgements

Bibliography

1 - Strand, S., Standnes, D.C., Austad, T. "New wettability test for chalk based on chromatographic separation of SCN- and SO4-2". *Journal of Petroleum Science and Engineering*, EUA, v. 52, p. 187-197, 2006

2 - Romanuka, J., et al. "Low Salinity EOR in Carbonates". *Eighteenth SPE Improved Oil Recovery Symposium*, Tulsa, EUA: Society of Petroleum Engineers, SPE 153869, 2012

3 - Fathi, S.J., Austad, T., Strand, S. "Smart Water as a Wettability Modifier in Chalk: The Effect of Salinity and Ionic Composition". *Energy & Fuels*, EUA, v. 24, p. 2514-1529, March 2010

4 - Austad, T., et al. "Conditions for a Low-Salinity Enhanced Oil Recovery (EOR) effect in Carbonate Reservoirs". *Energy & Fuels*, EUA, v. 26, p. 569-575, 2012

5 - Hiorth, A., Cahtles, L.M., Madland, M.V. "The Impact of Pore Water Chemistry on Carbonate Surface Charge and Oil Wettability". *Transport in Porous Media*, EUA, v. 85, p. 1–21, 2010

6 - Springer, N., Survey, G. "Resistivity Index Measurement Without The Porous Plate: a Desaturation Technique Based on Evaporation Produces Uniform Water Saturation Profiles and More Reliable Results for Tight North Sea Chalk" 2003

Table 1 - Composition of used brines

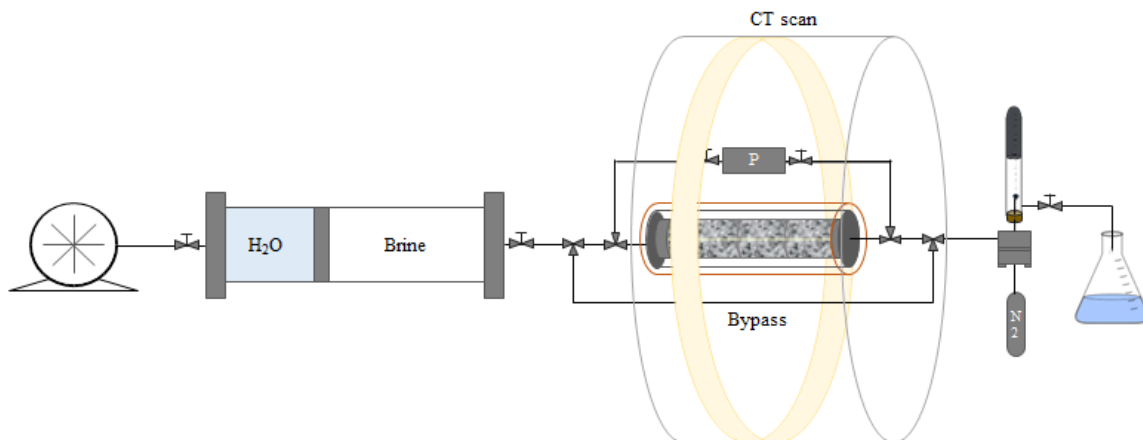| Íon	FW	SW	SW20d	SW0NaCL
	mg/L	mg/L	mg/L	mg/L
(Na^+)	58003,80	13664,68	683,24	1356,84
(K^+)	3984,67	444,75	206,55	444,75
(Mg^{2+})	392,96	33,00	1,65	33,00
(Ca^{2+})	8930,78	1472,93	73,65	1472,93
(Ba^{2+})	2,81	-	-	-
(Sr^{2+})	117,98	5,92	0,30	5,92
(Li^+)	126,07	-	-	-
(Cl^-)	110516,13	22058,52	1270,06	3078,35
(Br^-)	320,28	71,85	3,59	71,85
(SO_4^{2-})	79,80	2800,97	140,06	2800,97
(HCO^{3-})	55,93	42,85	2,14	42,85
TDS (ppm)	192,45	42,07	2,10	10,79

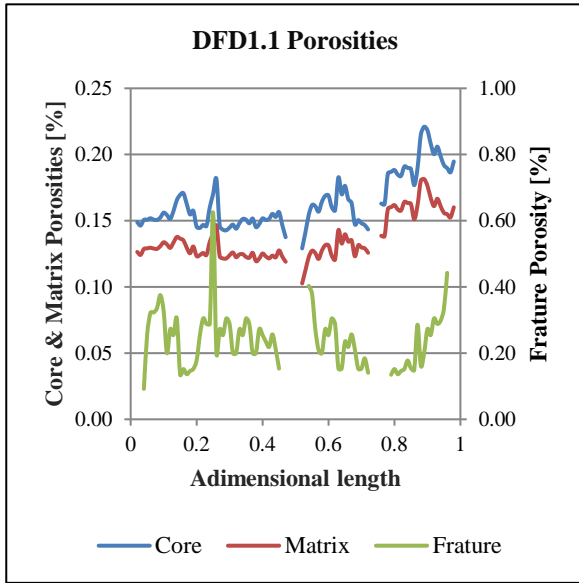Figure 1 - Schematic experimental apparatus

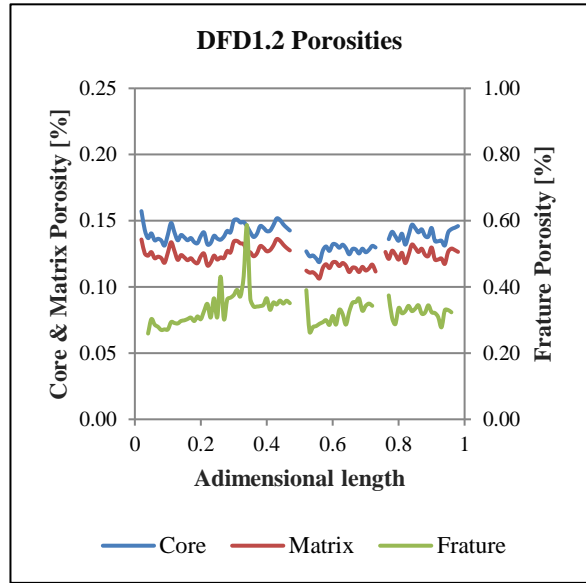Figure 2 - Porosity profiles of the DFD1.1 test

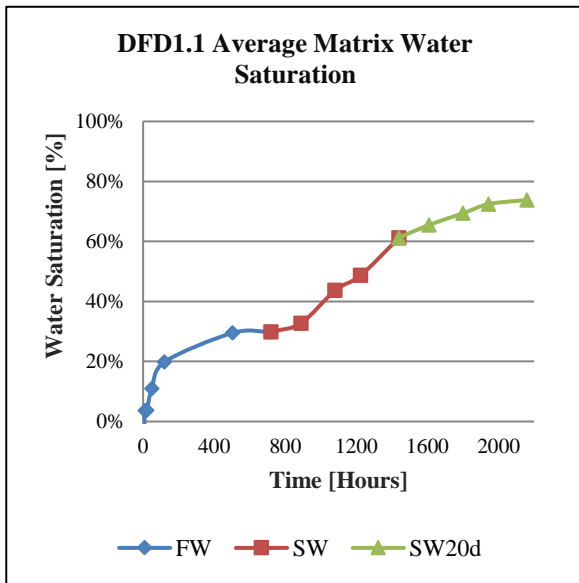
Figure 3 - Porosity profiles of the DFD1.2 test

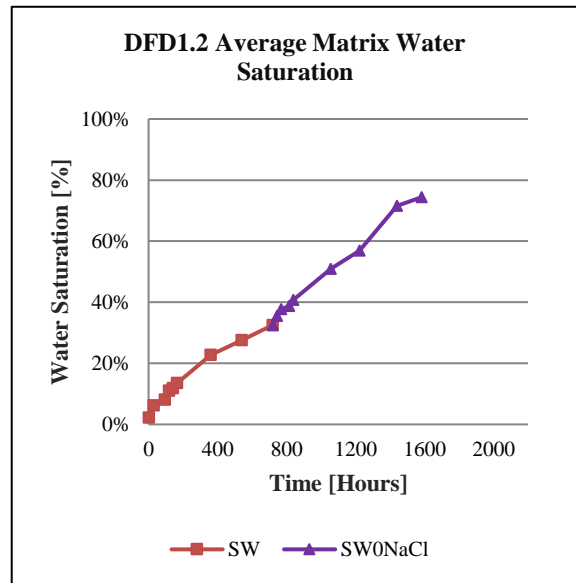Figure 4 – DFD1.1 Average Matrix Water Saturation

Figure 5 – DFD1.2 Matrix Average Water Saturation
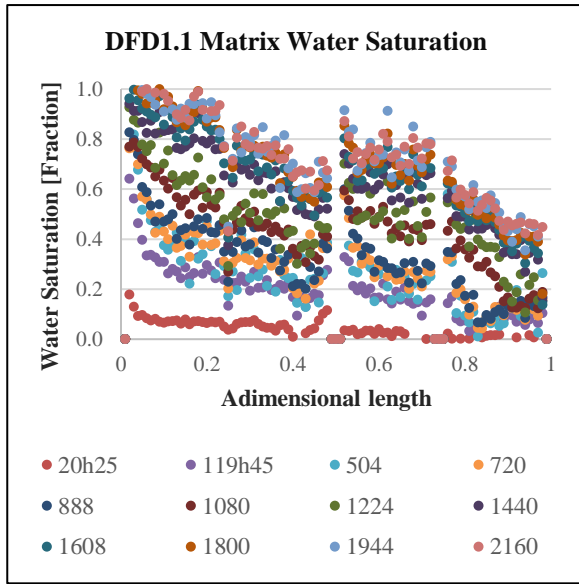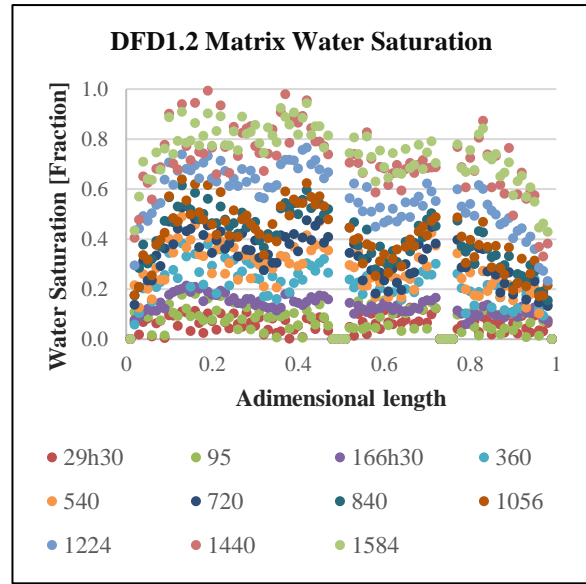
Figure 6 – DFD1.1 Matrix Water Saturation

Figure 7 – DFD1.1 Matrix Water Saturation

INVESTIGATION OF WETTABILITY ALTERATION OF CARBONATE ROCK IN PRESENCE OF SULFATE, CALCIUM AND MAGNESIUM IONS

Pouyan Ahmadi[1], Masoud Riazi[1], Mohammad Reza Malayeri[1]
[1]EOR Research Center, School of Chemical and Petroleum Engineering, Shiraz University,
I.R. Iran

ABSTRACT

Wettability alteration (WA) is one of the principal challenges of oil wet carbonate reservoirs. During primary migration, oil would be replaced with formation brine which contains many cationic ions such as Ca^{2+}, Mg^{2+} that would boost calcite or dolomite surface charge to more positive, the amount of positive charge in rock/brine and oil/brine contacts region is high due to high cations concentration in formation brine during oil migration. In practice, after many years of migration process, because of negatively charged oil components, attractive forces will be active thus it would absorb the oil component to the calcite or dolomite surface consequently the wettability would change to oil wet. For more production in water flooding process in tertiary recovery processes, the rock wettability should change to more water wet conditions. Low salinity water injection comprising of SO_4^{2-}, Ca^{2+}, Na^+ and Mg^{2+} ions is known as a WA method that by dilution of seawater or other accessible brines. In this study, based on active ions in WA mechanism, variation of them in a baseline seawater shows tangible results for better water wetness in case when monovalent and divalent ions are used. In the experiments, WA of seawater with 3-time sulfate, 6-time calcium and magnesium (SW-3S-6C-M), (SW-3S-C-6M), (SW-6S-C-3M), (SW-6S-3C-M), (SW-3S-0C-0M), (SW-0S-3C-0M), (SW-0S-0C-3M) and seawater, the contact angles were measured. The results showed that by increasing the amount of sulfate, WA always seems to tend to be more water wet. As for calcite at low temperature in the presence of sulfate the WA happened while no change was noted in the absence of sulfate. Magnesium seemed to have an impact at elevated temperatures and in this case SW-3S-C-6M showed best (from 129° to 30°) in comparison with other brines. Finally, it was found that without refreshing the brine in each step, the results were not appreciable.

INTRODUCTION

Carbonate reservoirs contains the majority of the world's oil reserves. These oil reservoirs are characterized with two types of porous media namely i) matrix blocks and ii) natural fractures.

EOR methods for fracture reservoirs are usually designed to facilitate the transmission between matrix and fractures. Neutral to oil wet carbonate reservoir implies weak spontaneous imbibition of water. One of such methods for enhanced oil recovery from carbonate reservoirs is to use smart salinity water imbibition with the help of altering wettability from oil-wet to neutral or water-wet. Should a block matrix be surrounded by water, if existed in the fractures, then imbibition is expected to occur simultaneously during wettability alteration (at the moment of contact of cores with smart water as a wettability alteration agent, WA process will be started from all pores which are located on the surfaces of the cores and continuous to invading in core). Many factors such as pressure, temperature, oil composition, injection fluids properties would influence chemical wettability alteration under reservoir conditions.

Wettability alteration during water flooding by adjusting injection brine composition is becoming economically more viable thus a matter of much interest [1]. The main objective of EOR by ion exchange (chemical) mechanism is to improve mobility of trapped oil during water flooding [2]. In range of pH<9, surface charge of carbonate rock are positive, thus by the use of diluted alkaline (Na_2CO_3) the surface charge will be altered to negative when an anionic surfactant is used [3]. The interaction between monomer of cationic surfactant and crude oil carboxylic materials forms a complex usually termed as "cationic surfactant". negatively charged carboxylic material of crude oil will be adsorbed by the monomer of the cationic surfactant [4] .In low permeable rock such as carbonate matrix as a result of using surfactant and brine, the interfacial tension will be decreased (about 0.3-1.0 mN/m) and the imbibition rate is expected to decrease even though the capillary forces increase as a result of more water wetness [5].

By the use of diluted Persian Gulf seawater by 2, 10, and 20 times, the amount of oil recovery from composite limestone cores has been increased [6]. Nonetheless, in chalky cap rock flooded with diluted SW due to the decrease in surface active ions the recovery factor has been decreased [7]. Seawater includes potentially active ions such as Ca^{2+}, Mg^{2+} and $SO4^{2-}$ that control surface charge of carbonate rock to forming organic-metal complex and change the wettability to more water wetness and improve imbibition process and recovery factor. Negative charge of sulfate ions reduces the carbonate surface positive charge and let the positive ions to get closer to the carbonate rock. Carbonate rock positive charge would, in turn, lead to adsorption of negative charge and thus calcium and magnesium can get closer to the carboxylic component and separate them from carbonate rocks. Chemical activity and mobility of cationic ions strongly depend on temperature of the bulk of fluids which are in contact with the rock surface [8]. Magnesium is a potentially determining ion due to small size and high charge density. It may become more reactive because of partial dehydration as temperature increases [9]. Some criteria for the interaction which should exist for a successful wettability alteration process are as follows [10]:

1- Mixed wet condition

2- Existence of divalent cations
3- Initial formation water must be present
4- Oil must contain polar components

Overall, the utilization of smart water is a viable option to alter rock wettability to water wet at reservoir conditions but the key parameters that control the wettability alteration are potential influential ions such as sulfate, calcium and magnesium and high reservoir temperature conditions. The present study aims to determine the best optimum salinity with ions strength equal to seawater by foreseeing of concentration of sulfate, calcite and magnesium.

EXPERIMENTAL SET UP AND PROCEDURE

The following procedure was carefully performed to discern the optimum concentration:
1. Water from the nearest and the most accessible sea with known ions concentration were taken as sample.
2. All brines are synthetic and by adjusting the salts concentrations, and ion strength (the total number of moles of salt per liter) was kept constant with decreasing or increasing concentrations of sodium chloride.
3. Carbonate rock that have previously been studied were carefully cut into thin pieces before maintaining initially for 14 days in the formation brine at 75°C to achieve original positive charge as it would exist at the reservoir conditions. This method is reliable since the thin section would reach its maximum positive charge for attraction of negative charge oil components.
4. Thin sections were then kept in crude oil in 75°C and 2500 psi for 20 days or about 500 hrs. It should be pointed out that the amount of oil wetness would be changed due to difference of minerals in each section and different oil components. Reactive surface area of the thin section, those carbonate rock parts are that during aging process will react with carboxylic components of crude oil.
5. All solutions were of the same ion strength with different concentration ratios of sulfate, calcium and magnesium to determine the best interaction with carbonate rock minerals.
6. All the prepared thin sections in specified time interval of 0, 48, 120, 360 hrs were placed in the refresh synthetic brine before measuring the contact angle.

In this study, a drop shape analysis (DSA100, KRUSS, Germany) apparatus was used for measurement of contact angel, as shown in Fig. 1.In brief, for contact angle measurement, a micro syringe was fitted with a U-shape needle and loaded with the fluid with lower density (i.e., crude oil) the syringe was placed in a motor driven piston and the tip of the U-shaped needle was positioned in an optically clear vessel and immersed in the aqueous phase. A carbonate rock thin section with thickness of about 1.5 mm was placed on a rubber block, then the injection continued to the point at which the drop be big enough and leave the needle and stick to the rock surface. Finally, the image of the drop on the thin section is analyzed.

Figure 1: Drop shape analysis –DSA 100

RESULTS AND DISCUSSION

Diluted seawater with and without refreshing

Figures 2 and 3 show the best results for 5d-SW (5 times diluted sea water brine by distilled water) with respect to seawater and 3-time diluted seawater. The superiority of 5d-SW is probably due to the amount of concentration near the rock surface and more chance for active ions like sulfate, magnesium and calcium to reach to the carboxylic component which are stuck to the carbonate rock and separate them from carbonate rock and alter the wettability from oil wet to water wet condition. Table 1 shows salt concentration of synthetic brines. Furthermore, the results show just a marginal change when diluted brine without refreshing were used. This is because initially WA changes which, in turn results in concentration reduction of sulfate, calcium and magnesium as reported in Table 2.

Table 1: Properties of diluted brines-absolute concentration

composition	SW(gram/liter)	3dSW(gram/liter)	5dSW(gram/liter)
Na+	17	5.67	3.4
Ca2+	0.55	0.18	0.11
Mg2+	1.8	0.6	0.36
K+	4.3	1.43	0.86
SO42-	3.2	1.07	0.64
HCO3-	0.75	0.25	0.15
Cl-	23.25	7.75	4.65

Table 2: Measured contact angle of different diluted sea water with and without refreshing brine.

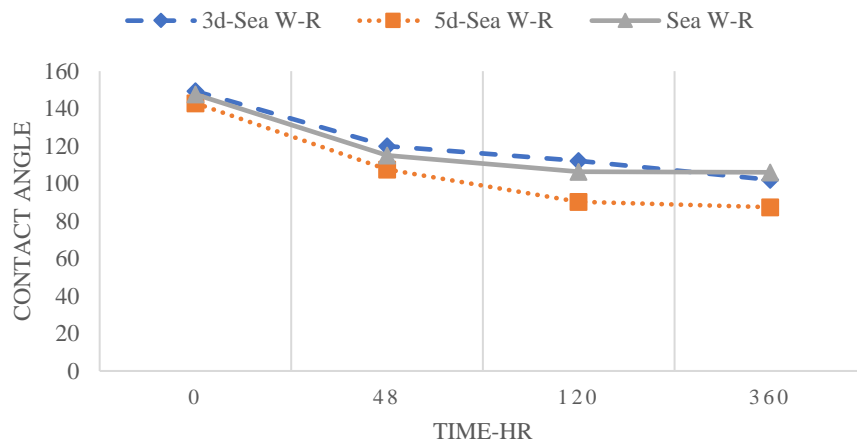| Brine	CA-0hr	CA-48hr	CA-120hr	CA-360hr
3d-Sea W-R	149.3	120.0	112.2	102.0
3d-Sea W-WR	116.0	-	-	110.0
5d-Sea W-R	142.9	107.6	90.2	87.4
5d-Sea W-WR	125.0	-	-	113.0
Sea W-R	147.6	115.1	106.33	106
Sea W-WR	128.1	-	-	122.3

REFRESHING BRINE

Figure 2: Wettability alteration trend in each step-refreshing brine
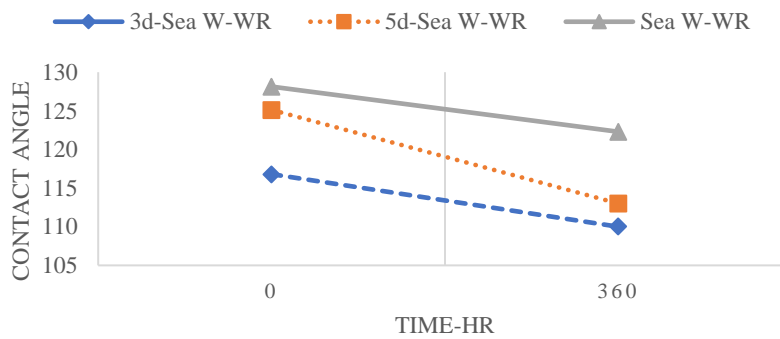
WITHOUT REFRESHING BRINE

Figure 3: Wettability alteration trend –without refreshing brine

Contact angel of synthetic brines with different ratios of active ions

Different concentration ratios of active ions (Table 3) for similar ion strength show the importance of the divalent cations during completion of wettability alteration process. As it can be seen from the above figure that Sea W-3S-C-6M has the maximum wettability alteration from 129.2 to 30.1 degrees as shown in Figure 5 and all changes of contact angle are reported in Table 4. The most important ion is sulfate because of its role in decreasing surface positive charge and allowing the cations to get closer to the carbonate surface and react with crude oil carboxylic components that are stuck to the rock surface.

As shown in Figure 4, in comparison to 6-time sulfate samples, wettability alteration for magnesium due to its chemical activity and surface density charge for SW-6S-C-3M (Figure 5) is more than SW-6S-3C-M (Figure 6). This implies that the concentration of sulfate ions must not exceed from an optimal because at high concentrations, the possibility of cations accessibility to the carbonate rock will be decreased.

Table 3: properties of brines with similar ion strength-absolute concentration

Composition	SW-6S-3C-M (gram/liter)	SW-6S-C-3M (gram/liter)	SW-3S-6C-M (gram/liter)	SW-3S-C-6M (gram/liter)
Na^+	17.93	13.76	15.88	5.02
Ca^{2+}	0.53	1.57	3.13	0.53
Mg^{2+}	1.81	5.43	1.81	10.84
K^+	0.43	0.43	0.43	0.43
SO_4^{2-}	19.85	19.85	9.93	9.93
HCO^{3-}	0.74	0.74	0.74	0.74
Cl^-	21	25.11	27.94	32.94

Table 4: Measured contact angle of different active ions (sulfate, calcium, magnesium).

Brine	CA-0hr	CA-48hr	CA-120hr	CA-360hr
Sea W-3S-6C-M	123.8	100	93.7	88
Sea W-3S-C-6M	129.2	100.1	50.6	30.1
Sea W-6S-M-3M	126.7	106	92	90
Sea W-6S-3C-M	118.5	101.2	92.4	90

WETTABILITY ALTERATION
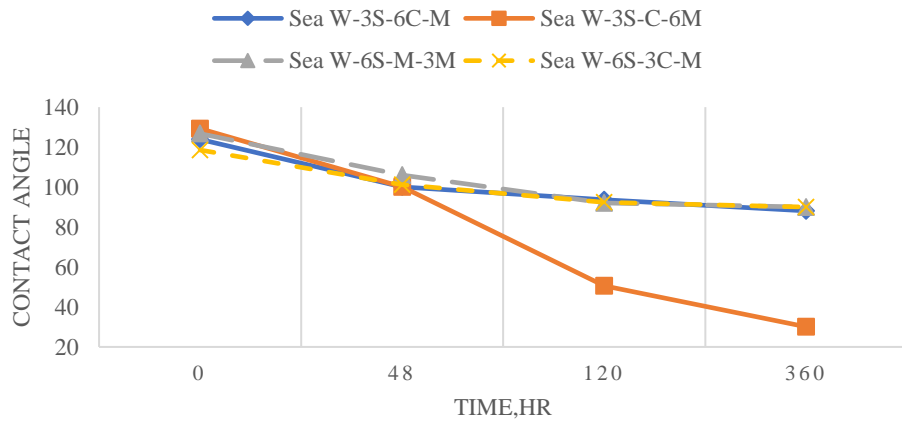
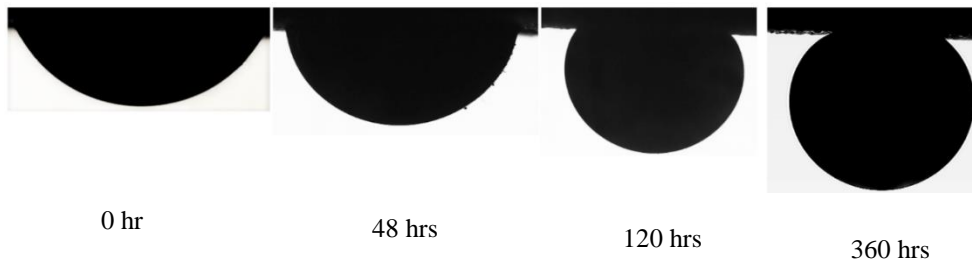Figure 4: Wettability alteration trend at different time intervals

0 hr   48 hrs   120 hrs   360 hrs

Figure 5: Contact angle of synthetic brine SW-3S-C-6M at different time intervals of 0, 48, 120, 360 hrs.

0 hr   48 hrs   120 hrs   360 hrs

Figure 6: Contact angle of synthetic SW-3S-6C-M at different time intervals of 0, 48, 120, 360 hrs.

CONCLUSIONS

- During the experiments as time elapsed, the ion concentration remained constant with refreshing brine which provided enough number of ions to react with crude oil carboxylic components thus more WA would be expected to occur as time elapses.

- Due to the size of oil wet carbonate rock surface area which was in contact with brine at different time intervals, the degree changes in WA faded as time elapsed.

- Sulfate accessibility to carbonate rock surface in competition with other monovalent ions will be increased by dilution of brine.

- For brines with ion strength close to seawater, the concentration of sulfate ions must be at optimal so that to assure that calcium and magnesium ions would be able to reach near the carbonate surface.

- Synthetic brine (SW-3S-C-6M) is the optimum active ions concentration for WA with ion strength equal to 0.63.

- For all synthetic brines, magnesium with compared to calcium played a more important role in WA.

ACKNOWLEDGEMENTS

REFERENCES

[1] Jadhunandan, Pudji P. Effects of brine composition, crude oil, and aging conditions on wettability and oil recovery. *Department of Petroleum Engineering, New Mexico Institute of Mining & Technology*, (1990).

[2] Morrow, Norman R., and Geoffrey Mason. "Recovery of oil by spontaneous imbibition." *Current Opinion in Colloid & Interface Science* 6.4 (2001).

[3] Hirasaki, George, and Danhua Leslie Zhang. "Surface chemistry of oil recovery from fractured, oil-wet, carbonate formations." *Spe Journal* 9.02 (2004).

[4] Høgnesen, Eli J., Dag C. Standnes, and Tor Austad. "Scaling spontaneous imbibition of aqueous surfactant solution into preferential oil-wet carbonates." *Energy & fuels* 18.6 (2004).

[5] M Stoll, J Hofman, DJ Ligthelm, MJ Faber"Toward field-scale wettability modification the limitations of diffusive transport." *SPE Reservoir Evaluation & Engineering* 11.03 (2008).

[6] AA Yousef, S Al-Saleh, AU Al-Kaabi "Laboratory investigation of novel oil recovery method for carbonate reservoirs." *Canadian Unconventional Resources and International Petroleum Conference*. Society of Petroleum Engineers, (2010).

[7] Fathi, S J., Austad, T., Strand S "Smart water" as a wettability modifier in chalk: The effect of salinity and ionic composition. *Energy & Fuels* 24(4), pp. (2010).

[8] Puntervold, Tina, Skule Strand, and Tor Austad. "Water Flooding of Carbonate Reservoirs– Effects of a Model Base and Natural Crude Oil Bases on Chalk Wettability." *IOR 2007-14th European Symposium on Improved Oil Recovery*. (2007).

[9] T Austad, S Strand, T Puntervold "New method to clean carbonate reservoir cores by seawater." *SCA2008-15 presented at the International Symposium of the Society of Core Analysts*. Vol. 29. (2008).

[10] Morrow, Norman, and Jill Buckley. "Improved oil recovery by low-salinity water flooding." *Journal of Petroleum Technology* 63.05 (2011).

GREATER-THAN-ONE RELATIVE PERMEABILITY IN MIXED-WET LIMESTONE

Magali Christensen, Luca Romanello, Yukie Tanino
School of Engineering, University of Aberdeen, UK

ABSTRACT

Waterflood relative permeability was measured in Indiana limestone under five mixed-wet conditions, as characterized by macroscopic contact angles on polished calcite which ranged from $\theta_w = 55°$ to $150°$, and two Darcy velocities: $U_w = 1.5$ μm/s and 30 μm/s. Oil relative permeability at initial oil saturation decreased and brine relative permeability at residual oil saturation increased with increasing θ_w under the conditions considered presently. Greater-than-one end-point relative permeability was observed at $\theta_w < 90°$ for oil and at $\theta_w > 130°$ for brine. End-point brine relative permeabilities were larger at the larger U_w under all oil-wet conditions considered, i.e., $\theta_w > 90°$. In contrast to recent literature that associate greater-than-one permeability to the flow of non-wetting fluid against surface, we observed enhanced permeability even when the flowing fluid was the wetting phase. Our results demonstrate that models assuming $k_r \leq 1$ underestimate fluid displacement for a wider range of contact angles than previously documented.

INTRODUCTION

In special core analysis [1, 2], empirical models [3, 4, 5], and pore network simulators [6, 7, 8], it is often assumed that two-phase permeability k_i cannot exceed single-phase permeability k, i.e., $k_{ri} = k_i/k \leq 1$, where k_{ri} is the relative permeability of flowing phase i. However, several laboratory studies report endpoint relative permeability exceeding one [9 and references therein; 10, 11], indicating that, at least under certain conditions, permeability to a fluid is enhanced by the presence of a second phase in the pore space.

In this paper, we consider waterflood relative permeability measurements in mixed-wet Indiana limestone at two of water injection Darcy velocity ranges, $U_w = 1.5 - 3.0$ and 30 μm/s. We present the dependence of relative permeability on advancing contact angle and identify conditions under which $k_{ri} > 1$.

MATERIALS

Rock

Indiana (USA) limestone cores were used as the porous medium, with a porosity of $\phi = 0.15$ and an absolute permeability of $k = 6.6 \pm 3.1$ mD, and of length $L = 51.03 \pm 0.04$ mm or 89.02 ± 0.24 mm. Indiana limestone is 99% calcite and is characterised by a wide pore size distribution [12]. All cores were cleaned by hot Soxhlet extraction with a mixture of methanol and toluene before use.

Fluids

In all experiments, the same aqueous solution of 5 wt.% sodium chloride and 1 wt.% potassium chloride was used as connate and flood water. Five oils were considered: n-decane, and 6.6×10^{-2} M solutions of cyclohexanecarboxylic acid, cyclohexanepropionic acid, cyclohexanebutyric acid, and cyclohexanepentanoic acid in n-decane. These organic acids, of similar molecular structure but different alkyl chain lengths, alter the wettability of calcite in order of increasing alkyl chain length (Fig. 1), resulting in dynamic advancing contact angles of $\theta_w = 55°, 110°, 125°, 135°,$ and $150°$ [13]. Interfacial tension for the fluid pairs considered, σ, can be found in Ref. [13].
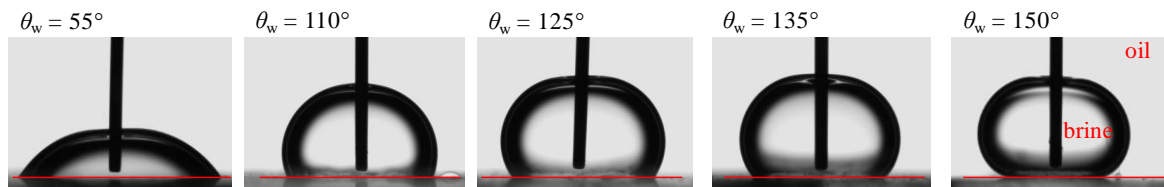

Figure 1. A drop of brine advancing on a polished calcite substrate submerged in, from left to right, n-decane and 6.6×10^{-2} M solutions of cyclohexanecarboxylic acid, cyclohexanepropionic acid, cyclohexanebutyric acid, and cyclohexanepentanoic acid in n-decane.

DISPLACEMENT EXPERIMENTS

Two sets of unsteady state relative permeability experiments were performed: one at low waterflood injection velocity [14] and one at high velocity [15].

Low Waterflood Velocity

Details of the coreflood apparatus and procedure can be found in Refs. [12, 13, 16]. The key steps were as follows [13]:

1. Each core was alternately evacuated and flushed with gaseous CO_2 to remove air, then flushed with degassed brine to fully saturate it. k was measured.
2. The test oil was injected into the core at constant pressure to establish initial oil saturation, S_{oi}, using the porous plate method.
3. Permeability to oil at initial oil saturation, $k_o(S_{oi})$, was measured.

4. Up to 100 pore volumes (pv) of degassed brine was injected at constant Darcy velocity of $U_w = 1.5\ \mu$m/s.

Core-averaged S_{oi} and S_{or} were measured by mass balance. The corresponding microscopic waterflood capillary number,

$$Ca = \frac{\mu_w U_w}{\sigma}, \tag{1}$$

where μ_w is the dynamic viscosity of the brine, varied between Ca = 3.1×10^{-8} and 9.7×10^{-8}, indicating that flow rates remained below the capillary desaturation threshold.

High Waterflood Velocity
Details of the coreflood apparatus and procedure can be found in Ref. [15]. The key steps are as follows:
1. Each core was evacuated for 24 hours to remove air. The core was then saturated with the equivalent of 60 pv of brine before k was measured.
2. Primary drainage was completed in two stages. First, Blandol was injected in the core at constant flow rate increased in discrete intervals. Second, 10 to 20 pv of the test oil were injected at constant flow rate until Blandol production ceased. The cores were left to age in the test oil for an average of 8 hours.
3. Brine was injected at constant rate of $U_w = 30\ \mu$m/s until oil production and the pressure drop across the length of the core approached steady state (Fig. 2).

The waterflood rate corresponds to Ca = $(1 - 2) \times 10^{-6}$. Pressure drop and effluent production was monitored throughout the waterflood, and core-averaged saturation was determined volumetrically.

k and $k_o(S_{oi})$ were calculated using the pressure drop across the core at steady state at constant flow rate as

$$k_i = \mu_i \frac{U_i}{\Delta P_i/L}, \tag{2}$$

where μ_i and U_i are the viscosity and Darcy velocity of the injected fluid i, and ΔP_i is the pressure drop across the core. In particular, $k_o(S_{oi})$ was calculated by measuring ΔP_i for a constant oil injection rate of $U_o = 60\ \mu$m/s [Ca = $(1.6 - 3.2) \times 10^{-6}$].

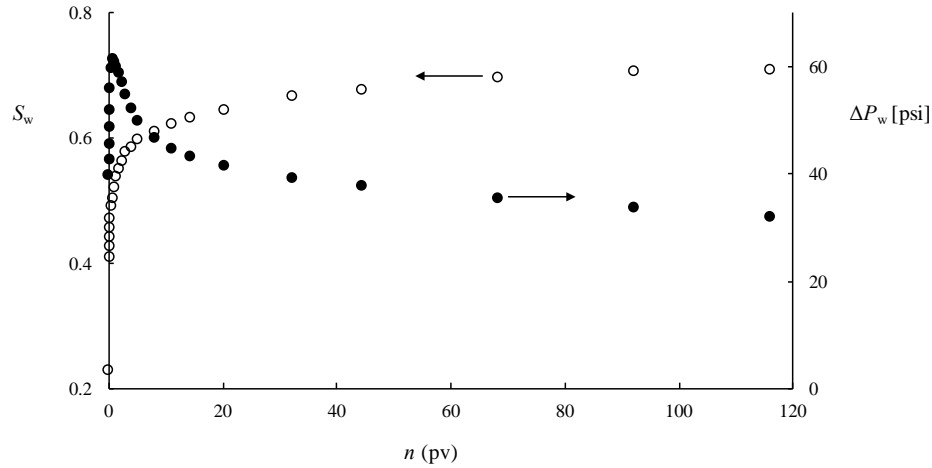**Figure 2.** Brine saturation (open circles) and ΔP_w (solid circles) during waterflood as a function of the cumulative number of pore volumes of brine injected for $U_\text{w} = 30 \ \mu\text{m/s}$, $\theta_\text{w} = 150°$.

Relative permeability determination

Relative permeabilities to oil k_ro and brine k_rw during waterflood were determined by iterative history matching of simulated ΔP_w after water breakthrough to measured values using software CYDAR$^{\text{TM}}$ (CYDAREX). First, waterflood (secondary imbibition) capillary pressure curves, $P_\text{c}^\text{B}(S_\text{w})$, of a Berea sandstone pore network from Ref. [12] were predicted for each oil/brine combination using a two-phase pore network simulator developed by Valvatne & Blunt [6]; details of the pore network are available in Ref. [12]. To account for differences in S_or, water saturation was rescaled as

$$\hat{S}_\text{w}(t) = \frac{S_\text{w}(t) - (1 - S_\text{oi})}{S_\text{oi} - S_\text{or}} \tag{3}$$

Similarly, P_c^B was scaled using the Leverett-J function, i.e.,

$$P_\text{c}\left(\hat{S}_\text{w}\right) = P_\text{c}^\text{B}\left(\hat{S}_\text{w}\right) \sqrt{\frac{k^\text{B}/\phi^\text{B}}{k/\phi}} \ , \tag{4}$$

where superscript B denotes properties of the Berea sandstone pore network. Brooks-Corey functions were used as input relative permeability curves [17]

$$k_\text{rw} = k_\text{rw}(S_\text{or}) \ \hat{S}_\text{w}^{\ \alpha_\text{w}} \quad , \quad k_\text{ro} = k_\text{ro}(S_\text{oi}) \ (1 - \hat{S}_\text{w})^{\alpha_\text{o}} \ , \tag{5}$$

where α_w, α_o, $k_\text{ro}(S_\text{oi})$, and $k_\text{rw}(S_\text{or})$ were fitting parameters whose values were determined by matching ΔP_w predicted by the simulator to measured values in the least squares sense after water breakthrough (e.g., Fig. 3).
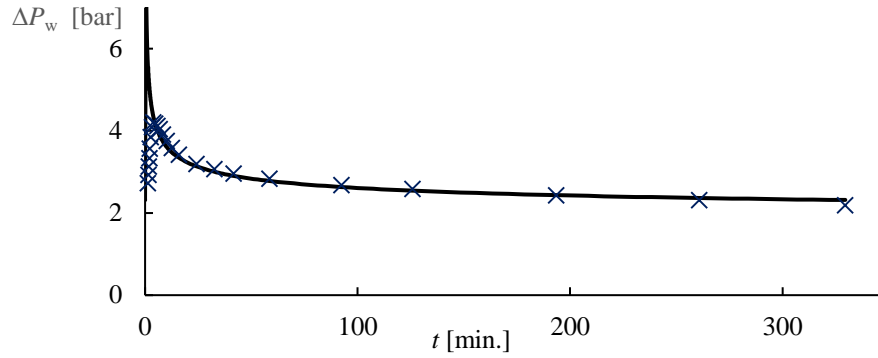
Figure 3. Measured (markers) and simulated (solid line) pressure drop across the length of the core. $U_w = 30$ μm/s; $\theta_w = 150°$.

RESULTS

Figure 4 presents best-fit Brooks–Corey functions for k_{rw} and k_{ro} at $\theta_w = 110°$, 135°, and 150° for Ca ~ 10^{-6} (solid lines) and for Ca ~ (3 to 10) $\times$ 10^{-8} (dashed). $k_{ro}(S_{oi})$ does not differ between the two Ca considered, but $k_{rw}(S_{or})$ is up to a factor of 3 larger at the larger Ca. $k_{ro}(S_{oi}) \lesssim 1$ for $\theta_w > 90°$, which is consistent with previous measurements in the literature for mixed-wet oil/brine/rock systems [20]. In contrast, $k_{rw} > 1$ at $\theta_w = 135°$ and 150° for large Ca at $S_w \gtrsim 0.6$ and $S_w \gtrsim 0.5$, respectively, suggesting that greater-than-one relative permeability may be a common state for mixed-wet oil/brine/rock systems.

Table 1. Summary of relative permeability measurements completed at $U_w = 1.5$ μm/s Corefloods are a subset of those reported in Ref. [14].

θ_w [°]	core	ϕ	L [mm]	k [mD]	S_{oi}	S_{or}	best-fit parameters			
							$k_{ro}(S_{oi})$	$k_{rw}(S_{or})$	α_w	α_o
55	M	0.15	89.02	8.8	0.86	0.37	1.40	0.11	1.9	1
110	W	0.15	88.97	6.3	0.88	0.25	0.90	0.40	1	2.6
125	O	0.14	88.50	3.8	0.89	0.32	1.10	0.56	1.1	2.8
135	AD	0.14	89.60	2.0	0.88	0.31	0.98	0.49	1.1	5
150	N	0.15	89.12	11.1	0.82	0.10	0.63	0.58	1.2	2.4

Table 2. Summary of relative permeability measurements completed at $U_w = 30$ μm/s.

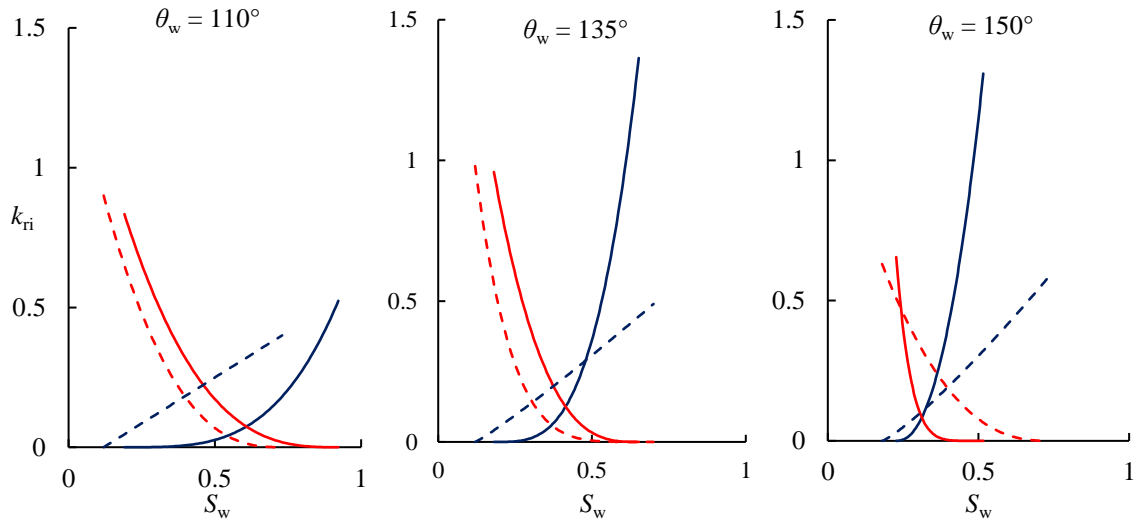| θ_w [°]	ϕ	L [mm]	k [mD]	S_{oi}	S_{or}	best-fit parameters			
						$k_{ro}(S_{oi})$	$k_{rw}(S_{or})$	α_w	α_o
110	0.15	51.07	7.4	0.81	0.08	0.83	0.52	3.5	2.9
135	0.14	51.05	3.6	0.82	0.35	0.96	1.4	3.4	3.0
150	0.15	50.98	9.2	0.77	0.48	0.65	1.3	5.9	2.3

Figure 4. Best-fit Brooks-Corey functions for oil (red) and brine (blue) relative permeabilities [Eq. (5)] for $U_w =$ 1.5 μm/s (dashed lines) and $U_w = 30$ μm/s (solid lines).

Permeability Enhancement

Consider a bundle of N identical, parallel capillary tubes of uniform radius r_p and length L distributed over a bulk cross-sectional area A; the bundle represents the rock and individual tubes represent pore channels spanning the length of the rock [21]. The porosity of the bundle is $\phi = (N\pi r_p^2)/A$. Flow in each tube is described by the Hagen-Poiseuille equation,

$$\mu \, \frac{U_p}{\Delta P/L} = \frac{r_p^2}{8},$$ (6)

where ΔP is the constant applied pressure drop, U_p is the resulting mean velocity within each tube, and subscript p denotes properties of a single pore channel (capillary tube). The left-hand-side of Eq. (6) is, by definition [Eq. (2)], the permeability of each tube, and $k_p = r_p^2/8$.

If the bundle contains a single phase, the net volumetric flux through the bundle is $U_p \, A_{\text{eff}}$ and the corresponding Darcy velocity is $U = U_p \, A_{\text{eff}}/A$ where $A_{\text{eff}} = N\pi \, r_p^2 = \pi A$ is the net cross-sectional area through which the fluid flows. It then follows that the permeability of the bundle, $k = \mu/(\Delta P/L)$, is related to the permeability of a single capillary tube as $k = k_p \, A_{\text{eff}} /A = k_p\phi$.

Next, consider a bundle containing two phases, where only one phase i is continuous and flowing. This scenario is equivalent to only N_c ($\leq N$) of the N tubes conducting fluid. Here, the net cross-sectional area conducting fluid is $A_{\text{eff}} = N_c \, \pi r_p^2 = (N_c/N) \, \phi A$. Finally, a non-conducting tube represents pore space occupied by the non-flowing phase j in the present experiments and,

accordingly, $1 - N_c/N = S_j$. The relative permeability of the flowing phase is thus given by

$$k_{ri} = \frac{k_p(1-S_j)\phi}{k_p\phi} = 1 - S_j = S_i. \tag{7}$$

Figure 5 presents end-point relative permeabilities, $k_{rw}(S_{or})$ and $k_{ro}(S_{oi})$, normalised by the respective saturations as a function of θ_w and the corresponding contact angle measured through the oil phase θ_o ($\equiv 180° - \theta_w$), respectively. From Eq. (7), $k_{ri}/S_i > 1$ indicates permeability enhancement correcting for the impact of reduced cross-sectional area available to flow due to the presence of the residual phase. k_{ri}/S_i increases with increasing θ_i for both phases, i.e., relative permeability increases as the grains become increasingly non-wetting towards the flowing phase. $k_{ro}(S_{oi})/S_{oi}$ does not differ between the two U_w considered, and $k_{ro}(S_{oi})/S_{oi} > 1$ for $\theta_o \geq 45°$ at both flow rates, indicating that enhanced permeability can occur even when the flowing phase is the wetting phase. In contrast, $k_{rw}(S_{or})/(1-S_{or}) > 1$ only at $\theta_w > 130°$, i.e., when brine is the non-wetting phase.
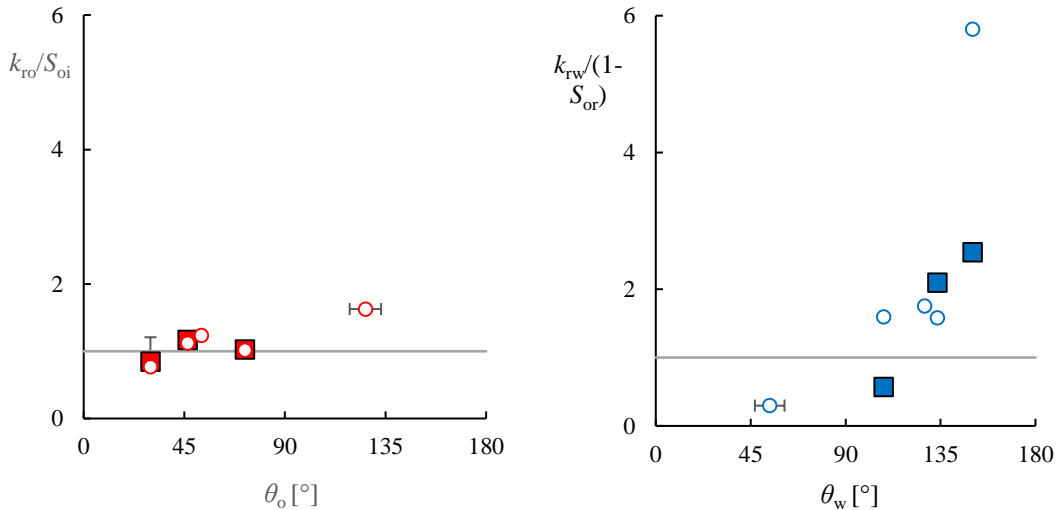

Figure 5. End-point relative permeability normalised by the saturation of the flowing phase as a function of the contact angle θ_i measured through the flowing phase i. $U_w = 30$ μm/s (solid squares) and $U_w = 1.5$ μm/s (open circles). Horizontal bars are standard errors of the mean. Vertical bar on (θ_o, k_{ro}/S_{oi}) = (30°, 0.85) depicts the disagreement between $k_{ro}(S_{oi})$ calculated using Eq. (2) and that in the best-fit Brooks-Corey function.

CONCLUSIONS

We present $k_r(S_w)$ curves for in Indiana limestone under different mixed wettability conditions. In addition, we compare end point brine and oil relative permeabilities to measurements completed at lower capillary numbers [14]. Relative oil and brine permeabilities decrease and increase, respectively, as θ_w increases, i.e., as the grains become increasingly non-wetting to the

flowing phase. Greater-than-one end-point relative permeability was observed at $\theta_w < 90°$ for oil and at $\theta_w > 130°$ for brine. In contrast to recent literature that associate enhanced permeability to the flow of non-wetting fluid against a solid surface, we observe enhanced permeability even when the flowing fluid was the wetting phase.

ACKNOWLEDGEMENTS

REFERENCES

1. Jerauld, G. (1997) Prudhoe bay gas/oil relative permeability, *SPE Res. Eng.*, 12(1), 66–73, doi:10.2118/35718-PA.
2. Al-Gharbi, M. S., X. Jing, M. Kraaijveld, J. B. Hognestad & P. O. Udeh (2007) SCAL relative permeability measurements and analyses for a cluster of fields in South Oman, in *Proc.,* International Petroleum Technology Conference, 4-6 Dec., International Petroleum Technology Conference, Dubai, UAE.
3. Honarpour, M., L. F. Koederitz & A. H. Harvey (1982) Empirical equations for estimating two-phase relative permeability in consolidated rock, *J. Petrol. Technol.*, 34(12), 2905–2908, doi:10.2118/9966-PA.
4. Burdine, N. T. (1953) Relative permeability calculations from pore size distribution data, *J. Petrol. Technol.*, 5(3), 71–78, doi:10.2118/225-G.
5. Lomeland, F., E. Ebeltoft & W. H. Thomas (2005) A new versatile relative permeability correlation, in *Proc.,* International Symposium of the Society of Core Analysts, 21-25 Aug., SCA2005-32, Toronto, Canada.
6. Valvatne, P. H. & M. J. Blunt (2004) Predictive pore-scale modeling of two-phase flow in mixed-wet media, *Water Resour. Res.*, 40(7), W07,406, doi:10.1029/2003WR002627.
7. Joekar-Niasar, V., S. M. Hassanizadeh & A. Leijnse (2008) Insights into the relationships among capillary pressure, saturation, interfacial area and relative

permeability using pore-network modeling, *Transp. Porous Med.*, 74(2), 201–219, doi:10.1007/s11242- 007-9191-7.

8. Ryazanov, A. V., M. I. J. van Dijke & K. S. Sorbie (2010) Pore-network prediction of residual oil saturation based on oil layer drainage in mixed-wet systems, in *Proc.,* SPE Improved Oil Recovery Symposium, 24-28 April, Society of Petroleum Engineers, Oklahoma, USA, doi:10.2118/129919-MS.

9. Berg, S., A. W. Cense, J. P. Hofman & R. M. M. Smits (2008) Two-phase flow in porous media with slip boundary condition, *Transport Porous Med.*, 74(3), 275–292.

10. Nowak, T. & R. Krueger (1951) The effect of mud filtrates and mud particles upon the permeabilities of cores, in *Drilling and Production Practice*, American Petroleum Institute.

11. Morrow, N. R., P. J. Cram & F. McCaffery (1973) Displacement studies in dolomite with wettability control by octanoic acid, *Soc. Petrol. Eng. J.*, 13(4), 221–232, doi: 10.2118/3993-PA.

12. Tanino, Y. & M. J. Blunt (2012) Capillary trapping in sandstones and carbonates: Dependence on pore structure, *Water Resour. Res.*, 48(8), doi:10.1029/2011WR011712.

13. Christensen, M. & Y. Tanino (2017) Waterflood oil recovery from mixed-wet limestone: dependence on contact angle, *Energy Fuel*, 31(2), 1529–1535, doi: 10.1021/acs.energyfuels.6b03249.

14. Christensen, M. & Y. Tanino (2017) Enhanced permeability due to apparent oil/brine slippage in limestone and its dependence on wettability, *Geophys. Res. Lett.*, doi: 10.1002/2017GL073603

15. Romanello, L. (2015) Impact of wettability on relative permeability, MSc thesis, University of Aberdeen.

16. Tanino, Y. & M. J. Blunt (2013) Laboratory investigation of capillary trapping under mixed-wet conditions, *Water Resour. Res.*, 49(7), 4311–4319, doi:10.1002/wrcr.20344.

17. Corey, A. T. (1954) The interrelation between gas and oil relative permeabilities, *Producers Monthly*, 19(1), 38–41.

18. Tie, H. & Morrow, N. R. (2005) Low-flood-rate residual saturations in carbonate rocks. *Proc*., International Petroleum Technology Conference, 21-23 Nov., Doha, Qatar.

19. Tanino, Y., B. Akamairo, M. Christensen & S. A. Bowden (2015) Impact of displacement rate on waterflood oil recovery under mixed-wet conditions, in *Proc.,* International Symposium of the Society of Core Analysts, SCA-A031, St. John's Newfoundland and Labrador, Canada.

20. Owens, W. W. & D. L. Archer (1971) The effect of rock wettability on oil-water relative permeability relationships, *J. Petrol. Technol.*, 23(7), 873–878, doi:10.2118/3034-PA.

21. Dullien, F. A. L. (1991) *Porous Media. Fluid Transport and Pore Structure*, 2nd ed., Academic San Diego, Calif.